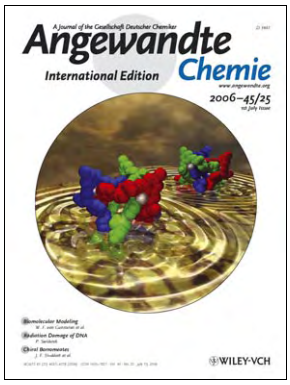
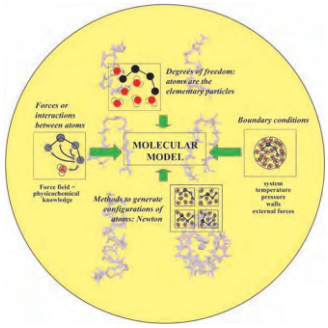
Cover Picture

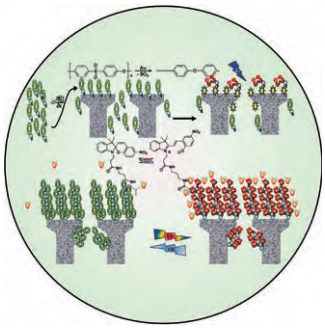


Cari D. Pentecost, Andrea J. Peters, Kelly S. Chichak, Gareth W. V. Cave, Stuart J. Cantrill, and J. Fraser Stoddart*

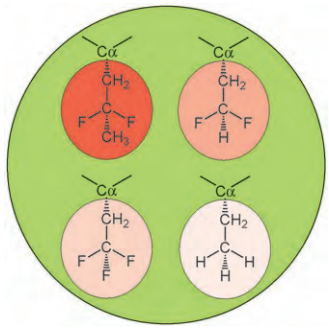
Chirality is transferred from 12 stereogenic centers, all of the same chirality, to the six templating zinc(II) ions in each enantiomer of an optically active Borromeate. Recognizing that the three-component Borromean link is topologically achiral, J. F. Stoddart et al. describe in their Communication on page 4099 ff. the dynamic stereospecific synthesis of both all-*R* and all-*S* enantiomers of the Borromeate and report the X-ray crystal structure of the all-*R* enantiomer.



Biomolecular Modeling
In their Review on page 4064 ff. W. F. van Gunsteren et al. introduce the basis for computational methods that describe the conformational dynamics in oligopeptides and related biomolecules.



Graft Polymerization and Switching
An optically reversible switching membrane surface is developed by G. Belfort and co-workers as described in their Communication on page 4094 ff. They combine their UV grafting process with the photoresponsive properties of spiropyran molecules.



Protein Modifications
B. Koksch et al. study in their Communication on page 4198 ff. the influence of fluoro substituents in the amino acid side chains on the interactions of a native polypeptide. The fluorination of alkyl groups has electrostatic and steric consequences for the stability of hydrophobic protein interactions.

Contents

VIP *The following Communications have been judged by at least two referees to be "very important papers" and will be published online at www.angewandte.org soon:*

*A. Narayanaswamy, H. Xu, N. Pradhan, X. Peng**
Single-Crystal Nanoflowers with Different Chemical Compositions and Physical Properties Grown by Limited Ligand Protection

J. L. Alonso, E. Cocinero, A. Lesarri, M. E. Sanz, J. López*
The Glycine–Water Complex

*A. Tao, P. Sinsermsuksakul, P. Yang**
Polyhedral Silver Nanocrystals with Distinct Scattering Signatures

J. van Bokhoven, C. Louis, J. Miller, M. Tromp, O. Safonova, P. Glatzel*
Activation of Oxygen on Gold–Alumina Catalysts: In situ High-Energy Resolution Fluorescence and Time-Resolved X-ray Spectroscopy

M. Brynda, R. Herber, P. Hitchcock, M. Lappert,* I. Nowik, P. Power,* A. Protchenko, A. Ruzicka, J. Steiner*
Higher Nuclearity Group 14 Metalloid Clusters: $[Sn_9\{Sn(NRR')\}_6]$ (R = 2,6-*i*$Pr_2C_6H_3$; R′ = $SiMe_3$ or $SiMe_2Ph$)

*O. Guillén-Villafuerte, G. García, B. Anula, E. Pastor, M. Blanco, M. A López-Quintela, A. Hernández-Creus, G. Planes**
Assembly of Subnanometric 2D Pt Nanoislands in Parallel Rows on Au(111) by Self-Assembly of Pt Clusters

News

Biochemistry:
R. R. Breaker honored ——— **4052**

Organic Chemistry:
D. W. C. MacMillan awarded ——— **4052**

Biochemistry:
Prize to J. K. Barton ——— **4052**

Books

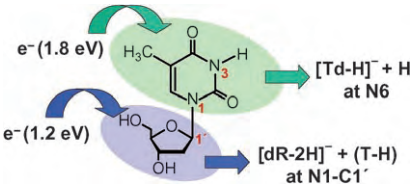
Master Mind — Daniel Charles — *reviewed by B. Friedrich* ——— **4053**

Highlights

Radiation Damage

P. Swiderek* ——— **4056 – 4059**

Fundamental Processes in Radiation Damage of DNA



Ionizing radiation (UV, X-rays, etc.) induces DNA damage not merely from the primary impact of high-energy quanta but, to a large extent, from secondary particles. Among these, low-energy electrons (see scheme) play an important role. Gas-phase studies that use crossed-molecular and monochromatic electron beams have provided new fundamental insight into the mechanism of radiation damage in DNA.

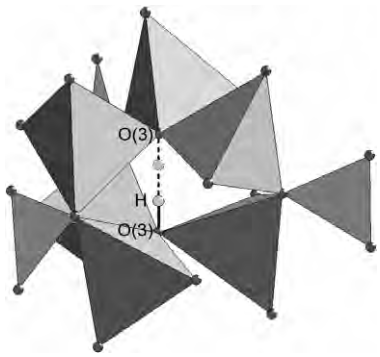
Correspondence

Borates

T. Delahaye, F. Boucher, M. Paris, O. Joubert, M. Caldes, Y. Piffard* ——— **4060 – 4062**

Some Experimental Evidence that $Zn_4O(BO_3)_2$ is $Zn_6O(OH)(BO_3)_3$

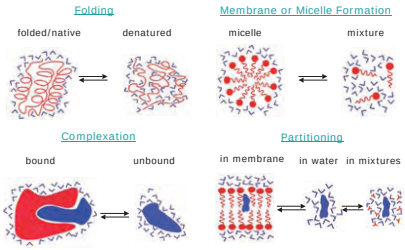
A combination of techniques show that the so-called zincoborate "$Zn_4O(BO_3)_2$" is in fact a zinc oxyhydroxyborate. The presence of hydrogen in the structure explains the constriction of the O(3)···O(3) distance through it being straddled by an O–H···O bridge and rules out the hypothesis of oxygen vacancies in the environment of boron.



InterScience
© 2006 Wiley-VCH Verlag GmbH & Co. KGaA, Weinheim

Reviews

Present day biomolecular modeling is limited in its application by four main problems: 1) the force-field problem, 2) the search problem, 3) the ensemble problem, and 4) the experimental problem. These four problems are discussed in this Review by using practical examples, and perspectives are outlined for overcoming the limitations of biomolecular modeling.

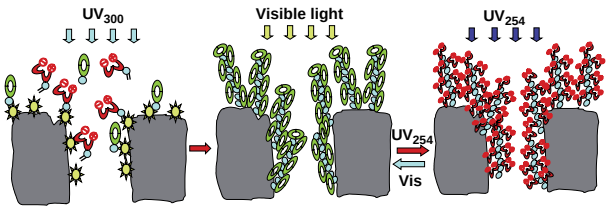


Molecular Dynamics

W. F. van Gunsteren,* D. Bakowies, R. Baron, I. Chandrasekhar, M. Christen, X. Daura, P. Gee, D. P. Geerke, A. Glättli, P. H. Hünenberger, M. A. Kastenholz, C. Oostenbrink, M. Schenk, D. Trzesniak, N. F. A. van der Vegt, H. B. Yu _____ **4064 – 4092**

Biomolecular Modeling: Goals, Problems, Perspectives

Communications



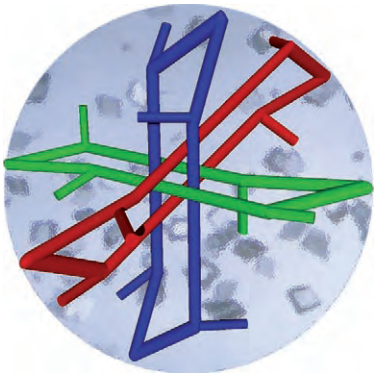
Lighting the way: Through the combination of a UV-grafting process with the photoresponsive properties of spiropyran molecules, an optically reversible switching membrane surface was developed. This process can be used in preference to inducing physical movement of long-chain SAMs toward an electrode and as a result improve many industrial opportunities including those dependent on surface wettability and molecular adhesion.

Membranes

A. Nayak, H. Liu, G. Belfort* **4094 – 4098**

An Optically Reversible Switching Membrane Surface

The fellowship of the rings: Circular dichroism measurements reveal that chirality is transferred from 12 stereogenic centers to 6 octahedral zinc(II) centers (see picture) in two enantiomeric pairs of chiral Borromeates, one of which has been found to be wholly asymmetric in the solid state by X-ray crystallography.



Dynamic Chemistry

C. D. Pentecost, A. J. Peters, K. S. Chichak, G. W. V. Cave, S. J. Cantrill, J. F. Stoddart* _____ **4099 – 4104**

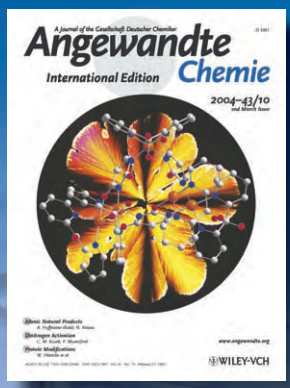
Chiral Borromeates

For the USA and Canada:
ANGEWANDTE CHEMIE International Edition (ISSN 1433-7851) is published weekly by Wiley-VCH PO Box 191161, D 69451 Weinheim, Germany. Air freight and mailing in the USA by Publications Expediting Inc. 200 Meacham Ave., Elmont, NY 11003. Periodicals postage paid at Jamaica NY 11431. US POSTMASTER: send address changes to *Angewandte Chemie*, Wiley-VCH, 111 River Street, Hoboken, NJ 07030. Annual subscription price for institutions: US$ 5685/5168 (valid for print and electronic / print or electronic delivery); for individuals who are personal members of a national chemical society prices are available on request. Postage and handling charges included. All prices are subject to local VAT/sales tax.

© 2006 Wiley-VCH Verlag GmbH & Co. KGaA, Weinheim

The best in chemistry –

for more than a hundred years



A Journal of the Gesellschaft Deutscher Chemiker

Angewandte
International Edition **Chemie**

www.angewandte.org

1888: ***The beginning of a success story***

Constant Innovations

1962: *First issue of the International Edition*
1976: *Graphical abstracts*
1979: *Cover pictures*
1988: *Centenary of Angewandte*
1989: *Routine use of color*
1991: *New section: Highlights*
1992: *Computerized editorial tracking system*
1995: *Internet service for readers*
1998: *Regular press service; full-text online*
2000: *New section: Essays; EarlyView: Communications available online ahead of the printed version*
2001: *New section: Minireviews*
2002: *Online submission of manuscripts*
2003: *Weekly publication; new section: News; new layout*
2004: *Backfiles (1962-1997); ManuscriptXpress: Online system for authors and referees*



Angewandte's advisors...

Roald Hoffmann
Cornell University
(Photo: Lois Anshus)

» As an applied theoretical chemist, I love it that the best chemical journal in the world has „applied" in its title. It's history, I know. But there is also the implication in this adjective that these sterling accounts of the new, these just-in-time reviews, these incisive essays that ***Angewandte Chemie*** *contains – that they all are of true utility, and are really used, by the finest chemists of our time. «*

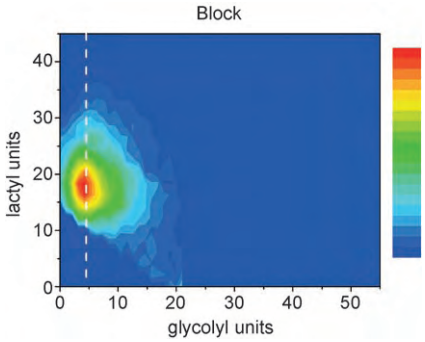
Angewandte Chemie International Edition *is a journal of the German Chemical Society (GDCh)*

GDCh

WILEY InterScience® DISCOVER SOMETHING GREAT

WILEY-VCH

1195/404_gu

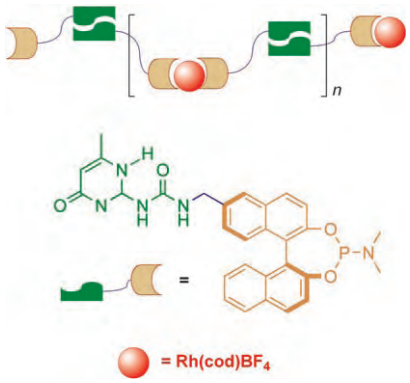


Software developed in house in combination with a recently developed method of MALDI-TOF MS enable not only the elucidation of individual chain structures of poly(lactide-*co*-glycolide), a polymer used extensively in the medical sector, but a full characterization of this copolymer including even its chemical composition and topology (random, gradient, block (see figure), or alternating).

Polymer Chemistry

S. Huijser, B. B. P. Staal, J. Huang, R. Duchateau,* C. E. Koning **4104 – 4108**

Chemical Composition and Topology of Poly(lactide-*co*-glycolide) Revealed by Pushing MALDI-TOF MS to Its Limit



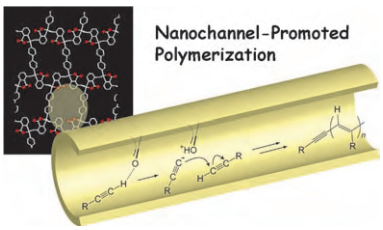
Noncovalent interactions are used to generate a polymeric supramolecular chiral catalyst (see picture). This heterogeneous catalyst, which is based on Feringa's MonoPhos/Rh^{I} system, is formed by orthogonal self-assembly of recognition motifs through hydrogen bonding and ligand-to-metal coordination interactions. It shows excellent asymmetric induction and reusability in the catalysis of the asymmetric hydrogenation of dehydro-α-amino acid and enamide derivatives.

Heterogeneous Catalysis

L. Shi, X. Wang, C. A. Sandoval, M. Li, Q. Qi, Z. Li, K. Ding* **4108 – 4112**

Engineering a Polymeric Chiral Catalyst by Using Hydrogen Bonding and Coordination Interactions

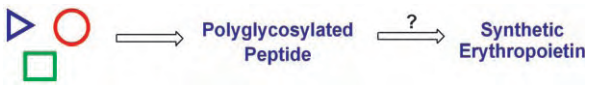
Get into the groove: Porous coordination polymers with basic interaction sites catalyze the fast and stereoselective polymerization of acetylene derivatives. The reactions take place in the one-dimensional nanochannels of the coordination polymer (see picture).



Polymerization

T. Uemura, R. Kitaura, Y. Ohta, M. Nagaoka, S. Kitagawa* **4112 – 4116**

Nanochannel-Promoted Polymerization of Substituted Acetylenes in Porous Coordination Polymers



The missing link: Reiterative ligations based on non-cysteine and cysteine-based acyl acceptors have been used to prepare synthetic polypeptides and proteins with multiple sites of glycosylation. Highly complex positionally defined glycopolypeptides corresponding to single glycoforms can be formed from simple components.

Glycoproteins

B. Wu, J. Chen, J. D. Warren, G. Chen, Z. Hua, S. J. Danishefsky* **4116 – 4125**

Building Complex Glycopeptides: Development of a Cysteine-Free Native Chemical Ligation Protocol

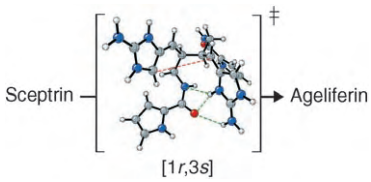
© 2006 Wiley-VCH Verlag GmbH & Co. KGaA, Weinheim

Contents

Alkaloids

B. H. Northrop, D. P. O'Malley, A. L. Zografos, P. S. Baran,* K. N. Houk* ——— **4126 – 4130**

Mechanism of the Vinylcyclobutane Rearrangement of Sceptrin to Ageliferin and Nagelamide E



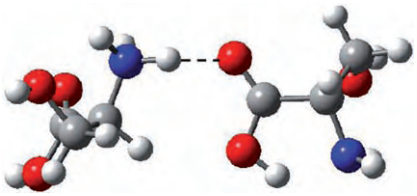
Naturally radical: The microwave-induced rearrangement of sceptrin to natural products ageliferin and nagelamide E results in approximately the same ratio as they are isolated from natural sources. Computational investigations show that the vinylcyclobutane–cyclohexene rearrangement occurs via diradical intermediates and support the involvement of this rearrangement in the biosynthesis of the natural products.

Zwitterions

X. Kong, I.-A. Tsai, S. Sabu, C.-C. Han, Y. T. Lee, H.-C. Chang,* S.-Y. Tu, A. H. Kung, C.-C. Wu ——— **4130 – 4134**

Progressive Stabilization of Zwitterionic Structures in $[H(Ser)_{2-8}]^+$ Studied by Infrared Photodissociation Spectroscopy

Does $(Ser)_2$ have a neutral structure? How does the zwitterion evolve with an increasing cluster size of serine (Ser)? Infrared spectroscopic and mass-spectrometric analysis of $[H(Ser)_n]^+$ ($n = 2$–8) shows progressive stabilization of the zwitterion with increasing cluster size, and the results of ab initio calculations based on density functional theory of $[H(Ser)_2]^+$ are also given (picture: a neutral structure; red O, blue N, gray C, white H).

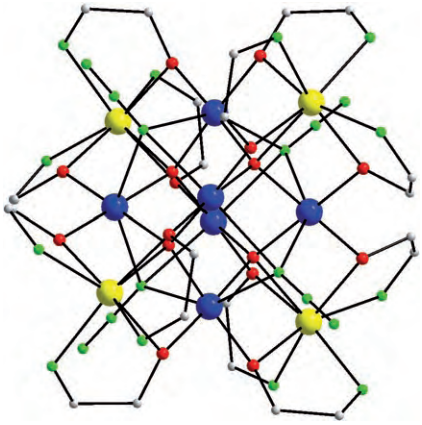


Magnetic Clusters

T. C. Stamatatos, K. A. Abboud, W. Wernsdorfer, G. Christou* ——— **4134 – 4137**

High-Nuclearity, High-Symmetry, High-Spin Molecules: A Mixed-Valence Mn_{10} Cage Possessing Rare T symmetry and an $S = 22$ Ground State

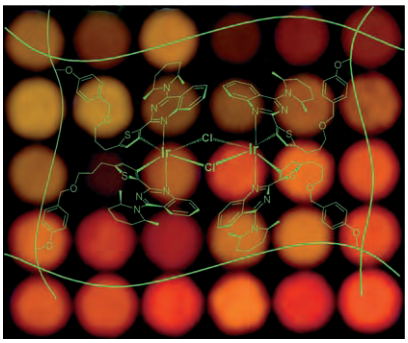
Taking the high road: The unification of azide and hmp^- (hmpH = 2-(hydroxymethyl)pyridine) ligands has provided a route to two salts of a new Mn_{10} cation with an aesthetically pleasing, high-symmetry structure. The cation (see excerpt of structure; Mn^{II} yellow, Mn^{III} blue, O red, N green, C gray) is completely ferromagnetically coupled and possesses an $S = 22$ ground state, one of the highest values ever reported.



Iridium Complexes

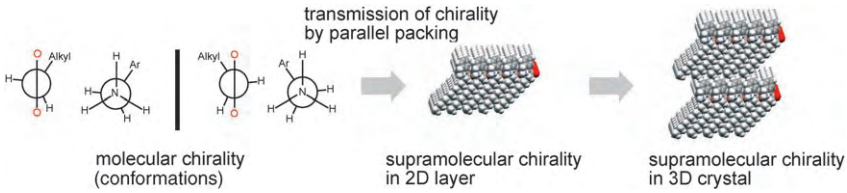
N.-M. Hsu, W.-R. Li* ——— **4138 – 4142**

Accelerated Discovery of Red-Phosphorescent Emitters through Combinatorial Organometallic Synthesis and Screening



Seeing red dots: A parallel solid-phase synthetic protocol was developed in the search for red-phosphorescent iridium complexes. Direct screening of resin-bound chloro-bridged dimers and leads was performed and validated (see picture), and two hits were identified. Their electroluminescent devices exhibited very high external quantum efficiencies.

© 2006 Wiley-VCH Verlag GmbH & Co. KGaA, Weinheim

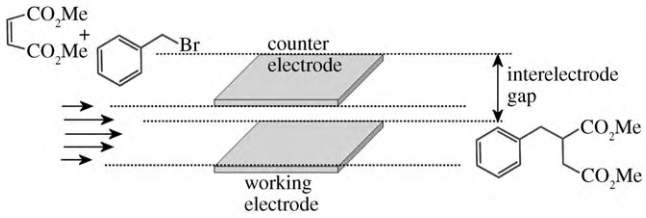


Something out of nothing: Chiral layered crystals are obtained from achiral 4-methylbenzylammonium myristate and pentadecanoate. The molecular chirality within a single molecule in these systems arises from the fixation of the conformation. It then spreads over the 2D layers and finally over the 3D crystal to generate supramolecular chirality by parallel assembly (see picture).

Chiral Assemblies

A. Tanaka, K. Inoue, I. Hisaki, N. Tohnai, M. Miyata,* A. Matsumoto **4142 – 4145**

Supramolecular Chirality in Layered Crystals of Achiral Ammonium Salts and Fatty Acids: A Hierarchical Interpretation

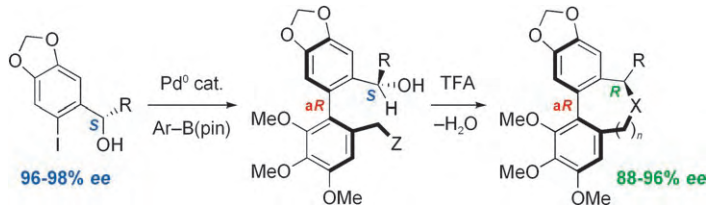


Currently coupled: A clean microreactor-based electrosyntheses in the absence of supporting electrolyte is demonstrated and shown to feature very simple cell geometries. As exemplified for the coupling reaction of various olefins with benzyl bromides, the height of the microfluidic cell and the flow rate are crucial for the minimization of unwanted side products and optimization of yields (see picture).

Microreactors

P. He, P. Watts, F. Marken, S. J. Haswell* **4146 – 4149**

Self-Supported and Clean One-Step Cathodic Coupling of Activated Olefins with Benzyl Bromide Derivatives in a Micro Flow Reactor



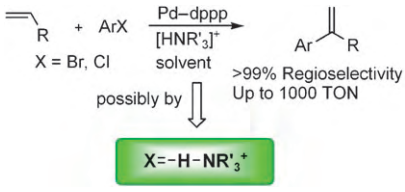
Return to sender: A biaryl configuration that is controlled by a benzylic stereocenter in an atropo-selective Suzuki coupling in turn controls the stereocenter configuration in an S_N1-type dehydrative cyclization performed at low temperature. Promising antimicrotubule biaryls of high optical purity are obtained in this manner. TFA = trifluoroacetic acid, pin = pinacolato.

Asymmetric Synthesis

A. Joncour, A. Décor, S. Thoret, A. Chiaroni, O. Baudoin* **4149 – 4152**

Biaryl Axis as a Stereochemical Relay for the Enantioselective Synthesis of Antimicrotubule Agents

No salt please: Halide scavengers AgOTf and TlOAc are not required for the Heck coupling of electron-rich olefins with aryl bromides and chlorides. Using ammonium additives, these reactions can be carried out in either an imidazolium ionic liquid or a common molecular solvent, thus furnishing 1,1′-disubstituted olefins in high yields with excellent regioselectivities.



Homogeneous Catalysis

J. Mo, J. Xiao* **4152 – 4157**

The Heck Reaction of Electron-Rich Olefins with Regiocontrol by Hydrogen-Bond Donors

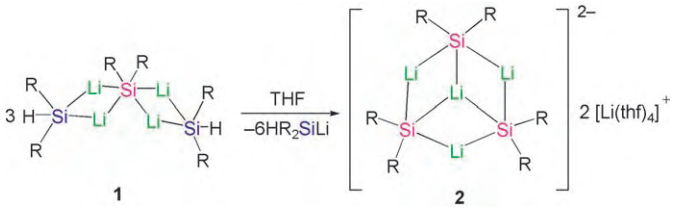
© 2006 Wiley-VCH Verlag GmbH & Co. KGaA, Weinheim

Contents

Silyllithium Compounds

D. Bravo-Zhivotovskii,* I. Ruderfer, S. Melamed, M. Botoshansky, A. Schmidt, Y. Apeloig* _____ **4157 – 4159**

$[\{(t\mathrm{Bu_2Me})_2\mathrm{Si}\}_3\mathrm{Li_4}]^{2-}$: An Aggregated Dianion of a 1,1-Dilithiosilane with a Unique Structural Motif



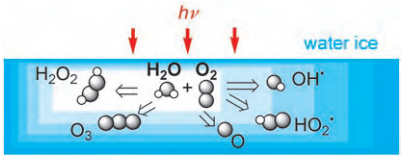
An anionic dilithium compound: The dianion $[(R_2Si)_3Li_4]^{2-}$ ($R = t\mathrm{Bu_2MeSi}$) as salt **2** was synthesized as the first of its kind by dissolving **1** in THF. The structure of **2** was solved by X-ray crystallography and studied by solid-state and solution NMR spectroscopy. Compound **2** reacts as a dilithiosilane.

Analytical Methods

S. Lacombe,* F. Bournel, C. Laffon, P. Parent _____ **4159 – 4163**

Radical Photochemistry in Oxygen-Loaded Ices

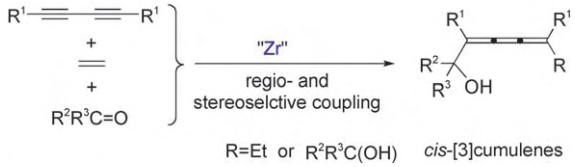
Ice to see you all: The photoproducts formed by irradiation of water and molecular oxygen ices are strongly dependent on the chemical composition of the medium. The observation of all the transient species (radicals and molecules, see picture) simultaneously will have applications in different fields such as astrochemistry and radiobiology.



Cumulene Synthesis

Y.-H. Liu,* H.-J. Gao, S.-L. Zhou _____ **4163 – 4167**

Highly Stereoselective Synthesis of TMS-, Alkyl-, or Aryl-Substituted *cis*-[3]Cumulenols via α-Alkynylated Zirconacyclopentenes

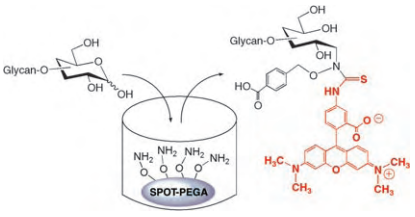


Double bonds come in threes: A highly stereoselective and potentially general method for the synthesis of tetrasubstituted *cis*-[3]cumulenes through zirconium-mediated coupling of 1,3-butadiynes with aldehydes or ketones is described (see scheme). Remarkably, the reaction occurs with completely different chemoselectivity to that usually observed with alkyl- or aryl-substituted zirconacyclopentenes.

Oligosaccharide Analysis

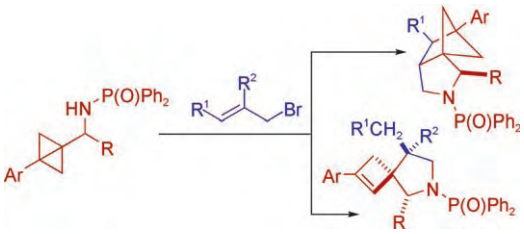
A. Lohse, R. Martins, M. R. Jørgensen, O. Hindsgaul* _____ **4167 – 4172**

Solid-Phase Oligosaccharide Tagging (SPOT): Validation on Glycolipid-Derived Structures



SPOT check: A simple technique for labeling oligosaccharides consists of capturing the sugars on beads functionalized with hydroxylamine groups bearing cleavable linkers. After sequential pipetting in and out of reagents, tagged sugars are released into solution (see picture; PEGA = polyethylene glycol–polyacrylamide resin) for analysis by electrophoresis or mass spectrometry.

© 2006 Wiley-VCH Verlag GmbH & Co. KGaA, Weinheim



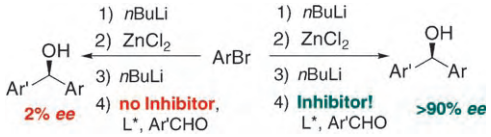
Direct access: Phase-transfer *N*-allylation and *N*-propargylation of (bicyclo-[1.1.0]butylmethyl)amines initiate diastereoselective pericyclic cascade reactions that culminate in novel spirocyclic and tricyclic pyrrolidine heterocycles through formal ene or [2+2] pathways.

Cycloaddition Reactions

P. Wipf,* M. A. A. Walczak _ **4172 – 4175**

Pericyclic Cascade Reactions of (Bicyclo[1.1.0]butylmethyl)amines

---



Stop that achiral catalyst! Chiral Lewis acid catalyzed aryl additions to aldehydes that originate from aryl halides generate products with very low *ee* values (see scheme, left), because the achiral metal halide by-products are much more efficient catalysts than those derived from chiral amino alcohols. A LiCl-selective inhibitor is introduced that enables a highly enantioselective one-pot arylation of aldehydes that begins with aryl bromides (right).

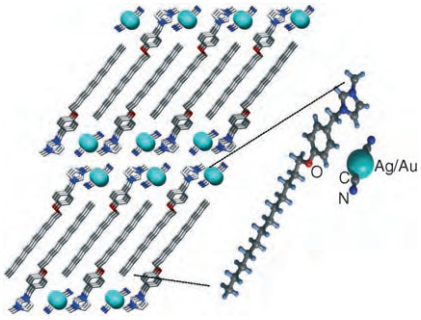
Asymmetric Catalysis

J. G. Kim, P. J. Walsh* _____ **4175 – 4178**

From Aryl Bromides to Enantioenriched Benzylic Alcohols in a Single Flask: Catalytic Asymmetric Arylation of Aldehydes

---

Precious particles: Dicyanoargentate(I) and dicyanoaurate(I) salts of an imidazolium cation form both crystalline (see structure and enlargement of the cation and anion) and smectic-A phases. Electrodeposition from the ionic liquid crystals provides a novel route to silver particles and gold nanoparticles.

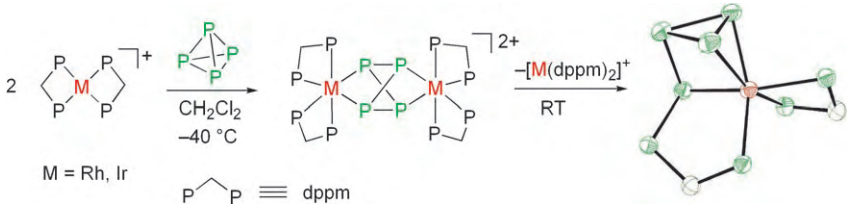


Liquid Crystals

W. Dobbs, J.-M. Suisse, L. Douce,* R. Welter _____ **4179 – 4182**

Electrodeposition of Silver Particles and Gold Nanoparticles from Ionic Liquid-Crystal Precursors

---



P's in a pod: White phosphorus reacts with $[M(dppm)_2]OTf$ (M = Rh, Ir; dppm = $PPh_2CH_2PPh_2$) to give $[M(dppm)(Ph_2PCH_2PPh_2PPPP)]OTf$ whereby a trihapto "P_5" ligand is assembled through P–P bond formation between one dppm PPh_2 group and an activated P_4 molecule (see scheme; P green, M red, C white, phenyl groups omitted). A bimetallic reaction pathway leading to the final product is proposed, as based on in situ ^{31}P NMR studies.

P_4 Activation

D. Yakhvarov,* P. Barbaro, L. Gonsalvi, S. Mañas Carpio, S. Midollini,* A. Orlandini, M. Peruzzini,* O. Sinyashin, F. Zanobini _____ **4182 – 4185**

A Snapshot of P_4 Tetrahedron Opening: Rh- and Ir-Mediated Activation of White Phosphorus

© 2006 Wiley-VCH Verlag GmbH & Co. KGaA, Weinheim

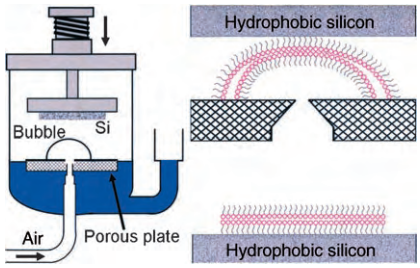
Contents

Surfaces

J.-J. Benattar,* M. Nedyalkov, F. K. Lee, O. K. C. Tsui ——— **4186 – 4188**

Adhesion of a Free-Standing Newton Black Film onto a Solid Substrate

Film transfer: A new method is presented to transfer free-standing Newton black films of surfactant onto a solid substrate (see picture). X-ray reflectivity and atomic force microscopy reveal that the deposited films have a high degree of molecular organization and good adhesion.

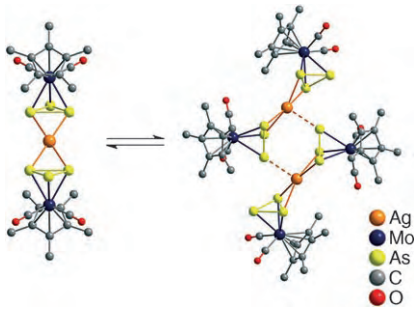


Arsenic Ligands

L. J. Gregoriades, H. Krauss, J. Wachter, A. V. Virovets, M. Sierka, M. Scheer* ——— **4189 – 4192**

The Potential of a *cyclo*-As_3-Ligand Complex in Supramolecular Chemistry

As_3 makes the connection: $[Cp^*Mo(CO)_2(\eta^3\text{-}As_3)]$ reacts with $Ag[Al\{OC(CF_3)_3\}_4]$ to yield a novel dimeric complex featuring the *cyclo*-As_3 ligand in an unusual face-bridging coordination mode. Analytical data and DFT calculations support the existence of a monomer–dimer equilibrium in solution (see scheme). $[Cp^*Mo(CO)_2(\eta^3\text{-}As_3)]$ also reacts with CuX (X = Cl, Br, I) to yield insoluble dimers consisting of planar Cu_2X_2 moieties.

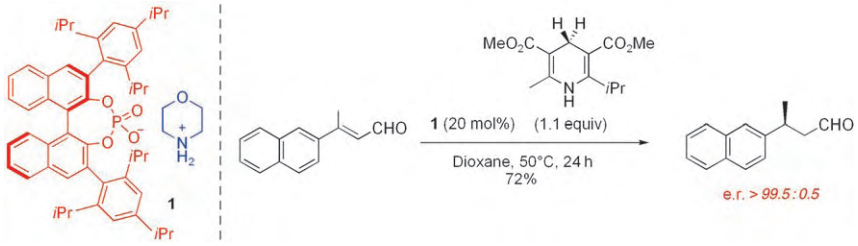


Organocatalysis

S. Mayer, B. List* ——— **4193 – 4195**

Asymmetric Counteranion-Directed Catalysis

Exceedingly high enantioselectivity in a catalytic reaction can be realized even when the chirality resides only in the counteranion of the catalyst. A salt (**1**) composed of an achiral ammonium cation and a chiral phosphate counteranion catalyzes asymmetric transfer hydrogenations of aromatic and aliphatic α,β-unsaturated aldehydes with a Hantzsch ester in excellent enantioselectivities (see scheme).

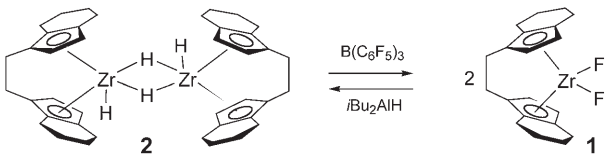


C–F Activation

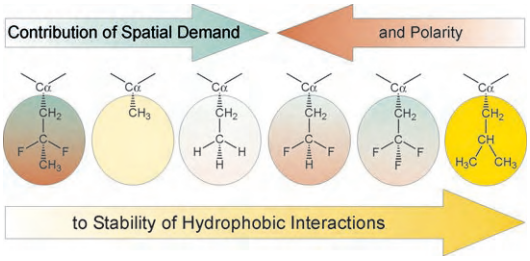
P. Arndt,* U. Jäger-Fiedler, M. Klahn, W. Baumann, A. Spannenberg, V. V. Burlakov, U. Rosenthal* **4195 – 4198**

Formation of Zirconocene Fluoro Complexes: No Deactivation in the Polymerization of Olefins by the Contact-Ion-Pair Catalysts $[Cp'_2ZrR]^+[RB(C_6F_5)_3]^-$

Not a catalyst killer: In the reaction of **2** with $B(C_6F_5)_3$, a nucleophilic aromatic substitution with C–F bond cleavage leads to the unexpected difluoride **1**. Although the formation of Zr–F species during olefin polymerization by $[Cp'_2ZrR]^+[RB(C_6F_5)_3]^-$ (Cp′ = substituted or unsubstituted η^5-cyclopentadienyl; R = Me, H) catalysts is often described as a deactivation, the catalyst precursor **2** can be regenerated from **1** through treatment with iBu_2AlH.



© 2006 Wiley-VCH Verlag GmbH & Co. KGaA, Weinheim



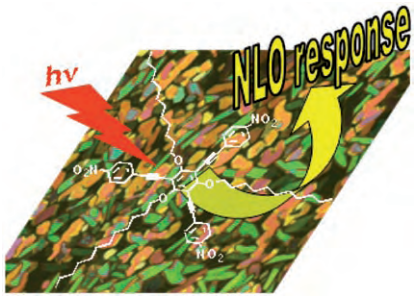
Give and take: The influence of fluoro substitution of amino acid side chains on their interaction profile in a native polypeptide environment was studied systematically. The fluorination of alkyl groups has opposing electrostatic and steric consequences for the stability of hydrophobic protein cores.

Protein Modification

C. Jäckel, M. Salwiczek, B. Koksch* ——— **4198 – 4203**

Fluorine in a Native Protein Environment—How the Spatial Demand and Polarity of Fluoroalkyl Groups Affect Protein Folding

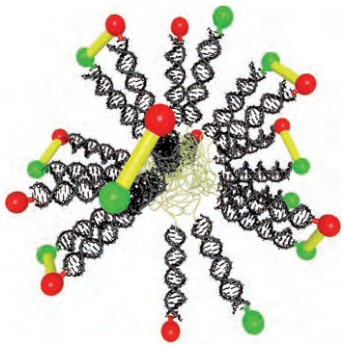
Octopolar tris[(phenyl)ethynyl]benzenes with high second-order nonlinear optical (NLO) activity form discotic liquid-crystalline mesophases whose properties depend on the length of the alkoxy chains. The molecules self-organize in a non-centrosymmetric fashion in the bulk phase which enables the construction of a simple, efficient, NLO device (see picture).



Functional Materials

G. Hennrich,* A. Omenat, I. Asselberghs, S. Foerier, K. Clays, T. Verbiest,* J. L. Serrano* ——— **4203 – 4206**

Liquid Crystals from C_3-Symmetric Mesogens for Second-Order Nonlinear Optics



Blocked up: Amphiphilic DNA-block copolymers were prepared in a fully automated single process by using a DNA synthesizer. These materials formed micelles in aqueous solution which were applied as a scaffold for DNA-templated organic reactions (see picture, red and green balls = reactants, yellow bar = new bond). For a novel fluorogenic reaction, the DNA-templated conversions were detected by fluorescence spectroscopy.

DNA-Templated Synthesis

F. E. Alemdaroglu, K. Ding, R. Berger, A. Herrmann* ——— **4206 – 4210**

DNA-Templated Synthesis in Three Dimensions: Introducing a Micellar Scaffold for Organic Reactions

The issues for June 2006 appeared online on the following dates
Issue 21: May 10. · Issue 22: May 18. · Issue 23: May 24. · Issue 24: June 1

Sources

Product and Company Directory

You can start the entry for your company in "Sources" in any issue of *Angewandte Chemie*.

If you would like more information, please do not hesitate to contact us.

Wiley-VCH Verlag – Advertising Department
Tel.: 0 62 01 - 60 65 65
Fax: 0 62 01 - 60 65 50
E-Mail: MSchulz@wiley-vch.de

Service

Keywords ——— *4214*

Authors ——— *4215*

Angewandte's Sister Journals ——— *4212 – 4213*

Preview ——— *4217*

© 2006 Wiley-VCH Verlag GmbH & Co. KGaA, Weinheim



Awarded...

US Academy awards R. R. Breaker

Ronald R. Breaker's research group at Yale University (New Haven, CT, USA) is interested in the structure and function of natural and synthetic nucleic acids: desoxyribozyme, ribozyme, enzyme kinetics of (desoxy)ribozymes, aptamers, and allosteric ribozymes as well as riboswitches. Breaker, together with Tina M. Henkin (Ohio State University, USA), was presented the 2006 Award in Molecular Biology of the National Academy of Sciences (USA). They have established a new mode of regulation of gene expression in which metabolites regulate the activity of their cognate pathways by directly binding to mRNA. Breaker recently reported in *Angewandte Chemie* on the molecular-recognition characteristics of *S*-adenosylmethionine-binding riboswitches.[1]



R. R. Breaker

Breaker studied biology and chemistry at the University of Wisconsin in Stevens Point (USA) and completed his PhD in 1992 at Purdue University (West Lafayette, IN, USA) under the guidance of P. T. Gilham on chemical and enzymatic synthesis of nucleic acids. He then joined G. F. Joyce at Scripps Research Institute in La Jolla, CA (USA), as a postdoctoral researcher. He joined the faculty at Yale University in 1995.

D. W. C. MacMillan receives Thieme–IUPAC Prize

David W. C. MacMillan (California Institute of Technology, Pasadena, USA) was presented with the Thieme–IUPAC Prize in Synthetic Organic Chemistry at the IUPAC International Conference on Organic Synthesis in Mexico. The award is in recognition of his work on the synthesis of chiral amines from amino acids to catalyze the enantioselective cycloaddition of dienes or 1,3-dipoles to α,β-unsaturated aldehydes through reversible formation of iminium ions. This approach has been applied to catalytic asymmetric Friedel–Crafts alkylations, and his work has found broad industrial application. His most recent contribution in *Angewandte Chemie* described the importance of controlling the geometry of the iminium species in enamine catalysis.[2]



D. W. C. MacMillan

MacMillan studied at Glasgow University (UK) and completed his PhD in 1990 at the University of California in Irvine (USA) under the guidance of L. E. Overman. Following postdoctoral work with D. A. Evans at Harvard University (Cambridge, MA, USA), he joined the University of California in Berkeley as an assistant professor in 1998. Two years later, he moved to Caltech and was appointed full professor. MacMillan and his group will soon move to Princeton University (New Jersey, USA).

Gibbs Medal to J. K. Barton

Jacqueline K. Barton (California Institute of Technology, Pasadena, USA) received the Willard Gibbs Award from the American Chemical Society (ACS) Chicago Section, which recognizes exceptional individuals whose pioneering work has opened new fields of chemical research. Barton's work has made an impact on the understanding of the molecular chemistry of DNA and its relevance to the development of a variety of diseases and inherited abnormalities. She pioneered the application of transition-metal complexes as tools to probe recognition and reactions of DNA. Her most recent report in *Angewandte Chemie* discussed the ultrafast dynamics of DNA-mediated electron transfer.[3] This is the first time that a husband and wife have both received the Gibbs Medal (P. B. Dervan, 1993), and only the second time that the award has been presented to a woman (M. Curie, 1921).



J. K. Barton

Barton studied at Barnard College and completed her PhD in 1979 with S. J. Lippard at Columbia University (New York). Following postdoctoral studies at Bell Laboratories and at Yale University with R. G. Shulman, she joined Hunter College in New York as an assistant professor. In 1983 she returned to Columbia University and was appointed full professor there two years later. She has been at Caltech since 1989.

[1] J. Lim, W. C. Winkler, S. Nakamura, V. Scott, R. R. Breaker, *Angew. Chem.* **2006**, *118*, 978; *Angew. Chem. Int. Ed.* **2006**, *45*, 964.

[2] I. K. Mangion, A. B. Northrup, D. W. C. MacMillan, *Angew. Chem.* **2004**, *116*, 6890; *Angew. Chem. Int. Ed.* **2004**, *43*, 6722.

[3] M. A. O'Neill, H.-C. Becker, C. Wan, J. K. Barton, A. H. Zewail, *Angew. Chem.* **2003**, *115*, 6076; *Angew. Chem. Int. Ed.* **2003**, *42*, 5896.

DOI: 10.1002/anie.200601982

WILEY InterScience DISCOVER SOMETHING GREAT
© 2006 Wiley-VCH Verlag GmbH & Co. KGaA, Weinheim

Radiation Damage

DOI: 10.1002/anie.200600614

Fundamental Processes in Radiation Damage of DNA

*Petra Swiderek**

Keywords:
DNA damage · gas-phase reactions · ionization · low-energy electrons · reaction mechanisms

The stability and correct replication of DNA as the carrier of the genetic information is of fundamental importance to all living organisms. Yet, exposure to ionizing radiation (UV, X-rays, etc.) induces damage in DNA,[1] thus putting life and its reproduction at risk. Motivated by the wish to obtain a detailed molecular-scale understanding of radiation damage, that is, the elementary steps leading eventually to effects like genome mutagenesis or cancer, different lines of research have evolved.

Ionization of nucleic acid bases has been identified as an initiating step of radiation damage and is thus studied with high energy resolution.[2] Following ionization, migration of the positive hole (i.e. a radical cation) along the DNA strand can occur. This process is investigated in DNA that is modified by adding electron-acceptor units that serve to inject a positive charge into the chain upon photoexcitation.[3] The results give evidence that hole migration preferably takes place through charge transfer to guanine (G) units, which are the most easily oxidized among the nucleobases. In the absence of G, adenine (A) acts as the intermediate charge carrier. Oxidative damage to DNA finally occurs on a $G^{+\bullet}$ site as a concurrent process to further charge migration.[3] Another example of radiation damage that is thought to be responsible for skin cancer, is the photochemical dimerization of the nucleic bases cytosine (C) and thymine (T) along the DNA chain under the effect of UV radiation.[4]

For a complete understanding, it is important to realize that radiation damage of DNA stems not merely from the primary impact of high-energy quanta, but to a large extent from secondary particles (i.e., ions, radicals, and ballistic electrons) that are created along the ionization path.[5] Most of these products, which are created in large quantities ($\approx 10^5$/MeV) and of which electrons are the most abundant, have energies below 30 eV.[6] Therefore, an important branch of current research on radiation damage focuses on the interaction of low-energy electrons, that is, electrons with a kinetic energy below 10–20 eV, with DNA or its constituents.[5] This work has provided evidence that a wealth of dissociative reaction pathways exist already at subionization energies (Figure 1).

In principle, investigations of the effect of low-energy electrons on DNA follow two different approaches: In a kind of top-down approach, damage of the DNA itself is quantified as a function of incident-electron energy (E_0). As an important model system, thin films of supercoiled plasmid DNA deposited onto a metallic substrate have been studied.[5] The products were analyzed ex situ by electrophoresis following electron exposure under ultrahigh vacuum (UHV),[7b,8] and in situ by measuring with MS electron-stimulated desorption (ESD) of negative fragments upon exposure of the sample to the electron beam.[9]

Ion yields of fragments in ESD from plasmid DNA are important only above 6–7 eV with a maximum around 10 eV, which can be attributed to formation and decay of temporary negative ion states (resonances).[9] Electrophoresis of the exposed DNA, on the other hand, shows that single-strand breaks (SSB) and double-strand breaks (DSB) occur (Figure 2). Recent and more-sensitive experiments demonstrated that SSB even take place for E_0 values below 1 eV.[8]

One opportunity to gain more insight into electron-induced damage in DNA is to perform model studies with self-assembled monolayers (SAMs) of short DNA single and double strands on a Au surface. A recent example used a

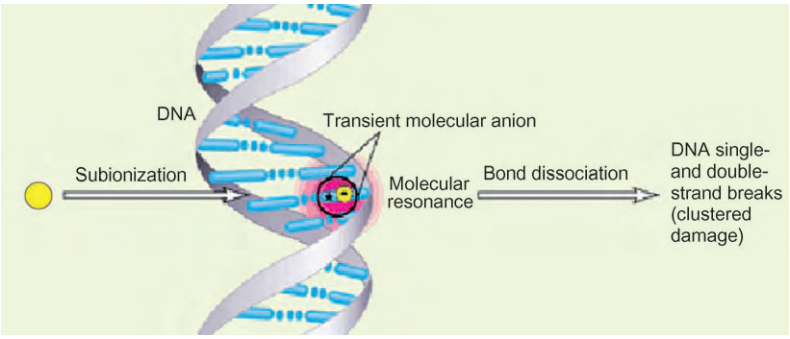


Figure 1. Interaction of low-energy electrons with DNA at energies below the ionization threshold leads to strand breaks. (Reproduced with permission from reference [7a]. Copyright *Science Magazine*, **2000**.)

[*] Prof. Dr. P. Swiderek
Universität Bremen
Fachbereich 2 (Biologie/Chemie)
Institut für Angewandte und Physikalische Chemie
Leobener Strasse, 28359 Bremen (Germany)
Fax: (+49) 421-218-4918
E-mail: swiderek@uni-bremen.de

InterScience
© 2006 Wiley-VCH Verlag GmbH & Co. KGaA, Weinheim

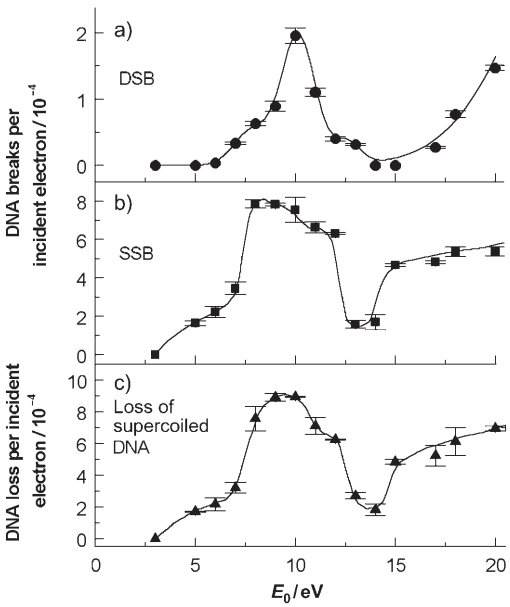


Figure 2. Quantum yields for induction of DSB (a), SSB (b), and for loss of the initial supercoiled plasmid DNA in the solid state (c) after exposure to low-energy electrons. (Reproduced with permission from reference [7b]. Copyright *Science Magazine*, **2000**.)

microarray technique in combination with fluorescent labels to quantify the amount of damage as function of electron exposure.[10] The chemical sensitivity of different nucleobases to low-energy electron impact and the effect of the base sequence on their stability were investigated by monitoring the desorption of neutral fragments from homo- and hetero-oligonucleotide–SAMs.[5] A study of photoelectron transmission through such SAMs provided further evidence that the probability of capturing electrons increases with the number of G bases and depends on their clustering in single-stranded oligomers.[11] Two-photon photoemission experiments demonstrated that, after attachment, the electron localizes either on the sugar–phosphate backbone or between the molecules in the SAM, with single-stranded DNA capturing electrons more efficiently than double-stranded DNA.[11]

An understanding of the origin of the described DNA damage requires further molecular level information of the processes following electron attachment. In a bottom-up type of approach that is complementary to the experiments described so far, low-energy electron interactions with single DNA constituents, namely the isolated bases, the sugar, and the phosphate units, are studied in detail before proceeding to investigate the same processes in successively larger units.[5] It is expected that this approach will unravel, step by step, the sequence of elementary processes following electron attachment to a specific constituent, namely migration of the excess electrons and preferred reactive pathways leading to DNA damage after final localization of the charge.

Gas-phase experiments are the natural choice to investigate the isolated DNA building blocks or units that contain only few of these building blocks. Crossed electron and molecular beams are combined with MS (Figure 3) to detect negatively charged products resulting from dissociative electron attachment (DEA). After the first demonstration that such studies on electron interaction with DNA constituents in the gas phase are feasible,[12] an increasing number of experiments on the isolated nucleobases have revealed their fragile nature. In fact, fragmentation occurs with an E_0 value as low as 0.5–1 eV,[5,13,14] that is, far below the ionization threshold. This is in accord with the results for plasmid DNA.[5,7,8] The dominant reaction path leads to the products $[M-H]^-$ (M = C, T, A, G) through loss of a single hydrogen atom.[5,13,14] In contrast to this, the sugar unit, deoxyribose, already undergoes more-severe fragmentation near 0 eV, suggesting that it represents a particularly weak part of the DNA strand.[15] Gas-phase studies of phosphate units have so far not been reported, but ESD on solid films of $NaPO_2(OH)_2$ showed desorption of OH^- around 8 eV.[5]



Figure 3. Experimental setup for measuring negatively charged products formed by low-energy electron attachment to gaseous DNA constituents. A molecular beam emanating from an oven (left) is crossed with a monochromatic electron beam from a hemispherical energy analyzer (top) with a typical resolution between 50–150 meV. Negatively charged products are separated and detected in a quadrupole mass spectrometer (right). Ion yields for specific masses are recorded as a function of E_0. Picture kindly provided by Paul Scheier.

Charge-injection studies have given evidence that migration of excess electrons on double-helical B-DNA preferably involves a thermally activated electron-hopping mechanism through the thymine (T) and cytosin (C) units. This was expected as these two nucleobases are more-easily reduced than A and G, with $T^{\bullet-}$ being the slightly more-favorable charge carrier.[3] In accord with this, specific effort has recently focused on elucidating the molecular details of low-energy electron-driven dissociative processes for T.[16–19]

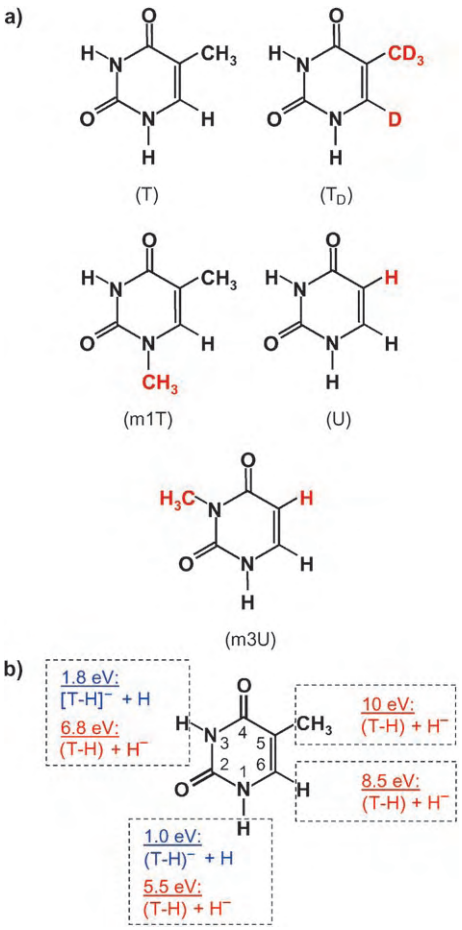
The energy dependence of the yields of negatively charged fragments upon low-energy electron attachment to T shows, as a result of resonant processes, a detailed structure.[18] An in-depth comparison of DEA by using partly deuterated T and uracil (U) as well as selectively methylated T and U (m1T and m3U, Scheme 1) has unraveled the dissociation processes taking place at different E_0 values. Formation of $[T-H]^-$, that is, abstraction of a neutral H from T, occurs over an energy range from 0.6–3 eV.[13,18,19] Selective deuteration of the carbon sites similarly leads to formation of $[T-H]^-$ but not of $[T-D]^-$ in the same range. This proves that the lowest-energy electron-attachment pathways are bond selective, that is, N–H bonds dissociate, whereas C–H bonds do not.[13] Furthermore, methylation of T at the N1 position (m1T) gives evidence of energy dependent site selectivity as formation of $[m1T-H]^-$ at $E_0 \approx 1$ eV is completely suppressed in m1T, whereas the signal around 1.8 eV remains.[19] The former is attributed to the dissociation of the N1–H bonds whereas the latter concerns the N3–H bond. This result is a fine example of

 © 2006 Wiley-VCH Verlag GmbH & Co. KGaA, Weinheim

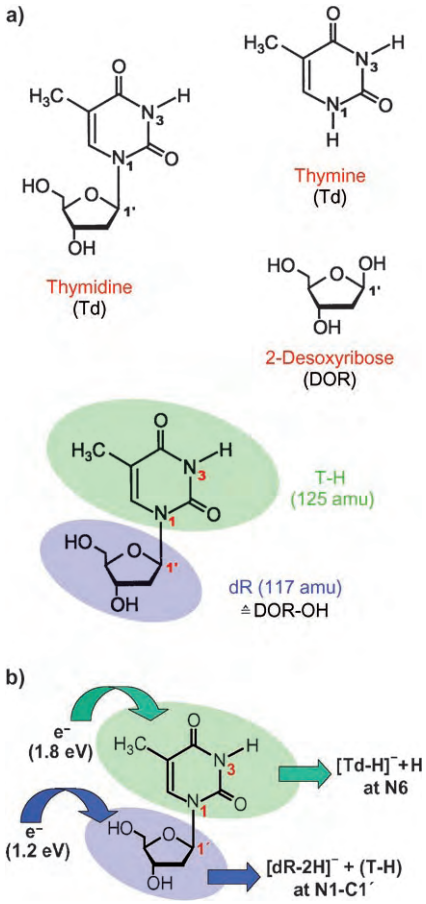
reaction control through low-energy electron attachment.

Similarly, the origin of H^- formed from T through DEA at an E_0 value between 5–11 eV has been elucidated by comparing the H^- or D^- ion yields for T, U, and their derivatives.[16,17] The results demonstrate that four different DEA pathways at 5.5, 6.8, 8.5, and 10 eV lead to strongly selective dissociation at the N1, N3, C6, and methyl sites, respectively (Scheme 1).

As a first step towards the full modeling of DNA in the sense of a bottom-up approach, the nucleoside thymidine (Td), which consists of T bound to a deoxyribose sugar (DOR) through the N1 position (Scheme 2a), has very recently been studied.[20] The results reveal two different electron-attachment pathways at low E_0 values (Scheme 2b). Attachment of 1.2 eV electrons occurs at the sugar unit and leads to rupture of the bond between the (T–H) and dR (=DOR–OH) units as evident by the observation of the product $[dR-2H]^-$. Direct electron attachment to the (T–H) unit at around 1.8 eV, on the other hand, leaves the Td essentially intact. Only H abstraction at the N3 site occurs, as is obvious from the observed fragment $[Td-H]^-$ and the close similarity of the DEA signal with that of m1T. Within the time frame of the experiment (several μs) an electron initially attached to the (T–H) unit does not migrate to the dR unit where it would induce bond rupture between the two units as observed at 1.2 eV. This is in striking contrast to a recent theoretical study[19] that predicted electron migration from low-lying π* MOs of the nucleobase to low-lying σ* MOs of the DNA backbone as discussed in reference [20].



Scheme 1. a) Different thymine-related molecules studied recently by DEA. b) Bond-selective (C–H compared with N–H) and site-selective (N3–H compared with N1–H and C6–H compared with CH_2–H) DEA to T achieved by proper tuning of the incident electron energy.[13,16–19] Graphs kindly provided by Paul Scheier.



Scheme 2. a) Nomenclature and masses of thymidine and its constituents. b) Energy-selective dissociation pathways following low-energy electron attachment to Td. Charge transfer from T–H to dR is not observed.[20] Graphs kindly provided by Eugen Illenberger.

So far, **Td** is the largest model DNA fragment studied by DEA in the gas phase. The next immediate step must and will include, besides a detailed study of the fragmentation pathways in other nucleobases, the addition of the phosphate unit to the nucleoside, thus forming a nucleotide. This will also lead to further questions including the effect of the addition of water molecules and of the formation of base pairs and stacks. Thus, more-sophisticated experimental techniques for the preparation of the molecular beam, for example, MALDI, and a controlled way to add, step by step, the hydration shell will be required at a certain point to proceed to larger units and to situations similar to that in actual living organisms.

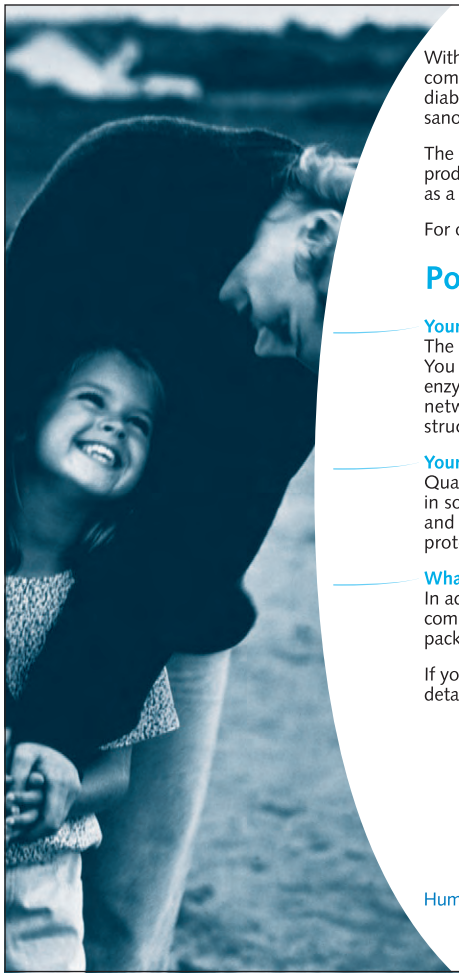
Nonetheless, much has been achieved as supported by results from charge-migration studies in which it was found that reductive charge transfer, that is, migration of an excess electron, does not induce DNA damage.[3] This seems to be in contrast with the general finding that electron attachment to DNA obviously leads to damage. On the other hand, the study of DEA in thymidine has revealed that electron attachment to the (T–H) unit in fact produces a situation that does not necessarily lead to dissociation of a bond between two constituents of DNA.[20] This is in full agreement with the view provided by the charge-migration measurements. The bottom-up approach in studies of radiation damage in DNA has thus proven to be a valuable one.

[1] R. V. Bensasson, E. J. Land, T. G. Truscott, *Excited States and free Radicals in Biology and Medicine*, Oxford University Press, New York, **1993**, p. 143.
[2] K.-W. Choi, J.-H. Lee, S. K. Kim, *J. Am. Chem. Soc.* **2005**, *127*, 15674.
[3] H.-A. Wagenknecht in *Charge Transfer in DNA* (Ed.: H.-A. Wagenknecht), Wiley-VCH, Weinheim **2005**, p. 1.
[4] J.-S. Taylor, *Acc. Chem. Res.* **1994**, *27*, 76.
[5] L. Sanche, *Eur. Phys. J. D* **2005**, *35*, 367.
[6] International Commission on Radiation Units and Measurements, ICRU Report 31 (ICRU, Washington, DC), **1979**.

© 2006 Wiley-VCH Verlag GmbH & Co. KGaA, Weinheim

[7] a) B. D. Michael, P. O'Neill, *Science* **2000**, *287*, 1603; b) B. Boudaïffa, P. Cloutier, D. Hunting, M. A. Huels, L. Sanche, *Science* **2000**, *287*, 1658.
[8] F. Martin, P. D. Burrow, Z. Cai, P. Cloutier, D. Hunting, L. Sanche, *Phys. Rev. Lett.* **2004**, *93*, 068101.
[9] X. Pan, P. Cloutier, D. Hunting, L. Sanche, *Phys. Rev. Lett.* **2003**, *90*, 208102.
[10] T. Solomun, C. Hultschig, E. Illenberger, *Eur. Phys. J. D* **2005**, *35*, 437.
[11] S. G. Ray, S. S. Daube, R. Naaman, *Proc. Natl. Acad. Sci. USA* **2005**, *102*, 15.
[12] M. A. Huels, I. Hahndorf, E. Illenberger, L. Sanche, *J. Chem. Phys.* **1998**, *108*, 1309.
[13] H. Abdoul-Carime, S. Gohlke, E. Illenberger, *Phys. Rev. Lett.* **2004**, *92*, 168103.
[14] S. Denifl, S. Ptasińska, M. Probst, J. Hrušák, P. Scheier, T. D. Märk, *J. Phys. Chem. A* **2004**, *108*, 6562.
[15] S. Ptasińska, S. Denifl, P. Scheier, T. D. Märk, *J. Chem. Phys.* **2004**, *120*, 8505.
[16] S. Ptasińska, S. Denifl, V. Grill, T. D. Märk, P. Scheier, S. Gohlke, M. A. Huels, E. Illenberger, *Angew. Chem.* **2005**, *117*, 1673; *Angew. Chem. Int. Ed.* **2005**, *44*, 1647.
[17] S. Ptasińska, S. Denifl, V. Grill, T. D. Märk, E. Illenberger, P. Scheier, *Phys. Rev. Lett.* **2005**, *95*, 093201.
[18] S. Ptasińska, S. Denifl, B. Mróz, M. Probst, V. Grill, E. Illenberger, P. Scheier, T. D. Märk, *J. Chem. Phys.* **2005**, *123*, 124302.
[19] S. Ptasińska, S. Denifl, P. Scheier, E. Illenberger, T. D. Märk, *Angew. Chem.* **2005**, *117*, 7101; *Angew. Chem. Int. Ed.* **2005**, *44*, 6941.
[20] S. Ptasińska, S. Denifl, S. Gohlke, P. Scheier, E. Illenberger, T. D. Märk, *Angew. Chem.*, **2006**, *118*, 1926; *Angew. Chem. Int. Ed.*, **2006**, *45*, 1893.
[21] J. Berdys, I. Anusiewicz, O. Skurski, J. Simons, *J. Am. Chem. Soc.* **2004**, *126*, 6441.

Vacancy



With around 100,000 employees, sanofi-aventis is one of the world's leading research-based pharmaceutical companies and is No. 1 in Europe. Our core therapeutic areas: cardiovascular disease, thrombosis, oncology, diabetis/metabolic disorders, central nervous system and internal medicine. And to prevent diseases, sanofi-aventis also develops vaccines.

The 10,000 people who work for the sanofi-aventis Group in Germany perform basic research and development, produce active ingreedients, and manufacture and market medicinal products. In so doing, we promote Germany as a business location and improve medical care for people everywhere.

For our Chemical Sciences department in Frankfurt we are searching

Postdoctoral scientists in synthetic & bioorganic chemistry (m/f)

Your role
The positions will be part of the EC-financed project "Chemical Proteomics by Activity Monitoring of Proteases". You will design and synthesize novel chemical probes to monitor and modulate the activity of proteolytic enzymes in the living cell. The position requires close interaction with the partnering institutions of the international network as well as with sanofi-aventis research teams in medicinal chemistry, combinatorial chemistry, structural biology and drug design.

Your profile
Qualified candidates will possess a Ph. D. in synthetic organic or bioorganic chemistry. Demonstrated success in solving challenging synthetic problems is a prerequisite for these positions. Experience in peptide chemistry and solid-state synthesis will be a strong advantage. Working knowledge of enzymology, particularly of proteolytic enzymes would be an additional asset.

What we offer
In addition to a challenging and interesting job in a competent and well-established team within an international company, we offer an attractive salary commensurate to your qualifications with an above-average compensation package as well as offer considerable support for your further professional and personal development.

If you would like to be considered, please send a resume indicating your full career history and current employment details to the address below or apply online at **www.sanofi-aventis.de**.

sanofi aventis
Because health matters

Sanofi-Aventis Deutschland GmbH
Human Resources Recruitment & Marketing • Industriepark Höchst • Gebäude H 831 • D-65926 Frankfurt am Main
E-Mail: ApplicationService@sanofi-aventis.com • www.sanofi-aventis.de

 © 2006 Wiley-VCH Verlag GmbH & Co. KGaA, Weinheim

Borates

DOI: 10.1002/anie.200503999

Some Experimental Evidence that $Zn_4O(BO_3)_2$ is $Zn_6O(OH)(BO_3)_3$

*Thibaud Delahaye, Florent Boucher, Michaël Paris, Olivier Joubert, Mayté Caldes, and Yves Piffard**

Keywords:
boron · hydrogen bonds · structure elucidation · zinc

Oxides exhibiting a disordered arrangement of oxygen vacancies are of potential interest as oxygen-ion conductors. In this respect, our attention has recently been drawn by the crystal structure of $Zn_4O(BO_3)_2$ in which one of the oxygen sites is not fully occupied, leading to an overall composition $Zn_{12}B_6O_{21}\square$ per rhombohedral unit cell.[1] However, on detailed examination of the structure data, some surprising features appear:

- The oxygen site that is only 5/6 occupied (O(2) in ref.[1]), belongs to the three-fold coordination of boron. That a BO_3 group, which can be considered as a polyanion, could exhibit an oxygen vacancy is unlikely and, to our knowledge, has never been reported to date.
- Bond valence sums calculations for the three oxygen sites show that, for O(3), this sum is anomalously low ($\Sigma O(3) = 1.49$ v.u.) compared to the expected value of 2 ($\Sigma O(1) = 1.97$ and $\Sigma O(2) = 2.00$ v.u.).[2,3] In addition, considering that O(3) is bonded to Zn only, the O(3)···O(3) distance is abnormally short (2.543(9) Å) for a distance between oxygen atoms from different ZnO_4 tetrahedra.

[*] Dr. Y. Piffard
Institut des Matériaux Jean Rouxel
UMR CNRS-Université de Nantes No. 6502
2, rue de la Houssinière—BP 32229
44322 Nantes Cedex 03 (France)
Fax: (+33) 2-4037-3995
E-mail: yves.piffard@cnrs-imn.fr
T. Delahaye, Dr. F. Boucher, Dr. M. Paris, Dr. O. Joubert, Dr. M. Caldes
Institut des Matériaux Jean Rouxel
UMR CNRS-Université de Nantes No. 6502
2, rue de la Houssinière—BP 32229
44322 Nantes Cedex 03 (France)

The first feature suggests that there is no oxygen vacancy in the structure and that, accordingly, two missing positive charges per unit cell have to be found to maintain charge balance in the formula. By taking into account both this preliminary conclusion and the second feature, the presence of a hydrogen atom between pairs of O(3) atoms becomes a reasonable assumption, because it would both induce an increase of the bond valence sum for O(3) and explain the constriction of the O(3)···O(3) distance by the straddling of a O–H···O bridge, that is, the formation of a strong hydrogen bond.

We describe herein some experiments which demonstrate that "$Zn_4O(BO_3)_2$" is in fact $Zn_6O(OH)(BO_3)_3$ (**1**) and we give a more accurate description of its structure thanks to a new determination from single-crystal X-ray diffraction data.

A slightly modified version of the hydrothermal reaction described in ref. [1] yielded small ($0.02 \leq$ max. dimension ≤ 0.06 mm), colorless, single crystals in the shape of faceted rhombohedra. The phase purity of the product was checked by comparison of the observed powder X-ray diffraction (XRD) pattern with that reported for "$Zn_4O(BO_3)_2$". The first support for our assumption was obtained by a difference thermoanalytical/thermogravimetric analysis coupled with an analysis of released gases by mass spectrometry (Setaram TG-DSC 111 system equipped with a Leybold Mass Spectrometer, heating rate 5 K min^{-1}, dry Argon stream) showing that the phase undergoes a water loss of 1.49 % in weight (the expected value for **1** is 1.50 %) at 670 °C. This temperature indicates a remarkable stability of the compound. The decomposition products were identified from the XRD pattern (at room temperature) of the sample heated at 750 °C, as ZnO and $Zn_3(BO_3)_2$, suggesting that the dehydration process occurs according to the hypothetical reaction given in Equation (1).

$$2\,Zn_6O(OH)(BO_3)_3 \rightarrow 3\,ZnO + 3\,Zn_3(BO_3)_2 + H_2O \quad (1)$$

The measured density ($\rho =$ 3.99(2) g cm^{-3}, AccuPyc 1330 system, He pressure, sample mass = 1.2605 g), is in better agreement with that calculated for **1** ($\rho = 3.98$ g cm^{-3}) than for "$Zn_4O(BO_3)_2$" ($\rho = 3.92$ g cm^{-3}).

Structural analysis of **1** by single-crystal XRD revealed the three-dimensional framework of vertex-sharing ZnO_4 tetrahedra and triangular BO_3 groups described in ref. [1] with however, and as expected, a better precision in the atomic coordinates (Table 1). This improvement leads to more regular oxygen environments for both Zn and B atoms, as can be appreciated from bond lengths given in Table 2, and to an O(3)···O(3) distance even shorter (2.456(4) Å) than that inferred from the previous study.

This strong overlapping of O(3) atoms, coming close to the critical O···O distance (2.42 Å) for which symmetric hydrogen bonds could theoretically be observed, is the signature of a very strong hydrogen bonding implying a linear or nearly linear O–H···O bridge.[4,5] Accordingly, the acid hydrogen atom (H(1)) was introduced in a statistically disordered (half-occupied) 4c site between pairs of O(3) atoms; it

 InterScience © 2006 Wiley-VCH Verlag GmbH & Co. KGaA, Weinheim

Table 1: Atomic coordinates and isotropic temperature factors for $Zn_6O(OH)(BO_3)_3$. Values from ref. [1] are given in italics for comparison.

Atom	W[a]	τ[b]	x	y	z	U_{eq}/U_{iso} [Å^2]
Zn(1)	12f	1.0	0.64005(5)	0.69493(5)	0.07925(5)	0.0087(3)
			0.6408(2)	*0.6925(2)*	*0.0794(2)*	*0.007(1)*
B(1)	6e	1.0	0.7276(6)	0.7724	0.25	0.008(3)
			0.728(2)	*0.772*	*0.25*	*0.005*[c]
O(1)	12f	1.0	0.5892(3)	0.8031(3)	0.2222(3)	0.0114(18)
			0.5854(8)	*0.8045(7)*	*0.2181(8)*	*0.007(2)*
O(2)	6e	1.0	0.3958(3)	0.75	0.1042	0.012(2)
		5/6	*0.396(2)*	*0.75*	*0.104*	*0.018(4)*
O(3)	4c	1.0	0.79695(12)	0.79695	0.79695	0.0097(15)
			0.7986(4)	*0.7986*	0.7986	*0.013(4)*
H(1)	4c	0.5	0.767(3)	0.767	0.767	0.02(4)[d]

[a] Wyckoff-site notation. [b] Occupancy. [c] Not refined in ref. [1]. [d] Isotropic thermal parameter; U_{eq} is defined as one-third of the trace of the orthogonalized U_{ij} tensor.

Table 2: Selected bond lengths [Å], bond valences (BV) [v.u.], and bond valence sums for $Zn_6O(OH)(BO_3)_3$.

	This work		From ref. [1]		
	Bond length [Å]	BV [v.u.]	Bond length [Å]	BV [v.u.]	
Zn(1)-O(1)	1.939(4)	0.530	1.906(5)	0.579	
Zn(1)-O(1)[a]	1.9581(17)	0.503	1.926(5)	0.549	
Zn(1)-O(2)	1.965(4)	0.494	1.962(5)	0.498	
Zn(1)-O(3)[b]	1.9632(8)	0.496	1.962(2)	0.498	
	ΣZn = 2.023		ΣZn =		2.124
B(1)-O(1)	1.374(7)	0.992	1.435	0.841	
B(1)-O(1)[c]	1.374(7)	0.992	1.435	0.841	
B(1)-O(2)[a]	1.372(4)	0.997	1.367	1.011	
	ΣB = 2.981		ΣB = 2.693		
O(3)-H(1)	0.78(5)[e]	0.63[f]			
O(3)-H(1)[d]	1.67(5)[e]	0.37[f]			
	ΣO(1) = 2.025		ΣO(1) = 1.969		
	ΣO(2) = 1.985		ΣO(2) = 2.007		
	ΣO(3) = 1.988		ΣO(3) = 1.494		
O(3)···O(3)	2.456(4)		2.543(9)		

[a] 1−z,1−x,1−y ; [b] −x,−y,−1−z; [c] 13/6−y,11/6−x,5/6−z ; [d] 3/2−z,3/2−y,3/2−x. [e] The H atom being closer to the O atom than it actually is, the bond valences marked [f] were determined from Figure 2 in ref. [3] with the use of the O(3)···O(3) distance.

was refined satisfactorily along with its isotropic thermal parameter (Table 1). However, since X-ray diffraction locates the centroid of the electron density rather than the position of the nucleus, the hydrogen atom appears to be closer to the oxygen atom than it actually is (Table 2). The O–H···O bridge straddles the small cavity centered on the 2a site and delimited by six ZnO_4 tetrahedra (Figure 1).

The ^{1}H magic-angle spinning (MAS) NMR spectrum (Bruker "Avance" 500 MHz spectrometer, TMS reference, MAS rate 14 kHz, 1000 s repetition time) shows a single resonance at δ = 14.5 ppm. This important downfield chemical shift is in fair agreement with the value (δ ≈ 16 ppm) that can be expected from the O(3)···O(3) distance.[6] It confirms that the hydrogen bond is strong.

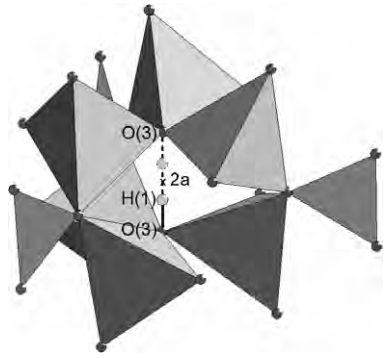


Figure 1. Perspective view of the cavity centered on the 2a site and straddled by the O–H···O bridge along the [111] axis (both statistically half-occupied H positions are represented).

The validity of the asymmetric versus symmetric hydrogen-bond model, arising from a statistical disorder between two positions on either side of the 2a site, was evaluated by means of density functional theory (DFT). The computation results show that the asymmetric configuration is more stable with an energy difference of 6 meV per formula unit. This low, but significant, activation energy barrier (≈ 70 K) agrees perfectly with the dynamic disorder observed at room temperature. Furthermore; the O–H (1.10 Å) and H···O (1.36 Å) optimized bond lengths fit rather well with those expected from the chemical shift.[7]

In summary, some experiments aimed at characterizing protons in solids, have shown that the so-called zincoborate "$Zn_4O(BO_3)_2$" is in fact a zinc oxyhydroxyborate. As expected, the introduction of the H atom into the structure now brings the bond-valence sum of O(3) to a more reasonable value of 1.988 and it rules out the hypothesis of oxygen vacancies in the environment of boron.

Experimental Section

Synthesis: 50-mL Teflon vessels were filled with the same amount of borax ($Na_2B_4O_7{\cdot}10H_2O$, 3.814 g), $Zn(NO_3)_2$ (6.43 g) and water (10 mL) as in the previous study,[1] and decreasing amounts of 4 M NaOH (from 3.44 g to 1.72 g) so as to decrease the starting pH value of the mixture down to ≈ 7. These vessels were placed in stainless steel bombs and heated as indicated previously (200 °C, 4 days). The preparation with the lowest starting pH value yielded the desired product in the form of small single crystals.

Crystal structure determination: The cell parameters (Table 3) were refined from the powder XRD pattern (INEL CPS 120 diffractometer, quartz monochromator, $Cu_{K\alpha1}$, λ = 1.540598 Å) using the program FULLPROF in the full pattern matching mode,[8] and its interface : the program WinPLOTR.[9] The single-crystal data collection was carried out on a Bruker-Nonius Kappa CCD diffractometer (graphite monochromated MoK-$L_{2,3}$ radiation, 600 s exposure time per frame). Intensity integration and standard Lorentz-polarization correction were performed with the Bruker-Nonius Eval-CCD program package. On account of both the shape and the

 © 2006 Wiley-VCH Verlag GmbH & Co. KGaA, Weinheim

Table 3: Crystallographic data for $Zn_6O(OH)(BO_3)_3$.

Empirical formula	$Zn_6O_{11}B_3H$
Formula weight	601.65
Crystal system	Rhombohedral
Space group	$R\bar{3}c$ (No. 167)
$a=b=c$ [Å]	9.9120(4)[a]
$\alpha=\beta=\gamma$ [°]	48.609(2)[a]
V [Å^3]	502.81(4)
Z	2
ρ_{calcd} [g cm^{-3}]	3.98
ρ_{meas} [g cm^{-3}]	3.99(2)
Absorption coefficient [mm^{-1}]	14.1
Crystal size [mm]	$0.04\times0.04\times0.05$
Data range	$6.56\leq\theta\leq35.06$
Reflections collected	3859
Independent reflections	737
Reflections with $I>3\sigma(I)$ (obs.)	610
Number of variables	35
$R(F)$[b]/$R_w(F)$[c] (obs. refl.)	0.0296/0.0220
$R(F)$[b]/$R_w(F)$[c] (all refl.)	0.0472/0.0229
$\Delta\rho_{max}/\Delta\rho_{min}$ [e$^-$ Å^{-3}] (all refl.)	1.50/−1.64
Extinction method	Lorentzian type I isotropic.[12]
Extinction coefficient	0.027(6)

[a] Refined from powder data. [b] $R(F)=\Sigma\,||F_o|-|F_c||/\Sigma\,|F_o|$. [c] $R_w(F)=[\Sigma w(|F_o|-|F_c|)^2/\Sigma w F_o^2]^{1/2}$ with $w=1/[\sigma^2(F_o)]$

very small size of the crystal an absorption correction was not deemed necessary. All other structure calculations were conducted with the Jana2000 program suite.[10] The structure was refined with anisotropic atomic displacement parameters for all non-H atoms. Further details on the crystal structure investigations may be obtained from the Fachinformationszentrum Karlsruhe, 76344 Eggenstein-Leopoldshafen, Germany (fax: (+49) 7247-808-666; e-mail: crysdata@fiz-karlsruhe.de), on quoting the depository number CSD-415925.

Electronic band structure calculations: Calculations were carried out with the VASP package,[11] within the DFT framework and using the PBE96 exchange and correlation potential. Complete structural optimizations were performed by calculating the Hellmann–Feynman (HF) forces on the atoms and HF stresses on the unit cell. As usually observed, the optimized cell parameters ($a=$ 10.031 Å (+1.2%), $\alpha=48.74°$) and average distances (Zn–O_{av} = 1.985 Å (+1.4%), B–O_{av} = 1.386 Å (+0.9%)) are slightly overestimated.

Received: November 10, 2005

[1] W. T. A. Harisson, T. E. Gier, G. D. Stucky, *Angew. Chem.* **1993**, *105*, 788; *Angew. Chem. Int. Ed. Engl.* **1993**, *32*, 724.

[2] N. E. Brese, M. O'Keeffe, *Acta Crystallogr. Sect. B* **1991**, *47*, 192.

[3] I. D. Brown, D. Altermatt, *Acta Crystallogr. Sect. B* **1985**, *41*, 244.

[4] I. D. Brown, *Acta Crystallogr. Sect. B* **1992**, *48*, 553.

[5] H. D. Lutz, *J. Mol. Struct.* **2003**,*646*, 227.

[6] H. Eckert, J. P. Yesinowski, L. A. Silver, E. M. Stolper, *J. Phys. Chem.* **1988**, *92*, 2055.

[7] E. Brunner, U. Sternberg, *Prog. Nucl. Magn. Reson. Spectrosc.* **1998**, *32*, 21.

[8] J. Rodríguez-Carvajal, *Phys. B* **1993**, *192*, 55. See also http://www-llb.cea.fr/fullweb/fp2k/fp2k.htm.

[9] T. Roisnel, J. Rodríguez-Carvajal, WinPLOTR: *a Windows tool for powder diffraction patterns analysis*, Materials Science Forum (Ed.: R. Delhez, E. J. Mittenmeijer), Proc. of the 7th European Powder Diffraction Conference (EPDIC7), **2000**, p. 118. See also http://www-llb.cea.fr/fullweb/winplotr/winplotr.htm.

[10] V. Petricek, M. Dusek, Jana2000, Structure Determination Software Programs. Institute of Physics, Praha, Czech Republic, **2000**.

[11] G. Kresse, J. Furthmüller, *Comput. Mater. Sci.* **1996**, *6*, 15; G. Kresse, J. Furthmüller, *Phys. Rev. B* **1996**, *54*, 11169.

[12] P. J. Becker, P. Coppens, *Acta Crystallogr. Sect. A* **1974**, *30*, 129.

 © 2006 Wiley-VCH Verlag GmbH & Co. KGaA, Weinheim

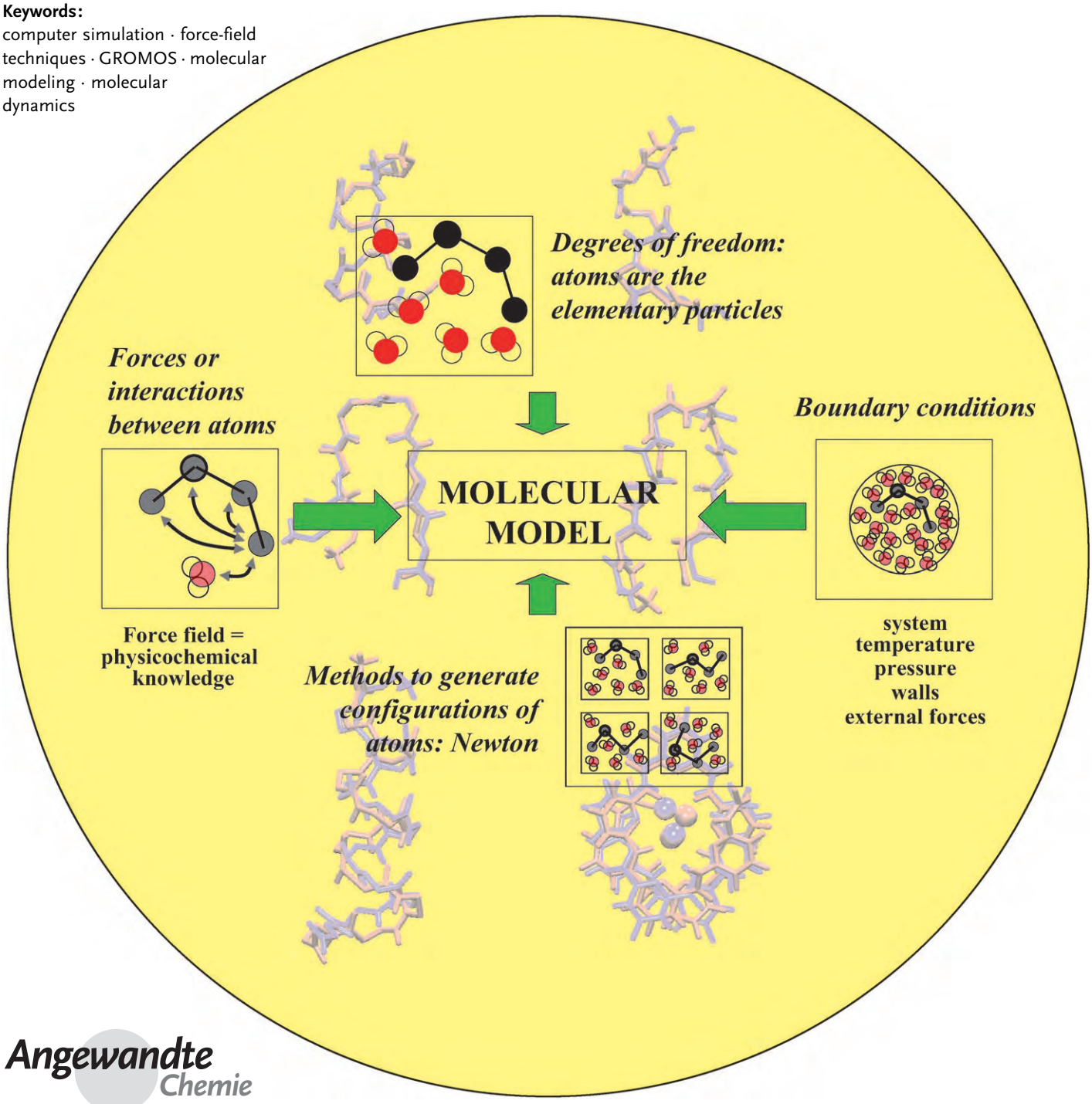
Molecular Dynamics

DOI: 10.1002/anie.200502655

Biomolecular Modeling: Goals, Problems, Perspectives

Wilfred F. van Gunsteren, Dirk Bakowies, Riccardo Baron, Indira Chandrasekhar, Markus Christen, Xavier Daura, Peter Gee, Daan P. Geerke, Alice Glättli, Philippe H. Hünenberger, Mika A. Kastenholz, Chris Oostenbrink, Merijn Schenk, Daniel Trzesniak, Nico F. A. van der Vegt, and Haibo B. Yu*

Keywords:
computer simulation · force-field techniques · GROMOS · molecular modeling · molecular dynamics



© 2006 Wiley-VCH Verlag GmbH & Co. KGaA, Weinheim

Computation based on molecular models is playing an increasingly important role in biology, biological chemistry, and biophysics. Since only a very limited number of properties of biomolecular systems is actually accessible to measurement by experimental means, computer simulation can complement experiment by providing not only averages, but also distributions and time series of any definable quantity, for example, conformational distributions or interactions between parts of systems. Present day biomolecular modeling is limited in its application by four main problems: 1) the force-field problem, 2) the search (sampling) problem, 3) the ensemble (sampling) problem, and 4) the experimental problem. These four problems are discussed and illustrated by practical examples. Perspectives are also outlined for pushing forward the limitations of biomolecular modeling.

From the Contents

1. Introduction	4065
2. The Force-Field Problem	4067
3. The Search Problem	4073
4. The Ensemble Problem	4080
5. The Experimental Problem	4083
6. Perspectives in Biomolecular Modeling	4087

1. Introduction

The role of computation in biology, biological chemistry, and biophysics has shown a steady increase over the past few decades. The continuing growth of computing power (in particular in the context of personal computers) has made it possible to analyze, compare, and characterize large and complex data sets that are obtained from experiments on biomolecular systems. This has in turn led to the formulation of models for biomolecular processes that are amenable to simulation or analysis on a computer. When undertaking a biomolecular modeling study of a particular system of interest, the level of modeling, that is, the spatial resolution, time scale, and degrees of freedom of interest, must be considered (Table 1).

Which level of modeling is chosen to describe a particular biomolecular process depends on the type of process. In this Review we focus on three of the four biomolecular processes illustrated in Figure 1: 1) polypeptide folding, 2) molecular complexation (e.g. protein–ligand, DNA–ligand, protein–DNA, etc.), 3) partitioning of molecules between different environments, such as lipid membranes, water, mixtures (e.g. water/urea, ionic solutions), and apolar solvents, and 4) the formation of lipid membranes or micelles out of mixtures of their components. These four processes play a fundamental role in the behavior of biomolecular systems and share the common feature that they are driven by weak, nonbonded interatomic interactions. Such interactions govern the thermodynamic properties of the condensed phase in which the four processes occur. Therefore, these processes are most promisingly modeled at the atomic or molecular level (third row in Table 1). Since the temperature range of interest basically lies between room and physiological temperatures, and energies involved in these processes are on the order of 1–10 $k_B T$ (which corresponds to tens of kJ mol^{-1}, k_B is the Boltzmann constant), the processes are largely determined by the laws of classical statistical mechanics. Although quantum mechanics governs the interactions between the electrons of the atoms and molecules as well as the motions of light particles such as protons, the nonbonded interactions can be very well described by a classical potential-energy function or force field as part of a classical Hamiltonian of the system of interest.[1]

Figure 2 shows the four choices to be made when modeling a biomolecular system: 1) which atomic or molecular degrees of freedom are explicitly considered in the model, 2) which interaction function or force field is used to describe the energy of the system as a function of the chosen degrees of freedom, 3) how these, generally many, degrees of freedom are to be sampled, and 4) how the spatial boundaries and external forces are modeled. As already mentioned, we mainly consider atomic and molecular degrees of freedom with the corresponding classical force fields and classical Newtonian dynamics to sample the degrees of freedom. System sizes that can be considered range up to 10^5 or

[*] Prof. Dr. W. F. van Gunsteren, Dr. D. Bakowies, R. Baron, Dr. I. Chandrasekhar, M. Christen, Prof. Dr. X. Daura, Dr. P. Gee, D. P. Geerke, Dr. A. Glättli, Dr. P. H. Hünenberger, M. A. Kastenholz, Dr. C. Oostenbrink, Dr. M. Schenk, D. Trzesniak, Dr. N. F. A. van der Vegt, Dr. H. B. Yu
Laboratory of Physical Chemistry
Swiss Federal Institute of Technology
ETH
8093 Zurich (Switzerland)
Fax: (+41) 44-632-1039
E-mail: wfvgn@igc.phys.chem.ethz.ch

Prof. Dr. X. Daura
ICREA, Institute of Biotechnology and Biomedicine
Universitat Autònoma de Barcelona
08193 Bellaterra (Barcelona) (Spain)

Dr. C. Oostenbrink
Pharmaceutical Sciences/Pharmacochemistry
Vrije Universiteit
De Boelelaan 1083 P262, 1081 HV Amsterdam (The Netherlands)

Dr. N. F. A. van der Vegt
Max-Planck-Institute for Polymer Research
Ackermannweg 10, 55128 Mainz (Germany)

Dr. H. B. Yu
Department of Chemistry
University of Wisconsin
1101 University Ave, Madison, WI 53706 (USA)

 © 2006 Wiley-VCH Verlag GmbH & Co. KGaA, Weinheim

Table 1: Examples of levels of modeling in computational biochemistry and molecular biology.

Methods	Degrees of freedom	Properties, processes	Time scale
quantum dynamics	atoms, nuclei, electrons	excited states, relaxation, reaction dynamics	picoseconds
quantum mechanics (ab initio, density functional, semiempirical, valence bond methods)	atoms, nuclei, electrons	ground and excited states, reaction mechanisms	no time scale
classical statistical mechanics (MD, MC, force fields)	atoms, solvent	ensembles, averages, system properties, folding	nanoseconds
statistical methods (database analysis)	groups of atoms, amino acid residues, bases	structural homology and similarity	no time scale
continuum methods (hydrodynamics and electrostatics)	electrical continuum, velocity continuum etc.	rheological properties	supramolecular
kinetic equations	populations of species	population dynamics, signal transduction	macroscopic

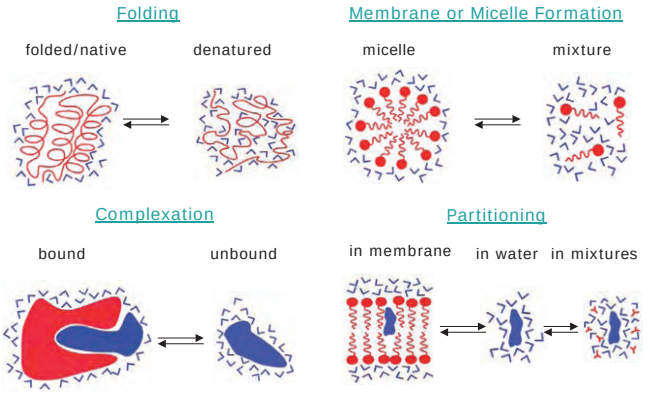


Figure 1. Four biomolecular processes that are governed by thermodynamic equilibria.

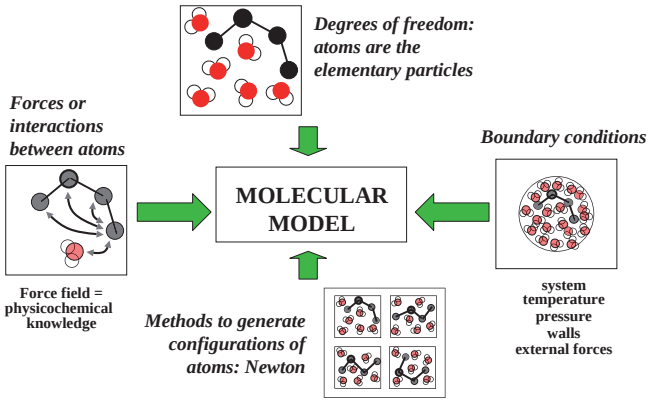


Figure 2. Four basic choices in the definition of a model for molecular simulation.

10^6 atoms or particles, which is still very small compared to Avogadro's number, that is, macroscopic sizes. For such small systems, the modeling of the boundary or surface will have a large effect on the calculated properties. Such surface effects can be minimized by using periodic boundary conditions, where the box that contains the molecular system is surrounded by an infinite number of copies of itself (Figure 3). This avoids surface effects at the expense of introducing periodicity artefacts.[2–5]

Present day biomolecular modeling is limited in its application by the four problems highlighted in Table 2: 1) the force-field problem, 2) the search (sampling) problem, 3) the ensemble (sampling) problem, and 4) the experimental problem. These four problems are the focus of the present Review and will be discussed and illustrated in Sections 2–5 by using examples from our own work. We stress that the aim of this Review is not to review the contributions of various research groups to the field.

The key reason why computer simulation is used in the study of biomolecular systems in spite of the above-mentioned



Wilfred F. van Gunsteren was born in 1947 in Wassenaar (The Netherlands). In 1968 he gained a BSc in physics at the Free University of Amsterdam; in 1976 he was awarded a "Meester" in Law, and in 1976 a PhD in nuclear physics. After postdoc research at the University of Groningen and at Harvard University he was, 1980–1987, senior lecturer and, until August 1990, Professor for Physical Chemistry at the University of Groningen. In 1990 he became professor of Computer Chemistry at the ETH Zürich. He is holder of a gold medal for research of the Royal Netherlands Chemical Scoiety. His main interests center on the physical fundamentals of the structure and function of biomolecules.

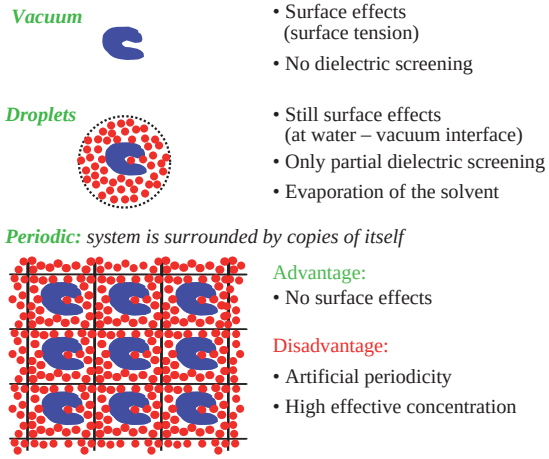


Figure 3. Three types of spatial boundary conditions used in molecular simulation.

© 2006 Wiley-VCH Verlag GmbH & Co. KGaA, Weinheim

Table 2: Four basic problems of biomolecular modeling.

1. force-field problem	A) very small (free) energy differences, many interactions B) entropic effects C) variety of atoms and molecules
2. search problem	A) convergence B) alleviating factors C) aggravating factors
3. ensemble problem	A) entropy B) averaging C) nonlinear averaging
4. experimental problem	A) averaging B) insufficient number of data C) insufficient accuracy of data

limitations to its accuracy resides in the fourth of the four reasons listed in Table 3: Only a very limited number of properties of a biomolecular system is actually accessible to experimental measurement, whereas in a computer simulation not only averages, but also distributions and time series of any definable quantity can be determined. Thus, computer simulation represents a complement to experiment by providing the detailed conformational and other distributions that determine the space and time averages obtained experimentally. As such, it is an indispensable tool to interpret experimental data. Moreover, it can be used to predict properties under environmental conditions that are difficult or expensive to realize. In the next four sections we illustrate the use, power, and limitations of biomolecular modeling in conjunction with experimental efforts with regard to the four processes of interest (Figure 1).

Table 3: Four reasons why computer simulation is used in science.

Simulation can replace or complement an experiment:	
1. experiment is impossible	collision of stars or galaxies weather forcast
2. experiment is dangerous	flight simulation explosion simulation
3. experiment is expensive	high pressure simulation wind channel simulation
4. experiment is blind	many properties cannot be observed on very short time scales and very small space scales

2. The Force-Field Problem

A biomolecular force field generally consists of potential-energy terms representing covalent interactions between atoms (such as bond-stretching, bond-angle bending, improper and proper dihedral-angle torsion) on the one hand and nonbonded interactions on the other hand between atoms in different molecules and between atoms in a molecule that are separated by more than two or three covalent bonds.[6,7]

Since nonbonded interactions govern the thermodynamic equilibria and processes of interest depicted in Figure 1, we focus on the formulation and parametrization of these potential-energy terms. Three problems dominate the topic of force-field development (Table 2, point 1, A–C).

A first problem is that the (free) energy differences driving the processes of Figure 1 are of the order of 1–10 $k_B T$ (which corresponds to tens of kJ mol^{-1}). These relatively small energies result from a summation over very many (10^6–10^8) atom pairs: A system of $N = 1000$ atoms has about $^1/_2 N(N-1) = 500\,000$ pairs of atoms contributing to the nonbonded interaction. To reach the requested accuracy for the total nonbonded energy, the accuracy of the individual terms in the summation (the atom-pair energies) must be higher. This difficulty becomes increasingly severe when trying to derive a force field of high accuracy for larger systems, that is, for larger values of N.

A second problem is to appropriately account for entropic effects. Since we are not interested in biomolecular systems at a temperature of −273.15 °C (0 K), we have to consider the contribution of entropy S to the free energy $F = U - TS$ of the system of interest. It is well known that entropy plays an essential role in all four of the processes shown in Figure 1. Changes in free energy that drive processes may result from changes in internal energy (U) or in entropy (S), which may work together or against each other depending on the relative strengths of the nonbonded interactions between the various components (atoms, molecules) of the system.[8,9] Figure 4 illustrates the phenomenon of energy–entropy compensation: two conformations x_1 and x_2 of a molecule may have $U(x_1) \ll U(x_2)$, while $F(x_1) > F(x_2)$ if at a given temperature $S(x_1) \ll S(x_2)$. The entropy is a measure of the extent of conformational space (x) accessible to the molecular system at a given temperature T.

Figure 4 also illustrates that searching for and finding the global energy minimum of a biomolecular system is meaningless when its entropy accounts for a sizeable fraction of its free energy. For example, $F = -24$ kJ mol^{-1}, $U = -41$ kJ mol^{-1}, and $TS = -17$ kJ mol^{-1} for liquid water at room temperature and pressure. The properties of water in

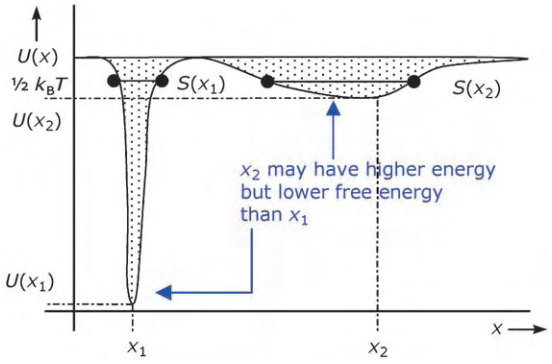


Figure 4. Energy–entropy compensation at finite temperatures.

© 2006 Wiley-VCH Verlag GmbH & Co. KGaA, Weinheim

the condensed phase can therefore only be described through a conformational distribution, which in turn can be generated by computer simulation. Similar considerations apply to biomolecular systems: an energy-minimized structure of a protein corresponds to a possible conformation at 0 K, and lacks information on the conformational distribution of the protein at physiological temperatures. This state of affairs has consequences for the development of force fields: if a force field is to be used in computer simulations above 0 K, its parameters should be derived or calibrated taking into account entropic effects for it to be consistent. In other words, calibration of force-field parameters involves computer simulations to generate configurational ensembles, which makes it a more costly task than when only single minimum-energy conformations or measured average structures are used.

A third problem in the development of a biomolecular force field is the enormous variety of chemical compounds for which adequate force-field parameters should be derived. If the force-field parameters are (to some extent) transferable between atoms or groups of atoms in different molecules, this problem may be (at least partially) alleviated. In general, putting the force-field terms on a physical (instead of a purely statistical) basis and keeping them simple and local will enhance the transferability of parameters from one compound to another. In addition, by keeping them computationally simple, the efficiency of biomolecular simulation can be enhanced, which facilitates the sampling of configurational space.

2.1. Functional Form of the Force-Field Terms

Most biomolecular force fields are composed of terms that possess a rather simple functional form.[6] The GROMOS force field, for example, consists of the following terms [Eqs. (1)–(8)]:[7,10]

$$V^{\mathrm{bond}}(\boldsymbol{r};K_{\mathrm{b}},b_0) = \sum_{n=1}^{N_{\mathrm{b}}} \tfrac{1}{4}K_{b_n}[b_n^2-b_{0_n}^2]^2 \tag{1}$$

$$V^{\mathrm{angle}}(\boldsymbol{r};K_\theta,\theta_0) = \sum_{n=1}^{N_\theta} \tfrac{1}{2}K_{\theta_n}[\cos(\theta_n)-\cos(\theta_{0_n})]^2 \tag{2}$$

$$V^{\mathrm{har}}(\boldsymbol{r};K_\xi,\xi_0) = \sum_{n=1}^{N_\xi} \tfrac{1}{2}K_{\xi_n}[\xi_n-\xi_{0_n}]^2 \tag{3}$$

$$V^{\mathrm{trig}}(\boldsymbol{r};K_\varphi,\delta,m) = \sum_{n=1}^{N_\varphi} K_{\varphi_n}[1+\cos(\delta_n)\cos(m_n\varphi_n)] \tag{4}$$

$$V^{\mathrm{LJ}}(\boldsymbol{r};\mathrm{C}_{12},\mathrm{C}_6) = \sum_{\text{pairs } i,j}\left[\frac{\mathrm{C}_{12}(i,j)}{r_{ij}^{12}}-\frac{\mathrm{C}_6(i,j)}{r_{ij}^{6}}\right] \tag{5}$$

$$V^{C}(\boldsymbol{r};q) = \sum_{\text{pairs } i,j}\frac{q_i\,q_j}{4\pi\varepsilon_0\varepsilon_1}\frac{1}{r_{ij}} \tag{6}$$

$$V^{\mathrm{RF}}(\boldsymbol{r};q) = \sum_{\text{pairs } i,j}\frac{q_i\,q_j}{4\pi\varepsilon_0\varepsilon_1}\frac{(-\frac{1}{2}C_{rf}\,r_{ij}^2)}{R_{rf}^3} \tag{7}$$

$$V^{\mathrm{RF_c}}(\boldsymbol{r};q) = \sum_{\text{pairs } i,j}\frac{q_i\,q_j}{4\pi\varepsilon_0\varepsilon_1}\frac{(\frac{1}{2}C_{rf}-1)}{R_{rf}} \tag{8}$$

The first four equations describe the four types of covalent (bonded) interactions mentioned before, while the last four specify the nonbonded interactions: the van der Waals interaction cast in the form of a Lennard–Jones term, the electrostatic Coulomb interaction between (partial) atomic charges q_i, the distance-dependent and distance-independent (constant) interactions arising from the dipolar reaction field (RF) induced by the charge distribution inside the cut-off sphere through the continuous dielectric medium outside this cut-off sphere. Since this force field covers a variety of molecules (including polypeptides, polysaccharides, nucleic acids, lipids), it contains a large set of parameters:[7] 52 types of bonds [Eq. (1)], 54 types of bond angles [Eq. (2)], 3 types of improper (harmonic) dihedral angles [Eq. (3)], 41 types of proper torsional (trigonometric) dihedral angles [Eq. (4)], van der Waals interactions of 53 types of atoms [Eq. (5)], and many different sets of atomic charges for the typical polar or charged groups of atoms in the molecules mentioned above [Eqs. (6)–(8)].[7,10]

The functional forms are chosen such that they are easy to compute. The nonbonded interactions only contain pair terms, and the more complex three- and four-body covalent terms [Eqs. (3) and (4)] are much fewer in number than the nonbonded pair terms. The solvent part of this biomolecular force field only contains nonbonded terms, the intramolecular degrees of freedom of solvent molecules are kept frozen. The major computational effort resides in evaluating the nonbonded interactions.

2.2. Calibration of Force-Field Parameters

Having specified the functional form of the interaction terms, the formidable task of finding appropriate, consistent values for the hundreds of force-field parameters remains to be addressed. This task involves the choice of type of data, type of systems, thermodynamic phase, and properties to be used as the calibration set for specific force-field parameters. The choices made for the GROMOS force field are summarized in Table 4. Since biomolecular systems are generally in the condensed phase, data for the condensed phase (experimental and theoretical) are used whenever possible. Furthermore, to maximize the transferability of parameters between groups of atoms in different molecules, only data for small molecules are used. When using data from large molecules such as proteins (e.g. from the protein data bank) properties of groups of atoms may be dependent on their particular environment in the folded molecule. Furthermore, the protein data bank contains structures measured at widely different thermodynamic conditions (pH value, ionic strength, etc.). Finally, certain properties will be strongly related to specific force-field parameters and only weakly to others. This situation offers the opportunity to reduce the calibration effort by optimizing specific subsets of parameters separately against a limited set of properties.

 © 2006 Wiley-VCH Verlag GmbH & Co. KGaA, Weinheim

Table 4: Choice of calibration sets of data, systems, properties, and thermodynamic phase for the derivation of the GROMOS biomolecular force-field parameter values.[7]

Type of data	Type of system	Phase	Type of properties	Force-field parameter
structural data (exptl)	small molecules	crystalline solid phase	molecular geometry: bond lengths, bond angles	b_0, θ_0, ξ_0
spectroscopic data (exptl)	small molecules	gas phase	molecular vibrations: force constants	K_b, K_θ, K_ξ
thermodynamic data (exptl)	small molecules, mixtures, solutions	condensed phase	heat of vaporization, density, partition coefficient, free energy of solvation	van der Waals: $C_{12}(i,j)$, $C_6(i,j)$, q_i(final)
dielectric data (exptl)	small molecules	condensed phase	dielectric permittivity, relaxation	charges q_i
transport data (exptl)	small molecules	condensed phase	diffusion and viscosity coefficients	$C_{12}(i,j)$, $C_6(i,j)$, q_i
electron densities (theor.)	small molecules	gas phase	quantum-chemical calculation of atom charges	charges q_i(initial)
energy profiles (theor.)	small molecules	gas phase	quantum-chemical calculation of torsional-angle rotational profiles	K_ϕ, δ, m

The following strategy was applied in developing the GROMOS force field (Table 4).[7] The geometric parameters for the covalent interaction terms were obtained from the crystal structures of small molecules, and the corresponding vibrational force constants came from infrared spectroscopic data on small molecules in the gas phase. The nonbonding interaction parameters C_{12}, C_6, and q were obtained by fitting heats of vaporization, densities of pure liquids, and free energies of solvation of small solutes in polar and apolar solvents as obtained from molecular dynamics (MD) simulations to data obtained by experiment. Dielectric permittivities and diffusion properties of liquids were used as secondary data in this parametrization. Electron densities obtained from quantum-mechanical calculations were only used to obtain an initial guess for partial atomic charges, because they may depend strongly on the environment (gas phase or condensed phase) as a result of polarization effects. Torsional-angle parameters were derived by fitting torsional-energy profiles to quantum-mechanical data, thus leaving the set of parameters for the nonbonding interactions untouched.

A biomolecular force field forms, in principle, a consistent set of parameters for both solute molecules (proteins, lipids, saccharides, nucleotides) and solvent molecules (water, alcohols, DMSO, chloroform, etc.). Changing a subset of parameters by taking them from other force fields or models may introduce inconsistencies and inaccuracy.

The simulation of peptide or protein folding (Figure 1) necessitates that the relative free energies of solvation of the 20 amino acid residues in polar solution (water) versus nonpolar solution (cyclohexane) as obtained from simulation compares well with the corresponding experimental data, since these differences are likely to largely determine the driving force for folding. Gibbs free energies of solvation obtained with the GROMOS 53A6 force field[7] are shown in Figure 5. The average absolute deviations from experiment for the 18 amino acid side chains (except Gly and Pro) are 1.0 kJ mol^{-1} in water and 2.0 kJ mol^{-1} in cyclohexane. Both values are smaller than the value of $k_B T$, which makes the 53A6 GROMOS force field suitable for studies on protein folding.

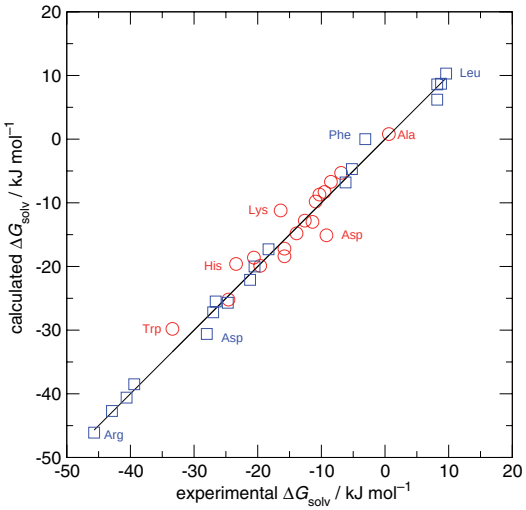


Figure 5. Comparison of the calculated (MD simulation using the GROMOS 53A6 force field) and experimental Gibbs free energies of solvation in cyclohexane (circles) and in water (squares) of 18 amino acid analogues (no Gly and Pro).[7]

© 2006 Wiley-VCH Verlag GmbH & Co. KGaA, Weinheim

2.3. Long-Range Forces

Electrostatic interactions play a major role in biomolecular systems. Compared to covalent and van der Waals interactions, their range is relatively long, because electrostatic interactions between molecules or parts of molecules at a distance r from each other decrease only slowly with increasing value of r:

1. The interaction energy between two charged molecules is proportional to r^{-1}, while the corresponding force, the (negative) spatial derivative of the energy, is proportional to r^{-2}.
2. The interaction energy between a neutral molecule with a dipole moment and a charged molecule is proportional to r^{-2}, while the corresponding force is proportional to r^{-3}.
3. The interaction energy between two neutral molecules with dipole moments is proportional to r^{-3}, while the corresponding force is proportional to r^{-4}.

Continuing this multipole expansion with quadrupole moments, octupole moments, etc. shows that even the interaction between two neutral molecules without dipole moments, but with quadrupole moments is longer ranged (proportional to r^{-5}) than the van der Waals dispersion interaction, which is proportional to r^{-6}. If we consider the electrostatic energy of a single charge, dipole, or quadrupole with all charges, dipoles, and quadrupoles surrounding it, we have to integrate the electrostatic interaction $V^{\mathrm{el}}(r)\,4\pi r^2$ from r to infinity, where $4\pi r^2\,\mathrm{d}r$ is the volume of the spherical shell between r and $r+dr$ surrounding the central charge, dipole, or quadrupole [Eq. (9)].

$$\int_0^\infty V^{\mathrm{el}}(r)\,4\pi r^2\,\mathrm{d}r \tag{9}$$

However, the integral (9) only converges under the conditions of Equation (10):

$$V^{\mathrm{el}}(r) \sim r^{-n},\ n > 3 \tag{10}$$

Thus, the total electrostatic energy of ionic systems depends on the spatial boundary conditions that restrict the range of the integral (9) in practical calculations. The gradual decrease of pair energies and forces with the interatomic separation r means that the results of simulations will depend on the way long-range interactions are treated in the force and energy calculations.

Two techniques are predominantly used currently to evaluate long-range (electrostatic) interactions in biomolecular systems (Figure 6). In the so-called lattice-sum methods the system is put into a particularly shaped box (cubic, rectangular, triclinic, truncated octahedral) and surrounded by an infinite number of identical copies of itself. In this way the boundary problem is moved to infinity, but, unfortunately, is not removed. Moreover, an artificial periodicity is enforced upon the system. Lattice-sum methods are the Ewald summation,[12] the particle–particle/particle–mesh (P^3M) method[13] and the particle–mesh–Ewald (PME) method.[14]

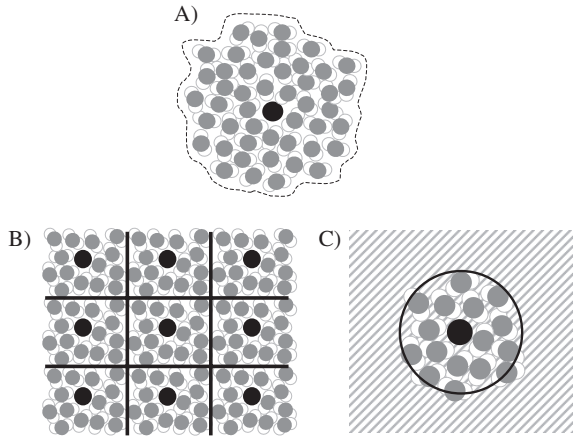


Figure 6. Two methods for calculating long-range electrostatic energies and forces in a molecular system: A) real system with explicit solvent; B) periodicity used in the Ewald, P^3M, and PME methods, and C) continuum approximations beyond a given cut-off distance.

An alternative method is to approximate the medium beyond a given cut-off distance R_{rf} from a specific atom or molecule by a dielectric continuum of uniform permittivity $\varepsilon_{\mathrm{rf}}$ and ionic strength I_{rf}.[15,16] Such a dielectric continuum produces a reaction field in response to the charge distribution inside the cut-off sphere with radius R_{rf}, which can easily be calculated for every atom or molecule [see Equations (7) and (8)]; the constant C_{rf} depends on R_{rf}, $\varepsilon_{\mathrm{rf}}$, and I_{rf}.[10,16]

Both methods are approximations of different type. The reaction-field approach is a mean-field approximation of the real charge distribution beyond a distance R_{rf}, and treats its dielectric response in a spherically symmetric way. It does not introduce artificial periodicity. The lattice-sum approach does not involve averaging, but treats interactions beyond the box size as periodic. Both approximations and their effects have been investigated for various systems.[3–5,17–19]

The effect of different treatments of the long-range electrostatic interactions on the free energy of hydration of a charged (ionic) solute in water is illustrated in Table 5.[20] The results show that the method used to handle long-range forces and its parameters (e.g. R_{rf}) are of great importance when parametrizing a force field. For example, the nonbonding parameters of the OPLS force field[28,29] have generally been obtained from calculations with cut-off radii $R_{\mathrm{c}} = 0.95$–1.5 nm, with the longer-range van der Waals interactions being included through correction formulae (see for example, Ref. [30]). The GROMOS force field was calibrated using $R_{\mathrm{c}} = 1.4$ nm and a reaction field force.

2.4. Testing Biomolecular Force Fields

Having developed a biomolecular force field through calibration of its parameters to reproduce a variety of properties of small molecules, this force field remains to be tested by application to biomolecular systems containing different, larger molecules in the condensed phase. Tests should include proteins, saccharides, or nucleotides in aqueous solution, and comparisons should be made for simulated

 © 2006 Wiley-VCH Verlag GmbH & Co. KGaA, Weinheim

Table 5: Computation of methodology-independent ionic hydration free energies from molecular dynamics simulations with explicit solvent.[a]

Method	N_w	R_{rf}	ΔF_{sim}	ΔF_{ncb}	ΔF_{per}	ΔF_{sum}	ΔF_{srf}	ΔF^0_{hyd}
P^3M	4	–	−45.8	0.0	−293.2	−61.9	−3.54	−390.82
P^3M	8	–	−118.7	0.0	−259.7	−69.8	−1.97	−436.62
P^3M	16	–	−164.8	0.0	−221.5	−74.5	−1.04	−448.15
P^3M	32	–	−209.9	0.0	−183.9	−77.1	−0.54	−457.67
P^3M	64	–	−249.0	0.0	−150.0	−78.4	−0.27	−464.02
P^3M	128	–	−279.8	0.0	−121.1	−79.1	−0.14	−466.45
P^3M	256	–	−303.8	0.0	−97.1	−79.4	−0.07	−466.71
P^3M	512	–	−324.8	0.0	−77.6	−79.6	−0.03	−468.35
P^3M	1024	–	−340.5	0.0	−61.8	−79.7	−0.02	−468.35
P^3M	2048	–	−353.5	0.0	−49.2	−79.7	−0.01	−468.73
RF	512	0.8	−275.9	−128.1	−1.47	−76.8	0.0	−468.55
RF	512	1.0	−298.6	−102.7	−3.76	−77.4	0.0	−468.77
RF	512	1.2	−311.0	−85.7	−6.76	−77.6	0.0	−467.49
RF	1024	0.8	−278.4	−128.1	−0.38	−76.8	0.0	−469.97
RF	1024	1.0	−300.8	−102.7	−1.26	−77.4	0.0	−468.49
RF	1024	1.2	−315.6	−85.7	−2.72	−77.6	0.0	−468.03
RF	2048	0.8	−277.9	−128.1	−0.07	−76.8	0.0	−469.20
RF	2048	1.0	−301.7	−102.7	−0.32	−77.4	0.0	−468.48
RF	2048	1.2	−318.4	−85.7	−0.87	−77.6	0.0	−468.98

[a] Standard hydration free energy ΔF_{hyd} of the sodium cation calculated for different system sizes (number of water molecules N_w) by using the P^3M[13,21,22] or reaction-field[15,16] (with different cutoff radii R_{rf}) methods for the treatment of electrostatic interactions. The SPC water model[23] was used together with the Lennard–Jones ion–water interaction parameters of Straatsma and Berendsen.[24] The simulations were carried out at constant volume, in periodic cubic boxes of edge $L=[(N_w+1)\rho^{-1}]^{1/3}$ with $\rho=33.427\ nm^{-3}$. For the P^3M method a spherical hat charge-shaping function of width 0.4 nm (or 0.26 nm for $N_w \leq 32$) was used,[25] together with an assignment function of order three, a finite-difference operator of order two, three alias vectors for the calculation of the optimal influence function, and a grid spacing of 0.05 nm (or 0.0166 nm for $N_w \leq 32$).[21] For the RF method, the reaction-field radius was set to R_{rf} and the solvent permittivity to 66.6. A cut-off truncation was applied based on the oxygen atom as the molecular center. The raw charging free energies ΔF_{sim} (calculated from the simulations using the scheme proposed by Hummer et al.,[26] based on three ionic charge states of 0, 0.5, and 1 *e*) are corrected (based on a solvent permittivity of 66.6 and an approximate ionic radius of 0.2 nm) for the effect of non-Coulombic interactions ΔF_{ncb}, for artificial periodicity ΔF_{per}, for the use of an improper summation scheme for the electrostatic potential ΔF_{sum} (conversion from P-sum to M-sum convention[27]), for the effect of the interfacial potential at the ionic surface on the average potential within the computational box ΔF_{srf}, for the work of cavity formation (ΔF_{cav}; 5.67 kJ mol^{-1}), and for the compression work ΔF_{cmp} (7.95 kJ mol^{-1}; corresponding to the standard-state correction for a gas at a reference pressure of 1 bar), leading to final standard (intrinsic) values ΔF^0_{hyd}.

properties with available experimental values of measurable ones. Here, one may think of comparing simulated conformational distributions in crystals with averages derived from measured X-ray diffraction data. NOE (nuclear Overhauser effect) intensities, ^3J-coupling constant, and chemical shift values calculated from simulations of solutes in solution may be compared with the corresponding averages derived from NMR experiments. However, reproduction by simulation of a particular folded structure derived from experiment is neither a necessary[31] nor a sufficient condition for a force field to be correct. The force field should be able to reproduce the conformational distribution of the solute as a function of the thermodynamic conditions; for example, it should predict the correct melting temperature of a particular fold.

A particular challenge to biomolecular force fields is the prediction of the fold of a polypeptide in solution as a function of its amino acid residue composition and the type of solvent. How well this challenge is met by the GROMOS force field is illustrated in Figures 7 and 8. Using the GROMOS force-field parameter sets, 43A1 and 45A3 left-handed or right-handed helices of different types as well as β turns were found as dominant conformations in MD simulations of β- and α-peptides in methanol or water (Figure 7), a result that is in agreement with the dominant conformations derived from NOE data.[32–37] However, since these parameter sets were shown to underestimate the magnitude of the hydration (Gibbs) free energies for amino acid analogues,[7,38,39] a reparametrization was carried out which led to the 53A6 set.[7] Figure 8 illustrates the improvement obtained by including solvation free energies of polar compounds into the calibration set in the context of the prediction of the correct fold of a β-dodecapeptide containing many polar side chains. While the 45A3 set could not reproduce the experimentally observed helix, the 53A6 set did. Properties that are less sensitive to small (free) energy differences were, however, well reproduced by both parameter sets.[36]

Thus, a particular force field can only be (in)validated by investigating molecular or system properties that are sensitive to the particular simulation parameters and conditions.

2.5. Perspectives in Force-Field Development

There is still room for improvement in current biomolecular force fields. First, the van der Waals parameters and partial charge distributions of charged moieties should be based on free energies of solvation, as has been done for those of apolar and polar neutral moieties.[7] Examples of such groups are the side chains of Arg, Lys, Asp, and Glu amino acid residues or phosphate groups occurring in DNA, RNA, and lipids. However, this is easier said than accurately done

 © 2006 Wiley-VCH Verlag GmbH & Co. KGaA, Weinheim

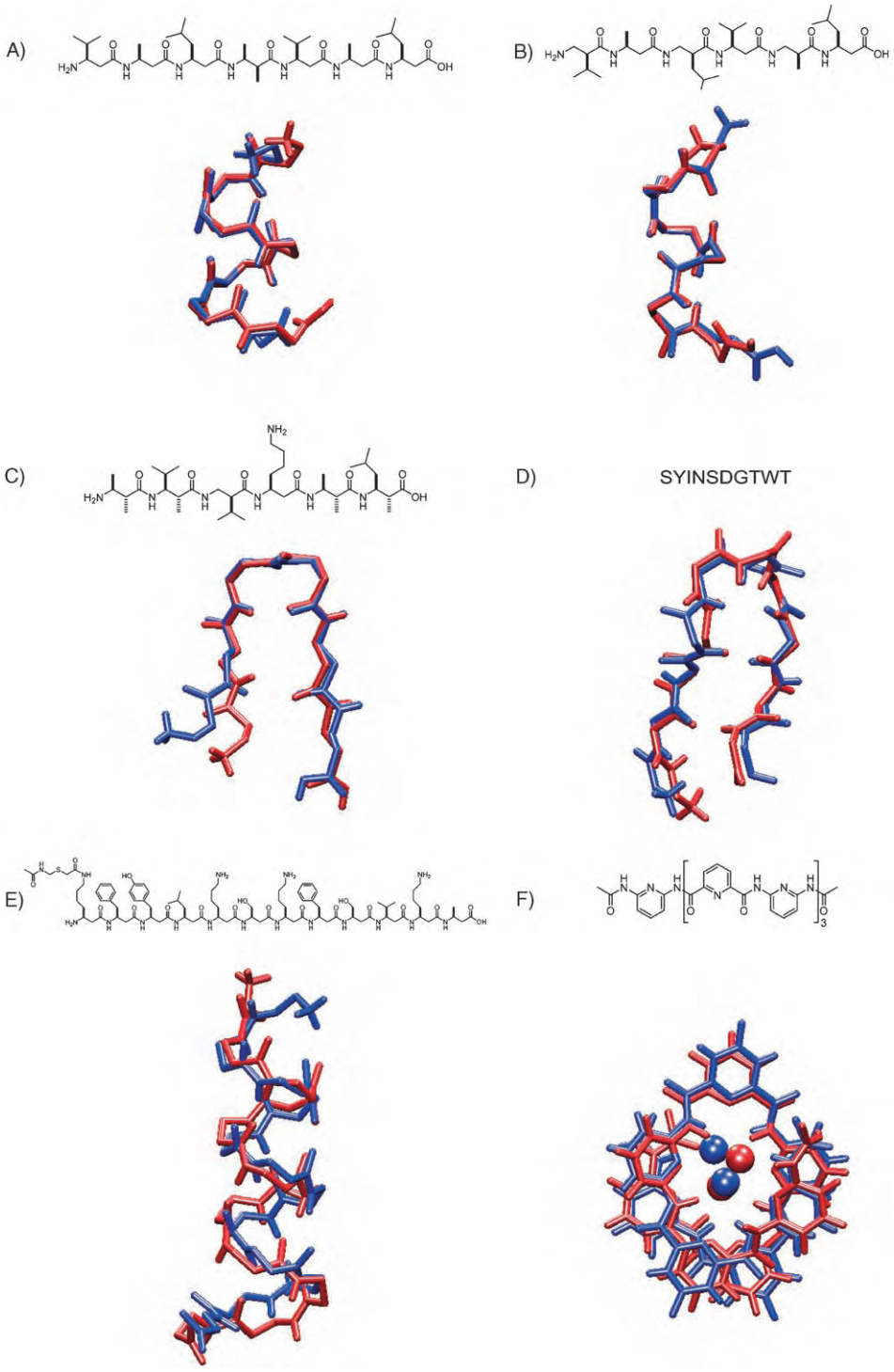


Figure 7. Folding of different polypeptides and peptoides into different folds in different solvents by MD simulation. The folded structure (red), modeled from the available NMR or X-ray experimental data, is superimposed on a folded structure (blue) representing the most populated conformation from the MD simulations of the folding/unfolding equilibrium.[32–37] The solvents are methanol (A–C, E), water (D), and water or chloroform (F). The versions of the GROMOS force field used are: 43A1 (A–D), 45A3 (F), and 53A6 (E).

because of the large solvation free energies of single ions (of the order of several hundred $k_B T$) and the technical difficulties in obtaining such data from experiment[40] and from simulations.[27]

Second, the properties of solvent mixtures, as these are used in experimental protein denaturation studies, should be evaluated as a function of their composition. The thermodynamic properties, such as energy and density of mixing, are of particular importance when the free energy of solvation and folding of solutes is to be calculated.[8,9,41–43] The properties of a mixture of two solvents need not be a linear function of its composition, as illustrated for water/dimethyl sulfoxide (DMSO) mixtures in Figure 9. Only the dielectric permittivity ε shows a linear behavior, while the other properties considered show different types of nonlinearity.[42]

Currently used biomolecular force fields treat the electronic polarization of the molecules in an average manner, which leads, however, to limited accuracy when systems under varying dielectric conditions are considered.[44–48] The limitation could be removed by the introduction of explicit polarizability into biomolecular force fields,[49,50] which requires, however, a more or less complete reparametrization of the force field, followed by extensive testing for realistic systems. Clearly, this is a formidable task. Recently, the first polarizable biomolecular force fields have been proposed.[51–53] Their performance in solvation free energy calculations or in reproducing folding equilibria has not yet been reported, and should be investigated.

To be able to efficiently simulate large biomolecular systems and slow processes, such as membrane or micelle formation, it would be helpful to formulate so-called coarse-grained molecular models, in which a number of covalently bound atoms are treated as a single particle or bead.[54–59] Such models can be made orders of magnitude faster in simulations than atomic models, at the expense of losing atomic detail. Models of this type have been successfully applied to membrane and micelle formation.[60] A comparison of the properties obtained from coarse-grained models with those from atomic models is required to evaluate the effect of the approximations and simplifications made.

 © 2006 Wiley-VCH Verlag GmbH & Co. KGaA, Weinheim

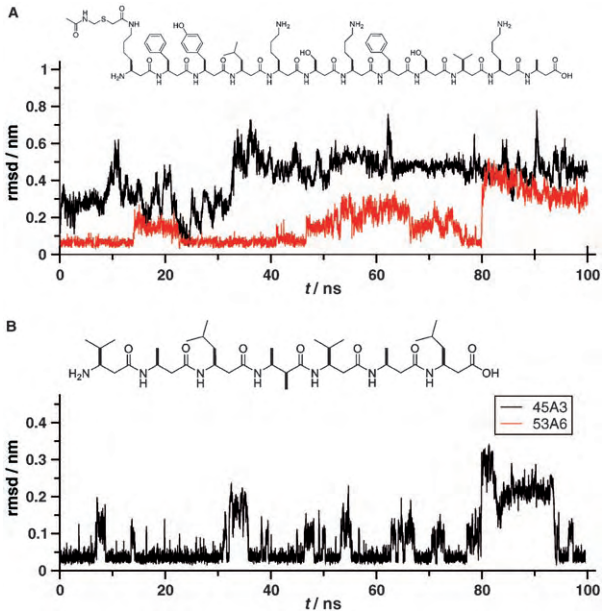


Figure 8. Root-mean-square deviation (rmsd) of the positions of backbone atoms in MD trajectory structures from the helical model structures derived from NMR data for two β-peptides in methanol. A) The peptide containing polar side chains only shows the experimental fold with the newer force-field parameter set 53A6.[36] B) The other peptide is equally well folded by using the old (45A3) and the new (53A6) force fields, and only data for the former are shown.

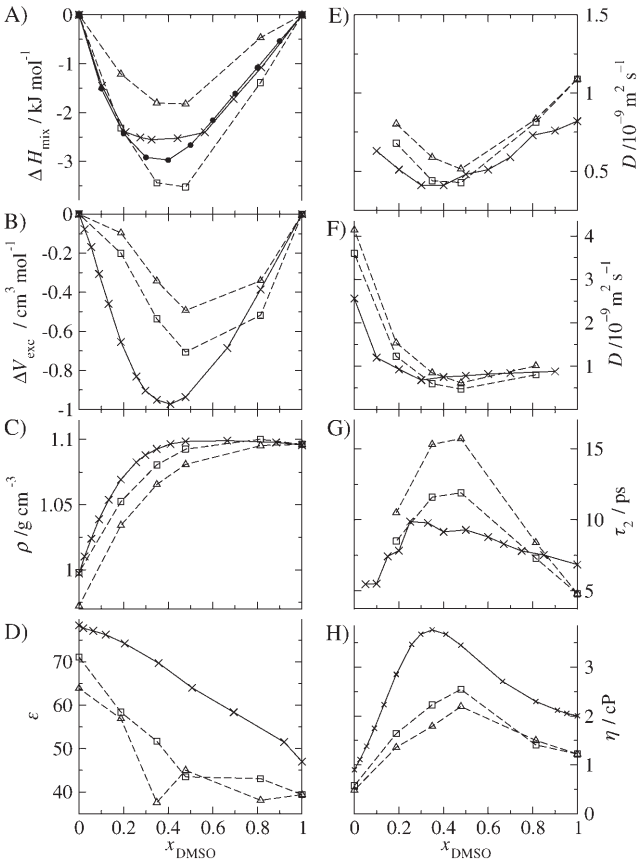


Figure 9. Properties of water/DMSO mixtures at 298 K and 1 atm as a function of the mole fraction of DMSO (x_{DMSO}) from MD simulations.[42] ΔH_{mix}: mixing enthalpy, ΔV_{exc}: excess volume, ρ: density, ε: relative dielectric permittivity, D: diffusion coefficient (panel E: DMSO, panel F: water), τ_2: rotational correlation time (DMSO), η: shear viscosity. Values from simulation: △ SPC water model, □ SPC/L water model; experimental values: × and ●.

3. The Search Problem

A biomolecular system is generally characterized by a very large number of degrees of freedom (10^4–10^6 or more). The motions along these degrees of freedom show a variety of characteristics, from highly harmonic to anharmonic, chaotic, and diffusive. Moreover, correlations are present that cover a wide range of time and spatial scales, from femtoseconds and tenths of nanometers to milliseconds and micrometers. The energy hypersurface of such a system, which is defined by the potential-energy function [e.g. Eqs. (1)–(8)], is therefore a very rugged surface, with energy basins and mountains of a wide range of depths or heights and spatial extent. This makes the search for the global energy minimum of such a high-dimensional function—or rather the search for those regions of the surface that contribute most to the free energy of the system—a daunting if not impossible task.

As mentioned before, the state of a biomolecular system cannot be described by a single global minimum energy configuration or structure, but only by a statistical-mechanical ensemble of configurations, in which the weight of a configuration x is given by the Boltzmann factor [Eq. (11); k_B is the Boltzmann constant and T the (absolute) temperature].

$$P(x) \sim \exp\left(-V(x)/k_B\,T\right) \tag{11}$$

The exponential weighting in Equation (11) implies that high-energy regions of the energy hypersurface will not contribute configurations that are relevant to the state of the system, unless they are very numerous (entropy). The equilibrium properties of the system are dominated by those parts of configuration space, for which $V(x)$ is low. Therefore, one of the fundamental challenges to biomolecular modeling is to develop methodology to efficiently search the vast biomolecular energy surface for regions of low energy.

Below, we only mention and classify the major techniques that are currently used to search and sample configuration space.[61–63] There are also search and sampling techniques in which not only the molecular coordinates x serve as variables, but also their Boltzmann probabilities $P(x)$. A discussion and examples of these so-called probability search techniques can be found in Refs. [61, 64, 65]

3.1. Methods to Search and Sample Configuration Space

A variety of search methods is available, each with its own particular strengths and weaknesses, which depend on the form of the function $V(x)$ and the number and types of degrees of freedom in the system. Two basic types of search methods can be distinguished: systematic and heuristic.

Systematic or exhaustive search methods scan the complete or a significant fraction of the configuration space of the

 © 2006 Wiley-VCH Verlag GmbH & Co. KGaA, Weinheim

biomolecular system. Particular subspaces can be excluded from the search without reduction in the quality of the solution found by applying rigorous arguments that mean that these subspaces cannot contain the desired solution.[66] Such arguments are based on a priori knowledge, often of physical or chemical nature, about the structure of the space or energy hypersurface to be searched. Systematic search techniques can only be applied to small molecules with only a few degrees of freedom,[67–70] because of the exponential growth of the required computing effort as the number of degrees of freedom included in the search increases.

Heuristic search methods, although visiting only a tiny fraction of the configuration space, aim at generating a representative (in the Boltzmann weighted sense) set of system configurations. These methods may generally be divided into three types (see also Table 7:

1. Nonstep methods, in which a series of system configurations is generated, which are independent of each other. An example is the so-called distance-geometry metric-matrix method,[72,73] which generates, at least in principle, an uncorrelated series of random configurations for a search problem that can be cast into a distance-based form.
2. Step methods that build a complete molecular or system configuration from configurations of fragments of the molecule or system in a step-wise manner. Examples are the build-up procedure of Gibson and Scheraga,[74,75] combinatorial build-up methods that make use of dynamic programming techniques,[76] and Monte Carlo (MC) chain-growing methods,[77,78] such as the so-called configurational bias Monte Carlo (CBMC) technique.[79]
3. Step methods, such as energy minimization (EM), Metropolis Monte Carlo (MC), molecular dynamics, and stochastic dynamics (SD),[80] that generate a new configuration of the complete system from the previous configuration. These methods can be further classified according to the way in which the step direction and step size are chosen (see Table 6). Energy minimization can be based on only energy values and random steps (simplex methods), or on energy and energy gradient values (steepest-descent and conjugate-gradient methods), or on second-order derivatives of the energy (Hessean matrix methods). In MC methods the step direction is taken at random, and the step size is limited by the Boltzmann acceptance criterion: when the energy of the system changes by $\Delta V < 0$, the step in configuration space is accepted, while for $\Delta V > 0$, the step is accepted with probability $\exp(-\Delta V/k_B T)$. In MD simulation the step is determined by the force (the negative of the local gradient $\partial V/\partial x$) and the inertia of the degrees of freedom, which serves as a short-time memory of the path followed so far. In SD simulations a random component is added to the force, the size of which is determined by the temperature of the system and the atomic masses and friction coefficients. In the potential-energy contour tracing (PECT) algorithm[81] and in the potential-energy annealing conformational search (PEACS) algorithm[71] the energy values are monitored and kept constant (PECT) or annealed (PEACS) to locate saddle points and pass over these. There exists a large variety of search procedures based on stepping through configuration space using a combination of the five mentioned basic elements (energy, gradient, Hessean, memory, and randomness) combined in one way or another.[61]

Table 6: Heuristic methods to search configuration space for configurations x with low energy $V(x)$.[a]

Reason for the change	Method				
	EM	MC	MD	SD	PEACS
energy	yes	yes	no	no	yes
energy gradient	yes	no	yes	yes	yes
second derevative of the energy	yes	no	no	no	no
memory	no	no	yes	yes	yes
randomness	yes	yes	no	yes	no

[a] EM: energy minimization, MC: Monte Carlo, MD: molecular dynamics, SD: stochastic dynamics, PEACS: potential energy annealing conformational search.[71]

The efficacy of search methods for biomolecular systems is severely restricted by the nature of the energy hypersurface $V(x)$ that is to be explored to find low-energy regions. The occurrence of a multitude of high-energy barriers between local minima means that the radius of convergence of the step methods is generally very small. Therefore, a variety of techniques has been developed to enhance the search and sampling power of searching methods. Three general types of search and sampling enhancement techniques are distinguished in Table 7.[61]

Table 7: Techniques to enhance the searching and sampling power of simulation methods.[a]

1. Deformation or smoothening of the potential-energy surface
a) omission of high-resolution structure factor data in structure refinement based on X-ray diffraction data
b) gradual introduction of longer range distance bounds - in structure refinement based on NOE data[82]
c) softening of the hard core of atoms in the nonbonding interaction ("soft-core" atoms)[83]
d) reduction of the ruggedness of the energy surface through a diffusion-equation type of scaling[83,84]
e) avoiding the repeated sampling of an energy well through local potential-energy elevation or conformational flooding[85,86]
f) softening of geometric restraints derived from experimental data (NMR, X-ray) through time averaging[87,88]
g) circumvention of energy barriers through an extension of the dimensionality of the Cartesian space (4D-MD)[89]
h) freezing of high-frequency degrees of freedom through the use of constraints[90]
i) coarse-graining the model by reduction of the number of interaction sites[54–59]

2. scaling the system parameters
a) temperature annealing[91]
b) mass scaling[92]
c) mean-field approaches[93]

3. multicopy searching and sampling
a) genetic algorithms[94]
b) replica-exchange and multicanonical algorithms[62]
c) cooperative search: SWARM [95]

[a] For details see Refs. [60–62] and references therein.

 © 2006 Wiley-VCH Verlag GmbH & Co. KGaA, Weinheim

3.1.1. Deformation or Smoothening of the Potential-Energy Hypersurface to Reduce Barriers

a) Generally, a smoothening of the potential-energy function $V(x)$ allows for a faster search for its minima. This technique has been applied to different problems, such as structure determination based on X-ray diffraction or NMR spectroscopic data, conformational search, and protein-structure prediction. In method Ia of Table 7, the electron density of a biomolecular crystal is smoothed by the omission of high-resolution diffraction intensities when back calculating the electron density from these through Fourier transforms. This smoothening enhances the radius of convergence of the structure refinement.

b) When building a protein structure from atom–atom distance data obtained from NMR spectroscopy, the convergence of the configurational search process is enhanced by gradually introducing distance restraints that connect atoms at longer distances along the polypeptide chain in the potential-energy function. This is called a variable-target function method.[82]

c) The hard core of atoms, that is, the strong repulsive interaction between overlapping atoms, is responsible for many barriers on the energy hypersurface of a molecular system. These barriers can be removed by making the repulsive short-range interactions between atoms "soft".[96–99] Atoms with soft cores smooth the energy surface and lead to strongly enhanced sampling.[83]

d) In the deformation methods based on the diffusion equation,[83,84] the deformation of the energy surface during a simulation is made proportional to the local curvature (second derivative) of the surface, which leads to a preferential smoothening of the sharpest peaks and valleys in the surface and a very efficient search.

e) Incorporation of information on the energy hypersurface obtained during the search into the potential-energy function is another possibility to enhance sampling. Once a local energy minimum is found, it is removed from the energy surface by a suitable local deformation of the potential-energy function. This idea is the basis of the deflation method,[100] the local-elevation search method,[85] recently also called meta-dynamics[101], and the method of conformational flooding.[86]

f) Another way to introduce a memory into the search is the use of a potential-energy term which uses a running average of a coordinate over the trajectory or ensemble generated so far rather than its instantaneous value.[102] Application of this type of time-dependent or ensemble-dependent restraints in protein-structure determination based on NMR spectroscopic or X-ray data leads to a much enhanced sampling of the molecular configuration space.[87,88]

g) Barriers in the energy hypersurface can be circumvented by an extension of the dimensionality of the configuration space beyond the three Cartesian ones. The technique of energy embedding locates a low-energy conformation in a high-dimensional Cartesian space and gradually projects this conformation to three-dimensional Cartesian space while perturbing its energy and configuration as little as possible.[103] Variations on the original procedure have been proposed.[104–107] Dynamic search methods can also be used in conjunction with an extension of the dimensionality. Energy barriers in three-dimensional space can be circumvented by performing MD simulations in four-dimensional Cartesian space,[89] and free-energy changes can be calculated.[108]

h) A long-used standard technique to smooth the energy surface is to freeze the highest-frequency degrees of freedom of a system through the application of constraints.[90,109–113] Bond-length constraints are applied as standard in biomolecular simulation and allow for a four times longer time step.[114] High-frequency motion can also be eliminated by using soft constraints:[115] the (bond-) constraint lengths change adiabatically as a result of the forces.

3.1.2. Scaling of System Parameters To Enhance Sampling

a) The technique of simulated temperature annealing[91] involves simulation or search at a high temperature T, followed by gradually cooling the system. By raising the temperature, the system may more easily surmount energy barriers, so a larger part of configurational space can be searched. The technique of simulated temperature annealing has been widely used in combination with MC, MD, and SD simulations. An example of potential-energy annealing can be found in Ref. [71].

b) Scaling of atomic masses can be used to enhance sampling. In the classical partition function and in case no constraints are applied, the integration over the atomic momenta can be carried out analytically, separately from the integration over the coordinates. Thus, the atomic masses do not appear in the configurational integral, which means that the equilibrium (excess) properties of the system are independent of the atomic masses. This freedom can be exploited in different ways to enhance the sampling. By increasing the mass of specific parts of a molecule, its relative inertia is enhanced, which eases the surmounting of energy barriers,[92] and may allow for larger time steps.

c) Enhanced sampling by a mean-field approximation is obtained by separating the biomolecular system into two parts (A and B), each of which moves in the average field of the other. The initial configuration of the system consists of N_A identical copies of part A and N_B identical copies of part B. The positions of corresponding atoms in the identical copies may be chosen to be identical. The force on atoms of each copy of part A exerted by the atoms in all copies of part B is scaled by a factor $N_B{}^{-1}$ to obtain the mean force exerted by part B on the individual atoms of part A. Likewise, the force on atoms of each copy of part B exerted by the atoms in all copies of part A is scaled by a factor $N_A{}^{-1}$. The forces between different copies of part A are zero, and so are the forces between different copies of part B. The MD simulation involves the integration of Newton's Equation of motion, $\boldsymbol{f} = m\boldsymbol{a}$, for all copies of parts A and B simultaneously. Thus, one obtains N_A individual trajectories of part A in the mean

 © 2006 Wiley-VCH Verlag GmbH & Co. KGaA, Weinheim

field of part B and vice versa. This situation comes at the loss of correct dynamics: Newton's third law, $\boldsymbol{f}_{AB} = -\boldsymbol{f}_{BA}$ is violated. The technique only enhances efficiency when the system is partitioned into parts of very different sizes (for example, $A \ll B$) and the bigger part is represented by one copy: $N_B = 1$. Enhanced searching and sampling procedures based on a mean-field approximation have been proposed in different forms,[93,116–127] and have been applied to the diffusion of CO molecules in the field of a protein molecule,[93,118] to the conformational equilibrium of protein side chains,[117] to the determination of protein-loop conformations,[123] and to the search for the minimum-energy conformations of polypeptides[126,127] and nucleic acid segments[128] as well as to the search for binding sites in enzymes.[129–131]

3.1.3. Multicopy Simulation with a Given Relationship between the Copies

In the mean-field approach, multiple copies of a part of the system were simulated. This idea has also been used in other ways to enhance searching and sampling (Table 7).

a) In genetic algorithms[132] a pool of copies of the biomolecular system in different configurations is considered, and new configurations are created and existing ones deleted by mutating and combining (parts of) configurations according to a given set of rules.
b) In the so-called replica-exchange algorithm multiple copies of the system are simulated by MC, MD, or SD, each at a distinct temperature. From time to time copies from simulations close in temperature are exchanged through an exchange probability based on the Boltzmann factor [Eq. (11)]. This leads, within the limit of infinite sampling, to Boltzmann-distributed (canonical) ensembles for each temperature.[133] So-called multicanonical algorithms are a generalization of this procedure.[62] These types of algorithms have been used to simulate proteins in vacuo.[133] The inclusion of solvent degrees of freedom may impair the efficiency of the algorithm.[134] Dynamic information is lost in the exchanges and for short sampling times the entropy content is likely to be biased at the lower and upper ends of the temperature range considered.
c) The so-called SWARM type of MD[95] is based on the idea of combining a collection (or swarm) of copies of the system each with its own trajectory into a cooperative multicopy system that searches configurational space. To build such a cooperative multicopy system, each copy is, in addition to physical forces arising from $V(x)$, subject to (artificial) forces that drive the trajectory of each copy towards an average of the trajectories of the swarm of copies. This effect is analogous to the intelligent and efficient behavior of a whole swarm of insects which can be achieved even in the absence of any particular intelligence or forethought of the individuals. SWARM-MD is less attracted by local minima and is more likely to follow an overall energy gradient toward the global energy minimum.

This overview of methods to search and sample configurational space is rather limited. More extensive reviews can be found in Refs. [61–63] Since biomolecular configurational space is too large to be exhaustively sampled, one generally has to use heuristic search methods in biomolecular modeling studies. The overview (Tables 6 and 7) of types of methods and tricks that can be used and combined to obtain a powerful search method may assist in the choosing of a combination of methods and tricks that will be particularly suited to the specific problem or energy hypersurface of interest.

3.2. Convergence of Simulated Properties

The time scales involved in the dynamics of different properties of biomolecular systems range from femtoseconds to seconds or even longer. Limited computing power means that current MD simulations of biomolecular systems cover nanoseconds to tens or hundreds of nanoseconds, depending on the system size. This poses the question as to whether such time periods are long enough to yield reliable trajectory averages for the different molecular or system properties. Trajectory averages will generally only be representative when the equilibration period of a simulation τ_{equil} is longer than the relaxation time $\tau_{relax}(Q)$ of the property Q [Eq. (12)] and when the sampling period τ_{sample} is much longer than $\tau_{relax}(Q)$ [Eq. (13)].

$$\tau_{equil} > \tau_{relax}(Q) \tag{12}$$

$$\tau_{sample} \gg \tau_{relax}(Q) \tag{13}$$

If conditions (12) or (13) are not fulfilled, the trajectory average $\langle Q(t)\rangle_t$ of the property Q will display a drift with time or erratic behavior.[135–137]

The time scale associated with the change or relaxation of a particular physical quantity calculated for a particular biomolecular system will depend on 1) the type of molecular system, 2) the thermodynamic state point, and 3) the particular quantity or property. This relationship is illustrated in Figure 10 for the dynamics of β-heptapeptides in methanol solution. At 298 K the dominant conformer is the 3_{14}-L helix, which completely unfolds and refolds only a few times within 100 ns (panel A). At 340 K many more (un)folding events are observed (panel B). Reducing the solvent viscosity to 1/3 (Panel C) or to 1/10 (Panel D) enhances the rate of the (un)folding process considerably, and leads to improved convergence of the statistics for the (un)folding equilibrium. Panel E illustrates that the presence of longer and charged side chains in the polypeptide solute slows down the (un)folding process, thereby reducing the sampling (compare with panel B).

Not only can different molecules or thermodynamic state points show different relaxation times, but different properties also can do so. The potential energy of the solute and the square of its total dipole moment (related to its dielectric permittivity) relax faster than, for example, the average atom-positional root-mean-square fluctuations for all atoms.[140,141] System properties, such as the free energy of folding,

 © 2006 Wiley-VCH Verlag GmbH & Co. KGaA, Weinheim

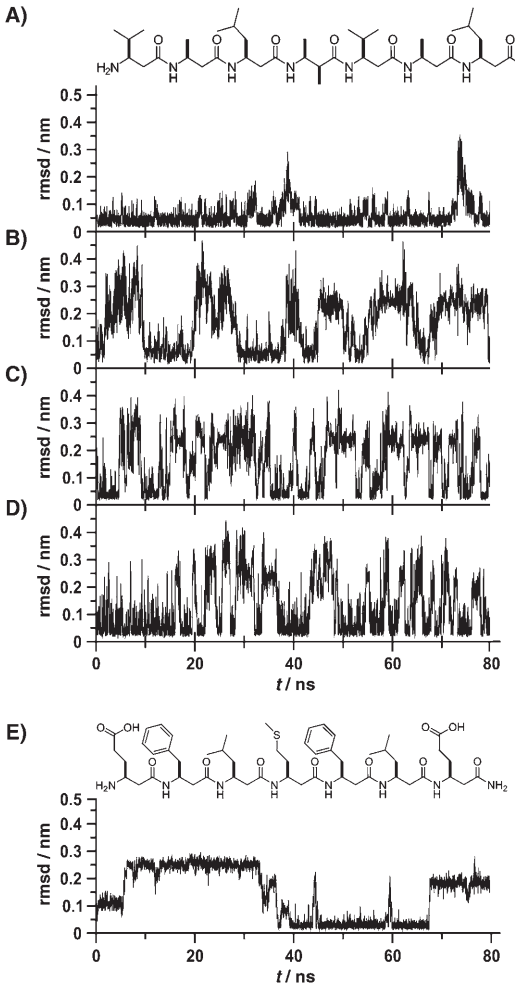


Figure 10. Root-mean-square deviation of the positions of backbone atoms in MD trajectory structures from the helical model structures derived from NMR data for two β-heptapeptides of identical chain lengths in methanol at 1 atm. The peptide with apolar side chains is simulated at 298 K (A) and at 340 K (B–D).[32,138] The viscosity of the methanol solvent is reduced by a factor of 3 (C) and by a factor of 10 (D) through mass scaling. Raising the temperature or reducing the solvent viscosity increases the rate of (un)folding. The peptide with a few polar side chains is simulated at 340 K in normal methanol (E). The polar side chains reduce the rate of (un)folding.[139]

converge even slower—in general more slowly than molecular properties.[1,142]

The relaxation and dynamics of the various properties of a biomolecular system can be analyzed in different ways:[135–137]

1. For equilibrium simulations one may monitor the time series of a property $Q(t)$, its average value $\langle Q(t)\rangle_t$, or fluctuations $\langle(Q(t)-\langle Q(t)\rangle_t)^2\rangle_t^{1/2}$, or calculate its autocorrelation function $\langle Q(t')Q(t'+t)\rangle_{t'}$. The decay time of the autocorrelation function or the build-up rate of the trajectory averages gives an indication of the magnitude of $\tau_{relax}(Q)$.[137]
2. When starting a simulation from a non-equilibrium initial state, the rate of relaxation of $Q(t)$ toward equilibrium, measured over many non-equilibrium trajectories, will give an indication of $\tau_{relax}(Q)$.
3. If different MD simulations starting from different initial states do not converge to the same trajectory average for property Q, it can be concluded that $\tau_{relax}(Q)$ is longer than the simulation period.[143]

Further examples of different relaxation times of properties in various systems can be found in Refs. [135–137, 140–143].

3.3. Alleviation of the Search and Sampling Problems

Although the search and sampling problem with regard to biomolecular systems looks formidable at first sight, the characteristics of the energy hypersurface may alleviate these problems. Simulations of (un)folding equilibria of polypeptides in solution using a thermodynamically calibrated force field and an explicit representation of the solvent molecules have shown that the unfolded or denatured state of these polypeptides contains much fewer conformations significantly populated at equlilibrium than there are possible polypeptide conformations. In the case of peptides possessing 20 rotatable torsional angles in their backbone, the use of physical, realistic force fields representing the particular (nonbonding) interactions between the various residues results in a reduction from 10^9 possible conformers to 10^3 relevant conformers.[144–146] This is illustrated in Figure 11, where the number of conformations visited during a MD simulation of a polypeptide and of another polymer of equal length are shown. This number grows sublinearly for the β-heptapeptide in methanol and levels off at about 200 conformations (Figure 11 A), whereas the number of visited (relevant) conformations for a poly(hydroxybutanoate) molecule of similar length in chloroform grows linearly with time (Figure 11 B), as would be expected considering the number of possible conformations for either molecule is about 10^9. The difference is due to the presence of hydrogen-bond donor and acceptor atoms in the β-heptapeptide, which restrict (through favorable hydrogen bonding) the conformational space accessible to the molecule

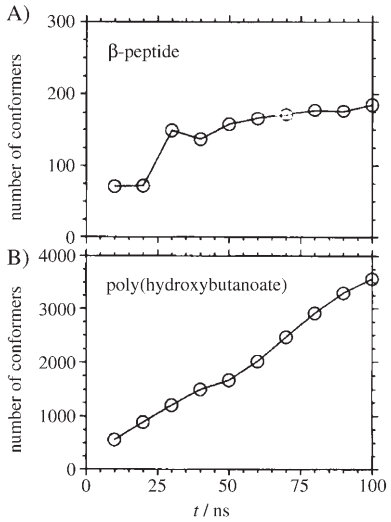


Figure 11. Number of conformations as a function of time from MD stimulation: A) A β-heptapeptide in methanol at 340 K;[138] b) $(Val\text{-}Ala\text{-}Leu)_2$-3-hydroxybutanoate in chloroform at 298 K.[147] For the definition of a conformation (cluster of structures) we refer to Ref. [138].

 © 2006 Wiley-VCH Verlag GmbH & Co. KGaA, Weinheim

at the given temperature. In the absence of hydrogen-bond donors in poly(hydroxybutanoate), this restriction is not present.[147]

When a realistic force field is used, most of the configuration space will have a very high energy, which indicates that the configuration space to be searched or sampled to predict the most stable fold of a polypeptide or protein does not grow exponentially with the system size or chain length.[144]

3.4. Aggravation of the Search and Sampling Problems

The free energy F of a system of N particles in a volume V at temperature T is a $6N$-dimensional integral over all particle coordinates $\boldsymbol{r}$ and momenta $\boldsymbol{p}$ of the Boltzmann factor of the system Hamiltonian (kinetic plus potential energy) [Eq. (14); h is Planck's constant)].

$$F_{NVT} = -k_B T \ln\left((N!\,h^{3N})^{-1} \int\int \exp(-H(\boldsymbol{p},\boldsymbol{r})/k_B T)\mathrm{d}\boldsymbol{p}\,\mathrm{d}\boldsymbol{r}\right) \quad (14)$$

The factor $N!$ must be omitted when dealing with distinguishable particles. Since the integrand—the Boltzmann factor—is everywhere positive, the omission of configurations in the integral leads to systematic (not canceling) errors. Equation (14) shows that not only will the global minimum energy structure or configuration determine the free energy or be representative for the configurational ensemble, but other configurations of higher energy and greater abundance will also do so. In other words, both energy U and entropy S contribute to the free energy [Eq. (15)].

$$F = U - TS \quad (15)$$

Solvent degrees of freedom may contribute significantly to the free energy of folding.[148] From a 200-ns MD simulation of the (un)folding equilibrium of a β-heptapeptide in methanol, the differences between the enthalpy H_{solute} and entropy S_{solute} of the peptide in the folded conformation and in the unfolded conformations could be calculated as $\Delta H^{folding}_{solute} = -64\ kJ\,mol^{-1}$ and $T\Delta S^{folding}_{solute} = -157\ kJ\,mol^{-1}$, which yields $\Delta G^{folding}_{solute} = +93\ kJ\,mol^{-1}$. However, the Gibbs free energy of folding as calculated for the whole system (peptide plus solvent) from the ratio between the folded and unfolded conformations appeared to be $\Delta G^{folding} = -8\ kJ\,mol^{-1}$. Thus, changes in solute free energy alone cannot explain the observed folding behavior. This underlines the important role of the solvent in peptide folding and that entropy calculations including solvent degrees of freedom are needed. Unfortunately, extensive sampling of solvent degrees of freedom aggravates the sampling problem.

Figure 12 illustrates another example of the observation that an ensemble of relevant conformations needs to be sampled to obtain accurate estimates of the free energy. It shows a superposition of the configurations of a protein–ligand complex that contribute most to the free energy of binding of the biphenyl ligand to the ligand-binding domain of the estrogen receptor. The configurations show sizeable

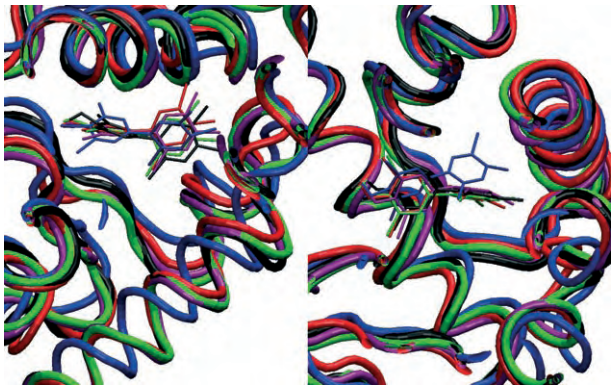


Figure 12. Calculation of the free energy of binding of 16 hydroxylated polychlorinated biphenyls to the ligand-binding domain of the estrogen receptor using MD simulation and the one-step perturbation technique.[149] Five protein–ligand structures that contribute most to the free energy of binding of a particular ligand are shown.

variation, and choosing only one of them to represent the ensemble would lead to an inaccurate estimate of the binding free energy.[149] In contrast to the assumptions of many standard ligand–protein docking algorithms, this example illustrates that inclusion of protein degrees of freedom in the sampling is probably necessary to obtain accurate results. This, unfortunately, aggravates the search and sampling problem of docking algorithms.

A last example of the aggravation of the sampling problem is the dependence of the magnitude of the hydrophobic effect on the size of a hydrophobic cluster and the composition of the solvent. Understanding the hydrophobic effect at the molecular level will help to understand the driving forces for protein folding in which this effect is thought to play an essential role. Figure 13 shows the free energy of cluster growth for clusters with 2 to 46 methane

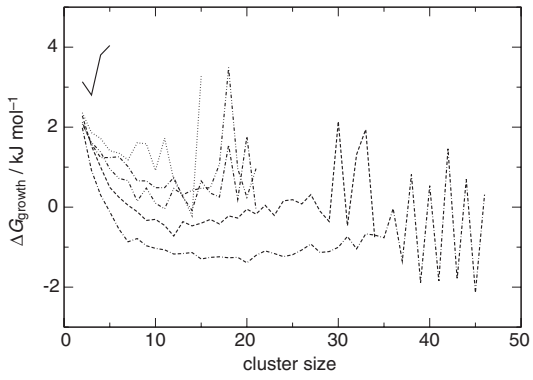


Figure 13. Gibbs free energy of methane cluster growth as a function of the cluster size for MD simulations of different methane/urea/water mixtures.[150] N_m is the number of methane molecules, N_u the number of urea molecules, and N_w the number of water molecules. Solid line: $N_m = 10$, $N_u = 0$, $N_w = 990$; dotted line: $N_m = 40$, $N_u = 0$, $N_w = 960$; dot-dashed line: $N_m = 50$, $N_u = 150$, $N_w = 800$; double dot-dashed line: $N_m = 50$, $N_u = 250$, $N_w = 700$; dashed line: $N_m = 50$, $N_u = 0$, $N_w = 950$; dot-double dashed line: $N_m = 64$, $N_u = 250$, $N_w = 686$; Large fluctuations at the end of the curves stem from poor statistics for large cluster sizes.

 © 2006 Wiley-VCH Verlag GmbH & Co. KGaA, Weinheim

molecules in urea/water mixtures at different urea concentrations.[150] Methane aggregation and cluster formation only becomes favorable at cluster sizes of at least five methane molecules. A second observation is that high urea concentrations result in slightly enhanced clustering of methane molecules, rather than in a reduction of the hydrophobic interactions. This result hints against a mechanism of protein denaturation by urea through a weakening of hydrophobic interactions.[151] The sampling problem is aggravated by the observed dependence of the free energy on the cluster size and urea concentration, because both these degrees of freedom need to be varied to obtain meaningful results.

3.5. Perspectives Regarding the Search and Sampling Problem

There is certainly still room to enhance the search and sampling efficiency of biomolecular simulation techniques; however, the past ten years have already shown encouraging progress that we expect to be of benefit also for the study of larger, more interesting and relevant biomolecular systems. In particular the technique of smoothening the potential-energy surface can enhance sampling through the use of soft-core atoms, local-elevation, and diffusion-equation types of deformation of the energy surface, and on another level through the formulation of coarse-grained models. The efficiency of local-elevation types of sampling[85] of the conformational space of a dipeptide in aqueous solution is illustrated in Figure 14. A much larger part of the Ramachandran map is covered in a much shorter simulation time than when using a standard MD simulation.

The so-called single-step perturbation methodology allows ligand-binding free energies or solvation free energies

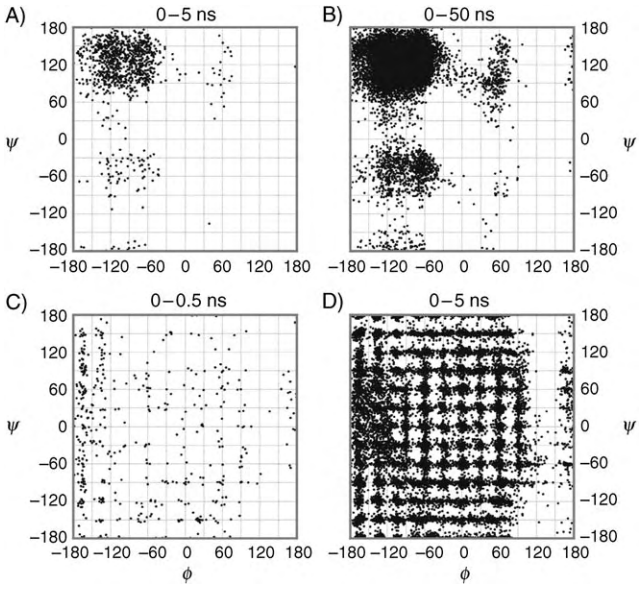


Figure 14. Ramachandran maps obtained from MD simulations of an alanine dipeptide in (SPC/E) water. φ/ψ distributions obtained by standard MD for 5 ns (A) and 50 ns (B), and by local-elevation (LE) MD for 0.5 ns (C) and 5 ns (D),[85] showing the much more rapid sampling of the LE-MD algorithm. Upon revisiting a conformation the LE potential energy is raised by 2.0 kJ mol^{-1}.

to be obtained for a great many compounds. This method uses only a few simulations involving nonphysical reference states with soft-core atoms chosen to widen the configurational ensemble and offers orders of magnitude gains in efficiency compared to standard (thermodynamic integration or perturbation) free energy calculations.[149,152–156] This is illustrated in Figure 15, where binding (Gibbs) free energies of 16 hydroxylated polychlorinated biphenyls to the estrogen receptor as

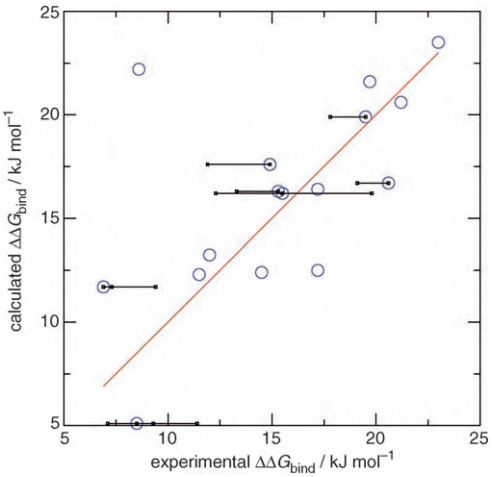


Figure 15. Experimental versus calculated relative Gibbs free energies of binding for 16 hydroxylated polychlorinated biphenyls to the estrogen receptor binding domain in solution.[149] The horizontal lines connect different experimental values for one compound. The calculated values were obtained from only two simulations and the one-step perturbation method. The GROMOS 43 A1 force field was used.

calculated using the single-step perturbation technique from only two MD simulations are compared to the corresponding experimental values.[149] The average deviation of the simulated values from the experimental ones is, at 2.5 kJ mol^{-1}, smaller than the variation of 4.2 kJ mol^{-1} in the experimental values themselves. Thus, the force field used and the sampling technique based on soft-core atoms are able to reproduce the experimental values within the accuracy of their measurement.

A reduction of the solvent viscosity (see Figure 10) may also lead to considerably enhanced sampling without affecting the nondynamic equilibrium properties of the system.

	number of amino acids in the protein	folding time (exptl/sim) in seconds	number of *possible* structures	number of *relevant* (observed) structures
peptide	10	10^{-8}	$3^{20} \approx 10^{9}$	10^{3}
protein	100	10^{-2}	$3^{200} \approx 10^{90}$	10^{9}

Assuming that the number of relevant unfolded structures is proportional to the folding time, only 10^9 protein structures need to be simulated instead of 10^{90} structures.

⇒ Folding mechanism is simpler than generally expected: searching through only 10^9 structures

⇒ Protein folding on a computer is possible before 2010

Figure 16. A surprising result after the simulation of many polypeptides: The number of unfolded conformations visited in MD simulations of (un)folding equilibria of a host of polypeptides and peptoids is much smaller than theoretically possible.[144–146]

© 2006 Wiley-VCH Verlag GmbH & Co. KGaA, Weinheim

The observation that the unfolded state of polypeptides contains much fewer relevant conformations than possible conformations opens up the possibility to simulate the reversible (un)folding of small proteins within not too many years (Figure 16).

4. The Ensemble Problem

Biomolecular modeling is hindered by the fact that the behavior of biomolecular systems is governed by statistical mechanics. If mechanics were applicable only, one could characterize such systems in terms of (global) minimum-energy structures. Statistical mechanics leads to the concept of the entropy of a system, that is, the negative derivative of the free energy F with respect to temperature [Eq. (16)]:

$$S_{\mathrm{NVT}} = -\left(\frac{\partial F}{\partial T}\right)_{\mathrm{NV}} = (U-F)/T \tag{16}$$

The entropy together with the energy of a system [Eq. (17)], that is, the average of the Hamiltonian of the system over the momenta and coordinates of all degrees of freedom, determines the free energy [Eq. (14)] of the system.

$$U_{\mathrm{NVT}} = \left(\frac{\partial(F/T)}{\partial(1/T)}\right)_{\mathrm{NV}} = \langle H(\boldsymbol{p},\boldsymbol{r})\rangle_{\boldsymbol{p},\boldsymbol{r}} \tag{17}$$

The Boltzmann average $\langle\cdots\rangle_{\mathbf{p},\mathbf{r}}$ of a quantity $Q(\boldsymbol{p},\boldsymbol{r})$, which depends on the (atomic) coordinates and momenta, is defined by Equation (18):

$$\langle Q(\boldsymbol{p},\boldsymbol{r})\rangle_{\boldsymbol{p},\boldsymbol{r}} = \frac{\int\int Q(\boldsymbol{p},\boldsymbol{r})\exp[-H(\boldsymbol{p},\boldsymbol{r})/k_{\mathrm{B}}T]\mathrm{d}\boldsymbol{p}\,\mathrm{d}\boldsymbol{r}}{\int\int \exp[-H(\boldsymbol{p},\boldsymbol{r})/k_{\mathrm{B}}T]\mathrm{d}\boldsymbol{p}\,\mathrm{d}\boldsymbol{r}} \tag{18}$$

The state of a system is generally characterized not by one configuration or structure, but by a Boltzmann ensemble of configurations or structures. This complicates biomolecular modeling, because it is easier to think of and handle single structures than to consider configurational ensembles. However, a number of (experimental) observations can only be understood by an analysis in terms of alternative structures present in an ensemble and in terms of entropy.

4.1. Free Energy, Energy, and Entropy of Solvation

Since the free energy F can be written as $F = U - TS$, different combinations of energy (U) and entropy (S) values may result in the same free energy. This can be illustrated through a calculation of the free energy of solvation ΔF_{S} of a solute in a binary solvent from MD simulations.[8] Figure 17 shows the Gibbs free energy ΔG_{S} (the equivalent of the quantity ΔF_{S} under constant pressure) of solvating a methane molecule in a mixture of water and a co-solvent (NaCl, DMSO and acetone) as a function of the co-solvent concentration or mole fraction. In NaCl, the value of ΔG_{S} increases as the co-solvent concentration increases, whereas in DMSO and acetone the value of ΔG_{S} decreases as the mole fraction of the co-solvent increases. The Gibbs free energy ΔG_{S} can be broken down into an energetic contribution, the change in the solute–solvent energy upon solvation (ΔU_{uv}), and an entropic contribution—the solute–solvent entropy change upon solvation ($-T\Delta S_{\mathrm{uv}}$) [Eq. (19)]:[8,157–159]

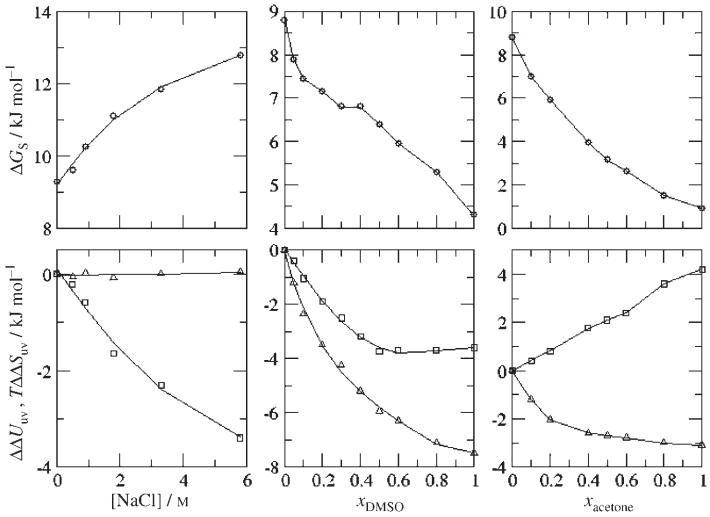


Figure 17. Gibbs free energy ΔG_s for the solvation of methane (upper panels) and solute–solvent energy $\Delta\Delta U_{uv}$ (triangles) and entropy $T\Delta\Delta S_{uv}$ (squares) relative to neat water (lower panels) as a function of the salt concentration NaCl (left panels), the mole fraction of DMSO (middle panels), and the mole fraction of acetone (right panels).[8] The calculations were performed by using the particle-insertion technique.

$$\Delta G_{\mathrm{S}} = \Delta U_{\mathrm{uv}} - T\Delta S_{\mathrm{uv}} \tag{19}$$

The lower panels in Figure 17 show these energetic and entropic contributions relative to neat water (indicated by $\Delta\Delta$) also as a function of the co-solvent concentration or mole fraction. The solvation of methane in aqueous solution is disfavored with increasing NaCl concentration as a result of an increasingly unfavorable solute–solvent entropy of solvation. On the other hand, solvation of methane in aqueous solution is favored both with increasing DMSO or acetone mole fraction, but the relative roles of solute–solvent energy and entropy are quite different, even though DMSO and acetone are structurally rather similar molecules. Solvation in DMSO is dominated by a favorable energy with increasing DMSO concentration, whereas solvation in acetone is dominated by a favorable entropy with increasing acetone concentration. Thus, comparable curves for ΔG_{S} are due to quite different solvation mechanisms. This example illustrates that entropy should be properly taken into account in biomolecular modeling studies.

The varying roles of energy and entropy in hydrophobic solvation is illustrated in Table 8 for a set of hydrophobic molecules in different aqueous solutions. Increasing the size of the hydrophobic solute in NaCl causes an increase in the $\Delta\Delta G_{\mathrm{S}}$ value as a consequence of an increase in $-T\Delta\Delta S_{\mathrm{uv}}$. In a

 © 2006 Wiley-VCH Verlag GmbH & Co. KGaA, Weinheim

Table 8: Thermodynamic data [kJ mol^{-1}] for solute transfer from pure water to co-solvent/water mixtures at 298 K and 1 atm as calculated from MD simulations.[9] Mole fractions are given in percent. Two different models (I and II) were used for acetone.

Solute	NaCl (11%)			Urea (15%)			DMSO (10%)[a]			Acetone(I) (10%)			Acetone(I) (50%)			Acetone(II) (10%)		
	$\Delta\Delta G_S$	$\Delta\Delta U_{uv}$	$T\Delta\Delta S_{uv}$	$\Delta\Delta G_S$	$\Delta\Delta U_{uv}$	$T\Delta\Delta S_{uv}$	$\Delta\Delta G_S$	$\Delta\Delta U_{uv}$	$T\Delta\Delta S_{uv}$	$\Delta\Delta G_S$	$\Delta\Delta U_{uv}$	$T\Delta\Delta S_{uv}$	$\Delta\Delta G_S$	$\Delta\Delta U_{uv}$	$T\Delta\Delta S_{uv}$	$\Delta\Delta G_S$	$\Delta\Delta U_{uv}$	$T\Delta\Delta S_{uv}$
helium	2.0	−0.4	−2.4	1.3	−0.1	−1.4	0.0	−0.2	−0.2	−0.4	−0.2	0.2	−1.7	−0.6	1.1	−0.1	−0.2	−0.1
neon	2.8	0.2	−2.6	1.1	−0.7	−1.8	−0.3	−0.7	−0.4	−0.7	−0.4	0.3	−2.4	−1.0	1.4	−0.4	−0.6	−0.2
argon	3.7	−0.1	−3.8	0.8	−2.3	−3.1	−0.9	−1.8	−0.9	−1.3	−1.0	0.3	−4.4	−2.1	2.3	−1.1	−1.7	−0.6
krypton	4.0	−0.2	−4.2	0.4	−3.2	−3.6	−1.2	−2.3	−1.1	−1.6	−1.2	0.4	−5.2	−2.6	2.6	−1.5	−2.3	−0.8
xenon	4.4	−1.2	−5.6	−0.5	−4.7	−4.2	−1.5	−2.7	−1.2	−2.2	−1.7	0.5	−6.8	−3.6	3.2	−2.1	−3.4	−1.3
methane	4.2	−0.2	−4.4	0.5	−3.1	−3.6	−1.1	−2.1	−1.0	−1.7	−1.2	0.5	−5.4	−2.6	2.8	−1.4	−2.2	−0.8
ethane	5.6	−0.8	−6.4	−0.9	−6.0	−5.1	−2.8	−4.4	−1.6	−2.9	−2.4	0.5	−8.4	−4.6	3.8	−2.6	−4.3	−1.7
propane	5.4	−0.3	−5.7	−2.2	−7.3	−5.1	−4.8	−5.8	−1.0	−5.8	−3.9	1.9	−13.0	−6.5	6.5	−4.8	−6.2	−1.4
n-butane	7.4	−1.2	−8.6	−2.7	−10.6	−7.9	−5.8	−7.9	−2.1	−6.4	−5.6	0.8	−15.7	−9.3	6.4	−4.3	−6.0	−1.7
iso-butane	5.7	−1.2	−6.9	−2.3	−10.2	−7.9	−6.5	−6.7	−0.2	−6.7	−4.9	1.8	−15.2	−7.7	7.5	−5.9	−7.7	−1.8
neo-pentane	8.2	−0.6	−8.8	−2.2	−10.9	−8.7	−6.0	−8.3	−2.3	−6.7	−4.3	2.4	−15.8	−7.1	8.7	−5.3	−9.7	−4.4

[a] To expedite statistical sampling, MD simulation runs were performed using an atomic mass of 15.9994 amu for the sulfur and water hydrogen atoms of DMSO. An MD time step of 4 fs was used.

urea/water mixture, $\Delta\Delta G_S$ is relatively independent of the solute size, because of energy–entropy compensation. In DMSO, $\Delta\Delta G_S$ becomes more favorable with increasing solute size, because of a strongly favorable energetic contribution, which is slightly counteracted by the entropy term $-T\Delta\Delta S_{uv}$. The picture again changes on changing from DMSO to acetone in that the entropy term now coacts with the solvation energy term, an effect that appears to increase with the acetone concentration. These results show that similar free energy changes, and thus the processes driven by them, can be due to very different mechanisms. A proper modeling of entropic effects is required to capture such molecular processes.

4.2. Temperature Dependence of Folding Equilibria

The folding-unfolding equilibrium of a polypeptide is not only determined by energy changes upon (un)folding, but also by entropy changes. This will make the corresponding conformational ensemble and folding pathways temperature-dependent. Figure 18 shows the most populated conformations of a β-heptapeptide in methanol at three different temperatures as obtained from MD simulations.[138] The quasivertical arrows between the rows indicate corresponding conformations at the different temperatures, while the horizontal arrows indicate the most dominant (un)folding pathways (from and) to the most stable (helical) conformation C1. Both the conformational ensemble and the (un)folding pathways are temperature-dependent, as expected, and this dependence can be investigated by MD simulation.

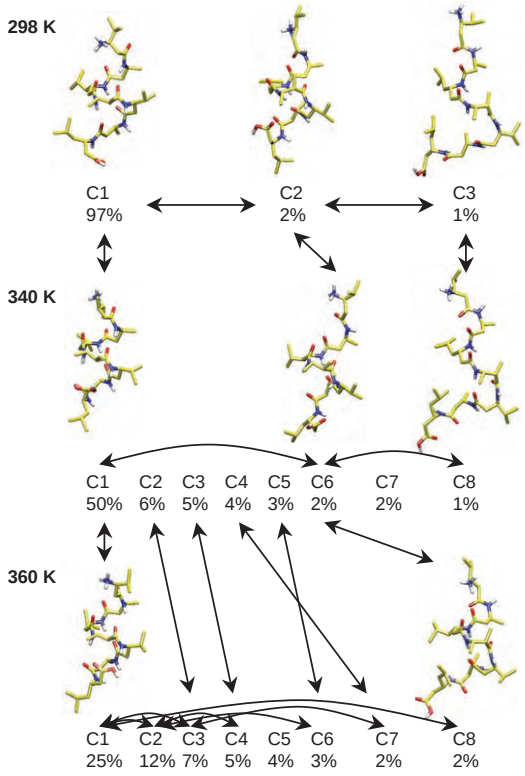


Figure 18. Most populated conformations of a β-heptapeptide in methanol from MD simulations at three different temperatures.[138] The quasi-vertical arrows indicate corresponding conformations at the different temperatures, while the horizontal arrows represent the dominant (un)folding pathways leading to the most stable (helical) conformation C1.

4.3. Different Conformations may Contribute to the Ensemble Averages

If different conformations are present in the ensemble of polypeptide conformations in solution, the measured average value of an observable, such as an NOE intensity or a ^3J-coupling constant, may not correspond to any realistic (that is, energetically accessible) conformation of the solute. This problem may be aggravated by a nonlinear dependence of the observable upon solute conformation. In such a case, structure determination based on NMR data will only lead to consistency with the experimentally measured observable values if conformational ensembles instead of single structures are considered. An example of such a case is the β-nonapeptide shown in Figure 19. Single-structure refinement based on 65 NOE intensities and 4 ^3J-coupling constants measured for the (unprotected) solute in methanol resulted in a 12/10-helical model structure. The hydrogen bonds charac-

© 2006 Wiley-VCH Verlag GmbH & Co. KGaA, Weinheim

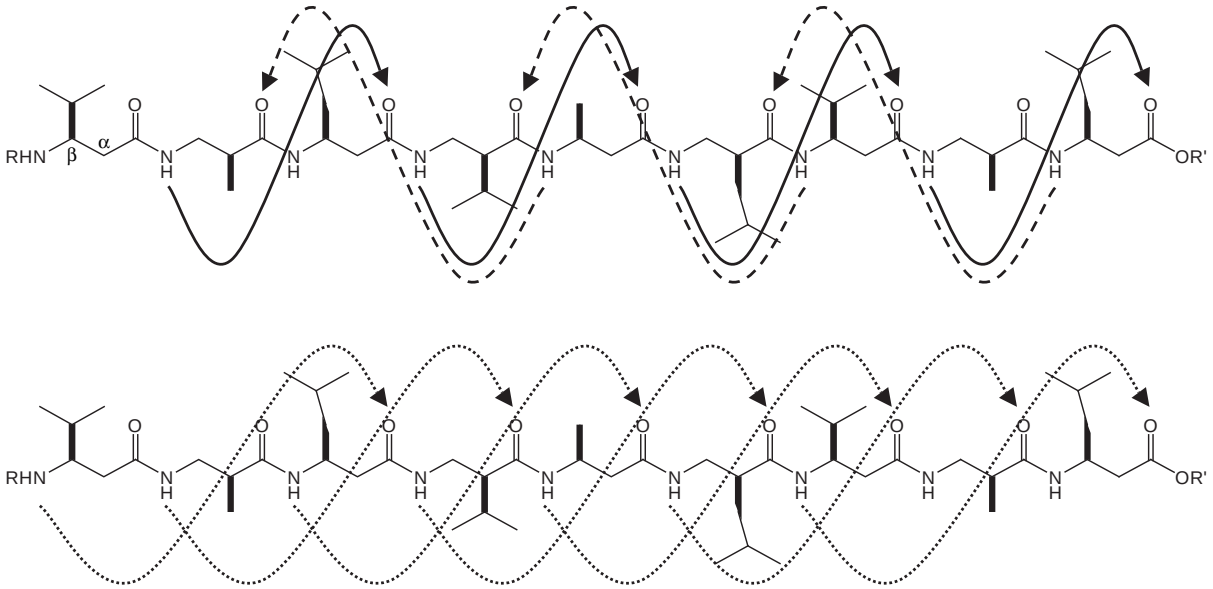


Figure 19. Structural formula of a β-nonapeptide with arrows indicating the hydrogen-bonding patterns characteristic of 12/10- and 3_{14}-helices. The 12/10-helix (top) is characterized by 10- (solid arrows) and 12-membered (dashed arrows) hydrogen-bonded rings, whereas the 3_{14}-helix (bottom) is characterized by 14-membered hydrogen-bonded rings (dotted arrows).

teristic for this type of helix are indicated in Figure 19 (dashed and solid arrows). However, three weak NOE intensities (2HN-5Hβ, 6HN-3Hβ, 7HN-4Hβ_{Re}) were omitted in the single-structure refinement, because of their incompatibility with the 12/10 helix.[160] A 100-ns MD simulation of the β-nonapeptide in methanol (without applying any NOE or ^3J-couping constant restraints) did essentially reproduce all measured NOE intensities and ^3J values.[161] Analysis of the MD trajectory showed that the three mentioned NOE intensities are due to a small percentage of an alternative 3_{14}-helical conformation (Figure 19, dotted arrows) in the conformational ensemble. This example shows that unrestrained MD simulation using a consistent, thermodynamically calibrated force field for both solute and solvent and including solvent degrees of freedom explicitly can contribute significantly to a correct interpretation of experimental data in terms of conformational distributions.

4.4. Perspectives in Calculating Entropies

While the determination of free-energy differences by MD simulation has become a standard procedure, for which a variety of techniques have been developed, total entropies and entropy differences are still seldom computed. However, entropy is the key property for understanding phenomena such as hydrophobic interactions, solvation, ligand binding, etc. Unfortunately, determining absolute entropies and entropy differences from MD simulation is not an easy task: it requires in principle the complete sampling of phase space. Generally, one can distinguish two types of methods to obtain reasonable estimates for entropies from MD simulations.

One type of methods focuses on conformational entropies, which consider not all, but only internal (conformational) nondiffusive degrees of freedom,[162–165] for example, in a protein.[166]

The other type of methods extends techniques that are successfully used to estimate free-energy differences from the calculation of entropy differences. To obtain free-energy differences between two states of a system or between two systems, the evaluation of the complete partition functions is not really needed. It is sufficient to extensively sample the relevant parts of phase or configuration space where the two states or systems differ. In contrast, the corresponding techniques to obtain entropy differences suffer from the fact that they require an accurate estimate of an ensemble average that includes the complete Hamiltonian operator H of the system in the two states, not only the part of the Hamiltonian operator that differs between the two states or systems ($\partial H/\partial\lambda$; see Figure 20).[142] The complete Hamiltonian operator is a sum over very many terms, of which only a few differ between the two states of the system. It therefore takes a very long time to obtain a precise ensemble. The most accurate methods are methods 3 and 4 of Figure 20. Method 4 yields only accurate solute–solvent entropies, not solvation entropies, which involve all solvent terms. This methodology was used to obtain the data shown in Table 8 and Figure 17.

The first type of methods is only suitable for estimating solute conformational entropies; it is of little help for diffusive systems such as solutions. The approaches used in the second type of methods (Figure 20) have recently been reviewed and evaluated.[142] Despite the progress made in developing methods, the possibility to accurately compute entropies is not good. None of the techniques considered seems suitable for the calculation of the entropy of ligand–protein binding or the entropy of polypeptide folding.

 © 2006 Wiley-VCH Verlag GmbH & Co. KGaA, Weinheim

Four Ways to Compute Entropy Differences

Coupling parameter λ approach

Hamiltonian is made function of λ: $H_a(\vec{p},\vec{r}) = H(\vec{p},\vec{r},\lambda_a) \rightarrow$ state a

$H_b(\vec{p},\vec{r}) = H(\vec{p},\vec{r},\lambda_b) \rightarrow$ state b

Free energy depends on λ:

$$F_{NVT}(\lambda) = -k_b T \ln\left(\left[h^{3N} N!\right]^{-1} \iint \exp\left(-H(\vec{p},\vec{r},\lambda)/k_b T\right) d\vec{p}\, d\vec{r}\right)$$

1. Entropy difference from energy difference and thermodynamic integration (TI) of the free energy

Free Energy Difference and End States Energy Difference

$$\Delta F_{ba}^{TI} = F(\lambda_b) - F(\lambda_a) = \int_{\lambda a}^{\lambda b} \frac{dF}{d\lambda} d\lambda = \int_{\lambda a}^{\lambda b} \left\langle \frac{\partial H}{\partial \lambda} \right\rangle_\lambda d\lambda$$ accurate

$$\Delta U_{ba} = \langle H \rangle_{\lambda_b} - \langle H \rangle_{\lambda_a}$$

$$= U(\lambda_b) - U(\lambda_a) = \Delta U_{ba}^{end}$$ not accurate

$$\Delta S_{ba}^{TI} = \frac{\Delta U_{ba}^{end} - \Delta F_{ba}^{TI}}{T}$$ not so accurate because of inaccuracy of energy

2. Entropy difference directly from TI

using $S = -\left(\frac{\partial F}{\partial T}\right)_{N,V}$ ⇨ $\Delta S_{ba}^{TI} = \frac{1}{k_b T^2} \int_{\lambda a}^{\lambda b} \left[\left\langle \frac{\partial H}{\partial \lambda} \right\rangle_\lambda \langle H \rangle_\lambda - \left\langle \frac{\partial H}{\partial \lambda} H \right\rangle_\lambda \right] d\lambda$

and $\left(\frac{\partial S}{\partial \lambda}\right)_{N,V,T}$ correlation between $\frac{\partial H}{\partial \lambda}$ and H not so accurate

↑ only λ-dependent terms; ↑ all terms

3. Entropy difference from finite temperature difference

using $S = -\left(\frac{\partial F}{\partial T}\right)_{N,T}$ ⇨ $\Delta S_{ba}^{\Delta T} = -\frac{\Delta F_{ba}^{TI}(T+\Delta T) - \Delta F_{ba}^{TI}(T-\Delta T)}{2\Delta T}$

difference between almost equal accurate values

4. Solvation entropy difference from solute-solvent entropy difference (using TI) and **end states solvent-solvent energy difference**

$$\Delta S_{ba}^{TI,all} = \frac{1}{k_B T^2} \int_{\lambda_a}^{\lambda_b} \left[\left\langle \frac{\partial H_{uv}}{\partial \lambda} \right\rangle_\lambda \langle H_{uv} \rangle_\lambda - \left\langle \frac{\partial H_{uv}}{\partial \lambda} H_{uv} \right\rangle \right] d\lambda + \frac{1}{T} \left[\langle H_{vv} \rangle_{\lambda_b} - \langle H_{vv} \rangle_{\lambda_a} \right]$$

$$= \Delta S_{ba}^{TI,uv} + \frac{\Delta U_{ba}^{end,vv}}{T}$$

accurate ↑ only solute-solvent terms; not so accurate ↑ all solvent terms; solvent: v solute: u

Figure 20. Four ways to compute entropy differences by using the coupling parameter technique and MD simulations.[142]

5. The Experimental Problem

Experimental data play an essential role in biomolecular modeling. First, they form the basis on which classical force fields are built (see Table 4). Without the experimental data mentioned there, classical force-field development would be virtually impossible. Quantum-chemical theoretical data alone do not suffice to build a force field. Second, the simulation methodology and the force field used can be validated and tested by comparison of simulated or calculated values for various molecular or system properties with experimentally measured ones.

Three problems arise with respect to roles of experimental data in biomolecular modeling: 1) Almost every experiment involves an averaging over time and the space or molecules, and, therefore, does not yield direct information on all configurations constituting a simulation trajectory. 2) Experimental data for biomolecular systems are scarce relative to the number of degrees of freedom involved. This makes the problem of deriving the conformational ensemble from experimental data for a biomolecular system under-determined. Many different ensembles may reproduce the same set of experimental data. 3) The experimental data may be of insufficient accuracy to be used to (in)validate simulation predictions. These three types of experimental problems with regard to biomolecular modeling will be illustrated in the following sections with examples.

5.1. The Averaging Limitation

A measurement of a quantity $Q(\boldsymbol{r})$ that can be expressed as a function of a molecular or system configuration $\boldsymbol{r}$ does not yield a value $Q^{obs} = Q(\boldsymbol{r})$ that depends on a single configuration $\boldsymbol{r}$, but yields an average over many molecules in the real (macroscopic) system and over the duration of the measurement [Eq. (20); the symbol $\langle \cdots \rangle$ denotes averaging].

$$Q^{obs} = \langle Q(\boldsymbol{r}) \rangle_{\text{molecules,time}} \tag{20}$$

In other words, only an average over the distribution $P(Q)$ of the quantity Q is measured (see Figure 21). The distribution itself is not measured. The detailed information on the distribution is lost by averaging, and very different distributions may yield the same average. The sensitivity of an average $\langle Q \rangle$ value of a particular quantity Q to the shape of the distribution $P(Q)$ or the shape of the conformational distribution $P(\boldsymbol{r})$ can be very different for different quantities Q.

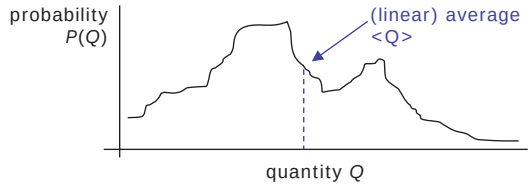


Figure 21. The averaging problem: the conformational distribution over which an average is measured cannot be derived from this average.

As an example, we consider the conformational distributions of an octapeptide $(Aib)_6$-Leu-Aib in DMSO solution and in the crystal (Figure 22). Since this peptide contains mainly achiral helix promoting Aib residues, the molecule is expected to be able to adopt both an *R*- and an *L*-helical conformation in solution. Indeed NOE intensities and ^3J values compatible with either *R*- or *L*-helices are observed in NMR experiments in solution.[167] In the crystal only the *R*-helical form is found.[168] However, the calculated ^3J values for the crystal structure are with 4.2 Hz significantly lower than the values of 6.9 Hz measured in solution. This observation

© 2006 Wiley-VCH Verlag GmbH & Co. KGaA, Weinheim

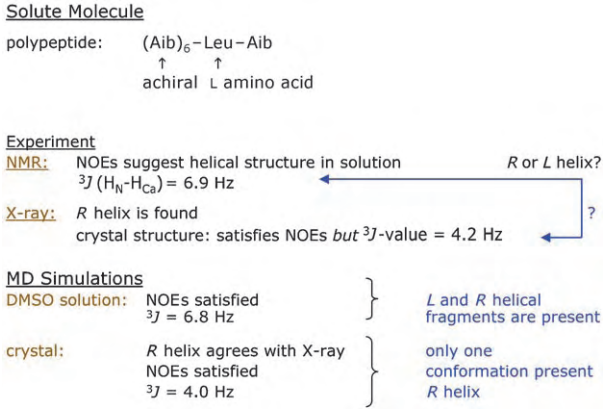


Figure 22. ^3J Coupling constants are dependent upon the conformational arrangement of an octapeptide, while in contrast NOE intensities are not sensitive.[169,170]

hints at different conformational distributions in solution and in the crystal. To investigate these, MD simulations of the octapeptide in DMSO solution and in the crystalline form were carried out.[169,170] These reproduced accurately the measured NOE intensities, ^3J values, and X-ray structure, and showed the differences in the conformational ensembles (Figure 23). In solution transient *R*- and *L*-helical fragments

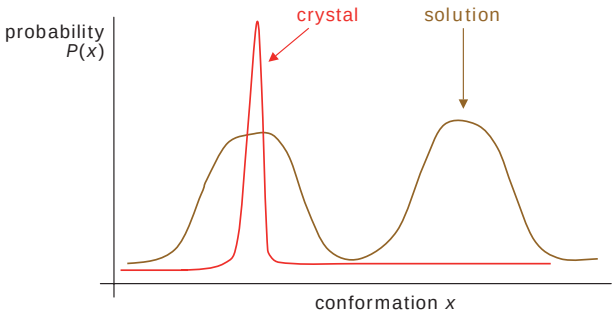


Figure 23. The conformational distribution in solution and in the crystal can be different. In the text, an example of an octapeptide is discussed.[169,170]

are present which led to a broad conformational ensemble with $\langle^3J\rangle = 6.8$ Hz, which coincides with the experimental value. In the crystal, a rather narrow *R*-helical conformational ensemble is found with $\langle^3J\rangle = 4.0$ Hz close to the ^3J value found from the X-ray structure. The simulations illustrate that the NOE intensities are not very sensitive to the shape of the conformational ensemble, as long as helical fragments are present; however, they cannot distinguish between the solution and crystal ensembles. In contrast, the ^3J-coupling constants reflect in this case the rather large differences between the two conformational ensembles.

In other cases, ^3J-coupling constants may be extremely insensitive to the underlying conformational distribution. This is illustrated in Figure 24, where simulated ^3J values for a β-heptapeptide in methanol are compared to experimental

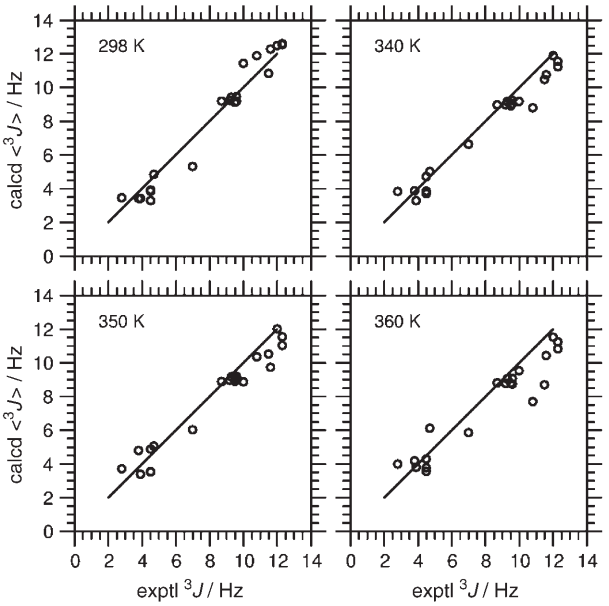


Figure 24. Comparison of the 21 experimental average ^3J-coupling constants measured at 298 K with the corresponding averaged ^3J-coupling constants calculated for the trajectory structures of 50-ns MD simulations of a β-heptapeptide in methanol at four different temperatures. The four conformational distributions are rather different: they contain 97%, 50%, 39%, and 25% 3_{14}-helical structures, respectively.[171]

values.[171] Four conformational distributions (generated at 298 K, 340 K, 350 K, and 360 K) that are rather different have been used: they contain 97%, 50%, 39% and 25% 3_{14}-helical structures, respectively.[171] However, the agreement with experiment is of equal quality for each of the four different distributions.

The loss of information through averaging in the measurement is not restricted to NMR experiments. Similar observations were made for circular dichroism (CD) spectra.[172] Figure 25 shows the measured CD spectra for two β-hexapeptides in methanol solution. The CD spectra are very similar, although the conformational ensembles for the two solutes were expected to be rather different since the double methylation at the α-carbon atom of peptide A inhibits the formation of a 3_{14}-helix, whereas peptide B, which only differs from peptide A in this respect, can and does adopt such a helix. This was confirmed by NOE intensities measured in NMR experiments. To resolve this puzzle, 100-ns MD simulations of each molecule were carried out and average CD spectra were calculated from the MD trajectories.[172] The spectra are of similar shape as the experimental ones, only the amplitudes are smaller. The conformations dominating the corresponding conformational ensembles are shown in Figure 26 together with the corresponding CD spectra. For peptide A, the CD spectrum is dominated by the second most populated (13%) conformation, not by the most populated one. The only helical conformation of peptide B (18% population) exhibits a spectrum quite different from the other conformations and from experiment.

This raises the question as to whether a particular spectrum can be assigned to a particular structure. In

 © 2006 Wiley-VCH Verlag GmbH & Co. KGaA, Weinheim

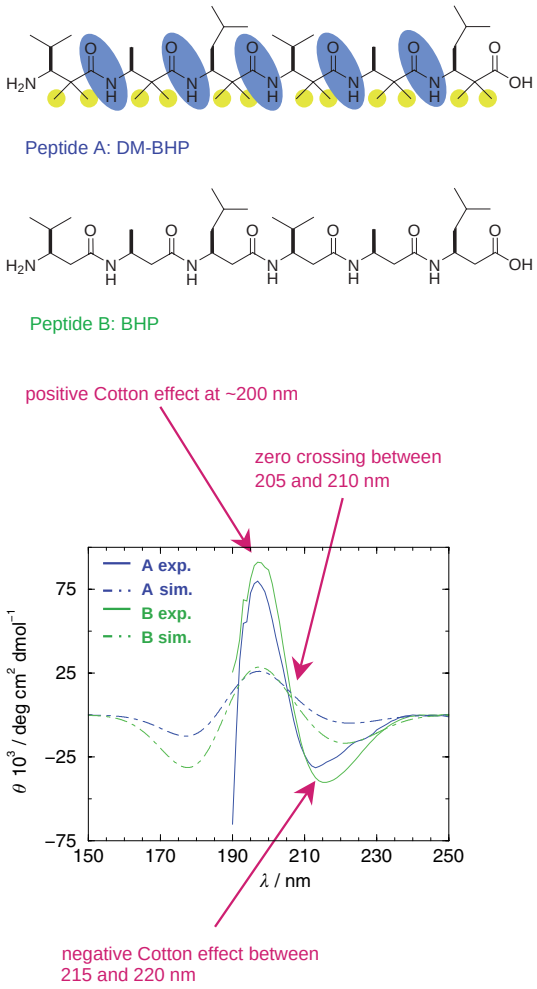


Figure 25. Experimental CD spectra and CD spectra calculated from 100-ns MD simulations of two β-hexapeptides in methanol at 298 K. Peptide B adopts a 3_{14}-helix, as confirmed by NMR experiments. Peptide A is doubly methylated at the α position and does not form a 3_{14}-helix, although a CD spectrum "typical" for a 3_{14}-helix is obtained.[172]

Figure 27 the six CD spectra with the largest amplitudes are displayed for each peptide together with the six MD trajectory structures that lead to these spectra. It is clear that the same spectrum can be generated by very different structures. Figure 28 shows a conformational clustering analysis of the combined MD trajectories of both peptides. It turns out that there is virtually no overlap between the two conformational ensembles of the peptides, although their CD spectra are very similar both in experiment and in simulation. This observation posts a cautionary note when interpreting CD spectra in terms of molecular conformations. The averaging problem means that no reliable conclusions about conformational preferences can be drawn from the measured CD spectra.

5.2. Insufficient Number of Experimental Data

If the number of experimental data on a biomolecular system is lower than the number of degrees of freedom, or if the different experimental data are correlated, they may not uniquely determine the solute conformation that dominates the conformational ensemble. An example of such a situation is illustrated in Figure 29 where NOE distances and ^3J-coupling constant values obtained from MD simulations[173] as well as from a set of 20 model structures derived during NMR structure refinement[174] are compared to the measured values for a β-hexapeptide in methanol. The NOE distances from the 100-ns MD simulations agree with the experimental values (only two small violations) and so do the ^3J values. The set of 20 NMR model structures also satisfies the experimental data, which simply reflects the fact that they were derived using the same data.[174] Figure 30 shows that there is relatively little overlap between the simulated conformational ensembles and the set of NMR model structures, yet the two sets of structures reproduce the experimental data. These data appear to be insufficient in number to uniquely determine

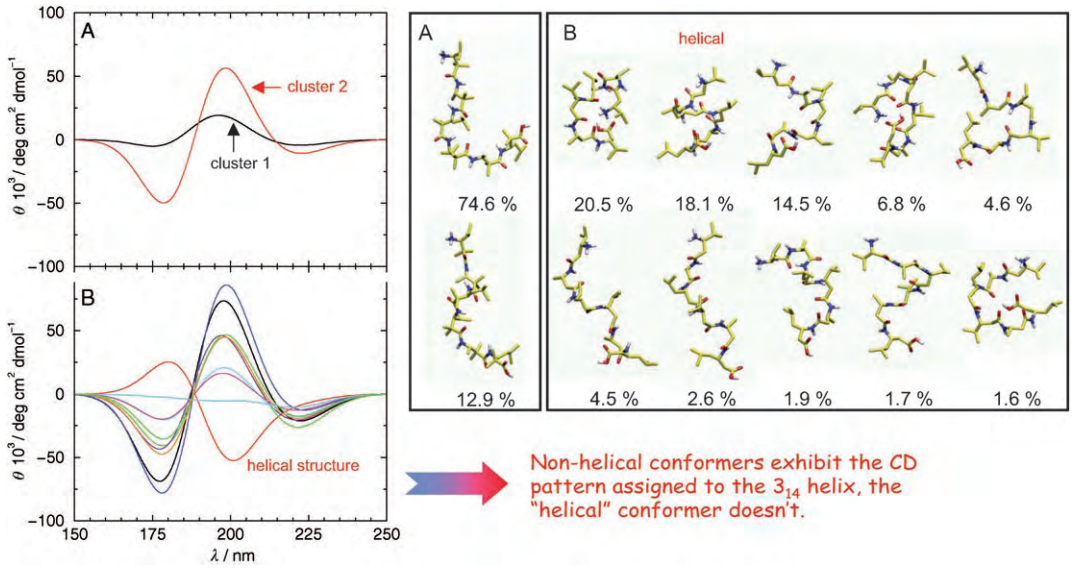


Figure 26. Dominant conformations in the MD trajectories of two β-hexapeptides A (methylated) and B (not methylated; see Figure 24) together with the corresponding CD spectra.[172] (Similarity criterion: RMSD of backbone atoms ≤0.09 nm; 10000 structures, 10 ps apart.)

 © 2006 Wiley-VCH Verlag GmbH & Co. KGaA, Weinheim

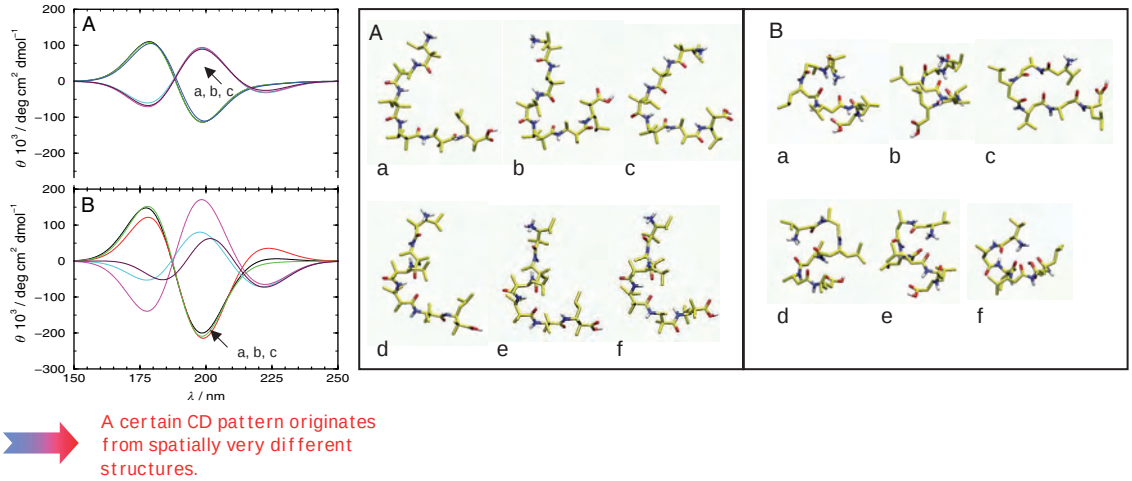


Figure 27. CD spectra for MD trajectory structures which show the largest CD signals, together with the corresponding structures of the two β-hexapeptides A and B.[172]

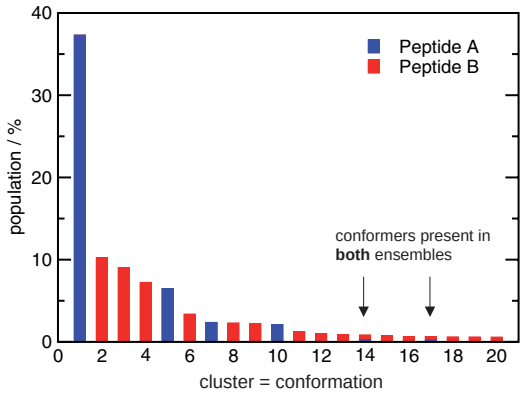


Figure 28. Conformational cluster analysis of the combined MD trajectories of both β-hexapeptides A (methylated, DM-BHP) and B (not methylated, BHP) confirm that, despite their similar CD spectra, there is virtually no overlap between the conformational ensembles of the two molecules.[172]

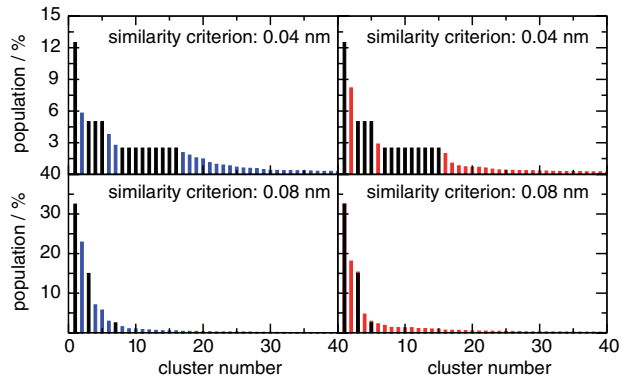
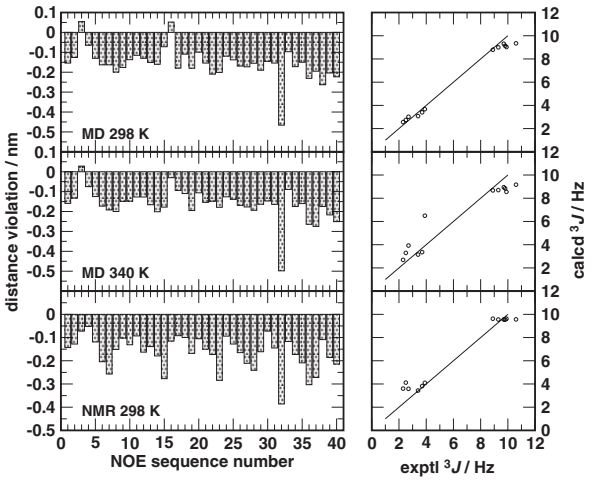


Figure 30. Conformational cluster analysis on combining the set of NMR model structures (black) for a β-octapeptide with an MD trajectory at 298 K (blue) or at 340 K (red), using two different similarity criteria for the atom-positional root-mean-square difference between the backbone atoms of the peptide structures.[173]



- 298 K:
  2 violations (~0.05 nm)

  average deviation from exptl J values: 0.44 Hz
- 340 K:
  1 violation (~ 0.03 nm)

  average deviation from exptl J values: 0.91 Hz
- NMR bundle
  no violation

  average deviation from exptl J values: 0.57 Hz

Figure 29. NOE distance-bound violations and ^3J-coupling constants for a β-octapeptide in methanol. The parameters were calculated from two 100-ns MD trajectories (not using the experimental data)[173] and from a set of 20 NMR model structures obtained by structure refinement based on the experimental NMR data.[174]

the dominant conformer: the MD trajectories suggest a 2.5_{12}-P helix to be dominant, whereas the set of NMR model structures suggest a 2_8-P-helix.[173]

5.3. Accuracy of Experimental Data

The accuracy of experimental data is finite and often insufficient to (in)validate simulation results. An example of this situation is found in Figure 15, where the disagreement between computed and measured binding free energies for a set of ligands to the estrogen receptor turns out to be smaller than the variation between different experimental values for the same ligands.

It is not easy to determine the accuracy of NOE distance bounds derived from NMR experiments on proteins in aqueous solution.

 © 2006 Wiley-VCH Verlag GmbH & Co. KGaA, Weinheim

In other words, how large must a violation of such NOE distance bounds be in an MD simulation to constitute a significant disagreement between simulation and experiment? Figure 31 shows the distribution of NOE distance bounds violations for 3.5-ns MD trajectories of the protein

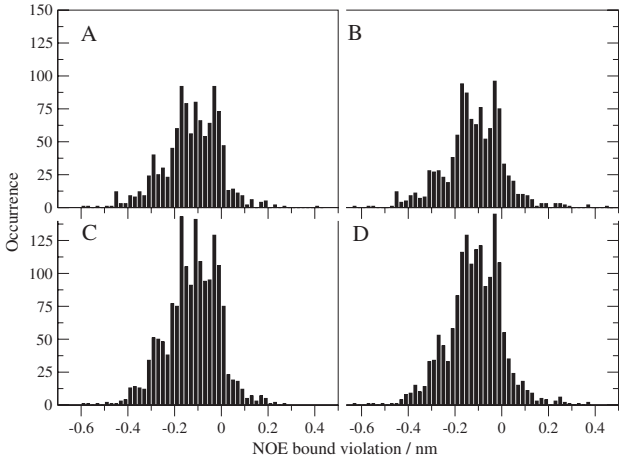


Figure 31. Distribution of r^{-3}-averaged ^{1}H-^{1}H NOE distances in two 3.5-ns MD simulations of hen egg white lysozyme in aqueous solution[175] relative to two sets of NOE distance bounds derived from NMR data. Positive values represent violations of the experimental NOE upper distance bounds. A, B) 1079 NOE distances calculated from the MD trajectories relative to the NOE distance bounds of Ref. [176] C, D) 1630 NOE distances calculated from the same MD trajectories relative to the more recent NOE distance bounds of Ref. [177] Left panels: MD simulation based on the GROMOS 43A1 force field. Right panels: MD simulation based on the GROMOS 45A3 force field.

hen egg white lysozyme in aqueous solution.[175] Two MD simulations based on different force-field parameter sets (Panels A and C, versus B and D) are analyzed in terms of two sets of experimentally determined NOE distance bounds (Panels A and B versus C and D). The experiment in 1993 produced 1079 distance bounds[176] while the more recent experiment in 2001 produced considerably more distance bounds, namely 1630.[177] A comparison of both experimental data sets with the single MD trajectories shows that the more recent, more abundant experimental data agree slightly better with the simulations (lower mean violation, fewer large violations) than the older data set. This result shows that experimental data may approach theoretical ones over time, which may serve as a cautionary note when drawing conclusions about (insufficient) quality of simulation results from observed discrepancies between simulated and measured data.

5.4. Perspectives in Comparing Simulated and Measured Data

Simulation studies are normally verified by a comparison of simulated and experimentally measured properties of the system considered.[178] The results of such a comparison between simulation and experiment can be classified as follows.[137,179,180]

Case 1: Agreement between simulation and experiment. This may arise from the following reasons:

a) The simulation adequately reflects the experimental system.
b) The property examined is insensitive to the details of the simulated trajectory. Variation of the simulation parameters would not change the agreement.
c) A compensation of errors has occurred. This situation can easily emerge if only a few (global or system) properties for a system with very many degrees of freedom are calculated and compared.

Case 2: No agreement between simulation and experiment is obtained as a consequence of one or both of the following reasons:

a) The simulation does not reflect the experimental system. The theory or model is incorrect, the simulated property is not converged, the software is at fault, or the software is incorrectly used.
b) The experimental data are incorrect or incorrectly interpreted, or both.

When comparing simulated with experimental results, the same properties should be compared. This is not always possible and sometimes only related properties are compared. For example, atom-positional mean-square fluctuations and crystallographic *B* factors both measure atomic mobility and disorder but are differently defined: the former measures the spatial distribution of a particular atom, whereas the latter measures the extent of the occupation of a given position in space by any atom that happens to be in that position.[181] As another example, protein folding rates as measured from simulated temperature renaturation may differ from those measured in an (un)folding induced by a co-solvent admixture.

With time, simulations will produce more accurate values for the various molecular and system properties, because of improved force fields and more extended equilibration and sampling. It is hoped that the improvement in experimental accuracy through improved measuring techniques may keep up with the improvements in modeling.

With regard to experimental data to be used in the development of a force field, a precise measurement of thermodynamic data such as heat of vaporization, heat of mixing, etc. for a wide variety of compounds at physiological conditions would be most beneficial for the further development of biomolecular modeling.

6. Perspectives in Biomolecular Modeling

The essential driving force behind the growth and development of the field of biomolecular modeling was, is, and will be the steady and rapid increase of computing power. Figure 32 shows there has been an average increase in computing power by a factor of 10 about every 5 years over the past few decades. This trend will probably continue in the near future, based on the on-going application of parallel computing. The possibility of parallel computing can be

 © 2006 Wiley-VCH Verlag GmbH & Co. KGaA, Weinheim

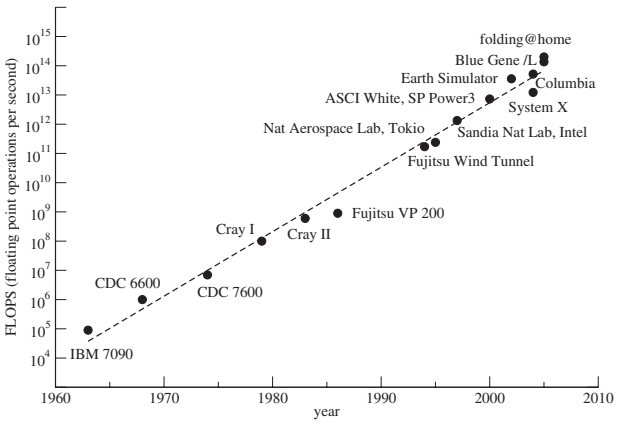


Figure 32. Development of computing power of the most powerful computers.

exploited in biomolecular simulation, since the most time-consuming part is the force or interaction calculation, which can be carried out in parallel for all atoms in the system. In particular, the advent of new hardware designed to solve the protein-folding problem through classical dynamical simulation opens up the possibility of more accurate simulations and new applications.[182]

A second driving force behind biomolecular modeling is the advancement of modeling techniques. For example, efficient algorithms to compute long-range electrostatic forces have become available.[13,21,27] Methods have been developed to extend and enhance sampling,[61,63,85,155,183] and biomolecular force fields have been refined.[7,184]

These driving forces have led to simulations of ever larger systems or over ever longer time periods (see Table 9). Practical applications of simulation address a variety of systems and processes: molecular complexation, ligand binding, polypeptide folding, transport across membranes, membrane formation, crystallization. Extrapolation of the efficiency increase in simulation by a factor 10 every 5 years leads to the predictions listed in Table 9. However, these are rather senseless predictions. First, computing power is unlikely to continue to grow for ever at the rate observed up until now. Second, when simulating ever-larger systems in atomic detail, more and more pair interactions need to be added to obtain the system energy. To obtain the same overall accuracy for a large system as for a small one, the accuracy of the pair interactions must be much higher for the large system. However, this accuracy is limited by the approximations on which a force-field description of the system rests. Third, one may question the value of a detailed atomic description of a macroscopic system. In other words, it still remains mandatory to formulate simple and approximate models (Figure 33) that contain just the necessary degrees of freedom to adequately represent the phenomenon of interest.

Table 9: History and extrapolated future of computer simulations of molecular dynamics. The future is deduced from extrapolation based on an observed increase of computing speed of a factor 10 every 5 years over the past decades (see Figure 31).

Year	Molecular system (type, size)	Length of the simulation [s]
1957	first molecular dynamics simulation (hard discs)	
1964	atomic liquid (argon)	10^{-11}
1971	molecular liquid (water)	5×10^{-12}
1977	protein in a vacuum	2×10^{-11}
1983	protein in water	2×10^{-11}
1989	protein–DNA complex in water	10^{-10}
1997	polypeptide folding in solvent	10^{-7}
2001	micelle formation	10^{-7}
200x	folding of a small protein	10^{-3}
And the future ...		
2001	biomolecules in water (ca. 10^4 atoms)	10^{-8}
2029	biomolecules in water (folding sooner?)	10^{-3}
2034	*E. coli* bacteria (ca. 10^{11} atoms)	10^{-9}
2056	mammalian cell (ca. 10^{15} atoms)	10^{-9}
2080	biomolecules in water (as fast as nature)	10^{6}
2172	human body (ca. 10^{27} atoms)	1

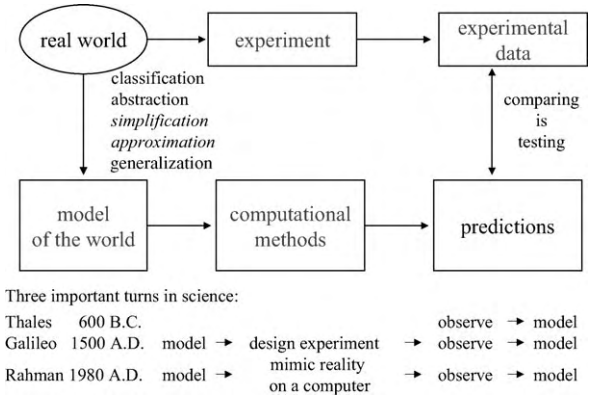


Figure 33. Computational physics, chemistry, and biology involve the formulation and testing of (mathematical) models of the real world.

The question remains, along which lines should current biomolecular models be extended, improved, or simplified? First, an appropriate description of enzyme reactions requires the inclusion of electronic degrees of freedom, one level up from the theoretical level of classical MD methods in Table 1. Hybrid quantum-classical (QM/MM) modeling will be further developed to this end.[49,185–187] To simulate proton-transfer reactions, it may be necessary to employ quantum-dynamical methodology,[188–191] which requires even more computing power than QM/MM calculations.[192] Second, at the classical level of modeling, improvements will come from the introduction of polarizability in biomolecular force fields,[44–48] from the incorporation of co-solvent effects through explicit simulation,[193] and from techniques to extend the sampling power of simulations.[61–63] Third, simplification of models by averaging over atomic degrees of freedom (coarse-graining)[54–59] will allow the simulation of slower processes, such as membrane formation.[60,194]

The reason for using simulation and modeling was indicated in Table 3: to provide a microscopic picture of unrivaled resolution in time, space, and energy that comple-

 © 2006 Wiley-VCH Verlag GmbH & Co. KGaA, Weinheim

ments the limited set of properties obtainable from experiment. Second, system parameters can be changed at will during the modeling study to study particular cause–effect relationships, thus leading to enhanced understanding of biomolecular systems.

The challenge when modeling a biomolecular system lies in a proper balance between the choices to be made regarding degrees of freedom, force field, sampling, and boundary conditions (see Figure 2). These choices will depend on three factors (Figure 34).

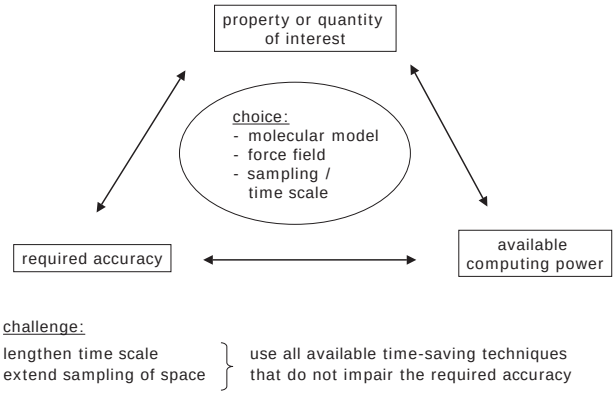


Figure 34. The choice of molecular model (degrees of freedom), force field, and extent of sampling depends on the property of interest, the required accuracy of the result, and the available computing power to generate the Boltzmann ensemble.

1. The properties of the biomolecular system one is interested in should be listed and the size of the configuration space (or time scale) to be searched and sampled should be estimated.
2. The required accuracy of the properties should be specified.
3. The available computing power should be estimated.

If the model selected is too simple, the phenomena of interest may be lost or the accuracy may be insufficient. If the model is too elaborate, sampling of the required extent of configuration space may be impossible. It is the art of biomolecular modeling to sail safely between these *Scylla* and *Charybdis*.[195]

The National Centre of Competence in Research (NCCR) in Structural Biology of the Swiss National Science Foundation is gratefully acknowledged for financial support. We thank Daniela Kalbermatter for her help in editing the manuscript.

Received: July 28, 2005

[1] M. P. Allen, D. J. Tildesley, *Computer simulation of liquids*, Oxford University Press, New York, **1987**.
[2] B. A. Luty, W. F. van Gunsteren, *J. Phys. Chem.* **1996**, *100*, 2581 – 2587.
[3] P. H. Hünenberger, J. A. McCammon, *J. Chem. Phys.* **1999**, *110*, 1856 – 1872.
[4] P. H. Hünenberger, J. A. McCammon, *Biophys. Chem.* **1999**, *78*, 69 – 88.
[5] W. Weber, P. H. Hünenberger, J. A. McCammon, *J. Phys. Chem. B* **2000**, *104*, 3668 – 3675.
[6] P. H. Hünenberger, W. F. van Gunsteren in *Computer Simulation of Biomolecular Systems, Theoretical and Experimental Applications*, *Vol. 3* (Eds.: W. F. van Gunsteren, P. K. Weiner, A. J. Wilkinson), Kluwer, Dordrecht, The Netherlands, **1997**, pp. 3 – 82.
[7] C. Oostenbrink, A. Villa, A. E. Mark, W. F. van Gunsteren, *J. Comput. Chem.* **2004**, *25*, 1656 – 1676.
[8] N. F. A. van der Vegt, W. F. van Gunsteren, *J. Phys. Chem. B* **2004**, *108*, 1056 – 1064.
[9] N. F. A. van der Vegt, D. Trzesniak, B. Kasumaj, W. F. van Gunsteren, *ChemPhysChem* **2004**, *5*, 144 – 147.
[10] W. F. van Gunsteren, S. R. Billeter, A. A. Eising, P. H. Hünenberger, P. Krüger, A. E. Mark, W. R. P. Scott, I. G. Tironi, *Biomolecular Simulation: The GROMOS96 Manual and User Guide*, Vdf Hochschulverlag, Zürich, **1996**.
[11] J. D. Jackson, *Classical Electrodynamics*, Wiley, New York, **1962**.
[12] P. Ewald, *Ann. Phys.* **1921**, *64*, 253 – 287.
[13] R. W. Hockney, J. W. Eastwood, *Computer simulation using particles*, 2nd ed., Institute of Physics Publishing, Bristol, **1988**.
[14] U. Essmann, L. Perera, M. L. Berkowitz, T. Darden, H. Lee, L. G. Pedersen, *J. Chem. Phys.* **1995**, *103*, 8577 – 8593.
[15] J. A. Barker, R. O. Watts, *Mol. Phys.* **1973**, *26*, 789 – 792.
[16] I. G. Tironi, R. Sperb, P. E. Smith, W. F. van Gunsteren, *J. Chem. Phys.* **1995**, *102*, 5451 – 5459.
[17] S. Boresch, O. Steinhauser, *J. Chem. Phys.* **2001**, *115*, 10793 – 10807.
[18] M. Bergdorf, C. Peter, P. H. Hünenberger, *J. Chem. Phys.* **2003**, *119*, 9129 – 9144.
[19] C. Peter, W. F. van Gunsteren, P. H. Hünenberger, *J. Chem. Phys.* **2003**, *119*, 12205 – 12223.
[20] M. A. Kastenholz, P. H. Hünenberger, *J. Phys. Chem. B* **2004**, *108*, 774 – 778.
[21] P. H. Hünenberger in *Simulation and theory of electrostatic interactions in solution: Computational chemistry, biophysics and aqueous solution* (Eds.: L. R. Pratt, G. Hummer) AIP, New York, **1999**, pp. 17 – 83.
[22] B. A. Luty, I. G. Tironi, W. F. van Gunsteren, *J. Chem. Phys.* **1995**, *103*, 3014 – 3021.
[23] H. J. C. Berendsen, J. P. M. Postma, W. F. van Gunsteren, J. Hermans in *Intermolecular Forces* (Ed.: B. Pullman), Reidel, Dordrecht, **1981**, pp. 331 – 342.
[24] T. P. Straatsma, H. J. C. Berendsen, *J. Chem. Phys.* **1988**, *89*, 5876 – 5886.
[25] P. H. Hünenberger, *J. Chem. Phys.* **2000**, *113*, 10464 – 10476.
[26] G. Hummer, L. R. Pratt, A. E. Garcia, *J. Phys. Chem.* **1996**, *100*, 1206 – 1215.
[27] M. A. Kastenholz, P. H. Hünenberger, *J. Chem. Phys.*, in press.
[28] W. L. Jorgensen, J. D. Madura, C. J. Swenson, *J. Am. Chem. Soc.* **1984**, *106*, 6638 – 6646.
[29] W. L. Jorgensen, D. S. Maxwell, J. Tirado-Rives, *J. Am. Chem. Soc.* **1996**, *118*, 11225 – 11236.
[30] L. D. Schuler, W. F. van Gunsteren, *Mol. Simul.* **2000**, *25*, 301 – 319.
[31] A. Glättli, W. F. van Gunsteren, *Angew. Chem.* **2004**, *116*, 6472 – 6476; *Angew. Chem. Int. Ed.* **2004**, *43*, 6312 – 6316.
[32] X. Daura, B. Jaun, D. Seebach, W. F. van Gunsteren, A. E. Mark, *J. Mol. Biol.* **1998**, *280*, 925 – 932.
[33] X. Daura, K. Gademann, B. Jaun, D. Seebach, W. F. van Gunsteren, A. E. Mark, *Angew. Chem.* **1999**, *111*, 249 – 253; *Angew. Chem. Int. Ed.* **1999**, *38*, 236 – 240.
[34] X. Daura, K. Gademann, H. Schäfer, B. Jaun, D. Seebach, W. F. van Gunsteren, *J. Am. Chem. Soc.* **2001**, *123*, 2393 – 2404.

 © 2006 Wiley-VCH Verlag GmbH & Co. KGaA, Weinheim

[35] C. M. Santiveri, M. A. Jiménez, M. Rico, W. F. van Gunsteren, X. Daura, *J. Pept. Sci.* **2004**, *10*, 546 – 565.
[36] C. Oostenbrink, T. A. Soares, N. F. A. van der Vegt, W. F. van Gunsteren, *Eur. Biophys. J.* **2005**, *34*, 273 – 284.
[37] I. Huc, V. Maurizot, H. Gornitzka, J.-M. Leger, *Chem. Commun.* **2002**, 578 – 579.
[38] A. Villa, A. E. Mark, *J. Comput. Chem.* **2002**, *23*, 548 – 553.
[39] M. R. Shirts, J. W. Pitera, W. C. Swope, V. S. Pande, *J. Chem. Phys.* **2003**, *119*, 5740 – 5761.
[40] Y. Marcus, *Ionic solvation*, Wiley, Chichester, **1985**.
[41] L. J. Smith, H. J. C. Berendsen, W. F. van Gunsteren, *J. Phys. Chem. A* **2004**, *108*, 1065 – 1071.
[42] D. P. Geerke, C. Oostenbrink, N. F. A. van der Vegt, W. F. van Gunsteren, *J. Phys. Chem. B* **2004**, *108*, 1436 – 1445.
[43] D. Trzesniak, N. F. A. van der Vegt, W. F. van Gunsteren, *Phys. Chem. Chem. Phys.* **2004**, *6*, 697 – 702; Erratum: D. Trzesniak, N. F. A. van der Vegt, W. F. van Gunsteren, *Phys. Chem. Chem. Phys.* **2004**, *6* (3rd August, 2004).
[44] T. A. Halgren, W. Damm, *Curr. Opin. Struct. Biol.* **2001**, *11*, 236 – 242.
[45] S. W. Rick, S. J. Stuart, *Rev. Comput. Chem.* **2002**, 89 – 146.
[46] B. Guillot, *J. Mol. Liq.* **2002**, *101*, 219 – 260.
[47] J. W. Ponder, D. A. Case, *Adv. Protein Chem.* **2003**, *56*, 27 – 85.
[48] H. B. Yu, W. F. van Gunsteren, *Comput. Phys. Commun.* **2005**, *172*, 69 – 85.
[49] A. Warshel, M. Levitt, *J. Mol. Biol.* **1976**, *103*, 227 – 249.
[50] D. Van Belle, I. Couplet, M. Prevost, S. J. Wodak, *J. Mol. Biol.* **1987**, *198*, 721 – 735.
[51] J. L. Banks, G. A. Kaminski, R. H. Zhou, D. T. Mainz, B. J. Berne, R. A. Friesner, *J. Chem. Phys.* **1999**, *110*, 741 – 754.
[52] S. Patel, C. L. Brooks, *J. Comput. Chem.* **2004**, *25*, 1 – 15.
[53] S. Patel, A. D. MacKerell, C. L. Brooks, *J. Comput. Chem.* **2004**, *25*, 1504 – 1514.
[54] A. Liwo, M. R. Pincus, R. J. Wawak, S. Rackofsky, H. A. Scheraga, *Protein Sci.* **1993**, *2*, 1715 – 1731.
[55] J. C. Shelley, M. Y. Shelley, *Curr. Opin. Colloid Interface Sci.* **2000**, *5*, 101 – 110.
[56] J. Barschnagel, K. Binder, P. Doruker, A. A. Gusev, O. Hahn, K. Kremer, W. L. Mattice, F. Müller-Plathe, M. Murat, W. Paul, S. Santos, U. W. Suter, V. Tries, *Adv. Polym. Sci.* **2000**, *152*, 41 – 156.
[57] M. Müller, K. Katsov, M. Schick, *J. Polym. Sci. Part B* **2003**, *41*, 1441 – 1450.
[58] A. Liwo, M. Khalili, H. A. Scheraga, *Proc. Natl. Acad. Sci. USA* **2005**, *102*, 2362 – 2367.
[59] S. J. Marrink, A. H. de Vries, A. E. Mark, *J. Phys. Chem. B* **2004**, *108*, 750 – 760.
[60] S. J. Marrink, H. J. Risselada, A. E. Mark, *Chem. Phys. Lip.* **2005**, *135*, 223 – 244.
[61] W. F. van Gunsteren, T. Huber, A. E. Torda in *Proc. Eur. Conf. Comput. Chem. (ECCC 1)*, American Institute of Physics, Conference Proceedings **1995**, *330*, 253 – 268.
[62] Y. Okamoto, *J. Mol. Graphics Modell.* **2004**, *22*, 425 – 439.
[63] K. Tai, *Biophys. Chem.* **2004**, *107*, 213 – 220.
[64] P. Koehl, M. Delaure, *J. Mol. Biol.* **1994**, *239*, 249 – 275.
[65] T. Huber, A. E. Torda, W. F. van Gunsteren, *Biopolymers* **1996**, *39*, 103 – 114.
[66] J. Desmet, M. DeMaeyer, B. Hazes, I. Lasters, *Nature* **1992**, *356*, 539 – 542.
[67] M. Lipton, W. C. Still, *J. Comput. Chem.* **1988**, *9*, 343 – 355.
[68] "Protein Structure and Engineering": D. D. Bensen, G. R. Marshall, *NATO ASI Ser. Ser. A* **1989**, *183*, 97 – 109.
[69] M. Saunders, K. N. Houk, Y.-D. Wu, W. C. Still, M. Lipton, G. Chang, W. C. Guida, *J. Am. Chem. Soc.* **1990**, *112*, 1419 – 1427.
[70] D. G. Covell, R. L. Jernigan, *Biochemistry* **1990**, *29*, 3287 – 3294.
[71] R. C. van Schaik, W. F. van Gunsteren, H. J. C. Berendsen, *J. Comput.-Aided Mol. Des.* **1992**, *6*, 97 – 112.
[72] G. M. Crippen, T. F. Havel, *Distance geometry and molecular conformation*, Wiley, New York, **1988**.
[73] T. F. Havel, *Biopolymers* **1990**, *29*, 1565 – 1585.
[74] K. D. Gibson, H. A. Scheraga, *J. Comput. Chem.* **1987**, *8*, 826 – 834.
[75] H. A. Scheraga in *Computer Simulation of Biomolecular Systems, Theoretical and Experimental Applications*, *Vol. 2* (Eds.: W. F. van Gunsteren, P. K. Weiner, A. J. Wilkinson), Escom Science Publishers, Leiden, **1993**, pp. 231 – 248.
[76] S. Vajda, C. DeLisi, *Biopolymers* **1990**, *29*, 1755 – 1772.
[77] J. Harris, S. A. Rice, *J. Chem. Phys.* **1988**, *88*, 1298 – 1306.
[78] B. Velikson, T. Garel, J.-C. Niel, H. Orland, J. C. Smith, *J. Comput. Chem.* **1992**, *13*, 1216 – 1233.
[79] D. Frenkel, G. C. A. M. Mooij, B. Smit, *J. Phys. Condens. Matter* **1992**, *4*, 3053 – 3076.
[80] W. F. van Gunsteren in *Computer Simulation of Biomolecular Systems, Theoretical and Experimental Applications*, *Vol. 2* (Eds.: W. F. van Gunsteren, P. K. Weiner, A. J. Wilkinson), Escom Science Publishers, Leiden, **1993**, pp. 3 – 36.
[81] R. M. J. Cotterill, J. K. Madsen in *Characterising Complex Systems* (Ed.: H. Bohr), World Scientific, Singapore, **1990**, p. 177 – 191.
[82] W. Braun, N. Go, *J. Mol. Biol.* **1985**, *186*, 611 – 626.
[83] T. Huber, A. E. Torda, W. F. van Gunsteren, *J. Phys. Chem. A* **1997**, *101*, 5926 – 5930.
[84] A. Piela, J. Kostrowicki, H. A. Scheraga, *J. Phys. Chem.* **1989**, *93*, 3339 – 3346.
[85] T. Huber, A. E. Torda, W. F. van Gunsteren, *J. Comput.-Aided Mol. Des.* **1994**, *8*, 695 – 708.
[86] H. Grubmüller, *Phys. Rev. E* **1995**, *52*, 2893 – 2906.
[87] A. E. Torda, R. M. Scheek, W. F. van Gunsteren, *J. Mol. Biol.* **1990**, *214*, 223 – 235.
[88] W. F. van Gunsteren, R. M. Brunne, P. Gros, R. C. van Schaik, C. A. Schiffer, A. E. Torda in *Methods in Enzymology: Nuclear Magnetic Resonance*, *Vol. 239* (Eds.: T. L. James, N. J. Oppenheimer), Academic Press, New York, **1994**, pp. 619 – 654.
[89] R. C. van Schaik, H. J. C. Berendsen, A. E. Torda, W. F. van Gunsteren, *J. Mol. Biol.* **1993**, *234*, 751 – 762.
[90] W. F. van Gunsteren, H. J. C. Berendsen, *Mol. Phys.* **1977**, *34*, 1311 – 1327.
[91] S. Kirkpatrick, C. D. Gelatt, M. P. Vecchi, *Science* **1983**, *220*, 671 – 680.
[92] B. Mao, A. R. Friedmann, *Biophys. J.* **1990**, *58*, 803 – 805.
[93] R. Elber, M. Karplus, *J. Am. Chem. Soc.* **1990**, *112*, 9161 – 9175.
[94] R. Unger, J. Moult, *J. Mol. Biol.* **1993**, *231*, 75 – 81.
[95] T. Huber, W. F. van Gunsteren, *J. Phys. Chem. A* **1998**, *102*, 5937 – 5943.
[96] M. Levitt, *J. Mol. Biol.* **1983**, *170*, 723 – 764.
[97] T. C. Beutler, A. E. Mark, R. C. van Schaik, P. R. Gerber, W. F. van Gunsteren, *Chem. Phys. Lett.* **1994**, *222*, 529 – 539.
[98] M. Zacharias, T. P. Straatsma, J. A. McCammon, *J. Chem. Phys.* **1994**, *100*, 9025 – 9031.
[99] V. Hornak, C. Simmerling, *J. Mol. Graphics Modell.* **2004**, *22*, 405 – 413.
[100] G. M. Crippen, H. A. Scheraga, *Proc. Natl. Acad. Sci. USA* **1969**, *64*, 42 – 49.
[101] A. Laio, M. Parrinello, *Proc. Natl. Acad. Sci. USA* **2002**, *99*, 12562 – 12566.
[102] A. E. Torda, R. M. Scheek, W. F. van Gunsteren, *Chem. Phys. Lett.* **1989**, *157*, 289 – 294.
[103] G. M. Crippen, *J. Comput. Chem.* **1982**, *3*, 471 – 476.
[104] E. O. Purisima, H. A. Scheraga, *Proc. Natl. Acad. Sci. USA* **1986**, *83*, 2782 – 2786.
[105] G. M. Crippen, *J. Phys Chem.* **1987**, *91*, 6341 – 6343.
[106] G. M. Crippen, T. F. Havel, *J. Chem. Inf. Comput. Sci.* **1990**, *30*, 222 – 227.

 © 2006 Wiley-VCH Verlag GmbH & Co. KGaA, Weinheim

[107] P. L. Weber, R. Morrison, D. L. Hare, *J. Mol. Biol.* **1988**, *204*, 483 – 487.
[108] T. C. Beutler, W. F. van Gunsteren, *J. Chem. Phys.* **1994**, *101*, 1417 – 1422.
[109] J.-P. Ryckaert, G. Ciccotti, H. J. C. Berendsen, *J. Comput. Phys.* **1977**, *23*, 327 – 341.
[110] H. C. Andersen, *J. Comput. Phys.* **1983**, *52*, 24 – 34.
[111] S. Miyamoto, P. A. Kollman, *J. Comput. Chem.* **1992**, *13*, 952 – 962.
[112] B. Hess, H. Bekker, H. J. C. Berendsen, J. G. E. M. Fraaije, *J. Comput. Chem.* **1997**, *18*, 1463 – 1472.
[113] V. Kräutler, W. F. van Gunsteren, P. H. Hünenberger, *J. Comput. Chem.* **2001**, *22*, 501 – 508.
[114] W. F. van Gunsteren, M. Karplus, *Macromolecules* **1982**, *15*, 1528 – 1544.
[115] M. Christen, W. F. van Gunsteren, *J. Chem. Phys.* **2005**, *122*, 144106.
[116] J. E. Straub, M. Karplus, *J. Chem. Phys.* **1991**, *94*, 6737 – 6739.
[117] A. Roitberg, R. Elber, *J. Chem. Phys.* **1991**, *95*, 9277 – 9287.
[118] G. Verkhivker, R. Elber, Q. H. Gibson, *J. Am. Chem. Soc.* **1992**, *114*, 7866 – 7878.
[119] G. Verkhivker, R. Elber, W. Nowak, *J. Chem. Phys.* **1992**, *97*, 7838 – 7841.
[120] A. Ulitsky, R. Elber, *J. Chem. Phys.* **1993**, *98*, 3380 – 3388.
[121] P. Amara, D. Hsu, J. E. Straub, *J. Phys. Chem.* **1993**, *97*, 6715 – 6721.
[122] J. P. Ma, D. Hsu, J. E. Straub, *J. Chem. Phys.* **1993**, *99*, 4024 – 4035.
[123] Q. Zheng, R. Rosenfeld, S. Vajda, C. DeLisi, *Protein Sci.* **1993**, *2*, 1242 – 1248.
[124] Q. Zheng, R. Rosenfeld, D. J. Kyle, *J. Chem. Phys.* **1993**, *99*, 8892 – 8896.
[125] K. A. Olszewski, L. Piela, H. A. Scheraga, *J. Phys. Chem.* **1992**, *96*, 4672 – 4676.
[126] K. A. Olszewski, L. Piela, H. A. Scheraga, *J. Phys. Chem.* **1993**, *97*, 260 – 266.
[127] K. A. Olszewski, L. Piela, H. A. Scheraga, *J. Phys. Chem.* **1993**, *97*, 267 – 270.
[128] C. Simmerling, J. L. Miller, P. A. Kollman, *J. Am. Chem. Soc.* **1998**, *120*, 7149 – 7155.
[129] H. Y. Liu, Z. H. Duan, Q. M. Luo, Y. Y. Shi, *Proteins Struct. Funct. Genet.* **1999**, *36*, 462 – 470.
[130] J. Zhu, H. B. Yu, H. Fan, H. Y. Liu, Y. Y. Shi, *J. Comput.-Aided Mol. Des.* **2001**, *15*, 447 – 463.
[131] J. Zhu, H. Fan, H. Y. Liu, Y. Y. Shi, *J. Comput.-Aided Mol. Des.* **2001**, *15*, 979 – 996.
[132] D. E. Goldberg, *Genetic Algorithms in Search, Optimisation and Machine Learning*, Addison-Wesley, Reading, **1989**.
[133] Y. Sugita, Y. Okamoto, *Chem. Phys. Lett.* **1999**, *314*, 141 – 151.
[134] R. Zhou, B. J. Berne, R. Germain, *Proc. Natl. Acad. Sci. USA* **2001**, *98*, 14931 – 14936.
[135] W. F. van Gunsteren, P. H. Hünenberger, A. E. Mark, P. E. Smith, I. G. Tironi, *Comput. Phys. Commun.* **1995**, *91*, 305 – 319.
[136] W. F. van Gunsteren, A. E. Mark, *J. Chem. Phys.* **1998**, *108*, 6109 – 6116.
[137] "Dynamics, Structure and Function of Biological Macromolecules": W. F. van Gunsteren, D. Bakowies, W. Damm, T. Hansson, U. Stocker, X. Daura, *NATO ASI Ser. Ser. A* **2001**, *315*, 1 – 26.
[138] X. Daura, W. F. van Gunsteren, A. E. Mark, *Proteins Struct. Funct. Genet.* **1999**, *34*, 269 – 280.
[139] A. Glättli, X. Daura, P. Bindschädler, B. Jaun, Y. R. Mahajan, R. I. Mathad, M. Rueping, D. Seebach, W. F. van Gunsteren, *Chem. Eur. J.* **2005**, *11*, 7276 – 7293.
[140] J. W. Pitera, M. Falta, W. F. van Gunsteren, *Biophys. J.* **2001**, *80*, 2546 – 2555.
[141] T. N. Heinz, W. F. van Gunsteren, P. H. Hünenberger, *J. Chem. Phys.* **2001**, *115*, 1125 – 1136.
[142] C. Peter, C. Oostenbrink, A. van Dorp, W. F. van Gunsteren, *J. Chem. Phys.* **2004**, *120*, 2652 – 2661.
[143] L. J. Smith, X. Daura, W. F. van Gunsteren, *Proteins Struct. Funct. Genet.* **2002**, *48*, 487 – 496.
[144] W. F. van Gunsteren, R. Bürgi, C. Peter, X. Daura, *Angew. Chem.* **2001**, *113*, 363 – 367; *Angew. Chem. Int. Ed.* **2001**, *40*, 351 – 355.
[145] W. F. van Gunsteren, D. Bakowies, R. Bürgi, I. Chandrasekhar, M. Christen, X. Daura, P. Gee, A. Glättli, T. Hansson, C. Oostenbrink, C. Peter, J. Pitera, L. Schuler, T. Soares, H. B. Yu, *Chimia* **2001**, *55*, 856 – 860.
[146] X. Daura, A. Glättli, P. Gee, C. Peter, W. F. van Gunsteren, *Adv. Protein Chem.* **2002**, *62*, 341 – 360.
[147] P. J. Gee, F. A. Hamprecht, L. D. Schuler, W. F. van Gunsteren, E. Duchardt, H. Schwalbe, M. Albert, D. Seebach, *Helv. Chim. Acta* **2002**, *85*, 618 – 632.
[148] H. Schäfer, X. Daura, A. E. Mark, W. F. van Gunsteren, *Proteins Struct. Funct. Genet.* **2001**, *43*, 45 – 56.
[149] C. Oostenbrink, W. F. van Gunsteren, *Proteins Struct. Funct. Genet.* **2004**, *54*, 237 – 246.
[150] C. Oostenbrink, W. F. van Gunsteren, *Phys. Chem. Chem. Phys.* **2005**, *7*, 53 – 58.
[151] L. J. Smith, R. M. Jones, W. F. van Gunsteren, *Proteins Struct. Funct. Genet.* **2005**, *58*, 439 – 449.
[152] H. Liu, A. E. Mark, W. F. van Gunsteren, *J. Phys. Chem.* **1996**, *100*, 9485 – 9494.
[153] J. W. Pitera, W. F. van Gunsteren, *J. Phys. Chem. B* **2001**, *105*, 11264 – 11274.
[154] C. Oostenbrink, W. F. van Gunsteren, *J. Comput. Chem.* **2003**, *24*, 1730 – 1739.
[155] C. Oostenbrink, W. F. van Gunsteren, *Chem. Eur. J.* **2005**, *11*, 4340 – 4348.
[156] C. Oostenbrink, W. F. van Gunsteren, *Proc. Natl. Acad. Sci. USA* **2005**, *102*, 6750 – 6754.
[157] H.-A. Yu, M. Karplus, *J. Chem. Phys.* **1988**, *89*, 2366 – 2379.
[158] B. Guillot, Y. Guissani, *J. Chem. Phys.* **1993**, *99*, 8075 – 8094.
[159] E. Gallicchio, M. M. Kubo, R. M. Levy, *J. Phys. Chem. B* **2000**, *104*, 6271 – 6285.
[160] M. Rueping, J. V. Schreiber, G. Lelais, B. Jaun, D. Seebach, *Helv. Chim. Acta* **2002**, *85*, 2577 – 2593.
[161] D. Trzesniak, A. Glättli, B. Jaun, W. F. van Gunsteren, *J. Am. Chem. Soc.* **2005**, 127, 14320 – 14329.
[162] M. Karplus, J. N. Kushick, *Macromolecules* **1981**, *14*, 325 – 332.
[163] J. Schlitter, *Chem. Phys. Lett.* **1993**, *215*, 617 – 621.
[164] H. Schäfer, A. E. Mark, W. F. van Gunsteren, *J. Chem. Phys.* **2000**, *113*, 7809 – 7817.
[165] J. Carlsson, J. Aqvist, *J. Phys. Chem. B* **2005**, *109*, 6448 – 6456.
[166] H. Schäfer, L. J. Smith, A. E. Mark, W. F. van Gunsteren, *Proteins Struct. Funct. Genet.* **2002**, *46*, 215 – 224.
[167] M. Bellanda, E. Peggion, R. Bürgi, W. F. van Gunsteren, S. Mammi, *J. Pept. Res.* **2001**, *57*, 97 – 106.
[168] A. Bavoso, E. Benedetti, B. DiBlasio, V. Pavone, C. Pedone, C. Toniolo, G. M. Bonora, F. Formaggio, M. Crisma, *J. Biomol. Struct. Dyn.* **1988**, *6*, 803 – 817.
[169] R. Bürgi, X. Daura, A. Mark, M. Bellanda, S. Mammi, E. Peggion, W. F. van Gunsteren, *J. Pept. Res.* **2001**, *57*, 107 – 118.
[170] H. B. Yu, M. Ramseier, R. Bürgi, W. F. van Gunsteren, *ChemPhysChem* **2004**, *5*, 633 – 641.
[171] X. Daura, I. Antes, W. F. van Gunsteren, W. Thiel, A. E. Mark, *Proteins Struct. Funct. Genet.* **1999**, *36*, 542 – 555.
[172] A. Glättli, X. Daura, D. Seebach, W. F. van Gunsteren, *J. Am. Chem. Soc.* **2002**, *124*, 12972 – 12978.
[173] A. Glättli, W. F. van Gunsteren, *Angew. Chem.* **2004**, *116*, 6472 – 6476; *Angew. Chem. Int. Ed.* **2004**, *43*, 6312 – 6316.

© 2006 Wiley-VCH Verlag GmbH & Co. KGaA, Weinheim

[174] K. Gademann, A. Häne, M. Rueping, B. Jaun, D. Seebach, *Angew. Chem.* **2003**, *115*, 1573 – 1575; *Angew. Chem. Int. Ed. Angew. Chem. Int. Ed. Engl.* **2003**, *42*, 1534 – 1537.
[175] T. A. Soares, X. Daura, C. Oostenbrink, L. J. Smith, W. F. van Gunsteren, *J. Biomol. NMR* **2004**, *30*, 407 – 422.
[176] L. J. Smith, M. J. Sutcliffe, C. Redfield, C. M. Dobson, *J. Mol. Biol.* **1993**, *229*, 930 – 944.
[177] H. Schwalbe, S. B. Grimshaw, A. Spencer, M. Buck, J. Boyd, C. M. Dobson, C. Redfield, L. J. Smith, *Protein Sci.* **2001**, *10*, 677 – 688.
[178] W. F. van Gunsteren, A. E. Mark, *J. Chem. Phys.* **1998**, *108*, 6109 – 6116.
[179] "Modelling of Molecular Structures, Properties": W. F. van Gunsteren in *Studies in Physical Theoretical Chemistry*, *Vol. 71* (Ed.: J.-L. Rivail), Elsevier, Amsterdam, **1990**, pp. 463 – 478.
[180] W. F. van Gunsteren, A. E. Mark, *Eur. J. Biochem.* **1992**, *204*, 947 – 961.
[181] P. H. Hünenberger, A. E. Mark, W. F. van Gunsteren, *J. Mol. Biol.* **1995**, *252*, 492 – 503.
[182] B. G. Fitch, R. S. Germain, M. Mendell, J. Pitera, M. Pitman, A. Rayshubskiy, Y. Sham, F. Suits, W. Swope, T. J. C. Ward, Y. Zhestkov, R. Zhou, *J. Parall. Distr. Comp.* **2003**, *63*, 759 – 773.
[183] J. Norberg, L. Nilsson, *Q. Rev. Biophys.* **2003**, *36*, 257 – 306.
[184] A. D. MacKerell, *J. Comput. Chem.* **2004**, *25*, 1584 – 1604.
[185] M. J. Field, P. A. Bash, M. Karplus, *J. Comput. Chem.* **1990**, *11*, 700 – 733.
[186] D. Bakowies, W. Thiel, *J. Phys. Chem.* **1996**, *100*, 10580 – 10594.
[187] A. Warshel, *Computer Modelling of Chemical Reactions in Enzymes and Solution*, Wiley, New York, **1991**.
[188] H. J. C. Berendsen, J. Mavri, *J. Phys. Chem.* **1993**, *97*, 13464 – 13468.
[189] S. R. Billeter, W. F. van Gunsteren, *Comput. Phys. Commun.* **1997**, *107*, 61 – 91.
[190] H. J. C. Berendsen, J. Mavri in *Theoretical Treatments of Hydrogen Bonding* (Ed.: D. Hadzi), Wiley, New York, **1997**, pp. 119 – 141.
[191] S. R. Billeter, S. P. Webb, T. Iordanov, P. K. Agarwal, S. Hammes-Schiffer, *J. Chem. Phys.* **2001**, *114*, 6925 – 6936.
[192] S. J. Benkovic, S. Hammes-Schiffer, *Science* **2003**, *301*, 1196 – 1202.
[193] T. Hansson, C. Oostenbrink, W. F. van Gunsteren, *Curr. Opin. Struct. Biol.* **2002**, *12*, 190 – 196.
[194] J. C. Shillcock, R. Lipowsky, *J. Chem. Phys.* **2002**, *117*, 5048 – 5061.
[195] *Scylla* and *Charybdis* are two monsters from Greek mythology that guarded the narrow waters of the Straits of Messina destroying ships as they attempted to navigate through.

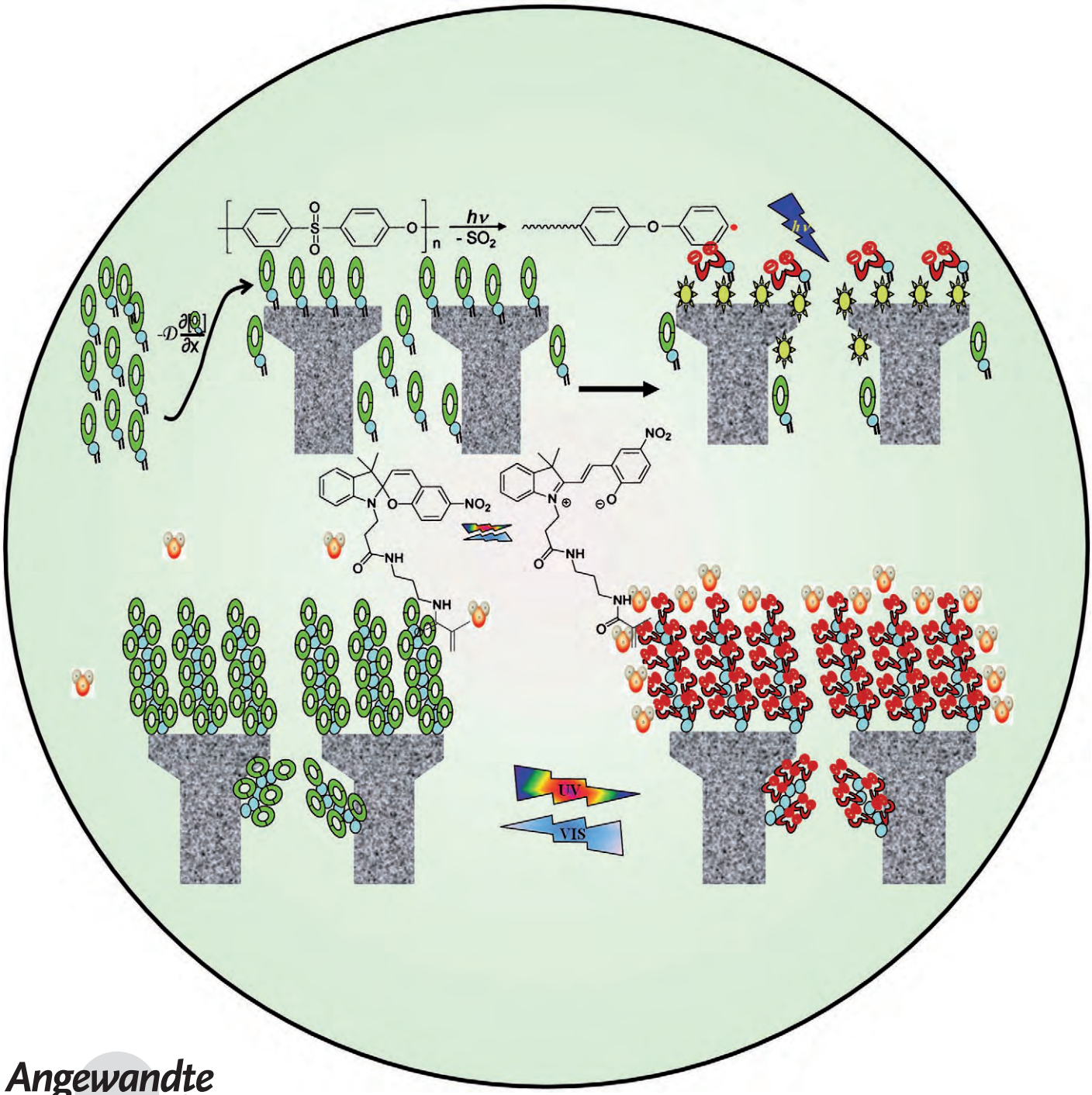
 © 2006 Wiley-VCH Verlag GmbH & Co. KGaA, Weinheim

Membranes

DOI: 10.1002/anie.200600581

An Optically Reversible Switching Membrane Surface**

*Arpan Nayak, Hongwei Liu, and Georges Belfort**



InterScience

© 2006 Wiley-VCH Verlag GmbH & Co. KGaA, Weinheim

The surface chemistry of synthetic membranes is of great interest to the bioprocessing of protein-containing solutions, to the filtration of medically relevant solutions, and to the performance of membrane-based sensors.[1] For biosensors, controlling the polarity of the membrane and reducing nonspecific protein adsorption would significantly improve signal to noise ratios. This may also be useful as a switch to control diffusive transport to biosensor elements (enzymes, chemoreceptors, etc) by changing the polarity of the protective membrane when desired. For bioprocessing, it has direct bearing on the efficacy of producing and delivering desirable proteins and other biologically derived molecules at high yield and purity.[2]

The performance of synthetic polymer membranes when filtering bioprocessing and biomedical fluids is severely limited by the interaction of proteins with membrane surfaces. Currently, expensive and labor-intensive methods such as controlling the pH and ionic strength of the feed solution, periodic cleaning, and back flushing are used to deal with the loss of filtration performance resulting from protein adhesion. It would therefore be extremely attractive to have an in situ cleaning procedure in which filtration performance could be re-established with minimum need for expensive cleaning chemicals and down time owing to back flushing. Synthesizing membranes with polymers that reduce such interactions has resulted in improved filtration performance.[3,4]

We suggest herein that grafting environmentally responsive polymers onto synthetic membranes by using simple inexpensive methods such as photograft-induced polymerization, which can be easily incorporated into the membrane synthesis process, may offer an alternative method to the approaches that use traditional protein-adhesion-resistant monomers such as polyethylene glycol and other hydrophilic monomers.[3,5] Specifically, we combine two known technologies, a patented UV-grafting process with the well-known photoresponsive properties of spiropyran molecules, to produce an optically reversible switching membrane surface.

Vinyl monomers with desirable functionality are easily grafted and polymerized onto UV-sensitive polymers such as poly(ether sulfone) (PES) membranes by using a UV-induced graft polymerization method (Figure 1 A).[6] Exposure of a PES synthetic membrane to 300-nm UV radiation produces radical sites onto which vinyl monomers such as vinyl spiropyran can graft and polymerize. The spiropyrans are comprised of a group of light-switchable photochromic organic molecules that are colorless, nonpolar, and in a "closed" form in the visible light.[7,8] When exposed to UV and visible light, spiropyrans isomerize and produce a colored polar "open" merocyanine form and a white nonpolar "closed" form, respectively (Figure 1 B–E, Figure 2).

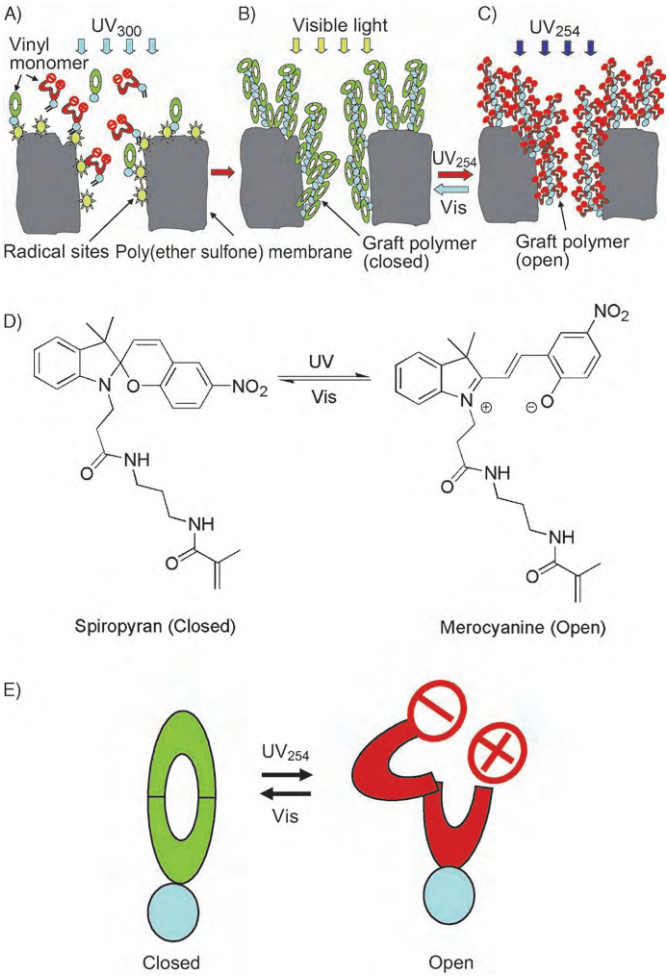


Figure 1. Schematic of graft polymerization and switching: A) Rensselaer's patented photografting process in which a synthetic ultrafiltration membrane formed from PES (photo sensitive polymer) is first dipped into a vinyl (spiropyran) monomer solution (1% w/v) in ethyl acetate for 1 h and then exposed to 300-nm UV irradiation to induce grating and polymerization. B) Exposure of the grafted PES membrane to visible light for 1 h resulting in the formation of the "closed" apolar white form of spiropyran. C) Exposure of the grafted "closed" form of the PES membrane to UV irradiation at 254 nm for 1 h formed the "open" polar red form of spiropyran. D) The chemical structure of the vinyl spiropyrans in two configurations as a function of UV and Vis irradiation. E) A schematic of the chemical structure of the vinyl spiropyrans in two configurations as a function of UV and visible (Vis) irradiation.

Light-switching of monolayers of azobenzene[9–11] and spiropyran[12] has been studied on solid substrates. Previously, binding of photochromic moieties to solid substrates required complicated and multi-step procedures,[13,14] whereas herein we use a relatively simple two-step dip and UV-irradiation process that could be easily incorporated into a commercial manufacturing process.[15] The challenge was to synthesize optically active vinyl spiropyran (1′-(2-propylcarbamylmethacrylamide)ethyl)-3′,3′-dimethyl-6-nitrospiro[2*H*-1]benzo-

[*] A. Nayak, H. Liu, Prof. G. Belfort
Howard P. Isermann Department of Chemical and Biological Engineering
Rensselaer Polytechnic Institute
Troy, New York 12180 (USA)
Fax: (+1) 518-276-4030
E-mail: belfog@rpi.edu

[**] We acknowledge the support of the US Department of Energy (Grant No. DE-FG02-90ER14114) and the National Science Foundation (Grant No. CTS-94-00610).

Supporting information for this article is available on the WWW under http://www.angewandte.org or from the author.

 © 2006 Wiley-VCH Verlag GmbH & Co. KGaA, Weinheim

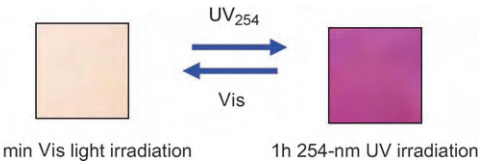


Figure 2. Color change of spiropyran-grafted PES membrane after exposure to UV irradiation at 254 nm for 1 h and visible light for 5 min in air.

pyran-2,2′-indoline) and determine whether the photografting process that uses UV light at 300 nm would allow the vinyl spiropyran molecules to graft and retain their switchable properties. A commercial PES 30-kDa synthetic membrane filter was chosen as a model membrane surface because of its high sensitivity to 300-nm UV radiation and because it is one of the most widely used polymeric materials that is used to produce commercial ultrafiltration membranes and support layers for reverse osmosis and nanofiltration membranes.[16]

The synthesized vinyl spiropyran was photografted onto the 30-kDa PES ultrafiltration membranes by using our standard grafting method. Attenuated total reflection Fourier transform infrared spectroscopy (ATR/FTIR) was used to demonstrate that the vinyl monomers were grafted onto the PES membranes. In Figure 3, ATR/FTIR spectra are compared for the unmodified PES membrane with those of the grafted-spiropyran-modified PES membranes. The peaks at 1410, 1487, 1579, and 1663 cm^{-1} are owing to the -SO_2 group, the aromatic-ring stretch of C=C, the aromatic C–H stretch, and the aromatic C=O stretch, respectively. The last peak may shift depending on the chemical and charge environment. Under exposed visible light for 5 min and on a dry membrane, the peak at $\approx$1663 cm^{-1} is maximized whereas the peak at $\approx$1720–5 cm^{-1} is reduced. Similarly, under 254-nm UV radiation for 1 h on a dry membrane, the peak at $\approx$1663 cm^{-1} is reduced whereas that at $\approx$1720–5 cm^{-1} is

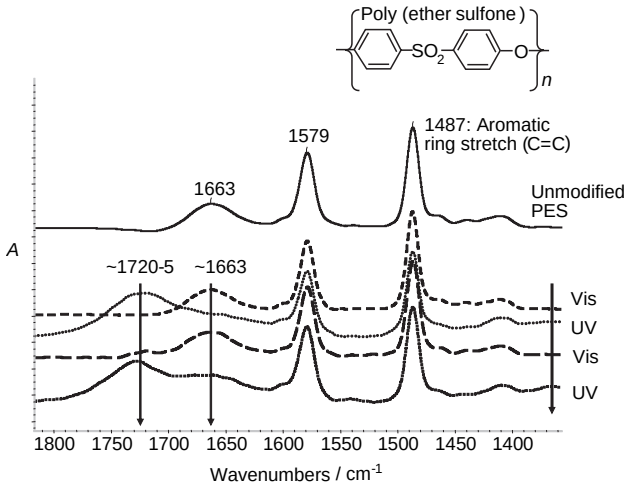


Figure 3. Five ATR/FTIR spectra of the unmodified (as received) PES ultrafiltration membrane and the spiropyran-grafted PES membrane after two cycles of exposure to UV irradiation at 254 nm for 1 h and visible light for 5 min. Note that the peak at $\approx$1663 cm^{-1} decreases whereas the peak at $\approx$1720–1725 cm^{-1} increases in intensity during exposure to UV at 254 nm.

increased. If the ratio of peak heights, $R = (h_{1720}/h_{1487})/(h_{1663}/h_{1487})$, is defined as a measure of the ratio of the relative chemical surface condition under ultraviolet radiation versus that under visible-light exposure, we can follow this ratio with changing irradiation exposure in Figure 4A. The reference peak at 1487 cm^{-1} is a measure of the carbon–carbon aromatic-ring stretch and is used as an internal standard as it is independent of the grafting process.

Similarly, measuring the sessile contact angle of the grafted dry PES membrane with a water droplet after alternating exposure to 254-nm UV (1 h) and visible light (5 min) demonstrates changes in surface wettability (Figure 4B). About a 16° drop in contact angle was obtained through this process. This is similar in magnitude to that reported by Lahann and co-workers who used electrical potential to induce a polarity change in a self-assembled polar molecule on a gold surface.[17] As protein–membrane interactions can determine success or failure for many processes including those mentioned above, we demonstrate, through two related experiments, that the switchable hydrophilic (on exposure to 254-nm UV light) and hydrophobic (with visible light) surfaces 1) exhibit low and high protein adsorbabilities, respectively, and 2) display high and low buffer-permeations rates after protein adsorption, respectively. Results for these two experiments are shown in Figure 4C,D. Bovine serum albumin (BSA; 67 kDa, pI 4.7) was used as a model protein for the adsorption experiments. Clearly, from the data shown in Figure 4C, the as-received PES membrane exhibited the highest adsorbed amount of BSA in 10 mM phosphate-buffered saline (PBS) buffer solution at pH 7.4 and 22 ± 1 °C followed by the grafted vinyl spiropyran in the "closed" (visible light) and "open" (254-nm UV light) configuration. The "closed" configuration of the vinyl spiropyran surface adsorbed about 26% more protein than the "open" configuration of the surface. These surfaces, with adsorbed protein on them, were then tested to see if this difference in protein adsorption translated into higher permeation flux. The modified membranes were then placed into a filtration test cell and the permeation rate of freshly prepared PBS at pH 7.4 and 22 ± 1 °C measured (Figure 4D). As expected, the "closed" configuration of the vinyl spiropyran gave about a 17% lower permeation flux as compared with the "open" configuration of the vinyl spiropyran surface. The contact-angle measurements of the base PES membrane, of the base PES membrane after washing with ethyl acetate solvent, and of the base PES membrane irradiated with 254-nm UV light for 1 h were also obtained (see the Supporting Information). No noticeable change in contact angle was observed in this control experiment. However, irradiation with UV light under wet rather than dry conditions reduces the switching time from "closed" to "open" conformation by about one third (data not shown).

The results presented herein demonstrate the reversible conversion of a photografted, photoresponsive, polymeric synthetic membrane surface from polar to nonpolar character. We have clearly shown that a UV/Vis-switchable moiety such as spiropyran can be grafted onto a commercial photoactive polymer such as PES by using a very simple photograft polymerization method. Both molecular (ATR/FTIR) and

 © 2006 Wiley-VCH Verlag GmbH & Co. KGaA, Weinheim

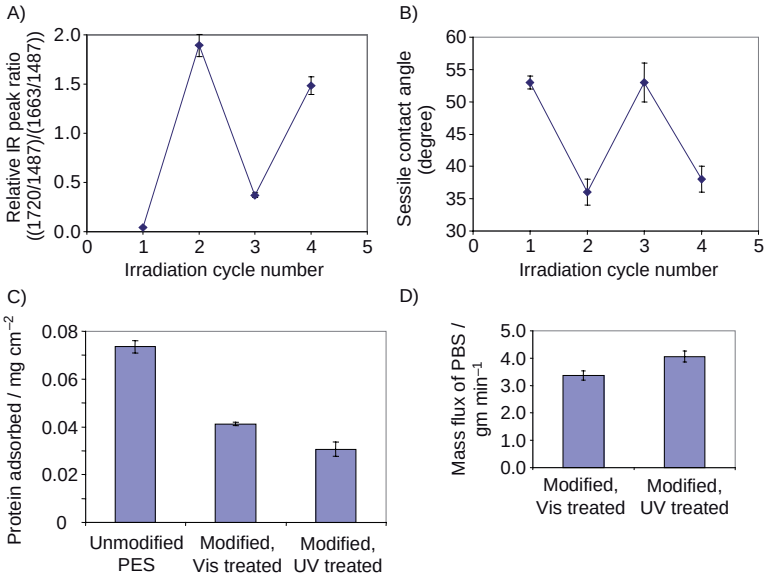


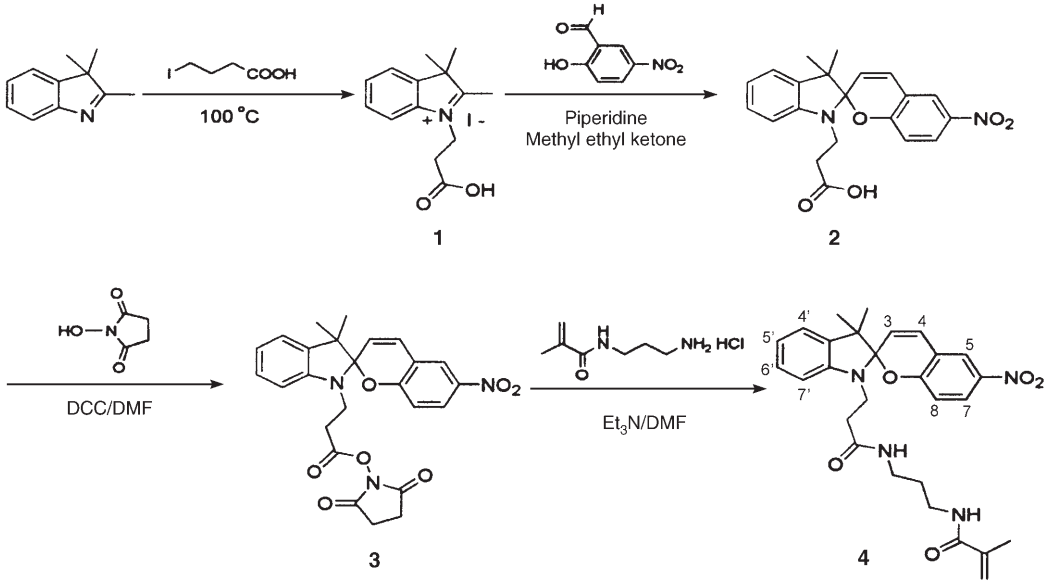
Figure 4. Summary data demonstrating the optically reversible switching of the wettability of the spiropyran grafted PES membrane surface after exposure to 254-nm UV light and visible light. A) Ratio of peak heights, $R=(h_{1720}/h_{1487})/(h_{1663}/h_{1487})$, from ATR/FTIR spectra from Figure 3 as a function of alternating exposure to 254-nm UV light (1 h) and visible light (5 min) or cycle number. B) Surface wettability changes as measured by the sessile contact angle of the grafted PES membrane with a water droplet after alternating exposure to 254-nm UV light (1 h) and visible light (5 min) or cycle number. C) Adsorption of BSA in PBS (10 mM; pH 7.4) at 22±1°C for 1 h on the as-received PES membrane and on modified PES membranes with grafted vinyl spiropyran in the "closed" (visible light) and "open" (254-nm UV light) configuration. D) Mass flux of PBS at pH 7.4 and 22±1°C permeating through modified PES membranes with grafted vinyl spiropyran in the "closed" (visible light) and "open" (254-nm UV light) configuration after exposure to BSA adsorption from (C).

classical (color, contact angle, protein adsorption, and subsequent buffer ultrafiltration) measurements were used to confirm the reversible polar–apolar reaction of grafted spiropyran owing to exposure of UV/Vis radiation. Rather than inducing a physical movement (conformational change) of long-chain SAMs toward an electrode by changing the surface potential of a gold substrate,[17,18] we have synthesized and grafted a photoresponsive molecule (vinyl spiropyran) onto a widely used industrial polymer. This was accomplished by combining two technologies, our patented UV grafting process with the well-known photoresponsive properties of spiropyran molecules, to produce an optically reversible switching membrane surface. The relative ease of this grafting and switching process should suggest many industrial opportunities including those dependent on surface wettability and molecular adhesion.

Future work will involve further optimization of the approach presented herein. Further research with triggers other than UV/Vis radiation, such as temperature, pH, and ionic strength, can be pursued with vinyl functional groups and photosensitive PES. Besides membrane filtration and sensors, there is a need to consider surface properties of materials for catheters, surgical instruments, and pulmonary breathing tubes that are exposed to body fluids, and for spot detection for genomic analysis and nanoprocessing in micro-fluidic devices.

Experimental Section

Vinyl spiropyran (1′-(2-(propylcarbamylmethacrylamide)ethyl)-3′,3′-dimethyl-6-nitrospiro[2H-1]benzo- pyran-2,2′-indoline): 3-aminopropyl methacrylamide hydrochloride was obtained from Polysciences Inc. All other chemicals were purchased from Aldrich Chemical Co. and used without further purification. 1-(2-carboxyethyl)-2,3,3-trimethylindolenine iodide (**1**), 1′-(2-carboxyethyl) −3′,3′-dimethyl −6- nitro spiro-[2H-1]benzopyran-2,2′-indoline (**2**), and 1′-(2-(carbosuccinimidyloxy)ethyl)-3′,3′-dimethyl-6-nitrospiro[2*H*-1]benzopyran-2,2′-indoline (**3**) were synthesized according to literature methods[19] (Scheme 1).



Scheme 1. Synthesis of the spiropyran-containing monomer compound **4**. DCC = dicyclohexyl carbodiimide.

 © 2006 Wiley-VCH Verlag GmbH & Co. KGaA, Weinheim

NMR spectra were measured on a Varian spectrometer by using tetramethylsilane (TMS) as the internal standard. Mass spectra were recorded by using electrospray ionization.

1′-(2-(Propylcarbamylmethacrylamide)ethyl)-3′,3′-dimethyl-6-nitrospiro[2H-1]benzo- pyran-2,2′-indoline (**4**): The mixture of **3** (3.26 g, 6.83 mmol), 3-aminopropyl methacrylamide hydrochloride (1.34 g, 7.50 mmol), and triethyl amine (1 mL, 7.19 mmol) was stirred in *N*,*N*-dimethylformamide (DMF; 50 mL) at room temperature for 20 h. After the evaporation of DMF, the residue was dissolved in chloroform, washed with water and then purified by silica-gel column chromatography (eluent, ethyl acetate/hexane; 1:1 v/v) to give **4** as a yellow solid (2.6 g, 76%). ^{1}H NMR (500 MHz, $CDCl_3$): $\delta = 7.99$ (m, 2H; 5-H and 7-H), 7.18 (t, 1H; 6′-H), 7.08 (d, 1H; 4′-H), 6.89 (m, 2H; 4-H and 5′-H), 6.75 (d, 1H; 8-H), 6.67 (d, 1H; 7′-H), 6.51 (m, 1H; NH), 6.39 (m, 1H; NH), 5.87 (d, 1H; 3-H), 5.74 (s, 1H; CH_2), 5.35 (s, 1H; CH_2), 3.68 (m, 1H; CH_2N), 3.51 (m, 1H; CH_2N), 3.20 (m, 4H; CH_2), 2.56 (m, 1H; CH_2CO), 2.44 (m, 1H; CH_2CO), 1.93 (s, 3H; CH_3), 1.58 (m, 2H; CH_2), 1.27 (s, 3H; CH_3), 1.17 ppm (s, 3H; CH_3); ^{13}C NMR (300 MHz, $CDCl_3$): $\delta = 18.9$, 20.1, 26.0, 29.8, 35.9, 36.3, 40.2, 53.1, 107.0, 115.7, 118.9, 120.0, 120.2, 122.0, 122.2, 123.0, 126.1, 128.0, 128.5, 136.1, 139.9, 141.2, 146.7, 159.7, 169.2, 171.9 ppm.

MS calcd $C_{28}H_{32}N_4O_5$: 504.24. Found $[M+H]^+$: 505.2, $[M+Na]^+$: 527.1.

Preparation of modified membranes: 30-kDa PES membranes were modified by using a UV-induced graft polymerization method as described in detail in Taniguchi, Belfort and co-workers.[3,6,15,16] A Rayonet photochemical chamber reactor system (Model RPR-100, Southern New England, Ultraviolet Co., Branford, CT) containing 300-nm UV lamps ($\approx$15% of the energy was at $<$280 nm) was used. The membranes were dipped in spyropyran monomer solution (1% *w*/*v* in ethyl acetate) for 1 h with stirring at 22 ± 1 °C, removed from the monomer solution, purged with N_2 for 10 min, and irradiated with 300-nm UV light in water-saturated N_2 for 4 min. After photografting, the membranes were again cleaned with ethyl acetate by shaking overnight to remove homopolymer and unreacted monomer from the membrane. Then, the modified membranes were vacuum dried for use.

ATR/FTIR: ATR/IR (Magna-IR 550 Series II, Thermo Nicolet Instruments Corp., Madison, WI) was used to obtain a measure of the degree of grafting. By using an incident angle of 45°, the penetration or sampling depth was approximately 0.1–1.0 μm. Spectra were collected at a gain of 8 and resolution of 2 cm^{-1} with 512 scans for each sample.

Synthetic membrane: The PES membrane with a 30-kDa molecular-weight cut off from lot 9140E was obtained from Pall Corp. (East Hills, NY). These Omega series have been slightly hydrophilized by the manufacturer by an undisclosed process as evidenced by the small carbonyl peak at $\approx$1663 cm^{-1}.

Contact angle: The sessile contact angle of water in air on the membrane substrates was measured by using an optical system (SIT camera, SIT66, Dage-MTI, Michigan, IN) converted to a video display. Water droplets of 2.5 μL were placed on the membrane substrates at different positions and the contact angles were measured. At least five measurements were made and the average reported.

BSA adsorption: BSA was dissolved in PBS buffer solution (10 mM; pH 7.4) to prepare a 1 mg mL^{-1} protein solution. Membrane swatches (3 cm^2) were immersed in the BSA solution for 2 h at 22 ± 1 °C. The amount of adsorbed protein was determined by staining with Ponceau S solution (Ponceau S (2%), trichloroacetic acid (30%), and sulfosalicylic acid (30%)). Membranes with adsorbed protein were immersed for 1 h into a solution of Ponceau S, washed thoroughly with deionized water, immersed for 1 h in acetic acid (5% v/v), and again washed with deionized water. Then the protein–dye complex was quantitatively eluted with NaOH solution (3 mL, 100 mM) for 1 h. Next, the membranes were removed, the solutions neutralized with HCl (50 μL, 6 M), and the absorbance of the red-colored solutions was measured at 515 nm. Protein amounts were calculated based on a calibration which was performed with known BSA amounts ($m_{BSA} = 0.001$–1 mg) onto clean unmodified PES membranes ($A_{515\,nm} = 0.6799\,m_{BSA} + 0.0754$; $R^2 = 0.9944$).

PBS filtration: PBS buffer solution (10 mM; pH 7.4) was used as the feed. The PBS buffer solution was composed of NaCl (137 mM) and KCl (2.7 mM) in deionized water. Membranes were immersed in the BSA solution (1 mg mL^{-1} in PBS buffer) for 5 min to induce protein adsorption. Then, PBS permeation flux through the membranes with adsorbed BSA was measured. A dead-end stirred cell (Model 8010, Millipore Corp., Bedford, MA) filtration system was used for PBS flux measurements through the membranes. The active membrane area was 3.8 cm^2. All filtration experiments were conducted at a constant transmembrane pressure of 69 kPa, a stirring rate of 500 rpm, and a system temperature of 22 ± 1 °C.

Received: February 13, 2006
Published online: May 16, 2006

Keywords: membranes · optical properties · polymerization · surface chemistry · UV/Vis spectroscopy

[1] "Interactions of proteins with polymeric synthetic membranes": G. Belfort, A. L. Zydney, *Biopolymers at Interfaces*, Marcel Dekker, New York, **2003**.
[2] L. J. Zeman, A. L. Zydney, *Microfiltration and Ultrafiltration Principles and Applications*, Marcel Dekker, New York, **1996**.
[3] M. Taniguchi, G. Belfort, *J. Membr. Sci.* **2004**, *231*, 147–157.
[4] M. J. Steuck, US Patent 4618533, **1986**.
[5] M. Ulbricht, H. Matuschewski, A. Oechel, H. G. Hicke, *J. Membr. Sci.* **1996**, *115*, 31–47.
[6] G. Belfort, M. Taniguchi, J. Pieracci, US Patent 6852769, **2005**.
[7] "Biological applications-Supramolecular chemistry": M. Inouye, *Organic, Photochromic and Thermochromic Compounds*, *Vol. 2*, Kluwer Academic, New York, **1999**, chap. 9.
[8] H. Bouas-Laurent, H. Dürr, *Pure Appl. Chem.* **2001**, *73*, 639–665.
[9] W. Jiang, G. Wang, Y. He, X. Wang, Y. An, Y. Song, L. Jiang, *Chem. Commun.* **2005**, 3550–3552.
[10] H. Ge, G. Wang, Y. He, X. Wang, Y. Song, L. Jiang, D. Zhu, *ChemPhysChem* **2006**, *7*, 575–578.
[11] K. Ichimura, S.-K. Oh, M. Nakagawa, *Science* **2000**, *288*, 1624–1626.
[12] B. C. Bunker, B. I. Kim, J. E. Houston, R. Rosario, A. A. Garcia, M. Hayes, D. Gust, S. T. Picraux, *Nano Lett.* **2003**, *3*, 1723–1727.
[13] R. Rosario, D. Gust, M. Hayes, F. Jahnke, J. Springer, A. A. Garcia, *Langmuir* **2002**, *18*, 8062–8069.
[14] S. Abbott, J. Ralston, G. Reynolds, R. Hayes, *Langmuir* **1999**, *15*, 8923–8928.
[15] J. Pieracci, D. W. Wood, J. V. Crivello, G. Belfort, *Chem. Mater.* **2000**, *12*, 2123–2133.
[16] B. Kaeslev, J. Pieracci, G. Belfort, *J. Membr. Sci.* **2001**, *194*, 245–261.
[17] J. Lahann, S. Mitragotri, T. -N. Tran, H. Kaido, J. Sundaram, I. S. Choi, S. Hoffer, G. A. Somorjai, R. Langer, *Science* **2003**, *299*, 371–374.
[18] U. Rant, K. Arinaga, S. Fujita, N. Yokoyama, G. Abstreiter, M. Tornow, *Nano Lett.* **2004**, *4*, 2441–2445.
[19] A. Fissi, O. Pieroni, G. Ruggeri, F. Ciardelli, *Macromolecules* **1995**, *28*, 302–309.

 © 2006 Wiley-VCH Verlag GmbH & Co. KGaA, Weinheim

Dynamic Chemistry

DOI: 10.1002/anie.200600817

Chiral Borromeates**

*Cari D. Pentecost, Andrea J. Peters, Kelly S. Chichak, Gareth W. V. Cave, Stuart J. Cantrill, and J. Fraser Stoddart**

The quest for topologically interesting molecules has led to the template-directed synthesis[1] of a wide range of molecular catenanes and knots.[2] Such molecules with interlocked and intertwined structures have nonplanar molecular graphs and can exhibit[3] topological chirality.[4] Although the classic example is the trefoil knot,[2,4] catenanes—characterized in knot theory by the Hopf link—can also display topological chirality, provided that both rings exhibit structural directionality.[5] By contrast, the Borromean rings (BRs)—characterized in knot theory by the Brunnian link—remain amphicheiral[6] even after orientation. Thus, the only way by which we can render BRs chiral is to introduce chirality in the form of elements that are planar, axial, or point (stereogenic) in nature.

Although the incorporation of stereogenic centers into mechanically interlocked molecules can be inconsequential, especially if the stereogenic centers are far removed from the rest of the functional groups in the molecule, the effects of such centers can often be amplified, particularly when they are able to influence nearby molecular structure, sometimes even inducing chirality.[7] Relatively simple transition-metal complexes containing 2,2′-bipyridyl ligands with appended stereogenic centers have been termed chirality generators (or CHIRAGENs)[8] because the absolute configuration of these centers can determine the absolute configuration induced at the metal coordination site. This kind of chirality transfer has been identified in tight-fitting, mechanically interlocked molecules such as the catenate investigated recently by Sauvage and co-workers[9] that contains an axially chiral binaphthyl unit. Herein, we report the preparation of two enantiomeric pairs of Borromean linked compounds[10,11] using Zn^{II} ions to template their formation from diaminobipyridine (**DAB**) ligands with one of two like stereogenic centers (i.e., (*R*,*R*) or (*S*,*S*)) and either 2,6-diformylpyridine (**DFP**) or its 4-chloro derivative **Cl-DFP**[12] to give the $(R)^{12}$ and $(S)^{12}$ enantiomers of the Borromean link compounds **BR**·12 TFA and **BRCl$_6$**·12 TFA (TFA = trifluoroacetate); that is, $(R)^{12}$-**BR**·12 TFA, $(S)^{12}$-**BR**·12 TFA, $(R)^{12}$-**BRCl$_6$**·12 TFA, and $(S)^{12}$-**BRCl$_6$**·12 TFA. It transpires that, as a consequence of introducing four stereogenic centers into each of three identical rings in these chiral Borromeates[13] such that they pair up in locations close to the six ions, these metal ions are surrounded by chiral coordination spheres as revealed by one X-ray crystal structure and several circular dichroism (CD) spectra.

The (*R*,*R*)- and (*S*,*S*)-**DAB**-H_n·*n* TFA precursors were each synthesized (see Supporting Information) in five steps from the (*R*) and (*S*) enantiomers, respectively, of *p*-hydroxyphenylglycine methyl ester hydrochloride. In four separate reactions, the chiral diaminobipyridine ligands, as their TFA^- salts, were treated at 70 °C for 24 h in *i*PrOH with equimolar amounts (0.10 mM) of either **DFP** or **Cl-DFP**, in the presence of $Zn(OAc)_2$ as the template to afford stereospecifically $(R)^{12}$-**BR**·12 TFA and $(S)^{12}$-**BR**·12 TFA, and $(R)^{12}$-**BRCl$_6$**·12 TFA and $(S)^{12}$-**BRCl$_6$**·12 TFA (Scheme 1). High-resolution electrospray ionization mass spectrometry (HR-ESI-MS) revealed peaks at *m*/*z* 1585.3302 and 1160.2263, and 1584.2427 and 1160.1778, respectively, for the triply and quadruply charged molecular ions from $(R)^{12}$-**BR**·12TFA and $(S)^{12}$-**BR**·12 TFA: the analogous *m*/*z* values for $(R)^{12}$-**BRCl$_6$**·12 TFA and $(S)^{12}$-**BRCl$_6$**·12 TFA are 1653.5458 and 1211.9171, and 1652.5632 and 1212.4001, respectively. Although the ^{1}H NMR spectra of all these compounds recorded in CD_3OD at 600 MHz were characterized by broad resonances, a singlet for the 12 imine protons was discernible at $\delta = 9.0$ ppm in all four spectra and peaks for most[14] of the other heterotopic protons in the chiral **BR**·12 TFA and **BRCl$_6$**·12 TFA compounds could be identified and assigned (Figure 1).

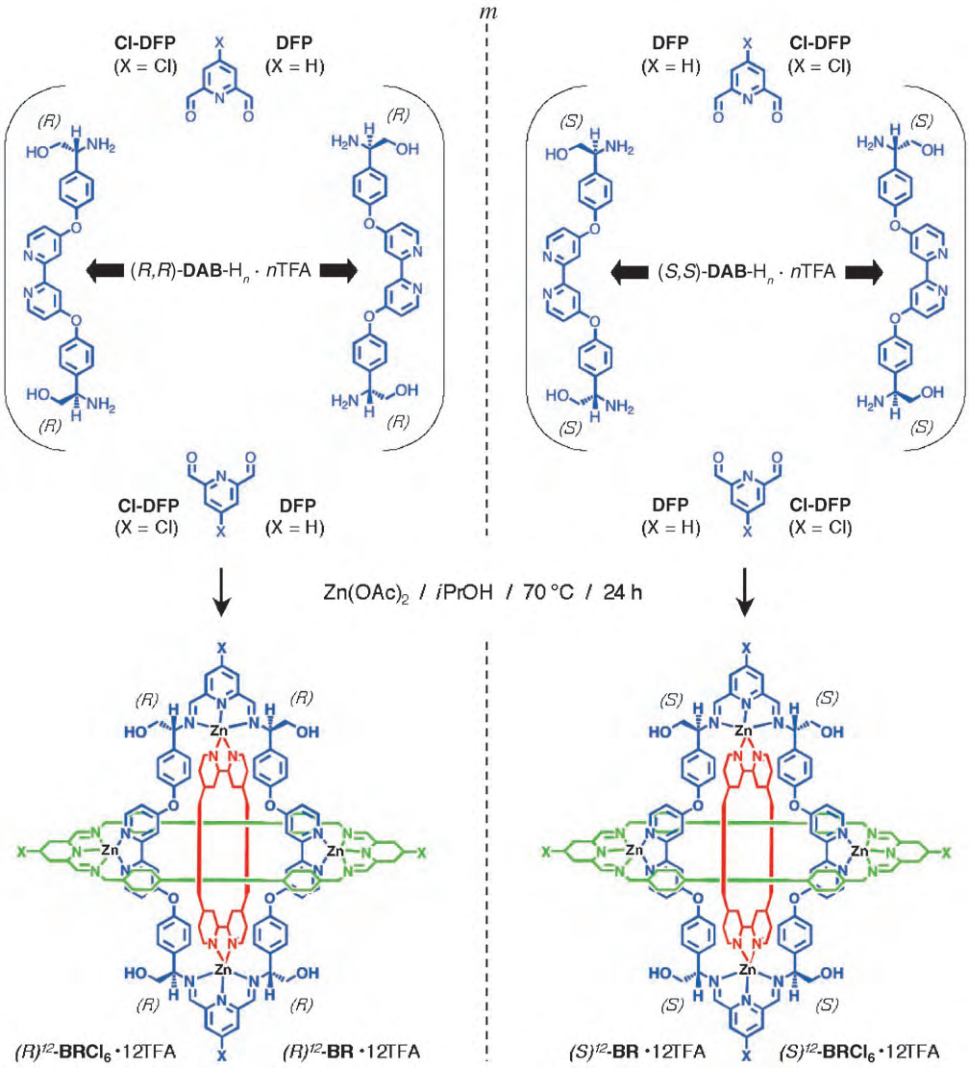
Single colorless crystals[15] of $(R)^{12}$-**BRCl$_6$**·12 TFA, suitable for X-ray crystallography,[16] were obtained by vapor diffusion of Et_2O into a methanolic solution of the compound.[17] The solid-state structure of the original, achiral Borromean rings[10a] indicated that all three macrocycles adopt chairlike conformations, such that they confer S_6 symmetry on the molecule. In the chiral Borromean rings, we expected the C_3 axis, which is collinear with the S_6 axis in the achiral progenitor, to be present in the solid-state structure. However, although the same chairlike conformations can also be observed (Figure 2a) in the orthogonal arrangement of the three macrocycles in $(R)^{12}$-**BRCl$_6$**$^{12+}$, the C_3 axis is not evident: the symmetry is reduced to C_1 on account of one of the three macrocycles adopting a flipped chairlike conformation (Figure 2b). On inspection of the three chairlike conformations in **BRCl$_6$**$^{12+}$, the CH_2OH groups are oriented in pairs with the pseudo-axial and pseudo-equatorial arrangements alternating between neighboring 60° segments (Figure 3). Moreover, beyond the molecule, the packing diagrams (Figure 4) show that these CH_2OH groups result in the formation of two very different hydrophilic solvent channels that run all the way through the lattice such that the channels are lined with only pseudo-axial CH_2OH groups or only pseudo-equatorial CH_2OH groups.

[*] C. D. Pentecost, Dr. A. J. Peters, Dr. K. S. Chichak, Dr. S. J. Cantrill, Prof. J. F. Stoddart
The California NanoSystems Institute, and
Department of Chemistry and Biochemistry
University of California, Los Angeles
405 Hilgard Avenue, Los Angeles, CA 90095-1569 (USA)
Fax: (+1) 310-206-1843
E-mail: stoddart@chem.ucla.edu
Dr. G. W. V. Cave
School of Biomedical and Natural Sciences
Nottingham Trent University
Nottingham, NG11 8NS (UK)

[**] The research at UCLA was supported by the National Science Foundation (NSF).

Supporting information for this article is available on the WWW under http://www.angewandte.org or from the author.

 © 2006 Wiley-VCH Verlag GmbH & Co. KGaA, Weinheim



Scheme 1. Schematic representation of $(R)^{12}$-**BR**·12TFA and $(S)^{12}$-**BR**·12TFA, in which only the blue ring depicts all of the atoms and bonds present in the macrocycles that make up the Borromeate ring structure. By using either the (*R*,*R*)- or the (*S*,*S*)-**DAB**-H$_n$·*n*TFA ligand, enantiomeric BRs with twelve stereogenic centers are formed.

The CD spectra[18] (Figure 5a) of the Boc-protected enantiomeric ligand precursors, (*R*,*R*)-**DAB** and (*S*,*S*)-**DAB**, constitute plots that are mirror images of each other, and both display optical activity at $\lambda < 255$ nm. Although not as simple to interpret, the enantiomeric BRs, $(R)^{12}$-**BRCl$_6$**·12TFA and $(S)^{12}$-**BRCl$_6$**·12TFA, also provide plots (Figure 5b) that are mirror images of each other. The trace from $(R)^{12}$-**BRCl$_6$**·12TFA shows strong Cotton effects at $\lambda_{min} = 224$ nm ($\Delta\varepsilon = -29.75\,\text{M}^{-1}\,\text{cm}^{-1}$) and $\lambda_{max} = 239$ nm ($\Delta\varepsilon = 49.0\,\text{M}^{-1}\,\text{cm}^{-1}$), most likely arising from the stereogenic centers appended to the bipyridyl ligand, considering that this higher-energy region is within the same range as the absorptions observed for the free ligand in Figure 5a. Likewise, the trace for $(S)^{12}$-**BRCl$_6$**·12TFA shows intense Cotton effects in that region: $\lambda_{max} = 220$ nm ($\Delta\varepsilon = 32.9\,\text{M}^{-1}\,\text{cm}^{-1}$) and $\lambda_{min} = 237$ nm ($\Delta\varepsilon = -49.0\,\text{M}^{-1}\,\text{cm}^{-1}$). At lower energy ($\lambda = 272$ nm), where the free ligand is optically inactive, a pair of antipodal CD absorptions are evident ($\Delta\varepsilon = 41.17$, $-27.6\,\text{M}^{-1}\,\text{cm}^{-1}$) corresponding to $(R)^{12}$-**BRCl$_6$**·12TFA and $(S)^{12}$-**BRCl$_6$**·12TFA, respectively. Equally interesting are the strong Cotton effects observed at $\lambda = 310$ nm, with $\Delta\varepsilon = -38.8\,\text{M}^{-1}\,\text{cm}^{-1}$ for $(R)^{12}$-**BRCl$_6$**·12TFA and $\Delta\varepsilon = 42.6\,\text{M}^{-1}\,\text{cm}^{-1}$ for $(S)^{12}$-**BRCl$_6$**·12TFA. This absorption range is especially characteristic of chirality associated with the metal centers, a situation which suggests that chirality has been induced by the stereogenic centers to the zinc coordination sphere.[19] Furthermore, the coordination spheres around the metals are themselves enantiomers of each other, as reflected by their opposing Cotton effects in the CD spectra of the enantiomeric BRs.

To eliminate the possibility that the size and shape of the Borromeate framework transmits chiral information of any form, the CD spectrum of the achiral progenitor was measured. It showed no CD response at all. As an additional verification that chirality is being induced at its metal centers, the $(R)^{12}$-**BRCl$_6$**·12TFA enantiomer was demetallated by

 © 2006 Wiley-VCH Verlag GmbH & Co. KGaA, Weinheim

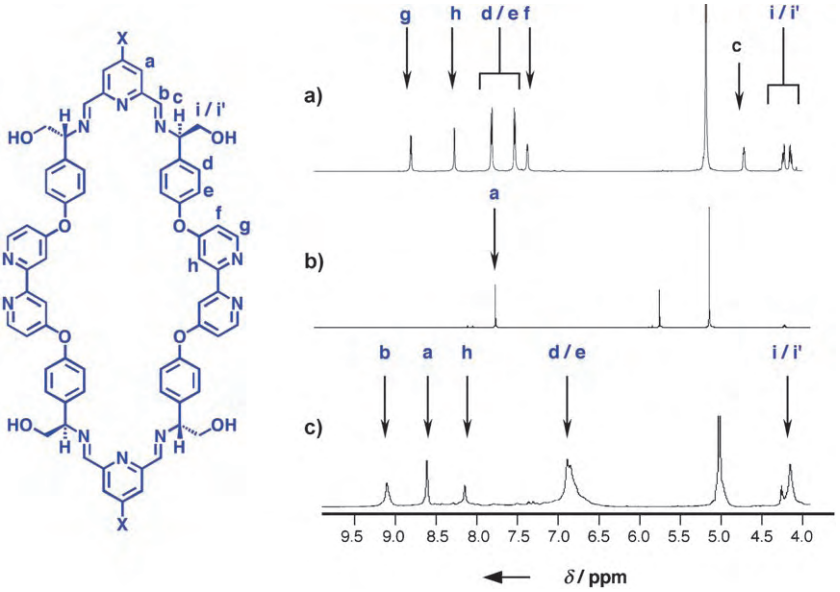


Figure 1. Partial ^{1}H NMR spectra (600 MHz) recorded in CD_3OD of a) the freshly deprotected (*R*,*R*)-**DAB**-H_n·*n*TFA ligand, b) **Cl-DFP**, and c) the $(R)^{12}$-**BRCl$_6$**·12TFA isomer. If the structure of the chiral Borromeate has C_1 symmetry in solution, then *all* the protons in the molecule are heterotopic. The observed line widths in the spectrum are consistent with this structural assignment.

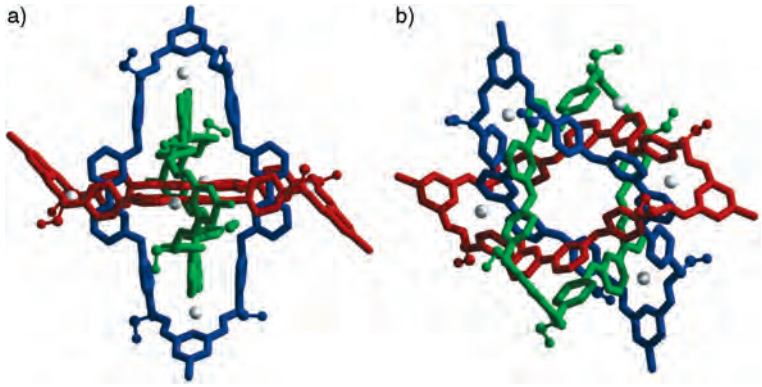


Figure 2. X-ray crystal structure of $(R)^{12}$-**BRCl$_6$**·12TFA viewed a) from an orthogonal perspective and b) down the core, revealing the low symmetry (C_1) resulting from one "flipped" chairlike macrocycle.

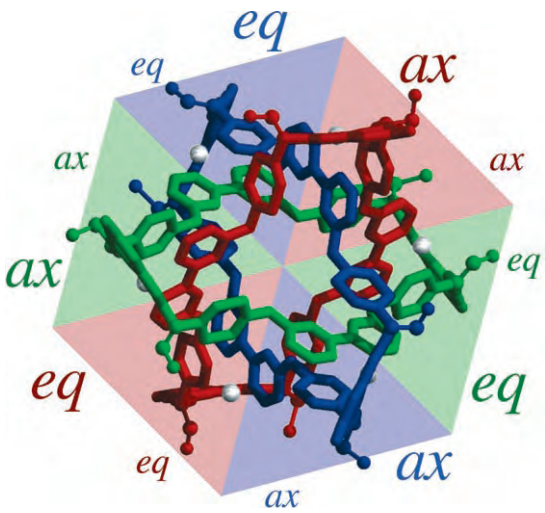


Figure 3. View of the X-ray crystal structure of $(R)^{12}$-**BRCl$_6$**·12TFA down the *c* axis with pendant alternating axial (ax) and equatorial (eq) CH_2OH groups.

reducing the 12 imine bonds. Application of a recently established procedure[13] for demetallation and reduction gives a mixture of single rings, linear fragments, and intact BRs—in this case, $(R)^{12}$-**BRCl$_6$H$_{24}$**—but without the metals; that is, the Borromeands. The CD spectrum (Figure 6) of the crude demetallated chiral BRs exhibits much weaker absorptions (at the same concentrations of 8.0 μM) in the absence of the metal. In fact, only two main absorptions are apparent at $\lambda_{min} = 248$ nm ($\Delta\varepsilon = -8.09\,M^{-1}cm^{-1}$) and at $\lambda_{max} = 277$ nm ($\Delta\varepsilon = 6.61\,M^{-1}cm^{-1}$): the first bands are within the optical activity range of the free ligand. Furthermore, the CD trace of demetallated $(R)^{12}$-**BRCl$_6$H$_{24}$** is conspicuously lacking any absorption at 310 nm, further suggesting that chirality was induced at the metal center. These results prompted us to examine the octahedral disposition of the ligands surrounding the Zn^{II} ions from the X-ray crystallographic data (Figure 7). From this distorted octahedron, it is apparent that the chiral ligands wrap around the metal in a helical, and thus chiral, fashion.[20] For comparison, we re-examined the X-ray crystal data for the original Borromeate and confirmed that each octahedron around the zinc in the achiral BR is an ideal octahedron with no distortion. Hence, we conclude that the presence of the nearby stereogenic centers disturbs the neighboring coordination sphere to produce chirality at metal centers in the optically active Borromeates.

In summary, two pairs of enantiomerically related Borromeates were synthesized stereospecifically from enantiomeric phenylglycine derivatives. All four optically active compounds have three macrocycles each containing four stereogenic centers. The one example whose crystal structure has been determined adopts an asymmetric conformation. All four compounds exhibit intense CD spectra in solution. Furthermore, the Zn^{II} octahedra, found in the X-ray crystal structure of one of the compounds, deviate substantially from ideal geometry, strongly suggesting that chirality is being transferred rather efficiently from the 12 stereogenic centers to the six Zn^{II} centers. Removal of the Zn^{II} ions and reduction of the imine bonds present in the macrocyles affords a Borromeand with a significantly different CD spectrum. In the fullness of time, the chiral Borromeates could find applications[21] in chemical biology and materials science; or they could remain what they are presently—that is, stereochemical curiosities.

 © 2006 Wiley-VCH Verlag GmbH & Co. KGaA, Weinheim

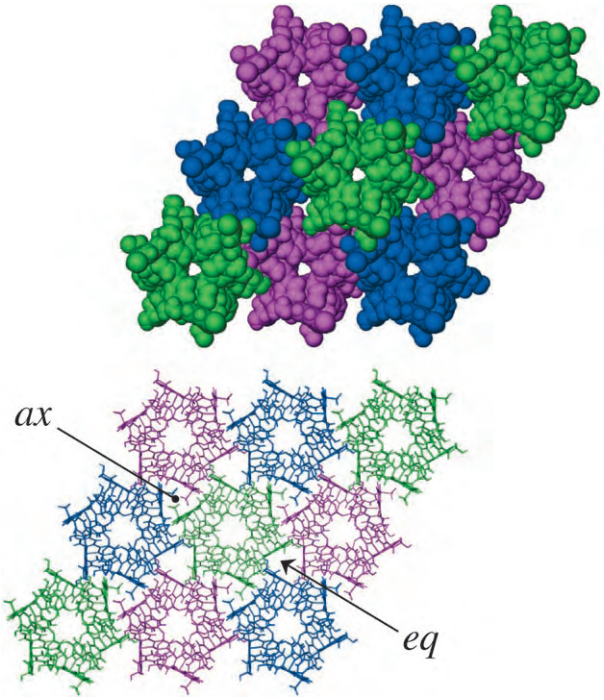


Figure 4. Packing diagram of $(R)^{12}$-**BRCl$_6$**·12TFA viewed down the *c* axis revealing alternating hydrophilic solvent channels. Depicted in the wire view are the equatorial (eq) and axial (ax) solvent channels. Hydrogen atoms, TFA counterions, and solvent molecules have been omitted for clarity.

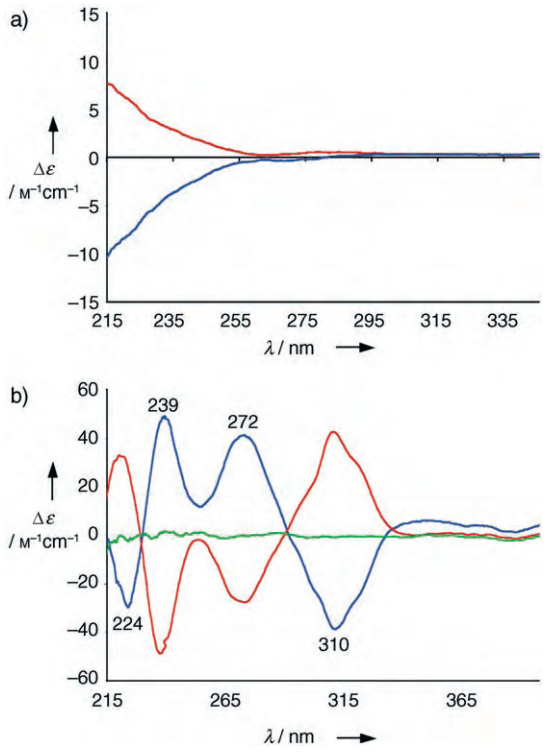


Figure 5. Circular dichroism spectra of a) the chiral ligand precursors, Boc-protected (*R*,*R*)-**DAB** (blue) and (*S*,*S*)-**DAB** (red), both recorded at a concentration of 0.02 μM in MeOH (22 °C), b) the enantiomeric chiral BRs $(R)^{12}$-**BRCl$_6$**·12TFA (blue) and $(S)^{12}$-**BRCl$_6$**·12TFA (red). The CD spectrum of the achiral (unmodified) BRs was taken as a control (green). All three samples were measured at a concentration of 8.0 μM in MeOH (22 °C). Boc = *tert*-butyloxycarbonyl.

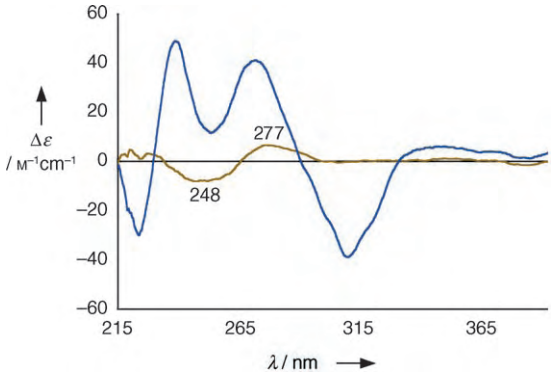


Figure 6. CD spectra of $(R)^{12}$-**BRCl$_6$**·12TFA (blue) and the crude reduced chiral Borromeand (brown). Both were obtained at a concentration of 8.0 μM in MeOH (22 °C).

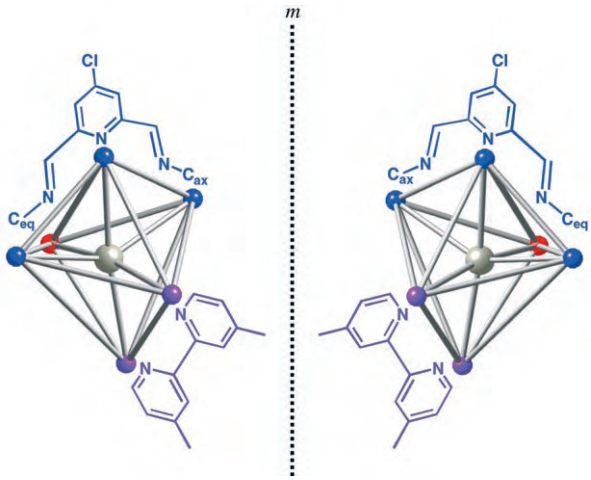


Figure 7. Distorted octahedron around the Zn^{II} atom, drawn from the X-ray crystal structure data (left) and its mirror image. The imine nitrogen atoms in the coordination sphere are not equivalent—one is flanked with a nearby pseudo-equatorial CH_2OH (C_{eq}) and the other is situated nearest a stereogenic center with a pseudo-axial CH_2OH (C_{ax}), thereby eliminating any planes of symmetry from the octahedron.

Experimental Section

$(R)^{12}$-**BRCl$_6$**·12TFA**:** The Boc protecting groups in (*R*,*R*)-**6** were removed by the addition of neat CF_3CO_2H (0.5 mL) to (*R*,*R*)-**6** (155 mg, 0.235 mmol) with stirring at room temperature for 15 min. The reaction mixture was concentrated to dryness, leaving a light pink oil. The excess of CF_3CO_2H was removed by two repeated addition and removal cycles of MeOH (5 mL) by rotary evaporation under reduced pressure. Any residual CF_3CO_2H was removed under high vacuum to leave (*R*,*R*)-**DAB**-H_n·*n*TFA as a pink sticky solid that is moisture-sensitive and was therefore carried onto the next step without delay. $Zn(OAc)_2$ (43 mg, 0.235 mmol) was added to a stirred solution (10 mL) containing (*R*,*R*)-**DAB**-H_n·*n*TFA (0.235 mmol) and 4-chloro-2,6-diformylpyridine (40 mg, 0.235 mmol) in *i*PrOH, and the reaction mixture was heated at 65 °C for 16 h to produce a pale yellow solution along with a white precipitate. The mixture was allowed to cool down to room temperature and filtered, and the precipitate was washed with *i*PrOH (3 × 5 mL) and Et_2O (3 × 5 mL). This procedure afforded $(R)^{12}$-**BRCl$_6$**·12TFA as a white powder (117 mg). Crystals suitable for X-ray crystallography were grown by vapor diffusion of

 © 2006 Wiley-VCH Verlag GmbH & Co. KGaA, Weinheim

Et_2O into a solution of $(R)^{12}$-**$BRCl_6$**·12 TFA in MeOH. Yield: 83%; $[\alpha]_D^{22} = -6.19$ ($c = 0.2$, MeOH); ^{1}H NMR (600 MHz, CD_3OD): $\delta =$ 4.01 (s, 24H), 6.54 (br, 12H), 6.74 (m, 48H), 8.02 (s, 12H), 8.49 (s, 12H); 9.00 ppm (s, 12H); resonances for the hydroxy protons were not observed as a result of exchange with the deuterium in the solvent. A resonance for the CH at the stereogenic center was not observed because it was obscured by the H_2O resonance; HR-ESI-MS: m/z calcd for $(C_{66}H_{52}Cl_2N_{10}O_8)_3Zn_6(CF_3CO_2)_{12}$: 5300.8528; found (%): 1653.5458 (90) $[M-3\,TFA]^{3+}$, 1211.9171 (100) $[M-4\,TFA]^{4+}$, 947.1281 (24) $[M-5\,TFA]^{5+}$, 769.9425 (6) $[M-6\,TFA]^{6+}$.

$(R)^{12}$-**$BRCl_6H_{24}$**: The Zn^{II}-containing BR complex $(R)^{12}$-**$BRCl_6$**·12 TFA (50 mg, 0.01 mmol) was dissolved in anhydrous EtOH under an Ar atmosphere at 22 °C. $NaBH_4$ (15 mg, 0.4 mmol) was added in one portion. The reaction mixture became cloudy immediately. It was stirred at 22 °C for 5 days. The reaction was then quenched by the addition of H_2O (5 mL), and the mixture was treated with an excess of ethylenediamine tetraacetic acid (EDTA; 175 mg) and heated under reflux for 30 min. Thereafter, the reaction mixture was allowed to cool down to room temperature and the solvents were removed under reduced pressure. The crude product was suspended in H_2O (15 mL) and filtered. The white filter cake was washed with H_2O (10 × 5 mL) to remove excess of salts and then finally with Et_2O (3 × 5 mL). This procedure afforded 26 mg of the crude product as a white solid containing both the reduced $(R)^{12}$-**$BRCl_6H_{24}$** and the free macrocycle in a 1.0:1.8 molar ratio, as determined from the integration of the resonances in the ^{1}H NMR spectrum. Therefore, this observation suggests that approximately 53% of the $(R)^{12}$-**$BRCl_6$**·12 TFA followed a pathway in which all 12 imine bonds were reduced and the three rings remained interlocked to produce $(R)^{12}$-**$BRCl_6H_{24}$**. The remaining 47% followed a pathway in which at least one of the rings was cleaved during the borohydride reduction to produce the two reduced macrocycles and one linear fragment. $(R)^{12}$-**$BRCl_6H_{24}$** and the component macrocyle mixture exhibited low solubilities in most solvents and therefore had to be used as the crude mixture. $[\alpha]_D^{22} = -5.1$ ($c = 0.1$, MeOH); selected ^{1}H NMR data (600 MHz, CD_3SOCD_3): $\delta = 3.59$ (s, 24H), 3.70 (s, 24H), 4.24 (dd, $J = 4.5$, 1.3 Hz, 12H), 4.10 (bs, 12H), 6.38 (m, 12H), 6.70 (d, $J =$ 9.0 Hz, 24H), 7.01 (d, $J = 9.0$ Hz, 24H), 7.28 (s, 12H), 7.46 (d, $J =$ 2.4 Hz, 12H), 7.89 ppm (d, $J = 6$ Hz, 12H) (see Supporting Information for full assignments). MALDI-MS: m/z calcd for $(C_{66}H_{60}N_{10}O_8)_3$: 1256.4; found: 1255.3 (100%) $[3M+H+Na]^+$.

Received: March 2, 2006

Keywords: chirality · Schiff bases · self-assembly · supramolecular chemistry · template synthesis

[1] a) *Templated Organic Synthesis* (Eds.: F. Diederich, P. J. Stang), Wiley-VCH, Weinheim, **2000**; b) G. A. Breault, C. A. Hunter, P. C. Mayers, *Tetrahedron* **1999**, *55*, 5265 – 5293; c) T. J. Hubin, D. H. Busch, *Coord. Chem. Rev.* **2000**, *200*, 5 – 52; d) J. F. Stoddart, H.-R. Tseng, *Proc. Natl. Acad. Sci. USA* **2002**, *99*, 4797 – 4800; e) M.-J. Blanco, J.-C. Chambron, M. C. Jiménez, J.-P. Sauvage, *Top. Stereochem.* **2003**, *23*, 125 – 173; f) F. Aricó, J. D. Badjić, S. J. Cantrill, A. H. Flood, K. C.-F. Leung, Y. Liu, J. F. Stoddart, *Top. Curr. Chem.* **2005**, *249*, 203 – 259.

[2] a) G. Schill, *Catenanes, Rotaxanes, and Knots*, Academic Press, New York, **1971**; b) D. B. Amabilino, J. F. Stoddart, *Chem. Rev.* **1995**, *95*, 2725 – 2828; c) T. J. Hubin, A. G. Kolchinski, A. L. Vance, D. H. Busch, *Adv. Supramol. Chem.* **1999**, *5*, 237 – 357; d) *Molecular Catenanes, Rotaxanes and Knots: A Journey Through the World of Molecular Topology* (Eds.: J.-P. Sauvage, C. Dietrich-Buchecker), Wiley-VCH, Weinheim, **1999**; e) S. J. Cantrill, A. R. Pease, J. F. Stoddart, *J. Chem. Soc. Dalton Trans.* **2000**, 3715 – 3734; f) L. Raehm, D. G. Hamilton, J. K. M. Sanders, *Synlett* **2002**, 1742 – 1761; g) O. Lukin, F. Vögtle, *Angew. Chem.* **2005**, *117*, 1480 – 1501; *Angew. Chem. Int. Ed.* **2005**, *44*, 1456 – 1477; h) C. Dietrich-Buchecker, B. X. Colasson, J.-P. Sauvage, *Top. Curr. Chem.* **2005**, *249*, 261 – 283.

[3] J.-C. Chambron, C. Dietrich-Buchecker, G. Rapenne, J.-P. Sauvage, *Chirality* **1998**, *10*, 125 – 133.

[4] a) C. Liang, K. Mislow, *J. Math. Chem.* **1995**, *16*, 27 – 34; b) C. Liang, K. Mislow, *J. Math. Chem.* **1995**, *18*, 1 – 24; c) K. Mislow, *Top. Stereochem.* **1999**, *22*, 1 – 82.

[5] a) J.-C. Chambron, D. K. Mitchell, J.-P. Sauvage, *J. Am. Chem. Soc.* **1992**, *114*, 4625 – 4631; b) S. Ottens-Hildebrandt, T. Schmidt, J. Harren, F. Vögtle, *Liebigs Ann.* **1995**, 1855 – 1860; c) C. Yamamoto, Y. Okamoto, T. Schmidt, R. Jäger, F. Vögtle, *J. Am. Chem. Soc.* **1997**, *119*, 10547 – 10548; d) A. Mohry, F. Vögtle, M. Nieger, H. Hupfer, *Chirality* **2000**, *12*, 76 – 83; e) C. Reuter, A. Mohry, A. Sobanski, F. Vögtle, *Chem. Eur. J.* **2000**, *6*, 1674 – 1682; f) A. Hori, A. Akasaka, K. Biradha, S. Sakamoto, K. Yamaguchi, M. Fujita, *Angew. Chem.* **2002**, *114*, 3403 – 3406; *Angew. Chem. Int. Ed.* **2002**, *41*, 3269 – 3272; g) C. P. McArdle, S. Van, M. C. Jennings, R. J. Puddephatt, *J. Am. Chem. Soc.* **2002**, *124*, 3959 – 3965; h) A. Hori, H. Kataoka, A. Akasaka, T. Okano, M. Fujita, *J. Polym. Sci. Part A* **2003**, *41*, 3478 – 3485; i) Recently, inherently chiral rotaxanes were discussed in the literature: see P. Mobian, N. Banerji, G. Bernardinelli, J. LaCour, *Org. Biomol. Chem.* **2006**, *4*, 224 – 231.

[6] Defined as "topologically achiral in 3-space", *amphicheiral* is a term that was introduced in 1877 by the Scottish physicist Peter Guthrie Tait, one of the pioneers of knot theory. With its original spelling intact, *amphicheiral* is still widely used in current mathematical literature on topology. See Ref. [4c].

[7] a) M. Kodaka, *J. Am. Chem. Soc.* **1993**, *115*, 3702 – 3705; b) E. Yashima, T. Matsushima, Y. Okamoto, *J. Am. Chem. Soc.* **1997**, *119*, 6345 – 6359; c) M. Asakawa, P. R. Ashton, W. Hayes, H. M. Janssen, E. W. Meijer, S. Menzer, D. Pasini, J. F. Stoddart, A. J. P. White, D. J. Williams, *J. Am. Chem. Soc.* **1998**, *120*, 920 – 931; d) J.-C. Meillon, N. Voyer, E. Biron, F. Sanschagrin, J. F. Stoddart, *Angew. Chem.* **2000**, *112*, 147 – 149; *Angew. Chem. Int. Ed.* **2000**, *39*, 143 – 145; e) M. Asakawa, G. Brancato, M. Fanti, D. A. Leigh, T. Shimizu, A. M. Z. Slawin, J. K. Y. Wong, F. Zerbetto, S. Zhang, *J. Am. Chem. Soc.* **2002**, *124*, 2939 – 2950.

[8] a) P. Hayoz, A. von Zelewsky, H. Stoeckli-Evans, *J. Am. Chem. Soc.* **1993**, *115*, 5111 – 5114; b) U. Knof, A. von Zelewsky, *Angew. Chem.* **1999**, *111*, 312 – 333; *Angew. Chem. Int. Ed.* **1999**, *38*, 302 – 322.

[9] M. Koizumi, C. Dietrich-Buchecker, J.-P. Sauvage, *Eur. J. Org. Chem.* **2004**, 770 – 775.

[10] a) K. S. Chichak, S. J. Cantrill, A. R. Pease, S.-H. Chiu, G. W. V. Cave, J. L. Atwood, J. F. Stoddart, *Science* **2004**, *304*, 1308 – 1312; b) K. S. Chichak, A. J. Peters, S. J. Cantrill, J. F Stoddart, *J. Org. Chem.* **2005**, *70*, 7956 – 7962.

[11] a) J. S. Siegel, *Science* **2004**, *304*, 1256 – 1258; b) C. A. Schalley, *Angew. Chem.* **2004**, *116*, 4499 – 4501; *Angew. Chem. Int. Ed.* **2004**, *43*, 4399 – 4401; c) S. J. Cantrill, K. S. Chichak, A. J. Peters, J. F. Stoddart, *Acc. Chem. Res.* **2005**, *38*, 1 – 9; d) D. H. Busch, *Top. Curr. Chem.* **2005**, *249*, 1 – 65; e) Borromean rings have been identified in the solid-state superstructures of a number of interwoven supramolecular architectures: see, for example: R. Liantonio, P. Metrangolo, F. Meyer, T. Pilati, W. Navarrini, G. Resnati, *Chem. Commun.* **2006**, 1819 – 1821, and references therein.

[12] K. S. Chichak, S. J. Cantrill, J. F. Stoddart, *Chem. Commun.* **2005**, 3391 – 3393.

[13] A. J. Peters, K. S. Chichak, S. J. Cantrill, J. F. Stoddart, *Chem. Commun.* **2005**, 3394 – 3396; we proposed therein that Borromean ring compounds that are assembled using metal ions, and that retain these metal ions as an intrinsic part of their structure, be referred to as "Borromeates". Furthermore, upon removal of

 © 2006 Wiley-VCH Verlag GmbH & Co. KGaA, Weinheim

the metal ions, the term "Borromeand" is suggested for the resulting metal-free compound.

[14] No resonance was observed for the methine protons attached to the stereogenic centers because it was obscured by a water resonance. It was also not possible to identify one of the two vicinal protons located on the bipyridyl ligands.

[15] Crystal data for $[(C_{66}H_{52}Cl_2N_{10}O_8)_3(ZnO_2CCF_3)_6]$-$(CF_3CO_2)_6 \cdot 10.5\,CH_3OH \cdot 1.5\,H_2O$, trigonal, $a = b = 31.293(4)$, $c = 24.348(5)$ Å, $V = 20.649(6)$ Å^3, space group $R3$, $Z = 3$, $\rho_{calcd} = 1.362\ g\,cm^{-3}$, $\lambda(Mo_{K\alpha}) = 0.71073$ Å, $F(000) = 8636$, $T = 120(2)$ K, 9818 unique reflections ($2\theta_{max} = 54.9°$), of which 4944 were observed [$I_o > 2\sigma(I)$]. Absolute structure parameter = 0.0121(15). Final R factors: $R_1 = 0.1661$, $wR_2 = 0.3865$ for 611 parameters.

[16] Single crystals of $(R)^{12}$-**BRCl$_6$**·12 TFA, suitable for X-ray crystallography, were obtained by vapor diffusion of Et_2O into a methanolic solution of the compound. A single colorless crystal ($0.32 \times 0.24 \times 0.185$ mm^3) was attached with oil to a thin glass fiber. Suitable crystals were extremely difficult to mount. Solvent loss was immediately evident as soon as the crystal was removed from the mother liquor. Data were collected on a Bruker-Nonius FR591 rotating anode diffractometer with $Mo_{K\alpha}$ radiation using the *phi* and *omega* scan modes (150-second exposure per frame). Data were corrected for absorption using the SADABS program, and structure solution and refinement were performed using the SHELX-97 software package. All non-hydrogen atoms, except those in the solvent molecules and counterions, were refined anisotropically while the hydrogen atoms were included at geometrically calculated positions and allowed to ride on their parent atoms. CCDC 299519 contains the supplementary crystallographic data for this paper. These data can be obtained free of charge from The Cambridge Crystallographic Data Centre via www.ccdc.cam.ac.uk/data_-request/cif.

[17] The enantiomeric pairs of BRs, $(R)^{12}$-**BRCl$_6$**·12 TFA and $(S)^{12}$-**BRCl$_6$**·12 TFA, were prepared in the form of the chlorinated derivatives in order to aid the growth of single crystals suitable for X-ray crystallography. Analysis of the X-ray data supported this notion (see Supporting Information). The molecular parameters (distances, angles, etc.) are not reported here, however they are not all that dissimilar from those found in the original Borromean rings (see Ref. [10a]). The X-ray crystal structure will be discussed in more detail in a full paper.

[18] CD Spectra were recorded on a JASCO J715 spectropolarimeter using a Xe lamp equipped with a PS-150 J power supply.

[19] a) H.-R. Mürner, H. Stoeckli-Evans, A. von Zelewsky, *Inorg. Chem.* **1996**, *35*, 3931 – 3935; b) H.-R. Mürner, A. von Zelewsky, G. Hopfgartner, *Inorg. Chim. Acta* **1998**, *271*, 36 – 39; c) O. Mamula, F. J. Monlien, A. Porquet, G. Hopfgartner, A. E. Merbach, A. von Zelewsky, *Chem. Eur. J.* **2001**, *7*, 533 – 539; d) K. Campbell, C. A. Johnson II, R. McDonald, M. J. Ferguson, M. M. Haley, R. R. Tykwinski, *Angew. Chem.* **2004**, *116*, 6093 – 6097; *Angew. Chem. Int. Ed.* **2004**, *43*, 5967 – 5971.

[20] a) C. J. Hawkins, *Absolute Configuration of Metal Complexes*, Wiley-VCH, New York, **1971**; b) A. von Zelewsky, *Stereochemistry of Coordination Compounds*, Wiley-VCH, Chichester, **1996**.

[21] The fact that $(R)^{12}$-**BRCl$_6$**·12 TFA is asymmetric in the solid state, and probably also in solution, raises an important issue—namely that these kinds of BRs can exist in more than one diastereoisomeric conformation. As such, we have a necessary yet insufficient property to be able to construct molecular switches.

 © 2006 Wiley-VCH Verlag GmbH & Co. KGaA, Weinheim

Polymer Chemistry

DOI: 10.1002/anie.200600594

Chemical Composition and Topology of Poly(lactide-*co*-glycolide) Revealed by Pushing MALDI-TOF MS to Its Limit**

Saskia Huijser, Bastiaan B. P. Staal, Juan Huang, Robbert Duchateau, and Cor E. Koning*

Poly(lactide-*co*-glycolide) (PLGA) is a copolymer used extensively in the medical sector as a material for drug-delivery implants, bone screws, and absorbable sutures. Especially in the field of drug delivery, the use of PLGA has grown rapidly over the last few decades owing to its good biocompatibility and biodegradability. As the degradation products of the polymer can be metabolized in the human body to carbon dioxide and water, surgical removal of the implants is generally not required. An understanding of the chemical structure and topology of the polymer and their correlation with its physical properties and morphology is of great importance in the endeavor to control the degradation characteristics of the polymer matrix. Although various studies on structure–property relationships have been performed, little is known about the exact topology of PLGA, which can form as a random, block, alternating, or gradient structure.

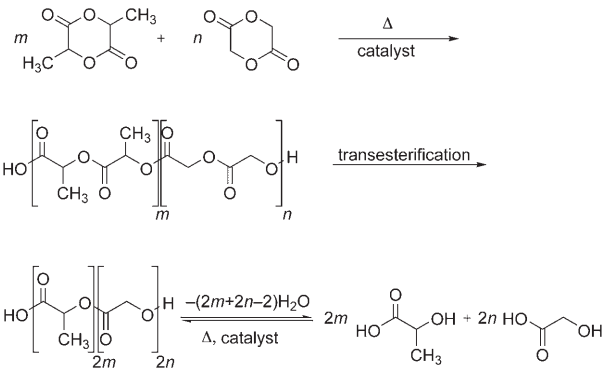
PLGA can be synthesized by direct melt polycondensation of the hydroxyacids lactic and glycolic acid, as well as by ring opening of lactide and glycolide (Scheme 1). Ring-opening polymerization can take place cationically,[1] anionically,[2] and by a metal-catalyzed coordination–insertion mechanism.[3] The latter method has drawn the most attention and is widely employed, as stereospecific polymers with high molecular weights can be obtained.[4] These different pathways each leave their fingerprint behind in the topology of the polymer. Generally, microstructures of a particular copolymer are characterized by high-resolution ^{13}C NMR spectroscopy, in which mainly the carbonyl signals are used because of their sensitivity to sequence effects. However, to obtain a highly resolved spectrum, long measuring times are required as well as powerful NMR instruments. Moreover, the spectra are complex, and the assignment of the peaks is not always straightforward.

[*] S. Huijser, B. B. P. Staal, J. Huang, Dr. R. Duchateau, C. E. Koning
Department of Chemical Engineering and Chemistry
Laboratory of Polymer Chemistry
University of Technology Eindhoven
Den Dolech 2, Helix, STO 1.37, P.O. Box 513, 5600 MB Eindhoven (The Netherlands)
Fax: (+31) 402-463-966
E-mail: r.duchateau@tue.nl

[**] The authors thank SenterNovem and Dolphys Medical for financial support and the Foundation of Emulsion Polymerization (SEP) for the use of the MALDI-TOF MS equipment.

Supporting information for this article is available on the WWW under http://www.angewandte.org or from the author.

WILEY InterScience DISCOVER SOMETHING GREAT
© 2006 Wiley-VCH Verlag GmbH & Co. KGaA, Weinheim



Scheme 1. Ring-opening polymerization of lactide and glycolide, and polycondensation of lactic and glycolic acid.

Albeit challenging, matrix assisted laser desorption/ionization time-of-flight mass spectrometry (MALDI-TOF MS) might be a suitable tool to disclose the fine structure even of complex copolymers, such as poly(lactide-*co*-glycolide). Initially, MALDI-TOF MS was developed for protein research, but because of the highly accurate information it provides on chemical structures, this characterization technique has gained increasing attention in polymer chemistry. Herein, we report a study on the composition and topology of PLGA which makes use of a recently developed method based on MALDI-TOF MS. Software developed in house enables not only the elucidation of individual chain structures, but a full characterization of the copolymer, including even its chemical composition and topology (random, gradient, block, or alternating).

Poly(lactide-*co*-glycolide) used in this study was synthesized by ring-opening polymerization of L- (LL) or D,L-lactide (DLL) and glycolide in the presence of tin(II) 2-ethylhexanoate ($Sn(Oct)_2$). The copolymer with a molar ratio of 80 L/20 G was characterized by DSC, SEC, and NMR spectroscopy. PLLGA (80 L/20 G) synthesized from the monomers L-lactide and glycolide had a number-average molecular weight of 9.9 $kg\,mol^{-1}$ with a polydispersity of 1.5, and the synthesis of PDLLGA (80 L/20 G) resulted in a polymer with a number-average molecular weight of 32.6 $kg\,mol^{-1}$ with a polydispersity of 1.6. Both copolymers were amorphous, with a T_g of 50.9 °C for PLLGA and 43.8 °C for PDLLGA. The ratio of lactide to glycolide in the polymer represented the feed ratio as determined by ^1H NMR spectroscopy.

MALDI-TOF MS spectra were generally recorded with potassium trifluoroacetate as the cationization agent, in the reflectron mode for good mass resolution. Software developed in house was used to simulate the spectrum and required the molar mass of 1) the repeating units, 2) possible end groups, and 3) the cation of the cationization agent as input data. The program makes use of Equation (1) to assign a

$$m_{th} = n_G M_G + m_L M_L + E_I + E_{II} + M^+ \quad (1)$$

certain combination of glycolyl and lactyl units with a given end group to an experimental value of m/z.[5]

E_I and E_{II} represent the masses of the end groups at either end of the chain, M_G represents the mass of the repeating glycolyl unit, M_L the mass of the repeating lactyl unit, and M^+ the mass of the cation. Multiple peak assignment, that is, more combinations of $n_G M_G$ and $m_L M_L$ found for a particular experimental value of m/z, is common, and an independent technique is required, such as ^1H NMR spectroscopy, to determine the correct chemical composition. Moreover, the presence of chains with different end groups and the small difference in mass between lactyl and glycolyl units resulted in overlapping isotope patterns.

A pattern of alternating high- and low-intensity isotope distributions was detected for both PLLGA and PDLLGA. The difference in m/z between adjacent isotope distributions is 14, which corresponds to the exchange of one glycolyl unit (58.01 $g\,mol^{-1}$) for one lactyl unit (72.02 $g\,mol^{-1}$) within a single chain (see enlargement of spectrum in Figure 1). The difference in m/z of 28 between the most abundant isotope distributions corresponds to the exchange of one glycolydyl unit (116.01 $g\,mol^{-1}$) for a lactydyl unit (144.04 $g\,mol^{-1}$).

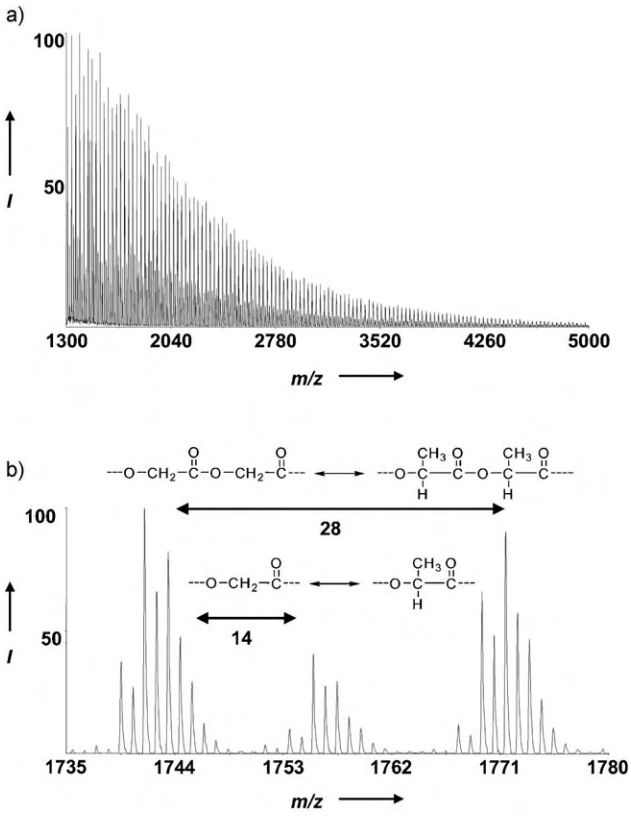


Figure 1. a) MALDI-TOF MS spectrum of PDLLGA and b) enlargement of part of the spectrum.

The ring opening of lactides generally results in linear chains end capped with hydroxy and carboxylic acid groups (referred to as an H–OH end group) and cyclic polymer structures (Figure 2 a,c). Occasionally, catalyst residues give rise to additional end groups, for example, an octanoyl end group as reported by Kowalski et al.[6] (Figure 2 d). Simulation of the experimental MALDI-TOF MS spectrum did not afford a unique solution, as cyclic structures, chains with an octanoyl end group, and chains with an H–OK end group

 © 2006 Wiley-VCH Verlag GmbH & Co. KGaA, Weinheim

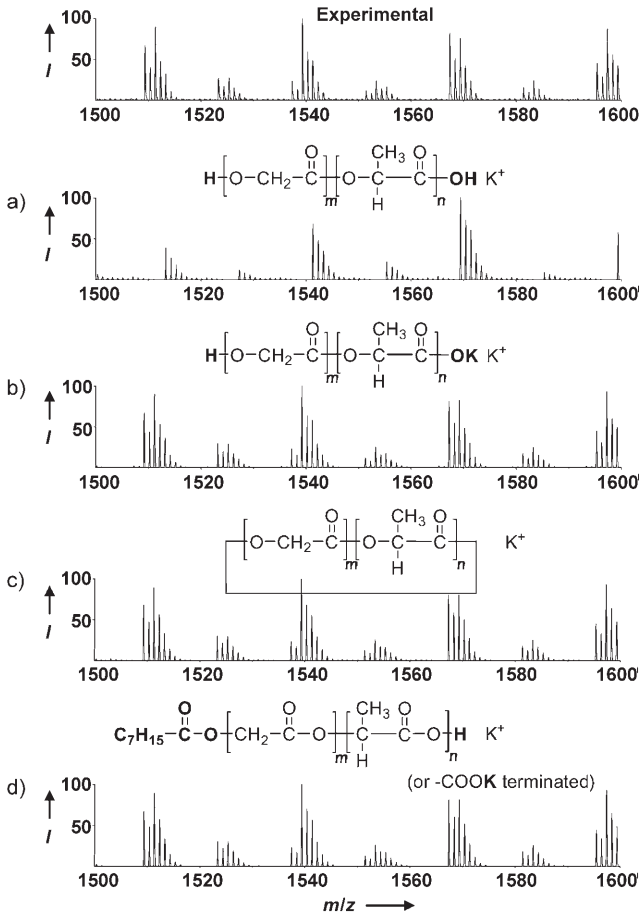


Figure 2. Experimental and a)–d) simulated isotope patterns for different end groups. (A complete spectrum was simulated, but for clarity only a selected range is shown.)

yielded virtually identical spectra (Figure 2). The occurrence of an H–OK end group is an artifact of MALDI-TOF MS, as the hydrogen atom of the carboxylic acid end group of an H–OH end-capped polymer is in this case exchanged by a cation of the cationization agent (Figure 2b). Comparison of the MALDI-TOF MS spectra recorded with potassium and sodium trifluoroacetate helped to determine the true end group. The spectrum measured with the sodium cationization agent was shifted −16 in m/z with respect to the spectrum measured with the potassium agent (Figure 3). This result automatically excludes the H–OK end group as a possible solution. The difference between an H–OK-terminated chain with a K^+ adduct and an H–ONa-terminated chain with a Na^+ adduct would be shown by a shift in the spectrum measured with sodium of −32 in m/z. The occurrence of H–OH-terminated chains can be ruled out as well for three different reasons: The first is that statistically, with the large excess of salt used, the exchange of a certain percentage of acidic protons for K^+/Na^+ would take place and result in the occasional difference of 32. Secondly, the presence of H–OH-terminated chains alone can not explain all the isotope distributions present. Finally, the calculated composition for H–OH-terminated chains differs too much from the composition of the copolymer as determined by ^{1}H NMR spectroscopy.

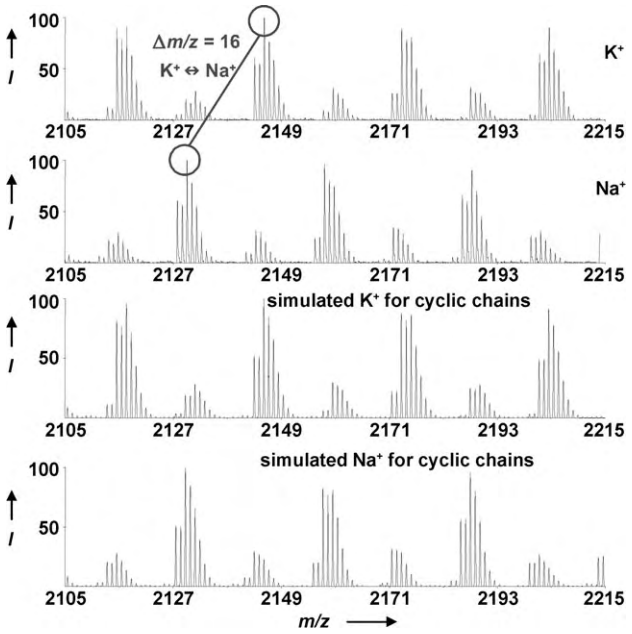


Figure 3. Enlargements of experimental and simulated spectra of PDLLGA recorded with K^+ and Na^+.

Although the presence of chains containing octanoyl end groups that originate from catalyst residues can not be excluded, their contribution is expected to be marginal because of the low catalyst concentration. Furthermore, these polymers should also undergo occasional deprotonation of the carboxylic acid end group; the expected shift of −32 m/z which would result was not detected. Therefore, the sequential difference of 16 m/z observed strongly suggests the presence of mainly cyclic structures. Both experimental and simulated isotope patterns of cyclic species ionized with potassium and sodium are shown in Figure 3. For sufficient mass resolution, MALDI-TOF MS is restricted to lower-molecular-weight fractions. The fact that the MALDI-TOF MS spectrum only shows cyclic structures does not exclude the possibility that linear chains are present in the higher-molecular-weight fraction of the material.

The software developed in house was also used to compute a contour plot, which represents the fingerprint of the polymer. Such contour plots were constructed to make the complex MALDI-TOF MS spectra of copolymers more accessible in general and are based on the work of Wilczek-Vera et al.[7,8] The contour plot is a 3D representation of a normalized matrix of the mass spectrum with lactyl units, glycolyl units, and the corresponding peak intensity on the axes. The shape and position of the plot reveals information on the topology of the polymer.[5,9,10] The contour plots appear to have been cut off, but this effect is simply a result of the fact that these MALDI-TOF MS spectra were not recorded at m/z values lower than 1250.

Interestingly, the computed contour plots show a peculiar pattern, which is characteristic for the presence mainly of chains both even- and odd-numbered in glycolyl units but only even-numbered in lactyl repeating units (Figure 4). The horizontal lines in the plot represent the polymer chains containing complete lactydyl units. This striped pattern would

 © 2006 Wiley-VCH Verlag GmbH & Co. KGaA, Weinheim

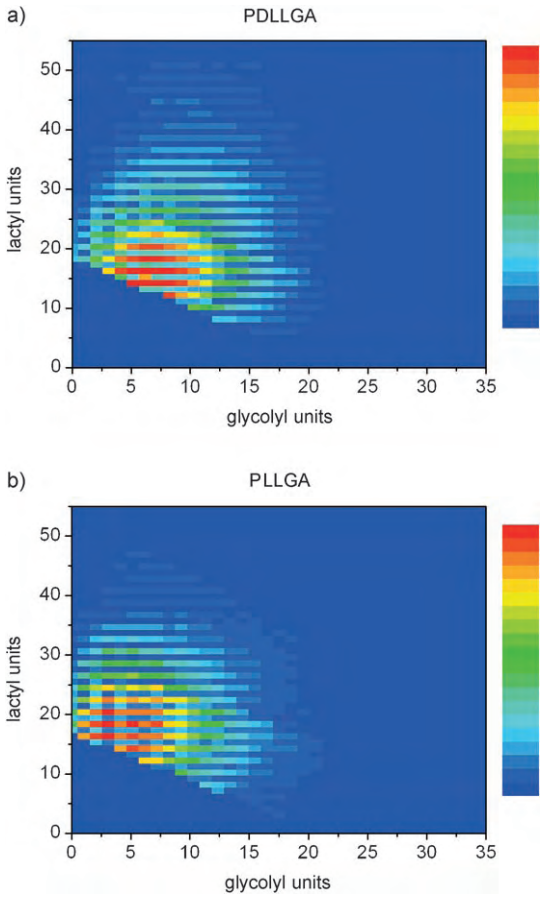


Figure 4. Contour plots of a) PDLLGA and b) PLLGA for cyclic structures. The colors indicate intensity; red represents the most abundant chains and corresponds to the isotope distributions of highest intensity in the spectrum shown in Figure 1.

be absent if chains with half-lactydyl (lactyl) units were present in an appreciable amount, which suggests that the $Sn(Oct)_2$ readily transesterifies glycolydyl units, but is not capable of transesterifying the lactydyl ester bond within the given reaction time. Similar contour plots are obtained for copolymer synthesized with D,L-lactide (racemic mixture of D-lactide and L-lactide) to those for copolymer synthesized with L-lactide, which indicates that $Sn(Oct)_2$ does not discriminate between the enantiomers in the transesterification. As expected, contour plots of PLGA synthesized by polycondensation of the hydroxyacids showed a homogeneous area, which is indicative of an equal distribution of even-numbered and odd-numbered chains.

As mentioned earlier, the contour plot reveals information on the topology of the polymeric material. A line drawn through the center of the contour plot is a measure of the average chemical composition. If this line crosses the origin and the slope remains constant the copolymer can be classified as random. If the line is curved but still crosses the origin, the plot represents a gradient copolymer. Finally, in the case of a block copolymer, the line does not cross the origin.[9,10]

Because of the discontinuity in the area, the shape and position of the contour plot in Figure 4 do not show unambiguously if we are dealing with a block or a random copolymer. Better insight into the topology is obtained when the plot is simulated with complete lactydyl units instead of lactyl units (Figure 5). Surprisingly, the contour plot of

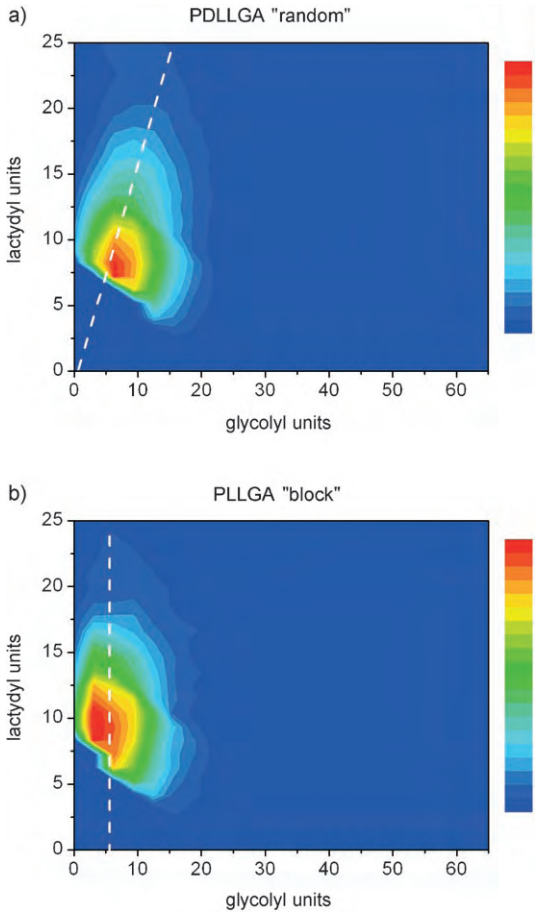


Figure 5. Contour plots of a) PDLLGA and b) PLLGA for cyclic structures plotted with lactydyl units.

PLLGA suggests a block copolymer, whereas that of PDLLGA points to a more random copolymer. Apparently, the configuration of lactide has an influence on the randomness of the copolymer. The more random character of PDLLGA relative to that of PLLGA suggests either that the rate of incorporation is higher for D-lactide than for L-lactide or that the transesterification of the D-LA–D-LA ester bond is more facile. As similar striped patterns are observed in the contour plots of PDLLGA and PLLGA, transesterification is unlikely to be the origin of this difference (Figure 4). Therefore, the topologies of both polymers are probably determined by a higher rate of incorporation of the racemic mixture of D-lactide and L-lactide relative to that of enantiomerically pure L-lactide.

In summary, MALDI-TOF MS has been used successfully to determine the composition, end groups, and topology of poly(lactide-*co*-glycolide). It was shown that the molecular characterization of copolymers by MALDI-TOF MS is a challenging task, but that intelligent software can be used to derive more information than would otherwise seem possible. Overlap of isotope distributions and multiple peak assign-

 © 2006 Wiley-VCH Verlag GmbH & Co. KGaA, Weinheim

ment are common and make the spectra more complicated, especially when comonomers only differ by a methyl group. Evidence was found for selective transesterification by Sn(Oct)$_2$ in the form of the presence of complete lactydyl units, as shown by a fingerprint of the MALDI-TOF MS spectrum. When these contour plots are used, MALDI-TOF MS can be employed as a powerful tool for the elucidation of even the topology of the polymer. Used together with NMR spectroscopy, the MALDI-TOF MS method presented can give a much better understanding of mechanistic processes, such as transesterification. Further studies on the MALDI-TOF MS analysis of PLGA synthesized enzymatically and by polycondensation have been carried out, the results of which will be published in the near future.

Experimental Section

Synthesis: A three-necked flask equipped with a mechanical stirrer was charged with a mixture of lactide (5.0 g, 34.7 mmol) and glycolide (1.0 g, 8.7 mmol). Tin(II) 2-ethylhexanoate (0.1 mol‰) was added after the monomers had melted completely. The mixture was stirred for 6 h under an argon atmosphere at 160 °C. The polymer was then dissolved in chloroform and precipitated with diethyl ether. The purified product was dried in vacuo at 40 °C for 48 h.

Analysis: MALDI-TOF MS analysis was performed with a Voyager DE-STR instrument (Applied Biosystems) equipped with a 337-nm nitrogen laser. An accelerating voltage of 25 kV was applied. Mass spectra were recorded in the reflectron mode (1000 shots). The polymer samples were dissolved in THF at a concentration of 1 mg mL^{-1}. The cationization agents used were potassium trifluoroacetate (Fluka, > 99 %) or sodium trifluoroacetate (Fluka, > 99 %) dissolved in THF at a concentration of 1 mg mL^{-1}. The matrix *trans*-2-(3-(4-*tert*-butylphenyl)-2-methyl-2-propenylidene)malononitrile (DCTB; Fluka) was dissolved in THF at a concentration of 40 mg mL^{-1}. Solutions of matrix (10 μL), salt (1 μL), and polymer (5 μL) were mixed, and the mixture was spotted by hand onto a stainless-steel MALDI target and left to dry. Baseline corrections and data analysis were performed by using Data Explorer version 4.0 from Applied Biosystems.

DSC Analysis: The glass transition temperatures of the purified material were measured using a TA Instruments Q100 DSC equipped with a refrigerated cooling system (RCS) and autosampler. The DSC cell was purged with nitrogen gas at a flow rate of 50 mL min^{-1}. Experiments were performed in aluminum hermetic pans using heating and cooling rate of 10 °C min^{-1}. The T_g was determined from the second heating curve by applying the half extrapolated tangent method.

SEC Analysis: SEC analysis was carried out using a Waters model 510 pump, a model 410 refractive index detector (at 40 °C), and a model 486 UV detector (at 254 nm) in series. Injections were done by a Waters model WISP 712 autoinjector using an injection volume of 50 μL. The columns used were a PLgel guard (5-μm particles) 50 × 7.5-mm^2 column, followed by two PLgel mixed-C (5-μm particles) 300 × 7.5-mm^2 columns at 40 °C in series. THF was used as eluent at a flow rate of 1.0 mL min^{-1}. For calibration polystyrene standards were used (Polymer Laboratories, $M_n = 580$ to 7.1×10^6 g mol^{-1}). Data acquisition and processing were performed using Waters Millennium 32 (v4.0) software.

Received: February 14, 2006
Published online: May 26, 2006

Keywords: analytical methods · copolymerization · mass spectrometry · ring-opening polymerization · stannous octoate

[1] H. R. Kricheldorf, I. Kreiser, *Makromol. Chem.* **1987**, *188*, 1861.
[2] H. R. Kricheldorf, I. Kreiser-Saunders, *Makromol. Chem.* **1990**, *191*, 1057.
[3] O. Dechy-Cabaret, B. Martin-Vaca, D. Bourissou, *Chem. Rev.* **2004**, *104*, 6147.
[4] B. M. Chamberlain, M. Cheng, D. R. Moore, T. M. Ovitt, E. B. Lobkovsky, G. W. Coates, *J. Am. Chem. Soc.* **2001**, *123*, 3229.
[5] See Supporting Information for more information about the simulation program used.
[6] A. Kowalski, A. Duda, S. Penczek, *Macromolecules* **2000**, *33*, 7359.
[7] G. Wilczek-Vera, P. O. Danis, A. Eisenberg, *Macromolecules* **1996**, *29*, 4036.
[8] G. Wilczek-Vera, Y. Yu, K. Waddell, P. O. Danis, A. Eisenberg, *Macromolecules* **1999**, *32*, 2180.
[9] B. B. P. Staal, PhD Thesis, University of Technology Eindhoven, **2005**, ISBN 90-386-2826-9, http://alexandria.tue.nl/extra2/200510540.pdf.
[10] R. X. E. Willemse, PhD Thesis, University of Technology Eindhoven, **2005**, ISBN 90-386-2816-1, http://alexandria.tue.nl/extra2/200510293.pdf.

 © 2006 Wiley-VCH Verlag GmbH & Co. KGaA, Weinheim

Heterogeneous Catalysis

DOI: 10.1002/anie.200600432

Engineering a Polymeric Chiral Catalyst by Using Hydrogen Bonding and Coordination Interactions**

*Lei Shi, Xingwang Wang, Christian A. Sandoval, Mingxing Li, Qiaoyan Qi, Zhanting Li, and Kuiling Ding**

Asymmetric catalysis of organic reactions to provide optically active products is of central importance to modern synthetic chemistry and the pharmaceutical industry.[1] Homogeneous

[*] L. Shi, X. Wang, Prof. Dr. C. A. Sandoval, Q. Qi, Prof. Dr. Z. Li, Prof. Dr. K. Ding
State Key Laboratory of Organometallic Chemistry
Shanghai Institute of Organic Chemistry
Chinese Academy of Sciences
354 Fenglin Road, Shanghai 200032 (P.R. China)
Fax: (+86) 21-6416-6128
E-mail: kding@mail.sioc.ac.cn
L. Shi, Prof. Dr. M. Li
Department of Chemistry
College of Sciences
Shanghai University
99 Shangda Road, Shanghai 200444 (P.R. China)

[**] Financial support from the National Natural Science Foundation of China, the Chinese Academy of Sciences, the Major Basic Research Development Program of China (grant no. G2000077506), and the Ministry of Science and Technology of Shanghai Municipality is gratefully acknowledged.

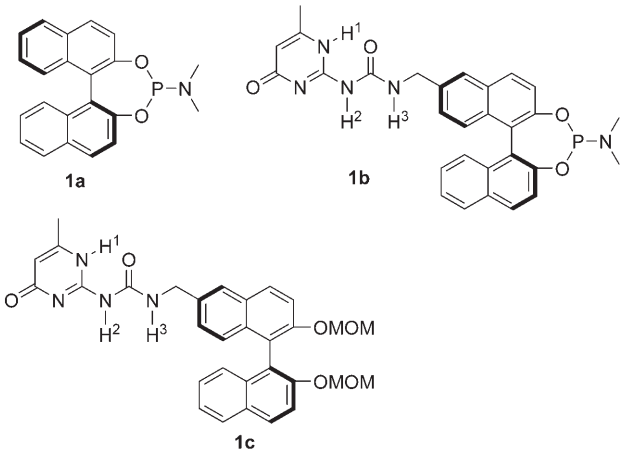
Supporting Information for this article is available on the WWW under http://www.angewandte.org or from the author.

WILEY InterScience DISCOVER SOMETHING GREAT
© 2006 Wiley-VCH Verlag GmbH & Co. KGaA, Weinheim

asymmetric catalysis offers many inherent advantages, such as high selectivity and catalytic activity, mild reaction conditions, some generality, and predictable manipulation. However, the difficulties associated with recovery and reuse of expensive chiral catalysts and the product contamination caused by metal leaching significantly limit practical applications.[2] The immobilization of chiral catalysts is considered as one of the most promising solutions to such problems.[2,3] In particular, the use of homochiral metal-organic polymers as heterogeneous catalysts for asymmetric reactions has provided a new strategy for chiral catalyst immobilization.[4,5] In such systems, chiral bridging ligands provide an enantio-discriminating environment, and the metal ions act as the catalytically active centers. Therefore, the design and synthesis of multitopic chiral ligands with diverse geometrical features is a central issue in the generation of homochiral metal-organic polymers for heterogeneous asymmetric catalysis. The common practice for this purpose is the use of covalent linkers to incorporate the coordinating chiral subunits into the ligand.[4,5] However, the preparation of covalent multitopic ligands is somewhat tedious, thus limiting their widespread applicability.

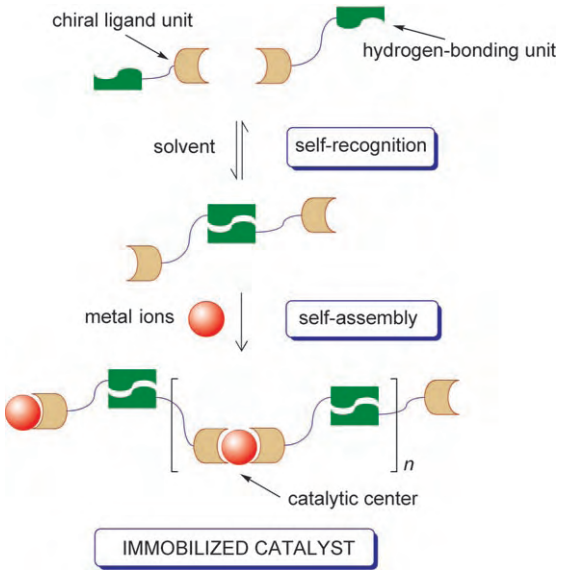
The use of noncovalent self-assembly, frequently hydrogen bonding (HB) and metal coordination, as a practical alternative to covalent-based chemistry has been recognized as one of the most important tools in the design and fabrication of complex molecules and functional systems.[6,7] Despite its tremendous potential, however, such systems have not been applied as heterogeneous catalysts for asymmetric reactions. We envisaged the use of chiral ligands possessing donor–acceptor moieties for the construction of multi-topic ligands through complementary or self-complementary hydrogen-bonding recognition motifs. Furthermore, in combination with current self-supporting strategies,[8] such assemblies are expected to spontaneously aggregate to yield immobilized catalytic systems (Scheme 1). Herein, we report the generation of a heterogeneous asymmetric catalyst by orthogonal self-assembly through hydrogen bonding and ligand-to-metal coordination interactions. The heterogeneous catalyst generated by this approach demonstrates excellent asymmetric induction in the catalytic synthesis of optically active α-amino acid and 1-phenylethylamine derivatives, without leaching of toxic metal ions into the product, and is easily recyclable.

Owing to its high association constant ($K_a = 6 \times 10^7\,M^{-1}$ in $CHCl_3$), ureido-4[1*H*]-ureidopyrimidone (UP) is among the most commonly used self-complementary hydrogen-bonding units for the construction of supramolecular systems.[9] Feringa's MonoPhos ligand **1a** is well-established in asymmetric catalysis; its rhodium(I) complex has been shown to catalyze hydrogenation of a number of substrates with excellent selectivity and reactivity.[10] To exemplify the above-mentioned strategy, UP and **1a** were integrated into one molecule, **1b**, which, in principle, can form a ditopic ligand through self-complementary hydrogen-bonding interactions in a suitable solvent. The ligand **1b** was prepared in



good yields by the reaction of hexamethylphosphorus triamide (HMPT) with a UP-containing 1,1′-bi-2-naphthol (binol) derivative (see the Supporting Information). The ^{1}H NMR spectra of **1b** and its analogue **1c** (without the chelating phosphorus moiety) show downfield resonances for the NH protons (between $\delta = 10.5$ and 13.0 ppm) indicative of strong quadruple hydrogen bonding (Figures 1a and 1b).

In order to clarify the "orthogonal" nature of the hydrogen bonding and metal-to-ligand coordination interactions in the course of supramolecular polymer formation,[7d–f] compound **1c** was mixed with $[Rh(cod)_2]BF_4$ (Figure 1c). Upon mixing, the ^{1}H NMR spectrum showed substantial changes in the NH region (Figures 1b and 1c), thus indicating disruption of the hydrogen bonds. However, when two equivalents of **1a** were added to the above system, the hydrogen-bonding pattern was recovered completely (Figure 1d). This implies that coordination of the rhodium(I) moieties by a phosphorus ligand (**1a**) is strong enough to overcome any disruption to the hydrogen bonds, and that the hydrogen-bonding units quickly reassemble. Thus, for combinations of **1b** with $[Rh(cod)_2]BF_4$, the formation of supramolecular polymers



Scheme 1. Generation of an immobilized catalyst through noncovalent interactions.

© 2006 Wiley-VCH Verlag GmbH & Co. KGaA, Weinheim

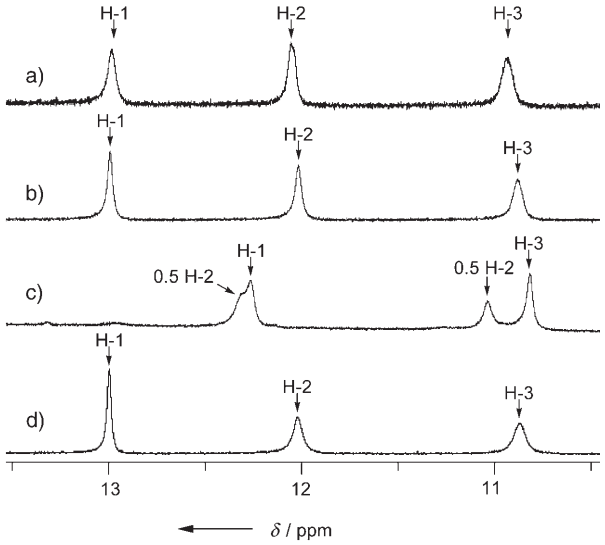
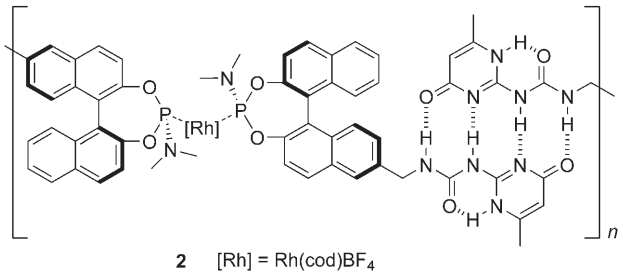


Figure 1. Sections of the ^{1}H NMR spectra (300 MHz) of a) **1b**, b) **1c**, c) **1c**/1 equiv $[Rh(cod)_2]BF_4$, and d) **1c**/1 equiv $[Rh(cod)_2]BF_4$/2 equiv **1a** in $CDCl_3$ (20 mM) at room temperature.

by "orthogonal" noncovalent interactions (hydrogen bonding and metal-to-ligand coordination) is guaranteed.

On the basis of the ^{1}H NMR results mentioned above, $[Rh(cod)_2]BF_4$ was added to a CH_2Cl_2 solution of **1b**, which resulted in the immediate precipitation of a yellow solid. The reaction mixture was stirred for one hour, and the solvent was subsequently removed under reduced pressure. The resulting powder was washed with toluene to remove soluble low-molecular-weight species. Elemental analysis (C, H, N, P) shows that the composition of the solids is consistent with the expected structure **2**. An SEM image indicates that **2** is



2 [Rh] = $Rh(cod)BF_4$

composed of micrometer-sized particles (Figure 2), while powder X-ray diffraction (XRD) shows that it is a noncrystalline solid (see the Supporting Information).

A comparison of the solid-state ^{31}P CP-MAS NMR spectra (Figure 3) of ligand **1b** ($\delta = 148.4$ ppm) and its assembled polymer **2** ($\delta = 135.7$ ppm) with those of authentic samples of **1a** ($\delta = 149.3$ ppm) and Rh^I/**1a** complex ($\delta = 135.3$ ppm) clearly demonstrates a similar coordination pattern in the solid state. The characteristic band at 1700 cm^{-1} for the pyrimidone carbonyl stretching vibration[11] in the FTIR spectrum of **1b** remains almost unchanged upon formation of the supramolecular polymer **2** (1699 cm^{-1}). This shows that

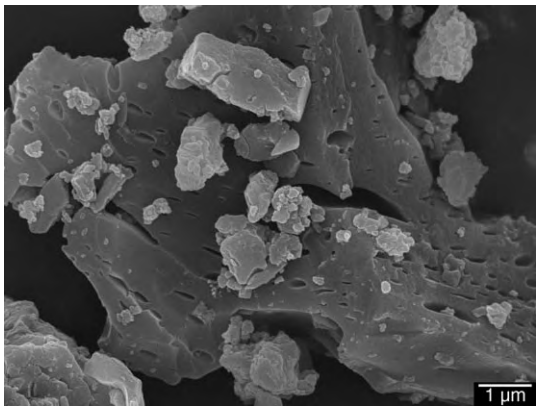


Figure 2. SEM image of catalyst **2**. The scale bar indicates 1 μm.

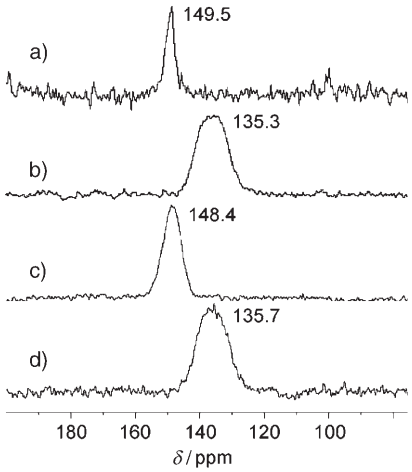


Figure 3. ^{31}P CP-MAS NMR spectra: a) **1a**, b) complex Rh^I/**1a**, c) **1b**, and d) **2**.

the UP functionalities are dimerized in the keto tautomer in both ligand **1b** and polymer **2**.

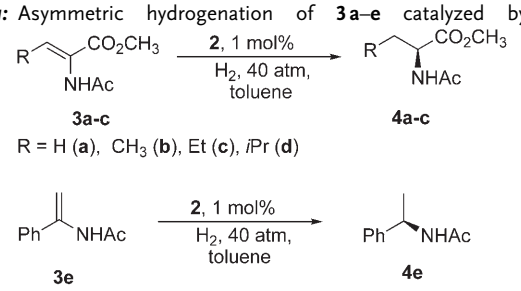
Thermal analysis of **2** shows that the polymer is fairly stable. The mass change (−3.1 %) below 150 °C is assigned to the loss of CH_2Cl_2 molecules included in the polymer (see the Supporting Information).

The supramolecular metal-organic polymer **2** is insoluble in less polar organic solvents such as toluene (see the Supporting Information), thus providing an excellent opportunity for conducting heterogeneous asymmetric reactions. As shown in Table 1, asymmetric hydrogenation of dehydro-α-amino acid derivatives (**3a–d**) and an enamide (**3e**) catalyzed by **2** proceeded smoothly with complete conversion within a standard 20 h. The products (**4a–e**) were obtained with 91–96 % *ee*,[12] comparable to values for the homogeneous system **1a**/Rh^I.[10a,13]

The remarkable advantage of the present polymeric supramolecular heterogeneous catalysts over its homogeneous counterpart is its facile recovery and reusability. Following completion of the hydrogenation, simple filtration under argon allows separation of the solid catalyst from the solution containing the product. The separated solid is then simply recharged with solvent and substrates for the next run. The

 © 2006 Wiley-VCH Verlag GmbH & Co. KGaA, Weinheim

Table 1: Asymmetric hydrogenation of **3a–e** catalyzed by **2**.[a]



Entry	Substrate	*t* [h]	*ee* [%][b]
1	**3a**	20	95 (*R*)
2	**3b**	20	96 (*R*)
3	**3c**	20	95 (*R*)
4	**3d**	20	93 (*R*)
5	**3e**[c]	40	91 (*R*)

[a] All reactions conducted in toluene at 25 °C under 40 atm of H_2, [**3**] = 1.0 M, [**2**] = 0.01 M (based on the $(MonoPhos)_2/Rh^I$ unit). Conversions were > 99% as determined by ^1H NMR spectroscopy. [b] Determined by HPLC (Chiralcel AD column) or GC (Supelco BETA-DEX225 column). Absolute configuration determined from the $[\alpha]_D$ values.[9] [c] [**3e**] = 0.2 M, [**2**] = 0.002 M.

supernatant of **2** does not give further hydrogenation of **3b** under otherwise identical experimental conditions, thus unambiguously demonstrating the heterogeneous nature of the present catalytic system. Furthermore, inductively coupled plasma (ICP) spectroscopic analyses of both the filtered organic solution and the isolated product **4b** did not provide any evidence for metal leaching within the detection limit of the instrument (1 ppm).

The reusability of the catalyst system was exemplified by the hydrogenation of **3b**. As shown in Table 2 for a standard reaction time of 20 h, the hydrogenation proceeds with near-quantitative conversion and constant enantioselectivity (96–92% *ee*) for at least 10 cycles with the same catalyst. Under the same conditions at a hydrogen pressure of 15 atm, a reaction profile of the hydrogenation showed that the catalyst activity is quite high, giving more than 90% conversion (96% *ee*) after only 2 h (see the Supporting Information). However,

Table 2: Reuse of catalyst **2** in the asymmetric hydrogenation of **3b**.[a]

Run	TOF [h^{-1}][b]	*ee* [%][c]
1	180	96
2	111	96
3	83	95
4	68	95
5	44	94
6	32	95
7	24	95
8	19	95
9	11	93
10	8	92

[a] All reactions conducted in toluene at 25 °C under 40 atm of H_2, [**3b**] = 1.0 M, [**2**] = 0.01 M (based on the $(MonoPhos)_2/Rh^I$ unit). Conversions were > 99% as determined by ^1H NMR spectroscopy. [b] Determined by ^1H NMR spectroscopy from a separate consecutive hydrogenation experiment at > 50% conversion. [c] Determined by GC (Supelco BETA-DEX 225 column).

the catalyst reactivity declined with consecutive hydrogenations, as shown by the lower turnover frequency (TOF) for each run (Table 2). Preliminary studies suggest that the absence of a hydrogen atmosphere during product/catalyst separation results in partial catalyst decomposition. A constant-flow reactor is currently under development to address this issue.

In conclusion, the heterogenization of a chiral catalyst using both supramolecular hydrogen bonding and ligand-to-metal coordination has been achieved and the resulting polymer characterized by various techniques. The chiral rhodium(I) complex demonstrates excellent asymmetric induction in the heterogeneous hydrogenation of dehydro-α-amino acid and enamide derivatives. Salient features of this catalyst, such as its simple preparation, facile recovery and reuse, as well as excellent stereocontrol performance, make it particularly interesting for practical asymmetric synthesis. This new concept will stimulate future research aimed at the development of heterogeneous chiral catalysts for asymmetric reactions based on noncovalent interactions.

Received: February 1, 2006
Revised: March 21, 2006
Published online: May 24, 2006

Keywords: asymmetric catalysis · heterogeneous catalysis · hydrogen bonding · hydrogenation · immobilization

[1] For examples, see: a) R. Noyori, *Asymmetric Catalysis in Organic Synthesis*, Wiley-Interscience, New York, **1994**; b) *Catalytic Asymmetric Synthesis*, *2nd ed.* (Ed.: I. Ojima), Wiley, New York, **2000**; c) *Comprehensive Asymmetric Catalysis*, *Vols. I–III* (Eds.: E. N. Jacobsen, A. Pfaltz, H. Yamamoto), Springer, Berlin, **1999**; d) *Lewis Acids in Organic Synthesis* (Ed.: H. Yamamoto), Wiley, New York, **2001**; e) *Asymmetric Catalysis on an Industrial Scale: Challenges, Approaches and Solutions* (Eds.: H. U. Blaser, E. Schmidt), Wiley-VCH, Weinheim, **2004**.

[2] *Chiral Catalyst Immobilization and Recycling* (Eds.: D. E. de Vos, I. F. Vankelecom, P. A. Jacobs), Wiley-VCH, Weinheim, **2000**.

[3] For comprehensive reviews, see: a) C. E. Song, S. Lee, *Chem. Rev.* **2002**, *102*, 3495–3524; b) Q. Fan, Y.-M. Li, A. S. C. Chan, *Chem. Rev.* **2002**, *102*, 3385–3466; c) D. E. de Vos, M. Dams, B. F. Sels, P. A. Jacobs, *Chem. Rev.* **2002**, *102*, 3615–3640; d) N. E. Leadbeater, M. Marco, *Chem. Rev.* **2002**, *102*, 3217–3274; e) D. E. Bergbreiter, *Chem. Rev.* **2002**, *102*, 3345–3384; f) D. Rechavi, M. Lemaire, *Chem. Rev.* **2002**, *102*, 3467–3494; g) L. Pu, *Chem. Rev.* **1998**, *98*, 2405–2494; h) S. Bräse, F. Lauterwasser, R. E. Ziegert, *Adv. Synth. Catal.* **2003**, *345*, 869–929.

[4] For a leading reference, see: a) J. S. Seo, D. Whang, H. Lee, S. I. Jun, J. Oh, Y. J. Jeon, K. Kim, *Nature* **2000**, *404*, 982–986. For a highlight, see: b) L.-X. Dai, *Angew. Chem.* **2004**, *116*, 5846–5850; *Angew. Chem. Int. Ed.* **2004**, *43*, 5726–5729. For a recent review, see: c) K. Ding, Z. Wang, X. Wang, Y. Liang, X. Wang, *Chem. Eur. J.* **2006**, DOI: 10.1002/chem.200501387.

[5] For recent examples, see: a) S. Takizawa, H. Somei, D. Jayaprakash, H. Sasai, *Angew. Chem.* **2003**, *115*, 5889–5892; *Angew. Chem. Int. Ed.* **2003**, *42*, 5711–5714; b) H. Guo, X. Wang, K. Ding, *Tetrahedron Lett.* **2004**, *45*, 2009–2012; c) X. Wang, K. Ding, *J. Am. Chem. Soc.* **2004**, *126*, 10524–10525; d) X. Wang, X. Wang, H. Guo, Z. Wang, K. Ding, *Chem. Eur. J.* **2005**, *11*, 4078–4088; e) Y. Liang, Q. Jing, X. Li, L. Shi, K. Ding, *J. Am.*

 © 2006 Wiley-VCH Verlag GmbH & Co. KGaA, Weinheim

Chem. Soc. **2005**, *127*, 7694 – 7695; f) X. Wang, L. Shi, M. Li, K. Ding, *Angew. Chem.* **2005**, *117*, 6520 – 6524; *Angew. Chem. Int. Ed.* **2005**, *44*, 6362 – 6366; g) H. Y. Peng, C. K. Lam, T. C. W. Mak, Z. W. Cai, W. T. Ma, Y. X. Li, H. N. C. Wong, *J. Am. Chem. Soc.* **2005**, *127*, 9603 – 9611. For heterogenization of Noyori's catalyst by formation of chiral porous hybrid solids in situ, see: h) A. Hu, H. L. Ngo, W. Lin, *J. Am. Chem. Soc.* **2003**, *125*, 11490 – 11491; i) A. Hu, H. L. Ngo, W. Lin, *Angew. Chem.* **2003**, *115*, 6182 – 6185; *Angew. Chem. Int. Ed.* **2003**, *42*, 6000 – 6003. For the use of a homochiral metal-organic coordination framework as a porous polymeric ligand for enantioselective addition of diethylzinc to aromatic aldehydes, see: j) C. D. Wu, A. Hu, L. Zhang, W. B. Lin, *J. Am. Chem. Soc.* **2005**, *127*, 8940 – 8941.

[6] For comprehensive reviews, see: a) J.-M. Lehn, *Supramolecular Chemistry—Concepts and Perspectives*, Wiley-VCH, Weinheim, **1995**; b) L. Brunsveld, B. J. B. Folmer, E. W. Meijer, R. P. Sijbesma, *Chem. Rev.* **2001**, *101*, 4071 – 4097; c) J.-M. Lehn, *Science* **2002**, *295*, 2400 – 2403; d) C. Schmuck, W. Wienand, *Angew. Chem.* **2001**, *113*, 4493 – 4499; *Angew. Chem. Int. Ed.* **2001**, *40*, 4363 – 4369; e) W. Gerhardt, M. Črne, M. Weck, *Chem. Eur. J.* **2004**, *10*, 6212 – 6221; f) B. Breit, *Angew. Chem.* **2005**, *117*, 6976 – 6986; *Angew. Chem. Int. Ed.* **2005**, *44*, 6816 – 6825.

[7] For selected examples, see: a) R. P. Sijbesma, F. H. Beijer, L. Brunsveld, B. J. B. Folmer, J. H. K. Ky Hirschberg, R. F. M. Lange, J. K. L. Lowe, E. W. Meijer, *Science* **1997**, *278*, 1601 – 1604; b) J. H. K. Ky Hirschberg, L. Brunsveld, A. Ramzi, J. A. J. M. Vekemans, R. P. Sijbesma, E. W. Meijer, *Nature* **2000**, *407*, 167 – 170; c) J. M. Pollino, L. P. Stubbs, M. Weck, *J. Am. Chem. Soc.* **2004**, *126*, 563 – 567; d) H. Hofmeier, A. Elghayoury, A. P. H. Schenning, U. S. Schubert, *Chem. Commun.* **2004**, 318 – 319; e) H. Hofmeier, R. Hoogenboom, M. E. L. Wouters, U. S. Schubert, *J. Am. Chem. Soc.* **2005**, *127*, 2913 – 2921; f) P. Y. W. Dankers, M. C. Harmsen, L. A. Brouwer, M. J. A. van Luyn, E. W. Meijer, *Nat. Mater.* **2005**, *4*, 568 – 574; g) B. Breit, W. Seiche, *J. Am. Chem. Soc.* **2003**, *125*, 6608 – 6609; h) B. Breit, W. Seiche, *Angew. Chem.* **2005**, *117*, 1666 – 1669; *Angew. Chem. Int. Ed.* **2005**, *44*, 1640 – 1643.

[8] See refs. [4b,c] and [5b–f].

[9] a) S. H. M. Sontjens, R. P. Sijbesma, M. H. P. van Genderen, E. W. Meijer, *J. Am. Chem. Soc.* **2000**, *122*, 7487 – 7493; b) X.-Z. Wang, X.-Q. Li, X.-B. Shao, X. Zhao, P. Deng, X.-K. Jiang, Z.-T. Li, Y.-Q. Chen, *Chem. Eur. J.* **2003**, *9*, 2904 – 2913.

[10] For leading references, see: a) M. Van den Berg, A. J. Minnaard, E. P. Schudde, J. Van Esch, A. H. M. De Vries, J. G. De Vries, B. L. Feringa, *J. Am. Chem. Soc.* **2000**, *122*, 11539 – 11540; b) M. van den Berg, A. J. Minnaard, R. M. Haak, M. Leeman, E. P. Schudde, A. Meetsma, B. L. Feringa, A. H. M. de Vries, C. E. P. Maljaars, C. E. Willans, D. Hyett, J. A. F. Boogers, H. J. W. Henderickx, J. G. de Vries, *Adv. Synth. Catal.* **2003**, *345*, 308 – 323; c) M. T. Reetz, G. Mehler, *Angew. Chem.* **2000**, *112*, 4047 – 4049; *Angew. Chem. Int. Ed.* **2000**, *39*, 3889 – 3890; d) C. Claver, E. Fernandez, A. Gillon, K. Heslop, D. J. Hyett, A. Martorell, A. G. Orpen, P. G. Pringle, *Chem. Commun.* **2000**, 961 – 962.

[11] J. H. K. Ky Hirschberg, F. H. Beijer, H. A. van Aert, P. C. M. M. Magusin, R. P. Sijbesma, E. W. Meijer, *Macromolecules* **1999**, *32*, 2696 – 2705.

[12] Recently, values of 99% *ee* have been reported for a related ligand: X. Jia, X. Li, L. Xu, Q. Li, X. Yao, A. S. C. Chan, *J. Org. Chem.* **2003**, *68*, 4539 – 4541.

[13] The enantioselectivity obtained for **3e** (91% *ee*) was higher than for the homogeneous counterpart (87–88% *ee*).[5c]

 © 2006 Wiley-VCH Verlag GmbH & Co. KGaA, Weinheim

Polymerization

DOI: 10.1002/anie.200600333

Nanochannel-Promoted Polymerization of Substituted Acetylenes in Porous Coordination Polymers**

*Takashi Uemura, Ryo Kitaura, Yusuke Ohta, Masataka Nagaoka, and Susumu Kitagawa**

In recent years, there has been considerable interest in porous coordination polymers (PCPs) composed of transition-metal ions and bridging organic ligands because of their potential applications in many areas, including storage, separation, and exchange processes.[1] In contrast to conventional microporous materials such as zeolites and activated carbon materials, PCPs have pore surfaces that can be rationally designed and functionalized by their constituents.[1,2] The versatile pore features of PCPs, such as redox activity, Lewis acidity, basicity, hydrophobicity, chirality, result from the precise arrangement of transition metals and organic functional groups, and should be of key importance for the creation of unique nanosized reaction fields based on the PCP materials.[3] Thus, functionalized PCPs bearing specific interaction sites in/on nanochannels have been envisioned for useful catalytic applications in organic and polymer syntheses, which allow several advantages: 1) reaction acceleration; 2) regulated and controlled reactions (stereo- and regiocontrols); 3) substrate specificity. All of these properties are similar to those of enzyme reactions in biological systems. However, the use of PCP nanochannels with such remarkable effects has been very limited to date.[3]

[*] Dr. T. Uemura, Dr. R. Kitaura,[+] Prof. Dr. S. Kitagawa
Department of Synthetic Chemistry and Biological Chemistry
Graduate School of Engineering
Kyoto University
Katsura, Nishikyo-ku, Kyoto 615-8510 (Japan)
Fax: (+81) 75-383-2732
E-mail: kitagawa@sbchem.kyoto-u.ac.jp
Y. Ohta, Prof. Dr. M. Nagaoka
Department of Complex Systems Science
Graduate School of Information Science
Nagoya University
Furo-chou, Chikusa-ku, Nagoya 464-8601 (Japan)
[+] Current address:
Department of Chemistry
Graduate School of Science
Nagoya University
Furo-chou, Chikusa-ku, Nagoya 464-8602 (Japan)

[**] We thank Prof. Y. Chujo of Kyoto University for access to GPC apparatus. This work was supported by a Grant-in-Aid for Scientific Research in a Priority Area "Chemistry of Coordination Space" (no. 434) and a Grant-in-Aid for Young Scientists (B; no. 17750125) from the Ministry of Education, Culture, Sports, Science and Technology, Government of Japan.

Supporting information for this article is available on the WWW under http://www.angewandte.org or from the author.

WILEY InterScience DISCOVER SOMETHING GREAT
© 2006 Wiley-VCH Verlag GmbH & Co. KGaA, Weinheim

Much attention has also been directed to the electronic and optical properties of poly(substituted acetylenes) for a wide range of applications such as conducting materials, nonlinear optics, polymer sensors, and components in molecular electronics.[4] In particular, the controlled polymerization of substituted acetylenes by using several types of catalysts (such as metal complexes, anions, cations, radicals) has been investigated with the aim of increasing catalytic activity, decreasing the formation of cyclic trimer by-products (substituted benzenes), and controlling the stereostructure (the *cis* and *trans* chain sequence) because the characteristic properties of poly(substituted acetylenes), such as conjugation length, supra-structures, and processability, can be precisely adjusted by changing the substituents and stereoregularity.[4,5] In addition, the design and understanding of well-defined nanostructures based on such π-conjugated polymers is one of the most challenging goals in contemporary polymer and solid-state sciences for their future application in the creation of nanosized molecule-based devices.[6]

Recently, we first demonstrated the use of PCP nanochannels as a field of polymerization,[7] which lead not only to a controlled reaction but also to new model systems for well-ordered single polymer chains in the nanochannel structures.[8] In this study, we have performed controlled and selective polymerizations of substituted acetylenes in one-dimensional specific nanochannels of $[Cu_2(pzdc)_2(L)]_n$ (**1**; pzdc = pyrazine-2,3-dicarboxylate, L = pillar ligands)[2b,9] with basic carboxylate oxygen atoms as catalytic interaction sites on the pore walls.

A pillared-layer microporous compound, $[Cu_2(pzdc)_2(pyrazine)]_n$ (**1a**), with one-dimensional channels (4.0 × 6.0 Å^2) has basic surface oxygen atoms that act as specific adsorption sites for acetylene molecules (HC≡CH), as a consequence of a double hydrogen-bonding interaction.[2b] The HC≡CH molecule is strongly fixed in the confined nanochannel of **1a** (**1a**⊃HC≡CH), which results in electron delocalization between the hydrogen atoms of the HC≡CH molecule and the carboxylate oxygen atoms.[2b] In addition, as is often the case with metal oxides, abstraction of one proton per HC≡CH molecule has been realized on such Lewis base sites of solid surfaces, even at room temperature.[10] These facts inspired us to postulate that the introduction of more-acidic monosubstituted acetylenes (i.e., acetylenes bearing an electron-withdrawing substitution group) in the channels of **1** would produce reactive acetylide species by C–H bond dissociation, which would subsequently initiate anionic polymerization of the substituted acetylenes. Moreover, the narrow nanochannel structure would direct the selectivity towards a polymerization with *trans* addition because of the prohibitive steric demand for the formation of trisubstituted benzenes and *cis* polymers. Thus, we carried out the polymerization of methyl propiolate (MP) in the nanochannel of $[Cu_2(pzdc)_2(4,4'\text{-bipyridine})]_n$ (**1b**; channel size 8.2 × 6.0 Å^2). In this experiment, the reaction of neat MP with the sky-blue complex **1b** for 12 h at room temperature provided a dark-green powder composite (**1b**⊃polyMP).[11] In the solid-state UV/Vis reflection spectrum of **1b**⊃polyMP there is an additional absorption around 450 nm, which can be attributed to the π-conjugated polyMP (Figure 1a). The

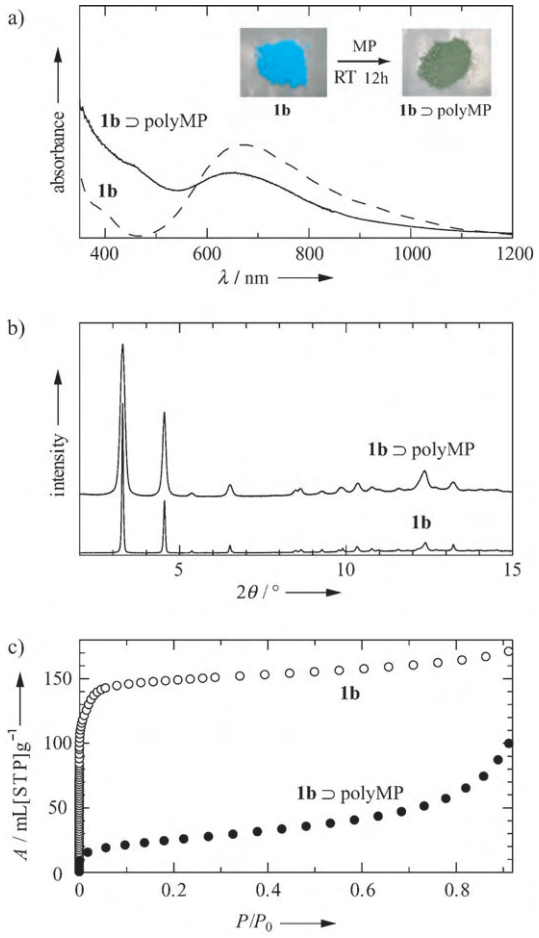


Figure 1. a) Solid-state UV/Vis reflection spectra, b) XRPD patterns under reduced pressure, and c) N_2 adsorption isotherms at 77 K, for **1b** and **1b**⊃polyMP.

resultant polyMP filled about 40% of the void space of the nanochannel, as estimated by thermogravimetric analysis (TGA). The X-ray powder-diffraction (XRPD) pattern of **1b**⊃polyMP shows that the channel structure of **1b** in this composite is preserved during polymerization (Figure 1b). A distinct change in the relative peak intensities and peak broadening after the polymerization are ascribed to the inclusion of the guest polyMP in the nanochannel of **1b** (Figure 1b).[7,12] Moreover, a dramatic decrease in the capacity of **1b**⊃polyMP at 77 K to adsorb nitrogen compared with **1b** is consistent with the encapsulation of polyMP in the channels (Figure 1c).[6b–d,12b]

Accommodated polyMP was released from the host framework **1b** by extraction with *N*,*N*-dimethyl formamide (DMF) at 80 °C.[13] The extracted polymer exhibited a weight-average molecular weight ($\bar{M}_w$) and number-average molecular weight ($\bar{M}_n$) of 4800 and 850, respectively, as measured by gel permeation chromatography (GPC) in DMF with polystyrene standard. The IR spectrum of the polymer shows a characteristic peak pattern of polyMP and provides information on its stereostructure (Figure 2a).[14] In the spectrum of the recovered polyMP, a peak around 700 cm^{-1}, which is specific to the *cis* form of polyMP, is hardly visible,[5c,14]

 © 2006 Wiley-VCH Verlag GmbH & Co. KGaA, Weinheim

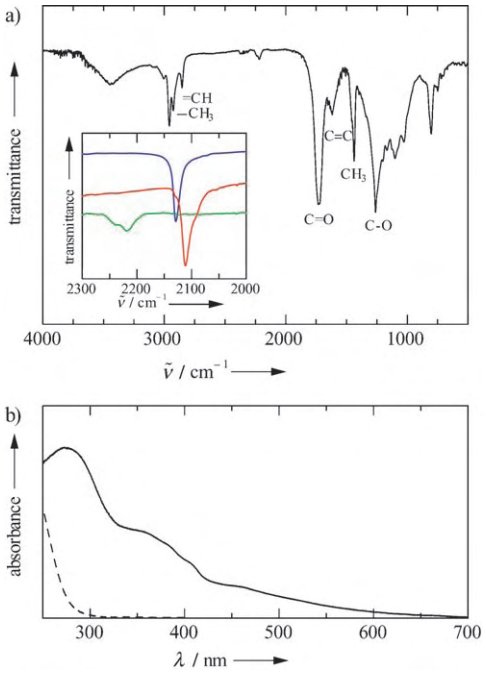


Figure 2. a) IR spectrum of polyMP prepared in **1b** shows characteristic bands of polyMP. Inset: IR spectra of neat MP (blue), MP in **1b** 5 min after the introduction of MP (red), and polyMP prepared in **1b** (green), in the region for stretching vibrations of substituted acetylenes. b) UV/Vis absorption spectra of polyMP prepared in **1b** (solid line) and monomer MP (dashed line) in chloroform.

whereas the presence of a band at 970 cm^{-1} suggests that the *trans* geometry is dominant in this polymer.[5c,14] Electronic conjugation in the polyMP backbone is strongly dependent on its stereostructure, which has a considerable effect on color and band gap. The red–brown color of the recovered polyMP is characteristic of *trans* geometry, and a band at a longer wavelength (> 480 nm) in the absorption spectrum of the polymer also supports the dominance of the highly conjugated *trans* form of polyMP (Figure 2b).[5e,13,14]

The overall polymerization is characterized by the nanochannel-promoted polymerization in PCP (Figure 3a). In this reaction, acidic MP is adsorbed into the nanochannel and interacts with the basic oxygen atoms on the pore surface. As a consequence of the acid–base interaction, C–H bond dissociation of MP produces a reactive acetylide species that initiates regulated polymerization (*trans*-selective polymerization) in the narrow nanochannel. To explain this reaction mechanism, we have conducted IR measurements of neat MP, MP in the channel of **1b**, and polyMP prepared in **1b** in the region of the C≡C stretching of substituted acetylenes (inset in Figure 2a). Compared to the neat MP ($\tilde{\nu}_{C\equiv C} = 2129\ cm^{-1}$), MP embedded in the nanochannel of **1b** shows a band at distinctly lower wavenumber (major and shoulder bands at 2111 and 2090 cm^{-1}, respectively), which is attributed to hydrogen bonding between the acetylene hydrogen atom of MP and the carboxylate oxygen atoms of the pore wall.[15] These shift values are found to be larger than that observed previously for **1a**⊃HC≡CH, thus indicating the very strong interaction between those two moieties.[2b] Clear evidence of initiation in this polymerization was obtained from the spectrum of polyMP prepared in **1b**. Although the spectrum does not show the band around 2100–2130 cm^{-1}, a weak band appears at 2219 cm^{-1}, in the region of disubstituted acetylenes. This new band, which is absent in polyMP prepared by other methods, is assignable to the polymer terminal unit from the acetylide initiator. In addition to this spectral evidence, molecular-mechanics structure optimization by using a universal force field (UFF)[16] also reproduced a specific hydrogen-bonding interaction between the MP monomer and the carboxylate moiety of the host **1b** (Figure 3b). The −C≡CH group of MP is clearly oriented towards the carboxylate oxygen atoms on the pore wall, and the acetylenic hydrogen atom and the oxygen atoms are close enough for an efficient hydrogen bonding (2.8 and 2.9 Å), which is consistent with the experimental results.

In a control experiment, MP was treated with sodium benzoate as a discrete model catalyst at room temperature and the mixture was left for one month, which gave only a trace amount of product. An increase in the reaction temperature to 70 °C resulted in a small quantity of yellow oily mixture (< 5 %) of cyclic trisubstituted benzenes as the major products and less-conjugated polyMP of *cis* geometry as a minor product, which contrasts with the result obtained in the nanochannels of **1b**. Our polymerization system with PCP is of considerable interest owing to several significant features

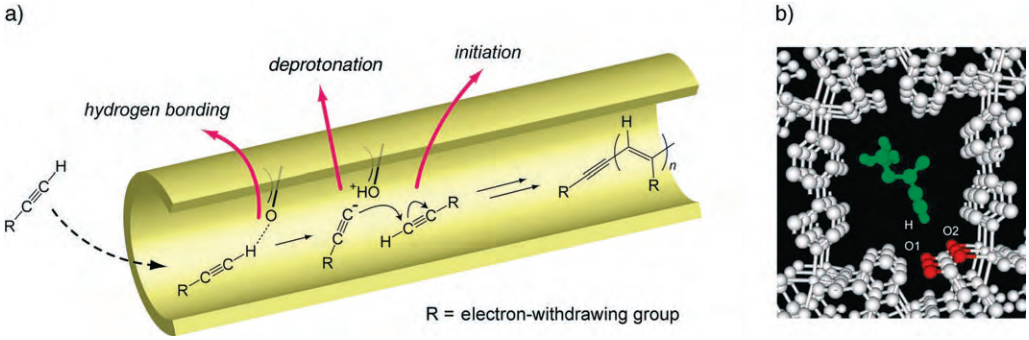


Figure 3. a) Mechanism of the nanochannel-promoted polymerization of acidic acetylenes in porous coordination polymers. b) Optimized structure of MP (green) incorporated in a nanochannel of **1b**. The distances between the MP hydrogen atom and oxygen atoms (red) of the pzdc ligand are 2.9 (H–O1) and 2.8 Å (H–O2). Hydrogen atoms of the host are omitted for clarity.

 © 2006 Wiley-VCH Verlag GmbH & Co. KGaA, Weinheim

such as a dramatic acceleration of the polymerization, no production of trisubstituted benzenes as by-products, and *trans*-selective polymerization. In this case, the basic carboxylate oxygen atoms are precisely arranged at appropriate positions of the narrow nanochannels, which enables a strong interaction between the monomer and carboxylate group and results in *trans*-selective polymerization.

To elucidate this polymerization specific to the channel properties of PCPs, we examined the reaction of MP in channels of different sizes of **1** (**1a**, 4.0×6.0 Å^2; **1c**, L = 1,2-di(4-pyridyl)ethylene, 10.3×6.0 Å^2) and the reactivity in a nonfunctionalized channel (without basic surface carboxylate moiety) of $[Cu_2(tp)_2(tren)]_n$ (**2**, tp = terephthalate, tren = triethylenediamine, 7.5×7.5 Å^2).[17] The pillared-layer complex **1c** with large pores was newly synthesized for this experiment.[9a,18] As expected, the polymerization of MP proceeded only in the channel of **1c** ($\bar{M}_w = 2760$, $\bar{M}_n = 710$), which shows that the monomer recognizes precisely the channel size as well as the surface functionality of PCPs. Investigations with different acetylene monomers have revealed distinct monomer selectivity, which is in agreement with the proposed polymerization mechanism. The reaction of acidic monosubstituted acetylenes (cyanoacetylene and 2-ethynylpyridine) with **1b** yields the corresponding polyacetylenes in the same manner;[19,20] in contrast, neither less-acidic monosubstituted acetylenes (phenylacetylene and 1-hexyne) nor non-acidic disubstituted acetylene (tetrolic acid methyl ester) is polymerized in the channels of **1b**. This result indicates that the strong hydrogen-bonding interaction (acid–base) between the monomers and the channel surface is a key factor to this unique spontaneous polymerization.

In conclusion, we have demonstrated that truly designable PCPs with specific basic interaction sites in the nanochannels allow the highly accelerated, stereocontrolled, and monomer-selective polymerization of substituted acetylenes. This methodology should contribute to the development of PCP materials for their application as unique and attractive catalysts that are distinct from inorganic zeolites. In addition, precisely aligned PCP nanochannels filled with π-conjugated substituted polyacetylenes should be a promising new class of host–guest nanostructures for applications such as nanoscale electronics and for fundamental investigations of these polymers in the isolated, single-chain state.

Experimental Section

1⊃polyMP: General polymerization procedure: In a pyrex reaction tube, **1b** (300 mg) was dried by evacuation at 110 °C for 5 h. After the vessel was filled with nitrogen, methyl propiolate (0.4 mL) was added and the reaction mixture was left at room temperature for 12 h. A thorough washing of the reaction mixture with $CHCl_3$ to remove unconverted monomer and surface polymer left the dark-green powder composite **1b**⊃polyMP.

Recovery of polyMP: **1b**⊃polyMP (600 mg) was suspended in DMF (30 mL) and heated at 80 °C for two days. After the mixture had been filtered, the solvent of the filtrate was removed by evaporation and the filtrate poured into Et_2O. The resulting precipitate was collected by filtration, washed with Et_2O, and dried under reduced pressure to give red–brown polyMP (16 mg).

Received: January 26, 2006
Revised: March 15, 2006
Published online: May 24, 2006

Keywords: alkynes · heterogeneous catalysis · inclusion compounds · nanostructures · polymerization

[1] a) B. Moulton, M. J. Zaworotko, *Chem. Rev.* **2001**, *101*, 1629; b) G. Férey, C. Mellot-Draznieks, C. Serre, F. Millange, *Acc. Chem. Res.* **2005**, *38*, 217; c) S. L. James, *Chem. Soc. Rev.* **2003**, *32*, 276; d) D. Bradshaw, J. B. Claridge, E. J. Cussen, T. J. Prior, M. J. Rosseinsky, *Acc. Chem. Res.* **2005**, *38*, 273; e) S. Kitagawa, R. Kitaura, S. Noro, *Angew. Chem.* **2004**, *116*, 2388; *Angew. Chem. Int. Ed.* **2004**, *43*, 2334.

[2] a) S. Kitagawa, S. Noro, T. Nakamura, *Chem. Commun*, **2006**, 701; b) R. Matsuda, R. Kitaura, S. Kitagawa, Y. Kubota, R. V. Belosludov, T. C. Kobayashi, H. Sakamoto, T. Chiba, M. Takata, Y. Kawazoe, Y. Mita, *Nature*, **2005**, *436*, 238; c) T. K. Maji, K. Uemura, H.-C. Chang, R. Matsuda, S. Kitagawa, *Angew. Chem.* **2004**, *116*, 3331; *Angew. Chem. Int. Ed.* **2004**, *43*, 3269; d) B. Chen, M. Eddaoudi, T. M. Reineke, J. W. Kampf, M. O'Keeffe, O. M. Yaghi, *J. Am. Chem. Soc.* **2000**, *122*, 11559; e) R. Kitaura, G. Onoyama, H. Sakamoto, R. Matsuda, S. Noro, S. Kitagawa, *Angew. Chem.* **2004**, *116*, 2738; *Angew. Chem. Int. Ed.* **2004**, *43*, 2684; f) D. Bradshaw, T. J. Prior, E. J. Cussen, J. B. Claridge, M. J. Rosseinsky, *J. Am. Chem. Soc.* **2004**, *126*, 6106; g) B. Kesanli, W. Lin, *Coord. Chem. Rev.* **2003**, *246*, 305.

[3] a) C.-D. Wu, A. Hu, L. Zhang, W. Lin, *J. Am. Chem. Soc.* **2005**, *127*, 8940; b) M. Fujita, Y. J. Kwon, S. Washizu, K. Ogura, *J. Am. Chem. Soc.* **1994**, *116*, 1151; c) H. J. Choi, M. P. Suh, *J. Am. Chem. Soc.* **2004**, *126*, 15844; d) J. S. Seo, D. Whang, H. Lee, S. I. Jun, J. Oh, Y. J. Jeon, K. Kim, *Nature* **2000**, *404*, 982; e) L. Pan, H. Liu, X. Lei, X. Huang, D. V. Olson, N. J. Turro, J. Li, *Angew. Chem.* **2003**, *115*, 560; *Angew. Chem. Int. Ed.* **2003**, *42*, 542.

[4] a) J. W. Y. Lam, B. Z. Tang, *Acc. Chem. Res.* **2005**, *38*, 745; b) K. J. S. Harrell, S. T. Nguyen in *Handbook of Advanced Electronic and Photonic Materials and Devices*, *Vol. 8*, Academic Press, San Diego, **2001**, pp. 131.

[5] a) C. I. Simionescu, V. Percec, *J. Polym. Sci. Polym. Symp.* **1980**, *67*, 43; b) T. Masuda, T. Higashimura, *Acc. Chem. Res.* **1984**, *17*, 51; c) M. Tabata, Y. Inaba, K. Yokota, Y. Nozaki, *J. Macromol. Sci. Part A* **1994**, *31*, 465; d) R. Nomura, J. Tabei, T. Masuda, *J. Am. Chem. Soc.* **2001**, *123*, 8430; e) K. Maeda, H. Goto, E. Yashima, *Macromolecules* **2001**, *34*, 1160; f) Y. Kishimoto, P. Eckerle, T. Miyatake, T. Ikariya, R. Noyori, *J. Am. Chem. Soc.* **1994**, *116*, 12131.

[6] For encapsulation of π-conjugated polymers and oligomers in ordered nanochannel structures, see: a) D. J. Cardin, *Adv. Mater.* **2002**, *14*, 553; b) C.-G. Wu, T. Bein, *Science* **1994**, *264*, 1757; c) A. G. Pattantyus-Abraham, M. O. Wolf, *Chem. Mater.* **2004**, *16*, 2180; d) V. S.-Y. Lin, D. R. Radu, M. K. Han, W. Deng, S. Kuroki, B. H. Shanks, M. Pruski, *J. Am. Chem. Soc.* **2002**, *124*, 9040; e) P. Sozzani, A. Comotti, S. Bracco, R. Simmonutti, *Angew. Chem.* **2004**, *116*, 2852; *Angew. Chem. Int. Ed.* **2004**, *43*, 2729; f) W. C. Molenkamp, M. Watanabe, H. Miyata, S. H. Tolbert, *J. Am. Chem. Soc.* **2004**, *126*, 4476.

[7] T. Uemura, K. Kitagawa, S. Horike, T. Kawamura, S. Kitagawa, M. Mizuno, K. Endo, *Chem. Commun.* **2005**, 5968.

[8] a) P. Sozzani, S. Bracco, A. Comotti, R. Simonutti, *Adv. Polym. Sci.* **2005**, *181*, 153; b) P. Sozzani, A. Comotti, S. Bracco, R. Simonutti, *Chem. Commun.* **2004**, 768; c) J. Lu, P. A. Mirau, A. E. Tonelli, *Prog. Polym. Sci.* **2002**, *27*, 357; d) K. A. Udachin,

 © 2006 Wiley-VCH Verlag GmbH & Co. KGaA, Weinheim

L. D. Wilson, J. A. Ripmeester, *J. Am. Chem. Soc.* **2000**, *122*, 12375.

[9] a) M. Kondo, T. Okubo, A. Asami, S. Noro, T. Yoshitomi, S. Kitagawa, T. Ishii, H. Matsuzaka, K. Seki, *Angew. Chem.* **1999**, *111*, 190; *Angew. Chem. Int. Ed.* **1999**, *38*, 140; b) R. Matsuda, R. Kitaura, Y. Kubota, T. C. Kobayashi, S. Horike, M. Takata, *J. Am. Chem. Soc.* **2004**, *126*, 14063.

[10] a) C. C. Chang, R. J. Kokes, *J. Am. Chem. Soc.* **1970**, *92*, 7517; b) C. C. Chang, R. J. Kokes, *J. Catal.* **1973**, *28*, 92; c) T. Z. Tabasaranskaya, A. A. Kadushin, *Kinet. Catal.* **1971**, *12*, 1334.

[11] Formation of trisubstituted benzenes is not observed in this polymerization system, which is confirmed by IR and ^{1}H NMR spectroscopies.

[12] a) P.-S. E. Dai, J. H. Lunsford, *J. Catal.* **1980**, *64*, 173; b) K. Moller, T. Bein, R. X. Fischer, *Chem. Mater.* **1998**, *10*, 1841.

[13] The poly(alkyl propiolates) are thermally quite stable and do not show any conformation change upon heating, see: H. Nakako, R. Nomura, M. Tabata, T. Masuda, *Macromolecules* **1999**, *32*, 2861.

[14] C. I. Simionescu, V. Bulacovschi, M. Grovu-Ivanoiu, A. Stanciu, *J. Macromol. Sci. Chem. A* **1987**, *24*, 611.

[15] a) G. C. Pimentel, A. L. McClellan, *The Hydrogen Bond*, W. H. Freeman, San Francisco, **1960**; b) A. M. DeLaat, B. S. Ault, *J. Am. Chem. Soc.* **1987**, *109*, 4232.

[16] a) A. K. Rappé, C. J. Casewit, K. S. Colwell, W. A. Goddard III, W. M. Skiff, *J. Am. Chem. Soc.* **1992**, *114*, 10024; b) C. J. Casewit, K. S. Colwell, A. K. Rappé, *J. Am. Chem. Soc.* **1992**, *114*, 10035.

[17] a) K. Seki, Y. Mori, *J. Phys. Chem. B* **2002**, *106*, 1380; b) K. Seki, *Langmuir* **2002**, *18*, 2441.

[18] Crystal data for **1c**⊃6 H_2O: $C_{24}H_{14}Cu_2N_6O_{14}$, $M_r = 737.50$, monoclinic, $P2_1/c$ (No. 14), $a = 4.7109(5)$, $b = 31.858(3)$, $c = 11.002(1)$ Å, $\beta = 96.008(8)°$, $V = 1642.0(3)$ Å^3, $Z = 4$, $R_1 = 0.027$, $R_w = 0.037$, $T = 298$ K. CCDC-295897 contains the supplementary crystallographic data for this paper. These data can be obtained free of charge from The Cambridge Crystallographic Data Centre via www.ccdc.cam.ac.uk/data_request/cif.

[19] Poly(cyanoacetylene): IR (KBr): $\tilde{\nu} = 2203$, 1659, 1497, 1348, 1190 cm^{-1}; $M_w = 15800$, $M_n = 6700$ (polystyrene standard). Poly(2-ethynylpyridine): IR (KBr): $\tilde{\nu} = 1616$, 1588, 1466, 1132, 754 cm^{-1}; $M_w = 1400$, $M_n = 420$ (polystyrene standard).

[20] a) C. B. Gorman, R. W. Vest, T. U. Palovich, S. Serron, *Macromolecules* **1999**, *32*, 4157; b) S. Subramanyam, A. Blumstein, *Macromolecules* **1992**, *25*, 4058.

 © 2006 Wiley-VCH Verlag GmbH & Co. KGaA, Weinheim

Glycoproteins

DOI: 10.1002/anie.200600538

Building Complex Glycopeptides: Development of a Cysteine-Free Native Chemical Ligation Protocol**

*Bin Wu, Jiehao Chen, J. David Warren, Gong Chen, Zihao Hua, and Samuel J. Danishefsky**

The development of increasingly efficient and general methods for the merging of complex peptidic fragments remains a central objective in the field of polypeptide and glycopolypeptide synthesis. A number of traditional native chemical ligation (NCL) techniques have been applied to the problem of polypeptide assembly through convergent ligation.[1] Nearly all of these require the presence of an N-terminal cysteine residue to function as the acyl acceptor. Given the relative scarcity of cysteine residues in nature, a clear impetus arises for the realization of new NCL capabilities.

Our laboratory has a major interest in the development of methods for the preparation of homogeneous, fully synthetic polypeptides, and even proteins, that display multiple sites of glycosylation. A particularly relevant glycoprotein, which serves to coordinate and focus our efforts in this field, is the naturally occurring erythropoietin alpha (EPO; Figure 1).[2]

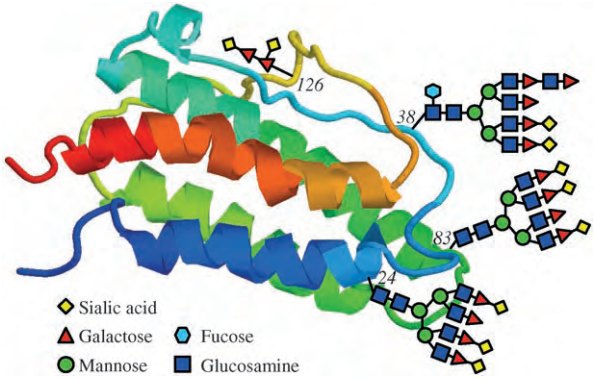


Figure 1. Structure of erythropoietin.

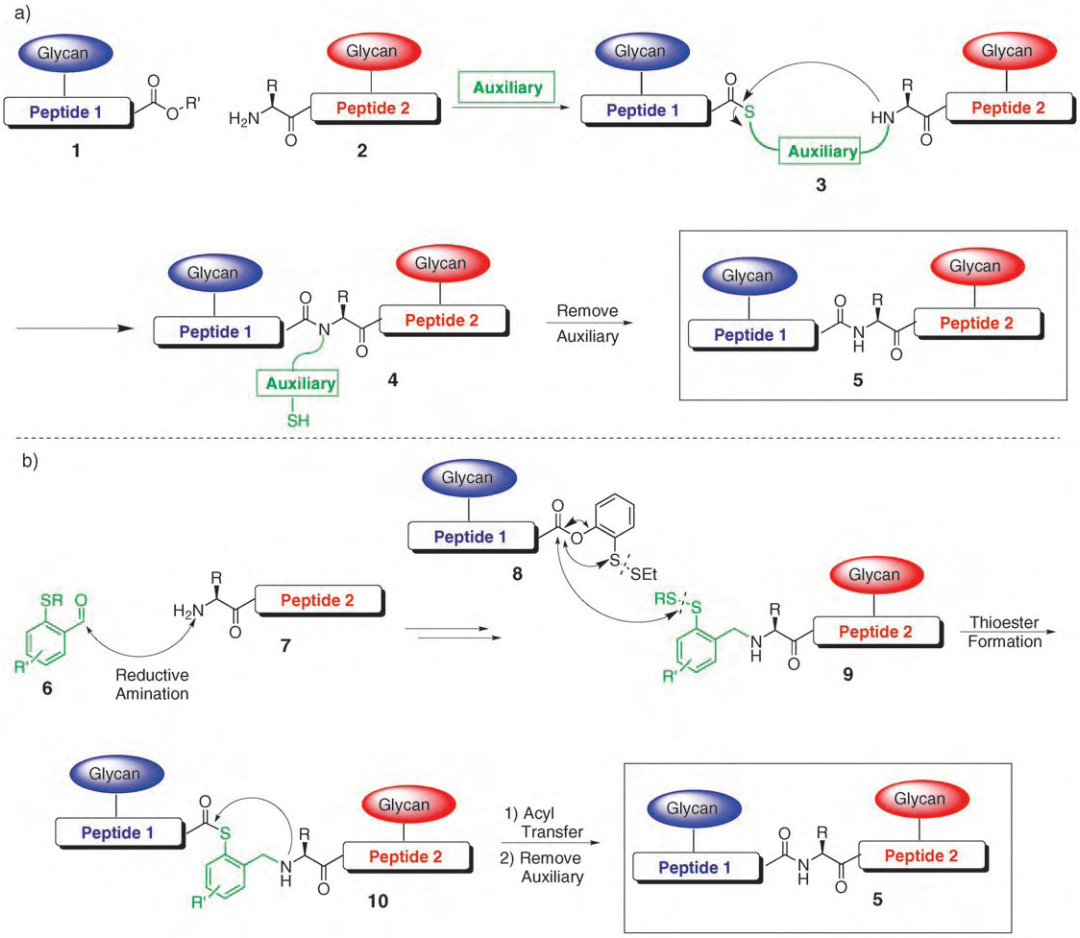
[*] Prof. S. J. Danishefsky
The Department of Chemistry
Columbia University
Havemeyer Hall, New York, NY 10027 (USA)
Fax: (+1) 212-772-8691
E-mail: s-danishefsky@ski.mskcc.org

Dr. B. Wu, Dr. J. Chen, Dr. J. D. Warren, Dr. G. Chen, Dr. Z. Hua, Prof. S. J. Danishefsky
The Laboratory for Bioorganic Chemistry
Sloan-Kettering Institute for Cancer Research
1275 York Avenue, New York, NY 10021 (USA)

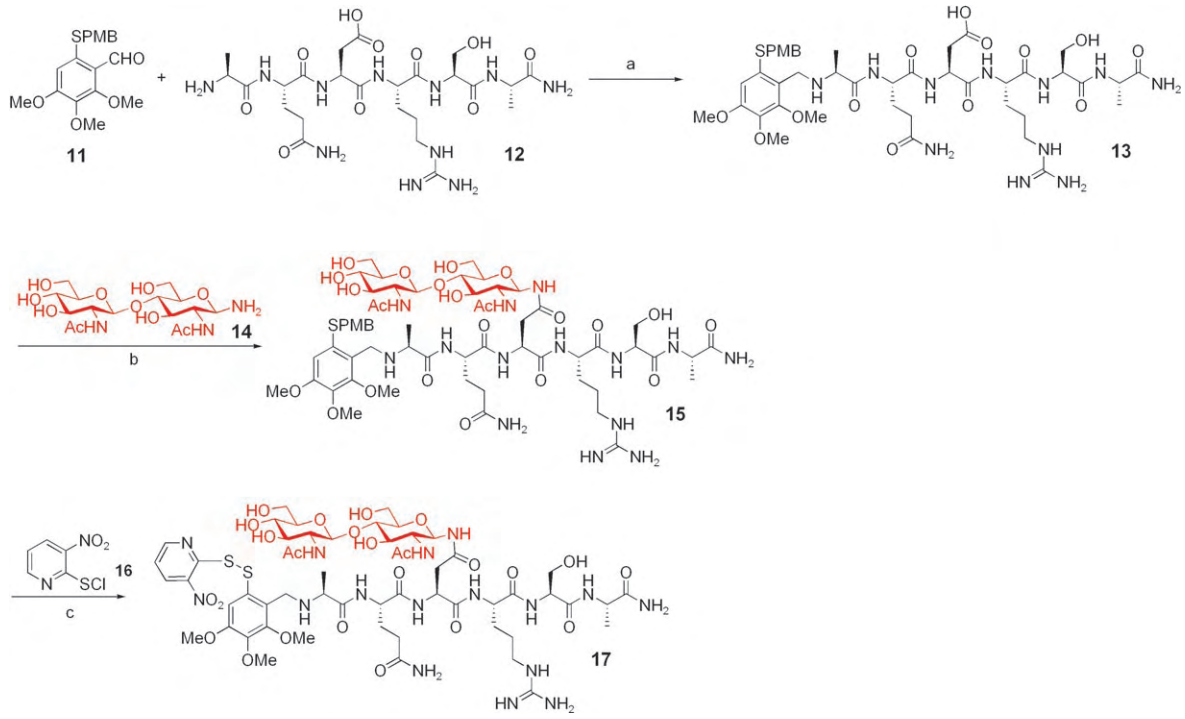
[**] This work was supported by the National Institutes of Health (Grant CA28824 to S.J.D., and CA62948 to J.D.W.) and by New York State Department of Health, New York State Breast Cancer Research and Education Fund (to B.W.).

Supporting information for this article is available on the WWW under http://www.angewandte.org or from the author.

WILEY InterScience DISCOVER SOMETHING GREAT
© 2006 Wiley-VCH Verlag GmbH & Co. KGaA, Weinheim

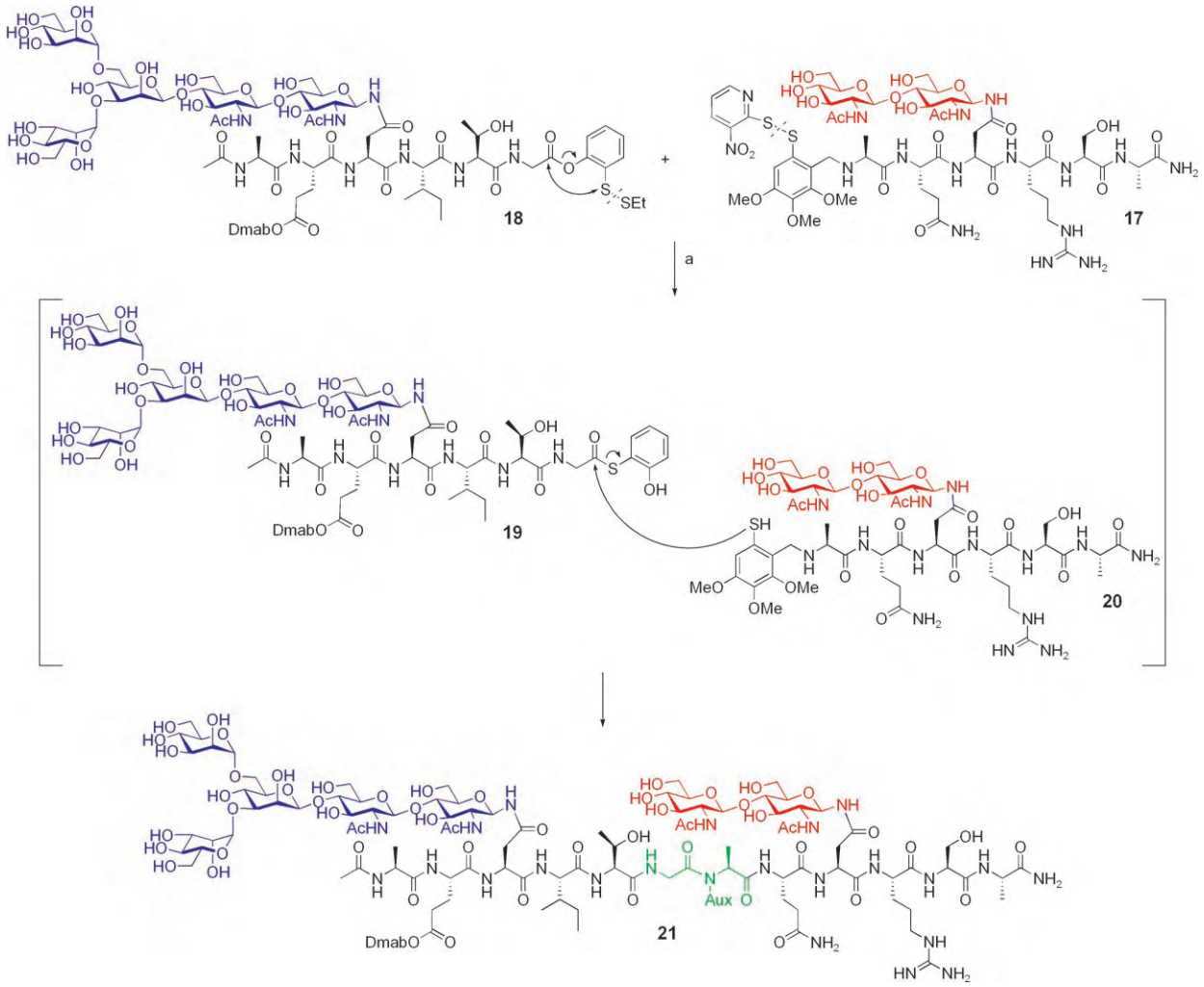


Scheme 1. Cysteine-free ligation strategy. See text for details.

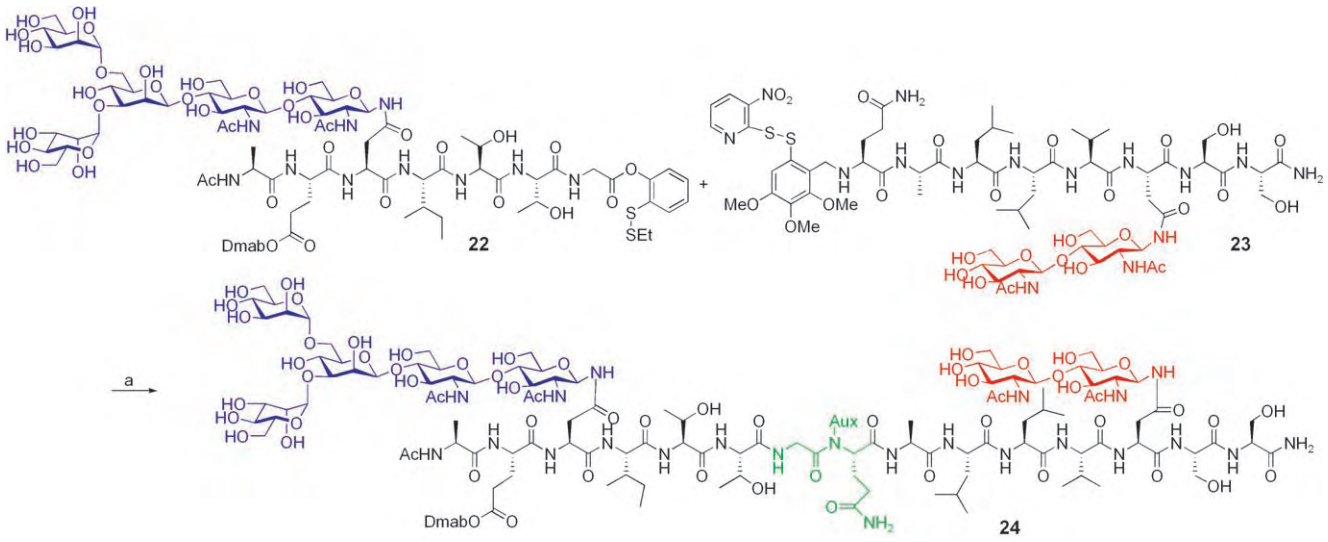


Scheme 2. Synthesis of compound **17**. Reaction conditions, a) $NaCNBH_3$, MeOH/DMF, 60%; b) **14**, HATU, iPr_2NEt, DMSO, 62%; c) **16**, TFE/CH_2Cl_2, 70%. Ac = acetyl, DMF = *N*,*N*-dimethylformamide, DMSO = dimethyl sulfoxide, HATU = *O*-(7-azabenzotriazol-1-yl)-*N*,*N*,*N*',*N*'-tetramethyluronium hexafluorophosphate, PMB = *para*-methoxybenzyl, TFE = 2,2,2-trifluoroethanol.

 © 2006 Wiley-VCH Verlag GmbH & Co. KGaA, Weinheim



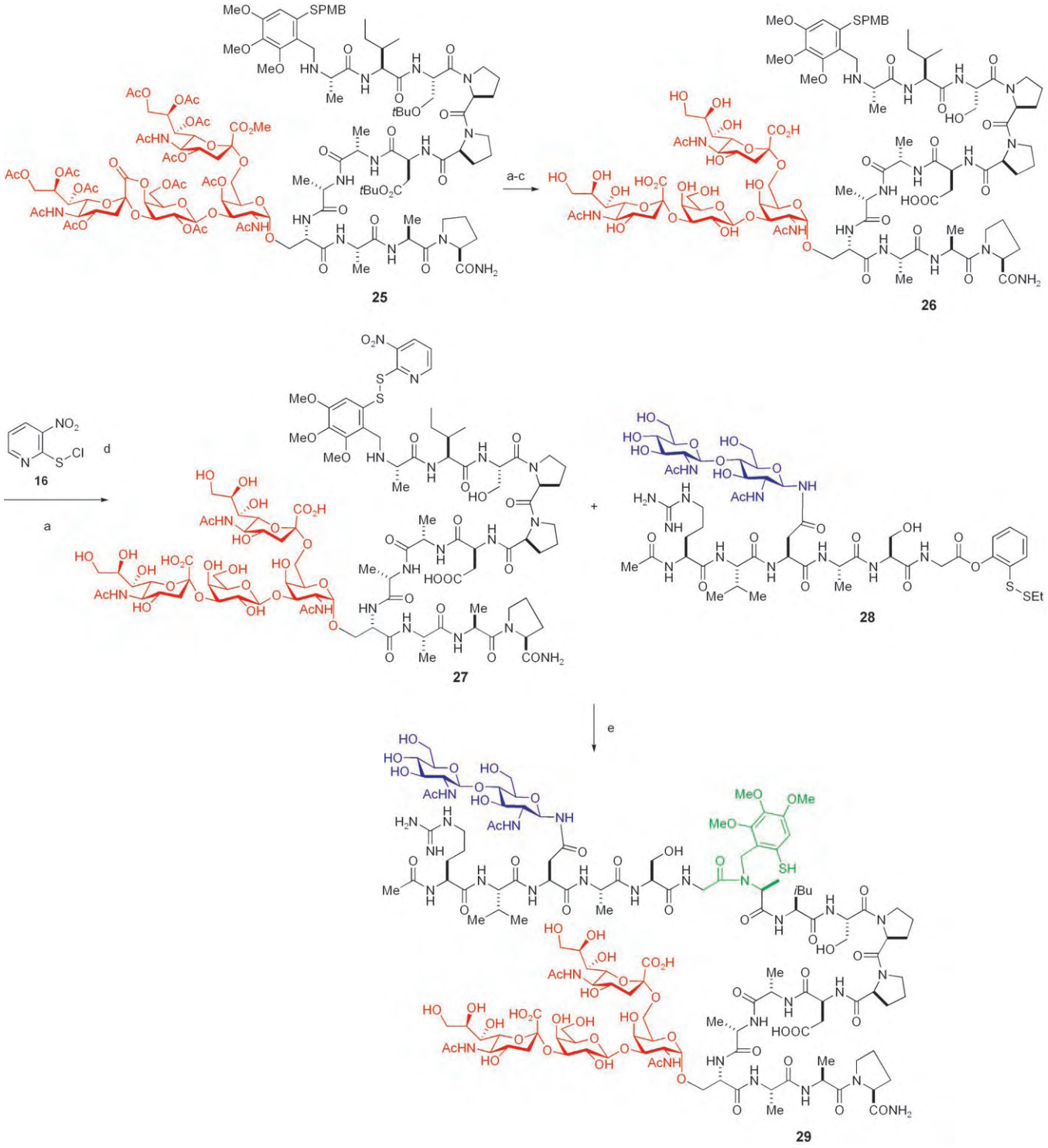
Scheme 3. Synthesis of **21**. Reaction conditions, a) TCEP, PBS (pH 8.0), 37%. Aux = auxiliary, Dmab = 4-{N-[1-(4,4-dimethyl-2,6-dioxocyclohexylidene)-3-methylbutyl]-amino}benzyl, PBS = phosphate-buffered saline buffer solution, TCEP = tricarboxyethylphosphine.



Scheme 4. Ligation of **22** and **23**. Reaction conditions, a) TCEP, DMF, Na_2HPO_4, 32 °C, 54%.

 © 2006 Wiley-VCH Verlag GmbH & Co. KGaA, Weinheim

This multiply glycosylated protein has found widespread therapeutic application in the treatment of anemia. Despite the clear-cut clinical importance of this compound, attempts to rigorously evaluate the role of glycosylation on the activity and stability of erythropoietin have thus far been complicated by the daunting difficulties associated with isolating significant quantities of homogeneous EPO.[3] On the basis of our long-term involvement in the arena of carbohydrate and glycopeptide total synthesis,[4] we reasoned that if the considerable powers of chemical synthesis were brought to bear on this problem in a principled and focused fashion, it might be possible to gain access to fully synthetic, homogeneous erythropoietins. Needless to say, such a capability would likely enable access to a range of EPO analogues for structure–activity-relationship investigations. Broadly speaking, an undertaking of this magnitude could well lead to the



Scheme 5. Ligation of O-linked glycodomains. Reaction conditions, a) TFA, PhOH, H_2O, TESH; b) 0.1 N NaOH, MeOH; c) H_2NNH_2, MeOH, 61% over 3 steps; d) **16**, TFE, 67%; e) TCEP, DMF, Na_2HPO_4, 65%. TFA = trifluoroacetic acid, TESH = triethylsilane.

 © 2006 Wiley-VCH Verlag GmbH & Co. KGaA, Weinheim

development of generally useful strategies and protocols of utility to the entire field of glycoprotein synthesis.

Erythropoietin is a 166-residue protein possessing four sites of glycosylation. Three of these are N linked to asparagine residues and one is O linked to a serine residue. In considering a strategy for the de novo synthesis of erythropoietin, we took note of the paucity of cysteine residues on the molecule. A maximally convergent route to erythropoietin would involve the preparation of the four different glycopeptide fragments, which would subsequently be joined through some form of ligation to furnish the fully glycosylated protein backbone. Thus, in light of the fact that the four cysteine residues of erythropoietin do not segregate into nearly equal-sized carbohydrate-bearing domains, we were led to consider glycopeptide ligation methods that do not require cysteine-based acyl acceptors. The development of a repertoire of ligation methods could well be critical to the success of our EPO-directed venture.

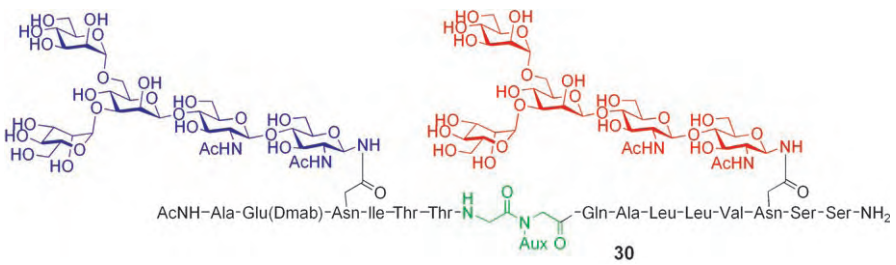
Scheme 1a shows, in the most general terms, a scenario wherein two differentially glycosylated peptide fragments (**1** and **2**) would be temporarily engaged through an auxiliary linker[5] such that the C-terminal coupling fragment would be activated as a thioester (**3**). Having been coaxed into proximity, the N-terminal coupling partner would attack the thioester, thus forming the key amide bond (**4**). Removal of the auxiliary would provide the doubly glycosylated peptide **5**. In this way, the limitation of a cysteine acyl acceptor situated at the N-terminus would have been removed.

One conceivable manifestation of this general strategy would commence with the covalent appendage of a sulfur-displaying auxiliary of the type **6** to the N terminus of an appropriate peptide fragment (**7**) through reductive amination.[6] In this early feasibility demonstration, we benefited from a recently disclosed clever idea of Dawson et al. for a non-cysteine-based ligation, albeit by a different organizing step.[7] The resultant intermediate would be advanced to the glycopeptide **9**. At this point, we envisioned joining the two fully functionalized glycopeptide fragments under conditions analogous to those that we had previously developed in the context of a cysteine-based NCL method.[5a] Thus, the coupling partner, **8**, would be equipped with a C-terminal phenolic ester, as shown in Scheme 1b. Under disulfide reducing conditions, the C-terminal coupling partner, **8**, would be activated to form a thioester with the auxiliary sulfur functionality of the N-terminal fragment, thus providing an intermediate of the type **10**. Amide-bond formation followed by auxiliary removal would provide the bifunctional glycopeptide **5**.

In the end, we elected to equip the sulfur atom of the auxiliary with a PMB protecting group.[8] We anticipated that deprotection of this group could be accomplished under mild conditions that are compatible with survival of glycopeptide functionality (see Scheme 2). Thus, aldehyde **11** was prepared through slight modification of a known procedure.[7a] Reductive amination with hexapeptide **12** provided **13** in 60% yield. This ability to connect a substantial N-terminal domain to the auxiliary by reductive amination is an important feature of this methodology. Next, the disaccharide **14** was appended to the peptide through reducing-end amination and aspartylation.[9] At this stage, we sought to convert the S–PMB group into an aromatic disulfide under mild conditions that would leave the sensitive glycopeptide functionality intact. We were pleased to find that, following treatment of **15** with sufenyl chloride **16** in TFE/DCM, compound **17** was obtained.[10] Notably, this transformation represents an appealing alternative to previously described conditions that typically require exposure to harsh reagents such as anhydrous HF or $Hg(OAc)_2$ and TFA.[6a,7a]

With the auxiliary-bearing glycopeptide fragment **17** in hand, we were now prepared to investigate the viability of our cysteine-free coupling strategy. In this context, we first examined a Gly–Ala ligation. As expected, upon exposure to TCEP in PBS buffer solution (pH 8.0), glycopeptides **17** and **18** each underwent reductive disulfide cleavage (see Scheme 3). Presumably, the C-terminal glycopeptide then suffered an O→S acyl transfer of the type previously described to generate the activated thioester (**19**).[11] As anticipated, **19** and **20** were temporarily joined through a thioester exchange reaction. Following intramolecular acyl transfer, the fully functionalized glycopeptide **21** was isolated in 37% yield.[12]

Encouraged by this early success, we next sought to explore the generality of the method by attempting ligation at a more challenging Gly–Gln center. Thus, glycopeptides **22** and **23** (Scheme 4) were prepared and subjected to ligation conditions (TCEP in PBS buffer solution; pH 8.0). Unfortunately, the yield of **24** was found to be quite low, and a significant quantity of carboxylic acid arising from the hydrolysis of **22** was observed. We postulated that, although in the previous instance (**17** + **18**→**21**) the rate-determining step of the sequence had been the joining of the two fragments through transthioesterification, in the case at hand, the increased steric hindrance around the reacting center had caused the intramolecular acyl transfer to become rate limiting. Consequently, hydrolysis of the tethered intermediate had the opportunity to intervene as a competitive side reaction. Although we were unable to improve upon the product distribution by adjusting the pH of the system, we did find that, by introducing DMF as a cosolvent with a small amount of Na_2HPO_4, we were able to isolate the ligation product **24** in a more-acceptable 54% yield.

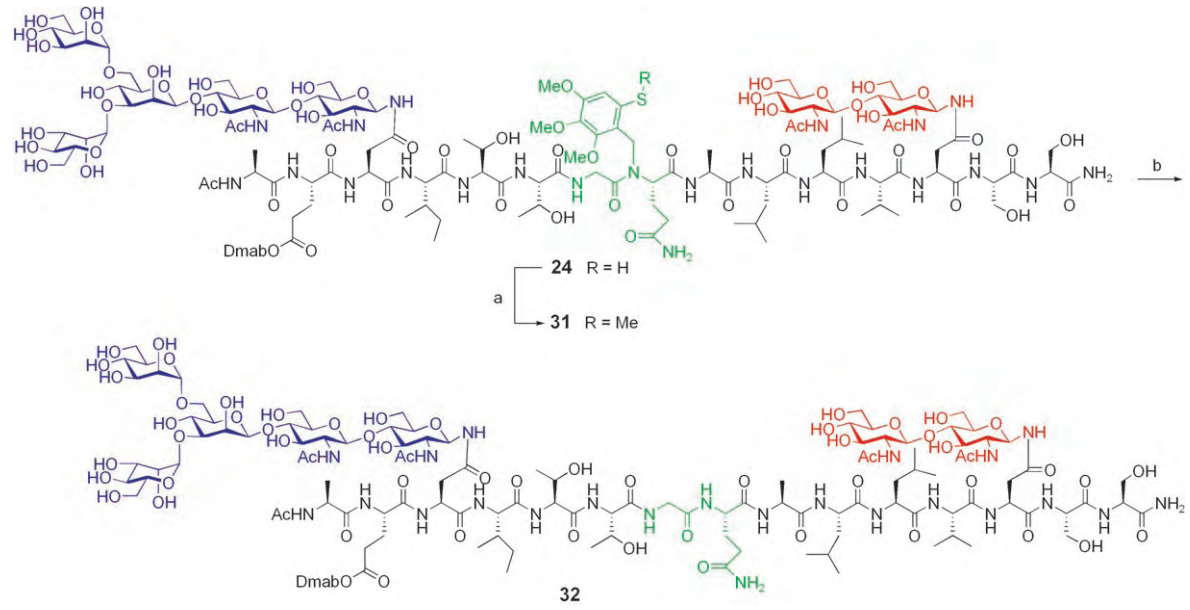


Scheme 6. Bifunctional glycopeptide.

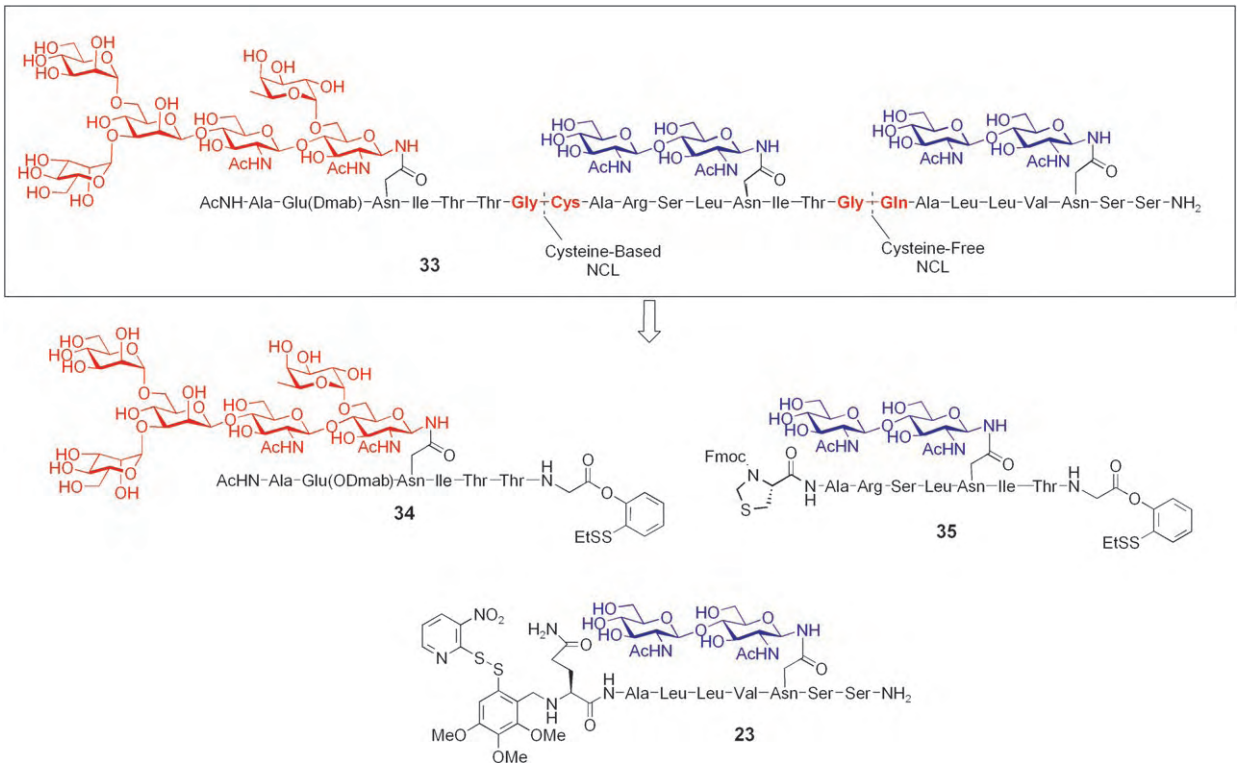
 © 2006 Wiley-VCH Verlag GmbH & Co. KGaA, Weinheim

Having demonstrated the capacity of our methods to successfully ligate two N-linked glycopeptide domains, we next sought to investigate its compatibility with O-linked glycodomains. Thus, intermediate **25** was advanced to **26** through a three-step sequence, as shown in Scheme 5.[13] The latter was converted into the N-terminal coupling partner, **27**, according to previously developed reaction conditions. We were pleased to find that, upon exposure to TCEP and DMF with Na_2HPO_4, **27** and **28** readily underwent cysteine-free native chemical ligation to provide glycopeptide **29**, which possesses both N- and O-linked carbohydrate domains. Notably, no carbohydrate decomposition products were observed.

We next validated our methodology in the context of more-complex glycan fragments, including those containing characteristic non-reducing and sialic acid moieties. The



Scheme 7. Synthesis of **32**. Reaction conditions, a) methyl *p*-nitrobenzene sulfonate; b) 95% TFA.



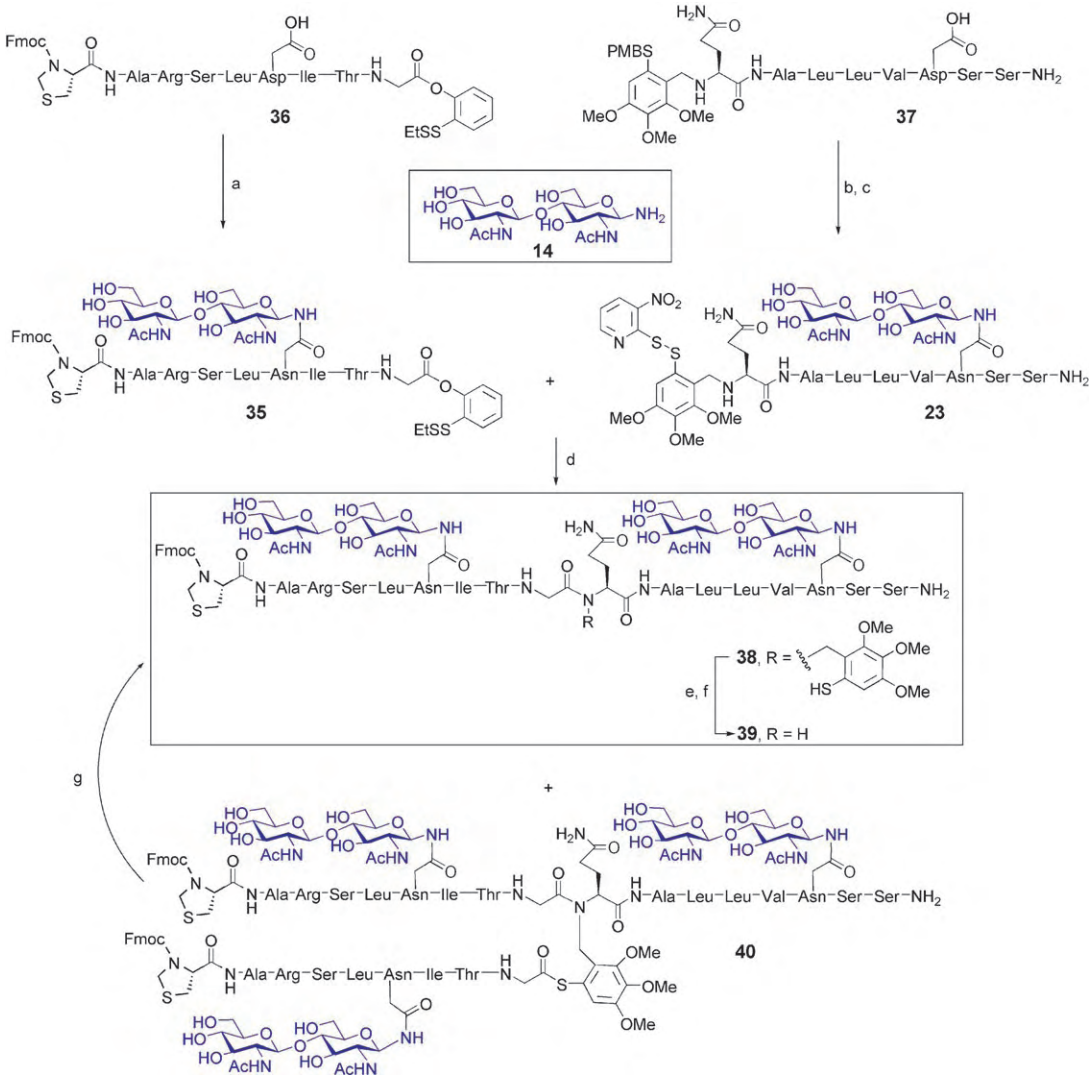
Scheme 8. Trifunctional glycopeptide.

© 2006 Wiley-VCH Verlag GmbH & Co. KGaA, Weinheim

extent of sialidation is apparently a determinant of EPO stability.[14] Thus, the coupling of two glycopeptide fragments, each displaying an N-linked core pentasaccharide, was found to proceed smoothly to provide the bifunctional glycopeptide **30** (Scheme 6).

The final phase of this investigation would be the development of appropriately mild conditions for the cleavage of the thiol auxiliary. In this context, TFA with a scavenger has been used in similar types of systems. However, in our hands, the treatment of the ligation product with 95% TFA with a triisopropyl silane (TIPS) scavenger resulted in a mixture of the desired native glycopeptide along with another compound of the same molecular weight as the starting glycopeptide. The latter was tentatively assigned to be the thioester intermediate, arising from acid-mediated intramolecular N→S acyl transfer.[15] Presumably, the otherwise endothermic step is driven by irreversible protonation of the benzylic amine. In light of this finding, a two-step sequence (Scheme 7) was devised for the removal of the auxiliary. First, intermediate **24** was treated with methyl *p*-nitrobenzene sulfonate.[16] This step accomplished selective methylation of the sulfur on the aromatic ring to provide intermediate **31**. The latter was not purified, rather, it was exposed to the action of 95% TFA, thereby providing the native glycopeptide **32**, free of any observable thioester by-product.

Having successfully field tested our novel cysteine-free ligation protocol in the context of a convergent bis-domainal glycopeptide synthesis, we next turned to the challenge of synthesizing longer peptide chains that contain more than two sites of glycosylation. Indeed, to consider the total synthesis of a complex glycoprotein, such as EPO, it would be critical to be able to couple, in a reiterative fashion, multiple glycopeptide fragments. Along these lines, we recently disclosed a method to generate differentially glycosylated trifunctional glycopeptides based on a cysteine-dependent native chemical ligation protocol.[17] As a demonstration of the applicability of our new non-cysteine NCL technology to complex targets, we



Scheme 9. Synthesis of **40**. Reaction conditions, a) **14**, HATU, iPr$_2$NEt, DMSO, 72%; b) **14**, HATU, iPr$_2$NEt, DMSO, 83%; c) TFE, DCM, **16**, 69%; d) TCEP, DMF, Na_2HPO_4, 58% (**38**) + 11% (**40**); e) methyl *p*-nitrobenzene sulfonate; f) 95% TFA; g) PhSH or MesNa, PBS. DCM = dichloromethane, Fmoc = 9-Fluorenylmethoxycarbonyl, MesNa = 2-mercaptoethane sulfonic acid, sodium salt.

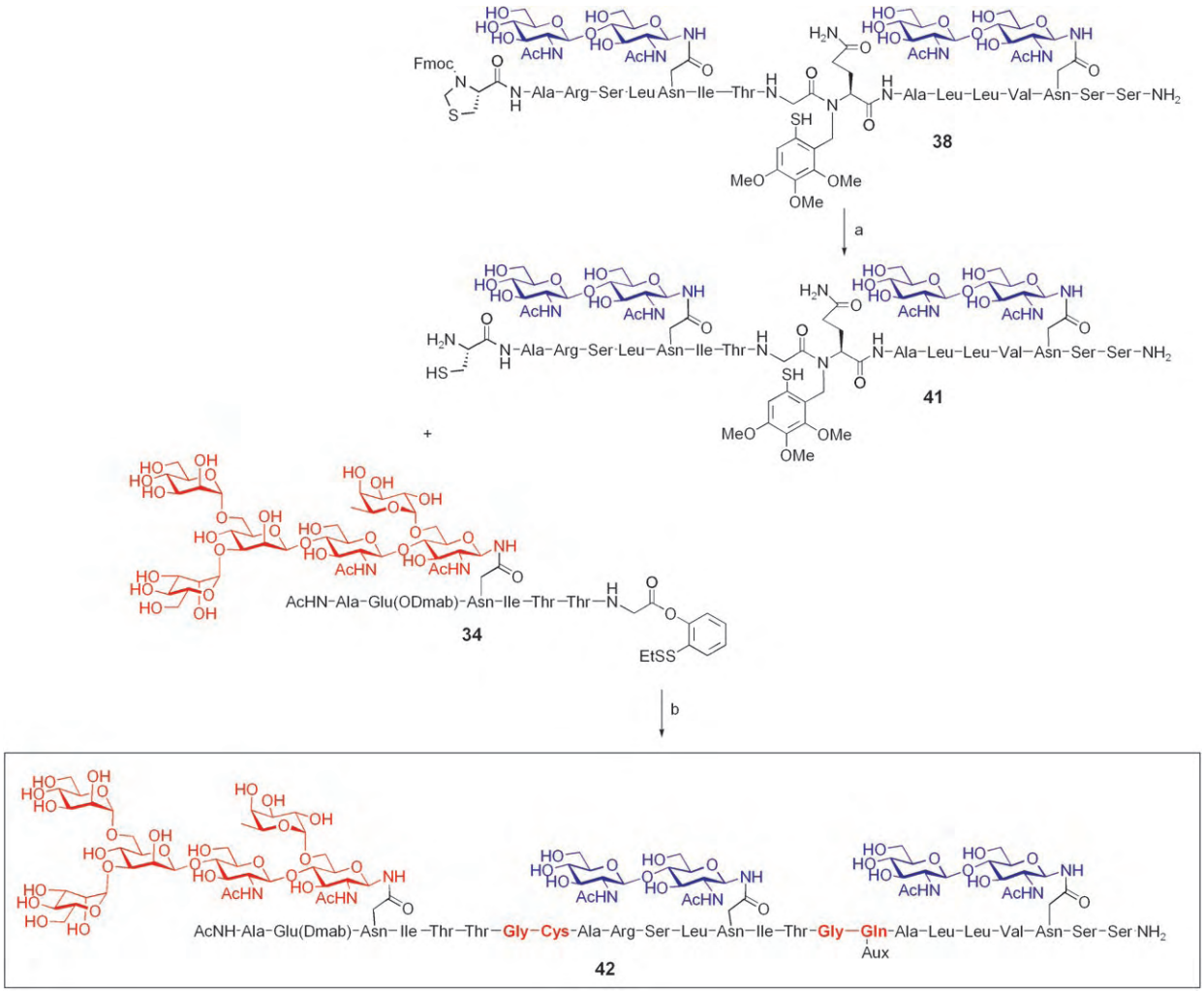
 © 2006 Wiley-VCH Verlag GmbH & Co. KGaA, Weinheim

next sought to apply a combination of our cysteine-dependent and cysteine-free NCL protocols to the preparation of the multiply glycosylated peptide, **33**. Under our synthetic plan, we would first prepare each of the three glycopeptide fragments (**34**, **35**, and **23**) according to glycal assembly and glycopeptide synthesis protocols that have been validated and optimized over the course of many years in our laboratory (Scheme 8).[4] Fragments **23** and **35** would then be joined according to our newly developed cysteine-free ligation method to form the Gly–Gln junction. Next, following deprotection of the N-terminal cysteine residue, the bifunctional peptide would be merged with glycopeptide **34** through cysteine-based ligation to afford the fully functionalized target compound.

Thus, polypeptides **36** and **37** were prepared for the cysteine-free ligation event. It is noted that the termini have been suitably equipped in anticipation of the reiterative sequence. Thus, peptide **37** bears the requisite N-terminal auxiliary for the cysteine-free coupling, whereas fragment **36**, which will serve as the middle glycopeptide component, incorporates the C-terminal phenolic ester for the first cysteine-free ligation as well as a 1,3-thiazolidine-4-carboxo (Thz)-protected N-terminal cysteine residue, which is unmasked prior to the second, cysteine-based ligation event.[18]

Each peptide fragment was subjected to glycosylation with disaccharide **14**, and, following conversion of the N-terminal auxiliary S–PMB group to the requisite disulfide, glycopeptides **35** and **23** were in hand. As hoped, the coupling of the two fragments proceeded readily in the presence of TCEP to afford the ligated product **38** in 58% yield, along with 11% of the thioester **40**. The latter could be converted into **38** upon treatment with thiophenol or MesNa.[19] At this stage, the thiol auxiliary could be removed according to the two-step sequence shown in Scheme 9 (**38**→**39**); alternatively, the auxiliary could also be maintained in the subsequent ligation event without causing detriment.

As we had previously demonstrated, the cysteine residue was readily unmasked through exposure of **38** to 10% morpholine in DMF (to remove the Fmoc group) followed by treatment with an aqueous solution of $MeONH_2 \cdot HCl$ (Scheme 10). Native chemical ligation between **41** and **34** was



Scheme 10. Synthesis of **42**. Reaction conditions, a) (i) 10% morpholine in DMF; (ii) 0.4 M $MeONH_2 \cdot HCl$, 60%; b) MesNa, TCEP, PBS (pH 8.0), 57%.

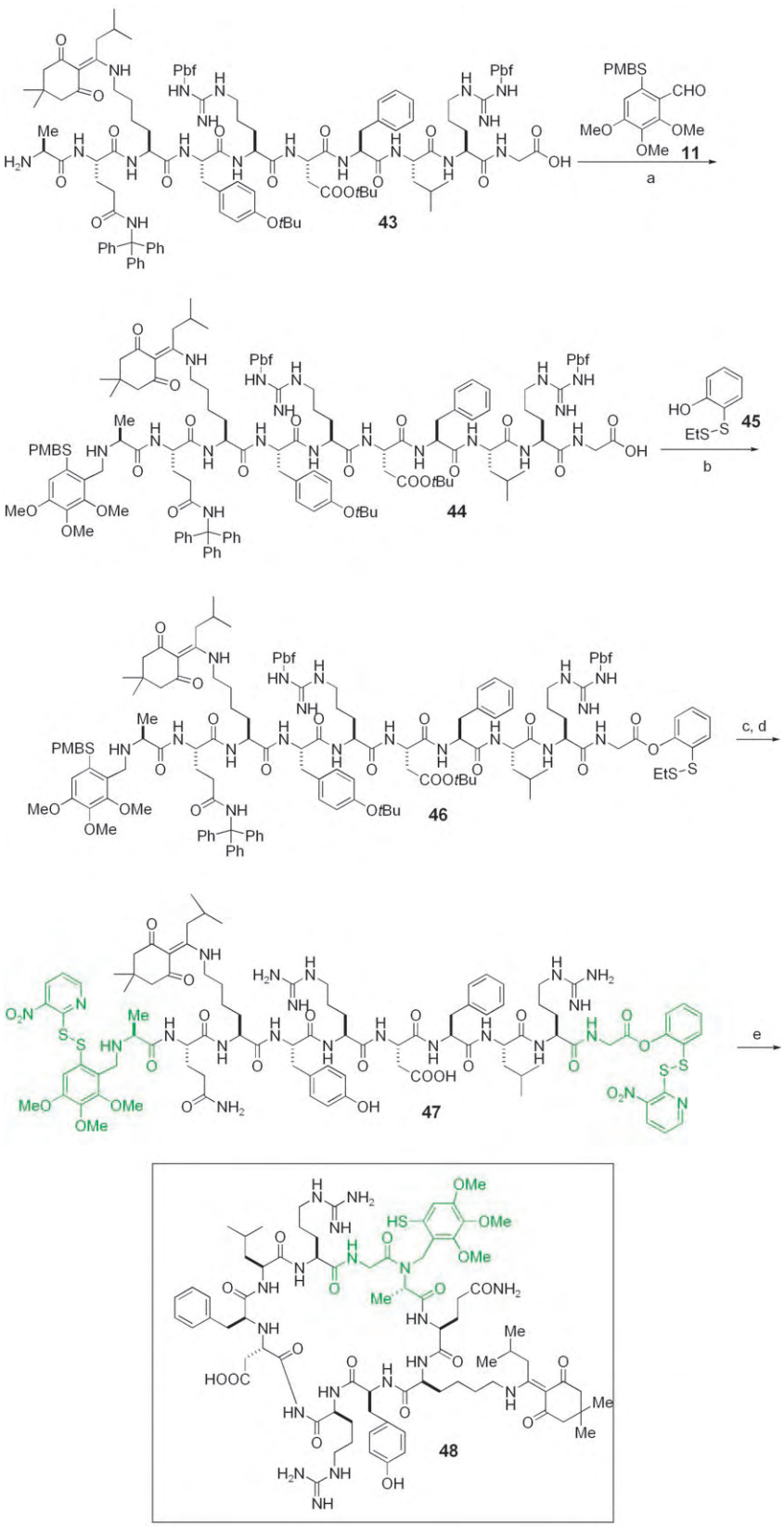
 © 2006 Wiley-VCH Verlag GmbH & Co. KGaA, Weinheim

carried out in the presence of MesNa and TCEP and afforded the multifunctional glycopeptide **42** in 57% yield.

Finally, the viability of our newly developed cysteine-free ligation protocol was demonstrated in another area of peptide chemistry of great interest to those at the forefront of chemistry and glycobiology, that is, the synthesis of cyclic peptides.[20] Cyclic peptides often possess enhanced biological specificity, activity, and metabolic stability in comparison to their linear counterparts. This is as a consequence of their constrained conformations and their enhanced levels of resistance to protease digestion. Although traditional strategies for cyclic-peptide formation are restricted to macrolactam or disulfide formation, Tam and co-workers[21] have disclosed that cyclic peptides can be accessed through native chemical ligation.[22] Recently, our research group reported on a newly modified protocol for native chemical ligation that allows for formation of cyclic peptides possessing a cysteine residue.[23] However, given the scarcity of cysteine residues in nature, the applicability of standard cysteine-based ligation methods may be somewhat limited. Clearly, the development of a broadly useful, cysteine-independent ligation protocol could well have profound ramifications for the field of cyclic-peptide synthesis.

The linear polypeptide **43** was prepared through solid-phase peptide synthesis. Reductive amination with aldehyde **11** served to introduce the N-terminal auxiliary (**44**). The C terminus was functionalized through HATU-mediated esterification with phenol **45**, providing **46**. Following protecting-group removal and exposure to 3-nitro-2-pyridinesulfenyl chloride, the requisite disulfide cyclization precursor was in hand. Thus, the linear peptide bis-disulfide (**47**) was treated with TCEP and Na_2HPO_4 in DMF to provide the desired cyclized peptide (**48**) in good yield. Importantly, no dimers or oligomers were observed in liquid chromatograpy–MS analysis (see Scheme 11).

Obviously, in undertaking a target of the complexity of erythropoietin, opportunities for complications and even failure are always inherent. However, we feel that in principle the basis of a realistic total synthesis of homogeneous erythropoietin has been set forth above. Always



Scheme 11. a) **11**, $NaCNBH_3$, MeOH, DMF, 66%; b) **45**, HATU, DIPEA, DMF; c) TFA, PhOH, TESH, H_2O, 57% for 2 steps; d) **16**, TFE, 60%; e) TCEP, Na_2HPO_4, DMF, 78%. DIPEA = *N*,*N*-diisopropylethylamine, Pbf = 2,2,4,6,7-pentymethyldihydrobenzofuran-5-sulfonyl.

 © 2006 Wiley-VCH Verlag GmbH & Co. KGaA, Weinheim

mindful of the risks, we remain busily engaged in pursuing this goal.

Received: February 9, 2006
Revised: April 5, 2006
Published online: May 19, 2006

Keywords: cysteine-free ligation · erythropoietin · glycoproteins · native chemical ligation · peptides

[1] a) P. E. Dawson, T. W. Muir, I. Clark-Lewis, S. B. H. Kent, *Science* **1994**, *266*, 776–779; b) J. Wilken, S. B. H. Kent, *Curr. Opin. Biotechnol.* **1998**, *9*, 412–426; c) G. J. Cotton, T. W. Muir, *Chem. Biol.* **1999**, *6*, R247–R256; d) D. S. Y. Yeo, R. Srinivasan, G. Y. J. Chen, S. Q. Yao, *Chem. Eur. J.* **2004**, *10*, 4664–4672.

[2] D. M. Ridley, F. Dawkins, E. Perlin, *J. Natl. Med. Assoc.* **1994**, *86*, 129–135. For examples of related chemical synthesis approaches to EPO, see: a) G. G. Kochendoerfer et al., *Science* **2003**, *299*, 884–887; b) N. Robertson, R. Ramage, *J. Chem. Soc. Perkin Trans. 1* **1999**, 1015–1021.

[3] a) R. Kornfeld, S. Kornfeld, *Annu. Rev. Biochem.* **1985**, *54*, 631–664; b) J. Roth, *Chem. Rev.* **2002**, *102*, 285–303.

[4] a) S. J. Danishefsky, M. T. Bilodeau, *Angew. Chem.* **1996**, *108*, 1482–1522; *Angew. Chem. Int. Ed. Engl.* **1996**, *35*, 1380–1419; b) S. J. Danishefsky, J. R. Allen, *Angew. Chem.* **2000**, *112*, 882–912; *Angew. Chem. Int. Ed.* **2000**, *39*, 836–863. For other examples of the chemical synthesis of glycopeptides, see: c) H. Hojo, Y. Matsumoto, Y. Nakahara, E. Ito, Y. Suzuki, M. Suzuki, A. Suzuki, Y. Nakahara, *J. Am. Chem. Soc.* **2005**, *127*, 13720–13725; d) H. Hojo, E. Haginoya, Y. Matsumoto, Y. Nakahara, K. Nabeshima, B. P. Toole, Y. Watanabe, *Tetrahedron Lett.* **2003**, *44*, 2961–2964; e) D. Macmillan, C. R. Bertozzi, *Angew. Chem.* **2004**, *116*, 1379–1383; *Angew. Chem. Int. Ed.* **2004**, *43*, 1355–1359; f) S. Mezzato, M. Schaffrath, C. Unverzagt, *Angew. Chem.* **2005**, *117*, 1677–1681; *Angew. Chem. Int. Ed.* **2005**, *44*, 1650–1654.

[5] a) J. D. Warren, J. S. Miller, S. J. Keding, S. J. Danishefsky, *J. Am. Chem. Soc.* **2004**, *126*, 6576–6578. Although the O→S acyl transfer method that we have developed and its application to complex glycopeptide synthesis had not previously been reported, the general concept of chemical ligation of polypeptides through 1) an organizing preliminary attachment, 2) acyl transfer, and 3) deconvolution with emergence of a peptide bond establishing the ligation has a distinguished intellectual history. For an early paper that can be so classified, see: b) M. Brenner, J. P. Zimmermann, J. Wehrmüller, P. Quitt, A. Hartmann, W. Schneider, U. Beglinger, *Helv. Chim. Acta.* **1957**, *40*, 1497–1517. The key seminal advance was incubated in a series of papers by Kemp and co-workers, see: c) D. S. Kemp, S.-L. Leung, D. J. Kerkman, *Tetrahedron Lett.* **1981**, *22*, 181–184; d) D. S. Kemp, D. J. Kerkman, *Tetrahedron Lett.* **1981**, *22*, 185–186; e) D. S. Kemp, D. J. Kerkman, S.-L. Leung, G. Hanson, *J. Org. Chem.* **1981**, *46*, 490–498; f) D. S. Kemp, *Biopolymers* **1981**, *20*, 1793–1804; g) D. S. Kemp, N. G. Galakatos, *J. Org. Chem.* **1986**, *51*, 1821–1829; h) D. S. Kemp, N. Fotouhi, *Tetrahedron Lett.* **1987**, *28*, 4637–4640; i) N. Fotouhi, N. G. Galakatos, D. S. Kemp, *J. Org. Chem.* **1989**, *54*, 2803–2817; j) D. S. Kemp, R. I. Carey, *J. Org. Chem.* **1993**, *58*, 2216–2222, see also: k) P. Botti, M. Villain, S. Manganiello, H. Gaertner, *Org. Lett.* **2004**, *6*, 4861–4864; l) D. W. Low, M. G. Hill, M. R. Carrasco, S. B. H. Kent, P. Botti, *Proc. Natl. Acad. Sci. USA* **2001**, *98*, 6554–6559.

[6] a) D. Macmillan, D. W. Anderson, *Org. Lett.* **2004**, *6*, 4659–4662; b) T. Kawakami, K. Akaji, S. Aimoto, *Org. Lett.* **2001**, *3*, 1403–1405.

[7] a) J. Offer, C. N. C. Boddy, P. E. Dawson, *J. Am. Chem. Soc.* **2002**, *124*, 4642–4646; b) J. Offer, P. E. Dawson, *Org. Lett.* **2000**, *2*, 23–26.

[8] Other S-protecting groups such as 2-cyanoethyl group (removable under basic conditions), and 2,4-dinitrophenyl (DNP; removable with Mes-Na) were also successfully applied to this approach to allow the incorporation of cysteine and tryptophan residues in the glycopeptides.

[9] S. T. Cohen-Anisfeld, P. T. Lansbury, *J. Am. Chem. Soc.* **1993**, *115*, 10531–10537.

[10] R. Matsueda, T. Kimura, E. T. Kaiser, G. R. Matsueda, *Chem. Lett.* **1981**, *6*, 737–740.

[11] Manuscripts detailing the mechanism study of the postulated O→S acyl shift are in preparation.

[12] The Dmab protecting group on the glutamic acid residue, installed for the selective incorporation of a carbohydrate moiety on the asparagine residue, was removed by diluted hydrazine solution and further confirmed the presence of a stable amide-linked ligation product. For other examples of hydrazine treatment of glycopeptides, see: a) Y. Shin, K. A. Winans, B. Backes, S. B. H. Kent, J. A. Ellman, C. R. Bertozzi, *J. Am. Chem. Soc.* **1999**, *121*, 11684–11689; b) T. Pohl, H. Waldmann, *J. Am. Chem. Soc.* **1997**, *119*, 6702–6710.

[13] J. B. Schwarz, S. D. Kuduk, X.-T Chen, D. Sames, P. W. Glunz, S. J. Danishefsky, *J. Am. Chem. Soc.* **1999**, *121*, 2662.

[14] E. Tsuda, G. Kawanishi, M. Ueda, S. Masuda, R. Sasaki, *Eur. J. Biochem.* **1990**, *188*, 405–411.

[15] J. Vizzavona, F. Dick, T. Vorherr, *Bioorg. Med. Chem. Lett.* **2002**, *12*, 1963–1965.

[16] J. P. Tam, Q. Yu, *Biopolymers* **1998**, *46*, 319–327.

[17] B. Wu, J. D. Warren, J. Chen, G. Chen, Z. Hua, S. J. Danishefsky, *Tetrahedron Lett.* **2006**, In Press.

[18] D. Bang, S. B. H. Kent, *Angew. Chem.* **2004**, *116*, 2588–2592; *Angew. Chem. Int. Ed.* **2004**, *43*, 2534–2538.

[19] T. Kawakami, M. Sumida, K. Nakamura, T. Vorherr, S. Aimoto, *Tetrahedron Lett.* **2005**, *46*, 8805–8807.

[20] a) D. F. Veber, R. M. Freidinger, *Trends Neurosci.* **1985**, *8*, 392–396; b) E. J. Milner-White, *Trends Pharmacol. Sci.* **1989**, *10*, 70–74.

[21] a) L. Zhang, J. P. Tam, *J. Am. Chem. Soc.* **1997**, *119*, 2363–2370; b) J. P. Tam, Y.-A Lu, *Tetrahedron Lett.* **1997**, *38*, 5599–5602.

[22] For other examples of the use of NCL in the synthesis of cyclic peptides, see: a) Y. Shao, W. Y. Lu, S. B. H. Kent, *Tetrahedron Lett.* **1998**, *39*, 3911–3914; b) W. D. F. Meutermans, S. W. Golding, G. T. Bourne, L. P. Miranda, M. J. Dooley, P. F. Alewood, M. L. Smythe, *J. Am. Chem. Soc.* **1999**, *121*, 9790–9796; c) S. Tchertchian, O. Hartley, P. Botti, *J. Org. Chem.* **2004**, *69*, 9208–9214; d) V. M. Cardona, O. Hartley, P. Botti, *J. Pept. Res.* **2003**, *61*, 152–157.

[23] J. Chen, J. D. Warren, B. Wu, G. Chen, Q. Wan, S. J. Danishefsky, *Tetrahedron Lett.* **2006**, *47*, 1969–1972.

 © 2006 Wiley-VCH Verlag GmbH & Co. KGaA, Weinheim

Alkaloids

DOI: 10.1002/anie.200600514

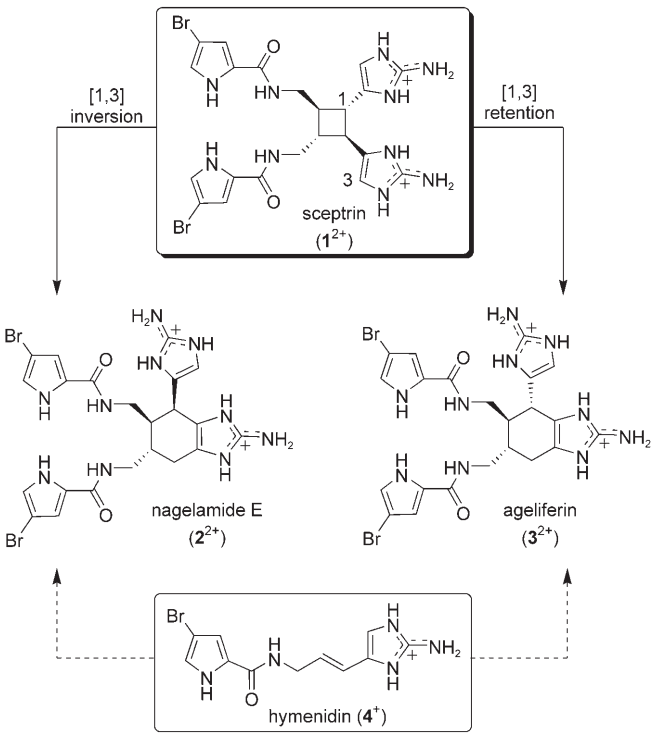
Mechanism of the Vinylcyclobutane Rearrangement of Sceptrin to Ageliferin and Nagelamide E**

Brian H. Northrop, Daniel P. O'Malley, Alexandros L. Zografos, Phil S. Baran, and K. N. Houk**

Chemical transformations that have been the focus of extensive physical organic studies are sometimes later discovered to be operative in natural processes. The Bergman cyclization of (*Z*)-3-ene-1,5-diynes, for example, was explored mechanistically and found to involve *p*-benzyne diradical intermediates.[1] A little over a decade later, it was discovered that the Bergman cyclization was a critical component of the biological activity of a newly discovered class of enediyne natural antibiotics that have potent antitumor activity.[2]

We now provide theoretical evidence that the well-studied vinylcyclobutane–cyclohexene rearrangement, which involves a 1,4-diradical "*para* intermediate",[3] is involved not only in a synthetic but also a biosynthetic process. The recent synthesis[4] of the antiviral compound ageliferin ($\mathbf{3}^{2+}$)[5] from sceptrin ($\mathbf{1}^{2+}$)[6] led to the proposed involvement of a vinylcyclobutane–cyclohexene rearrangement[7] (Scheme 1). Therefore, a reaction previously of interest for mechanistic reasons is likely to be an important step in a biosynthesis.

Dimeric pyrrole–imidazole alkaloids[8] are believed to be derived from hymenidin ($\mathbf{4}^{+}$)[4] and related structures (see Scheme 1). The reigning biosynthetic hypothesis[4,9] is that nagelamide E ($\mathbf{2}^{2+}$) and $\mathbf{3}^{2+}$ are likely formed from two equivalents of $\mathbf{4}^{+}$ through an enzymatic "Diels–Alderase",



Scheme 1. Solid arrows: The vinylcyclobutane rearrangements of $\mathbf{1}^{2+}$ to $\mathbf{2}^{2+}$ and $\mathbf{3}^{2+}$. Atoms that become bonded in the [1,3] shift are labeled 1 and 3 on $\mathbf{1}^{2+}$. Dashed arrows: $\mathbf{4}^{+}$ as a possible precursor to complex pyrrole–imidazole alkaloids $\mathbf{2}^{2+}$ and $\mathbf{3}^{2+}$ by an enzymatic "Diels–Alderase".

but recent results[4] suggest the involvement of the vinylcyclobutane–cyclohexene rearrangement of $\mathbf{1}^{2+}$ to $\mathbf{2}^{2+}$. Such rearrangements are alternatives to the previous biosynthetic hypothesis for the formation of $\mathbf{2}^{2+}$ and $\mathbf{3}^{2+}$. Subsequent to our initial report on the synthesis of $\mathbf{3}^{2+}$,[4] preparation of the natural product in larger quantities led to the isolation of small quantities of a compound tentatively assigned as an epimer of $\mathbf{3}^{2+}$. This compound was later reported as the natural product $\mathbf{2}^{2+}$,[10] which was isolated by Kobayashi and co-workers from an unidentified *Agelas* marine sponge along with $\mathbf{3}^{2+}$ in a ratio of 1:24. Herein, we report the first total synthesis of $\mathbf{2}^{2+}$ and computational studies that have led to a clear understanding of the mechanism and stereoselectivity of this remarkable rearrangement.

Microwave irradiation of $\mathbf{1}^{2+}$ in water at 200 °C for 5 minutes followed by purification by reversed-phase HPLC gave a 40% yield of $\mathbf{3}^{2+}$, 50% recovery of $\mathbf{1}^{2+}$,[4] and a small amount of $\mathbf{2}^{2+}$. Although the amount of isolated $\mathbf{2}^{2+}$ varied somewhat and the small quantities of material involved made precise measurements difficult, the yield was consistently around 2% (ca. 1:20 ratio with $\mathbf{3}^{2+}$). Microwave heating of pure $\mathbf{3}^{2+}$ at 200 °C was found to generate a mixture of $\mathbf{3}^{2+}$ and $\mathbf{2}^{2+}$. A final concentration of 2:1 was reached after 7 minutes, and further heating led only to decomposition. This result suggests either that $\mathbf{1}^{2+}$ could be the direct biosynthetic precursor to both $\mathbf{3}^{2+}$ and $\mathbf{2}^{2+}$ or that $\mathbf{1}^{2+}$ could be an indirect precursor through the epimerization of $\mathbf{3}^{2+}$. Given the small amounts of $\mathbf{2}^{2+}$ isolated relative to $\mathbf{3}^{2+}$, it is also possible that

[*] D. P. O'Malley, Dr. A. L. Zografos, Prof. P. S. Baran
Department of Chemistry
The Scripps Research Institute
10550 North Torrey Pines Road, La Jolla, CA 92037 (USA)
Fax: (+1) 858-784-7375
E-mail: pbaran@scripps.edu
B. H. Northrop, Prof. K. N. Houk
Department of Chemistry and Biochemistry
University of California, Los Angeles
607 Charles E. Young Drive East, Los Angeles, CA 90095 (USA)
Fax: (+1) 310-206-1843
E-mail: houk@chem.ucla.edu

[**] We thank Dr. D. H. Huang and Dr. L. Pasternack for assistance with the NMR spectroscopy; Biotage for a generous donation of microwave process vials, which were used extensively during these studies; and the Department of Defense and the Hertz Foundation for pre-doctoral fellowships (D.P.O.). Financial support for this work was provided by The Scripps Research Institute, Amgen, Dupont, Eli Lilly, GlaxoSmithKline, Roche, the Searle Scholarship Fund, NIH/NIGMS (GM-073949 to P.S.B), the National Science Foundation (research grant CHE-0240203 to K.N.H), and IGERT (a (MCTP)-DGE-0114443 fellowship to B.H.N.).

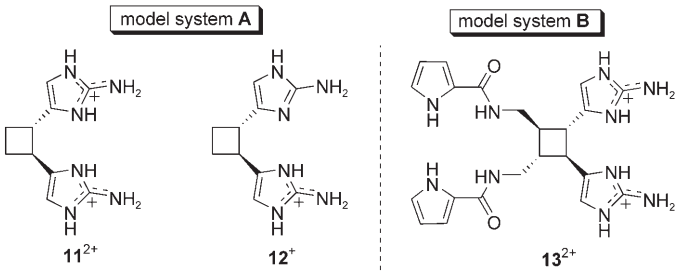
Supporting information for this article is available on the WWW under http://www.angewandte.org or from the author.

InterScience
© 2006 Wiley-VCH Verlag GmbH & Co. KGaA, Weinheim

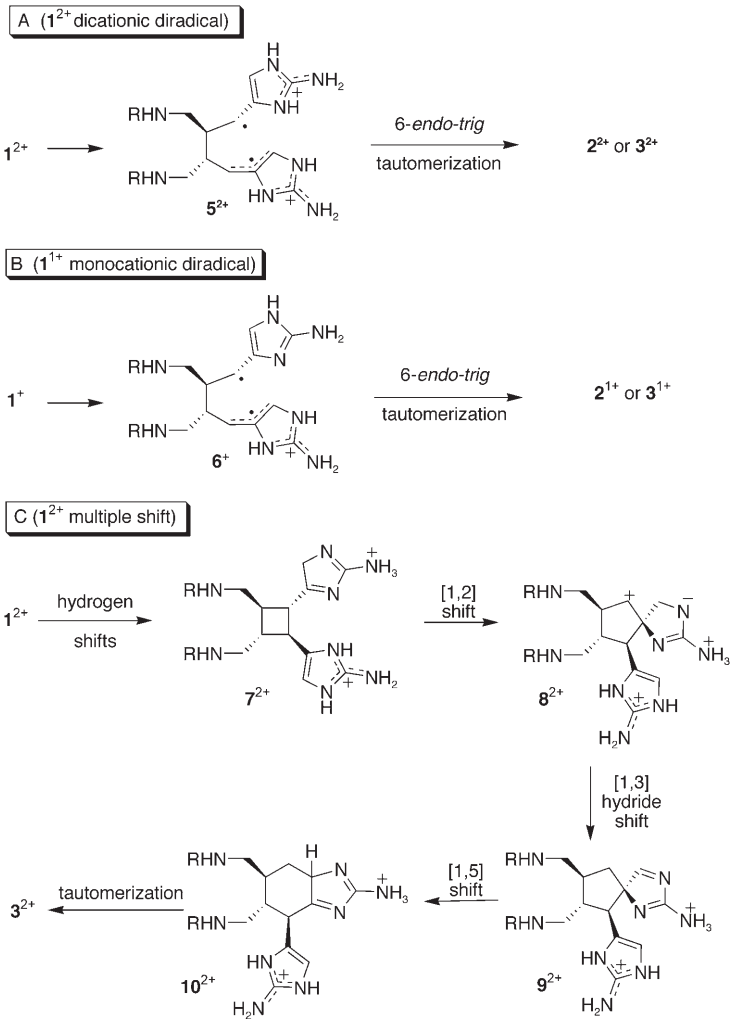
$\mathbf{2}^{2+}$ is an artifact produced from $\mathbf{3}^{2+}$ during isolation rather than a compound produced in nature. The isolation of $\mathbf{2}^{2+}$ was significant, as it involves inversion of the imidazole-bearing stereocenter, as opposed to the retention of configuration in the formation of $\mathbf{3}^{2+}$.

Experimental[7,11] and theoretical[12] investigations show that the rearrangements of substituted vinylcyclobutanes to cyclohexenes proceed via diradicals, although no distinct intermediates are present on the potential-energy surface. Simple vinylcyclobutanes rearrange to give a mixture of all four stereochemical outcomes (suprafacial or antarafacial with inversion or retention, hereafter referred to as: si, sr, ai, and ar) and often show a slight preference for symmetry-allowed products si and ar.[7,11–12] However, subtle stereochemical changes in the starting vinylcyclobutane may invert this preference and lead to the symmetry forbidden products sr and ai.[7,11] The rearrangements of $\mathbf{1}^{2+}$ to $\mathbf{3}^{2+}$ and $\mathbf{2}^{2+}$ could occur by three possible mechanisms.[4,13] Vinylcyclobutane rearrangement via a dicationic diradical ($\mathbf{1}^{2+}$; Scheme 2A) or a monocationic diradical ($\mathbf{1}^{1+}$; Scheme 2B), followed by tautomerization, are both possible. In addition, a dicationic multiple-shift mechanism with $\mathbf{1}^{2+}$ (Scheme 2C) that involves a 1,2 and a 1,5 shift combined with several tautomerizations could occur. While retention or inversion of configuration at the migrating carbon atom can unambiguously be observed in the product stereochemistries, $\mathbf{3}^{2+}$ and $\mathbf{2}^{2+}$ lack the stereochemical indicators necessary to determine whether the rearrangement proceeds suprafacially or antarafacially.

Computational studies of the rearrangements of $\mathbf{1}^{2+}$ were performed on the two model systems shown in Scheme 3.



Scheme 3. Simplified model compounds used in the computational study of the rearrangements of $\mathbf{1}^{2+}$.



Scheme 2. A)–C) Three potential mechanisms for the rearrangement of $\mathbf{12}^{+}$ to nagelamide E ($\mathbf{2}^{2+}$) and ageliferin ($\mathbf{3}^{2+}$) that have been studied computationally.

Model system A ($\mathbf{11}^{2+}$ and $\mathbf{12}^{+}$) lacks the neutral side chains of $\mathbf{12}^{+}$, whereas model system B ($\mathbf{12}^{2+}$) includes the side chains but replaces both pyrrole bromine atoms with hydrogen atoms. Stationary points were optimized at the UB3LYP/6-31G* level for model system A (16 heavy atoms) and at the UHF/6-31G* level for model system B (34 heavy atoms) with the GAUSSIAN03 program.[13] Density functional theoretical (DFT) calculations at the UB3LYP/6-31G* level have been shown to give reliable predictions for the energetics of hydrocarbon diradical species[12a,d,15] relative to those of other density functional methods (e.g., BPW91[11c]) or complete active space self-consistent field (SCF) methods.[12b–d,15d] UB3LYP/6-31G* enthalpies at 298 K and conductorlike polarizable continuum model (CPCM) solvation free energies[16] in H_2O were computed. Minimum energy reaction pathways were constructed for each of the proposed mechanisms.

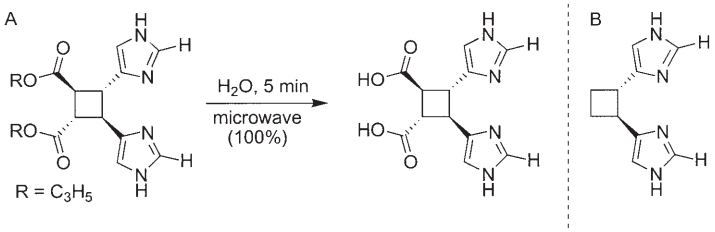
Cleavage of the cyclobutane ring of dicationic sceptrin model $\mathbf{11}^{2+}$ to form the diradical species[17] analogous to $\mathbf{5}^{2+}$ requires 30.5 kcal mol^{-1}. A dicationic diradical intermediate analogous to $\mathbf{5}^{2+}$ is formed and is 6.8 kcal mol^{-1} more stable than the ring-opening transition state. This behavior is in contrast to the flat potential surfaces that are typical of hydrocarbon rearrangements that involve diradicals.[12,15] Coulombic repulsion between the cationic aminoimidazole rings of the reactant is relieved in the diradical intermediate, as the inter-aminoimidazolyl distance increases by 2.5 Å. Closure of the diradical requires 7.8 kcal mol^{-1} and gives the si product. The sr ring-closure transition state is 1.3 kcal mol^{-1} higher in energy than the si ring-closure transition state.

Ring opening of the monocationic[17] model compound $\mathbf{12}^{+}$ requires 35.8 kcal mol^{-1} and leads to a flat potential-energy surface, typical of the hydrocarbon

 © 2006 Wiley-VCH Verlag GmbH & Co. KGaA, Weinheim

vinylcyclobutane rearrangement. The experimental ΔH^{+} value for the rearrangement of divinylcyclobutane to form vinylcyclohexene is 34.0 kcal mol^{-1},[18] while the same barrier computed with DFT is 31.3 kcal mol^{-1}.[12c] These results indicate that a 2-aminoimidazole group and a vinyl group stabilize a radical to nearly the same extent and led us to calculate radical stabilization energies (RSE) of 2-aminoimidazole, protonated 2-aminoimidazole, and 2-H imidazole. RSEs, calculated at the UB3LYP/6-31G* level relative to the allyl radical,[19] were found to be 2.5–3.9 kcal mol^{-1} lower than that of the allyl radical for all substituents, thus indicating no large difference in their ability to stabilize a radical. Both si and sr ring-closing transition states have been located for monocationic sceptrin model compound **12**$^{+}$; both are lower energy than the monocationic diradical intermediate (by 3.0 and 1.4 kcal mol^{-1}, respectively) when zero point energy and solvation are included.

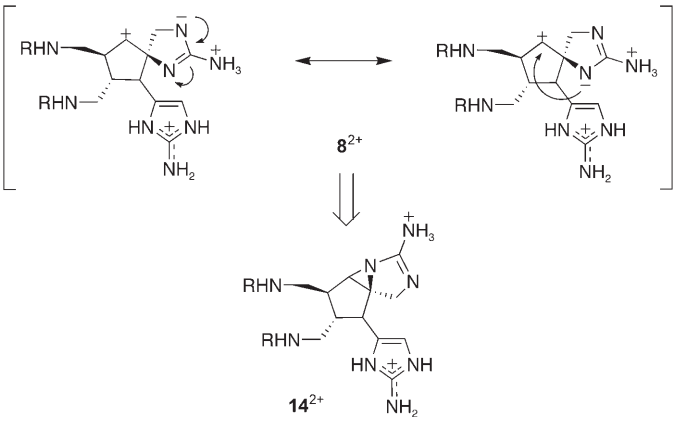
The ring opening of *trans*-1,2-di(4-imidazolyl)cyclobutane (Scheme 4), a neutral analogue of **11**$^{2+}$ and **12**$^{+}$, requires



Scheme 4. A) Microwave irradiation of the known allylurocanate dimer results in hydrolysis and no rearrangement. B) Model system of the neutral **1**$^{2+}$ analogue used in computational studies.

47.2 kcal mol^{-1}. Baran et al. have shown that exposure of the structurally similar allylurocanate dimer to microwave radiation at 200 °C in H_2O resulted in 100 % of the hydrolysis product and none of the rearrangement product, thus indicating the 2-aminoimidazolyl moiety of **1**$^{2+}$ is necessary for rearrangement.[4]

Computational studies of the dicationic multiple-shift mechanism were also performed. Formation of an intermediate species analogous to **7**$^{2+}$ is only 28.7 kcal mol^{-1} higher in energy than the starting sceptrin model compound **11**$^{2+}$. However, the subsequent [1,2] shift does not lead to the spiro intermediate **8**$^{2+}$, as postulated in Scheme 2c. Instead, all attempts to optimize the spiro intermediate model compound of **8**$^{2+}$ led to the tricyclic intermediate analogue of **14**$^{2+}$ shown in Scheme 5. Rearrangement through the multiple-shift mechanism via the analogue of **14**$^{2+}$ requires 37.7 kcal mol^{-1}, which exceeds the barriers to rearrangement of the monocationic **12**$^{+}$ and dicationic **11**$^{2+}$ model systems by 1.9 and 6.2 kcal mol^{-1}, respectively. Computations involving this model system indicate that the rearrangement of **1**$^{2+}$ most likely proceeds through a stepwise diradical process that starts from dicationic sceptrin (**1**$^{2+}$). It remains possible that two equivalents of **4**$^{+}$ may undergo a [2 + 2] dimerization to give **1**$^{2+}$, which can then rearrange to give **2**$^{2+}$ and **3**$^{2+}$. However, computations predict it to be unlikely for two equivalents of **4**$^{+}$ to react in a concerted [4 + 2] manner to give **2**$^{2+}$ or **3**$^{2+}$. The concerted transition state that leads to **2**$^{2+}$ and **3**$^{2+}$ from two equivalents of **4**$^{+}$ is 6 kcal mol^{-1} higher in energy than the stepwise diradical pathway. Additionally, Lindel and co-workers recently reported[20] the failure of oroidin, which is brominated **4**$^{+}$, to undergo Diels–Alder reactions to give dibromoageliferin.



Scheme 5. The formation of the high-energy tricyclic intermediate **14**$^{2+}$ from structure **8**$^{2+}$ through the dicationic multiple-shift reaction pathway (Scheme 2C).

In the more complete model system B **13**$^{2+}$, the ring-closing transition states that lead to the sr and si rearranged products **3**$^{2+}$ and **2**$^{2+}$ were optimized at the UHF/6-31G* level. The effects of solvation by H_2O were computed with CPCM solvation calculations. The most noteworthy difference between the sr and si transition states is the existence of three hydrogen-bonding interactions present in the sr ring-closing transition state (Figure 1). These are not observed in the si ring-closing transition state that leads to **2**$^{2+}$. Ring closure to **3**$^{2+}$ is predicted to be 1.7 kcal mol^{-1} more favorable than formation of **2**$^{2+}$ on account of these stabilizing hydrogen-bonding interactions. This $\Delta\Delta H^{+}$ value predicts **3**$^{2+}$ to be preferentially formed over **2**$^{2+}$ in a ratio of 22:1, which is in good agreement with the experimental results. In both the si closing transition state and the resulting **2**$^{2+}$, the *trans* relationship between the migrating 2-aminoimidazolyl group and the pyrrole side chain α to the allylic radical renders them incapable of forming similar hydrogen-bonding interactions.

In summary, computational studies on the vinylcyclobutane rearrangements of sceptrin to ageliferin and nagelamide E lead to the conclusion that rearrangement occurs via diradical intermediates starting from dicationic sceptrin (**1**$^{2+}$). Hydrogen-bonding interactions present in the 6-*endo-trig* closing transition state favor the formation of the [1*r*,3*s*] product, ageliferin. We have also reported the first total synthesis of nagelamide E. The fact that nagelamide E and ageliferin are synthesized by thermal rearrangement in approximately the same ratio as they are isolated from nature is remarkable and suggests the possible involvement of a similar process in the biosynthesis of these compounds.

 © 2006 Wiley-VCH Verlag GmbH & Co. KGaA, Weinheim

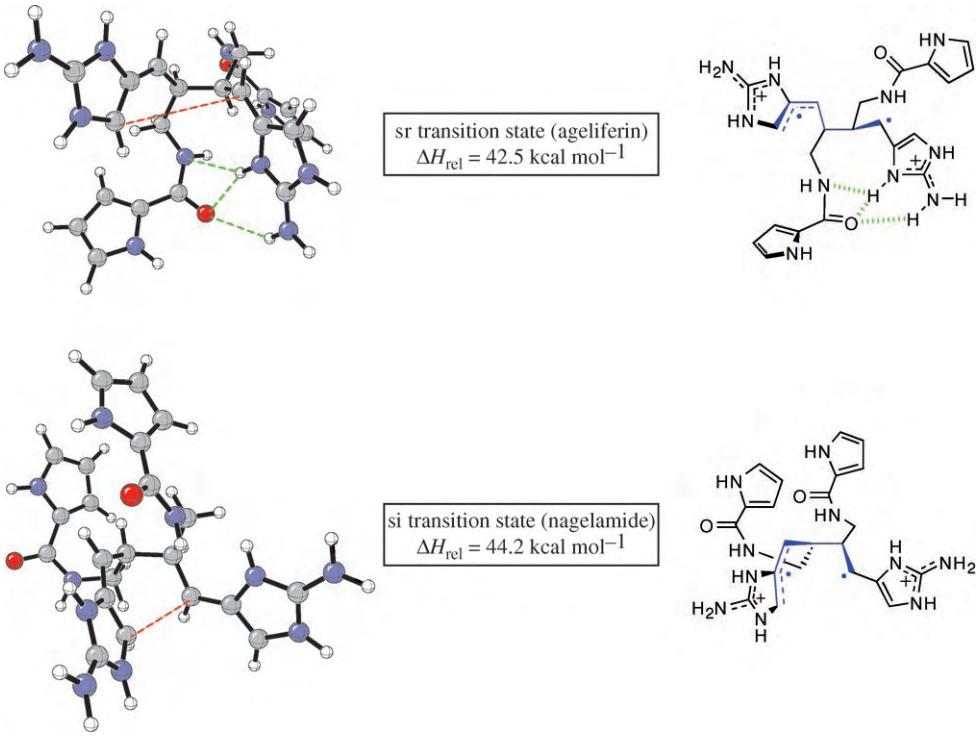


Figure 1. Optimized structures of the sr and si ring-closing transition states (model system B), which lead to $\mathbf{3}^{2+}$ and $\mathbf{2}^{2+}$, respectively. Dashed green lines indicate hydrogen-bonding interactions. Dashed red lines indicate the formation of covalent bonds. Bonds highlighted in blue (ChemDraw structures) indicate those that become the cyclohexene ring upon covalent bond formation.

Received: February 7, 2006
Published online: May 16, 2006

Keywords: alkaloids · biosynthesis · computational chemistry · natural products · rearrangement

[1] a) R. G. Bergman, *Acc. Chem. Res.* **1973**, *6*, 25–31; b) N. Darby, C. U. Kim, J. A. Salaun, K. W. Shelton, S. Takada, S. Masamune, *J. Chem. Soc. D* **1971**, *23*, 1516–1517; c) A. Basak, S. Mandal, S. S. Bag, *Chem. Rev.* **2003**, *103*, 4077–4094.

[2] a) K. Edo, M. Mizugaki, Y. Koide, H. Seto, K. Furihata, N. Otake, N. Ishida, *Tetrahedron Lett.* **1985**, *26*, 331–334; b) K. C. Nicolaou, A. L. Smith, *Acc. Chem. Res.* **1992**, *25*, 497–503.

[3] The 1,3- and 1,4-diradicals formed, for example, in vinylcyclopropane (K. N. Houk, M. Nendel, O. Wiest, J. W. Storer, *J. Am. Chem. Soc.* **1997**, *119*, 10545–10546) and vinylcyclobutane[12d] rearrangements are formed on flat potential-energy surfaces (Doering's "caldera": W. v. E. Doering, J. L. Eklmanis, K. D. Belfield, F. G. Klärner, B. Krawczyk, *J. Am. Chem. Soc.* **2001**, *123*, 5532–5541) and have lifetimes like those of transition states ($\approx 10^3$ fs; C. Doubleday, Jr., C. Suhrada, K. N. Houk, *J. Am. Chem. Soc.* **2006**, *128*, 90–94; E. W.-G. Diau, J. L. Herek, Z. H. Kim, A. H. Zewail, *Science* **1998**, *279*, 847–851) rather than intermediates. We refer to these structures as "*para* intermediates".

[4] P. S. Baran, D. P. O'Malley, A. L. Zografos, *Angew. Chem.* **2004**, *116*, 2728–2731; *Angew. Chem. Int. Ed.* **2004**, *43*, 2674–2677.

[5] a) P. A. Keifer, M. E. S. Koker, R. E. Schwartz, R. G. Hughes, Jr., D. Rittschof, K. L. Rinehart, *26th Interscience Conference on Antimicrobial Agents and Chemotherapy*, New Orleans, Sep. 28–Oct. 1, **1986**, No. 1281; b) K. L. Rinehart, *Pure Appl. Chem.* **1989**, *61*, 525–528; c) J. Kobayashi, M. Tsuda, T. Murayama, H. Nakamura, Y. Ohizumi, M. Ishibashi, M. Iwamura, T. Ohta, S. Nozoe, *Tetrahedron* **1990**, *46*, 5579–5586; d) P. A. Keifer, R. E. Schwartz, M. E. S. Koker, R. G. Hughes, D. Rittschof, K. L. Rinehart, *J. Org. Chem.* **1991**, *56*, 2965–2975; e) D. H. Williams, D. J. Faulkner, *Tetrahedron* **1996**, *52*, 5381–5390.

[6] a) R. P. Walker, D. J. Faulkner, D. Van Engen, J. Clardy, *J. Am. Chem. Soc.* **1981**, *103*, 6772–6773; b) P. S. Baran, A. L. Zografos, D. P. O'Malley, *J. Am. Chem. Soc.* **2004**, *126*, 3726–3727.

[7] For an extensive review of vinylcyclobutane arrangements, see: P. A. Leber, J. E. Baldwin, *Acc. Chem. Res.* **2002**, *35*, 279–287.

[8] a) H. Hoffmann, T. Lindel, *Synthesis* **2003**, 1753–1783; b) D. E. N. Jacquot, T. Lindel, *Current Org. Chem.* **2005**, *9*, 1551–1565.

[9] A. Al Mourabit, P. Potier, *Eur. J. Org. Chem.* **2001**, 237–243.

[10] T. Endo, M. Tsuda, T. Okada, S. Mitsuhashi, H. Shima, K. Kikuchi, Y. Mikami, J. Fremont, J. Kobayashi, *J. Nat. Prod.* **2004**, *67*, 1262–1267; we are grateful to Prof. Kobayashi for providing NMR spectra of compound **2**.

[11] a) J. E. Baldwin, R. C. Burrell, *J. Am. Chem. Soc.* **2001**, *123*, 6718–6719; b) J. E. Balwdin, R. C. Burrell, *J. Am. Chem. Soc.* **2003**, *125*, 15869–15877; c) W. v. E. Doering, E. A. Barsa, *J. Am. Chem. Soc.* **2004**, *126*, 12353–12362.

[12] a) B. R. Beno, S. Wilsey, K. N. Houk, *J. Am. Chem. Soc.* **1999**, *121*, 4816–4826; b) S. Wilsey, K. N. Houk, A. H. Zewail, *J. Am. Chem. Soc.* **1999**, *121*, 5772–5786; c) P. Caramella, P. Quadrelli, L. Toma, S. Romano, K. S. Khuong, B. Northrop, K. N. Houk, *J. Org. Chem.* **2005**, *70*, 2994–3008; d) B. H. Northrop, K. N. Houk, *J. Org. Chem.* **2005**, *70*, 3–13.

[13] In the original report of the sceptrin–ageliferin vinylcyclobutane rearrangement (Ref. [4]), three mechanisms were proposed: a "homolytic cleavage" mechanism involving diradicals, an "ionic" mechanism involving a charge-separated species, and a "tandem-shift" mechanism. Through computational investigations reported herein, minimum-energy reaction pathways for both the "homolytic cleavage" and "ionic" mechanism were shown to involve diradicals. The nomenclature of the three mechanisms has been modified herein to reflect this: the previous "homolytic cleavage" mechanism is referred to as "dicationic diradical" and the "ionic" mechanism is referred to as "monocationic diradical".

[14] Gaussian 03, Revision C.02, M. J. Frisch, et al.; see the Supporting Information.

[15] a) O. Wiest, D. C. Montiel, K. N. Houk, *J. Phys. Chem. A* **1997**, *101*, 8378–8388; b) C. P. Suhrada, K. N. Houk, *J. Am. Chem. Soc.* **2002**, *124*, 8796–8797; c) A. G. Leach, K. N. Houk, *J. Am. Chem. Soc.* **2002**, *124*, 14820–14821; d) A. G. Leach, E. Goldstein, K. N. Houk, *J. Am. Chem. Soc.* **2003**, *125*, 8330–8339.

[16] V. Barone, M. Cossi, *J. Phys. Chem. A* **1998**, *102*, 1995–2001.

[17] $<S^2>$ values for open-shell structures that originate from the dicationic $\mathbf{13}^{2+}$ and monocationic $\mathbf{14}^{+}$ model systems ranged from 0.45 to 1.03. Closed-shell, charge-separated intermediates

 © 2006 Wiley-VCH Verlag GmbH & Co. KGaA, Weinheim

located along the monocationic $\mathbf{1}^{1+}$ ionic pathway were found to be 7.4–10.5 kcal mol^{-1} less stable than the diradical structures.
[18] a) G. S. Hammond, C. D. DeBoer, *J. Am. Chem. Soc.* **1964**, *86*, 899 – 902; b) J. A. Berson, P. B. Dervan, *J. Am. Chem. Soc.* **1973**, *95*, 267 – 269; c) J. A. Berson, P. B. Dervan, R. Malherbe, J. A. Jenkins, *J. Am. Chem. Soc.* **1976**, *98*, 5937 – 5968.
[19] The experimentally determined radical stabilization energy of the allyl radical is 14.2 ± 1.2 kcal mol^{-1} at 298 K (J. A. Seetula, *Phys. Chem. Chem. Phys.* **1999**, *1*, 4727 – 4731); therefore, calculations predict RSE values of 10.2–11.7 kcal mol^{-1} for 2-aminoimidazole, protonated 2-aminoimidazole, and 2-H imidazole.
[20] C. Pöverlein, G. Breckle, T. Lindel, *Org. Lett.* **2006**, *8*, 819 – 821.

 © 2006 Wiley-VCH Verlag GmbH & Co. KGaA, Weinheim

Zwitterions

DOI: 10.1002/anie.200600597

Progressive Stabilization of Zwitterionic Structures in $[H(Ser)_{2-8}]^+$ Studied by Infrared Photodissociation Spectroscopy**

Xianglei Kong, I-An Tsai, Sahadevan Sabu, Chau-Chung Han, Yuan T. Lee, Huan-Cheng Chang, Shih-Yu Tu, A. H. Kung, and Chih-Che Wu*

Although amino acids are known to exist as zwitterions in aqueous solution and crystals, they should exist in their neutral form in the gas phase because zwitterionic charge separation is not energetically favored in the absence of a solvent.[1–3] However, it is also known that zwitterionic amino acids can be stabilized by noncovalent interactions with proximal molecules or ions.[4,5] For example, monomeric glycine is non-zwitterionic in the gas phase,[2,6] but clustering with five water molecules transforms glycine into its zwitterion.[7] Recently, the clusters of serine have attracted much attention from both experimentalists and theorists.[8–14] The protonated serine octamer, $[H(Ser)_8]^+$, first appeared as a "magic number" cluster in electrospray ionization (ESI) mass spectra and showed a pronounced preference for homochirality.[8,9] Several structures have been proposed for this cluster ion based on tandem mass spectrometry, ion mobility, and H/D exchange experiments.[8–12] Although most of the proposed structures contain all zwitterionic serine constituents, an H/D-exchange study indicated that isomers with both neutral and zwitterionic structures can form in the ESI source.[12b]

Infrared spectroscopy in combination with mass spectrometry and ab initio calculations has been proven to be an effective approach To deduce the structural information of gas-phase cluster ions.[15] McLafferty and co-workers demonstrated that it is possible to obtain infrared photodissociation spectra of protonated amino acid complexes with a pulsed infrared laser coupled to a Fourier-transform ion-cyclotron resonance (FTICR) mass spectrometer;[13] the spectra of $[H(Ser)_n]^+$ can be similarly obtained. Herein, we present infrared spectra of these cluster ions ($n = 2$–8) and address the questions of whether the serine dimer has a neutral structure and how the zwitterionic structure evolves as n increases. Results of ab initio calculations based on density functional theory (DFT) for the isomeric structures of $[H(Ser)_2]^+$ are also reported. By closely examining the infrared spectra of $[H(Ser)_{2-8}]^+$ in the frequency range 3400–3750 cm^{-1} for the free carboxy and hydroxymethyl OH stretches, a size effect on the structural transition from neutral to zwitterionic forms of serine subunits has been identified.

Figure 1a shows a typical FTICR mass spectrum of homochiral serine clusters produced by ESI. The spectrum is dominated by two peaks that correspond to $[H(Ser)_2]^+$ and $[H(Ser)_8]^+$.[16] The abundance of cluster ions of intermediate size ($n = 3$–7) is clearly too low to acquire their infrared photodissociation spectra. In a first attempt to overcome this difficulty, $[H(Ser)_8]^+$ was isolated in the ICR cell by radio-frequency (RF) sweeps and then fragmented by collision with pulsed argon gas (2×10^{-7} Torr) to produce smaller cluster ions of $n = 3$–6 (Figure 1b). The seemingly less stable heptamer was later produced by in-source collision-induced dissociation (CID) by increasing the ion-transmission energy in the region of the ESI source (Figure 1c). Mass selection was performed in the ICR cell to isolate the desired fragment ions for infrared spectroscopic measurements with an optical parametric oscillator (OPO) laser.

A typical infrared spectrum of $[H(Ser)_2]^+$ at room temperature is shown in Figure 2b. The spectrum was obtained by recording the dissociation fractions of all fragment ions versus total ions against laser frequency. The general feature of the spectrum (normalized with laser power) is in good agreement with the result of Oh et al., who used a similar setup but with a low-repetition-rate pulsed

[*] Dr. X. Kong, S. Sabu, Dr. C.-C. Han, Dr. Y. T. Lee, Dr. H.-C. Chang, S.-Y. Tu, Dr. A. H. Kung
Institute of Atomic and Molecular Sciences
Academia Sinica
Taipei 106 (Taiwan)
Fax: (+886) 2362-0200
E-mail: hcchang@po.iams.sinica.edu.tw
I.-A. Tsai, Dr. Y. T. Lee
Department of Chemistry
National Taiwan University
Taipei 106 (Taiwan)
Dr. C.-C. Han, Dr. Y. T. Lee, Dr. H.-C. Chang
Genomics Research Center
Academia Sinica
Nankang 115 (Taiwan)
Dr. A. H. Kung
Department of Photonics
National Chiao Tung University
Hsinchu 300 (Taiwan)
Dr. C.-C. Wu
Department of Applied Chemistry
National Chi Nan University
Puli, Nantou 545 (Taiwan)

[**] This study was supported by the Academia Sinica and the National Science Council (Grant No. NSC 92-3112-B-001-012-Y under the National Research Program for Genomic Medicine) of Taiwan, Republic of China. We thank Professors O. P. Charkin, H. B. Oh, and F. W. McLafferty for insightful discussions.

Supporting information for this article is available on the WWW under http://www.angewandte.org or from the author.

InterScience DISCOVER SOMETHING GREAT
© 2006 Wiley-VCH Verlag GmbH & Co. KGaA, Weinheim

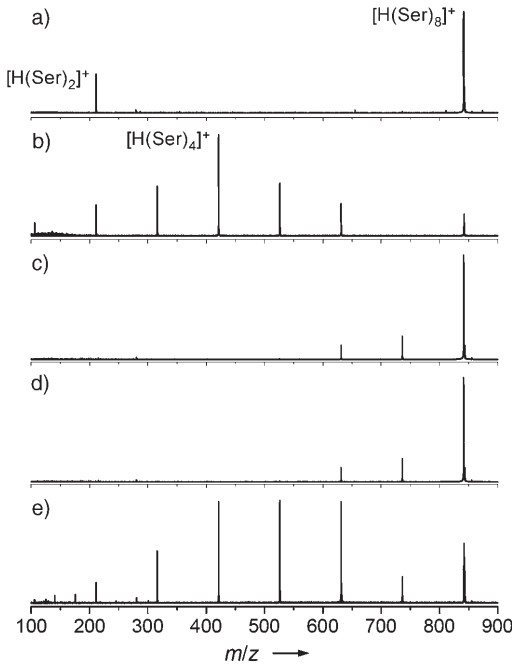


Figure 1. FTICR mass spectra of: a) protonated serine clusters produced directly from ESI; b) protonated serine cluster fragments after in-cell CID of isolated octamers; c) protonated serine clusters with in-source CID; d,e) protonated serine cluster fragments after infrared photodissociation of isolated octamers at 3672 cm^{-1} for 0.5 and 2.0 s, respectively.

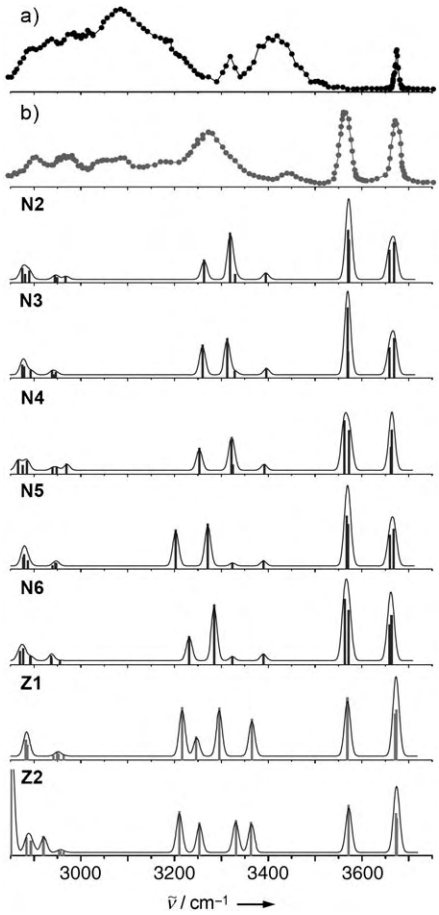


Figure 2. Comparison of experimental infrared spectra of a) $[H(Ser)_8]^+$ and b) $[H(Ser)_2]^+$ in the frequency range 2850–3750 cm^{-1}. The calculated $[H(Ser)_2]^+$ spectra shown underneath were obtained by the B3LYP/6-311++G(d,p) level of calculation and scaled with a single factor, ×0.954. The structures of isomers **N2**–**N6**, **Z1**, and **Z2** are depicted in Figure 3.

OPO laser.[13] The stronger absorption peaks at 3565 and 3672 cm^{-1} are ascribed to the stretching modes of free carboxy OH bonds on the C terminus and free hydroxymethyl OH bonds of the serine side chains, respectively. To assist the spectral interpretation, calculations performed at the B3LYP/6-31+G* level identified 86 stable isomers for this dimeric ion. Of these isomers, only seven are zwitterionic. The main reason that the number of stable neutral structures is far more than that of zwitterionic structures is because the COOH group can act as a proton acceptor, proton donor, or simultaneously as both, thus the probability of forming hydrogen bonds is high. The differences in total energy of these isomers are less than 20 kcal mol^{-1} (see the Supporting Information). Table 1 gives the energetics of the six lowest-energy neutral structures and the two lowest-energy zwitterionic structures, as depicted in Figure 3.[17] As can be seen, the neutral structures (**N1**–**N6**) are all significantly more stable than the zwitterionic structures (**Z1** and **Z2**) according to the MP2/6-311++G(d,p) and CCSD/6-31+G(d,p) levels of calculations. Although the structure of the serine dimer cannot be determined uniquely as a result of the complexity of the hydrogen-bonding network, a comparison of the experimental spectrum with the calculated spectra indicates that the $[H(Ser)_2]^+$ isomer with a neutral structure is most likely to be responsible for our observation (Figure 2b).

Table 1: Relative energies (in kcal mol^{-1}) of eight low-energy isomers obtained at three different levels of calculations.

Method[a]	N1[b]	N2	N3	N4	N5	N6	Z1	Z2
B3LYP/6-311++G(d,p)	0.00	0.66	1.22	1.19	1.16	1.50	1.91	3.18
	(0.00)[c]	(0.73)	(1.05)	(1.19)	(1.23)	(1.47)	(1.90)	(3.24)
	(0.00)[d]	(1.79)	(1.77)	(1.77)	(1.91)	(1.92)	(1.81)	(3.81)
MP2/6-311++G(d,p)	0.00	−4.07	−2.79	−2.93	−2.46	−1.95	2.06	3.27
	(0.00)[c]	(−4.00)	(−2.95)	(−2.93)	(−2.39)	(−1.98)	(2.06)	(3.33)
CCSD/6-31+G(d,p)	0.00	−3.87	−2.66	−2.47	−2.47	−1.72	2.63	3.96
	(0.00)[c]	(−3.80)	(−2.83)	(−2.47)	(−2.41)	(−1.76)	(2.63)	(4.02)

[a] All energy calculations were conducted based on the structures optimized by B3LYP/6-311++G(d,p). The calculated total electronic energies of **N1** with the B3LYP, MP2, and CCSD methods are −798.5996675, −796.538688, and −796.278142 hartree, respectively. [b] Structures of the isomers are depicted in Figure 3. [c] Values in this row include zero-point energy (ZPE) corrections based on the frequencies calculated by B3LYP/6-311++G(d,p). [d] Values in this row represent Gibbs free energies at 298 K.

For example, a comparison of the intensities of the absorption bands ascribable to the free OH stretching vibrations of the carboxy group and the hydroxymethyl group yields an experimentally observed ratio of 1.3 ± 0.1, which agrees favorably with that calculated for **N2**–**N6** (≈ 1.4), but is in

 © 2006 Wiley-VCH Verlag GmbH & Co. KGaA, Weinheim

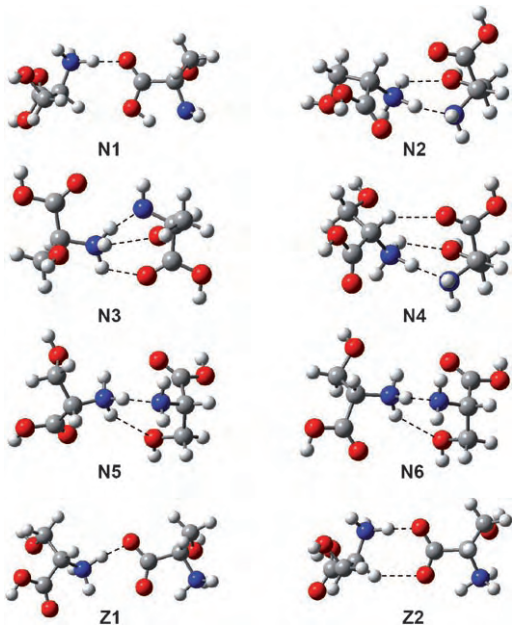


Figure 3. Lowest-energy isomers of $[H(Ser)_2]^+$ optimized by B3LYP/6-311++G(d,p), with six neutral (**N1**–**N6**) and two zwitterionic (**Z1**–**Z2**) structures. The red, blue, gray, and white spheres denote O, N, C, and H atoms, respectively. Note that the structures of **N2**–**N6** are all dominated by linear neutral and ionic N–H^+···N hydrogen bonds, instead of N–H^+···O, because the amino group has a much higher proton affinity than both the carboxy group on the C terminus and the hydroxy group on the serine side chain.

apparent disparity with that calculated for **Z1** and **Z2** (≈ 0.7). We assign the bands at approximately 2900 cm^{-1} to CH stretching vibrations and the bands at 3270 cm^{-1} predominantly to the stretching modes of NH_3^+ groups involved in intermolecular or intramolecular N–H···O hydrogen bonding.

Figure 2a shows the photodissociation spectrum of $[H(Ser)_8]^+$. Mass spectra of the corresponding photofragments are given in Figure 1d,e, in which evidence is given of the octamer degrading successively into smaller clusters upon exposure to resonating infrared photons. The sharp feature observed at 3674 cm^{-1}, again, corresponds to the free aliphatic OH stretching mode of serine. Its frequency matches that of the free OH stretch of CH_3OH in $[H(CH_3OH)_{4,5}]^+$ to within 3 cm^{-1}.[18a] Relative to that of $[H(Ser)_2]^+$, the bandwidth of this OH stretching absorption band is significantly smaller (8 versus 18 cm^{-1}), thus indicating that the aliphatic OH bonds in this octamer have more uniform environments. Distinct from the dimer case, however, no sign of the free carboxy OH stretching absorption was found in the spectrum within the limit of our experimental sensitivity. Additionally, a new and relatively sharp band (bandwidth ≈ 33 cm^{-1}) appears in the spectrum of $[H(Ser)_8]^+$ at 3324 cm^{-1}. The band can be ascribed to the free NH stretches of NH_3^+ groups in zwitterionic serines, as its frequency is close to the corresponding vibration in $[NH_4(H_2O)_3]^+$, 3375 cm^{-1}.[19] The observation of this distinct free NH stretching absorption band for the NH_3^+ ion cores, together with the disappearance of the free OH stretches of the COOH groups, corroborates the suggestion that the dominant structure of the $[H(Ser)_8]^+$ cluster probed in our experiment is zwitterionic.[20]

It is instructive to compare our infrared spectroscopic observations with previous measurements of ion mobility. For $[H(Ser)_8]^+$, Counterman and Clemmer[10] and Julian et al.[9b] independently determined the collisional cross section of this octamer to be 191 and 187 $Å^2$, respectively. By comparing these measured values with calculated cross sections for various neutral and zwitterionic structures, they concluded that only compact, cagelike structures stabilized by electrostatic interactions between the carboxyate groups and the ammonium groups of zwitterionic serines are consistent with their experimental findings. The present observation is in good agreement with their conclusion but additionally indicates that not all hydroxymethyl groups of the serine subunits are involved in hydrogen bonding, as manifested by the sharp band at 3674 cm^{-1} in Figure 2a.

Between the two extreme cases studied, $n=2$ and $n=8$, we found evidence for the progressive stabilization of the zwitterionic structure with increasing cluster size. Figure 4

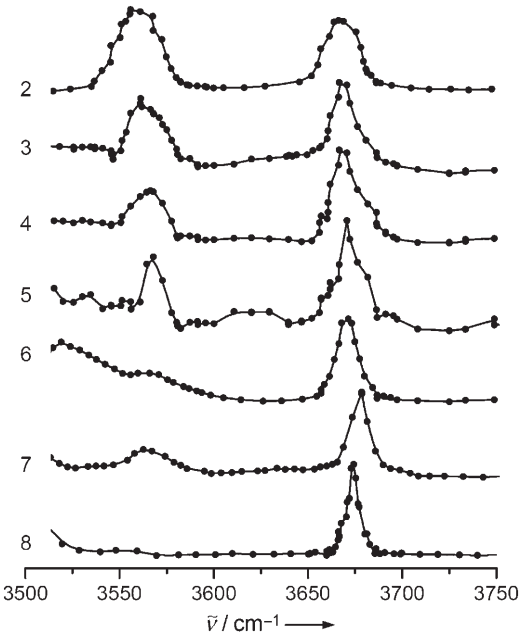


Figure 4. Infrared photodissociation spectra of sized-selected $[H(Ser)_n]^+$, $n=2$–8, in the free OH stretching region. Note the progressive decrease in intensity of the free carboxy OH stretching absorption band with increasing cluster size at ≈ 3565 cm^{-1}.

shows the size-dependent spectra of $[H(Ser)_{2-8}]^+$ in the free OH stretching region.[21] The band intensity ratio of the carboxy OH stretches versus the hydroxymethyl OH stretches decreases progressively from 1.3 to 0.2 as n increases from 2 to 6. The most notable changes occur between $n=5$ and $n=6$. Similar to that of $[H(Ser)_8]^+$, the spectrum of $[H(Ser)_6]^+$ shows only a very weak band that corresponds to free carboxy OH stretches at approximately 3565 cm^{-1}, which reflects that the structure of $[H(Ser)_6]^+$ is also compact and predominantly zwitterionic. In contrast, the intensity ratio of these two absorption bands in the spectra of $[H(Ser)_{3-5}]^+$ and $[H(Ser)_7]^+$ varies substantially from 0.4 to 1.2, which strongly suggests that the structures of these clusters are mixtures of neutral and zwitterionic forms.

 © 2006 Wiley-VCH Verlag GmbH & Co. KGaA, Weinheim

To conclude, we have provided infrared spectroscopic evidence for progressive stabilization of the zwitterionic structures in homochiral $[H(Ser)_{2-8}]^+$ clusters. Our results are in line with those reported by Beauchamp and co-workers,[9b] who pointed out this intriguing effect based on DFT calculations. However, to provide further insight into this size-dependent structural transition, which is also expected to be found in other amino acid clusters, more calculations and experiments are required.

Experimental Section

Mass spectra of protonated serine clusters were acquired by using an FTICR mass spectrometer (APEX IV, Bruker-Daltonics) equipped with a 7.0 tesla actively shielded superconducting magnet and an external ESI source. Protonated homochiral serine clusters were produced by spraying a sample solution (1 mM L-serine in 30% methanol solution containing 1% formic acid) through an electrically grounded, gas-assisted nebulization system. The ESI-generated ions, after passing through the differentially pumped regions, were accumulated in a hexapole ion trap for ≈ 1 s and finally pulsed into the ICR cell. Inside the cell, the ions of interest were isolated by RF clean-up sweeps and thermalized with pulsed argon gas at a pressure of $\approx 2 \times 10^{-7}$ Torr.

Infrared photodissociation spectra of $[H(Ser)_{2-8}]^+$ were obtained by excitation of the OH, NH, and CH stretching vibrations in the frequency range of 2800–3800 cm^{-1} by using a home-built pulsed OPO laser.[22] The singly resonant OPO was constructed with a periodically poled lithium niobate (PPLN) crystal in a grazing-incidence grating optical cavity. The PPLN crystal was pumped by an acousto-optic Q-switched Nd:YAG laser (210S, Lightwave Electronics) at a repetition rate of 4 kHz. As the storage time of ions in the ICR cell is in the order of seconds, a high-repetition-rate light source provided a better duty cycle in signal acquisition than a low-repetition-rate laser of 10–30 Hz.[23] By resonating the signal wavelength, the idler output wavelength of the OPO laser was tunable from 2.5 to 3.5 μm with a bandwidth of ≈ 1 cm^{-1}. The output wavelength was measured with an optical spectrum analyzer (86142 A, Hewlett Packard) and calibrated against atmospheric water absorption with an uncertainty of ± 1 cm^{-1}. The typical laser output power was 100 mW.

Ab initio calculations were carried out extensively for $[H(Ser)_2]^+$. Because of the complexity of the system, even for monomeric serine itself,[24,25] a complete search for all possible potential minima was impractical. Nonetheless, a wide range of hydrogen-bonding network structures, including those of neutral and zwitterionic forms, were designed based on our previous studies of protonated ammonia,[19] methanol,[18] and formamide[26] clusters and optimized with the semi-empirical method, AM1. Ten salt-bridge conformations and 100 ion-molecule conformations were then selected and optimized by the DFT calculation at the B3LYP/6-31+G* level. A split valence double-ζ basis set and extra polarization and diffuse functions (6-311++G**) were further used for geometry optimization and frequency calculation for eight lowest-energy isomers predicted by B3LYP/6-31+G*. The final energies were refined by single-point calculations with MP2/6-311++G(d,p) and CCSD/6-31+G(d,p) methods. All calculations were performed by using the Gaussian 03 program.[27]

Received: February 15, 2006
Published online: May 23, 2006

Keywords: cluster compounds · density functional calculations · IR spectroscopy · mass spectrometry · zwitterions

[1] a) J. H. Jensen, M. S. Gordon, *J. Am. Chem. Soc.* **1991**, *113*, 7917–7924; b) J. H. Jensen, M. S. Gordon, *J. Am. Chem. Soc.* **1995**, *117*, 8159–8170.
[2] Y. Ding, K. Krogh-Jespersen, *Chem. Phys. Lett.* **1992**, *199*, 261–266.
[3] C. J. Chapo, J. B. Paul, R. A. Provencal, K. Roth, R. J. Saykally, *J. Am. Chem. Soc.* **1998**, *120*, 12956–12957.
[4] T. Wyttenbach, M. Witt, M. T. Bowers, *J. Am. Chem. Soc.* **2000**, *122*, 3458–3464.
[5] R. R. Julian, J. L. Beauchamp, W. A. Goddard III, *J. Phys. Chem. A* **2002**, *106*, 32–34.
[6] a) M. J. Locke, R. L. Hunter, R. T. McIver, *J. Am. Chem. Soc.* **1979**, *101*, 272–273; b) M. J. Locke, R. T. McIver, *J. Am. Chem. Soc.* **1983**, *105*, 4226–4232.
[7] S. J. Xu, M. Nilles, K. H. Bowen, *J. Chem. Phys.* **2003**, *119*, 10696–10701.
[8] a) R. G. Cooks, D. Zhang, K. J Koch, F. C. Gozzo, M. N. Eberlin, *Anal. Chem.* **2001**, *73*, 3646–3655; b) Z. Takats, S. C. Nanita, R. G. Cooks, G. Schlosser, K. Vekey, *Anal. Chem.* **2003**, *75*, 1514–1523; c) Z. Takats, S. C. Nanita, R. G. Cooks, *Angew. Chem.* **2003**, *115*, 3645–3647; *Angew. Chem. Int. Ed.* **2003**, *42*, 3521–3523; d) S. C. Nanita, R. G. Cooks, *J. Phys. Chem. B* **2005**, *109*, 4748–4753; e) S. C. Nanita, R. G. Cooks, *Angew. Chem.* **2006**, *118*, 568–583; *Angew. Chem. Int. Ed.* **2006**, *45*, 554–569.
[9] a) R. Hodyss, R. R. Julian, J. L. Beauchamp, *Chirality* **2001**, *13*, 703–706; b) R. R. Julian, R. Hodyss, B. Kinnear, M. F. Jarrold, J. L. Beauchamp, *J. Phys. Chem. B* **2002**, *106*, 1219–1228.
[10] A. E. Counterman, D. E. Clemmer, *J. Phys. Chem. B* **2001**, *105*, 8092–8096.
[11] C. A. Schalley, P. Weis, *Int. J. Mass Spectrom.* **2002**, *221*, 9–19.
[12] a) P. Ustyuzhanin, J. Ustywhanin, C. Lifshitz, *Int. J. Mass Spectrom.* **2003**, *223*, 491–498; b) U. Mazurek, O. Geller, C. Lifshitz, M. A. McFarland, A. G. Marshall, B. G. Reuben, *J. Phys. Chem. A* **2005**, *109*, 2107–2112.
[13] H. B. Oh, C. Lin, H. Y. Hwang, H. Zhai, K. Breuker, V. Zabrouskov, B. Y. Carpenter, F. W. McLafferty, *J. Am. Chem. Soc.* **2005**, *127*, 4076–4083.
[14] F. Pollreisz, A. Gomory, G. Schlosser, K. Vekey, I. Solt, A. G. Csaszar, *Chem. Eur. J.* **2005**, *11*, 5908–5916.
[15] H.-C. Chang, C.-C. Wu, J.-L. Kuo, *Int. Rev. Phys. Chem.* **2005**, *24*, 553–578.
[16] The identities of these cluster ions were confirmed based on isotope separations in a high-resolution mass spectrum (see the Supporting Information).
[17] The most-stable structures suggested in ref. [14] have energies of 1–4 kcal mol^{-1} higher than **N1**–**N6** and **Z1** and **Z2**. It is therefore very unlikely that they are the global-minimum structures of $[H(Ser)_2]^+$.
[18] a) H.-C. Chang, J. C. Jiang, S. H. Lin, Y. T. Lee, H.-C. Chang, *J. Phys. Chem. A* **1999**, *103*, 2941–2944; b) C.-C. Wu, J. C. Jiang, D. W. Boo, S. H. Lin, Y. T. Lee, H.-C. Chang, *J. Chem. Phys.* **2000**, *112*, 176–188.
[19] Y.-S. Wang, H.-C. Chang, J. C. Jiang, S. H. Lin, Y. T. Lee, H.-C. Chang, *J. Am. Chem. Soc.* **1998**, *120*, 8777–8788.
[20] It is possible that the disappearance of the transition for the free carboxy OH stretch can be caused by a red shift of the band because of intramolecular or intermolecular hydrogen bonding. However, experiments of H/D exchange reactions between CH_3OD and $[H(Ser)_8]^+$ with and without ion isolation in our ICR mass spectrometer showed only one type of isomer (see the Supporting Information). A comparison of our experimental conditions and results with those of Mazurek et al.[12b] does not lend support to the presence of neutral structures.
[21] As previously found for other protonated molecular clusters,[15,18,19,26] the absorption bands of hydrogen-bonded OH

 © 2006 Wiley-VCH Verlag GmbH & Co. KGaA, Weinheim

and NH stretches are broad and congested and thus provide little structural information.
[22] C. S. Yu, A. H. Kung, *J. Opt. Soc. Am. B* **1999**, *16*, 2233 – 2238.
[23] X. Qian, T. Zhang, C. Y. Ng, A. H. Kung, M. Ahmed, *Rev. Sci. Instrum.* **2003**, *74*, 2784 – 2790.
[24] S. Gronert, R. A. J. O'Hair, *J. Am. Chem. Soc.* **1995**, *117*, 2071 – 2081.
[25] R. Miao, C. Jin, G. Yang, J. Hong, C. Zhao, L. Zhu, *J. Phys. Chem. A* **2005**, *109*, 2340 – 2349.
[26] a) C.-C. Wu, J. C. Jiang, I. Hahndorf, C. Chaudhuri, Y. T. Lee, H.-C. Chang, *J. Phys. Chem. A* **2000**, *104*, 9556 – 9565; b) C. Chaudhuri, J. C. Jiang, C.-C. Wu, X. Wang, H.-C. Chang, *J. Phys. Chem. A* **2001**, *105*, 8906 – 8915.
[27] M. J. Frisch, G. W. Trucks, H. B. Schlegel, G. E. Scuseria, M. A. Robb, J. R. Cheeseman, J. A. Montgomery, Jr., T. Vreven, K. N. Kudin, J. C. Burant, J. M. Millam, S. S. Iyengar, J. Tomasi, V. Barone, B. Mennucci, M. Cossi, G. Scalmani, N. Rega, G. A. Petersson, H. Nakatsuji, M. Hada, M. Ehara, K. Toyota, R. Fukuda, J. Hasegawa, M. Ishida, T. Nakajima, Y. Honda, O. Kitao, H. Nakai, M. Klene, X. Li, J. E. Knox, H. P. Hratchian, J. B. Cross, C. Adamo, J. Jaramillo, R. Gomperts, R. E. Stratmann, O. Yazyev, A. J. Austin, R. Cammi, C. Pomelli, J. W. Ochterski, P. Y. Ayala, K. Morokuma, G. A. Voth, P. Salvador, J. J. Dannenberg, V. G. Zakrzewski, S. Dapprich, A. D. Daniels, M. C. Strain, O. Farkas, D. K. Malick, A. D. Rabuck, K. Raghavachari, J. B. Foresman, J. V. Ortiz, Q. Cui, A. G. Baboul, S. Clifford, J. Cioslowski, B. B. Stefanov, G. Liu, A. Liashenko, P. Piskorz, I. Komaromi, R. L. Martin, D. J. Fox, T. Keith, M. A. Al-Laham, C. Y. Peng, A. Nanayakkara, M. Challacombe, P. M. W. Gill, B. Johnson, W. Chen, M. W. Wong, C. Gonzalez, J. A. Pople, Gaussian 03, Revision B.01, Gaussian, Inc., **2004**.

 © 2006 Wiley-VCH Verlag GmbH & Co. KGaA, Weinheim

Magnetic Clusters

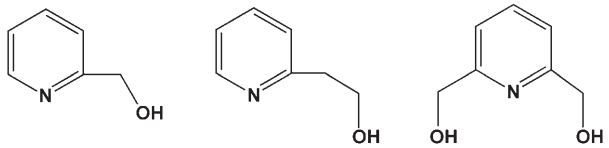
DOI: 10.1002/anie.200600691

High-Nuclearity, High-Symmetry, High-Spin Molecules: A Mixed-Valence Mn_{10} Cage Possessing Rare *T* symmetry and an $S = 22$ Ground State**

*Theocharis C. Stamatatos, Khalil A. Abboud, Wolfgang Wernsdorfer, and George Christou**

Polynuclear transition-metal clusters in intermediate oxidation states continue to attract great attention, mainly because of their fascinating physical properties and the aesthetic beauty and complexity of their structures. An interesting subarea of this chemistry is the small but growing family of molecules that, in their ground states, have unusually large numbers of unpaired electrons. Several molecular cluster compounds with abnormally high spin (*S*) values have been prepared, with the highest values to date being $S = 51/2$ for a $[Mn^{II}_6Mn^{III}_{18}Mn^{IV}]$ complex[1] and a cyano-bridged $[Mn^{II}_9Mo^{V}_6]$ system.[2] The study of such molecules has shown that the large *S* value results from either ferromagnetic (or ferrimagnetic) exchange interactions between the metal centers and/or spin-frustration effects from the presence in certain M_x topologies of competing antiferromagnetic exchange interactions that prevent (frustrate) the preferred spin alignments that would normally yield low-spin species.[3] In addition, it has recently become apparent that a fairly large ground-state *S* value is one of the necessary (but not sufficient) requirements for molecules to be able to exhibit the phenomenon of single-molecule magnetism.[4] The synthesis of new high-spin molecules is thus of great interest and importance. However, it is difficult to predict what type of topology and structure will lead to a high-spin cluster and even more difficult to then achieve the synthesis of such a species.[5]

In the majority of polynuclear clusters, magnetic exchange interactions are propagated mainly by bridging OH^-, OR^-, O^{2-}, or RCO_2^- groups (or a combination of these), ligands which usually lead to antiferromagnetic coupling. One approach to increasing the ground state *S* value is replacement of some or all of the above ligands with groups that give ferromagnetic coupling. One of the best of the latter is the azide (N_3^-) group when it bridges metal ions in the 1,1 (end-on) fashion, in which case the exchange coupling is ferromagnetic for a wide range of M-N-M angles.[6] We also have a long-standing interest in the use of pyridine-based alkoxide ligands (Scheme 1) in Mn cluster chemistry, and have found that the anion of 2-(hydroxymethyl)pyridine (hmp^-) is a versatile N,O-chelating and -bridging ligand whose alkoxide arm often supports ferromagnetic coupling between the metal atoms it bridges.[7,8]



Scheme 1. Pyridyl alcohol ligands (from left to the right) 2-(hydroxymethyl)pyridine (hmpH), 2-(2-hydroxyethyl)pyridine (hepH), and 2,6-pyridinedimethanol ($pdmH_2$).

We now report that use of both N_3^- and hmp^- groups in certain reactions with Mn salts leads to the two remarkable decanuclear, mixed-valence complexes $[Mn^{II}_4Mn^{III}_6O_4(N_3)_4(hmp)_{12}](X)_2$ [$X = N_3^-$ (**1**), ClO_4^- (**2**)]. The Mn_{10} cation in each of these complexes possesses an aesthetically pleasing structure of high (*T*) symmetry, is completely ferromagnetically coupled, and has a resulting $S = 22$ ground state, one of the highest values yet reported. In addition, this cation is the first example in which μ_3-1,1,1-azido ligands bridge *exclu-*

[*] T. C. Stamatatos, Dr. K. A. Abboud, Prof. Dr. G. Christou
Department of Chemistry
University of Florida
Gainesville, FL 32611-7200 (USA)
Fax: (+1) 352-392-8757
E-mail: christou@chem.ufl.edu
Dr. W. Wernsdorfer
Laboratoire Louis Néel-CNRS, BP-166
Grenoble, Cedex 9 (France)

[**] This work was supported by the U.S. National Science Foundation (Grant CHE-0414155).

InterScience
© 2006 Wiley-VCH Verlag GmbH & Co. KGaA, Weinheim

sively Mn^{3+} ions, and thus presages a potentially rich new area of Mn^{III} clusters with high spin values.

The reaction of $Mn(NO_3)_2{\cdot}H_2O$, hmpH, Et_3N, and NaN_3 in a 1:1:1:1 ratio in MeCN/MeOH gave a dark brown solution from which crystals of $[Mn_{10}O_4(N_3)_4(hmp)_{12}](N_3)_2$ (**1**) were subsequently isolated in 20% yield. Use of $Mn(ClO_4)_2{\cdot}6H_2O$ gave the isostructural complex $[Mn_{10}O_4(N_3)_4(hmp)_{12}](ClO_4)_2{\cdot}$MeCN (**2**·MeCN) in a much higher yield of 75%. The same reaction in which only MeOH was used gave the known complex $[Mn^{II}_2Mn^{III}_2(N_3)_2(hmp)_6]_n(ClO_4)_{2n}$ (**3**), which is a one-dimensional chain.[8]

The structure of the cation $[Mn_{10}O_4(N_3)_4(hmp)_{12}]^{2+}$ (Figure 1)[9] consists of ten Mn ions with a tetra-face-capped

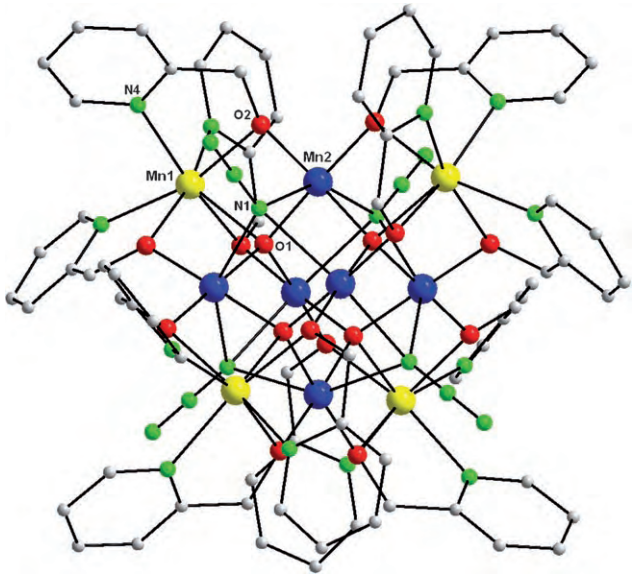


Figure 1. Partially labelled PovRay representation of the cation of **1** (Mn^{II} yellow, Mn^{III} blue, O red, N green, C gray). H atoms have been omitted for clarity.

octahedral topology. The central octahedron comprises six Mn^{3+} ions, and the eight faces of this octahedron are bridged by four μ_3-N_3^- ions and four μ_4-O^{2-} ions (Figure 2), with the latter also bridging to four external Mn^{2+} ions that thus cap four non-adjacent faces of the octahedron. The μ_3-N_3^- ions bind in an $\eta^1{:}\eta^1{:}\eta^1$ (end-on) fashion. The Mn^{II}/Mn^{III} oxidation states were established by consideration of bond lengths, bond-valence-sum (BVS) calculations,[10] and the presence of the Jahn–Teller distortions expected for octahedral Mn^{III} centers. All Mn^{3+} ions (Mn2 and its symmetry-related counterparts) are six-coordinate with near-octahedral geometry and thus display a Jahn–Teller distortion, which is observed in the form of an axial elongation of the two *trans* Mn–N_{azide} bonds (2.412(3) Å). The four Mn^{2+} ions (Mn1 and its symmetry-related counterparts) are seven-coordinate with distorted face-capped octahedral geometry in which the capping atom is the oxide atom O1 ($d(Mn^{2+}$–$O^{2-})$: 2.304(4) Å). The peripheral ligation about the $[Mn_{10}(\mu_4\text{-}O)_4(\mu_3\text{-}N_3)_4]^{14+}$ core is provided by the twelve hmp^- groups; three hmp^- groups bind terminally through their N atoms to each of the exterior Mn^{2+} ions, and their alkoxide arms bridge

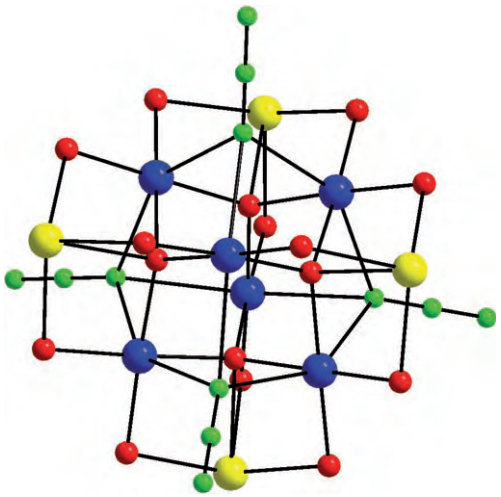


Figure 2. The core of complex **1** (Mn^{II} yellow, Mn^{III} blue, O red, N green, C gray). The hmp^- ligands, except for their O atoms, have been omitted.

each Mn^{2+} ion (Mn1) to Mn^{3+} ions (Mn2). There are only weak intermolecular interactions, which involve the hmp pyridyl rings.

Complexes **1** and **2** join only a handful of previously described mixed-valence Mn_{10} clusters[11] and are the first of the $[Mn^{II}_4Mn^{III}_6]$ type. The $[Mn_{10}(\mu_4\text{-}O)_4(\mu_3\text{-}N_3)_4]^{14+}$ core has T_d symmetry, but inclusion of the hmp groups removes the σ_d planes and S_4 axes of symmetry, and the complete $[Mn^{II}_4Mn^{III}_6O_4(N_3)_4(hmp)_{12}]^{2+}$ cation consequently has the rare T point-group symmetry, which is crystallographically imposed; the point group T is the rotational subgroup of T_d.

Solid-state direct current (dc) magnetic susceptibility (χ_M) data for complex **2**·MeCN were collected in the temperature range 5.0–300 K in an applied field of 1 kG (0.1 T).[12] The $\chi_M T$ value steadily increases from 53.78 $cm^3\,mol^{-1}\,K$ at 300 K to a maximum of 231.56 $cm^3\,mol^{-1}\,K$ at 10 K, before dropping to 220.23 $cm^3\,mol^{-1}\,K$ at 5.0 K (Figure 3). The spin-only ($g=2$) value for a non-interacting $[Mn^{II}_4Mn^{III}_6]$ unit is 35.5 $cm^3\,mol^{-1}\,K$. This value indicates ferromagnetic exchange interactions within **2**, and the value at 10 K strongly suggests a very large ground-state spin value; the sharp decrease at the lowest temperatures is assigned to Zeeman

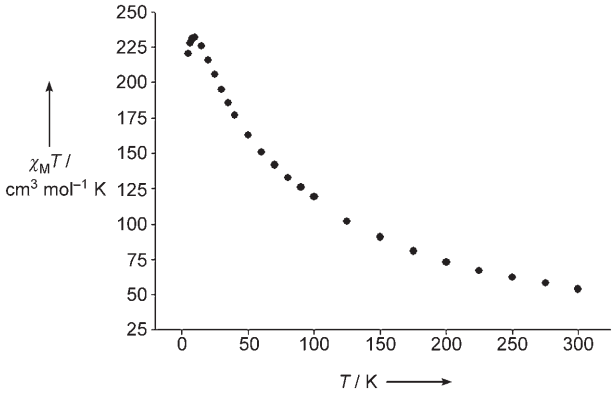


Figure 3. $\chi_M T$ versus T plot for complex **2**·MeCN in a 1-kG field.

© 2006 Wiley-VCH Verlag GmbH & Co. KGaA, Weinheim

effects, zero-field splitting (ZFS), and/or weak intermolecular interactions. The value at 10 K is consistent with an $S = 22$ ground state, the maximum possible value for this cluster, and a g factor slightly less than 2.0, as expected for a Mn^{II}/Mn^{III} complex; the spin-only ($g = 2$) value for a state with $S = 22$ is 253 $cm^3 mol^{-1} K$.

In order to confirm the ground state of **2**·MeCN, magnetization (M) data were collected in the ranges 0.1–5 T and 1.8–10.0 K, and these are plotted as $M/N\mu_B$ versus H/T in Figure 4.

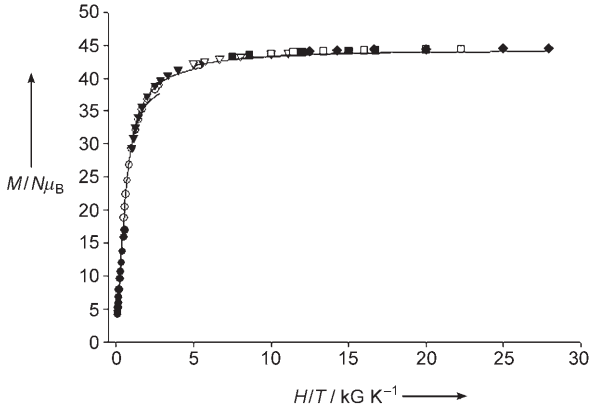


Figure 4. Plot of reduced magnetization ($M/N\mu_B$) versus H/T for **2**·MeCN in the temperature range 1.8–10 K and in fields of 0.1 T (●), 0.5 T (○), 1.0 T (▼), 2.0 T (▽), 3.0 T (■), 4.0 T (□), 5.0 T (◆). Solid lines are the fit; see the text for the fitting parameters.

The various isofield lines are virtually superimposed, thus indicating essentially no zero-field splitting within the ground state, and the saturation value of $M/N\mu_B \approx 44$ is consistent with a spin value of $S = 22$. The data were fit by matrix diagonalization to a model that assumes only the ground state is populated, includes axial zero-field splitting ($D\hat{S}_z^2$) and the Zeeman interaction, and carries out a full powder average. The best fit (solid lines in Figure 4) gave $S = 22$, $g = 2.00 \pm 0.0013$, and $D = -0.0112 \pm 0.0003\ cm^{-1}$, thus confirming a very high-spin ground state with little or no magnetic anisotropy. The latter attribute was anticipated from the high (cubic) symmetry of the molecule because, although Mn^{3+} ions have significant single-ion anisotropy, the molecular anisotropy is the tensoral sum of the single-ion values, and this sum should be essentially zero given the cubic symmetry and the resulting orientations of the six Mn^{III} Jahn–Teller axes.[3,13] This supposition is borne out by the experimental observation of $D \approx 0$ for **1** and **2**.

The presence of the $S = 22$ ground state was further supported by alternating current (ac) susceptibility experiments, in which a weak field of 3.5 G that was oscillating at a particular frequency was applied to the sample. Alternating current susceptibility studies use no dc field and thus are an excellent complementary tool for determining S by avoiding potential complications from a large dc field. The in-phase susceptibility (χ_M') for **2**·MeCN is shown as $\chi_M'T$ versus T in Figure 5, and $\chi_M'T$ is temperature-independent at about 244 $cm^3 mol^{-1} K$ from 15 K down to about 8 K. This temperature-independent value is consistent with a spin value of $S = 22$ and a g factor of about 1.96, thus in satisfying agreement

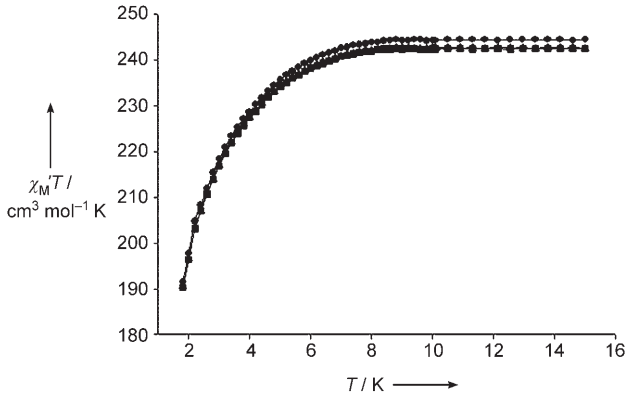


Figure 5. In-phase ac susceptibility ($\chi_M'T$) measurements of complex **2**·MeCN measured below 15.0 K at 50 Hz (▲), 250 Hz (■), and 1000 Hz (●).

with the dc magnetization fits. The temperature-independent $\chi_M'T$ value also indicates no population of excited states in this temperature range. At lower temperatures, $\chi_M'T$ decreases slightly, and we assign this effect to weak intermolecular interactions, both dipolar and superexchange in nature.

There is no out-of-phase (χ_M'') ac susceptibility signal down to 1.8 K, which indicates an insignificant barrier (vs. kT, where k is the Boltzmann constant) to magnetization relaxation. To explore whether slow relaxation might become apparent at even lower temperatures, magnetization versus dc field scans were performed on a single crystal of **2**·MeCN down to 0.04 K, with the field applied in turn along three perpendicular axes of the crystal. All of the measurements gave essentially superimposable scans, as shown for one field direction in Figure 6. There is also clearly no hysteresis observed. The combined results indicate an isotropic crystal and fast magnetization relaxation even at 0.04 K, thus consistent with $D \approx 0$.

In summary, the combination of azide and hmp^- ligands in Mn cluster chemistry has yielded an unusual cation that has both a very high ($S = 22$) ground-state spin value and high (T)

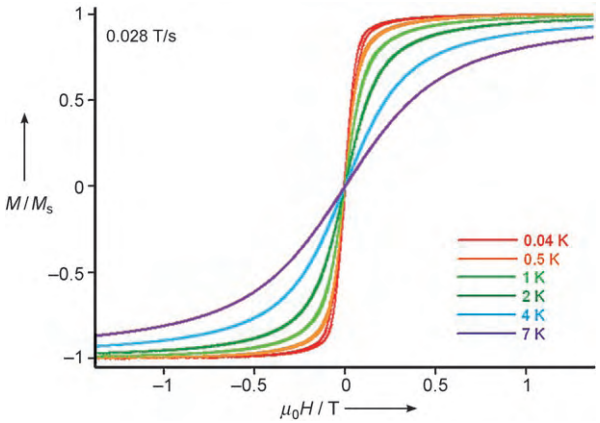


Figure 6. Plot of magnetization versus applied dc field scans for a single crystal of complex **2**·MeCN at the indicated field sweep rate and temperatures. The magnetization is normalized to its saturation value.

 © 2006 Wiley-VCH Verlag GmbH & Co. KGaA, Weinheim

symmetry. Such a high S value is extremely rare; in fact, it is the second-highest in Mn chemistry to date and very similar in magnitude to the value $S = 23$ for an Fe_{14} cluster, which is the largest spin value in Fe chemistry.[14] The value $S = 22$ for **1** and **2** is the maximum for a $[Mn^{II}_4Mn^{III}_6]$ species, thus indicating that all interactions are ferromagnetic. This attribute is consistent with the presence of end-on-bridging N_3^- groups on the $\{Mn^{III}_3\}$ faces of the central octahedron, as well as with the bridging of each $Mn^{II}Mn^{III}$ pair by two separate O atoms with rather acute Mn-O-Mn angles (ca. 101–105°), as both of these bridging modes are known to yield ferromagnetic interactions.[6,7,15] Also rare is the high, aesthetically pleasing symmetry of this cation, which continues to emphasize the versatility of Mn chemistry.

Experimental Section

1: Solid NaN_3 (0.13 g, 2.0 mmol) was added to a stirred, pale yellow solution of hmpH (0.19 mL, 2.0 mmol) and Et_3N (0.28 mL, 2.0 mmol) in MeCN/MeOH (20 mL, 20:1 v/v). To this solution was added solid $Mn(NO_3)_2{\cdot}H_2O$ (0.36 g, 2.0 mmol), which caused a rapid color change to dark brown. The resulting dark brown solution was stirred for a further 2 h and filtered, and the filtrate was left undisturbed at ambient temperature. After 3 days, X-ray quality dark brown hexagonal crystals appeared and were collected by filtration, washed with MeCN (2 × 5 mL), and dried in vacuo. The yield was 20%. Elemental analysis (%) calcd for $C_{72}H_{72}Mn_{10}N_{30}O_{16}$: C 39.98, H 3.36, N 19.43; found: C 39.77, H 3.32, N 19.54.

2·MeCN: This complex was prepared in the same manner as complex **1**, except that $Mn(ClO_4)_2{\cdot}6H_2O$ (0.50 g, 2.0 mmol) was used in place of $Mn(NO_3)_2{\cdot}H_2O$. Dark brown hexagonal crystals of the product were isolated, collected by filtration, washed with MeCN (2 × 5 mL), and dried in vacuo. The yield was 75%. Elemental analysis (%) calcd for $C_{74}H_{75}Mn_{10}N_{25}O_{24}Cl_2$: C 38.33, H 3.26, N 15.10; found: C 38.31, H 3.10, N 14.98; selected IR data (KBr): $\tilde{\nu} = 3334$ (m), 3068 (m), 2902 (w), 2784 (m), 2048 (vs), 1602 (s), 1567 (m), 1482 (m), 1434 (s), 1367 (m), 1210 (m), 1291 (m), 1248 (w), 1223 (w), 1153 (m), 1082 (vs), 1048 (m), 1010 (m), 817 (m), 758 (s), 729 (m), 671 (vs), 622 (vs), 549 (m), 467 cm^{-1} (m).

Safety note: Perchlorate and azide salts are potentially explosive; such compounds should be synthesized and used in small quantities, and should be treated with utmost care at all times.

Received: February 21, 2006
Revised: March 23, 2006
Published online: May 16, 2006

Keywords: azides · cluster compounds · magnetic properties · manganese · N,O ligands

[1] M. Murugesu, M. Habrych, W. Wernsdorfer, K. A. Abboud, G. Christou, *J. Am. Chem. Soc.* **2004**, *126*, 4766–4767.

[2] J. Larionova, M. Gross, M. Pilkington, H. Andres, H. Stoeckli-Evans, H. U. Güdel, S. Decurtins, *Angew. Chem.* **2000**, *112*, 1579–1683; *Angew. Chem. Int. Ed.* **2000**, *39*, 1605–1609.

[3] G. Aromi, M. J. Knapp, J.-P. Claude, J. C. Huffman, D. N. Hendrickson, G. Christou, *J. Am. Chem. Soc.* **1999**, *121*, 5489–5499.

[4] a) R. Sessoli, D. Gatteschi, D. N. Hendrickson, G. Christou, *MRS Bull.* **2000**, *25*, 66–71; b) W. Wernsdorfer, N. Aliaga-Alcade, D. N. Hendrickson, G. Christou, *Nature* **2002**, *416*, 406–409; c) S. Hill, R. S. Edwards, N. Aliaga-Alcade, G. Christou, *Science* **2003**, *302*, 1015–1018; d) R. Sessoli, D. Gatteschi, A. Caneschi, M. A. Novak, *Nature* **1993**, *365*, 141–143.

[5] a) G. S. Papaefstathiou, A. Escuer, R. Vicente, M. Font-Bardia, X. Solans, S. P. Perlepes, *Chem. Commun.* **2001**, 2414–2415; b) G. S. Papaefstathiou, S. P. Perlepes, A. Escuer, R. Vicente, M. Font-Bardia, X. Solans, *Angew. Chem.* **2001**, *113*, 908–910; *Angew. Chem. Int. Ed.* **2001**, *40*, 884–886.

[6] E. Ruiz, J. Cano, S. Alvarez, P. Alemany, *J. Am. Chem. Soc.* **1998**, *120*, 11122–11129.

[7] a) J. Yoo, A. Yamaguchi, M. Nakano, J. Krzystek, W. E. Streib, L.-C. Brunel, H. Ishimoto, G. Christou, D. N. Hendrickson, *Inorg. Chem.* **2001**, *40*, 4604–4616; b) E. C. Yang, D. N. Hendrickson, W. Wernsdorfer, M. Nakano, L. N. Zakharov, R. D. Sommer, A. L. Rheingold, M. Ledezma-Gairaud, G. Christou, *J. Appl. Phys.* **2002**, *91*, 7382–7384; c) N. C. Harden, M. A. Bolcar, W. Wernsdorfer, K. A. Abboud, W. E. Streib, G. Christou, *Inorg. Chem.* **2003**, *42*, 7067–7076; d) C. A. Christmas, H.-L. Tsai, L. Pardi, J. M. Kesselman, P. K. Gantzel, R. K. Chadha, D. Gatteschi, D. F. Harvey, D. N. Hendrickson, *J. Am. Chem. Soc.* **1993**, *115*, 12483–12490.

[8] L. Lecren, O. Roubeau, C. Coulon, Y.-G. Li, X. F. L. Goff, W. Wernsdorfer, H. Miyasaka, R. Clerac, *J. Am. Chem. Soc.* **2005**, *127*, 17353–17363.

[9] a) Crystal-structure data for **1**: $C_{72}H_{72}Mn_{10}N_{30}O_{16}$, $M_r = 2163.00$, cubic, space group $P4_3/n$, $a = 16.3101(3)$ Å, $V = 4338.80(14)$ Å^3, $Z = 2$, $\rho_{calcd} = 1.656$ g cm^{-3}, $T = 173(2)$ K, 25543 reflections collected, 1670 unique ($R_{int} = 0.1262$), $R1 = 0.0266$ and $wR2 = 0.0577$, based on 1670 reflections with $I > 2\sigma(I)$. The asymmetric unit consists of half of the Mn_{10} cluster and one-eighth of a combination of N_3^- and MeCN disordered in the same position. The disorder of the counter ion and MeCN molecule is the only possibility of balancing the crystal charges whereby the ratio of cluster to counter ion is 3:1, thus necessitating two-thirds occupancy of the N_3^- anion with one-third of MeCN. Crystal-structure data for **2**·MeCN: $C_{74}H_{75}Cl_2Mn_{10}N_{25}O_{24}$, $M_r = 2283.44$, cubic, space group $P4_3/n$, $a = 16.5474(5)$ Å, $V = 4531.0(2)$ Å^3, $Z = 2$, $\rho_{calcd} = 1.674$ g cm^{-3}, $T = 173(2)$ K, 27284 reflections collected, 1755 unique ($R_{int} = 0.0582$), $R1 = 0.0351$ and $wR2 = 0.0840$, based on 1755 reflections with $I > 2\sigma(I)$; b) CCDC-298873 and CCDC-298874 contain the supplementary crystallographic data for this paper. These data can be obtained free of charge from The Cambridge Crystallographic Data Centre via www.ccdc.cam.ac.uk/data_request/cif.

[10] a) Bond-valence-sum (BVS) calculations for the Mn ions of **1** gave values of 1.98 (for Mn1) and 2.97 (for Mn2); b) W. Liu, H. H. Thorp, *Inorg. Chem.* **1993**, *32*, 4102–4105; c) I. D. Brown, D. Altermatt, *Acta Crystallogr. Sect. B* **1985**, *41*, 244–247.

[11] a) C. Cavaluzzo, Q. Chen, J. Zubieta, *J. Chem. Soc. Chem. Commun.* **1993**, 131–132; b) D. P. Goldberg, A. Caneschi, C. D. Delfs, R. Sessoli, S. J. Lippard, *J. Am. Chem. Soc.* **1995**, *117*, 5789–5800.

[12] The magnetic behavior of the two complexes is similar. As a result of the high yield of complex **2** (compared to that of **1**), magnetic data are presented only for the former cluster.

[13] a) H.-L. Tsai, S. Wang, K. Folting, W. E. Streib, D. N. Hendrickson, G. Christou, *J. Am. Chem. Soc.* **1995**, *117*, 301–317; b) P. King, W. Wernsdorfer, K. A. Abboud, G. Christou, *Inorg. Chem.* **2005**, *44*, 8659–8669.

[14] D. M. Low, L. F. Jones, A. Bell, E. K. Brechin, T. Mallah, E. Riviere, S. J. Teat, E. J. L. McInnes, *Angew. Chem.* **2003**, *115*, 3911–3914; *Angew. Chem. Int. Ed.* **2003**, *42*, 3781–3784.

[15] D. Foguet-Albiol, T. A. O'Brien, W. Wernsdorfer, B. Moulton, M. J. Zaworotko, K. A. Abboud, G. Christou, *Angew. Chem.* **2005**, *117*, 919–923; *Angew. Chem. Int. Ed.* **2005**, *44*, 897–901.

 © 2006 Wiley-VCH Verlag GmbH & Co. KGaA, Weinheim

Iridium Complexes

DOI: 10.1002/anie.200600004

Accelerated Discovery of Red-Phosphorescent Emitters through Combinatorial Organometallic Synthesis and Screening**

*Nai-Mu Hsu and Wen-Ren Li**

Dedicated to Professor Madeleine M. Joullié

The combinatorial approach of synthesis and screening has become the focus of intense interest as a tool for drug discovery in the pharmaceutical industry.[1] Promising developments in medicinal chemistry subsequently pointed the way for material chemists to use this approach to discover diverse catalysts and materials such as liquid crystals[2] and luminescent emitters,[3] among others.[4] Most of these materials are organic compounds. The combinatorial synthesis of organometallic materials is not a common trend yet. Bernhard and co-workers applied the basics of the combinatorial approach to solution synthesis for the discovery of transition-metal-based luminophores.[5] Elsewhere, Binnemans and co-workers coupled luminescent lanthanide(III) complexes on a Merrifield resin through a functionalized ligand.[6] However, a complete combinatorial synthetic sequence and high-throughput screening are yet to be developed to discover organometallic compounds with desired properties.[7]

In the last decade, material chemists have become interested in developing organometallic complexes based on Ir,[8] Os,[9] Ru,[10] and Pt[11] for their applications in organic light-emitting diodes (OLEDs). OLEDs hold great potential for application in flat-panel displays owing to their excellent properties, such as self-luminescence, flexibility, fast response, good contrast, and low energy consumption. Light-emitting materials doped in OLEDs offer an improvement in efficiency and the possibility to tune the color. Fluorescent[12] and phosphorescent emitters with high luminescence efficiencies have been extensively used for this purpose. However, studies have proved that devices based on phosphorescent materials are more efficient than those based on fluorescent materials. For example, bis(2-(2′-benzothienyl)pyridinato-$N,C^{3'}$)-iridium(acetylacetonate) ([$(btp)_2$Ir(acac)]) was used as the dopant for red-light emission and an external quantum efficiency of 6.5% and power efficiency of 2.2 lm W^{-1} at 1 mA cm^{-2} were reported.[8]

Notwithstanding the success in increasing the external quantum efficiency, research on OLEDs is still focused on the improvement of the emission efficiency and the color purity by developing high-efficiency phosphorescent materials on the device architectures. As ligands can affect both the quantum yield and the emission wavelength of iridium complexes significantly, these complexes appear to be excellent candidates to use as electrophosphorescence emitters in OLEDs. Consequently, the development of new organic ligands for iridium complexes is highly desirable in order to maximize the external quantum efficiency and the color purity of devices. On the basis of several studies to improve efficiencies, aminoquinazolines were selected as cyclometalating ligands because of their polarity and potential stability.[8–11] Herein, we report a series of efficient red-phosphorescent emitters discovered by using combinatorial organometallic solid-phase synthesis and screening methodology.

For OLED applications, compounds that emit in a specific color range are desirable. While rational design of compounds with specific emission wavelengths and high quantum yields is difficult, combinatorial solid-phase synthesis appears to be a powerful tool in developing libraries of iridium complexes. The key to discover excellent emitters on solid supports lies in the screening methodology. A crucial feature of the screening methodology is to obtain information about basic photophysical characteristics, namely the wavelength (λ_{em}) and quantum yield (Φ_{PL}) of emission. However, to achieve this aim, the spacer used to link emitters to resins should have no interference in the photophysical characteristics. Hence, the choice of spacer becomes crucial. The use of a conjugated spacer system will affect wavelengths and quantum yields. Saturated alkyl or alkoxy spacers have the advantage of being stable under the reaction sequences. These spacers are non-conjugated systems that allow common solid-phase resins to be used, such as polystyrene-type polymers, in the synthesis of the emitter, an operation that is otherwise impossible owing to the conjugated or aromatic nature of the resins.

Along with the above-mentioned properties, the spacers should mimic aromatic substitution on the heterocyclic system. The selected spacers Ar^m ($m = 1$–3) mimic alkyl phenyl, alkoxy phenyl, and thiophene substitutions, respectively (Figure 1). This strategy of mimicking aromatic substitution in spacers enabled us to process rapid screening. It was found that resin-bound lead compounds **1**(Ar^mR^n) reveal wavelengths and quantum yields of emission that are very close to those of cleaved products **2**(Ar^mR^n) and the respective emitters without a spacer, namely **3**(R^n), **4**(R^n), and **5**(R^n) (Figure 1). These spacers also imparted enough flexibility to accommodate the synthesis of a unique bis-cyclometalated Ir^{III} μ-chloro-bridged dimer **6** (Scheme 1) linked through its four ligands to one resin through spacers. To the best of our knowledge, this kind of assembly has not been reported before.

The parallel solid-phase syntheses (Scheme 1) of resin-bound leads **1**(Ar^mR^n) and the cleaved products **2**(Ar^mR^n) were carried out using Wang resin (1% divinylbenzene (DVB) cross-linked; loading: 1.0 mmol g^{-1}). Wang resin was

[*] N.-M. Hsu, Prof. Dr. W.-R. Li
Department of Chemistry and
Center for Nano Science and Technology
National Central University
Chung-Li, Taiwan 32054 (Taiwan)
Fax: (+886) 3-427-7972
E-mail: ch01@ncu.edu.tw

[**] The authors are grateful to the National Science Council, ROC, for financial support of this work (grant NSC 93-2113-M-008-009). We are also thankful to Chitec Technology Co., Ltd. for supplying electroluminescent device testing data.

Supporting information for this article is available on the WWW under http://www.angewandte.org or from the author.

InterScience
© 2006 Wiley-VCH Verlag GmbH & Co. KGaA, Weinheim

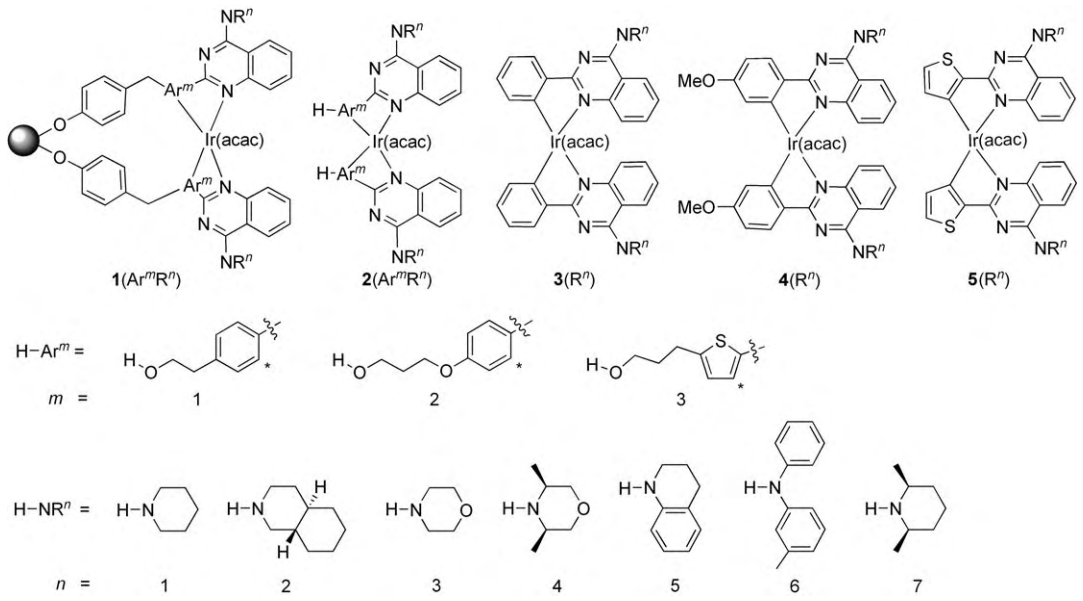
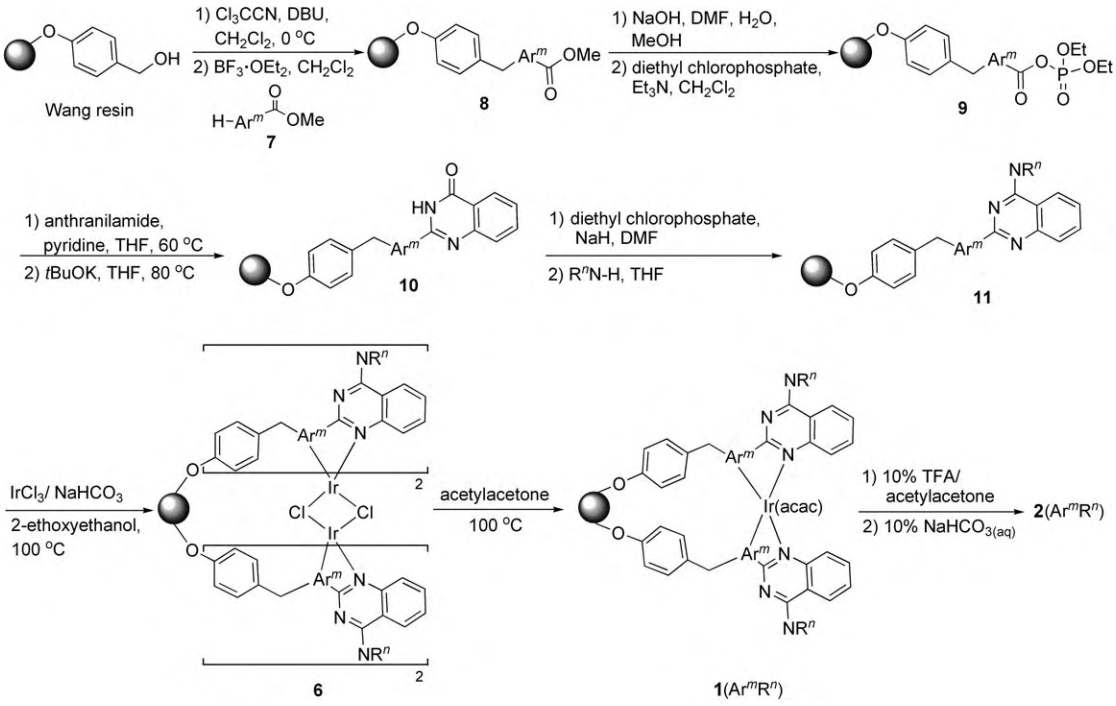


Figure 1. General structures of leads **1**(Ar^mR^n), cleaved products **2**(Ar^mR^n), and emitters **3**(R^n)–**5**(R^n). The aryl group binds to Ir through the positions marked with an asterisk in Ar^m. acac = acetylacetonate



Scheme 1. Solid-phase synthesis of leads **1**(Ar^mR^n) and cleaved products **2**(Ar^mR^n). DBU = 1,8-diazabicyclo[5.4.0]undec-7-ene; DMF = *N*,*N*-dimethylformamide; TFA = trifluoroacetic acid.

activated as its trichloroacetimidate and linked with the derivatives **7** through their hydroxy groups to obtain the resin-bound esters **8**.[13] Hydrolysis of esters **8** was carried out using sodium hydroxide in the presence of DMF, MeOH, and water, and the resulting acids were derivatized as mixed anhydrides **9**.[14] Anthranilamide was coupled with anhydrides **9** to give N-acylated products, which were cyclized under basic conditions to afford the resin-bound quinazolin-4-one derivatives **10**. Of the various bases tested,[15] *t*BuOK was found to be the best and was employed in the synthesis of the library. Resins **10** were treated with sodium hydride followed by diethyl chlorophosphate, and the resulting *o*-phosphorylated products were reacted with R^nNH to give the resin-bound quinazolines **11**.[16] During the synthetic sequences, at several stages, a small portion of the compounds was taken out and either monitored by magic-angle spinning gel-phase NMR spectroscopy or cleaved to check whether the reaction had gone to completion. Whenever necessary, the previous steps

 © 2006 Wiley-VCH Verlag GmbH & Co. KGaA, Weinheim

were repeated. The purity (>50%) of compounds **11** was crucial for the success of the following organometallic reactions. The resins **11** were treated with iridium trichloride hydrate in the presence of $NaHCO_3$ and 2-ethoxyethanol to give the dimers **6**.[8,17] The formation of the chloro-bridged dimer **6** linked through its four ligands through spacers to form a polymer-bound complex within the same resin was proved by analysis of the polarized optical microscope picture. Ir^{III} μ-chloro-bridged dimers **6** were sensitive to pH at high temperature. The pH value was maintained around 7 by adding $NaHCO_3$ to avoid decomposition of the dimers. Further treatment of the resins with acetylacetone afforded the desired iridium complexes **1**.[18]

The polymer-bound lead complexes **1** are stable in air, and no decomposition was noted over the period of 3 months at room temperature. When 10, 20, and 40% trifluoroacetic acid (TFA) in CH_2Cl_2 or 2-ethoxyethanol was employed to cleave resin **1**, decomposition of the iridium complexes was observed. However, 10% TFA in acetylacetone followed by treatment with aqueous $NaHCO_3$ (10%) was found to be adequate to cleave the resin completely while keeping the iridium complex intact to afford products **2**. The compounds **2** were purified by normal-phase HPLC and obtained in 30–45% yields from the Wang resin, which corresponds to about 90% yield per transformation in this 12-step solid-phase procedure. This range of yields is enough to measure photophysical properties because only a very low concentration of the complexes in the polymer is required for luminescence to be studied. Moreover, problems with concentration quenching would probably arise when the concentration of the complex on the polymer is too high.

The combinatorial technique does not carry full merits if the rapid synthesis is not accompanied with the facile and speedy method of screening synthesized libraries for the desired properties. Combinatorial screening using a microplate reader was developed to search for highly luminescent materials from the synthesized library of the resin-bound compounds **1**, **6**, **10**, and **11**. Screening of a few representative resin-bound leads is displayed in Figure 2, and their emission maxima are summarized in Tables 1 and 2. The resin-bound leads of significant interest were cleaved to afford compounds **2**, and the corresponding emitters **3**–**5** were prepared by using a similar protocol to that described in Scheme 1. These three groups, namely resin-bound leads **1**, cleaved products **2**, and emitters **3**–**5**, were compared for their photophysical properties (Table 2). Table 1, which lists the wavelengths of resin-bound organic compounds 1A–3F, indicates that the screening method (Figure 2) used here should be suitable to identify fluorescent organic emitters. Also during the reaction sequence the purity of chloro-bridged dimer **6** (4A–6C) and the completion of previous reaction step was assured by the disappearance of the emission between 400 and 500 nm. Analysis of the quantitative photophysical properties data (Table 2, 6D–8F) showed that the deviations in emission maxima of leads **1**, cleaved products **2**, and the corresponding emitters **3**–**5** are within a very narrow range of 11 nm. In addition, the quantum yields[19] of the products **2** and those of emitters **3**–**5** differ from each other by only 0.08. When wavelengths are close, the brightness of resin-bound leads **1** are proportionally correlated with quantum yields of the cleaved products **2** and the respective emitters **3**–**5**. This result can be seen from Figure 2 and Table 2 by comparing leads **1** [7B: **1**(Ar^1R^5); 8B: **1**(Ar^2R^5); 8C: **1**(Ar^2R^6); 8F: **1**(Ar^3R^7)], cleaved products **2** [**2**(Ar^1R^5); **2**(Ar^2R^5); **2**(Ar^2R^6); **2**(Ar^3R^7)], and the respective emitters **3**–**5** [**3**(R^5); **4**(R^5); **4**(R^6); **5**(R^7)]. Moreover, spectral characteristics (Figure 3) observed for the above-mentioned three groups of compounds (**1**, **2**, and **3**–**5**) further validated the screening protocol. The full width at half maximum (FWHM) and shapes of the emission spectra are very similar in each case for the compounds on beads, the respective cleaved products, and corresponding emitters. Thus, naked-eye observation of the brightness coupled with

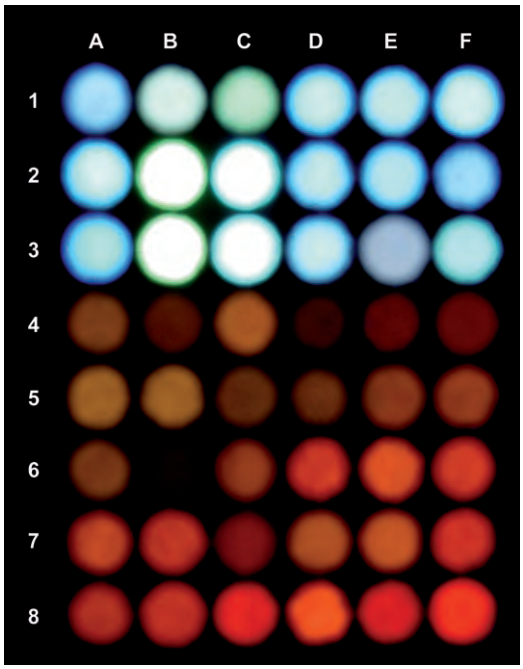


Figure 2. Screening of a library of representative resin-bound leads (see Tables 1 and 2).

Table 1: Emission maxima of resin-bound compounds **6**, **10**, and **11**.

Resin[a]	Compound	λ_{em} [nm]	Resin[a]	Compound	λ_{em} [nm]
1A	**10**(Ar^1)	514	3F	**11**(Ar^3R^7)	488
1B	**10**(Ar^2)	522	4A	**6**(Ar^1R^1)	585
1C	**10**(Ar^3)	541	4B	**6**(Ar^1R^2)	600
1D	**11**(Ar^1R^1)	470	4C	**6**(Ar^1R^3)	604
1E	**11**(Ar^1R^2)	440	4D	**6**(Ar^1R^4)	599
1F	**11**(Ar^1R^3)	456	4E	**6**(Ar^1R^5)	605
2A	**11**(Ar^1R^4)	472	4F	**6**(Ar^1R^6)	619
2B	**11**(Ar^1R^5)	507	5A	**6**(Ar^2R^1)	578
2C	**11**(Ar^1R^6)	528	5B	**6**(Ar^2R^2)	580
2D	**11**(Ar^2R^1)	528	5C	**6**(Ar^2R^3)	573
2E	**11**(Ar^2R^2)	436	5D	**6**(Ar^2R^4)	590
2F	**11**(Ar^2R^3)	400	5E	**6**(Ar^2R^5)	604
3A	**11**(Ar^2R^4)	435	5F	**6**(Ar^2R^6)	615
3B	**11**(Ar^2R^5)	515	6A	**6**(Ar^3R^3)	614
3C	**11**(Ar^2R^6)	485	6B	**6**(Ar^3R^6)	644
3D	**11**(Ar^3R^3)	421	6C	**6**(Ar^3R^7)	613
3E	**11**(Ar^3R^6)	476			

[a] Refers to Figure 2.

 © 2006 Wiley-VCH Verlag GmbH & Co. KGaA, Weinheim

Table 2: A comparison of the photophysical properties of resin-bound leads **1**(Ar^mR^n), cleaved products **2**(Ar^mR^n), and emitters **3**(R^n)–**5**(R^n).

Resin[a]	Leads **1**	λ_{em} [nm]	Products **2**	λ_{em} [nm]	Φ_{PL}	Emitters	λ_{em} [nm]	Φ_{PL}
6D	**1**(Ar^1R^1)	598	**2**(Ar^1R^1)	594	0.52	**3**(R^1)	598	0.54
6E	**1**(Ar^1R^2)	594	**2**(Ar^1R^2)	592	0.48	**3**(R^2)	595	0.49
6F	**1**(Ar^1R^3)	590	**2**(Ar^1R^3)	590	0.47	**3**(R^3)	595	0.46
7A	**1**(Ar^1R^4)	601	**2**(Ar^1R^4)	598	0.36	**3**(R^4)	600	0.35
7B	**1**(Ar^1R^5)	625	**2**(Ar^1R^5)	624	0.28	**3**(R^5)	628	0.24
7C	**1**(Ar^1R^6)	632	**2**(Ar^1R^6)	637	0.27	**3**(R^6)	643	0.31
7D	**1**(Ar^2R^1)	588	**2**(Ar^2R^1)	588	0.37	**4**(R^1)	588	0.41
7E	**1**(Ar^2R^2)	590	**2**(Ar^2R^2)	585	0.37	**4**(R^2)	586	0.41
7F	**1**(Ar^2R^3)	592	**2**(Ar^2R^3)	592	0.51	**4**(R^3)	592	0.49
8A	**1**(Ar^2R^4)	591	**2**(Ar^2R^4)	587	0.37	**4**(R^4)	590	0.45
8B	**1**(Ar^2R^5)	619	**2**(Ar^2R^5)	624	0.35	**4**(R^5)	627	0.31
8C	**1**(Ar^2R^6)	630	**2**(Ar^2R^6)	634	0.58	**4**(R^6)	633	0.62
8D	**1**(Ar^3R^3)	616	**2**(Ar^3R^3)	613	0.46	**5**(R^3)	612	0.50
8E	**1**(Ar^3R^6)	655	**2**(Ar^3R^6)	652	0.24	**5**(R^6)	653	0.24
8F	**1**(Ar^3R^7)	635	**2**(Ar^3R^7)	636	0.69	**5**(R^7)	636	0.67

[a] Refers to Figure 2.

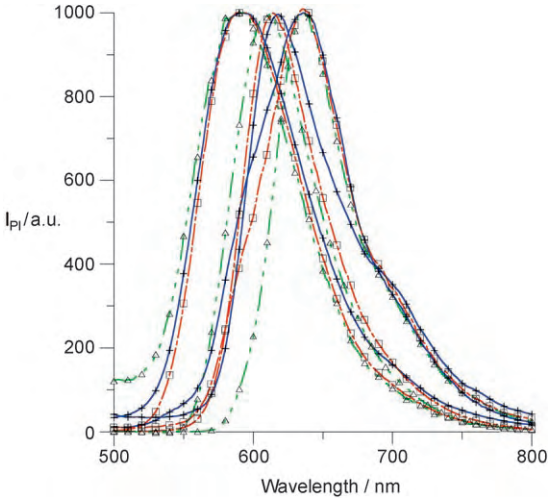


Figure 3. A comparison of the photoluminescence (PL) spectra of resin-bound leads **1**, cleaved products **2**, and emitters **4**–**5**. Emission maxima are provided in parentheses (λ_{em} [nm]): Blue line (+): **1**(Ar^2R^3) (592); **1**(Ar^3R^3) (616); **1**(Ar^3R^7) (635). Red line (□): **2**(Ar^2R^3) (592); **2**(Ar^3R^3) (613); **2**-(Ar^3R^7) (636). Green line (△): **4**(R^3) (592): **5**(R^3) (612): **5**(R^7) (636). λ_{ex} = 370 nm.

the determination of emission maxima on beads before cleavage can lead to the identification of potentially bright light-emitting hits. By using this combinatorial screening technique, two optimum red emitters **4**(R^6) and **5**(R^7) were identified.

To evaluate the electroluminescent properties of the identified hits, several electroluminescent (EL) devices were fabricated using these iridium complexes as dopant emitters. The electroluminescent characteristics of **4**(R^6) and **5**(R^7) are summarized in Table 3. In devices **A**–**F**, **4**(R^6) and **5**(R^7) were doped into a light-emitting layer at a concentration of 8% to afford the optimum external quantum efficiency. Device **B** shows excellent electroluminescent characteristics for OLEDs deposited with a 50-nm-thick layer of Alq. A maximum external quantum efficiency of 15.2% and a power efficiency of 10.0 lm W^{-1} were obtained at 4.5 V. The device also emitted strong red light at 630 nm with a maximum brightness of 54919 cd m^{-2} at 18.0 V. Device **F** was prepared using **5**(R^7) as the dopant emitter in the CBP layer and using a 60-nm-thick layer of deposited Alq. The device revealed an emission maximum at 630 nm, external quantum efficiency of 20.3%, current efficiency of 16.6 cd A^{-1}, and power efficiency of 12.2 lm W^{-1} at 4.25 V. The corresponding CIE (Commission Internationale de l'Eclairage) coordinates are $x = 0.649$, $y = 0.349$ for **4**(R^6) in device **B**, and $x = 0.666$, $y = 0.332$ for **5**(R^7) in device **F**, which coincide with the National Television Standards Committee (NTSC) red specification.

In conclusion, we have demonstrated that a rapid combinatorial synthesis and screening methodology can be successfully applied to discover luminescent materials. This efficient synthetic protocol has been applied to prepare a library of new red-phosphorescent Ir complexes through assembly of a novel resin-bound bis-cyclometalated Ir^{III} μ-chloro-bridged dimer. The spacers used adequately mimicked alkyl or alkoxy substitutions on aromatic heterocyclic ligand systems and imparted enough flexibility. The photophysical

Table 3: Electrophosphorescence data for iridium complexes **4**(R^6) and **5**(R^7).[a]

Device	Device structure	*V* [V]	η_{ext} [%]	η_c [cd A^{-1}]	η_p [lm W^{-1}]	CIE (*x*, *y*)
A	ITO/α-NPB (60 nm)/**4**(R^6):CBP (8%, 30 nm)/ BCP (30 nm)/Alq (40 nm)/LiF (0.5 nm)/Al	4.75	13.8	13.6	9.0	0.647, 0.351
B	ITO/α-NPB (60 nm)/**4**(R^6):CBP (8%, 30 nm)/ BCP (30 nm)/Alq (50 nm)/LiF (0.5 nm)/Al	4.5	15.2	14.9	10.0	0.649, 0.349
C	ITO/α-NPB (60 nm)/**4**(R^6):CBP (8%, 30 nm)/ BCP (30 nm)/Alq (60 nm)/LiF (0.5 nm)/Al	5.0	15.4	13.8	8.7	0.651, 0.347
D	ITO/α-NPB (60 nm)/**5**(R^7):CBP (8%, 30 nm)/ BCP (30 nm)/Alq (40 nm)/LiF (0.5 nm)/Al	4.25	18.9	17.8	13.2	0.661, 0.337
E	ITO/α-NPB (60 nm)/**5**(R^7):CBP (8%, 30 nm)/ BCP (30 nm)/Alq (50 nm)/LiF (0.5 nm)/Al	4.0	19.6	17.1	13.4	0.665, 0.334
F	ITO/α-NPB (60 nm)/**5**(R^7):CBP (8%, 30 nm)/ BCP (30 nm)/Alq (60 nm)/LiF (0.5 nm)/Al	4.25	20.3	16.6	12.2	0.666, 0.332

[a] ITO: indium tin oxide; α-NPB: *N*,*N*′-di(naphthalen-1-yl)-*N*,*N*′-diphenylbenzidine; CBP: 4,4′-*N*,*N*′-dicarbazolebiphenyl; BCP: 2,9-dimethyl-7-diphenyl-1,10-phenanthroline; Alq: tris(8-hydroxy-quinolinato)aluminum. The data for external quantum efficiency (η_{ext}), current efficiency (η_c), and power efficiency (η_p) are the maximum values of the device.

© 2006 Wiley-VCH Verlag GmbH & Co. KGaA, Weinheim

properties that were measured for this library of emitters were astonishingly accurate considering that the resins were analyzed directly. The strong coherence among the data from resin-bound leads, cleaved products, and corresponding emitters confirm that luminescent properties of pure emitter complexes can be predicted directly by screening resins. Our screening data analysis also resulted in the identification of two hits with high quantum yields. The EL devices based on these complexes emitted saturated red electroluminescence with high quantum efficiency and power efficiency and satisfied NTSC red specifications. The present solid-phase synthetic methodology and screening technique are not only useful for accelerating the discovery of luminescent complexes but also may find broad applications in the field of organometallics and combinatorial chemistry.

Received: January 1, 2006
Revised: March 11, 2006
Published online: May 30, 2006

Keywords: combinatorial chemistry · iridium · luminescence · materials science · solid-phase synthesis

[1] a) R. E. Dolle, C. MacLeod, B. Martinez-Teipel, W. Barker, P. R. Seida, T. Herbertz, *Angew. Chem.* **2005**, *117*, 5980; *Angew. Chem. Int. Ed.* **2005**, *44*, 5830; b) R. E. Dolle, *J. Comb. Chem.* **2005**, *7*, 739.

[2] T. Haino, M. Tanaka, K. Ideta, K. Kubo, A. Mori, Y. Fukazawa, *Tetrahedron Lett.* **2004**, *45*, 2277.

[3] a) M.-S. Schiedel, C. A. Briehn, P. Bauerle, *Angew. Chem.* **2001**, *113*, 4813; *Angew. Chem. Int. Ed.* **2001**, *40*, 4677; b) C. A. Briehn, P. Bauerle, *Chem. Commun.* **2002**, 1015; c) G. R. Rosania, J. W. Lee, L. Ding, H.-S. Yoon, Y.-T. Chang, *J. Am. Chem. Soc.* **2003**, *125*, 1130.

[4] a) X.-D. Xiang, X. Sun, G. Briceno, Y. Lou, K.-A. Wang, H. Chang, W. G. Wallace-Freedman, S.-W. Chen, P. G. Schultz, *Science* **1995**, *268*, 1738; b) B. Jandeleit, D. J. Schaefer, T. S. Powers, H. W. Turner, W. H. Weinberg, *Angew. Chem.* **1999**, *111*, 2468; *Angew. Chem. Int. Ed.* **1999**, *38*, 2494; c) Q. Li, J.-S. Lee, C. Ha, C. B. Park, G. Yang, W. B. Gan, Y.-T. Chang, *Angew. Chem.* **2004**, *116*, 6491; *Angew. Chem. Int. Ed.* **2004**, *43*, 6331; d) V. del Amo, A. P. McGlone, C. Foster, A. P. Davis, *J. Comb. Chem.* **2005**, *7*, 1.

[5] M. S. Lowry, W. R. Hudson, R. A. Pascal, Jr., S. Bernhard, *J. Am. Chem. Soc.* **2004**, *126*, 14129.

[6] P. Lenaerts, K. Driesen, R. V. Deun, K. Binnemans, *Chem. Mater.* **2005**, *17*, 2148.

[7] a) N. E. Leadbeater, *J. Org. Chem.* **2001**, *66*, 2168; b) J. A. Cassel, S. Leue, N. I. Gachkova, N. C. Kann, *J. Org. Chem.* **2002**, *67*, 9460; c) N. E. Leadbeater, E. L. Sharp, *Organometallics* **2003**, *22*, 4167; d) S. van Zutphen, M. S. Robillard, G. A. van der Marel, H. S. Overkleeft, H. den Dulk, J. Brouwer, J. Reedijk, *Chem. Commun.* **2003**, 634.

[8] a) C. Adachi, M. A. Baldo, S. R. Forrest, S. Lamansky, M. E. Thompson, R. C. Kwong, *Appl. Phys. Lett.* **2001**, *78*, 1622; b) D. Kolosov, V. Adamovich, P. Djurovich, M. E. Thompson, C. Adachi, *J. Am. Chem. Soc.* **2002**, *124*, 9945; c) A. Tsuboyama, H. Iwawaki, M. Furugori, T. Mukaide, J. Kamatani, S. Igawa, T. Moriyama, S. Miura, T. Takiguchi, S. Okada, M. Hoshino, K. Ueno, *J. Am. Chem. Soc.* **2003**, *125*, 12971.

[9] S. Bernhard, X. Gao, G. G. Malliaras, H. D. Abruna, *Adv. Mater.* **2002**, *14*, 433.

[10] Y.-L. Tung, S.-W. Lee, Y. Chi, L.-S. Chen, C.-F. Shu, F.-I. Wu, A. J. Carty, P.-T. Chou, S.-M. Peng, G.-H. Lee, *Adv. Mater.* **2005**, *17*, 1059.

[11] J. Brooks, Y. Babayan, S. Lamansky, P. I. Djurovich, I. Tsyba, R. Bau, M. E. Thompson, *Inorg. Chem.* **2002**, *41*, 3055.

[12] G. Barbarella, L. Favaretto, G. Sotgiu, M. Zambianchi, A. Bongini, C. Arbizzani, M. Mastragostino, M. Anni, G. Gigli, R. Cingolani, *J. Am. Chem. Soc.* **2000**, *122*, 11971.

[13] a) C. W. Phoon, S. F. Oliver, C. Abell, *Tetrahedron Lett.* **1998**, *39*, 7959; b) A. Bianco, J. Furrer, D. Limal, G. Guichard, K. Elbayed, J. Raya, M. Piotto, J.-P. Briand, *J. Comb. Chem.* **2000**, *2*, 681.

[14] a) A. Kamal, G. S. K. Reddy, S. Raghavan, *Bioorg. Med. Chem. Lett.* **2001**, *11*, 387; b) M. R. Wiley, S. D. Lepore, *J. Org. Chem.* **2000**, *65*, 2924.

[15] a) D. P. Rotella, Z. Sun, Y. Zhu, J. Krupinski, R. Pongrac, L. Seliger, D. Normandin, J. E. Macor, *J. Med. Chem.* **2000**, *43*, 5037; b) J. Hanusek, M. Sedlak, P. Simunek, V. Sterba, *Eur. J. Org. Chem.* **2002**, 1855.

[16] a) R. Y. Ning, R. I. Fryer, P. B. Madan, B. C. Sluboski, *J. Org. Chem.* **1976**, *41*, 2724; b) D. J. Kertesz, M. Marx, *J. Org. Chem.* **1986**, *51*, 2315.

[17] X. Chen, J.-L. Liao, Y. Liang, M. O. Ahmed, H.-E. Tseng, S.-A. Chen, *J. Am. Chem. Soc.* **2003**, *125*, 636.

[18] M. K. Nazeeruddin, R. Humphry-Baker, D. Berner, S. Rivier, L. Zuppiroli, M. Graetzel, *J. Am. Chem. Soc.* **2003**, *125*, 8790.

[19] G. Jones II, W. R. Jackson, C.-Y. Choi, W. R. Bergmark, *J. Phys. Chem.* **1985**, *89*, 294.

 © 2006 Wiley-VCH Verlag GmbH & Co. KGaA, Weinheim

Chiral Assemblies

DOI: 10.1002/anie.200504424

Supramolecular Chirality in Layered Crystals of Achiral Ammonium Salts and Fatty Acids: A Hierarchical Interpretation**

Akira Tanaka, Katsunari Inoue, Ichiro Hisaki, Norimitsu Tohnai, Mikiji Miyata, and Akikazu Matsumoto*

The formation of chiral crystals from achiral compounds has attracted much attention because chemical reactions of achiral compounds under asymmetric conditions can lead to absolute asymmetric synthesis,[1] which could be the key to the

[*] A. Tanaka, K. Inoue, Dr. I. Hisaki, Dr. N. Tohnai, Prof. Dr. M. Miyata
Department of Material and Life Science
Graduate School of Engineering, Osaka University
2-1 Yamadaoka, Suita 565-0871 (Japan)
Fax: (+81) 6-6879-7406
E-mail: miyata@mls.eng.osaka-u.ac.jp
Prof. Dr. A. Matsumoto
Department of Applied Chemistry
Graduate School of Engineering, Osaka City University
Sugimoto, Sumiyoshi-ku, Osaka 558-8585 (Japan)

[**] A.T. expresses his special thanks to the Center of Excellence (21COE) program "Creation of Integrated EcoChemistry of Osaka University". This work was also supported by a Grant-in-Aid for Scientific Research (15350070) from the Ministry of Education, Culture, Sports, Science, and Technology, Japan.

InterScience
© 2006 Wiley-VCH Verlag GmbH & Co. KGaA, Weinheim

origin of homochirality of life.[2] Some chiral systems are known in the solid state, in which robust supramolecular motifs, such as hydrogen-bonded networks and π–π stacking, are adopted to obtain chiral crystals with helical[1e,3] and layered structures.[4] However, even in these sophisticated supramolecular systems the nature of the relationship between the molecular structures and the appearance of supramolecular chirality[5] in the crystals still remains ambiguous. Simpler achiral molecules, such as linear fatty acids, on the other hand, are expected to form chiral crystal structures in which the appearance of supramolecular chirality could be explicable on the basis of single molecules. These acids have readily analyzable structures, and thus a number of studies on their solid-state structure have been reported (e.g., layered crystal structures), including our recent results that show how certain amines and carboxylic acids form robust organic layer crystals involving a planar hydrogen-bonded network.[6]

Very few chiral crystal structures of such simple fatty acids have been reported. However, to our surprise, the chirality in the crystal structures is not discussed at all.[7] To understand the formation of chiral crystals composed of achiral compounds, a systematic way of thinking is also required. Herein, we propose a hierarchical approach to the generation of chiral layered crystals that start from achiral molecules (Figure 1).

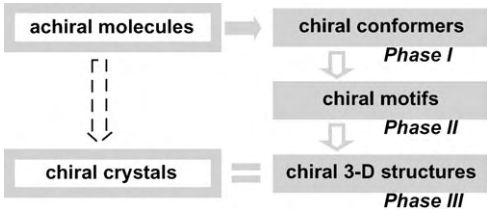
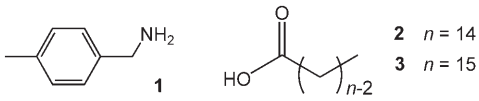


Figure 1. A hierarchical interpretation of supramolecular chirality in crystals generated from achiral molecules.

This approach includes the following three steps: 1) generation of chirality in an achiral single molecule as a result of fixing its conformation in an asymmetric way; 2) assembly into a chiral zero-, one-, or two-dimensional layer motif, in which the chirality in the single molecules spreads throughout the whole layer motif through regular noncovalent interactions, such as hydrogen bonds; and 3) formation of a chiral crystal, in which the chiral layers pile up directionally to form a three-dimensional chiral structure. This approach would be adopted generally in crystals composed of various types of supramolecular assemblies.

Herein, we describe the preparation of two types of novel chiral layered crystals containing 4-methylbenzylamine (**1**) and the linear fatty acids myristic acid (**2**) and pentadecanoic acid (**3**), respectively, and the hierarchical interpretation of their chiral crystal structures.



The chiral crystals were obtained from 4-methylbenzylamine (**1**) and the linear fatty acid in THF. After evaporation of the solvent, the resulting powdery salts were recrystallized from several solvents to give single crystals suitable for X-ray diffraction studies. Figure 2 shows the crystal structures of ammonium myristate **1**·**2**[8] and pentadecanoate **1**·**3**,[9] both of which exhibit layered packing. In both crystals the carboxylate and ammonium ions assemble separately in planes with an identical inclination. A single layer is defined as a set of carboxylate and ammonium layers linked by a planar hydrogen-bonded network (see Figure 2a and 2c for **1**·**2**). The carboxylate and ammonium ions in a single layer in a crystal of **1**·**2** align in the same way as those in **1**·**3** (Figure 2b). However, the stacking manner is completely different between the two crystal systems: each single layer in the crystal of **1**·**2** stacks in a parallel way, whereas those of **1**·**3** stack in an opposite way with a 180° rotation. As a consequence, the crystal structure of **1**·**2** includes only translation as a chiral symmetry element, and thus belongs to the chiral space group $P1$, whereas the structure of **1**·**3** has a twofold helical axis perpendicular to each single layer and thus belongs to the chiral space group $P2_1$.

The X-ray single crystallographic analysis also revealed that the carboxylic group and the alkyl group of the alkyl carboxylate are staggered, as shown in the Newman projection in Figure 3 (top). The fixation of its conformation provides chirality to the twisted carboxylate in the crystal, thus forming *P* or *M* enantiomers.[10] The 4-methylbenzylammonium ion in the crystal is also chiral for the same reasons as

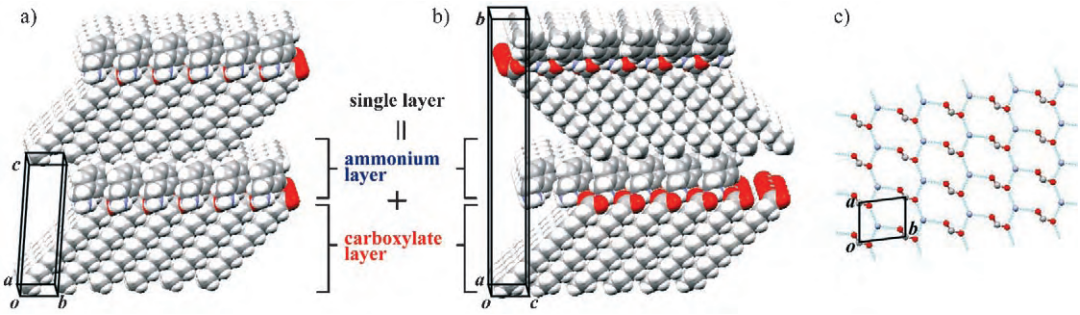


Figure 2. Chiral layered structures of the ammonium carboxylates **1**·**2** (a) and **1**·**3** (b). c) The planar hydrogen-bonded network in **1**·**2**. A set of carboxylate and ammonium layers is connected to construct a single layer. All figures are presented for the *P* crystal. C gray, N blue, O red, H white.

© 2006 Wiley-VCH Verlag GmbH & Co. KGaA, Weinheim

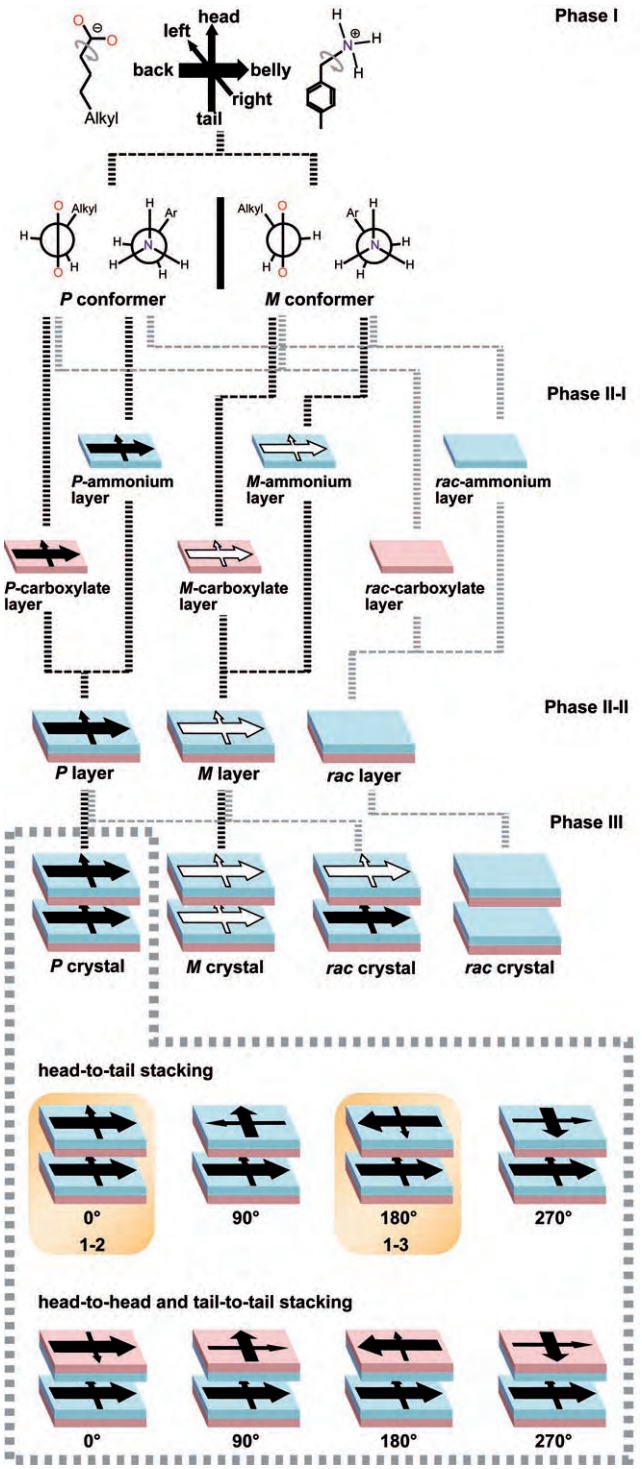


Figure 3. A hierarchical classification of layered crystals based on chirality and directionality. Three distinguishable axes are defined for conformationally chiral carboxylate and ammonium ions (phase I). These assemble to construct *P*-, *M*-, and *rac*-carboxylate and ammonium layers, respectively (phase II-I). The pink and blue plates denote the carboxylate and ammonium layers, black and white arrows denote *P* and *M* conformers, and thick and thin arrows denote back-to-belly and right-to-left axes, respectively. Single layers result from attaching the carboxylate and ammonium layers (phase II-II). Stacking of the single layers yields four types of layered crystals (phase III). The gray dotted box at the bottom shows the possible stacking manners of the single layers in terms of stacking faces and degrees of rotation. The difference of the degrees of stacking gives the two types of chiral layered crystals (**1·2** and **1·3**).

for the carboxylate. Thus, supramolecular chirality in the layered structures of **1·2** and **1·3** is attributed to the transmission of molecular chirality within the single twisted molecules of the single layer by regular assembly, and finally throughout the whole crystal by parallel stacking of these single layers.

We have previously reported that molecular-assembly mechanisms of complex chiral compounds, such as steroids, can be understood by considering the directionality within the molecules as defined by three distinguishable axes,[11] in which the directionality of the helical aggregations is derived from the directionality of the chiral component itself and reflects on the directionality of the entire molecular assembly. In the same way, three axes can be defined for the conformationally chiral carboxylate and ammonium ions and then the 2D aggregation and layered stacking of these ions can be classified by their directionality (Figure 3).

The directionality within the chiral carboxylate and ammonium ions is initially defined by three axes (phase I in Figure 3). In the case of the carboxylate, the head and tail are defined as the carboxylic group and alkyl chain, respectively, and the belly and back as the sides with odd and even numbers of carbon atoms (thick arrow), respectively. Right and left are then spontaneously generated on the carboxylate (thin arrow). In the case of the ammonium ion, the head and tail are defined by the amino group and the methyl group on the aromatic ring near the amino group, respectively, and the back is the opposite side of the edge. Right and left are also generated spontaneously by this procedure.

The assembly manner of the carboxylate and ammonium ions in the single layer can now be clearly shown by defining the directionality of the chiral molecules (phase II-I in Figure 3). The *P* or *M* carboxylates assemble independently in planes with an identical inclination that connects the belly to the back along the crystallographic *a* axis and right to left along the *b* axis (see Figure 2a for the *P* carboxylate), respectively, which leads to two carboxylate layers that are mirror images of each other. The ammonium ions also form a layer. The ammonium ion has a planar body, and this plane lies parallel to a diagonal axis between the *a* and *b* axes, which means that the belly and back lie along the diagonal axis (see Figure 2a for the *P* ammonium). The *P* and *M* ammonium ions assemble independently in the plane to form two kinds of ammonium layers that are mirror images of each other. *P* and *M* conformers are also known to aggregate in *rac*-carboxylate and *rac*-ammonium layers in which supramolecular chirality is not generated, although this behavior is not observed in this system.[6]

A single layer in the crystal contains carboxylate and ammonium layers. Although there are several possible combinations, only layers having certain combinations of chirality can be attached together to form *P*, *M*, and *rac* layers (phase II–II in Figure 3) as formation of a single layer requires the concordance of the period and shape of the unit cell, thus corresponding to chirality, between the carboxylate and ammonium layers.

As the chiral carboxylate and ammonium layers possess directionality, the single layers with supramolecular chirality also have directionality that can be defined by using the three

 © 2006 Wiley-VCH Verlag GmbH & Co. KGaA, Weinheim

distinguishable axes—right and left sides, belly and back sides, and head and tail sides—and adapting them to that of the carboxylate for simplicity.

Finally, the stacking manner of these three kinds of layers determines whether or not supramolecular chirality is generated in the layered crystals (phase III in Figure 3). Stacking of only *P* layers leads to a *P* crystal and stacking of only *M* layers leads to an *M* crystal. A mixture of *P* and *M* layers, however, leads to a *rac* crystal, as does stacking of *rac* layers. Taking into account the directionality of the single layers, there are several ways of stacking them. Indeed, a difference in the stacking of the chiral single layers provides the two types of chiral layered structures observed in the crystals of **1·2** and **1·3**. The gray box in Figure 3 shows selected stacking patterns of the single layers with directionality in the chiral layered structure. It is expected that each single layer contacts in a head-to-tail or head-to-head and tail-to-tail manner. Moreover, each layer is assumed to stack with a rotation of 0, 90, 180, and 270°. In this way, there are at least eight ways to stack a single layer. 4-Methylbenzylammonium myristate (**1·2**) stacks in a head-to-tail manner with a 0° rotation, whereas 4-methylbenzylammonium pentadecanoate (**1·3**) stacks in a head-to-tail manner with a 180° rotation. The difference between the two types of chiral structures arises only from the degree of rotation of the layer stacking, and is presumably due to the even/odd effect of the alkyl chain in the carboxylate.

In summary, we have shown that supramolecular chirality in layered crystals of 4-methylbenzylammonium myristate and pentadecanoate can be understood at the molecular, single-layer, and whole-crystal levels on the basis of a hierarchical interpretation. In a future study, we expect that a correlation between the molecular structure and the stacking manner will reveal the fundamental cause of the generation of this chirality.

Received: December 13, 2005
Revised: April 4, 2006
Published online: May 24, 2006

Keywords: chirality · crystal engineering · hydrogen bonds · layered compounds · supramolecular chemistry

[1] a) T. Suzuki, T. Fukushima, Y. Yamashita, T. Miyashi, *J. Am. Chem. Soc.* **1994**, *116*, 2793–2803; b) H. Irngartinger, P. W. Fettel, V. Siemund, *Eur. J. Org. Chem.* **1998**, 2079–2082; c) S. Kohmoto, Y. Ono, H. Masu, K. Yamaguchi, K. Kishikawa, M. Yamamoto, *Org. Lett.* **2001**, *3*, 4153–4155; d) M. Sakamoto, S. Kobaru, T. Mino, T. Fujita, *Chem. Commun.* **2004**, 1002–1003; e) H. Koshima, H. Kawanishi, M. Nagano, H. Yu, M. Shiro, T. Hosoya, H. Uekusa, Y. Ohashi, *J. Org. Chem.* **2005**, *70*, 4490–4497.

[2] a) B. S. Green, M. Lahav, D. Ravinovich, *Acc. Chem. Res.* **1979**, *12*, 191–197; b) A. Sekine, K. Hori, Y. Ohashi, M. Yagi, F. Toda, *J. Am. Chem. Soc.* **1989**, *111*, 697–699; c) G. Kaupp, M. Haak, *Angew. Chem.* **1993**, *105*, 727–728; *Angew. Chem. Int. Ed. Engl.* **1993**, *32*, 694–695.

[3] a) I. Azumaya, D. Uchida, T. Kato, A. Yokoyama, A. Tanatani, H. Takayanagi, T. Yokozawa, *Angew. Chem.* **2004**, *116*, 1384–1387; *Angew. Chem. Int. Ed.* **2004**, *43*, 1360–1363; b) H. Koshima, S. Honke, J. Fujita, *J. Org. Chem.* **1999**, *64*, 3916–3921; c) S. Jayanty, T. P. Radhakrishnan, *Chem. Eur. J.* **2004**, *10*, 2661–2667; d) H. Koshima, M. Nagano, T. Asahi, *J. Am. Chem. Soc.* **2005**, *127*, 2455–2463.

[4] B. Gong, C. Zheng, H. Zeng, J. Zhu, *J. Am. Chem. Soc.* **1999**, *121*, 9766–9767.

[5] a) L. P. García, D. B. Amabilino, *Chem. Soc. Rev.* **2002**, *31*, 342–356; b) S. Ferlay, O. Felix, M. W. Hosseini, J. M. Planeix, N. Kyritsakas, *Chem. Commun.* **2002**, 702–703; c) M. A. M. Timoneda, M. C. Calama, D. N. Reinhoudt, *Chem. Soc. Rev.* **2004**, *33*, 363–372; d) X. Huang, C. Li, S. Jiang, X. Wang, B. Zhang, M. Liu, *J. Am. Chem. Soc.* **2004**, *126*, 1322–1323.

[6] a) K. Sada, K. Inoue, T. Tanaka, A. Tanaka, A. Epergyes, S. Nagahama, A. Matsumoto, M. Miyata, *J. Am. Chem. Soc.* **2004**, *126*, 1764–1771; b) K. Sada, K. Inoue, T. Tanaka, A. Epergyes, A. Tanaka, N. Tohnai, A. Matsumoto, M. Miyata, *Angew. Chem.* **2005**, *117*, 7221–7224; *Angew. Chem. Int. Ed.* **2005**, *44*, 7059–7062.

[7] Only three examples were found in a search of the Cambridge Structural Database, although the authors do not refer to chirality; see: a) V. Ketmann, E. Kello, V. Vrabel, J. Garaj, M. Karvas, M. Goghova, J. Durmis, *Acta Crystallogr. Sect. C* **1989**, *45*, 787–791; b) V. B. Gaillard, W. Paciorek, K. Schenk, G. Chapuis, *Acta Crystallogr. Sect. B* **1996**, *52*, 1036–1047; c) D. Braga, L. Maini, G. Sanctis, K. Rubini, F. Grepioni, M. R. Chierotti, R. Gobetto, *Chem. Eur. J.* **2003**, *9*, 5538–5548.

[8] Crystal data for **1·2**: $C_{22}H_{39}NO_2$, $M_r = 349.56$, triclinic, space group $P\bar{1}$ (no. 1), $a = 4.784(1)$, $b = 5.651(1)$, $c = 20.278(4)$ Å, $\alpha = 85.19(2)$, $\beta = 86.68(2)$, $\gamma = 82.42(2)°$, $V = 540.9(2)$ Å^3, $T = 213.2$ K, $Z = 1$, $\mu(Cu_{K\alpha}) = 5.16$ cm^{-1}, $\rho_{calcd} = 1.073$ g cm^{-3}, 4199 reflections measured, 1739 of which were unique ($R_{int} = 0.073$) and were used in all calculations. The final *R*1 and *wR*2 values were 0.077 (observed data) and 0.209 (observed data), respectively.

[9] Crystal data for **1·3**: $C_{23}H_{41}NO_2$, $M_r = 363.58$, monoclinic, space group $P2_1$ (no. 4), $a = 4.7364(6)$, $b = 41.125(5)$, $c = 5.6194(9)$ Å, $\beta = 97.76(1)°$, $V = 1084.5(3)$ Å^3, $T = 93.2$ K, $Z = 2$, $\mu(Cu_{K\alpha}) = 5.31$ cm^{-1}, $\rho_{calcd} = 1.113$ g cm^{-3}, 11804 reflections measured, 1973 of which were unique ($R_{int} = 0.031$) and were used in all calculations. The final *R*1 and *wR*2 values were 0.046 (observed data) and 0.111 (observed data), respectively. CCDC-286085 (**1·2**) and -286086 (**1·3**) contain the supplementary crystallographic data for this paper. These data can be obtained free of charge from The Cambridge Crystallographic Data Centre via www.ccdc.cam.ac.uk/data_request/cif.

[10] Although the strict definition of chirality within the twisted molecules can be expressed as +synclinal and −synclinal according to the Klyne–Prelog method, the shortened forms are adopted here for clarity; see: W. Klyne, V. Prelog, *Experientia* **1960**, *16*, 521.

[11] a) M. Miyata, K. Sada, *Comprehensive Supramolecular Chemistry. Vol. 6* (Eds.: D. D. MacNicol, F. Toda, R. Bishop), Pergamon, Oxford, **1996**, pp. 147–176; b) K. Kato, K. Inoue, N. Tohnai, M. Miyata, *J. Inclusion Phenom. Macrocycl. Chem.* **2004**, *48*, 61–67; c) "Separations and Reactions in Organic Supramolecular Chemistry": M. Miyata, N. Yoswathananont, K. Nakano, K. Sada in *Perspectives in Supramolecular Chemistry*, *Vol. 8* (Eds.: F. Toda, R. Bishop), Wiley, New York, **2004**, pp. 87–122, chap. 4; d) T. Watabe, K. Kato, N. Tohnai, M. Miyata in *Structure and Dynamics in Macromolecular Systems with Specific Interactions* (Eds.: K. Adachi, T. Sato), Osaka University Press, **2005**, pp. 157–167.

 © 2006 Wiley-VCH Verlag GmbH & Co. KGaA, Weinheim

Microreactors

DOI: 10.1002/anie.200600951

Self-Supported and Clean One-Step Cathodic Coupling of Activated Olefins with Benzyl Bromide Derivatives in a Micro Flow Reactor**

*Ping He, Paul Watts, Frank Marken, and Stephen J. Haswell**

Electrosynthesis offers a clean and versatile method for the generation of anion and cation radical intermediates.[1] The addition of electrons to, or the removal of electrons from, neutral organic substrates can be achieved under relatively mild reaction conditions and may lead to powerful electrosynthetic strategies. A possible role of electrosynthesis in "green chemistry" has been highlighted by several authors,[2] particularly in combination with the recently emerging microreactor technology.[3a–c] Microreactors have numerous practical advantages including safe operating, easy modulation, and easy scale-up for industrial production when compared with batch reactors.[3d,e] The combination of electrosynthesis with microreactors has made electrochemistry more accessible even in the absence of electrolyte.[4]

In synthetic chemistry, C–C-bond-formation processes are of considerable importance and new methods are constantly sought with the aim of obtaining clean, simple, and efficient synthetic routes. Herein, we describe a C–C-bond-formation method based on the electro-reductive coupling of activated olefins and benzyl bromide derivatives. The coupling products such as 2-benzyl succinic acid dimethyl ester are important classes of compounds owing to their utility as intermediates in the synthesis of important targets such as natural antibiotics,[5a] pyrrolidines,[5b] metalloproteinase inhibitors,[5c] inhibitors towards human leukocytes,[5d] cephalotaxine,[5e] and monoesters of alkylated succinic acids.[5f] Several methods have been reported[5b,g,h] for this class of compounds, most of which involve multi-step processes and require the presence of metal catalysts. Alternatively, a photochemical procedure based on electron transfer to a photo-sensitizer has been proposed for the coupling of methylbenzene and dimethylsuccinate,[5i] but the method resulted in a complex mixture of reaction products. In contrast, the process described herein is based on a clean one-step cathodic coupling process carried out under microreactor flow through conditions to generate higher yields of products when compared with conventional synthetic methods. Considerable benefits of the novel electrochemical process are 1) simple operation, 2) no need for chemical reagents or electrolytes, 3) simple work-up, and 4) a surprisingly high yield.

Initially, the coupling of dimethyl fumarate with benzyl bromide was selected for study by cyclic voltammetry experiments. Both dimethyl fumarate and dimethyl maleate are known to be reduced in one-electron processes, both leading to the dimethyl fumarate radical anions as the intermediate followed by slow hydrodimerization.[6] The reduction of benzyl bromide is usually found to be chemically irreversible leading to the formation of dibenzyl products. The one-electron reduction of benzyl bromide proceeds through the benzyl radical intermediate. The two-electron reduction of benzyl bromide to give a benzyl carbanion may occur at sufficiently negative potentials, at mercury pool electrodes,[7] or in the presence of electrophilic reagents such as protons. Figure 1 A shows typical (conventional) cyclic voltammograms for the reduction of benzyl bromide (curve a), dimethyl fumarate (curve b), and dimethyl fumarate in the presence of benzyl bromide (curve c). The reduction of dimethyl fumarate occurs as a reversible one-electron process. In the presence of benzyl bromide, the peak current of the reduction wave for dimethyl fumarate remains and the re-oxidation wave after reversal of the scan direction completely disappears. A complete loss of the anodic peak reveals a rapid chemical reaction of the dimethyl fumarate radical anion with benzyl bromide. From the peak current in Figure 1 A (and based on additional microelectrode experiments, see Supporting Information), the process can be identified as a one-electron process. As will be shown below, on a longer time scale during the course of electrolysis, transfer of a second electron occurs and is attributed to a further unidentified processes.

During the main electrode reaction, the interaction of the primary fumarate radical anion and benzyl bromide is believed to lead to rapid C–C coupling. The coupling, followed by loss of bromide, occurs only if a sufficient driving force for this process is available. The parameter ΔE ($E_{1/2,\mathrm{df}} - E_{1/2,\mathrm{bb}}$) describes the potential difference for the reduction of the dimethyl fumarate (df) and for benzyl bromide (bb) and is obtained here as an approximate measure of the energy balance in the intermolecular electron transfer. If ΔE becomes too high, the energy for the C–Br bond heterolysis will be insufficient.

Preparative microreactor electrolyses were conducted in a flow cell (see Figure 2) to isolate and identify products by using GC/MS as well as ^{1}H and ^{13}C NMR spectroscopy and to optimize yields for the coupling of dimethyl fumarate (or dimethyl maleate) with benzyl bromide. The solution containing 5 mM dimethyl fumarate (or dimethyl maleate) and 5 mM benzyl bromide in DMF (*N*,*N*-dimethylformamide) was continuously pumped through the cell in which two platinum electrodes with a working area of 45 mm^2 were positioned with an inter-electrode gap of 160 μm or 320 μm. The coupling reactions were conducted galvanostatically and product samples were collected in a product vial for 5 min. Table 1 summarizes the conversion and product distribution for the

[*] Dr. P. He, Dr. P. Watts, Prof. S. J. Haswell
Department of Chemistry
University of Hull, Hull, HU6 7RX (UK)
Fax: (+44) 148-246-6416
E-mail: s.j.haswell@hull.ac.uk
Dr. F. Marken
Department of Chemistry
University of Bath, Bath, BA2 7AY (UK)

[**] We thank the EPSRC for funding.

Supporting information for this article is available on the WWW under http://www.angewandte.org or from the author.

InterScience
© 2006 Wiley-VCH Verlag GmbH & Co. KGaA, Weinheim

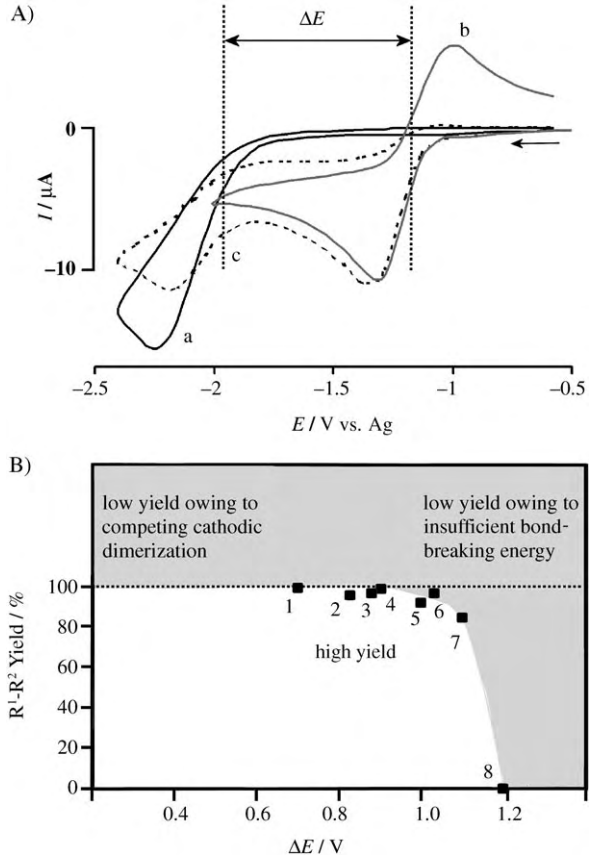


Figure 1. A) Cyclic voltammograms (scan rate 10 $V s^{-1}$) obtained at a platinum disc electrode (diameter 0.5 mm) immersed in 0.1 M nBu_4NBF_4/DMF for: a) 3 mM benzyl bromide, b) 3 mM dimethyl fumarate, and c) 3 mM dimethyl fumarate in the presence of 3 mM benzyl bromide. The parameter ΔE when compared to the energy for heterolytic C–Br bond fission allows the driving force for the reaction to be assessed (see text). B) Plot of the yield of the R^1–R^2 coupling product (see Table 1) versus the gap in halfwave potential for: 1) dimethyl fumarate/benzyl bromide, 2) dimethyl fumarate/4-bromobenzyl bromide, 3) dimethyl fumarate/1-phenylethylbenzyl bromide, 4) fumaronitrile/benzyl bromide, 5) dimethyl fumarate/4-methoxybenzyl bromide, 6) fumaronitrile/4-bromobenzyl bromide, 7) maleic anhydride/bisbromomethylbenzene, 8) maleic anhydride/benzyl bromide.

range of conditions employed in this study. Both conversion and product distribution are strongly dependent on the electrode gap, the flow rate, and the applied current. For a 320-μm inter-electrode gap (Table 1, entries 1 and 2), 47% and 77% conversion to the desired coupling product can be achieved with significant homo-coupling side products. An increase in current was found to enhance only homo-dimerization of the olefin or benzyl bromide. For an inter-electrode gap of 160 μm (Table 1, entries 3–7), relatively lower voltages (4–4.4 V) were required to obtain sufficiently high levels of conversion (>95%). Interestingly, unwanted dimerization of olefins was found to be less than 2% plus a very small amount of toluene (from debromination of benzyl bromide) and no dimerization of benzyl bromide was detected. The best result obtained was 98% of 2-benzyl dimethylsuccinate with only 2% of the homo-dimer tetramethyl butanetetracarboxylate and toluene at a flow rate of 10 or 15 μL min^{-1} (Table 1, entries 5 and 6, respectively). At higher flow rates, the possibility of homo-dimerization of the olefin was observed (Table 1, entry 7).

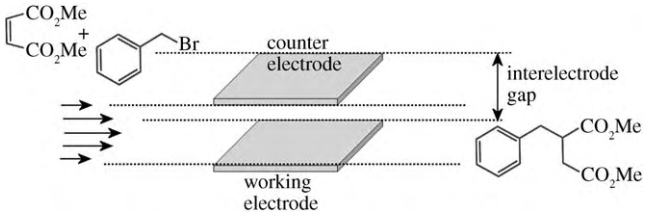


Figure 2. Schematic representation of the C–C coupling reaction during electrosynthesis in a microreactor. A flow of reagents through a rectangular duct with the working and counter electrodes facing each other results in the formation of products.

This electrochemical procedure was also scaled up in a "parallel" microreactor cell containing two equally sized sets of electrodes. Again, dimethyl fumarate was completely converted to give the cross-coupling product 2-benzyldimethylsuccinate with only 2% of olefin dimer and toluene. In this case, a volumetric flow rate equivalent to 30 μL min^{-1} (i.e. 15 μL $min^{-1} \times 2$ flow cells) was achieved, which is double the flow rate of the single cell and hence producing twice the quantity of the product in a given time. Other benzyl bromide derivatives such as 4-methoxybenzyl bromide, 4-methylbenzyl bromide, 4-bromobenzyl bromide, 4-iodobenzyl bromide, and 1-phenylethyl bromide were also examined for coupling reactions with dimethyl fumarate using the same microreactor

Table 1: Data for the preparative electrolysis of activated olefins in the presence of benzyl bromides in a micro flow cell without intentionally added supporting electrolyte.[a]

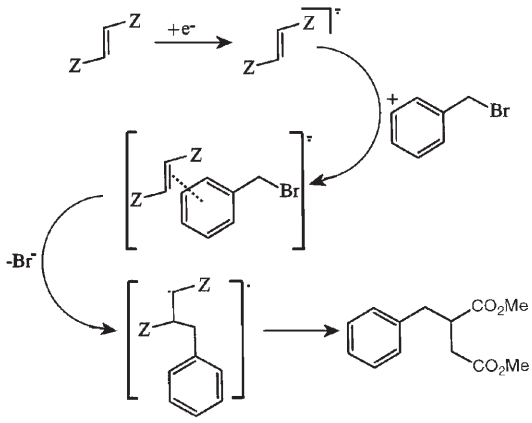
No.	*I* [mA]	Olefin R^1	R^2-Br R^2	Flow [μL min^{-1}]	Conv. [%][b]	Distribution [%] R^1-R^2	others[c]
1	0.6	dimethyl maleate	benzyl	20	47	89	11
2	1.5	dimethyl maleate	benzyl	20	77	70	30
3	0.6	dimethyl maleate	benzyl	10	100	98	2
4	0.6	dimethyl maleate	benzyl	15	100	98	2
5	0.6	dimethyl fumarate	benzyl	10	100	98	2
6	0.6	dimethyl fumarate	benzyl	15	100	98	2
7	0.6	dimethyl fumarate	benzyl	20	100	94	6
8	0.6	dimethyl fumarate	4-methoxybenzyl	10	100	94	6
9	0.6	dimethyl fumarate	4-methylbenzyl	10	100	94	6
10	0.6	dimethyl fumarate	4-bromobenzyl	10	100	99	1
11	0.6	dimethyl fumarate	4-iodobenzyl	10	100	99	1
12	0.6	dimethyl fumarate	1-phenylethyl	10	100	98	2
13	0.5	fumaronitrile	benzyl	10	100	96	4
14	0.5	fumaronitrile	4-methylbenzyl	10	100	93	7
15	0.5	fumaronitrile	4-bromobenzyl	10	100	95	5
16	0.3	maleic anhydride	dibromide	10	82	84	16[d]

[a] Olefin 5 mM, halide 5 mM, solvent DMF; the electrode gap is 320 μm for entries 1 and 2, and 160 μm for entries 3–16. [b] Conversion was determined based on the quantity of olefin before and after reaction using *n*-decane as an internal standard. [c] Other products result from dimerization of olefin and debromination of benzyl bromides; no dimerization of benzyl bromides is detected except for entry 2. [d] Other side products are 1,2-dimethylbenzene and 2-methylbenzyl bromide.

© 2006 Wiley-VCH Verlag GmbH & Co. KGaA, Weinheim

as that used in entry 3 in Table 1. All preparative electrolyses gave excellent yields (94%) of cross-coupling products with very small amount of olefin dimer and debrominated products (Table 1, entries 8–12). The formation of bromine due to oxidation of bromide was not observed presumably owing to the limited overlap of diffusion layers within the flow cell. Current efficiencies for all processes are typically 40–50%. These data suggest that overall two moles of electrons are consumed for each mole of product formed by electrolysis. Cyclic voltammetry data (short time scale) do not show evidence for the transfer of the second electron. However, the time scale for the electrolysis process is different and the second electron transfer may occur in the later stages of the process, for example, involving solvent.

From the results obtained, it can be seen that the presence of benzyl bromide suppresses olefin hydrodimerization, indicating that the reaction between olefin radical anion and benzyl bromide is fast. The neutral benzyl radical intermediate,[4d] which is short-lived[8] and known to either dimerize (to give bibenzyl) or to abstract a hydrogen atom to produce toluene,[9] appears to be an unlikely free intermediate. The absence of bibenzyl and only a small amount of toluene indicate fast direct coupling of the dimethyl fumarate radical anion with benzyl bromide. Scheme 1 describes a



Scheme 1. Plausible mechanistic reaction pathway for the C–C coupling process.

plausible reaction pathway. The mild conditions employed during electrolysis are consistent with a one-electron pathway, and a related transition metal complex mediated reduction of benzyl bromide also has been shown to proceed through a one-electron pathway.[10] However, in this particular study it is not clear whether the final step proceeds through a second-electron transfer process or not and this will require further study.

Further coupling reactions between fumaronitrile and benzyl bromides as well as between maleic anhydride and 1,2-bis(bromomethyl)benzene were investigated. Formally equivalent (but more laborious and less effective) conventional synthetic reactions have been described in the literature, for example, a photochemical process in the presence of organometallic catalysts for the coupling of benzyl bromide with fumaronitrile,[11] a sacrificial zinc approach,[12a] a photochemical approach,[12b] and a direct Diels–Alder reaction[12c,d] for coupling of maleic anhydride with dibromides. Interestingly, in a flow microreactor cell excellent yields (>93%) for coupling of fumaronitrile and bromides (Table 1, entries 13–15) and 84% yields for coupling of maleic anhydride and 1,2-bis(bromomethyl)benzene (Table 1, entry 16) can be obtained.

For the proposed mechanism, the differences between the approximate reduction halfwave potentials for the olefin and benzyl bromide, ΔE, may be understood as part of a thermodynamic cycle.[13] It is observed that conversion is dependent on the reduction potential difference ΔE. For the coupling reaction of dimethyl fumarate and benzyl bromide with ΔE of 0.7 V up to 100% conversion can be achieved, and for the coupling reaction of dimethyl fumarate and 4-methoxybenzyl bromide with ΔE of 1.1 V 91% conversion are obtained at a flow rate of 15 $\mu L\,min^{-1}$ under the same conditions. It is also observed that coupling reactions of benzyl chloride with dimethyl fumarate, and that of maleic anhydride with all benzyl bromide derivatives ($\Delta E > 1.2$ V) except 1,2-bis(bromomethyl)benzene ($\Delta E = 1.1$ V) fail to produce any cross-coupling products. The benzyl bromides are recovered unreacted. A schematic plot of maximum yield versus ΔE (Figure 1B) suggests a threshold of $\Delta E \approx 1.1$ V for successful coupling. This value is in approximate agreement (ΔE is slightly high due to uncertainty in half wave potential for the benzyl bromide reduction) with the value expected for dissociation of the C–Br bond: $\Delta E = 0.85$ V (the gas phase bond energy for benzyl bromide is $D_o = 82\,kJ\,mol^{-1}$).[14]

We have demonstrated that clean microreactor-based electrosyntheses in the absence of supporting electrolyte are feasible even with very simple cell geometries. The height of the microfluidic cell and the flow rate have been shown to be crucial for the minimization of unwanted side products and optimization of yields. More work will be required for a better understanding of the spatial distribution of reagents, the electron transfer process in microreactor systems, as well as for the optimization and scale up of processes in the microreactor cell. For an energy-efficient use of microreactor electrosynthesis, the resistive losses during electrosynthesis will need further investigation and better electrode designs may help in optimizing the efficiency of the process. It is very likely that clean one-step electrosynthetic coupling processes in microfluidic reactors are applicable for a wider range of reactions.

Experimental Section

Cyclic voltammetric (CV) experiments were carried out with an Autolab PGSTAT30 system in a conventional three-electrode cell and in the presence of supporting electrolyte. A Pt disc (diameter 0.5 mm), a Pt wire, and a silver wire (both diameter 0.1 mm) were used as the working electrode, the counter electrode, and the reference electrode, respectively. For preparative microreactor electrolyses, a Harvard PHD 2000 syringe pump was used to pump the reaction solution containing olefin (5 mM) and benzyl bromide (5 mM) in DMF without the addition of electrolyte through the microreactor cell in which two platinum foil electrodes with a working area of 45 mm^2 were positioned with an inter-electrode distance of 160 μm and 320 μm.[4d] All reactions were conducted galvanostatically and

 © 2006 Wiley-VCH Verlag GmbH & Co. KGaA, Weinheim

product samples were continuously collected 5 times and each run took 5 min. Reactions were analyzed by GC (Shimadzu GC-17 A, FID, column CPSIL8) using decane as an internal standard. The replicate analysis shows RSD less than 5%. The products were also identified using ^{1}H and ^{13}C NMR spectroscopy (Jeol GX400) in $CDCl_3$ as well as mass spectrometry (Varian 2000).

Received: March 10, 2006
Published online: May 23, 2006

Keywords: C–C coupling · electrochemical synthesis · flow cells · microreactors · olefins

[1] J. Utley, *Chem. Soc. Rev.* **1997**, *26*, 157.
[2] a) P. T. Anastas, T. C. Williamson, *Green Chemistry*, Oxford University Press, Oxford, **1998**, pp. 167; b) E. Steckhan, T. Arns, W. R. Heineman, G. Hilt, D. Hoorman, J. Jorissen, L. Kroner, B. Lewall, H. Putter, *Chemosphere* **2001**, *43*, 63; c) D. Pletcher, N. L. Weinberg, *Chem. Eng.* **1992**, *99*, 98.
[3] a) *Microreaction Technology* (Ed.: W. Ehrfeld), Springer, Berlin, **1998**; b) W. Ehrfeld, V. Hessel, H. Löwe, *Microreactors: New Technology for Modern Chemistry*, Wiley-VCH, Weinheim, **2000**; c) V. Hessel, S. Hardt, H. Löwe, *Chemical Micro Process Engineering*, Wiley-VCH, Weinheim, **2004**; d) S. Taghavi-Moghadam, A. Kleemann, K. G. Golbig, *Org. Process Res. Dev.* **2001**, *5*, 652; e) T. Kawaguchi, H. Miyata, K. Ataka, K. Mae, J. Yoshida, *Angew. Chem.* **2005**, *117*, 2465; *Angew. Chem. Int. Ed.* **2005**, *44*, 2413.
[4] a) C. A. Paddon, G. J. Pritchard, T. Thiemann, F. Marken, *Electrochem. Commun.* **2002**, *4*, 825; b) D. Horii, M. Atobe, T. Fuchigami, F. Marken, *Electrochem. Commun.* **2005**, *7*, 35; c) R. Horcajada, M. Okajima, S. Suga, J. Yoshida, *Chem. Commun.* **2005**, 1303; d) P. He, P. Watts, F. Marken, S. J. Haswell, *Electrochem. Commun.* **2005**, *7*, 918.
[5] a) J. P. Devlin, W. D. Ollis, J. E. Thorpe, R. S. Wood, B. J. Broughton, P. J. Warren, K. R. H. Wooldbridge, D. E. Wright, *J. Chem. Soc. Perkin Trans. 1* **1975**, 830; b) N. A. Porter, D. M. Scott, I. J. Rosenstein, B. Giese, A. Veit, H. G. Zeitz, *J. Am. Chem. Soc.* **1991**, *113*, 1791; c) D. E. Levy, F. Lapierre, W. Liang, W. Ye, C. W. Lange, X. Li, D. Grobelny, M. Casabonne, D. Tyrrell, K. Holme, A. Nadzan, R. E. Galardy, *J. Med. Chem.* **1998**, *41*, 199; d) W. C. Groutas, M. J. Brubaker, M. A. Stanga, J. C. Castrisos, J. P. Crowley, E. J. Schatz, *J. Med. Chem.* **1989**, *32*, 1607; e) R. B. Bates, R. S. Cuther, R. M. Freeman, *J. Org. Chem.* **1977**, *42*, 4162; f) G. Sabitha, R. Srividya, J. S. Yadav, *Tetrahedron* **1999**, *55*, 4015; g) S. C. Bergmeier, K. A. Ismail, *Synthesis* **2000**, 1369; h) R. Ballini, G. Bosica, D. Fiorini, P. Righi, *Synthesis* **2002**, 681; i) M. Mella, M. Fagnoni, A. Albini, *Eur. J. Org. Chem.* **1999**, *9*, 2137.
[6] a) C. Degrand, H. Lund, *Nouv. J. Chim.* **1977**, *1*, 35; b) E. A. Casanova, M. C. Dutton, D. J. Kalota, J. H. Wagenknecht, *J. Electrochem. Soc.* **1993**, *140*, 2565.
[7] a) J. G. Lawless, D. E. Bartak, M. D. Hawley, *J. Am. Chem. Soc.* **1969**, *91*, 7121; b) D. E. Bartak, M. D. Hawley, *J. Am. Chem. Soc.* **1972**, *94*, 640; c) J. Grimshaw, *Electrochemical Reactions and Mechanisms in Organic Chemistry*, Elsevier, Amsterdam, **2000**, pp. 98–103; d) *Organic Electrochemistry* (Eds.: H. Lund, O. Hammerich), Marcel Dekker, New York, **2001**, and references therein.
[8] D. Zhou, H. Carrero, J. F. Rusling, *Langmuir* **1996**, *12*, 3067.
[9] a) "Acyclic Aliphatic Halides": M. D. Hawley in *Encyclopedia of Electrochemistry of the Elements, Organic Section*, *Vol. 14* (Eds.: A. J. Bard, H. Lund), Marcel Dekker, New York, **1980**, pp. 83–103; b) O. R. Brown, H. R. Thirsk, B. Thornton, *Electrochim. Acta* **1971**, *16*, 495; c) C. P. Andrieux, A. L. Gorande, J. M. Saveant, *J. Am. Chem. Soc.* **1992**, *114*, 6892.
[10] a) D. Zhou, H. Carrero, J. F. Rusling, *Langmuir* **1996**, *12*, 3067; b) C. P. Andrieux, A. Le Gorande, J. M. Savéant, *J. Am. Chem. Soc.* **1992**, *114*, 6892; c) A. J. Fry, A. H. Singh, *J. Org. Chem.* **1994**, *59*, 8172; d) N. Sadler, S. L. Scott, A. Bakac, J. H. Espenson, M. S. Ram, *Inorg. Chem.* **1989**, *28*, 3951.
[11] B. Giese, G. Thoma, *Helv. Chim. Acta* **1991**, *74*, 1135.
[12] a) B. H. Han, B. P. Hee, *J. Org. Chem.* **1982**, *47*, 751; b) A. Ouchi, Y. Koga, *Chem. Commun.* **1996**, *17*, 2075; c) J. H. P. Utley, Y. Gao, J. Gruber, R. Lines, *J. Mater. Chem.* **1995**, *5*, 1297; d) A. Ouchi, Z. Li, M. Sakuragi, T. Majima, *J. Am. Chem. Soc.* **2003**, *125*, 1104.
[13] J. H. P. Utley, S. Ramesh, X. Salvatella, S. Szunerits, M. Motevalli, M. F. Nielsen, *J. Chem. Soc. Perkin Trans. 2* **2001**, 153.
[14] A. Freedman, S. C. Yang, M. Kawasaki, R. Bersohn, *J. Chem. Phys.* **1980**, *72*, 1028.

 © 2006 Wiley-VCH Verlag GmbH & Co. KGaA, Weinheim

Asymmetric Synthesis

DOI: 10.1002/anie.200600451

Biaryl Axis as a Stereochemical Relay for the Enantioselective Synthesis of Antimicrotubule Agents**

*Agnès Joncour, Anne Décor, Sylviane Thoret, Angèle Chiaroni, and Olivier Baudoin**

Dedicated to the memory of Pierre Potier

Allocolchicine (**1**) and steganacin (**2**) are two naturally occurring chiral biaryls that inhibit the polymerization of tubulin into microtubules in a similar way to colchicine.[1–3] Recently, colchicine-type antimicrotubule agents got a second wind with the discovery that a prodrug of *N*-acetylcolchinol (**3**; NAC) caused the selective destruction of tumor vasculature.[4] Steganacin (**2**) contains a stereogenic biaryl axis with a stable a*R* configuration, with atropisomerization being prevented by the eight-membered bridging ring conformation.[3] In contrast, the seven-membered ring of allocolchicinoids **1** and **3** allows atropisomerization, and these molecules occur as a mixture of equilibrating atropisomers.[2] The biaryl-axis configuration of **1**–**3** and analogues was shown to be a crucial

[*] A. Joncour, Dr. A. Décor, S. Thoret, A. Chiaroni,[+] Dr. O. Baudoin
Institut de Chimie des Substances Naturelles
CNRS, Avenue de la Terrasse
91198 Gif-sur-Yvette (France)
Fax: (+33) 1-690-77247
E-mail: baudoin@icsn.cnrs-gif.fr

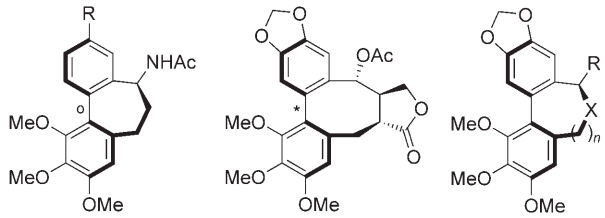
[+] X-ray crystal structure analysis.

[**] We thank M.-E. Tran Huu Dau for the AM1 calculations, F. Guéritte and D. Guénard for support, and E. Bacqué for a useful suggestion. This work was financially supported by the ICSN-CNRS.

Supporting information for this article is available on the WWW under http://www.angewandte.org or from the author.

© 2006 Wiley-VCH Verlag GmbH & Co. KGaA, Weinheim

parameter for their tubulin-binding properties, the activity being often restricted to a*R* atropisomers.[1] We report herein a versatile enantioselective synthesis of bioactive biaryls **4**, simple new hybrid analogues of **1**–**3** containing a heterocyclic



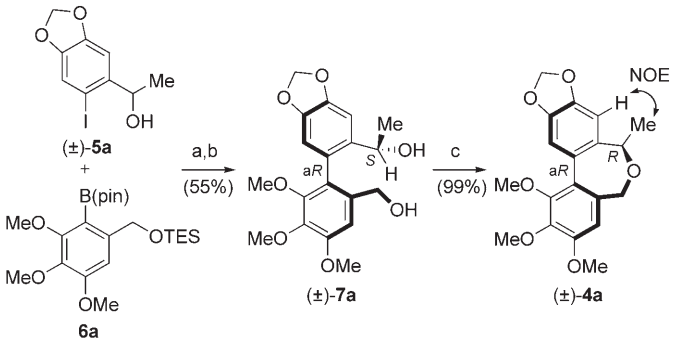
allocolchicine (**1**): R = CO_2Me
N-acetylcolchinol (**3**): R = OH

steganacin (**2**)

4

bridge, by using the biaryl stereogenic axis as a stereochemical relay.[5] First, the biaryl configuration is controlled by a benzylic stereocenter through an atropo-diastereoselective Suzuki coupling,[6] then the biaryl axis relays its stereochemical information to the temporarily destroyed stereocenter in a S_N1-type dehydrative cyclization.

Our synthetic strategy was initially implemented with racemic dibenzoxepine (**4a**; Scheme 1), thus following on from our early investigations.[7] The reoptimized Suzuki coupling of racemic iodide **5a** with boronate **6a** catalyzed by $Pd(OAc)_2$/**L1**[8] followed by removal of the triethylsilyl (TES) group on the major diastereoisomer (d.r. = 87:13 for the Suzuki coupling) gave biphenyl diol **7a** in 55% yield. The *S*,a*R* relative configuration of **7a** was determined by X-ray diffraction analysis.[9] As expected, no atropisomerization of **7a** was detected at temperatures below 160°C. We found that the dehydrative cyclization of **7a** occurred in the presence of CSA in acetone, probably through an intramolecular S_N1 process, thus furnishing racemic **4a** in quantitative yield. The *R*,a*R* relative configuration of **4a** was deduced from NOESY

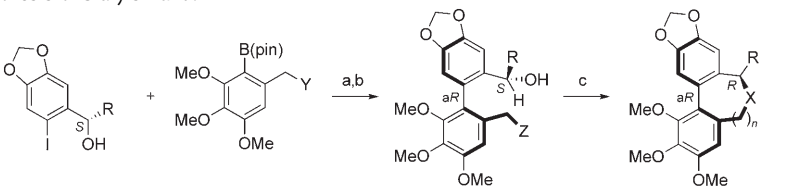


Scheme 1. Synthesis of racemic dibenzoxepine (**4a**). Reagents and conditions: a) (±)-**5a**, **6a** (1.5 equiv), $Pd(OAc)_2$ (5 mol%), **L1** (10 mol%), $Ba(OH)_2{\cdot}8H_2O$ (1.1 equiv), dioxane/H_2O (9:1; *c* = 1 M), 100°C (d.r. = 87:13); b) nBu_4NF, THF, 20°C; c) CSA (1.0 equiv), acetone, 20°C (99%). **L1** = 2-(dicyclohexylphosphino)-2′-(*N*,*N*-dimethylamino)biphenyl, CSA = camphorsulfonic acid, pin = pinacolato.

experiments (Scheme 1). Similar to other allocolchicinoids,[2] **4a** occurred as a 96:4 mixture of interconverting a*R*/a*S* atropisomers in $CDCl_3$, as shown by the presence of exchange correlations on the NOESY spectrum.[10] We were delighted to find that racemic **4a** significantly inhibited the assembly of microtubules in vitro, with an IC_{50} value of 13.1(±2.9) μM versus 8.2(±1.6) μM for (−)-colchicine.

We next embarked on an asymmetric synthesis of (*R*,a*R*)-**4a** and other analogues, on the assumption that only this enantiomer was responsible for the antimicrotubule activity of (±)-**4a**. Our general strategy for the asymmetric synthesis of tricyclic biaryls **4a**–**d** with a seven or eight-membered bridging ring containing an oxygen or nitrogen atom is depicted in Table 1. The *S* enantiomer of **5a** was obtained in 72% yield and 97% *ee* from 3,4-methylenedioxyacetophenone by reduction with catalytic (*R*)-CBS-oxazaborolidine (CBS = Corey, Bakshi, Shibata), followed by electrophilic

Table 1: Enantioselective synthesis of biaryls **4a**–**d**.[a]



(*S*)-**5a**: R = Me
(*R*)-**5a**: R = Me
(*S*)-**5b**: R = Et

6a: Y = OTES
6b: Y = NH*t*Boc
6c: Y = CH_2OTES

7a: R = Me, Z = OH
7b: R = Et, Z = OH
7c: R = Me, Z = NH*t*Boc
7d: R = Me, Z = CH_2OH

4a: *n* = 1, R = Me, X = O
4b: *n* = 1, R = Et, X = O
4c: *n* = 1, R = Me, X = NH
4d: *n* = 2, R = Me, X = O

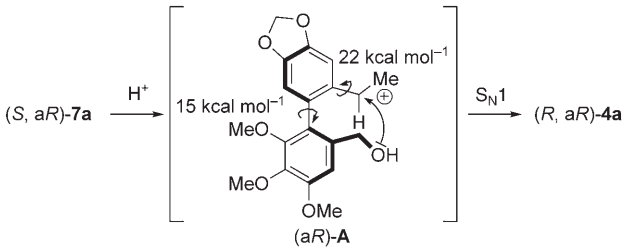
Entry	Iodide	*ee* [%][b]	Suzuki coupling					Dehydrative cyclization			
			Boronate	Ligand	Product[c]	Yield [%][d]	d.r.[e]	Product[c]	*T* [°C]	Yield [%][g]	*ee* [%][b]
1	(*S*)-**5a**	97	**6a**	**L1**	(*S*, a*R*)-**7a**	54	87:13	(*R*, a*R*)-**4a**[f]	−50	86	96
2	(*R*)-**5a**	96	**6a**	**L1**	(*R*, a*S*)-**7a**	34	87:13	(*S*, a*S*)-**4a**[f]	−50	86	94
3	(*S*)-**5b**	98	**6a**	**L1**	(*S*, a*R*)-**7b**	42	74:26	(*R*, a*R*)-**4b**[f]	−78	77	95
4	(*S*)-**5a**	97	**6b**	**L1**	(*S*, a*R*)-**7c**	39	60:40	(*R*, a*R*)-**4c**	−78	95	88
5	(*S*)-**5a**	97	**6c**	**L2**	(*S*, a*R*)-**7d**	57	81:19	(*R*, a*R*)-**4d**	−50	84	96

[a] Reaction conditions: a) iodide (1 equiv), boronate (1.5 equiv), $Pd(OAc)_2$ (5 mol%), **L1** or **L2** (10 mol%), $Ba(OH)_2{\cdot}8H_2O$ (1.1 equiv), dioxane/H_2O (9:1; *c* = 1 M), 100°C (**L2** = 2-dicyclohexylphosphino-2′,6′-dimethoxy-1,1′-biphenyl); b) for **7a**–**b** and **7d**: nBu_4NF, THF, 20°C; c) TFA (5 equiv), CH_2Cl_2. [b] Measured by chiral HPLC, using the racemic mixture as a reference. [c] Relative configuration determined by NOESY experiments, absolute configuration confirmed by superimposition of the CD spectrum on an authentic sample of (−)-NAC (**3**; see the Supporting Information). [d] Yield of the isolated major diastereoisomer from steps (a) and (b). [e] Measured by ^{1}H NMR spectroscopic analysis of the crude mixture obtained in step (a). [f] Configuration of the major atropisomer (the compound occurs as a mixture of interconverting atropisomers). [g] Yield of the isolated product.

© 2006 Wiley-VCH Verlag GmbH & Co. KGaA, Weinheim

iodination. Atropo-diastereoselective Suzuki coupling with boronate **6a** followed by removal of the TES group on the major diastereoisomer provided (*S*,a*R*)-**7a** in 54% yield (entry 1). The stereochemically crucial dehydration of this compound was first attempted under the same conditions as the racemic mixture at 20°C. This step gave **4a** with 74% *ee* in favor of the putative *R*,a*R* enantiomer. Gratifyingly, carrying out the cyclization at −50°C with trifluoroacetic acid (TFA) in CH_2Cl_2 allowed almost complete conservation of the optical purity (96% *ee*, 86% yield). The *R*,a*R* absolute configuration of the product was confirmed by the superimposition of its CD spectrum on that of an authentic sample of (−)-NAC (**3**). Repeating the same reaction sequence from enantiomeric (*R*)-**5a** (synthesized in 96% *ee*) furnished (*S*, a*S*)-**4a** in 94% ee (entry 2). Introduction of another alkyl group on the oxepine ring proved feasible, as illustrated by the synthesis of the ethyl analogue (*R*,a*R*)-**4b** (entry 3). This analogue was obtained with 95% *ee* from (*S*)-**5b** (98% *ee*).[11] The dibenzazepine analogue (*R*,a*R*)-**4c** could be obtained accordingly, starting from (*S*)-**5a** and boronate **6b** (entry 4). In this case, a small loss of optical purity was observed (88% *ee*), although the dehydration occurred at −78°C. Cleavage of the *tert*-butyloxycarbonyl (*t*Boc) group was observed upon warming the reaction mixture to room temperature. Finally, dibenzoxocine (*R*,a*R*)-**4d** (eight-membered median ring) was synthesized with 96% *ee* from (*S*)-**5a** and boronate **6c** containing a homologated side chain. In this case, **L2** (S-Phos)[12] gave a better yield than **L1** in the Suzuki coupling. Compound **4d** occurred as a single atropisomer in solution, contrary to **4a**,**b**, because of the presence of the larger bridging ring, similar to stegane-type molecules.[3]

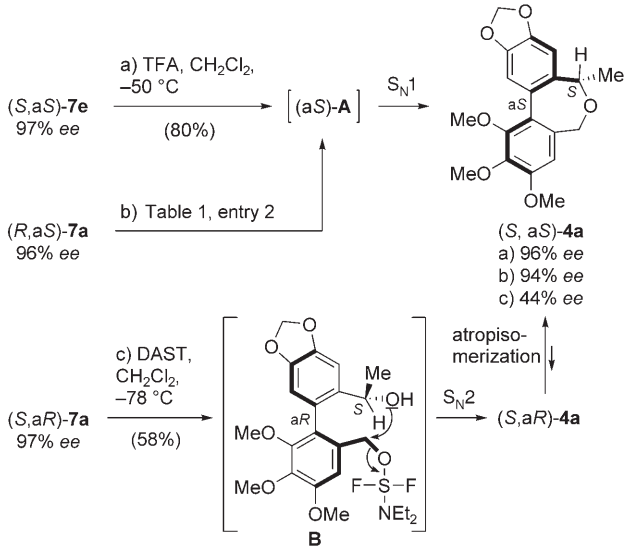
The stereoselectivity of the dehydrative cyclization of diol (*S*,a*R*)-**7a** can be rationalized by the formation of chiral benzylic cation (*aR*)-**A**,[13] in which the C^+–H bond eclipses the biaryl axis to minimize $A^{1,3}$ allylic strain (Scheme 2). At



Scheme 2. Proposed cationic cyclization intermediate.

low temperature, this intermediate is configurationally stable and trapped by the internal nucleophile, thus giving (*R*,a*R*)-**4a** with inversion of configuration at the benzylic stereocenter. An atropisomerization barrier of 15 kcal mol^{-1} was calculated for **A** (AM1 method), whereas the rotation barrier of the C(Ar)–C^+ bond was significantly higher (22 kcal mol^{-1}), as expected from conjugation with the aromatic ring. This behavior indicates that the observed racemization of (*R*,a*R*)-**4a** at higher temperatures might occur preferably by atropisomerization. Overall, the biaryl axis, therefore, functions as a stereochemical relay for the benzylic stereocenter that is temporarily destroyed in intermediate **A**.

Additional evidence of a chiral carbocationic intermediate in the dehydrative cyclization was provided by the reaction of the minor diastereoisomer (*S*,a*S*)-**7e** obtained in a small amount after Suzuki coupling of (*S*)-**5a** with **6a** and deprotection (Scheme 3, path a). This reaction furnished



Scheme 3. Stereoconvergent syntheses of (*S*,a*S*)-**4a**.

(*S*,a*S*)-**4a** with 96% *ee*, most likely through the same carbocationic intermediate (a*S*)-**A** as that formed from (*R*,a*S*)-**7a** (path b). A third stereoconvergent pathway could be devised for the synthesis of (*S*,a*S*)-**4a** (path c). When diol (*S*,a*R*)-**7a**, which was previously converted into (*R*,a*R*)-**4a** with TFA (Table 1, entry 1), was treated with (diethylamino)sulfur trifluoride (DAST) in CH_2Cl_2 at −78°C, (*S*,a*S*)-**4a** was obtained as the major enantiomer in 44% *ee*. This result can be best rationalized by the regioselective reaction of the primary alcohol of **7a** with DAST to give intermediate **B**, followed by intramolecular S_N2.[14] This reaction would produce (*S*,a*R*)-**4a**, which interconverts into the more stable atropisomer (*S*,a*S*)-**4a**. The loss of optical purity could be ascribed either to incomplete regioselectivity in the reaction of the diol with DAST or to a mixed S_N2/S_N1 mechanism.

The antimicrotubule activity of biaryls **4a–d** was examined and compared to that of (−)-colchicine and (−)-NAC (**3**). First, no activity was found for (*S*,a*S*)-**4a**, as expected. The IC_{50} values for the inhibition of the microtubule assembly for the target compounds and the reference compounds were: 2.9(±0.7) μM for NAC (**3**); 8.2(±1.6) μM for colchicine; 12.3(±2.5) μM for (*R*, a*R*)-**4a**; 4.9(±0.4) μM for (*R*, a*R*)-**4b**; 11.1(±2.0) μM for (*R*, a*R*)-**4d**. Dibenzazepine (*R*,a*R*)-**4c** was found to be inactive. Thus, all oxygen-containing analogues were strong inhibitors of tubulin polymerization, with (*R*,a*R*)-**4b** being the most active (1.7× more active than colchicine).[15]

In conclusion, we have reported a general and efficient enantioselective synthesis of potent antimicrotubule biaryls

 © 2006 Wiley-VCH Verlag GmbH & Co. KGaA, Weinheim

by using a novel type of asymmetry relay by a biaryl stereogenic axis. These molecules could represent promising new leads for the development of vascular-targeting agents.

Received: February 2, 2006
Published online: May 10, 2006

Keywords: antimicrotubule agents · asymmetric synthesis · atropisomerism · carbocations · Suzuki coupling

[1] O. Baudoin, F. Guéritte in *Studies in Natural Product Chemistry*, *Vol. 29* (Ed.: Atta-ur-Rahman), Elsevier Science, Amsterdam, **2003**, pp. 355–417.
[2] a) O. Boyé, A. Brossi in *The Alkaloids*, *Vol. 41* (Eds.: A. Brossi, G. A. Cordell), Academic Press, New York, **1992**, pp. 125–176; b) Q. Shi, K. Chen, S. L. Morris-Natschke, K.-H. Lee, *Curr. Pharm. Des.* **1998**, *4*, 219–248.
[3] a) D. L. Sackett, *Pharmacol. Ther.* **1993**, *59*, 163–228; b) J. Chang, J. Reiner, J. Xie, *Chem. Rev.* **2005**, *105*, 4581–4609.
[4] Reviews: a) M. A. Jordan, L. Wilson, *Nat. Rev. Cancer* **2004**, *4*, 253–265; b) P. E. Thorpe, *Clin. Cancer Res.* **2004**, *10*, 415–427; c) F. Donate, *Drugs Future* **2005**, *30*, 695–706.
[5] Recent examples with axially chiral amides: a) J. Clayden, A. Lund, L. Vallverdú, M. Helliwell, *Nature* **2004**, *431*, 966–971; b) M. Petit, A. J. B. Lapierre, D. P. Curran, *J. Am. Chem. Soc.* **2005**, *127*, 14994–14995.
[6] Reviews: a) O. Baudoin, *Eur. J. Org. Chem.* **2005**, 4223–4229; b) G. Bringmann, A. J. Price Mortimer, P. A. Keller, M. J. Gresser, J. Garner, M. Breuning, *Angew. Chem.* **2005**, *117*, 5518–5563; *Angew. Chem. Int. Ed.* **2005**, *44*, 5384–5427.
[7] O. Baudoin, A. Décor, M. Cesario, F. Guéritte, *Synlett* **2003**, 2009–2012.
[8] a) J. P. Wolfe, S. L. Buchwald, *Angew. Chem.* **1999**, *111*, 2570–2573; *Angew. Chem. Int. Ed.* **1999**, *38*, 2413–2416; b) J. P. Wolfe, R. A. Singer, B. H. Yang, S. L. Buchwald, *J. Am. Chem. Soc.* **1999**, *121*, 9550–9561.
[9] CCDC-296412 ((±)-(*S*,a*R*)-**7a**) contains the supplementary crystallographic data for this paper. These data can be obtained free of charge from The Cambridge Crystallographic Data Centre via www.ccdc.cam.ac.uk/data_request/cif.
[10] The structures of both atropisomers were computed using random search calculations. The NOE interactions observed for the major a*R* atropisomer (Scheme 1) corresponds to a H(Ar)–CH_3 distance of 2.2 Å, whereas this distance is 3.6 Å in the a*S* atropisomer.
[11] All target compounds **4a–d** were first synthesized in racemic form to serve as references for chiral HPLC analysis.
[12] a) S. D. Walker, T. E. Barder, J. R. Martinelli, S. L. Buchwald, *Angew. Chem.* **2004**, *116*, 1907–1912; *Angew. Chem. Int. Ed.* **2004**, *43*, 1871–1876; b) T. E. Barder, S. D. Walker, J. R. Martinelli, S. L. Buchwald, *J. Am. Chem. Soc.* **2005**, *127*, 4685–4696.
[13] F. Mühlthau, O. Schuster, T. Bach, *J. Am. Chem. Soc.* **2005**, *127*, 9348–9349.
[14] D. F. Shellhamer, D. T. Anstine, K. M. Gallego, B. R. Ganesh, A. A. Hanson, K. A. Hanson, R. D. Henderson, J. M. Prince, V. L. Heasley, *J. Chem. Soc. Perkin Trans. 2* **1995**, 861–866.
[15] By comparison (±)-steganacin (**2**) is 1.4× less active than colchicine: F. Zavala, D. Guénard, J.-P. Robin, E. Brown, *J. Med. Chem.* **1980**, *23*, 546–549.

 © 2006 Wiley-VCH Verlag GmbH & Co. KGaA, Weinheim

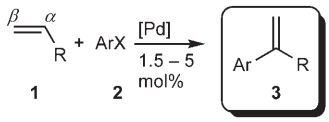
Homogeneous Catalysis

DOI: 10.1002/anie.200600799

The Heck Reaction of Electron-Rich Olefins with Regiocontrol by Hydrogen-Bond Donors

*Jun Mo and Jianliang Xiao**

Considerable progress has been made in the Heck arylation of electron-deficient olefins in the past several years; these olefins generally form linear products.[1,2] However, this is not the case with electron-rich olefins, the intermolecular arylation of which is usually complicated by the formation of a mixture of regioisomers. This problem can be addressed by employing aryl triflates or by adding stoichiometric silver or thallium salts when aryl iodides and bromides are chosen.[3–5] However, triflates are thermally labile and are generally not commercially available, and the inorganic additives create new problems, that is, waste salts, toxicity, and added cost. Additionally, when applied to intermolecular arylation these methods generally afford low turnover numbers (TONs) and turnover frequencies (TOFs), with some reactions requiring exceedingly long times and high catalyst loadings [Eq. (1); OTf = triflate].[5d]



(1)

X	Salt	*t* [h]	Ref.
OTf	–	0.3–24	[5a,b,e,f]
I	TlOAc	0.8–12	[5f]
Br	AgOTf	>24	[5f]
Br	TlOAc	0.7–144	[5c,d,f]

We recently demonstrated that imidazolium ionic liquids in combination with readily available $Pd(OAc)_2$ and 1,3-bis(diphenylphosphino)propane (dppp) form an excellent catalytic system, with which electron-rich olefins can be arylated highly regioselectively by aryl halides without recourse to triflates or any halide scavengers, for example, AgOTf or TlOAc.[6–9] However, the observed TOF ($< 2\ h^{-1}$) and TON (< 40) values are again relatively low. Herein, we report that the regioselective Heck reaction of electron-rich olefins can be greatly accelerated by hydrogen-bond-donating ammonium salts, not only in ionic liquids but in common molecular solvents as well. The use of common solvents would

[*] J. Mo, Prof. Dr. J. Xiao
Liverpool Centre for Materials and Catalysis
Department of Chemistry, University of Liverpool
Liverpool L69 7ZD (UK)
Fax: (+44) 151-794-3589
E-mail: j.xiao@liv.ac.uk

Supporting information for this article is available on the WWW under http://www.angewandte.org or from the author.

WILEY InterScience DISCOVER SOMETHING GREAT
© 2006 Wiley-VCH Verlag GmbH & Co. KGaA, Weinheim

further extend the applicability of the Heck chemistry in synthesis, as until now "the use of additives such as AgOTf or TlOAc or of an ionic liquid solvent is generally required to obtain high α/β selectivity in the Heck reaction of aryl halides" for this class of olefin.[10]

Our recent study indicates that the arylation of electron-rich olefins by Pd–dppp catalysis is inhibited by bromide ions in the ionic liquid 1-butyl-3-methylimidazolium tetrafluoroborate ([bmim][BF_4]).[6a] This behavior is clearly seen in Figure 1 for the arylation of butyl vinyl ether by bromoacetophenone. The dramatic decrease in the arylation rate with increasing bromide concentration suggests that there is an equilibrium before the rate controlling step [Eq. (2)]. An important conclusion then is that the HBr generated from each arylation cycle must be effectively scavenged by NEt_3, as the reaction would otherwise be practically stopped before reaching an approximate conversion of 25%. The trapping of the bromide anions could be brought about by possible hydrogen bonding between $[HNEt_3]^+$ and Br^-, thus rendering the equilibrium in favor of the right side [Eq. (2)]. Hydrogen bonding is indicated as the N–H proton of [$HNEt_3$][BF_4] (0.01M in $CDCl_3$) moves progressively from $\delta = 7.55$ to 10.91 ppm in the ^{1}H NMR spectra upon addition of up to two equivalents of [Br][NBu_4]. Indeed, examples of such hydrogen bonds are abundant in the literature.[11]

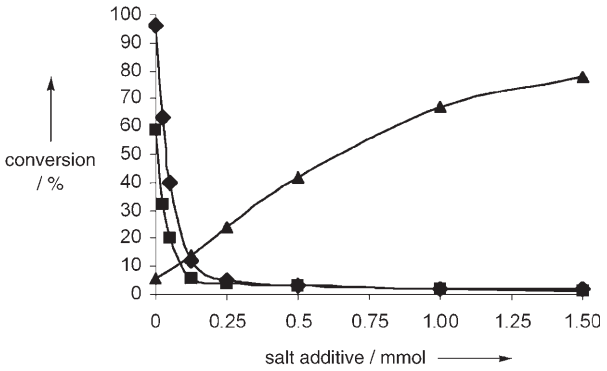
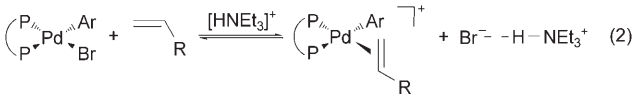
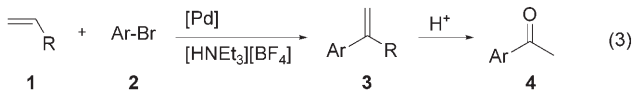


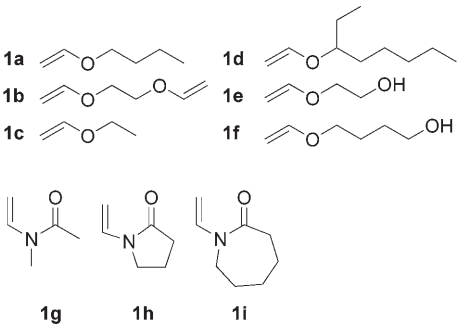
Figure 1. The effect of salt additives on the conversion of bromoacetophenone (**2a**) with butyl vinyl ether (**1a**) at different reaction times: ■ nBu_4NBr, 6 h; ◆ nBu_4NBr, 12 h; ▲ [$HNEt_3$][BF_4], 1 h. Reaction conditions: **1a** (2.0 mmol), **2a** (1.0 mmol), $Pd(OAc)_2$ (2.5 mol%), dppp (5.0 mol%), and Et_3N (1.5 equiv) in [bmim][BF_4] (2 mL) at 115°C.



Given the adverse effect of the bromide ions, introduction of the potential hydrogen-bond donor $[HNEt_3]^+$ should enhance the reaction rates. The accelerating effect of $[HNEt_3]^+$ is clearly revealed in Figure 1. A remarkable illustration of the effect is the comparison between the conversion observed in the presence of 1.5 equivalents of [NBu_4][Br] over 12 hours versus that in the presence of 1.5 equivalents of [$HNEt_3$][BF_4] over 1 hour; the conversions for the former and the latter were 2 and 78%, respectively (Figure 1)! Further evidence in support of the possible involvement of hydrogen bonding came from the observation that replacing [$HNEt_3$][BF_4] with [NBu_4][BF_4] brought about no significant effect on the reaction rate; but reintroduction of [$HNEt_3$][BF_4] did considerably accelerate the reaction in [bmim][BF_4] (see the Supporting Information). We also carried out the same arylation in the presence of 1.5 equivalents of [NBu_4][Br] with increasing palladium loading. However, this approach did not lead to any increase in the conversion (<3%), thus indicating that the inhibition of bromide ions takes place before the reductive elimination of HBr.[12,13]

Based on these investigations, the arylation of electron-rich olefins **1a–i** was carried out with a variety of aryl bromides in [bmim][BF_4] in the presence of [$HNEt_3$][BF_4] [Eq. (3)]. As can be seen from Table 1, all the reactions



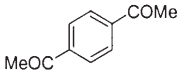
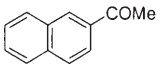
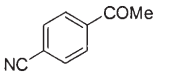
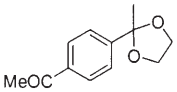
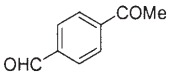
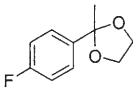
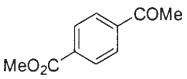
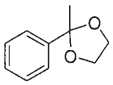
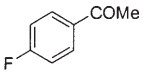
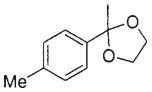
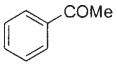
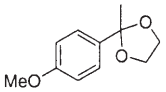
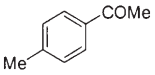
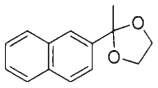
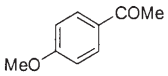
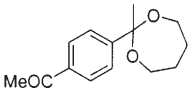
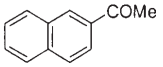
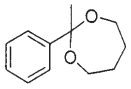
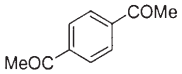
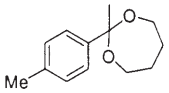
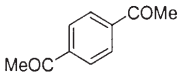
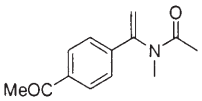
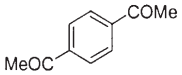
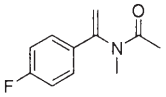
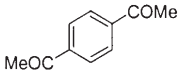
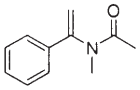
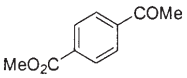
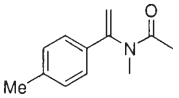
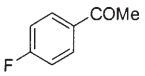
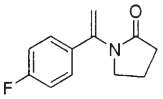
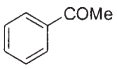
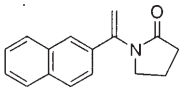
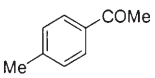
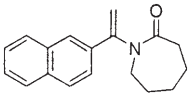


finished with >99:1 regioselectivity of the branched/linear products with good-to-excellent yields. In the case of butyl vinyl ether **1a** (Table 1, entries 1–9), the reactions were all completed in less than 3 hours, regardless of the nature of the substituents on the aryl rings. The isolated products were the ketone **4**, following the acidification of **3**. This outcome is remarkable in comparison with the previous results, in which the reactions needed up to 36 hours for completion without [$HNEt_3$][BF_4].[6a] The vinyl ethers **1b–d** underwent similar, fast arylation by bromoacetophenone **2a** (Table 1, entries 10–12). Most interestingly, the palladium loading could be lowered to 0.1 mol% in the presence of the hydrogen-bond donor, thus bringing the TOF and TON values to up to 83 h^{-1} and 1000, respectively (Table 1, entries 13–18). This result represents the highest TON value ever reported for the internal arylation of electron-rich olefins.

The hydroxyalkyl vinyl ethers **1e–f** could also be arylated, with cyclization of the resulting products to give cyclic ketals. This chemistry was shown to be feasible in dimethylformamide (DMF) by Larhed and Hallberg using aryl triflates or halide scavengers for ArX (X = Br, I); however, the reaction tends to be slow.[5d] Under the present conditions, the reaction was completed within 4 hours, thus providing a practical

 © 2006 Wiley-VCH Verlag GmbH & Co. KGaA, Weinheim

Table 1: $[HNEt_3]^+$-Accelerated regioselective arylation of olefins **1a–i**.[a]

Entry	Olefin	ArBr	Product		*t* [h]	Yield [%]	Entry	Olefin	ArBr	Product		*t* [h]	Yield [%]
1	**1a**	**2a**		**4a**	1.5	94	18[c]	**1a**	**2i**		**4i**	12	91
2	**1a**	**2b**		**4b**	3	89	19	**1e**	**2a**		**3ea**	2	88
3	**1a**	**2c**		**4c**	1.5	90	20	**1e**	**2e**		**3ee**	2	96
4	**1a**	**2d**		**4d**	1.5	95	21	**1e**	**2f**		**3ef**	2	97
5	**1a**	**2e**		**4e**	1.5	96	22	**1e**	**2g**		**3eg**	2	90
6	**1a**	**2f**		**4f**	1.5	94	23	**1e**	**2h**		**3eh**	4	88
7	**1a**	**2g**		**4g**	2	88	24	**1e**	**2i**		**3ei**	4	89
8	**1a**	**2h**		**4h**	3	87	25	**1f**	**2a**		**3fa**	4	83
9	**1a**	**2i**		**4i**	1.5	93	26	**1f**	**2f**		**3ff**	4	91
10[b]	**1b**	**2a**		**4a**	2	97	27	**1f**	**2g**		**3fg**	4	87
11	**1c**	**2a**		**4a**	2	92	28[d]	**1g**	**2a**		**3ga**	4	84
12	**1d**	**2a**		**4a**	2	86	29[d]	**1g**	**2e**		**3ge**	4	81
13[c]	**1a**	**2a**		**4a**	12	91	30[d]	**1g**	**2f**		**3gf**	4	80
14[c]	**1a**	**2d**		**4d**	12	93	31[d]	**1g**	**2g**		**3gg**	4	74
15[c]	**1a**	**2e**		**4e**	12	94	32[d]	**1h**	**2e**		**3he**	4	86
16[c]	**1a**	**2f**		**4f**	12	90	33[d]	**1h**	**2i**		**3hi**	4	83
17[c]	**1a**	**2g**		**4g**	16	87	34[d]	**1i**	**2i**		**3ii**	4	70

[a] Reaction conditions: **1** (2.0 equiv), **2** (1.0 mmol), $[HNEt_3][BF_4]$ (1.5 equiv), $Pd(OAc)_2$ (2.5 mol%), dppp (5.0 mol%), and iPr_2NH (1.5 equiv) in $[bmim][BF_4]$ (2 mL) at 115 °C; 100% conversion and >99:1 regioselectivity for all, as determined by ^1H NMR spectroscopic analysis. Yields of the isolated products; **4** was obtained after acidification of **3**. [b] 0.75 equivalents of **1b** were used. [c] $Pd(OAc)_2$ (0.1 mol%) and dppp (0.2 mol%) were used. [d] Conditions: **1g–i** (1.0 mmol), $Pd(OAc)_2$ (4 mol%), dppp (8 mol%) in DMSO (1 mL), and $[bmim][BF_4]$ (1 mL).

 © 2006 Wiley-VCH Verlag GmbH & Co. KGaA, Weinheim

alternative to the synthesis of ketals, which may find use in the synthesis of anti-HIV agents (Table 1, entries 19–27).[14]

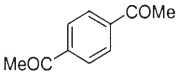
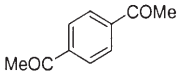
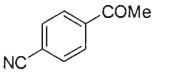
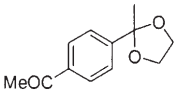
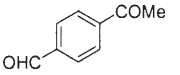
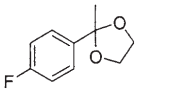
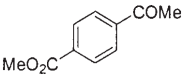
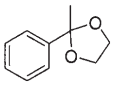
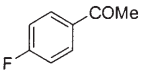
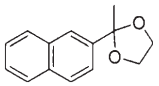
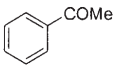
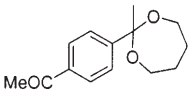
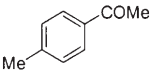
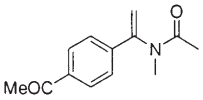
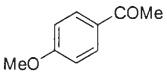
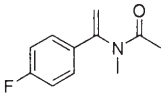
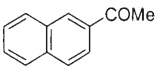
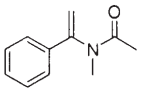
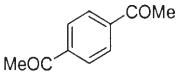
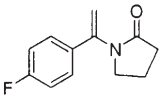
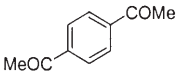
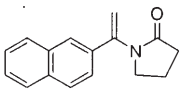
Recently, we reported the first examples of the regioselective arylation of **1g–i** by aryl halides in a mixed solvent of [bmim][BF_4] and dimethyl sulfoxide (DMSO).[6a,15] Again the reactions appeared to be sluggish and required more than 30 hours to complete. In stark contrast, under similar conditions but in the presence of [$HNEt_3$][BF_4], all the reactions went to completion within 4 hours (Table 1, entries 28–34).

The acceleration of the reaction rates was also seen in common solvents. Thus, under conditions identified for [bmim][BF_4] but replacing the ionic liquid with DMF, bromoacetophenone **2a** was olefinated with butyl vinyl ether **1a** with a 38% conversion in 1 hour and gave the α-arylated olefin exclusively according to ^{1}H NMR spectroscopic analysis. By way of contrast, the reaction in the absence of [$HNEt_3$][BF_4] was sluggish and much less selective toward the α-olefin in DMF (75:25 regioselectivity), thus suggesting that the ammonium additive exerts a significant promotion effect on the ionic pathway of the Heck reaction.[3,4] A limited screening shows that the combination of [H_2NiPr_2][BF_4] with DMF is a good choice in terms of effectiveness and cost (see the Supporting Information). Under such conditions, the conversion of **2a** is 12 times that observed without the ammonium salt with exclusive α regioselectivity.

The wider applicability of the new chemistry is demonstrated with the arylation of olefins **1a–h** with aryl bromides **2a–i** (Table 2). Thus, in the presence of [H_2NiPr_2][BF_4] in DMF, all the reactions shown in Table 2 finished with > 99:1 regioselectivity in favor of the branched products with high yields. Relative to those in [bmim][BF_4] (Table 1), however, the reactions in DMF generally required longer reaction times to complete.

Under the action of the ammonium additive, aryl chlorides could also, for the first time, be coupled regiose-

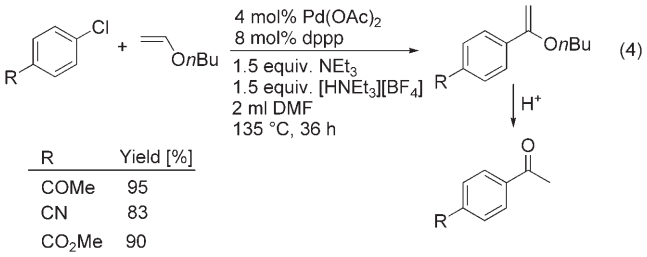
Table 2: [H_2NiPr_2]$^+$-Accelerated regioselective arylation of olefins **1a–h** in DMF.[a]

Entry	Olefin	ArBr	Product		*t* [h]	Yield [%]	Entry	Olefin	ArBr	Product		*t* [h]	Yield [%]
1	**1a**	**2a**		**4a**	4	90	12	**1d**	**2a**		**4a**	4	88
2	**1a**	**2b**		**4b**	8	83	13[c]	**1e**	**2a**		**3ea**	8	85
3	**1a**	**2c**		**4c**	4	87	14[c]	**1e**	**2e**		**3ee**	8	90
4	**1a**	**2d**		**4d**	4	88	15[c]	**1e**	**2f**		**3ef**	8	86
5	**1a**	**2e**		**4e**	4	85	16[c]	**1e**	**2i**		**3ei**	12	84
6	**1a**	**2f**		**4f**	4	91	17[c]	**1f**	**2a**		**3fa**	16	78
7	**1a**	**2g**		**4g**	6	83	18[d]	**1g**	**2a**		**3ga**	16	76
8	**1a**	**2h**		**4h**	10	82	19[d]	**1g**	**2e**		**3ge**	16	75
9	**1a**	**2i**		**4i**	4	89	20[d]	**1g**	**2f**		**3gf**	16	72
10[b]	**1b**	**2a**		**4a**	4	92	21[d]	**1h**	**2e**		**3he**	16	80
11	**1c**	**2a**		**4a**	4	90	22[d]	**1h**	**2i**		**3hi**	16	77

[a] Reaction conditions: **1** (2.0 equiv), **2** (1.0 mmol), [H_2NiPr_2][BF_4] (1.5 equiv), $Pd(OAc)_2$ (2.5 mol%), dppp (5.0 mol%), and NEt_3 (1.5 equiv) in DMF (2 mL) at 115 °C; 100% conversion and > 99:1 regioselectivity for all, as determined by ^{1}H NMR spectroscopic analysis. Yield of the isolated products; **4** was obtained after acidification of **3**. [b] 0.75 equivalents of **1b** were used. [c] The reaction was continued, upon addition of dry HOAc (5 mL) at 80 °C, for a further 2 h at 80 °C before workup.[5d] [d] Reaction conditions: **1g–h** (1.0 mmol), $Pd(OAc)_2$ (4 mol%), and dppp (8 mol%) in DMSO (2 mL).

 © 2006 Wiley-VCH Verlag GmbH & Co. KGaA, Weinheim

lectively with electron-rich olefins. For example, the vinyl ether **1a** was smoothly arylated by activated chlorides [Eq. (4)], thus furnishing the corresponding ketones in high



(4)

R	Yield [%]
COMe	95
CN	83
CO_2Me	90

yields. However, these reactions necessitated harsher conditions and failed with deactivated chlorides under the conditions employed.

In conclusion, we have demonstrated that ammonium salts that can act as hydrogen-bond donors exert a remarkable accelerating effect on the rates of the regioselective arylation of electron-rich olefins by aryl halides in ionic liquids and common solvents. More than two decades ago, tetraalkylammonium salts, such as $[NBu_4][Cl]$, were discovered to accelerate the Heck reaction.[16] The Jeffery conditions can be successfully employed for palladium catalysts containing monodentate phosphines or no ligands. Under such conditions, the Heck reaction presumably proceeds by the neutral pathway,[3] which involves anion-ligated palladium species, as indicated by the extensive studies of Amatore and Jutand.[17] In contrast, the Pd–dppp catalysis described herein is typical of the Heck reaction proceeding by the cationic pathway,[3,4] although the detailed mechanism of the rate acceleration by $[H_nNR_{4-n}]^+$ ($n = 1, 2$) remains open for discussion, particularly with regard to the proposed effect of hydrogen bonding on the equilibrium shown in Equation (2). To the best of our knowledge, the chemistry presented represents the first generic method to conduct the regioselective Heck reaction of electron-rich olefins with aryl halides with no need for silver or thallium-based halide scavengers.

Experimental Section

A typical procedure for the arylation of vinyl ether **1a**: An oven-dried, two-necked round-bottom flask containing a stir bar was charged with an aryl halide **2** (1.0 mmol), $Pd(OAc)_2$ (6 mg, 0.025 mmol), dppp (21 mg, 0.05 mmol), $[HNEt_3][BF_4]$ (284 mg, 1.5 mmol), and $[bmim][BF_4]$ (2 mL) under nitrogen at room temperature. Following degassing three times, **1a** (204 mg, 2.0 mmol) and $HNiPr_2$ (153 mg, 1.5 mmol) were injected sequentially. The flask was placed in an oil bath, and the reaction mixture was stirred and heated at the desired temperature. After an appropriate reaction time, the flask was removed from the oil bath and cooled to room temperature. A small sample was then taken for NMR spectroscopic analysis. To the rest of the mixture, aqueous HCl (5%, 5 mL) was added and following stirring for 0.5 h, CH_2Cl_2 (20 mL) was added. After separation of the CH_2Cl_2 phase, the aqueous layer was extracted with CH_2Cl_2 (2×20 mL) and the combined organic layers were washed with water until neutral, dried (Na_2SO_4), filtered, and concentrated in vacuo. The aryl methyl ketone **4** was isolated by flash chromatography on silica gel using a mixture of ethyl acetate and hexane (1:99 to 10:90) as the eluent. The identity and purity of the product was confirmed by ^1H and ^{13}C NMR spectroscopic, mass-spectrometric, high-resolution mass-spectrometric, and elemental analysis.

Received: March 1, 2006
Published online: May 23, 2006

Keywords: Heck reaction · homogeneous catalysis · hydrogen bonding · ionic liquids · regioselectivity

[1] Recent reviews: a) M. Shibasaki, E. M. Vogl, T. Ohshima, *Adv. Synth. Catal.* **2004**, *346*, 1533; b) R. B. Bedford, C. S. J. Cazin, D. Holder, *Coord. Chem. Rev.* **2004**, *248*, 2283; c) S. Bräse, A. de Meijere in *Metal-Catalyzed Cross-Coupling Reactions*, *Vol. 1* (Eds.: A. de Meijere, F. Diederich), Wiley-VCH, Weinheim, **2004**, p. 217; d) M. Larhed, A. Hallberg in *Handbook of Organopalladium Chemistry for Organic Synthesis*, *Vol. 1* (Ed.: E.-I Negishi), Wiley-Interscience, New York, **2002**, p. 1133; e) A. F. Littke, G. C. Fu, *Angew. Chem.* **2002**, *114*, 4350; *Angew. Chem. Int. Ed.* **2002**, *41*, 4176; f) I. P. Beletakaya, A. V. Cheprakov, *Chem. Rev.* **2000**, *100*, 3009.

[2] Commercial applications: a) A. Zapf, M. Beller, *Top. Catal.* **2002**, *19*, 101; b) J. G. de Vries, *Can. J. Chem.* **2001**, *79*, 1086; c) A. Eisenstadt, D. J. Ager in *Fine Chemicals through Heterogeneous Catalysis* (Eds.: R. A. Sheldon, H. van Bekkum), Wiley-VCH, Weinheim, **1998**, p. 576.

[3] W. Cabri, I. Candiani, *Acc. Chem. Res.* **1995**, *28*, 2.

[4] Examples of mechanistic studies: a) R. J. Deeth, A. Smith, J. M. Brown, *J. Am. Chem. Soc.* **2004**, *126*, 7144; b) H. von Schenck, B. Akermark, M. Svensson, *J. Am. Chem. Soc.* **2003**, *125*, 3503; c) H. von Schenck, B. Akermark, M. Svensson, *Organometallics* **2002**, *21*, 2248.

[5] Recent examples of regioselective arylation: a) A. L. Hansen, T. Skrydstrup, *J. Org. Chem.* **2005**, *70*, 5997; b) K. S. A. Vallin, Q. Zhang, M. Larhed, D. P. Curran, A. Hallberg, *J. Org. Chem.* **2003**, *68*, 6639; c) P. Nilsson, M. Larhed, A. Hallberg, *J. Am. Chem. Soc.* **2001**, *123*, 8217; d) M. Larhed, A. Hallberg, *J. Org. Chem.* **1997**, *62*, 7858; e) W. Cabri, I. Canadiniani, A. Bedeschi, R. Santi, *J. Org. Chem.* **1993**, *58*, 7421; f) W. Cabri, I. Canadiniani, A. Bedeschi, S. Penco, R. Santi, *J. Org. Chem.* **1992**, *57*, 1481.

[6] a) J. Mo, L. Xu, J. Xiao, *J. Am. Chem. Soc.* **2005**, *127*, 751; b) L. Xu, W. Chen, J. Ross, J. Xiao, *Org. Lett.* **2001**, *3*, 295.

[7] The first examples of the Heck reaction in ionic liquids: D. E. Kaufmann, M. Nouroozian, H. Henze, *Synlett* **1996**, 1091.

[8] Recent examples of Heck coupling in ionic liquids: a) D. Zhao, Z. Fei, T. Geldbach, R. Scopelliti, P. J. Dyson, *J. Am. Chem. Soc.* **2004**, *126*, 15876; b) J. Xiao, B. Twamley, J. M. Shreeve, *Org. Lett.* **2004**, *6*, 3845; c) H. Hagiwara, Y. Sugawara, T. Hoshi, T. Suzuki, *Chem. Commun.* **2005**, 2942; d) C. C. Cassol, A. P. Umpierre, G. Machado, S. I. Wolke, J. Dupont, *J. Am. Chem. Soc.* **2005**, *127*, 3298; e) V. Calo, A. Nacci, A. Monopoli, E. Ieva, N. Cioffi, *Org. Lett.* **2005**, *7*, 617.

[9] Recent reviews on ionic liquids: a) N. Jain, A. Kumar, S. Chauhan, S. M. S. Chauhan, *Tetrahedron* **2005**, *61*, 1015; b) T. Welton, *Coord. Chem. Rev.* **2004**, *248*, 2459; c) J. Dupont, R. F. de Souza, P. A. Z. Suarez, *Chem. Rev.* **2002**, *102*, 3667; d) R. Sheldon, *Chem. Commun.* **2001**, 2399; e) P. Wasserscheid, W. Keim, *Angew. Chem.* **2000**, *112*, 3926; *Angew. Chem. Int. Ed.* **2000**, *39*, 3772.

[10] A. F. Littke, G. C. Fu, *J. Am. Chem. Soc.* **2001**, *123*, 6989.

[11] A recent review: J. M. Llinares, D. Powell, K. Bowman-James, *Coord. Chem. Rev.* **2003**, *240*, 57.

[12] Under the conditions of **1a** (2.0 equiv), **2a** (1.0 mmol), nBu_4NBr (1.5 equiv), $Pd(OAc)_2$ (10 mol%), dppp (20 mol%), and Et_3N

 © 2006 Wiley-VCH Verlag GmbH & Co. KGaA, Weinheim

(1.5 equiv) in [bmim][BF_4] (2 mL) at 115 °C for 24 h, the conversion of **2a** was < 3 %.
[13] The formation of [L_2Pd^0] from [L_2PdHX] can be slow, see: I. D. Hills, G. C. Fu, *J. Am. Chem. Soc.* **2004**, *126*, 13178.
[14] A. Bengtson, M. Larhed, A. Hallberg, *J. Org. Chem.* **2002**, *67*, 5852.
[15] This reaction is also feasible with arylboronic acids: M. M. S. Andappan, P. Nilsson, H. von Schenck, M. Larhed, *J. Org. Chem.* **2004**, *69*, 5212; for a more recent example of very efficient regioselective Heck coupling of enamides, see Ref. [5a].
[16] a) T. Jeffery, *J. Chem. Soc. Chem. Commun.* **1984**, 1287; b) R. C. Larock, S. Babu, *Tetrahedron Lett.* **1987**, *28*, 5291; c) T. Jeffery, *Tetrahedron* **1996**, *52*, 10113, and references therein.
[17] C. Amatore, A. Jutand, *Acc. Chem. Res.* **2000**, *33*, 314, and references therein.

 © 2006 Wiley-VCH Verlag GmbH & Co. KGaA, Weinheim

Silyllithium Compounds

DOI: 10.1002/anie.200600308

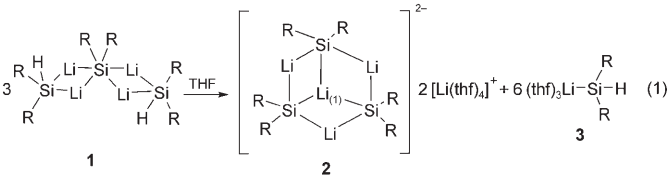
$[\{(t\mathrm{Bu_2Me})_2\mathrm{Si}\}_3\mathrm{Li_4}]^{2-}$: An Aggregated Dianion of a 1,1-Dilithiosilane with a Unique Structural Motif**

Dmitry Bravo-Zhivotovskii, Ilya Ruderfer, Semyon Melamed, Mark Botoshansky, Asher Schmidt, and Yitzhak Apeloig**

In memory of Vadim A. Pestunovich

The chemistry of geminal dilithio reagents of the general type R_2ELi_2 (E = C,[1] Si,[2,3] Ge[4]) is a rapidly developing field. However, the structures of these compounds and their aggregation preferences are still largely unknown. Thus, only a few R_2SiLi_2 compounds have been characterized by X-ray crystallography, all as solvated unaggregated structures.[2e,f,3c] Recently, we reported the structure of unsolvated **1** [see Eq. (1)], which has a unique R_2SiLi_4 core fragment, formed by co-aggregation of one molecule of R_2SiLi_2 with two molecules of R_2SiHLi.[5] Also for solvated geminal dilithio organic compounds R_2CLi_2[1a] only limited structural information is available, although they have important synthetic applications.[1b,6] A solvated dimeric aggregate of a 1,1-dilithiogermane was reported.[4] Gaining structural information on R_2ELi_2 reagents is important because of their synthetic applications[6] and because the chemistry of organolithium and silyllithium reagents is solvent-dependent.[7,8]

Herein we report isolation, X-ray structure analysis, and NMR spectroscopic studies of silyllithium aggregate **2** [Eq. (1), R = tBu$_2$MeSi], which contains the first known



(1)

aggregated silyllithium dianion $[(R_2Si)_3Li_4]^{2-}$. The formation of an aggregated anionic metallic core is common for clusters of Group 13 elements, e.g., $(RIc)_n^{m-}$ (Ic = Al, Ga, In)[9] and for transition metal complexes,[10] but such aggregates were not yet observed for RLi compounds.

When **1** is dissolved in THF two compounds are produced [Eq. (1)]: solvated silyllithium **3**[5] and **2** in 6:1 molar ratio. The formation of aggregate **2** in THF is unexpected, because in most previous cases studied addition of THF led to solvated lithiosilanes[11] or dilithiosilanes.[3c] Evaporation of THF solvent and addition of hexane allowed the separation of hexane-insoluble **2** from hexane-soluble **3**. Crystallization of crude **2** from toluene yielded red crystals suitable for X-ray crystallography.[12] An ORTEP plot of the anion of **2** is shown in Figure 1.

Compound **2** is a new aggregated solvated form of the known dilithiosilane R_2SiLi_2[3d–h] (R = tBu$_2$MeSi) containing three R_2SiLi_2 molecules and eight THF molecules (Figure 1). Its structure consists of $[(R_2Si)_3Li_4]^{2-}$ cluster dianions with a starlike tetralithium core, and with two lithium cations each solvated by four THF molecules. The distance between the solvated lithium cations and the closest silicon atom of around 9 Å indicates that **2** has an ionic structure. The structure of **2** is reminiscent of known ate complexes of the type $(Li^+)_2[R'_3M]^{2-}$, where M = Cu.[13] In **2**, M is the central Li atom (Li1) and R′ is R_2LiSi.

The structure of **2** is very unusual. It has a nearly planar central Si_3Li_3 hexagon and a central lithium atom (Li1) which is located 0.4 Å above the hexagon plane[14] (the sum of the Si1-Li1-Si4, Si1-Li1-Si7, and Si4-Li1-Si7 bond angles is 355.2°, and that of the Li4-Li1-Li3, Li4-Li1-Li2, and Li2-Li1-Li3 bond angles is 348.3°). Li1 is somewhat closer to one of the lithium atoms (Li4) than to the other two (Li2 and Li3). Two of the three Li–Li bonds are in the regular Li–Li bond-length range[15] (2.53 and 2.62 Å) while the third is unusually short (2.18 Å). The Si–Li bond lengths in **2** vary quite significantly (2.42–2.76 Å) but are all in the range of other known Si–Li bond lengths.[11]

[*] Dr. D. Bravo-Zhivotovskii, I. Ruderfer, S. Melamed, Dr. M. Botoshansky, Prof. A. Schmidt, Prof. Y. Apeloig
Department of Chemistry and
the Lise Meitner–Minerva Center for Computational Quantum Chemistry
Technion—Israel Institute of Technology
Haifa 32000 (Israel)
Fax: (+972) 4-829-4601
E-mail: chrbrzh@tx.technion.ac.il
chrapel@tx.technion.ac.il

[**] This research was supported by the Israel Science Foundation administrated by the Israel Academy of Sciences and Humanities, the Fund for the Promotion of Research at the Technion, and the Minerva Foundation in Munich. M.B. and D.B.-Z. are grateful to the Ministry of Immigrant Absorption, State of Israel for a Kamea scholarship. The authors thank Dr. Yael Balazs for helpful discussions and technical assistance.

Supporting information for this article is available on the WWW under http://www.angewandte.org or from the author.

 © 2006 Wiley-VCH Verlag GmbH & Co. KGaA, Weinheim

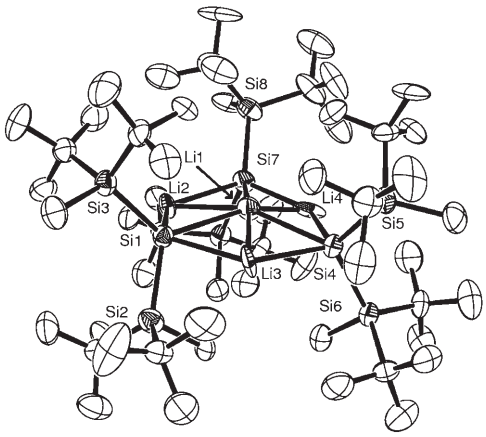


Figure 1. ORTEP plot of the anion of **2**. Hydrogen atoms are omitted for clarity. Selected distances [Å] and angles [°]: Li1-Li3 2.53(2), Li1-Li2 2.62(2), Li1-Li4 2.18(3), Si1-Li3 2.556(16), Si1-Li2 2.613(17), Si1-Li1 2.76(2), Si4-Li4 2.497(16), Si4-Li3 2.610(18), Si4-Li1 2.69(2), Si7-Li4 2.422(17), Si7-Li2 2.675(16), Si7-Li1 2.687(19), Si1-Si2 2.333(5), Si1-Si3 2.350(5); Si2-Si1-Si3 114.89(18), Li3-Si1-Li2 112.6(6), Li3-Si1-Li1 56.6(6), Li2-Si1-Li1 58.3(6), Li4-Si4-Li3 105.1(7), Li4-Si4-Li1 49.6(7), Li3-Si4-Li1 56.9(6), Li4-Si7-Li2 106.2(7), Li4-Si7-Li1 50.2(8), Li2-Si7-Li1 58.5(6), Li4-Li1-Li3 118.7(10), Li4-Li1-Li2 116.1(10), Li2-Li1-Li3 113.5(9), Si1-Li1-Si4 117.4(6), Si1-Li1-Si7 118.7(8), Si4-Li1-Si7 119.1(8), Li3-Li1-Si4 60.0(5), Si4-Li1-Li4 60.6(6); Si1-Li3-Li4-Si7 0.7(5), Si1-Li3-Si4-Li4 −5.7(14), Si1-Li2-Si7-Li4 15.0(12), Li2-Si7-Li4-Si4 −11.9(16), Li2-Si1-Li3-Si4 10.4(15).

Compound **2** was also studied by solid-state and solution NMR spectroscopy. In the solid state the ^{29}Si MAS-NMR chemical shifts of the dianionic Si atoms (Si1, Si4, Si7) appear at −239 and −243 ppm, while in THF solution the signal is shifted slightly to higher field (−254 ppm). These chemical shifts are similar to those of the unsolvated neutral aggregate **1** ($\delta = -251$ ppm) and are shifted downfield by 30–40 ppm relative to that of the central silicon atom in solvated $[(i\mathrm{Pr}_3\mathrm{Si})_2\mathrm{SiLi}_2(\mathrm{thf})_4]$ ($\delta = -282$ ppm).[3c] However, they are strongly shifted to higher field in comparison to those of $[(\mathrm{Me}_3\mathrm{Si})_3\mathrm{SiLi}]_2$ ($\delta = -189$ ppm).[16]

The solid-state ^{7}Li MAS-NMR spectrum of **2** shows two signals: a narrow signal at 0.1 ppm, assigned to the THF-solvated Li^+ cations and a broad signal at 7 ppm corresponding to the four core lithium atoms of **2**.[17] This is the most downfield $\delta(^7\mathrm{Li})$ value reported, except for $[(\mathrm{Li}(\mathrm{dme}_2)]_2$-$[1,2,4,5\text{-}(\mathrm{Me}_3\mathrm{Si})_4\mathrm{C}_6\mathrm{H}_2]$, for which $\delta(^7\mathrm{Li}) = 10.7$ ppm was explained by the strong deshielding effect on the lithium atom of paratropic ring currents resulting from the presence of an 8π antiaromatic system.[18]

The ^{7}Li chemical shifts of solvated silyllithium compounds are around 0.5 ppm,[19] while those of aggregated silyllithium[19] and organolithium[20] compounds are around 3 ppm. Compound **1**, a coaggregate of mono- and dilithium silyl units, has $\delta(^7\mathrm{Li})$ values of 4.2 and 5.4 ppm.[5] The observed $\delta(^7\mathrm{Li})$ value of 7 ppm in **2** is further downfield and consistent with **2** being an aggregate of dilithiosilane.

In THF solution we observed a broad peak from 4.0 ppm to −0.5 ppm and a peak at 6.3 ppm.[17] The significantly lower intensity of the latter indicates that in solution most of **2** dissociates into other silyllithium derivatives.

Compound **2** reacts with water and with MeCl to form in high yields the corresponding disubstitution products R_2SiH_2 and R_2SiMe_2, respectively. Thus, **2** reacts as a 1,1-dilithiosilane.

In conclusion, we have prepared and structurally characterized the first aggregated silyllithium dianion, $[(R_2Si)_3Li_4]^{2-}$, which reacts as a 1,1-dilithiosilane. We are continuing to study the chemistry of **2** and other related dimetal organosilicon compounds.

Experimental Section

Standard Schlenk techniques were used for all syntheses and sample manipulations. **2**: **1** (2.5 g, 2.3 mmol) in THF (20 mL) was gently warmed to 40–60 °C until it had completely dissolved (storage of **1** in THF at room temperature for several days led to substantial decomposition). Immediately afterwards the THF was evaporated. The resulting solid product was washed with hexane (3 × 20 mL) to remove **3**. Crystallization of the crude solid from toluene gave 0.9 g (0.5 mmol, 65 % yield based on **1**) of red crystals of **2**. Solid-state ^{29}Si MAS-NMR (25 °C, TMS): $\delta = 27.7$, 24.8, 23.2 ($\mathrm{Si}(t\mathrm{Bu})_2\mathrm{Me}$), −238.6, −243.2 ppm ($\mathrm{Si}_2\mathit{Si}\mathrm{Li}_4$); solid-state ^{7}Li MAS-NMR (25 °C, LiCl): $\delta = 7$ (br), 0.1 ppm. Solution ^{29}Si NMR (99.4 MHz, THF with $[D_6]$DMSO capillary, 25 °C, TMS): $\delta = 28.5$ (br; $\mathrm{Si}(t\mathrm{Bu})_2\mathrm{Me}$), −254 ppm (br; $\mathrm{Si}_2\mathit{Si}\mathrm{Li}_4$). Solution ^{7}Li NMR (73.6 MHz, THF with DMSO capillary, 25 °C, LiCl in MeOH) $\delta = 6.3$ (br, low-intensity peak), broad peak from 4 to −0.5 ppm.[17]

Received: January 24, 2006
Revised: March 21, 2006
Published online: May 16, 2006

Keywords: anions · cluster compounds · lithium · silicon

[1] a) C. Strohmann, D. Schildbach in *The Chemistry of Organolithium Compounds* (Eds.: Z. Rappoport, I. Marek), Wiley, Chichester, **2004**, pp. 941–996; b) I. Marek, J. F. Normant, *Chem. Rev.* **1996**, *96*, 3241–3267.

[2] a) J. H. Hong, P. Boudjouk, S. Castellino, *Organometallics* **1994**, *13*, 3387–3389; b) U. Bankwitz, H. Sohn, D. R. Powell, R. West, *J. Organomet. Chem.* **1995**, *499*, C7–C9; c) S.-B. Choi, P. Boudjouk, *Tetrahedron Lett.* **2000**, *41*, 6685–6688; d) H. Sohn, *J. Organomet. Chem.* **2004**, *689*, 134–138; e) R. West, H. Sohn, U. Bankwitz, J. Calabrese, Y. Apeloig, T. Mueller, *J. Am. Chem. Soc.* **1995**, *117*, 11608–11609; f) S.-B. Choi, P. Boudjouk, P. Wei, *J. Am. Chem. Soc.* **1998**, *120*, 5814–5815; several disodium and dipotassium silole derivatives are also known: g) W. C. Joo, J. H. Hong, S. B. Choi, H. E. Son, C. H. Kim, *J. Organomet. Chem.* **1990**, *391*, 27–36; h) W. P. Freeman, T. D. Tilley, G. P. A. Yap, A. L. Rheingold, *Angew. Chem.* **1996**, *108*, 960–962; *Angew. Chem. Int. Ed. Engl.* **1996**, *35*, 882–884; i) Y. Liu, T. C. Stringfellow, D. Ballweg, I. A. Guzei, R. West, *J. Am. Chem. Soc.* **2002**, *124*, 49–57.

[3] a) S. K. Mehrotra, H. Kawa, J. R. Baran, Jr., M. M. Ludvig, R. J. Lagow, *J. Am. Chem. Soc.* **1990**, *112*, 9003–9004; b) N. Tokitoh, K. Hatano, T. Sadahiro, R. Okazaki, *Chem. Lett.* **1999**, 931–932; c) A. Sekiguchi, M. Ichinohe, S. Yamaguchi, *J. Am. Chem. Soc.* **1999**, *121*, 10231–10232; d) M. Ichinohe, Y. Arai, A. Sekiguchi, N. Takagi, S. Nagase, *Organometallics* **2001**, *20*, 4141–4143; e) A. Sekiguchi, R. Izumi, V. Ya. Lee, M. Ichinohe, *J. Am. Chem. Soc.* **2002**, *124*, 14822–14823; f) N. Nakata, R. Izumi, V. Ya. Lee, M. Ichinohe, A. Sekiguchi, *J. Am. Chem. Soc.* **2004**, *126*, 5058–5059; g) A. Sekiguchi, S. Inoue, M. Ichinohe, Y. Arai, *J. Am.*

 © 2006 Wiley-VCH Verlag GmbH & Co. KGaA, Weinheim

Chem. Soc. **2004**, *126*, 9626 – 9629; h) N. Nakata, R. Izumi, V. Ya. Lee, M. Ichinohe, A. Sekiguchi, *Chem. Lett.* **2005**, 582 – 583.
[4] a) N. Tokitoh, K. Hatano, T. Sasaki, T. Sasamori, N. Takeda, N. Takagi, S. Nagase, *Organometallics* **2002**, *21*, 4309 – 4311; b) V. Ya. Lee, H. Yasuda, M. Ichinohe, A. Sekiguchi, *Angew. Chem.* **2005**, *117*, 6536 – 6539; *Angew. Chem. Int. Ed.* **2005**, *44*, 6378 – 6381; c) A. Sekiguchi, R. Izumi, S. Ihara, M. Ichinohe, V. Ya. Lee, *Angew. Chem.* **2002**, *114*, 1668 – 1670; *Angew. Chem. Int. Ed.* **2002**, *41*, 1598 – 1600.
[5] D. Bravo-Zhivotovskii, I. Ruderfer, S. Melamed, M. Botoshansky, B. Tumanskii, Y. Apeloig, *Angew. Chem.* **2005**, *117*, 749 – 753; *Angew. Chem. Int. Ed.* **2005**, *44*, 739 – 743.
[6] a) J. F. K. Muller, *Eur. J. Inorg. Chem.* **2000**, 789 – 799; b) C. M. Thomson in *Dianion Chemistry in Organic Synthesis*, CRC Press, Boca Raton, **1994**.
[7] M. Schlosser in *Organometallics in Synthesis: a Manual* (Ed.: M. Schlosser), Wiley, Chichester, **2002**, pp. 5 – 352.
[8] a) G. Korogodsky, M. Bendikov, D. Bravo-Zhivotovskii, Y. Apeloig, *Organometallics* **2002**, *21*, 3157 – 3161; b) D. Bravo-Zhivotovskii, G. Korogodsky, Y. Apeloig, *J. Organomet. Chem.* **2003**, *686*, 58 – 65; c) R. Balasubramanian, J. Oliver, *J. Organomet. Chem.* **1980**, *197*, C7 – C11.
[9] a) G. Linti, H. Schnöckel, *Coord. Chem. Rev.* **2000**, *206–207*, 285 – 319; b) R. B. King, G. H. Robinson, *J. Organomet. Chem.* **2000**, *597*, 54 – 60; c) R. B. King, *Inorg. Chem.* **1989**, *28*, 2796; d) J.-T. Zhao, J. D. Corbett, *Inorg. Chem.* **1995**, *34*, 378.
[10] F. A. Cotton, G. Wilkinson, C. A. Murillo, M. Bochmann in *Advanced Inorganic Chemistry*, 6th ed., Wiley, New York, **1999**, pp. 652 – 674.
[11] a) P. Lickiss, C. Smith, *Coord. Chem. Rev.* **1995**, *145*, 75 – 124; b) K. Tomao, A. Kawachi, *Adv. Organomet. Chem.* **1995**, *38*, 1 – 58; c) J. Belzner, U. Dehnert in *The Chemistry of Organic Silicon Compounds*, *Vol. 2* (Eds.: Z. Rappoport, Y. Apeloig), Wiley, Chichester, **1998**, pp. 779 – 825; d) A. Sekiguchi, V. Y. Lee, M. Nanjo, *Coord. Chem. Rev.* **2000**, *210*, 11 – 45.
[12] Crystallographic data for **2**: $C_{86}H_{170}Li_6Si_9O_8$, $M_r = 1626.67$, monoclinic, space group *Cc*, $a = 18.831(4)$, $b = 24.571(5)$, $c = 24.113(5)$ Å, $\beta = 96.34(2)°$, $V = 11089(4)$ Å^3, $Z = 4$, Nonius Kappa CCD, $Mo_{K\alpha}$ radiation (0.71073 Å), 220 K, $2\theta_{max} = 50°$, $R = 0.0673$ ($I > 2\sigma I$), $wR2 = 0.1109$ ($I > 2\sigma I$), $R_w = 0.2312$ (all data), GOF = 0.838. CCDC 283189 contains the supplementary crystallographic data for this paper. These data can be obtained free of charge from The Cambridge Crystallographic Data Centre via www.ccdc.cam.ac.uk/data_request/cif..
[13] E. Nakamura, S. Mori, *Angew. Chem.* **2000**, *112*, 3902 – 3924; *Angew. Chem. Int. Ed.* **2000**, *39*, 3750 – 3771.
[14] Deviations [Å] from the mean plane (calculated by MPLA in SHELXL97): Si1 0.1042(0.0116), Si4 0.0(0.0116), Si7 0.1086(0.0108), Li2 −0.1425(0.0111), Li3 −0.0295(0.0121), Li4 −0.0409(0.0121); the distance of Li1 from the hexagon plane is 0.416(0.0241) Å).
[15] T. Stey, D. Stalke in *The Chemistry of Organolithium Compounds* (Eds.: Z. Rappoport, I. Marek), Wiley, Chichester, **2004**, pp. 47 – 120.
[16] K. Klinkhammer, *Chem. Eur. J.* **1997**, *3*, 1418 – 1431.
[17] For ^{7}Li MAS-NMR and ^{7}Li NMR spectra of **2**, see Supporting Information.
[18] A. Sekiguchi, K. Ebata, C. Kabuto, H. Sakurai, *J. Am. Chem. Soc.* **1991**, *113*, 7081 – 7082.
[19] M. Nanjo, A. Sekiguchi, H. Sakurai, *Bull. Chem. Soc. Jpn.* **1998**, *71*, 741 – 747.
[20] W. Bauer in *Lithium Chemistry* (Eds.: A. M. Sapse, P. von R. Schleyer), Wiley, New York, **1995**, pp. 125 – 172.

 © 2006 Wiley-VCH Verlag GmbH & Co. KGaA, Weinheim

Analytical Methods

DOI: 10.1002/anie.200504509

Radical Photochemistry in Oxygen-Loaded Ices

Sandrine Lacombe, Fabrice Bournel, Carine Laffon, and Philippe Parent*

The photochemistry of molecular oxygen and water films is a fundamental and growing field of investigation for which the main interest is a full understanding of the "far-out" chemistry[1–6] relevant to the new field of astrobiology.[7–9] Another field of interest concerns the study of oxygen and water radiation chemistry relevant to the medical applications of radiobiology.[10] Indeed, oxygen-derived radicals are known to play an important role in the biochemistry of living cells exposed to ionizing radiation. Therefore, a better understanding of the basic physicochemical processes involved in the transformation of oxygen and aqueous media exposed to ionizing radiation is of fundamental interest.

The last decade has seen a proliferation of studies concerning the chemical reactivity of condensed molecular films submitted to different types of ionizing radiation. The reactivity of molecular oxygen and ozone films induced by electronic,[11] ionic,[12] and UV/IR[13] irradiation as well as the reactivity of water ice[14–18] has been extensively studied. In most of these studies, ozone (O_3) and hydrogen peroxide (H_2O_2) molecules, transient species such as the hydroperoxy ($HO_2^{\bullet}$) and the hydroxyl ($OH^{\bullet}$) radicals, and atomic oxygen are often mentioned as possible intermediate products. To the best of our knowledge there are two direct techniques that have been used to characterize the chemical composition of films in situ. IR spectroscopy led to the observation of O_3 in a molecular-oxygen film irradiated by UV light.[14] The same technique allowed the observation of H_2O_2 and $OH^{\bullet}$ in water ice irradiated by high energy ions[19] and by UV light.[17,20] In these studies the chemical analysis was not complete—in particular, the atomic oxygen and the $HO_2^{\bullet}$ radicals were not detected. In earlier studies Taub and Eiben[21] used electron spin resonance spectroscopy to follow the production of $OH^{\bullet}$ and $HO_2^{\bullet}$ as radiolytic products from crystalline ice irradiated with high energy electrons. However the radicals were observed at temperatures up to 0 °C, which is in contradiction with many recent studies, and requires reconsideration of their identification. The ESR technique has more recently been successfully applied as a direct technique for the observation of radicals in water ice irradiated by γ rays, with

[*] Dr. S. Lacombe
Laboratoire des Collisions Atomiques et Moléculaires
Université Paris Sud 11
91405 Orsay Cedex (France)
Fax: (+33) 1-6915-7671
E-mail: sandrine.lacombe@lcam.u-psud.fr
Dr. F. Bournel, Dr. C. Laffon, Dr. P. Parent
Laboratoire de Chimie Physique-Matière et Rayonnement
Université Pierre et Marie Curie
75231 Paris Cedex 05 (France)

© 2006 Wiley-VCH Verlag GmbH & Co. KGaA, Weinheim

$OH^{\bullet}$ and $HO_2^{\bullet}$ being detected simultaneously.[18] However, in this case the film characterization remained incomplete since the other radiolysis products such as the $O^{\bullet}$ radicals, H_2O_2, and O_2 were absent.

Here we show a complete in situ measurement of all the oxygen-derived radiolysis products. We can thus clearly analyze the final chemical composition of an irradiated matrix as a function of the irradiation dose and the initial composition of the film. In the case of oxygen-loaded films we observe the presence of atomic oxygen as well as ozone, whereas ozone does not appear in the irradiated pure water ice. In the condensed films containing water, the irradiation induces the production of radicals, for example, $OH^{\bullet}$, $O^{\bullet}$, and $HO_2^{\bullet}$, as well as H_2O_2. These results indicate the advantage of low-temperature near-edge X-ray absorption fine structure (NEXAFS) spectroscopy as a direct and powerful probe technique which allows the simultaneous detection of the products (molecules or radicals) in situ. It opens up exciting new perspectives in the advances of chemical analysis, dose-dependence analysis, and the kinetic study of irradiated condensed media.

The oxygen k-edge absorption spectra of a pure O_2 film measured before and after irradiation are presented in Figure 1. The results have been background-subtracted and normalized at 552 eV. Spectrum a corresponds to the typical NEXAFS spectrum of non-irradiated condensed oxygen.[23] Spectra b–d were measured after three successive irradiations of the film.

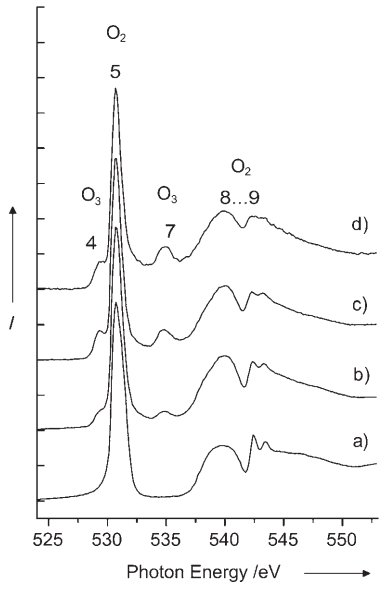


Figure 1. O K-edge photoabsorption spectrum of a molecular O_2 film, before irradiation (a) and after increasing irradiation (b: 1/3×1.6, c: 2/3×1.6, d: 1.6 eV mol^{-1}). The background has been subtracted from the spectra and they have been vertically shifted for clarity. The assignment of the peaks is given in Table 1.

The peaks 5, 8, and 9 are characteristic of the electronic transitions of molecular oxygen O1s→π*, O1s→σ* ($^2\Sigma$ state), and O1s→σ* ($^4\Sigma$ state), respectively.[23] Peak 5 is found at 530.7 eV as previously reported[23,24] and is used here as the energy reference for the other measurements. In addition to the structures arising from O_2 molecules (peaks 5, 8, and 9) we observe two new features (peaks 4 and 7) after irradiation. According to previous measurements[24] these two structures correspond to the NEXAFS signature of O_3 in the condensed phase. Peak 4 corresponds to the $O_{terminal}1s\rightarrow\pi^*(2b_1)$ transition in O_3. Peak 7 is asymmetric, as in the gas phase, and consists of two (not resolved) contributions: $O_{central}1s\rightarrow\pi^*(2b_1)$ and $O_{terminal}1s\rightarrow\sigma^*(7a_1)$. This structure is shifted to slightly lower energy relative to that in the gas phase (0.6 eV). Since peak 4 remains at the same position, the corresponding orbitals (π* and $O_{terminal}1s$) are not perturbed by the condensed phase environment. The $O_{central}1s$ orbital, which is an inner orbital, should not be perturbed either. Therefore, we explain this low energy shift of peak 7 by the perturbation of the external molecular orbital σ* of ozone, which sees its bonding character modified as a result of the solvation in the condensed matrix.[23] Finally our results show chemical changes in the irradiated O_2 film, in particular the synthesis of O_3, which agrees with previous measurements.[11]

The simplest mechanism for the synthesis of O_3 consists of the following two-step reaction:

1) O_2 dissociates by photoexcitation[25,26] or dissociative electron attachment:[27] $O_2 + h\nu$ (or e^-)→$O(^1D)$ or $O(^3P)$ or $O^-(^2P)$, and associated products;
2) O_3 is synthesized in the presence of atomic and molecular oxygen by the exothermic reaction: $O_2 + O\rightarrow O_3$.[28] There is no atomic oxygen released in the film (no peak at 527.2 eV). The reaction of O^- with O_2, which presents an energy threshold, is not considered as a favorite pathway for the formation of O_3.

O_3 may further dissociate by photolysis, by electron-stimulated dissociation,[25,29] or by collision.[16] The maximum intensity of the O_3 peak corresponds to the maximum concentration of O_3 when an equilibrium between the production/destruction of the product is achieved. The spectra presented in Figure 1 have been measured under the same experimental conditions. The peak intensities are thus indicative of the chemical composition of the film. According to the absorption cross-sections of Gejo et al.,[24] the estimated proportion of O_3 produced in pure O_2 is on the order of 8% at saturation.

The role of the environment on the chemical reactivity of the film was investigated by performing measurements with different heterogeneous films: O_2 in an inert matrix (argon) and O_2 in a reactive matrix (H_2O). The NEXAFS spectra obtained after irradiation of the pure O_2 layer at saturation and of the film composed of O_2/Ar (50%:50%) are presented in Figure 2. Irradiation of the heterogeneous film leads to the production of O_3 (peaks 4 and 7) as observed in the pure O_2 medium. The intensity of O_3 relative to O_2 decreases from approximately 8% in the pure O_2 film, as mentioned previously, to 4% in the O_2/Ar mixture. The decrease in the rate of O_3 synthesis by a factor of two in Ar corresponds to the dilution factor of O_2 in Ar. Under these conditions the irradiation of O_2 leads to the formation of atomic oxygen but half of it interacts with the surrounding oxygen molecules to produce O_3, while the second half migrates to be trapped in

 © 2006 Wiley-VCH Verlag GmbH & Co. KGaA, Weinheim

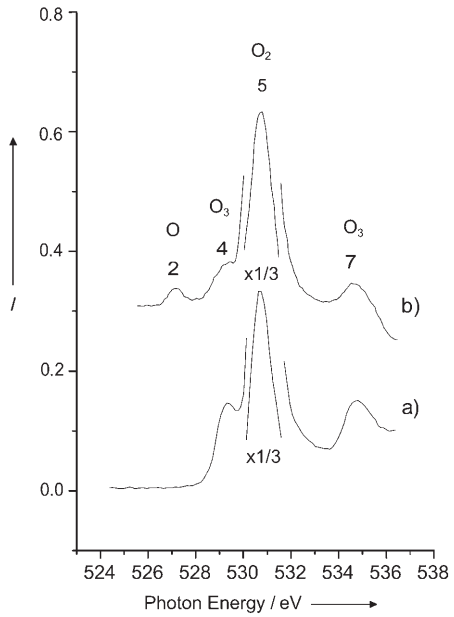


Figure 2. O K-edge absorption spectra obtained after irradiation of a) pure O_2 and b) 50:50 O_2/Ar films. The results have been background-subtracted and normalized to peak 5. The spectra have been vertically shifted for clarity. The identification of the peaks is given in Table 1.

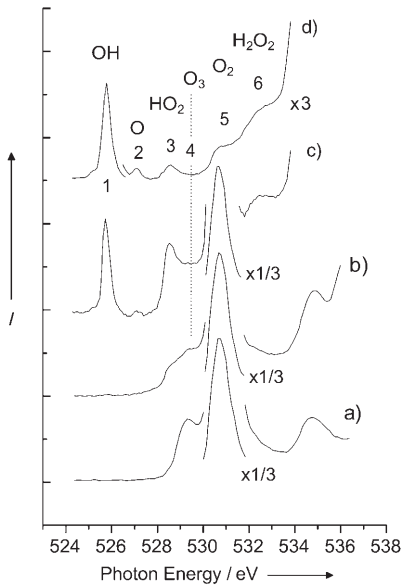


Figure 3. O K-edge absorption spectra obtained after irradiation of pure and heterogeneous films a) pure O_2, b) 50:50 O_2/H_2O, c) 10:90 O_2/H_2O, and d) pure water ice. The results have been background-subtracted. Spectra a–c have been normalized against peak 5. Spectrum d has been normalized against peak 1 of spectrum 2 c. The spectra have been vertically shifted for clarity. The identification of the peaks is given in Table 1.

the Ar matrix. This proposal is supported by the observation of peak 2 at 527.2 eV which corresponds to atomic oxygen[30] (Table 1). The spectra measured with 10 % and 50 % O_2 in the water ice, as well as the spectra obtained with pure O_2 and pure H_2O condensed films are shown in Figure 3.

Table 1: Energy position of the different features observed in the successive NEXAFS measurements.

Peak	Energy [eV] ($\pm$0.1 eV)	Electronic transition
1	525.8	$OH^{\bullet}$ ($O1s \rightarrow 2p_O$)[30,31] (1π)
2	527.2	$O^{\bullet}$ ($O1s \rightarrow 2p_O$)[30,31] (2p)
3	528.6	$HO_2^{\bullet}$ ($O1s \rightarrow \pi^*_{O\text{-}O}$) ($2A''$)
4	529.3	O_3 ($O1s_{terminal} \rightarrow \pi^*_{O\text{-}O\text{-}O}$)[24] ($2B_1$)
5	530.7	O_2 ($O1s \rightarrow \pi^*_{O\text{-}O}$)[23,24] ($1\pi_g$)
6	532.6	H_2O_2 ($O1s \rightarrow \sigma^*_{O\text{-}O}$)[33] ($3B_u$)
7	534.8	O_3 ($O1s_{central} \rightarrow \pi^*_{O\text{-}O}$)[24] ($2B_1$)
		O_3 ($O1s_{terminal} \rightarrow \sigma^*_{O\text{-}O}$)[24] ($4B_2$)
		and/or
		H_2O ($O\ 1s \rightarrow \sigma^*_{O\text{-}H}$)[22] ($4a_1$)
8···9	540···	O_2($O1s \rightarrow \sigma^*_{O\text{-}O}$)[23] ($2\sigma_u$) ($^2\Sigma$, $^4\Sigma$)

Before irradiation O_2 does not react chemically with H_2O at 25 K. After irradiation the spectra indicate the presence of new products. The very low temperature means that transient species are stabilized in the condensed media and can be characterized by absorption spectroscopy. We were thus able to identify three different radicals. Peaks 1 and 2 are characteristic of the hydroxyl radical ($OH^{\bullet}$) and of atomic oxygen ($O^{\bullet}$), respectively.[30,31] Atomic oxygen in particular has already been mentioned as coexisting with water ice through formation of the complex $H_2O{\cdot}O$.[32] The structure observed at 532.6 eV (peak 6) corresponds to hydrogen peroxide (H_2O_2).[33] To the best of our knowledge, the species giving rise to peak 3 at 528.5 eV has not been characterized yet. The intensity of this peak varies differently with the composition of the film from those of $OH^{\bullet}$, $O^{\bullet}$, O_2, O_3, and H_2O_2, thus showing that peak 3 is related to another chemical species. The fact that peak 3 increases in intensity in 10:90 O_2/H_2O indicates that the concentration of the product is enhanced by reactions that mix the O_2 and H_2O photoproducts or/and O_2 and H_2O reactant molecules. Such reactions lead to $H^{\bullet}$, H_2 (which are not detected), $OH^{\bullet}$, $O^{\bullet}$, O_3, O_2, H_2O_2, and $HO_2^{\bullet}$. Among these six oxygen compounds, five have been already identified ($OH^{\bullet}$, $O^{\bullet}$, O_2, O_3, and H_2O_2), but not the $HO_2^{\bullet}$ radical. We therefore assign peak 3 to $HO_2^{\bullet}$. $HO_2^{\bullet}$, an expected product from the radiolysis of pure water ice,[15,16,19,21] is also observed in Figure 3 trace d. Peak 3 is less intense in the 50:50 O_2/H_2O mixture than in the 10:90 O_2/H_2O mixture; this observation is explained by the decrease in H and $OH^{\bullet}$ availability as the water content decreases, as discussed below. Similar to the $OH^{\bullet}$ transition, peak 3 corresponds to the less energetic excitation, for example, from the inner shell (O1s) to the low-lying orbital (that is, the half-occupied π orbital). Peak 3 is the first identification of the hydroperoxyl radical ($HO_2^{\bullet}$) by NEXAFS spectroscopy.

We have shown that this experimental method consists of a direct chemical analysis of the medium, which allows the simultaneous observation of the different products, such as neutral molecules and radicals, synthesized at the early stage of irradiation. In particular, these results show how strongly the presence of molecular oxygen influences the reactivity of the ice under irradiation. This procedure gives an insight into

 © 2006 Wiley-VCH Verlag GmbH & Co. KGaA, Weinheim

the processes involved in the chemistry of the film. The reactions (1)–(5) are exothermic in the condensed phase and give rise to the production of the hydroperoxyl radical and hydrogen peroxide:[16]

$$O_2 + H^{\cdot} \rightarrow HO_2^{\cdot} \quad \Delta H = -2.00\,eV \tag{1}$$

$$O^{\cdot} + OH^{\cdot} \rightarrow HO_2^{\cdot} \quad \Delta H = -2.73\,eV \tag{2}$$

$$OH^{\cdot} + H_2O_2 \rightarrow HO_2^{\cdot} + H_2O \quad \Delta H = -1.28\,eV \tag{3}$$

$$H^{\cdot} + HO_2^{\cdot} \rightarrow 2\,OH^{\cdot} \quad \Delta H = -1.67\,eV \tag{4}$$

$$OH^{\cdot} + OH^{\cdot} \rightarrow H_2O_2 \quad \Delta H = -2.17\,eV \tag{5}$$

The production of H_2O_2, which is thermodynamically allowed in the condensed phase, consists of the interaction of two hydroxyl radicals (reaction 5). Recently it has been shown that the dissociation of O_2 by electron attachment and production of negative ions, leads to the formation of H_2O_2 by an exothermic reaction between O^- and H_2O.[34,38] This process would explain the increase in H_2O_2 relative to $OH^{\cdot}$ in the presence of 10% O_2 in ice. Other reactions which are exothermic in aqueous solutions ($HO_2^{\cdot} + HO_2^{\cdot} \rightarrow H_2O_2 + O_2$)[35] or in the gas phase ($O(1D) + H_2O \rightarrow H_2O_2$),[36] have been proposed to explain the synthesis of H_2O_2.[34,37] However, the transposition of these results to the condensed phase is not apparent. It has also been proposed that H_2O_2 can be produced by dissociation of a complex such as $H{-}OH{\cdots}O_3 \rightarrow 2\,H_2O_2$, which is not compatible with our findings since O_3 is not observed in the irradiated water ice.[20] The synthesis of $HO_2^{\cdot}$ takes place through the three reactions (1)–(3). The bimolecular reaction (1), which involves a molecule of the matrix (O_2) and a dissociation product ($H^{\cdot}$), must be more efficient than reactions (2) and (3), which involve two dissociation products. The increase in the intensity of peak 3 relative to that of peaks 1, 2, and 6 when water is loaded with 10% oxygen (Figure 3c) is consistent with a higher yield of reaction (1) in the presence of O_2. When the proportion of O_2 reaches 50% in the film (Figure 3b), peaks 1, 3, and 6 should decrease with the amount of water in the mixture (by a factor of approximately 2). Peak 1 ($OH^{\cdot}$) however disappears totally. This observation shows that reaction (2) becomes more efficient when atomic oxygen is present in the film (because of O_2 dissociation). Peak 3 ($HO_2^{\cdot}$), however, does not increase since the rates of reactions (1)–(3) also decrease with the water proportion. Finally, peak 2 (O) disappears as a consequence of reaction (2) occurring, as well as through the competitive synthesis of ozone ($O_2 + O \rightarrow O_3$).

In conclusion, the radiation chemistry of condensed molecular films has been investigated by NEXAFS spectroscopy. Experiments performed at low temperature with different heterogeneous films of O_2 mixed with inert (Ar) and reactive (H_2O) media have underlined the crucial role of the environment. We present here, in particular, the first simultaneous observation of all the transients (molecules and radicals) produced in an irradiated molecular film. This method is thus directly applicable to astrochemistry: the simultaneous analysis of the transient species produced in ices submitted to irradiation would give a more complete picture of the photochemistry in interstellar and stratospheric ice particles. This technique also has applications in an another field of the radiation chemistry; in particular it is promising for the study of the properties of complex molecules of medical interest, such as radiosensitizers. Such molecules are known to enhance the lethal effect of ionizing radiation in living cells, which is commonly attributed to the production of $OH^{\cdot}$ radicals in the medium.[10] NEXAFS spectroscopy would therefore be a valuable tool for studying the radiation chemistry of radiosensitizing molecules trapped in water ice and would thus greatly advance the understanding of their function at a molecular level.

Experimental Section

The NEXAFS experiments were performed on the SACEMOR UHV experimental setup on the high-energy SM-PGM monochromator ($E/\Delta E = 5000$) of the SuperACO SA2 bending magnet beamline (LURE—Orsay, France).[22] The data presented here were recorded in the total electron yield (TEY) mode. The films were deposited at 25 K by background exposure of a clean Pt(111) surface to the desired proportions of oxygen (99.99%, Air Liquide), argon (99.99%, Messer), and/or ultrapure water at a rate of 0.1 Langmuir (1 Langmuir $= 1 \times 10^{-6}$ Torr s). The film compositions were deduced from the mass spectra of the gas mixtures recorded during the dosing (assuming a sticking coefficient of unity for O_2, H_2O, and Ar at 25 K). The films were typically 100 monolayers thick. The synchrotron beam was used for irradiation. The accumulated dose for a saturation concentration of the photoproducts (see below) is on the order of 1.6 eV mol^{-1}. The measurements resulting from the irradiation of the sample either with monochromatic beams of 530.7 eV (resonant excitation to the electronic state of the oxygen), 520 eV, or 540 eV (out of the oxygen resonance) or with a white beam (continuous light from 3 to 900 eV) did not show any significant difference. We can deduce that the energy of the primary photon excitation (in the 500 eV range) does not play a key role: the photoprocess is thus dominated by interactions of the material with the low-energy secondary electrons produced by the primary photon interaction, regardless of whether the photon interaction is resonant on an electronic state (monochromatic beam) or not (white beam).[14] The white beam, whose photon flux is 200 times higher than the monochromatic beam, was used to reduce the time of irradiation. The NEXAFS spectra were recorded under low-intensity monochromatic conditions, so the irradiation damage to the films during the acquisition was negligible.

Received: December 19, 2005
Revised: March 28, 2006
Published online: May 16, 2006

Keywords: analytical methods · EXAFS spectroscopy · photochemistry · radical reactions · water chemistry

[1] a) E. Herbst, *Angew. Chem.* **1990**, *102*, 627; *Angew. Chem. Int. Ed.* **1990**, *29*, 595; b) H. Roberts, E. Herbst, *Astron. Astrophys.* **2002**, *395*, 233.
[2] T. E. Madey, R. E. Johnson, T. M. Orlando, *Surf. Sci.* **2002**, *500*, 838.
[3] R. W. Carlson, M. S. Anderson, R. E. Johnson, W. D. Smythe, A. R. Hendrix, C. A. Barth, L. A. Soderblom, G. B. Hansen, T. B. McCord, J. B. Dalton, R. N. Clark, J. H. Shirley, A. C. Ocampo, D. L. Matson, *Science* **1999**, *283*, 2062.
[4] C. Ponnamperuna, *Icarus* **1976**, *29*, 321.

 © 2006 Wiley-VCH Verlag GmbH & Co. KGaA, Weinheim

[5] Y. Aikawa, N. Ohashi, E. Herbst, *Astron. Astrophys.* **2003**, *593*, 906.
[6] M. T. Sieger, W. C. Simpson, T. M. Orlando, *Nature* **1998**, *394*, 554.
[7] E. L. Shock, *Nature* **2002**, *416*, 380.
[8] A. Brack, *Adv. Space Res.* **1999**, *24*, 417.
[9] J. Whitfield, *Nature* **2004**, *430*, 288.
[10] a) A. Chatterjee, W. R. Holley, *Int. J. Quantum Chem.* **2004**, *39*, 709 – 727; b) K. Kobayashi, H. Frohlich, N. Usami, C. Le Sech, K. Takakura, *Radiat. Res.* **2002**, *157*, 32.
[11] S. Lacombe, F. Cemic, K. Jacobi, N. Hedhili, Y. Le Coat, R. Azria, M. Tronc, *Phys. Rev. Lett.* **1997**, *79*, 1146.
[12] D. A. Bahr, M. Fama, R. A. Vidal, R. A. Baragiola, *J. Geophys. Res.* **2001**, *106*, 33, 285.
[13] L. Schvriver-Mazzuoli, *Phys. Chem. Earth C* **2001**, *26*, 495.
[14] T. M. Orlando, M. T. Sieger, *Surf. Sci.* **2003**, *528*, 1.
[15] R. A. Baragiola, *Planet. Space Sci.* **2003**, *51*, 953.
[16] R. E. Johnson, T. I. Quickenden, *J. Geophys. Res.* **1997**, *102*, 10, 985.
[17] F. Borget, T. Chiavassa, A. Allouche, J. P. Aycard, *J. Phys. Chem. B* **2001**, *105*, 449.
[18] A. Plonka, E. Szajdzinska-Pietek, J. Bednarek, A. Hallbrucher, E. Mayer, *Phys. Chem. Chem. Phys.* **2000**, *2*, 1587.
[19] O. Gomis, M. A. Satorre, G. Strazzula, G. Leto, *Planet. Space Sci.* **2004**, *52*, 371.
[20] L. Schvriver-Mazzuoli, L. Barreau, C. A. Schriver, *Chem. Phys.* **1990**, *140*, 429.
[21] a) K. Eiben, *Angew. Chem.* **2003**, *115*, 652; *Angew. Chem. Int. Ed.* **2003**, *42*, 619; b) I. A. Taub, K. Eiben, *J. Chem. Phys.* **1968**, *49*, 2499.
[22] P. Parent, C. Laffon, C. Mangeney, F. Bournel, M. Tronc, *J. Chem. Phys.* **2002**, *117*, 10842.
[23] J. Stöhr, *NEXAFS Spectroscopy*, *Vol. 25* (Ed.: R. Gomer), Springer Series in Surface Sciences, Springer, Berlin, **1992**, p. 236.
[24] T. Gejo, K. Okada, T. Ibuki, *Chem. Phys. Lett.* **1997**, *277*, 497 – 501.
[25] M. Allan, *J. Phys. B* **1995**, *28*, 4329.
[26] K. Wakiya, *J. Phys. B* **1978**, *11*, 3913.
[27] R. Azria, L. Parenteau, L. Sanche, *Phys. Rev. Lett.* **1987**, *59*, 638.
[28] H. I. Schiff, *Appl. At. Collision Phys.* **1982**, *1*, 293.
[29] J. D. Skalny, S. Matejcik, A. Kiendler, A. Stamatovic, T. D. Märk, *Chem. Phys. Lett.* **1996**, *255*, 112.
[30] M. Alagia, M. Coreno, M. de Simone, R. Richter, S. Stranges, *J. Electron Spectrosc. Relat. Phenom.* **2001**, *114–116*, 85.
[31] S. Stranges, R. Richter, M. Alagia, *J. Chem. Phys.* **2002**, *116*, 3676.
[32] L. Khriatchev, M. Petterson, M. Jolkkonen, S. Pehkonen, M. Rasanen, *J. Chem. Phys.* **2000**, *112*, 2187.
[33] E. Rühl, A. P. Hitchcock, *Chem. Phys.* **1991**, *154*, 323.
[34] X. Pan, A. D. Bass, J. P. Jay-Gerin, L. Sanche, *Icarus* **2004**, *172*, 521.
[35] B. H. J. Bielski, D. E. Cabelli, R. L. Arudi, A. B. Ross, *J. Phys. Chem.* **1985**, *89*, 1041.
[36] R. Sayos, C. Oliva, M. Gonzàlez, *J. Chem. Phys.* **2000**, *113*, 6736.
[37] P. D. Cooper, R. E. Johnson, T. I. Quickenden, *Icarus* **2003**, *166*, 444.
[38] H. S. W. Massey, *Negative Ions*, Cambridge University Press, **1976**, p. 513.

 © 2006 Wiley-VCH Verlag GmbH & Co. KGaA, Weinheim

Cumulene Synthesis

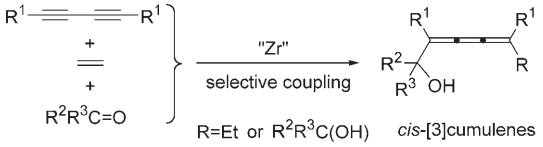
DOI: 10.1002/anie.200600520

Highly Stereoselective Synthesis of TMS-, Alkyl-, or Aryl-Substituted *cis*-[3]Cumulenols via α-Alkynylated Zirconacyclopentenes**

Yuanhong Liu, Hongjun Gao, and Shaolin Zhou*

[3]Cumulenes have attracted much attention in recent years because they have potential applications in antitumor-drug design[1] and as advanced materials with unique electronic and photonic properties, for example, as molecular wires, nonlinear optical systems, ferromagnets, conjugated polymers, etc.[2] They also serve as useful building blocks for two-dimensional carbon networks such as radialenes.[3] Although a number of methods are available for the construction of cumulenes,[1,4] most of them lead to a mixture of *E* and *Z* isomers.

Surprisingly, the stereoselective synthesis of cumulenes with reasonable generality is quite rare.[5] The *cis*-selective synthesis of acyclic cumulenes has been achieved either by Ru- or Ir-catalyzed dimerization[5a–c] of terminal alkynes with $[Ru(CO)(PPh_3)_3H_2]$ or $[\{Ir(cod)Cl\}_2]$ (cod = cycloocta-1,5-diene) as the catalyst precursor, a method that was restricted to *tert*-butyl or trimethylsilyl acetylenes, or by alkylation of alkylthiovinyl–copper(I) compounds by starting from specific substituted α-(methylthio)vinyl cuprates.[5d,e] These methods are useful for the synthesis of disubstituted *cis*-[3]cumulenes. However, there has been no example of the stereoselevtive formation of fully substituted [3]cumulenes. We report herein the first stereoselective preparation of tetrasubstituted cumulene derivatives through Zr-mediated coupling reactions of 1,3-butadiynes with aldehydes or ketones to afford *cis*-[3]cumulenols [Eq. (1)].[6]



(1)

[*] Prof. Y.-H. Liu, Dr. H.-J. Gao, Dr. S.-L. Zhou
State Key Laboratory of Organometallic Chemistry
Shanghai Institute of Organic Chemistry
Chinese Academy of Sciences
354 Fenglin Lu, Shanghai 200032 (P.R. China)
Fax: (+86) 21-6416-6128
E-mail: yhliu@mail.sioc.ac.cn

[**] TMS = trimethylsilyl. We thank the National Natural Science Foundation of China, the Chinese Academy of Science, and the Science and Technology Commission of Shanghai Municipality (grant no.: 04QMX1446) for financial support. We also thank Prof. Tamotsu Takahashi for his helpful discussions.

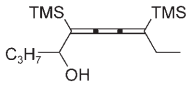
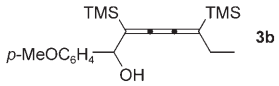
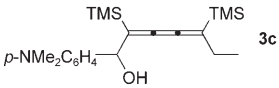
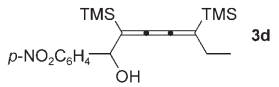
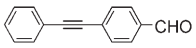
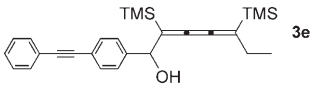
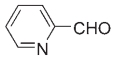
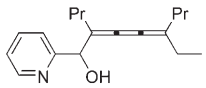
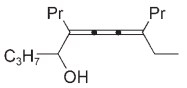
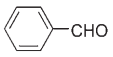
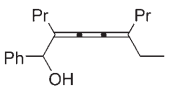
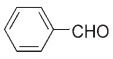
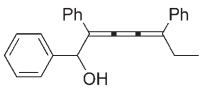
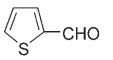
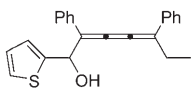
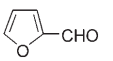
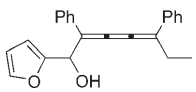
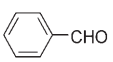
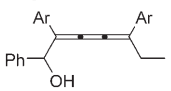
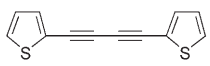
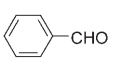
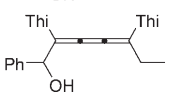
Supporting information for this article is available on the WWW under http://www.angewandte.org or from the author.

© 2006 Wiley-VCH Verlag GmbH & Co. KGaA, Weinheim

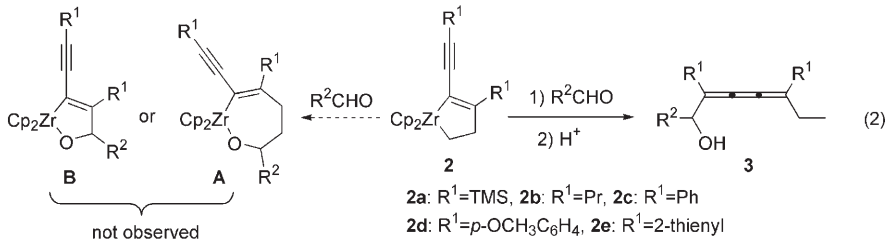
Takahashi et al. have reported that the reaction of conjugated diynes R(C≡C)$_2$R, **1**, with [Cp$_2$Zr-(H$_2$C≡CH$_2$)] (Cp = cyclopentadienyl), prepared from [Cp$_2$ZrEt$_2$] in situ, gave α-alkynylzirconacyclopentenes **2**,[7] which afforded dideuterated enynes after deuteriolysis and α-alkynylcyclopentenenones by treatment with CO/I$_2$.[7b] It has also been demonstrated that the strong interaction of a triple bond in the α position of the zirconacyclopentene with the Cp$_2$Zr moiety prevented the zirconacyclopentene from reacting with a second alkyne, such as another molecule of the diyne.[7a,b]

We now found that simple treatment of zirconacycles **2** with 1 equivalent of aldehyde at room temperature for 1–6 h readily afforded *cis*-[3]cumulenols **3** in good yields after hydrolysis [Eq. (2)]. To our surprise, the C–C bond formation occurred exclusively at the alkynylic carbon atom substituted with the R^1 group, whereas the expected products derived from direct insertion into a Zr–C(sp^3) bond [Eq. (2), complex **A**] or from **B** through a β,β′ C–C bond cleavage reaction were not detected. The chemoselectivity in this case is in marked contrast to that observed with alkyl- or aryl-substituted zirconacyclopentenes, since only insertion of aldehydes into the alkyl–zirconium bond to afford the seven-membered oxazirconacycles has been reported[8] in these zirconacyclopentenes so far.

Table 1: Formation of *cis*-[3]cumulenes via α-alkynylated zirconacyclopentenes.[a]

Entry	Butadiyne	Aldehyde	Product	Yield [%][b]
1	TMS–≡–≡–TMS **1a**	C_3H_7CHO	 **3a**	67
2	**1a**	MeO–C$_6$H$_4$–CHO	 **3b**	67
3	**1a**	Me$_2$N–C$_6$H$_4$–CHO	 **3c**	58
4	**1a**	O$_2$N–C$_6$H$_4$–CHO	 **3d**	66
5	**1a**		 **3e**	70
6	Pr–≡–≡–Pr **1b**		 **3f**	61
7	**1b**	C_3H_7CHO	 **3g**	64
8	**1b**		 **3h**	71
9	Ph–≡–≡–Ph **1c**		 **3i**	65
10	**1c**		 **3j**	62
11	**1c**		 **3k**	55
12	Ar–≡–≡–Ar Ar=*p*-MeOC$_6$H$_4$		 **3l**	55
13[c]			 **3m**	35

[a] All the reactions were carried out at room temperature for 1–6 h. [b] Yields of isolated products. [c] Thi = 2-thienyl.



(2)

Representative results are given in Table 1. A wide range of 1,3-butadiynes, including TMS-, alkyl-, aryl-, and heteroaryl-substituted ones, participated in the cumulene formation reactions. In all cases, the cumulene products, **3a**–**m**, were obtained with high *cis* selectivity (> 99 % by NMR spectroscopy). X-ray crystal structure analysis of **3d** provided unequivocal evidence for the stereochemical assignment (Figure 1).[9] The central C=C bond (C(2)-C(3) = 1.258(7) Å) is significantly shorter than both terminal C=C bonds (C(1)-C(2) = 1.334(7) Å, C(3)-C(4) = 1.315 (7) Å), a result that is indicative of electronically different bonding situations.[10]

Zirconacycles prepared from diaryldiynes are reported to undergo reductive elimination upon heating and previously reported coupling reactions of alkynes or alkenes with these zirconacycles occurred only after reductive elimination at 50 °C.[7c] In our reaction, the zirconacycles **2c**–**e** reacted with aldehydes at room temperature within 1 h completely, with no observation of the

 © 2006 Wiley-VCH Verlag GmbH & Co. KGaA, Weinheim

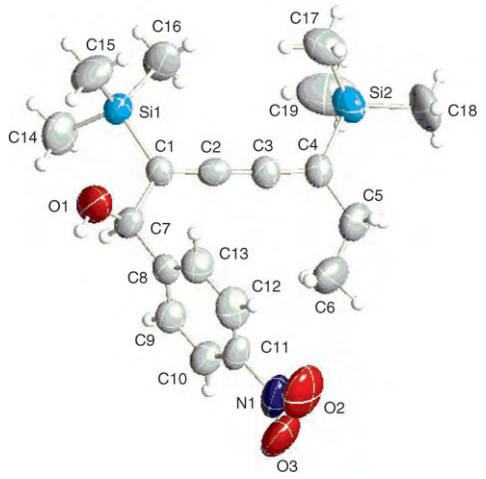


Figure 1. The X-ray crystal structure of **3d**. Selected bond lengths [Å] and bond angles [°]: Si(1)-C(1) 1.875(5), C(1)-C(2) 1.334(7), C(2)-C(3) 1.258(7), C(3)-C(4) 1.315(7), C(1)-C(7) 1.521(6); C(2)-C(1)-Si(1) 120.6(4), C(3)-C(2)-C(1) 178.8(6), C(2)-C(3)-C(4) 176.4(6), C(2)-C(1)-C(7) 121.0(4).

products induced by reductive elimination. Interestingly, it was confirmed that zirconacycle **2b**, derived from an alkyl-substituted butadiyne, did not react with alkynes or alkenes; however, it readily underwent coupling reactions with aldehydes to furnish cumulenes **3f**,**g**,**h** in 61, 64, and 71% yields (Table 1, entries 6–8), respectively.

The reaction could be applied to a wide variety of aliphatic aldehydes as well as aromatic ones bearing electron-donating or electron-withdrawing substituents. The functionalities of MeO, NMe_2, NO_2, and alkynyl groups in the aromatic ring were tolerated during the reaction, thereby affording the corresponding products **3b**–**e** in 58–70% yields (Table 1, entries 2–5). A number of heteroaryl aldehydes could be incorporated successfully into the sequence; for example, when 2-pyridinecarboxaldehyde or 2-thiophencarboxaldehyde were employed, the corresponding cumulenes **3f** and **3j** were obtained in 61 and 62% yields, respectively (Table 1, entries 6 and 10). It was also found that a *cis–trans* isomerization occurred upon addition of a trace amount of iodine;[5f] for example, a 2.8:1 (*Z*/*E*) mixture of **3d** and its isomer was formed within 0.5 h at room temperature.

It has been demonstrated that cumulenes are generally unstable and most of the known [3]cumulenes are aryl- or *tert*-butyl-substituted because of their greater stability towards oxygen and acids. Only a limited number of procedures for the preparation of alkyl-substituted buta-1,2,3-trienes have been reported.[4e] Cumulene derivatives **3**, obtained by this new method, were sufficiently stable to allow purification by chromatography on alumina or silica gel; this eventually led to the successful isolation of the products. Their ^{1}H and ^{13}C NMR spectra were consistent with the proposed structures. The ^{13}C NMR spectra displayed two characteristic resonances at $\delta = 169$–173 (TMS-substituted cumulenes), 152–155 (phenyl-substituted cumulenes), or 153–158 ppm (alkyl-substituted cumulenes), which could be assigned to the allenic-type sp-hybridized carbon atoms of **3**. An attractive advantage of this strategy is the single-pot construction of cumulenes and also the flexibility possible in the assembly of the products by using appropriate combinations of butadiynes and carbonyl derivatives.

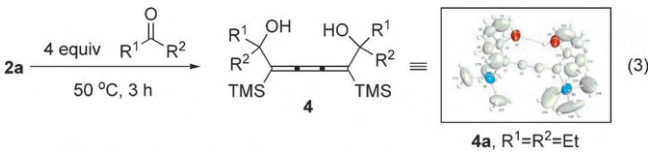
More interestingly, we found that the reaction of **2a** with 4 equivalents of ketones[11] afforded [3]cumulenic diols **4** in reasonable yields after hydrolysis [Eq. (3)]. The products **4** were obtained with high *Z* stereoselectivity. The tetraethyl-substituted product **4a** formed good single crystals for X-ray crystallography,[12] which clearly showed the cumulenic skeleton [see Eq. (3)]. Unsymmetrical ketones afforded (*Z*)-**4** as a mixture of diastereomers (Table 2). However, the reaction of

Table 2: Formation of (*Z*)-[3]cumulenic diols **4**.

R^1	R^2	Product	Yield [%][a]	d.r.[b]
Et	Et	**4a**	60	–
Me	Et	**4b**	55	1.2:1
Me	Hex	**4c**	42	1.1:1
Me	*i*Pr	**4d**	55	1.1:1
Me	*i*Bu	**4e**	45	1.1:1
Me	Pr	**4f**	44	1.6:1
Me	isopentyl	**4g**	46	1.2:1

[a] Yields of isolated products. [b] Diastereomeric ratio.

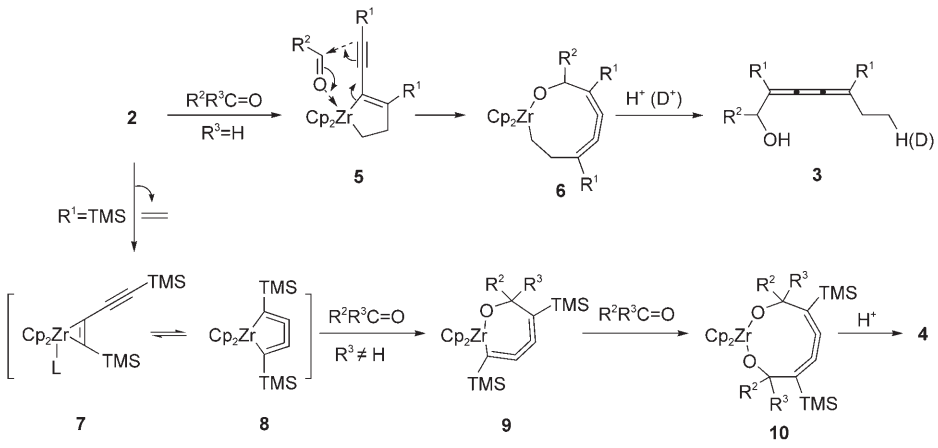
2a with methylphenylketone or diphenylketone failed to produce any detectable products due to the lower reactivity of aryl ketones. This reaction is of interest when related to the results of a reaction reported by Rosenthal and co-workers between a five-membered zirconacyclocumulene and carbon dioxide, in which a double insertion occurred to give the cumulenic dicarboxylate [Cp*Zr{O(C=O)C(SiMe$_3$)=C=C=C-(SiMe$_3$)C(=O)O}] (Cp* = pentamethylcyclopentadienyl).[13] This strongly suggests that a similar intermediate of oxazirconacycle with a cyclic cumulene moiety may exist in our system.



(3)

On the basis of the above observations, a possible reaction mechanism is proposed in Scheme 1. The interaction of an aldehyde with zirconacycle **2**, presumably via intermediate **5**, gives a nine-membered oxazirconacycle **6** with a cyclic cumulene structure. Hydrolysis of **6** affords the desired products **3**. The stereoselectivity might be induced by strong coordination of the aldehyde to the zirconium center. An NMR study of the reaction of **2a** with *p*-methoxybenzaldehyde indicated the formation of **6b** (R^1 = TMS, R^2 = *p*-$MeOC_6H_4$) in 75% yield. The ^{1}H NMR spectrum of **6b** in C_6D_6/THF (2:1) showed two sets of singlets at $\delta = 5.60$ and 5.81 ppm, and the ^{13}C NMR spectrum revealed two singlets at $\delta = 110.5$ and 111.1 ppm, which were assigned to Cp ligands. The signals at $\delta = 38.1$ and 41.8 ppm are assignable to a $(CH_2)_2$ unit attached to the zirconium atom, and the low-field

 © 2006 Wiley-VCH Verlag GmbH & Co. KGaA, Weinheim



Scheme 1. Proposed mechanism for the formation of *cis* cumulenes.

signals ($\delta = 173.7$ and 175.4 ppm) are characteristic for sp carbon atoms in cumulenic skeletons.

In a deuteration experiment with benzaldehyde and **2a**, the monodeuterated compound [D]**3n** was obtained in 60% yield with high deuterium incorporation (D = 90%). To account for the formation of cumulenic diols **4**, a zirconocene–butadiyne complex **7** (an η^2 complex)[14] formed through a β,β′ C–C bond cleavage reaction was suggested; this complex might form an equilibrium with zirconacyclocumulene **8** (an η^4 complex). A double insertion of a ketone into **8** would lead to the formation of (*Z*)-**4** after hydrolysis. In this reaction, the η^2 and η^4 complexes of Cp_2Zr with 1,4-bis(trimethylsilyl)-1,3-butadiyne were formed in situ from complex **2** by using the ethylene unit in the zirconacyclopentene as a spectator ligand. With Cp^*_2Zr, such complexes do exist, but the reactivity of these complexes is restricted to only small molecules (for example, carbon dioxide) due to steric reasons.[13,14]

In summary, we have shown that zirconium-mediated coupling of 1,3-butadiynes with aldehydes or ketones provides access to an efficient, general, and one-pot method for the *cis*-selective synthesis of tetrasubstituted [3]cumulenols. Remarkably, the reaction occurs with complete chemoselectivity with respect to the α-alkynylated zirconacyclopentenes, which is different to that of the reactions with alkyl- or aryl-substituted zirconacyclopentenes reported so far. Clarification of the reaction mechanism and further application of this chemistry are in progress.

Experimental Section

Typical procedure for the cross-coupling reaction of α-alkynylated zirconacyclopentenes with aldehydes: EtMgBr (1.0 M THF solution, 2.5 mmol) was added to a solution of $[Cp_2ZrCl_2]$ (0.365 g, 1.25 mmol) in THF (5 mL) at −50 °C. After the reaction mixture was stirred for 1 h at the same temperature, 1,4-bis(trimethylsilyl)buta-1,3-diyne (0.19 g, 1 mmol) was added and the reaction mixture was warmed to room temperature and stirred for 2 h. *p*-Methoxybenzaldehyde (0.12 mL, 1 mmol) was added and the mixture was stirred for 6 h. The reaction mixture was quenched with 5% HCl and extracted with ethyl acetate. The extract was washed with water and brine, then dried over Na_2SO_4. The solvent was evaporated in vacuo and the residue was purified by chromatography over silica gel (petroleum ether (60–90 °C)/ethyl acetate 20:1). The (*Z*)-[3]cumulenol derivative (*Z*)-1-(4-methoxyphenyl)-2,5-bis(trimethylsilyl)-hepta-2,3,4-trien-1-ol **3b** (241 mg, 67%) was obtained as a light-yellow oil: ^{1}H NMR ($CDCl_3$, Me_4Si): $\delta = 0.20$ (s, 9H), 0.37 (s, 9H), 1.30 (t, $J = 6.9$ Hz, 3H), 2.54 (q, $J = 7.2$ Hz, 2H), 3.11 (s, 1H), 3.96 (s, 3H), 5.50 (s, 1H), 7.03 (m, 2H), 7.45 ppm (m, 2H); ^{13}C NMR ($CDCl_3$, Me_4Si): $\delta = -1.42$, −0.82, 13.28, 28.78, 55.16, 75.60, 113.65, 128.67, 130.05, 133.79, 135.02, 159.18, 169.62, 170.51 ppm; HRMS (MALDI/DHB): calcd for $C_{20}H_{32}O_2Si_2Na$ $[M+Na]^+$: 383.1839; found: 383.1828. DHB = 2,5-dihydroxybenzoic acid.

General procedure for the cross-coupling reaction of α-alkynylated zirconacyclopentenes with ketones: In the procedure described above, *p*-methoxybenzaldehyde was replaced by a ketone (4 mmol), the mixture was stirred for 3 h at 50 °C, and chromatography was over alumina. (*Z*)-[3]cumulenic diol derivatives **4a–g** were obtained as white solids or light-yellow oils. Data for 3,8-diethyl-4,7-bis(trimethylsilyl)-deca-4,5,6-triene-3,8-diol (**4a**): Column chromatography afford it as a white solid (220 mg, 60%); ^{1}H NMR ($CDCl_3$, Me_4Si): $\delta = 0.20$ (s, 18H), 0.83 (t, $J = 7.4$ Hz, 12H), 1.61–1.71 (m, 8H), 2.37 ppm (br s, 2H); ^{13}C NMR ($CDCl_3$, Me_4Si): $\delta = 0.71$, 8.06, 34.22, 81.74, 135.26, 171.66 ppm; HRMS (MALDI/DHB): calcd for $C_{20}H_{40}O_2Si_2Na$ $[M+Na]^+$: 391.2465; found: 391.2457.

Received: February 8, 2006
Published online: May 16, 2006

Keywords: aldehydes · butadiynes · cumulenes · stereoselective synthesis · zirconium

[1] a) N. Ishida, K. Miyazaki, K. Kumagai, M. Rikimaru, *J. Antibiot.* **1965**, *18*, 68; b) A. G. Myers, S. B. Cohen, B.-M. Kwon, *J. Am. Chem. Soc.* **1994**, *116*, 1670; c) K. Fujiwara, H. Sakai, M. Hirama, *J. Org. Chem.* **1991**, *56*, 1688; d) K. K. Wang, B. Liu, Y. Lu, *J. Org. Chem.* **1995**, *60*, 1885, and references therein.

[2] a) W. Skibar, H. Kopacka, K. Wurst, C. Salzmann, K. Ongania, F. F. de Biani, P. Zanello, B. Bildstein, *Organometallics* **2004**, *23*, 1024; b) B. Bildstein, *Coord. Chem. Rev.* **2000**, *206–207*, 369; c) S. Ermer, S. Lovejoy, D. Leung, R. Spitzer, G. Hansen, R. Stone in *Proceedings of The International Society of Optical Engineering, Vol. 1560, Nonlinear Optical Properties of Organic Materials IV* (Ed.: K. D. Singer), SPIE, Washington, **1991**, p. 120; d) I. Kinoshita, M. Kijima, H. Shirakawa, *Macromol. Rapid Commun.* **2000**, *21*, 1205; e) M. Kijima, I. Kinoshita, H. Shirakawa, *Synth. Met.* **1999**, *101*, 145; f) M. N. Schkunov, R. K. Meyer, W. Gellermann, R. E. Benner, Z. V. Vardeny, J. B. Lin, T. Barton, *Synth. Met.* **1997**, *84*, 969.

[3] a) M. Iyoda, S. Tanaka, H. Otani, M. Nose, M. Oda, *J. Am. Chem. Soc.* **1988**, *110*, 8494; b) F. Diederich, Y. Rubin, *Angew. Chem.* **1992**, *104*, 1123; *Angew. Chem. Int. Ed. Engl.* **1992**, *31*, 1101.

[4] a) H. Hopf, *Classics in Hydrocarbon Chemistry*, Wiley-VCH, Weinheim, **2000**, p. 171; b) H. Hopf in *The Chemistry of Ketenes, Allenes, and Related Compounds, Part 2* (Ed.: S. Patai), Wiley-Interscience, Chichester, **1980**, p. 781; c) L. Brandsma, H. D. Verkruijsse in *Synthesis of Acetylenes, Allenes and Cumulenes*, Elsevier, New York, **1981**; d) "Cumulenes": H. Fischer in *The Chemistry of Alkenes* (Ed.: S. Patai), Wiley-Interscience, London, **1964**, p. 1025; e) X.-P. Cao, M.-K. Leung, *J. Chem.*

 © 2006 Wiley-VCH Verlag GmbH & Co. KGaA, Weinheim

Soc. Perkin Trans. 1 **1995**, 193; f) H.-F. Chow, X.-P. Cao, M.-K. Leung, *J. Chem. Soc. Chem. Commun.* **1994**, 2121, and references therein.

[5] a) Y. Wakatsuki, H. Yamazaki, N. Kumegawa, T. Satoh, J. Y. Satoh, *J. Am. Chem. Soc.* **1991**, *113*, 9604; b) Y. Wakatsuki, H. Yamazaki, N. Kumegawa, P. S. Johar, *Bull. Chem. Soc. Jpn.* **1993**, *66*, 987; c) T. Ohmura, S. Yorozuya, Y. Yamamoto, N. Miyaura, *Organometallics* **2000**, *19*, 365; d) H. Westmijze, J. Meijer, P. Vermeer, *Tetrahedron Lett.* **1975**, 2923; e) W. G. M. van den Hoek, J. Kroon, H. Kleijn, H. Westmijze, P. Vermeer, H. J. T. Bos, *J. Chem. Soc. Perkin Trans. 2* **1979**, 4231; f) for the *E*-selective synthesis of 1,4-dialkylbutatrienes, see: T. Yoshida, R. M. Williams, E. Negishi, *J. Am. Chem. Soc.* **1974**, *96*, 3688; g) E. Negishi, T. Yoshida, A. Abramovitch, G. Lew, R. M. Williams, *Tetrahedron* **1991**, *47*, 343.

[6] a) For an SmI_2-promoted nonstereoselective synthesis of [3]cumulenols, see: J. M. Aurrecoechea, E. Pérez, M. Solay, *J. Org. Chem.* **2001**, *66*, 564; b) for Ti-mediated formation of [3]cumulenols without definition of the configuration, see: C. Delas, H. Urabe, F. Sato, *Chem. Commun.* **2002**, 272.

[7] a) T. Takahashi, K. Aoyagi, V. Denisov, N. Suzuki, D. Choueiry, E. Negishi, *Tetrahedron Lett.* **1993**, *34*, 8301; b) T. Takahashi, Z. Xi, Y. Nishihara, S. Huo, K. Kasai, K. Aoyagi, V. Denisov, E. Negishi, *Tetrahedron* **1997**, *53*, 9123; c) Y. Liu, W. Sun, K. Nakajima, T. Takahashi, *Chem. Commun.* **1998**, 1133.

[8] For the reaction of zirconacyclopentenes with aldehydes, see: a) T. Takahashi, M. Kageyama, V. Denisov, R. Hara, E. Negishi, *Tetrahedron Lett.* **1993**, *34*, 687; b) C. Copéret, E. Negishi, Z. Xi, T. Takahashi, *Tetrahedron Lett.* **1994**, *35*, 695; c) E. Negishi, D. Choueiry, T. B. Nguyen, D. R. Swanson, *J. Am. Chem. Soc.* **1994**, *116*, 9751; d) S. L. Buchwald, R. B. Nielsen, *Chem. Rev.* **1988**, *88*, 1047; e) C. Zhao, T. Yu, Z. Xi, *Chem. Commun.* **2002**, 142; f) C. Zhao, J. Yan, Z. Xi, *J. Org. Chem.* **2003**, *68*, 4355.

[9] CCDC 285026 contains the supplementary crystallographic data for **3d**. These data can be obtained free of charge from The Cambridge Crystallographic Data Centre via www.ccdc.cam.ac.uk/data_request/cif.

[10] P. A. Morken, N. C. Baenziger, D. J. Burton, P. C. Bachand, C. R. Davis, S. D. Pedersen, S. W. Hansen, *J. Chem. Soc. Chem. Commun.* **1991**, 566.

[11] For the reaction of zirconacyclopentenes with ketones, see: a) references [8a,b]; b) T. Takahashi, C. Xi, Z. Xi, M. Kageyama, R. Fischer, K. Nakajima, E. Negishi, *J. Org. Chem.* **1998**, *63*, 6802; c) T. Takahashi, M. Kotora, R. Hara, Z. Xi, *Bull. Chem. Soc. Jpn.* **1999**, *72*, 2591; d) Z. Xi, R. Guo, S. Mito, H. Yan, K. Kanno, K. Nakajima, T. Takahashi, *J. Org. Chem.* **2003**, *68*, 1252.

[12] CCDC 297419 contains the supplementary crystallographic data for **4a**. These data can be obtained free of charge from The Cambridge Crystallographic Data Centre via www.ccdc.cam.ac.uk/data_request/cif.

[13] P. Pellny, F. G. Kirchbauer, V. V. Burlakov, W. Baumann, A. Spannenberg, U. Rosenthal, *J. Am. Chem. Soc.* **1999**, *121*, 8313.

[14] a) U. Rosenthal, V. V. Burlakov, P. Arndt, W. Baumann, A. Spannenberg, *Organometallics* **2005**, *24*, 456; b) U. Rosenthal, V. V. Burlakov, P. Arndt, W. Baumann, A. Spannenberg, *Organometallics* **2003**, *22*, 884; c) U. Rosenthal, *Angew. Chem.* **2003**, *115*, 1838; *Angew. Chem. Int. Ed.* **2003**, *42*, 1794; d) U. Rosenthal, *Angew. Chem.* **2004**, *116*, 3972; *Angew. Chem. Int. Ed.* **2004**, *43*, 3882.

 © 2006 Wiley-VCH Verlag GmbH & Co. KGaA, Weinheim

Oligosaccharide Analysis

DOI: 10.1002/anie.200600642

Solid-Phase Oligosaccharide Tagging (SPOT): Validation on Glycolipid-Derived Structures**

*Anders Lohse, Rita Martins, Malene Ryborg Jørgensen, and Ole Hindsgaul**

Glycosylation is the most abundant form of post-translational modification of proteins. Over 50% of all protein sequences are glycosylated in eukaryotic systems.[1] Glycosylated lipids are also widespread in animal cells: they constitute up to 5–10% of the cell membrane content and are responsible for a wide array of pathological disorders.[2]

The structural analysis, or sequencing, of the oligosaccharide chains of glycoproteins and glycolipids is much more complex than that of DNA or proteins, as the molecules are generally branched and the linkage between sugar residues introduces a new α or β stereocenter. The major analytical approaches[3] rely on the detection of oligosaccharides either by mass spectrometry (MS) or pulsed amperometry. Oligosaccharides released from glycoproteins or glycolipids by chemical or enzymatic methods are also frequently labeled at the reducing end to afford increased sensitivity of detection.[4] The insertion of fluorescent tags followed by analysis by chromatography or electrophoresis is common practice. The above approaches, however, remain complex endeavors that require a combination of sophisticated equipment and a high degree of expertise in both sample handling and data analysis.

There would be clear advantages in any technique that could sequester a reducing oligosaccharide from solution and allow its further manipulation (including tagging) while immobilized on a solid phase, for example, on beads or glass surfaces such as slides. This is the rationale behind solid-phase oligosaccharide tagging (SPOT) that would involve only pipetting and washing. The advantages are:

- Once the oligosaccharide is "captured" it remains covalently bound to the beads, so there would be no sample loss during subsequent manipulations.
- Large excesses of tagging (or other) reagents could be used to drive reactions to completion, as they would be washed away without sample loss or dilution.
- If the immobilized oligosaccharide remained sterically accessible to enzymes and lectins (or antibodies), biological oligosaccharide recognition and enzyme-assisted

[*] Dr. A. Lohse, Dr. R. Martins, Dr. M. R. Jørgensen, Prof. O. Hindsgaul
Carlsberg Laboratory
2500 Valby, Copenhagen (Denmark)
Fax: (+45) 3327-4708
E-mail: hindsgaul@crc.dk

[**] This work was supported by the Danish Technical Research Council (STVF).

Supporting information for this article is available on the WWW under http://www.angewandte.org or from the author.

© 2006 Wiley-VCH Verlag GmbH & Co. KGaA, Weinheim

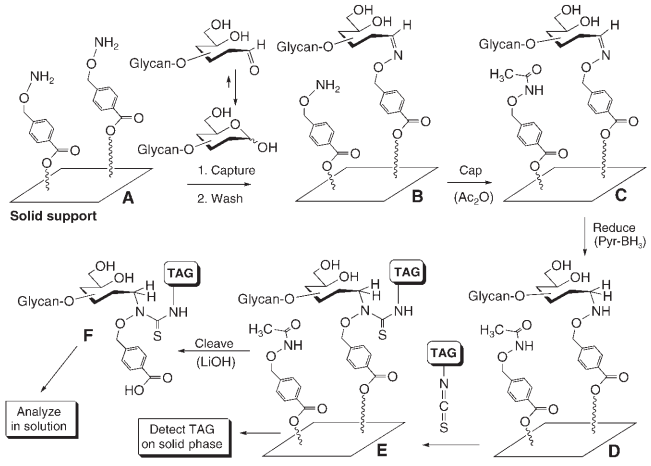
sequencing procedures already in use in glycomics could be applied.

- If a cleavable linker was present in the capture molecule, a "processed" (for example, fluorescently tagged) oligosaccharide could be released into solution in a small volume for further analysis.

Recently, Nishimura and co-workers[5] showed that polymeric beads functionalized with hydroxylamine groups could be used to capture reducing oligosaccharides from complex samples. After washing away the non-carbohydrate debris, the oligosaccharide could be released back into solution for further analysis. This convenient cleanup procedure, termed "glyco-blotting", yielded superior MS data for use in fragmentation sequencing. Shin and co-workers[6] later showed that oligosaccharides could be captured on glass array slides functionalized with hydrazide or hydroxylamine groups, and detected on the slides using fluorescently tagged lectins.

Herein, we show that a system can be devised where solid supports bearing hydroxylamine groups can capture oligosaccharides from solution. Furthermore, the immobilized product can be efficiently chemically manipulated while on the solid phase, and then released back into solution for analysis. We demonstrate the SPOT process on glycolipid-derived structures.

The chemistry described in Scheme 1 was developed for SPOT. Structure **A** shows benzyl hydroxylamine capture

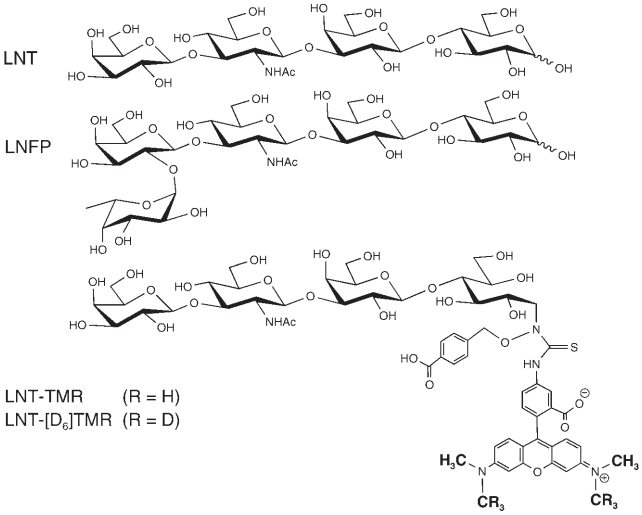


Scheme 1. The chemistry underlying SPOT.

groups attached through a cleavable ester linkage to a solid support, optionally through a spacer molecule. An appropriate spacer would be needed if access of a captured sugar molecule to a protein active site, such as that of a glycosidase or lectin, was required. Incubation of **A** with a solution containing a reducing sugar results in its capture to form an oxime (**B**), along with an excess of unreacted capture groups. The oxime is expected to be a mixture of tautomers including cyclic forms (not shown).[7] The excess unreacted hydroxylamines in **B** could now be capped (for example, by reaction with an amine-reactive compound such as acetic anhydride (Ac_2O)) to give **C**, under conditions in which neither the oxime nor the immobilized sugar OH groups react. Reduction of the oxime double bond in **C** would then give the *N*,*O*-alkylhydroxylamine **D**, now with a reactive sp^3 nitrogen atom. Tagging of the active nitrogen atom in **D** can be accomplished under conditions in which the sugar OH groups do not react (for example, by using aryl isothiocyanates) to give **E**. Base treatment of **E** then releases the tagged sugar **F** into solution for analysis. In the process, the immobilized oligosaccharide(s) in **B**–**E** should be detectable by lectins or antibodies, thus yielding potentially valuable information on their structure(s).

The process described has, as its key step, the selective inactivation of excess capture groups prior to reduction and insertion of a tag on the sugar. In this way, a single tag is added only to the sugar molecule, even though an excess of tagging agent is used. The excess tagging agent, and indeed all reagents used, are easily washed away from the immobilized sugar, which thereby remains in a small volume.

The feasibility of the SPOT process was evaluated by using two simple, model reducing oligosaccharides derived from glycolipids (Scheme 2): the linear tetrasaccharide lacto-



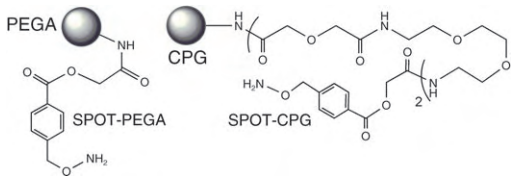
Scheme 2. Structures of LNT, LNFP, and fluorescently tagged products of LNT. TMR = tetramethylrhodamine.

N-tetraose (LNT) and its fucosylated product lacto-*N*-fucopentaose (LNFP). These specific structures were selected because they are commercially available in pure form, as are the glycosidases required to cleave their terminal sugar residues for eventual enzyme-assisted sequencing.

Two different solid supports were investigated in the evaluation of SPOT: PEGA-1900,[8] a polyethylene glycol–polyacrylamide resin that swells in both organic and aqueous solvents and has functionalizable amino groups incorporated in the range of 0.5 mmol g^{-1}; and controlled-pore glass (CPG), which comprises nonswellable, rigid particles having pores of size >1400 Å and near 30 μmol g^{-1} incorporated amino groups. The PEGA beads should be more useful when a high density of capture groups is required, whereas the CPG beads would be favored when an immobilized oligosaccharide should be accessible to a protein probe. For these reasons, the

 © 2006 Wiley-VCH Verlag GmbH & Co. KGaA, Weinheim

amino groups on the PEGA beads were functionalized directly with the cleavable hydroxylamine capture groups (no spacer) to give SPOT-PEGA beads (Scheme 3), whereas the silylpropylaminated CPG was functionalized with a 40-



Scheme 3. Structures of solid supports, showing the capture group, cleavable linker, and optional spacer.

atom polyethylene glycol derived spacer prior to the incorporation of the capture groups to give SPOT-CPG beads (Scheme 3). Experimental details are provided in the Supporting Information.

Examination of the optimal conditions for the capture of oligosaccharides showed that the conditions for >95% capture differed between the two bead types. For SPOT-PEGA beads, dimethyl sulfoxide/acetic acid (DMSO/AcOH, 7:3), 70°C, and reaction for 3 h were found to be optimal. Capping was achieved with acetic anhydride/methanol (Ac_2O/MeOH; 1 h) and reduction was effected with pyridine/borane (Pyr-BH_3; 10 min). For SPOT-CPG beads, incubation overnight at 55°C in aqueous citrate/phosphate buffer (pH 5.0) proved ideal for the capture process. The capping and reduction steps were performed as for the SPOT-PEGA beads. Extensive washing of the beads was performed between steps, with the beads placed in syringes with frits on a vacuum manifold.

In a typical experiment, the capture of LNT (70 μg) on SPOT-PEGA beads (5 mg, ca. 30 μL) at 70°C for 3 h was followed by capping, reduction, fluorescence tagging with tetramethylrhodamine-5-isothiocyanate (TMR-NCS), and cleavage with an aqueous solution of LiOH. The brilliant red solution obtained was neutralized with aqueous AcOH and diluted to a final volume of 3 mL. An aliquot of this sample was further diluted 100 to 1000-fold with water, and a 22-nL portion was injected for micellar capillary electrophoresis (CE) with conventional (non-laser) fluorescence detection at 570 nm. A portion of about 10^{-8} of the sample was used for the analysis.

The electropherogram of the SPOT-labeled product is shown in Figure 1. A highly efficient chemical sequence is indicated, with the LNT-TMR (Scheme 2) eluting near 16 min (the structure was verified by MS and was independently confirmed by solution synthesis), and the only significant impurity (marked X, Figure 1) being a peak at 23 min. This latter impurity was isolated by HPLC, was found by MS to have a m/z of 624, and has the structure shown for LNT-TMR but with the sugar replaced by a methyl group. This compound arises from the scavenging of trace contaminating formaldehyde from the air and/or the solvents used. It does not interfere in the present analysis, but efforts are under way to minimize its formation.

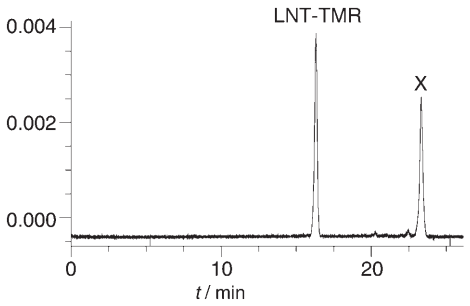


Figure 1. Capillary electropherogram of crude LNT-TMR. X denotes a non-carbohydrate side product.

We next examined the suitability of SPOT-PEGA beads for the insertion of a tag that would be of use in MS. We chose the *p*-bromophenyl (BrPh) group, as the unique isotope pattern (^{79}Br/^{81}Br 1:1) of the bromine atom can confirm that a product is indeed labeled. Incorporation of a bromine label also allows the very efficient "editing" of mass spectra as a result of the mass defect properties of this atom.[9] We therefore tagged the intermediate **D** (Scheme 1) with *p*-bromophenyl isothiocyanate, washed the beads, cleaved the linker with an aqueous base, and neutralized the sample as before. The removal of salts from the product LNT-BrPh (Figure 2) prior to MS analysis was effected by adsorption on C-18 resin, washing with water, and elution with an aqueous solution of MeOH. The mass spectrum of the crude product is shown in Figure 2 and confirms the quality of the tagged sample.

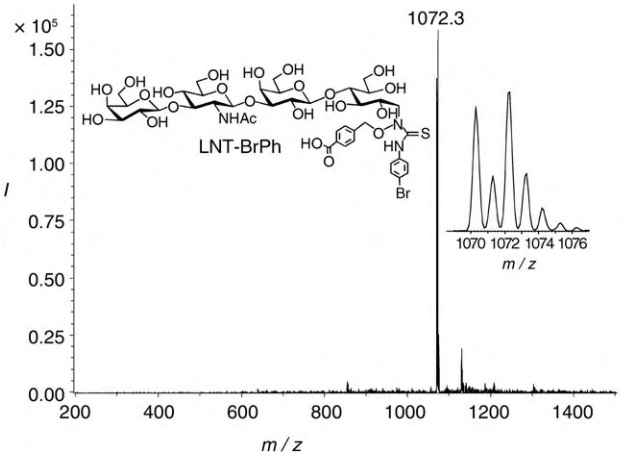


Figure 2. Structure and mass spectrum of LNT-BrPh, with the ^{79}Br and ^{81}Br isotopes highlighted in the inset.

We then set up a "dummy run" to evaluate a potential dual application of SPOT in both fluorescence tagging and CE analysis as just described, and in a differential glycomics[10] setting where the concentration of the same compound in two different samples would be estimated by MS using stable, isotope-encoded tagging species (Figure 3). For this experiment, we chemically synthesized TMR-NCS with two trideuteromethyl groups ([D_6]TMR-NCS). Separate samples containing LNT at concentrations of 1.0 and 0.5 μM

 © 2006 Wiley-VCH Verlag GmbH & Co. KGaA, Weinheim

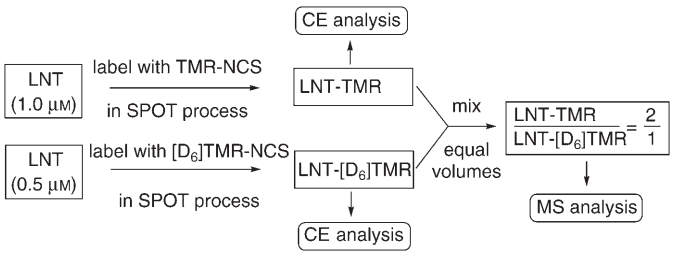


Figure 3. Flow chart for estimating the relative concentrations of LNT in two different samples, by both CE and MS analysis.

were run through the SPOT process (Scheme 1), each using 5 mg of SPOT-PEGA beads. The more concentrated sample was labeled with TMR-NCS and the other by using [D_6]TMR-NCS. CE analysis of the two cleaved and neutralized samples revealed identical retention times for LNT-TMR and LNT-[D_6]TMR (see Scheme 2 for structures). As expected, the integral of the peak for LNT-[D_6]TMR was half that of the unlabeled compound (Figure 4).

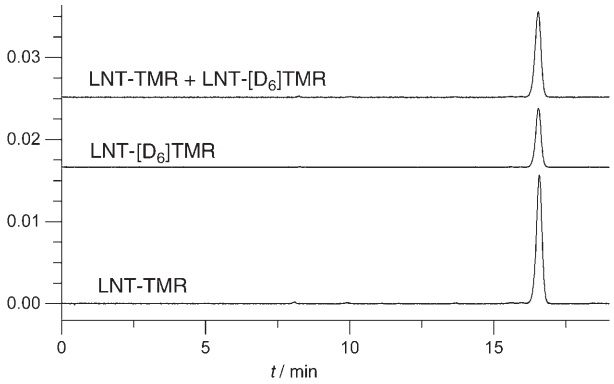


Figure 4. Capillary electropherograms of the LNT samples labeled as in Figure 3.

Identical volumes of each sample were then mixed together, following the flow diagram of Figure 3, and the resulting solution was desalted on C-18 resin prior to analysis by electrospray MS. CE analysis of the mixture (Figure 4, top trace) confirmed their expected co-elution. The mass spectrum obtained in the negative-ion mode is shown in Figure 5, and unambiguously reports the relative abundance of LNT in the two investigated samples.

To show that the composition of a mixture of oligosaccharides could be quantitated by the SPOT method, an equimolar mixture of LNT and LNFP was prepared by careful weighing of the commercial compounds. This time, SPOT-CPG beads were used. Surprisingly, the electropherogram of the product obtained after SPOT labeling with TMR-NCS showed that the compounds were present in the ratio LNT/LNFP 100:74 (Figure 6). We initially thought that either the labeling of the smaller oligosaccharide was more efficient, or that the excitation/emission properties of the labeled compounds differed. However, the fully relaxed 600-MHz

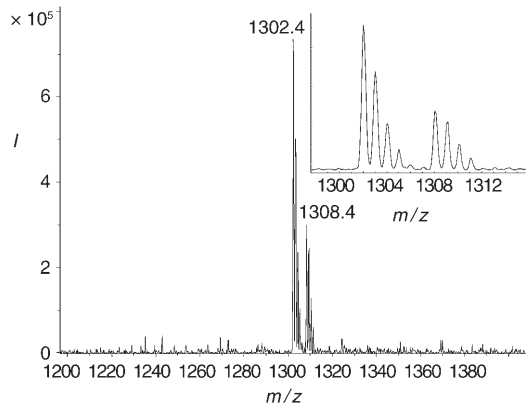


Figure 5. Electrospray mass spectrum of a mixture of equal volumes of the LNT solutions labeled as in Figure 3. The inset highlights the isotope patterns for nonlabeled and [D_6]-labeled LNT-TMR.

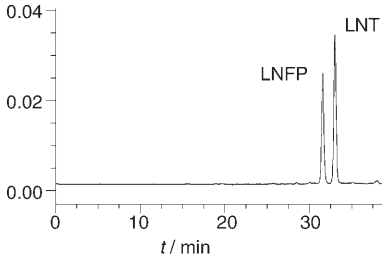


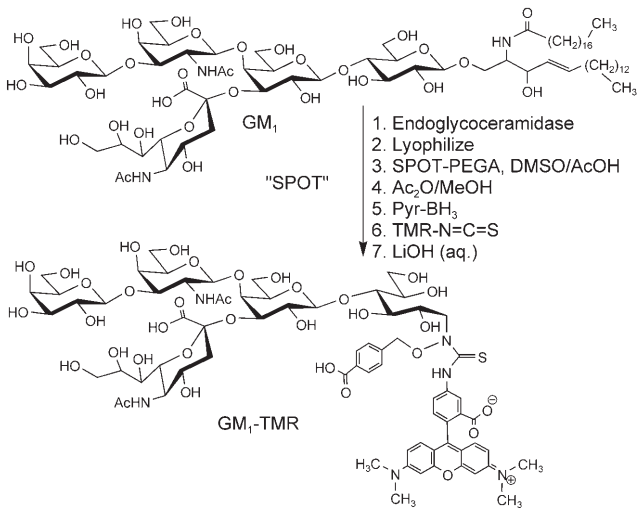
Figure 6. Capillary electropherogram of a mixture of LNT and LNFP SPOT-labeled with TMR.

^{1}H NMR spectrum of the mixture used for capture and tagging revealed that the compounds were in fact present in the ratio 100:79 (data not shown). The conclusion is therefore that the SPOT process does not significantly discriminate between the oligosaccharides of different size used here in the capture, subsequent chemistry, and analysis steps. The LNFP sample was most likely contaminated with salt and/or moisture, or an error in weighing was made.

Finally, we evaluated the entire SPOT process on a real-life glycolipid, the brain-derived ganglioside GM_1 (Scheme 4). The ganglio series of glycolipids are known to be good substrates for the commercial recombinant endoglycoceramidase II (Takara Bio), and the ceramide was indeed completely cleaved in an overnight incubation. The reaction mixture was lyophilized, the residue was redissolved in DMSO/AcOH, SPOT-PEGA beads were added, and the entire sequence of reactions developed on LNT was repeated. The CE and MS of the product GM_1-TMR are shown in Figure 7. The quality of the product validates the SPOT process.

We have demonstrated that reducing oligosaccharides can be captured on both swellable resins like PEGA, which are water and organic solvent compatible, and on rigid surfaces such as glass (CPG). Herein, immobilized hydroxylamine groups have been used as the capture reagents to produce immobilized oximes. Following a sequence of capping, reduction, and tagging with aryl isothiocyanates, a single tag is installed at the reducing end. Excess tagging (and other)

 © 2006 Wiley-VCH Verlag GmbH & Co. KGaA, Weinheim



Scheme 4. Sequence of reactions for SPOT labeling of ganglioside GM_1.

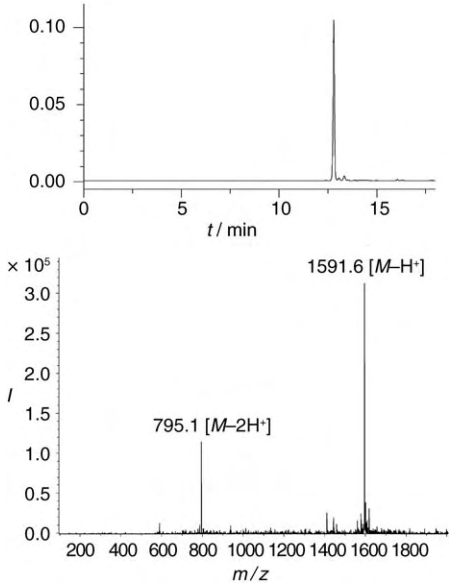


Figure 7. Characterization of the SPOT-labeled GM_1-TMR obtained as described in Scheme 4. Top: capillary electropherogram. Bottom: electrospray mass spectrum.

reagent is removed by simple washing. As a cleavable linker is installed between the capture group and the solid support, the tagged oligosaccharide can be released into solution for analysis by a variety of techniques. The types of tags used were selected to permit detection by fluorimetry and/or MS.

The two key advantages of SPOT are: 1) the simplicity of all the manipulations—which involve only pipetting and washing, and require no prior experience in the handling of oligosaccharides—means that valuable oligosaccharides cannot be lost once they are reduced after immobilization; and 2) a single protocol is used for labeling and release, irrespective of the tag used. The same captured oligosaccharide can therefore be rapidly derivatized with several different tags, and analyzed by a variety of different techniques.

The results presented are clearly those of a model study, designed only to test the feasibility of the chemistry used for capture, capping, reduction, tagging, and release. The central consideration for the chemistries developed is that, in real-life situations, very little oligosaccharide may be available for analysis. This means that the concentration of oligosaccharide in solution might be very low. Thus, it is essential that the concentration of immobilized capture groups is high for a bimolecular reaction to occur, and these capture groups must therefore be present in a large excess. In all of the experiments presented, the hydroxylamine capture groups were in fact present in at least a tenfold molar excess of the target oligosaccharide. As a result, it was necessary to be able to inactivate this excess prior to the tagging step, which would, for the same reasons, require a large excess of tagging agent. The sequence of chemical reactions developed proved to be highly efficient at achieving these objectives.

As presented herein, the capture and tagging of oligosaccharides using the SPOT process is highly efficient ($>90\,\%$) with SPOT-PEGA beads down to the range of 1 nmol oligosaccharide/mg beads. The lower level of capture group incorporation in SPOT-CPG requires a tenfold higher concentration of oligosaccharide to approach the same efficiency. The release of tagged oligosaccharide from the beads was judged to be complete under the saponification conditions used, as all of the visible red color was removed from CPG-SPOT beads.

There are certainly many challenges that remain before SPOT can be applied to real-life situations, especially to crude samples such as cell or tissue extracts. However, these are the same challenges that exist today for solution labeling techniques: complex mixtures of glycans will be present and their release from glycoproteins or glycolipids, by either enzymatic or chemical means, must be quantitative, as should their labeling. Furthermore, the labeling of N-linked oligosaccharides at the reducing end GlcNAc residue is more difficult than at the reducing Glc residue used herein. An additional challenge will be learning to eliminate trace compounds containing aldehydes and ketones, whether present in the biological samples or in the solvents and reagents used. These same compounds are present in the solution labeling techniques used today, but they are either removed by "sample processing" prior to labeling or react and become labeled. These undesired reaction products, which include excess labeling agent, are then removed in subsequent sample processing steps with attendant potential losses of oligosaccharide components. It is hoped that such sample processing steps, with their potential selective sample losses, can be avoided with the further development of the SPOT technique.

Received: February 17, 2006
Published online: May 19, 2006

Keywords: fluorescent probes · glycolipids · glycosylation · isotopic labeling · oligosaccharides

 © 2006 Wiley-VCH Verlag GmbH & Co. KGaA, Weinheim

[1] R. Apweiler, H. Hermjakob, N. Sharon, *Biochim. Biophys. Acta* **1999**, *1473*, 4 – 8.
[2] T. Kolter, K. Sandhoff, *Angew. Chem.* **1999**, *111*, 1632 – 1670; *Angew. Chem. Int. Ed.* **1999**, *38*, 1532 – 1568.
[3] For recent reviews on oligosaccharide analysis, see: a) P. M. Rudd, R. A. Dwek, *Curr. Opin. Biotechnol.* **1997**, *8*, 488 – 497; b) A. Dell, H. R. Morris, *Science* **2001**, *291*, 2351 – 2356; c) Z. Shriver, S. Raguram, R. Sasisekharan, *Nat. Rev. Drug Discovery* **2004**, *3*, 863 – 873; d) M. V. Novotny, Y. Mechref, *J. Sep. Sci.* **2005**, *28*, 1956 – 1968; e) W. Morelle, J. C. Michalski, *Curr. Anal. Chem.* **2005**, *1*, 29 – 57.
[4] For recent reviews on oligosaccharide tagging in solution, see: a) Y. Mechrev, M. Novotny, *Chem. Rev.* **2002**, *102*, 321 – 369; b) N. V. Shilova, N. V. Bovin, *Russ. J. Bioorg. Chem.* **2003**, *29*, 309 – 324.
[5] S. Nishimura, K. Niikura, M. Kurogochi, T. Matsushita, M. Fumoto, H. Hinou, R. Kamitani, H. Nakagawa, K. Deguchi, N. Miura, K. Monde, H. Kondo, *Angew. Chem.* **2005**, *117*, 93 – 98; *Angew. Chem. Int. Ed.* **2005**, *44*, 91 – 96.
[6] M. Lee, I. Shin, *Org. Lett.* **2005**, *7*, 4269 – 4272.
[7] a) W. von Deyn, W. S. York, P. Albersheim, A. G. Darvill, *Carbohydr. Res.* **1990**, *201*, 135 – 144; b) M. Pauly, W. S. York, R. Guillen, P. Albersheim, A. G. Darvill, *Carbohydr. Res.* **1996**, *282*, 1 – 12; c) S. L. Ramsay, C. Freeman, P. B. Grace, J. W. Redmond, J. K. MacLeod, *Carbohydr. Res.* **2001**, *333*, 59 – 71.
[8] R. M. Ferreras, J. M. Delaisse, N. T. Foged, M. P. Meldal, *J. Pept. Sci.* **1998**, *4*, 195 – 210.
[9] M. P. Hall, S. Ashrafi, I. Obegi, R. Petesch, J. N. Peterson, L. V. Schneider, *J. Mass Spectrom.* **2003**, *38*, 809 – 816.
[10] For recent reviews on differential proteomics, see: a) L. Monteoliva, J. P. Aalbar, *Briefings Funct. Genomics Proteomics* **2004**, *3*, 220 – 239; b) S. Julka, F. E. Regnier, *Briefings Funct. Genomics Proteomics* **2005**, *4*, 158 – 177; c) L. V. Schneider, M. P. Hall, *Drug Discovery Today* **2005**, *10*, 353 – 363. For examples of stable-isotope tagging in differential glycomics, see: d) H. Zhang, X.-J. Li, D. B. Martin, R. Aebersold, *Nat. Biotechnol.* **2003**, *21*, 660 – 666; e) J. Yuan, N. Hashii, N. Kawasaki, S. Itoh, T. Kawanishi, T. Hayakawa, *J. Chromatogr. A* **2005**, *1067*, 145 – 152.

 © 2006 Wiley-VCH Verlag GmbH & Co. KGaA, Weinheim

Cycloaddition Reactions

DOI: 10.1002/anie.200600723

Pericyclic Cascade Reactions of (Bicyclo-[1.1.0]butylmethyl)amines**

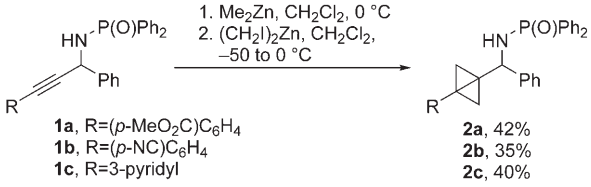
Peter Wipf and Maciej A. A. Walczak*

Dedicated to Professor Heinz Heimgartner

Cyclopropanes and cyclobutanes are often used as scaffolds in selective functionalizations and in the expansion of molecular complexity.[1,2] In contrast, applications of bicyclo-[1.1.0]butanes[3] in organic synthesis have been much more limited.[4] Because of their impressive strain energy of 64 kcal mol^{-1},[5] the latter compounds readily undergo electrophilic, nucleophilic, and radical additions as well as cycloaddition reactions.[3] Of special interest for bicyclobutane chemistry is the high π character of the central C–C bond, which can be utilized for the synthesis of cyclobutene derivatives.[6]

We recently described a cascade reaction initiated by the hydrozirconation of alkynes followed by transmetalation to dimethylzinc and addition to alkynyl imines.[7] Exposure of the resulting *N*-metalated intermediates to the cyclopropanation conditions developed by Furukawa et al.[8] resulted in an unprecedented series of C–C bond-formation and -cleavage processes, thus leading to bicyclo[1.1.0]butanes and (dicyclopropylmethyl)amines.[7a]

Bicyclo[1.1.0]butanes can also be obtained by direct cyclopropanation of propargyl phosphinylamides[9] (Scheme 1). Treatment of **1a–c** with Me_2Zn followed by addition of $(CH_2I)_2Zn$ at −50 °C provided **2a–c**.[10] Conjugated propargylamides with electron-withdrawing substitu-



Scheme 1. Synthesis of bicyclobutanes by a directed Simmons–Smith reaction.

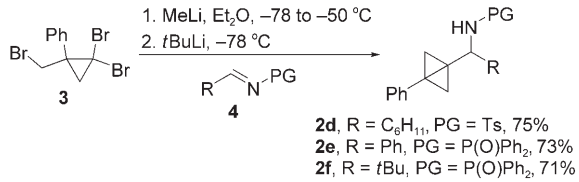
[*] Prof. P. Wipf, M. A. A. Walczak
Department of Chemistry
University of Pittsburgh
Pittsburgh, PA 15260 (USA)
Fax: (+1) 412-624-0787
E-mail: pwipf@pitt.edu

[**] This work was supported by the National Science Foundation (CHE-0315205). We thank Dr. Steve Geib for the X-ray crystallographic analysis and Juan Arredondo for help with the acquisition of the NMR spectra.

Supporting information for this article is available on the WWW under http://www.angewandte.org or from the author.

InterScience
© 2006 Wiley-VCH Verlag GmbH & Co. KGaA, Weinheim

ents in the aryl group provide higher yields in this transformation. Alternatively, bicyclobutanes **2** can be accessed by addition of bicyclo[1.1.0]butyllithium to the activated imines (Scheme 2).[11] Treatment of **3** with MeLi followed by transmetallation with *t*BuLi and addition to imines **4** furnished bicyclobutanes **2d–f** in high yields.



Scheme 2. Synthesis of bicyclobutanes by addition of bicyclo-[1.1.0]butyllithium. PG = protecting group, Ts = *p*-toluenesulfonyl.

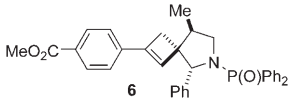
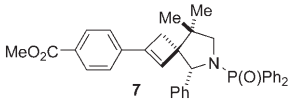
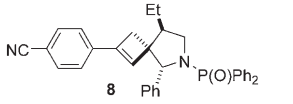
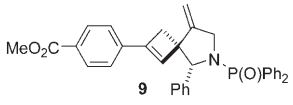
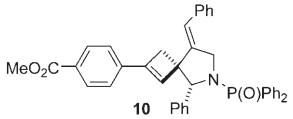
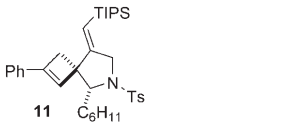
Based on the ease of insertion of zinc carbenoids into the bicyclobutane scaffold,[7] we decided to explore the intramolecular cycloadditions with alkenes and alkynes.[12] Under modified phase-transfer conditions[13] (allyl bromide, Bu_4NHSO_4, 50% aq. NaOH, toluene), *N*-allylation of **2e** proceeded efficiently; however, instead of the expected product, we found that the initial product underwent a spontaneous formal ene reaction[14] to give spirocycle **5** in 63% yield as the only detectable diastereomer based on the ^{1}H NMR spectroscopic analysis of the crude reaction mixture (Scheme 3).[15]



Scheme 3. Cascade *N*-allylation—an Alder ene reaction.

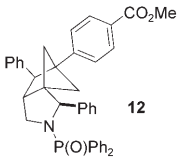
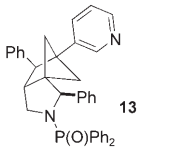
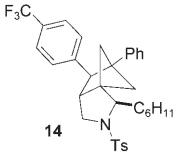
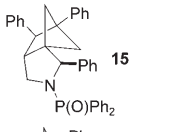
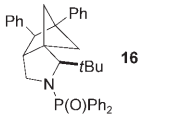
For a further investigation of the scope of this novel cascade process (Table 1), various bicyclobutane derivatives were reacted with allyl, 2-methylallyl, crotyl, propargyl, 3-phenylpropargyl, and 3-triisopropylsilylpropargyl bromides (entries 1–6, respectively). The course of the reaction was dependent on the substitution of the allyl moiety and the electronic environment at the bicyclobutane ring. For example, reaction of **2a** with 3-bromo-2-methylbutene led to the *N*-allylated intermediate (90% yield), which underwent conversion into **7** in 80% yield under reflux conditions in toluene. To directly convert **2a** into **7**, our initial conditions had to be modified—the reaction was carried out at elevated temperatures in the presence of a mixture of powdered NaOH and K_2CO_3 (entry 2).[12] Interestingly, when bicyclobutanes **2** were treated with cinnamyl bromides, the pathway changed from an Alder ene reaction to a formal [2+2] cycloaddition, thus leading to the first synthesis of 3-azatricyclo[5.1.1.0^{1,5}]nonanes (Table 2).[16,17] Yields in this remarkable conversion ranged from modest (32% with the pyridine-substituted **2c**; entry 2) to excellent (93%; entry 1), and both aromatic and aliphatic groups α to the pyrrolidine nitrogen atoms were well tolerated. It is, however, important to note that with our current experimental protocol only bicyclobutanes conju-

Table 1: Reactions of bicyclobutanes with allyl and propargyl bromides.

Entry	Substrates	Product	Yield [%]
1	**2a**, allyl bromide	 **6**	82
2	**2a**, 3-bromo-2-methyl-propene	 **7**	66[a,b]
3	**2b**, (*E*)-crotyl bromide	 **8**	51[a]
4	**2a**, propargyl bromide	 **9**	87
5	**2a**, 3-phenylpropargyl bromide	 **10**	49
6	**2d**, 3-triisopropylsilyl-propargyl bromide	 **11**	62

[a] The reaction was carried out in the presence of a mixture of powdered NaOH and K_2CO_3. [b] Obtained as a 2.9:1 mixture of diastereoisomers; only the major isomer is shown.

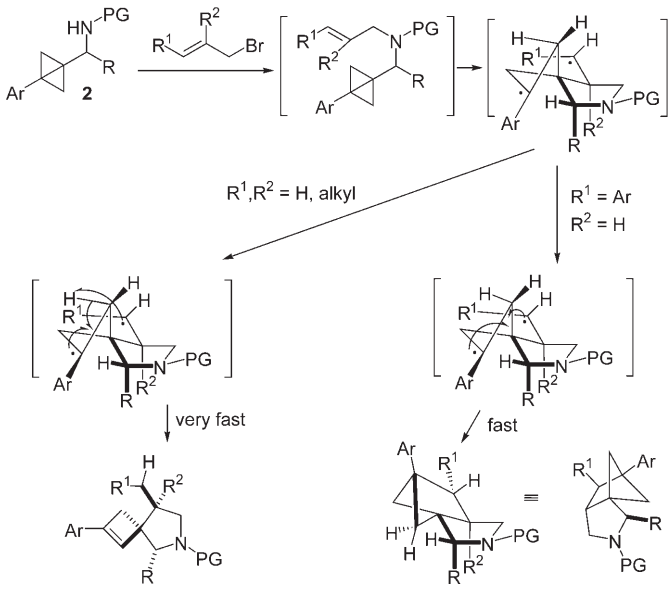
Table 2: Reactions of bicyclobutanes with cinnamyl bromides.

Entry	Substrates	Product	Yield [%]
1	**2a**, (*E*)-cinnamyl bromide	 **12**	93
2	**2c**, (*E*)-cinnamyl bromide	 **13**	32
3	**2d**, 1-((*E*)-3-bromoprop-1-enyl)-4-(trifluoro-methyl)benzene	 **14**	68
4	**2e**, (*E*)-cinnamyl bromide	 **15**	59
5	**2f**, (*E*)-cinnamyl bromide	 **16**	54

 © 2006 Wiley-VCH Verlag GmbH & Co. KGaA, Weinheim

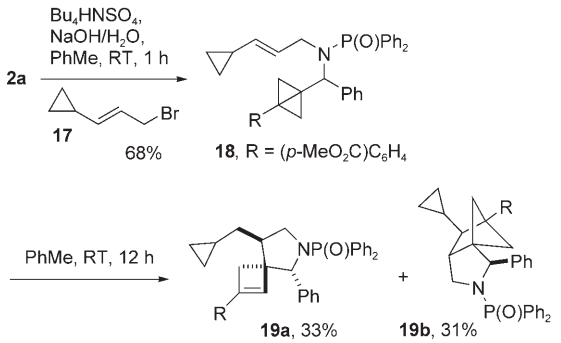
gated to aromatic rings were found to undergo either the intramolecular ene or the [2+2] reaction.[18]

Scheme 4 summarizes our mechanistic model of the two competing reaction pathways for the reactions of bicyclobutanes with allyl bromides. A stepwise addition of the π system across the central bicyclobutane C–C σ bond leads to a putative biradical species,[12b,c,d,e,19] which in case of alkyl substituents at R^1 rapidly abstracts the inside hydrogen atom to form the spirocyclic butene.[12c] If the biradical species is stabilized by an aromatic group at R^1, its prolonged lifetime allows for a ring inversion of the cyclobutane and radical recombination in a formal [2+2] cycloaddition process, thus yielding the tricyclic pyrrolidine system.



Scheme 4. A mechanistic hypothesis that involves ene and [2+2] reaction pathways of bicyclobutanes **2**.

To probe the lifetime of the proposed biradical intermediates[12b,c,d,e,19] in the conversion of **2a** into **6** and **12**, we introduced a cyclopropylallyl substituent (Scheme 5).[20] Bicyclobutane **2a** was allowed to react with freshly prepared bromide **17** and the unstable amide **18** was obtained in 68% yield. Compound **18** underwent spontaneous conversion into equimolar amounts of **19a** and **19b** upon standing at room temperature. The lack of cyclopropane ring-opened products is not unusual for short-lived biradical intermediates,[21a] and the bifurcation in the reaction pathway with the cyclopropane substituent at R^1 supports our hypothesis of a common intermediate for both spirocycle and tricycle formation. A nonconcerted pathway for the formal [2+2] process was further supported by the reaction of **2a** with (*Z*)-cinnamyl bromide, which afforded **12** in 52% yield under our standard conditions instead of the diastereomeric product derived from a stereospecific process.[21b] Thus, the lifetime of the intermediate biradical is sufficiently long to allow σ-bond rotation at R_1 to give the more stable *anti* conformer.



Scheme 5. A mechanistic study with cyclopropane as a radical trap.

In summary, we have established a direct synthetic access to (bicyclo[1.1.0]butylmethyl)amines from propargyl phosphinamides through a Simmons–Smith reaction with Et_2Zn/CH_2I_2 or by addition of bicyclo[1.1.0]butyllithium to activated imines. Phase-transfer conditions proved optimal for the introduction of *N*-allyl or *N*-propargyl substituents, and the resulting amides underwent highly diastereoselective cascade rearrangements by formal ene or [2+2] pathways to yield novel spirocyclic and tricyclic pyrrolidine heterocycles.

Received: February 24, 2006
Published online: May 19, 2006

Keywords: bicyclobutanes · cascade reactions · pericyclic reactions · pyrrolidines · spirocycles

[1] a) H. Lebel, J.-F. Marcoux, C. Molinaro, A. B. Charette, *Chem. Rev.* **2003**, *103*, 977–1050; b) W. A. Donaldson, *Tetrahedron* **2001**, *57*, 8589–8627.
[2] a) N.-Y. Fu, S.-H. Chan, H. N. C. Wong in *The Chemistry of Cyclobutanes* (Eds.: Z. Rappoport, J. F. Liebman), Wiley, New York, **2005**, pp. 357–440; b) J. C. Namyslo, D. E. Kaufmann, *Chem. Rev.* **2003**, *103*, 1485–1538; c) E. Lee-Ruff, G. Mladenova, *Chem. Rev.* **2003**, *103*, 1449–1484.
[3] S. Hoz in *The Chemistry of Cyclopropyl Group* (Ed.: Z. Rappoport), Wiley, New York, **1987**, pp. 1121–1192.
[4] a) Y. Gaoni, *Tetrahedron* **1989**, *45*, 2819–2840; b) H. Takaya, T. Suzuki, Y. Kumagai, M. Hosoya, H. Kawauchi, R. Noyori, *J. Org. Chem.* **1981**, *46*, 2854–2861; c) P. G. Gassman, M. J. Mullins, *Tetrahedron Lett.* **1980**, *21*, 2219–2222.
[5] K. B. Wiberg, G. M. Lampman, R. P. Ciula, D. S. Connor, P. Schertler, J. Lavanish, *Tetrahedron* **1965**, *21*, 2749–2769.
[6] a) J. M. Schulman, G. J. Fisanick, *J. Am. Chem. Soc.* **1970**, *92*, 6653–6654; b) W. R. Moore, C. R. Costin, *J. Am. Chem. Soc.* **1971**, *93*, 4910–4912.
[7] a) P. Wipf, C. R. J. Stephenson, K. Okumura, *J. Am. Chem. Soc.* **2003**, *125*, 14694–14695; b) P. Wipf, C. Kendall, C. R. J. Stephenson, *J. Am. Chem. Soc.* **2003**, *125*, 761–768.
[8] a) J. Furukawa, N. Kawabata, J. Nishimura, *Tetrahedron* **1968**, *24*, 53–58; b) A. B. Charette, N. Wilb, *Synlett* **2002**, 176–178.
[9] P. Wipf, C. R. J. Stephenson, M. A. A. Walczak, *Org. Lett.* **2004**, *6*, 3009–3012.
[10] The remainder of the material was starting material **1** or rearranged allylcyclopropylbenzylamine.
[11] a) A. Duker, G. Szeimies, *Tetrahedron Lett.* **1985**, *26*, 3555–3558; b) J. Weber, U. Haslinger, U. H. Brinker, *J. Org. Chem.* **1999**, *64*, 6084–6086.
[12] a) E. P. Blanchard, Jr., A. Cairncross, *J. Am. Chem. Soc.* **1966**, *88*, 487–495; b) A. Cairncross, E. P. Blanchard, Jr., *J. Am. Chem. Soc.* **1966**, *88*, 496–504; c) M. Pomerantz, G. W. Gruber, R. N. Wilke, *J. Am. Chem. Soc.* **1968**, *90*, 5040–5041; d) P. G. Gassman, G. D. Richmond, *J. Am. Chem. Soc.* **1970**, *92*, 2090–

 © 2006 Wiley-VCH Verlag GmbH & Co. KGaA, Weinheim

2096; e) M. Pomerantz, R. N. Wilke, G. W. Gruber, U. Roy, *J. Am. Chem. Soc.* **1972**, *94*, 2752 – 2758.
[13] E. Slusarska, A. Zwierzak, *Synthesis* **1980**, 717 – 719.
[14] a) W. Oppolzer, *Pure Appl. Chem.* **1981**, *53*, 1181 – 1201; b) K. Mikami, M. Shimizu, *Chem. Rev.* **1992**, *92*, 1021 – 1050.
[15] The structure of **5** was assigned based on the X-ray analysis of the ketoaldehyde derived from cleavage of the cyclobutene ring.
[16] The relative stereochemistry of **12** was assigned based on NOESY analysis.
[17] A steric argument was used to rationalize the selectivity of the ene versus [2+2] pathway for simple bicyclo[1.1.0]butanes (see reference [12]); prior pericyclic reactions of bicyclo-[1.1.0]butanes were limited to structurally simple substrates, and no further synthetic applications were reported.
[18] Reaction of 3-phenylbicyclo[1.1.0]butyllithium with acetaldehyde or benzaldehyde followed by phase-transfer alkylation resulted in a low yield of the alkylated product.
[19] For a demonstration of the radical nature of reactions of bicyclo[2.1.0]pentane with alkenes, see: a) P. G. Gassman, K. T. Mansfield, T. J. Murphy, *J. Am. Chem. Soc.* **1969**, *91*, 1684 – 1689; b) P. G. Gassman, K. T. Mansfield, *J. Am. Chem. Soc.* **1968**, *90*, 1524 – 1526.
[20] J. P. Stevenson, W. F. Jackson, J. M. Tanko, *J. Am. Chem. Soc.* **2002**, *124*, 4271 – 4281.
[21] a) T. Linker, *Angew. Chem.* **1997**, *109*, 2150 – 2152; *Angew. Chem. Int. Ed. Engl.* **1997**, *36*, 2060 – 2062; b) alkene *Z*/*E* isomerization during *N*-alkylation was not responsible for the lack of stereospecificity; (*Z*)-cinnamyl bromide when treated with *N*-(3-*p*henylprop-2-ynyl)diphenylphosphinylamide gives an alkylated product with an intact *Z* double-bond configuration in 67% yield.

 © 2006 Wiley-VCH Verlag GmbH & Co. KGaA, Weinheim

Asymmetric Catalysis

DOI: 10.1002/anie.200600741

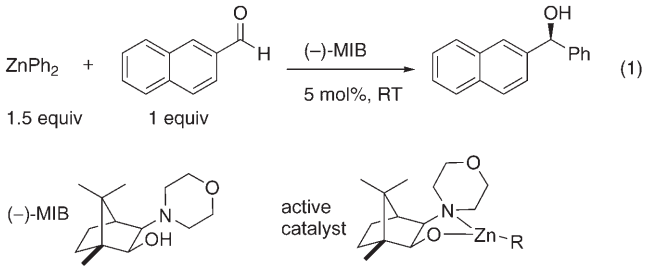
From Aryl Bromides to Enantioenriched Benzylic Alcohols in a Single Flask: Catalytic Asymmetric Arylation of Aldehydes**

*Jeung Gon Kim and Patrick J. Walsh**

Dedicated to Professor Madeleine Joullié

The catalytic asymmetric addition of aryl groups to aldehydes has generated an enormous amount of attention.[1] The resulting diarylmethanols are important constituents of biologically active compounds, such as clemastine,[2] orphenadrine,[3,4] neobenodine,[3,4] chloropheniramine,[5,6] cizolirtine,[7] and carbinoxamine.[8] Although the majority of enantioselective aldehyde arylation reactions rely on the use of costly diphenylzinc ($55–75 g^{-1}), important advances in the use of other aryl transfer reagents, such as arylboronic acids[9,10] and $Ph_2Si(OMe)_2$,[11] have been reported. Although a limited number of aryl boronic acids are commercially available, they are quite expensive as well (e.g., $PhB(OH)_2$ $225.00 mol^{-1} from Aldrich). A more practical and versatile method would begin with aryl bromides, many of which are commercially available and inexpensive (compare PhBr $2.50 mol^{-1} from Aldrich). There are no reports, however, of successful catalytic asymmetric aryl additions to aldehydes that begin with aryl bromides.[12,13] Herein, we disclose a one-pot method that begins with aryl bromides for the in situ generation of aryl zinc intermediates and their catalytic asymmetric addition to aldehydes to afford highly enantioenriched diarylmethanols and benzylic alcohols.

We chose to examine the amino alcohol ligand MIB developed by Nugent[14,15] in the asymmetric addition of commercial $ZnPh_2$ to 2-naphthylaldehyde [Eq. (1)]. We were



pleased to find that phenylation proceeded in toluene with 94% enantioselectivity (Table 1, entry 1). Unfortunately, transmetalation of phenyllithium with $ZnCl_2$ in toluene was unsuccessful because of the insolubility of $ZnCl_2$ in this medium. In contrast, ethereal solvents are known to promote transmetalation reactions. The asymmetric addition in diethyl ether, however, gave a low enantioselectivity (60%; Table 1, entry 2). In an attempt to balance both the solvating properties of diethyl ether, needed for the transmetalation, and the low polarity of toluene, we examined *tert*-butyl methyl ether (*t*BuOMe). A reaction mixture of commercial $ZnPh_2$, (−)-MIB, and 2-naphthylaldehyde in *t*BuOMe furnished the product in 88% *ee* (Table 1, entry 3). A solvent system of *t*BuOMe and hexanes (1:3) exhibited about the same

Table 1: Commercially available $ZnPh_2$ versus $ZnPh_2$ formed in situ.

Entry	$ZnPh_2$	Solvent	*ee* [%]
1	commercial	toluene	94
2	commercial	Et_2O	60
3	commercial	*t*BuOMe	88
4	commercial	*t*BuOMe/Hex (1:3)	89
5	in situ	*t*BuOMe/Hex (1:3)	2

[*] Dr. J. G. Kim, Prof. P. J. Walsh
P. Roy and Diana T. Vagelos Laboratories
University of Pennsylvania
Department of Chemistry
231 South 34th Street, Philadelphia, PA 19104-6323 (USA)
Fax: (+1) 215-573-6743
E-mail: pwalsh@sas.upenn.edu

[**] We thank the National Institutes of Health (National Institute of General Medical Sciences) and the National Science Foundation for support of this research.

Supporting information for this article is available on the WWW under http://www.angewandte.org or from the author.

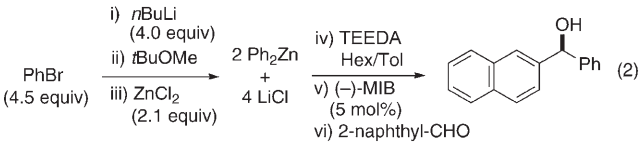
 © 2006 Wiley-VCH Verlag GmbH & Co. KGaA, Weinheim

enantioselectivity as *t*BuOMe alone (89%; Table 1, entry 4). Having identified a suitable solvent for the asymmetric addition, we focused on the in situ generation of diphenylzinc.

The preparation of $ZnPh_2$ was performed by metalation of 4.5 equivalents bromobenzene in *t*BuOMe with 4 equivalents of a freshly titrated solution of *n*BuLi (2.5 M in hexanes), transmetalation of the resultant PhLi with 2.1 equivalents of $ZnCl_2$, and the addition of hexanes to precipitate LiCl. The use of solutions prepared as described in the asymmetric addition to 2-naphthylaldehyde in the presence of 5 mol% of (−)-MIB resulted in the formation of the product with 2% enantioselectivity (Table 1, entry 5). We hypothesized that the LiCl, generated en route to $ZnPh_2$, likely promoted the addition faster than the amino alcohol based catalyst promotes the asymmetric addition. Similar proposals were advanced by Seebach[12] and Bolm[16] in reactions that began with Grignard reagents or PhLi. Based on their observations, we set out to design an inhibitor to reduce the undesired LiCl promoted addition.

To develop a selective inhibitor for lithium chloride we took advantage of the differences in coordination chemistry between the lithium salts and the zinc-based catalyst. It is proposed that three coordinate amino alcohol based catalysts possess a single open coordination site [Eq. (1)].[17] In contrast, the lithium salts likely have at least two available coordination sites. Structures of $[tmeda{\cdot}LiCl]_n$ (TMEDA = *N*,*N*,*N*′,*N*′-tetramethylethylene diamine) contain four-coordinate lithium centers with bridging chlorides.[18,19] Furthermore, we expected that the zinc catalyst is more sterically saturated than the lithium salts. Based on these points, we chose to examine bulky multidentate diamines as inhibitors that would chelate to lithium, but bind to the zinc catalyst in a monodentate fashion.

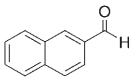
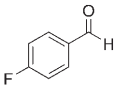
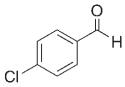
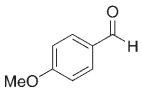
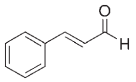
A series of chelating diamines was evaluated as LiCl inhibitors in the asymmetric addition with $ZnPh_2$ prepared in situ under the conditions employed in Table 1, entry 5. In this study, it was found that addition of toluene (or hexanes) after transmetalation aided the precipitation of the lithium salts. Subsequent injection of tetraethylethylene diamine (TEEDA, 0.8 equiv) resulted in addition with 89% enantioselectivity, the same value obtained under salt-free conditions with commercially available diphenylzinc [Eq. (2) and Table 1, entry 4]. Achieving of the same enantioselectivity in the absence or presence of LiCl indicates that the diamine effectively inhibits the LiCl-promoted addition pathway.



(2)

Under the conditions outlined above, unfunctionalized aryl bromides (bromobenzene, 2-bromotoluene, and 2-bromonaphthalene) were employed to prepare diarylzinc reagents [Eq. (2)]. TEEDA was then added followed by MIB and the aldehyde. In this fashion, aryl aldehydes gave addition products with high enantioselectivities (80–92%) and yields (78–99%). *trans*-Cinnamaldehyde and cyclohexanecarboxaldehyde underwent addition with 84 and 85% enantioselectivities (Table 2, entries 12 and 13, respectively).

Table 2: Catalytic asymmetric aryl additions to aldehydes from Ar_2Zn.

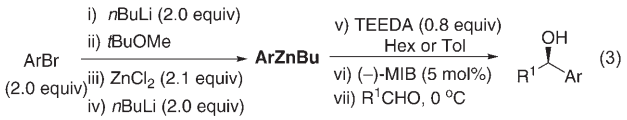
Entry	ArBr	Aldehyde	*ee* [%]	Yield [%]
1	phenyl		92	99
2	2-tolyl		92	90
3	2-naphthyl		89	96
4	phenyl		84	89
5	2-tolyl		80	92
6	phenyl		90	85 (*S*)[a]
7	2-tolyl		80	86
8	2-naphthyl		87	96
9	phenyl		90	90 (*S*)[a]
10	2-tolyl		87	78
11	2-naphthyl		91	99
12	phenyl		84	91
13	phenyl		85	92
14	2-naphthyl		82	92

[a] Absolute configuration.

During early investigations of phenyl additions with $ZnPh_2$, it was realized that the uncatalyzed addition was fast and competitive with the catalyzed reaction pathway, thus resulting in low enantioselectivity.[20–22] To circumvent this problem, Bolm and co-workers introduced the mixed zinc reagent Et/Zn/Ph formed from combination of $ZnEt_2$ and $ZnPh_2$.[22–28] Enantioselectivities with Et/Zn/Ph and planar chiral catalyst were up to 38% higher than those that employed the same catalyst with $ZnPh_2$ alone.

Based on the successful application by Bolm of mixed alkyl aryl zinc reagents,[9] we wished to develop an in situ route to these species to increase the levels of enantioselectivity in the aryl addition reactions. In our strategy to prepare the mixed alkyl aryl zinc intermediates in situ, we chose to avoid the use of dialkyl zinc reagents and focused on the more readily available alkyl lithium reagents instead. Thus, 2.0 equivalents of aryl bromide and 2.1 equivalents of $ZnCl_2$ were employed. Metalation of PhBr with *n*BuLi and addition to $ZnCl_2$ resulted in the generation of Ph/Zn/Cl. A second equivalent of *n*BuLi was then added to produce Ph/Zn/Bu, which was used in situ in the asymmetric addition reaction after the addition of 0.8 equivalents of TEEDA [Eq. (3)]. We were pleased to find that the enantioselectivity observed with

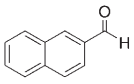
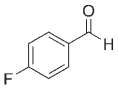
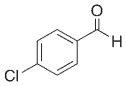
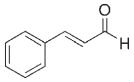
 © 2006 Wiley-VCH Verlag GmbH & Co. KGaA, Weinheim



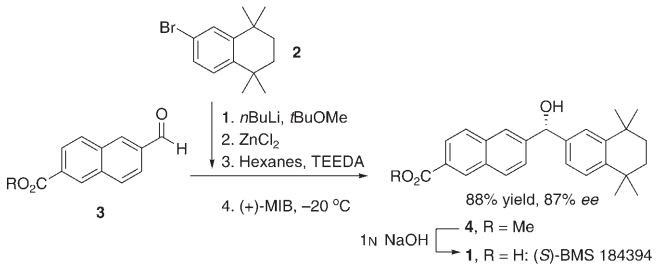
the Ph/Zn/Bu generated in situ was higher than that with Ph_2Zn and equal to that of Ph/Zn/Et (generated from commercial Ph_2Zn and Et_2Zn), despite the 4 equivalents of LiCl formed in the preparation of Ph/Zn/Bu.

A variety of substituted and functionalized aryl bromides underwent enantioselective addition to benzaldehyde derivatives under the conditions in Equation (3) with enantioselectivities around 95% (Table 3, entries 2–9). These include 2-bromotoluene, 2-bromonaphthylene, 4-bromoanisole, 4-bromofluorobenzene, and 4-bromochlorobenzene. α,β-Unsaturated aldehydes underwent addition with enantioselectivities between 81 and 88%, whereas cyclohexanecarboxaldehyde again gave slightly lower enantioselectivities (78 and 82%). The results in Table 3 indicate that various aryl bromides can now be employed as starting materials in the catalytic asymmetric arylation of aldehydes.

Table 3: Catalytic asymmetric aryl additions to aldehydes with ArZnBu.

Entry	ArBr	Aldehyde	*ee* [%]	Yield [%]
1	Ph_2Zn + Et_2Zn		97	98
2	phenyl		97	90
3	4-methoxyphenyl		93	96
4	4-fluorophenyl		97	75
5	4-chlorophenyl		95	78
6	phenyl		96	80
7	4-methoxyphenyl		93	84
8	2-tolyl		95	73
9	2-naphthyl		96	79
10	4-methoxyphenyl		83	82
11	4-fluorophenyl		88	64
12	4-chlorophenyl		87	55
13	phenyl		88	95
14	4-fluorophenyl		84	74
15	4-chlorophenyl		81	68
16	2-naphthyl		82	76
17	4-methoxyphenyl		78	84

To demonstrate the utility of our method, we chose to prepare the precursor to BMS184394 (**1**, Scheme 1), an retinoic acid receptor (RAR) γ-selective retinoid with activity against various skin diseases and cancers, in particular breast cancer and acute promyelocytic leukemia.[29–31] Although



Scheme 1. Formal synthesis of (*S*)-BMS184394.

both (*R*)- and (*S*)-BMS184394 are RAR γ-selective, the *S* enantiomer is significantly more potent than the *R* enantiomer.[30] Enantioselective synthesis of this compound proved difficult. Currently, the only enantioselective route to this drug candidate employed two sequential enzymatic kinetic resolutions that required 2 and 3.5 days (43% yield and 95% *ee*).[30] As with any kinetic resolution, the maximum yield is 50% and the desired compound must be separated from the undesired derivatized product. In principle, secondary diarylmethanols could be prepared enantioselectively by asymmetric reduction of diaryl ketones. This approach has proven quite challenging, however, because it is difficult for catalysts to differentiate between the lone pairs on the carbonyl oxygen atom when the aryl groups are similar in size, thus resulting in low enantioselectivities.[32–36]

Using our method, 3.0 equivalents aryl bromide (**2**, Scheme 1) were combined with *n*BuLi followed by $ZnCl_2$ to generate the mixed aryl butyl zinc reagent. TEEDA (1.5 equiv) in hexanes was added followed by (+)-MIB (5 mol%) and the aldehyde **3**. The addition product **4** was produced with 87% enantioselectivity in 88% yield (Scheme 1). Conversion into (*S*)-BMS184394 can be accomplished by saponification of the ester.[30] The one-pot enantioselective arylation of **3** demonstrates the potential utility of our method for the synthesis of enantioenriched biologically active benzylic alcohols.

In summary, we have developed a versatile method to generate secondary benzylic alcohols with high levels of enantioselectivity and yields. The importance of this method is that one can now begin the asymmetric arylation of aldehydes with aryl bromides, many of which are readily available. In contrast, previous methods employed preformed aryl boron reagents to generate salt-free aryl zinc intermediates or began with diphenylzinc. The introduction of a diamine, such as TEEDA, was the key to the success of this method. In the absence of TEEDA, the addition reaction is promoted by LiCl, thus generating racemic products. TEEDA prohibits the LiCl by-product from promoting the addition reaction, thus allowing the addition to proceed through the chiral zinc catalyst. Importantly, it is not necessary to filter,[16] centrifuge,[13] or isolate the pyrophoric aryl zinc reagents, as required with previous methods, in the presence of the diamine, thus increasing the attractiveness of our method for large-scale applications. This method enables the synthesis of a variety of benzylic alcohols that were previously difficult to access in enantioenriched form.

 © 2006 Wiley-VCH Verlag GmbH & Co. KGaA, Weinheim

Experimental Section

Preparation of (4-fluorophenyl-4-methoxyphenyl)methanol (Table 3, entry 7): A nitrogen-purged Schlenk flask was charged with 4-bromoanisole (100.1 μL, 0.8 mmol) and *t*BuOMe (1 mL) and cooled to −78 °C. Freshly titrated *n*BuLi (0.32 mL, 2.5 M in hexanes, 0.8 mmol) was added dropwise, and the solution was stirred for 1 h. The dry-ice bath was replaced with an ice bath, $ZnCl_2$ (114.5 mg, 0.84 mmol) was added, and the reaction mixture was stirred for 30 min. Additional *n*BuLi (0.32 mL, 2.5 M in hexanes, 0.8 mmol) was added to the reaction mixture, which was then stirred for 4.5 h at room temperature. Toluene (5 mL) and TEEDA (68 μL, 0.32 mmol) were added, and the solution was stirred for 1 h. After the addition of (−)-MIB (4.8 mg, 0.02 mmol, 5 mol %), the reaction cooled to 0 °C for 30 min, and *p*-fluorobenzaldehyde (43 μL, 0.4 mmol) was added. The reaction was stirred at 0 °C and monitored by TLC. After completion (18 h), the reaction mixture was quenched with H_2O (20 mL) and extracted with ethyl acetate (3 × 20 mL). The organic layer was dried over $MgSO_4$, filtered, and the solvent was removed under reduced pressure. The crude product was purified by column chromatography on silica gel (hexanes/EtOAc, 95:5) to give the product (77.7 mg, 84 % yield, 93 % *ee*) as a white solid. M.p. 52 °C; $[\alpha]_D^{20} = (+)13.846$ (c = 0.195, THF); ^{1}H NMR (C_6D_6, 300 MHz): $\delta = 2.17$ (s, 1H), 3.38 (s, 3H), 5.50 (s, 1H), 6.81–6.95 (m, 4H), 7.17–7.29 (m, 4H) ppm; $^{13}C\{^1H\}$ NMR (C_6D_6, 75 MHz): 55.0, 75.3, 114.3, 115.4 (d, J = 21.2 Hz), 128.4, 128.7 (d, J = 8.0 Hz), 136.9, 141.0 (d, J = 3.0 Hz), 159.7, 162.6 ppm (d, J = 243 Hz); IR (neat): $\tilde{\nu}$ = 3421, 2957, 2837, 1609, 1504, 1248, 1033, 831 cm^{-1}; HRMS calcd for $C_{13}H_{13}FO_2$ $[M]^+$: 232.0900, found: 232.0900; determination conditions for the *ee*: Chiralpak AS-H, hexanes/isopropylamine (95:5), flow rate = 0.5 mL min^{-1}, t = 20.0 min, 22.1 min.

Received: February 26, 2006
Published online: May 24, 2006

Keywords: addition reactions · alcohols · aldehydes · asymmetric catalysis · zinc reagents

[1] C. Bolm, J. P. Hildebrand, K. Muñiz, N. Hermanns, *Angew. Chem.* **2001**, *113*, 3382; *Angew. Chem. Int. Ed.* **2001**, *40*, 3284.
[2] A. Ebnother, H.-P. Weber, *Helv. Chim. Acta* **1976**, *59*, 2462.
[3] A. F. Casy, A. F. Drake, C. R. Ganellin, A. D. Mercer, C. Upton, *Chirality* **1992**, *4*, 356.
[4] P. Müller, P. Nury, G. Bernardinelli, *Eur. J. Org. Chem.* **2001**, 4137.
[5] M. N. G. James, G. J. B. Williams, *Can. J. Chem.* **1974**, *52*, 1872.
[6] A. Shafi′ee, G. Hite, *J. Med. Chem.* **1969**, *12*, 266.
[7] A. Torrens, J. A. Castrillo, A. Claparols, J. Redondo, *Synlett* **1999**, 765.
[8] V. Barouh, H. Dall, D. Patel, G. Hite, *J. Med. Chem.* **1971**, *14*, 834.
[9] C. Bolm, J. Rudolph, *J. Am. Chem. Soc.* **2002**, *124*, 14850.
[10] J. Rudolph, F. Schmidt, C. Bolm, *Synthesis* **2005**, 840.
[11] D. Tomita, R. Wada, M. Kanai, M. Shibasaki, *J. Am. Chem. Soc.* **2005**, *127*, 4138.
[12] Two additions of aryl groups to aldehydes beginning from aryl bromides are reported; each gave less than 10 % enantioselectivity; see: B. Weber, D. Seebach, *Tetrahedron* **1994**, *50*, 7473.
[13] Seebach reported that transmetalation of PhLi with [TiCl(O*i*Pr)$_3$] and addition to benzaldehydes gave high enantioselectivities only if the reactions were subject to centrifugation to remove LiCl and the addition of 30 mol % of [12]crown-4 to inhibit the remaining LiCl; see reference [12].
[14] W. A. Nugent, *Chem. Commun.* **1999**, 1369.
[15] Y. K. Chen, S. J. Jeon, P. J. Walsh, W. A. Nugent, *Org. Synth.* **2005**, *82*, 87.
[16] Generation of $ZnPh_2$ from PhLi and $ZnBr_2$ followed by filtration through Celite and addition of dimethoxy poly(ethylene glycol) (to inhibit traces of remaining LiBr) and addition to 4-chlorobenzaldehyde afforded the diaryl methanol in up to 93 % enantioselectivity in 8–31 % yield; see: J. Rudolph, N. Hermanns, C. Bolm, *J. Org. Chem.* **2004**, *69*, 3997.
[17] M. Kitamura, S. Okada, S. Suga, R. Noyori, *J. Am. Chem. Soc.* **1989**, *111*, 4028.
[18] D. Hoffmann, A. Dorigo, P. von R. Schleyer, H. Reif, D. Stalke, G. M. Sheldrick, E. Weiss, M. Geissler, *Inorg. Chem.* **1995**, *34*, 262.
[19] S. Chitsaz, J. Pauls, B. Neumüller, *Z. Naturforsch. B* **2001**, *56*, 245.
[20] P. I. Dosa, J. C. Ruble, G. C. Fu, *J. Org. Chem.* **1997**, *62*, 444.
[21] W.-S. Huang, L. Pu, *J. Org. Chem.* **1999**, *64*, 4222.
[22] J. Rudolph, C. Bolm, P.-O. Norrby, *J. Am. Chem. Soc.* **2005**, *127*, 1548.
[23] C. Bolm, N. Hermanns, J. P. Hildebrand, K. Muñiz, *Angew. Chem.* **2000**, *112*, 3607; *Angew. Chem. Int. Ed.* **2000**, *39*, 3465.
[24] C. Bolm, M. Kesselgruber, N. Hermanns, J. P. Hildebrand, G. Raabe, *Angew. Chem.* **2001**, *113*, 1536; *Angew. Chem. Int. Ed.* **2001**, *40*, 1488.
[25] C. Bolm, N. Hermanns, M. Kesselgruber, J. P. Hildebrand, *J. Organomet. Chem.* **2001**, *624*, 157.
[26] S. Ozcubukcu, F. Schmidt, C. Bolm, *Org. Lett.* **2005**, *7*, 1407.
[27] J. Rudolph, T. Rasmussen, C. Bolm, P.-O. Norrby, *Angew. Chem.* **2003**, *115*, 3110; *Angew. Chem. Int. Ed.* **2003**, *42*, 3002.
[28] M. Fontes, X. Verdaguer, L. Solà, M. A. Pericàs, A. Riera, *J. Org. Chem.* **2004**, *69*, 2532
[29] B. P. Klaholz, A. Mitschler, D. Moras, *J. Mol. Biol.* **2000**, *302*, 155.
[30] K. L. Yu, P. Spinazze, J. Ostrowski, S. J. Currier, E. J. Pack, L. Hammer, T. Roalsvig, J. A. Honeyman, D. R. Tortolani, P. R. Reczek, M. M. Mansuri, J. E. Starrett, *J. Med. Chem.* **1996**, *39*, 2411.
[31] S. M. Thacher, J. Vasudevan, R. A. S. Chandraratna, *Curr. Pharm. Des.* **2000**, *6*, 25.
[32] R. Noyori, M. Yamakawa, S. Hashiguchi, *J. Org. Chem.* **2001**, *66*, 7931
[33] E. J. Corey, C. J. Helal, *Tetrahedron Lett.* **1996**, *37*, 4837.
[34] T. Ohkuma, M. Koizumi, H. Ikehira, T. Yokozawa, R. Noyori, *Org. Lett.* **2000**, *2*, 659.
[35] E. J. Corey, C. J. Helal, *Tetrahedron Lett.* **1995**, *36*, 9153.
[36] H. Ushio, K. Mikami, *Tetrahedron Lett.* **2005**, *46*, 2903.

 © 2006 Wiley-VCH Verlag GmbH & Co. KGaA, Weinheim

Liquid Crystals

DOI: 10.1002/anie.200600929

Electrodeposition of Silver Particles and Gold Nanoparticles from Ionic Liquid-Crystal Precursors**

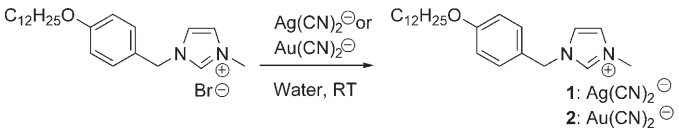
William Dobbs, Jean-Moïse Suisse, Laurent Douce, and Richard Welter*

Dedicated to Stéphane Bellemin-Laponnaz

The convergence of two distinct fields of ionic liquid chemistry, those of imidazolium salts and liquid crystals, could lead to a vast range of new materials.[1] Uniting the properties of imidazolium derivatives, which have low melting points, low volatility, nonflammability, high chemical and radiochemical stability, tunable conductivity, and wide electrochemical windows, with those of liquid crystals, which have many forms of labile macroscopic ordering, raises fascinating prospects.[1,2] A particular challenge is the synthesis of nanoparticles of controllable form for applications in electronics, catalysis, and materials science.[3] Solvents based on imidazolium and pyridinium salts have been successfully used to prepare and stabilize gold nanoparticles or nanorods, for example, but the literature concerning mesomorphic pyridinium and imidazolium salts incorporating metalloanions is very limited.[4–8] A significant recent report is the use of an ionic liquid crystal, *N*-dodecylpyridinium tetrachlorocuprate(II), mixed with the hydrophobic reducing agent 6-*O*-palmitoyl ascorbic acid, as a template to synthesize copper(I) chloride nanoplatelets.[9]

We now present a strategy for a more versatile exploitation of liquid-crystal template effects, which is illustrated by the electrolysis of imidazolium liquid crystals containing dicyanoargentate(I) and dicyanoaurate(I) anions to produce silver and gold nanoparticles. The key to this approach is the coupling of the self-organization of the imidazolium metallate to the use of electrochemical reduction, the latter providing the means to control the particle size and form of the electrodeposited metals by variation of parameters such as the potential and the current density.

Many mesomorphic imidazolium salts can be readily prepared by simple metathesis reactions involving precipitation from aqueous solutions containing the appropriate anions. In investigating this chemistry, we sought to use anions incorporating transition metals to endow the products with properties such as redox activity and variable conductivity. Thus, we have synthesized dicyanoargentate(I) (**1**) and dicyanoaurate(I) (**2**) derivatives of 3-(4-dodecyloxybenzyl)-1-methyl-1*H*-imidazolium in good yield (over 80%) from the bromide starting material (Scheme 1).[10] Both complex salts are highly insoluble in water and are isolated in pure form by simply washing the reaction precipitates with water.



Scheme 1. Precipitation of **1** and **2** from water.

Compounds **1** and **2** were characterized by ^{1}H NMR, ^{13}C{^{1}H} NMR, and FT-IR spectroscopy, and elemental analysis. Distinctive signals assigned to the CH group at the 2-position of the imidazolium ring appear in the ^{1}H NMR spectra of **1** and **2** at $\delta = 9.05$ and 8.77 ppm, and in their ^{13}C{^{1}H} NMR spectra at $\delta = 136.14$ and 135.50 ppm, respectively. The IR spectra of **1** and **2** show typical cyanometallate vibrations at $\tilde{\nu}(\mathrm{CN}) = 2131$ and 2140 cm^{-1}, respectively.[11]

Single crystals of **1** and **2** were obtained by the slow diffusion of ether into dichloromethane solutions, and the structures of the compounds were determined by X-ray diffraction (see Supporting Information). As the crystal structures of **1** and **2** are isotypic, we only describe that of **2**, which is shown in Figure 1. In the cation, the *n*-alkyl chains and the phenyl groups are approximately orthogonal (87(1)°) to the plane of the imidazolium ring.

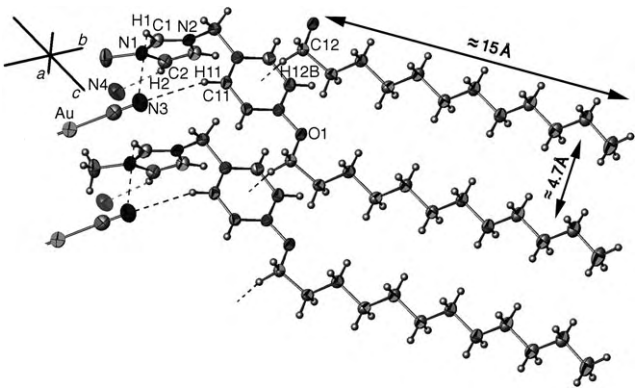


Figure 1. ORTEP representation of part of the crystal structure of **2**. Dashed lines indicate nonclassical hydrogen bonds. Thermal ellipsoids enclose 50% of the electron density.

[*] W. Dobbs, J.-M. Suisse, Dr. L. Douce
Institut de Physique et Chimie des Matériaux de Strasbourg
Groupe des Matériaux Organiques
UMR 7504, CNRS-Université Louis Pasteur
BP 43, 23 rue du Loess, 67034 Strasbourg Cedex 2 (France)
Fax: (+33) 388-107-246
E-mail: Laurent.Douce@ipcms.u-strasbg.fr
Prof. R. Welter
Laboratoire DECOMET
UMR 7177-LC003, CNRS-Université Louis Pasteur
4 rue Blaise Pascal, 67000 Strasbourg Cedex (France)

[**] We are especially grateful to Dr. J. Harrowfield for the critical evaluation of the manuscript. We also thank A. De Cian and B. Heinrich for the X-ray diffraction studies, and J. Faerber for the scanning electron micrographs. This work was supported by the Institut de Physique et Chimie des Matériaux de Strasbourg, the Université Louis Pasteur, and NANORGYSOL A.N.R.

Supporting information for this article is available on the WWW under http://www.angewandte.org or from the author.

 © 2006 Wiley-VCH Verlag GmbH & Co. KGaA, Weinheim

The packing in the crystal structure can be described as a pseudo-lamellar system with a stacking direction along the *c* axis (Figure 2). Nonclassical hydrogen bonds (N4···H2–C2, N3···H1–C1, and N3···H11–C11) associate the $[Au(CN)_2]^-$ anion with the rigid imidazolium and phenyl rings of the cation (Figure 1). Moreover, a C–H···π interaction occurs between C12–H12B and the phenyl ring (the distance between H12B and the centroid of the ring is 2.76 Å). The rigid phenyl and imidazolium rings form a unit of approximately 7 Å in length. These units, together with the $[Au(CN)_2]^-$ anions, comprise layers that are completely segregated by the flexible chains of approximately 15 Å in length. The layers are stacked along the *c* axis at a repeat distance of approximately 27 Å (Figure 2).

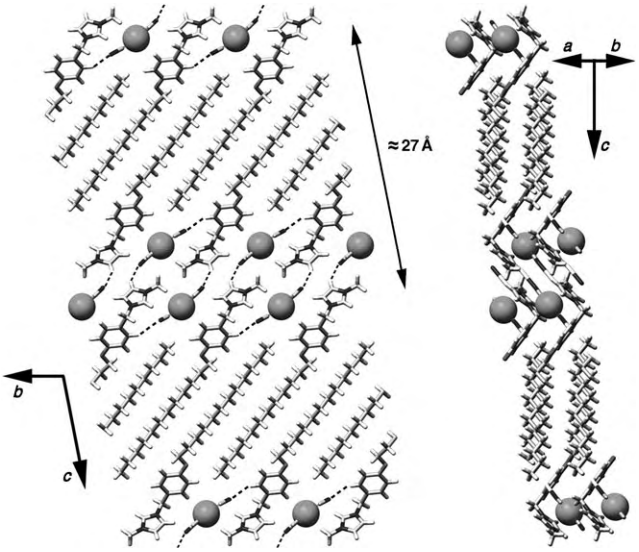


Figure 2. Two views of the crystal structure of **2**. Dashed lines indicate nonclassical hydrogen bonds. Au spheres; C, H, N, O rods.

The formation of true crystals of **1** and **2** at ambient temperatures is not unexpected, since the balance of factors influencing crystallinity and mesomorphism is subtle. The amphiphilic character of these materials leads, however, to the expectation that mesomorphism should be exhibited at higher temperatures.

The mesomorphic behavior and phase-transition temperatures of **1** and **2** were characterized by polarizing optical microscopy (POM), differential scanning calorimetry (DSC), and powder X-ray diffraction (XRD). The DSC thermograms registered upon heating and cooling reveal for both **1** and **2** the presence of two sharp peaks indicative of reversible first-order phase transitions. The first peak (at low temperature with a large enthalpy change) is related to the appearance of a liquid-crystal phase, while the second peak is due to its melting into an isotropic liquid. These observations can be summarized by Equations (1) and (2), in which the phase-transition temperatures and enthalpy changes are indicated.

$$\mathbf{1}\ \text{Crystal} \underset{\text{partial crystallization}}{\overset{61\,^\circ\text{C}\ (42.95\ \text{kJ mol}^{-1})}{\rightleftharpoons}} \text{Smectic A} \underset{158\,^\circ\text{C}\ (0.55\ \text{kJ mol}^{-1})}{\overset{157\,^\circ\text{C}\ (0.54\ \text{kJ mol}^{-1})}{\rightleftharpoons}} \text{Liquid} \quad (1)$$

$$\mathbf{2}\ \text{Crystal} \underset{\text{partial crystallization}}{\overset{66\,^\circ\text{C}\ (54.23\ \text{kJ mol}^{-1})}{\rightleftharpoons}} \text{Smectic A} \underset{112\,^\circ\text{C}\ (0.49\ \text{kJ mol}^{-1})}{\overset{112\,^\circ\text{C}\ (0.50\ \text{kJ mol}^{-1})}{\rightleftharpoons}} \text{Liquid} \quad (2)$$

The optical textures observed upon slow cooling from the isotropic melt show the emergence of a typical smectic-A phase: initially bâtonnets (rods) appear, and these turn into focal conic structures (Figure 3).



Figure 3. Polarizing optical microscope images of the smectic-A phase of **2**. Upon formation of the liquid-crystal phase, rods (left) initially appear, followed by focal conic structures (right).

The lamellar arrangement of the liquid-crystal phase was also established by XRD. Because of the high X-ray mass attenuation coefficients of gold and silver atoms, we prepared thin films of **1** and **2** between two mica slides with a 100-μm separation. The smectic-A structures produced diffraction patterns containing one sharp reflection in the small-angle region, which arises from the regular arrangement of the molecules in layers with separations of $d = 37.0$ and 36.0 Å at 100 °C for **1** and **2**, respectively. A broad band at $d = 4.6$ Å in the wide-angle region of the patterns is related to the disordered (liquid-like) conformation of the alkyl chains. The diffraction patterns are consistent with a head-to-tail molecular arrangement of the cations within the layers, as observed for imidazolium salts containing PF_6^-, BF_4^-, Br^-, and SCN^- anions, in which the lamellar spacings are approximately 37 Å.[10]

To investigate the possibility of forming nanoparticles from **1** and **2** by electrodeposition, we sandwiched the compounds between two indium tin oxide (ITO) coated glass slides separated by a 100-μm spacer. The electrodeposition was conducted at constant potential for 15 minutes. In Figure 4, scanning electron micrographs (SEM) of the gold particles obtained by electrodeposition of **2** from the isotropic liquid state at 117 °C (top) and from the liquid-crystal state at 111 °C (bottom) are shown. The particles formed by electrodeposition from the isotropic liquid are nanodots (20–30 nm) aggregated into spheres or multiglobular shapes (100 nm). In contrast, the morphology of the nanoparticles deposited from the liquid crystal at 111 °C is completely different, consisting of leaflike forms interlocked in rosettes.

Application of the same electrodeposition procedure to the isotropic liquid of the silver derivative **1** led to essentially polydisperse silver spheres at 170 °C (Figure 5, top). Electrodeposition at 152 °C from the mesomorphic phase of **1** led to hexagonal platelets in an amorphous silver gangue (Figure 5,

 © 2006 Wiley-VCH Verlag GmbH & Co. KGaA, Weinheim

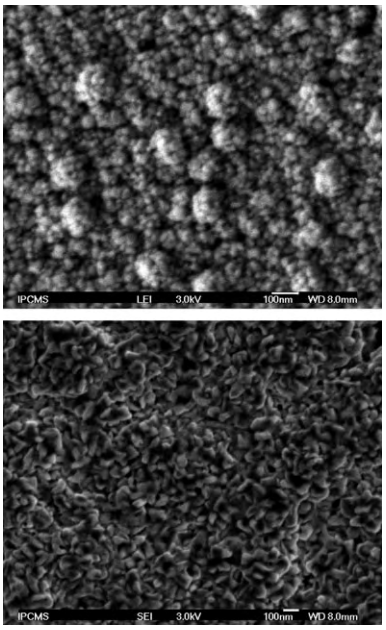


Figure 4. SEMs of spherical gold nanoparticles electrodeposited ($E = 1.78$ V) from the isotropic liquid phase of **2** (top), and of leaflike gold forms electrodeposited ($E = 2.27$ V) from the lamellar liquid-crystal phase of **2** (bottom). White scale bars: 100 nm.

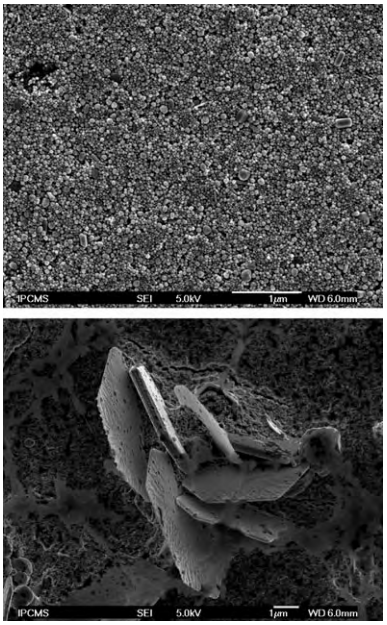


Figure 5. SEMs of spherical silver nanoparticles electrodeposited ($E = 1.21$ V) from the isotropic liquid phase of **1** (top), and of hexagonal silver platelets electrodeposited ($E = 1.70$ V) from the lamellar liquid-crystal phase of **1** (bottom). White scale bars: 1 μm.

bottom). These platelets are remarkably similar to the CuCl platelets obtained from a lamellar ionic liquid-crystal precursor.[9]

In summary, we report the full characterization of the first mesomorphic compounds based on imidazolium cyanometallates. The structures of their crystalline phases have also been determined. Work is in progress on the modification of the structures to provide ambient-temperature mesophases and other forms of self-organization. Of particular significance is the demonstration herein that the supramolecular structure of the liquid-crystal phase can be used to influence the morphology of metal nanoparticles deposited by electrochemical reduction.

Experimental Section

1: Compound **1** was obtained by anion metathesis in water. An aqueous solution (25 mL) of potassium dicyanoargentate (467 mg, 2.35 mmol) was added to 3-(4-dodecyloxybenzyl)-1-methyl-1*H*-imidazolium bromide (1.03 g, 2.35 mmol) dissolved in water (50 mL). A precipitate of **1** formed immediately, and was collected by filtration and washed with water. Recrystallization by slow diffusion of ether into a dichloromethane solution led to a white crystalline solid, yield: 1.22 g, 92%. ^{1}H NMR (300 MHz, $CDCl_3$): $\delta = 0.89$ (t, ^3J(H,H) = 6.6 Hz, 3H, CH_3 aliphatic chain), 1.27 (br s, 16H, CH_2 aliphatic chain), 1.39–1.47 (m, 2H, CH_2 aliphatic chain), 1.76 (q, ^3J(H,H) = 6.8 Hz, 2H, OCH$_2$CH_2), 3.98 (t, ^3J(H,H) = 6.6 Hz, 2H, OCH_2), 4.03 (s, 3H, CH_3N), 5.31 (s, 2H, NCH_2Ph), 6.97 (d, ^3J(H,H) = 8.6 Hz, 2H, C*H* phenyl), 7.24–7.26 (m, 2H, NC*H* imidazolium), 7.35 (d, ^3J (H,H) = 8.6 Hz, 2H, C*H* phenyl), 9.05 ppm (s, 1H, NC*H*N imidazolium); ^{13}C NMR (75 MHz, $CDCl_3$): $\delta = 14.09$ (*C*H$_3$ aliphatic chain), 22.65, 25.99, 29.13, 29.31, 29.37, 29.54, 29.57, 29.60, 29.63, 31.88 (*C*H$_2$ aliphatic chain), 36.95 (N*C*H$_3$), 53.52 (N*C*H$_2$Ph), 67.26 (O*C*H$_2$), 115.57 (*C*H phenyl), 122.08, 123.38 (N*C*H imidazolium), 123.42 (*C* phenyl), 123.65 (N*C*H imidazolium), 130.60 (*C*H phenyl), 136.14 (N*C*HN imidazolium), 144.74 (*C*N), 160.37 ppm (*C* phenyl); IR: $\tilde{\nu}$ = 3154, 2915, 2846, 2131, 1515, 1255, 1248 cm^{-1}. Elemental analysis (%) calcd for $C_{25}H_{37}AgN_4O$: C 58.0, H 7.2, N 10.8; found: C 58.0, H 7.4, N 10.0.

2: The same experimental procedure was used as for **1**, with potassium dicyanoaurate (164 mg, 0.57 mmol) and 3-(4-dodecyloxybenzyl)-1-methyl-1*H*-imidazolium bromide (250 mg, 0.57 mmol). White solid, yield: 275 mg, 80%. ^{1}H NMR (300 MHz, $CDCl_3$): δ = 0.89 (t, ^3J(H,H) = 6.6 Hz, 3H, CH_3 aliphatic chain), 1.27 (br s, 16H, CH_2 aliphatic chain), 1.39–1.47 (m, 2H, CH_2 aliphatic chain), 1.80 (q, ^3J(H,H) = 6.8, 2H, OCH$_2$CH_2), 3.98 (t, ^3J(H,H) = 6.6, 2H, OCH_2), 4.03 (s, 3H, CH_3N), 5.31 (s, 2H, NCH_2Ph), 6.97 (d, ^3J(H,H) = 8.6 Hz, 2H, C*H* phenyl), 7.24–7.26 (m, 2H, NC*H* imidazolium), 7.35 (d, ^3J(H,H) = 8.6 Hz, 2H, C*H* phenyl), 8.77 ppm (s, 1H, NC*H*N imidazolium); ^{13}C NMR (75 MHz, $CDCl_3$): $\delta = 14.11$ (*C*H$_3$ aliphatic chain), 22.67, 26.00, 29.14, 29.33, 29.38, 29.56, 29.59, 29.62, 29.65, 31.90 (*C*H$_2$ aliphatic chain), 37.05 (N*C*H$_3$), 53.70 (N*C*H$_2$Ph), 68.29 (O*C*H$_2$), 115.65 (*C*H phenyl), 122.26, 122.99 (N*C*H imidazolium), 123.74 (*C* phenyl), 130.82 (*C*H phenyl), 135.50 (N*C*HN imidazolium), 151.17 (*C*N), 160.47 ppm (*C* phenyl); IR: $\tilde{\nu}$ = 3101, 2916, 2846, 2140, 1515, 1256, 1249 cm^{-1}. Elemental analysis (%) calcd for $C_{25}H_{37}AuN_4O$: C 49.5, H 6.15, N 9.2; found: C 49.1, H 6.3, N 8.9.

DSC: Perkin Elmer Q1000, heating/cooling rate of 2 °C min^{-1}. Polarizing optical microscope: Leitz Orthoplan, Mettler FP82 hot stage. Powder XRD: $Cu_{K\alpha 1}$ radiation, powder samples in Lindemann capillaries, INSTEC hot stage, image plate. SEM: JEOL JMS 6700F with a Noran Vantage energy-dispersive X-ray spectrometer.

Single-crystal XRD: The selected crystals were mounted on a Nonius KappaCCD area-detector diffractometer ($Mo_{K\alpha}$, λ = 0.71073 Å). Cell parameters were determined from reflections recorded in ten frames (1.0° in ϕ, 20 s). The structures were solved using direct methods (SHELXS97) and refined against F^2 (SHELXL97). All non-hydrogen atoms were refined anisotropically. Hydrogen atoms were generated according to stereochemistry and refined using a riding model. Further details of the data collections (Denzo) and structure refinements are given in the Supporting Information. **1**: colorless crystal, $0.11 \times 0.10 \times 0.09$ mm^3, $C_{25}H_{37}AgN_4O$, $M_r = 517.46$ g mol^{-1}, triclinic, space group $P\bar{1}$, a =

 © 2006 Wiley-VCH Verlag GmbH & Co. KGaA, Weinheim

4.6840(10), $b = 10.238(2)$, $c = 27.212(5)$ Å, $\alpha = 98.83(5)$, $\beta = 90.90(5)$, $\gamma = 102.64(5)°$, $V = 1256.7(5)$ Å^3, $Z = 2$, $\rho_{calcd} = 1.367$ g cm^{-3}, $\mu(Mo_{K\alpha}) = 0.825$ mm^{-1}, 7341 reflections, $1.52 < \theta < 30.05°$, 7341 independent, 4275 with $I > 2\sigma(I)$, 280 parameters, $R_1 = 0.0607$, $wR_2 = 0.1821$, $S = 1.072$, max. residual electron density = 1.235 e Å^{-3}. **2**: colorless crystal, $0.10 \times 0.10 \times 0.10$ mm^3, $C_{25}H_{37}AuN_4O$, $M_r = 606.55$ g mol^{-1}, triclinic, space group $P\bar{1}$, $a = 4.68600(10)$, $b = 10.1620(2)$, $c = 27.2730(5)$ Å, $\alpha = 99.1470(7)$, $\beta = 91.5350(8)$, $\gamma = 100.1550(10)°$, $V = 1260.11(4)$ Å^3, $Z = 2$, $\rho_{calcd} = 1.599$ g cm^{-3}, $\mu(Mo_{K\alpha}) = 5.860$ mm^{-1}, 11179 reflections, $1.51 < \theta < 30.05°$, 7317 independent, 5999 with $I > 2\sigma(I)$, 280 parameters, $R_1 = 0.0304$, $wR_2 = 0.0661$, $S = 1.052$, max. residual electron density = 1.470 e Å^{-3}. CCDC-600951 (**1**) and CCDC-600952 (**2**) contain the supplementary crystallographic data for this paper. These data can be obtained free of charge from The Cambridge Crystallographic Data Centre via www.ccdc.cam.ac.uk/data_request/cif.

Received: March 9, 2006
Published online: May 24, 2006

Keywords: electrodeposition · gold · liquid crystals · nanostructures · silver

[1] H. Ohno, *Electrochemical Aspects of Ionic Liquids*, Wiley-Interscience, New York, **2005**; P. Wasserscheid, T. Welton, *Ionic Liquids in Synthesis*, Wiley-VCH, Weinheim, **2003**; J. Dupont, R. F. de Souza, P. A. Z. Suarez, *Chem. Rev.* **2002**, *102*, 3667; J. W. Goodby, G. W. Gray, H.-W. Spiess, V. Vill, D. Demus, *Handbook of Liquid Crystals*, Wiley-VCH, Weinheim, **1998**.

[2] F. Endres, *ChemPhysChem* **2002**, *3*, 144; D. Allen, G. Baston, A. E. Bradley, T. Gorman, A. Haile, I. Hamblett, J. E. Hatter, M. J. F. Healey, B. Hodgson, R. Lewin, K. V. Lovell, B. Newton, W. R. Pitner, D. W. Rooney, D. Sanders, K. R. Seddon, H. E. Sims, R. C. Thied, *Green Chem.* **2002**, *4*, 152; A. J. Arduengo III, *Acc. Chem. Res.* **1999**, *32*, 913; A. J. Arduengo, T. Bannenberg, *The Strem Chemiker* **2002**, *19*, 1.

[3] G. Cao, *Nanostructures and Nanomaterials: Synthesis, Properties and Applications*, Imperial College Press, London, **2004**; M.-C. Daniel, D. Astruc, *Chem. Rev.* **2004**, *104*, 293.

[4] K. Binnemans, *Chem. Rev.* **2005**, *105*, 4148.

[5] G. T. Wei, Z. Yang, C. Y. Lee, H-Y Yang, C. R. Wang, *J. Am. Chem. Soc.* **2004**, *126*, 5036; C. Scheeren, G. Machado, J. Dupont, P. Fichtner, S. Ribiero-Texeira, *Inorg. Chem.* **2003**, *42*, 4738.

[6] F. Neve, O. Francescangeli, A. Cripini, *Inorg. Chim. Acta* **2002**, *338*, 51; F. Neve, O. Francescangeli, A. Cripini, J. Charmant, *Chem. Mater.* **2001**, *13*, 2032; F. Neve, S. Armentano, A. Cripini, O. Francescangeli, *Chem. Mater.* **1998**, *10*, 1904.

[7] C. K. Lee, H. H. Peng, I. J. B. Lee, *Chem. Mater.* **2004**, *16*, 530; C. Hardacare, J. D. Holbrey, P. B. McCornac, S. E. J. McMath, M. Nieuwenhuyzen, K. R. Seddon, *J. Mater. Chem.* **2001**, *11*, 346; E. R. Schreiter, J. E. Stevens, M. F. Ortwerth, G. Freeman, *Inorg. Chem.* **1999**, *38*, 3935; C. J. Bowlas, D. W. Bruce, K. R. Seddon, *Chem. Commun.* **1996**, 1652.

[8] Y. Yoshida, K. Muroi, A. Otsuka, G. Saito, M. Takahashi, T. Yoko, *Inorg. Chem.* **2004**, *43*, 1458.

[9] A. Taubert, P. Steiner, A. Mantion, *J. Phys. Chem. B* **2005**, *109*, 15542; A. Taubert, *Acta Chim. Slov.* **2005**, *52*, 183; A. Taubert, *Angew. Chem.* **2004**, *116*, 5494; *Angew. Chem. Int. Ed.* **2004**, *43*, 5380.

[10] W. Dobbs, L. Douce, L. Allouche, A. Louati, F. Malbosc, R. Welter, *New J. Chem.* **2006**, *30*, 528.

[11] K. Nakamoto, *Infrared and Raman Spectra of Inorganic and Coordination Compounds*, 4th ed., Wiley-Interscience, New York, **1986**.

 © 2006 Wiley-VCH Verlag GmbH & Co. KGaA, Weinheim

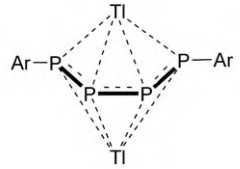
P4 Activation

DOI: 10.1002/anie.200601048

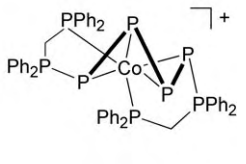
A Snapshot of P_4 Tetrahedron Opening: Rh- and Ir-Mediated Activation of White Phosphorus**

Dmitry Yakhvarov, Pierluigi Barbaro, Luca Gonsalvi, Sonia Mañas Carpio, Stefano Midollini,* Annabella Orlandini, Maurizio Peruzzini,* Oleg Sinyashin, and Fabrizio Zanobini*

The reactivity of white phosphorus with transition metals is characterized by a vast diversity of bonding situations which result in various $\{P_x\}$ units that range from single phosphido atoms to high-nuclearity polyphosphorus ligands.[1] When the tetraphosphorus array is preserved, different topologies are observed in which the P_4 molecule either remains intact and behaves as a monohapto[2] or dihapto ligand,[2c,3] or is activated by the opening of one or more edges to generate acyclic P_4 chains.[1a–d] These ligands reach their thermodynamic minima either by bridging two metal moieties[4] or by undergoing electrophilic or nucleophilic attack from ancillary ligands to form new P–H, P–C, or P–P bonds,[5] as exemplified by the recently reported dithallium salt of $Ar_2P_4^{2-}$ (**1**, $Ar = C_6H_3$-2,6-(C_6H_3-2,6-iPr$_2$)$_2$)[5c] and the unique cobalt complex $[Co(Ph_2PCH_2PPh_2PPPPPh_2PCH_2PPh_2)]BF_4$ (**2**-BF_4)



1, Ar = C_6H_3-2,6-(C_6H_3-2,6-iPr$_2$)$_2$



2

[*] Dr. D. Yakhvarov, Prof. O. Sinyashin
A. E. Arbuzov Institute of Organic and Physical Chemistry
Russian Academy of Sciences
Arbuzov str. 8, 420088 Kazan (Russian Federation)
Fax: (+7) 8432-732-253
E-mail: yakhvar@iopc.knc.ru

Dr. P. Barbaro, Dr. L. Gonsalvi, Dr. S. Mañas Carpio, Dr. S. Midollini, Dr. A. Orlandini, Dr. M. Peruzzini, Dipl. Chem. F. Zanobini
Istituto di Chimica dei Composti Organometallici
ICCOM CNR
Via Madonna del Piano, 10, 50019 Sesto Fiorentino (Italy)
Fax (+39) 055-5225-203
E-mail: stefano.midollini@iccom.cnr.it
mperuzzini@iccom.cnr.it

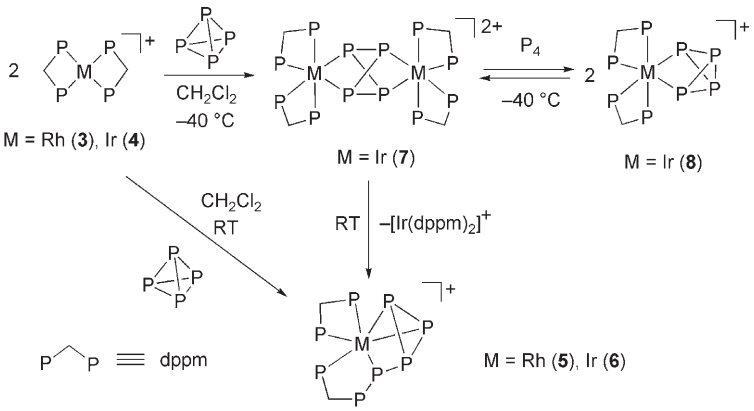
[**] The stay of D.Y. in Florence was supported by the INTAS YS fellowship program 2003 (Fellowship Ref. Nr. 03-55-2050). S.M.C. thanks the "Ministerio de Ciencia y Tecnologia" (Spain) for a postdoctoral grant. Thanks are due to Thermphos Int. (Vlissingen, Netherlands) for a generous loan of white phosphorus, to the NMR service of "FIRENZE HYDROLAB", a project sponsored by Ente Cassa di Risparmio di Firenze, and to Dr. A. Raffaelli (ICCOM CNR, Pisa) for running the ESI-MS spectrum of **5**-OTf.

Supporting information for this article is available on the WWW under http://www.angewandte.org or from the author.

WILEY InterScience DISCOVER SOMETHING GREAT
© 2006 Wiley-VCH Verlag GmbH & Co. KGaA, Weinheim

which was prepared in our group more than two decades ago.[6] The mechanism of formation of the cobalt(I)-coordinated 1,4-disubstituted zigzag tetraphosphabutadiene P_6 chain in **2** is not clearly understood as yet. Herein, we describe the synthesis and characterization of new rhodium and iridium species related to **2** which result from an unexpected bimetallic P_4-activation pathway.

Reaction of $[M(dppm)_2]OTf$ (M = Rh (**3**-OTf), Ir (**4**-OTf); dppm = $PPh_2CH_2PPh_2$, OTf = trifluoromethanesulfonate)[7] with white phosphorus in CH_2Cl_2 at room temperature under nitrogen and subsequent work up led to the isolation of $[M(dppm)(Ph_2PCH_2PPh_2PPPP)]OTf$ as either orange (M = Rh (**5**-OTf)) or light yellow (M = Ir (**6**-OTf), Scheme 1)



Scheme 1. Reactions of **3** and **4** with P_4. The Ph groups of the dppm ligands have been omitted.

microcrystals. Complexes **5**-OTf and **6**-OTf were characterized by ^1H and ^{31}P NMR spectroscopy, ESI mass spectrometry, elemental analysis, and single-crystal X-ray crystallography. The structure of the complex cation in **5**-OTf is presented in Figure 1 a,[8] and Figure 2 shows a plot of the experimental and computed $^{31}P\{^1H\}$ NMR spectra of **5**-PF_6 with the labeling scheme taken from the ORTEP drawing in Figure 1 a (NMR spectroscopic values for **5** and **6** are given in the Supplementary Information).

The structure of **5**-OTf consists of the $[Rh(dppm)(Ph_2PCH_2PPh_2PPPP)]^+$ cation and a triflate anion. In the complex cation, the metal is pseudo-octahedrally coordinated by a dppm ligand and by the new $Ph_2PCH_2PPh_2PPPP$ ligand, which originates from the attack of one terminal dppm Ph_2P group on the P_4 molecule. The whole activation process results in the cleavage of two P–P edges (P5–P7 and P5–P8) and subsequent attack on P5 by one dppm PPh_2 terminal group. Alternatively, the coordination polyhedron can be described as a trigonal bipyramid in which the P7–P8 bond occupies one site with an η^2-type coordination in the equatorial plane, and the P2-Rh1-P5 linkage forms the axis of the bipyramid. The bond lengths better represent the latter bonding picture, as the P7–P8 bond reveals the shortest P–P separation (2.118(3) Å) in the {PPPP} group, and the other P–P bonds (P6–P5, P6–P7, and P6–P8) average to 2.214(7) Å.[9] Notably, the latter value is practically unchanged in comparison with the average P–P

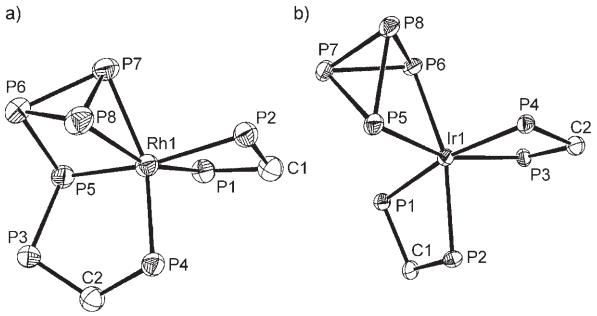


Figure 1. ORTEP drawings of the complex cations in **5**-OTf (a) and **8**-OTf (b); thermal ellipsoids are set at 30% probability. H atoms and phenyl groups are omitted. Selected bond lengths/separations [Å] and angles [°]: **5**-OTf: Rh1-P1 2.357(2), Rh1-P2 2.398(2), Rh1-P4 2.348(2), Rh1-P5 2.343(2), Rh1-P7 2.426(3), Rh1-P8 2.431(3), P3-P5 2.206(3), P5-P6 2.202(3), P6-P7 2.225(4), P6-P8 2.216(4), P7-P8 2.118(3), P5···P7 2.992(4), P5···P8 3.158(4); P1-Rh1-P8 159.60(9), P2-Rh1-P5 162.64(8), P4-Rh1-P7 153.29(9), P1-Rh1-P4 98.04(8), P1-Rh1-P7 108.20(9), P4-Rh1-P8 102.31(9), P7-Rh1-P8 51.71(9). **8**-OTf: Ir1-P1 2.349(2), Ir1-P2 2.435(2), Ir1-P3 2.418(2), Ir1-P4 2.327(2), Ir1-P5 2.411(2), Ir1-P6 2.430(2), P5-P7 2.231(3), P5-P8 2.237(3), P6-P7 2.233(3), P6-P8 2.214(3), P7-P8 2.162(3), P5···P6 2.760(3); P1-Ir1-P4 169.52(7), P3-Ir1-P5 159.52(7), P2-Ir1-P6 164.09(7).

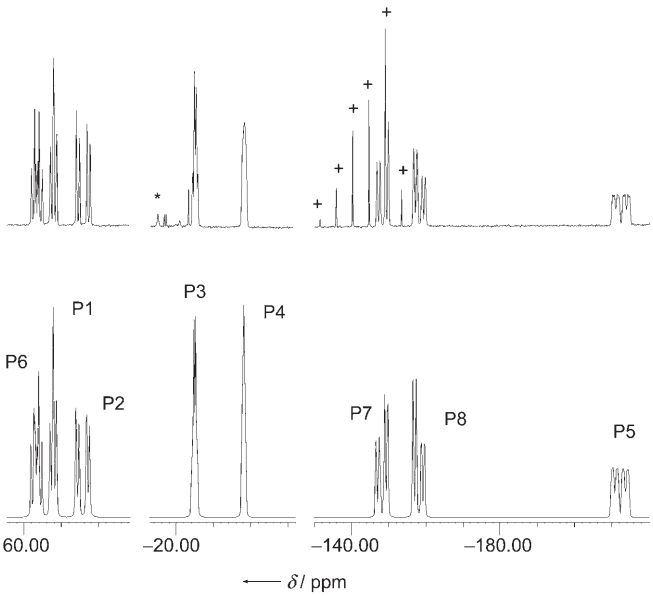
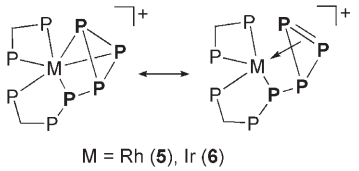


Figure 2. Computed (bottom) and experimental (top) $^{31}P\{^1H\}$ NMR spectra of **5**-PF_6 (400.13 MHz, CD_2Cl_2, 294 K); unidentified impurity denoted with ⋆; some of the signals of the partially superimposed PF_6 septet denoted with +.



bond lengths determined for the free P_4 molecule (2.21 Å).[10] A similar bonding situation was found for the rhodium derivatives $[\{MeC(CH_2PPh_2)_3\}Rh(\eta^1{:}\eta^2\text{-}P_4RR')]^+$, which dis-

 © 2006 Wiley-VCH Verlag GmbH & Co. KGaA, Weinheim

play metrical parameters and NMR data in agreement with a trigonal bipyramidal geometry.[11]

Compounds **5**-OTf and **6**-OTf are soluble in halogenated solvents, THF, and acetone. The $^{31}P\{^1H\}$ NMR spectra in CD_2Cl_2 indicate that the solid-state structures of **5** and **6** are preserved in solution. The spectrum of **5** exhibits a temperature-invariant ABCDEFGHX splitting pattern ($X = ^{103}Rh$), which simplifies to an ABCDEFGH pattern for the iridium complex **6** (see the Supporting Information).

Complexes **5** and **6** display a new P_4 topology formed by a *cyclo*-P_3 ring that is bound to a functionalized P atom;[12] this ligand array may be viewed as an intermediate along the P_4-activation process leading to the ligand in **2**. Indeed, further cleavage of the P6–P8 bond and subsequent attack on a PPh_2 group of a chelating dppm ligand could certainly account for the formation of the tetraphosphabutadiene unit $\{Ph_2PCH_2PPh_2PPPPPh_2PCH_2PPh_2\}$ that was found in the cobalt derivative **2**.[13] Monitoring the reactions of **3**-OTf and **4**-OTf with P_4 by in situ ^{31}P NMR spectroscopy provided useful hints about the activation mechanism. The strategy was to exploit the higher kinetic inertness of the Ir complex in the NMR monitoring of the reaction of **4**-OTf with P_4. White phosphorus immediately reacted with the iridium precursor already at −40 °C to afford a highly fluxional intermediate species **7** which displayed three featureless resonances at $\delta =$ −55.9, −62.1, and −82.6 ppm with identical intensity corresponding to four P atoms each. Lowering the temperature to −90 °C did not affect the broadness of these signals, thus indicating that a low-energy process is responsible for the observed fluxionality of **7**. Increasing the temperature to 25 °C slowly gave the final compound **6** in almost quantitative yield after about four days (Scheme 1). However, when the solution was kept at −40 °C, a new set of resonances appeared in the spectrum within 20 minutes, as ascribable to the Ir^{III} complex $[Ir(dppm)_2(\eta^2\text{-}P_4)]OTf$ (**8**-OTf) which results from the oxidative addition of P_4 to **7**-OTf. After a week at −20 °C, brown crystals of **8**-OTf precipitated.[14] The structure of **8**-OTf consists of a $[(dppm)_2Ir(\eta^2\text{-}P_4)]^+$ cation and a triflate anion, as well as a disordered dichloromethane molecule (Figure 1b). In **8**, the metal center is hexacoordinated by the four phosphorus donors of two dppm ligands and by an η^2-coordinated tetraphosphabicyclobutadienide ligand. The bond lengths in the P_4 moiety are comparable with those of other reported butterfly P_4 ligands.[2]

Dissolving **8**-OTf in CH_2Cl_2 did not directly produce **6**, but gave rise to an equilibrium between **8** and **7** with release of free P_4 (singlet at $\delta = -527$ ppm).[15] To elucidate the nature of **7**, stock solutions of **4**-OTf and P_4 in CD_2Cl_2 were carefully mixed at low temperature (−40 °C) in four screw-cap 5 mm NMR tubes to prepare solutions of **4**-OTf/P_4 in ratios of 1:0.25, 1:0.50, 1:1, and 1:2, and these solutions were independently analyzed by ^{31}P NMR spectroscopy at low temperature. The results of this experiment show that: 1) at the lowest P_4 concentration (1:0.25 **4**-OTf/P_4), only 50% of the iridium complex is consumed to form **7**, and the other signals correspond to unreacted **4**; 2) doubling the amount of P_4 (1:0.50 **4**-OTf/P_4) gives **7** as the only NMR-detectable iridium species, and all the added P_4 is consumed; and 3) further increase of P_4 concentration (1:1 or 1:2 **4**-OTf/P_4) does not change the product distribution and gives only free P_4 and **7**. As all experiments were performed quickly, no significant amount of **8** was detected. On this basis, we may conclude that the mononuclear species **8** is not directly related to the activation process and that a bimetallic complex of the form $[\{Ir(dppm)_2\}_2(\mu,\eta^2\text{:}\eta^2\text{-}P_4)]^{2+}$, which features a doubly activated tetraphosphorus molecule tethering two $\{Ir(dppm)_2\}$ fragments, is the most likely attribution for **7**. This conclusion is in line with literature data reporting double-edge activation of P_4 as observed in, for example, $[\{Cp^*Co(CO)\}_2(\mu,\eta^2\text{:}\eta^2\text{-}P_4)]$[4a] and $[\{HC(CMeNAr)_2\}_2Al_2(\mu,\eta^2\text{:}\eta^2\text{-}P_4)]$ (Ar = 2,6-*i*$Pr_2C_6H_3$),[4e] although species with $\mu,\eta^1\text{:}\eta^2\text{-}P_4$ or $\mu,\eta^1\text{:}\eta^1\text{-}P_4$ ligands, which could account for the observed fluxionality of **7** and for the formation of **6** by nucleophilic attack of one dppm PPh_2 group on the activated P_4 ligand, cannot be ruled out at this stage for the Ir complex. The occurrence of a bimetallic activation of white phosphorus by Mo^{III} complexes has been recently proposed.[16] Theoretical studies are in progress to clarify the nature of **7**, whose identification represents a step forward in understanding the activation of elemental phosphorus by transition metals and may eventually lead to large-scale applications. The reactivity of the novel complexes **5** and **6** is also currently under investigation.

In summary, we have shown that: 1) as in recent reports in N_2 chemistry,[17] bimetallic cooperativity is relevant to P_4 activation; 2) a new bonding mode for the P_4 ligand which catches the metal-mediated opening of the P_4 molecule in action has been elucidated; and 3) the ancillary phosphane ligands may actively participate in opening the P_4 cage, thus confirming that the activation/degradation of white phosphorus is favored by strong nucleophiles.[18]

Experimental Section

5-OTf: A solution of P_4 (0.030 g, 0.24 mmol) in THF (4 mL) was added to a solution of **3**-OTf (0.21 g, 0.19 mmol) in acetone (10 mL) at room temperature with continuous stirring. The resulting brown solution was concentrated under a current of nitrogen to about 5 mL, and then ethanol (10 mL) was added. After further concentration under nitrogen, allowing the solution to stand at room temperature for one day gave orange-brown X-ray quality crystals. The crystals were filtered, washed with acetone/pentane (1:1), and dried in a current of nitrogen at room temperature. Yield: 0.125 g, 58%. Elemental analysis (%) calcd for $C_{51}H_{44}F_3O_3P_8RhS$: C 53.51, H 3.87; found: C 53.38, H 3.97; ESI-MS: *m*/*z* (%): 995.4 (100) $[Rh(dppm)(Ph_2PCH_2PPh_2PPPP)]^+$; ^1H NMR (400.13 MHz, CD_2Cl_2, 294 K): $\delta = 8.4$–6.5 (m, 40H, Ph), 4.8–4.2 ppm (m, 4H, CH_2); $^{31}P\{^1H\}$ NMR: see Figure 2 and the Supporting Information. Metathesis of the triflate counteranion with NH_4PF_6 gave the PF_6 salt **5**-PF_6 in practically quantitative yield.

6-OTf: A solution of P_4 (0.026 g, 0.21 mmol) in THF (3 mL) was added to a solution of **4**-OTf (0.200 g, 0.17 mmol) in CH_2Cl_2 (15 mL) at room temperature. The resulting reddish-brown solution was stirred at room temperature until the color turned to orange-yellow (ca. 4 days). Then ethanol (10 mL) was added, and the solution was concentrated under a gentle current of nitrogen until precipitation started. After the solution stood for one day at room temperature, solid **6** separated as light yellow X-ray-quality crystals. The crystals were filtered, washed with CH_2Cl_2/pentane (1:3), and dried in a current of nitrogen. Yield: 0.110 g, 56%. Elemental analysis (%) calcd for $C_{51}H_{44}F_3IrO_3P_8S$: C 49.64, H 3.59; found: C 49.59, H 3.70; ^1H NMR (400.13 MHz, CD_2Cl_2, 294 K): $\delta = 7.6$–7.0 (m, 40H, Ph),

 © 2006 Wiley-VCH Verlag GmbH & Co. KGaA, Weinheim

4.87 ppm (m, 4H, CH_2); $^{31}P\{^1H\}$ NMR: see the Supporting Information.

Details of the synthesis of **3**-OTf and **4**-OTf, as well as of the crystal-structure determination of **5**-OTf and **8**-OTf, are provided in the Supporting Information, which also includes complete ORTEP drawings of **5**-OTf and **8**-OTf, tables reporting the $^{31}P\{^1H\}$ NMR spectroscopic data for **5** and **6**, and copies of significant ^{31}P NMR spectra.

Received: March 16, 2006
Published online: May 16, 2006

Keywords: iridium · P ligands · phosphorus · rhodium · structure elucidation

[1] a) K. H. Whitmire, *Adv. Organomet. Chem.* **1998**, *42*, 1–145; b) O. J. Scherer, *Acc. Chem. Res.* **1999**, *32*, 751–762; c) M. Peruzzini, I. de los Rios, A. Romerosa, F. Vizza, *Eur. J. Inorg. Chem.* **2001**, 593–608; d) M. Ehses, A. Romerosa, M. Peruzzini, *Top. Curr. Chem.* **2002**, *120*, 107–140; e) M. Peruzzini, R. R. Abdreimova, Y. Budnikova, A. Romerosa, O. J. Scherer, H. Sitzmann, *J. Organomet. Chem.* **2004**, *689*, 4319–4331; f) M. Peruzzini, L. Gonsalvi, A. Romerosa, *Chem. Soc. Rev.* **2005**, *34*, 1038–1047.

[2] a) P. Dapporto, S. Midollini, L. Sacconi, *Angew. Chem.* **1979**, *91*, 510; *Angew. Chem. Int. Ed. Engl.* **1979**, *18*, 469–470; b) T. Gröer, G. Baum, M. Scheer, *Organometallics* **1998**, *17*, 5916–5919; c) M. Peruzzini, M. Marvelli, A. Romerosa, R. Rossi, F. Vizza, F. Zanobini, *Eur. J. Inorg. Chem.* **1999**, 931–933; d) I. de los Rios, J. R. Hamon, P. Hamon, C. Lapinte, L. Toupet, A. Romerosa, M. Peruzzini, *Angew. Chem.* **2001**, *113*, 4028–4030; *Angew. Chem. Int. Ed.* **2001**, *40*, 3910–3911; e) M. Di Vaira, S. Seniori Costantini, P. Stoppioni, P. Frediani, M. Peruzzini, *Dalton Trans.* **2005**, 2234–2236.

[3] M. Di Vaira, S. Seniori Costantini, P. Stoppioni, P. Frediani, M. Peruzzini, Book of abstracts, XXth IUCR Congress, Florence, Italy, **2005**, C303-P.07.01.37.

[4] a) O. J. Scherer, M. Swarowsky, H. Swarowsky, G. Wolmershäuser, *Angew. Chem.* **1988**, *100*, 738–739; *Angew. Chem. Int. Ed. Engl.* **1988**, *27*, 694–695; b) O. J. Scherer, M. Swarowsky, H. Swarowsky, G. Wolmershäuser, *Organometallics* **1989**, *8*, 841–842; c) O. J. Scherer, G. Schwarz, G. Wolmershäuser, *Z. Anorg. Allg. Chem.* **1996**, *622*, 951–957; d) V. A. Miluykov, O. G. Sinyashin, P. Lönnecke, E. Hey-Hawkins, *Mendeleev Commun.* **2003**, 212–213; e) Y. Peng, H. Fan, H. Zhu, H. W. Roesky, J. Magull, C. E. Hughes, *Angew. Chem.* **2004**, *116*, 3525–3527; *Angew. Chem. Int. Ed.* **2004**, *43*, 3443–3445.

[5] a) E. Hey, M. F. Lappert, J. L. Atwood, S. G. Bott, *J. Chem. Soc. Chem. Commun.* **1987**, 597–598; b) P. J. Chirik, J. A. Pool, E. Lobkovsky, *Angew. Chem.* **2002**, *114*, 3613–3615; *Angew. Chem. Int. Ed.* **2002**, *41*, 3463–3465; c) A. R. Fox, R. J. Wright, E. Rivard, P. P. Power, *Angew. Chem.* **2005**, *117*, 7907–7911; *Angew. Chem. Int. Ed.* **2005**, *44*, 7729–7733.

[6] a) F. Cecconi, C. A. Ghilardi, S. Midollini, A. Orlandini, *J. Am. Chem. Soc.* **1984**, *106*, 3667–3668; b) F. Cecconi, C. A. Ghilardi, S. Midollini, A. Orlandini, *Inorg. Chem.* **1986**, *25*, 1766–1770.

[7] The preparations of **3**-OTf and **4**-OTf are detailed in the Supporting Information.

[8] Crystal data for **5**-OTf: $C_{51}H_{44}F_3O_3P_8RhS$, $M_r = 1144.59$, triclinic, space group $P\bar{1}$, $a = 19.755(6)$, $b = 12.139(3)$, $c = 11.744(3)$ Å, $\alpha = 73.75(2)$, $\beta = 108.20(2)$, $\gamma = 102.55(2)°$, $V = 2542(1)$ Å^3, $Z = 2$, $\rho_{calcd} = 1.495$ Mg m^{-3}, $\mu(Cu_{K\alpha}) = 5.926$ mm^{-1}, $F(000) = 1164$. A total of 4103 reflections were collected at room temperature on a Philips PW 1100 automatic diffractometer with $Cu_{K\alpha}$ radiation. The structure was solved by direct methods and refined by full-matrix F^2. The phenyl rings were treated as rigid bodies, and anisotropic temperature factors were assigned only to non-hydrogen and non-carbon atoms to ensure a good parameter-to-data ratio. Some constraints were applied to the disordered triflate anion. The hydrogen atoms were introduced in calculated positions with thermal factors 20% larger than those of the corresponding carbon atoms. $R_1 = 0.0584$ and $wR_2 = 0.1478$ for 3610 reflections ($I > 2\sigma(I)$). CCDC-299453 contains the supplementary crystallographic data for **5**-OTf. These data can be obtained free of charge from The Cambridge Crystallographic Data Centre via www.ccdc.cam.ac.uk/data_request/cif.

[9] A similar structure has been ascertained by X-ray crystallography for the isomorphous iridium complex **6**-OTf: triclinic, space group $P\bar{1}$, $a = 19.822(10)$, $b = 12.113(6)$, $c = 11.820(6)$ Å, $\alpha = 73.47(6)$, $\beta = 108.26(9)$, $\gamma = 103.14(9)°$; A. Orlandini et al., unpublished results.

[10] Chemical Society Special Publication No. 18, Chemical Society, London, **1965**.

[11] P. Barbaro, A. Ienco, C. Mealli, M. Peruzzini, O. J. Scherer, G. Schmitt, F. Vizza, G. Wolmershäuser, *Chem. Eur. J.* **2003**, *9*, 5195–5210.

[12] The zirconium complex $[Cp_2Zr\{\eta^1{:}\eta^1\text{-}P_4(PR_2)_2\}]$ shows a correlated structural motif in which the tetraphosphorus ligand is part of a P_6 moiety which incorporates two phosphido units originally coordinated to zirconium.[5a]

[13] The thermal lability of **5** and **6** does not allow to verify directly this mechanistic proposal. Studies on the corresponding dppm–Co system are in progress to confirm this hypothesis.

[14] $[Ir(dppm)_2(\eta^2\text{-}P_4)]OTf{\cdot}0.5\,CH_2Cl_2$ (**8**-OTf·0.5 CH_2Cl_2): $^{31}P\{^1H\}$ NMR (81.015 MHz, CD_2Cl_2, 233 K): $\delta = -51.5$ (m, 2P, dppm), −81.30 (m, 2P, dppm) −236.90 (m, 2P, P_4), −250.80 ppm (m, 2P, P_4). Crystal data for **8**-OTf·0.5 CH_2Cl_2: $C_{51.5}H_{45}ClF_3IrO_3P_8S$, $M_r = 1276.34$, monoclinic, space group $P2_1/c$, $a = 14.126(9)$, $b = 17.032(9)$, $c = 25.226(8)$ Å, $\beta = 102.22(2)°$, $V = 5932(5)$ Å^3, $Z = 4$, $\rho_{calcd} = 1.429$ Mg m^{-3}, $\mu(Mo_{K\alpha}) = 2.594$ mm^{-1}, $F(000) = 2540$. A total of 10391 reflections were collected on an Oxford CCD automatic diffractometer with $Mo_{K\alpha}$ radiation at 190 K. The structure was solved by direct methods and refined by full-matrix F^2. All the non-hydrogen atoms, except for those of the disordered solvent molecule, were assigned anisotropic temperature factors. The phenyl rings were refined as rigid groups of D_{6h} symmetry. The hydrogen atoms were introduced in calculated positions with temperature factors 20% larger than those of the respective carbon atoms. $R_1 = 0.0677$ and $wR_2 = 0.1682$ for 8757 reflections ($I > 2\sigma(I)$). CCDC-604167 contains the supplementary crystallographic data for **8**-OTf·0.5 CH_2Cl_2. These data can be obtained free of charge from The Cambridge Crystallographic Data Centre via www.ccdc.cam.ac.uk/data_request/cif.

[15] In situ NMR studies on the rhodium precursor **3**-OTf and P_4 did not give the analogue of **8**, but confirmed that the formation of **5** is preceded by the formation of a fluxional three-band species similar to **7** ($^{31}P\{^1H\}$ NMR: $\delta = -13.02$ (br d, $^1J_{RhP}$ 95 Hz), −51.98 (br d $^1J_{RhP}$ 76 Hz), −59.84 ppm (br s)). For the Rh system, the concentration of this intermediate does not grow substantially at any temperature in the ^{31}P NMR spectrum as it transforms into **5** at a much faster rate than **7** transformed into **6** (ca. 1 hour at −40 °C; immediately at room temperature).

[16] F. H. Stephens, M. J. A. Johnson, C. C. Cummins, O. P. Kryatova, S. V. Kryatov, E. V. Rybak-Akimova, J. E. McDonough, C. D. Hoff, *J. Am. Chem. Soc.* **2005**, *127*, 15191–15200.

[17] F. Studt, B. A. MacKay, S. A. Johnson, B. O. Patrick, M. D. Fryzuk, F. Tuczek, *Chem. Eur. J.* **2005**, *11*, 604–608, and references therein.

[18] a) A. Schmidpeter, S. Lochshmidt, S. Sheldrick, *Angew. Chem.* **1985**, *97*, 214–215; *Angew. Chem. Int. Ed. Engl.* **1985**, *24*, 226–227, and references therein; b) J. P. Bezombes, P. B. Hitchcock, M. Lappert, J. E. Nycs, *Dalton Trans.* **2004**, 499–501.

 © 2006 Wiley-VCH Verlag GmbH & Co. KGaA, Weinheim

Surfaces

DOI: 10.1002/anie.200600367

Adhesion of a Free-Standing Newton Black Film onto a Solid Substrate**

Jean-Jacques Benattar, Michael Nedyalkov, Fuk Kay Lee, and Ophelia K. C. Tsui*

Newton black films (NBFs) are self-assembled molecular bilayers of surfactant that usually contain a residual hydration layer in the core upon maximal drainage.[1–10] Because the films are so thin, optical light reflected from the interfaces interferes destructively, thereby giving NBFs a black appearance and hence their name.

We recently reported a process for the insertion of protein molecules into an NBF by controlling the chemical potential of the protein molecules in the solution from which the NBF is extracted and self-assembled.[11–13] Such a process has been shown to allow the formation of a dense monolayer of protein molecules, which can be water soluble (for example, bovine serum albumin) or insoluble (for example, the outer membrane protein OmpA), inside the NBF bilayer. Since the driving force is independent of the nature of the objects being inserted, sufficiently small molecules or nanoparticles that can be made soluble in water by an appropriate surfactant would be suitable candidates for this process. It may thus provide a powerful method for making 2D assemblies of a large variety of molecules and nanoparticles, thereby opening up new opportunities for fundamental research and new technologies.[14–16]

NBFs have only been made in the fragile free-standing form to date. To make such films amenable to practical applications, it is therefore necessary to find ways of depositing them onto a solid substrate. Herein, we show for the first time the transfer of an NBF to a solid substrate by bringing the substrate into contact with a "black bubble". A very large area (a few square centimeters) of the film can be transferred. The bubble is made from an aqueous solution of surfactant (hexaethylene glycol monododecyl ether ($C_{12}E_6$)) and the substrate is hydrophobized silicon. Results from X-ray reflectivity (XR) and atomic force microscopy (AFM) studies show a high degree of molecular organization in the deposited film.

The apparatus is shown in Figure 1. The main components are an air-tight glass chamber and a porous plate that is used to control the bubble drainage, which limits the top level of the solution. A conduit at the bottom connects the chamber to a reservoir containing the surfactant solution. A hole drilled in the center of the porous plate is connected to a gas pipe. The solution from the reservoir is allowed to fill the chamber, flushing the top of the porous plate. The substrate is mounted face-down on a vertical translation stage at the top of the chamber. An air bubble is formed on the porous plate by slowly injecting air through the pipe. Water is allowed to drain from the bubble until the top of the bubble appears black. The substrate is then steadily lowered towards the bubble, until the bubble film adheres to the substrate.

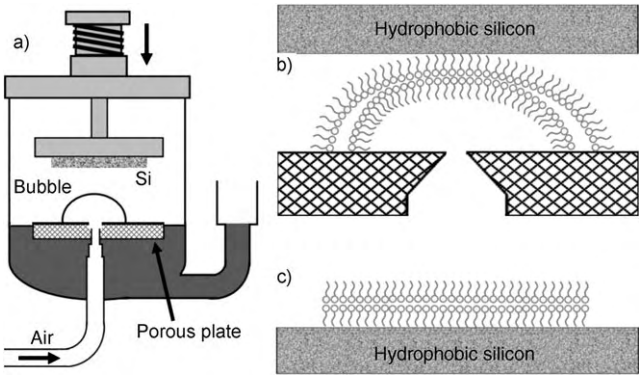


Figure 1. Schematic drawings illustrating the transfer of an NBF film from a "black bubble" (note that the film and the porous plate are not drawn at the same scale). a) A bubble is formed on the porous plate inside the chamber. b) When the top of the bubble film turns black, the silicon substrate is lowered to make contact with a the bubble. c) A black film is transferred onto the silicon substrate.

Figure 2a shows the XR curve of a free-standing $C_{12}E_6$ NBF. It exhibits three distinct interference fringes. We fitted the curve by using the optical matrix formalism,[17] which assumes that the film is composed of a succession of slabs, and obtained the roughness at each interface, along with the thickness and electron density profile along the film normal. By assuming the $C_{12}E_6$ film to be a symmetric trilayer consisting of a central layer sandwiched between two identical external layers, the thickness of the film was deduced to be 60 Å, consistent with the value previously found for NBFs of this surfactant[7,11] and with the thickness reported for its monolayer.[18] The interfacial roughness is approximately 3 Å, which shows that the film is well ordered and homogeneous. The results are summarized in Table 1.

Figure 2b shows the XR curve of a similarly prepared $C_{12}E_6$ film transferred onto a silicon substrate. Two interference fringes with reduced definition are found. The fitted values of the film thickness and interfacial roughness are 48 and 7 Å, respectively. The fitting parameters are summarized

[*] Dr. J.-J. Benattar, Dr. M. Nedyalkov,[+] Dr. F. K. Lee
Service de Physique de l'Etat Condensé (CNRS URA 2464)
DSM/DRECAM/SPEC, CEA Saclay
91191 Gif sur Yvette Cedex (France)
Fax: (+33) 169-088-786
E-mail: Jean-Jacques.Benattar@cea.fr
Dr. O. K. C. Tsui
Department of Physics
Hong Kong University of Science and Technology
Clear Water Bay, Hong Kong (China)

[+] Permanent address:
Department of Physical Chemistry
University of Sofia
Blvd. James Bourchier 1, 1126 Sofia (Bulgaria)

[**] We thank Prof. Ichinose and Dr. Jin of the NIMS (Japan) for fruitful discussions on the formation of black films. We also acknowledge financial support from the France/Hong Kong Joint Research Scheme F-HK20/03T.

InterScience
© 2006 Wiley-VCH Verlag GmbH & Co. KGaA, Weinheim

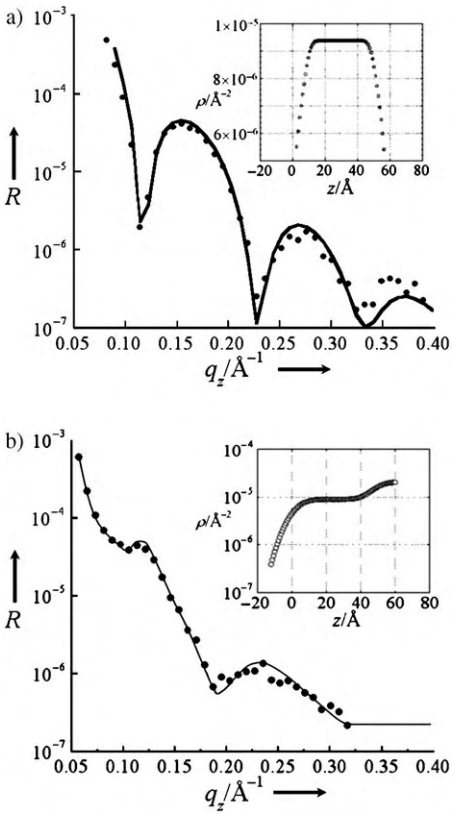


Figure 2. Plot of the reflectivity R as a function of the normal wave vector q_z for a) a free-standing $C_{12}E_6$ film and b) a transferred film. Solid circles are experimental data. The solid line in (a) is a model fit to the XR data, as detailed in the text. The solid line in (b) is a guide for the eye. The insets are profiles of the electron density along the film normals, deduced from fits of the corresponding XR data.

Table 1: Results of the fit to the XR data for a free-standing $C_{12}E_6$ film based on the model discussed in the text.

Layer	Thickness [Å]	δ[a]	Roughness [Å]
External	7.94	2.50×10^{-6}	3
Core	44.06	3.55×10^{-6}	3

[a] δ is the real part of the refractive index. $\delta=\lambda^2 r_e\rho/2\pi$, where $\lambda=$ 1.5405 Å is the X-ray wavelength, r_e is the classical electron radius, and ρ is the mean electron density.

in Table 2. The thickness of the deposited film is reduced by 12 Å and the interfacial roughness is increased by 3–4 Å compared with the free-standing film, which suggests that there is a morphological change caused by the transfer.

The thickness obtained by XR is an average value over the footprint of the incident X-ray, therefore the reduction of the total thickness, as well as the increase in the interfacial roughness suggest that there could be a small unevenness in

Table 2: Fitting parameters of the XR curve for a film of $C_{12}E_6$ deposited on a silicon substrate.

Layer	Thickness [Å]	δ	Roughness [Å]
Film	48	3.40×10^{-6}	7
Bulk Si	–	7.82×10^{-6}	6

the deposition, which may also explain the reduced contrast found in the interference fringes. It is possible that some local parts of the bilayer are torn off during the transfer. Another possibility is that the alkyl chains become tilted from the surface normal.[18] The quality of the film transfer is expected to improve with further experiments.

The XR measurements can only provide information about the structure along the film normal. AFM, however, can give complementary information about the in-plane structure of the film surface and the details of any local inhomogeneity. Figure 3 shows AFM topographic images of

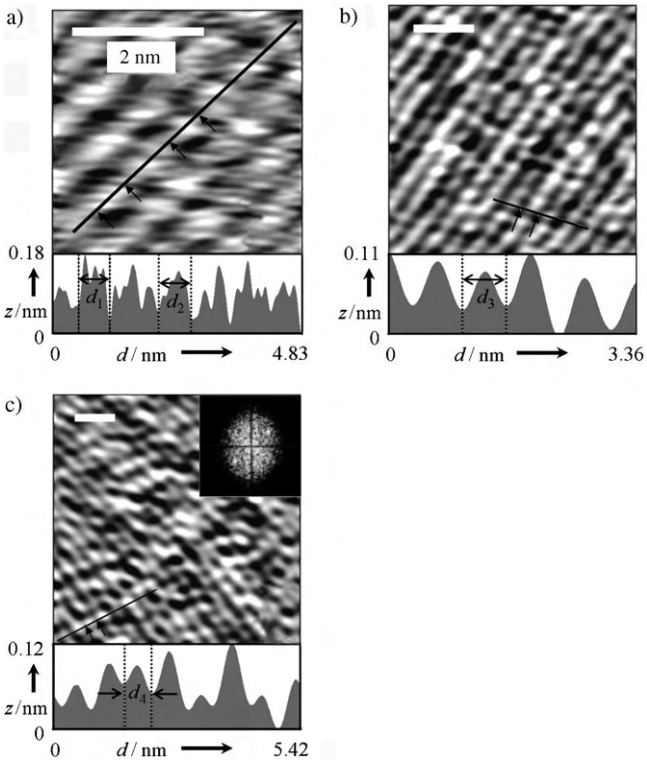


Figure 3. AFM topographic images of the transferred $C_{12}E_6$ films with different scan sizes of a) 4×4, b) 8×8, and c) 12×12 nm^2. The cross-sectional profile along an arbitrarily line drawn across the image is shown beneath each image. The distances d_1, d_2, d_3, and d_4 (bounded by arrows in images) are 0.60, 0.62, 0.61, and 0.60 nm, respectively. All scale bars represent 2 nm. The inset of (c) is the 2D Fourier transform of the real image in the main panel. High-frequency noise in the images was removed by Fourier filtering.

transferred $C_{12}E_6$ films with different scan sizes of a) 4×4, b) 8×8, and c) 12×12 nm^2 along different scan directions. Despite the different scan conditions employed for the imaging, all three images consistently show a chain structure with a periodicity of approximately 0.6 nm, close to the shortest distance between nearest-neighbor molecules.[19] The 2D Fourier transform shown in the inset of Figure 3c reveals a rather long correlation length for the surfactant molecules. The AFM topographic image of the same film over a much larger area of 2 μm^2 is shown in Figure 4, in which the surface can be seen to be quite homogeneous without noticeable aggregations. Hence, we deduce that the reduction of the total film thickness by 12 Å arises from a tilting of the surfactant

 © 2006 Wiley-VCH Verlag GmbH & Co. KGaA, Weinheim

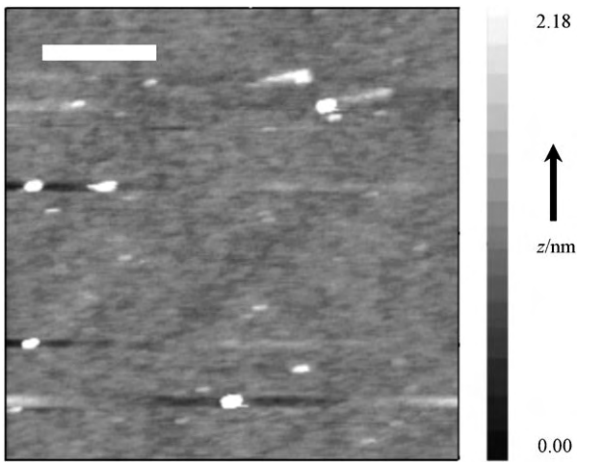


Figure 4. AFM image of a $C_{12}E_6$ film deposited on a silicon substrate, which shows that the film is continuous and smooth. A height (z) scale is to the right of the image. The white scale bar represents 500 nm. The bright spots are probably particulates from the air.

molecules after the transfer. In addition, no distortion is found in the image from a second scan of the same area, thus, showing that the transferred bilayer film is strongly adhered to the hydrophobic silicon substrate.

Free-standing black films have been studied for centuries, but with only a limited variety of techniques. In this study, we have succeeded for the first time in transferring a free-standing NBF onto a solid substrate, thereby allowing simultaneous characterization by XR and AFM. The data show that the molecular ordering of the black film is essentially preserved. This method may thus allow a more complete picture of an NBF's molecular structure to be determined. However, it is still in the early stages of development, and work is in progress to optimize the transfer process. In future studies, we will apply the insertion process to make an NBF with a variety of entities, including protein molecules, silver nanoparticles, and carbon nanotubes, in the core before transfer. The incorporation of nanoparticles or nanotubes is expected to lead to applications in electromechanical[15] or optoelectronic[20] devices, respectively.

Experimental Section

Materials: The nonionic surfactant hexaethylene glycol monododecyl ether ($C_{12}E_6$) was purchased from Sigma (Steinheim, Germany), and was used without further purification. NBFs of $C_{12}E_6$ were chosen for this study, because they have been extensively studied.[7,11] Furthermore, large and stable NBFs of $C_{12}E_6$ can usually be formed at a concentration higher than 0.5 mg mL^{-1}, which is approximately 15 times the critical micelle concentration. All solutions were prepared in ultrapure water (18.2 MΩ, milli-Q system), sonicated, and then filtered. The temperature was maintained at 23 ± 1 °C. Two-inch-diameter n-type Si (111) wafers (5–15 Ωcm) were used. They were first cleaned in a mixture of concentrated sulfuric acid and 33% hydrogen peroxide solution (3:1 ratio) at 120 °C for 10 min to remove any organic contaminants. The wafers were then treated to make the surface hydrophobic by putting them in 40% NH_4F for 20 min. They were then rinsed with ultrapure water and dried in argon gas for 30 min. This treatment produces atomically flat Si (111) surfaces with silicon monohydride terminations oriented normal to the surface.[21,22]

Characterization: XR experiments were carried out with a high-resolution reflectometer (Nonius OptiX) and a copper tube as an X-ray source ($\lambda = 1.5405$ Å). The free-standing films were drawn vertically by lifting a metallic frame at a slow constant rate inside an air-tight chamber in order to maintain a saturated vapor atmosphere. We measured the ratio $R(\theta) = I(\theta)/I_o$ at different incident angles θ, where I_o is the intensity of the incident X-ray beam and $I(\theta)$ is the intensity of the beam reflected off the film. From the specular reflectivity, we could deduce the interfacial roughness, the film thickness, and the electron density profile. The in-plane structure of the surfactant film was investigated by AFM topographic imaging with a Seiko Instruments (Chiban, Japan) SPA300HV model equipped with a platinum-coated silicon integrated cantilever tip with a spring constant of 0.03–0.08 N m^{-1} and a tip radius of less than 32 nm (manufacturing specification). During imaging, the AFM was operated in the contact force mode with an applied normal force of approximately 50 pN.

Received: January 27, 2006
Revised: March 13, 2006
Published online: May 23, 2006

Keywords: black films · deposition · film transfer · surfactants · thin films

[1] O. Belorgey, J. J. Benattar, *Phys. Rev. Lett.* **1991**, *66*, 313.
[2] D. Exerowa, P. M. Kruglyakov, *Foam and Foam Films: Theory, Experiment, Application*, Elsevier, Amsterdam, **1998**.
[3] D. Sentenac, J. J. Benattar, *Phys. Rev. Lett.* **1998**, *81*, 160.
[4] F. Millet, J. J. Benattar, P. Perrin, *Phys. Rev. E* **1999**, *60*, 2045.
[5] F. Millet, J. J. Benattar, P. Perrin, *Macromolecules* **2001**, *34*, 7076.
[6] N. Cuvillier, F. Millet, V. Petkova, M. Nedyalkov, J. J. Benattar, *Langmuir* **2000**, *16*, 5029.
[7] J. J. Benattar, Q. Shen, S. Bratskaya, V. Petkova, M. P. Krafft, B. Pucci, *Langmuir* **2004**, *20*, 1047.
[8] V. Petkova, C. Sultanem, M. Nedyalkov, J. J. Benattar, M. E. Leser, C. Schmitt, *Langmuir* **2003**, *19*, 6942.
[9] C. Sultanem, S. Moutard, J. J. Benattar, F. Djedaïni-Pilard, B. Perly, *Langmuir* **2004**, *20*, 3311.
[10] J. Jin, J. Huang, I. Ichinose, *Angew. Chem.* **2005**, *117*, 4608; *Angew. Chem. Int. Ed.* **2005**, *44*, 4532.
[11] J. J. Benattar, M. Nedyalkov, J. Prost, A. Tiss, R. Verger, C. Guilbert, *Phys. Rev. Lett.* **1999**, *82*, 5297.
[12] V. Petkova, J. J. Benattar, M. Nedyalkov, *Biophys. J.* **2002**, *82*, 541.
[13] V. Petkova, J.-J. Benattar, M. Zoonens, J.-L. Popot, A. Polidori, S. Jasseron, B. Pucci, *Langmuir* **2006**, submitted.
[14] Y. Cui, Q. Wei, H. Park, C. M. Lieber, *Science* **2001**, *293*, 1289.
[15] R. H. Baughman, C. Cui, A. A. Zakhidov, Z. Iqbal, J. N. Barisci, G. M. Spinks, G. G. Wallace, A. Mazzoldi, D. De Rossi, A. G. Rinzler, O. Jaschinski, S. Roth, M. Kertesz, *Science* **1999**, *284*, 1340.
[16] Z. Zhong, D. Wang, Y. Cui, M. W. Bockrath, C. M. Lieber, *Science* **2003**, *302*, 1377.
[17] M. Born, E. Wolf, *Principles of Optics*, Pergamon, London, **1984**, pp. 51–60.
[18] J. R. Lu, Z. X. Li, R. K. Thomas, E. J. Staples, I. Tucker, J. Penfold, *J. Phys. Chem.* **1993**, *97*, 8012.
[19] D. C. McDermott, J. R. Lu, E. M. Lee, R. K. Thomas, A. R. Rennie, *Langmuir* **1992**, *8*, 1204.
[20] P. V. Kamat, *J. Phys. Chem. B* **2002**, *106*, 7729.
[21] G. S. Higashi, Y. J. Chabal, G. W. Trucks, K. Raghavachari, *Appl. Phys. Lett.* **1990**, *56*, 656.
[22] G. S. Higashi, R. S. Becker, Y. J. Chabal, A. J. Becker, *Appl. Phys. Lett.* **1991**, *58*, 1656.

 © 2006 Wiley-VCH Verlag GmbH & Co. KGaA, Weinheim

Arsenic Ligands

DOI: 10.1002/anie.200600815

The Potential of a *cyclo*-As_3-Ligand Complex in Supramolecular Chemistry**

*Laurence J. Gregoriades, Hannes Krauss, Joachim Wachter, Alexander V. Virovets, Marek Sierka, and Manfred Scheer**

Dedicated to Professor Hansgeorg Schnöckel on the occasion of his 65th birthday

The self-organisation of discrete units to form supramolecular aggregates and networks has become one of the foremost areas of chemical research.[1] Contrary to familiar methods in this field which make use of N- and O-donor-containing ligands, respectively, for connecting different metal centers, our strategy until now has been focused on the use of P_n-ligand complexes as connecting moieties. We have already shown that the tetrahedrane complex $[\{CpMo(CO)_2\}_2(\mu,\eta^2\text{-}P_2)]$ can be used as an efficient building block for the formation of oligomers and polymers[2,3] in the presence of Cu^I and Ag^I salts and that the pentaphosphaferrocene complexes $[Cp^xFe(\eta^5\text{-}P_5)]$ ($Cp^x = C_5Me_5$ (Cp*), C_5Me_4Et) form 1D and 2D polymers[4] as well as spherical fullerene-like aggregates[5,6] upon reaction with Cu^I halides. The Florentine groups of Stoppioni and Peruzzini were able to show that $[(triphos)M(\eta^3\text{-}P_3)]$ (M = Co, Rh, or Ir; triphos = 1,1,1-tris-(diphenylphosphanylmethyl)ethane) coordinates with Cu^I, Ag^I, or Au^I centers to form monocationic complexes.[7] For M = Co, the reaction with CuBr resulted in a multidecker complex containing a $\{(CuBr)_6\}$ middle deck.[8] In view of the versatility of P_n-ligand complexes as supramolecular ligands, we became interested in exploring the potential of As_n-ligand complexes as such.[9]

Although the reactivity of As_n-ligand complexes has been investigated to some extent,[10] no supramolecular aggregates featuring these compounds as connecting moieties have been reported. We report herein the use of **1**[11] as a ligand in coordination chemistry. The reactions of **1** with the Cu^I halides yielded the dimeric Cu_2X_2-bridged complexes **2** (X = Cl), **3** (X = Br), and **4** (X = I), which demonstrate the intermolecular coordination ability of arsenic to form stacked aggregates. Furthermore, with a Ag^I salt the novel oligomeric complex **5** was obtained in which the *cyclo*-As_3 ligands are bound in an unexpected bridging coordination mode in the solid state and which shows unusual dynamic behavior in solution.

$[Cp^*Mo(CO)_2(\eta^3\text{-}As_3)]$ **1**

$[\{Cu(\mu\text{-}X)[Cp^*(CO)_2Mo(\mu,\eta^3\text{:}\eta^2\text{-}As_3)]\}_2]$ **2 – 4**

$[Ag_2\{Cp^*Mo(CO)_2(\mu,\eta^3\text{:}\eta^2\text{-}As_3)\}_2\text{-}\{Cp^*Mo(CO)_2(\mu,\eta^3\text{:}\eta^2\text{:}\eta^2\text{-}As_3)\}_2][Al\{OC(CF_3)_3\}_4]_2$ **5**

Complex **1** reacts with the Ag^I salt of the weakly coordinating anion $[Al\{OC(CF_3)_3\}_4]^-$ [12] in a 2:1 stoichiometry to produce the dicationic complex **5**. Interestingly, a 1:1 reaction stoichiometry led nevertheless to the formation of **5**, thus suggesting that the 2:1 product represents a thermodynamic minimum of this system. The yellow compound **5** is light-sensitive and is soluble in CH_2Cl_2, THF, and CH_3CN. In contrast, the orange needles of **2**–**4** remain unchanged upon exposure to light and are insoluble in most common solvents.

All products were structurally characterized by X-ray diffraction analysis.[13] Compounds **2**–**4** are isostructural and crystallize in the monoclinic space group $P2_1/c$ (Figure 1). The complexes consist of planar four-membered Cu_2X_2 rings, and each Cu^I center is side-on coordinated by an As–As edge of the *cyclo*-As_3 moiety of a unit of **1**. The copper-bound As–As

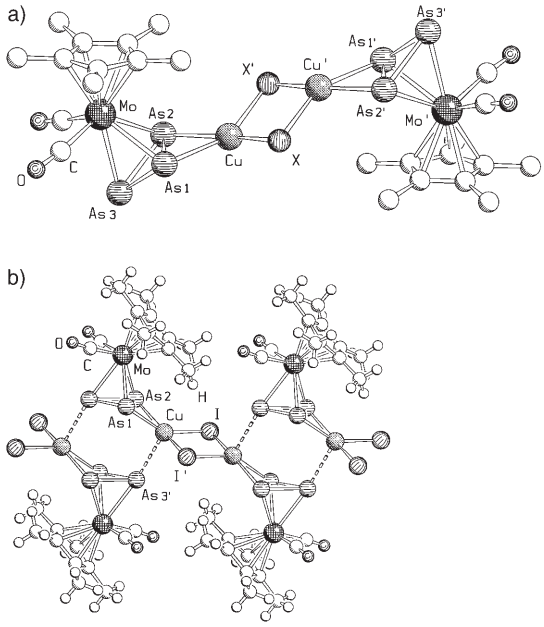


Figure 1. a) Molecular structure of **2**–**4** in the crystal; hydrogen atoms are omitted for clarity. b) Arrangement of the molecules of **4** along the crystallographic *b* axis.

[*] Dr. L. J. Gregoriades, Dipl.-Chem. H. Krauss, Dr. J. Wachter, Prof. Dr. M. Scheer
Institut für Anorganische Chemie
Universität Regensburg
93040 Regensburg (Germany)
Fax: (+49) 941-943-4439
E-mail: manfred.scheer@chemie.uni-regensburg.de
Dr. A. V. Virovets
Nikolaev Institute of Inorganic Chemistry
Siberian Division of RAS
Acad. Lavrentyev str. 3, Novosibirsk 630090 (Russia)
Dr. M. Sierka
Institut für Chemie
Humboldt-Universität zu Berlin
Unter den Linden 6, 10099 Berlin (Germany)

[**] This work was comprehensively supported by the Deutsche Forschungsgemeinschaft and the Fonds der Chemischen Industrie. M. Sierka gratefully acknowledges Prof. Joachim Sauer and the Humboldt-Universität zu Berlin for providing computing facilities.

 © 2006 Wiley-VCH Verlag GmbH & Co. KGaA, Weinheim

edges in **2**–**4** are elongated by 0.15–0.18 Å (Table 1) in comparison with the starting material **1** (2.377(2) Å),[11] whereas all other bonds remain essentially unchanged.

Table 1: Comparison of selected bond lengths [Å] and angles [°] in **2**–**4**.

	2 X = Cl	**3** X = Br	**4** X = I
As1–As2	2.543(1)	2.557(1)	2.532(1)
As1–As3	2.378(1)	2.387(1)	2.380(1)
As2–As3	2.385(1)	2.397(1)	2.390(1)
As1–Cu	2.449(1)	2.465(1)	2.479(1)
As2–Cu	2.436(1)	2.458(1)	2.469(1)
Cu–As3′	2.955(1)	2.878(1)	2.818(1)
Cu–X	2.330(1)	2.475(1)	2.630(1)
Cu–X′	2.357(1)	2.493(1)	2.642(1)
As1-As2-As3	57.58(1)	57.51(2)	57.74(2)
As1-As3-As2	64.56(2)	64.60(3)	64.12(2)
As1-As2-Cu	58.88(1)	58.86(2)	59.44(2)
As2-As1-Cu	58.36(1)	58.56(2)	59.02(2)
As1-Cu-As2	62.76(2)	62.58(3)	61.55(2)
As1-Cu-X	102.95(3)	100.74(3)	98.40(2)
As2-Cu-X′	99.77(3)	98.63(3)	98.57(2)
Cu-X-Cu′	88.21(3)	85.76(3)	83.44(2)
X-Cu-X′	91.79(3)	94.24(3)	96.56(2)

In the structures of the products each Cu atom is in a nearly planar coordination geometry (sum of angles: 355.1–357.3°; the deviation of the As1 atom from the X-Cu-X′ plane increases in the order X = Cl < Br < I (0.93, 1.04, 1.13 Å)). However, the most significant difference between the structures of the products is the degree of intermolecular aggregation through coordination of the As3 atoms to the Cu atoms of neighboring molecules. This coordination leads to stacking of the molecules along the crystallographic *b* axis, and the intermolecular As3–Cu distance decreases in the order **2** > **3** > **4** (2.955(1), 2.878(1), 2.818(1) Å). Considering the sum of the van der Waals radii of As and Cu (3.4 Å[14]), a tetragonal-pyramidal geometry can be inferred for the Cu atoms.[15] The Cu–As bond lengths are comparable with those found in $[Cu\{As_2(SiMe_3)_2\}\{As_4(SiMe_3)_4\}]^-$.[16]

The solid-state structure of the dication in **5** (Figure 2)[13] consists of two Ag^+ cations bridged by two units of **1**, in which the *cyclo*-As_3 moieties are coordinated in an unusual η^2:η^2 fashion. This coordination mode is novel for As_n-ligand complexes[10] and reveals the higher propensity of As_n ligands to be π-coordinated, whereas for P_n-ligand complexes σ donation tends to be favored. Two further units of **1**, one per Ag center, are attached through η^2 coordination of the As_3 rings. Although each Ag atom is bonded to six As atoms, owing to the π-coordination mode, the Ag center is in a trigonal environment. As would be expected from the π-coordination mode, the As1–As2 (2.452(2) Å), As2–As3 (2.464(2) Å), and As4–As5 (2.528(2) Å) edges are noticeably longer than the As–As bonds in uncoordinated **1** (2.377(2) Å),[11] whereas the uncoordinated edges in **5** remain essentially unchanged. The Ag–As bond lengths

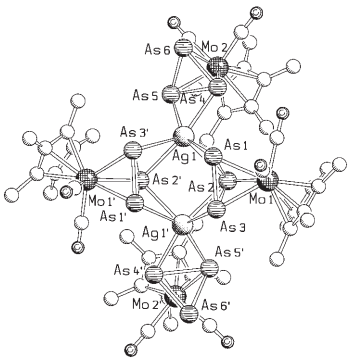
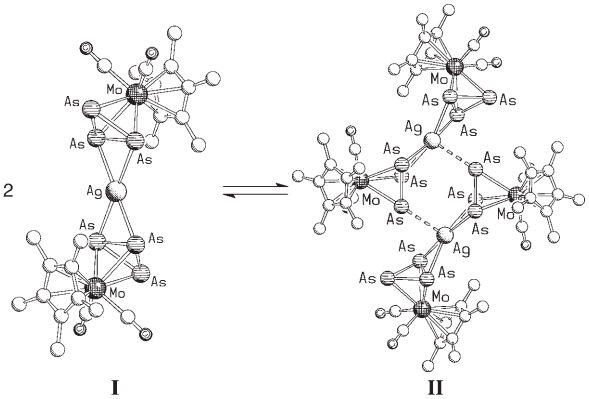


Figure 2. Structure of the dication of **5** in the crystal; hydrogen atoms omitted for clarity. Selected bond lengths [Å] and angles [°]: As1-As2 2.452(2), As1-As3 2.368(2), As2-As3 2.464(2), As4-As5 2.528(2), As4-As6 2.371(2), As5-As6 2.369(2), Ag1-As1 2.828(1), Ag1-As2 2.806(1), Ag1-As2′ 2.823(1), Ag1-As3′ 2.780(1), Ag1-As4 2.704(2), Ag1-As5 2.665(1); As1-Ag1-As2 51.59(4), As1-Ag1-As2′ 105.02(4), As1-Ag1-As3′ 82.26(4), As1-Ag1-As4 96.65(4), As1-Ag1-As5 151.49(5), As2-Ag1-As2′ 90.09(4), As2′-Ag1-As3′ 52.16(4), As2-Ag1-As3′ 111.33(4), As2-Ag1-As4 101.54(4), As2′-Ag1-As4 158.17(5), As2-Ag1-As5 135.13(5), As2′-Ag1-As5 102.72(4), As3′-Ag1-As4 135.69(5), As3′-Ag1-As5 110.35(5), As4-Ag1-As5 56.17(4).

(2.665(1)–2.828(1) Å) are, on average, longer than those found in previously reported $[Ag(AsPh_3)_4]^+$ salts (2.643(4)–2.700(5) Å).[17]

In the ESI-MS spectra of **5** in CH_2Cl_2, the fragment with the highest relative abundance is attributable to the monocation $[Ag\{Cp^*Mo(CO)_2As_3\}_2]^+$ (**I**), which indicates that **5** dissociates to a monomeric species in solution. Vapor-pressure osmometric (VPO) measurements were carried out at 28 °C in CH_2Cl_2 and yield a molecular mass of 2756 ± 138 g mol^{-1}. These results suggest an equilibrium between the $[Al\{OC(CF_3)_3\}_4]^-$ salt of monomer **I** (2099 g mol^{-1}) and the dimer **5** (4198 g mol^{-1}), noticeably in favor of the monomer (monomer/dimer ca. 3:1).

To determine the validity of the proposed monomer–dimer equilibrium, density functional theory (DFT) calculations were performed on monocation **I** and dication **II** (Scheme 1). The structure optimization of the monocation **I** both in the gas phase and in CH_2Cl_2 solution with the



Scheme 1. Proposed equilibrium of the monocation **I** and dication **II** (DFT-calculated structures) in CH_2Cl_2 at room temperature.

 © 2006 Wiley-VCH Verlag GmbH & Co. KGaA, Weinheim

conductor-like screening model (COSMO)[18] yielded a C_{2h}-symmetric geometry in which the Ag^I center is coordinated to two units of **1** through two As–As edges in a linear fashion, and these five atoms are coplanar. For the dication **II** the structure which was calculated both in the gas phase and in CH_2Cl_2 solution differs significantly from that observed in the solid state. The calculated structure exhibits C_2 symmetry with each Ag^+ cation bound to the As–As edges of two units of **1**, and these monocationic moieties are held together by two rather long Ag···As contacts (3.008 Å, COSMO result), which are shorter than the sum of the van der Waals radii of the two elements (3.7 Å).[14] In the solid state, the units of **1** coordinate to both Ag^I centers of the dication exclusively through the As–As edges. The dication in solution can thus be viewed as two weakly associated monocations, a structure which is reminiscent of those observed in the products **2**–**4** with weak intermolecular Cu···As interactions.

In the gas phase the dication **II** is unstable. The calculated gas-phase free energy of formation ΔG of the dication from the monocation **I** at 28 °C is 149 kJ mol^{-1}. In CH_2Cl_2 solution at 28 °C the reaction is slightly exergonic with $\Delta G = -19.7$ kJ mol^{-1}. The endergonic nature of the formation of **II** in the gas phase as well as the two somewhat long Ag···As contacts therein explain why only the monocation is detected in the ESI-MS spectra, whereas the exergonic formation in solution explains the crystallization of the dimer rather than the monomer.

Based on the theoretical calculations and experimental data, an equilibrium between the monocation **I** and the dication **II** can be postulated for solutions of the dimer **5** (Scheme 1). These results shed light on the finding that only one signal is observed in the solution ^{31}P NMR spectrum of the dicationic complex **6**,[2] which was formed by the reaction of $[\{Cp^*Mo(CO)_2\}_2(\mu,\eta^2\text{-}P_2)]$ with $Ag(O_3SCF_3)$, without any detectable coupling to the $^{107}Ag/^{109}Ag$ nuclei. Obviously, these Ag-containing cationic systems demonstrate dynamic equilibria in solution, which could be elucidated here with the novel *cyclo*-As_3 system **5**.

$$[Ag_2\{Cp_2Mo_2(CO)_4(\mu,\eta^2{:}\eta^2\text{-}P_2)\}_2\text{-}\{Cp_2Mo_2(CO)_4(\mu,\eta^2{:}\eta^1{:}\eta^1\text{-}P_2)\}_2](CF_3SO_3)_2 \quad \mathbf{6}$$

The results have shown that by using the *cyclo*-As_3-ligand complex **1** and the Ag^I salt of the weakly coordinating anion $[Al\{OC(CF_3)_3\}_4]^-$, the novel dimeric complex **5** is formed. This unprecedented homoleptic silver complex features the *cyclo*-As_3 ligand complex in an unusual face-bridging coordination mode. ESI-MS measurements reveal the existence of monocations in solution, and VPO measurements indicate that a monocation–dication equilibrium exists, which was clarified by DFT calculations. The isolation of **5** and the Cu_2X_2-bridged dimers **2**–**4**, which exhibit stacking through weak intermolecular interactions, demonstrates the high potential of the *cyclo*-As_3 complex **1** as a supramolecular ligand and thus signals the establishment of a new field of research for As_n-ligand complexes.

Experimental Section

All manipulations were performed under nitrogen with glovebox and Schlenk techniques. Solvents were purified and degassed by standard procedures. Compounds **1**[11] and $Ag[Al\{OC(CF_3)_3\}_4]$[12] were prepared according to literature procedures. IR spectra were recorded on a Varian FTS 800 spectrometer. Solution NMR spectra were acquired on a Bruker Avance 400 MHz spectrometer. ESI-MS spectra were measured on a Finnigan Thermoquest TSQ 7000 mass spectrometer. VPO measurements were performed on a Knauer K-7000 vapor pressure osmometer.

2–**4**: A solution of CuX (X = Cl: 57 mg, 0.57 mmol; X = Br: 70 mg, 0.49 mmol; X = I: 66 mg, 0.35 mmol) in acetonitrile (10 mL) was layered carefully over a solution of **1** (for **2** (X = Cl): 98 mg, 0.19 mmol; for **3** (X = Br): 83 mg, 0.16 mmol; for **4** (X = I): 60 mg, 0.12 mmol) in CH_2Cl_2 (10 mL). After 3 days, orange rodlike crystals of **2** and **3** could be isolated. Crystals of **4** were obtained after storing the solution at −30 °C. All products were washed with pentane (2 mL) and dried in vacuum.

2: Yield: 91 mg (78 %); ESI-MS (CH_3CN): *m*/*z* (%): 1187 (11) $[M-Cl]^+$, 1089 (100) $[M-CuCl_2]^+$, 618 (84) $[^1/_2M-Cl+CH_3CN]^+$; IR (KBr): $\tilde{\nu}(CO) = 1962$, 1922 cm^{-1}. Elemental analysis (%) calcd for $As_6C_{24}Cl_2Cu_2H_{30}Mo_2O_4$ (1221.9): C 23.59, H 2.47; found: C 23.43, H 2.46. **3**: Yield: 74 mg (70 %); ESI-MS (CH_3CN): *m*/*z* (%): 1231 (20) $[M-Br]^+$, 1087 (100) $[M-CuBr_2]^+$, 618 (63) $[^1/_2M-Br+CH_3CN]^+$; IR (KBr): $\tilde{\nu}(CO) = 1963$, 1924 cm^{-1}. Elemental analysis (%) calcd for $As_6C_{24}Br_2Cu_2H_{30}Mo_2O_4$ (1310.8): C 21.99, H 2.31; found: C 21.89, H 2.07. **4**: Yield: 45 mg (55 %); ESI-MS (CH_3CN): *m*/*z* (%): 1278 (29) $[M-I]^+$, 1087 (100) $[M-CuI_2]^+$, 618 (61) $[^1/_2M-I+CH_3CN]^+$; IR (KBr): $\tilde{\nu}(CO) = 1965$, 1924 cm^{-1}. Elemental analysis (%) calcd for $As_6C_{24}I_2Cu_2H_{30}Mo_2O_4$ (1404.8): C 20.52, H 2.15; found: C 20.52, H 1.99.

5: A solution of **1** (100 mg, 0.20 mmol) and $Ag[Al\{OC(CF_3)_3\}_4]\cdot CH_2Cl_2$ (113 mg, 0.10 mmol) in CH_2Cl_2 (10 mL) was stirred at room temperature for 12 h in the dark. The yellow solution was filtered over diatomaceous earth, which was subsequently washed with CH_2Cl_2 (2 × 3 mL), and the combined filtrate and washings were stored in a freezer at −28 °C. Bright yellow-orange needles of $\mathbf{5}\cdot 2.5\,CH_2Cl_2$ were deposited within a week and were filtered at −30 °C, washed with pentane (2 × 3 mL), and dried in vacuum at room temperature. The solvent in the crystal lattice was completely removed during the drying process. Yield: 180 mg (88 %); ^1H NMR (CD_2Cl_2, 400.13 MHz, 27 °C): $\delta = 2.09$ ppm (s, CH_3); $^{13}C\{^1H\}$ NMR (CD_2Cl_2, 100.63 MHz, 27 °C): $\delta = 12.89$ (s, CH_3), 102.66 (s, Cp*), 121.68 (q, $^1J_{FC} = 293$ Hz; CF_3), 220.79 ppm (s, CO); ^{27}Al NMR (CD_2Cl_2, 104.26 MHz, 27 °C): $\delta = 33.66$ ppm (s, $[Al\{OC(CF_3)_3\}_4]^-$); ^{19}F NMR (CD_2Cl_2, 376.47 MHz, 27 °C): $\delta = -75.58$ ppm (s, CF_3); positive-ion ESI-MS (CH_2Cl_2, RT): *m*/*z* (%): 1644.7 (0.1) $[Ag\{Cp^*Mo(CO)_2As_3\}_3]^+$, 1130.8 (100) $[Ag\{Cp^*Mo(CO)_2As_3\}_2]^+$, 1102.7 (20) $[Ag\{Cp^*Mo(CO)_{1.5}As_3\}_2]^+$, 1076.7 (7) $[Ag\{Cp^*Mo(CO)As_3\}_2]^+$, 1046.6 (1) $[Ag\{Cp^*Mo(CO)_{0.5}As_3\}_2]^+$, 1020.6 (2) $[Ag\{Cp^*MoAs_3\}_2]^+$; negative-ion ESI-MS (CH_2Cl_2, RT): *m*/*z* (%): 967.1 (100) $[Al\{OC(CF_3)_3\}_4]^-$; IR (CH_2Cl_2): $\tilde{\nu}(CO) = 2006$ (m), 1952 cm^{-1} (m); IR (KBr): $\tilde{\nu}(CO) = 2018$ (s), 2007 (s), 1974 (s), 1958 cm^{-1} (s); molecular mass calcd for $C_{80}H_{60}Ag_2Al_2As_{12}F_{72}Mo_4O_{16}$: 4197.75 g mol^{-1}; found (osmometric, CH_2Cl_2, 28 °C): 2756 ± 138 g mol^{-1}. Elemental analysis (%) calcd for $C_{40}H_{30}AgAlAs_6F_{36}Mo_2O_8$ (2098.88): C 22.89, H 1.44; found: C 22.99, H 1.49.

Structure optimizations and vibrational analyses at the DFT level were performed using the TURBOMOLE program package.[19] The BP86[20] exchange-correlation functional was used along with the triple zeta plus polarization (TZVP) basis set on all atoms.[21] To speed up calculations, the Coulomb part was evaluated using the MARI-J method along with TZVP auxiliary basis set.[22]

Received: March 2, 2006
Published online: May 24, 2006

 © 2006 Wiley-VCH Verlag GmbH & Co. KGaA, Weinheim

Keywords: arsenic · copper · molybdenum · self-assembly · silver

[1] Recent reviews: a) N. C. Gianneschi, M. S. Masar III, C. A. Mirkin, *Acc. Chem. Res.* **2005**, *38*, 825 – 837; b) M. Ruben, J. Rojo, F. J. Romero-Salguero, L. H. Uppadine, J.-M. Lehn, *Angew. Chem.* **2004**, *116*, 3728 – 3747; *Angew. Chem. Int. Ed.* **2004**, *43*, 3644 – 3662; c) L. Carlucci, G. Ciani, D. M. Proserpio, *Coord. Chem. Rev.* **2003**, *246*, 247 – 289; d) G. F. Swiegers, T. J. Malefetse, *Coord. Chem. Rev.* **2002**, *225*, 91 – 121; e) B. J. Holliday, C. A. Mirkin, *Angew. Chem.* **2001**, *113*, 2076 – 2097; *Angew. Chem. Int. Ed.* **2001**, *40*, 2022 – 2043; f) S. Leininger, B. Olenyuk, P. J. Stang, *Chem. Rev.* **2000**, *100*, 853 – 908.

[2] J. Bai, E. Leiner, M. Scheer, *Angew. Chem.* **2002**, *114*, 820 – 823; *Angew. Chem. Int. Ed.* **2002**, *41*, 783 – 786.

[3] M. Scheer, L. Gregoriades, J. Bai, M. Sierka, G. Brunklaus, H. Eckert, *Chem. Eur. J.* **2005**, *11*, 2163 – 2169.

[4] J. Bai, A. V. Virovets, M. Scheer, *Angew. Chem.* **2002**, *114*, 1808 – 1811; *Angew. Chem. Int. Ed.* **2002**, *41*, 1737 – 1740.

[5] J. Bai, A. V. Virovets, M. Scheer, *Science* **2003**, *300*, 781 – 783.

[6] M. Scheer, J. Bai, B. P. Johnson, R. Merkle, A. V. Virovets, C. E. Anson, *Eur. J. Inorg. Chem.* **2005**, 4023 – 4026.

[7] a) M. Di Vaira, M. P. Ehses, M. Peruzzini, P. Stoppioni, *Polyhedron* **1999**, *18*, 2331 – 2336; b) M. Di Vaira, P. Stoppioni, M. Peruzzini, *J. Chem. Soc. Dalton Trans.* **1990**, 109 – 113.

[8] M. F. Cecconi, C. A. Ghilardi, S. Midollini, A. Orlandini, *J. Chem. Soc. Chem. Commun.* **1982**, 229 – 230; in the case of the Ir complex the cationic species $[\{(triphos)IrP_3\}_3Cu_5Br_4]^+$ was obtained: F. Cecconi, C. A. Ghilardi, S. Midollini, A. Orlandini, *Angew. Chem.* **1983**, *95*, 554 – 555; *Angew. Chem. Int. Ed. Engl.* **1983**, *22*, 554 – 555. For a sandwich complex with a *cyclo*-As_3 ligand between two {(triphos)M} fragments (M = Co, Ni), see: M. Di Vaira, S. Midollini, L. Sacconi, *J. Am. Chem. Soc.* **1979**, *101*, 1757 – 1763.

[9] For supramolecular aggregates based on $[\{CpMo(CO)_2\}_2(\mu,\eta^2\text{-}Sb_2)]$, see: H. V. Ly, M. Parvez, R. Roesler, *Inorg. Chem.* **2006**, *45*, 345 – 351.

[10] Review articles: a) O. J. Scherer, *Acc. Chem. Res.* **1999**, *32*, 751 – 762; b) K. H. Whitmire, *Adv. Organomet. Chem.* **1998**, *42*, 1 – 145; c) O. J. Scherer, *Angew. Chem.* **1990**, *102*, 1137 – 1155; *Angew. Chem. Int. Ed. Engl.* **1990**, *29*, 1104 – 1122.

[11] I. Bernal, H. Brunner, W. Meier, H. Pfisterer, J. Wachter, M. L. Ziegler, *Angew. Chem.* **1984**, *96*, 428 – 429; *Angew. Chem. Int. Ed. Engl.* **1984**, *23*, 438 – 439.

[12] I. Krossing, *Chem. Eur. J.* **2001**, *7*, 490 – 502.

[13] The crystal structure analyses of **2**–**4** were performed on an STOE IPDS diffractometer and that of **5** on an Oxford Diffraction Xcalibur 3 CCD diffractometer with $Mo_{K\alpha}$ radiation ($\lambda = 0.71073$ Å). The structures were solved by direct methods with the program SHELXS-97,[23a] and full-matrix least-squares refinement on F^2 was performed in SHELXL-97[23b] with anisotropic displacements for non-H atoms. Hydrogen atoms were located in idealized positions and refined isotropically according to the riding model. The $[Al(OC(CF_3)_3)_4]^-$ anion has a strong tendency to be disordered in two ways: a) rotation of CCF_3 about the C–C bond and b) rotation of the whole $OC(CF_3)_3$ group about the O–C bond. In the structure of **5** we observed both effects, which led to a somewhat elevated wR_2 value. **2**: $C_{24}H_{30}As_5Cl_2Cu_2Mo_2O_4$, $M_r = 1221.88$, crystal dimensions $0.40 \times 0.20 \times 0.12$ mm^3, monoclinic, space group $P2_1/c$ (No. 14), $a = 9.855(1)$, $b = 8.460(1)$, $c = 20.090(2)$ Å, $\beta = 95.97(1)°$, $T = 173(1)$ K, $Z = 2$, $V = 1665.8(2)$ Å^3, $\rho_{calcd} = 2.436$ Mg m^{-3}, $\mu = 8.099$ mm^{-1}, 10084 reflections collected, 3100 unique reflections ($R_{int} = 0.0440$, $2\theta_{max} = 52°$), 186 parameters, $R_1 = 0.0260$, $wR_2 = 0.0706$. **3**: $C_{12}H_{15}As_3BrCuMoO_2$, $M_r = 655.39$, crystal dimensions $0.30 \times 0.20 \times 0.08$ mm^3, monoclinic, space group $P2_1/c$ (No. 14), $a = 9.908(2)$, $b = 8.467(2)$, $c = 20.340(4)$ Å, $\beta = 95.46(3)°$, $T = 173(1)$ K, $Z = 4$, $V = 1698.6(6)$ Å^3, $\rho_{calcd} = 2.563$ Mg m^{-3}, $\mu = 10.138$ mm^{-1}, 9897 reflections collected, 3037 unique reflections ($R_{int} = 0.0477$, $2\theta_{max} = 52°$), 186 parameters, $R_1 = 0.0341$, $wR_2 = 0.0922$. **4**: $C_{12}H_{15}As_3ICuMoO_2$, $M_r = 702.39$, crystal dimensions $0.26 \times 0.20 \times 0.05$ mm^3, monoclinic, space group $P2_1/c$ (No. 14), $a = 10.018(1)$, $b = 8.421(1)$, $c = 20.745(2)$ Å, $\beta = 95.08(1)°$, $T = 123(1)$ K, $Z = 4$, $V = 1743.2(3)$ Å^3, $\rho_{calcd} = 2.676$ Mg m^{-3}, $\mu = 9.358$ mm^{-1}, 14674 reflections collected, 3370 unique reflections ($R_{int} = 0.0465$, $2\theta_{max} = 52°$), 186 parameters, $R_1 = 0.0273$, $wR_2 = 0.0724$. **5**·2.5 CH_2Cl_2: $C_{82.5}H_{65}Ag_2Al_2As_{12}Cl_5F_{72}Mo_4$, $M_r = 4410.10$, crystal dimensions $0.51 \times 0.19 \times 0.08$ mm^3, monoclinic, space group $C2/c$ (No. 15), $a = 36.467(2)$, $b = 18.221(1)$, $c = 20.434(1)$ Å, $\beta = 103.43(1)°$, $T = 100(1)$ K, $Z = 4$, $V = 13206.3(13)$ Å^3, $\rho_{calcd} = 2.218$ Mg m^{-3}, $\mu = 3.914$ mm^{-1}, 28407 reflections collected, 10531 unique reflections ($R_{int} = 0.0450$, $2\theta_{max} = 50°$), 889 parameters, $R_1 = 0.0798$, $wR_2 = 0.2228$. CCDC-298992–298995 (**2**–**5**) contain the supplementary crystallographic data for this paper. These data can be obtained free of charge from The Cambridge Crystallographic Data Centre via www.ccdc.cam.ac.uk/data_request/cif.

[14] Holleman-Wiberg, *Lehrbuch der Anorganischen Chemie*, Walther de Gruyter, Berlin, **1995**, p. 1339.

[15] Although the positions of the H atoms were calculated by using a freely rotational HFIX instruction, the geometry and the distance hints at weak interactions between the Cu and H atoms (sum of the van der Waals radii: 2.8 Å;[14] intramolecular Cu···H9 distance in **4** (2.760 Å)). Thus a pseudo-octahedral geometry at the Cu atom can also be inferred.

[16] J. Besinger, J. Treptow, D. Fenske, *Z. Anorg. Allg. Chem.* **2002**, *628*, 512 – 515.

[17] a) M. Nardelli, C. Pelizzi, G. Pelizzi, P. Tarasconi, *J. Chem. Soc. Dalton Trans.* **1985**, 321 – 331; b) A. Bonardi, A. Cantoni, C. Pelizzi, G. Pelizzi, P. Tarasconi, *J. Organomet. Chem.* **1991**, *402*, 281 – 288; c) U. M. Tripathi, A. Bauer, H. Schmidbaur, *J. Chem. Soc. Dalton Trans.* **1997**, 2865 – 2868; d) G. A. Bowmaker, Effendy, R. D. Hart, J. D. Kildea, E. N. da Silva, B. W. Skelton, A. H. White, *Aust. J. Chem.* **1997**, *50*, 539 – 552.

[18] A. Klamt, G. Schürmann, *J. Chem. Soc. Perkin Trans. 2* **1993**, *5*, 799 – 805.

[19] a) R. Ahlrichs, M. Bär, M. Häser, H. Horn, C. Kölmel, *Chem. Phys. Lett.* **1989**, *162*, 165 – 169; b) O. Treutler, R. Ahlrichs, *J. Chem. Phys.* **1995**, *102*, 346 – 354.

[20] a) A. D. Becke, *Phys. Rev. A* **1988**, *38*, 3098 – 3100; b) S. H. Vosko, L. Wilk, M. Nusair, *Can. J. Phys.* **1980**, *58*, 1200 – 1211; c) J. P. Perdew, *Phys. Rev. B* **1986**, *33*, 8822 – 8824; erratum: J. P. Perdew, *Phys. Rev. B* **1986**, *34*, 7406.

[21] a) A. Schäfer, H. Horn, R. Ahlrichs, *J. Chem. Phys.* **1992**, *97*, 2571 – 2577; b) A. Schäfer, C. Huber, R. Ahlrichs, *J. Chem. Phys.* **1994**, *100*, 5829 – 5835; c) K. Eichkorn, F. Weigend, O. Treutler, R. Ahlrichs, *Theor. Chem. Acc.* **1997**, *97*, 119 – 124.

[22] a) K. Eichkorn, O. Treutler, H. Öhm, M. Häser, R. Ahlrichs, *Chem. Phys. Lett.* **1995**, *242*, 652 – 660; b) M. Sierka, A. Hogekamp, R. Ahlrichs, *J. Chem. Phys.* **2003**, *118*, 9136 – 9148.

[23] a) G. M. Sheldrick, SHELXS-*97*, Universität Göttingen, **1997**; b) G. M. Sheldrick, SHELXL-*97*, Universität Göttingen, **1997**.

 © 2006 Wiley-VCH Verlag GmbH & Co. KGaA, Weinheim

Organocatalysis

DOI: 10.1002/anie.200600512

Asymmetric Counteranion-Directed Catalysis**

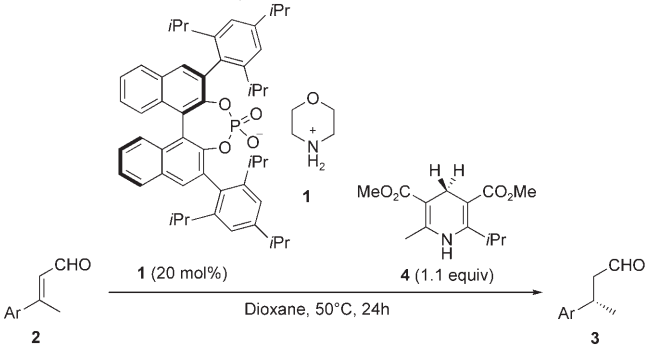
*Sonja Mayer and Benjamin List**

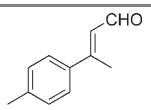
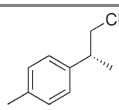
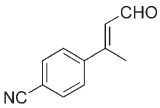
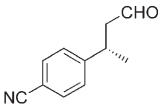
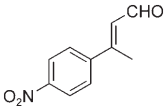
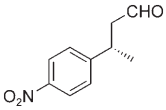
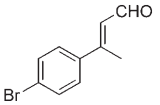
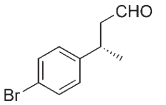
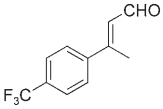
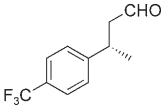
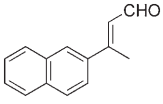
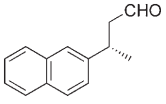
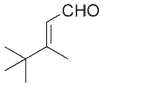
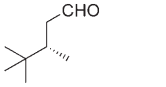
Most chemical reactions proceed via charged intermediates or transition states. Such "polar reactions" can be influenced by the counterion, especially if conducted in organic solvents, where ion pairs are ineffectively separated by the solvent. Although efficient asymmetric catalytic transformations involving anionic intermediates with chiral, cationic catalysts have been realized (for example, in phase-transfer catalysis),[1] analogous versions of *inverse* polarity with reasonable enantioselectivity have been illusive, despite several attempts.[2] We report here a catalytic organic salt that consists of an achiral ammonium cation and a chiral phosphate anion, which catalyzes transfer hydrogenations with remarkably high enantioselectivities.

Recently, a metal-free biomimetic transfer hydrogenation of α,β-unsaturated aldehydes was discovered in our research group and independently by MacMillan and co-workers.[3] The reaction is catalyzed by salts of chiral amines and proceeds via iminium ion intermediates. The process utilizes a Hantzsch dihydropyridine as the reductant and synthetic NADH analogue. Intrigued by the observation of a strong counteranion effect on the yield and enantioselectivity of the reaction, and inspired by the recent introduction of chiral phosphates as asymmetric Brønsted acid catalysts,[4] we hypothesized that catalytic salts of achiral amines and chiral phosphoric acids could induce asymmetry in the process. We expected the asymmetry of the chiral phosphate anion to influence the enantioselectivity of the reaction through a stereochemical communication within the iminium phosphate ion pair.

We have now screened such salts, which are easily prepared by mixing various commercially available primary and secondary amines with known chiral binaphthol-derived phosphoric acids. Several ammonium phosphate salts gave products in significant enantioselectivities. Remarkably, we consistently observed the highest enantiomeric ratios (e.r.) with ammonium salts of the sterically hindered chiral phosphoric acid derivative 3,3′-bis(2,4,6-triisopropylphenyl)-1,1′-binaphthyl-2,2′-diyl hydrogen phosphate (TRIP), which we recently introduced as powerful catalysts for imine reductions and Pictet–Spengler cyclizations.[4i,j] Its morpholine salt **1** was identified as widely applicable and a highly enantioselective catalyst for our organocatalytic transfer hydrogenation. Thus, treating α,β-unsaturated aldehydes **2** with a slight excess of dihydropyridine **4** and a catalytic amount of salt **1** at 50 °C in dioxane for 24 h gave the corresponding saturated aldehydes **3** in high yields and in enantioselectivities between 98:2 and >99:1 e.r. (Table 1).[5]

Table 1: Asymmetric counterion-mediated organocatalytic transfer hydrogenation of α,β-unsaturated aldehydes.



Entry	Substrate		Product		Yield [%]	e.r.[a]
1		**2a**		**3a**	87	98:2
2		**2b**		**3b**	84	99:1
3		**2c**		**3c**	90	99:1
4		**2d**		**3d**	67	98:2
5		**2e**		**3e**	63	99:1
6		**2f**		**3f**	72	>99:<1
7		**2g**		**3g**	<5	n.d.

[a] Determined by GC. n.d. = not determined.

Although our new catalyst was ineffective in converting the sterically hindered substrate **2g**, the enantioselectivities with aromatic substrates **2a**–**2f** are the highest reported for this reaction. Significantly, the previously developed chiral amine based catalysts that we and McMillan and co-workers have studied have not been of use for sterically *nonhindered* aliphatic substrates. For example, citral (**5**), of which the hydrogenation product citronellal (**6**) is an intermediate in the

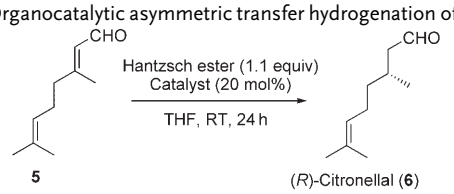
[*] S. Mayer, Prof. Dr. B. List
Max-Planck-Institut für Kohlenforschung
Kaiser-Wilhelm-Platz 1, 45470 Mülheim an der Ruhr (Germany)
Fax: (+49) 208-306-2999
E-mail: list@mpi-muelheim.mpg.de

[**] Technical assistance by Simone Marcus, Jutta Rosentreter, Michael Stadler, and Dr. Jung Woon Yang is gratefully acknowledged. We thank the Max-Planck Institut, Degussa, Lanxess, and Wacker for support of our work, the Deutsche Forschungsgemeneinschaft for the priority program "Organocatalysis" (SPP1179), and Novartis for a Young Investigator Award.

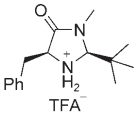
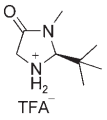
 © 2006 Wiley-VCH Verlag GmbH & Co. KGaA, Weinheim

industrial synthesis of menthol and used as a perfume ingredient, could not readily be used. We could not achieve high enantioselectivity for this particular substrate with either our previous system[3b] or with that of MacMillan and coworkers[3c] (Table 2). However, with our novel chiral counteranion catalyst **1**, citral is converted into (*R*)-citronellal (**6**) with an e.r. value of 95:5 (Table 2, entry 3). This is the highest enantioselectivity so far reported for a catalytic asymmetric (transfer) hydrogenation of citral.[6]

Table 2: Organocatalytic asymmetric transfer hydrogenation of (*E*)-citral.

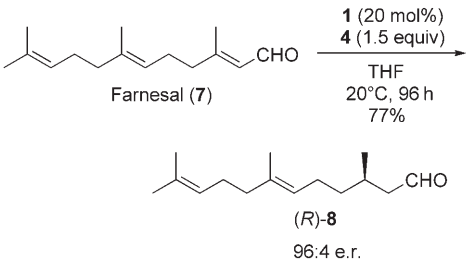


5 (*R*)-Citronellal (**6**)

Entry	Catalyst	Product	Yield [%]	e.r.[a]
1[b]		(*S*)-**6**	58[a]	70:30[c]
2[b]		(*S*)-**6**	82[a]	70:30[d]
3[e]	**1**	(*R*)-**6**	71	95:5

[a] Determined by GC. [b] Commercially available Hantzsch ethyl ester was used and gave a higher e.r. value than ester **4**. [c] Using the conditions reported in Ref. [3b]. [d] Using the conditions reported in Ref. [3c]. [e] Hantzsch ester **4** was used.

Similarly, farnesal (**7**) gave (*R*)-dihydrofarnesal (**8**) in 77% yield and 96:4 e.r. [Eq. (1)]. Enantiomerically enriched



Farnesal (**7**) (*R*)-**8**

96:4 e.r. (1)

2,3-dihydrofarnesal (**8**) has been identified as a marking pheromone of several bumblebee species, a constituent of the scent of orchids and the blossom fragrance of *Citrus limon*, and in fresh juniper needles.[7] To our knowledge, the reaction described herein constitutes the first asymmetric synthesis of **8**.

Although all the experiments reported here have been conducted with diastereomerically pure *E* isomers, initial experiments indicate that our new catalyst system is stereoconvergent and a rapid *E*–*Z* equilibration precedes the hydrogenation, as can be seen by NMR spectroscopic studies. Thus both *E* and *Z* isomers as well as their mixtures provide the same enantiomeric product, a phenomenon which has previously been observed in the versions catalyzed by chiral amines. We believe the reaction proceeds via an iminium ion intermediate since salts of tertiary amines (e.g. triethylamine) are ineffective. Asymmetric induction presumably occurs in the cationic transition state of the reaction by virtue of a stereochemical communication with the chiral phosphate counteranion, possibly through CH···O hydrogen-bonding interactions. The details of these interactions will be elucidated in future investigations.

In summary, we have developed a new catalyst salt (**1**) that consists of an achiral ammonium ion and a chiral phosphate anion which catalyzes highly enantioselective transfer hydrogenations of α,β-unsaturated aldehydes to the corresponding saturated derivatives. Our new catalyst considerably widens the substrate scope of the iminium catalytic transfer hydrogenation by allowing the use of sterically nonhindered α,β-unsaturated aldehydes. The underlying principle, namely asymmetric counteranion-directed catalysis (ACDC), is a new strategy for highly enantioselective synthesis and may turn out to be of general utility for other reactions that proceed via cationic intermediates.

Experimental Section

General procedure**:** Catalyst **1** (84.0 mg, 0.1 mmol, 20 mol%) was added to a stirred solution of the α,β-unsaturated aldehyde **2** (0.5 mmol) in dioxane (THF with aldehydes **5** and **7**; 5 mL) at 50°C (RT with aldehydes **5** and **7**). After five minutes, dihydropyridine **4** (139 mg, 0.55 mmol; 189 mg, 0.75 mmol for aldehyde **7**) was added. After 24 h (96 h for **7**), the mixture was poured into distilled water (20 mL) and extracted with dichloromethane (Et_2O with aldehydes **5** and **7**; 2 × 15 mL). The combined organic layers were dried ($MgSO_4$), filtered, and concentrated. Flash chromatography (SiO_2, ethyl acetate/hexane or diethyl ether/pentane) provided the pure products **3**, **6**, and **8**. Aldehydes **2a**–**g** were synthesized according to previously reported methods and their analytical data as well of those of aldehydes **3** correspond to literature values.[8] The absolute configuration of **3f** was determined by measurement of its known optical rotation.[9] Enantiomeric ratios were determined by GC analysis on a chiral stationary phase. The absolute configuration of (*R*)-citronellal (**6**) was determined by comparison with a commercial sample.

Received: February 7, 2006
Revised: March 22, 2006
Published online: May 24, 2006

Keywords: asymmetric organocatalysis · binaphthol derivatives · iminium ions · ion pair catalysis · transfer hydrogenation

[1] For reviews, see the special edition on "Asymmetric Organocatalysis": *Acc. Chem. Res.* **2004**, *37*, 487–631.
[2] For a review, see: a) J. Lacour, V. Hebbe-Viton, *Chem. Soc. Rev.* **2003**, *32*, 373–382; see also: b) D. B. Llewellyn, B. A. Arndtsen, *Tetrahedron: Asymmetry* **2005**, *16*, 1789–1799; c) R. Dorta, L. Shimon, D. Milstein, *J. Organomet. Chem.* **2004**, *689*, 751–758; d) C. Carter, S. Fletcher, A. Nelson, *Tetrahedron: Asymmetry* **2003**, *14*, 1995–2004.
[3] a) J. W. Yang, M. T. Hechavarria Fonseca, B. List, *Angew. Chem.* **2004**, *116*, 6829–6832; *Angew. Chem. Int. Ed.* **2004**, *43*, 6660–6662; b) J. W. Yang, M. T. Hechavarria Fonseca, N. Vignola, B. List, *Angew. Chem.* **2005**, *117*, 110–112; *Angew. Chem. Int. Ed.*

 © 2006 Wiley-VCH Verlag GmbH & Co. KGaA, Weinheim

2005, *44*, 108 – 110; c) S. G. Ouellet, J. B. Tuttle, D. W. C. MacMillan, *J. Am. Chem. Soc.* **2005**, *127*, 32 – 33.

[4] a) T. Akiyama, J. Itoh, K. Yokota, K. Fuchibe, *Angew. Chem.* **2004**, *116*, 1592 – 1594; *Angew. Chem. Int. Ed.* **2004**, *43*, 1566 – 1568; b) T. Akiyama, H. Morita, J. Itoh, K. Fuchibe, *Org. Lett.* **2005**, *7*, 2583 – 2585; c) T. Akiyama, Y. Saitoh, H. Morita, K. Fuchibe, *Adv. Synth. Catal.* **2005**, *347*, 1523 – 1526; d) T. Akiyama, Y. Tamura, J. Itoh, H. Morita, K Fuchibe, *Synlett* **2006**, 141 – 143; e) D. Uraguchi, M. Terada, *J. Am. Chem. Soc.* **2004**, *126*, 5356 – 5367; f) D. Uraguchi, K. Sorimachi, M. Terada, *J. Am. Chem. Soc.* **2004**, *126*, 11804 – 11805; g) D. Uraguchi, K. Sorimachi, M. Terada, *J. Am. Chem. Soc.* **2005**, *127*, 9360 – 9361; h) M. Rueping, E. Sugiono, C. Azap, T. Theissmann, M. Bolte, *Org. Lett.* **2005**, *7*, 3781 – 3783; i) S. Hoffmann, A. Seayad, B. List, *Angew. Chem.* **2005**, *117*, 7590 – 7593; *Angew. Chem. Int. Ed.* **2005**, *44*, 7424 – 7427; j) J. Seayad, A. M. Seayad, B. List, *J. Am. Chem. Soc.* **2006**, *128*, 1086 – 1087; k) G. B. Rowland, H. Zhang, E. B. Rowland, S. Chennamadhavuni, Y. Wang, J. C. Antilla, *J. Am. Chem. Soc.* **2005**, *127*, 15696 – 15697; l) R. I. Storer, D. E. Carrera, Y. Ni, D. W. C. MacMillan, *J. Am. Chem. Soc.* **2006**, *128*, 84 – 86.

[5] Alternative dialkyl 2,6-dimethyl-1,4-dihydropyridine-3,5-dicarboxylate Hantzsch esters have been screened for the reduction of substrate **2c**: bis-*tert*-butyl (82:18 e.r.), bisneopentyl (83:17 e.r.), mixed methyl-*tert*-butyl (85:15 e.r.). The use of alternative substituents in the 2,6 positions of the Hantzsch ester leads to diminished enantioselectivities. Alternative amines that were screened with the TRIP counteranion using **2c** as substrate are: pyrrolidine (98:2 e.r.), dibenzylamine (97:3 e.r.), *O*,*N*-dimethylhydroxylamine (94:6 e.r.), and methylamine (90:10 e.r.). Other chiral phosphate and carboxylate counteranions have been studied but typically gave lower e.r. values. The full details of the catalyst screen will be reported in due course.

[6] a) "Optical active citronellal" (Rhone-Poulenc Industries S.A., Fr.), JP 78-80630, **1979**; b) T.-P. Dang, P. Aviron-Violet, Y. Colleuille, J. Varagnat, *J. Mol. Catal.* **1982**, *16*, 51 – 59; c) G. Kortvelyessy, *Acta Chim. Hung.* **1985**, *119*, 347 – 354.

[7] A. Luxova, K. Urbanova, I. Valterova, M. Terzo, A.-K. Borg-Karlson, *Chirality* **2004**, *16*, 228 – 233, and references therein.

[8] a) R. Martin, I. Islas, A. Moyano, M. A. Pericas, A. Riera, *Tetrahedron* **2001**, *57*, 6367 – 6374; b) M. I. Al-Hassan, *Gazz. Chim. Ital.* **1985**, *115*, 441; c) M. Akhtar, L. Jallo, A. Johnson, *J. Chem. Soc. Chem. Commun.* **1982**, *1*, 44 – 46; d) A. I. Meyers, A. Nabeya, H. W. Adickes, I. R. Politzer, *J. Am. Chem. Soc.* **1969**, *91*, 764 – 765.

[9] T. Lee, J. B. Jones, *J. Am. Chem. Soc.* **1997**, *119*, 10260 – 10268.

 © 2006 Wiley-VCH Verlag GmbH & Co. KGaA, Weinheim

C–F Activation

DOI: 10.1002/anie.200600361

Formation of Zirconocene Fluoro Complexes: No Deactivation in the Polymerization of Olefins by the Contact-Ion-Pair Catalysts $[Cp'_2ZrR]^+[RB(C_6F_5)_3]^-$**

Perdita Arndt, Ulrike Jäger-Fiedler, Marcus Klahn, Wolfgang Baumann, Anke Spannenberg, Vladimir V. Burlakov, and Uwe Rosenthal**

In memory of Erhard Kurras

Certain ion pairs $[Cp'_2MMe]^+[MeB(C_6F_5)_3]^-$ (M = Ti, Zr; Cp′ = substituted or unsubstituted η^5-cyclopentadienyl), formed by the formal abstraction of methyl anions from dimethyl complexes $[Cp'_2MMe_2]$ of the Group 14 transition metals by the strong Lewis acid $B(C_6F_5)_3$, are highly active catalysts for the polymerization of α-olefins.[1] Zirconocene complexes of olefins, alkynes, and butadiene were also later activated for catalytic olefin polymerization in a similar way.[2]

Recently, we described the reactions of complexes containing two M–C σ bonds, including the zirconacyclopropenes $[Cp'_2Zr(\eta^2\text{-}RC_2R)]$ ($R = SiMe_3$)[3a] and several five-membered zirconacycles,[3b,c] with $B(C_6F_5)_3$. A typical example is [*rac*-(ebthi)Zr(η^2-$Me_3SiC_2SiMe_3$)] (**A**; ebthi = 1,2-ethylene-1,1′-bis(η^5-tetrahydroindenyl)),[4a] which undergoes electrophilic substitution at the five-membered ring of the ebthi ligand upon reaction with $B(C_6F_5)_3$, forming the alkenyl complex **B** [Eq. (1)].[4b] In this complex, the boranate group is substituted at the 3-position of the five-membered ring, and one of its *ortho* fluorine atoms is coordinated to the zirconium center. The σ-bound alkenyl group at the zirconium center participates in an additional agostic interaction.[4b]

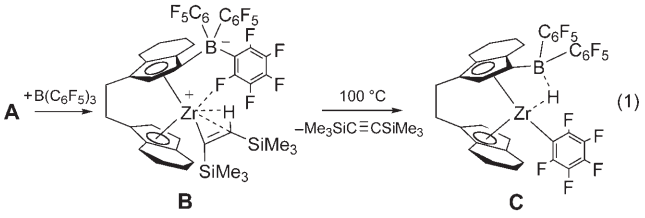
Upon thermolysis of **B** [Eq. (1)], bis(trimethylsilyl)acetylene is eliminated, and with the cleavage of one B–C bond,

[*] Dr. P. Arndt, U. Jäger-Fiedler, M. Klahn, Dr. W. Baumann, Dr. A. Spannenberg, Prof. Dr. U. Rosenthal
Leibniz-Institut für Katalyse e.V.
an der Universität Rostock
Albert-Einstein-Strasse 29a, 18059 Rostock (Germany)
Fax: (+49) 381-1281-51176
E-mail: perdita.arndt@ifok-rostock.de
uwe.rosenthal@ifok-rostock.de
Dr. V. V. Burlakov
Nesmeyanov Institute of Organoelement Compounds
Russian Academy of Sciences
Vavilov Street 28, 117813 Moscow (Russia)

[**] We are grateful to the Deutsche Forschungsgemeinschaft (Research Training Group 1213 and SPP 1118, project no. RO 1269/6) and the Russian Foundation for Basic Research (project code 05-03-32515) for financial support. We thank our technical staff, in particular Petra Bartels and Regina Jesse, for skilled assistance. Cp′ = substituted or unsubstituted η^5-cyclopentadienyl; R = Me, H.

Supporting information for this article is available on the WWW under http://www.angewandte.org or from the author.

 © 2006 Wiley-VCH Verlag GmbH & Co. KGaA, Weinheim WILEY InterScience DISCOVER SOMETHING GREAT



one C_6F_5 group is transferred from boron to zirconium. The resulting complex **C** contains one bridging μ-hydrogen atom between the boron and zirconium centers.[4b]

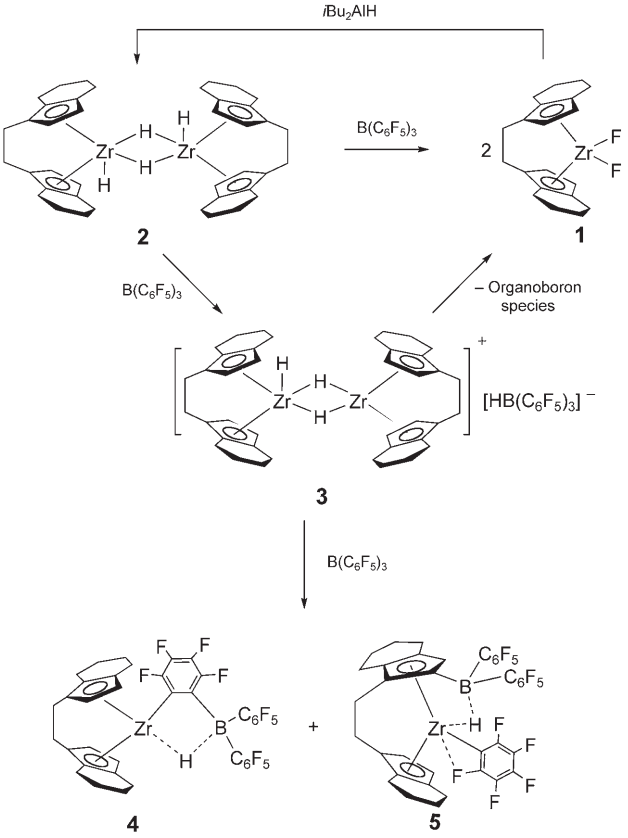
Complexes **B** and **C** can serve as model compounds for the two most frequently reported side reactions leading to catalyst poisoning and decreased productivity.[5a] The first deactivation pathway is the transfer of a C_6F_5 group to the cationic metal centre (**C**).[4b,5] The second consists of the transfer of a fluoride anion to the metal center (via intermediates such as **B**). It has been proposed that the formation of catalytically inactive zirconocene fluorides is an important deactivation process.[5a]

Nevertheless, we recently found that the difluoride [*rac*-(ebthi)ZrF_2] (**1**),[6b,c] in contrast to the analogous dichloride,[6a] is an efficient catalyst for ethylene polymerization after activation with *i*Bu_3Al (or *i*Bu_2AlH).[7a–c] In the literature, there are several empirical reports of Ti–F and Zr–F olefin-polymerization catalysts.[7d–f] To understand these results, we studied the reaction of **1** with two equivalents of *i*Bu_2AlH and found that hydride anions replace the fluoride ligands of **1** to give the complex [{*rac*-(ebthi)ZrH(μ-H)}$_2$] (**2**) (Scheme 1).[8a,b] Interestingly, the reaction of the dichloride [*rac*-(ebthi)$ZrCl_2$] with *i*Bu_2AlH under analogous conditions does not lead to a hydride; rather, only the starting material is isolated.[8a] The fluoride anion is apparently a more labile ligand than the chloride anion in this system, which explains the easier abstraction of a fluoride ligand to give an active catalyst system. The cleavage of the Zr–F bonds by Al–H groups with the formation of Zr–H and Al–F bonds is accepted as the reason for this "fluoride effect".[7,8]

Zirconocene hydrides have frequently been used for the activation of C–F bonds. In a series of outstanding papers, Jones and co-workers have described the cleavage of C–F bonds in alkanes, arenes, and olefins using [$Cp^*_2ZrH_2$] (Cp^* = η^5-pentamethylcyclopentadienyl).[9]

In light of the surprising results mentioned above for zirconocene difluorides in the catalytic polymerization of olefins, we describe herein the effective cleavage of C–F bonds in $B(C_6F_5)_3$ by complex **2**, which is formed by the reaction of Zr–F and Al–H species.

The reaction of **2** with $B(C_6F_5)_3$ in toluene at 90 °C for 14 days leads to a nearly quantitative formation of **1** (Scheme 1). A small amount of complex **5** is formed as a byproduct. To elucidate the reaction pathway, not only was the intermediate **3** isolated, but NMR spectroscopic experiments were also carried out. In these experiments, compounds such as **4** and **5**, which are difficult to characterize or isolate because of their instability, were detected. Note that the system is extremely sensitive with respect to slight changes in reaction conditions. Variations in the conditions can change



Scheme 1. Elementary steps of C–F bond activation in the reaction of **2** with $B(C_6F_5)_3$.

the product composition or lead to inseparable mixtures of other complexes, which could not yet be characterized.

Orange crystals of complex **3** form very quickly at 20 °C in toluene, *n*-hexane, or benzene. The insolubility and instability of this complex prevents a detailed NMR spectroscopic investigation or recrystallization. Therefore, only low-quality crystals could be obtained for X-ray crystal-structure analysis. Nevertheless, it was possible to confirm that **3** consists of an ion pair of the type [{*rac*-(ebthi)Zr(μ-H)}$_2$]$^+$[$HB(C_6F_5)_3$]$^-$;[14] in analogy to the ion pair [Cp^*_2ZrH]$^+$[$HB(C_6F_5)_3$]$^-$,[10] the presence of one terminal hydrogen atom in the cation is postulated (Scheme 1), but could not be located.

Complex **3** reacts slowly (60 °C, 5–7 h) with additional $B(C_6F_5)_3$ to give the yellow mononuclear complex [*rac*-(ebthi)Zr(μ-H){*o*-$C_6F_4B(C_6F_5)_2$}] (**4**) and varying amounts of complex **5**. The molecular structure of **4** contains the typical {*rac*-(ebthi)Zr} unit; the zirconium center is bonded to an *ortho*-metalated phenyl ring of the boranate anion, as well as a hydride ligand (H1; Figure 1).[15] The positional and thermal parameters of H1 could not be refined. However, in the $^1H\{^{11}B\}$ NMR spectrum of **4** a signal ($\delta = 1.27$ ppm) assigned to the hydride ligand is detected in the region of the *rac*-(ebthi)-ligand signals. Further NMR spectroscopic investigations were hampered by the instability of **4** in solution. Nevertheless, high yields of **1** can be obtained by the reaction of **2** with $B(C_6F_5)_3$ or by the thermolysis of complex **3**.

Only one other example of a similar fluoride transfer from $B(C_6F_5)_3$ to zirconium has been described: starting from

 © 2006 Wiley-VCH Verlag GmbH & Co. KGaA, Weinheim

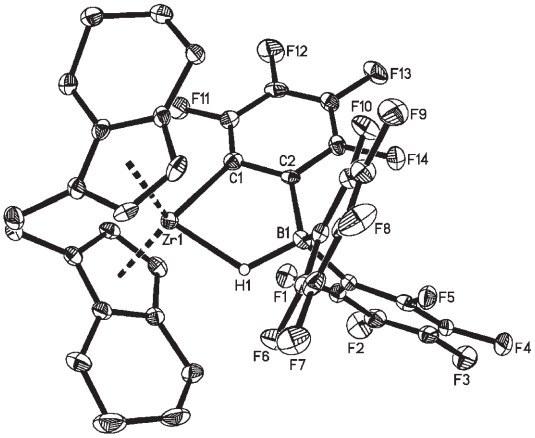


Figure 1. ORTEP representation of **4**. Thermal ellipsoids are set at 30% probability. Hydrogen atoms (with the exception of H1) are omitted for clarity. Selected bond lengths [Å] and angles [°]: Zr1–C1 2.222(4), C1–C2 1.414(6), B1–C2 1.647(7); Zr1-C1-C2 103.4(3), C1-C2-B1 121.9(4).

$[Cp^*_2ZrMe]^+[MeB(C_6F_5)_3]^-$, Marks and co-workers obtained $[Cp^*_2(Me)Zr(\mu\text{-}F)Zr(Me)Cp^*_2]^+[MeB(C_6F_5)_3]^-$,[5c] which can be viewed as an adduct of $[Cp^*_2ZrMe]^+[MeB(C_6F_5)_3]^-$ and $[Cp^*_2Zr(Me)F]$. This product is probably formed through either a transfer of one C_6F_5 group to the metal center, with the formation of $[Cp^*_2Zr(Me)C_6F_5]$ and $MeB(C_6F_5)_2$, followed by an *ortho*-fluoride abstraction to give $[Cp^*_2Zr(Me)F]$ and organoboron species, or through a direct fluoride transfer to the zirconium centre.

Complex **5**, which is formed in 10 to 30% yield depending on the reaction temperature and time, was shown by X-ray crystallography to be an isomer of complex **C**.[4b,16] In **5**, the *rac*-(ebthi) ligand is substituted by the boranate group at the 2-position of the cyclopentadienyl ring, whereas in **C**, the ring is substituted at the 3-position. Additionally, one *ortho* fluorine atom of the zirconium-bound C_6F_5 group weakly coordinates the zirconium center in **5** (Figure 2).[4b]

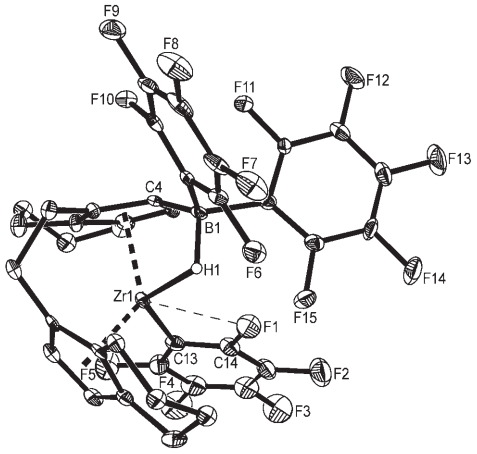
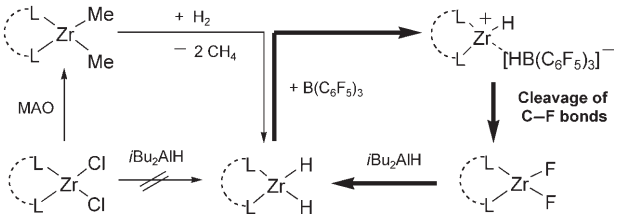


Figure 2. ORTEP representation of **5**. Thermal ellipsoids are set at 30% probability. Hydrogen atoms (with the exception of H1) are omitted for clarity. Selected bond lengths [Å] and angles [°]: Zr1–C13 2.319(8), Zr1···F1 2.604(5), F1–C14 1.389(8), B1–C4 1.593(10); C13-C14-F1 114.0(7).

The formation of the difluoride **1** (by nucleophilic aromatic substitution on $B(C_6F_5)_3$), as well as complexes **5** and **C** (by C_6F_5-group migration) is relevant for the catalytic polymerization of olefins. Complexes such as **5** and **C** are completely inactive, and their formation clearly represents a deactivation process. The formation of **1** from **2** and $B(C_6F_5)_3$ by C–F bond cleavage, often described as a deactivation process, is not in fact a deactivation, because **1** can be reconverted into **2** through treatment with iBu$_2$AlH (Scheme 1).

These results, obtained through the stepwise reactions of isolated complexes, have important consequences for catalytic olefin polymerization in general: mixtures of zirconocene halides such as $[Cp'_2ZrCl_2]$, methylalumoxane (MAO; as an activator and scavenger), and fluorosubstituted arylboranes such as $B(C_6F_5)_3$ are often used to produce catalytically active systems. Hydrogen gas is also added to the system to control the molecular weight of the polymer. Marks and coworkers have shown that the methyl complex $[Cp^*_2ZrMe_2]$ reacts with hydrogen to produce the hydride $[Cp^*_2ZrH_2]$, with elimination of methane. The hydride subsequently reacts with $B(C_6F_5)_3$ to form the active ion pair $[Cp^*_2ZrH]^+[HB(C_6F_5)_3]^-$ (Scheme 2).[10]



Scheme 2. Mechanisms of catalyst activation and deactivation. L-----L = Cp'_2.

In relation to these steps, the formation of fluoro complexes by C–F bond cleavage was only discussed as a deactivation process.[5] Our results clearly show that Zr–F complexes can be reconverted into Zr–H complexes, which are very active catalysts, through interaction with Al–H groups (Scheme 2).

It has been noted that *"In many instances organometallic fluorides have been the unexpected products of fluorine abstraction in the decomposition of complexes of fluorinated anions."*[11] This observation, in the case of reactions involving the fluorinated arylborane $B(C_6F_5)_3$ and the boranates $[RB(C_6F_5)_3]^-$ (R = Me, H), was previously considered to be a marginal problem and interpreted exclusively as the result of a deactivation process.

There are, in fact, many examples of $B(C_6F_5)_3$ effecting electrophilic substitution at cyclopentadienyl ligands (leading to complexes such as **B**),[3] but few examples of nucleophilic aromatic substitution involving $B(C_6F_5)_3$. Erker and co-workers,[12a,b] and others[12c] have described that the positive inductive effect of boron is sometimes overcompensated in $B(C_6F_5)_3$ by the fluoro substituents, making this special Lewis acid susceptible to nucleophilic attack at the electron-deficient arene rings.

The unexpected formation of **1** and its activity as a precatalyst in olefin polymerization, explained herein, con-

 © 2006 Wiley-VCH Verlag GmbH & Co. KGaA, Weinheim

firm the statement that *"early transition metal fluoride complexes do not preclude catalytic chemistry."*[13] In this context, our results offer a new perspective on the deactivation of olefin-polymerization catalysts.

Received: January 27, 2006
Published online: May 16, 2006

Keywords: borate ligands · C—F activation · homogeneous catalysis · polymerization · zirconocene fluorides

[1] Review: H. H. Brintzinger, D. Fischer, R. Mülhaupt, B. Rieger, R. Waymouth, *Angew. Chem.* **1995**, *107*, 1255 – 1283; *Angew. Chem. Int. Ed. Engl.* **1995**, *34*, 1143 – 1171, and references therein.

[2] Reviews: a) W. E. Piers, *Chem. Eur. J.* **1998**, *4*, 13 – 18; b) G. Erker, *Acc. Chem. Res.* **2001**, *34*, 309 – 317, and references therein.

[3] a) U. Rosenthal, V. V. Burlakov, P. Arndt, W. Baumann, A. Spannenberg, V. B. Shur, *Eur. J. Inorg. Chem.* **2004**, 4739 – 4749, and references therein; b) V. V. Burlakov, P. Arndt, W. Baumann, A. Spannenberg, U. Rosenthal, *Organometallics* **2004**, *23*, 5188 – 5192; c) M. A. Bach, T. Beweries, V. V. Burlakov, P. Arndt, W. Baumann, A. Spannenberg, U. Rosenthal, W. Bonrath, *Organometallics* **2005**, *24*, 5916 – 5918.

[4] a) C. Lefeber, W. Baumann, A. Tillack, R. Kempe, H. Görls, U. Rosenthal, *Organometallics* **1996**, *15*, 3486 – 3490; b) P. Arndt, W. Baumann, A. Spannenberg, U. Rosenthal, V. V. Burlakov, V. B. Shur, *Angew. Chem.* **2003**, *115*, 1455 – 1458; *Angew. Chem. Int. Ed.* **2003**, *42*, 1414 – 1418.

[5] Examples: a) T. Wondimagegn, Z. Xu, K. Vanka, T. Ziegler, *Organometallics* **2005**, *24*, 2076 – 2085, and references therein; b) T. Wondimagegn, Z. Xu, K. Vanka, T. Ziegler, *Organometallics* **2004**, *23*, 3847 – 3852; c) X. Yang, C. L. Stern, T. J. Marks, *J. Am. Chem. Soc.* **1994**, *116*, 10015 – 10031.

[6] a) F. R. W. P. Wild, L. Zsolnai, G. Huttner, H. H. Brintzinger, *J. Organomet. Chem.* **1982**, *232*, 233 – 247; b) D. Thomas, W. Baumann, A. Spannenberg, R. Kempe, U. Rosenthal, *Organometallics* **1998**, *17*, 2096 – 2102; c) A. Spannenberg, P. Arndt, W. Baumann, V. V. Burlakov, U. Rosenthal, S. Becke, T. Weiß, *Organometallics* **2004**, *23*, 3819 – 3825.

[7] a) S. Becke, U. Rosenthal, (Bayer AG), DE 199 32 409A1 (18. 01. **2001**); b) S. Becke, U. Rosenthal, (Bayer AG), US 6,303,718 B1 (16. 10. **2001**); c) S. Becke, U. Rosenthal, P. Arndt, W. Baumann, A. Spannenberg, (Bayer AG), DE 101 10 227A1 (05. 09. **2002**); d) J. N. Pedeutour, H. Cramail, A. Deffieux, *J. Mol. Catal. A* **2001**, *174*, 81 – 87; e) C. Schwecke, W. Kaminsky, *Macromol. Rapid Commun.* **2001**, *22*, 508 – 512; f) Y. Qian, H. Zhang, X. Qian, J. Huang, C. Shen, *J. Mol. Catal. A* **2003**, *192*, 25 – 33.

[8] a) A. Spannenberg, P. Arndt, W. Baumann, V. V. Burlakov, U. Rosenthal, S. Becke, T. Weiß, *Organometallics* **2004**, *23*, 4792 – 4795; b) R. B. Grossmann, R. A. Doyle, S. L. Buchwald, *Organometallics* **1991**, *10*, 1501 – 1505.

[9] a) B. L. Edelbach, B. M. Kraft, W. D. Jones, *J. Am. Chem. Soc.* **1999**, *121*, 10327 – 10331; b) B. M. Kraft, R. J. Lachicotte, W. D. Jones, *J. Am. Chem. Soc.* **2000**, *122*, 8559 – 8560; c) B. M. Kraft, R. J. Lachicotte, W. D. Jones, *J. Am. Chem. Soc.* **2001**, *123*, 10973 – 10979; d) B. M. Kraft, W. D. Jones, *J. Organomet. Chem.* **2002**, *658*, 132 – 140; e) B. M. Kraft, W. D. Jones, *J. Am. Chem. Soc.* **2002**, *124*, 8681 – 8689; f) B. M. Kraft, R. J. Lachicotte, W. D. Jones, *Organometallics* **2002**, *21*, 727 – 731; g) W. D. Jones, *Dalton Trans.* **2003**, 3991 – 3995.

[10] T. J. Marks, X. Yang, C. L. Stern, *Angew. Chem.* **1992**, *104*, 1406 – 1408; *Angew. Chem. Int. Ed. Engl.* **1992**, *31*, 1375 – 1377.

[11] E. F. Murphy, R. Murugavel, H. W. Roesky, *Chem. Rev.* **1997**, *97*, 3425 – 3468.

[12] Examples: a) S. Döring, G. Erker, R. Fröhlich, O. Meyer, K. Bergander, *Organometallics* **1998**, *17*, 2183 – 2187; b) D. Vagedes, G. Kehr, D. König, K. Wedeking, R. Fröhlich, G. Erker, C. Mück-Lichtenfeld, S. Grimme, *Eur. J. Inorg. Chem.* **2002**, 2015 – 2021; c) A. N. Chernega, A. J. Graham, M. L. H. Green, J. Haggitt, J. Lloyd, C. P. Mehnert, N. Metzler, J. Souter, *J. Chem. Soc. Dalton Trans.* **1997**, 2293 – 2303.

[13] J. L. Kiplinger, T. G. Richmond, *J. Am. Chem. Soc.* **1996**, *118*, 1805 – 1806.

[14] Crystal-structure analysis of **3**: $C_{58}H_{51}BF_{15}Zr_2$, $M_r = 1226.24$, $0.2 \times 0.2 \times 0.1$ mm, orange prisms, space group $P2_1/n$, monoclinic, $a = 10.946(2)$, $b = 20.243(4)$, $c = 22.602(5)$ Å, $\beta = 100.86(3)°$, $V = 4918.5(17)$ Å^3, $Z = 4$, $\rho_{calcd} = 1.656$ g cm^{-3}, 17564 reflections measured, 5159 independent, 3562 observed ($I > 2\sigma(I)$), $R1 = 0.057$, $wR2$(all data) $= 0.141$, 696 parameters. The terminal hydride ligand was not located.

[15] Crystal-structure analysis of **4**: $C_{38}H_{25}BF_{14}Zr$, $M_r = 849.61$, $0.4 \times 0.3 \times 0.2$ mm, yellow prisms, space group $P2_12_12_1$, orthorhombic, $a = 11.562(2)$, $b = 12.493(2)$, $c = 22.206(4)$ Å, $V = 3207.5(10)$ Å^3, $Z = 4$, $\rho_{calcd} = 1.759$ g cm^{-3}, 17145 reflections measured, 5104 independent, 3749 observed ($I > 2\sigma(I)$), $R1 = 0.034$, $wR2$(all data) $= 0.061$, 487 parameters.

[16] Crystal-structure analysis of **5**: $C_{39.67}H_{24}BF_{15}Zr$, $M_r = 887.62$, $0.3 \times 0.2 \times 0.1$ mm, colorless prisms, space group $P\bar{3}$, trigonal, $a = 23.082(3)$, $c = 12.474(3)$ Å, $V = 5755.5(16)$ Å^3, $Z = 6$, $\rho_{calcd} = 1.537$ g cm^{-3}, 16976 reflections measured, 5992 independent, 2908 observed ($I > 2\sigma(I)$), $R1 = 0.053$, $wR2$(all data) $= 0.153$, 507 parameters. CCDC-295535 (**3**), CCDC-295534 (**4**), and CCDC-295536 (**5**) contain the supplementary crystallographic data for this paper. These data can be obtained free of charge from The Cambridge Crystallographic Data Centre via www.ccdc.cam.ac.uk/data_request/cif.

 © 2006 Wiley-VCH Verlag GmbH & Co. KGaA, Weinheim

Protein Modification

DOI: 10.1002/anie.200504387

Fluorine in a Native Protein Environment—How the Spatial Demand and Polarity of Fluoroalkyl Groups Affect Protein Folding**

*Christian Jäckel, Mario Salwiczek, and Beate Koksch**

Noncanonical amino acids with newly designed side-chain functionalities are powerful tools that can be used to improve structural, biological, and pharmacological properties of peptides and proteins.[1] Incorporating fluorine in the design of artificial amino acids has become a prominent strategy to enhance the structural stability of peptides and proteins.[1,2]

[*] C. Jäckel, M. Salwiczek, Prof. Dr. B. Koksch
Department of Chemistry and Biochemistry
Free University of Berlin
Takustrasse 3, 14195 Berlin (Germany)
Fax: (+49) 308-385-5644
E-mail: koksch@chemie.fu-berlin.de

[**] This work was supported by the Deutsche Forschungsgemeinschaft (KO1976/2-1) and the Graduiertenkolleg (#788).

Supporting information for this article is available on the WWW under http://www.angewandte.org or from the author.

© 2006 Wiley-VCH Verlag GmbH & Co. KGaA, Weinheim

The decrease in polarizability of the carbon framework and the increase of the surface area upon fluorination increases the hydrophobicity of a molecule.[3] Consequently, the incorporation of fluoroalkyl groups can significantly increase diffusion across membranes such as the blood–brain barrier[4] and improve the pharmacokinetical properties of peptide-based drugs. The carbon–fluorine bond is highly dipolar, which enables its participation in polar interactions.[5] The strong inductive effect of the fluorine atom combined with its high electronegativity affects the acidity and basicity of nearby functional groups.[6] Consequently, fluorination of alkyl groups induces polarization of C–H bonds in proximity to the site of fluorine substitution.

Besides the question of fluorine's capability to participate in hydrogen bonds,[7] some other important features of fluorinated alkyl groups are still subjects of debate or are even unstudied, marking a profound drawback for the directed application of fluorine in peptide and protein engineering.[8] 1) Literature values for the steric demand of a trifluoromethyl group range from twice the bulk of methyl[9] to close to the size of phenyl and *tert*-butyl.[10] Those values mostly depend on the experimental methods and their interpretation.[9,11] Recent reports suggest that CF_3 better mimics bulkier alkyl groups rather than methyl in protein binding pockets.[12] 2) The influence of fluorine's inductive effect on the polarity of the C–F bond as well as nearby C–H bonds in a hydrophobic protein environment has not been studied yet. 3) The ability of fluoroalkylated amino acids to enhance the structural stability of hydrophobic protein domains is attributed either to a general increase in hydrophobicity[13] or to the formation of specific fluorine–fluorine interaction cores, the "fluorous effect".[14] Clarifying these issues is indispensible for making use of fluorine's potency in the composition of de novo designed protein domains.

We recently presented a screening system for the investigation of the properties that fluorinated amino acids display in a native polypeptide environment.[15,16] This system is based on a 41 amino acid residue, α-helical coiled-coil peptide that folds into an antiparallel homodimer.[17] The primary structure of the α-helical coiled coil is composed of heptad repeats that are designated with letters from *a* to *g*. Positions *a* and *d* are typically occupied by amino acids with alkyl side chains, which form a zipperlike hydrophobic-interaction core in the folded state. Positions *e* and *g* contain charged residues that form interhelical salt bridges.[18] The α-helical coiled-coil motif is known to react highly sensitively even on single mutations in one of the recognition domains.[19] It provides a hydrophobic as well as a polar environment. The complex molecular interactions of fluoroalkyl groups with native polypeptides can thus be studied systematically.

In our screening system, residues Lys8 in the charged domain and Leu9 in the hydrophobic core serve as substitution positions for the fluorinated amino acids (Figure 1). The antiparallel orientation of the α-helical coiled-coil peptide dimer insures that the nonnatural building blocks exclusively interact with native amino acid residues in precisely defined positions at the opposite helix strand (Glu29 in the charged domain and Leu30, Leu33, combined with Leu37 in the hydrophobic domain).

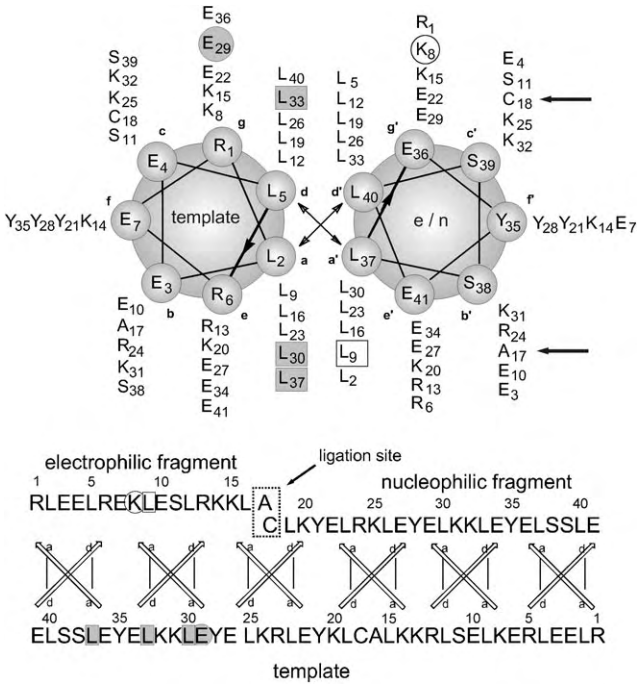


Figure 1. Helical-wheel and sequence representation of the original peptide. Substitution positions within the hydrophobic domain are highlighted with open squares and those within the charged interface with open circles. Their interaction partners are highlighted with shaded squares and circles, respectively. The ligation site of the electrophilic and nucleophilic fragments is marked with arrows.

Screen I measures the structural stability of the fluorine-modified α-helical peptide dimers. Screen II is based on the self-replication properties of α-helical coiled-coil peptides.[19] Therefore, we synthesized fluorine-modified electrophilic peptides that undergo a thioester-mediated chemical ligation with a nucleophilic coiled-coil fragment and determined the rate of peptide-bond formation in the autocatalyzed reaction cycle.[20] Both screens in this study have been proven to be sufficiently sensitive to detect the difference of even a single fluorine atom within the side chain of an amino acid.[15] Applying this screening system, we systematically studied fluorinated amino acids of varying side-chain length and degree of fluoro substitution. Here we present the first systematic study of the properties of fluoroalkyl groups and their impact on amino acid interactions in native polypeptide environments.

Based on the widespread argument that a trifluoromethyl group is approximately as large as an isopropyl group,[21] the side chain of (*S*)-4,4,4-trifluoroethylglycine (TfeGly, Figure 2) should have space-filling properties similar to those of native leucine. Therefore, our investigation started with the amino

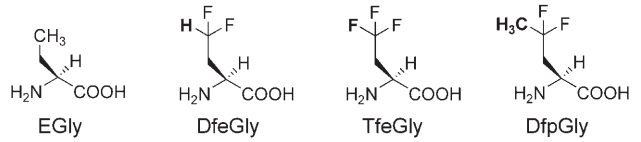


Figure 2. Structures of (*S*)-ethylglycine and its fluorinated analogues.

 © 2006 Wiley-VCH Verlag GmbH & Co. KGaA, Weinheim

acid (*S*)-ethylglycine (EGly) and its analogue (*S*)-4,4-difluoroethylglycine (DfeGly). To systematically enhance the steric demand of the amino acid side chain, the remaining hydrogen of the difluoromethyl group in DfeGly was either replaced by fluorine, which resulted in (*S*)-4,4,4-trifluoroethylglycine (TfeGly), or by a methyl group to give (*S*)-4,4-difluoropropylglycine (DfpGly).

The peptide containing the canonical amino acid alanine served as a control. Electrophilic peptide fragments containing the original residues (Leu and Lys) as well as the fluorinated and control amino acids in either of the substitution positions Leu9 and Lys8 were synthesized and ligated to the nucleophilic fragment on a preparative scale to obtain the full-length α-helical coiled-coil peptides.

Screen I for thermal stability: Thermal unfolding experiments (CD spectroscopy) show that all substitutions in position Leu9 of the hydrophobic core strongly destabilize the α-helical coiled coil relative to the original sequence (Figure 3a). The melting temperatures (T_m) of all substituted peptides are lowered by 14.9–22.3 K (Figure 4). The incorporation of alanine (Leu9Ala) causes a hole in the hydrophobic-core packing that destabilizes the folding motif. Elongation of the Ala methyl side chain by one methyl (Leu9EGly) slightly diminishes this effect. A stepwise increase in side-chain volume by subsequent fluorination of the EGly methyl group further increases the peptide melting temperatures (Leu9-DfeGly and Leu9TfeGly).

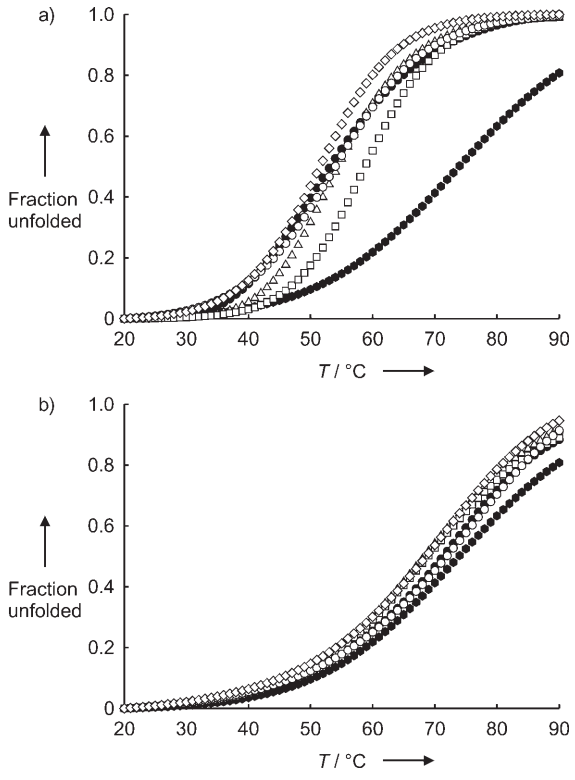


Figure 3. Thermal unfolding profiles of a) Leu9- and b) Lys8-substituted peptides. Denaturation was recorded with CD spectroscopy following the change of minimum at 222 nm with steadily increasing temperature. Original peptide (filled hexagons); othe peptides with the following substitutions: Ala (●), EGly (○), DfeGly (△), TfeGly (□), DfpGly (◇).

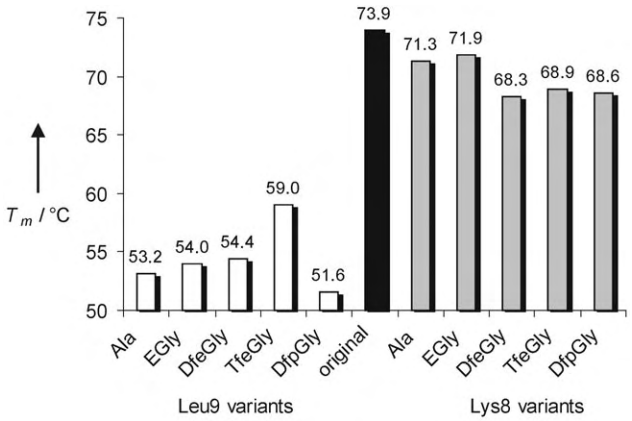


Figure 4. Melting temperatures of the original peptide and its variants. T_m is defined as the temperature at which 50% of the peptide is unfolded.

Interestingly, this effect is marginal for the difluoro analogue ($\Delta T_m = 0.4$ K), while the peptide possessing just one more fluorine atom (Leu9TfeGly) shows an increase in thermal stability by 5 K. An additional enlargement of the side chain by replacement of one of the fluorine atoms of TfeGly by methyl (Leu9DfpGly) leads to a dramatic loss of structural stability compared to that of the Leu9TfeGly variant. Apparently the strong electronegativity of the fluorine substituents causes a polarization of hydrogen atoms in all the adjacent alkyl groups that dramatically disturbs hydrophobic-core packing in the case of DfpGly. Importantly, the extent of destabilization increases along with the number of alkyl hydrogen atoms polarized by fluorine. Although DfpGly carries the most space-filling side chain of the investigated amino acids, the thermal stability of the Leu9DfpGly variant falls behind even that of the alanine variant. It has been reported recently that polar interactions of a CF_3 group can stabilize peptide secondary structure and, thereby, even overcompensate the destabilizing impact of enhanced steric demand.[22] Our results demonstrate that the electrostatic consequences of alkyl fluorination can have a much stronger influence on hydrophobic interactions in a protein than the increase in molecular volume upon stepwise fluorination does (Figure 5).

All substitutions of lysine at position 8 of the charged interaction domain have a much lower impact on the stability of the α-helical coiled-coil motif than the Leu9 variants do (Figure 3b). The decrease in melting temperatures of 2.0–5.6 K is caused by the loss of the stabilizing salt bridge Lys8–Glu29 upon Lys8 substitution. The two nonfluorinated analogues (Lys8Ala and Lys8EGly) and all of the fluorinated variants (Lys8DfeGly, Lys8TfeGly, and Lys8DfpGly) show similar stability (Figure 4). Remarkably, fluorination of the solvent-exposed alkyl side chains in this position (Lys8-DfeGly, Lys8TfeGly, and Lys8DfpGly) causes an additional loss of structural stability. We conclude that fluorine–fluorine interactions in the unfolded state of the peptide have an impact on the monomer–dimer equilibrium. Encouraged by this finding, we focused on the issue of the "fluorous effect" in further experiments. Therefore, we investigated the self-

 © 2006 Wiley-VCH Verlag GmbH & Co. KGaA, Weinheim

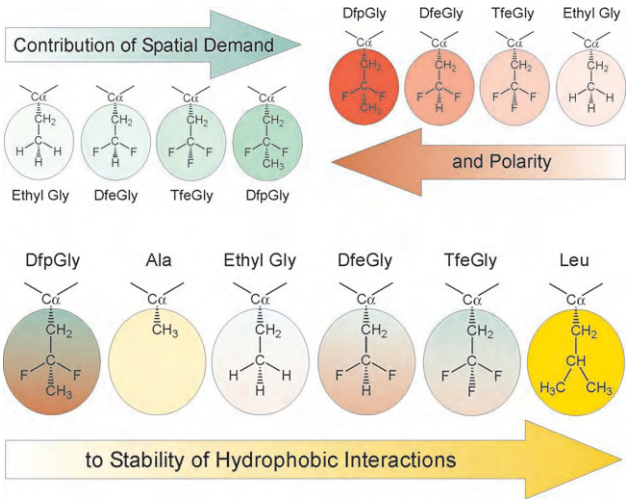


Figure 5. Influence of polarity and spatial demand of fluoroalkyl groups on stability of hydrophobic protein domains.

replication properties of the fluorine-modified α-helical coiled-coil peptides.

Screen II for self-replication: The native chemical ligation of electrophilic and nucleophilic peptides in the replicase reaction was catalyzed by the annealing of both fragments with a complementary full-length monomer that serves as a template for coiled-coil formation (Figure 6).[23] The reaction of the C-terminal benzylthiolester of the electrophilic peptides with the N-terminal cysteine of the nucleophilic peptide resulted in the formation of a peptide bond.[20] Control experiments under conditions that disturb or completely prevent the formation of the coiled-coil structure without affecting ligation chemistry proved the rate of noncatalyzed background ligation reactions to be negligible (Figures S2–S4 in the Supporting Information). Each ligation product acts as a new catalyst for peptide-bond formation in the next cycle.

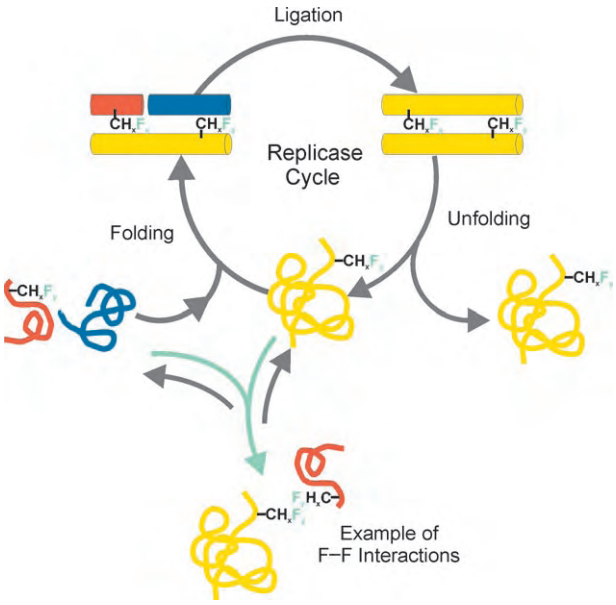


Figure 6. Template-assisted autocatalyzed peptide ligation (replicase) and the influence of fluorine–fluorine interactions on the reaction cycle. The amide-bond-forming process is based on the Kent strategy (see the Supporting Information).[20] Yellow: ligation product, red: electrophilic peptide thioester, blue: nucleophilic peptide.

The effect that an amino acid substitution in both of the recognition domains has on the stability of the protein folding motif will influence the peptide self-replication. This effect can be detected by means of the product formation rate. Fluorine–fluorine interactions between amino acids in the electrophilic peptide fragments and the monomeric catalysts might impede the α-helical coiled-coil folding and, therefore, would inhibit the reaction cycle. Consequently, the "fluorous effect" would cause slower product formation. With this screen we studied amino acids with alkyl side chains of the same length but with different fluorine content (EGly, DfeGly, and TfeGly).

The ligation reactions of electrophilic peptides with the original sequence and EGly in position Leu9 (Figure 7a) show that a decrease in the spatial demand in the hydrophobic core of the α-helical coiled coil remarkably reduces the rate of product formation. In contrast, a stepwise increase in volume by subsequent fluorination of the EGly side chain (Leu9-DfeGly and Leu9TfeGly) does not accelerate but further decelerates the reaction. As this effect correlates with the number of fluorine atoms in the amino acid side chain, it can be contributed to an inhibition of the reaction cycle by F–F interactions.

Comparison of the replicase experiments of the unsubstituted electrophilic peptide and the variant carrying EGly in position 8 (Lys8EGly) shows that a destabilization of the α-helical coiled-coil folding motif by alterations within the

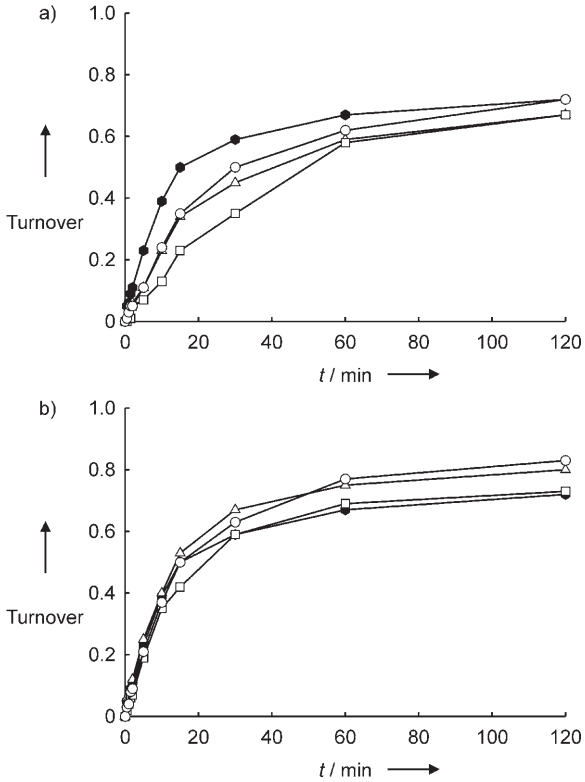


Figure 7. Replicase turnover rates of a) Leu9- and b) Lys8-substituted electrophilic fragments with the nucleophilic fragment. Original peptide (filled hexagons); other peptides with the following substitutions: EGly (○), DfeGly (△), TfeGly (□).

 © 2006 Wiley-VCH Verlag GmbH & Co. KGaA, Weinheim

charged interaction domain increases the product formation rate (Figure 7b). In contrast, fluorination of the EGly side chain does not lead to an additional acceleration of the reaction cycle. Again, a stepwise deceleration is observed that correlates with the fluorine content. This effect has also been observed in the case of Leu9-modified peptides.

These findings indicate that the inhibition of the replication cycle by stepwise fluorination of the ethylglycine side chain in both recognition domains of the peptide is caused by specific fluorine–fluorine interactions between fluorinated amino acids in the unfolded peptides. This interpretation is in agreement with the preferred formation of homodimers which was observed in studies of "self-sorting" α-helical coiled-coil peptides with fluoro- and hydrocarbon cores.[24] In other words, fluorine in a native polypeptide environment prefers to interact with fluorine. This effect can be overcompensated by the strong tendency of the α-helical coiled-coil folding motif for secondary-structure formation which we use as tool for our studies. However, one has to be aware that the fluorine–fluorine interaction is strong enough to direct ligand–receptor interactions as well as peptide and protein folding.

We have described the first systematic study on how fluoro substitution of amino acid side chains influences their interaction profile in a native polypeptide environment. We demonstrate the opposing electrostatic and steric consequences that fluorination of alkyl groups has on stability of hydrophobic protein cores and prove that fluorine–fluorine interactions have a significant impact on peptide folding. More fluorinated amino acids varying in side-chain length and fluorine content will be studied using the described screening system. These studies will provide the basis for the directed application of fluorine's unique properties for the rational design of peptides and proteins.

Experimental Section

Materials: Resins for solid-phase peptide synthesis (SPPS) were obtained from Bachem. Standard Fmoc amino acids were obtained from Novabiochem, Iris Biotech, and MultiSynTech. Racemic TfeGly was prepared by malonic ester synthesis using diethyl acetamidomalonate and trifluoroethanol, which was first converted into the corresponding triflate.[25] Stereochemical resolution was carried out using hog kidney acylase. DfeGly and DfpGly were prepared stereoselectively starting from hexafluoroacetone-protected aspartic acid using diethylaminosulfur trifluoride (DAST) as a direct fluorination agent.[26]

Peptide synthesis: Peptides were synthesized on a SyroXP (MultiSynthTech GmbH, Germany) or an ACT 90 (AdvancedChemTech, USA) peptide synthesizer according to standard Fmoc/*t*Bu strategy. C-terminal activation was carried out using TCTU/HOBt/DIEA and DIC/HOAt for coupling to fluorinated amino acids. The electrophilic peptide fragments were synthesized on a sulfamyl butyryl resin. Peptide thioesters were obtained by activation of the resin with iodoacetonitrile and subsequent cleavage of the peptide with benzylmercaptan.[27] The nucleophilic peptide was synthesized on a Wang resin. Peptides were purified by preparative HPLC using CH_3CN/H_2O gradients containing 0.1% trifluoroacetic acid (TFA).

Chemical ligation: Preparative ligation of the nucleophilic and electrophilic peptides was carried out at peptide concentrations of 290 μM at pH 7 (200 mM phosphate buffer). Tris(2-carboxyethyl)-phosphine (TCEP) was added to a final concentration of 280 μM to prevent cysteine residues from forming disulfide bonds. Ligation products were purified by HPLC using a CH_3CN/H_2O gradient containing 0.1% TFA.

Replication experiments: Reactions were performed in 200 mM phosphate buffer at pH 7 and 22°C. Concentrations of both the electrophilic and nucleophilic peptides were 100 μM. TCEP was added to a final concentration of 250 μM to prevent formation of disulfide bonds. Reactions were started by addition of the electrophilic peptide, and aliquots were removed at set times. Analysis of the reaction progress was carried out by analytical HPLC; the fluorescence emission of the Tyr residues in the nucleophilic peptide and the ligation products was measured ($\lambda_{ex} = 230$ nm; $\lambda_{em} = 310$ nm).

Thermal unfolding experiments: Melting curves were recorded by observing the CD signal at 222 nm on a Jasco J715 spectropolarimeter with a heating rate of $3\,K\,min^{-1}$. Peptide concentrations were 20 μM at pH 7.4 in 5 M Gdn·HCl. Path lengths were 0.1 cm. The thermal melting profiles were fitted by using a sigmoidal five-parameter curve fit.

Received: December 9, 2005
Revised: February 28, 2006
Published online: May 11, 2006

Keywords: amino acids · fluorine · fluorous effect · peptides · protein modification

[1] A. J. Link, M. L. Mock, D. A. Tirrell, *Curr. Opin. Biotechnol.* **2003**, *14*, 603–609.
[2] N. C. Yoder, K. Kumar, *Chem. Soc. Rev.* **2002**, *31*, 335–341.
[3] J. C. Biffinger, H. W. Kim, S. G. DiMagno, *ChemBioChem* **2004**, *5*, 622–627.
[4] G. Gerebtzoff, X. Li-Blatter, H. Fischer, A. Frentzel, A. Seelig, *ChemBioChem* **2004**, *5*, 676–684.
[5] J. A. Olsen, D. W. Banner, P. Seiler, B. Wagner, T. Tschopp, U. Obst-Sander, M. Kansy, K. Müller, F. Diederich, *ChemBioChem* **2004**, *5*, 666–675.
[6] B. E. Smart, *J. Fluorine Chem.* **2001**, *109*, 3–11.
[7] a) J. D. Dunitz, *ChemBioChem* **2004**, *5*, 614–621; b) E. Carosati, S. Sciabola, G. Cruciani, *J. Med. Chem.* **2004**, *47*, 5114–5125.
[8] C. Jaeckel, B. Koksch, *Eur. J. Org. Chem.* **2005**, 4483–4503.
[9] F. Leroux, *ChemBioChem* **2004**, *5*, 644–649.
[10] K. Mikami, Y. Itoh, M. Yamanaka, *Chem. Rev.* **2004**, *104*, 1–16.
[11] C. Wolf, W. A. Koenig, C. Roussel, *Liebigs Ann.* **1995**, 781–786.
[12] M. Zanda, *New J. Chem.* **2004**, *28*, 1401–1411.
[13] a) K.-H. Lee, H.-Y. Lee, M. M. Slutsky, J. T. Anderson, E. N. G. Marsh, *Biochemistry* **2004**, *43*, 16277–16284; b) J.-C. Horng, D. P. Raleigh, *J. Am. Chem. Soc.* **2003**, *125*, 9286–9287.
[14] a) A. Niemz, D. A. Tirrell, *J. Am. Chem. Soc.* **2001**, *123*, 7407–7413; b) B. Bilgicer, K. Kumar, *Proc. Natl. Acad. Sci. USA* **2004**, *101*, 15324–15329; c) B. Bilgicer, A. Fichera, K. Kumar, *J. Am. Chem. Soc.* **2001**, *123*, 4393–4399; d) Y. Tang, G. Ghirlanda, N. Vaidehi, J. Kua, D. T. Mainz, W. A. Goddard III, W. F. DeGrado, D. A. Tirrell, *Biochemistry* **2001**, *40*, 2790–2796; e) Y. Tang, D. A. Tirrell, *J. Am. Chem. Soc.* **2001**, *123*, 11089–11090; f) Y. Tang, G. Ghirlanda, W. A. Petka, T. Nakajima, W. F. DeGrado, D. A. Tirrell, *Angew. Chem.* **2001**, *113*, 1545–1548; *Angew. Chem. Int. Ed.* **2001**, *40*, 1494–1496.
[15] C. Jaeckel, W. Seufert, S. Thust, B. Koksch, *ChemBioChem* **2004**, *5*, 717–720.
[16] S. K. Ritter, *Chem. Eng. News* **2005**, *83*, 35–40.
[17] K. Pagel, B. Seiwert, K. Seeger, S. Berger, A. Mark, B. Koksch, *Org. Biomol. Chem.* **2005**, *3*, 1189–1194.
[18] J. Mason, K. M. Arndt, *ChemBioChem* **2004**, *5*, 170–176.
[19] a) K. Severin, D. H. Lee, J. A. Martinez, M. R. Ghadiri, *Chem. Eur. J.* **1997**, *3*, 1017–1024; b) A. Saghatelian, Y. Yokobayashi, K. Soltani, M. K. Ghadiri, *Nature* **2001**, *409*, 797–801.
[20] P. E. Dawson, T. W. Muir, I. Clark-Lewis, S. B. H. Kent, *Science* **1994**, *266*, 776–779.

 © 2006 Wiley-VCH Verlag GmbH & Co. KGaA, Weinheim

[21] D. O'Hagan, H. S. Rzepa, *Chem. Commun.* **1997**, *7*, 645 – 652.
[22] J. Xiao, B. Weisblum, P. Wipf, *J. Am. Chem. Soc.* **2005**, *127*, 5742 – 5743.
[23] K. Severin, D. H. Lee, A. J. Kennan, M. R. Ghadiri, *Nature* **1997**, *389*, 706 – 709.
[24] B. Bilgicer, X. Xing, K. Kumar, *J. Am. Chem. Soc.* **2001**, *123*, 11815 – 11816.
[25] T. Tsushima, K. Kawada, S. Ishihara, N. Uchida, O. Shiratori, J. Higaki, M. Hirata, *Tetrahedron* **1988**, *44*, 5375 – 5387.
[26] a) D. Winkler, K. Burger, *Synthesis* **1996**, 1419 – 1421; b) S. N. Osipov, T. Lange, P. Tsouker, J. Spengler, L. Hennig, B. Koksch, S. Berger, S. M. El-Kousy, K. Burger, *Synthesis* **2004**, 1821 – 1829.
[27] a) G. W. Kenner, J. R. McDermott, R. C. Sheppard, *Chem. Commun.* **1971**, 636 – 637; b) R. Ingenito, E. Bianchi, D. Fattori, A. Pessi, *J. Am. Chem. Soc.* **1999**, *121*, 11369 – 11374.

 © 2006 Wiley-VCH Verlag GmbH & Co. KGaA, Weinheim

Functional Materials

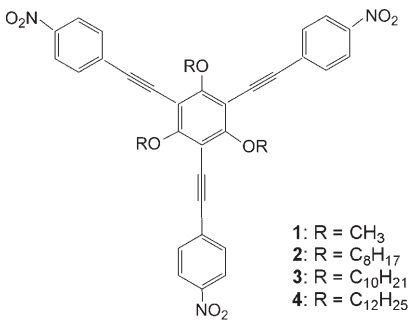
DOI: 10.1002/anie.200600019

Liquid Crystals from C_3-Symmetric Mesogens for Second-Order Nonlinear Optics**

Gunther Hennrich, Ana Omenat, Inge Asselberghs, Stijn Foerier, Koen Clays, Thierry Verbiest,* and José Luis Serrano**

The construction of nanoscale photonic devices from functional molecular building blocks in a bottom-up approach is a promising strategy to meet the growing demand for miniaturization in electronics and photonics.[1] The controlled supramolecular arrangement of single molecules through noncovalent interactions can be the key to bridging the gap between chemistry (molecule design) and physics (bulk application).[2] In the field of nonlinear optics (NLO) organic molecules have been promising candidates for more than two decades. Tailormade molecular materials can be obtained in a nearly infinite variety by organic synthesis.[3] However, the predominant tendency toward centrosymmetric ordering of the single molecules in the bulk phase often impedes the preparation of self-assembled NLO-active material from molecular building units.[4] Therefore, the number of applications of organic-molecule-based NLO devices is still limited.[5] The synthesis of octopolar NLO chromophores, non-centrosymmetric molecules with no dipole moment, is a promising strategy to overcome this problem on the molecular level.[6] Amongst the plethora of organic structures, octopolar trisalkynylbenzenes have been shown recently to display extremely high second-order NLO activity.[7] The abundance of this structural motif in liquid crystals is also striking. Star-shaped alkynylbenzenes are flat, rigid, extended aromatic systems that are ideally suited to forming noncovalent interactions such as π–π stacking and van der Waals interactions.[8] Typically, this leads to the formation of different types of liquid-crystalline mesophases.[9]

We describe here the first members of a new family of discotic 1,3,5-trisalkynylbenzenes (**1**–**4**) with octopolar symmetry. The donor–acceptor substitution of the arylethynylbenzene scaffold results in degenerate charge transfer within the octopolar structure, and as a consequence, in an efficient second-order NLO response. Long alkoxy chains are incorporated into the central benzene core to favor the formation of different mesophases, depending on the chain lengths. The synthesis of compounds **1**–**4** is based on the threefold Sonogashira coupling of (*p*-nitrophenyl)acetylene with prefunctionalized 1,3,5-trialkoxy-2,4,6-triiodobenzenes in the same manner as described recently.[10]



In solution, all octopolar compounds display a broad, unstructured absorption band above 350 nm, indicative of efficient charge transfer from the electron-rich benzene core to the electron-deficient periphery. Owing to the presence of the nitro substituents, the molecules are virtually nonfluorescent. This facilitates the accurate determination of the quadratic hyperpolarizabilities β by means of hyper-Rayleigh scattering.[11] A high second-order nonlinear optical response

[*] Dr. G. Hennrich
Departamento de Química Orgánica
Universidad Autónoma de Madrid
Cantoblanco, 28049 Madrid (Spain)
Fax: (+34) 91-497-3966
E-mail: gunther.hennrich@uam.es
Dr. I. Asselberghs, S. Foerier, Prof. K. Clays, Prof. T. Verbiest
Department of Chemistry
University of Leuven
Celestijnenlaan 200D, 3001 Leuven (Belgium)
Fax: (+32) 16-327-982
E-mail: thierry.verbiest@fys.kuleuven.be
Dr. A. Omenat, Prof. J. L. Serrano
Departamento de Química Orgánica
Facultad de Ciencias-ICMA
Universidad de Zaragoza-CSIC
50009 Zaragoza (Spain)
Fax: (+34) 976-761-209
E-mail: joseluis@unizar.es

[**] This work was supported by the MEC, Spain (BQU2000–0226 and Ramón y Cajal contract for G.H.), the CICYT of Spain, the FEDER funds (EU, project MAT2003-07806-C01), and by the Diputación General de Aragón, as well as by the University of Leuven (GOA/2006/03), the Institute for the Promotion of Innovation through Science and Technology in Flanders (IWT-Vlaanderen), the FWO-V (G.0297.04), and the Belgian government (IUAP/5). I.A. acknowledges a fellowship from the Flemish Fund for Scientific Research. (FWO-V).

Supporting information for this article is available on the WWW under http://www.angewandte.org or from the author.

 © 2006 Wiley-VCH Verlag GmbH & Co. KGaA, Weinheim

is observed in accordance with the activities reported for similar octopolar systems (Table 1).[7,12] Generally, increasing chain lengths lead to bathochromically shifted absorption maxima, enhanced absorptivities, and enhanced β values.

Table 1: Spectroscopic data for **1**–**4** measured in CH_2Cl_2.

Cmpd.	λ_{max}(abs) [nm]	ε_{max} [$cm^2\,mol^{-1}$]	$\beta_{xxx,800}$ [10^{-30} esu]	$\beta_{xxx,0}$ [10^{-30} esu]
1	351	20070	145 ± 2	30 ± 1
2	358	47916	273 ± 4	52 ± 1
3	359	52092	320 ± 20	48 ± 3
4	359	51612	340 ± 20	52 ± 3

Since the donor capacity of the alkoxy substituents is practically independent of the length of the alkyl chain,[13] we attribute intramolecular effects, for example, folding of the alkoxy chains, to be responsible for these tendencies.[14] A similar phenomenon has been reported for related cyclic acetylene systems.[15]

Recently, it has been reported that compounds consisting of a rigid aromatic core substituted with polar or polarizable groups and without flexible side chains in their structure exhibit discotic mesophases.[16] Therefore, it is not surprising that compounds **2**–**4**, which incorporate a rigid aromatic core, terminal nitro groups, and three alkyloxy side chains, show some type of discotic mesomorphism as well. Indeed, **2**–**4** show liquid-crystal properties, which we studied by polarized light optical microscopy, differential scanning calorimetry, and X-ray diffraction. The optical properties, transition temperatures, and enthalpies are summarized in Table 2.

Table 2: Optical and thermal properties of compounds **2**–**4**: Phase transition temperatures T and enthalpies ΔH.

Cmpd.	Phase T [°C] (ΔH [kJ mol^{-1}])[a]
2	C 120.3 (20.8) N_D 143.7 (0.3) I
3	C 40.0 (4.0) C′ 59.9 Col_h 68.5 (12.0)[b] N_D 111.9 (0.7) I
4	C 65–78 (9.7) Col_h–N_D–I[c]

[a] Second heating scan; C, C′: crystalline, Col_h: hexagonal columnar mesophase, N_D: discotic nematic mesophase, I: isotropic liquid. [b] Enthalpy for both transitions C–Col_h -N_D [c] Broad peak including the transitions C–Col_h–N_D–I.

Compound **2** exhibits a discotic nematic mesophase which is identified by its typical droplet texture under the microscope (Figure 1). This assignment was confirmed by X-ray diffraction studies in the mesophase. The driving force to this nematic order must be the interactions between polar groups along with the stacking of the planar core of the molecules. Compounds **3** and **4**, which have decyloxy and dodecyloxy chains, respectively, exhibit both a hexagonal columnar mesophase and a discotic nematic mesophase. The characteristic mosaic textures of the columnar mesophases are shown in Figure 2. The increase of the chain length favors a columnar stacking of the molecules with a C_3 symmetry since the intercolumnar space is filled in an efficient manner with the alkyl chains, which act as a lubricant between the rigid discotic columns.

However, in both cases the X-ray diffraction data indicates large lattice distances too great for discrete intermolecular π stacking. With a value of 30.7 Å obtained for **4**, we propose a unit cell that is composed of a linear dimeric assembly, subsequently forming columnar stacks. A possible interaction between NO_2 groups of two adjacent molecules, the supposed driving force for a supramolecular dimerization, is expected to be weak and cannot be detected by UV/Vis spectroscopy in either the columnar mesophase or in the isotropic liquid.[14] The hexagonal columnar and the discotic nematic mesophases are centrosymmetric, but compound **3** presents a positive NLO response as seen in the SHG measurements. Therefore, molecules of **3** must arrange in a non-centrosymmetric superstucture. This fact can be explained by an orientation effect induced by the cell walls leading to a non-centrosymmetric arrangement of the mesomorphic material.

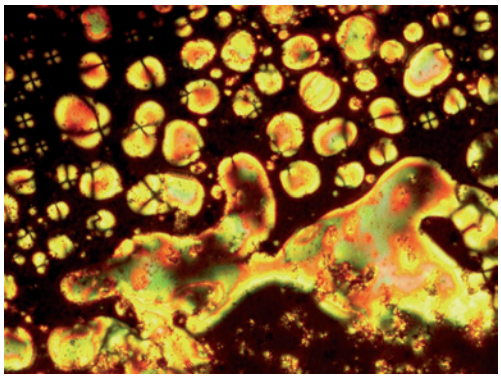


Figure 1. Nematic droplets of **2** at 143 °C upon cooling from the isotropic liquid.

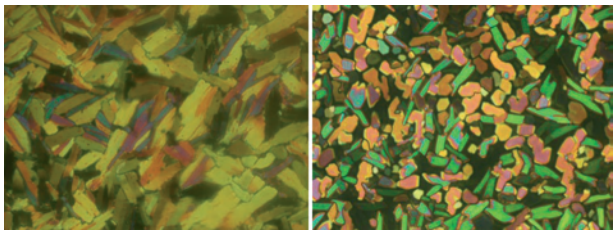


Figure 2. Hexagonal columnar mesophases. Left: In the second heating process of **3** at 62 °C; right: in the second cooling process of **4** at 69 °C.

For the preparation of an NLO device based on the LC material, films of **3** 100 microns thick were prepared by heating a small amount of solid **3** between two glass slides above the melting point, followed by rapid cooling to room temperature. The glass surface was not subjected to any previous treatment. The thickness of the sample was controlled by using 100-micron spacers. The sample was placed on a heating stage for measurements of second-harmonic intensity versus temperature. The second-harmonic generation (SHG) experiments were conducted by irradiating the sample at a 45° angle of incidence with the fundamental beam from a Nd:YAG laser (1064 nm, 10 Hz, 5-ns pulses) and detecting the second-harmonic light in reflection. SHG measurements at room temperature on a solid sample of **3** show a fairly low second-harmonic response, as would be expected for a disoriented sample. Presumably, the small

 © 2006 Wiley-VCH Verlag GmbH & Co. KGaA, Weinheim

amount of SHG observed is due to a surface contribution. Upon heating, the second-harmonic response suddenly increased when the temperature of the sample surpassed 40 °C, which corresponds to the LC phase transition (Figure 3). This sudden increase in SHG can only be

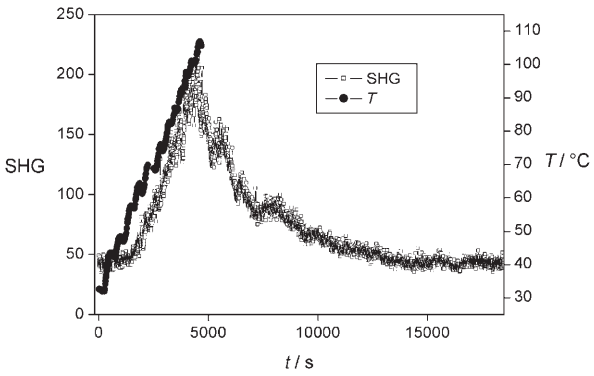


Figure 3. Plots of the temperature of **3** (●) and the second-harmonic signal intensity (□, in arbitrary units) versus time *t*.

explained by a change in the sample symmetry. Since SHG is only allowed in non-centrosymmetric media, breaking of inversion symmetry must occur. In fact, the octopolar symmetry of the molecule combined with the discotic liquid-crystalline character of the sample at this temperature confirms this assumption. Upon further heating until the clearing point, the second harmonic intensity suddenly started to decrease since the sample becomes a centrosymmetric isotropic liquid. While these preliminary measurements results on solid samples, which were repeated reproducibly several times on the same sample, are only qualitative, the important point to make here is that the sample spontaneously assembles into a non-centrosymmetric structure. In any case, the second-order NLO activity detected is comparable to that of conventional poled-polymer systems.[17] This provides us with a very simple sample preparation method, eliminating the need for tedious orientation methods such as electric-field poling or the Langmuir–Blodgett technique. Hence, these materials could be very useful for nonlinear-optical applications.

In summary, the properties of the different liquid-crystalline mesophases formed by the highly NLO-active octopoles **2**–**4** can be adjusted easily by changing the length of the alkoxy chains in the molecules. Molecules of **3** self-organize in a non-centrosymmetric fashion in the bulk phase which allows for the construction of a first example of a simple, efficient NLO device. Ongoing research is directed towards the optimization of both the LC properties and the device fabrication and performance (different supports, surface treatment etc.).

Experimental Section

2–**4**: 1,3,5-Triiodo-2,4,6-trialkoxybenzene (0.5 mmol) was stirred together with $[PdCl_2(PPh_3)_2]$ (0.075 mmol, 53 mg) and CuI (0.075 mmol, 14 mg) in Ar-degassed diisopropylamine (5 mL) for 30 min at room temperature before (*p*-nitrophenyl)acetylene (2.5 mmol, 354 mg) was added. The mixture was heated at 80 °C for 48 h. The solvent was removed; the remaining solid was suspended in water (50 mL) and extracted with ethyl acetate (3 × 25 mL). The combined organic layers were dried ($MgSO_4$) and concentrated in vacuo to give the crude solid product which was purified by column chromatography on silica gel (hexane/EtOAc 20:1) and final recrystallization.

1,3,5-Tris[(4-nitrophenyl)ethynyl]-2,4,6-tris(octyloxy)benzene (**2**): Recrystallized from EtOH; Yield: 148 mg, 33 %. ^{1}H NMR (300 MHz, $CDCl_3$): $\delta = 8.25$ (d_{AB}, $J = 8.8$ Hz; 6H), 7.65 (d_{AB}, $J = 8.8$ Hz; 6H), 4.38 (t, $J = 6.5$ Hz, 6H), 1.89 (q, $J = 6.5$ Hz, 6H), 1.56 (q, $J = 7.0$ Hz, 6H), 1.51–1.29 (m, 24H), 0.84 ppm (t, $J = 7.0$ Hz, 9H); ^{13}C NMR (125 MHz, $CDCl_3$): $\delta = 164.4$, 147.1, 131.9, 130.1, 123.8, 107.2, 95.5, 86.6, 75.3, 31.7, 30.6, 29.5, 29.3, 26.3, 22.6, 14.0 ppm. MALDI-MS: *m*/*z*: 898 [M^+]. C,H,N analysis (%) calcd for $C_{54}H_{63}N_3O_9$: C 72.16, H 7.02, N 4.68; found: C 71.80, H 6.96, N 4.74.

1,3,5-Tris[(4-nitrophenyl)ethynyl]-2,4,6-tris(decyloxy)benzene (**3**): Recrystallized from *i*PrOH; Yield: 137 mg, 28 %. ^{1}H NMR (300 MHz, $CDCl_3$): $\delta = 8.25$ (d_{AB}, $J = 8.6$ Hz; 6H), 7.65 (d_{AB}, $J = 8.6$ Hz; 6H), 4.38 (t, $J = 6.5$ Hz, 6H), 1.89 (q, $J = 7.0$ Hz, 6H), 1.56 (q, $J = 6.5$, 6H), 1.20 (brs, 36H), 0.86 ppm (t, $J = 7.0$ Hz, 9H); ^{13}C NMR (125 Hz, $CDCl_3$): $\delta = 164.4$, 147.1, 131.9, 130.1, 123.8, 107.2, 95.6, 86.7, 75.3, 31.9, 30.6, 29.7, 29.6, 29.4, 26.3, 26.1, 22.7, 14.1 ppm; MALDI-MS: *m*/*z*: 982 [M^+]. C,H,N analysis (%) calcd for $C_{60}H_{75}N_3O_9$: C 73.32, H 7.64, N, 4.28; found: C 73.08, H 7.68, N 4.32.

1,3,5-Tris[(4-nitrophenyl)ethynyl]-2,4,6-tris(dodecyloxy)benzene (**4**): Precipitated from CH_2Cl_2/MeOH; Yield: 106 mg, 20 %. ^{1}H NMR (300 MHz, $CDCl_3$): $\delta = 8.25$ (d_{AB}, $J = 8.6$ Hz; 6H), 7.65 (d_{AB}, $J = 8.6$ Hz; 6H), 4.38 (t, $J = 6.5$ Hz, 6H), 1.89 (q, $J = 7.0$ Hz, 6H), 1.57 (q, $J = 6.5$ Hz, 6H), 1.21 (brs, 48H), 0.87 ppm (t, $J = 7.0$ Hz, 9H); ^{13}C NMR (125 MHz, $CDCl_3$): $\delta = 164.4$, 147.4, 132.0, 130.4, 124.6, 107.2, 95.6, 86.8, 75.5, 32.3, 31.0, 30.8, 30.3, 30.0, 29.8, 29.6, 29.4, 26.6, 22.9, 14.1 ppm. MALDI-MS: *m*/*z*: 1066 [M^+]. C,H,N analysis (%) calcd for $C_{66}H_{87}N_3O_9$: C 74.30, H 8.16, N 3.94; found: C 73.85, H 8.42, N 3.83.

Received: January 3, 2006
Revised: March 13, 2006
Published online: May 24, 2006

Keywords: benzene derivatives · liquid crystals · materials science · nonlinear optics · self-assembly

[1] a) *Electronic Materials: The Oligomer Approach*, (Eds.: K. Müllen, G. Wegner), Wiley-VCH, Weinheim, **1998**; b) R. A. Wassel, C. B. Gorman, *Angew. Chem.* **2004**, *116*, 5230–5233; *Angew. Chem. Int. Ed.* **2004**, *43*, 5120–5123.

[2] J.-M. Lehn, *Supramolecular Chemistry: Concepts and Perspectives*, VCH, Weinheim, **1995**.

[3] F. Meyers, S. R. Marder, J. W. Perry in *Chemistry of Advanced Materials: An Overview* (Eds.: L. V. Interrante, M. J. Hampden-Smith), Wiley-VCH, Weinheim, **1998**, pp. 207–269.

[4] C. Bosshard, K. Sutter, P. Prêtre, J. Hulliger, M. Flörsheimer, P. Kaatz, P. Günther, *Organic Nonlinear Optical Materials*, *Vol. 1*, Gordon & Breach, Amsterdam, **1995**.

[5] a) O. R. Evans, W. Lin, *Acc. Chem. Res.* **2002**, *35*, 511–522; b) M. Muthuraman, R. Masse, J.-F. Nicoud, G. R. Desiraju, *Chem. Mater.* **2001**, *13*, 1473–1479; c) K. E. Van Cott, M. Guzy, P. Neyman, C. Brands, J. R. Heflin, J. R. Gibson, R. W. Davis, *Angew. Chem.* **2002**, *114*, 3370–3372; *Angew. Chem. Int. Ed.* **2002**, *41*, 3236–3238; .

[6] J. Zyss, I. Ledoux, *Chem. Rev.* **1994**, *94*, 77–105.

[7] a) J. J. Wolff, F. Siegler, R. Matschiner, R. Wortmann, *Angew. Chem.* **2000**, *112*, 1494–1498; *Angew. Chem. Int. Ed.* **2000**, *39*, 1436–1439; b) B. Traber, J. J. Wolff, F. Rominger, T. Oeser, R.

 © 2006 Wiley-VCH Verlag GmbH & Co. KGaA, Weinheim

Gleiter, M. Goebel, R. Wortmann, *Chem. Eur. J.* **2004**, *10*, 1227 – 1238.
[8] a) L. Brunsveld, B. J. B. Folmer, E. W. Meijer, R. P. Sijbesma, *Chem. Rev.* **2001**, *101*, 4701 – 4097; b) S. Kumar, S. K. Varshney, *Angew. Chem.* **2000**, *112*, 3270 – 3272; *Angew. Chem. Int. Ed.* **2000**, *39*, 3140 – 3142; c) H.-F. Hsu, M.-C. Lin, W.-C. Lin, Y.-H. Lai, S.-Y. Lin, *Chem. Mater.* **2003**, *15*, 2115 – 2118; d) M. L. Bushey, T.-Q. Nguyen, W. Zhang, D. Horoszewski, C. Nuckolls, *Angew. Chem.* **2004**, *116*, 5562 – 5570; *Angew. Chem. Int. Ed.* **2004**, *43*, 5446 – 5433; e) A. Grafe, D. Janietz, T. Frese, J. H. Wendorff, *Chem. Mater.* **2005**, *17*, 4979 – 4984.
[9] a) P. H. J. Kouwer, W. F. Fager, W. J. Mijs, S. J. Picken, *J. Mater. Chem.* **2003**, *13*, 458 – 469; b) K. Pieterse, A. Lauritsen, A. P. H. J. Schenning, J. A. J. M. Vekemans, E. W. Meijer, *Chem. Eur. J.* **2003**, *9*, 5597 – 5604.
[10] G. Hennrich, *Tetrahedron* **2004**, *60*, 9871 – 9876.
[11] E. Hendrickx, K. Clays, A. Persoons, *Acc. Chem. Res.* **1998**, *31*, 675 – 683.
[12] G. Hennrich, I. Asselberghs, K. Clays, A. Persoons, *J. Org. Chem.* **2004**, *69*, 5077 – 5081.
[13] C. Hansch, A. Leo, R. W. Taft, *Chem. Rev.* **1991**, *91*, 165 – 195.
[14] No concentration-dependent spectral shifts were observed in the range of 10^{-6}–2×10^{-5} mol L^{-1}. The solvatochromism observed in MeOH, CH_3CN, CH_2Cl_2, and *n*-hexane is less than 15 nm.
[15] S. Höger, V. Enkelmann, K. Bonard, C. Tschierske, *Angew. Chem.* **2000**, *112*, 2355 – 2358; *Angew. Chem. Int. Ed.* **2000**, *39*, 2267 – 2270.
[16] J. Barberá, O. A. Rakitin, M. B. Ros, T. Torroba, *Angew. Chem.* **1998**, *110*, 308 – 312; *Angew. Chem. Int. Ed.* **1998**, *37*, 296 – 299.
[17] D. M. Burland, R. D. Miller, C. A. Walsh, *Chem. Rev.* **1994**, *94*, 31 – 75.

 © 2006 Wiley-VCH Verlag GmbH & Co. KGaA, Weinheim

DNA-Templated Synthesis

DOI: 10.1002/anie.200600524

DNA-Templated Synthesis in Three Dimensions: Introducing a Micellar Scaffold for Organic Reactions**

*Fikri E. Alemdaroglu, Ke Ding, Rüdiger Berger, and Andreas Herrmann**

Nowadays, a large variety of organic reactions and conversions can be carried out in a DNA-templated format.[1–9] Based on these developments, applications employing the concept of nucleic acid templated synthesis have already been realized. These include nucleic acid detection,[8,10,11] sequence-specific DNA modifications,[12–15] screening libraries of synthetic molecules,[4,5,16] and the discovery of new reactions.[17] These successful examples are based on three different nucleic acid template architectures, the A + B + A′B′-, A + BB′A′- and A + A′-templates. A/B and A′/B′ denote complementary oligonucleotides (ODNs) and + symbols indicate separate molecules. This basic set of templates was complemented by the so called Ω and T architectures, which allow distance dependent reactions and transformations involving three functional groups to proceed efficiently in a DNA-templated fashion.[18] Beside these single-stranded (ss) templates, the DNA double helix itself was exploited as a reaction scaffold by using major- or minor-grove-binding motifs for the prearrangement of the reactants.[19,20] Both ss and double-stranded (ds) templates represent one dimensional objects, whereas the so called Y-shaped template, which catalyzes the coupling of three different ODNs to a tris-linker molecule, can be regarded as a two dimensional scaffold.[21]

In this contribution, a novel template architecture is introduced which allows DNA-templated organic reactions to proceed in three-dimensional space. The template consists of amphiphilic DNA-block copolymer micelles with a hydrophobic core and a ss-DNA shell. Instead of Watson-Crick base pairing, aggregation of hydrophobic polymer blocks aligns the DNA of the corona so that it acts as a template in DNA-templated organic synthesis. The ss-DNA of the corona is hybridized with ODNs which are equipped with different reactants. Depending on the functionalization of either the 5′ or 3′ ends, various organic reactions are performed sequence specifically on the surface of the micelles (5′ end) or at the hydrophobic/hydrophilic interface (3′ end). The three-dimensional template architecture is of great importance for the advancement of nucleic acid templated synthesis because it might allow DNA-templated reactions to occur while they are being shielded from the aqueous environment.

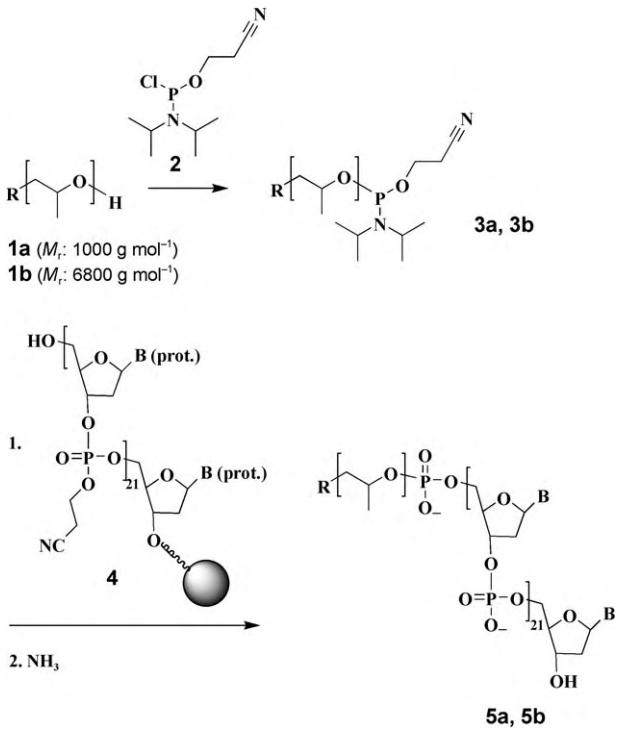
In dilute aqueous solutions, polyelectrolyte-block copolymers self-assemble into three-dimensional spherical micelles with a charged corona and a hydrophobic core.[22] Such nanocontainers, which are composed of amphiphilic-block copolymers, are important as drug delivery vehicles in which lipophilic drugs are incorporated into the hydrophobic interior and then later released.[23] Recently, new types of micellar aggregates were introduced that consist of a ss-DNA corona and a poly(D,L-lactic-*co*-glycolic acid) (PLGA) or a polystyrene (PS) hydrophobic core.[24,25] These micelles were applied for the delivery of antisense ODNs[24] and for selective hybridization with DNA-coated gold nanoparticles.[25] Both organic polymer blocks, PLGA and PS, exhibit relative high glass transition temperatures (T_G; T_G (PS) = 90 °C, T_G (PLGA) = 30 °C), which are known to prevent direct dissolving in aqueous solution[26] and hinder investigation of the micellar properties because the "frozen" micelles do not reach the state of thermodynamic equilibrium.[22] Herein, DNA-*b*-polypropyleneoxide (PPO) polymers (T_G (PPO) = −70 °C) were prepared (Scheme 1) to overcome these shortcomings as well as to provide a polymer with

[*] F. E. Alemdaroglu, K. Ding, Dr. R. Berger, Dr. A. Herrmann
Max Planck Institute for Polymer Research
Ackermannweg 10, 55128 Mainz (Germany)
Fax: (+49) 6131-379-100
E-mail: andherrm@mpip-mainz.mpg.de

[**] This work, as part of the European Science Foundation EUROCORES Programme BIONICS, was supported by funds from the DFG and the EC Sixth Framework Programme. Additional funding was provided through the ERA-CHEMISRY Programme. The help of Dr. Roland Bauer for creating graphical representations is gratefully acknowledged. We also thank Prof. Hans-Jürgen Butt for his support.

Supporting information for this article is available on the WWW under http://www.angewandte.org or from the author.

 InterScience © 2006 Wiley-VCH Verlag GmbH & Co. KGaA, Weinheim

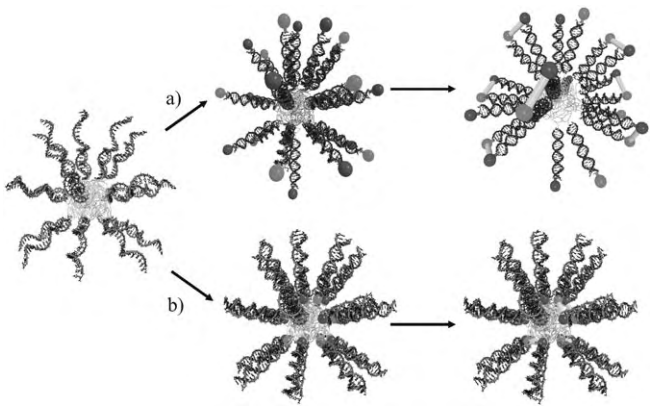


Scheme 1. Synthesis of DNA-*b*-PPO **5a** and **5b**. B(prot.) = protected nucleobase, R = $CH_3(CH_2)_3$.

proven biocompatibility toward different cell types when administered as a constituent component of amphiphilic-block-copolymer micelles.[27]

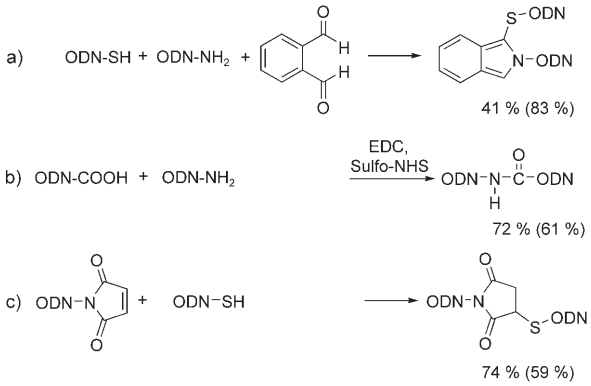
Inspired by the synthetic strategy of Mirkin and co-workers,[25] hydroxy-group-terminated PPOs **1** were reacted with phosphoramidite chloride **2** to yield the corresponding phosphoramidite-PPO derivatives **3**. The activated PPOs **3** were then coupled to the 5′ end of the ODN **4** (22 mer, sequence: 5′-CCTCGCTCTGCTAATCCTGTTA-3′) on the solid support by using a DNA-synthesizer. After separation from the substrate, deprotection of the protecting groups, and purification by polyacrylamide gel electrophoresis (PAGE), the DNA-*b*-PPOs **5** were obtained (Scheme 1). Coupling efficiencies of the large polymer moieties were remarkably high with yields reaching 41 and 32 % for PPO polymers with molecular weights of 1000 and 6800 g mol^{-1}, respectively. The experimental outcome of the coupling reaction suggests that the use of a DNA-synthesizer is superior to a grafting approach in solution[24] or a manual attachment procedure.[25] This is because automation guarantees high reproducibility and efficient exposure of the phosphoramidite polymer to the solid phase.

As it is well accepted for polyelectrolyte-block copolymers that the polyelectrolyte chains within the corona of the micelle are well ordered and almost completely stretched,[28] it was hypothesized that these bioorganic nanoparticles could serve as supramolecular scaffolds for DNA-templated organic reactions. In our initial studies, we investigated reactions proceeding at the surface of the micelle (Scheme 2 a). The DNA-*b*-PPO **5b** was dissolved in buffer solution and hybridized with equimolar amounts of ODNs (22 mer,



Scheme 2. Schematic representation of DNA-templated synthesis applying DNA-block copolymers. The micelles resulting from these polymeric architectures consist of a hydrophobic core and a shell of DNA. Single stranded micelles can be either hybridized with oligonucleotides that are equipped with reactants at the 5′ or at the 3′ ends (light and dark gray balls, respectively). The subsequent chemical reaction (bar = new bond) proceeds at the surface of the micelle or at the hydrophobic/hydrophilic interface, respectively.

sequence: 5′-TAACAGGATTAGCAGAGCGAGG-3′) that were equipped with different reactants at the 5′ ends including sulfhydryl, amino, carboxylic acid, and malimide groups. With this set of reactants, three different reactions were carried out (Scheme 3).



Scheme 3. DNA-templated reactions carried out either on the surface or within the interior of the DNA-block-copolymer micelles. a) Isoindole formation, b) amide-bond formation, and c) Michael addition. The numbers in parentheses indicate the yields achieved inside the micelles. EDC = 1-ethyl-3-(3-dimethylaminopropyl)carbodiimide, sulfo-NHS = *N*-hydroxysulfosuccinimide.

First, a trimolecular coupling between a ss-thiol, a ss-amine, and a free *o*-phthalaldehyde was performed to produce a fluorescent isoindole[29,30] on the surface of the micelles. The desired product was confirmed through PAGE (Figure 1 a, lane 1) and fluorescence measurements (characteristic emission maxima at 440 and 460 nm). This novel, fluorogenic DNA-templated reaction turned out to be a highly efficient tool for optimizing reaction conditions for

 © 2006 Wiley-VCH Verlag GmbH & Co. KGaA, Weinheim

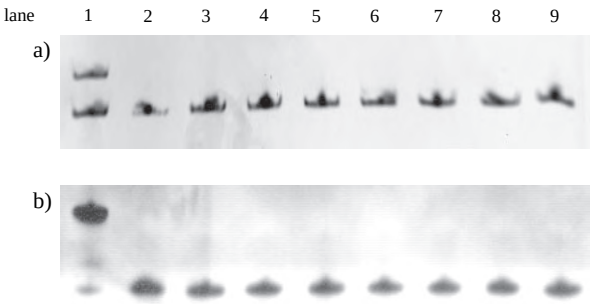


Figure 1. Analysis by denaturing PAGE of the DNA-templated isoindole formation by using the micellar scaffold a) at the surface of the micelles and b) at the interface of the biological and the organic polymer segment. Lane 1 shows the fully matching reaction conditions that resulted in product formation. The product band is represented by the band with lower electrophoretic mobility. Lane 2–9 contained the control experiments where reaction conditions were modified in contrast to lane 1 accordingly. Lanes 2 and 3: Use of complementary sequences with respect to the template but without terminal amino and sulfhydryl groups, respectively. Lanes 4 and 5: Application of mismatching ODNs with respect to the template modified with amino and sulfhydryl functionalities. Lane 6: Reaction without *o*-phthalaldehyde. Lane 7: Reaction without the micelles. Lane 8: Conversion with the template sequence but without PPO attachment. Lane 9: Applying the DNA-block copolymer **5b** as a template below the critical micelle concentration (cmc).

DNA-templated organic synthesis and to monitor the different control reactions that were necessary to prove the applicability and efficiency of the method. In the control experiments, similar reaction protocols were carried out as described above but with some alterations that are described in the legend of Figure 1. For all of these control reactions, a fluorescence signal and band corresponding to the reaction product in the gel could not be detected. These results impressively demonstrate the efficiency of the micellar template. Through the hybridization of the reaction in the DNA-block-copolymer micelle, the molarities of the reaction partners were increased, which in turn helps the chemical conversion proceed. Interestingly, the yield of fluorophore formation on the micelle scaffold was 41%, which was higher than that obtained with the A + B + A′B′-, the A + BB′A′-, and the A + A′-architectures for the same reaction (see the Supporting Information). As a second DNA-*b*-PPO scaffold supported transformation, amide-bond formation was carried out on the surface of the micelles by hybridization with carboxy- and amine-functionalized ODNs in the presence of EDC and sulfo-NHS as activation reagents. The yield of peptide bond formation was 72%, which is comparable to yields achieved by Liu et al. for the same reaction with an A + A′-template.[3]

Finally, to further prove the generality of the DNA-block-copolymer scaffold and its sequence-specific chemistry at the surface, a Michael addition between a thiol- and a malimide-modified ODN was performed. The yield was again very high (74%) and was comparable to results achieved previously with A + BB′A′- and A + A′-templates.[4] For the amide-bond formation and the Michael addition, the same controls as for the fluorogenic reaction were carried out but again did not show any product formation as confirmed by PAGE (see the Supporting Information).

To fully exploit the potential of the DNA-*b*-PPO micelles for templated transformations, reactions at the interface of the hydrophobic core and the hydrophilic corona were investigated by using the same set of reactions described above. To conduct these experiments, a simple change to 3′ modified ODNs was required (Scheme 2b). After hybridization of the micelles with the appropriately functionalized ODNs, isoindole (Figure 1b, Figure 2) and amide-bond formation as well as Michael-addition were all detected by means of fluorescence and/or PAGE. The reactions proceeded with yields of 83, 61, and 59%, respectively, in a sequence-selective manner as demonstrated by comparison with the control experiments. Notably, the isoindole formation worked much more efficiently at the hydrophilic/hydrophobic interface than at the surface of the micelle. An explanation for this is that the *o*-phthalaldehyde might accumulate within the hydrophobic core leading to significant higher reaction yields when the reactants were directed to the centre of the micelle.

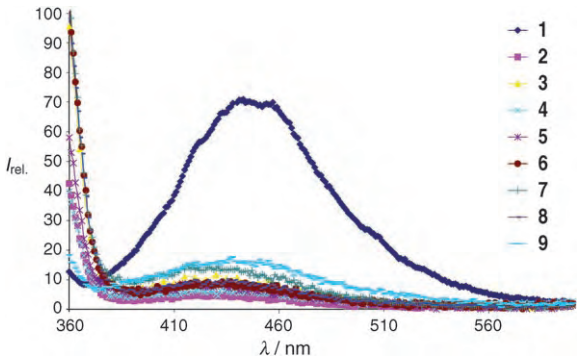


Figure 2. Fluorescence spectroscopic analysis of the isoindole formation at the hydrophilic/hydrophobic interface of the micelles. A fluorescence signal was only obtained for fully matching reaction conditions (1). The corresponding control experiments (2–9; see legend of Figure 1 for conditions) resulted in low emission intensities. Excitation wavelength was 350 nm.

As the DNA-block copolymer **5b** efficiently catalyzes DNA-templated organic reactions, the structural properties of the micelles were elucidated in more detail. Micelles of **5b** with a ss-DNA corona exhibited a diameter of 11.3 ± 2 nm as detected by dynamic light scattering (DLS). To investigate if hybridization and chemical-bond formation influenced the structural features of the micelles, they were visualized by scanning force microscopy (SFM) before and after amide-bond formation. The SFM image taken before the DNA-templated reaction showed spherical micelles, which were visualized by soft-tapping mode in the reaction buffer and on a mica surface (Figure 3a). Inspection of the micelles after addition of the bond forming reagents by SFM resulted in very similar images (data not shown). Histograms of the height distribution before and after the reaction were also evaluated (Figure 3b and c). The height of the micelles ranged from 6 to 18 nm with an average height of 10.4 ± 1.8 nm before the reaction and 11.0 ± 2.0 nm after amide-

 © 2006 Wiley-VCH Verlag GmbH & Co. KGaA, Weinheim

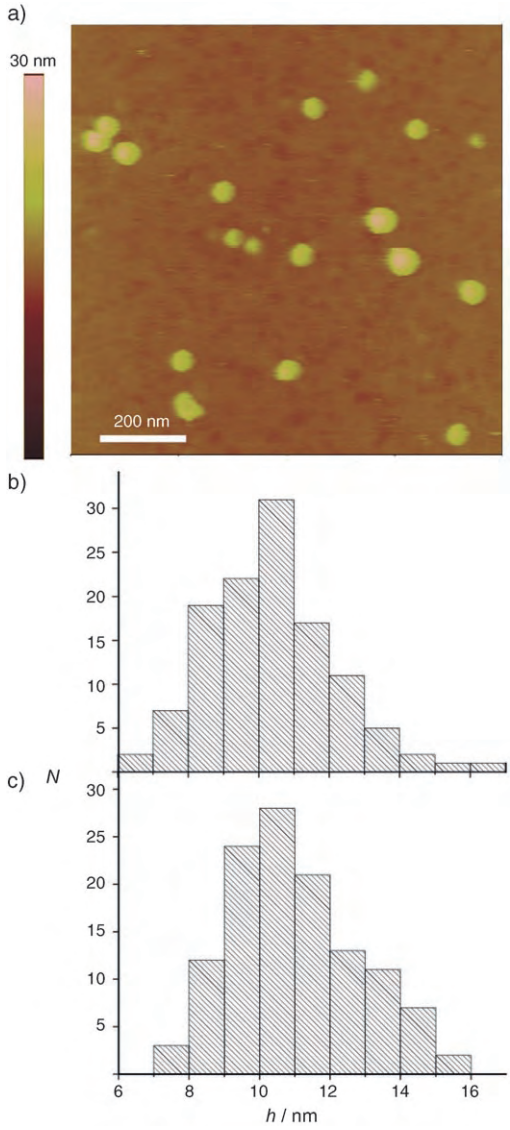


Figure 3. Structural properties of the DNA-block copolymer micelles investigated by SFM. a) SFM topographical image of double stranded micelles of **5b** hybridized with amino- and carboxyl-modified ODNs before amide bond formation. The height is indicated with a color scale bar on the left. The *z*-scale in this image is 30 nm. The height of the micelles was expressed in histograms before (b) and after (c) the chemical reaction occurred.

bond formation. Upon the chemical reaction, no significant changes in the height distributions were detected. This indicates that the bond formation has very little influence on the structural properties of the micelles. A detailed study of how the structural properties of DNA-block copolymer micelles are influenced by molecular parameters (e.g. degree of polymerization of the constituent segments, block length ratio, and hybridization with different sequences) will be the subject of future studies.

Cross-linking reactions within micelles, either in the corona[31–34] or in the core,[35–37] are known and were mainly used to stabilize their spherical shapes. Unfortunately, conventional cross-linking moieties need to be incorporated during the preparation of the block polymers and the subsequent transformations are usually not very well defined. Alternatively, the approach described herein represents a significant advancement with respect to performing chemistry in micelles. Aggregates of amphiphilic DNA-block copolymers are a novel, highly modular platform of programmable objects that allow functionalization of micelles post-synthesis with virtually any chemical moiety through DNA hybridization and the execution of chemical reactions within predetermined submicellar compartments.

In conclusion, a new synthesis for a so-far unknown type of DNA-block copolymer was presented. The synthesis of this amphiphilic biological polymeric hybrid material, which proceeded in high yields, was performed fully automated in a single process by using a DNA synthesizer. The DNA-*b*-PPO polymers formed spherical micelles in aqueous solution, which were characterized by light scattering and SFM, exhibiting a hydrophobic core and a ss-DNA polyelectrolyte shell. It was demonstrated for the first time that various chemical reactions can be performed in a perfectly controlled and programmed manner within the volume of the micelle representing a spherical 3D object.

The DNA strands of the corona were organized by hydrophobic interactions of the organic polymer segments in such a fashion that several DNA-templated organic reactions proceeded in a sequence-specific manner either at the surface of the micelles or at the interface between the biological and the organic polymer blocks. The yields of reactions employing the micellar template were equivalent or better than existing template architectures. Furthermore, hydrophobic reactants can accumulate within the core of the micelle to produce much higher yields than achieved with conventional templates. Finally, with the help of a novel fluorogenic reaction, the DNA-templated organic reaction was detected by fluorescence spectroscopy allowing easy optimization of reaction conditions for new template architectures.

In the future, the application of the fluorogenic reaction will be investigated with regard to DNA detection and the potential for the identification of single-nucleotide polymorphisms. The unique micellar template will further be investigated for its suitability in carrying out DNA-templated reactions that can not proceed in aqueous environments but within the hydrophobic environment of the core are possible. DNA-block-copolymer micelles are also appealing candidates to carry out chemical synthesis in living cells as reactions might be able to proceed when shielded from the cellular environment.

Methods

For the preparation of phosphoramidite functionalized polymers, DNA-PPO-diblock copolymers, and the corresponding micelles, refer to the Supporting Information.

DNA-templated synthesis: Reactions with the 3D template were carried out by mixing the DNA-PPO-diblock copolymer micelles composed of **5b** with equimolar quantities of the reactant functionalized ODNs. The functional groups were adjusted to a 1:1 ratio. In the case of the isoindole formation, *o*-phthaldialdehyde was used in twofold excess. Concentrations of the micelle template were 250–550 nM in a reaction buffer solution that contained 3-(4-morpholinyl) 1-propanesulfonic acid (MOPS; 80 mM; pH 7.5) and NaCl (100–

 © 2006 Wiley-VCH Verlag GmbH & Co. KGaA, Weinheim

500 mM). The following sequences were used and are written in the 5′ to 3′ direction. **5b**: CCTCGCTCTGCTAATCCTGTTA, matching reactants: TAACAGGATTAGCAGAGCGAGG, non-matching reactants: GCAGATTCTTGGAACTATGCTT, AAAACACAGTGACGGCCTAGCC.

The reactions were analyzed by denaturing PAGE followed by ethidium bromide or SYBR safe staining (molecular probes). The yields were quantified by charge-coupled-device-based densitometry of the product and template bands. For the isoindole formation, fluorescence spectra of the product were recorded on a fluorescence plate reader (SpectraMax M2, Molecular devices) as additional structural proof.

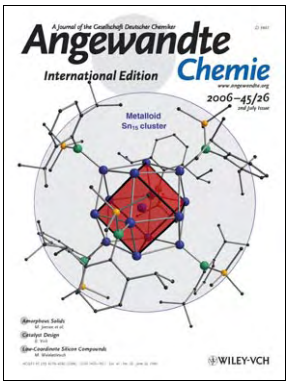
Received: February 8, 2006
Published online: May 17, 2006

Keywords: biological organic hybrid materials · block copolymers · DNA · nanostructures · self-assembly

[1] X. Y. Li, D. R. Liu, *Angew. Chem.* **2004**, *116*, 4956; *Angew. Chem. Int. Ed.* **2004**, *43*, 4848.
[2] D. Summerer, A. Marx, *Angew. Chem.* **2002**, *114*, 93; *Angew. Chem. Int. Ed.* **2002**, *41*, 89.
[3] Z. J. Gartner, M. W. Kanan, D. R. Liu, *Angew. Chem.* **2002**, *114*, 1847; *Angew. Chem. Int. Ed.* **2002**, *41*, 1796.
[4] Z. J. Gartner, D. R. Liu, *J. Am. Chem. Soc.* **2001**, *123*, 6961.
[5] Z. J. Gartner, M. W. Kanan, D. R. Liu, *J. Am. Chem. Soc.* **2002**, *124*, 10304.
[6] J. L. Czlapinski, T. L. Sheppard, *J. Am. Chem. Soc.* **2001**, *123*, 8618.
[7] R. L. Letsinger, T. F. Wu, *J. Am. Chem. Soc.* **1994**, *116*, 811.
[8] Z. C. Ma, J. S. Taylor, *Proc. Natl. Acad. Sci. USA* **2000**, *97*, 11159.
[9] J. Brunner, A. Mokhir, R. Kraemer, *J. Am. Chem. Soc.* **2003**, *125*, 12410.
[10] Y. Z. Xu, N. B. Karalkar, E. T. Kool, *Nat. Biotechnol.* **2001**, *19*, 148.
[11] A. Mattes, O. Seitz, *Angew. Chem.* **2001**, *113*, 3277; *Angew. Chem. Int. Ed.* **2001**, *40*, 3178.
[12] A. Demesmaeker, R. Haner, P. Martin, H. E. Moser, *Acc. Chem. Res.* **1995**, *28*, 366.
[13] J. F. R. Ortigao, A. Ruck, K. C. Gupta, R. Rosch, R. Steiner, H. Seliger, *Biochimie* **1993**, *75*, 29.
[14] D. Magda, R. A. Miller, J. L. Sessler, B. L. Iverson, *J. Am. Chem. Soc.* **1994**, *116*, 7439.
[15] Q. B. Zhou, S. E. Rokita, *Proc. Natl. Acad. Sci. USA* **2003**, *100*, 15452.
[16] Z. J. Gartner, B. N. Tse, R. Grubina, J. B. Doyon, T. M. Snyder, D. R. Liu, *Science* **2004**, *305*, 1601.
[17] M. W. Kanan, M. M. Rozenman, K. Sakurai, T. M. Snyder, D. R. Liu, *Nature* **2004**, *431*, 545.
[18] Z. J. Gartner, R. Grubina, C. T. Calderone, D. R. Liu, *Angew. Chem.* **2003**, *115*, 1408; *Angew. Chem. Int. Ed.* **2003**, *42*, 1370.
[19] K. J. Luebke, P. B. Dervan, *J. Am. Chem. Soc.* **1989**, *111*, 8733.
[20] A. T. Poulin-Kerstien, P. B. Dervan, *J. Am. Chem. Soc.* **2003**, *125*, 15811.
[21] L. H. Eckardt, K. Naumann, W. M. Pankau, M. Rein, M. Schweitzer, N. Windhab, G. von Kiedrowski, *Nature* **2002**, *420*, 286.
[22] S. Förster, V. Abetz, A. H. E. Müller, *Adv. Polym. Sci.* **2004**, *166*, 173.
[23] C. Allen, D. Maysinger, A. Eisenberg, *Colloids Surf. B* **1999**, *16*, 3.
[24] J. H. Jeong, T. G. Park, *Bioconjugate Chem.* **2001**, *12*, 917.
[25] Z. Li, P. Fullhart, C. A. Mirkin, *Nano Lett.* **2004**, *4*, 1055.
[26] J. Selb, Y. Gallot, *Makromol. Chem.* **1980**, *181*, 809.
[27] D. W. Miller, E. V. Batrakova, T. O. Waltner, V. Y. Alakhov, A. V. Kabanov, *Bioconjugate Chem.* **1997**, *8*, 649.
[28] G. Zhang, R. J. Barlow, A. Eisenberg, *Macromolecules* **1995**, *28*, 6055.
[29] M. Roth, *Anal. Chem.* **1971**, *43*, 880.
[30] P. de Montigny, J. F. Stobaugh, R. S. Givens, R. G. Carlson, K. Srinivasachar, L. A. Sternson, T. Higuchi, *Anal. Chem.* **1987**, *59*, 1096.
[31] K. B. Thurmond, T. Kowalewski, K. L. Wooley, *J. Am. Chem. Soc.* **1996**, *118*, 7239.
[32] H. Y. Huang, E. E. Remsen, T. Kowalewski, K. L. Wooley, *J. Am. Chem. Soc.* **1999**, *121*, 3805.
[33] V. Butun, N. C. Billingham, S. P. Armes, *J. Am. Chem. Soc.* **1998**, *120*, 12135.
[34] J. F. Ding, G. J. Liu, *Macromolecules* **1998**, *31*, 6554.
[35] M. Iijima, Y. Nagasaki, T. Okada, M. Kato, K. Kataoka, *Macromolecules* **1999**, *32*, 1140.
[36] Y. Y. Won, H. T. Davis, F. S. Bates, *Science* **1999**, *283*, 960.
[37] Y. Kakizawa, A. Harada, K. Kataoka, *J. Am. Chem. Soc.* **1999**, *121*, 11247.

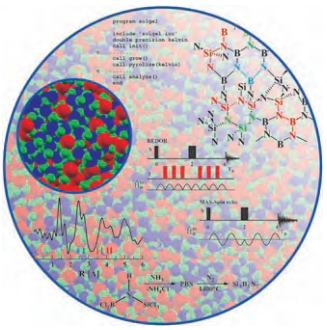
 © 2006 Wiley-VCH Verlag GmbH & Co. KGaA, Weinheim

Cover Picture

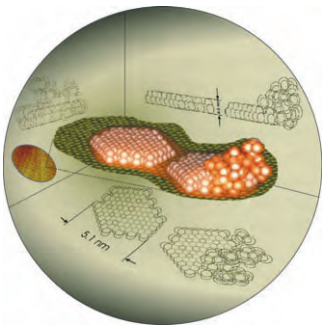


Marcin Brynda, Rolfe Herber,* Peter B. Hitchcock, Michael F. Lappert,* Israel Nowik, Philip P. Power,* Andrey V. Protchenko, Aleš Růžička, and Jochen Steiner

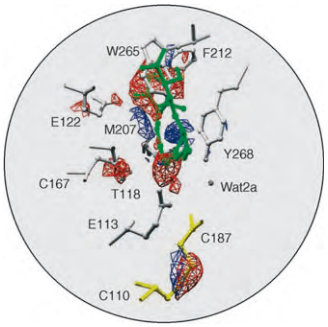
Metalloid Clusters possess more metal–metal than metal–ligand contacts and contain metal atoms that participate only in metal–metal interactions. The metalloid cluster shown features a body-centered Sn_{15} core and six amido ligands (Sn blue, N green, Si yellow, C black). In the Communication by M. F. Lappert, P. P. Power, R. Herber, and co-workers on page 4333 ff., the synthesis and structures of two such clusters are presented along with Mössbauer spectra, which show two distinct Sn environments.



Structure Elucidation
Significant progress in the elucidation of the structure of the amorphous ceramic $Si_3B_3N_7$ has been possible through the combination of experimental methods and computer simulations, as discussed by M. Jansen et al. in their Review on page 4244 ff.



Nanoparticle Arrays
In their Communication on page 4266 ff., G. A. Planes and co-workers describe the assembly of Pt clusters into so-called nanoislands and the alignment of the latter into parallel rows on a gold surface.



Chemistry of Sight
Two Communications—that of T. Okada and H. Nakamichi on page 4270 ff., as well as that of V. Buss and co-workers on page 4274 ff.—address the structure of bathorhodopsin, the first intermediate of the rhodopsin visual cycle.

Contents

VIP *The following Communications have been judged by at least two referees to be "very important papers" and will be published online at www.angewandte.org soon:*

*A. Narayanaswamy, H. Xu, N. Pradhan, X. Peng**
Single-Crystal Nanoflowers with Different Chemical Compositions and Physical Properties Grown by Limited Ligand Protection

J. L. Alonso, E. Cocinero, A. Lesarri, M. E. Sanz, J. López*
The Glycine–Water Complex

*A. Tao, P. Sinsermsuksakul, P. Yang**
Polyhedral Silver Nanocrystals with Distinct Scattering Signatures

J. van Bokhoven, C. Louis, J. Miller, M. Tromp, O. Safonova, P. Glatzel*
Activation of Oxygen on Gold–Alumina Catalysts: In Situ High-Energy Resolution Fluorescence and Time-Resolved X-ray Spectroscopy

Books

Chemistry of Peptide Synthesis — N. Leo Benoiton — *reviewed by S. Kent* — **4234**

Candid Science IV — Magdolna Hargittai, István Hargittai — *reviewed by G. B. Kauffman* — **4235**

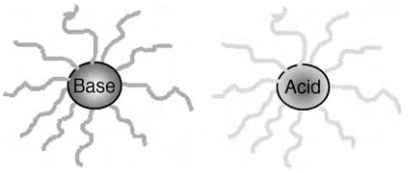
Highlights

Catalyst Design

B. Voit* — **4238 – 4240**

Sequential One-Pot Reactions Using the Concept of "Site Isolation"

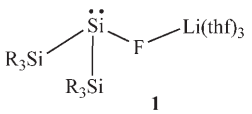
Acidic and basic sites can be isolated by incorporation in the core of star-shaped polymers (see picture). Fréchet, Hawker, and co-workers have used these polymer-based catalysts for homogeneous-phase one-pot multistep reactions. Similarly, Kaneda et al. have demonstrated the site-isolation concept in heterogeneous systems by use of different types of layered clays.



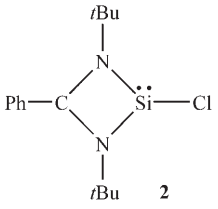
Low-Coordinate Compounds

M. Weidenbruch* — **4241 – 4242**

A Stable Silylenoid and a Donor-Stabilized Chlorosilylene: Low-Coordinate Silicon Compounds—A Never-Ending Story?



1



2

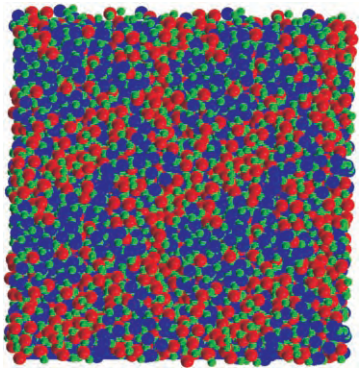
And so on: The silylenoid **1** and the stabilized chlorosilylene **2** represent new types of low-coordinate silicon compounds, which, on account of the presence of a silicon–halogen bond in each, should form the basis of interesting subsequent chemistry.

InterScience

© 2006 Wiley-VCH Verlag GmbH & Co. KGaA, Weinheim

Reviews

Teaming up for results: The structure of the amorphous ceramic $Si_3B_3N_7$ has been investigated by combining experimental data with computer simulations. Of the many structural models generated (see picture for an example; Si red, B blue, N green), those that consider the actual synthesis route of the material agree most closely with the experimental results.

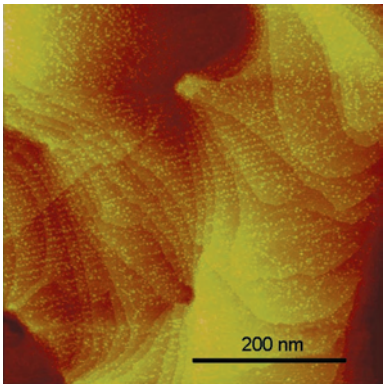


Amorphous Compounds

M. Jansen,* J. C. Schön, L. van Wüllen ——— **4244 – 4263**

The Route to the Structure Determination of Amorphous Solids: A Case Study of the Ceramic $Si_3B_3N_7$

Communications



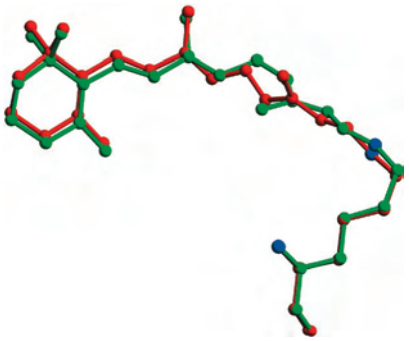
Good organizational skills: Evidence for the formation of Pt clusters during classical microemulsion synthesis was obtained by scanning tunneling microscopy. The Pt clusters were spontaneously assembled on an Au(111) surface to form high-aspect-ratio objects. 2D nanoislands form and subsequently self-assemble in parallel rows of several hundreds of nanometers in length.

Nanostructures VIP

O. Guillén-Villafuerte, G. García, B. Anula, E. Pastor, M. C. Blanco, M. A. López-Quintela, A. Hernández-Creus, G. A. Planes* ——— **4266 – 4269**

Assembly of Subnanometric 2D Pt Nanoislands in Parallel Rows onto Au(111) by Self-Organization of Pt Clusters

A curved retinal: Difference electron-density data between the photoreceptor protein rhodopsin and its primary photoreaction intermediate bathorhodopsin have provided a crystallographic model for the *cis–trans* isomerization of the chromophore retinal therein during the primary process in dim-light vision (see picture; the curved polyene structure of retinal in bathorhodopsin is shown in red, while that in rhodopsin is colored green).



Chemistry of Vision (1) VIP

H. Nakamichi, T. Okada* — **4270 – 4273**

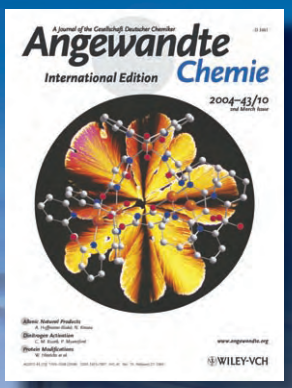
Crystallographic Analysis of Primary Visual Photochemistry

For the USA and Canada:
ANGEWANDTE CHEMIE International Edition (ISSN 1433-7851) is published weekly by Wiley-VCH PO Box 191161, D 69451 Weinheim, Germany. Air freight and mailing in the USA by Publications Expediting Inc. 200 Meacham Ave., Elmont, NY 11003. Periodicals postage paid at Jamaica NY 11431. US POSTMASTER: send address changes to *Angewandte Chemie*, Wiley-VCH, 111 River Street, Hoboken, NJ 07030. Annual subscription price for institutions: US$ 5685/5168 (valid for print and electronic / print or electronic delivery); for individuals who are personal members of a national chemical society prices are available on request. Postage and handling charges included. All prices are subject to local VAT/sales tax.

© 2006 Wiley-VCH Verlag GmbH & Co. KGaA, Weinheim

The best in chemistry –

for more than a hundred years



A Journal of the Gesellschaft Deutscher Chemiker

Angewandte
International Edition **Chemie**

www.angewandte.org

1888: ***The beginning of a success story***

Constant Innovations

1962: First issue of the International Edition
1976: Graphical abstracts
1979: Cover pictures
1988: Centenary of Angewandte
1989: Routine use of color
1991: New section: Highlights
1992: Computerized editorial tracking system
1995: Internet service for readers
1998: Regular press service; full-text online
2000: New section: Essays; EarlyView: Communications available online ahead of the printed version
2001: New section: Minireviews
2002: Online submission of manuscripts
2003: Weekly publication; new section: News; new layout
2004: Backfiles (1962-1997); ManuscriptXpress: Online system for authors and referees



Angewandte's advisors...

Seiji Shinkai
Kyushu University, Fukuoka

» ***Angewandte Chemie*** *is my favorite journal and I am honored to serve on its International Advisory Board. The research essence of an article can be understood rapidly because text and illustrations are finely harmonized. Furthermore, the high quality contents, which have a strong impact, are published very quickly.* *«*

Angewandte Chemie International Edition *is a journal of the German Chemical Society (GDCh)*

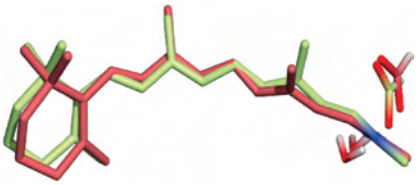
GDCh

WILEY InterScience® DISCOVER SOMETHING GREAT

WILEY-VCH

11901404_gu

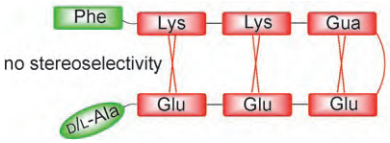
Seeing double: Quantum-mechanical refinement of the X-ray crystal structure of bathorhodopsin (see picture; before optimization green; optimized structure red) highlights the twisted geometry of the chromophore. Calculated Raman, UV/Vis, and CD spectral properties of this first intermediate of the rhodopsin visual cycle agree with those observed experimentally.

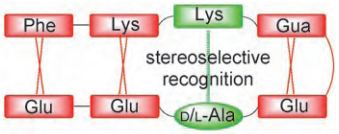


Chemistry of Vision (2)

M. Schreiber, M. Sugihara, T. Okada, V. Buss* ——— **4274 – 4277**

Quantum Mechanical Studies on the Crystallographic Model of Bathorhodopsin



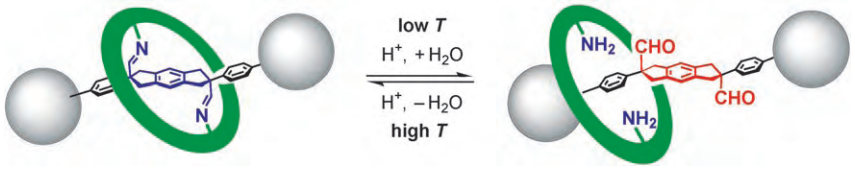


All in a row: The screening of a combinatorial library with 320 substrates shows that an artificial triscationic receptor efficiently binds anionic tetrapeptides in water with association constants up to $K_a = 27\,000\ M^{-1}$. Moreover, the receptor shows a remarkable sequence-dependent stereoselectivity between D-Ala and L-Ala in certain positions of the tetrapeptide.

Peptide Receptors

C. Schmuck,* P. Wich ——— **4277 – 4281**

Sequence-Dependent Stereoselectivity in the Binding of Tetrapeptides in Water by a Flexible Artificial Receptor

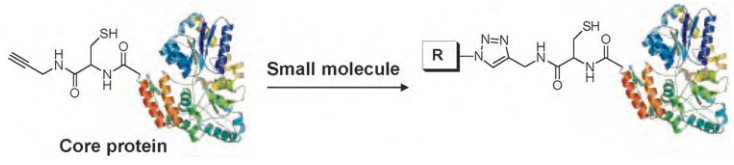


Building bridges: Imine bridges between the axle and ring components in rotaxanes allow simple rotaxane synthesis and a novel method for motion control to be developed. The submolecular mobility in this rotaxane-type assembly is regulated by the imine-bond formation/cleavage (see scheme). The relative abundance of the [2]rotaxane increases with decreasing temperature under dynamic equilibrium conditions.

Supramolecular Chemistry

H. Kawai,* T. Umehara, K. Fujiwara, T. Tsuji,* T. Suzuki ——— **4281 – 4286**

Dynamic Covalently Bonded Rotaxanes Cross-Linked by Imine Bonds between the Axle and Ring: Inverse Temperature Dependence of Subunit Mobility



Out of site: A protein expression system was combined with Cu^{I}-catalyzed 1,2,3-triazole formation to modify a target protein at its C terminus. The immobilized core protein can be modified by diverse small molecules in a site-specific manner (see picture). Protein conjugation with a diazido linker gives a homodimeric protein, and microarrays can be fabricated by site-specific covalent binding to functionalized surfaces.

Protein Modification

P.-C. Lin, S.-H. Ueng, M.-C. Tseng, J.-L. Ko, K.-T. Huang, S.-C. Yu, A. K. Adak, Y.-J. Chen, C.-C. Lin* ——— **4286 – 4290**

Site-Specific Protein Modification through Cu^{I}-Catalyzed 1,2,3-Triazole Formation and Its Implementation in Protein Microarray Fabrication

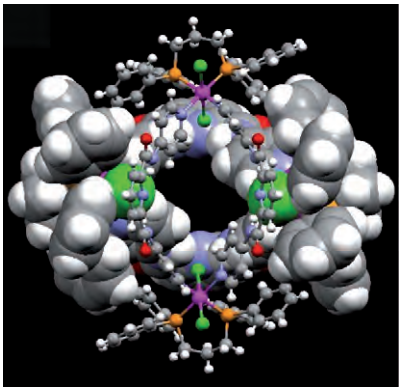
© 2006 Wiley-VCH Verlag GmbH & Co. KGaA, Weinheim

Contents

Metallacycles

Y. J. Park, J.-S. Kim, K.-T. Youm, N.-K. Lee, J. Ko,* H.-s. Park,* M.-J. Jun* _____ **4290 – 4294**

A Self-Complementary Assembly of Metallamacrocycles Directed by Ru–Cl···H–N Hydrogen Bonds and Its Reversible Dichotomy by Halide Anions in Solution

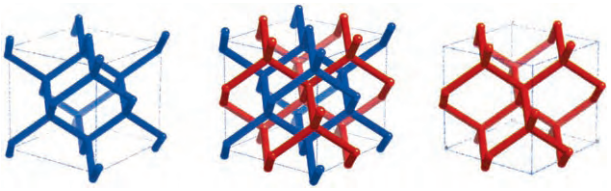


Back and forth: Reaction of $[RuCl_2(PPh_3)_3]$, 1,3-bis(diphenylphosphino)propane, and an amido ligand yields the coordination-driven self-assembly of two ruthenamacrocycles through NH···Cl–Ru, π···π, and C–H···π interactions (see picture; purple Ru, green Cl, orange P, red O, blue N, gray C, white H). Reversible dissociation/association behavior of this complex in solution is controlled by halide ions.

Mesoporous Materials

C. Gao, Y. Sakamoto,* K. Sakamoto, O. Terasaki, S. Che* _____ **4295 – 4298**

Synthesis and Characterization of Mesoporous Silica AMS-10 with Bicontinuous Cubic $Pn\bar{3}m$ Symmetry



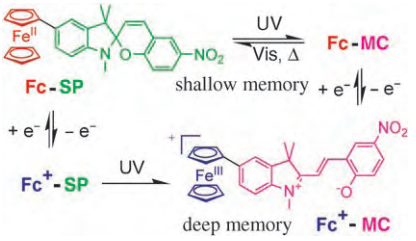
Woven into place: By precisely controlling the neutralization degree of the anionic surfactant template, mesoporous silica with different structures was prepared, such as AMS-10. Detailed characterizations of AMS-10 show that it is a novel bicontinuous cubic $Pn\bar{3}m$ mesophase. The mesostructure is composed of an interwoven enantiomeric pair of 3D networks (see picture).

Photochromism

S. Nagashima, M. Murata, H. Nishihara* _____ **4298 – 4301**

A Ferrocenylspiropyran That Functions as a Molecular Photomemory with Controllable Depth

Deep memory: A photochromic molecule can control the stability of its merocyanine (MC) form by changing the oxidation state of the ferrocene (Fc) moiety (see picture). This ferrocenyl–spiropyran (SP) system works not only in solution but also in a polymer electrolyte.

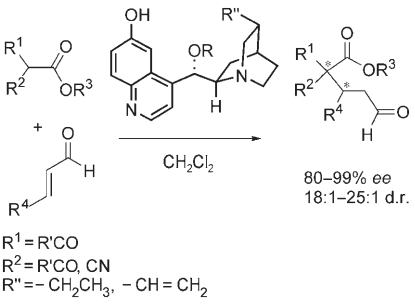


Organocatalysis

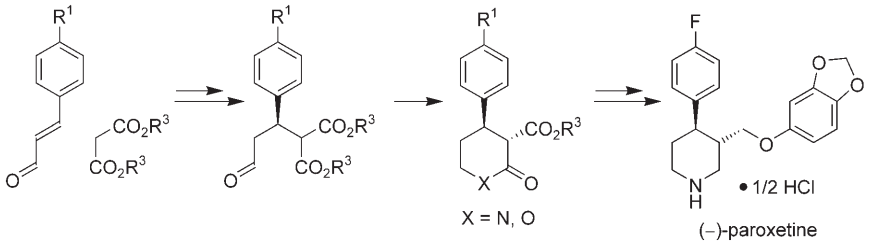
F. Wu, R. Hong, J. Khan, X. Liu, L. Deng* _____ **4301 – 4305**

Asymmetric Synthesis of Chiral Aldehydes by Conjugate Additions with Bifunctional Organocatalysis by Cinchona Alkaloids

A highly efficient asymmetric conjugate addition of carbonyl donors to α,β-unsaturated aldehydes is realized with 6′-OH cinchona alkaloids as bifunctional organocatalysts. A wide range of α-substituted β-ketoesters and α-substituted α-cyanoacetates can be employed as donors, whereas acrolein and β-substituted α,β-unsaturated aldehydes are suitable acceptors for this enantioselective addition.



© 2006 Wiley-VCH Verlag GmbH & Co. KGaA, Weinheim

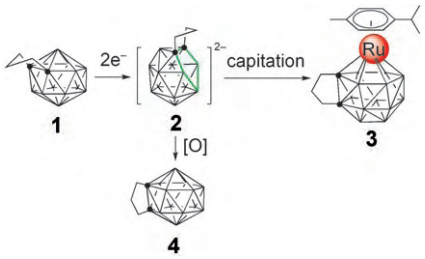


In addition: The scope of the title reaction is demonstrated by the synthesis of chiral lactones and lactams. The latter class of compounds is very important for the preparation of the pharmaceutical compounds such as (−)-paroxetine and (+)-femoxetine.

Organocatalysis

S. Brandau, A. Landa, J. Franzén, M. Marigo, K. A. Jørgensen* **4305 – 4309**

Organocatalytic Conjugate Addition of Malonates to α,β-Unsaturated Aldehydes: Asymmetric Formal Synthesis of (−)-Paroxetine, Chiral Lactams, and Lactones

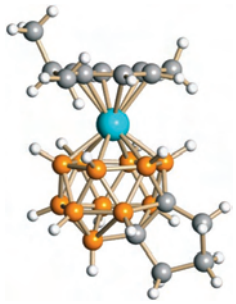


Adding corners: A metallacarborane with 15 vertices was prepared by reduction of 14-vertex carborane **1** to *nido*-carborane dianion **2** and subsequent reaction with $[\{(p\text{-cymene})RuCl_2\}_2]$ to give **3** (see scheme). The key to obtaining successively larger clusters is prevention of redox reactions (such as that to give **4**).

Metallacarboranes

L. Deng, J. Zhang, H.-S. Chan, Z. Xie* **4309 – 4313**

Synthesis and Structure of 14- and 15-Vertex Ruthenacarboranes

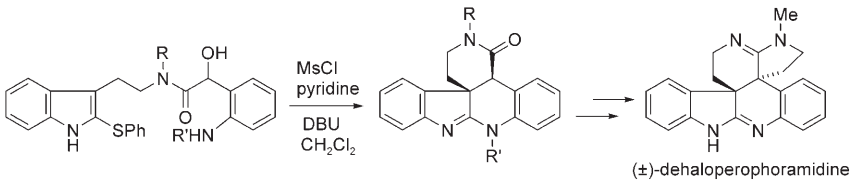


Cornering heteroboranes: The 15-vertex heteroborane 1-(*p*-cymene)-8,14-μ-$(CH_2)_3$-1,8,14-*closo*-$RuC_2B_{12}H_{12}$ has been prepared (see structure; B orange, Ru blue, C gray). The RuC_2B_{12} polyhedron has the form of a pentacosahedron (24 triangular faces and 1 quadrilateral face). In solution at elevated temperatures the structure is in tautomeric equilibrium by a "square–diamond–square" rearrangement involving the quadrilateral face.

Metallacarboranes

R. D. McIntosh, D. Ellis, G. M. Rosair, A. J. Welch* **4313 – 4316**

A 15-Vertex Heteroborane



Closing the ring: The cyclization of a 2-thioindole with an electrophilic substituent serves as the key transformation in a synthetic strategy for the generation of indole alkaloids of the perophoramidine and communesin class. DBU = 1,8-diazabicyclo[5.4.0]undec-7-ene, Ms = methanesulfonyl chloride.

Natural Product Synthesis

A. Sabahi, A. Novikov, J. D. Rainier* **4317 – 4320**

2-Thioindoles as Precursors to Spiro-Fused Indolines: Synthesis of (±)-Dehaloperophoramidine

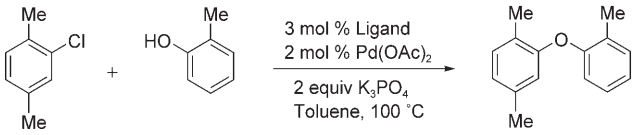
© 2006 Wiley-VCH Verlag GmbH & Co. KGaA, Weinheim

Contents

C–O Bond Formation

C. H. Burgos, T. E. Barder, X. Huang, S. L. Buchwald* ——— **4321 – 4326**

Significantly Improved Method for the Pd-Catalyzed Coupling of Phenols with Aryl Halides: Understanding Ligand Effects

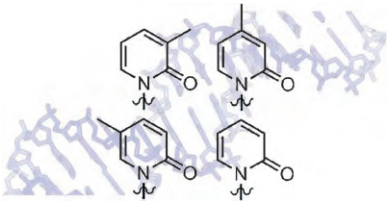


A variety of diaryl ethers were synthesized by the Pd-catalyzed reaction of (hetero)-aryl halides and phenols. These reactions were achieved through the use of two new di-*tert*-butylphosphino biaryl ligands that overcome several limitations of previously described methods.

Non-natural Base Pairs

A. M. Leconte, S. Matsuda, G. T. Hwang, F. E. Romesberg* ——— **4326 – 4329**

Efforts towards Expansion of the Genetic Alphabet: Pyridone and Methylpyridone Nucleobases

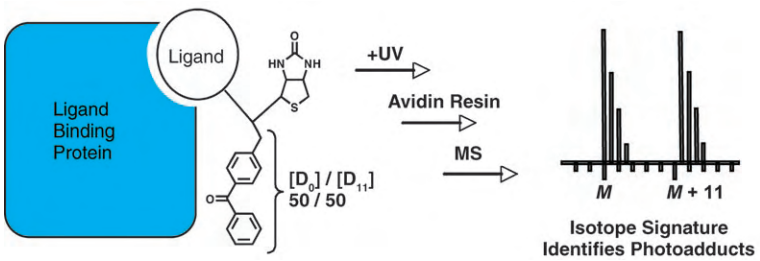


Getting on with it: A common problem with hydrophobic non-natural base pairs—the inefficient extension following such a base pair—is reduced by using the methylpyridone scaffold, which simultaneously limits another frequent problem of non-natural bases: mispairs with deoxyadenosine.

Chemical Genetics

S. M. Lamos, C. J. Krusemark, C. J. McGee, M. Scalf, L. M. Smith, P. J. Belshaw* ——— **4329 – 4333**

Mixed Isotope Photoaffinity Reagents for Identification of Small-Molecule Targets by Mass Spectrometry

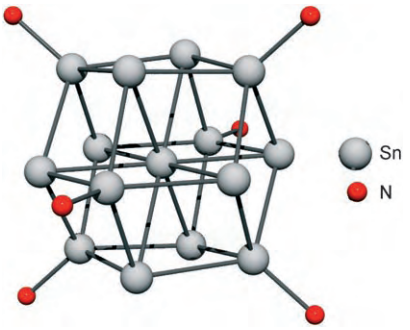


Twin peaks: A facile and economic route has been developed for the incorporation of deuterated benzophenones (a widely used photoaffinity tag) into probes. Attachment of these mixed-isotope labels to the immunosuppressive drug CsA facilitated the mass spectrometric identification of a target of CsA (see picture) from a mixture of proteins.

Cluster Compounds

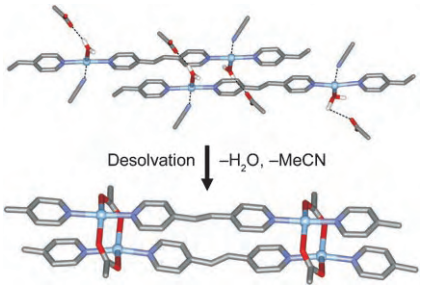
M. Brynda, R. Herber,* P. B. Hitchcock, M. F. Lappert,* I. Nowik, P. P. Power,* A. V. Protchenko, A. Růžička, J. Steiner ——— **4333 – 4337**

Higher-Nuclearity Group 14 Metalloid Clusters: $[Sn_9\{Sn(NRR')\}_6]$



A perfect tin! Two 15-nuclear tin metalloid clusters $[Sn_{15}Z_6]$ ($Z = N(2,6\text{-}iPr_2C_6H_3)(SiMe_2X)$; X = Me, Ph), having an unprecedented body-centered metal core (see picture; only N atoms of the amide ligands shown), were prepared by reduction of the appropriate amidotin(II) chloride with KC_8 or $Li[BHsBu_3]$. Mössbauer spectra showed two distinct quadrupole-splitting sites in the ratio of 1.5:1 for the Sn_9 atoms and the six amido-bound tin atoms.

© 2006 Wiley-VCH Verlag GmbH & Co. KGaA, Weinheim

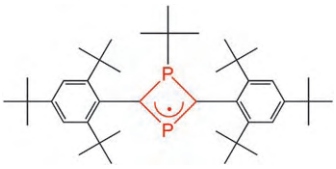


Rungs of a ladder: A solvated linear 1D coordination polymer $[Ag(\mu\text{-bpe})(H_2O)](CF_3CO_2)\cdot CH_3CN$ (bpe = 4,4′-bipyridylethylene) with no parallel dispositions of the double bonds in the crystal structure undergoes photodimerization when desolvated. This finding is attributed to the lateral movements of adjacent linear strands on desolvation, which form a ladderlike structure (see picture; Ag light blue, C gray, N purple, O red).

Crystal Engineering

M. Nagarathinam, J. J. Vittal* ——— 4337 – 4341

Anisotropic Movements of Coordination Polymers upon Desolvation: Solid-State Transformation of a Linear 1D Coordination Polymer to a Ladderlike Structure

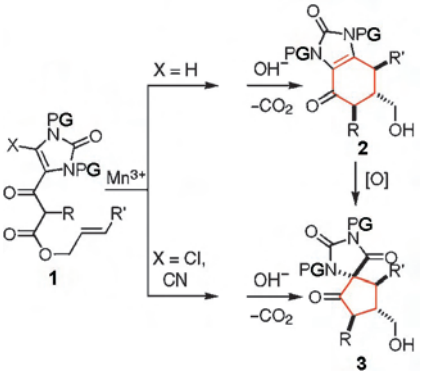


Radically stable: An extremely stable P-heterocyclic organic radical was isolated after oxidation of a sterically encumbered 1,3-diphosphacyclobutenyl anion generated from Mes*C≡P (Mes* = 2,4,6-$tBu_3C_6H_2$). The structure of the 1,3-diphosphacyclobuten-4-yl radical, as determined by X-ray analysis, was comparable to data obtained from EPR analysis and a computational model.

Phosphorus Heterocycles

S. Ito,* M. Kikuchi, M. Yoshifuji,* A. J. Arduengo, III, T. A. Konovalova, L. D. Kispert ——— 4341 – 4345

Preparation and Characterization of an Air-Tolerant 1,3-Diphosphacyclobuten-4-yl Radical



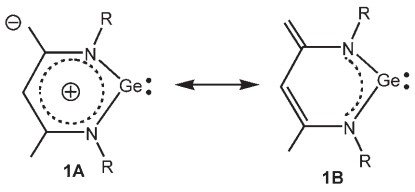
In control: A cyclization reaction of an allylic β-imidazolinonyl-β-ketoester **1** is carried out in a Mn^{III}-promoted radical cascade. The reaction pathway (5-*exo*/6-*endo* or 5-*exo*/5-*exo*) can be directed to construct the central cyclopentyl and cyclohexenyl core skeletons (**2** and **3**) of two classes of oroidin dimers with regiocontrol. An oxidative rearrangement can also be used to convert **2** into **3**. PG = protecting group.

Cascade Reactions

X. Tan, C. Chen* ——— 4345 – 4348

Regiocontrol in Mn^{III}-Mediated Oxidative Heterobicyclizations: Access to the Core Skeletons of Oroidin Dimers

An electronic chameleon: The planar cyclogermylene **1** can be described by the resonance structures **1A** and **1B**. It is accessible in 79% yield by dehydrohalogenation of the corresponding (β-diketiminato)chlorogermylene by $LiN(SiMe_3)_2$. Although the contribution of the dipolar resonance structure **1A** is relatively small, its influence is seen in the transformations of **1** with Me_3SiOTf or 1,2-dibromoethane. R = 2,6-diisopropylphenyl.



Main-Group-Element Compounds

M. Driess,* S. Yao, M. Brym, C. van Wüllen ——— 4349 – 4352

A Heterofulvene-Like Germylene with a Betain Reactivity

© 2006 Wiley-VCH Verlag GmbH & Co. KGaA, Weinheim

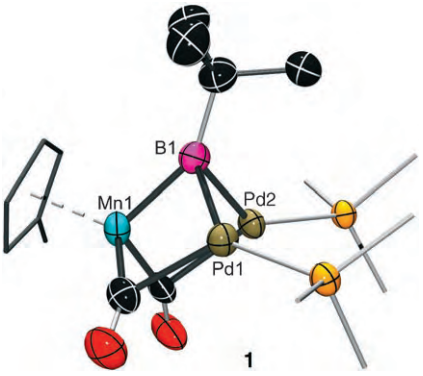
Contents

Borylene Complexes

H. Braunschweig,* C. Burschka, M. Burzler, S. Metz, K. Radacki ——— **4352 – 4355**

Molecular Structure and Cluster Formation of a *tert*-Butylborylene Complex

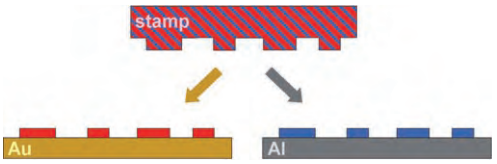
B finds a new hive: The X-ray structure of $[\mu\text{-B}t\text{Bu}\{(\eta^5\text{-C}_5\text{H}_5)\text{Mn(CO)}_2\}_2]$ represents the first crystallographic characterization of an alkylborylene complex. Its substituted counterpart $[\mu\text{-B}t\text{Bu}\{(\eta^5\text{-C}_5\text{H}_4\text{Me})\text{-Mn(CO)}_2\}_2]$ reacts cleanly with $[\text{Pd}(\text{PCy}_3)_2]$ (Cy = cyclohexyl) to form the first heterometallic μ_3-borylene complex **1**, for which DFT and ELF computations indicate a localized bonding situation.



Microcontact Printing

D. Burdinski,* M. Saalmink, J. P. W. G. van den Berg, C. van der Marel ——— **4355 – 4358**

Universal Ink for Microcontact Printing

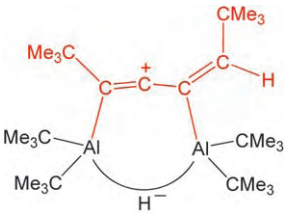


Hot off the press: A single mixed ink composition comprising aliphatic thiol and phosphonic acid inks has been used for the soft lithographic patterning of metal and metal oxide surfaces by microcontact printing and wet chemical etching. The method takes advantage of the intrinsic selectivity of the ink transfer to different substrate materials.

Hydroalumination

W. Uhl,* J. Grunenberg, A. Hepp, M. Matar, A. Vinogradov ——— **4358 – 4361**

Facile Formation of a Persistent Butadien-2-yl Cation Stabilized by Hyperconjugation with an Al–C Bond



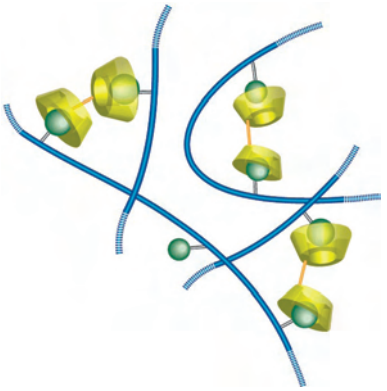
An aluminating discovery: Hydroalumination of 1,4-di(*tert*-butyl)butadiyne with di(*tert*-butyl)aluminum hydride affords a persistent butadien-2-yl cation (red in scheme). The stabilization of this compound is achieved in particular by hyperconjugation with an Al–C bond, and the effective chelating coordination by the aluminum atoms prevents the migration of the hydride ion to the electrophilic cationic carbon atom.

Hydrogels

O. Kretschmann, S. W. Choi, M. Miyauchi, I. Tomatsu, A. Harada, H. Ritter* ——— **4361 – 4365**

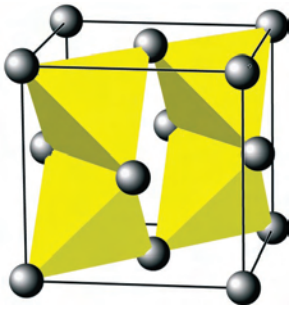
Switchable Hydrogels Obtained by Supramolecular Cross-Linking of Adamantyl-Containing LCST Copolymers with Cyclodextrin Dimers

En route to intelligent hydrogels: Copolymers of *N*-isopropylacrylamide containing adamantyl groups can be cross-linked noncovalently with cyclodextrin dimers. This results in thermosensitive hydrogels with cloud points that are lower than those of the pure copolymers. Addition of monomeric methylated cyclodextrin results in an increase in the cloud points but has no significant influence on the viscosity of the copolymer solution.



© 2006 Wiley-VCH Verlag GmbH & Co. KGaA, Weinheim

Mistaken identity: The high-pressure synthesis of PtN in the zinc blende structure type is refuted on the basis of first-principles electronic-structure calculations, which demonstrate that this low-density phase is energetically unstable and cannot be produced at high pressure. The denser cooperite structure type is preferable for PtN (see picture; NPt_4 tetrahedra are yellow).

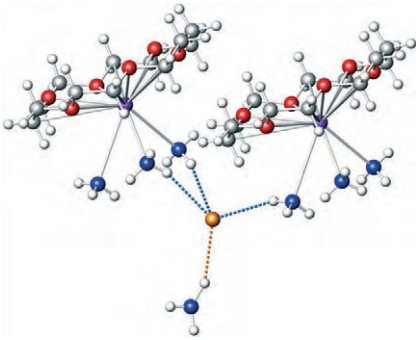


Solid-State Structures

J. von Appen, M.-W. Lumey, R. Dronskowski* ——— 4365 – 4368

Mysterious Platinum Nitride

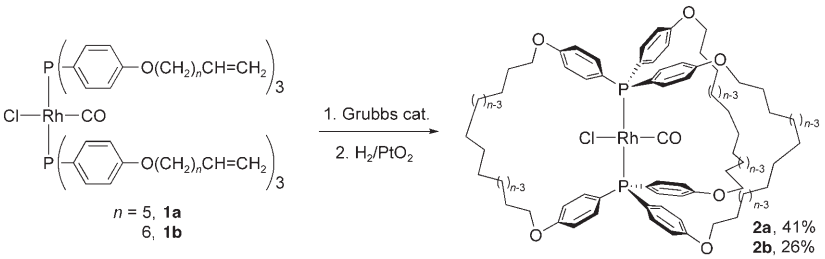
Golden bridge: In the title complex, the auride anion acts as an acceptor in N–H···Au$^-$ hydrogen bonds (see molecular structure; C gray, H white, N blue, O red, Au orange, Rb violet). For the first time, experimental values for an H···Au$^-$ distance and the corresponding N-H-Au angle could be determined.



Hydrogen Bonds

H. Nuss, M. Jansen* ——— 4369 – 4371

[Rb([18]crown-6)$(NH_3)_3$]Au·NH_3: Gold as Acceptor in N–H···Au$^-$ Hydrogen Bonds



Molecular Rotors

L. Wang, F. Hampel, J. A. Gladysz* ——— 4372 – 4375

"Giant" Gyroscope-Like Molecules Consisting of Dipolar Cl-Rh-CO Rotators Encased in Three-Spoke Stators That Define 25–27-Membered Macrocycles

Yet another feat for the Grubbs catalyst: Reactions with **1a**,**b** followed by hydrogenations give **2a**,**b**. The sizeable cavities of **2**, which were characterized crystallographically, allow for rapid Cl-Rh-CO rotation in solution. Reactions with ArC≡CLi give ArC≡C–Rh–CO species; when the aryl group is sufficiently large, it is confined between two macrocycles, blocking rotation.

Sources

Product and Company Directory

You can start the entry for your company in "Sources" in any issue of *Angewandte Chemie*.

If you would like more information, please do not hesitate to contact us.

Wiley-VCH Verlag – Advertising Department
Tel.: 0 62 01 - 60 65 65
Fax: 0 62 01 - 60 65 50
E-Mail: MSchulz@wiley-vch.de

Service

Keywords ——— 4378

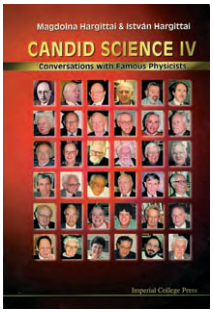
Authors ——— 4379

Angewandte's Sister Journals ——— 4376 – 4377

Preview ——— 4381

© 2006 Wiley-VCH Verlag GmbH & Co. KGaA, Weinheim

Candid Science IV



Conversations with Famous Physicists. By *Magdolna Hargittai* and *István Hargittai*. Imperial College Press, London 2004. xvi + 711 pp., hardcover £ 118.00.—ISBN 1-86094-414-0

During his six-year tenure (1995–2000) as editor-in-chief of Springer-Verlag's quarterly magazine *The Chemical Intelligencer*, István Hargittai, Professor of Chemistry at the Budapest University of Technology and Economics, sometimes in collaboration with his wife Magdolna (Magdi), Research Professor of Structural Chemistry of the Hungarian Academy of Sciences, interviewed more than 120 eminent scientists. Some of these interviews were not published in the magazine, and many have appeared in a handier and more permanent form—the *Candid Science* series. The first five volumes of this critically acclaimed series, each containing three dozen interviews, have been published, the first two of which have been reviewed in *Angewandte Chemie* (Vol. I: **2001**, p. 2179; Vol. III: **2004**, p. 1909). Also, according to Hargittai, the series "may extend to a seventh volume eventually" (Hargittai, I., e-mail to G. B. Kauffman, June 6, 2005).

For the first three volumes, Magdi acted only as editor. In this fourth volume she shares authorship with István. The Hargittais uncover the stories behind the most important achievements in 20th-century physics, directly from some of its most distinguished participants. The interviewees tell about their backgrounds, families, personal and professional lives, childhoods, influences, career choices, motivations, aspirations, heroes, mentors and influences, choice of co-workers, hardships and triumphs, *modus operandi*, philosophies, hobbies, nonscientific interests, and their major discoveries.

The interviews are usually by-products of the Hargittais' scientific and family travels; some were squeezed into programs of scientific meetings or the centennial celebrations of the Nobel Prizes in 2001 in Stockholm. The Hargittais contacted each interviewee in advance, set up a date, recorded the conversation on audiotape, and sent the transcript to the interviewee for correction and possible change. They never tried to deal with topics with which the interviewees seem uncomfortable, and they tactfully asked them to ignore questions they did not want to discuss. Therefore, the interviewees are often candid in their responses to questions that the Hargittais do ask. According to István, "Acting in this way rather than looking to reveal some "dark secrets" has been helpful in getting closer to our interviewees in a human sense than it might be possible by a more aggressive approach".

Hence the titles of the books in the series are quite appropriate, as are their subtitles. Their contents are more like candid informal conversations rather than formal interviews. In reply to the Hargittais' serious questions, a number of the interviewees answered with humor.

Most of the scientific subjects are discussed either by their originators or most prominent authorities. They include astronomy; astrophysics; radioastronomy; the fullerenes; Higgs's W, Z, and Ω particles; quarks; Grand Unified Theory; gravitation; quantum mechanics; extraterrestrial intelligence; astrophysics; the superconducting supercollider; the GALLEX experiment; nonconservation of parity; the Big Bang theory; dark matter; the solar neutrino problem; microwave background radiation; chemistry of interstellar space; antiprotons; Michael Frayn's play *Copenhagen*; Schrödinger's cat; quasicrystals; black holes; the Orion project (a bomb-propelled spaceship); paranormal phenomena; fractals; and phase transitions.

Among related topics, one finds discussions of government and public service, gender bias and feminism, Nobel politics, research planning, the Great Depression, serendipity, discovery and patenting of discoveries, teaching, nepotism, administration, the McCarthy era, war research, religious beliefs, the reconciling of science and religion, history of science, aging, authorship of articles, the scientific establishment, experiment vs. theory, science and nationalism, missed opportunities, the public image of physics and science, science literacy, greatest challenge, comparisons between universities and research institutes, the role of imagination in science, compulsory retirement and its effect on a person's work, feelings on being "scooped", the social responsibility of scientists, work in progress, their legacy, and advice to young people.

The collection begins and ends with recollections. The first conversation deals largely with Eugene P. Wigner's account of scientists from the earlier years of 20th-century physics, a clear link with the past. It is not really an interview but a summary of a series of conversations that István had during Wigner's visit to the University of Texas in 1969. The last entry, a summary of a conversation with David Schoenberg that includes direct quotes about his contacts with Russian physicists Peter Kapitza and Lev Landau, should introduce Western scientists to their counterparts in the East and turn their attention to the future.

The earliest-born physicist interviewed is the Australian, the late Marcus L. E. Oliphant (born 1901), co-discoverer with Ernest Rutherford of tritium and helium-3, a leading participant in the Manhattan Project and the establishment of radar during World War II, and co-founder of the Australian National University. The youngest interviewee is the German-born Wolfgang Ketterle (born 1957), Professor of Physics at the Massachusetts Institute of Technology and 2001 Nobel physics laureate.

The interviews flow naturally, and often introduce the next one. Rudolf Mößbauer follows John N. Bahcall, reflecting their common interest in cosmic neutrinos; Ketterle follows his mentor David E. Pritchard; Laszlo Tisza, whose 1944 article was one of the forerunners of the Bose–Einstein condensation, follows Ketterle, one of its discoverers a half-century later; and Joseph H. Taylor and Russell A. Hulse, the discoverers of double pulsars, follow Antony Hewish and Jocelyn Bell Burnell, the discoverers of pulsars.

Versatility is a prominent characteristic among many of the interviewees, as a number of them have switched areas several times in the course of their

 © 2006 Wiley-VCH Verlag GmbH & Co. KGaA, Weinheim

careers. Some, such as Leon M. Lederman, began as chemistry majors; Edward Teller studied chemical engineering; Freeman J. Dyson and John C. Polkinghorne were mathematicians; and Mildred S. Dresselhaus was a musician.

In most cases the interviewees' human feelings shine through their words. Nobel laureates describe how the Prize affected their lives, research, and careers. Most are modest and admit the role of luck in their good fortune.

Many of the physicists worked on the Manhattan Project, and their beliefs about the decision to use the nuclear bombs against Japan are varied. None of the interviewees was in favor of U.S. President Ronald Reagan's flawed "Star Wars" project. Several scientists discussed their differences with other scientists and competitors. For example, according to Valentine L. Telegdi, Leon M. Lederman "… tried to defame our experiment. He tried to tell people that we never did our experiment, and that I invented our results, that I faked them!" (p. 171). Telegdi also stated: "Edward Teller suffers from a disease that has not been uncommon among Jewish people in the past two or three hundred years; he thinks that he is the messiah" (p. 185). A number of other interviewees expressed negative feelings about Teller.

However, most interviewees are well acquainted with each other and are mutually supportive, and their names often appeared in each other's interviews. Some offer suggestions as to Nobel-caliber scientists whose candidacy was overlooked, either because of the three-person rule for sharing a Prize, or for other reasons.

The question about differences between physics and chemistry provoked various responses: "The physicists at ETH considered chemists a lower form of life" (p. 164). "Chemistry is a matter of care, observation, and hard work. Physics begins with hard work and very often leads nowhere, but is always exciting" (p. 310). "Physics is much more of a macho thing than chemistry, at least in the U.S., but still once you're doing the work, it is all right to be a woman" (p. 552).

I also learned many surprising or little-known facts: although Murray Gell-Mann presented his Nobel address, he never submitted it for publication (p. 49); Telegdi picked up his wife on a Zürich street (p. 164); the Hiroshima (U-235) bomb was not tested, but the plutonium implosion bomb was (p. 301); radar was discovered independently by at least four different countries including England, the United States, France, and Germany (p. 327); Leo Szilard liked to be homeless, never had a home, and lived in hotel rooms (p. 461); and "[former] Secretary of State [George] Schultz is a Princetonian, a relatively intelligent man, except that he has a tiger tattooed on his behind" (p. 593).

The date and exact locale of each interview is provided, along with a biographical sketch. This volume contains more unpublished interviews than the two previous ones, and only five interviews had appeared in the same or different form in *The Chemical Intelligencer*. Twenty (more than half) of the interviewees are Nobel laureates, and several are recipients of the Wolf Prize in Physics, the National Medal of Science, and the Templeton Prize for Progress toward Research or Discoveries about Spiritual Realities. Only three of the scientists are women (Dresselhaus, Bréchignac, and Burnell), so further advances in the struggle against sexism are still needed. All three were married (the first two to scientists who are less famous than they are, and Burnell is divorced), and they explained how they balanced marriage and parenting with their careers.

More than a third of the interviewees are Jewish, so many of them discuss the issues of Judaism, the reasons for the preponderance of Jews among scientists of the first rank, the Holocaust, Israel, and anti-Semitism. Although many of the interviewees are not religious, as expected of a diverse group of highly individual persons with strong opinions, they do not always agree on this or other topics. Weinberg, Ne'eman, Telegdi, Bréchignac, Alferov, and Anderson are declared atheists, while most of the others are not religious in the formal, organized sense. Burnell and Taylor are Quakers, and in 1979 Polkinghorne resigned his Cambridge professorship and trained for the Anglican priesthood, in which he was ordained in 1982.

In response to the question about future trends, Wheeler predicted: "I think that in the first part of the next century we are going to have an enormous war bigger than any war we've ever had. I do not know how it is going to develop" (p. 429). On the other hand, Philip W. Anderson hoped "My wishful thinking is that physics will spread out more toward complexity, geophysics, cosmology, and astrophysics, and most of all, biology" (p. 600).

The interviews include one or several portraits, many photographed by István or Magdi. The volume contains 158 illustrations—formal and informal photos of interviewees both as adults and as children, their families, colleagues, students, equipment, experiments, medals, sculptures at the Fermilab, Fitch's parents' ranch, a Lego model, radar scope photographs, Ketterle's scientific "family tree", and fractal curves.

The Hargittais' questions appear in italics, and the much longer responses appear in Roman type. Three of the interviewees (Wigner, Oliphant, and Teller) are now deceased, emphasizing the importance of acquiring oral histories promptly. István corresponded with Teller up to a few weeks before his death and includes excerpts from two letters clarifying Teller's feelings about his characterization as "father of the hydrogen bomb," a designation that he despised.

A name index (10 double-column pages with boldface page numbers referring to interviews) is provided, but no subject index. A cumulative index of interviewees (three double-column pages) for all volumes published to date is included. The number of mistakes is small and limited to readily detected proper nouns, typographical errors, or grammatical errors made by the interviewees themselves.

I heartily recommend this attractive volume, suitable for either complete reading or browsing, to historians of physics and of science, to practicing scientists, and to students, who will surely benefit from these inspiring stories by some of the leading luminaries of physics.

George B. Kauffman
California State University
Fresno, CA (USA)

DOI: 10.1002/anie.200485395

 © 2006 Wiley-VCH Verlag GmbH & Co. KGaA, Weinheim

Catalyst Design

DOI: 10.1002/anie.200504353

Sequential One-Pot Reactions Using the Concept of "Site Isolation"

*Brigitte Voit**

Keywords:
heterogeneous catalysis · homogeneous catalysis · isolated active sites · one-pot reactions · synthetic methods

In modern synthetic chemistry researchers often emulate nature, as it easily masters highly selective reactions in complex systems and the construction of structurally advanced and functional molecules. Today drugs and synthetic or biomimetic macromolecules with very complex structures and with specific function can be prepared by multistep synthesis owing to great progress in catalysis and the development of highly selective reactions under mild reaction conditions, polymeric and inorganic catalyst supports, and automated supported synthesis. A limiting factor, or at least one determining costs, however, is the necessary isolation and purification of intermediates between reaction steps when the reactive components of one reaction step quench or deactivate the reagents of the subsequent step. If multistep reactions could be carried out in a single reactor in high yield without complex reactor design or specific purification procedures, biomimetic synthetic approaches as well as any technical process for the production of organic compounds would strongly profit.[1]

Already 25 years ago, Patchornik et al.[2] defined the principle and requirements of sequential multistep one-pot reactions, termed "wolf-and-lamb" reactions, involving insoluble polymeric reagents. They investigated two-stage reactions in which a starting material was modified successively by two polymeric transfer reagents. The analogous soluble reagents reacted with each other rapidly in solution, but they were rendered mutually inactive upon attachment to the respective polymeric phases. Thus, multipolymer systems of insoluble polymeric reagents were identified, being unique in that reactions can only take place within the matrix of the polymeric reagent. Since then, polymers with functional sites as solid supports in heterogeneous catalysis, for example in mixed-bed reactors, have been used widely.[3–5] This approach goes back to the ground-breaking work by Astle and Zaslowsky[6] and Manecke and Storck[7] on polymeric reagents. In recent investigations of sol–gel processes with encapsulated opposing reagents by Gelman et al.[8] the concept of "wolf-and-lamb" reactions has been rediscovered and has emerged as a powerful tool to probe "site-isolation" effects in cross-linked solid materials.

Recently, two new, impressively effective concepts for site isolation in one-pot multistep reactions have been reported that are very different in their details. Kaneda et al.[9] report on the parallel use of two types of layered clays as inorganic catalysts, acid and base, for one-pot heterogeneous catalysis. Quenching is not possible because of the specific location of the acidic and basic groups. In contrast, Fréchet and Hawker et al.[10] used core-confined catalytic sites, again acid and base, shielded by a star-shaped polymer architecture in one-pot multistep homogenous catalysis.

Layered clays, for example, Ti^{4+}-exchanged montmorillonite (Ti^{4+}-mont) and Mg–Al hydrotalcite (HT), $Mg_6Al_2(OH)_{16}CO_3$, are known to be strong Brønsted acids and bases, respectively, in organic synthesis.[11] Kaneda et al.[9] used these two types of inorganic catalysts in a single reactor. Ti^{4+}-mont is an excellent solid Brønsted acid catalyst as a result of the Ti^{4+} centers in the interlayer spacings. In contrast, HT is a promising solid base catalyst, and the surface of the particles display tunable basicity. Both active sites can now act independently without mutual destruction as acid and base in one-pot reaction sequences since the large HT particles cannot enter the narrow spaces between the layers of the Ti-mont (Figure 1).

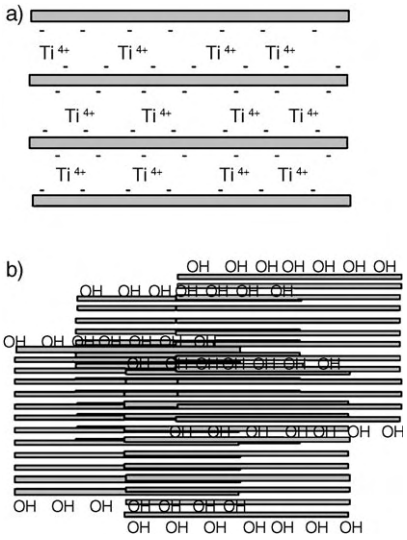


Figure 1. a) Ti^{4+}-mont as a Brønsted acid with isolated active sites and b) Mg-Al hydrotalcite (HT) as a solid base with basic groups on the surface.

[*] Prof. Dr. B. Voit
Leibniz-Institut
für Polymerforschung Dresden e.V.
Hohe Strasse 6
01069 Dresden (Germany)
Fax: (+49) 351-4658-565
E-mail: voit@ipfdd.de

InterScience
© 2006 Wiley-VCH Verlag GmbH & Co. KGaA, Weinheim

The authors demonstrate the potential of their concept with several examples. First, they describe a tandem reaction consisting of deprotection and aldol condensation starting from dimethyl acetal of benzaldehyde. The product was obtained in 93% yield only when both clay types were present. Even the production of the intermediate benzaldehyde was achieved only in 30% yield when Ti^{4+}-mont was applied alone, since then the missing aldol condensation step did not provide the necessary amount of water needed for complete reaction. A number of other aldol condensations with different starting materials were also effective as one-pot reactions; in addition a tandem reaction consisting of the introduction of a protecting group and a Michael addition was described. HT-supported palladium nanoparticles were also prepared which acted as hydrogenation catalyst and as base simultaneously.[12] In this way another type of catalytic site could be introduced and the number of reactions possible in a one-pot reaction sequence increased.

Scheme 1 outlines three- and four-step reaction sequences performed in one pot using Ti^{4+}-mont and HT, and Ti^{4+}-mont and Pd/HT, respectively. Cyanoacetic acid is converted in three steps in the presence HT into an epoxynitrile, a useful intermediate in heterocycle synthesis. When Pd/HT is employed, a hydrogenation step is possible, and after addition of acrylonitrile, 2-carbomethoxy-2-benzylglutaronitrile can be isolated in excellent yields. This demonstrates most convincingly how well the concept of site isolation works: the acid sites within the Ti^{4+}-mont layers are shielded from any negative interaction with the surface basic groups of the comparable large HT particles. At the same time, the acidic and basic sites are easily accessible for the organic compounds in solution.

In contrast, the concept described by Fréchet and Hawker et al.[10] is intended for a fully homogenous and organic catalytic system and is related to the polymer-based catalysts employed by Manecke[7] and Patchornik et al.[2] Isolation of the catalytic sites is achieved by preparing a starlike structure where the core-confined catalytic sites are shielded by polymer chains. How effectively a polymeric shell can shield highly reactive sites was demonstrated by Nuyken et al.[13] In their "micellar catalysis" approach a metathesis catalyst was shielded from the surrounding water in the micelle "core" formed by amphiphilic polyoxazoline block copolymers.

In their work Fréchet and Hawker et al.[10] prepared star polymers by the "arm-first" approach using nitroxide-mediated living radical polymerization. Thus, a polystyrene macroinitiator was prepared and subsequently used to copolymerize styrene, phenyl-4-styrenesulfonate, and divinylbenzene simultaneously, resulting in a cross-linked core shielded by many polystyrene arms. The phenylsulfonate esters were then hydrolyzed and acidified, leading to the active acid catalyst. As a result of the controlled synthetic methods, high control over the arm length and the total molar mass and molar mass could be achieved (polydispersity (PDI) = 1.19, M_w = 260000 g mol^{-1}) leading to roughly 100 catalytic sites per molecule. The corresponding core-confined amino base (PDI = 1.86, M_w = 640000 g mol^{-1}) with about 350 catalytic groups per molecule was prepared in the same way, but now the reactive core comonomer was a styrene with a pendant (methyl-(pyridyl)amino)methyl unit and poly-(*N*-isopropylacrylamide) macroinitiators served as arms (Figure 2).

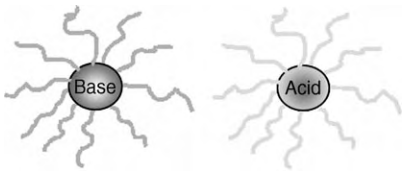
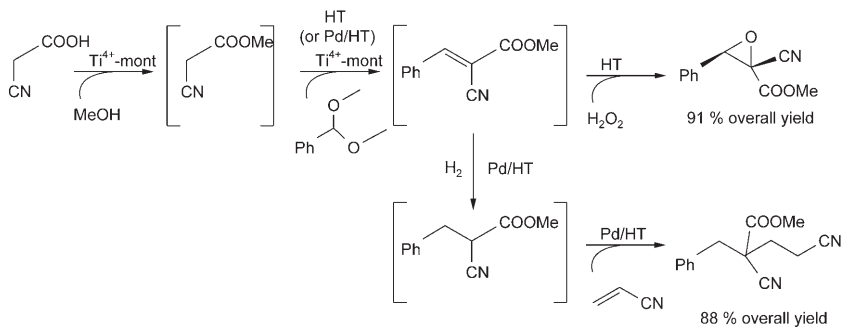


Figure 2. A star-shaped polymer with core-confined acidic and basic sites.[10] Basic group: -CH_2-N(CH_3)-py (py = 4-pyridyl); acidic group: -C_6H_4-SO_3H.

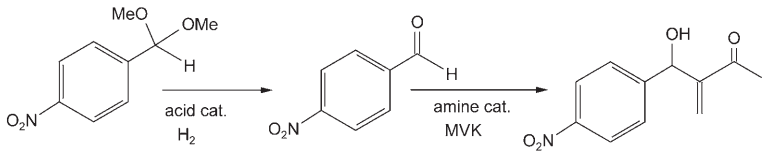
The obtained high-molecular-weight star polymers with the core-confined catalytic sites were fully soluble in organic solvents like DMF, but the acidic reactive sites were fully shielded from the basic reactive sites in the corresponding cores. However, low-molecular-weight compounds could easily penetrate the polymeric shell and had the necessary access to the catalytic sites to be converted to the desired products. The authors demonstrated the effectiveness of their concept on the acid-catalyzed deprotection of 4-nitrobenzaldehyde dimethyl acetal and the subsequent nucleophilic amine-base-catalyzed Baylis–Hillman reaction of 4-nitrobenzaldehyde with methyl vinyl ketone (MVK, Scheme 2). Only in the presence of both polymer-bound and core-confined catalysts was the Baylis–Hillman adduct obtained in 65% yield. No other combination, for example free *p*-toluene sulfonic acid (PTSA) and dimethylaminopyridine (DMAP) together or in combination with one of the star-shaped polymeric catalysts, resulted in the final products. Also the intermediate, 4-nitrobenzaldehyde, was observed in all other cases only in traces owing to deactivation of the acid catalyst by the base.

An additional control experiment proved further that simply polymer-bound catalysts are not sufficient; effective shielding of the active sites from each other is essential. Block copolymers of the same composition as the star



Scheme 1. One-pot multistep reaction sequence possible by using Ti^{4+}-mont, which has isolated Brønsted acid sites, and Mg–Al hydrotalcite (HT), which has active basic sites on the surface. Alternatively, Pd/HT can as serve as a catalyst instead of HT.[9]

 © 2006 Wiley-VCH Verlag GmbH & Co. KGaA, Weinheim



Scheme 2. One-pot reaction sequence consisting of deprotection and the Baylis–Hillman reaction carried out by using a star-shaped polymer with core-confined acidic and basic groups.[10].

polymers but prepared without the cross-linking agent divinyl benzene and thus not showing any core–shell-type structure could not be used to carry out the one-pot reaction sequence shown in Scheme 2. So far, the yields of the described reaction are not as high as those of the tandem reactions described by Kaneda et al.,[9] and only a two-step reaction sequence has been studied. However, this is clearly the first example of site isolation for a reaction sequence in a homogenous catalytic system. It can be expected that many more examples will come, quickly allowing for very complex reaction sequences in one pot since the concept of polymeric reagents shows great flexibility in catalytic sites that can be attached to or integrated in the polymeric chain.

Both concepts of site isolation, although very different in detail, mean a big step forward towards the challenging goal of simplifying multistep organic reaction sequences and providing the synthetic tools for the engineering of complex and/or biomimetic molecules.

Published online: May 26, 2006

[1] Review: K. C. Nicolaou, T. Montagnon, S. A. Snyder, *Chem. Commun.* **2003**, 551 – 564.
[2] B. J. Cohen, M. A. Kraus, A. Patchornik, *J. Am. Chem. Soc.* **1981**, *103*, 7620 – 7629.
[3] W. T. Ford in *Polymeric Reagents and Catalysts*, *ACS Symposium Series 308* (Ed.: W. T. Ford), ACS, Washington DC, **1986**, chap. 11, pp. 247 – 285.
[4] P. M. Lange, F. Martinola, S. Oeckl, *Hydrocarbon Process.* **1985**, *12*, 51.
[5] W. Neier, *Chem. Ind.* **1981**, *33*, 632.
[6] M. J. Astle, J. A. Zaslowsky, *Ind. Eng. Chem.* **1952**, *44*, 2867 – 2871.
[7] G. Manecke, W. Storck, *Encycl. Polym. Sci. Eng.* **1986**, *5*, 725 – 755; G. Manecke, W. Storck, *Angew. Chem.* **1978**, *90*, 691 – 704; *Angew. Chem. Int. Ed. Engl.* **1978**, *17*, 657 – 670.
[8] F. Gelman, J. Blum, D. Avnir, *New J. Chem.* **2003**, *27*, 205 – 207; F. Gelman, J. Blum, D. Avnir, *Angew. Chem.* **2001**, *113*, 3759 – 3761; *Angew. Chem. Int. Ed.* **2001**, *40*, 3647 – 3649; F. Gelman, J. Blum, D. Avnir, *J. Am. Chem. Soc.* **2000**, *122*, 11 999 – 12 000.
[9] K. Motokura, N. Fujita, K. Mori, T. Mizugaki, K. Ebitani, K. Kaneda, *J. Am. Chem. Soc.* **2005**, *127*, 9674 – 9675.
[10] B. Helms, S. J. Guillaudeu, Y. Xie, M. McMurdo, C. J. Hawker, J. M. J. Fréchet, *Angew. Chem.* **2005**, *117*, 6542 – 6545; *Angew. Chem. Int. Ed.* **2005**, *44*, 6384 – 6387.
[11] K. Motokura, D. Nishimura, K. Mori, T. Mizugaki, K. Ebitani, K. Kaneda, *J. Am. Chem. Soc.* **2004**, *126*, 5662.
[12] K. Motokura, N. Fujita, K. Mori, T. Mizugaki, K. Ebitani, K. Kaneda, *Tetrahedron Lett.* **2005**, *46*, 5507 – 5510.
[13] J. O. Krause, M. T. Zarka, U. Anders, R. Weberskirch, O. Nuyken, M. R. Buchmeiser, *Angew. Chem.* **2003**, *115*, 6147 – 6151; *Angew. Chem. Int. Ed.* **2003**, *42*, 5965 – 5969.

 © 2006 Wiley-VCH Verlag GmbH & Co. KGaA, Weinheim

Low-Coordinate Compounds

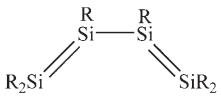
DOI: 10.1002/anie.200601414

A Stable Silylenoid and a Donor-Stabilized Chlorosilylene: Low-Coordinate Silicon Compounds—A Never-Ending Story?

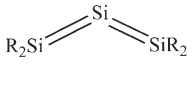
*Manfred Weidenbruch**

Keywords:
halogens · low-coordinate compounds · silicon · silylenes · silylenoids

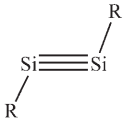
As recently as 25 years ago, molecular compounds that contained silicon atoms with a coordination number of less than four were considered solely in terms of reactive intermediates that could not be isolated. This state of affairs changed in 1981 when West, Fink, and Michl reported the formation of the first stable molecule containing an Si–Si double bond.[1] Since then, more than 50 compounds with this structural constituent have been described.[2] The last ten years have witnessed the appearance of the tetrasilabuta-1,3-diene **1**,[3] a spiropentasiladiene,[4] the trisilaallene **2**,[5] and, provisionally, the first disilynes **3** with an Si–Si triple bond.[6]



1

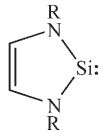


2

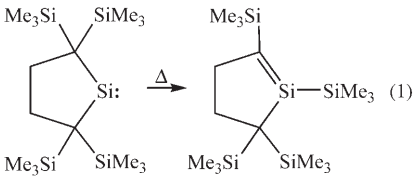


3

The same is true for the more-or-less stable diamino silylenes,[7] for example **4**, and the donor-atom-free silylene **5**,



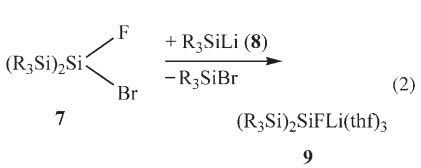
4



5 **6**

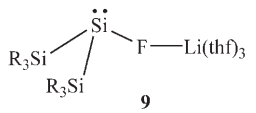
which, however, readily undergoes isomerization to the silene **6** with an endocyclic Si–C double bond [Eq. (1)].[8] The cation $[Cp^*Si]^+$ ($Cp^* = C_5Me_5$), a derivative of SiH^+, formally belongs to this series, but, owing to the η^5 coordination of the Cp* ring, should rather be counted as a higher-coordinate silicon compound.[9]

The chemistry of low-coordinate silicon compounds is by no means complete, as has impressively been demonstrated by the formation and characterization of a stable silylenoid and a tricoordinate chlorosilylene. Reaction of the bromofluorosilane **7** ($R_3Si = tBu_2MeSi$) with the silyl lithium compound **8** in THF resulted in yellow crystals of the fluorosilylenoid **9** [Eq. (2)], which was characterized not only by an X-ray crystal structure analysis but also by high-level molecular calculations.[10] The central silicon atom of **9** has a trigonal pyramidal environment consisting of the two silyl groups and the fluorine atom. According to calculations on the model compound **9′**,

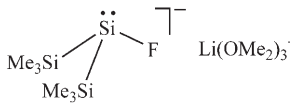


7 **9**

(2)



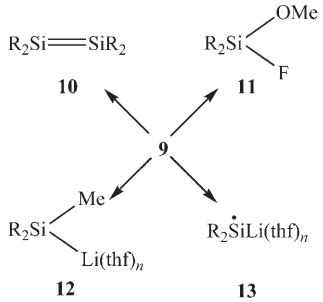
9



9′

the silylenoid exists predominantly as an ion pair with an almost completely ionic Si–F bond.

Thus, not surprisingly, photolysis or thermolysis of **9** proceeds through elimination of LiF to afford the known disilene **10**.[11] Furthermore, depending on the nature of the reaction partner, **9** can react not only as a nucleophile but also as an electrophile. Thus, for example, reaction with methanol furnishes the silane **11**, and the reaction with methyllithium affords the silyl lithium compound **12**. Reactions with lithium or



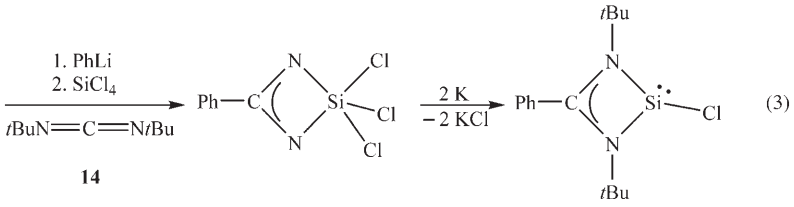
10 **11** **12** **13**

[*] Prof. Dr. M. Weidenbruch
Institut für Reine und Angewandte Chemie
Universität Oldenburg
Postfach 25 03
26111 Oldenburg (Germany)
Fax: (+49) 441-798-3352
E-mail:
manfred.weidenbruch@uni-oldenburg.de

© 2006 Wiley-VCH Verlag GmbH & Co. KGaA, Weinheim

tert-butyllithium give rise to the radical **13**, which was recently obtained by a different route.[12]

The chlorosilylene **16** similarly contains a tricoordinate silicon atom and was first prepared by Roesky et al.[13] by the following route. Treatment of the carbodiimide **14** with phenyllithium and subsequent reaction with $SiCl_4$ gave the silane **15**. Reductive elimination of chlorine was effected by treatment with potassium to afford colorless crystals of compound **16** in low yield [Eq. (3)].



(3)

An X-ray crystallographic analysis of **16** showed that the amidinate group is bonded to the silicon atom in a chelate-type manner and, together with the chlorine atom, forms a trigonal pyramidal geometry at the silicon atom. Noteworthy is the acute N-Si-N angle of 68.35°, which, according to natural bond orbital (NBO) calculations, results from the overlap of two orbitals of the nitrogen atoms with predominantly s character and a purely p orbital from the silicon atom. The bonding situation in **16** is comparable with that of $[\{(SiMe_3)C(PMe_2\}_2Si]$,[14] in which, however, the silicon atom has a coordination number of four.

Compound **16** is the first thermally stable chlorosilylene. Although gaseous silicon dichloride can be generated by the high-temperature reaction of silicon with silicon tetrachloride, on cooling it forms perchloropolysilane $(SiCl_2)_n$.[15,16] Astonishingly, the carbon analogues of **9** and **16** have not yet been reported. It may be anticipated that the reactive Si–Cl bond in **16** will provide synthetic access to other thermally stable silicon(II) compounds.

[1] R. West, M. J. Fink, J. Michl, *Science* **1981**, *214*, 1341.

[2] Recent review articles: a) P. P. Power, *Chem. Rev.* **1999**, *99*, 3463; b) M. Weidenbruch in *The Chemistry of Organic Silicon Compounds*, *Vol. 3* (Eds.: Z. Rappoport, Y. Apeloig), Wiley, Chichester, **2001**, chap. 5, p. 391.

[3] M. Weidenbruch, S. Willms, W. Saak, G. Henkel, *Angew. Chem.* **1997**, *109*, 2612; *Angew. Chem. Int. Ed. Engl.* **1997**, *36*, 2503.

[4] T. Iwamoto, C. Kabuto, M. Kira, *J. Am. Chem. Soc.* **1999**, *121*, 886.

[5] S. Ishida, T. Iwamoto, C. Kabuto, M. Kira, *Nature* **2003**, *421*, 725.

[6] a) N. Wiberg, W. Niedermayer, G. Fischer, H. Nöth, M. Suter, *Eur. J. Inorg. Chem.* **2002**, 1066; b) A. Sekiguchi, R. Kinjo, M. Ichinohe, *Science* **2004**, *305*, 1755; c) N. Wiberg, S. K. Vasisht, G. Fischer, P. Mayer, *Z. Anorg. Allg. Chem.* **2004**, *630*, 1823; d) Highlight: M. Weidenbruch, *Angew. Chem.* **2005**, *117*, 518; *Angew. Chem. Int. Ed.* **2005**, *44*, 514.

[7] a) M. Denk, R. Lennon, R. Hayashi, R. West, A. V. Belyakov, H. P. Verne, A. Haaland, M. Wagner, N. Metzler, *J. Am. Chem. Soc.* **1994**, *116*, 2691; b) B. Gerhus, M. F. Lappert, J. Heinicke, R. Boese, D. Bläser, *J. Chem. Soc. Chem. Commun.* **1995**, 1931; c) J. Heinicke, A. Oprea, M. K. Kindermann, T. Karpati, L. Nyulászi, T. Veszprémi, *Chem. Eur. J.* **1998**, *4*, 541.

[8] M. Kira, S. Ishida, T. Iwamoto, C. Kabuto, *J. Am. Chem. Soc.* **1999**, *121*, 9722.

[9] P. Jutzi, A. Mix, B. Rummel, W. W. Schoeller, B. Neumann, H.-G. Stammler, *Science* **2004**, *305*, 849.

[10] G. Molev, D. Bravo-Zhivotovskii, M. Karni, B. Tumanskii, M. Botoshansky, Y. Apeloig, *J. Am. Chem. Soc.* **2006**, *128*, 2784.

[11] A. Sekiguchi, S. Inoue, M. Ichinoe, Y. Arai, *J. Am. Chem. Soc.* **2002**, *124*, 15160.

[12] D. Bravo-Zhivotovskii, I. Ruderfer, S. Melamed, M. Botoshansky, B. Tumanskii, Y. Apeloig, *Angew. Chem.* **2005**, *117*, 749; *Angew. Chem. Int. Ed.* **2005**, *44*, 739.

[13] C.-W. So, H. W. Roesky, J. Magull, R. B. Oswald, *Angew. Chem.* **2006**, *118*, 4052; *Angew. Chem. Int. Ed.* **2006**, *45*, 3948.

[14] H. H. Karsch, U. Keller, S. Gamper, G. Müller, *Angew. Chem.* **1990**, *102*, 297; *Angew. Chem. Int. Ed. Engl.* **1990**, *29*, 295.

[15] M. Schmeisser, P. Voss, *Z. Anorg. Allg. Chem.* **1964**, *334*, 50.

[16] J. R. Koe, D. R. Powell, J. J. Buffy, S. Hayase, R. West, *Angew. Chem.* **1998**, *110*, 1514; *Angew. Chem. Int. Ed.* **1998**, *37*, 1441.

 © 2006 Wiley-VCH Verlag GmbH & Co. KGaA, Weinheim

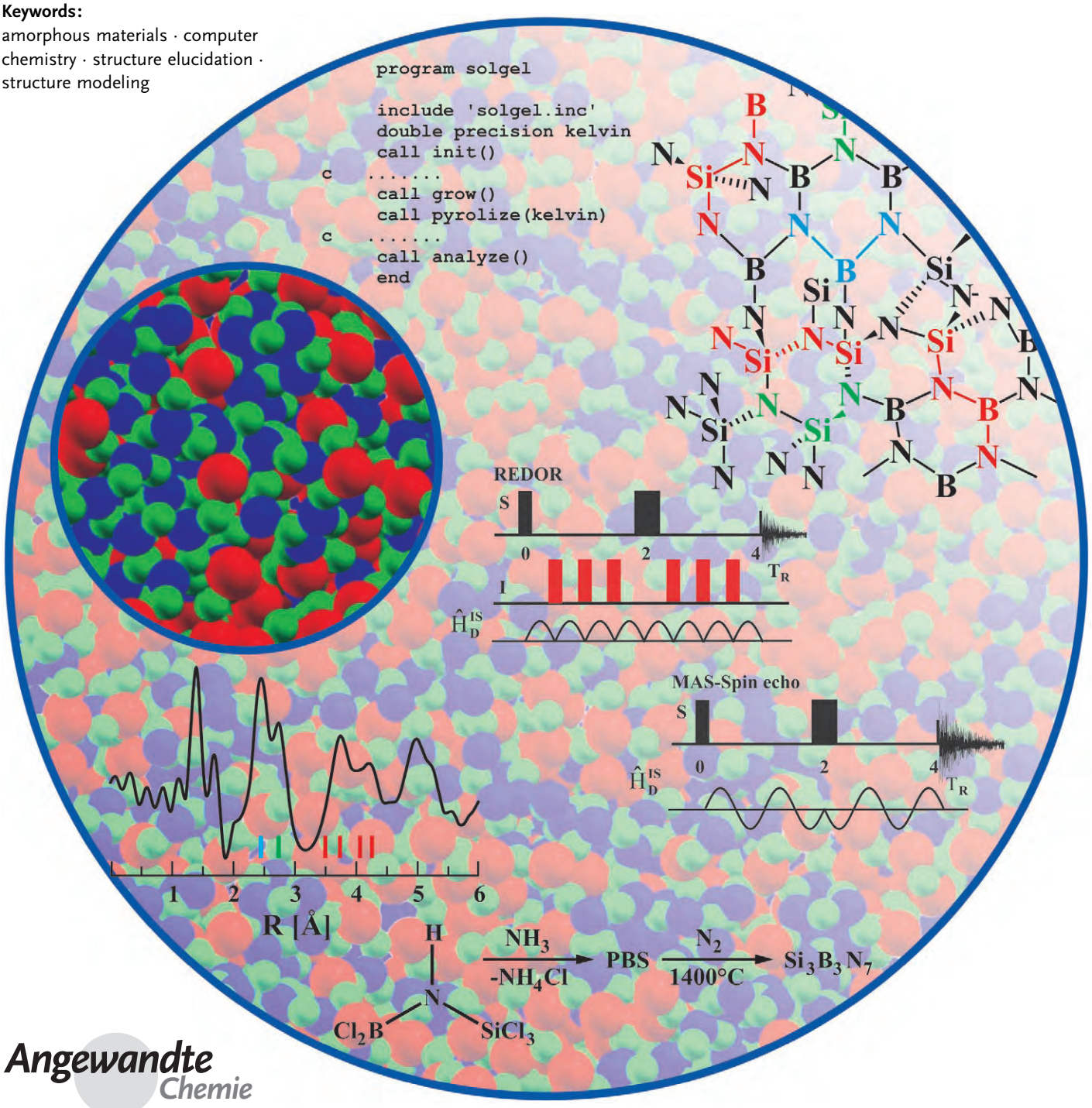
Amorphous Compounds

DOI: 10.1002/anie.200504193

The Route to the Structure Determination of Amorphous Solids: A Case Study of the Ceramic $Si_3B_3N_7$

Martin Jansen, J. Christian Schön, and Leo van Wüllen*

Keywords:
amorphous materials · computer chemistry · structure elucidation · structure modeling



© 2006 Wiley-VCH Verlag GmbH & Co. KGaA, Weinheim

$Si_3B_3N_7$ is the parent compound of a new class of amorphous ceramics containing silicon, boron, nitrogen, and carbon that display a unique spectrum of properties. It consists of a random network in which the constituent elements are linked by predominantly covalent bonds. Similarly to quartz glass, the composition of amorphous $Si_3B_3N_7$ is virtually stoichiometric. As all three of its constituent elements can serve as the objects of various structural probes, $Si_3B_3N_7$ was selected as the basis of a systematic structural investigation, in which methods for the structure determination of solids without translational symmetry could be validated and improved. However, as the complete amorphous structure cannot be deduced from experimental data, these results must be complemented by computer simulations. Thus, five classes of structure models were generated and compared to experimental results. Only the models generated by following the actual synthesis route as closely as possible agreed well with the experimental data.

From the Contents

1. Introduction 4245

2. Experimental Approaches to the Determination of Characteristic Structural Features in $Si_3B_3N_7$ 4247

3. Theory 4255

4. Summary and Conclusion 4260

1. Introduction

1.1. Concepts

Among the states of condensed matter, those classified as "amorphous" are probably the least understood, and dealing with them remains a scientific challenge.[1–6] Most of the conceptual, experimental, and theoretical intricacies associated with this class of solids originate from their thermodynamic metastability. For every solid chemical compound there exists a sequence of crystalline polymorphs. Some of these are thermodynamically stable under appropriate conditions, while the remainder are only kinetically stable at sufficiently low temperatures.[7–9] However, for identical chemical compositions, an essentially infinite number of "amorphous" atomic configurations, contributing to different metastable states of the system, can be generated. Consequently, compounds for which different amorphous structures are accessible—a well-known example is amorphous ice[10,11]—can exhibit different macroscopic properties, depending on the synthesis route and the details of their pretreatment. The differing properties, thus, reflect the history of the compound.

The nonequilibrium character and history dependence of amorphous compounds are the major reasons for the difficulties encountered in defining a comprehensive and unambiguous classification of these compounds. The criteria of existing classifications, which are typically based on thermodynamics, structure, or chemical composition,[2,3,5] for the most part, apply only to selected aspects of amorphous compounds. We prefer a standardized definition that, on one hand, covers all phenomena related to noncrystalline solids, and on the other hand, allows a more subtle differentiation among these phenomena.

The essential features of an amorphous material or a glass are a lack of long-range translational order, as well as an inherent tendency to undergo structural changes over time. Thus, it is possible to differentiate the amorphous state from other states of matter through the use of a two-dimensional map with the coordinates "degree of static disorder" and "degree of dynamic disorder" (Figure 1). This diagram is subdivided into two regions by a line separating globally ergodic[12] and nonergodic systems. Of course, the location of this border cannot be absolutely determined, because whether a chemical system appears ergodic or not depends on the time span that the observer is willing, or able, to follow the evolution of a given material, and on the external conditions, such as temperature and pressure.[8] The diagram covers the full range of possible dynamic phenomena, including the transition to ergodic behavior, and differentiates amorphous compounds from materials with structural periodicity. In addition, this description encompasses all aspects of the chemistry and physics of nonperiodic materials, which are otherwise conventionally subsumed under the terms glass, random network, metallic glass, or amorphous solid. These collective terms stem from the different preparation methods, the special structural or physical properties, and the chemical natures of the compounds.

From a theoretical point of view, the key to understanding the static and dynamic properties of an amorphous compound is the structure of its energy landscape,[13–21] that is, the potential-energy hypersurface over the space of all atomic configurations of the system (the so-called configuration space). Of course, the full energy landscape of a chemical system contains both amorphous and crystalline regions, each being the union of a large number of configurations. Herein, we focus on the part of the landscape of $Si_3B_3N_7$ that contains the amorphous state.

[*] Prof. Dr. M. Jansen, Priv.-Doz. Dr. J. C. Schön, Priv.-Doz. Dr. L. van Wüllen[+]
Max-Planck-Institut für Festkörperforschung
Heisenbergstrasse 1, 70569 Stuttgart (Germany)
Fax: (+49) 711-689-1502
E-mail: m.jansen@fkf.mpg.de

[+] Present address:
Institut für Physikalische Chemie
Westfälische Wilhelms-Universität Münster
Corrensstrasse 30/36, 48149 Münster (Germany)

© 2006 Wiley-VCH Verlag GmbH & Co. KGaA, Weinheim

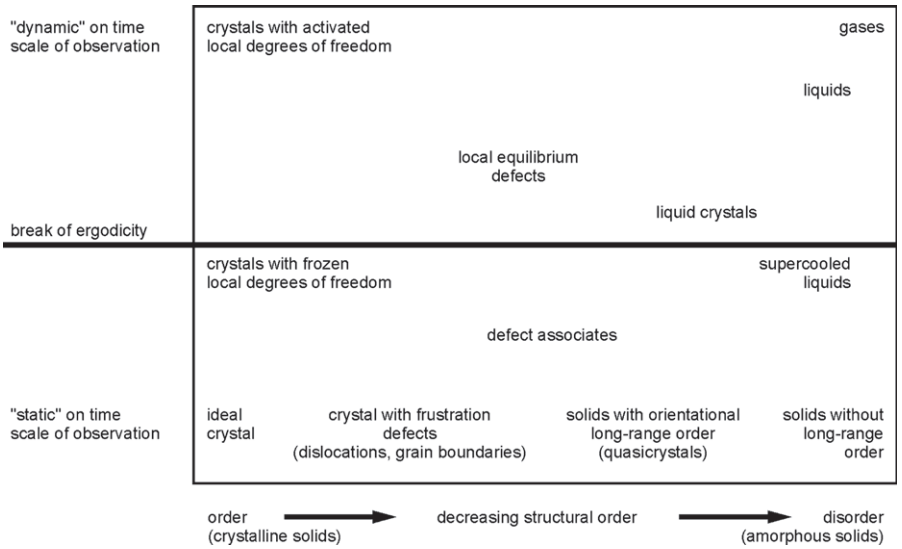


Figure 1. Placement of amorphous and other states of matter on a map with the coordinates "degree of dynamic disorder" and "degree of static disorder".

1.2. The Problem of Structure Determination for Amorphous Materials

As the properties of a solid crucially depend on the spatial arrangement of the atoms, knowledge of the microscopic structure of a material is an indispensable prerequisite for all attempts to understand and purposefully optimize its properties. The difficulty involved in determining the structures of amorphous compounds is one of the main reasons that these compounds have not always received their due attention.

Although experiments can yield valuable structural information, this information is diffuse, as a multitude of different atomic configurations can reproduce the experimental data within the error limits. Structure modeling with theoretical methods offers a possible solution. However, if we were to rely on theory alone, we would need to develop models that imitate an actual synthesis route, for example, the cooling of a melt, a pressure-induced amorphization, an atom-beam or vapor deposition, or a sol–gel process. Unless these different routes all lead to structurally identical amorphous compounds (that is, unless the details of the synthesis route are unimportant for the structure of the amorphous state) we face the currently impossible task of exactly reproducing the synthesis process in the simulation.

Clearly, if we want to surmount this barrier, it is necessary to combine experiment with theoretical modeling of the amorphous compound. In principle, amorphous atomic configurations of a given compound can be generated by employing advanced computational techniques with the incorporation of experimental information (without considering the actual synthesis route). However, innumerable plausible solutions will be obtained using this method, and there is no straightforward way to assign one of the simulated structure models to a real sample. Furthermore, each of the experimental structural probes provides only partial information. As the individual analytical tools reveal quite different features of the structure, it is difficult to correlate the results and to generate a complete and consistent structural model.

Therefore, our approach consists of first acquiring as many structural data as possible for the material under consideration. These findings are then combined with results from theoretical model calculations to produce a complete structural picture for the amorphous compound. On the theoretical side, a large ensemble of structural configurations must be generated. The region of this configuration space containing the real amorphous compound is then selected by taking the experimental data into account. The circle closes when the resulting structure reproduces the experimentally determined properties, validating its correctness.

1.3. The Case Study: $Si_3B_3N_7$

Ten years ago, the Sonderforschungsbereich 408 was founded in Bonn to develop appropriate theoretical and experimental methods for the elucidation of the "amorphous structures" of inorganic nonmetallic solids. One particularly fascinating compound investigated as part of this long-term



Martin Jansen studied chemistry at the Universität Giessen, where he gained his doctorate in 1973. After his habilitation in 1978, he accepted a professorial chair for inorganic chemistry at the Universität Hannover. In 1987, he moved to the Universität Bonn. Since 1998, he has been a member of the Scientific Council of the Max Planck Society and a director of the MPI for Solid-State Research in Stuttgart. His research interests include preparative solid-state chemistry, crystal chemistry, materials research, and the structure–property relationships of solids. He is a member of the Advisory Board of Angewandte Chemie.



J. Christian Schön studied physics at the Universität Bonn and at MIT, where he received his MSc in mathematical physics in 1982, and his PhD in theoretical solid-state physics in 1988. He then undertook postdoctoral studies at San Diego State University until the end of 1991. After being a visitor at the University of Odense, he was a postdoc at Copenhagen University. From 1993 to 1999, he worked at the Institute for Inorganic Chemistry of the Universität Bonn, where he completed his habilitation on energy landscapes of crystalline and amorphous solids in 1997. Since 1999, he has been working as a senior scientist at the MPI for Solid-State Research in Stuttgart.

 © 2006 Wiley-VCH Verlag GmbH & Co. KGaA, Weinheim

project was the amorphous silicon boron nitride $Si_3B_3N_7$. This compound consists of a novel prototypical random network of silicon and boron atoms, which are interconnected by nitrogen atoms through chemical bonds of predominantly covalent character.[22–28] The discovery of $Si_3B_3N_7$ was seminal to the exploration of a new class of amorphous ceramics for high-temperature applications, in the system Si/B/N/C.[22–32] In spite of their metastable character, these inorganic random networks exhibit high durability under thermal and mechanical loads. They surpass the well-known crystalline ceramics SiC and Si_3N_4 with respect to the combination of all properties relevant to high-temperature applications in air. For example, no weight loss is observed for amorphous $Si_3B_3N_7$ and $SiBN_3C$ up to approximately 1900 or 2150 K, respectively. The elastic constants of these materials are quite high (for example, the bulk modulus of $SiBN_3C$ is 200–300 GPa), and in spite of their low densities of approximately 1.8–1.9 $g\,cm^{-3}$, they exhibit a high fracture toughness.[23,26,27]

In contrast to many other amorphous materials of technological interest, $Si_3B_3N_7$ cannot be produced by conventional glass formation, that is, by quenching from a melt, the reason being that $Si_3B_3N_7$, and its binary components BN and Si_3N_4 melt incongruently under standard conditions. Nor has it been possible to produce $Si_3B_3N_7$ by sintering micrometer-sized powders of BN and Si_3N_4. Instead, a sol–gel synthesis starting from a single-component precursor such as $(SiCl_3)NH(BCl_2)$ (TADB) can be employed.[22] The use of monomers such as TADB, which contain two metalloid cations in the desired ratio linked by a nitrogen bridge, circumvents the concentration fluctuations in the preceramic polymer that result from the differing aminolysis reaction rates when two independent boron and silicon sources are used.[26,27] The periphery of the TADB molecule is fully functionalized by chlorine, which allows an easy polymerization of the intermediate amides through aminolysis and subsequent polycondensation (Figure 2). Thus, in the synthesis of amorphous $Si_3B_3N_7$, the precursor TADB molecules undergo aminolysis in NH_3, are subsequently linked into oligomers and polymers by condensation, and are finally pyrolyzed under an N_2 atmosphere to produce the ceramic.[22,23,26,33]

The resulting ceramic $Si_3B_3N_7$ is an air-stable white powder for which thermal decomposition, with the evolution of N_2, begins at 1900 K and proceeds rapidly at 2000 K. In diffraction experiments with X-rays (synchrotron radiation), neutrons, or electrons, Bragg reflections were not observed. The bulk composition of the product corresponds to $Si_3B_3N_7$, within the error limits of several analytical methods, and no variation in composition with synthesis charge was noticed. Furthermore, no lateral compositional inhomogeneities were observed to a resolution of 1 μm by energy dispersive X-ray (EDX) and wavelength dispersive X-ray (WDX) spectroscopy, or to a resolution of 1 nm by energy-filtered transmission electron microscopy (EFTEM).[34]

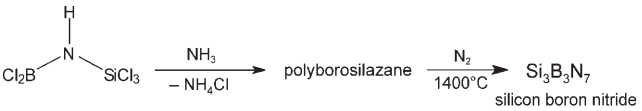


Figure 2. Synthesis of amorphous $Si_3B_3N_7$ starting from TADB.

While our investigations were motivated in part by the desire to better understand this new, promising class of ceramic materials, the main driving force was to utilize $Si_3B_3N_7$ as a case study, in which the tools available for analyzing the microstructures of amorphous materials could be tested and sharpened. This system has served us as a "*Drosophila*" for solid-state research. Only through the joint application of experimental and theoretical methods was it possible to develop a consistent structural model for amorphous $Si_3B_3N_7$.

2. Experimental Approaches to the Determination of Characteristic Structural Features in $Si_3B_3N_7$

2.1. Experimental Methods

The lack of translational periodicity in amorphous solids renders it impossible to follow the standard structure-determination protocol of using diffraction techniques to produce a complete three-dimensional structure in a single experiment. As a consequence, one has to resort to as many alternative structural probes as possible to study various structural aspects of the amorphous material. A successful strategy for the structure determination of an amorphous solid commences with a partition of the complex problem into the three categories of short-range order (1–2 Å), medium-range order (2–8 Å), and long-range order (> 8 Å).[35] Within each of these categories, as many different experimental tools as possible should be employed to probe the structural features, since the immanent distribution of bond lengths and angles often entails broad overlapping signals. These signals are difficult to disentangle, making an unambiguous interpretation problematic. Therefore, only the combined results of different experiments within a given category—yielding overlapping or complementary information—can pave the way to a successful description of the structure of an amorphous solid.

The microscopic tools available for the characterization of amorphous solids may be divided into three groups (Table 1): local probes, interference methods, and direct-imaging meth-



Leo van Wüllen studied chemistry at the Universität Münster and completed his doctorate there with Prof. Müller-Warmuth in 1993. After a two-year postdoctoral stay with Prof. Eckert and Prof. Ford at the University of California in Santa Barbara, he continued his research at the Universität Münster (1996) and then at the MPI for Solid-State Research in Stuttgart (1998–2003). In 2002, he completed his habilitation in physical chemistry at the Universität Münster, where he has continued his research on new NMR strategies for the characterization of the structure and dynamics of inorganic materials since 2003.

© 2006 Wiley-VCH Verlag GmbH & Co. KGaA, Weinheim

Table 1: Toolbox of probes that can be used to study the structural aspects of amorphous solids.

Local probes	Interference methods	Direct-imaging methods
IR Raman NMR EELS XANES XPS	PCFs from X-ray, neutron, and electron scattering experiments EXAFS	SEM AFM TEM

ods. Local probes that are frequently applied include infrared (IR) spectroscopy, Raman spectroscopy, X-ray photoelectron spectroscopy (XPS), X-ray absorption near-edge fine structure (XANES) spectroscopy, electron energy loss spectroscopy (EELS), and nuclear magnetic resonance (NMR) spectroscopy. Interference methods employing neutrons, electrons, or photons (X-rays) can be used to produce atomic pair correlation functions (PCFs) from which characteristic distances can be deduced. In recent years, direct-imaging techniques, such as atomic force microscopy (AFM),[36] scanning electron microscopy (SEM), or transmission electron microscopy (TEM), have evolved into very promising microscopic tools for elucidating structural aspects of amorphous solids to subnanometer or even atomic resolution.[37] In the following Sections, the body of experimental data obtained for $Si_3B_3N_7$ with the toolbox of available structural probes (Table 1) will be presented.

2.2. Experimental Results and Strategy

According to the approach to the structural characterization of amorphous solids described in Section 2.1, the first step is the evaluation of the short-range order (1–2 Å). In the case of $Si_3B_3N_7$ presented here, a set of complementary and overlapping approaches, including NMR and XANES spectroscopy, and scattering techniques, were employed. In a second step, the medium-range order (2–8 Å) of the material was addressed using dipolar solid-state NMR spectroscopic techniques and PCFs (from the various scattering techniques). In this step, information is harvested about the network connectivity—the interconnection of the polyhedral building blocks identified in the first step into an extended three-dimensional network. Long-range order is the focus of the final step. For $Si_3B_3N_7$, electron microscopic imaging techniques were used to investigate structural features at a length scale of >8 Å, including homogeneity and phase separation.

2.2.1. Short-Range Order

The short-range order of $Si_3B_3N_7$ was evaluated using solid-state NMR and XANES spectroscopy, and scattering techniques. The B K-edge XANES spectra of $Si_3B_3N_7$, cubic BN (c-BN), and hexagonal BN (h-BN) are shown in Figure 3a.[38,39] While the spectrum of h-BN is dominated by a strong $1s\rightarrow\pi^*$ resonance at 191.8 eV and a doublet at 198 eV ($1s\rightarrow\sigma^*$ resonances), in the spectrum of c-BN, the $1s\rightarrow\pi^*$

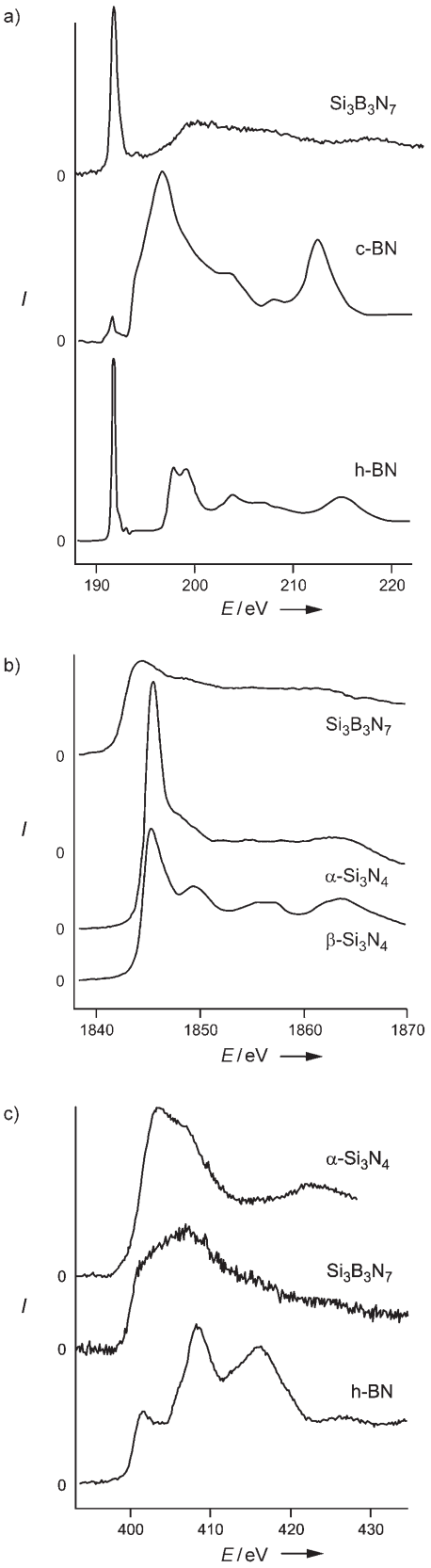


Figure 3. a) B K-edge XANES spectra of $Si_3B_3N_7$, c-BN, and h-BN.[38,39] b) Si K-edge XANES spectra of $Si_3B_3N_7$, α-Si_3N_4, and β-Si_3N_4.[40] c) N K-edge XANES spectra of $Si_3B_3N_7$, α-Si_3N_4, and h-BN.

 © 2006 Wiley-VCH Verlag GmbH & Co. KGaA, Weinheim

resonance is replaced by a strong 1s→σ* resonance at 198 eV. A comparison of these spectra to that of $Si_3B_3N_7$, in which a strong 1s→π* resonance is observed, suggests that the boron atoms in $Si_3B_3N_7$ are involved in planar BN_3 units comparable to those in h-BN. The Si K-edge XANES spectrum of $Si_3B_3N_7$ is shown in Figure 3b together with the spectra of α-Si_3N_4 and β-Si_3N_4.[40] The broad resonance at 1844 eV is indicative of the Si 1s→3p transition. The similarities (for example, in the position of the first peak) between the spectrum of $Si_3B_3N_7$ and those of the reference compounds α-Si_3N_4 and β-Si_3N_4 suggest that the silicon atoms in $Si_3B_3N_7$ are involved in SiN_4 groups. The N K-edge XANES spectra of $Si_3B_3N_7$, α-Si_3N_4, and h-BN are presented in Figure 3c. The resonances at 402–404 eV in the spectra of α-Si_3N_4 and h-BN originate from a 1s→π* transition, and the resonances at 406 or 408 eV, respectively, originate from a 1s→σ* transition. The spectrum of $Si_3B_3N_7$ can be interpreted as a superposition of the spectra of α-Si_3N_4 and h-BN and, thus, indicates a coexistence of various approximately trigonal-planar $NB_{3-x}Si_x$ $(0 \le x \le 3)$ environments. As an important conclusion, XANES spectroscopy indicates that trigonal-planar BN_3 and tetrahedral SiN_4 species are the two main constituents of the inorganic network in $Si_3B_3N_7$.

Further evidence for the existence of these network polyhedra can be gained by inspection of the PCFs obtained from neutron,[41,42] electron,[34] and X-ray (synchrotron radiation)[41] scattering experiments. The PCFs determined from these experiments are plotted in Figure 4, and the peak maxima relevant for the characterization of the short-range order are listed in Table 2. Considering all of the possible element–element bonds in $Si_3B_3N_7$ (Si–Si, Si–B, Si–N, B–B, B–N, N–N), the first peak maximum in the PCFs is only consistent with a B–N bond in a trigonal-planar BN_3 environment. The B–N bond length in the trigonal-planar BN_3 units of h-BN is 1.45 Å, while that in the tetrahedral BN_4 units of c-BN is 1.56 Å. Noting the Si–N bond lengths of 1.71–1.75 Å in α-Si_3N_4, the second peak maximum in the PCFs can be assigned to Si–N bonds. In addition, as the assignment of bonds is unambiguous, coordination numbers can be calculated from the PCFs. For silicon and boron, the numbers of nitrogen neighbors determined from this analysis are 3.7–3.8 and 2.8–2.9, respectively. The scattering experiments, thus, lend definite support to the suggestion given above that BN_3 and SiN_4 units are the basic building blocks of the network in $Si_3B_3N_7$.

To confirm these results and to check for the presence of additional local species, high-resolution magic angle spinning (MAS) NMR spectroscopy was performed on $Si_3B_3N_7$, as an additional independent probe. In MAS experiments, the internal interactions whose orientational dependencies scale with the second Legendre polynomial $(P_2(\cos\beta) = 0.5(3\cos^2\beta - 1))$, that is, the chemical-shift interaction, the homo- and heteronuclear dipolar couplings, and the first-order quadrupolar interaction, are averaged out by rapidly rotating the sample about an axis oriented at 54.7° relative to the magnetic field. The ^{11}B, ^{15}N, and ^{29}Si MAS NMR spectra of $Si_3B_3N_7$ are compiled in Figure 5. For the spin-$^1/_2$ nuclei ^{15}N and ^{29}Si, only the isotropic part of the chemical-shift tensor survives the MAS process. The isotropic chemical shift δ_{iso} of

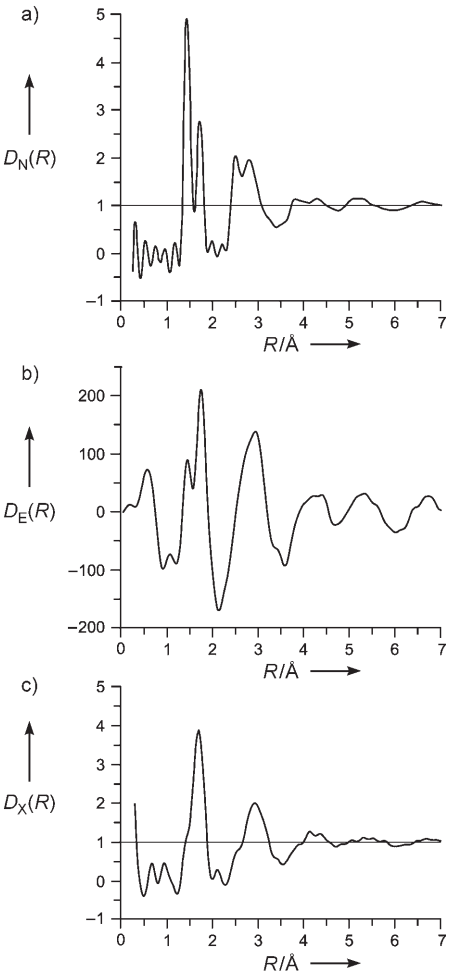


Figure 4. Total PCFs from a) neutron ($D_N(R)$; $Q_{max} = 50$ Å^{-1}),[41,42] b) electron ($D_E(R)$; $Q_{max} = 30$ Å^{-1}),[34] and c) X-ray ($D_X(R)$; $Q_{max} = 24$ Å^{-1})[41] scattering experiments on $Si_3B_3N_7$. *R* is the internuclear distance; Q_{max} is the maximum momentum transfer; the horizontal lines in (a) and (c) are to guide the eye.

Table 2: Positions [Å] of the first and second peak maxima in the PCFs from electron, X-ray, and neutron scattering experiments on $Si_3B_3N_7$.

Scattering method	First peak	Second peak
Electron	1.44	1.72
X-Ray	1.41	1.71
X-Ray ^{11}B[a]	1.40	1.72
Neutron	1.45	1.72

[a] On a $Si_3{}^{11}B_3N_7$ sample.

−45.5 ppm observed for the ^{29}Si nuclei in $Si_3B_3N_7$ suggests that the silicon atoms occupy tetrahedral coordination environments of nitrogen atoms (for example, for α-Si_3N_4 $\delta_{iso} = -46$ and −48 ppm),[43,44] confirming the results mentioned above. To obtain an acceptable signal-to-noise ratio in the ^{15}N MAS NMR spectrum of $Si_3B_3N_7$, a sample enriched to 100% with the isotope ^{15}N was necessary. A slightly asymmetric, broad, and featureless signal at 59 ppm with a half width of 25 ppm can be identified in the spectrum. The chemical-shift range of this signal encompasses the chemical

 © 2006 Wiley-VCH Verlag GmbH & Co. KGaA, Weinheim

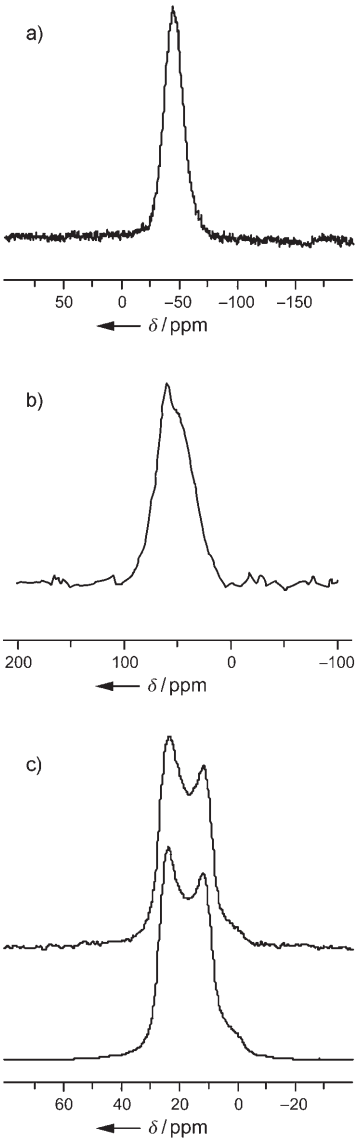


Figure 5. a) ^{29}Si, b) ^{15}N, and c) ^{11}B MAS NMR spectra of $Si_3B_3N_7$.[44] The lower curve in (c) is a simulation of the ^{11}B MAS NMR spectrum with the parameters given in the text.

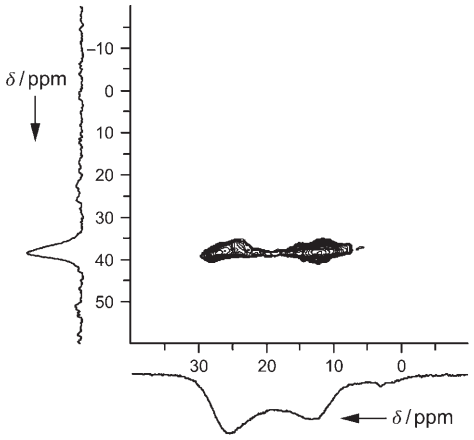


Figure 6. Two-dimensional ^{11}B MQMAS NMR spectrum of $Si_3B_3N_7$, as well as projections onto the vertical F_1 and horizontal F_2 frequency axes. In the projection onto the F_1 axis, only one isotropic signal, assigned to trigonally coordinated boron, is observed.

shifts for ^{14,15}N nuclei in h-BN at 63 ppm[45,46] and in α-Si_3N_4 at 30 ppm.[47] This evidence points to a mixed $NB_{3-x}Si_x$ environment; however, a further deconvolution of the signal into contributions from the different building units was not possible.

Unlike the spectra for the spin-$^1/_2$ nuclei ^{15}N and ^{29}Si, which are determined solely by the isotropic chemical shift, the MAS NMR spectra of the spin-$^3/_2$ nucleus ^{11}B in $Si_3B_3N_7$ are dominated by second-order quadrupolar coupling, the only interaction that scales with the fourth Legendre polynomial and that is, thus, not completely averaged out by the MAS process. A simulation of the line shape observed in the MAS NMR spectrum (lower curve in Figure 5c) yields an isotropic chemical shift δ_{iso} of 30.4 ppm, a quadrupolar coupling constant C_Q of 2.9 MHz, and an asymmetry parameter η_Q of 0.1. These values are in excellent agreement with those published for h-BN ($\delta_{iso} = 30.4$ ppm, $C_Q = 2.9$ MHz, $\eta_Q = 0$).[46,48] However, the possibility that a minor fraction of the boron atoms in $Si_3B_3N_7$ are involved in tetrahedral BN_4 units cannot be excluded on the basis of the MAS NMR spectroscopy. The ^{11}B signal for such a species would resonate at 0–5 ppm and would, therefore, overlap with the quadrupole-broadened resonance of the boron nuclei in BN_3 environments, possibly escaping detection. This problem can be overcome by employing techniques capable of averaging the fourth Legendre polynomial. Among the various strategies developed—dynamic angle spinning (DAS),[49,50] double rotation (DOR),[51,52] and multiple quantum MAS (MQMAS)[53–57]—the latter has attracted much attention because of the versatility and ease of use of the approach.

In MQMAS NMR spectroscopy, the evolution of a multiple quantum coherence is correlated with the evolution of a single quantum coherence in a two-dimensional experiment under conditions of fast MAS. This approach results in a separation of the isotropic chemical shift and the quadrupole-broadened line shape. The ^{11}B MQMAS NMR spectrum of $Si_3B_3N_7$ is plotted in Figure 6. The projection onto the horizontal F_2 frequency axis represents the conventional MAS NMR spectrum of $Si_3B_3N_7$, whereas the projection onto the vertical F_1 frequency axis produces the isotropic spectrum; the quadrupole broadening is effectively eliminated in this projection. The fact that only one isotropic resonance at 30.5 ppm is observed confirms that exclusively trigonally coordinated boron species are present in $Si_3B_3N_7$.

The combined results from the scattering experiments and MAS NMR spectroscopy allow a deeper insight into the distribution of local strain within the amorphous network. As the various scattering experiments produce rather sharp maxima in their respective PCFs, indicating a relatively narrow distribution of bond lengths within the amorphous network, the extremely broad line width in the ^{29}Si MAS NMR spectrum necessarily originates in a wide

 © 2006 Wiley-VCH Verlag GmbH & Co. KGaA, Weinheim

distribution of N-Si-N bond angles. Together with the comparatively marginal line broadening in the ^{11}B (MQ)MAS NMR spectra, which is a consequence of the rigidity of the BN_3 units, these findings imply that in $Si_3N_3B_7$ the majority of the local deformations that are inherently present in an amorphous network are located within the SiN_4 tetrahedra.

2.2.2. Medium-Range Order

The combined results from the various local probes unambiguously identified trigonal-planar BN_3 and tetrahedral SiN_4 units as the network-forming polyhedra of amorphous $Si_3N_3B_7$. The next logical step in the structure elucidation involves the investigation of the interconnection of these local building units into an extended three-dimensional network. To determine this medium-range order, predominantly two sources of information can be tapped. One strategy involves analyzing the PCFs to longer distances (2–5 Å). As shown in Figure 4, the PCFs exhibit distinct maxima at 2.5–3.0 and 4.3 Å. The maxima at 2.49 and 2.9 Å discernable in the neutron PCF are typical signatures of adjacent nitrogen atoms within a BN_3 triangle or a SiN_4 tetrahedron, respectively. Further information is not readily available from the PCFs, as the inherent shortcoming of this approach, the lack of elemental selectivity, entails a severe overlap of the signatures of partial PCFs for different atom pairs. This problem can be at least partially overcome by employing isotopic contrast techniques that rely on the different scattering lengths b_i of two isotopes of the same element (for example, $b_i(^{14}N) = 9.37 \times 10^{-15}$ m, $b_i(^{15}N) = 6.44 \times 10^{-15}$ m).

The results of neutron scattering experiments on $Si_3B_3N_7$ using isotopic contrast variation for nitrogen are shown in Figure 7. By taking the Fourier transform of the difference of

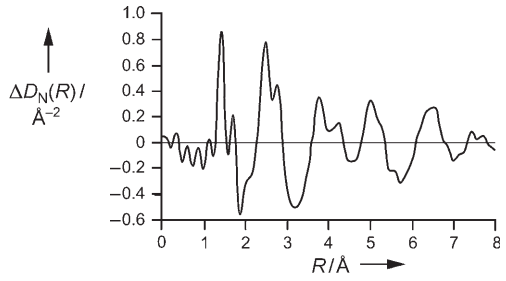


Figure 7. Fourier transform $\Delta D_N(R)$ of the first-order difference function $\Delta N(Q)$ determined from neutron scattering experiments on $Si_3{}^{11}B_3N_7$ and $Si_3{}^{11}B_3{}^{15}N_7$. The Fourier transform corresponds to a PCF containing only distances R involving nitrogen.[41]

the intensities measured for two samples with different isotopic concentrations (in this case, $Si_3{}^{11}B_3N_7$–$Si_3{}^{11}B_3{}^{15}N_7$), the contribution of atom pairs not containing nitrogen can be filtered out of the total PCF.[41,42] The noticeably reduced intensity of the maximum at 2.74 Å in the difference function (Figure 7) presents clear evidence that this peak arises from an atom pair not involving nitrogen. This result necessarily indicates a Si–B correlation and is the first indirect experimental evidence of Si-N-B connectivity within the amorphous network of $Si_3B_3N_7$.

Solid-state NMR spectroscopy offers more direct evidence of Si-N-B connectivity and allows its quantification. At this length scale, the magnetic dipolar interactions, which are characterized by the dipolar coupling constant D [Eq. (1)],

$$D = \frac{\gamma_I \gamma_S \frac{\mu_0}{4\pi} \hbar}{2\pi r^3} \quad (1)$$

can be utilized to analyze structural features. In Equation (1), γ_I and γ_S denote the magnetogyric ratios for the two different nuclei involved, r corresponds to their separation, μ_0 is the permeability of vacuum, and $\hbar$ is the Planck constant over 2π. The heteronuclear dipolar interaction, normally averaged out by the process of MAS, can be selectively re-introduced by employing advanced pulse techniques such as rotational echo double resonance (REDOR)[58–63] or rotational echo adiabatic passage double resonance (REAPDOR).[64–66] The common physical basis of these approaches is the manipulation of the dipolar interaction through rotor-synchronized radio-frequency pulses, as illustrated in Figure 8 for the REDOR

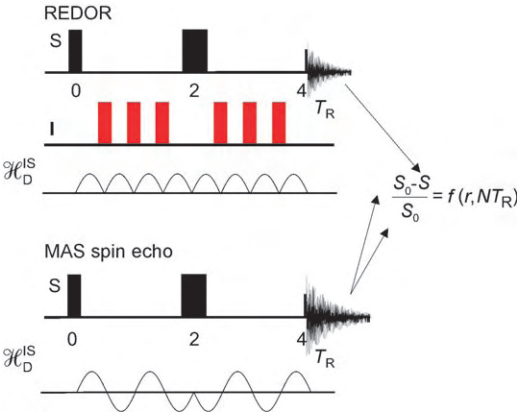


Figure 8. The principle of REDOR. The heteronuclear dipolar interaction between nuclei S and I described by the Hamiltonian $\mathcal{H}_D^{IS}$, averaged out over one rotor period T_R, is reintroduced by rotor-synchronized pulses for the I-spin species. The S-spin signal is detected using a rotor-synchronized spin-echo sequence. The dipolar coupling between the I and S spins leads to an attenuation of the intensity of the S-spin signal (S) relative to that of the reference signal (S_0) acquired without I-spin pulses. If the evolution time $N T_R$ is varied and the normalized difference signal $(S_0\text{-}S)/S_0 = \Delta S/S_0$ monitored as a function of the evolution time, a REDOR curve is obtained, from which internuclear distances r can be determined.

sequence. In the case of an isolated two-spin system, the REDOR evolution curves can be analyzed using Equations (1) and (2) to determine the internuclear distance r.[60] In

$$\frac{\Delta S}{S_0} = 1 - \frac{1}{4\pi S_0} \int_0^{\pi} \int_0^{2\pi} \cos\left[2\sqrt{2} N T_R D \sin 2\vartheta \sin\varphi\right] \sin\vartheta \, d\vartheta \, d\varphi \quad (2)$$

Equation (2), $\Delta S/S_0$ denotes the normalized difference signal, N the number of rotor cycles, and T_R the rotation period

© 2006 Wiley-VCH Verlag GmbH & Co. KGaA, Weinheim

(Figure 8); the polar angles ϑ and φ relate the principal-axis system to the laboratory system.

For $Si_3B_3N_7$, however, such a simplified analysis is not appropriate. A number of complications, for example, the distribution of bond lengths and angles inherently present in amorphous solids, the possible existence of multiple spin interactions, and the quadrupolar nature of the ^{11}B nucleus have to be taken into account. Consequently, a knowledge of the effects of these perturbations is a prerequisite for the successful analysis of the dipolar evolution curves.[67] Figure 9a illustrates the effect of a Gaussian distribution of B–Si distances on the resulting $^{11}B\{^{29}Si\}$ REDOR evolution curve. The important observation is that the initial part of the REDOR curve is virtually unaffected by the bond-length distribution. Only at longer evolution times does a damping of the oscillations in the REDOR curve become noticeable. Similarly, a variation in the angle α spanned by the two B–Si internuclear vectors in a SiB_2 three-spin system has little effect on the initial part of the evolution curves, as shown in Figure 9b.[67] Thus, when the data analysis is confined to the initial part of the evolution curves, perturbations such as multiple spin interactions and distribution effects may be harnessed. The analysis of medium-range order employing dipolar NMR spectroscopic approaches then boils down to the elucidation of the second coordination sphere around a central boron or silicon atom. If the internuclear distances (from the analysis of the PCFs; see Section 2.2.1) are used as input parameters, then the analysis of dipolar NMR spectroscopic data allows the number of silicon or boron atoms that are next-nearest neighbors to a central boron or silicon atom to be determined.

For the experiments, we employed a sample of $Si_3B_3N_7$ that was 100% isotopically enriched with the isotope ^{29}Si. The results of the $^{11}B\{^{29}Si\}$ REDOR experiment on this sample are collected in Figure 10.[69,70] The spectra reveal an attenuation of the intensity of the REDOR signal relative to that of the reference signal with increasing evolution time. The resulting REDOR evolution curve (filled circles in Figure 10b) can now be analyzed in terms of the numbers of silicon atoms in the second coordination sphere around boron. The assumption of a single B–Si interaction with an internuclear distance r of 2.74 Å produces the dotted line in Figure 10b, and the simulation of a BSi_2 three-spin system ($r = 2.74$ Å, $\alpha = 60°$) produces the dashed line. A superposition of these two contributions according to $0.44\,(BSi_2) + 0.56\,(BSi)$ (solid line in Figure 10b) results in a satisfactory fit to the initial part of the REDOR curve. From this fit, an average of 1.4 ± 0.1

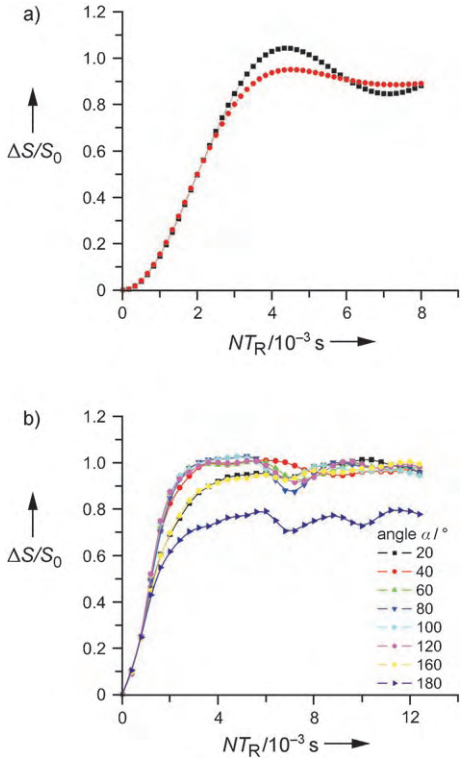


Figure 9. a) Simulated $^{11}B\{^{29}Si\}$ REDOR evolution curves for an isolated BSi two-spin system calculated assuming a fixed B–Si distance r of 2.74 Å (■), or assuming a Gaussian distribution about $r = 2.74$ Å with half width of 0.5 Å (●). b) Simulated REAPDOR evolution curves for a SiB_2 three-spin system calculated for various B-Si-B angles α of 20–180°.[67] The simulation package SIMPSON was used for the calculations.[68]

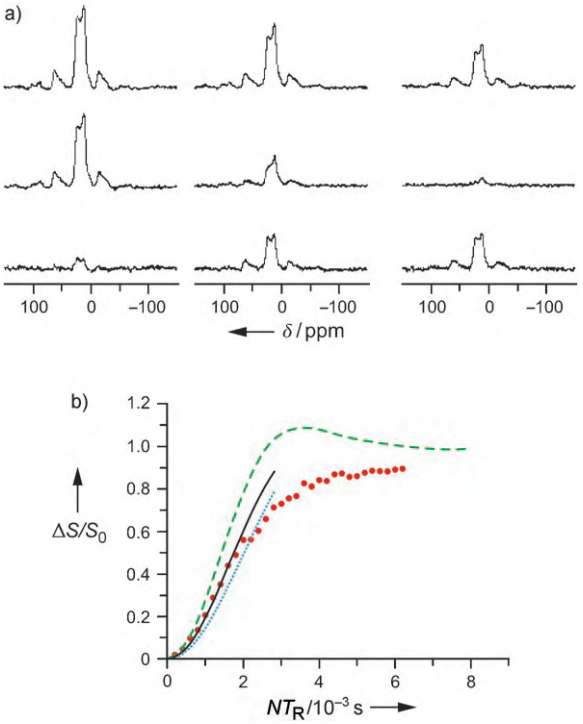


Figure 10. a) ^{11}B MAS spin-echo NMR (top), $^{11}B\{^{29}Si\}$ REDOR NMR (middle), and difference (bottom) spectra of $Si_3B_3N_7$ as a function of the evolution time NT_R (increasing to the right). The increasing attenuation of the REDOR signal with evolution time is clearly evident.[69] b) Resulting REDOR evolution curve (●), as well as simulated REDOR dephasing curves calculated assuming a single B–Si dipolar interaction (•••••) or a BSi_2 three-spin system (-----), with $r = 2.74$ Å in both cases. The solid line corresponds to a weighted superposition of these two contributions according to $0.44\,(BSi_2) + 0.56\,(BSi)$.

 © 2006 Wiley-VCH Verlag GmbH & Co. KGaA, Weinheim

silicon atoms per BN_3 unit is calculated; that is, boron is connected (via the three nitrogen atoms) to 1.4 silicon atoms on average in $Si_3N_3B_7$. We note that this number is considerably smaller than expected assuming a homogeneous elemental distribution, in which case boron should have 3.43 silicon and 2.57 boron next-nearest neighbors per BN_3 unit, and silicon should have 4.57 silicon and 3.43 boron next-nearest neighbors per SiN_4 unit.

Two further independent experiments were conducted to verify this result. The first was a $^{29}Si\{^{11}B\}$ REAPDOR experiment (a variation of the REDOR approach optimized for quadrupolar nuclei on the dephasing channel), which conversely to the $^{11}B\{^{29}Si\}$ REDOR experiment, allows the number of boron atoms around a SiN_4 unit to be determined. The results of the $^{29}Si\{^{11}B\}$ REAPDOR experiment are presented in Figure 11.[67,70] In this case, the simulation leads

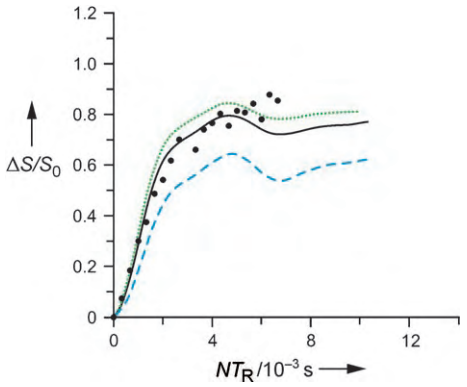


Figure 11. $^{29}Si\{^{11}B\}$ REAPDOR evolution curve for $Si_3B_3N_7$ (●; $\nu_{MAS} = 5$ kHz, $\nu_{RF}(^{11}B) = 89$ kHz), as well as simulated REAPDOR dephasing curves calculated assuming a single Si–B dipolar interaction (-----) or a SiB_2 three-spin system (•••••), with $r = 2.74$ Å in both cases.[67]

to an average value of 1.8 ± 0.2 boron atoms per SiN_4 unit; that is, the silicon atoms are connected (via nitrogen atoms) to an average of 1.8 boron atoms. Again, the result is not compatible with the assumption of a homogeneous distribution of silicon and boron in the network and, thus, lends support to the results of the $^{11}B\{^{29}Si\}$ REDOR experiment.

A complementary way of acquiring information about the medium-range order in $Si_3B_3N_7$ is to establish the number of homonuclear next-nearest neighbors for a central boron or silicon atom. This objective can be accomplished with the help of static spin-echo decay spectroscopy, which produces quantitative results for spin-$^1/_2$ nuclei such as ^{29}Si. At short echo times 2τ, the spin-echo decay I/I_0 can generally be described by the Gaussian function $I/I_0 = \exp(-(2\tau)^2 M_2/2)$.[71] The second moment M_2 is related to the internuclear distances r_{ij} by the Van Vleck equation [Eq. (3)], where S is

$$M_2 = \frac{3}{5}\left(\frac{\mu_0}{4\pi}\right)^2 \gamma_S{}^4 S(S+1)\hbar^2 \sum_{i \neq j} r_{ij}{}^{-6} \qquad (3)$$

the spin quantum number.[72] Because of the r^{-6} dependence, the contribution of the first two coordination spheres usually amounts to 90–95 % of the total second moment. Therefore, an estimate of M_2 allows the number of homonuclear next-nearest neighbors to be calculated, allowing an independent verification of the REDOR and REAPDOR results.

A fit of the ^{29}Si spin-echo data (Figure 12) leads to a second moment of 3.1×10^6 rad^2 s^{-2}. Assuming a Si–Si distance of 2.98 Å (again, from the PCFs), each Si–Si pair contributes

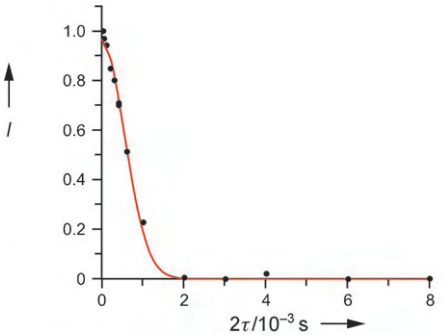


Figure 12. Plot of the intensity of the ^{29}Si spin-echo NMR signal of $Si_3B_3N_7$ as a function of the echo time 2τ (●).[67] A fit of the data (——) leads to a second moment M_2 of 3.1×10^6 rad^2 s^{-2}.

0.56×10^6 rad^2 s^{-2} to the second moment. Thus, an average of 5.6 silicon atoms occupy the second coordination sphere of each silicon atom. This value agrees with the results from the REAPDOR experiment: approximately two boron atoms (according to the $^{29}Si\{^{11}B\}$ REAPDOR experiment) and approximately six silicon atoms (according to the ^{29}Si spin-echo decay experiment) complete the second coordination sphere of each silicon atom.

2.2.3. *Long-Range Order*

The applicability of all interference-based methods for the structural characterization of amorphous solids is confined to length scales of less than 8 Å, as the inherent distribution of bond lengths and angles in these materials entails a rapid decay of the PCFs at longer distances. Approximately the same distance cutoff holds for the dipolar NMR spectroscopic approaches. As a consequence, neither of these methods holds much promise for the elucidation of structural features beyond 8 Å. However, it is in this regime that effects such as the precipitation of nanocrystals or phase separation in multinary systems, which severely affect the material's properties, can occur. The relevant length scale is, however, accessible by direct-imaging methods such as SEM, AFM, or TEM (EFTEM).[34] The latter, EFTEM, was used to characterize the amorphous ceramic $Si_3B_3N_7$. Apart from producing the electron-scattering-based PCFs presented in Sections 2.2.1 and 2.2.2, TEM was also used to provide elemental maps of silicon, boron, and nitrogen with high lateral resolution. Figure 13 shows the EELS spectrum of $Si_3B_3N_7$ in the region of the B K edge. With an imaging electron-energy filter attached to the TEM, an energy window of the EELS spectrum can be selected and an image of the spatial energy distribution of the inelastically scattered electrons in this window produced. Usually three such images are

© 2006 Wiley-VCH Verlag GmbH & Co. KGaA, Weinheim

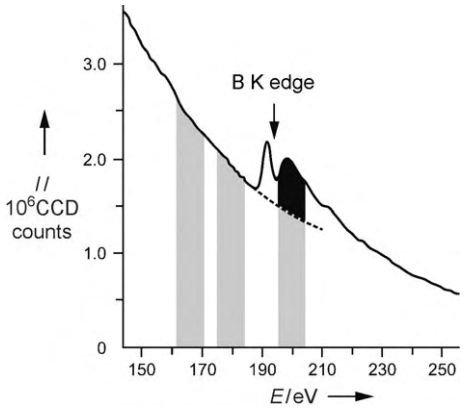


Figure 13. EELS spectrum of $Si_3B_3N_7$ in the region of the B K edge. The extrapolated background (calculated from two pre-edge images shown as gray bands) is subtracted from the post-edge image (gray/black band) to obtain the concentration of boron.[34]

acquired: two pre-edge images, which are used to calculate a background image, and an image beyond the ionization edge (post-edge image). After the background is subtracted from the post-edge image, pixel by pixel, the remaining electron intensity stems from the element under investigation. Thus, the distribution of the element can be qualitatively displayed as a map, and the concentration of the element quantified in any pixel of the elemental map. For a $Si_3B_3N_7$ sample, elemental maps (with a lateral resolution of 0.7 nm) of boron, nitrogen, and silicon, as well as a bright-field image, all of the same sample area, are shown in Figure 14. The important result is that homogeneous distributions are observed for silicon, boron, and nitrogen in the elemental maps.[34] In particular, the images contain no indication of phase separation, segregation, or clustering. Note, however, that the sample thickness of approximately 5 nm could cause projection effects. At this thickness, the vertical resolution is approximately a factor of seven less than the lateral resolution, and the resulting projection (averaging) effects could mask a possible phase separation.[73] The macroscopic ordering of $Si_3B_3N_7$ was also characterized through a density measurement with a helium pycnometer. The observed density of 1.899 $g\,cm^{-3}$ can be compared to the densities calculated for different structural models.

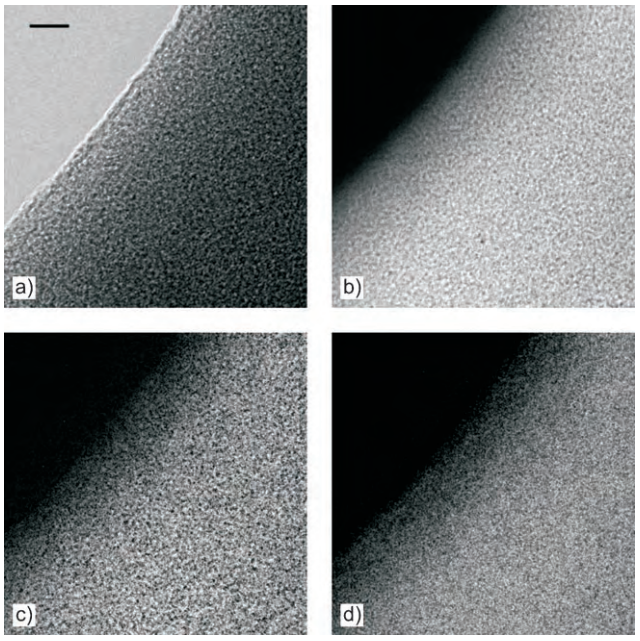


Figure 14. TEM images of $Si_3B_3N_7$: a) bright-field image, and elemental maps of b) silicon, c) boron, and d) nitrogen for the same sample region (at the same scale; scale bar = 5 nm).[34]

2.3. The Structure of $Si_3B_3N_7$ "Seen" by Experiment

In this Section, we summarize the experimental findings for $Si_3B_3N_7$ with respect to short-range and intermediate-range order. Through the use of XANES spectroscopy, scattering techniques, and MAS NMR spectroscopy, tetrahedral SiN_4, and trigonal planar BN_3 and $NB_{3-x}Si_x$ units were identified as the polyhedra that dominate the short-range order of $Si_3B_3N_7$ (Figure 15). Local deformations seem to accumulate within the N-Si-N angles. The interconnection of the local building blocks in the amorphous network was probed with dipolar NMR spectroscopic methods and with the PCFs obtained from scattering experiments. The Si-N-B linkages identified in the neutron PCFs by employing isotopic contrast techniques were confirmed and quantified with the help of $^{11}B\{^{29}Si\}$ REDOR, $^{29}Si\{^{11}B\}$ REAPDOR, and ^{29}Si spin-echo NMR spectroscopy. The results suggest a partial segregation of the boron and silicon atoms at intermediate length scales (2–8 Å), as indicated in Figure 15 d,e. According to the NMR spectroscopic investigations, a central boron atom is surrounded by four to five boron atoms[67] and only one or two silicon atoms in the second coordination sphere. Correspondingly, a central silicon atom is connected (via the four nitrogen atoms in the first coordination sphere) to six silicon atoms and two boron atoms, on average, in the second coordination sphere. These short- and intermediate-range network fragments serve as a basis and a test for the modeling work described in the following Section.

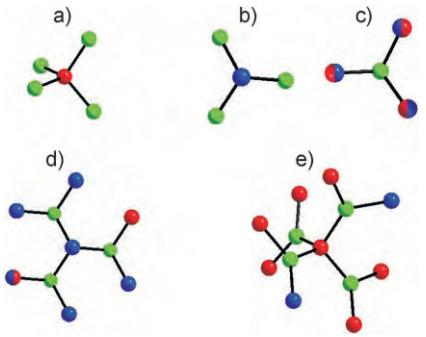


Figure 15. Experimentally identified network fragments in amorphous $Si_3B_3N_7$: local network polyhedra a) SiN_4, b) BN_3, and c) $NB_{3-x}Si_x$; d) and e) extended fragments consistent with the NMR spectroscopic experiments. Si red, B blue, N green.

 © 2006 Wiley-VCH Verlag GmbH & Co. KGaA, Weinheim

3. Theory

The experimental data alone are not sufficient to derive a complete structural model for amorphous $Si_3B_3N_7$. Computational modeling is required to achieve this goal.

3.1. Overview of the Modeling Procedures

As it was not clear at the outset, whether particular features of the actual synthesis would play a role in the structural and bulk properties of the amorphous compound, five different classes of $Si_3B_3N_7$ models (A–E) were generated in different ways:[74]

A: quenching from the melt,
B: sintering of subnanometer-sized crystallites,[75]
C: formation of clusters of $Si_3B_3N_7$ using a molecular modeling procedure designed by Gladden[76] and adapted by Wefing,[77] followed by sintering of the clusters,
D: random atom-beam deposition, modeled using a random close-packing algorithm[78],
E: the actual (rather involved) polymer-precursor route, which is similar to a sol–gel process.[79,80]

All models of classes A–E involved 700–1300 atoms, and the simulation/relaxation parts of the modeling process were performed using both molecular dynamics and Monte Carlo simulations at constant volume and pressure. In models of class A, the starting configurations were all well-equilibrated melts. In models of class B, the simulations started from a mixture of BN and Si_3N_4 nanocrystallites. The clusters to be sintered in models of class C were generated using the cited build-up and build-down algorithm. Finally, the starting configurations of models of class D were generated by an optimal placement of silicon and boron atoms in the holes of a random configuration of nitrogen atoms.

As the polymer-precursor route was the one used to synthesize the experimentally investigated samples of $Si_3B_3N_7$, we give a short description of the stepping-stone process that we used to model (E) this route (details can be found in references [79,80]). Initially, the precursor molecules are in solution with an excess of NH_3; the rate of reaction of the molecules depends on the number of available reaction sites per molecule and on the concentration of molecules in the solution. Once several precursor molecules have joined into a larger aggregate, this oligomer will move much more slowly than the remaining precursor and NH_3 molecules. Thus, the oligomers become essentially stationary and serve as condensation centers for the still-mobile reactants. We can, therefore, model this latter phase of the polymerization as a multiple condensation process of individual oligomers and monomers. At the end of this stage, we are left with many isolated oligomers, which begin to cross-link to form the polymer. This development is modeled by placing the oligomers randomly on a lattice and shrinking the average distance between them until the oligomers can interact and form bonds. The final pyrolysis stage, which transforms the polymer into a ceramic, is simulated by a Monte Carlo simulation at 1200 K, well below the (calculated) melting temperature T_{melt} of the system ($T_{melt}(Si_3B_3N_7{}^{cryst}) = 2500$ K and $T_{melt}(Si_3B_3N_7{}^{amorph}) = 2000$ K) of the system. Nevertheless, under these conditions, most of the dangling bonds still present in the polymer are eliminated.

In each of the cases A–E, raw models were generated, which were subsequently (locally) minimized by energy, using Monte Carlo and conjugate-gradient methods at constant volume and pressure. We employed an empirical potential from the literature,[81] which was derived from ab initio calculations on molecular fragments and from structural and elastic data for the binary compounds Si_3N_4 and BN. Various structural properties of the models generated were analyzed: the radial PCFs and angle distribution functions (ADFs), the mean coordination numbers within the first and second neighbor spheres of the atoms, and the ring statistics. Direct comparisons can then be made with the experimentally determined PCFs and the observed first and second coordination spheres. The ADFs are only indirectly accessible from the experimental data; the same holds true for information about the third coordination sphere, and the size and distribution of rings within the network. In Section 3.2, the structural properties of the models are briefly described, and their similarities and differences, both with respect to each other and with respect to the experimental data, are discussed.

3.2. Structural Properties of Models Belonging to the Five Classes

3.2.1. Pair Correlation Functions

In Figure 16, the experimental and calculated X-ray and neutron PCFs are compared. The functions calculated from all of the models have the same general shape as the experimental functions. As is apparent from Table 3, the various peaks in the experimental PCFs can be associated with specific interatomic distances within the first and second neighbor spheres (see also Figure 17). The best quantitative agreement is found for the crystal-fragment (class B) and the sol–gel (class E) models.

A great advantage of the availability of structure models generated by computer is that they allow the analysis of features of the amorphous structure that are not directly accessible by experiment. Thus, we can, for example, extend the peak assignments given in Section 2. In Figure 17, the partial PCFs for neutron and X-ray scattering experiments calculated for models of class A and B are presented. The assignment of the first peaks and shoulders up to 3.1 Å agrees with that in Table 3, while the shallow peaks between 3.8 and 4.2 Å in the experimental PCFs (Figures 16 and 17) can now be associated with third-neighbor Si–N and B–N distances, and the oscillations at 5.0–5.5 Å with N–N and Si–N distances (Table 3). In addition, small peaks occur at approximately 2.05, 2.2, and 2.6 Å in the B–B, Si–B, Si–Si, and N–N partial PCFs (Figure 17), indicating the presence of edge-sharing polyhedra in the structural models. However, these features are not clearly visible in the experimental PCFs.

© 2006 Wiley-VCH Verlag GmbH & Co. KGaA, Weinheim

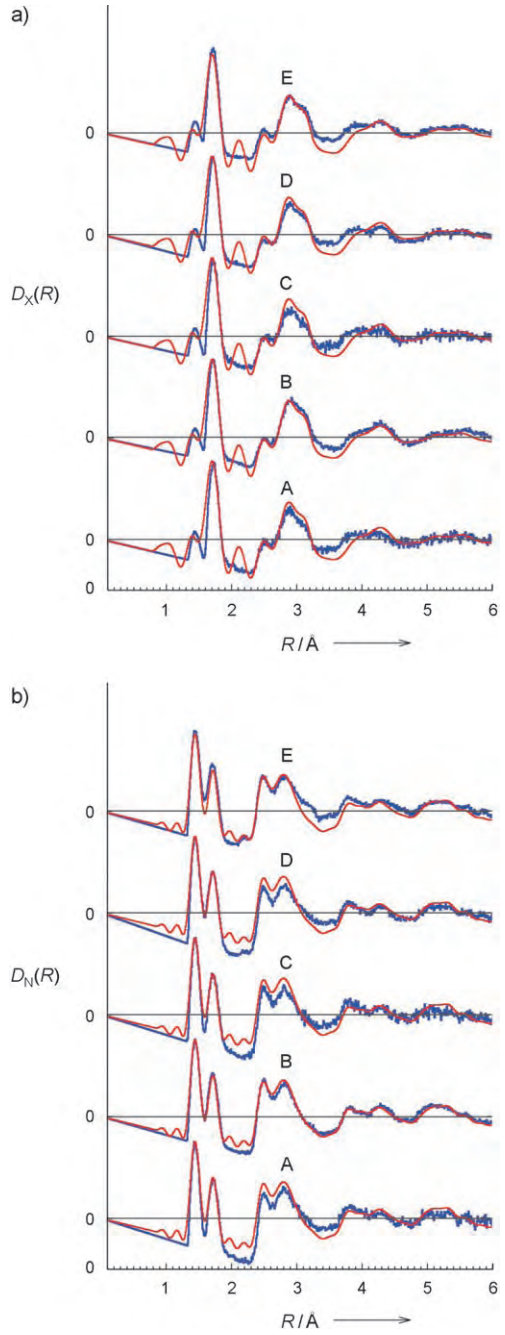


Figure 16. Comparison of PCFs from a) X-ray ($D_X(R)$) and b) neutron ($D_N(R)$) experiments (——) on $Si_3B_3N_7$ with those calculated (——) for models of the five classes A (melt), B (nanocrystallite), C (molecular modeling), D (random close packing), and E (sol–gel).[74]

3.2.2. *Local Coordination and Angle Distribution Functions*

Regarding the distribution of coordination numbers in the optimized models, the silicon atoms are mainly fourfold coordinated, whereas the boron and nitrogen atoms are mainly threefold coordinated. Comparing the silicon and boron atoms, we find that the boron atoms achieve their ideal coordination number more often than the silicon atoms (that is, the variation about the mean coordination number is larger for silicon), and that coordination defects are more frequently encountered at the silicon centers than at the boron centers. These results hold for all model classes. Differences between the models of different classes are found in the distribution of the nitrogen coordination spheres $NB_{3-x}Si_x$. For models derived from classes A, C, and D, the distribution of $NB_{3-x}Si_x$ units reveals a preference for $NBSi_2$ and NB_2Si units, while the models of classes B and E contain a higher percentage of NSi_3 and NB_3 units.

Table 3: Positions [Å] of the peak maxima in the experimental PCFs of $Si_3B_3N_7$ and the corresponding interatomic distances [Å] in the models.

Peak (experiment)[a]	Pairs/distances (model)[b]
1.43	B–N (I) 1.43
1.72	Si–N (I) 1.72
2.5	N–N (I) 2.50, B–B (I) 2.50
2.8	N–N (II) 2.71, Si–B (I) 2.75
3.0	B–N (II) 2.90, Si–Si (I) 3.0
3.8	B–N (III) 3.80
4.2	Si–N (II) 4.20, B–B (II) 4.25
5.0–5.5	N–N (III) 5.2, B–B (III) 5.0, B–N (IV) 5.2, Si–Si (II) 5.5

[a] Average of the peak maxima in the PCFs from X-ray, neutron, and electron scattering experiments. [b] Average of the interatomic distances from models of classes A–E; roman numerals distinguish different distances for the same atom pairs.

Similarly to the ring-size distributions discussed in Section 3.2.3, the ADFs are easily calculated for computer-generated models, but are not directly accessible by experiment. Nevertheless, knowledge of these distribution functions can assist us in interpreting the more subtle aspects of the experimental data. As is apparent in Figure 18, the maxima in the ADFs for the N-Si-N, N-B-N, and X-N-Y (X, Y = Si, B) angles in all models correspond to those expected for tetrahedral or trigonal coordination. Furthermore, the N-Si-N and, in particular, the X-N-Y distributions for all models exhibit a small peak near 90°. This result agrees with the observation that a small number of edge-sharing SiN_4 tetrahedra and BN_3 triangles are present in all of the models. The interatomic distances d_{90}(X-Y) corresponding to these 90° angles are d_{90}(B-B) ≈ 2.02 Å, d_{90}(Si-B) ≈ 2.23 Å, and d_{90}(Si-Si) ≈ 2.44 Å. As these values are similar to other relevant interatomic distances, they will at most result in small shoulders on larger peaks in the total experimental PCFs.

3.2.3. *Second Coordination Spheres and Ring Statistics*

Whereas all models yielded similar distributions for the distances and angles in the first coordination spheres, the second (cation–cation) coordination spheres reveal the differences between the model classes. Models of classes B and E contain more Si–Si and B–B contacts between next-nearest neighbors than all other models and are, thus, in best agreement with experiment. A comparison of the ring-size distributions for the different models (Table 4) shows that models of classes A–C contain approximately 5–7% four-membered rings (Si_2N_2, B_2N_2, and $SiBN_2$), and models of classes D and E approximately 8–10%. The four-membered rings are associated with small peaks near 90° in the ADFs and with small shoulders in the partial PCFs. No preference

© 2006 Wiley-VCH Verlag GmbH & Co. KGaA, Weinheim

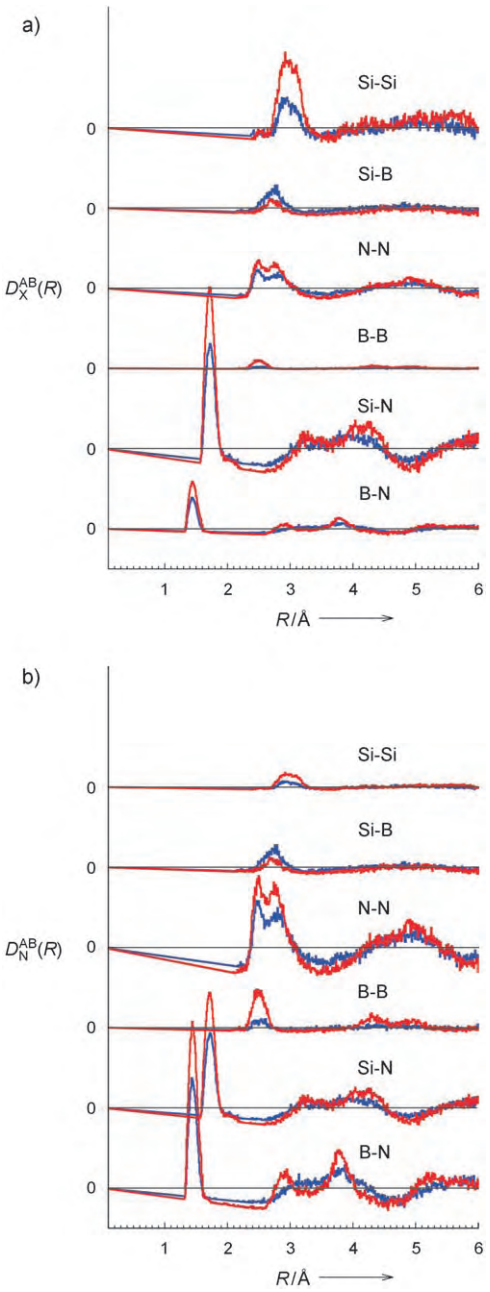


Figure 17. Comparison of the a) X-ray ($D_X^{AB}(R)$) and b) neutron ($D_N^{AB}(R)$) partial PCFs calculated for models of $Si_3B_3N_7$ of classes A (——) and B (——).[74]

Table 4: Fraction of rings with four, six, or eight atoms in models of $Si_3B_3N_7$ of classes A–E.

	4-rings	6-rings[a]	8-rings
A	0.05	0.28 [0.01]	0.39
B	0.06	0.41 [0.35]	0.32
C	0.07	0.27 [0.02]	0.37
D	0.10	0.24 [0.06]	0.36
E	0.08	0.28 [0.11]	0.31

[a] Relative fraction of borazene rings given in brackets.

for edge sharing between two SiN_4 tetrahedra over edge sharing between a SiN_4 tetrahedron and a BN_3 triangle is observed in the compositional distribution of the four-membered rings. The highest fraction of six-membered rings is found in the crystal-fragment models of class B, which initially contain a considerable number of borazene (B_3N_3) and Si_3N_3 rings, approximately 40% of the six-membered rings each. A significant part of the initial structure remains intact after the sintering. In contrast, in the models of classes A, C, and D, mainly mixed-cation six-membered rings are found. Models of class E exhibit a larger number of borazene rings.

3.2.4. Main Structural Differences Among the Model Classes

The differences in the structures of the models of different classes are most apparent in the second coordination spheres (in particular, the B–B, Si–B, and Si–Si partial PCFs; Figure 17). The melt models of class A (blue curves) contain more Si–B, and less B–B and Si–Si next-nearest-neighbor pairs than the crystal-fragment models of class B (red curves). An accumulation of homoatomic B–B and Si–Si contacts between next-nearest neighbors corresponds to concentration fluctuations at a subnanometer scale, as is clearly visible in the complete structure models of classes A and E depicted in Figure 19. With respect to the second coordination sphere, models of class B resemble those of class E, while models of classes C and D resemble those of class A. This division of the models into two groups is also apparent in the ring-size distributions, as models of classes B and E show an increased presence of borazene rings. The alternating arrangement of the cations in the structural models generated by quenching from the melt (class A) is reminiscent of the empirical Löwenstein rule.[82] This observation suggests that the actual a-$Si_3B_3N_7$ ceramic synthesized by the sol–gel route would probably be less stable than a hypothetical ceramic synthesized by quenching from the melt, a hypothesis that is supported by the fact that the average energy of models of class A is lower than that of models of class E (see Section 3.3).

It is important to note that the differences among the PCFs of the various model classes are greater than those within a given model class (Table 5). Thus, it should be possible to distinguish among various amorphous modifications of $Si_3B_3N_7$, once their syntheses by the various routes have been realized.

3.3. Density and Stability of Voids

The macroscopic density is another quantity that can be used to compare the theoretical models with experiment. However, the density is one of the most difficult quantities to model in amorphous compounds, as it depends crucially on the conformation of the network on a length scale of 0.5–2 nm, which is nearly inaccessible by experiment (except possibly by small-angle X-ray or neutron scattering under favorable conditions). Therefore, information important for the modeling, for example, whether small voids of 0.5–2 nm diameter are contained in the real compound, is not available. The densities calculated for the various models are shown in

 © 2006 Wiley-VCH Verlag GmbH & Co. KGaA, Weinheim

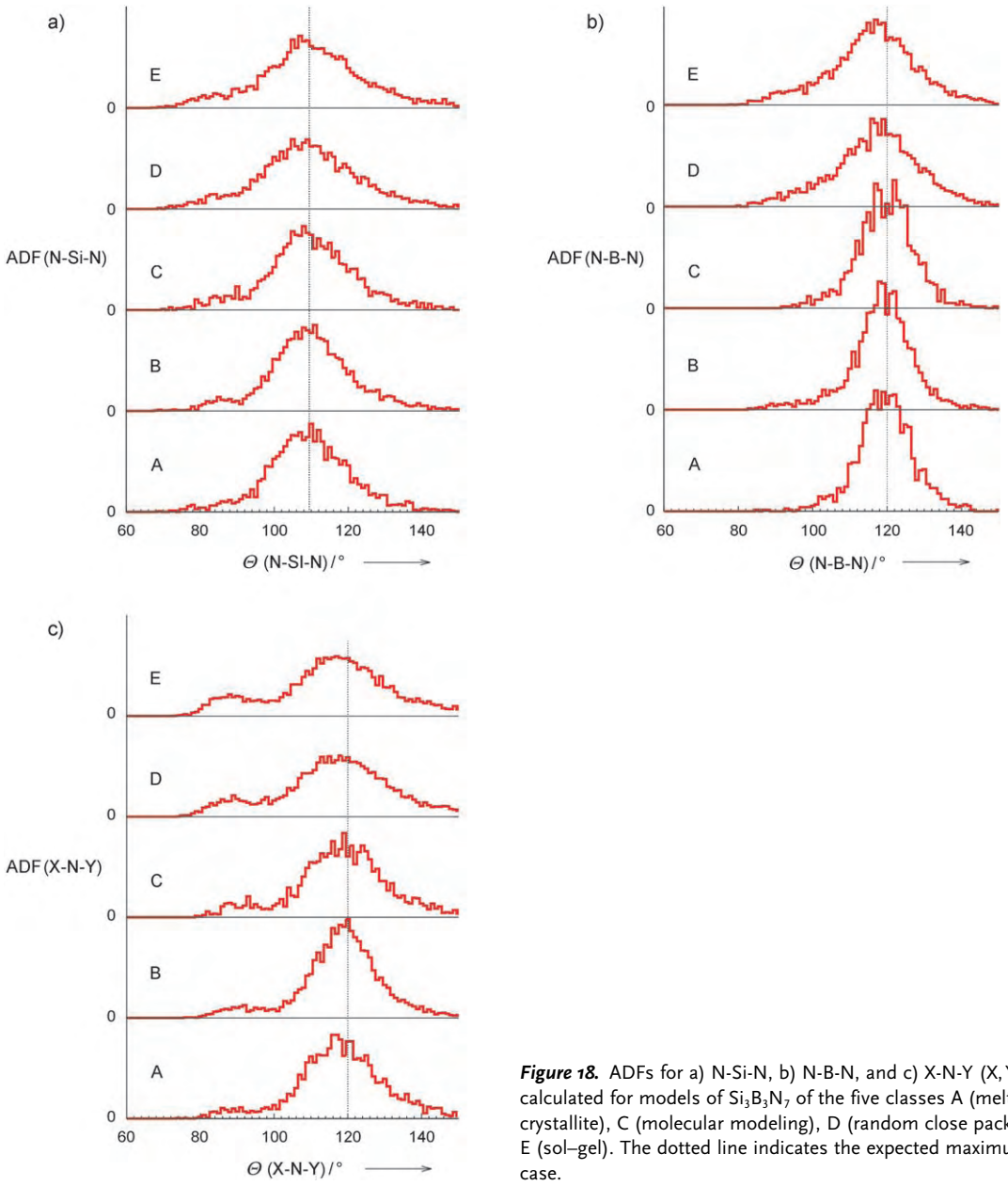


Figure 18. ADFs for a) N-Si-N, b) N-B-N, and c) X-N-Y (X, Y = Si, B) calculated for models of $Si_3B_3N_7$ of the five classes A (melt), B (nanocrystallite), C (molecular modeling), D (random close packing), and E (sol–gel). The dotted line indicates the expected maximum in each case.

Figure 20.[74] Again, the closest agreement with experiment is observed for the crystal-fragment models of class B and the sol–gel models of class E. However, if the void volume is subtracted from the total volume of each model, the remaining (void-free) regions of the models exhibit densities of 2.5–2.8 $g\,cm^{-3}$. These values compare well with the density of hypothetical crystalline $Si_3N_3B_7$ polymorphs (2.9 $g\,cm^{-3}$),[7,83] and the appropriately weighted average of the experimental densities of crystalline h-BN and β-Si_3N_4 (2.75 $g\,cm^{-3}$). This observation suggests that the reason for the surprisingly low experimental of amorphous $Si_3B_3N_7$ might be the presence of stable voids (cages) with radii of 3–10 Å, a hypothesis that is difficult to verify experimentally.

The polymer-precursor route is expected to lead to many defects and, hence, to the formation of cavities of all sizes in the actual structure of amorphous $Si_3B_3N_7$. The fact that the final densities of the sol–gel models (class E) agree best with the experimental density is self-consistent, and justifies faith in the model-generating procedure. According to the plots of density versus potential energy for models chosen from all classes (Figure 20), the higher the density, the lower the energy. This finding underlines the importance of taking the details of the synthesis route into account in the models of amorphous $Si_3B_3N_7$. Attempts to simply find the amorphous configuration with the lowest energy would clearly miss the mark and instead generate structures with densities that are much too high.

The distribution of void sizes calculated for models of $Si_3B_3N_7$ of classes A and E is shown in Figure 21.[84] Both structures exhibit tiny voids with radii of less than 2 Å, which reflect the general packing constraints of the SiN_4 polyhedra and BN_3 triangles within the covalent network. In this respect,

 © 2006 Wiley-VCH Verlag GmbH & Co. KGaA, Weinheim

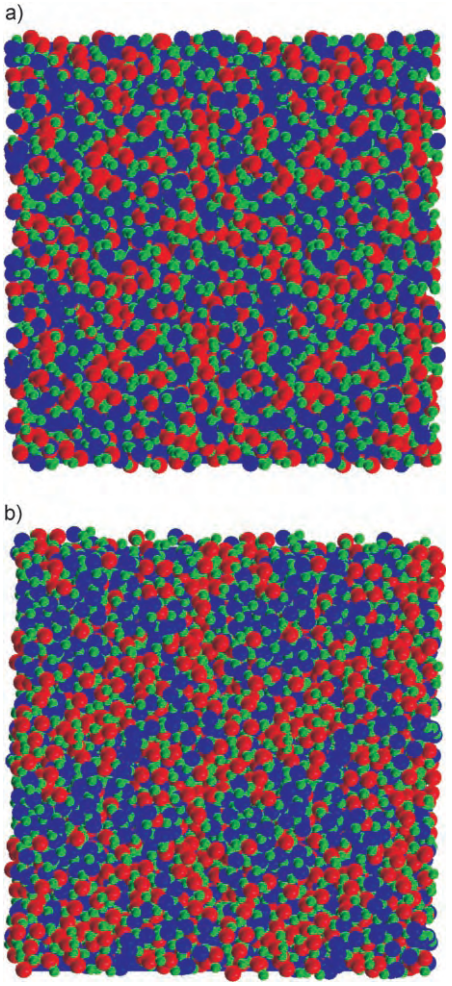


Figure 19. Structure models of amorphous $Si_3B_3N_7$ of a) class A (melt) and b) class E (sol–gel). The cation distribution is homogeneous in (a) and heterogeneous in (b). The structures are depicted as ball models with an edge length of ca. 4.5 nm; Si red, B blue, N green.

Table 5: Spread in the calculated neutron PCFs within the models ($\Delta_{YY}D_N(R)$) and between the models ($\Delta_{YZ}D_N(R)$) of $Si_3B_3N_7$ of classes Y, Z = A–E.[a]

	A	B	C	D	E
A	0.15	0.38	0.32	0.17	0.93
B	0.38	0.09	0.44	0.30	0.60
C	0.32	0.44	0.20	0.25	0.81
D	0.17	0.30	0.25	0.18	0.71
E	0.93	0.60	0.81	0.71	0.13

[a] The internal spread in the PCFs $\Delta D^Y(R)$ within a class Y containing n_Y models is $\Delta_{YY}D^Y(R) = (1/N_R)\sum_{i=1}^{N_R}\sum_{m=1}^{n_Y}[D^m(R_i) - \langle D^Y(R_i)\rangle]^2$, where $\langle D^Y(R_i)\rangle = (1/n_Y)\sum_{m=1}^{n_Y} D^m(R_i)$ is the average value of the PCF at a distance R_i, $D^m(R_i)$ is the value of the PCF at R_i in model m of class Y, and N_R is the number of distances R_i included. To compare the PCFs of models of different classes Y and Z, we calculate $\Delta_{YZ}D(R) = (1/N_R)\sum_{i=1}^{N_R}$ - $[\langle D^Y(R_i)\rangle - \langle D^Z(R_i)\rangle]^2$.

both classes of model resemble the (hypothetical) crystalline compound,[7] which by its nature, exhibits a very narrow size distribution. However, the model configurations generated by

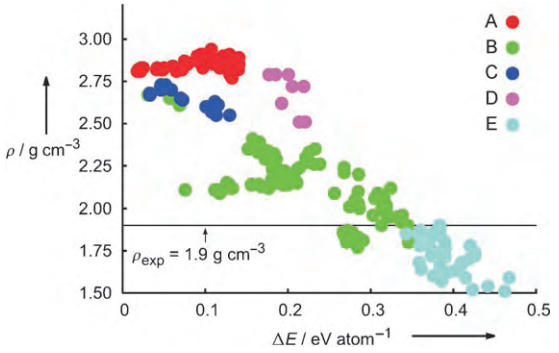


Figure 20. Plot of the density ρ versus the energy difference ΔE (between the energy of the model of the amorphous compound and that of the hypothetical crystalline compound[7]) for models of $Si_3B_3N_7$ of classes A (melt), B (nanocrystallite), C (molecular modeling), D (random close packing), and E (sol–gel).[74] The horizontal line indicates the experimentally determined density of $Si_3B_3N_7$.

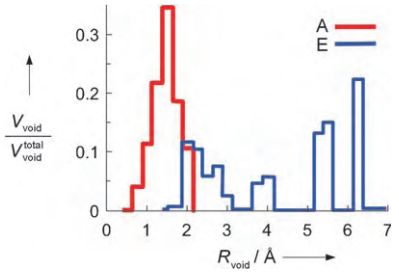


Figure 21. Distribution of voids of radii R_{void} for models of $Si_3B_3N_7$ of classes A (melt) and E (sol–gel), expressed in terms of the void volume V_{void} normalized to the total volume V_{void}^{total} of all voids in the model.

the sol–gel route (class E) contain many comparatively large voids with radii up to 7 Å. Annealing at low temperatures over a long period of time leads to redistributive coarsening in both the quenched-melt (class A) and the sol–gel (class E) models, but the effects are not very large, and no significant changes in the overall densities of the models are observed. In contrast, when the crystal-fragment (class B) or the sol–gel (class E) models are heated beyond the melting temperature at constant pressure, the densities increase from 2.2 or 1.9 g cm^{-3}, respectively, to 2.6 g cm^{-3}, owing to the elimination of larger voids. This observation again shows that the quenched-melt models (class A) are thermodynamically more stable than, for example, the sol–gel models (class E). However, during the polymer-precursor synthesis, the system remains far below the melting temperature. Thus, the large voids in amorphous $Si_3B_3N_7$ should be relatively stable (to approximately 1500 K).

An investigation of the stability of voids in a 5200-atom system with an initial density of 1.9 g cm^{-3} over a wide range of temperatures below the melting point produced a slow overall densification.[84] The density increased approximately logarithmically with time. In this process, larger voids were more stable than smaller ones. Therefore, the large voids contained in amorphous $Si_3B_3N_7$ should remain stable to a temperature of approximately 1500 K. The same logarithmic

 © 2006 Wiley-VCH Verlag GmbH & Co. KGaA, Weinheim

time dependence is found for the slow improvement in energy during the aging process, as observed in long-time simulations for $Si_3B_3N_7$ models at temperatures below the melting point.[85] The effect of high pressures on the nanoporous material could have great ramifications for potential applications.[84] Constant-pressure (1–50 GPa) simulations at 300 K show that the system can be compacted significantly, and that much of the densification is irreversible. For pressures exceeding 15 GPa, a saturation density value of approximately 2.8–3.0 $g\,cm^{-3}$ is observed after pressure release. In comparison, at a temperature of 1500 K, a much faster densification to approximately 2.8 $g\,cm^{-3}$ is observed for all pressures above 1 GPa.[86]

3.4. Bulk Properties

Once a credible structural model has been constructed, the physical properties of the compound can be calculated. In this Section, a short overview of various bulk properties of amorphous $Si_3B_3N_7$ is given.

The calculation of the vibrational (phonon) density of states (VDOS)[74,89] and the bulk modulus B[74] (70–180 GPa) of the different models was performed with the GULP program.[88] The overall shapes of the VDOS curves are the same for models of all classes (Figure 22). All of the curves exhibit peaks at approximately 1500 and 1000 cm^{-1}, which are most likely associated with B–N and Si–N stretching modes, respectively.[90] The speed of sound v_S can be estimated by studying the time evolution of a heat pulse;[92] in the case of amorphous $Si_3B_3N_7$, a value of $v_S \approx 3–4 \times 10^3\,m\,s^{-1}$ is obtained.[93] This value falls in the range of speeds of sound found experimentally for crystalline β-Si_3N_4 ($1.1 \times 10^3\,m\,s^{-1}$) and h-BN ($7 \times 10^3\,m\,s^{-1}$). Similarly, we can simulate and measure the heat conductivity κ by generating a steady-state heat flow through the system;[92] for amorphous $Si_3B_3N_7$, we find a heat conductivity of approximately 4 $W\,m^{-1}\,K^{-1}$, which varies only slightly with temperature.[93] As experimental conductivity values typically exceed the simulated values by a factor 3–5,[92,93] the true value for amorphous $Si_3B_3N_7$ should be $\kappa \approx 15\,W\,m^{-1}\,K^{-1}$.

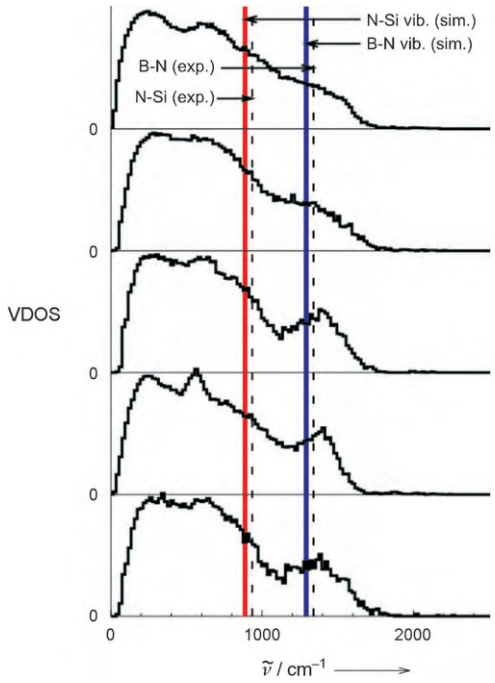


Figure 22. Calculated VDOS for models of $Si_3B_3N_7$ of classes A (bottom) to E (top).[74] The red and blue vertical lines correspond to vibrations dominated by contributions from SiN_4 and BN_3 building units, respectively; the dashed vertical lines indicate the positions of N–Si and B–N vibrations in experimental IR spectra of $Si_3B_3N_7$.[91]

We have also calculated a metastable phase diagram for the $Si_3B_3N_7$ system by performing long-time Monte Carlo simulations over a large range of temperatures and volumes for a system containing 702 atoms.[89,94] The term "metastable phase diagram" seems appropriate here, as in the solid state, the phase with the lowest energy corresponds to a weighted mixture of β-Si_3N_4 and h-BN. The phases with the next-lowest energies are the crystalline modifications of $Si_3B_3N_7$.[7,83] Of course, for very small crystallites, the polycrystalline mixture of β-Si_3N_4 and h-BN begins to lose stability compared to the amorphous phase; the critical particle diameter at which this occurs is approximately 30 Å.[89,94] This result explains the failure of attempts to synthesize amorphous $Si_3B_3N_7$ by sintering a mixture of BN and Si_3N_4 microcrystallites (diameter of approximately 500 nm).[23] A comparison of the corresponding free energies yields a very rough estimate of the pressure needed to suppress the evolution of N_2 from the condensed phase of $Si_3N_3B_7$ near its melting temperature; at 2000 K, this limiting pressure is approximately 4 GPa.

Finally, it is of great practical interest to gain some insight into possible aging phenomena in the amorphous ceramic $Si_3B_3N_7$. Information about the likelihood of structural changes, such as the separation of crystalline phases, at typical application temperatures is especially important, as these changes would probably weaken the amorphous network. Our simulations for $Si_3B_3N_7$ indicate a slow aging with a logarithmic time dependence at temperatures between 1200 and 1700 K.[85] Furthermore, $Si_3B_3N_7$ quenched from the melt should exhibit a glass transition in the temperature range 1700–2500 K, assuming the application of a N_2 partial pressure that is high enough to prevent decomposition of the ternary melt.

4. Summary and Conclusion

Thus far, $Si_3B_3N_7$ has been only accessible as a noncrystalline random network. Since no significant deviations from the ideal composition are observed in a-$Si_3B_3N_7$, the compound parallels the prototypical glassy system, quartz glass, in this respect, and may be regarded as a ternary nitride analogue of a-SiO_2. Of course, the more complicated composition of $Si_3B_3N_7$ implies that structure analyses are more difficult. On the other hand, the broader choice of atoms that are sensitive to various structural probes is expected to yield a larger spectrum of information.

The use of as many different structure-sensitive probes as possible has provided quite consistent results. In particular,

 © 2006 Wiley-VCH Verlag GmbH & Co. KGaA, Weinheim

the application of overlapping probes that monitor the same structural property, as well as combinations of complementary probes has helped to generate less ambiguous and more reliable experimental results. It is now well established that the first coordination sphere of silicon is tetrahedral in $Si_3B_3N_7$, and that those of boron and nitrogen are trigonal planar. Interestingly, the line shapes observed in the NMR spectra of $Si_3B_3N_7$ vary significantly in their inhomogeneous line broadening. While the quadrupolar transition for boron yields a line shape that fully matches the boron signal recorded for h-BN, the resonance for silicon exhibits a pronounced broadening, compared to that of α-Si_3N_4. Thus, in amorphous $Si_3B_3N_7$, boron occupies a virtually ideal trigonal-planar coordination environment, while most of the deformations, which are a consequence of the inevitable mechanical strain in the amorphous network, occur in the silicon coordination spheres. Similarly, the nitrogen resonance in the NMR spectrum of $Si_3B_3N_7$ is also clearly broadened, which is understandable given that four different approximately trigonal-planar $NB_{3-x}Si_x$ units contribute to the signal. Surprisingly, in the next-nearest neighbor shells, a kind of segregation is observed: instead of a random distribution of cations, a preference for cations of the same type as the central cation in the second coordination sphere (for example, silicon atoms as the next-nearest neighbors of silicon) is found.

These observations from probes sensitive to the local environment were complemented by measurements of medium- and long-range spatial correlations in the $Si_3B_3N_7$ system. The PCFs determined by X-ray (synchrotron radiation) and neutron scattering revealed all of the expected structural features; however, it is not possible to generate a complete structure from these pieces of the mosaic. One reason for this difficulty, is simply the lack of solid information concerning structural features at length scales between a few ångströms and a few nanometers. A second reason is that all of the structural probes yield only statistical information at best. As a consequence, a multitude of different structural models that reproduce the measurement data can be constructed, and no further criteria are available to distinguish among them.

Thus, it is necessary to complement the experiments with computer simulations. Structural models were generated by computational techniques and validated through comparison to the experimental results. As it was not obvious at the outset to what extent the synthesis route would determine the structural features of the amorphous ceramic, five different classes of models were generated for $Si_3B_3N_7$, each corresponding to a different (hypothetical) synthesis route (quenching from the melt, sintering of nanocrystals, growth and sintering of clusters, film deposition, and the actual polymer-precursor route). A comparison of these models to the experimental findings reveals that the short-range order in models of all classes agrees with the experimental data. However, beyond the nearest-neighbor peaks, the PCFs of the different model classes exhibit statistically significant differences. Satisfactory agreement with the experimental data is only found for two models, the nanocrystallite and the polymer-precursor models. These two models also show the best agreement with experiment regarding the inhomogeneous distribution of next-nearest neighbors. Note that the atomic configurations of these two classes of structural models have systematically higher energies than those of the other three model classes. This result implies that the partial separation of the cations at a subnanometer scale cannot be understood on a purely thermodynamic basis with energy minimization as the only criterion.

The best simulated models even agree with details of the experimental results. For example, the largest deviations from an ideal local environment in the models are found for the silicon atoms. These deviations are visible in the variation of the local coordination number and in the broad distribution of N-Si-N angles found by experiment. Even the edge sharing of polyhedra found in the calculated models can be identified as shoulders in the experimental PCFs, which were not previously assigned. The good agreement observed for both global and local structural properties makes us confident that a structural model coming close to reality has been achieved.

The rather low density found experimentally for $Si_3B_3N_7$ (only two thirds of the value expected for a binary mixture of h-BN and β-Si_3N_4) indicates that the amorphous compound has a rather open structure. Comparably low densities were also found for models simulated according to the polymer-precursor route (as the only one of the five model classes). The simulated relaxation of configurations with subnanometer-sized pores at constant temperature reveals a high structural stability to relatively high temperatures. With a knowledge of the structure, additional bulk properties of $Si_3B_3N_7$, such as the specific heat, the bulk modulus, or the thermal conductivity, can now be calculated; however, the corresponding experiments have not yet been performed.

To conclude, the investigations presented here strongly emphasize the fact that the structure of an amorphous material can only be successfully modeled by considering its synthesis route. Thus, in the case of amorphous $Si_3B_3N_7$, the modeling process must include the steps of polycondensation in solution, the aging of the polymer, and finally, the pyrolysis that forms the amorphous ceramic.

The work presented here was generously funded by the Fonds der Chemischen Industrie, the Max Planck Society, and the Deutsche Forschungsgemeinschaft (SFB 408 at the Rheinische-Friedrich-Wilhelms-Universität Bonn). The authors would like to thank all students and colleagues for their support in achieving the results. Their contributions are acknowledged by citing the respective publications. It is our particular pleasure to acknowledge the always pleasant and efficient cooperation with all of our colleagues in the SFB 408. Finally, we would like to thank Dr. Alexander Hannemann for his competent assistance in preparing the manuscript.

Received: November 24, 2005

[1] W. H. Zachariasen, *J. Am. Chem. Soc.* **1932**, *54*, 3841 – 3851.
[2] R. Zallen, *The Physics of Amorphous Solids*, Wiley, New York, **1983**.

 © 2006 Wiley-VCH Verlag GmbH & Co. KGaA, Weinheim

[3] S. R. Elliott, *Physics of Amorphous Materials*, Longman Scientific & Technical, Essex, **1990**.
[4] C. A. Angell, *Science* **1995**, *267*, 1924 – 1934.
[5] C. A. Angell, B. E. Richards, V. Velikov, *J. Phys. Condens. Matter* **1999**, *11*, A75 – A94.
[6] D. J. Wales, *Energy Landscapes with Applications to Clusters, Biomolecules and Glasses*, Cambridge University Press, **2004**.
[7] J. C. Schön, M. Jansen, *Angew. Chem.* **1996**, *108*, 1358 – 1377; *Angew. Chem. Int. Ed. Engl.* **1996**, *35*, 1286 – 1304.
[8] J. C. Schön, M. Jansen, *Z. Kristallogr.* **2001**, *216*, 307 – 325; J. C. Schön, M. Jansen, *Z. Kristallogr.* **2001**, *216*, 361 – 383.
[9] M. Jansen, *Angew. Chem.* **2002**, *114*, 3896 – 3917; *Angew. Chem. Int. Ed.* **2002**, *41*, 3747 – 3766.
[10] O. Mishima, L. D. Calvert, E. Whalley, *Nature* **1985**, *314*, 76 – 78.
[11] C. A. Tulk, C. J. Benmore, J. Urquidi, D. D. Klug, J. Neuefeind, B. Tomberli, P. A. Egelstaff, *Science* **2002**, *297*, 1320 – 1323.
[12] Formally, a system is termed ergodic if, for all observables, the time average along (infinitely long) trajectories equals the ensemble average. If this is the case, equilibrium statistical mechanics applies to the system under investigation. For many practical purposes, a system exhibiting ergodicity can be regarded as being in thermodynamic equilibrium. Signatures of nonergodic behavior include aging phenomena, a dependence of observables on process rates, or violations of the fluctuation-dissipation theorem. Note that even if the system as a whole is nonergodic, some subsystems might approximate ergodicity on the time scale of the observation. Such so-called locally ergodic regions[8] correspond to metastable compounds, for example.
[13] M. Goldstein, *J. Chem. Phys.* **1969**, *51*, 3728 – 3739.
[14] F. H. Stillinger, T. A Weber, *Phys. Rev. A* **1982**, *25*, 978 – 989.
[15] F. H. Stillinger, *Science* **1995**, *267*, 1935 – 1939.
[16] C. A. Angell, *The Landscape Paradigm* **1996**, 1 – 30.
[17] A. Heuer, *Phys. Rev. Lett.* **1997**, *78*, 4051 – 4054.
[18] J. C. Schön, P. Sibani, *J. Phys. A* **1998**, *31*, 8165 – 8178.
[19] W. Kob, *J. Phys. Condens. Matter* **1999**, *11*, R85 – R115.
[20] S. Sastry, P. G. Debenedetti, F. H. Stillinger, T. B. Schroder, J. C. Dyre, S. C. Glotzer, *Physica A* **1999**, *270*, 301 – 308.
[21] L. Angelani, G. Parisi, R. Ruocco, G. Viliani, *Phys. Rev. E* **2000**, *61*, 1681 – 1691.
[22] H. P. Baldus, O. Wagner, M. Jansen in *Mater. Res. Soc. Symp. Proc.*, *Vol. 271* (Eds.: M. J. Hampden-Smith, W. G, Klemperer, C. J. Brinker), p. 821–826, MRS, Warrendale, **1992**.
[23] M. Jansen, P. Baldus, *Angew. Chem.* **1997**, *109*, 338 – 354; *Angew. Chem. Int. Ed. Engl.* **1997**, *36*, 328 – 344.
[24] M. Jansen, *Solid State Ionics* **1997**, *101–103*, 1 – 7.
[25] M. Jansen, H. Jüngermann, *Curr. Opin. Solid State Mater. Sci.* **1997**, *2*, 150 – 157.
[26] "Amorphous Multinary Ceramics in the Si–B–N–C System": M. Jansen, B. Jäschke, T. Jäschke, *Struct. Bonding (Berlin)* **2002**, *101*, 138 – 191, and references therein.
[27] P. Baldus, M. Jansen, D. Sporn, *Science* **1999**, *285*, 699 – 703.
[28] K. Su, E. E. Remsen, G. A. Zank, L. G. Sneddon, *Chem. Mater.* **1993**, *5*, 547 – 556.
[29] O. Funayama, T. Kato, Y. Tashiro, T. Isoda, *J. Am. Ceram. Soc.* **1993**, *76*, 717 – 723.
[30] F. Aldinger, M. Weinmann, J. Bill, *Pure Appl. Chem.* **1998**, *70*, 439 – 448.
[31] D. Srivastava, E. N. Duesler, R. T. Painer, *Eur. J. Inorg. Chem.* **1998**, *6*, 855 – 859.
[32] R. Riedel, A. Kienzle, W. Dressler, L. Ruwisch, J. Bill, F. Aldinger, *Nature* **1996**, *382*, 796 – 798.
[33] Depending on the details of the synthesis (for example, choice of precursor, linking agent, atmosphere, and temperature program for pyrolysis), different ceramics (containing varying amounts of carbon, for example) are produced. Herein, we focus on the prototypical amorphous ternary nitride $Si_3B_3N_7$, as its composition is well defined, in contrast to that of amorphous $SiBN_3C$, for example.
[34] D. Heinemann, W. Assenmacher, W. Mader, M. Kroschel, M. Jansen, *J. Mater. Res.* **1999**, *14*, 3746 – 3753.
[35] The distance criterion that we use to define medium-range order in this discussion is the one commonly used in NMR spectroscopy. Alternative definitions focus on the relative orientation of coordination polyhedra and, thus, define medium-range order as starting at approximately 4 Å.
[36] G. Binnig, H. Rohrer, C. Gerber, E. Weibel, *Appl. Phys. Lett.* **1982**, *40*, 178 – 180.
[37] W. Raberg, V. Lansmann, M. Jansen, K. Wandelt, *Angew. Chem.* **1997**, *109*, 2760 – 2762; *Angew. Chem. Int. Ed. Engl.* **1997**, *36* 2646 – 2648.
[38] R. Franke, St. Bender, I. Arzberger, J. Hormes, M. Jansen, H. Jüngermann, J. Löffelholz, *Fresenius J. Anal. Chem.* **1996**, *354*, 874 – 878.
[39] R. Franke, St. Bender, H. Jüngermann, M. Kroschel, M. Jansen, *J. Electron Spectrosc.* **1999**, *101–103*, 641 – 645.
[40] R. Franke, J. Hormes, *SFB-408-Arbeits- und Ergebnisbericht 1995 – 1997*, Bonn, **1998**.
[41] R. M. Hagenmayer, U. Müller, C. J. Benmore, J. Neuefeind, M. Jansen, *J. Mater. Chem.* **1999**, *9*, 2865 – 2870.
[42] R. M. Hagenmayer, U. Müller, M. Jansen, *Physica B* **2000**, *276–278*, 423 – 424.
[43] K. R. Carduner, C. S. Blackwell, W. B. Hammond, F. Reidinger, G. R. Hatfield, *J. Am. Chem. Soc.* **1990**, *112*, 4676 – 4679.
[44] U. Müller, W. Hoffbauer, M. Jansen, *Chem. Mater.* **2000**, *12*, 2341 – 2346.
[45] G. Jeschke, M. Jansen, *Angew. Chem.* **1998**, *110*, 1342 – 1343; *Angew. Chem. Int. Ed.* **1998**, *37*, 1282 – 1283.
[46] G. Jeschke, W. Hoffbauer, M. Jansen, *Solid State Nucl. Magn. Reson.* **1998**, *12*, 1 – 7.
[47] R. K. Harris, M. J. Leach, D. P. Thompson, *Chem. Mater.* **1990**, *2*, 320 – 323.
[48] G. Jeschke, M. Kroschel, M. Jansen, *J. Non-Cryst. Solids* **1999**, *260*, 216 – 227.
[49] B. F. Chmelka, K. T. Mueller, A. Pines, J. Stebbins, Y. Wu, J. W. Zwanziger, *Nature* **1989**, *339*, 42 – 43.
[50] K. T. Mueller, J. H. Baltisberger, E. W. Wooten, A. Pines, *J. Phys. Chem.* **1992**, *96*, 7001 – 7004.
[51] A. Samoson, E. Lippmaa, *J. Magn. Reson.* **1989**, *84*, 410 – 416.
[52] K. T. Mueller, Y. Wu, B. F. Chmelka, J. Stebbins, A. Pines, *J. Am. Chem. Soc.* **1991**, *113*, 32 – 38.
[53] A. Medek, J. S. Harwood, L. Frydman, *J. Am. Chem. Soc.* **1995**, *117*, 12779 – 12787.
[54] A. Medek, L. Frydman, *J. Braz. Chem. Soc.* **1999**, *10*, 263 – 277.
[55] J.-P. Amoureux, M. Pruski, D. P. Lang, C. Fernandez, *J. Magn. Reson.* **1998**, *131*, 170 – 175.
[56] J.-P. Amoureux, C. Fernandez, S. Steuernagel, *J. Magn. Reson. Ser. A* **1996**, *123*, 116 – 118.
[57] L. B. Alemany, S. Steuernagel, J.-P. Amoureux, R. L. Callender, A. K. Barron, *Solid State Nucl. Magn. Reson.* **1999**, *14*, 1 – 18.
[58] T. Gullion, J. Schaefer, *J. Magn. Reson.* **1989**, *81*, 196 – 200.
[59] Y. Pan, T. Gullion, J. Schaefer, *J. Magn. Reson.* **1990**, *90*, 330 – 340.
[60] A. E. Bennet, R. G. Griffin, S. Vega, *NMR Basic Principles and Progress*, *Vol. 33*, Springer, Berlin, **1994**.
[61] L. van Wüllen, B. Gee, L. Züchner, M. Bertmer, H. Eckert, *Ber. Bunsen-Ges.* **1996**, *100*, 1539 – 1549.
[62] L. van Wüllen, L. Züchner, W. Müller-Warmuth, H. Eckert, *Solid State Nucl. Magn. Reson.* **1996**, *6*, 203 – 212.
[63] T. Gullion, *Magn. Reson. Rev.* **1997**, *17*, 83 – 131.
[64] T. Gullion, *J. Magn. Reson.* **1995**, *117*, 326 – 329.
[65] T. Gullion, *Chem. Phys. Lett.* **1995**, *246*, 325 – 330.
[66] L. Chopin, S. Vega, T. Gullion, *J. Am. Chem. Soc.* **1998**, *120*, 4406 – 4409.

 © 2006 Wiley-VCH Verlag GmbH & Co. KGaA, Weinheim

[67] L. van Wüllen, U. Müller, M. Jansen, *Chem. Mater.* **2000**, *12*, 2347 – 2352.
[68] M. Baks, J. T. Rasmussen, N. C. Nielsen, *J. Magn. Reson.* **2000**, *147*, 296 – 330.
[69] L. van Wüllen, U. Müller and M. Jansen, *Angew. Chem.* **2000**, *112*, 2574 – 2576; *Angew. Chem. Int. Ed.* **2000**, *39*, 2519 – 2521.
[70] L. van Wüllen, M. Jansen, *J. Mater. Chem.* **2001**, *11*, 223 – 229.
[71] D. Lathrop, D. Franke, R. Maxwell, T. Tepe, R. Flesher, Z. Zhang, H. Eckert, *Solid State Nucl. Magn. Reson.* **1992**, *1*, 73 – 83.
[72] J. H. van Vleck, *Phys. Rev.* **1948**, *74*, 1168 – 1183.
[73] K. D. Schulmeister, Dissertation, Universität Bonn, **2003**.
[74] A. Hannemann, J. C. Schön, H. Putz, T. Lengauer, M. Jansen, *Phys. Rev. B* **2004**, *70*, 144201.
[75] A. Hannemann, J. C. Schön, C. Oligschleger, M. Jansen in *Proc. DGK-Workshop on Struktur und Eigenschaften nichtkristalliner Materialien – Meßdaten und Strukturmodelle (Wolfersdorf, September 1999)* (Ed.: B. Müller), Universität Jena **1999**; see also: Cond-Mat/0001319.
[76] L. F. Gladden, *J. Non-Cryst. Solids* **1990**, *119*, 318 – 330.
[77] S. Wefing, *J. Non-Cryst. Solids* **1999**, *244*, 89 – 111.
[78] A. Hannemann, J. C. Schön, M. Jansen, *Comput. Phys. Commun.* **2002**, *144*, 284 – 296.
[79] J. C. Schön, A. Hannemann, M. Jansen, *J. Phys. Chem. B* **2004**, *108*, 2210 – 2217.
[80] A. Hannemann, J. C. Schön, M. Jansen, *J. Mater. Chem.* **2005**, *15*, 1167 – 1178.
[81] M. Gastreich, C. M. Marian, J. D. Gale, *Phys. Rev. B* **2000**, *62*, 3117 – 3123.
[82] U. Müller, *Anorganische Strukturchemie*, Teubner, Stuttgart, **1992**.
[83] P. Kroll, R. Hoffmann, *Angew. Chem.* **1998**, *110*, 2616 – 2620; *Angew. Chem. Int. Ed.* **1998**, *37*, 2527 – 2530.
[84] A. Hannemann, J. C. Schön, M. Jansen, *Philos. Mag.* **2005**, *85*, 2621 – 2639.
[85] A. Hannemann, J. C. Schön, M. Jansen, P. Sibani, *J. Phys. Chem. B* **2005**, *109*, 11770 – 11776.
[86] Preliminary experimental measurements of the density of $Si_3B_3N_7$ after the application of high pressures[87] appear to be in good qualitative agreement with our simulations.
[87] P. Balog, personal communication, **2003**.
[88] J. D. Gale, *J. Chem. Soc. Faraday Trans.* **1997**, *93*, 629 – 637.
[89] A. Hannemann, Dissertation, Universität Bonn, **2003**.
[90] Comparison with an experimental IR spectrum[91] collected at an early stage in the pyrolysis indicates a qualitative agreement between the calculated and observed results.
[91] O. Wagner, Diplomarbeit, Universität Bonn, **1991**.
[92] C. Oligschleger, J. C. Schön, *Phys. Rev. B* **1999**, *59*, 4125 – 4133.
[93] J. C. Schön, A. Hannemann, G. Sethi, M. Jansen, P. Salamon, R. Frost, L. Kjeldgaard in *Proc. XXIII Workshop on structure and kinetics of nucleation and crystallization in non-crystalline materials* (Ed.: B. Müller), Jena, September **2002**; see also: cond-mat/0212279.
[94] A. Hannemann, J. C. Schön, M. Jansen, *Phys. Rev. E*, submitted.

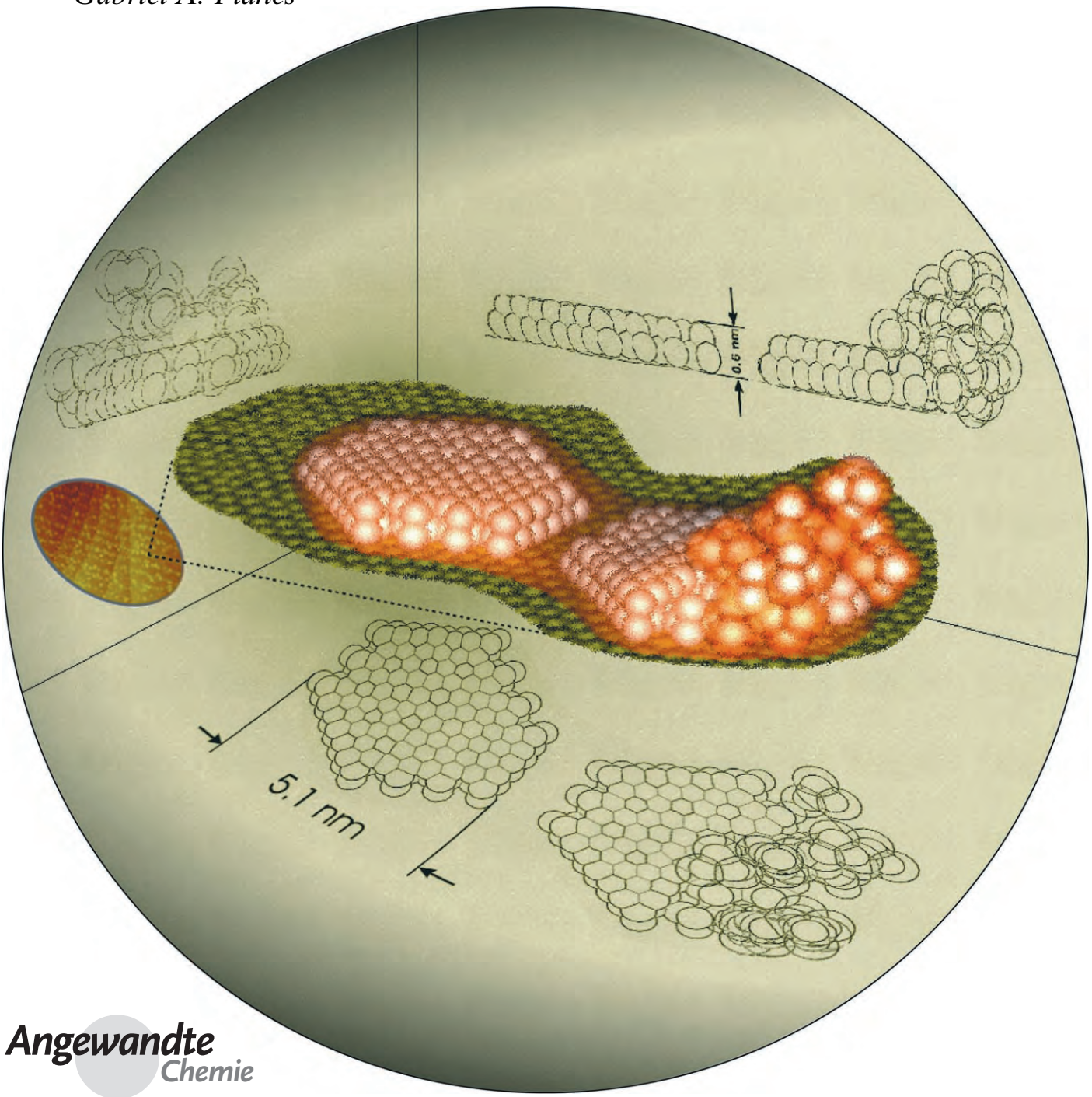
 © 2006 Wiley-VCH Verlag GmbH & Co. KGaA, Weinheim

Nanostructures

DOI: 10.1002/anie.200600826

Assembly of Subnanometric 2D Pt Nanoislands in Parallel Rows onto Au(111) by Self-Organization of Pt Clusters**

*Olmedo Guillén-Villafuerte, Gonzalo García, Benito Anula, Elena Pastor, María C. Blanco, Manuel A. López-Quintela, Alberto Hernández-Creus, and Gabriel A. Planes**



WILEY InterScience DISCOVER SOMETHING GREAT

© 2006 Wiley-VCH Verlag GmbH & Co. KGaA, Weinheim

The synthesis of ordered nanomaterials is one of the key points in the development of novel nanotechnologies. For this purpose, simple routes to prepare building nanoblocks and their self-assembly is of special importance in the bottom-up approach.[1] One of the most extensively studied ways to obtain nanoparticles is the microemulsion technique.[1–5] In this method, small quantities of water are added to a solution of surfactant/oil; the resulting mixture is known as a water-in-oil microemulsion. If a metal precursor is contained within the water droplets, the addition of a reducing agent can result in the formation of metal particles inside these aqueous nanoreactors.[6]

It has been recently demonstrated by in situ X-ray absorption spectroscopy studies that very small Pt clusters (diameters of less than 1 nm), with a coordination number per Pt atom as low as three, are the final product inside the micelle during the synthesis of Pt nanoparticles.[7] However, a posterior aggregation that produces larger nanoparticles occurs so frequently that it is difficult to find particles deposited on surfaces with sizes below 2–3 nm; in particular, TEM measurements in the same report showed contrasting results due to cluster aggregation during the drying process. On the other hand, metallic surfaces are frequently used to assemble stable nanometric or subnanometric structures by different techniques.[8] Nevertheless, this is usually a slow and expensive process. Herein, Pt clusters are assembled on two different hierarchical levels. The first level involves the formation of a 2D island over an Au(111) surface. At the same time, this island self-organizes to form patterns of parallel rows of several hundred of nanometers in length to give rise to a second hierarchical level.

As a result of the high resolution at atomic scale, scanning tunneling microscopy (STM) was used to examine the morphology of the Pt nanoparticles deposited on the metal surface. These Pt nanoparticles were prepared by applying a modification of the method previously described by Rivadulla et al.[9] Pt clusters were formed following this synthesis using a low excess (25%) of reducing agent (microemulsion A). Transmission electron microscopy (TEM) analyses[9] were performed to measure the particle size. Thus, a few drops of microemulsion A were deposited onto a TEM grid. Figure 1 confirms the existence of nanoparticles (dark spots) with a diameter range of 5.1 ± 0.8 nm. This value agrees with those previously reported.[9]

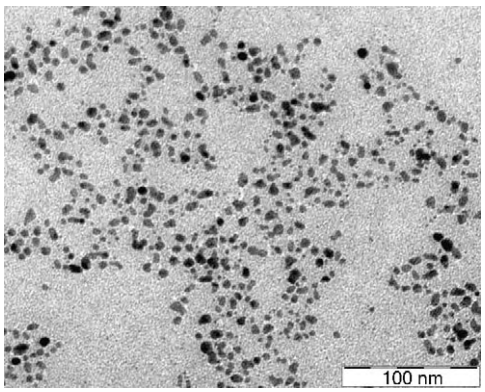


Figure 1. TEM image of Pt nanoparticles obtained from water-in-oil microemulsion A (using a PHILIPS CM-12 transmission electron microscope operating at 100 kV).

To obtain a more accurate idea of the spatial structure of these particles, 1 μL of microemulsion A was dropped on the Au (111) surface for STM studies. Then, the sample was washed copiously with acetone and finally with milli-Q water. Figure 2 shows a typical STM image (right) and the corresponding cross-section of the deposit (left). This result reveals that the gold surface is covered with circular structures. The dimensions obtained from the cross-sectional analysis show that these Pt deposits are 4–6 nm in diameter, in good agreement with data obtained from TEM. Surprisingly, the maximum in height reached by the Pt nanoparticles never exceeds 0.8 nm, with most of them around 0.6-nm high.[10] That is, the aspect ratio is more like that of flat disks than spheres. Thus, a single nanoisland is estimated to be composed of a total of about 500 Pt atoms.

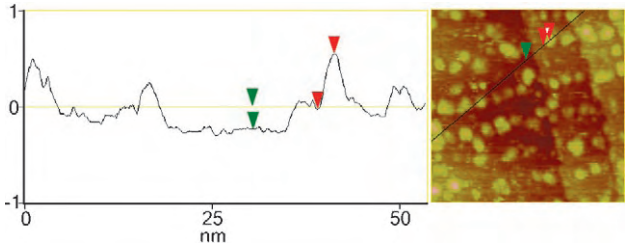


Figure 2. Cross-sectional analysis (left) and 52×52 nm^2 STM image (right) showing Pt nanoislands. The height of an island (red pointers) and that of a typical Au(111) monoatomic step (green pointers) are indicated for comparison.

In good agreement with previous findings,[7,11,12] the results described herein support the idea of a pool of isolated clusters, with each one formed from a few Pt atoms, in the aqueous medium of each droplet. Contrary to Ref. [7], in which Pt clusters probably collapse during the drying process

[*] O. Guillén-Villafuerte, G. García, B. Anula, Prof. E. Pastor, Prof. A. Hernández-Creus, Dr. G. A. Planes
Departamento de Química Física
Facultad de Química
Universidad de La Laguna
Astrofísico F. Sánchez s/n
38071 La Laguna, Tenerife (Spain)
Fax: (+34) 922-31-8033
E-mail: gplanes@ull.es
Prof. M. C. Blanco, Prof. M. A. López-Quintela
Laboratorio de Magnetismo y Nanotecnología
Instituto de Investigacións Tecnológicas
Universidade de Santiago de Compostela
15782 Santiago de Compostela (Spain)

[**] Financial support from MEC (MAT2005-06669-C03-02, NAN2004-09333-C05-04, MAT2005-07554-C02-01, and BQU 2005-03222) is gratefully acknowledged. O.G.V. acknowledges Cajacanarias, G.G. thanks the MEC for an FPI grant, and G.A.P. acknowledges MEC for a fellowship.

 © 2006 Wiley-VCH Verlag GmbH & Co. KGaA, Weinheim

onto the carbon-coated grid, the interaction between an individual drop and Au (111) surface freezes the pool of clusters in a side-to-side configuration, thereby maximizing the Pt–Au contact surface and avoiding such agglomerations. This result then raises the question of the exact nature and structure of microemulsion-synthesized nanoparticles, and also confirms those reported in Ref. [7]. Under some experimental conditions, namely kinetics/concentration control, the formation of clusters from a few atoms is favored.

The second and more important finding is the trend of the islands to form straight, parallel lines in a long-range arrangement, as can be seen in the STM images given in Figure 3 A. Domains with rows of around 400 nm in length are

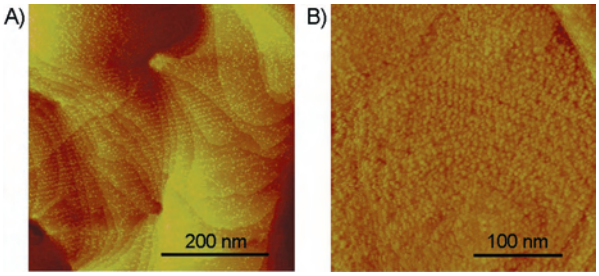


Figure 3. A) 500×500 nm^2 STM images of Au(111) surface showing the Pt nanoisland array. B) Surface after chemical reduction.

observed. Figure 3 A also reveals that rows of Pt islands are growing (approximately equally spaced, about 5 nm) in directions that are not those of the Au(111) steps. Moreover, the absence of Au reconstruction under such experimental conditions was verified, and the influence of the substrate as being directly responsible for this order was discarded.

To clarify the possible cause for spacing between the Pt rows, the same Pt-modified Au(111) plate was subsequently exposed to a dilute solution of aqueous hydrazine. STM analysis indicates that, after reduction, the surface is fully covered with a monolayer of Pt nanoislands of the same size as before. However, it is now difficult to appreciate the Au(111) substrate (see Figure 3 B). The same feature is achieved when reduced electrochemically (data not shown). This result points out that unreduced Pt ions, which are present initially in some micelles in microemulsion A, are filling the space between Pt rows. It has been shown that Pt ions can remain unreduced or partially reduced inside micelles.[7] These Pt ions are able to survive the hard cleaning process, probably by being stabilized inside the aqueous core of the attached micelle. A similar STM analysis was carried out with nanoparticles obtained by the microemulsion synthesis but using a higher excess of hydrazine during preparation of the particles (100 % excess, microemulsion B). The corresponding image revealed that the surface is initially fully covered with such nanoislands (data not shown).

To check further if the Pt ions are really needed for the space between the rows, complementary experiments were carried out with a 1:3 w/w mixture of the microemulsion containing only Pt_n clusters (microemulsion B) and a microemulsion containing only perchloric acid (microemulsion C). The same results were obtained as in the case of using microemulsion A, that is, the formation of spaced Pt nanoislands rows over the Au(111) surface was observed. Therefore, it appears that these micelles have no special effect on ordering and that they are merely excluded during construction of the Pt island array and limited to form the interline gap.

The most surprising fact that we wish to comment on here is not the single rows of Pt nanoislands but the capability of the system to form them by selecting between micelles that contain Pt_n clusters and those that are free of clusters. The trend of nanoparticles to connect and thereby form long nanowires has been found for other hybrid inorganic–organic structures.[13] The present system seems to obey the model of mesoscale transformation induced by crystallization, in which crystallization and surfactant reorganization are the driving force for the process.[14] In our case, the presence of surfactant molecules attached to Pt clusters avoids further crystallization while they are in a microemulsion. This idea is supported by the long-term stability of the microemulsion. At this first stage, permanent association of the micelle is impossible and all micelles in the microemulsion are isomorphs. However, during the deposition process, the micelles closely pack at the surface. Note that this theory is unable to explain the observed linear order.

The key point is that during deposition onto Au(111) (nanoisland formation), the isomorphic character of the micelles that contain clusters is significantly altered. The presence of a local crystalline order supplied by the Au(111) surface reinforces the trend of cluster aggregates to suffer an amorphous-to-crystalline transition when contacting with the surface. The formation of such an ordered array of clusters breaks the initial symmetry, and the anchored surfactant molecules are now reorganized according to the new situation. Hence, interparticle organizations, which probably involve association of surfactant molecules, unleash the mesoscale assembly. As cooperative particle interactions are energetically suitable for cluster-filled micelles only, the presence of cluster-empty micelles leads to a segregation process that produces the observed spaced linear arrays.

In summary, our results clearly show a hierarchical organization of Pt clusters at two different levels. The process starts with a pool of clusters inside the droplets of the microemulsion. On depositing the solution over the surface, two organization levels appear: The first, related to the interaction between microemulsion droplets and the surface (in this particular case Au) promotes the formation of a monolayer composed of circular arrays of those clusters. The diameters of the islands correspond approximately to the observed nanoislands by TEM, but they are only 0.6 nm in height. The next and more complex level implies the spontaneous formation of alternated lines, of hundred of nanometers long, composed of empty and cluster-filled micelles. Moreover, this atypical level of order can not be understood in classical terms, such as surface structure of the substrate or simple arrangement of undistinguishable objects, and it is a property governed (at least partially) by the nature of the micellar contents.

 © 2006 Wiley-VCH Verlag GmbH & Co. KGaA, Weinheim

Finally, our results also agree with recently reported findings,[7,11,15] thus showing that the formation of nanoparticles proceeds through special stable clusters that can be identified and, in some cases, also conveniently stabilized and isolated in appreciable amounts.[11] Owing to the key importance for future developments in the bottom-up building concept of materials science, studies devoted to understand more accurately the effect of parameters on the mechanism for patterning are specially interesting. Studies focused on clarifying the properties of Pt clusters and nanoislands, as well as the structural characterization of the clusters, are now in progress.

Experimental Section

Platinum nanoparticles were obtained by reduction of H_2PtCl_6 (8% wt; Aldrich) with hydrazine monohydrate (99.0% Fluka) using a water/oil microemulsion of water/polyethyleneglycol-dodecylether (BRIJ 30)/*n*-heptane.[9] The size of the microemulsion droplet is determined by the molar ratio (R) of water to surfactant.[2] In this work, R was fixed to six. The concentration of the surfactant was 16.54% w/w and that of the H_2PtCl_6 solution employed in the synthesis was 0.2 M (in the aqueous phase).

Briefly, synthesis of the nanoparticles proceeded as follows. First, two microemulsions were prepared, one of them containing hexachloroplatinic acid in the aqueous phase, and the second one containing hydrazine. Both microemulsions were left stirring during several hours until a clear homogeneous solution was obtained (this is a key point in the synthesis: shorter times promoted the appearance of a dark precipitate during synthesis). After that, they were combined under stirring to form a single microemulsion. The final solution has a clear red color. Solid deposits were never detected, even for aged microemulsions of Pt nanoparticles. UV/Vis spectra did not reveal a peak at 300 nm, which was attributed to agglomeration of the particles in Ref. [9], and did not change over time (several months) thus suggesting an especially stable cluster system.

Two different microemulsions containing Pt nanoparticles were prepared. Microemulsion A contained a low excess (25%) of the reducing agent, whereas microemulsion B contained a 100% excess of hydrazine. During the reduction process, the color of the microemulsion changed from yellow-orange to red-brown. A third microemulsion without Pt (microemulsion C), containing an aqueous solution of perchloric acid (0.2 M), was prepared for comparison purposes.

The electrochemical reduction was carried out in a thermostated three-electrode cell using a computer-controlled Heka PG 310 potentiostat/galvanostat, with 0.1 M perchloric acid as electrolyte. A potential of 0.20 V (vs RHE) was applied until complete reduction of Pt ions occurred.

STM images (constant current mode) were taken with a Nanoscope IIE (Digital Instrument, Santa Barbara, CA) using commercial and electrochemically etched Pt-Ir tips. All images were acquired in air. Typical tunneling currents and applied voltages to obtain good-quality images were 0.6–0.8 nA and 0.3–0.6 V, respectively, at scan rates ranging from 0.5 to 2 Hz. Au plates (1×0.5 cm^2; arrandee) were used as the substrate. After flame annealing, these plates consisted of micrometer-sized Au(111) preferred oriented crystals with atomically smooth terraces separated by monoatomic steps in height. The height of these steps (0.24 ± 0.02 nm) was used to calibrate the piezotube of the STM in the z direction. Several STM samples were prepared and investigated, and different sites over each modified surface were analyzed. The STM and electrochemical experiments as well as the microemulsion synthesis were carried out at room temperature. For micelle deposition over Au(111), the Au plate was maintained at 60 °C.

Received: March 2, 2006
Revised: March 31, 2006

Keywords: nanostructures · platinum · scanning probe microscopy · self-assembly

[1] a) S. H. Sun, C. B. Murria, D. Séller, A. Moser, *Science* **2000**, *287*, 1989–1992; b) A. N. Shipway, E. Katz, I. Willner, *ChemPhysChem* **2000**, *1*, 18–52.
[2] M. A. López-Quintela, *Curr. Opin. Colloid Interface Sci.* **2003**, *8*, 137–144.
[3] a) C. Petit, A. Taleb, M. P. Pileni, *J. Phys. Chem. B* **1999**, *103*, 1805–1810; b) M. A. López-Quintela, J. Rivas, *J. Colloid Interface Sci.* **1993**, *158*, 446–451; c) C. Petit, P. Lixon, M. P. Pileni, *J. Phys. Chem.* **1993**, *97*, 12974–12983; d) M. P. Pileni, *J. Phys. Chem.* **1993**, *97*, 6961–6973.
[4] a) K. Osseo-Asare in *Handbook of Microemulsion Science and Technology* (Eds.: P. Kumar, K. L. Mittal), Marcel Dekker, New York, **1999**, p. 549; b) L. Liz, M. A. López-Quintela, J. Mira, J. Rivas, *J. Mater. Sci.* **1994**, *29*, 3797–3801; c) J. A. López-Pérez, M. A. López-Quintela, J. Mira, J. Rivas, S. W. Charles, *J. Phys. Chem. B* **1997**, *101*, 8045–8047.
[5] M. Antonietti, R. Basten, S. Lohmann, *Macromol. Chem. Phys.* **1995**, *196*, 441–446.
[6] For recent reviews, see: a) M. A. López-Quintela, C. Tojo, M. C. Blanco, L. García-Rio, J. R. Leis, *Curr. Opin. Colloid Interface Sci.* **2004**, *9*, 264–278; b) I. Capek, *Adv Colloid Interface Sci.* **2004**, *110*, 49–79.
[7] Y. W. Tsai, Y. L. Tseng, L. S. Sarma, D. G. Liu, J. F. Lee, J. Hwang, *J. Phys. Chem. B* **2004**, *108*, 8148–8152.
[8] J. Mühlbach, K. Sattler, E. Recknagel, *Surf. Sci.* **1981**, *106*, 188–194.
[9] J. F. Rivadulla, M. C. Vergara, M. C. Blanco, M. A. López-Quintela, J. Rivas, *J. Phys. Chem. B* **1997**, *101*, 8997–9004.
[10] For all particles that are at least 0.3 nm high, 40% of them reach 0.6 nm, only 10% achieve 0.7 nm, and no nanoparticles of over 0.8 nm in height were found.
[11] "Procedure for the synthesis of atomic quantum clusters": M. A. López-Quintela, J. Rivas, Spanish patent application No.P200502041, **2005**.
[12] a) A. J. García-Bastida, J. Rivas, M. A. López-Quintela, *Trans. Mater. Res. Soc. Jpn.* **2004**, *29*, 351–356; b) J. Rivas, A. J. Garcia-Bastida, M. A. Lopez-Quintela, C. Ramos, *J. Magn. Magn. Mater.*, in press.
[13] a) Z. Tang, N. A. Kotov, M. Giersig, *Science* **2002**, *297*, 237–240; b) M. Giersig, I. Pastoriza-Santos, L. M. Liz-Marzán, *J. Mater. Chem.* **2004**, *14*, 607–610.
[14] For reviews, see: H. Colfen, S. Mann, *Angew. Chem.* **2003**, *115*, 2350–2365; *Angew. Chem. Int. Ed.* **2003**, *42*, 2350–2365.
[15] a) T. Yonezawa, K. Yasui, N. Kimikuza, *Langmuir* **2001**, *17*, 271–273; b) M. Zhao, L. Sun, R. M. Crooks, *J. Am. Chem. Soc.* **1998**, *120*, 4877–4878; c) S. H. Chen, K. Kimura, *Langmuir* **1999**, *15*, 1075–1082; d) J. T. Petty, J. Zheng, N. V. Hud, R. M. Dickson, *J. Am. Chem. Soc.* **2004**, *126*, 5207–5212; e) K. Esumi, T. Hosoya, A. Suzuki, K. Torigoe, *J. Colloid Interface Sci.* **2000**, *229*, 303–306; f) G. H. Woehrle, M. G. Warner, J. E. Hutchinson, *J. Phys. Chem. B* **2002**, *106*, 9979–9981; g) T. G. Schaaff, R. L. Whetten, *J. Phys. Chem. B* **2000**, *104*, 2630–2641; h) Y. Negishi, T. Tsukuda, *J. Am. Chem. Soc.* **2003**, *125*, 4046–4047; i) T. G. Schaaff, M. N. Shafigullin, J. T. Khoury, I. Vezmar, R. L. Whetten, *J. Phys. Chem. B* **2001**, *105*, 8785–8796; j) R. L. Donkers, D. Lee, R. W. Murray, *Langmuir* **2004**, *20*, 1945–1952.

 © 2006 Wiley-VCH Verlag GmbH & Co. KGaA, Weinheim

Chemistry of Vision (1)

DOI: 10.1002/anie.200600595

Crystallographic Analysis of Primary Visual Photochemistry**

*Hitoshi Nakamichi and Tetsuji Okada**

Photochemical *cis–trans* isomerization of the retinylidene chromophore is the mechanism of the primary visual process in the eye. 11-*cis*-Retinal is covalently linked not only to the dim-light photoreceptor protein rhodopsin but also to each of the three color pigments in humans. All of these proteins belong to the superfamily of G protein coupled receptors (GPCRs). To achieve extreme sensitivity for photon detection, the photoisomerization reaction to the all-*trans* form in these pigments has to be strictly designed for efficient formation of the active form of the protein moiety, which catalyzes guanosine diphosphate to triphosphate (GDP–GTP) exchange in the α-subunit of the G protein. To understand the molecular mechanism of this primary photochemistry, detailed structural analysis is required. Recent advances in X-ray crystallographic studies of rhodopsin[1–3] have opened a way to investigate the photoreaction with subatomic resolution.

The first intermediate that can be trapped following light absorption by rhodopsin is bathorhodopsin (Figure 1 a). Formation of bathorhodopsin occurs on an ultrafast timescale of a few hundred femtoseconds at room temperature.[4] It exhibits a high quantum yield of 0.67[5] and stores about two-thirds of the photon energy (36 kcal mol^{-1}),[6] which is used to drive the formation of subsequent intermediates. Spectroscopic studies at low temperature or with time resolution yielded indirect structural data for this photochemical intermediate. Resonance Raman spectra of trapped bathorhodopsin indicated a strongly distorted chromophore in the region where the isomerization has taken place;[7] this distortion was recently substantiated and quantified to some extent.[8] Photoaffinity labeling studies of the bathorhodopsin intermediate indicated that the "loose" end of the chromophore, that is, the β-ionone ring, does not change its position relative to the dark state,[9] confirming the notion that the perturbation caused by the photoreaction is initially localized on a relatively small part of the chromophore. This view is supported by recent solid-state NMR spectroscopic observations of the methyl groups of the β-ionone ring which show that the ring is retained through strong selective interactions within the binding site into the activated state.[10] Also, magic-angle spinning solid-state NMR spectra of isotopically labeled bathorhodopsin revealed only minor differences in chemical shifts compared to rhodopsin, indicating that the protein environment of the chromophore, in particular the interaction with the counterion Glu113, does not change significantly.[11]

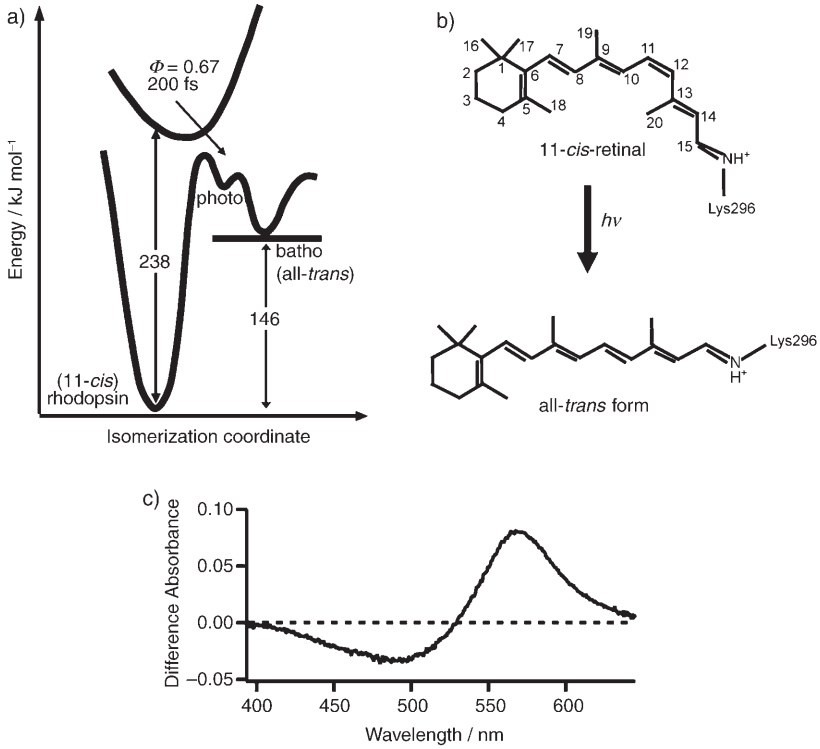


Figure 1. The primary photochemistry in vision involves 11-*cis* to all-*trans* photoisomerization of retinal. a) Schematic drawing of energy changes during the photoisomerization reaction. The photochemical precursor of bathorhodopsin is not detectable under cryogenic conditions. b) Chemical structure of the two isomeric forms of retinal before and after photoisomerization. The numbering scheme of carbon atoms is shown for 11-*cis*-retinal. c) Spectral changes observed upon conversion from rhodopsin to bathorhodopsin in a three-dimensional crystal at 105 K. A difference spectrum before and after illumination with 488 nm light is shown.

[*] H. Nakamichi, Dr. T. Okada
Biological Information Research Center
National Institute of Advanced Industrial Science and Technology
2-41-6 Aomi, Koto-ku, Tokyo 135-0064 (Japan)
Fax: (+81) 3-3529-5379
E-mail: t-okada@aist.go.jp
and
Core Research for Evolution Science and Technology (CREST)
Japan Science and Technology Agency (Japan)

[**] We are grateful to H. Sakai and M. Kawamoto for excellent support at BL41XU of SPring-8, to T. Yoshizawa, Y. Shichida, M. Sakurai, E. M. Landau, and J. Navarro for critical reading of the early draft of the manuscript, and to M. Schreiber, M. Sugihara, and V. Buss for preparation of the manuscript. This research was supported in part by grants from MEXT (15687005) and by NEDO. The coordinate file of bathorhodopsin has been deposited with the Protein Data Bank (ID: 2G87).

Supporting information for this article is available on the WWW under http://www.angewandte.org or from the author.

InterScience
© 2006 Wiley-VCH Verlag GmbH & Co. KGaA, Weinheim

Herein, we report the first structural view of bathorhodopsin examined by X-ray crystallography of illuminated rhodopsin crystals under cryogenic conditions. Structural changes in the protein environment induced by the conformational change of the chromophore suggest possible pathways towards the activated state of rhodopsin.

To study the structural differences between rhodopsin and bathorhodopsin, X-ray diffraction data were collected from frozen crystals with and without illumination. Crystals exposed to light with a wavelength of 488 nm at 95 K produced a red-shifted absorption spectrum (Figure 1c), which was similar to that of bathorhodopsin in solution. Under almost identical conditions to this offline spectroscopy, crystals were illuminated during collection of the diffraction data. The building of the model of bathorhodopsin was guided by difference electron densities, which were calculated with two data sets obtained before and after illuminating a crystal that reveals only a negligible amount of twinning (data set 2, see Supporting Information). Most of the large peaks were found only in the limited regions around the retinal unit (Figure 2a) and consistently in the two molecules in the asymmetric unit. The residues associated with the prominent peaks (3.5 σ) are Cys110, Glu113, Thr118, Glu122, Cys167, Cys187, Met207, Phe212, Trp265, Tyr268, and Lys296 (Figure 2b,c). A control difference map calculated with two data sets collected sequentially from a crystal without illumination showed no significant signals, indicating that the effect of radiation damage to the crystal was negligible (data not shown).

The pattern of difference densities corresponding to retinal was unexpected: a pair of strong positive and negative densities appeared at the β-ionone ring and around the C11=C12 bond (Figure 2b,c). This finding is not consistent with a simple one-bond flip for the photoisomerization process. We confirmed these differences between rhodopsin and bathorhodopsin in a number of data sets, two of which are shown in the Supporting Information. The structure refinement of bathorhodopsin was continued with one of these data sets, data set 1. Although the resolution of our data is not very high and is comparable with that of the lowest resolution model of the primary K state of bacteriorhodopsin, the clear difference electron densities calculated from the data with negligible twinning provide strong evidence for the magnitude and direction of the atomic displacement.[12]

Difference electron-density maps were also used to determine the ranges of amino acid residues that should be included in the refinement. We chose Asp83–Thr94, Cys110–Glu122, Glu181–Gly188, Tyr206–Phe212, Trp265–Gly270, and Pro291–Ala299 as the region that was large enough to cover all of the possible differences between rhodopsin and bathorhodopsin. Then, by taking only the reproducible and substantial structural differences, 11 residues as noted above were selected in the final alternate conformation refinement with an optimized ratio of rhodopsin and bathorhodopsin (see Experimental Section).

The structural change of the retinal polyene chain from rhodopsin to bathorhodopsin is small at the carbon atoms C9, which has a methyl group attached, and C13 (Figure 3a,b). The C11=C12 bond is displaced towards the cytoplasmic side, in the vicinity of Trp265 in transmembrane helix (TMH)-VI, while the chain from C7 to C9 and the β-ionone ring move downward in a seesaw-like fashion with C9 at the center (Figure 3c). The dihedral angle around the C11=C12 bond changes from about −40° to −155° upon isomerization, with a substantial rotation of the methyl group at C13 in the same direction as the pre-twist in rhodopsin. Overall, the polyene chain of retinal is quite distorted, with all dihedral angles around the double bonds lying in the range from −150° to −170°. The largest twist among the

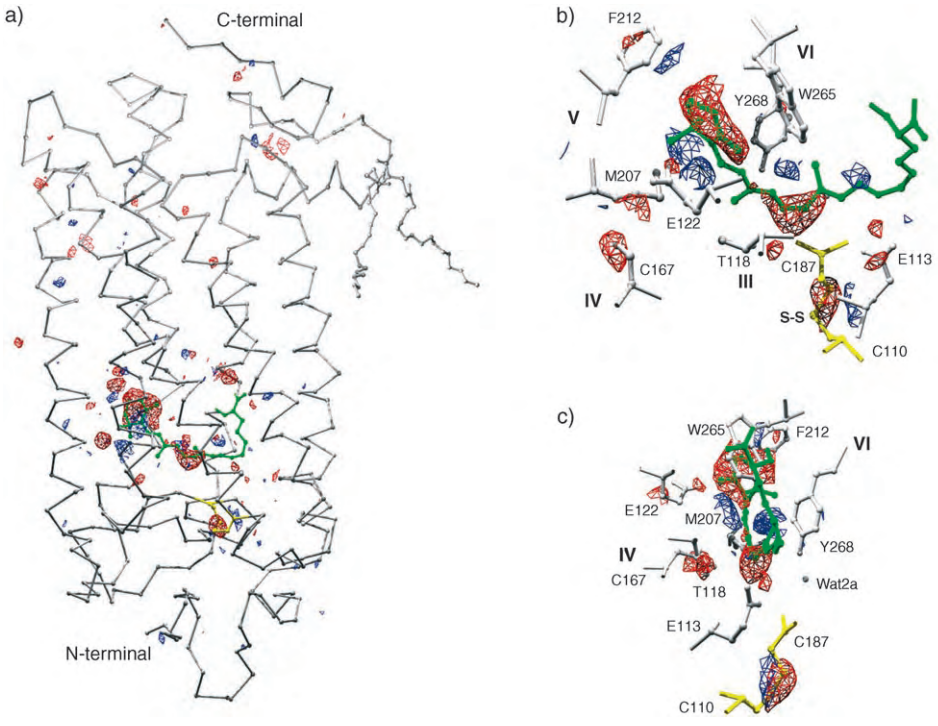


Figure 2. Difference electron densities between the illuminated and ground state of rhodopsin at 95 K (see text for details). a) $F_{light}-F_{dark}$ map calculated to 2.7 Å resolution is superimposed on the α-carbon trace of the structure of rhodopsin. The map is contoured to 3.5 σ (red, negative; blue, positive) for one of the two molecules in an asymmetric unit. The chromophore (11-*cis*-retinal + Lys296) and a disulfide bond between Cys110 and Cys187 are colored green and yellow, respectively. b) An expanded view of the map shown in part (a) highlighting the region around retinal and the residues associated with difference electron densities. c) A different view of the same region as in part (b) rotated approximately 90° around a vertical axis. The helices are numbered III–VI.

 © 2006 Wiley-VCH Verlag GmbH & Co. KGaA, Weinheim

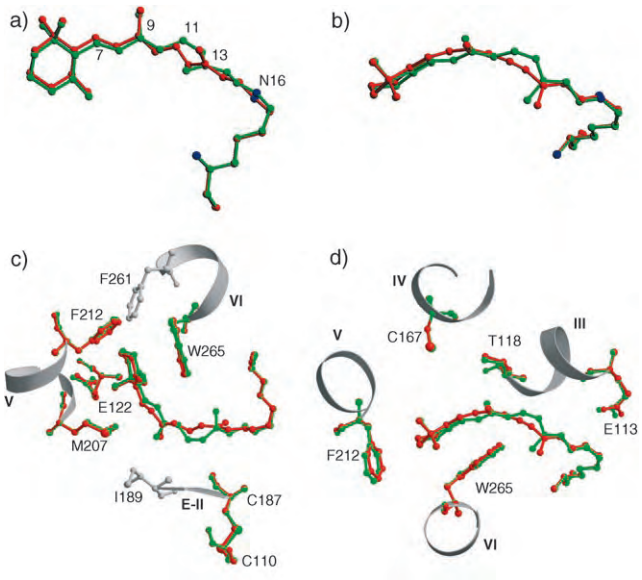


Figure 3. Structural changes from rhodopsin (green) to bathorhodopsin (red). a) A view of retinal and Lys296 linked through a protonated Schiff base from the direction similar to Figure 1b. Nitrogen atoms are shown in blue (see Supporting Information for a stereochemical view of this figure). b) A different view of the chromophore rotated approximately 90° around a horizontal axis, highlighting the curvature along the polyene chain in bathorhodopsin. c) Part of the retinal-binding pocket and the structural changes viewed from the direction similar to that used in Figure 2a, b. d) A different view of the retinal-binding site.

single bonds is found at the C12–C13 position. This first crystallographic model of the retinal in bathorhodopsin has not been predicted by previous models such as the hula-twist mechanism (see Reference [13] for more details).

The position of the Schiff base does not change significantly, whereas a small displacement of the side chain of Glu113 is consistently found in all the data sets containing bathorhodopsin (Figure 3d). As a result, the distance between the protonated Schiff base (the position of nitrogen atom N16) and the counterion (average of OE1 and OE2 of E113) increases slightly from 3.6 Å (chain A) and 3.4 Å (chain B) in rhodopsin to 3.9 Å (chain A) and 3.7 Å (chain B) in bathorhodopsin. This constant difference of 0.3 Å between the two states may not be large compared with the differences of 0.2 Å between the two molecules in the asymmetric unit for both rhodopsin and bathorhodopsin. Whether such an increase in the distance between the Schiff base and counterion is consistent with theoretical considerations is discussed in Reference [13]. This parameter also affects the estimation of energy storage in bathorhodopsin.

A small but substantial displacement of the polyene chain in retinal from C8 to C10 causes perturbation at Thr118 in TMH-III, which in turn moves outward from the core of protein. Another interesting feature in TMH-III is the difference electron density around the S–S bond that connects Cys110 and Cys187 in the second extracellular loop (E-II). The carbonyl oxygen atom of Cys187 is one of the atoms that is in close contact with retinal. Its distance to C12 of the retinal chain is about 3 Å in rhodopsin. As a result of the configurational change in bathorhodopsin, the restraint keeping the positions of these two atoms disappears. As a consequence, the carbonyl oxygen atom of Cys187 relaxes, with a concomitant dislocation of the S–S bond (Figure 3c). We speculate that all these features associated with TMH-III and E-II indicate the initial trigger evoked in rhodopsin for a further thermal activation process, which will be discussed later.

A pair of clear positive and negative difference densities appears reproducibly at the side chain of Phe212 in TMH-V, which forms part of the binding pocket for the β-ionone ring (Figure 2b). Owing to the translational dislocation of the cyclohexene ring upon isomerization, the aromatic ring of Phe212 moves inward to fill part of the space that the chromophore occupied in rhodopsin (Figure 3d). Interestingly, the position of that residue is also near to the agonist-binding site in adrenergic receptors[14,15] that may share a common activation mechanism with rhodopsin. Similarly, the side chain of Trp265 in TMH-VI rotates slightly to partially balance the loss of interaction with the β-ionone ring. Because most rhodopsin-like GPCRs share tryptophan at this position, our model of bathorhodopsin suggests a general mechanism of activation for this class of GPCRs.

Our findings from crystallography studies provide valuable insights into the molecular mechanisms by which the primary process of vision is mediated, and we propose the following thermal activation process. We postulate that photon absorption causes isomerization of retinal in a seesaw-like mechanism, which initiates a small displacement of the β-ionone ring (Figure 3c). The direction of this movement is defined by the binding pocket that has a space at the extracellular side of the ring. The only residues that are within 4.5 Å from atoms C16, C17, and C7 are Ile189 in E-II and Met207 in TMH-V, whereas the cytoplasmic side (C3, C4, and C18) is surrounded by the peptide from Gly121 to Glu122, the side chains of Phe212, Phe261, and Trp265. Similarly, atoms C11 and C12 do not have any residues within 5 Å at the cytoplasmic side, but the peptide from Cys187 to Gly188 is running at the extracellular side. The disulfide bond between Cys187 and Cys110 provides support that can make the isomerization efficient. Thus, we suggest that the binding pocket for 11-*cis*-retinal is designed to achieve dual function, holding the retinal as an inverse agonist in the dark, and allowing efficient photoconversion to an agonist.

The methyl group attached to C9 appears to function as a scaffold for these movements to occur efficiently. This interpretation is supported by previous studies, which suggested the important role of this group in the activation of rhodopsin.[16–18] In the ground state, five atoms from Thr118, Ile189, Tyr191, and Tyr268 are located within 4.5 Å from C19. The nonbonded interactions with these residues appear to be critical for stabilizing the 11-*cis* form in the dark and for leading to efficient photoisomerization. In contrast, restraints at this position would be less advantageous for the isomerization of 9-*cis*-rhodopsin, which exhibits similar properties to rhodopsin except for its lower quantum yield.[5]s

Our model of bathorhodopsin also agrees with the previous observation that the β-ionone ring is in the vicinity of Trp265 in both rhodopsin and bathorhodopsin but

 © 2006 Wiley-VCH Verlag GmbH & Co. KGaA, Weinheim

approaches Ala169 at TMH-IV in the later intermediates.[9] The curved structure of retinal in bathorhodopsin appears to be consistent with a prediction that it would relax by moving toward TMH-IV (Figure 3d). The initial movement of the β-ionone ring toward the extracellular side prevents a steric clash with TMH-III, mainly at Glu122 (Figure 3c). Then, the distorted all-*trans*-retinal in bathorhodopsin would relax by further movement of the β-ionone ring toward TMH-IV, presumably through a cavity surrounded by Thr118, Glu122, and Cys167 (Figure 3d). Then, the constraints imposed by the retinal on some key residues such as Trp265 and Phe261 in TMH-VI will vanish, allowing the helix freedom to assume the structure of the active state by rigid body movement[19] and/or rotational motion.[20] Photon energy stored in bathorhodopsin would be necessary for these possible dynamic events to occur. Thus, we suggest that the flexible conjugated polyene of retinal is ideal to work as an extremely sensitive photodetector (for more details, see also Reference [13]).

Experimental Section

Microspectrophotometry: Three-dimensional crystals of bovine rhodopsin were grown as reported previously.[2] The changes in the visible absorption spectra of the crystals were recorded by a system based on a 3DX microspectrophotometer with an ANDOR CCD detector. A crystal mounted on the goniometer head was illuminated under a stream of cold (105 K) nitrogen gas by argon laser light, which was depolarized and aligned along the long axis of crystals to maximize the extent of photoreaction. The temperature at the crystal position was recorded by a thermocouple for the goniometer head.

Data collection: All of the X-ray diffraction data sets were collected on a MAR165 CCD detector at BL41XU of SPring-8, with a beam wavelength of 1 Å. The temperature at the position of the crystal was kept at 95 K during data collection. To illuminate the crystals, depolarized argon laser light (488 nm, 2–7 mW) was aligned in a manner similar to that for the offline microspectroscopy experiment and brought to the crystal during data collection. (See Supporting Information for more details.)

Model building and refinement: For the refinement of bathorhodopsin, a model of rhodopsin at 2.2 Å[2] was used as a starting model. Using phases of this structure and after rigid body refinement, F_o-F_o maps were calculated for a number of ground-state (F_{dark}) and illuminated (F_{light}) data sets with different laser light intensities to obtain reproducible structural differences between rhodopsin and bathorhodopsin. We first considered the contribution from the possible 9-*cis* form in the illuminated crystals as described in the Supporting Information. The structure factors were used after appropriate treatment of the twin fractions of the data sets determined by the method described by Yeates.[21] The occupancy of rhodopsin (α) in an illuminated crystal was estimated for each of the data sets by performing alternate conformation refinement of the structure of the intermediate with its occupancy of $1-\alpha$ while the rest (rhodopsin) was fixed. The amino acids included in refinement were Cys110, Glu113, Thr118, Glu122, Cys167, Cys187, Met207, Phe212, Trp265, Tyr268, and Lys296. The value of α was changed from 0.4 to 0.75 in steps of 0.05, and the resulting R_{cryst}, R_{free}, and bonds/angles root-mean-square deviations were compared. Finally, occupancy refinement of the two conformations converged to yield values of $\alpha = 0.65$ with CNS v.1.1.[22] We also carried out the selected-atom structure refinement of the intermediates by using extrapolated structure factor amplitudes $(F_{light}-\alpha F_{dark})/(1-\alpha)$ and found that the results, including the optimal value of α, were almost the same as those for the alternate conformation refinement.

Received: February 15, 2006
Published online: April 4, 2006

Keywords: isomerization · protein structures · receptors · rhodopsin · X-ray diffraction

[1] K. Palczewski, T. Kumasaka, T. Hori, C. A. Behnke, H. Motoshima, B. A. Fox, I. Le Trong, D. C. Teller, T. Okada, R. E. Stenkamp, M. Yamamoto, M. Miyano, *Science* **2000**, *289*, 739–745.
[2] T. Okada, M. Sugihara, A. N. Bondar, M. Elstner, P. Entel, V. Buss, *J. Mol. Biol.* **2004**, *342*, 571–581.
[3] J. Li, P. C. Edwards, M. Burghammer, C. Villa, G. F. X. Schertler, *J. Mol. Biol.* **2004**, *343*, 1409–1438.
[4] R. W. Schoenlein, L. A. Peteanu, R. A. Mathies, C. V. Shank, *Science* **1991**, *254*, 412–415.
[5] J. B. Hurley, T. G. Ebrey, B. Honig, M. Ottolenghi, *Nature* **1977**, *270*, 540–542.
[6] A. Cooper, *Nature* **1979**, *282*, 531–533.
[7] I. Palings, E. M. M. van den Berg, J. Lugtenburg, R. A. Mathies, *Biochemistry* **1989**, *28*, 1498–1507.
[8] E. C. Y. Yan, Z. Ganim, M. A. Kazmi, B. S. W. Chang, T. P. Sakmar, R. A. Mathies, *Biochemistry* **2004**, *43*, 10867–10876.
[9] B. Borhan, M. L. Soutu, H. Imai, Y. Shichida, K. Nakanishi, *Science* **2000**, *288*, 2209–2212.
[10] P. J. R. Spooner, J. M. Sharples, S. C. Goodall, P. H. M. Bovee-Geurts, M. A. Verhoeven, J. Lugtenburg, A. M. A. Pistorius, W. J. DeGrip, A. Watts, *J. Mol. Biol.* **2004**, 343, 719–730.
[11] S. O. Smith, J. Courtin, H. J. M. de Groot, M. Gebhard, J. Lugtenburg, *Biochemistry* **1991**, *30*, 7409–7415.
[12] Y. Matsui, K. Sakai, M. Murakami, Y. Shiro, S. Adachi, H. Okumura, T. Kouyama, *J. Mol. Biol.* **2002**, *324*, 469–481.
[13] M. Schreiber, M. Sugihara, T. Okada, V. Buss, *Angew. Chem.* **2006**, *118*, 4380–4383; *Angew. Chem. Int. Ed.* **2006**, *45*, 4274–4277.
[14] D. D. Oprian, *J. Bioenerg. Biomembr.* **1992**, 24, 211–217.
[15] C. D. Strader, M. R. Candelore, W. S. Hill, I. S. Sigal, R. A. F. Dixon, *J. Biol. Chem.* **1989**, *264*, 13572–13578.
[16] U. M. Ganter, E. D. Schmid, D. Perez-Sala, R. R. Rando, F. Siebert, *Biochemistry* **1989**, *28*, 5954–5962.
[17] M. Han, M. Groesbeck, S. O. Smith, T. P. Sakmar, *Biochemistry* **1998**, *37*, 538–545.
[18] C. K. Meyer, M. Bohme, A. Ockenfels, W. Gartner, K. P. Hofmann, O. P. Ernst, *J. Biol. Chem.* **2000**, *275*, 19713–19718.
[19] D. L. Farrens, C. Altenbach, K. Yang, W. L. Hubbell, H. G. Khorana, *Science* **1996**, *274*, 768–770.
[20] L. Shi, G. Liapakis, R. Xu, F. Guarnieri, J. A. Ballesteros, J. A. Javitch, *J. Biol. Chem.* **2002**, *277*, 40989–40996.
[21] T. O. Yeates, *Methods Enzymol.* **1997**, 276, 344–358.
[22] A. T. Brünger, P. D. Adams, G. M. Clore, W. L. DeLano, P. Gros, R. W. Grosse-Kunstleve, J. S. Jiang, J. Kuszewski, M. Nilges, N. S. Pannu, R. J. Read, L. M. Rice, T. Simonson, G. L. Warren, *Acta. Crystallogr. Sect. D* **1998**, *54*, 905–921.

 © 2006 Wiley-VCH Verlag GmbH & Co. KGaA, Weinheim

Chemistry of Vision (2)

DOI: 10.1002/anie.200600585

Quantum Mechanical Studies on the Crystallographic Model of Bathorhodopsin**

*Marko Schreiber, Minoru Sugihara, Tetsuji Okada, and Volker Buss**

Rhodopsin is the pigment that mediates light/dark vision in the eyes of vertebrates. After photoexcitation, the chromophore of rhodopsin, 11-*cis*-retinal, isomerizes in an extremely fast reaction to form the all-*trans* isomer, thus starting a sequence of dark events that finally reaches the signaling state of the protein and activates the visual cascade. Formation of the first photoproduct, photorhodopsin, is complete within 200 fs and captures more than 50% of the photon energy, which is expended during the subsequent events. Within a few picoseconds photorhodopsin relaxes to bathorhodopsin, which is the first thermally equilibrated intermediate of the rhodopsin photocycle and can be trapped at cryogenic temperatures.[1,2] The preceding paper reports the first crystallographic analysis of this intermediate.[3] The main alteration is found to be the configurational change of the chromophore from the twisted 11-*cis* form in rhodopsin to the distorted all-*trans* form, with distinct but smaller changes in the chromophore environment.

Theoretical calculations can help to assess and improve protein X-ray data. Modeling the protein matrix is usually reliable owing to the use of standard computer software during the refinement process. The treatment of an active center, such as the chromophore embedded in the protein, may not reach the same level of accuracy as a result of its specific electronic structure, and the use of rigorous quantum mechanics may be required.[4] Herein, we describe the results of a theoretical study of the bathorhodopsin chromophore based on the X-ray crystal structure. The stability of the chromophore geometry inside the binding pocket was tested with DFTB,[5] a self-consistent charge density-functional tight-binding method. On the basis of the optimized geometry, DFT calculations were performed for the analysis of specific Raman bands and multiconfigurational CASPT2[6] calculations were performed to obtain UV/Vis and circular dichroism (CD) spectral data. Details of the DFTB and the excited-state calculations are provided in the Experimental Section. The results are discussed with reference to an analogous treatment of rhodopsin.[7]

A comparison of the X-ray crystal structure and the optimized chromophore structure is shown in Figure 1. The pattern of alternating bond lengths which is typical for the rhodopsin chromophore[7] is preserved in the batho intermediate. The calculated alternation is weaker than that determined experimentally, as is commonly observed for methods that include electron correlation.[8] Calculated bond angles agree well with experiment; a discrepancy is noted only for the bond angles at C7, C8, and C9. Previous crystal models of rhodopsin at different resolution[7] showed differences of

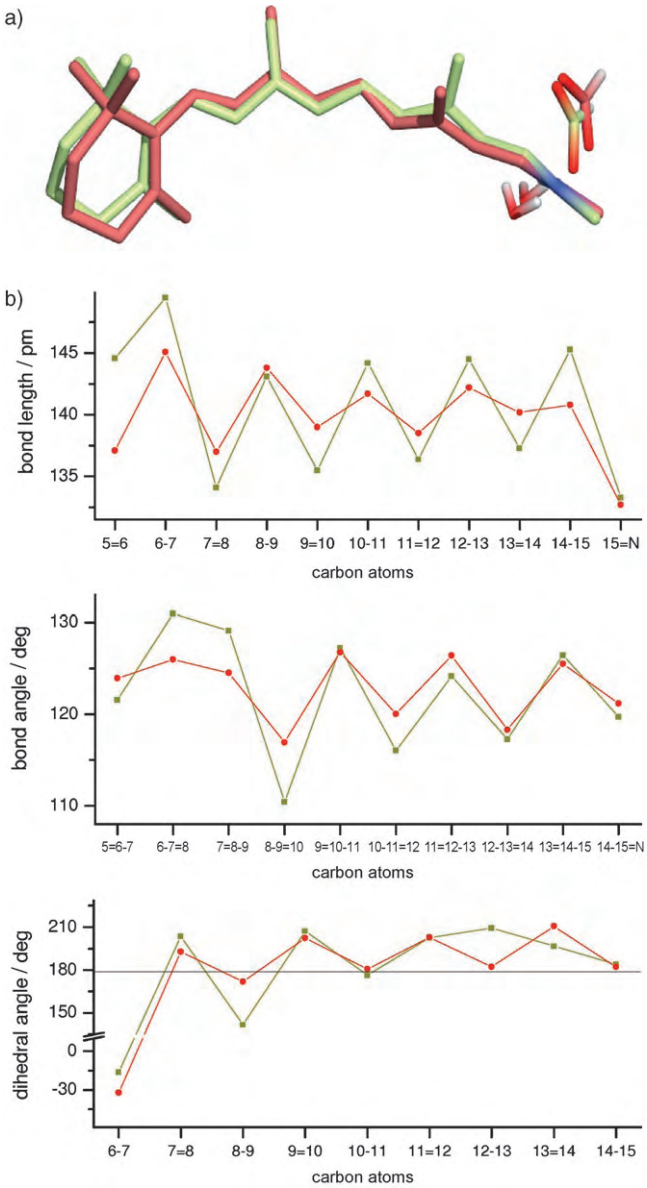


Figure 1. The bathorhodopsin chromophore including Glu113 and wat2b before (green) and after quantum mechanical optimization (red) inside the binding pocket. a) Overlay of the chromophore structures. b) Comparison of the internal coordinates.

[*] Dr. M. Schreiber, Dr. M. Sugihara, Prof. Dr. V. Buss
FB6/Theoretische Chemie
Universität Duisburg-Essen
47048 Duisburg (Germany)
Fax: (+49) 203-379-2772
E-mail: theobuss@uni-duisburg.de
Dr. T. Okada
Biological Information Research Center
National Institute of Advanced Industrial Science and Technology
2-41-6 Aomi, Koto-ku, Tokyo 135-0064 (Japan)

[**] We thank Dr. O. Weingart for helpful discussions. This research was supported in part by grants from MEXT (15687005), JST (CREST), NEDO, and the DFG (Forschergruppe FOR490).

Supporting information for this article is available on the WWW under http://www.angewandte.org or from the author.

WILEY InterScience DISCOVER SOMETHING GREAT
© 2006 Wiley-VCH Verlag GmbH & Co. KGaA, Weinheim

more than five degrees in a few bond angles; further improvement of the X-ray crystal structure of bathorhodopsin may provide bond angles that are closer to the values obtained from the current quantum mechanics model.

The dihedral angles exhibit a pattern which is more obvious in the calculated than in the experimental structure: except for the sterically hindered C6–C7 bond, the conformation about all single bonds is almost planar-*trans* with deviations between 0 and 8°. In contrast, all double bonds are strongly twisted, from 19° (the C15–N16 bond) to 36° (the C13–C14 bond). This same alternation is also evident in the experimental structure except for the C8–C9 and the C12–C13 bonds. Substantial twist of the C12–C13 single bond obtained from the X-ray model is consistent with results from recent resonance Raman spectroscopy,[9] but a planar-*trans* conformation fits the vibrational data as well (see below). The twist at the C8–C9 bond remains to be confirmed. We conclude that the highly distorted X-ray chromophore model is reasonably stable and shows only small changes after DFTB optimization.

Preferential torsion of the double bonds in bathorhodopsin has been found in molecular dynamics simulations of the rhodopsin photoreaction[10,11] and in a minimum energy path calculation.[12] Out-of-plane deformation of double bonds is more costly compared to that of single bonds and may be relevant with respect to the mechanism of energy storage in the photoproduct. The resulting shape of the chromophore is remarkably simple. With all bonds twisted from the planar all-*trans* geometry in the same (positive) direction, the chromophore adopts an elongated corkscrew-like structure with right-hand screw sense (positive helicity).

Resonance Raman spectroscopy can be used to probe the local conformation of the chromophore. In particular, the hydrogen out-of-plane (HOOP) wagging modes at C11 and C12 have been taken as evidence for the distorted C11=C12 *trans* geometry of retinal in bathorhodopsin.[13] These modes are strongly coupled in rhodopsin at 969 cm^{-1}; they uncouple in bathorhodopsin and appear as a C11 HOOP mode at 920 cm^{-1} and as a C12 HOOP mode at 858 cm^{-1}. We calculated the energies of these modes based on the model structures by using density functional theory (Figure 2). With the generally used scaling factor for the frequencies,[9] we found the C11-H/C12-H mode at 987 cm^{-1} in rhodopsin which decouples to a mainly C11 HOOP mode at 956 cm^{-1} and a nearly isolated C12 HOOP mode at 881 cm^{-1} in bathorhodopsin, with absolute energies and the energy splitting in good agreement with experimental data.

Figure 3 shows the bathorhodopsin and rhodopsin chromophores after optimization within their respective binding pockets. There is a large clockwise rotation (as viewed from the Schiff base nitrogen) of the C13–C20 bond by 140°, from −17° in rhodopsin to −157° in bathorhodopsin, with resulting large displacements of the C12 and C14 hydrogen atoms. Rotation of the C11=C12 bond within the restricted binding pocket is possible because the other bonds, in particular the double bonds, rotate in the opposite direction (Figure 3b).

The mechanism of photoisomerization of rhodopsin has been discussed in the past. To account for the fast rate and the high efficiency of the reaction, Warshel proposed a volume-conserving process in which the *cis* link of the C11=C12 bond in rhodopsin shifts to the C15=N16 bond in bathorhodopsin in a so-called "bicycle-pedal motion".[14] According to molecular dynamics studies,[15] the isomerization starts locally at the C11=C12 bond and spreads rapidly to rotations of the other double bonds in a bicycle-pedal-like motion until it is aborted as the molecule returns to the ground state. From a comparison of the two conformations before and after isomerization, it appears that the batho chromophore structure is determined by the same requirements that govern the dark-state structure of the chromophore:[16] to provide for the least-strained conformation of the configurationally inverted unsaturated chain that connects the two ends fixed in the protein matrix.

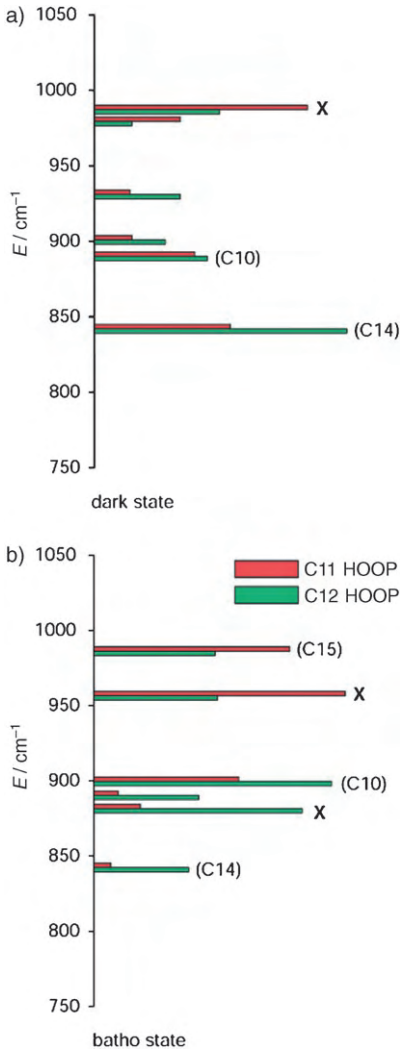


Figure 2. Calculated energies and relative contributions of the C11 and C12 HOOP vibrations to the normal modes of the optimized rhodopsin (a) and bathorhodopsin (b) chromophores. Crosses refer to modes that are discussed in the text; in the other modes, the HOOP vibration indicated in parentheses is a major contributor.

Table 1 summarizes the calculated energies and spectral parameters. The ground-state energy of the chromophore–glutamate complex of bathorhodopsin is raised by 12.7 kcal mol^{-1} relative to rhodopsin. The increase in the distance to

 © 2006 Wiley-VCH Verlag GmbH & Co. KGaA, Weinheim

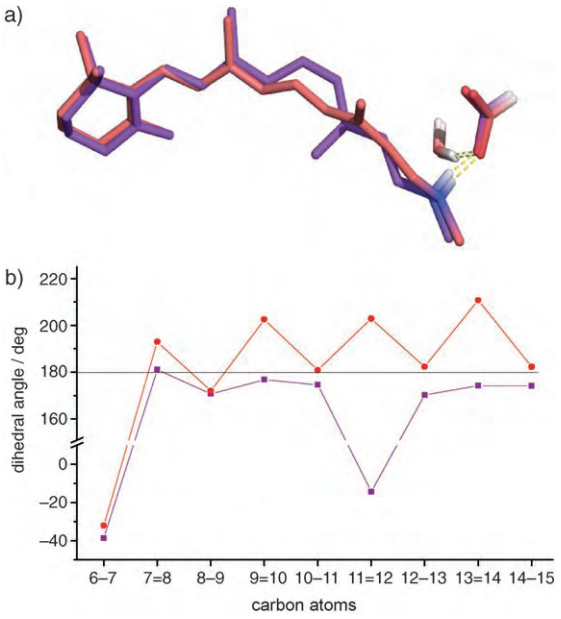


Figure 3. Change in the structure of the chromophore including Glu113 and wat2b from rhodopsin (blue) to bathorhodopsin (red). a) Overlay of the two structures. b) Dihedral angles along the retinal chain (see also Supporting Information).

Table 1: Calculated energies and spectral parameters of retinal chromophores.

Structure	State	E_{CASPT2}[a]	f[b]	R[c]
11-*cis*-retinal pSb[d]	S_0	−870.7110		
	S_1	1.88 (659)	0.93	0.16
Rhodopsin[e]	S_0	−1136.3419		
	S_1	2.52 (492)	0.82	0.29
Bathorhodopsin[e]	S_0	−1136.3217		
	S_1	2.35 (528)	0.81	−0.39

[a] S_0 energies [au]; S_1 energies [eV] relative to S_0 (values in parentheses are given in nm). [b] Oscillator strength. [c] Rotatory strength [au]. [d] The chromophore without counterion; pSb = protonated Schiff base. See Ref. [18] for more details. [e] Chromophore including glutamate and wat2b according to Figure 3.

Glu113 by 0.3 Å which is found experimentally (but not theoretically) in the conversion of rhodopsin to bathorhodopsin would raise the energy by another 7.3 kcal mol^{-1}. Compared to the increase in energy of bathorhodopsin by 36 kcal mol^{-1} relative to rhodopsin,[17] this result implies that between 23.3 and 16 kcal mol^{-1} is stored as strain between the chromophore and the binding pocket as both adjust to the new configuration of the chromophore.

The remaining data in Table 1 refer to the properties of the excited state of the chromophore in different configurations and surroundings. For the bare 11-*cis*-retinal pSb without counterion, the calculated S_1 energy corresponds to a λ_{max} value of 659 nm.[18] Recently, the absorbance of all-*trans*-retinal pSb in the gas phase was determined and found to peak at 610 nm.[19] This result is in very good agreement with the value of 600 nm which we calculate for the totally relaxed all-*trans* chromophore.[20] Additionally, the red shift to be expected from the configurational change and bond torsion[19] renders the calculated value for the *cis* chromophore very reasonable.

The presence of the charged Glu113 residues shifts the absorbance close to the experimental value of rhodopsin (498 nm) despite the fact that no charges and polarization of the protein are considered. In calculations reported elsewhere,[11] the glutamate-induced blue shift of the chromophore agrees with that observed herein. However, the bare chromophore is blue-shifted strongly relative to that observed by us, possibly a consequence of the different basis set and the chromophore geometry employed.

The position of the Glu113 residue affects not only the ground state of the chromophore but also the $S_0 \rightarrow S_1$ gap. We calculated the excitation energy as a function of the glutamate distance for a model chromophore (see Supporting Information) and extrapolated a red shift of 20 nm for the rhodopsin chromophore when the counterion is moved from 2.7 to 3.4 Å, the experimentally observed distance. The calculated shift for rhodopsin to bathorhodopsin (36 nm) is in very good agreement with that determined experimentally (44 nm). Note that the position of Glu113 does not change in the two quantum mechanical structures. If one allows for the experimentally determined increase in the counterion distance by 0.3 Å, the absorbance of bathorhodopsin is shifted by only 7 nm to 43 nm relative to the dark state. We conclude that movement of the counterion is not a major contributor to the red shift of the intermediate.

Circular dichroism spectroscopy can be used to monitor the overall shape of an inherently chiral chromophore; specifically, the absolute conformation of enantiomeric or pseudoenantiomeric geometries may be distinguished. For the α band in rhodopsin which peaks at 495 nm, the rotatory strength is approximately +0.1 au; in bathorhodopsin, the band inverts and is red-shifted by 45 nm, with a rotatory strength of −0.4 au.[21] The α bands of rhodopsin and bathorhodopsin calculated on the basis of the quantum mechanical geometries agree in sign and magnitude with those determined experimentally. Both the sign inversion of the rotatory strength and its marked increase in bathorhodopsin, a consequence of configurational change and the prominent helical geometry of the chromophore, are correctly reproduced by the calculations.

In summary, quantum mechanical calculations on the first crystallographic model of bathorhodopsin have provided additional structural details of the chromophore. On the basis of these structures reasonable agreement was found between calculated and experimental resonance Raman, UV/Vis, and CD spectral properties. These studies are a step towards a comprehensive picture of the molecular mechanism for the highly efficient photodetection in rhodopsin.

Experimental Section

Computational model: Of the two molecules in the asymmetric unit of the crystal, chain B of bathorhodopsin[3] was chosen as the basis for the model. The chain consists of the chromophore, 28 selected amino acid residues, and two water molecules close to the counterion. Twenty-seven of the amino acids were employed in our optimization of the rhodopsin binding pocket,[8] and we introduced Tyr192, which

 © 2006 Wiley-VCH Verlag GmbH & Co. KGaA, Weinheim

forms a hydrogen bond to Glu181. Except for Glu113, which is negatively charged, all amino acids were considered neutral; the chromophore carries a positive charge. The complete amino acid residues were considered. Where the backbone chain was interrupted, hydrogen atoms were filled in to saturate the free valences. During the computations, the backbone atoms were kept fixed in space.

Quantum mechanical platforms: The chromophore with the binding pocket around was optimized using the DFTB code.[5] For the calculation of UV/Vis and CD spectral data, CASPT2 calculations were performed on the chromophore including Glu113 and wat2b. The (12/12) active space included all π-type electrons and orbitals. For the basis, an atomic natural orbital (ANO)[22] set was employed contracted to 4s3p1d for the heavy atoms and 2s for hydrogen; the level shift was 0.3 au. Transition dipole moments were calculated in the velocity formalism and combined with CASPT2 energies. For the vibrational spectra, we used DFT (B3LYP//6-31G**).

Received: February 14, 2006
Revised: April 25, 2006
Published online: May 26, 2006

Keywords: density functional calculations · protein structures · retinal · rhodopsin · UV/Vis spectroscopy

[1] "Structure and Mechanism of Vertebrate Visual Pigments": W. J. DeGrip, K. J. Rothschild in *Handbook of Biological Physics*, *Vol. 3* (Eds.: D. G. Stavenga, W. J. DeGrip, E. N. Pugh, Jr.), Elsevier Science Press, Amsterdam, **2000**, pp 1 – 54.
[2] T. Okada, O. P. Ernst, K. Palczewski, K. P. Hofmann, *Trends Biochem. Sci.* **2001**, *26*, 2759 – 2767.
[3] H. Nakamichi, T. Okada, *Angew. Chem.*, DOI: 10.1002/ange.200600595/*Angew. Chem. Int. Ed.*, DOI: 10.1002/anie.200600595.
[4] U. Ryde, K. Nilsson, *J. Am. Chem. Soc.* **2003**, *125*, 14232 – 14233.
[5] M. Elstner, D. Porezag, G. Jungnickel, J. Elsner, M. Haugk, T. Frauenheim, S. Suhai, G. Seifert, *Phys. Rev. B* **1998**, 58, 7260 – 7268.
[6] K. Andersson, P.-A. Malmqvist, B. O. Roos, A. J. Sadley, K. Wolinski, *J. Phys. Chem.* **1990**, *94*, 5483 – 5488.
[7] T. Okada, M. Sugihara, A. N. Bondar, M. Elstner, P. Entel, V. Buss, *J. Mol. Biol.* **2004**, *342*, 571 – 581.
[8] M. Sugihara, V. Buss, P. Entel, M. Elstner, T. Frauenheim, *Biochemistry* **2002**, *41*, 15259 – 15266.
[9] E. C. Y. Yan, Z. Ganim, M. A. Kazmi, B. S. W. Chang, T. P. Sakmar, R. A. Mathies, *Biochemistry* **2004**, *43*, 10867 – 10876.
[10] J. A. Gascon, V. S. Batista, *Biophys. J.* **2004**, 87, 2931 – 2941.
[11] U. F. Röhrig, L. Guidoni, A. Laio, I. Frank, U. Rothlisberger, *J. Am. Chem. Soc.* **2004**, *126*, 15328 – 15329.
[12] T. Andruniow, N. Ferre, M. Olivucci, *Proc. Natl. Acad. Sci. USA* **2004**, *101*, 17908 – 17913.
[13] I. Palings, E. M. M. van den Berg, J. Lugtenburg, R. A. Mathies, *Biochemistry* **1989**, *28*, 1498 – 1507.
[14] A. Warshel, *Nature* **1976**, *260*, 679 – 683.
[15] O. Weingart, unpublished results.
[16] M. Sugihara, J. Hufen, V. Buss, *Biochemistry* **2006**, *45*, 801 – 810.
[17] A. Cooper, *Nature* **1979**, *282*, 531 – 533.
[18] M. Schreiber, V. Buss, *Int. J. Quantum Chem.* **2003**, 95, 882 – 889.
[19] L. H. Andersen, I. B. Nielsen, M. B. Kristensen, M. O. A. El Ghazaly, S. Haake, M. Brondsted Nielsen, M. A. Petersen, *J. Am. Chem. Soc.* **2005**, *127*, 12347 – 12350.
[20] S. Sekharan, O. Weingart, V. Buss, *Biophys. J.*, DOI: 10.1529/biophysj.106.087122.
[21] S. Horiuchi, F. Tokunaga, T. Yoshizawa, *Biochim. Biophys. Acta* **1980**, *591*, 445 – 457.
[22] K. Pierloot, B. Dumez, P. O. Widmark, B. O. Roos, *Theor. Chim. Acta* **1995**, 90, 87 – 114.

 © 2006 Wiley-VCH Verlag GmbH & Co. KGaA, Weinheim

Peptide Receptors

DOI: 10.1002/anie.200601046

Sequence-Dependent Stereoselectivity in the Binding of Tetrapeptides in Water by a Flexible Artificial Receptor**

Carsten Schmuck and Peter Wich*

Dedicated to Professor Ronald Breslow on the occasion of his 75th birthday

The binding of small oligopeptides by artificial receptors under physiological conditions (in water) still remains a challenging task. Although early work in this area was limited to peptide recognition in organic solvents,[1] some progress has been made in the last few years for peptide binding in more polar solvents. Some examples of oligopeptide binding in aqueous solvents based on metal–ligand[2] or hydrophobic interactions,[3] and, most recently, purely electrostatic interactions (H-bonds and ion pairs)[4] have been reported. For the identification of artificial peptide receptors, combinatorial libraries have been successfully employed by us and other groups.[5] In some cases, receptors found in this way even demonstrate pronounced selectivity for closely related substrates at least in qualitative on-bead binding assays. However, a quantitative confirmation of the reported on-bead substrate selectivities in free solution is lacking. For example, Chamorro and Liskamp[6] reported the screening of a large combinatorial receptor library derived from a cyclotriveratrylene with three attached peptide arms for the binding of D-Ala-D-Ala. By using a color-coded substrate, efficient receptors could be identified from a qualitative screening in which the dipeptide binds more efficiently than the related depsipeptide D-Ala-D-Lac. No quantitative information on binding affinities or substrate selectivity was provided. In another example, Kilburn et al. recently reported on the screening of a large combinatorial library of "tweezer receptors" (>15000 members) for the binding of the tripeptide *N*-Ac-L-Lys-D-Ala-D-Ala. Again, by using a qualitative binding assay, receptors were identified and the most promising one was then resynthesized and studied in more detail.[7] Weak binding with low-mM affinities was found for two diastereomeric tripeptides with the resin-bound receptor, but no binding data in free solution could be obtained. Therefore, the demonstration of efficient stereoselectivity in the binding of

[*] Prof. Dr. C. Schmuck, Dipl.-Chem. P. Wich
Institut für Organische Chemie
Universität Würzburg
Am Hubland, 97074 Würzburg (Germany)
Fax: (+49) 931-888-4625
E-mail: schmuck@chemie.uni-wuerzburg.de

[**] We thank the DFG (SFB 630) and the Fonds der Chemischen Industrie for ongoing financial support of our work.

Supporting information for this article is available on the WWW under http://www.angewandte.org or from the author.

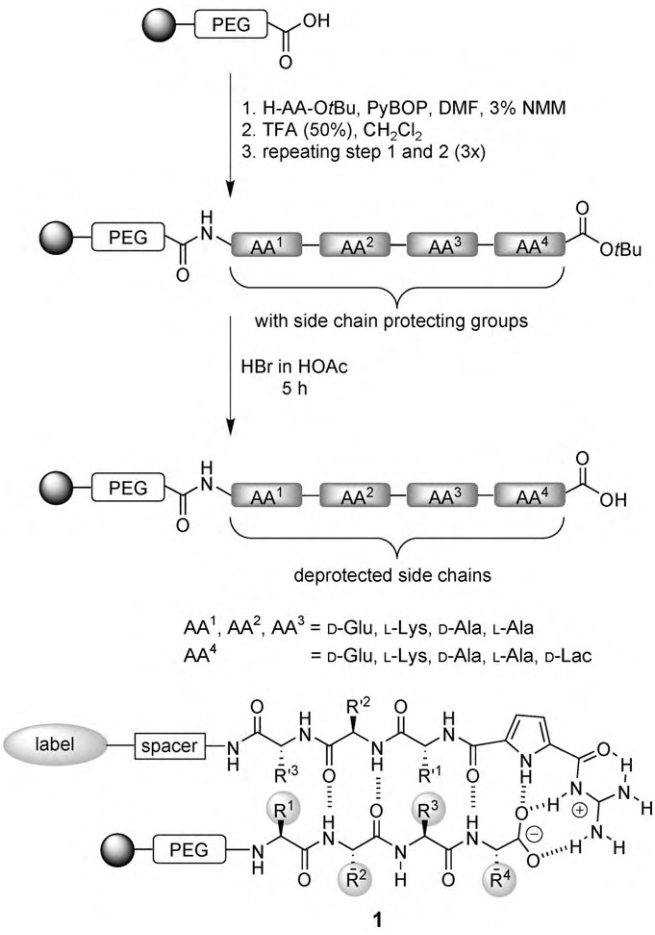
© 2006 Wiley-VCH Verlag GmbH & Co. KGaA, Weinheim

oligopeptides in water still remains an unsolved problem. Herein, we report that the fully flexible peptide receptor **1** shows not only significant substrate selectivity but also a remarkable sequence dependent stereoselectivity in the binding of polar tetrapeptides in water.

Recently, we demonstrated that the tris-cationic receptor **1** (Gua-Lys-Lys-Phe; Gua = guanidiniocarbonyl pyrrole) efficiently binds the tetrapeptide D-Glu-L-Lys-D-Ala-D-Ala-OH with $K_a > 10^4\,M^{-1}$ in buffered water.[4] This polar tetrapeptide is interesting owing to its resemblance to a bacterial peptidoglycan which plays a crucial role in cell wall synthesis and antibiotic activity.[8] Receptor **1** was identified from a combinatorial screening of a small but focused receptor library with 512 members by using a fluorescence-labeled derivative of this tetrapeptide. From a screening of the whole library a detailed quantitative structure–binding relationship could be established. This relationship showed that complex formation is dominated by electrostatic interactions. Following this approach to use rather small but custom designed combinatorial libraries that can be fully analyzed quantitatively in detail, we have now screened receptor **1** for its binding selectivity against a combinatorial library of 320 different but closely related substrates.

The substrate library was prepared by inverse solid-phase peptide synthesis on TentaGel as shown in Scheme 1. To introduce structural diversity, a combinatorial split-and-mix synthesis was performed based on the IRORI radiofrequency tagging technology.[9] In each coupling step, the following four amino acids were used as their *tert*-butyl esters: D-Glu(OBzl), L-Lys(Cbz), D-Ala, and L-Ala (Bzl = benzyl, Cbz = carbobenzoxy). D-Lac was also incorporated at the fourth position of the C terminus of the substrate[10] giving rise to a total library size of $4\times4\times4\times5 = 320$ substrates. It was necessary during the course of the library synthesis to develop a modified protocol for the cleavage of the benzyl-protected glutamate side chains as the standard protocol normally used in the literature (25% HBr in HOAc, 16 h)[11] also led to a complete cleavage of the tetrapeptides from the solid support. This cleavage was owing to the TentaGel being more acid sensitive than the standard Merrifield resin.[12] Time-dependent cleavage studies with a model peptide (resin-Ala-Glu(OBz)-Lys(Z)-Phe-NH_2) synthesized on TentaGel showed that after more than 2 h of treatment with 33% HBr in HOAc the glutamate side chains were cleaved (as determined by a malachite-green test[13]), whereas the resin started to decompose only after 10 h. Therefore, after the library synthesis, we used a 5 h treatment with 33% HBr in HOAc to remove all benzylic protecting groups.

The 320 solid-phase-bound deprotected substrates were then screened for their binding affinity towards receptor **1** by first using a qualitative on-bead screening assay through incubation of the library members with the Dansyl-labeled receptor **1** in aqueous buffer solution. This assay showed that even at concentrations as low as 5 μM, receptor **1** efficiently and with high selectivity binds to some of the substrates within the library (Figure 1). We then performed a quantitative screening assay of the whole substrate library. From the change in UV absorption of the solution before and after incubation with the labeled receptor and the known loading



Scheme 1. Synthesis of a combinatorial library containing 320 tetrapeptides and depsipeptides by inverse solid-phase peptide synthesis on tentagel and schematic representation of the complex formed with the triscationic guanidiniocarbonyl pyrrole peptide receptor **1** (spacer = ε-aminocaproic acid, $R'^1 = R'^2$ = Lys, R'^3 = Phe). AA = amino acid, Ac = acetyl, PyBOP = (benzotriazol-1-yloxy)tripyrrolidinophosphonium hexafluorophoslate, DCM = dichloromethane, DMF = *N*,*N*-dimethylformamide, NMM = *N*-methylmorpholine, PEG = polyethylene glycol, Py = pyridine, TFA = trifluoroacetic acid.

of the resin, the binding constants can be calculated by using a procedure described earlier.[4a] Some selected binding constants are given in Table 1. The best binding substrate in this library is D-Glu-D-Glu-D-Glu-D-Glu-D-Glu-OH (substrate **2**, $K_a = 26\,500\,M^{-1}$), which is not surprising for a tris-cationic receptor molecule. The binding affinity is remarkably high, keeping in mind that both receptor and substrate are fully flexible molecules. This emphasizes that multiple charge interactions can be very efficient even in water. As the binding is dominated by electrostatic interactions, the weakest binding affinities with $K_a \le 100\,M^{-1}$ are observed for those substrates that contain only nonpolar (Ala/Lac) or positively charged (Lys) side chains (e.g. substrates **10** or **11**). Only overall negatively charged substrates are bound efficiently. Binding of L-Lys-L-Lys-L-Lys-L-Lys-OH could not even be detected in this assay. Overall, the binding constants vary by more than a factor of 300, which is a remarkable substrate selectivity for such a small and flexible receptor, especially as the 320 substrates within the library are structurally very similar. The

 © 2006 Wiley-VCH Verlag GmbH & Co. KGaA, Weinheim

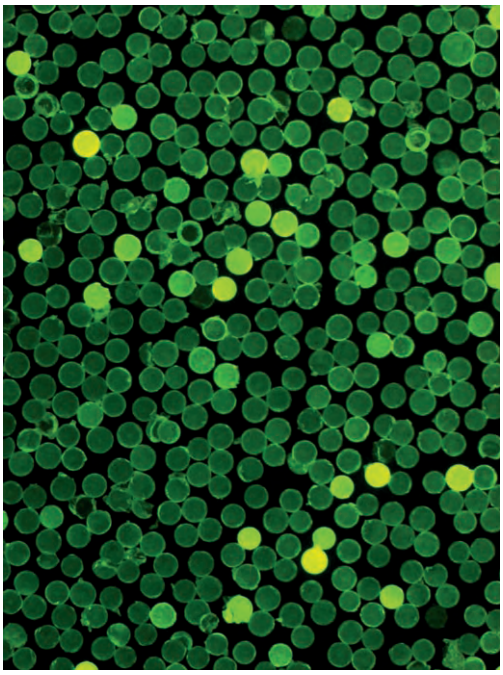


Figure 1. Incubation of the solid-phase bound substrate library with the fluorescence-labeled receptor **1** reveals a selective interaction with only some substrates within the library despite their structural close resemblance (aqueous buffer, pH 6.10, [**1**] = 5 μM).

Table 1: Selected association constants obtained from a quantitative on-bead assay for the binding of different substrates by receptor **1**.

Substrate	AA[1]	AA[2]	AA[3]	AA[4]	K_a [M^{-1}][a]
2	D-**Glu**	D-**Glu**	D-**Glu**	D-**Glu**	26500
3	L-Ala	D-**Glu**	D-**Glu**	D-**Glu**	8500
4	D-**Glu**	D-**Glu**	D-Ala	D-**Glu**	5000
5	D-**Glu**	D-Ala	L-Ala	D-**Glu**	4800
6	D-Ala	L-Ala	D-**Glu**	D-**Glu**	2600
7	D-Ala	D-Ala	L-Ala	D-**Glu**	1200
8	D-Ala	D-**Glu**	L-Ala	D-Ala	700
9	D-Ala	L-Ala	D-**Glu**	D-Ala	600
10	L-Lys	D-Ala	L-Ala	L-Lys	< 100
11	L-Ala	L-Ala	L-Ala	D-Ala	< 100

[a] Estimated error limit of the assay in $K_a \pm 30\%$.

substrates have three different side chains (Ala, Lys, and Glu) and differ only in the absolute configuration of either one building block (D/L-Ala) or the nature of one chemical linkage (Ala compared with Lac).

Even more surprising than the pronounced substrate selectivity is that receptor **1** also shows a distinct sequence-dependent stereoselectivity (Table 2): The receptor prefers D-Ala over its enantiomer L-Ala (K_a up to a factor of 10 greater) but only within certain sequences. Stereoselectivity is only observed for tetrapeptides that contain not more than one D/L-Ala located next to three D-Glu. This stereoselectivity is only found when the D/L-Ala is located in positions 2–4 of the tetrapeptide substrate, but not when it is in the N-terminal position 1. For example, although substrates **12** and **3** show nearly identical binding affinities ($K_a \approx 8000\,M^{-1}$), the association constants drops from $K_a = 5000\,M^{-1}$ to $< 1000\,M^{-1}$ if the

Table 2: Changes in the binding constant upon the exchange of D-Ala for L-Ala or D-Lac in various positions of the substrate as obtained from a quantitative on-bead screening.

Substrate	AA[1]	AA[2]	AA[3]	AA[4]	K_a [M^{-1}][a]
12	D-**Ala**	D-Glu	D-Glu	D-Glu	7900
3	L-**Ala**	D-Glu	D-Glu	D-Glu	8500
13	D-Glu	D-**Ala**	D-Glu	D-Glu	5200
14	D-Glu	L-**Ala**	D-Glu	D-Glu	600
4	D-Glu	D-Glu	D-**Ala**	D-Glu	5000
15	D-Glu	D-Glu	L-**Ala**	D-Glu	900
16	D-Glu	D-Glu	D-Glu	D-**Ala**	2100
17	D-Glu	D-Glu	D-Glu	L-**Ala**	200
18	D-Glu	D-Glu	D-Glu	D-**Lac**	300

[a] Estimated error limit of the assay in $K_a \pm 30\%$.

L-Ala is introduced in position 2 or 3 (compare substrates **13** and **14**, and **4** and **15**, respectively). The drop in affinity is even more pronounced if the L-Ala is positioned directly opposite the guanidiniocarbonyl pyrrole anion binding site (substrates **16** and **17**; $K_a = 2100\,M^{-1}$ and $K_a < 200\,M^{-1}$, respectively).

This remarkable and unexpected sequence dependent stereoselectivity was independently confirmed by UV-titration studies in free solution. First we determined the binding of Ac-D-Glu-D-Glu-D-Glu-D-Glu-OH **2** to the unlabelled receptor **1** in free solution. Aliquots of the tetrapeptide substrates were added to a solution of receptor **1** in buffered water ($[\mathbf{1}]_o = 50\,\mu M$, pH 6.10, 1.5 mM bis(2-hydroxyethyl)-imino-tris(hydroxymethyl)methane (Bis-Tris) buffer solution). From the decrease in the UV absorption of the pyrrole band at $\lambda = 300$ nm upon substrate addition, the binding constant was calculated by using a nonlinear least-square fitting procedure for a 1:1 complex formation (Figure 2). The complex stoichiometry was confirmed by a Job-plot extracted from the titration data.[14] The calculated association constant, $K_a = 23700\,M^{-1}$, for complex formation in free solution is in good agreement with the result from the on-bead screening ($K_a = 26500\,M^{-1}$).

We then tested the binding of two pairs of diastereomeric tetrapeptides, D-Glu-D-Glu-D/L-Ala-D-Glu-OH and D/L-Ala-D-Glu-D-Glu-D-Glu-OH, for their affinity to the unlabelled receptor **1** in free solution. Again UV titrations were performed by using the same conditions as described above. Stereoselectivity is only observed when the D-Ala/L-Ala exchange takes place at position 3 of the tetrapeptide but not at the N terminus (position 1). The two substrates D/L-Ala-D-Glu-D-Glu-D-Glu-OH (**12** and **3**) are bound with similar affinities by receptor **1** ($K_a = 5100\,M^{-1}$ and $4800\,M^{-1}$, respectively). However, from the two diastereomers D-Glu-D-Glu-D/L-Ala-D-Glu-OH (**4** and **15**) the one with D-Ala is preferred ($K_a = 4500\,M^{-1}$ versus $1400\,M^{-1}$, respectively) as was also found in the on-bead screening. Hence, even though the absolute binding constants determined on bead and in free solution differ (for example, owing to the different concentrations of buffer salts used in the experiments and also the influence of the solid support itself), the relative trends are the same.

Such a pronounced stereoselectivity owing to the change in the absolute stereochemistry of a single amino acid within a tetrapeptide is remarkable, even more so as the D-Ala/L-Ala

 © 2006 Wiley-VCH Verlag GmbH & Co. KGaA, Weinheim

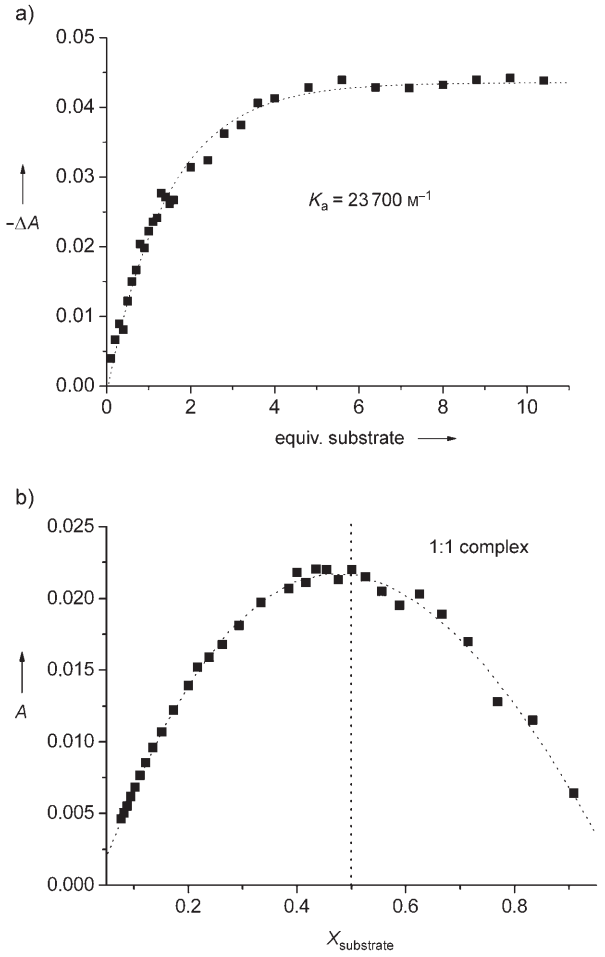


Figure 2. a) Binding isotherm at $\lambda = 300$ nm for the complexation of *N*-Ac-D-Glu-D-Glu-D-Glu-D-Glu-OH **2** by receptor **1** as obtained from a UV titration ($[\mathbf{1}]_0 = 50\ \mu M$, 1.5 mM Bis-Tris buffer solution, pH 6.1; data corrected for absorption changes owing to dilution). The dotted line represents the curve-fitting for a 1:1 complexation. b) Job plot obtained from the titration confirming the 1:1 binding stoichiometry. $X_{substrate}$ = molar fraction of the substrate.

pair is the smallest stereochemical change possible within a peptide. Most likely, stereoselectivity requires a rather well defined complex structure and is only possible when the position of the D-Ala/L-Ala exchange is fixated at both sides by strong charge interactions between receptor and substrate. The alanine itself can only form H-bonds to the receptor that are, in water, too weak to play a significant role for complex formation. Hence, either a glutamate or the C-terminal carboxylate is needed next to this position. Both groups are negatively charged and allow for strong electrostatic interactions with the tris-cationic receptor, either with the lysines or the guanidiniocarbonyl pyrrole moiety, that stabilizes the complex around the Ala. This would explain why stereoselectivity is not found for other peptide sequences within the library besides those cited in Table 2. For example, if there is another alanine next to the exchange position, the complex around the D/L-Ala exchange is perhaps too flexible to allow for a discrimination. Hence, only sequences with just one D/L-Ala pair with three glutamates show stereoselectivity. Also, no stereoselectivity is observed when the alanine is in the N-terminal position next to three glutamates (substrates **12** and **3** in Table 2). In this case only the first three amino acids of the tetrapeptide substrate are efficiently bound by the receptor, whereas the N-terminal alanine does not contribute significantly to the stability of the complex. Most likely, this terminal alanine is simply a dangling end as depicted in Figure 3. Hence, it does not matter if a D-Ala or a L-Ala is present at this position.

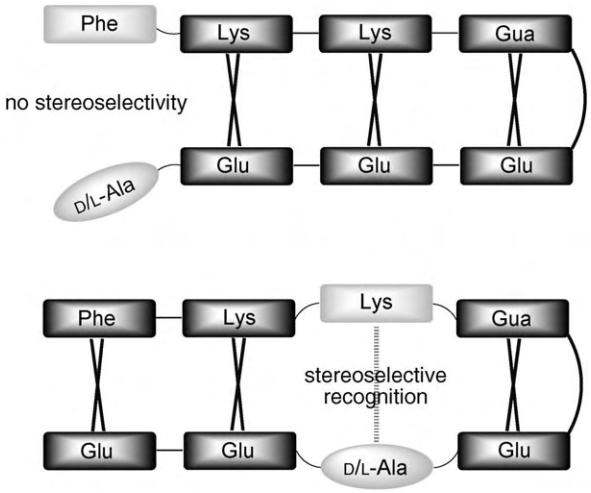


Figure 3. The stereoselectivity of receptor **1** depends on the sequence of the bound substrate. Stereoselectivity is only observed when the position where the D-Ala/L-Ala exchange takes place is fixated at both sides by strong electrostatic interactions between receptor (top) and substrate (bottom).

In good agreement with this multipoint-binding model is also the observation that the exchange of D-Ala for D-Lac at the C-terminal position of the substrate also significantly reduces the binding affinity. Although the peptide is bound with $K_a = 2100\ M^{-1}$, the affinity for the depsipeptide drops to $K_a \approx 300\ M^{-1}$ (substrates **16** and **18** in Table 2). This modification exchanges an attractive H-bond from a carbonyl CO of the receptor to an amide NH of the peptide substrate for a dipol–dipol repulsion with the ester oxygen of the depsipeptide. For such a small exchange to show up in the binding affinities, a well-defined complex structure around this position is needed. The same exchange is the origin of an upcoming bacterial resistance against the antibiotic vancomycin.[15] In this case the complex formed between vancomycin and the dipeptide fragment D-Ala-D-Ala is also well defined owing to the rigid structure of the antibiotic. Because of the extensive hydrophobic shielding of the substrate within the complex, the drop in affinity for the depsipeptide is even more pronounced. However, for an artificial receptor this is, to the best of our knowledge, the highest selectivity between this biological model dipeptide and the depsipeptide reported so far.

In conclusion, we have shown that first, the one-armed flexible peptide receptor **1** efficiently binds anionic tetrapeptides such as **2**, even in water, with association constants up to $K_a \approx 27\,000\ M^{-1}$. Second, even very closely related substrates are efficiently discriminated against as could be shown by

 © 2006 Wiley-VCH Verlag GmbH & Co. KGaA, Weinheim

screening a combinatorial library of 320 substrates. Third, a remarkable stereoselectivity between D-Ala and L-Ala is found both on the solid support as well as in free solution, but only in certain sequences that allow formation of overall well-defined complexes. Forth, the receptor is also capable of distinguishing a peptide from a depsipeptide. We are currently exploring how to further improve the selectivity of such receptors in free solution by introducing additional hydrophobic shielding elements.

Received: March 16, 2006
Published online: May 31, 2006

Keywords: amino acids · artificial peptide receptors · combinatorial chemistry · molecular recognition · supramolecular chemistry

[1] For reviews on the early work of peptide recognition, see: a) H.-J. Schneider, *Angew. Chem.* **1993**, *105*, 890 – 892; *Angew. Chem. Int. Ed. Engl.* **1993**, *32*, 848 – 850; b) M. W. Peczuh, A. D. Hamilton, *Chem. Rev.* **2000**, *100*, 2479 – 2493.

[2] For selected examples of oligopeptide binding in aqueous solvents based on metal-ligand interactions, see: a) A. T. Wright, E. V. Anslyn, *Org. Lett.* **2003**, *5*, 1341 – 1344; b) T. Mizutani, K. Wada, S. Kitagawa, *Chem. Commun.* **2002**, 1626 – 1627; c) S. Sun, M. A. Fazal, B. C. Roy, S. Mallik, *Org. Lett.* **2000**, *2*, 911.

[3] For examples of peptide recognition based on hydrophobic interactions, see: a) C. Schmuck, M. Heil, *ChemBioChem* **2003**, *4*, 1232 – 1238; b) M. Sirish, H.-J. Schneider, *Chem. Commun.* **1999**, 907 – 908; c) R. Xu, G. Greiveldinger, L. E. Marenus, A. Cooper, J. A. Ellman, *J. Am. Chem. Soc.* **1999**, *121*, 4898 – 4899; d) M. Davies, M. Bonnat, F. Guillier, J. D. Kilburn, M. Bradley, *J. Org. Chem.* **1998**, *63*, 8696 – 8703; e) R. Breslow, Z. Yang, R. Ching, G. Trojandt, F. Odobel, *J. Am. Chem. Soc.* **1998**, *120*, 3536 – 3537.

[4] For peptide recognition in water mainly based on electrostatic interactions, see: a) C. Schmuck, M. Heil, *Chem. Eur. J.* **2006**, *12*, 1339 – 1348; b) C. Schmuck, M. Heil, J. Scheiber, K. Baumann, *Angew. Chem.* **2005**, *117*, 7374 – 7379; *Angew. Chem. Int. Ed.* **2005**, *44*, 7208 – 7212.

[5] For review articles on the use of combinatorial receptor libraries, see: a) N. Srinivasan, J. D. Kilburn, *Curr. Opin. Chem. Biol.* **2004**, *8*, 305 – 310; b) B. Linton, A. D. Hamilton, *Curr. Opin. Chem. Biol.* **1999**, *3*, 307 – 312; c) Y. R. DeMiguel, J. M. K. Sanders, *Curr. Opin. Chem. Biol.* **1998**, *2*, 417 – 421; d) W. C. Still, *Acc. Chem. Res.* **1996**, *29*, 155 – 163.

[6] C. Chamorro, R. M. J. Liskamp, *Tetrahedron* **2004**, *60*, 11145 – 11157.

[7] J. Shepherd, T. Gale, K. B. Jensen, J. D. Kilburn, *Chem. Eur. J.* **2006**, *12*, 713 – 720.

[8] a) C. C. McComas, B. M. Crowley, D. L. Boger, *J. Am. Chem. Soc.* **2003**, *125*, 9314 – 9315; b) C. T. Walsh, *Nature* **2000**, *406*, 775 – 781; c) D. H. Williams, B. Bardsley, *Angew. Chem.* **1999**, *111*, 1264 – 1286; *Angew. Chem. Int. Ed.* **1999**, *38*, 1172 – 1193; d) M. Nieto, H. R. Perkins, *Biochem. J.* **1971**, *123*, 780 – 803.

[9] For a description of the IRORI tagging system, see: a) K. C. Nicolaou, J. A. Pfefferkorn, H. J. Mitchell, A. J. Roecker, S. Barluenga, G.-Q. Cao, R. L. Affleck, J. E. Lillig, *J. Am. Chem. Soc.* **2000**, *122*, 9954 – 9967; b) X.-Y. Xiao, Z. Parandoosh, M. P. Nova, *J. Am. Chem. Soc.* **1997**, *119*, 6029 – 6033.

[10] We determined the necessary coupling conditions of the *tert*-butyl ester of D-Lac compared to normal amino acids by synthesis of a model peptide sequence on *p*-methyl-benzyldryl-amine (MBHA) resin. The free amino function of this resin was transformed with the help of Z-Glu(O*t*Bu) into a carboxylate function allowing an analogous N to C solid-phase peptide-synthesis protocol like in the combinatorial library. The only difference is the higher acid sensitivity of the MBHA resin compared to TentaGel. It also allows the cleavage of the C-terminal *tert*-butyl esters with 50% TFA. In addition, the synthesized peptide can be cleaved with trifluoromethane sulfonic acid (TFMSA; 10% in TFA) and then analyzed with NMR spectroscopic techniques. These tests showed that it is possible to use the same conditions as those for like for amino acids to guarantee the quantitative coupling of D-Lac.

[11] S. Sano, S. Kawanashi, *J. Am. Chem. Soc.* **1975**, *97*, 3480 – 3484.

[12] However, the latter can not be used here as it does not swell in aqueous solutions and hence does not allow subsequent on-bead binding studies in water. For this purpose the hydrophilic TentaGel is the best choice.

[13] M. E. Attardi, G. Porcu, M. Taddei, *Tetrahedron Lett.* **2000**, *41*, 7391 – 7394.

[14] P. McCarthy, *Anal. Chem.* **1978**, *50*, 2165 – 2165.

[15] C. T. Walsh, S. L. Fisher, I.-S. Park, M. Prahalad, Z. Wu, *Chem. Biol.* **1996**, *3*, 21 – 28.

 © 2006 Wiley-VCH Verlag GmbH & Co. KGaA, Weinheim

Supramolecular Chemistry

DOI: 10.1002/anie.200600750

Dynamic Covalently Bonded Rotaxanes Cross-Linked by Imine Bonds between the Axle and Ring: Inverse Temperature Dependence of Subunit Mobility**

Hidetoshi Kawai, Takeshi Umehara, Kenshu Fujiwara, Takashi Tsuji,* and Takanori Suzuki*

Establishing methods to control submolecular movements of rotaxane components is a prerequisite for the development of artificial devices that function through translational and rotational motion at the molecular level. During the last decade, many systems capable of controlling interactions among components through external stimuli, such as metal binding, change in pH value, electrochemistry, light, or temperature, have been developed to realize on/off switching

[*] Dr. H. Kawai, T. Umehara, Prof. K. Fujiwara, Prof. T. Tsuji, Prof. T. Suzuki
Division of Chemistry
Faculty of Science
Hokkaido University, Sapporo 060-0810 (Japan)
Fax: (+81) 11-706-2714
E-mail: kawai@sci.hokudai.ac.jp

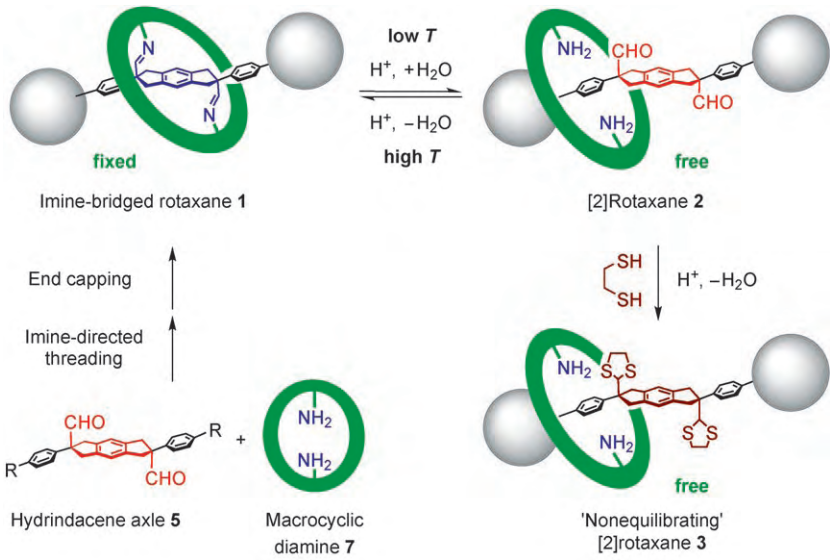
[**] We are grateful to K. Watanabe of the GC-MS and NMR Laboratory (Hokkaido University) for the mass-spectrometric analyses and to Dr. Y. Kumaki of the High-Resolution NMR Laboratory (Hokkaido University) for the ROESY and variable-temperature NMR measurements. This study was supported by JSPS KAKENHI (No. 16750024).

Supporting information for this article is available on the WWW under http://www.angewandte.org or from the author.

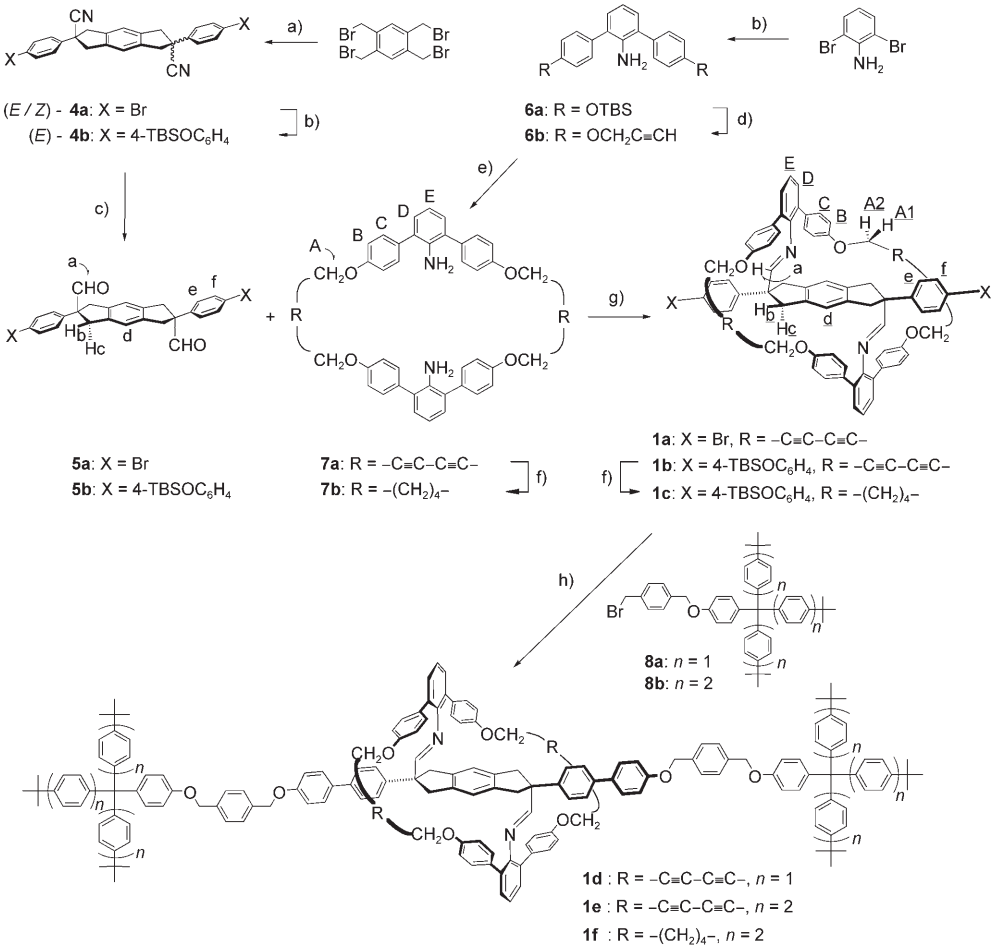
© 2006 Wiley-VCH Verlag GmbH & Co. KGaA, Weinheim

of subunit mobility or change in the position of the ring on the axle in rotaxanes (molecular shuttles).[1]

The use of dynamic covalent bonds,[2] which can be formed and broken reversibly under mild conditions, to link components seems promising for this purpose. There are no precedents for the use of the imine bond[3] as a cross-linkable/cleavable motif between the axle and ring components of rotaxanes,[4] yet we found it very useful for constructing interlocked compounds able to control the subunit mobility. The imine compounds in general can be equilibrated with the corresponding amine–aldehyde pair under hydrolytic conditions. Accordingly, the novel assembly can adopt the imine-bridged rotaxane (strictly, [1]rotaxane[5]), in which the ring is covalently fixed on the axle, or the [2]rotaxane, in which the ring can freely move on the axle (Scheme 1). Furthermore, the [2]rotaxane



Scheme 1. Dynamic formation of [2]rotaxanes **2** from imine-bridged rotaxanes **1** under acidic hydrolysis/dehydration conditions, and the transformation of **2** into [2]rotaxane **3** by dithioacetalization of the formyl groups.



Scheme 2. Synthesis of imine-bridged rotaxanes **1**: a) 4-Br$C_6H_4CH_2CN$, cat. PhCH_2NEt_3Cl, PhMe/40% NaOH, 65 °C (19 and 28% for (*E*)- and (*Z*)-**4a**, respectively); b) 4-TBSO$C_6H_4B(OH)_2$, [Pd(PPh_3)$_4$], PhH/EtOH/2 M Na_2CO_3, 80 °C (98% for (*E*)-**4b**; 97% for **6a**); c) DIBAL, PhH (for **5a**) or CH_2Cl_2 (for **5b**), 25 °C (94% for **5a**, 84% for **5b**); d) TBAF, then Cs_2CO_3, propargyl bromide, THF, 25 °C (87%); e) $Cu(OAc)_2$, CH_3CN, 80 °C (79%); f) H_2, 10% Pd/C, THF, 25 °C (>99% for **7b**; >99% for **1c**); g) TFA, 4-Å ms, PhH, reflux (>99% for **1a**; 95% for **1b**); h) TBAF, then Cs_2CO_3, **8a** or **8b**, THF/DMF, 25 °C (68% for **1d**; 52% for **1e**, 69% for **1f**). DIBAL = diisobutylaluminum hydride, TBAF = tetrabutylammonium fluoride, TFA = trifluoroacetic acid, 4-Å ms = 4-Å molecular sieves, DMF = dimethylformamide, TBS = *tert*-butyldimethylsilyl.

© 2006 Wiley-VCH Verlag GmbH & Co. KGaA, Weinheim

2 generated by hydrolysis could be transformed to another [2]rotaxane **3** by protection of the functional groups, thus preventing its participation in the dynamic regeneration of the imine-bridged rotaxane. In this way, we expected that the independent mobility of the axle and ring components in this novel type of rotaxane can be regulated based on the controllable reversibility of the dynamic covalent bond.

Herein, we report the preparation of novel assembly **1** by threading an axle bearing two formyl groups into a macrocyclic diamine, directed by cross-linking imine bond formation,[6] and attaching bulky end groups. We also report that [2]rotaxane **2** is successfully generated in equilibrium with **1** in an acidic medium, in which the relative abundance of **2** increases with decreasing temperature, and that **2** is trapped by ethanedithiol to afford "nonequilibrating" [2]rotaxane **3**.

The axle molecule **5** was designed by exploiting the well-defined geometrical features of the hydrindacene (1,2,3,5,6,7-hexahydro-*s*-indacene) skeleton.[7] The less-bulky carbaldehyde groups at the 2,6-positions preferentially occupy the pseudoaxial positions, and so can work as linkers with the amino groups of macrocycle **7** at opposing sides of the molecular plane. The bromo-terminated dicarbaldehyde axle **5a** and TBSO-terminated axle **5b** were prepared from 1,2,4,5-tetrakis(bromomethyl)benzene (Scheme 2). Macrocyclic diamine **7a** was prepared from 2,6-diarylaniline **6a** by oxidative coupling.

Upon mixing equimolar amounts of **5a** and macrocycle **7a** in $CDCl_3$ at 298 K, the ^1H NMR spectrum showed a new set of resonances just after the addition of a catalytic amount of TFA or silica gel. The newly generated species resonated at a higher field than most of the protons of both components (Figure 1). Signals that arose from **5a** and **7a** remained detectable for several hours. However, the addition of 4-Å ms to this sample or azeotropic refluxing in benzene led to the quantitative formation of doubly bridged pseudorotaxane **1a**.

Imine-bridged pseudorotaxane **1a** was isolated intact by column chromatography on alumina or gel-permeation chromatography (GPC). X-ray analysis of the THF solvate unambiguously revealed the threading of the hydrindacene axle through the macrocycle to create C_i-symmetric **1a** (Figure 2).[8] An imine-directed threading of a longer axle

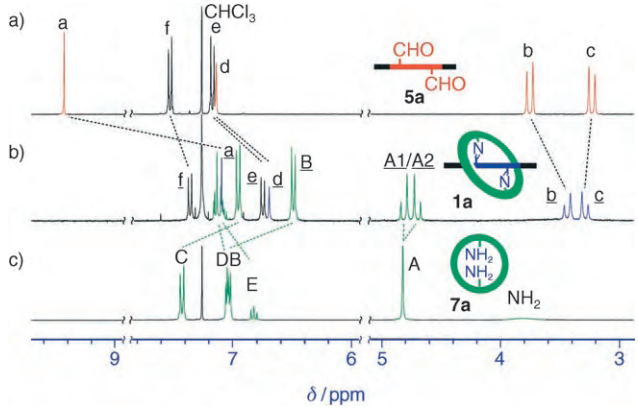


Figure 1. ^1H NMR spectra (300 MHz, $CDCl_3$) of a) hydrindacene axle **5a**, b) imine-bridged pseudorotaxane **1a**, and c) macrocycle **7a**. The lettering corresponds to the assignments shown in Scheme 2.

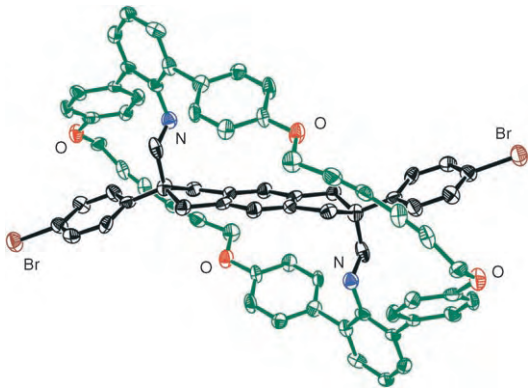


Figure 2. X-ray structure of imine-bridged pseudorotaxane **1a** in a THF solvate. Hydrogen atoms and solvents are omitted for clarity.

5b into **7a** quantitatively afforded **1b**. Imine-bridged pseudorotaxane **1c** with its flexible macrocycle was quantitatively obtained by hydrogenation of **1b** over 10% Pd/C. Finally, end groups were attached to **1b** and **1c** by one-pot desilylation–benzylation reactions with **8a** or **8b** to afford imine-bridged rotaxanes **1d**, **1e**, or **1f** (see Figure 3b and the Supporting Information[9]).

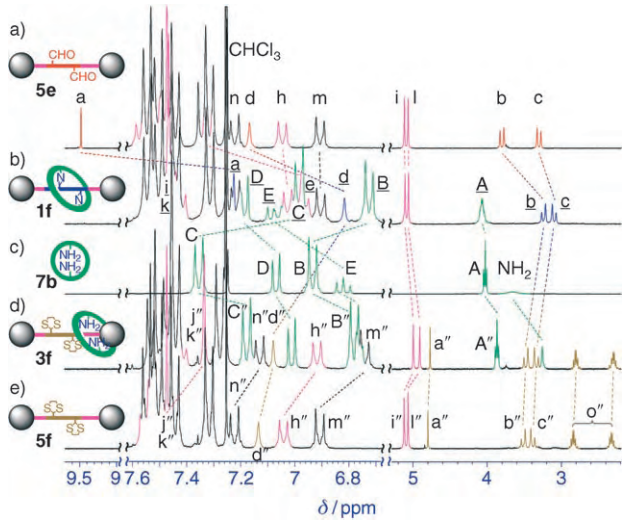
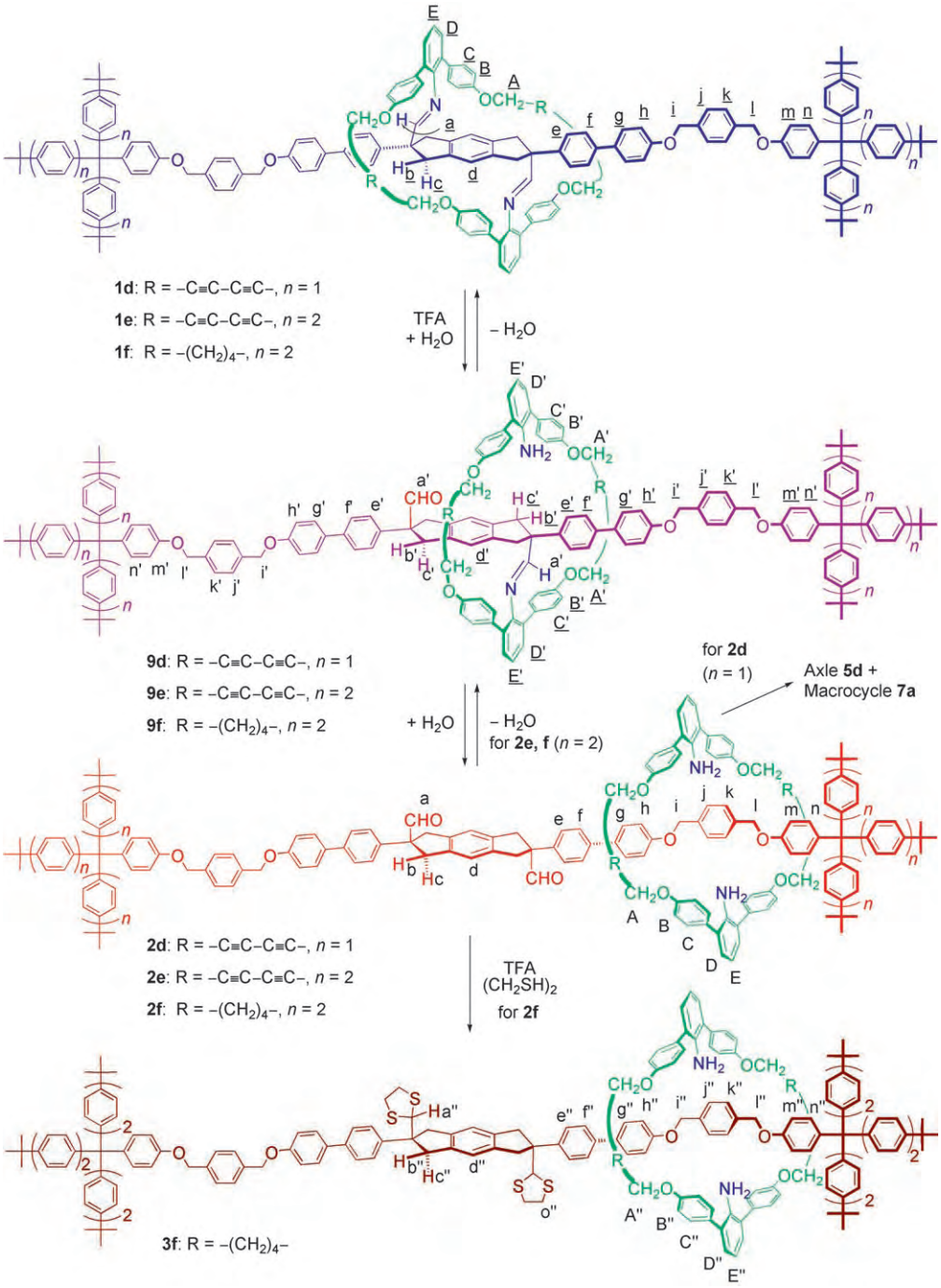


Figure 3. ^1H NMR spectra (300 MHz, $CDCl_3$, 298 K) of a) axle **5e**, b) imine-bridged rotaxane **1f**, c) macrocycle **7b**, d) dithioacetalized [2]rotaxane **3f**, and e) dithioacetalized axle **5f**. The lettering correspond to the assignments shown in Scheme 3.

With these imine-bridged rotaxanes in hand, we studied the dynamic generation of the [2]rotaxanes **2** under acidic hydrolysis conditions. The addition of TFA to a solution of **1a** or **1b** in wet $CHCl_3$ led to the quantitative (> 95%) formation of the axle, **5a** or **5b**, and the macrocycle **7a**. Similar hydrolysis and dethreading was observed for **1d** with 4-[tris(4′-*tert*-butylphenyl)methyl]phenoxy end groups (Scheme 3). These results obviously indicate the lability of the imine bonds in **1** toward acidic hydrolysis and the ready dethreading of the resultant pseudorotaxanes with the insufficiently bulky end groups.

 © 2006 Wiley-VCH Verlag GmbH & Co. KGaA, Weinheim



Scheme 3. Generation of [2]rotaxanes **2** from the imine-bridged rotaxanes **1** by acidic hydrolysis and transformation to the "nonequilibrating" [2]rotaxane **3**.

In striking contrast, compound **1f** exhibited dynamic behavior in its hydrolysis. Thus, a new set of resonances, including a C*H*O signal at $\delta = 9.4$ ppm, appeared upon addition of TFA to **1f** in $CDCl_3$ at 298 K. Another set of resonances was observed when the spectrum was recorded at 258 K, and interestingly both new sets of signals enhanced in intensity at the expense of those from **1f** as the recording temperature was lowered (see Figure 4 and the Supporting Information). The scrutiny of those sets of spectra revealed that the former spectrum was of a species low in symmetry and was consistent with the structure of the partially hydrolyzed monoimine **9f**, whereas the latter was simpler and in good agreement with that expected for the desired [2]rotaxane **2f** (see the Supporting Information).[10] The upfield shifts of the xylylene CH_2 protons in **2f**, but not in **9f**, relative to **1f** suggest relocation of the macrocycle toward the end group from the central hydrindacene moiety. The observed temperature dependence of the equilibrated ratios indicates that the dynamic generation of **2f** and **9f** by hydrolysis of the imine bonds are enthalpy-driven processes, whereas the reverse

 © 2006 Wiley-VCH Verlag GmbH & Co. KGaA, Weinheim

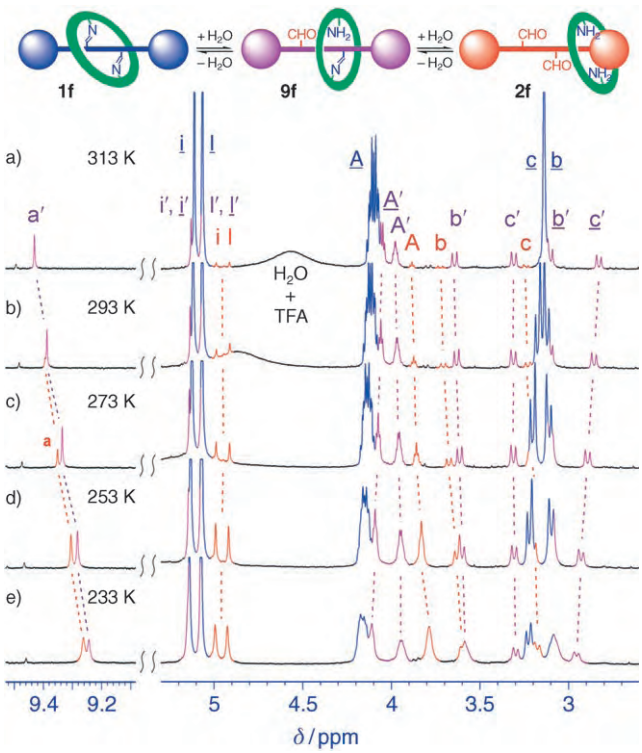


Figure 4. ^{1}H NMR spectra (600 MHz, 0.08% TFA/$CDCl_3$ (v/v)) of the hydrolyzed mixture containing imine-bridged rotaxane **1 f**, monoimine **9 f**, and [2]rotaxane **2 f**. An equilibrated ratio of **1 f**/**9 f**/**2 f** is shown in parenthesis at a) 313 K (81:18:≈1), b) 293 K (72:24:4), c) 273 K (64:30:6), d) 253 K (52:34:14), and e) 233 K (42:36:22). The lettering corresponds to the assignments shown in Scheme 3.

formation of the imine bonds are entropy driven. The release of water molecules upon the intramolecular condensation in **2 f** and **9 f** may contribute to the gain in entropy in those steps. Importantly, the increasing ratio of **2 f** at low temperature signifies that the submolecular mobility in this system (that is, the translational and rotational movement of macrocycle with respect to the axle) is enhanced as the temperature decreases. This thermosetting behavior is in sharp contrast to that of ordinary rotaxanes restricted by noncovalent interactions, in which the submolecular mobility is suppressed at lower temperature.

We could obtain the "nonequilibrating" [2]rotaxane **3 f** from the imine-bridged rotaxane **1 f** in good yield (75%) through the dithioacetalization of the formyl groups (ethanedithiol, TFA, wet $CHCl_3$) in situ. The [2]rotaxane structure of **3 f** was supported by field-desorption mass-spectrometric and ^{1}H NMR spectroscopic analysis (Figure 3 d). The ^{1}H NMR spectrum of **3 f** in $CDCl_3$ revealed that the xylylene protons (CH_2; $H_{i'',1''}$) of the tether groups of **3 f** ($\delta = 4.91$ and 5.00 ppm) were shielded relative to those of **1 f** ($\delta = 5.06$ and 5.11 ppm) or the dithioacetalized axle **5 f** ($\delta = 5.07$ and 5.12 ppm), and no peak-splitting was observed over a temperature range of 188–298 K in CD_2Cl_2. The central hydrindacene part of **3 f** ($\delta = 3.48$ ($H_{b''}$), 3.34 ($H_{c''}$), and 7.08 ppm ($H_{d''}$)) was not magnetically shielded, and their resonances appear in the similar region to those of **5 f** ($\delta = 3.51$, 3.38, and 7.13 ppm). These results indicate that the macrocycle of **3 f** preferentially resides around the tether groups and rapidly shuttles between the two xylylene spacers, as in the case of [2]rotaxane **2 f**.

In summary, by using diformylhydrindacene **5** as a synthetic platform, we have demonstrated the validity of a novel threading method directed by imine-bond formation. From the resultant imine-bridged [2]rotaxane **1**, two types of [2]rotaxane **2** and **3** were generated through the imine-bond cleavage, that is, acidic hydrolysis that leads to a dynamic mixture containing **2** and thioacetalization of **2** to give **3** in situ. More importantly, the submolecular mobility in this novel assembly could be regulated by the imine-bond formation/cleavage between the macrocycle and axle: the imine-bond formation allows control over the ability of the macrocycle to be able to move over the axle or not. This restriction of motion must be important for "ratcheting",[11] a crucial requirement for the preparation of molecular machines that are more complex than simple switchable molecular shuttles. Another outstanding feature of the present system is the temperature dependence of a proportion of **2** under the hydrolytic equilibration: as the temperature is lowered, the proportion of **2** relative to **1** is increased. Increasing submolecular mobility as a bulk with lowering of temperature is unusual, and we are investigating the exploitation of this peculiar behavior.

Received: February 27, 2006
Published online: May 31, 2006

Keywords: entropy · imines · molecular dynamics · rotaxanes · template synthesis

[1] a) *Molecular Catenanes, Rotaxanes, and Knots* (Eds.: J.-P. Sauvage, C. Dietrich-Buchecker), Wiley-VCH, Weinheim, **1999**; b) V. Balzani, A. Credi, F. M. Raymo, J. F. Stoddart, *Angew. Chem.* **2000**, *112*, 3484–3530; *Angew. Chem. Int. Ed.* **2000**, *39*, 3348–3391; c) Molecular Machines Special Issue, *Acc. Chem. Res.* **2001**, *34*, 409–522; d) *Molecular Switches* (Eds.: B. L. Feringa), Wiley-VCH, Weinheim, **2001**; e) V. Balzani, A. Credi, *Chem. Rec.* **2001**, *1*, 422–435; f) *Molecular Devices and Machines* (Eds.: V. Balzani, M. Venturi, A. Credi), Wiley-VCH, Weinheim, **2003**; g) E. R. Kay, D. A. Leigh in *Functional Synthetic Receptors* (Eds.: T. Schrader, A. D. Hamilton), Wiley-VCH, Weinheim, **2005**, chap. 7.

[2] a) J.-M. Lehn, *Chem. Eur. J.* **1999**, *5*, 2455–2463; b) G. R. L. Cousins, S.-A. Poulsen, J. K. M. Sanders, *Curr. Opin. Chem. Biol.* **2000**, *4*, 270–279; c) S. J. Rowan, S. J. Cantrill, G. R. L. Cousins, J. K. M. Sanders, J. F. Stoddart, *Angew. Chem.* **2002**, *114*, 938–993; *Angew. Chem. Int. Ed.* **2002**, *41*, 898–952; d) J.-M. Lehn, *Proc. Natl. Acad. Sci. USA* **2002**, *99*, 4763–4768; e) R. L. E. Furlan, S. Otto, J. K. M. Sanders, *Proc. Natl. Acad. Sci. USA* **2002**, *99*, 4801–4804; f) S. Otto, R. L. E. Furlan, J. K. M. Sanders, *Curr. Opin. Chem. Biol.* **2002**, *6*, 321–327; g) J.-M. Lehn, *Science* **2002**, *295*, 2400–2403.

[3] a) H. Schiff, *Justus Liebigs Ann. Chem.* **1864**, *131*, 118; b) R. W. Layer, *Chem. Rev.* **1963**, *63*, 489–510; c) *The Chemistry of the Amino Group* (Ed.: S. Patai), Wiley, London, **1968**, chap. 7; d) N. Giuseppone, J.-M. Lehn, *Chem. Eur. J.* **2006**, *12*, 1715–1722.

[4] Imine-bond formation has been utilized to construct individual axle or ring components in interlocked compounds, such as rotaxanes and a Borromean ring, see: a) J. Y. Sze, H. W. Gibson, *Polym. Prepr. Am. Chem. Soc. Div. Polym. Chem.* **1992**, *33*, 331–332; b) S. J. Cantrill, S. J. Rowan, J. F. Stoddart, *Org. Lett.* **1999**,

 © 2006 Wiley-VCH Verlag GmbH & Co. KGaA, Weinheim

1, 1363 – 1366; c) S. J. Rowan, J. F. Stoddart, *Org. Lett.* **1999**, *1*, 1913 – 1916; d) P. T. Glink, A. I. Oliva, J. F. Stoddart, A. J. P. White, D. J. Williams, *Angew. Chem.* **2001**, *113*, 1922 – 1927; *Angew. Chem. Int. Ed.* **2001**, *40*, 1870 – 1875; e) M. Horn, J. Ihringer, P. T. Glink, J. F. Stoddart, *Chem. Eur. J.* **2003**, *9*, 4046 – 4054; f) D. Nepal, S. Samal, K. E. Geckeler, *Macromolecules* **2003**, *36*, 3800 – 3802; g) L. Hogg, D. A. Leigh, P. J. Lusby, A. Morelli, S. Parsons, J. K. Y. Wong, *Angew. Chem.* **2004**, *116*, 1238 – 1241; *Angew. Chem. Int. Ed.* **2004**, *43*, 1217 – 1221; h) E. Katz, L. Sheeney-Haj-Ichia, I. Willner, *Angew. Chem.* **2004**, *116*, 3354 – 3362; *Angew. Chem. Int. Ed.* **2004**, *43*, 3292 – 3300; i) F. Aricó, T. Chang, S. J. Cantrill, S. I. Kahn, J. F. Stoddart, *Chem. Eur. J.* **2005**, *11*, 4655 – 4666; j) K. S. Chichak, S. J. Cantrill, A. R. Pease, S.-H. Chiu, G. W. V. Cave, J. L. Atwood, J. F. Stoddart, *Science* **2004**, *304*, 1308 – 1312.

[5] a) C. Reuter, A. Mohry, A. Sobanski, F. Vögtle, *Chem. Eur. J.* **2000**, *6*, 1674 – 1682; b) C. Reuter, W. Wienand, C. Schmuck, F. Vögtle, *Chem. Eur. J.* **2001**, *7*, 1728 – 1733; c) K. Hiratani, M. Kaneyama, Y. Nagawa, E. Koyama, M. Kanesato, *J. Am. Chem. Soc.* **2004**, *126*, 13 568 – 13 569.

[6] For other methods for the preparation of interlocked compounds through covalent-bond formation, see: a) G. Schill, A. Lüttringhaus, *Angew. Chem.* **1964**, *76*, 567 – 568; *Angew. Chem. Int. Ed. Engl.* **1964**, *3*, 546 – 547; b) K. Hiratani, J. Suga, Y. Nagawa, H. Houjou, H. Tokuhisa, M. Numata, K. Watanabe, *Tetrahedron Lett.* **2002**, *43*, 5747 – 5750; c) A. Godt, *Eur. J. Org. Chem.* **2004**, 1639 – 1654; d) N. Kameta, K. Hiratani, Y. Nagawa, *Chem. Commun.* **2004**, 466 – 467.

[7] a) H. Kawai, R. Katoono, K. Nishimura, S. Matsuda, K. Fujiwara, T. Tsuji, T. Suzuki, *J. Am. Chem. Soc.* **2004**, *126*, 5034 – 5035; b) H. Kawai, R. Katoono, K. Fujiwara, T. Tsuji, T. Suzuki, *Chem. Eur. J.* **2005**, *11*, 815 – 824.

[8] X-ray crystal structural data for **1a**·4THF (collected at 103 K): $C_{90}H_{82}Br_2N_2O_8$, $M_r = 1479.45$, triclinic $P\bar{1}$, $a = 11.185(5)$, $b = 12.645(3)$, $c = 14.799(7)$ Å, $\alpha = 67.08(5)$, $\beta = 82.55(6)$, $\gamma = 68.39(5)°$, $V = 8461.0(1)$ Å^3, $\rho_{calcd}(Z=1) = 1.370$ g cm^{-3}, $\mu = 1.196$ cm^{-1}, 7611 independent reflections ($R_{int} = 0.131$) and 509 parameters, $R1(F^2) = 0.092$ ($I > 2\sigma I$), $wR2(F^2) = 0.244$ (all data). Estimated standard deviations for bond lengths and angles are 0.009–0.02 Å and 0.6–1.0° for non-hydrogen atoms. CCDC-252150 contains the supplementary crystallographic data for this paper. These data can be obtained free of charge from The Cambridge Crystallographic Data Centre via www.ccdc.cam.ac.uk/data_request/cif.

[9] See the Supporting information.

[10] As **1e** has more rigid macrocycles than **1f**, most of the ^{1}H NMR signals, except for those of the end groups, broadened under the hydrolytic conditions, thus suggesting that the hydrolysis that generates **9e** and **2e** might proceed to some extent; however, the expected C*H*O signals were not clearly discernible and the propargyl methylene protons on the macrocycle remained nonequivalent to each other. Thus, the equilibration among **1e**, **9e**, and **2e** seems to be heavily in favor of **1e** under the hydrolytic conditions, and as a result the preorganization of the macrocycle favors imine formation.

[11] a) J. V. Hernández, E. R. Kay, D. A. Leigh, *Science* **2004**, *306*, 1532 – 1537; b) M. N. Chatterjee, E. R. Kay, D. A. Leigh, *J. Am. Chem. Soc.* **2006**, *128*, 4058 – 4073.

 © 2006 Wiley-VCH Verlag GmbH & Co. KGaA, Weinheim

Protein Modification

DOI: 10.1002/anie.200600756

Site-Specific Protein Modification through Cu^{I}-Catalyzed 1,2,3-Triazole Formation and Its Implementation in Protein Microarray Fabrication**

*Po-Chiao Lin, Shau-Hua Ueng, Mei-Chun Tseng, Jia-Ling Ko, Kuo-Ting Huang, Sheng-Chieh Yu, Avijit Kumar Adak, Yu-Ju Chen, and Chun-Cheng Lin**

Site-specific modification of proteins is an important yet challenging task in biochemical and biophysical research. In particular, during the fabrication of protein microarrays, the activity of the protein may be significantly influenced by its orientation on the solid surface.[1] Although many reports have detailed the noncovalent immobilization of proteins with orientational control (for example, biotin–streptavidin and His tag–Ni interactions), there are few such methods for the site-specific covalent immobilization of proteins.[2] However, the most commonly used chemistries for protein modification, such as amide-bond formation and reductive amination, involve random covalent-bond formation,[3] which inevitably has a negative impact on protein activity and, hence, the sensitivity of activity-based assays. Thus, given the presence of multiple reactive amino acids in proteins under physiological conditions, there is a considerable need for highly selective orthogonal reactions.[4] To address this issue, we have combined the intein fusion protein expression system with Cu^{I}-catalyzed 1,2,3-triazole formation to specifically modify a target protein at its C terminus. Furthermore, the use of a diazido linker yielded a covalent link between monomers of a homodimeric protein. We also applied this method to the fabrication of a protein microarray by site-

[*] P.-C. Lin, Prof. Y.-J. Chen, Prof. C.-C. Lin
Department of Chemistry
National Tsing Hua University
Hsinchu (Taiwan)
Fax: (+886) 3-571-1082
E-mail: cclin66@mx.nthu.edu.tw
and
Chemical Biology and Molecular Biophysics
Taiwan International Graduate Program
Academia Sinica, Taipei (Taiwan)

P.-C. Lin, Dr. S.-H. Ueng, M.-C. Tseng, J.-L. Ko, K.-T. Huang, S.-C. Yu, Dr. A. K. Adak, Prof. Y.-J. Chen, Prof. C.-C. Lin
Institute of Chemistry and Genomic Research Center
Academia Sinica, Taipei (Taiwan)

J.-L. Ko
Department of Chemistry
National Taiwan Normal University
Taipei (Taiwan)

[**] We acknowledge financial support from the National Tsing Hua University (Academia Sinica Research Project on Nano Science and Technology) and the National Science Council, Taiwan.

Supporting information for this article is available on the WWW under http://www.angewandte.org or from the author.

WILEY InterScience DISCOVER SOMETHING GREAT

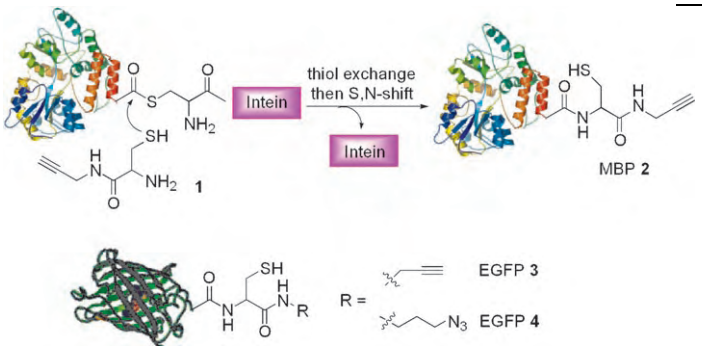
© 2006 Wiley-VCH Verlag GmbH & Co. KGaA, Weinheim

specific covalent-bond formation, which resulted in the retention of the protein activity.

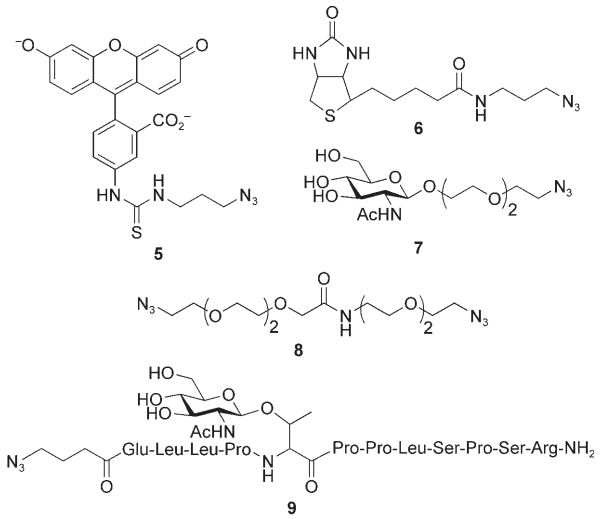
Recent studies have shown that site-specific modification of proteins can be achieved either by incorporating non-natural amino acids containing orthogonally reactive groups[5] or by the technique of expressed protein ligation (EPL)[6] to include terminal cysteine-containing molecules at the C termini. Although EPL has been used to attach a wide variety of molecules to target proteins[6–11] and to fabricate protein microarrays,[10–12] it has limited practical application for diverse modifications because of the instability of thioesters in proteins. As a result of the rapid expansion of array-based methods with diverse applications, there is an urgent need to develop methodologies to establish core template proteins that may be readily modified in a variety of ways; moreover, the systems must be amenable to long-term storage.

To develop an efficient and practical ligation method, Sharpless et al. and Meldal et al. exploited the effective formation of 1,2,3-triazoles between azides and terminal acetylenes in the presence of a Cu^I catalyst.[13] This azide–alkyne cycloaddition offers good reproducibility and a high degree of specificity and biocompatibility with water, which makes it potentially appropriate for a variety of in vitro and in vivo applications.[14–18] The Cu^I-catalyzed azide–alkyne cycloaddition[13] is highly predictable, very fast, and resistant to side reactions. Herein, we describe the use of EPL and the Cu^I-catalyzed formation of 1,2,3-triazole to achieve C-terminal protein modification and to fabricate a protein microarray by site-specific covalent-bond formation.

To demonstrate the concept, maltose binding protein (MBP) was chosen as the target protein because it has a good expression yield as an intein fusion protein in *Escherichia coli*.[7] MBP was expressed using the commercially available IMPACT (intein-mediated purification with affinity chitin-binding tag) vector system. The fusion protein was purified with chitin beads and treated with cysteine alkyne **1**, followed by a spontaneous S–N acyl shift to give core-alkynated MBP **2** (Scheme 1). The purified MBP **2** had a mass of 43217 Da, as determined by electrospray mass spectrometry. By a similar method, we prepared core-modified enhanced green fluorescent proteins (EGFPs) **3** and **4**, which contain alkyne and azide functional groups at their respective C termini. Initially, we used core-alkynated MBP **2** as the core template protein, with the C-terminal alkyne available for ligation with various azido molecules. To demonstrate the general applicability of the approach, **2** was conjugated with several target azide-containing molecules, such as fluorescein isothiocyanate (FITC; **5**), biotin (**6**), *N*-acetylglucosamine (**7**), diazide linker (**8**), and a glycopeptide (**9**; Scheme 2).



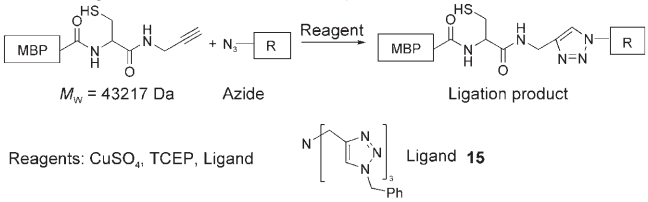
Scheme 1. Preparation of recombinant alkynated MBP **2**, EGFP **3**, and EGFP **4**.



Scheme 2. Azido molecules for ligation with alkynated MBP **2**.

Conjugation of **2** with azido molecules was achieved by 1,2,3-triazole formation catalyzed by Cu^I, which was produced from the reaction of $CuSO_4$ (1 mM) with tris(carboxyethyl)-phosphine (TCEP; 2 mM) in phosphate-buffered saline (PBS; pH 8.0, 0.1M; Table 1). As unligated and ligated **2** have similar masses (difference of <1 kDa) and hydrophobicity, common protein separation methods, such as SDS-PAGE and size-exclusion HPLC, could not be used to distinguish them. Thus, electrospray mass spectrometry was used to monitor both unligated and ligated **2** during the reaction and to evaluate the efficiency of cycloaddition.

Table 1: Ligation of various azido compounds with MBP **2**.



Azide	Ligation product	M_{obs} [Da]	M_{calcd} [Da]
5	**10**	43704	43704
6	**11**	43539	43544
7	**12**	43596	43594
8	**13**	43619	43606
9	**14**	44838	44836

In an attempt to maintain the native protein structure, the initial ligation between alkynated MBP **2** and **5** was performed overnight at 0 °C. However, these conditions resulted in a low product yield. To increase the reaction rate and yield, tri(triazolyl)amine ligand **15**

 © 2006 Wiley-VCH Verlag GmbH & Co. KGaA, Weinheim

(2 mM)[15] was added and the reaction temperature was increased to 25 °C. As depicted in Figure 1 a, the electrospray mass spectrum revealed the time-dependent reactant/product ratio during the reaction. The *m*/*z* value of 43 704 clearly

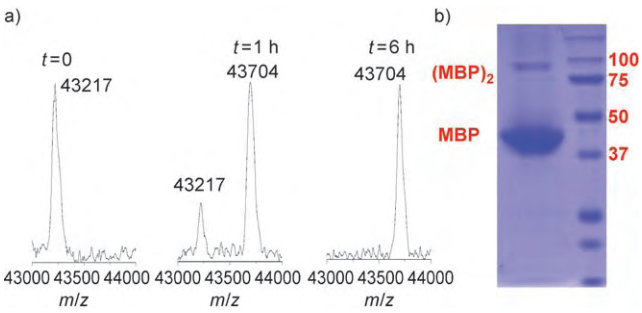


Figure 1. a) Ligation of alkynated MBP **2** and FITC (**5**) with reaction times of 0, 1, and 6 h. b) SDS-PAGE of homoligation of alkynated MBP 2 and **13**.

showed that ligation was complete in 6 hours, thus forming FITC-modified MBP **10** and indicating the efficiency of C-terminal modification. To demonstrate the application and versatility of the site-specific modification method, we tested some common reagents in bioevaluation, such as fluorescent probes and affinity tags. The observed masses of the modified protein products under different ligation reactions are shown in Table 1. The consistency between the calculated and observed masses of ligated proteins unambiguously shows that the correct ligation products were obtained. The observed yields clearly demonstrate that alkyne–azide cycloaddition presents a very efficient method for protein conjugation. In general, all ligations were complete within 12 h.

In addition to ligation with small molecules, the linker-conjugated MBP **13** was designed to demonstrate the applicability of the method to protein–protein conjugation. Alkynated MBP **2** was ligated with excess diazido linker **8** to give MBP **13**, which was again conjugated with MBP **2** to yield a covalently linked MBP homodimer (see Figure 1 b). SDS-PAGE of the ligation product showed a new band migrating at approximately 86 kDa, which is in good agreement with the expected mass of a covalent homodimer of MBP **2** (monomer 43 kDa). The ligation reaction was inefficient, however, probably because of the short length of the polyethylene glycol linker, which resulted in steric hindrance during close contact with the second MBP molecule. This putative steric effect was more significant with shorter linkers (data not shown). Further optimization of linker length, thereby minimizing steric hindrance, could improve the effective yield of the protein modification.

To demonstrate the utility of 1,2,3-triazole formation during the fabrication of a protein microarray, the alkyne-modified EGFP **3** and azide-modified EGFP **4** were used as fluorescent proteins that were covalently and site-specifically attached to glass slides by triazole formation, respectively. To prepare the alkynated and azidated glass slides, a slide coated with amino groups was incubated with glutaric acid bis-*N*-hydroxysuccinimide ester (10 mM) and then treated with 3-azidopropanylamine (10 mM) or monopropargylamine (10 mM) followed by capping with ethanolamine (Figure 2). The alkynated EGFP **3** (2.7 μg mL^{-1}) and azidated EGFP **4** (2.4 μg mL^{-1}) were spotted on the azide- and alkyne-functionalized glass slides, respectively, and unmodified EGFP

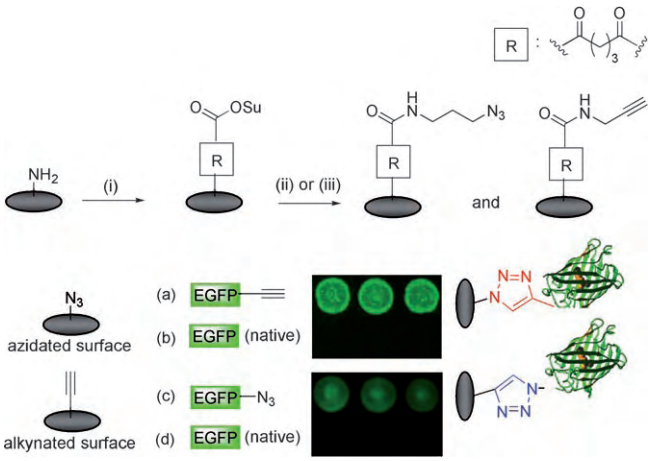


Figure 2. Fabrication of an EGFP microarray by 1,2,3-triazole formation for a) alkynated EGFP **3** and b) native EGFP with azido slide; c) azido-EGFP **4** and d) native EGFP with alkynated slide. Reaction conditions: i) immersed in a solution of glutaric acid bis-*N*-hydroxysuccinimide ester (10 mM) in DMF at room temperature for 24 h; ii) a solution of 3-azidopropanylamine (10 mM) in DMF, and iii) a solution of monopropargylamine (10 mM) in DMF incubated with activated slide in the presence of *N*,*N*-diisopropylethylamine (100 mM) at room temperature for 24 h.

was used as control for both functionalized glass slides. The ligation reaction was incubated for 12 h at room temperature in the presence of $CuSO_4$ (2 mM) and TCEP (4 mM) in PBS buffer (pH 8.0), and the protein-modified slide was then extensively washed with PBST (PBS + 0.04 % Tween 20). Positive EGFP fluorescence, as measured at 530 nm, was evident for both ligations on the glass slides, whereas the negative control gave no signal (Figure 2). These results indicate that chemoselective attachment was achieved by 1,2,3-triazole formation and that the protein tertiary structure was maintained.

However, the azide-modified slide presented a much better surface for efficient protein ligation relative to the alkyne-modified surface (Figure 2 a versus 2 c). This effect may be because Cu^I coordinates with alkynes in solution more rapidly and with higher affinity than with the azide, thereby enhancing the rate of 1,2,3-triazole formation with the surface azido group.[19] A similar preference for the surface functional group has also been reported when labeling azido-modified cowpea mosaic virus with an alkynated dye molecule through triazole formation.[15b] Significantly, in the current study a protein concentration of only 1 μM was needed to achieve well-detectable levels of immobilization, which demonstrates that Cu^I-catalyzed 1,2,3-triazole formation is a very efficient reaction in surface chemistry.[12]

To address the importance of orientation in protein immobilization, alkynated MBP **2** was covalently attached to a glass slide in a site-specific manner by triazole formation, as described in the fabrication of the EGFP microarray.

 © 2006 Wiley-VCH Verlag GmbH & Co. KGaA, Weinheim

Biotinylated maltose **16** was then used as the probe to interact with **2** on the glass surface, followed by fluorescence visualization with streptavidin-Cy3. As shown in Figure 3a, the relative intensity of the signal measured at 570 nm indicated that chemoselective attachment was achieved by 1,2,3-triazole formation.

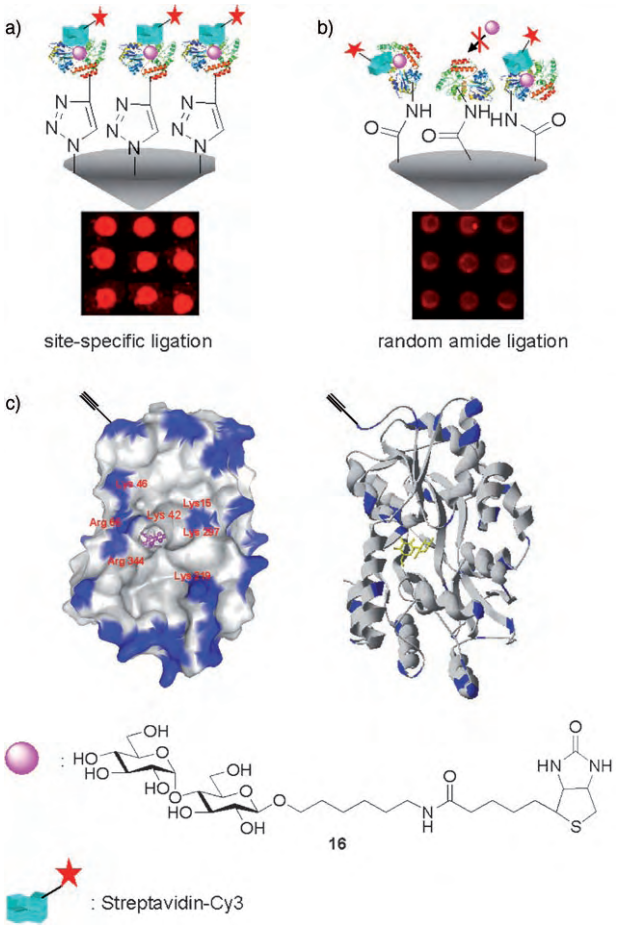


Figure 3. Fabrication of a protein microarray by a) site-specific covalent-bond (1,2,3-triazole) formation or b) random amide-bond formation. c) X-ray structure of MBP, with blue moieties indicating Lys and Arg residues.

To compare the effect of site-specific or random conjugation on maltose binding activity, MBP **2** was immobilized on *N*-hydroxysuccinimide (OSu)-activated slides by random amide-bond formation (Figure 3b). The site-specific immobilization technique yielded higher protein binding activity (Figure 3a versus 3b). The X-ray crystal structure of MBP[20] reveals that seven of 41 lysine and arginine residues on the protein surface are located near the maltose binding site (Figure 3c). These amino-containing residues may react with reagents involved in protein immobilization, which could, upon covalent attachment to a solid surface, cause a partial or complete blockade of the maltose binding site. By contrast, the C terminus of MBP is far from the binding site, and thus immobilization at this site would have minimal impact on the native conformation of the maltose binding site. Our data demonstrate that the site-specific fabrication of a protein array preserves greater protein activity relative to random protein attachment methods, thereby significantly improving assay sensitivity.

In conclusion, by combining the intein fusion protein expression system with Cu^{I}-catalyzed 1,2,3-triazole formation, the target protein was efficiently modified at its C terminus. This method allows the immobilized core template protein to be modified by diverse small molecules in a site-specific manner. In addition, site-specific protein–protein conjugation was achieved by using a diazido linker, a method that should be applicable to the preparation of protein heterodimers. Moreover, we demonstrated the importance of site-specific immobilization of a protein in an array-based assay; when protein molecules are oriented in an optimal manner, the native conformation is more likely to be preserved, thereby retaining greater activity. Given the flexibility and ease of this site-specific modification/immobilization technique, the procedure reported herein constitutes an efficient and reproducible method for the fabrication of protein microarrays or other solid-phase assays.

Received: February 27, 2006
Published online: May 31, 2006

Keywords: copper · dimerization · ligation · nitrogen heterocycles · protein modifications

[1] T. Cha, A. Guo, X.-Y. Zhu, *Proteomics* **2005**, *5*, 416–419.
[2] a) K.-Y. Tomizaki, K. Usui, H. Mihara, *ChemBioChem* **2005**, *6*, 782–799; b) A. D. De Araújo, J. M. Palomo, J. Cramer, M. Köhn, H. Schröder, R. Wacker, C. Niemeyer, K. Alexandrov, H. Waldmann, *Angew. Chem.* **2006**, *118*, 302–307; *Angew. Chem. Int. Ed.* **2006**, *45*, 296–301.
[3] G. T. Hermanson, *Bioconjugate Techniques*, Academic Press, San Diego, **1996**.
[4] For a review, see: G. A. Lemieux, C. R. Bertozzi, *Trends Biotechnol.* **1998**, *16*, 506–513.
[5] L. Wang, P. G. Schultz, *Angew. Chem.* **2004**, *116*, 34–66; *Angew. Chem. Int. Ed.* **2005**, *44*, 34–66.
[6] T. W. Muir, *Annu. Rev. Biochem.* **2003**, *72*, 249–289.
[7] T. J. Tolbert, C.-H. Wong, *J. Am. Chem. Soc.* **2000**, *122*, 5421–5428.
[8] J. A. Pezza, K. N. Allen, D. R. Tolan, *Chem. Commun.* **2004**, 2412–2413.
[9] T. Durek, K. Alexandrov, R. S. Goody, A. Hildebrand, I. Heinemann, H. Waldmann, *J. Am. Chem. Soc.* **2004**, *126*, 16368–16378.
[10] M. Lovrinovic, R. Seidel, R. Wacker, H. Schroeder, O. Seitz, M. Engelhard, R. S. Goody, C. M. Niemeyer, *Chem. Commun.* **2003**, 822–823.
[11] M.-L. Lesaicherre, R. Y. P. Lue, G. Y. J. Chen, Q. Zhu, S. Q. Yao, *J. Am. Chem. Soc.* **2002**, *124*, 8768–8769.
[12] J. A. Camarero, Y. Kwon, M. A. Coleman, *J. Am. Chem. Soc.* **2004**, *126*, 14730–14731.
[13] a) V. V. Rostovtsev, L. G. Green, V. V. Fokin, K. B. Sharpless, *Angew. Chem.* **2002**, *114*, 2708–2721; *Angew. Chem. Int. Ed.* **2002**, *41*,2596–2599; b) C. W. Tornøe, C. Christensen, M. Meldal, *J. Org. Chem.* **2002**, *67*, 3057–3064; c) for a review, see: V. D. Bock, H. Hiemstra, J. H. Van Maarseveen, *Eur. J. Org. Chem.* **2006**, 51–68.
[14] a) H. C. Kolb, K. B. Sharpless, *Drug Discovery Today* **2003**, *8*, 1128–1137; b) A. Krasinski, Z. Radic, R. Manetsch, J. Raushel, P. Taylor, K. B. Sharpless, H. C. Kolb, *J. Am. Chem. Soc.* **2005**, *127*, 6686–6692.

 © 2006 Wiley-VCH Verlag GmbH & Co. KGaA, Weinheim

[15] a) T. R. Chan, R. Hilgraf, K. B. Sharpless, V. V. Fokin, *Org. Lett.* **2004**, *6*, 2853 – 2855; b) Q. Wang, T. R. Chan, R. Hilgraf, V. V. Fokin, K. B. Sharpless, M. G. Finn, *J. Am. Chem. Soc.* **2003**, *125*, 3192 – 3193.
[16] A. E. Speers, B. F. Cravatt, *Chem. Biol.* **2004**, *11*, 535 – 546.
[17] a) J. P. Collman, N. K. Devaraj, C. E. D. Chidsey, *Langmuir* **2004**, *20*, 1051 – 1053; b) N. K. Devaraj, G. P. Miller, W. Ebina, B. Kakaradov, J. P. Collman, E. T. Kool, C. E. D. Chidsey, *J. Am. Chem. Soc.* **2005**, *127*, 8600 – 8601; c) J. K. Lee, Y. S. Chi, I. S. Choi, *Langmuir* **2004**, *20*, 3844 – 3847.
[18] M. C. Bryan, F. Fazio, H.-K. Lee, C.-Y. Huang, A. Chang, M. D. Best, D. A. Calarese, O. Blixt, J. C. Paulson, D. Burton, I. A. Wilson, C.-H. Wong, *J. Am. Chem. Soc.* **2004**, *126*, 8640 – 8641.
[19] S. Punna, J. Kuzelka, Q. Wang, M. G. Finn, *Angew. Chem.* **2005**, *117*, 2255 – 2260; *Angew. Chem. Int. Ed.* **2005**, *44*, 2215 – 2220.
[20] N. V. Adikesavan, S. S. Mahmood, S. Stanley, Z. Xu, N. Wu, M. Thibonnier, M. Shoham, *Acta Crystallogr. F* **2005**, *61*, 341.

 © 2006 Wiley-VCH Verlag GmbH & Co. KGaA, Weinheim

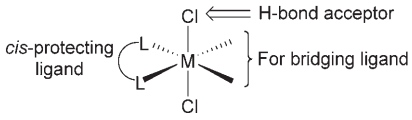
Metallacycles

DOI: 10.1002/anie.200600154

A Self-Complementary Assembly of Metallamacrocycles Directed by Ru–Cl···H–N Hydrogen Bonds and Its Reversible Dichotomy by Halide Anions in Solution**

Young Jun Park, Jik-Soo Kim, Kyoung-Tae Youm, Nam-Kyu Lee, Jaejung Ko, Hye-seo Park,* and Moo-Jin Jun**

The coordination-directed self-assembly approach is an extremely powerful strategy for the synthesis of various 2- and 3D metallasupramolecules and can provide a structural and functional basis for its potential application toward molecular sensing and catalysis by using supramolecular chemistry.[1] In particular, discrete 3D self-assemblies derived from the multiple noncovalent interactions between monomeric metallo-subunits, such as chains, squares, and/or cages, are very intriguing because they are structurally complex but symmetrically simple and synthetically convenient to make.[2] Whereas various functional groups have been utilized for such purposes, little attention has been paid to metal–halide bonds, although they are well known as hydrogen-bond acceptors in molecular recognition and crystal engineering.[3] The halides are usually destined to be eliminated, presumably as a result of limited coordination sites on the metal center for incoming ligands.[1] These facts prompted us to explore the way to get the metal–halide groups to participate in both the coordination-directed and noncovalent self-assembly processes without their abstraction. Considering the molecular library model,[1g] we envisioned that the octahedral geometry of a transition metal might provide a novel approach for the use of metal–halide bonds as a self-assembly motif. For example, octahedral transition-metal centers with axial halide and *cis*-protecting ligands could serve as a 90° building block. The axial halide, then, may participate in hydrogen bonding with suitably functionalized bridging ligands.



Herein, we demonstrate the unprecedented self-complementary dimer of Ru^{II} metallamacrocycles which uses the intact metal–halide bonds in the coordination-directed self-assembly process and its reversible dissociation/association behavior, which is controlled by halide anions in solution.

The ligand *N*,*N*′-bis(pyridin-4-yl)pyridine-2,6-dicarboxamide (**1**) was quite suitable for our purpose because it has central amide protons as hydrogen-bonding donors and is well known for bridging two metal centers, thus giving metallamacrocycles.[4] In addition, its bisamide configuration has proven to be very useful in hydrogen-bonding-mediated rotaxane formation[5] and anion recognition[6] with metallasupramolecules. As a precursor for the metal center, $[RuCl_2(PPh_3)_3]$ (**2**) was chosen for its ability to give a *trans*-Cl_2-*cis*-N_2-*cis*-P_2 coordination environment around the Ru^{II} center by reaction with a chelating phosphine and N-donor ligands.[7]

Stirring equimolar amounts of **1**, **2**, and 1,3-bis(diphenylphosphino)propane (DPPP) in acetone at room temperature yielded the orange solid of $\mathbf{3}_2$ in good yield (87%; Scheme 1).

A single-crystal X-ray structure determination of $\mathbf{3}_2$ unambiguously revealed an interesting supramolecular association between two severely folded molecules of Ru^{II} metallamacrocycle **3** (Figure 1).[8]

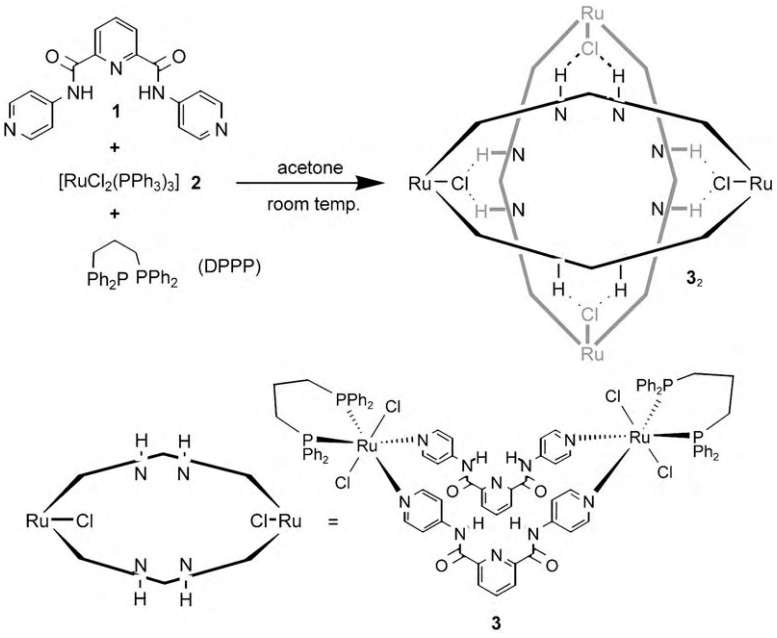
The folded metallacycles **3**, self-complementary monomers of $\mathbf{3}_2$, are oriented orthogonally to each other. This orthogonal assembly seems to be directed by N-H···Cl-Ru hydrogen bonds. Though the eight hydrogen-bonding distances (H···Cl: 2.68–2.72 Å) indicated a rather weak inter-

[*] Prof. Dr. J. Ko
Department of Chemistry
Korea University
Chochiwon, Chugnam 339-700 (Korea)
Fax: (+82) 41-867-5396
E-mail: jko@korea.ac.kr
Dr. Y. J. Park, J.-S. Kim, Dr. K.-T. Youm, N.-K. Lee, Prof. H.-s. Park, Prof. Dr. M.-J. Jun
Department of Chemistry and Center for Bioactive Molecular Hybrids
Yonsei University
Seoul 120-749 (Korea)
Fax: (+82) 2-364-7050
E-mail: hsp@yonsei.ac.kr
mjjun@yonsei.ac.kr

[**] This work was supported by the Korean Science and Engineering Foundation (KOSEF; Grant No. R01-2001-00053). We thank the Center for Bioactive Molecular Hybrids for their support for H.-s.P. and Yong Joo Jun for his help with the ^{31}P NMR spectroscopic measurements.

Supporting information for this article is available on the WWW under http://www.angewandte.org or from the author.

InterScience
© 2006 Wiley-VCH Verlag GmbH & Co. KGaA, Weinheim



Scheme 1. Synthesis of $\mathbf{3}_2$.

action[3a], the difference in Ru–Cl bond lengths found in two crystallographically independent NH···Cl_A-Ru-Cl_B moieties (Ru–Cl_A: 2.4531(11) and 2.4537(12) Å; Ru–Cl_B: 2.4196(12) and 2.4292(13) Å) may be found from these hydrogen-bonding interactions. The resulting hourglass-shaped internal cavity has the volume of 355 $Å^3$ (calculated by PLATON[9]), but no other molecules were found in the cavity of the assembly. On the other hand, the additional stabilizing interactions might be intermolecular π···π and C-H···π contacts between the phenyl groups of DPPP and pyridine rings of **1**. There are approximately 16 short contacts within the sum of their van der Waals radii. The exact extent of the contribution of each noncovalent interaction to the observed structure of $\mathbf{3}_2$ is not clear at the present time. However, the role of the chelating phosphine moieties seems to be important in forming the discrete structure of $\mathbf{3}_2$, because only DPPP gave an informative ^{1}H NMR spectrum out of the chelating phosphines investigated (see the Supporting Information).

Another interesting feature of the solid-state structure of $\mathbf{3}_2$ is the infinite 1D tubular array found in the packing diagram (Figure 2).

Each dimeric $\mathbf{3}_2$ unit is stacked along the crystallographic *b* axis with the next forming four hydrogen-bonding pairs between the carbonyl oxygen atom and the 3,5-protons of the central pyridine groups. It is noteworthy that the hydrogen-bonding interactions are also networked in a self-complementary fashion in this case.

The complex $\mathbf{3}_2$ gave well-resolved but rather unusual ^{1}H NMR spectra in solution (CD_2Cl_2),

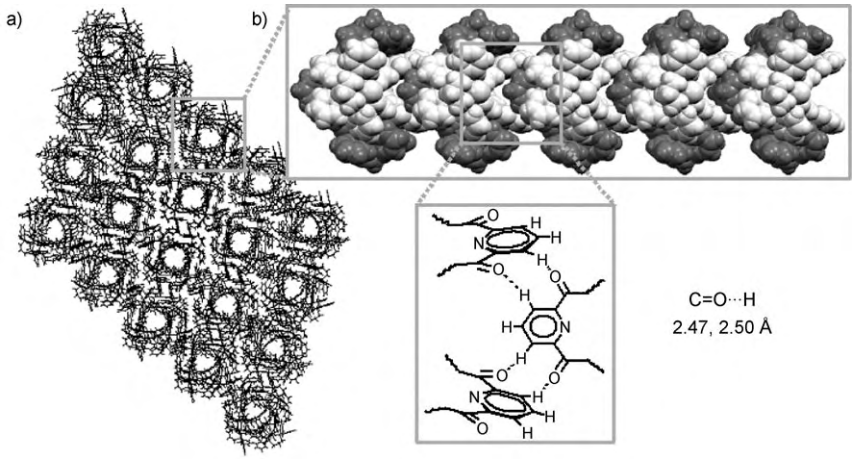


Figure 2. Packing diagram of $\mathbf{3}_2$. a) Perspective view along the *b* axis showing an infinite 1D tubular array. b) Side view of one of the infinite 1D tubes showing intermolecular hydrogen bonding.

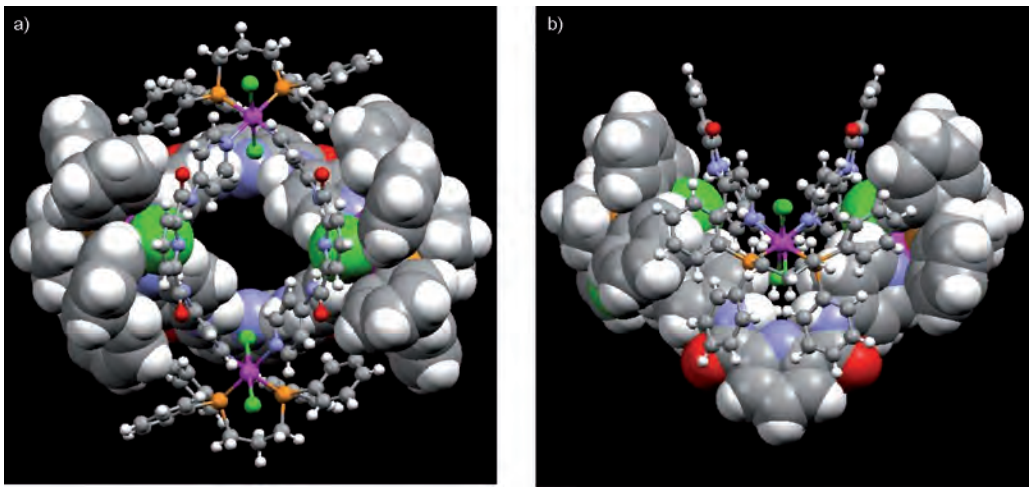


Figure 1. X-ray structure of $\mathbf{3}_2$. a) Top and b) side views. Purple = Ru, green = Cl, orange = P, red = O, blue = N, gray = C, and white = H. One of two metallamacrocycles is presented as a CPK model.

 © 2006 Wiley-VCH Verlag GmbH & Co. KGaA, Weinheim

along with a single, sharp ^{31}P NMR resonance, thus indicating a single symmetric species. For example, NMR signals for the α and β protons of the coordinated pyridine group of **1** were observed in four different fields. The corresponding chemical-shift assignments are depicted in Figure 3a (determined by DQF-COSY, NOESY, and variable-temperature NMR spectroscopic analysis; see the Supporting Information).

The broken local C_2 symmetry of the terminal pyridine groups of **1** suggests that those protons in solution are surrounded by the rigid unsymmetrical environments, as in the solid-state structure of $\mathbf{3}_2$. In addition, NOE interaction studies show that cross-peaks between H_d and the phenyl protons of DPPP might be an intermolecular spatial correlation based on the solid-state structure of $\mathbf{3}_2$ because the intramolecular spatial correlation is too distal to be observed (Figure 4).

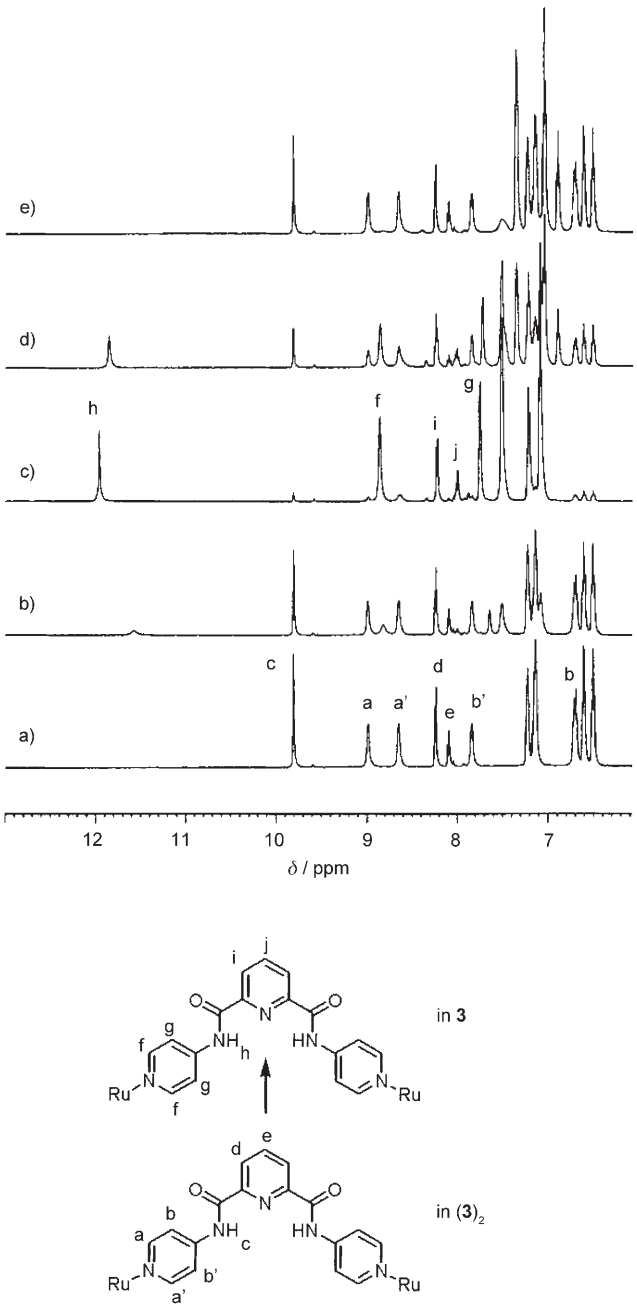


Figure 3. Partial ^1H NMR spectra (CD_2Cl_2) showing reversible dissociation and association of $\mathbf{3}_2$ upon addition of TEACl followed by $NaBPh_4$. a) $\mathbf{3}_2$ alone, b) 1 equiv of TEACl, c) 6 equiv of TEACl, d) 1 equiv of $NaBPh_4$, and e) excess $NaBPh_4$.

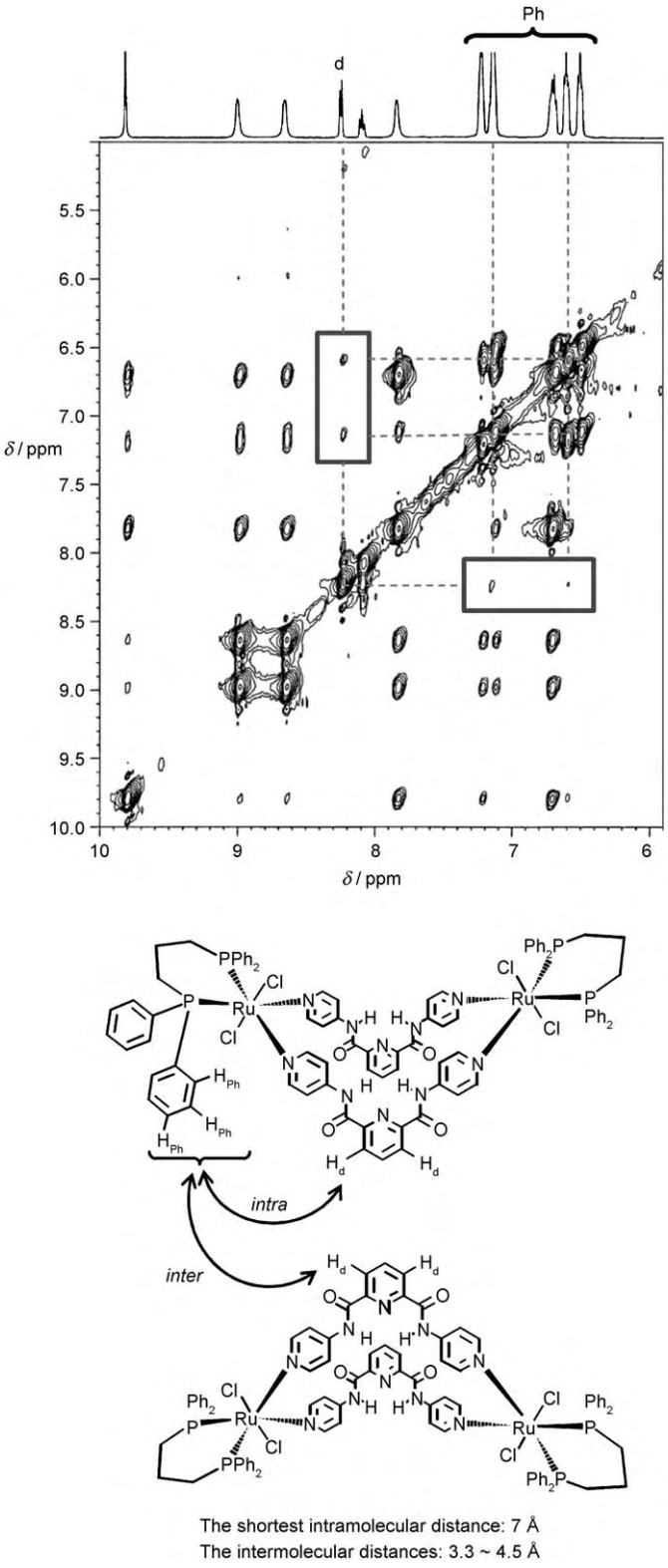


Figure 4. Partial NOESY spectrum of $\mathbf{3}_2$, and the intermolecular spatial correlation between H_d and phenyl protons (gray box).

 © 2006 Wiley-VCH Verlag GmbH & Co. KGaA, Weinheim

More definite evidence of the self-complementary assembly of $\mathbf{3}_2$ in solution was obtained by the following ^{1}H NMR experiments: Upon addition of chloride anions, as the tetraethylammonium (TEA) salt, new peaks started to grow accompanied by a diminishment of the original peaks of $\mathbf{3}_2$, and the local C_2 symmetry of the terminal pyridine groups of **1** was re-established when six equivalents of TEACl were added (Figure 3b,c). In addition, these ^{1}H NMR spectral changes are quite different from those observed by the variable-temperature ^{1}H NMR experiments (see the Supporting Information), especially in the aromatic region.

When the homogeneous mixture of $\mathbf{3}_2$ and eight equivalents of TEACl in CH_2Cl_2 stood for several days in a closed vial, the orange crystals could be obtained in good yield. Fortunately, this new species could be characterized by single-crystal X-ray structure determination and was the dissociation product of $\mathbf{3}_2$, the flattened monomer **3** with bound two chloride ions (Figure 5).[10] It is noteworthy that all Ru–Cl bond lengths are now almost identical (2.4054(17)–2.4070(15) Å) to those of $\mathbf{3}_2$.

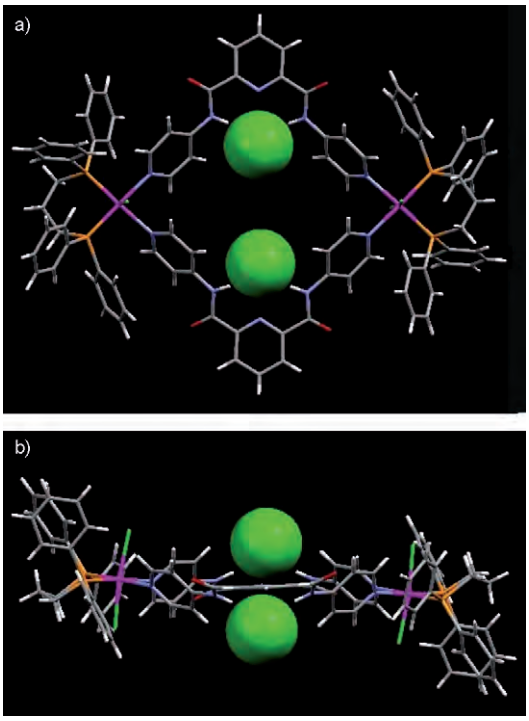


Figure 5. X-ray structure of **3**·2 TEACl·H_2O·2 CH_2Cl_2. a) Top and b) side views. Purple = Ru, green = Cl, orange = P, red = O, blue = N, gray = C, and white = H. Two chloride anions are presented as a CPK model. Solvents, water molecules, and TEA cations are omitted for clarity.

Although a direct correlation between the solid structure of **3**·2 TEACl·H_2O·2 CH_2Cl_2 and the major species observed in the mixture of $\mathbf{3}_2$ and eight equivalents of TEACl by ^{1}H and ^{31}P NMR spectroscopy (see the Supporting Information) should be done carefully,[11] their relationship could be considered from two points of view: First, both species observed by X-ray crystallography and NMR spectroscopy are each major products in the solid and solution states. Second, the ^{1}H NMR spectra of $\mathbf{3}_2$ obtained by gradually addition of increased amounts of TEACl could be restored to the original spectra of $\mathbf{3}_2$ by addition of $NaBPh_4$ (thereby causing elimination of NaCl) and successive simple shakings of the NMR tube at room temperature (Figure 3). In other words, it seems to be that the self-assembled structure of $\mathbf{3}_2$ can be halved by the chloride anions in solution into the disassembled state, such as the structure of **3**·2 TEACl·H_2O·2 CH_2Cl_2, and reassembled into the original structure of $\mathbf{3}_2$ by eliminating the chloride anions. Such a reversible dissociation/association of self-assembled molecules by chemical stimuli is a potentially useful property in supramolecular chemistry.[12]

To assess the relative response of $\mathbf{3}_2$ toward other anions, preliminary ^{1}H NMR experiments were carried out by adding five equivalents of other kinds of TEA salts, and the intensity ratio of amide protons (H_h and H_c in Figure 3) was compared with that of the chloride. Complex $\mathbf{3}_2$ showed a rather weak response to bromide and a very weak one to iodide, and there was no interaction at all with NO_3^-, ClO_4^-, BF_4^-, and PF_6^-. The relative strengths to dissociate $\mathbf{3}_2$ into **3** were approximately 2 (Br^-) and 200 (I^-) times weaker than that of Cl^-.[13]

In summary, we have shown a novel self-assembled dimer of Ru^{II} metallamacrocycles with noncovalent interactions, including hydrogen bonding between the Ru–Cl and N–H bonds, and its reversible dissociation/association process, which can be selectively controlled by anions in solution. More detailed studies on the solution behavior of $\mathbf{3}_2$ and its application in supramolecular chemistry are underway.

Experimental Section

Compound $\mathbf{3}_2$: Equimolar amount of ligand **1** (0.16 g, 0.5 mmol), $[RuCl_2(PPh_3)_3]$ (**2**; 0.48 g), and DPPP (0.21 g) were suspended in acetone (200 mL) and stirred at room temperature. The initial brown turbid solution gradually turned to a clear orange. After 6 h, the solution was evaporated to dryness, and the residue was dissolved in CH_2Cl_2 (20 mL) and filtered to remove any insoluble materials. *n*-Hexane (100 mL) was added to the filtrate. The resulting yellow precipitate was collected on the sintered glass, washed with methanol and *n*-hexane, and dried in vacuo to yield $\mathbf{3}_2$ as a yellow–orange solid (0.39 g, yield = 87%). ^{1}H NMR (CD_2Cl_2, 500 MHz): δ = 9.8 (s, 2H, NH), 9.0(s, 2H, PyH_α), 8.6 (s, 2H, PyH_α), 8.2 (d, 2H, $PyH_{3,5}$, J = 7.8 Hz), 8.0 (t, 1H, PyH_4, J = 7.8 Hz), 7.8 (s, 2H, $PyH_{\beta'}$), 7.2–7.1 (m, 12H, PPh), 6.7–6.4 (m, 8H + 2H, PPh + PyH_β), 3.1 (br t, 2H, PCH), 2.2 (m, 1H, PCH_2CH), 2.0 (br s, 2H, PCH), 1.5 ppm (br s, 1H, PCH_2CH); ^{13}C NMR (CD_2Cl_2, 125 MHz): δ = 163.0, 154.1, 151.9, 148.8, 144.7, 138.9, 137.6, 136.0, 134.5, 132.5, 128.9, 128.7, 127.2, 127.0, 126.6, 114.0, 27.8, 20.1 ppm; ^{31}P NMR (CD_2Cl_2, 202 MHz): δ = 38.2(s) ppm; IR (KBr): $\tilde{\nu}$ = 3055, 1700, 1580, 1511, 1421, 1336, 1210, 1125, 1092, 973, 836, 743, 696, 650, 514 cm^{-1}; elemental analysis (%) calcd for $C_{176}H_{156}Cl_8N_{20}O_8P_8Ru_4$: C 58.48, H 4.35, N 7.75; found: C 58.43, H 4.57, N 7.55. Single crystals of X-ray quality were grown by slow diffusion of *n*-hexane into the solution of $\mathbf{3}_2$ in CH_2Cl_2.

Compound **3**·2 TEACl·H_2O·2 CH_2Cl_2: IR (KBr): $\tilde{\nu}$ = 3462, 2956, 2919, 2356, 1695, 1593, 1516, 1419, 1342, 1219, 1135, 1004, 840, 748, 697, 533 cm^{-1}; elemental analysis (%) calcd for

 © 2006 Wiley-VCH Verlag GmbH & Co. KGaA, Weinheim

$C_{104}H_{118}Cl_6N_{12}O_4P_4Ru_2$: C 58.40, H 5.56, N 7.86; found (after vacuum drying): C 58.37, H 5.62, N 7.91.

Received: January 14, 2006
Revised: April 14, 2006
Published online: May 30, 2006

Keywords: coordination modes · hydrogen bonds · metal halides · metallamacrocycles · self-assembly

[1] For recent reviews: a) M. Ruben, J. Rojo, F. J. Romero-Salguero, L. H. Uppadine, J.-M. Lehn, *Angew. Chem.* **2004**, *116*, 3728; *Angew. Chem. Int. Ed.* **2004**, *43*, 3644; b) S. R. Seidel, P. J. Stang, *Acc. Chem. Res.* **2002**, *35*, 972; c) G. F. Swiegers, T. J. Malefetse, *Coord. Chem. Rev.* **2002**, *225*, 91; d) B. J. Holliday, C. A. Mirkin, *Angew. Chem.* **2001**, *113*, 2076; *Angew. Chem. Int. Ed.* **2001**, *40*, 2022; e) F. A. Cotton, C. Lin, C. A. Murillo, *Acc. Chem. Res.* **2001**, *34*, 759; f) M. Fujita, K. Umemoto, M. Yoshizawa, N. Fujita, T. Kusukawa, K. Biradha, *Chem. Commun.* **2001**, 509; g) S. Leininger, B. Olenyuk, P. J. Stang, *Chem. Rev.* **2000**, *100*, 853; h) D. L. Caulder, K. N. Raymond, *J. Chem. Soc. Dalton Trans.* **1999**, 1185; i) D. L. Caulder, K. N. Raymond, *Acc. Chem. Res.* **1999**, *32*, 975; j) P. N. W. Baxter, J.-M. Lehn, G. Baum, D. Fenske, *Chem. Eur. J.* **1999**, *5*, 102; k) M. Fujita, *Chem. Soc. Rev.* **1998**, *27*, 417.

[2] For some recent examples: a) H.-J. van Manen, V. Paraschiv, J. J. García-López, H. Schönherr, S. Zapotoczny, G. J. Vancso, M. Crego-Calama, D. N. Reinhoudt, *Nano Lett.* **2004**, *4*, 441; b) R. García-Zarracino, H. Höpfl, *Angew. Chem.* **2004**, *116*, 1533; *Angew. Chem. Int. Ed.* **2004**, *43*, 1507; c) A. Md. Alam, M. Nethaji, M. Ray, *Angew. Chem.* **2003**, *115*, 1984; *Angew. Chem. Int. Ed.* **2003**, *42*, 1940; d) A. J. Goshe, I. M. Steele, B. Bosnich, *J. Am. Chem. Soc.* **2003**, *125*, 444; e) L. J. Childs, N. W. Alcock, M. J. Hannon, *Angew. Chem.* **2002**, *114*, 4418; *Angew. Chem. Int. Ed.* **2002**, *41*, 4244; f) K. M. Kim, J. S. Park, Y.-S. Kim, Y. J. Jun, T. Y. Kang, Y. S. Sohn, M.-J. Jun, *Angew. Chem.* **2001**, *113*, 2524; *Angew. Chem. Int. Ed.* **2001**, *40*, 2458; g) S.-Y. Yu, T. Kusukawa, K. Biradha, M. Fujita, *J. Am. Chem. Soc.* **2000**, *122*, 2665; h) L. J. Childs, N. W. Alcock, M. J. Hannon, *Angew. Chem.* **2001**, *113*, 1113; *Angew. Chem. Int. Ed.* **2001**, *40*, 1079.

[3] a) T. Steiner, *Angew. Chem.* **2002**, *114*, 50; *Angew. Chem. Int. Ed.* **2002**, *41*, 48; b) G. Aullón, D. Bellamy, L. Brammer, E. A. Bruton, A. G. Orpen, *Chem. Commun.* **1998**, 653; c) G. P. A. Yap, A. L. Rheingold, P. Das, R. H. Crabtree, *Inorg. Chem.* **1995**, *34*, 3474; d) A. Angeloni, P. C. Crawford, A. G. Orpen, T. J. Podesta, B. J. Shore, *Chem. Eur. J.* **2004**, *10*, 3783; e) L. Brammer, *Chem. Soc. Rev.* **2004**, *33*, 476.

[4] a) Z. Qin, M. C. Jennings, R. J. Puddephatt, *Inorg. Chem.* **2003**, *42*, 1956; b) Z. Qin, M. C. Jennings, R. J. Puddephatt, *Inorg. Chem.* **2002**, *41*, 3967; c) Z. Qin, M. C. Jennings, R. J. Puddephatt, *Chem. Commun.* **2001**, 2676.

[5] a) K.-S. Jeong, Y. L. Cho, S.-U. Chang, T.-Y. Park, J. U. Song, *J. Org. Chem.* **1999**, *64*, 9459; b) K.-S. Jeong, Y. L. Cho, J. U. Song, H.-Y. Chang, M.-G. Choi, *J. Am. Chem. Soc.* **1998**, *120*, 10982; c) K.-S. Jeong, Y. L. Choi, S.-U. Chang, H.-Y. Chang, *Angew. Chem.* **2000**, *112*, 1758; *Angew. Chem. Int. Ed.* **2000**, *39*, 1692; d) S.-Y. Chang, H.-Y. Jang, K.-S. Jeong, *Chem. Eur. J.* **2003**, *9*, 1535.

[6] a) S.-S. Sun, A. J. Lees, *Chem. Commun.* **2000**, 1687; b) P. D. Beer, F. Szemes, V. Balzani, C. M. Sala, M. G. B. Drew, S. W. Dent, M. Maestri, *J. Am. Chem. Soc.* **1997**, *119*, 11864.

[7] F. H. Jardine, *Prog. Inorg. Chem.* **1984**, *31*, 265.

[8] Crystal data for $\mathbf{3}_2$: $C_{88}H_{78}Cl_4N_{10}O_4P_4Ru_2$, $M_r = 1807.42$, monoclinic, space group $C2/c$, $a = 39.6773(5)$, $b = 15.1882(3)$, $c = 37.4826(6)$ Å, $\beta = 115.3320(15)°$, $V = 20416.0(6)$ Å^3, $Z = 8$, $T = 150(1)$ K. Refinement of 1009 parameters on 23033 independent reflections out of 61496 measured reflections ($R_{int} = 0.0731$) led to $R_1 = 0.0683$ ($I > 2\sigma(I)$), $wR_2 = 0.1793$, and GOF = 1.006. CCDC-277154 contains the supplementary crystallographic data for this paper. These data can be obtained free of charge from The Cambridge Crystallographic Data Centre via www.ccdc.cam.ac.uk/data_request/cif.

[9] A. L. Spek, *PLATON, A Multipurpose Crystallographic Tool*, Utrecht University, Utrecht (Netherlands), **2003**.

[10] Crystal data for **3**: $C_{107}H_{126}Cl_{12}N_{12}O_6P_4Ru_2$, $M_r = 2427.62$, triclinic, space group $P\bar{1}$, $a = 10.8060(3)$, $b = 14.8440(5)$, $c = 19.6340(5)$ Å, $\alpha = 75.8720(13)$, $\beta = 74.5810(16)$, $\gamma = 88.5470(14)°$, $V = 2941.56(15)$ Å^3, $Z = 1$, $T = 150(2)$ K. Refinement of 686 parameters with 73 restrains on 13462 independent reflections out of 35562 measured reflections ($R_{int} = 0.0945$) led to $R_1 = 0.0904$ ($I > 2\sigma(I)$), $wR_2 = 0.2535$, and GOF = 1.060. CCDC-277155 contains the supplementary crystallographic data for this paper. These data can be obtained free of charge from The Cambridge Crystallographic Data Centre via www.ccdc.cam.ac.uk/data_request/cif.

[11] The single crystals were obtained from the homogeneous solution of $\mathbf{3}_2$ and 8 equivalents of TEACl in CH_2Cl_2 after 4–5 days in 80–90% yields without any cosolvent. However, after spontaneous crystallization in CH_2Cl_2, the crystals of $\mathbf{3}\cdot 2\,TEACl\cdot H_2O\cdot 2\,CH_2Cl_2$ were almost insoluble in common organic solvents, including MeOH. The solubility problem made it impossible to obtain clear NMR spectra of $\mathbf{3}\cdot 2\,TEACl\cdot H_2O\cdot 2\,CH_2Cl_2$ as a pure form. Similar difficulties were encountered during the ^{13}C NMR measurement of $\mathbf{3}_2$ in the presence of 8 equivalents of TEACl because the long data-acquisition period and the limited volume of NMR solvent caused crystal formation of the $\mathbf{3}\cdot 2\,TEACl$ species.

[12] J.-M. Lehn, *Supramolecular Chemistry, Concepts, and Perspectives*, VCH, Weinheim, **1995**.

[13] An organic dianion with an appropriate geometry, such as the terephthalate, can also change the ^1H NMR spectral features of $\mathbf{3}_2$. A full study on the relation between the shape of the dianions and the mode of interactions will be reported elsewhere. We greatly appreciate one of the referees for his/her kind suggestions about these experimental ideas. In the case of fluoride anions, irreversible decomposition of $\mathbf{3}_2$ into an intractable product was observed.

 © 2006 Wiley-VCH Verlag GmbH & Co. KGaA, Weinheim

Mesoporous Materials

DOI: 10.1002/anie.200504114

Synthesis and Characterization of Mesoporous Silica AMS-10 with Bicontinuous Cubic *Pn*$\bar{3}$*m* Symmetry**

*Chuanbo Gao, Yasuhiro Sakamoto,**
*Kazutami Sakamoto, Osamu Terasaki, and Shunai Che**

It is well known that various mesoporous materials can be synthesized based on the self-assembly of surfactant and inorganic precursors. Mesoporous materials have attracted a great deal of attention because of their controllable structures and compositions, which make them suitable for wide applications in catalysis, environmental clean-up, and in the design of advanced materials. Since the first reports of mesoporous materials (FSM-16[1] and M41S family[2]) by Yanagisawa et al. and Mobil Research, respectively, a variety of other phases have been reported. Until now, many well-ordered mesoporous materials have been successfully synthesized and it has been claimed that these have different mesostructures such as orthorhombic (*Pmmm*[3] etc.), tetragonal ($P4_2/mnm$,[4] $P4/mmm$[3]), three-dimensional (3D) hexagonal ($P6_3/mmc$[5]), micellar cubic ($Pm\bar{3}n$,[6,7] $Fd\bar{3}m$,[8,9] $Im\bar{3}m$,[7,10] $Fm\bar{3}m$,[11] $Pm\bar{3}m$,[10] etc.), bicontinuous cubic ($Ia\bar{3}d$,[2,12] $Im\bar{3}m$[13] and $Pn\bar{3}m$[14]), rectangular ($c2mm$[15]), two-dimensional (2D) hexagonal ($p6mm$[2,16]), and lamellar phase.[2] Most structures have been proposed on the basis of a combination of powder X-ray diffraction (XRD) studies and an accumulated knowledge of liquid-crystalline phases, whilst only a few have been precisely determined by electron crystallography. Elaborate synthesis under well-controlled conditions and careful structural studies are required to form mesoporous crystals with the $Pn\bar{3}m$ space group.

Recently, we reported the preparation of ordered mesoporous structures using anionic surfactants and co-structure-directing agents (CSDAs).[17] The introduction of CSDAs into the reaction system makes it feasible to produce electrostatic interactions between anionic surfactants and inorganic species and to control the packing parameter. These are key factors in the formation of highly ordered mesophases and to select a certain structure. Various mesophases, including lamellar, 2D hexagonal $p6mm$, tetragonal $P4_2/mnm$, 3D hexagonal $P6_3/mmc$, cubic $Pm\bar{3}n$, cubic $Fd\bar{3}m$, cubic $Ia\bar{3}d$, modulated structure, and a chiral mesostructure with helical arrangement of the pores, were successfully prepared based on this synthesis route,[4,9,17–19] though some of them have not been observed even in liquid-crystal systems.

Herein, we report a new mesoporous structure, AMS-10 (anionic surfactant templated mesoporous silica 10), which exhibits bicontinuous double diamond cubic $Pn\bar{3}m$ symmetry, prepared with anionic surfactant *N*-myristoyl-L-glutamic acid (C_{14}GluA) as template and *N*-trimethoxylsilylpropyl-*N*,*N*,*N*-trimethylammonium chloride (TMAPS) as CSDA. The packing of the micelle was controlled by simply adjusting the neutralization degree of the C_{14}GluA surfactant.

Different mesophases ranging from tetragonal $P4_2/mnm$ (cage type, AMS-9), cubic $Fd\bar{3}m$ (cage type, AMS-8), to 2D hexagonal $p6mm$ (cylindrical, AMS-3), and an unknown mesophase (denoted as AMS-10) were obtained by decreasing the amount of NaOH that was added into the reaction system (Figure 1). The neutralization degree of the surfactant increased with the amount of NaOH that was added into the system. The first three types of mesostructure were characterized by high-resolution transmission electron microscopy (HRTEM; see Supporting Information). They gave many reflections with similar magnitude of scattering vectors, and these reflections could only be resolved by a single-crystal experiment. Their electron diffractions were separately observed as a single-crystal experiment and are consistent with their XRD patterns. It is inferred that AMS-10 may exhibit a lower curvature close to bicontinuous cubic $Ia\bar{3}d$ from the sequence of the mesophases.

The XRD pattern of AMS-10 shows two intense and well-resolved peaks in the range $1° < 2\theta < 2°$ with a d spacing ratio of about $\sqrt{3}/\sqrt{2}$, which is quite rare in the mesoporous silica reported earlier. We can index the two peaks by any crystal systems. If it is assumed as cubic, the two peaks can be indexed to 110 and 111 reflections, or to 200 and 211 reflections, and so on. From a set of electron diffraction patterns or HRTEM images, we can conclude that the crystal belongs to the cubic system. The HRTEM images taken with the [100], [110], and [111] incidences are shown in Figure 2. The Fourier transform diffractogram of the image of [100] incidence shows the reflection conditions $0kl$: $k + l = 2n$ and $00l$: $l = 2n$, and that of the [110] incidence shows the conditions hkl: none and hhl: none. From these results, two space groups are possible, $Pn\bar{3}$ (201) or $Pn\bar{3}m$ (224). The space group $Pn\bar{3}m$ was chosen because of its high symmetry. Thus, the first two peaks of the XRD pattern can be concluded to be 110 and 111 reflections based on a cubic

[*] Dr. Y. Sakamoto, Prof. O. Terasaki
Structural Chemistry
Arrhenius Laboratory
Stockholm University
10691 Stockholm (Sweden)
Fax: (+46) 816-3118
E-mail: yasuhiro@struc.su.se
C. Gao, Prof. S. Che
School of Chemistry and Chemical Technology
State Key Laboratory of Composite Materials
Shanghai Jiao Tong University
800 Dongchuan Road, Shanghai 200240 (P.R. China)
Fax: (+86) 21-5474-1297
E-mail: chesa@sjtu.edu.cn
Dr. K. Sakamoto
Research Center, Shiseido Co., LTD
2-2-1, Hayabuchi, Tsuzuki-ku, Yokohama 224-8558 (Japan)

[**] This work was supported by the National Natural Science Foundation of China (grant no. 20425102 and 20521140450), the China Ministry of Education, and the Shanghai Science Foundation (0452nm061 and 05XD14010). O.T. thanks the Swedish Science Research Council (VR) and Japan Science and Technology Agency (JST) for financial support.

Supporting information for this article is available on the WWW under http://www.angewandte.org or from the author.

 © 2006 Wiley-VCH Verlag GmbH & Co. KGaA, Weinheim

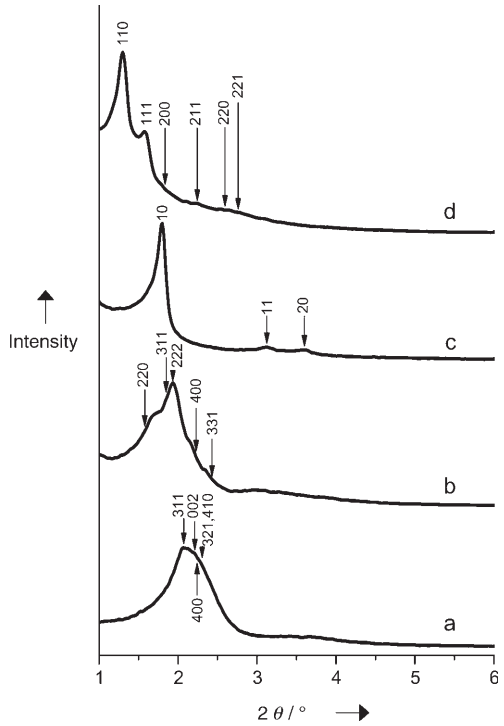


Figure 1. XRD patterns of calcined mesoporous silica prepared with C_{14}GluA as surfactant and TMAPS as CSDA and by precisely adjusting the acidity of the reaction system. The compositions of the gels are C_{14}GluA/TMAPS/TEOS/H_2O/NaOH = 1:1.5:15:1983:*x*; a) *x* = 2 ($P4_2/mnm$), b) *x* = 1.5 ($Fd\bar{3}m$), c) *x* = 1 ($p6mm$), and d) *x* = 0.75 ($Pn\bar{3}m$; AMS-10).

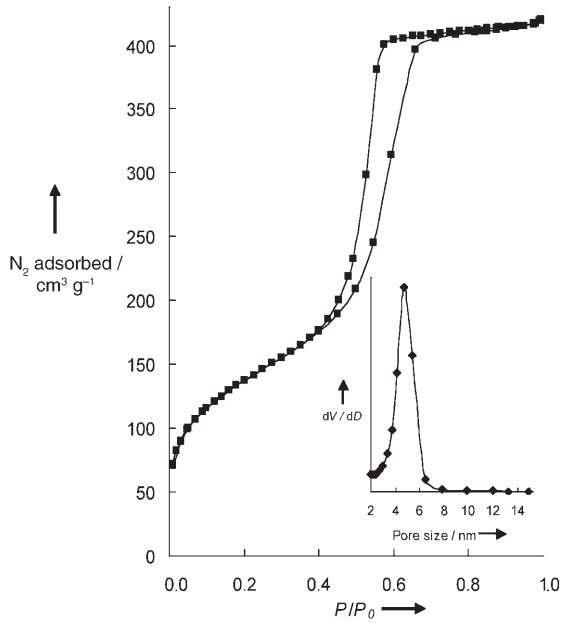


Figure 3. Nitrogen adsorption isotherm and pore size distribution (calculated by the BJH method based on the adsorption branch) of the calcined mesoporous silica AMS-10.

$Pn\bar{3}m$ space group, and it can be calculated from the 110 peak that the unit cell of AMS-10 is 9.6 nm. Also, the mesophase is highly ordered as can be derived from the large uniform areas of the HRTEM images.

Nitrogen adsorption and desorption isotherms of AMS-10 (Figure 3) show a typical type IV isotherm with an evident hysteresis loop in the range $0.45 < P/P_0 < 0.7$. The specific surface area and pore volume of the material are 493 $m^2 g^{-1}$ and 0.65 $cm^3 g^{-1}$, respectively. The pore diameter is about 4.7 nm calculated by the BJH method based on the adsorption branch of the isotherm, which is larger than that of common mesophases prepared with anionic surfactants.

A 3D reconstruction of the structure was conducted on the basis of the analysis of Fourier diffractograms taken from TEM images along high-symmetry zone axes of AMS-10. Table 1 shows crystal structure factors, both amplitude and phase, extracted from thin parts of crystals along three different zone axes, namely the [100], [110], and [111] directions. The origin of the symmetry was taken at the inversion center of $Pn\bar{3}m$ (origin choice 2); that is, the phase should be 0 or π. The electrostatic potential density map of AMS-10 was obtained by taking inverse Fourier summation of these crystal structure factors (not shown here). With a silica density of about 2.2 $g cm^{-3}$ and a pore volume of 0.65 $cm^3 g^{-1}$ from nitrogen adsorption data, the 3D pore structure of AMS-10 was determined (Figure 4a). The pore volume fraction therein corresponds to 58.8%. It can be calculated that AMS-10 has a pore diameter of 4.6 nm and wall thickness of 2.2 nm, values that are consistent with those calculated from nitrogen adsorption measurements. As can be

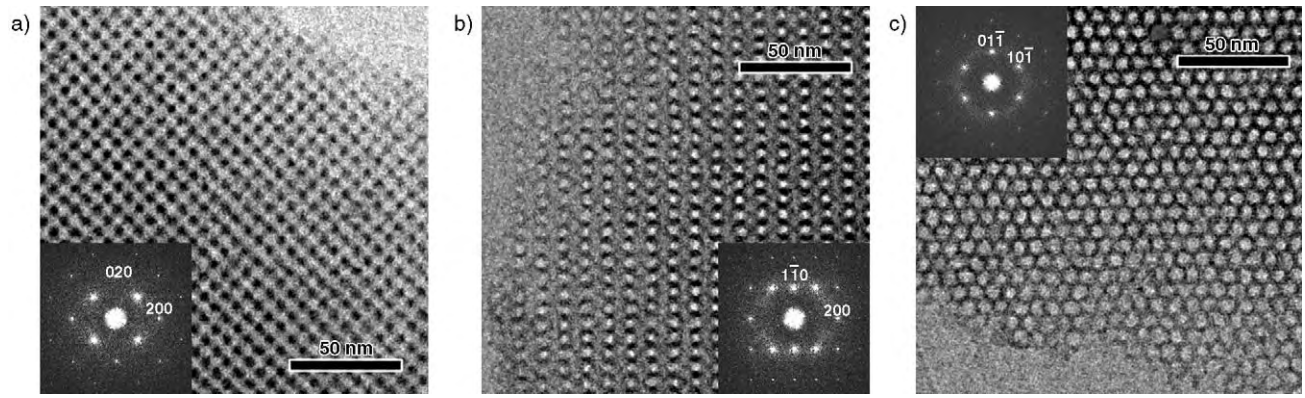


Figure 2. HRTEM images and Fourier diffractograms of the calcined mesoporous silica AMS-10. The images were taken along the zone axes as follows: a) [100], b) [110], and c) [111].

 © 2006 Wiley-VCH Verlag GmbH & Co. KGaA, Weinheim

Table 1: Crystal structure factors (amplitudes and phases) extracted from HRTEM images of calcined AMS-10 ($a = 9.6$ nm).

h	k	l	$h^2+k^2+l^2$	d [nm]	Amplitude	Phase
1	1	0	2	6.80	100.00	π
1	1	1	3	5.55	57.09	0
2	0	0	4	4.81	13.13	0
2	1	1	6	3.92	3.40	π
2	2	0	8	3.40	0.79	π
2	2	1	9	3.20	0.57	0
3	1	0	10	3.04	0.42	π
3	1	1	11	2.90	0.06	0
2	2	2	12	2.77	0.20	π
3	2	1	14	2.57	0.13	0
4	0	0	16	2.40	0.10	0
3	2	2	17	2.33	0.10	π
3	3	0	18	2.27	0.07	0
4	2	0	20	2.15	0.01	π
4	3	3	34	1.65	0.05	0
4	4	2	36	1.60	0.02	0
7	1	0	50	1.36	0.01	0
6	3	3	51	1.35	0.01	0

seen from Figure 4a, b, the silica wall of the AMS-10 follows a typical diamond minimal surface (D surface) in analogy to the gyroid minimal surface (G surface) as observed for the silica wall of MCM-48.[12] From this result, we conclude that AMS-10 has a bicontinuous structure composed of an enantiomeric pair of 3D mesoporous networks that are interwoven as shown in Figure 4c. Each network, which is divided by a D surface, consists of tetrahedral connection of pores at the $\bar{4}3m$ position, 2*a* site (Wyckoff notation), although in the case of a bicontinuous cubic $Ia\bar{3}d$ structure each network that is divided by a G-surface consists of three connected pores at the 32 position, 16*b* site (Wyckoff notation).

The surfactants C_nGluA ($n = 12$–18) with different chain lengths also gave rise to the ordered bicontinuous cubic $Pn\bar{3}m$ mesostructure in combination with either TMAPS or 3-aminopropyltrimethoxylsilane (APS). The neutralization degree of the surfactant is crucial to form the specific mesophase in both synthesis systems. The effect of the neutralization degree on the formation of mesostructures can be explained in terms of the surface charge density (σ) of the surfactant micelles, which increases with the amount of NaOH added into the carboxylic acid surfactant solution. It is useful to introduce the surfactant packing parameter, $g = v/a\,l$, where v is the chain volume, a is the effective hydrophobic/hydrophilic interfacial area, and l is the chain length.[20] The lower charge density contributes to a partial decrease in the electrostatic repulsion between the charged surfactant head groups and a decrease in the effective head group area of surfactant, a, therefore resulting in an increase in the g value. It is well-known that the g parameter of lyotropic liquid-crystal phases increases in the order: micellar tetragonal $P4_2/mnm$, micellar cubic $Fd\bar{3}m <$ cylindrical 2D hexagonal $p6mm <$ bicontinuous cubic $Pn\bar{3}m$.[21] Thus, it is reasonable that a lower charge density of the micelle surface facilitates the formation of the cubic $Pn\bar{3}m$ mesophase with a larger g parameter.

In summary, mesoporous silica AMS-10 with a novel bicontinuous cubic mesophase $Pn\bar{3}m$ was synthesized by using an anionic surfactant as template. Detailed characterizations were performed through XRD, HRTEM, and nitrogen adsorption studies, and a 3D structure was derived from these results and those obtained through electron crystallography. Precise control of the neutralization degree of the anionic surfactant is key to the synthesis of AMS-10 and also proves a feasible and simple means to achieve mesophase control of anionic surfactant templated mesoporous silica (AMS). Because of its characteristic mesoporous structure, this bicontinuous cubic mesoporous material could be useful, for example, as biocompatible materials for the encapsulation, controlled release, and delivery of drugs and biomolecules.

Experimental Section

TMAPS (Azmax) and tetraethyl orthosilicate (TEOS; TCI) were purchased and used as received. The synthetic method of glutamic acid derived surfactant C_{14}GluA is described in the Supporting Information.

In a typical synthesis of AMS-10, NaOH (7.5 g of 0.1 mol L^{-1} solution) was added to a solution of C_{14}GluA (0.357 g, 1 mmol) in deionized water (28.2 g) stirring at 60 °C. After the solution became homogeneous a mixture of TMAPS (0.773 g; 50% in methanol,

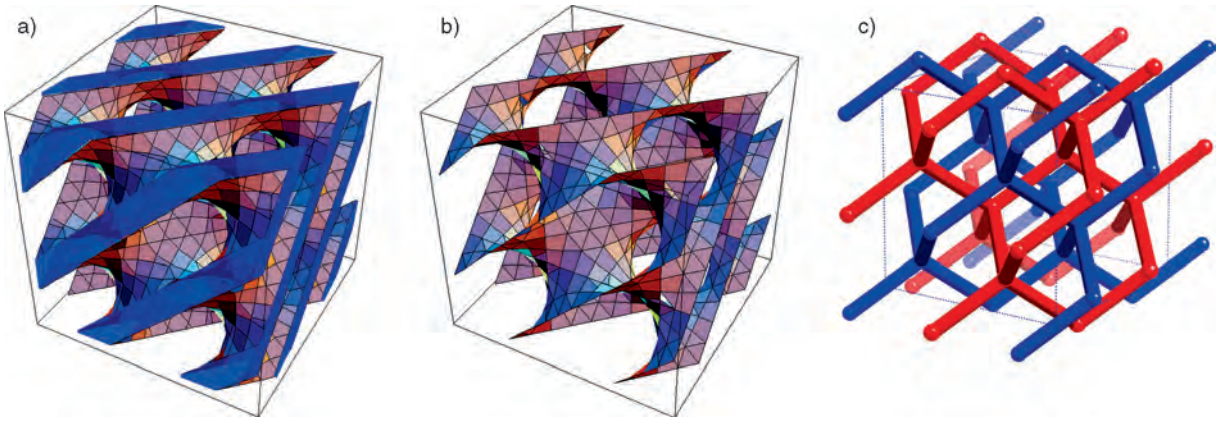


Figure 4. 3D structure of a) the bicontinuous cubic $Pn\bar{3}m$ mesoporous silica AMS-10 (as derived from electron crystallography), b) the D surface, and c) the 3D networks of double diamond structure divided by the D surface. They show a 2×2×2 unit cell.

 © 2006 Wiley-VCH Verlag GmbH & Co. KGaA, Weinheim

1.5 mmol) and TEOS (3.12 g, 15 mmol) was added, and the mixture was stirred at 60 °C for 10 min. The molar composition of the final gel was C_{14}GluA/TMAPS/TEOS/H_2O/NaOH = 1:1.5:15:1983:0.75. The reaction system was then kept static for 2 days at 60 °C to allow the product to hydrolyze, condense, and age. To remove the surfactant, the as-synthesized mesoporous silica was calcined at 550 °C for 6 h or extracted using a mixture of HCl (37 wt %) and ethanol (90 % w/w) for 12 h.

XRD patterns were recorded on a Rigaku X-ray diffractometer D/MAX-2200/PC with $Cu_{K\alpha}$ radiation (40 kV, 20 mA) at a rate of 1.0 deg min^{-1} over the range of $1° < 2\theta < 6°$. HRTEM was performed with a JEOL JEM-3010 microscope operating at 300 kV (Cs = 0.6 mm, point resolution 1.7 Å). Images were recorded with a CCD camera (MultiScan model 794, Gatan, 1024 × 1024 pixels, pixel size 24 × 24 μm^2) at 50000–80000 magnification under low-dose conditions. The adsorption/desorption isotherms were measured with an ASAP2100 using N_2 as adsorbate at 77 K. The specific surface area was calculated by the BET method, and the pore size was obtained from the maxima of the pore size distribution curve calculated by the BJH method by using the adsorption branch of the isotherm.

Received: November 18, 2005
Revised: February 11, 2006
Published online: May 26, 2006

Keywords: electron diffraction · electron microscopy · mesoporous materials · surfactants · template synthesis

[1] T. Yanagisawa, T. Shimizu, K. Kuroda, C. Kato, *Bull. Chem. Soc. Jpn.* **1990**, *63*, 988–992.
[2] J. S. Beck, J. C. Vartuli, W. J. Roth, M. E. Leonowicz, C. T. Kresge, K. D. Schmitt, C. T.-W. Chu, D. H. Olson, E. W. Sheppard, S. B. McCullen, J. B. Higgins, J. L. Schlenkert, *J. Am. Chem. Soc.* **1992**, *114*, 10834–10843.
[3] S. Shen, A. E. Garcia-Bennett, Z. Liu, Q. Lu, Y. Shi, Y. Yan, C. Yu, W. Liu, Y. Cai, O. Terasaki, D. Zhao, *J. Am. Chem. Soc.* **2005**, *127*, 6780–6787.
[4] A. E. Garcia-Bennett, N. Kupferschmidt, Y. Sakamoto, S. Che, O. Terasaki, *Angew. Chem.* **2005**, *117*, 5451–5456; *Angew. Chem. Int. Ed.* **2005**, *44*, 5317–5322.
[5] Q. Huo, R. Leon, P. M. Petroff, G. D. Stucky, *Science* **1995**, *268*, 1324–1327.
[6] Q. Huo, D. I. Margolese, U. Ciesla, P. Feng, T. E. Gier, P. Sieger, R. Leon, G. D. Stucky, *Nature* **1994**, *368*, 317–321.
[7] Y. Sakamoto, M. Kaneda, O. Terasaki, D. Zhao, J. M. Kim, G. D. Stucky, H. J. Shin, R. Ryoo, *Nature* **2000**, *408*, 449–453.
[8] S. Shen, Y. Li, Z. Zhang, J. Fan, B. Tu, W. Zhou, D. Zhao, *Chem. Commun.* **2002**, 2212–2213.
[9] A. E. Garcia-Bennett, K. Miyasaka, O. Terasaki, S. Che, *Chem. Mater.* **2004**, *16*, 3597–3605.
[10] D. Zhao, Q. Huo, J. Feng, B. F. Chmelka, G. D. Stucky, *J. Am. Chem. Soc.* **1998**, *120*, 6024–6036.
[11] a) Y. Sakamoto, I. Díaz, O. Terasaki, D. Zhao, J. Pérez-Pariente, J. M. Kim, G. D. Stucky, *J. Phys. Chem. B* **2002**, *106*, 3118–3123; b) J. Fan, C. Yu, F. Gao, J. Lei, B. Tian, L. Wang, Q. Luo, B. Tu, W. Zhou, D. Zhao, *Angew. Chem.* **2003**, *115*, 3254–3258; *Angew. Chem. Int. Ed.* **2003**, *42*, 3146–3150.
[12] A. Carlsson, M. Kaneda, Y. Sakamoto, O. Terasaki, R. Ryoo, S. H. Joo, *J. Electron Microsc.* **1999**, *48*, 795–798.
[13] a) A. C. Finnefrock, R. Ulrich, A. Du Chesne, C. C. Honeker, K. Schumacher, K. K. Unger, S. M. Gruner, U. Wiesner, *Angew. Chem.* **2001**, *113*, 1247–1251; *Angew. Chem. Int. Ed.* **2001**, *40*, 1207–1211; b) A. Jain, G. E. S. Toombes, L. M. Hall, S. Mahajan, C. B. W. Garcia, W. Probst, S. M. Gruner, U. Wiesner, *Angew. Chem.* **2005**, *117*, 1252–1255; *Angew. Chem. Int. Ed.* **2005**, *44*, 1226–1229.
[14] a) I. Honma, H. S. Zhou, D. Kundu, A. Endo, *Adv. Mater.* **2000**, *12*, 1529–1533; b) S. A. El-Safty, T. Hanaoka, *Chem. Mater.* **2003**, *15*, 2892–2902.
[15] D. Zhao, Q. Huo, J. Feng, J. Kim, Y. Han, G. D. Stucky, *Chem. Mater.* **1999**, *11*, 2668–2672.
[16] D. Zhao, J. Feng, Q. Huo, N. Melosh, G. H. Fredrickson, B. F. Chmelka, G. D. Stucky, *Science* **1998**, *279*, 548–552.
[17] S. Che, A. E. Garcia-Bennett, T. Yokoi, K. Sakamoto, H. Kunieda, O. Terasaki, T. Tatsumi, *Nat. Mater.* **2003**, *2*, 801–805.
[18] A. E. Garcia-Bennett, O. Terasaki, S. Che, T. Tatsumi, *Chem. Mater.* **2004**, *16*, 813–821.
[19] S. Che, Z. Liu, T. Ohsuna, K. Sakamoto, O. Terasaki, T. Tatsumi, *Nature* **2004**, *429*, 281–284.
[20] J. N. Israelachvili, D. J. Mitchell, B. W. Ninham, *J. Chem. Soc. Faraday Trans. 2* **1976**, *72*, 1525–1568.
[21] J. M. Seddon, J. Gulik-Krzywicki, H. Delacroix, *Phys. Chem. Chem. Phys.* **2000**, *2*, 4485–4493.

 © 2006 Wiley-VCH Verlag GmbH & Co. KGaA, Weinheim

Photochromism

DOI: 10.1002/anie.200600535

A Ferrocenylspiropyran That Functions as a Molecular Photomemory with Controllable Depth**

*Sayoko Nagashima, Masaki Murata, and Hiroshi Nishihara**

Spiropyran (SP) derivatives,[1] such as 1′,3′,3′-trimethyl-6-nitrospiro[2*H*-1-benzopyran-2,2′-indoline], belong to a class of organic photochromic compounds that have been intensively investigated and have potential applications as molecular electronic devices, optical switches, and memories.[2] These dyes are converted into the colored merocyanine (MC) form upon irradiation with UV light, but revert to the colorless SP form when left in the dark or upon irradiation with visible light. The open MC form has a larger dipole moment than the closed SP form, and thus the stability of the MC form strongly depends on the electronic effects of the substituent(s) of the indolium and phenyl moieties, the solvent polarity, and the metal complexation.[3] If the donor–acceptor nature of the substituent can be controlled by a redox reaction, we can switch the balance of thermody-

[*] S. Nagashima, Dr. M. Murata, Prof. H. Nishihara
Department of Chemistry, School of Science
The University of Tokyo
7-3-1 Hongo, Bunkyo-ku, Tokyo 113-0033 (Japan)
Fax: (+81) 3-5841-8063
E-mail: nisihara@chem.s.u-tokyo.ac.jp

[**] This work was supported by Grants-in-Aid for Scientific Research (nos. 16047204 (area 434) and 17205007), by a grant from The 21st Century COE Program for Frontiers in Fundamental Chemistry from MEXT, and by CREST, JST (Japan).

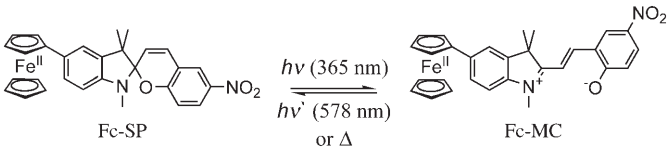
Supporting Information for this article is available on the WWW under http://www.angewandte.org or from the author.

WILEY InterScience DISCOVER SOMETHING GREAT
© 2006 Wiley-VCH Verlag GmbH & Co. KGaA, Weinheim

namic stability, and thus the memory depth, between the SP and MC forms. Herein, we report a new system in which the stability of the MC form can be completely and reversibly switched by a combination of SP/MC photoisomerization and a ferrocene/ferrocenium redox cycle.[4]

A 5-ferrocenylspiropyran (Fc-SP) was synthesized by condensation of 2-hydroxy-5-nitrobenzaldehyde and 5-ferrocenyl-substituted Fischer's Base in methanol (see the Supporting Information). A reversible Fe^{III}/Fe^{II} redox wave is observed at −0.03 V versus ferrocenium/ferrocene (Fc^+/Fc) in dichloromethane in the cyclic voltammogram of Fc-SP (see the Supporting Information). The UV/Vis spectrum of Fc-SP in methanol shows a π–π* transition band at $\lambda_{max} = 345$ nm ($\varepsilon = 2.9 \times 10^4\ M^{-1}cm^{-1}$; see the Supporting Information). The electron donation of the ferrocene moiety results in a lower energy of the π–π* band of Fc-SP relative to unsubstituted spiropyrans.

Irradiation of a pale-yellow solution of Fc-SP in methanol with UV light ($\lambda = 365$ nm) gave a red-purple solution with an absorption maximum wavelength of 530 nm (see the Supporting Information), which can be ascribed to the generation of the MC form (Fc-MC; Scheme 1). The molar ratio of the MC



Scheme 1. Photoisomerization of Fc-SP.

form was estimated from the photo-generated ^1H NMR spectral changes in [D_4]MeOH (see the Supporting Information) to be 75% in the photostationary state (PSS).

The λ_{max} value, yield in the PSS, and the thermodynamic stability of the MC form depend on the solvent polarity. Fc-MC exhibits negative solvatochromism, that is, its λ_{max} decreases with an increase in the Reichard empirical solvent polarity parameter, $E_T(30)$[5] (see the Supporting Information). The λ_{max} value of Fc-MC is red-shifted relative to that of the unsubstituted MC (see the Supporting Information) as a result of the ferrocene moiety acting as a donor with a resonance stabilization effect. Also, the yield of the MC form in the PSS during irradiation with UV light is lower, and thermal isomerization from the MC to the SP form is faster, in solvents with lower polarity. In dichloromethane, for example, Fc-MC ($\lambda_{max} = 578$ nm) was formed with a yield of 56% in the PSS, which is lower than the 75% obtained in methanol, although it isomerizes to Fc-SP within a few hours at 20°C, much faster than in methanol.

Next, we attempted to combine the redox and photochemical changes of Fc-SP in dichloromethane. When a dichloromethane solution of Fc-SP was oxidized to Fc^+-SP with a stoichiometric amount of 1,1′-dichloroferrocenium hexafluorophosphate ($E^{0\prime} = 0.19$ V versus Fc^+/Fc),[6] new absorption peaks appeared at 515 and 1250 nm (compare Figure 1a and b and left inset). When this oxidized solution was irradiated with 365-nm light for a length of time sufficient

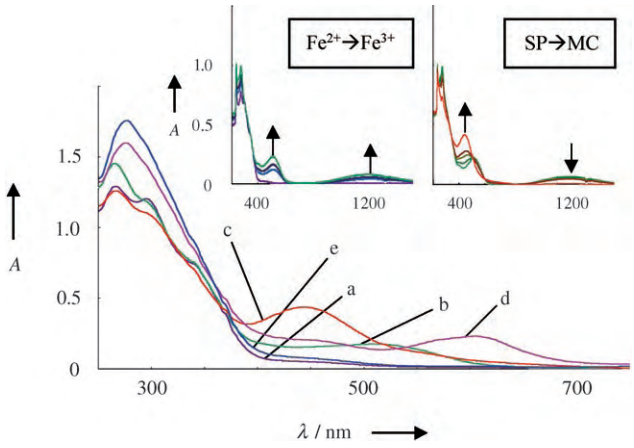


Figure 1. Sequential spectral changes of Fc-SP in dichloromethane: a) Initial state (Fc-SP), b) after oxidation with 1.0 equivalent of [Fe(η^5-$C_5H_4Cl)_2$]PF_6, c) after irradiation with 365-nm light, d) after reduction with 1.0 equivalent of [Fe(η^5-$C_5Me_5)_2$], and e) after standing at 20°C. Inset: UV/Vis–near-IR spectral changes from (a) to (b) (left) and from (b) to (c) (right).

to reach the PSS, the 1250-nm band vanished and a new band appeared at 445 nm (Figure 1c), that is, a marked blue shift occurs upon photoirradiation. The 445-nm band was ascribed to the isomerization from the SP to the MC form, based on the finding that subsequent reduction gave Fc-MC (see below). It should be noted that the complete disappearance of the 1250-nm band signifies that only the MC form is present in the PSS of the oxidized state, whereas the MC molar ratio in the PSS of the Fc state reaches only 56% (Figure 2A).

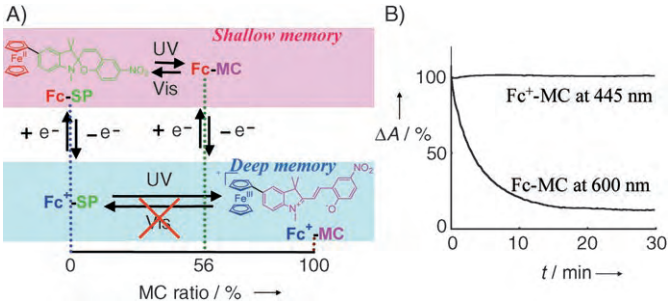


Figure 2. A) Photo- and redox reactions of Fc-SP/Fc-MC. B) The decrease in absorbance at λ_{max} of the MC forms at 20°C in CH_2Cl_2 before and after oxidation with [Fe(η^5-$C_5H_4Cl)_2$]PF_6 under irradiation with 365-nm light to reach the PSS.

The ratio of the MC form remained constant after oxidation; irradiation of Fc^+-MC with UV or visible light could not cause reversion to the SP form (Figure 2B), and thermal isomerization to the SP form hardly proceeded. In other words, Fc^+-MC is very stable towards light and heat. Previous methods to stabilize the MC state are mainly based on the Coulomb interaction of the phenolate anion with nearby cationic species.[3] The reason for the unique MC stabilization by Fc^+ in the present study has not been fully clarified, but the large blue shift of λ_{max} for Fc^+-MC relative to

© 2006 Wiley-VCH Verlag GmbH & Co. KGaA, Weinheim

Fc-MC suggests a strong electronic effect of Fc^+ as a result of π conjugation.

Chemical reduction of Fc^+-MC with a stoichiometric amount of decamethylferrocene ($E^{0\prime} = -0.59$ V versus Fc^+/Fc)[7] allowed us to reach the MC PSS, as confirmed by the appearance of the characteristic band of Fc-MC (Figure 1 d), and the MC form reverted thermally to the SP form (Figure 1 e). This reversible redox and photoisomerization cycle (Figure 2 A) indicates that the Fc state corresponds to a shallow (deletable) photomemory and the Fc^+ state to a deep (undeletable) photomemory.

The reversible redox and photoisomerization cycle was also studied in a polymer matrix. Poly(ethylene oxide) and polyvinylchloride (PVC) films containing Fc-SP show a coloring to purple ($\lambda_{max} = 545$ nm) and blue ($\lambda_{max} = 578$ nm), respectively, upon irradiation with UV light (365 nm; see Figure 3 A and the Supporting Information), thus indicating

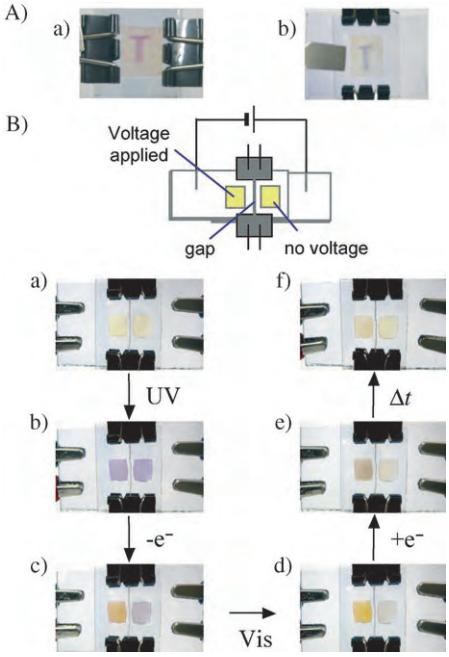


Figure 3. A) Optical changes of Fc-SP in a) poly(ethylene oxide) and b) PVC films with a photomask after irradiation at 365 nm. B) Optical changes of Fc-SP/PVC films upon irradiation at 365 nm (a–b), application of an electric field of 2 V (b–c), irradiation at 546 nm (c– d), application of an electric field of 0 V (d– e), and in the absence of further treatment (e– f). On the right-hand side an identical film sample is shown that was not subjected to the redox process (that is, to which the potential was not applied).

the formation of the MC form; this color change can be reversed thermally or by irradiation with 546-nm light. Oxidation and re-reduction of Fc-SP in a PVC film containing Bu_4NBF_4 as an electrolyte sandwiched by two ITO electrodes occurs reversibly when the voltage between the two ITO electrodes is controlled between 0 and 2 V.

Figure 3 B shows the results for two identical films to only one of which (the left one) an electric field was applied. Upon irradiation at 365 nm, both of the films become purple (a to b). When charged with electricity at the ITO electrode cell, only the film on the left-hand side turns from purple to orange as a result of the oxidation of Fc-SP (c). When the films are irradiated with visible light, the color goes back to yellow (d). When the current is switched off, the re-reduction of Fc-SP takes place in the left-hand film, as seen by a change in color from yellow to brown (e). The brown color is due to a mixture of the oxidized and re-reduced MC forms in the film. When left without further treatment, the film reverts to yellow (f). These color changes demonstrate the change in readiness of the SP–MC conversion as a result of the redox change of the ferrocene site.

In conclusion, a photochromic molecule with an ability to switch between two isomeric structures by a redox change has been created. This phenomenon has been demonstrated both in solution and in solid polymer electrolytes. The system is expected to provide a new approach for the realization of molecule-based devices, and should be important in the field of semiconductor computer technology based on "random-access memory" and "read-only memory", in which the control of memory depth is becoming increasingly important.

Experimental Section

Synthesis of **1** (prepared according to a report on the synthesis of 3-ferrocenylnitrobenzene): Ferrocene (6.69 g, 0.0361 mol) was added to sulfuric acid (specific gravity = 1.84, 40 mL). The resulting deep-blue ferrocenium solution was stirred at room temperature for 3 h. A solution of sodium nitrite (0.80 g, 0.0116 mol) in water (5 mL) at less than 0 °C was added dropwise to a solution of 5-amino-1,3,3-trimethyl-2-methyleneindoline (1.83 g, 0.0972 mol) in 1:1 water/hydrochloric acid (specific gravity 1.18, 10 mL) with stirring. The mixture was stirred at less than 0 °C for 3 h to ensure complete diazotization. Copper powder (2.0 g) was added to the ferrocenium solution as a catalyst, and the diazonium solution was then added dropwise with vigorous stirring. The nitrogen effervescence ceased after stirring for 4 h, and ascorbic acid (5.0 g) was added to reduce the starting ferrocenium to ferrocene. The product was extracted with dichloromethane. The combined organic extracts were dried with sodium sulfate, filtered through Celite, and the solvent was eliminated. The dark solid thus obtained was purified by column chromatography on alumina with an increasing proportion of ethyl acetate in *n*-hexane as the eluent. The first yellow-orange band was eluted with pure hexane and yielded unchanged ferrocene. The third yellow band, which eluted with ethyl acetate/hexane (50:50), was collected. The yellow component was evaporated to yield 97.9 mg (0.274 mmol, 2.81 %) of **1** as a brown solid. ^{1}H NMR (400 MHz, CD_2Cl_2, room temperature): $\delta = 1.37$ (s, 6 H), 3.03 (s, 3 H), 3.84 (s, 2 H), 4.03 (s, 5 H), 4.23 (t, $J = 2.0$ Hz, 2 H), 4.53 (t, $J = 2.0$ Hz, 2 H), 6.45 (d, $J = 8.0$ Hz, 1 H), 7.18 (d, $J = 1.6$ Hz, 1 H), 7.25 ppm (dd, $J =$ 8.0, 1.6 Hz, 1 H); MALDI-TOF-MS: m/z 357 [M^+].

Synthesis of Fc-SP: Compound **1** (38.8 mg, 1.09 mmol) and 2-hydroxy-5-nitrobenzaldehyde (18.7 mg, 1.11 mmol) were stirred at room temperature in anhydrous methanol for 1.5 h. The resulting mixture was separated by column chromatography on alumina using ethyl acetate/hexane (1:5, v/v) as the eluent. The yellow band was collected and the solvent evaporated to yield 20.3 mg (0.400 mmol, 36.9 %) of Fc-SP as a greenish-yellow powder. Elemental analysis (%) calcd for $C_{29}H_{26}FeN_2O_3$: C 68.79, H 5.18, N 5.53; found C 68.54, H 5.31, N 5.31; ^{1}H NMR (400 MHz, CD_2Cl_2, room temperature): $\delta =$ 1.21 (s, 3 H), 1.32 (s, 3 H), 2.74 (s, 3 H), 4.05 (s, 5 H), 4.26 (t, $J = 1.9$ Hz, 2 H), 4.53 (t, $J = 1.9$ Hz, 2 H), 5.89 (d, $J = 10.4$ Hz, 1 H), 6.49 (d, $J =$ 8.0 Hz, 1 H), 6.82 (d, $J = 10.0$ Hz, 1 H), 6.97 (d, $J = 10.4$ Hz, 1 H), 7.21 (d, $J = 1.7$ Hz, 1 H), 7.33 (dd, $J = 10.0$, 1.7 Hz, 1 H), 8.00 (dd, $J = 8.0$,

 © 2006 Wiley-VCH Verlag GmbH & Co. KGaA, Weinheim

2.9 Hz, 1H), 8.02 ppm (d, $J = 2.9$ Hz, 1H); MALDI-TOF-MS: m/z 506 [M^+].

Polymer-electrolyte experiment: Photoirradiation was carried out with a USHIO high-pressure mercury lamp as the light source. The bright lines were selected with a monochromator (Jasco, CT-10) or with a glass filter (Toshiba). Two kinds of polymer were investigated. One polyelectrolyte (FB-011, DAISO Research Laboratories; thickness: 40 μm) consisted of the ternary copolymer of ethylene oxide (EO), 2-(2-methoxyethoxy)ethyl glycidyl ether (EM-2), and allyl glycidyl ether (AGE), with an EO/EM-2/AGE molar ratio of 82:12:1.8. Lithium bis(trifluoromethansulfonyl)imide (LiTFSI) was added as a supporting salt ([Li]/[O] = 0.06:1). The other polymer (Toughnyl, Japan Wavelock Co.; thickness: 100 μm) contained PVC. A solution of nBu$_4$NBF$_4$ was introduced into the PVC film as an electrolyte and the solvents evaporated. The Fc-SP solution was swollen in these polymer films and the solvent was removed. The dried polymer films were pitched with two ITO-coated glass electrodes. The voltage was controlled with a Hokuto Denko HSV-100 automatic polarization system.

Received: February 9, 2006
Published online: May 31, 2006

Keywords: photochromism · photomemory · redox chemistry · sandwich complexes · spiro compounds

[1] a) G. Berkovic, V. Krongauz, V. Weiss, *Chem. Rev.* **2000**, *100*, 1741 – 1754; b) S. Kobatake, M. Irie, *Annu. Rep. Prog. Chem. Sect. C* **2003**, *99*, 277 – 313; c) G. Such, A. R. Evans, H. L. Yee, P. T. Davis, *J. Macromol. Sci. Part C* **2003**, *43*, 547 – 579.

[2] a) Z. F. Liu, K. Hashimoto, A. Fujishima, *Nature* **1990**, *347*, 658 – 660; b) T. Ikeda, O. Tsutsumi, *Science* **1995**, *268*, 1873 – 1875; c) *Photochromism: Memories and Switches* (Ed.: M. Irie), *Chem. Rev.* **2000**, *100*, 1683 – 1890; d) K. Ichimura, S.-K. Oh, M. Nakagawa, *Science* **2000**, *288*, 1624 – 1626.

[3] a) H. Goerner, *Phys. Chem. Chem. Phys.* **2001**, *3*, 416 – 423; b) L. Evans, G. E. Collins, R. E. Shaffer, V. Michelet, J. D. Winkler, *Anal. Chem.* **1999**, *71*, 5322 – 5327; c) M. Tanaka, M. Nakamura, M. A. A. Salhin, T. Ikeda, K. Kamada, H. Ando, Y. Shibutani, K. Kimura, *J. Org. Chem.* **2001**, *66*, 1533 – 1537; d) J. T. C. Wojtyk, P. M. Kazmaier, E. Buncel, *Chem. Mater.* **2001**, *13*, 2547 – 2551; e) B. G. Jeliazkova, S. Minkovska, T. Deligeorgiev, *J. Photochem. Photobiol. A* **2005**, *171*, 153 – 160.

[4] Redox-initiated photoisomerization of ferrocene-attached photochromic molecules has been reported; see: a) M. Kurihara, A. Hirooka, S. Kume, M. Sugimoto, H. Nishihara, *J. Am. Chem. Soc.* **2002**, *124*, 8800 – 8801; b) A. Sakamoto, A. Hirooka, K. Namiki, M. Kurihara, M. Murata, M. Sugimoto, H. Nishihara, *Inorg. Chem.* **2005**, *44*, 7547 – 7558.

[5] a) K. Dimroth, C. Reichardt, T. Siepmann, F. Bohlmann, *Justus Liebigs Ann. Chem.* **1963**, *661*, 1; b) C. Reichardt, *Justus Liebigs Ann. Chem.* **1971**, *752*, 64.

[6] M. Kurosawa, T. Nankawa, T. Matsuda, K. Kubo, M. Kurihara, H. Nishihara, *Inorg. Chem.* **1999**, *38*, 5113 – 5123.

[7] J. Ruiz, D. Astruc, *C. R. Acad. Sci. Ser. IIc* **1998**, *1*, 21 – 27.

 © 2006 Wiley-VCH Verlag GmbH & Co. KGaA, Weinheim

Organocatalysis

DOI: 10.1002/anie.200600867

Asymmetric Synthesis of Chiral Aldehydes by Conjugate Additions with Bifunctional Organocatalysis by Cinchona Alkaloids**

*Fanghui Wu, Ran Hong, Jihan Khan, Xiaofeng Liu, and Li Deng**

The aldehyde is arguably the most versatile carbonyl functionality. Furthermore, it is more active than any other carbonyl functionality toward a plethora of nucleophilic reactions. This unique combination of functional versatility and activity renders chiral aldehydes highly valuable intermediates in asymmetric synthesis. The emergence of numerous catalytic enantioselective reactions that involve aldehydes as either nucleophiles or electrophiles further enhances the synthetic value of chiral aldehydes. Enantioselective transformations of the readily available prochiral aldehydes are now emerging as a fundamentally important approach toward optically active aldehydes. In particular, great strides have been made in the development of enantioselective bond formations with the α-carbon atom of prochiral aldehydes with chiral enamine catalysis,[1,2] enantioselective cycloadditions and Friedel–Crafts reactions with chiral immonium catalysis,[3] and conjugate additions of aryl boronic acids and silyl nitronates to α,β-unsaturated aldehydes by chiral transition-metal catalysis[4] and chiral phase-transfer catalysts,[5] respectively. Despite its synthetic importance, the highly enantioselective and general conjugate addition of carbonyl donors to α,β-unsaturated aldehydes remains elusive, even with considerable efforts.[6–8] Herein, we wish to report significant progress toward the development of such a reaction with cinchona-alkaloid-derived organic catalysts.

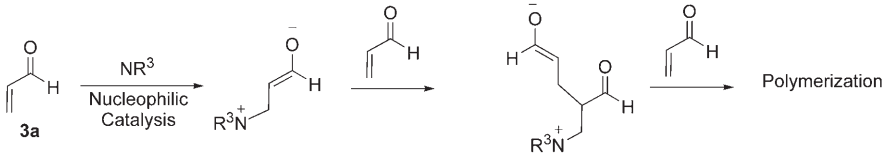
At the outset of our investigations, we were concerned that the decomposition of **3a** could be triggered by cinchona alkaloids as nucleophilic catalysts (Scheme 1) in light of the well-documented nucleophilic catalysis of 1,4-diazabicyclo-[2.2.2]octane (DABCO) and quinuclidine in the Morita–Baylis–Hillman (MBH) reaction.[9] Indeed, **3a** was found to rapidly undergo decomposition to form insoluble oligomers or polymers in the presence of DABCO, quinuclidine, or β-isocupreidine. On the other hand, mechanistic studies by us established that cinchona alkaloids, such as dihydroquinidine

[*] F. Wu, Dr. R. Hong, J. Khan, X. Liu, Prof. L. Deng
Department of Chemistry
Brandeis University
Waltham, MA 02454-9110 (USA)
Fax: (+1) 781-736-2516
E-mail: deng@brandeis.edu

[**] This work was supported financially by the National Institutes of Health (GM-61591). We thank Stephen C. Wilson for his contribution to the studies described herein.

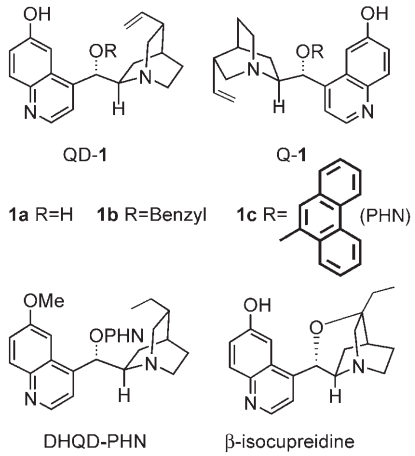
Supporting information for this article is available on the WWW under http://www.angewandte.org or from the author.

 © 2006 Wiley-VCH Verlag GmbH & Co. KGaA, Weinheim



Scheme 1. Possible polymerization pathway of acrolein (**3a**) initiated by tertiary amine nucleophilic catalysis. NR^3 = achiral or chiral tertiary amine.

9-*O*-(9'-phenanthryl) ether (DHQD–PHN), as a chiral hydrogen-bond donor functioned as a general base catalyst rather than a nucleophilic catalyst for the highly enantioselective alcoholysis of *N*-carboxyanhydrides.[10] More recent mechanistic studies from our laboratories indicated that 6′-OH cinchona alkaloids **1a–c** (Scheme 2) were able to promote a

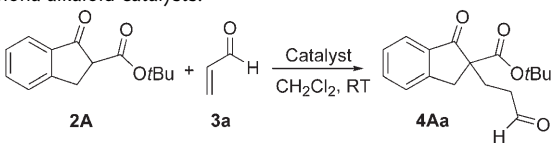


Scheme 2. Structures of cinchona-alkaloid catalysts **1**, DHQD–PHN, and β-isocupreidine. QD = quinidine, Q = quinine

variety of efficient enantioselective conjugate additions[11] as acid–base bifunctional organic catalysts from their ability to interact with the nucleophiles and electrophiles as hydrogen-bond acceptors and donors, respectively. We were pleased to find that, in stark contrast to DABCO, quinuclidine, and β-isocupreidine, 6′-OH cinchona alkaloids **1a–c** did not promote the polymerization of **3a**. These and previous results[10,11] indicate that 6′-cinchona alkaloids **1a–c** were effective general base catalysts but poor nucleophilic catalysts. We therefore suspected that **1a–c** might efficiently promote conjugate additions of carbonyl donors to **3a** without provoking polymerizations of the latter.

Our hypothesis was validated by the examination of various cinchona alkaloids as catalysts for the conjugate addition of **2A** to **3a** (Scheme 2). As summarized in Table 1, reactions with cinchona alkaloids **1a–c** rapidly went to completion to produce the 1,4-adduct **4Aa** as the only detectable product. In the presence of only 1.0 mol% of either Q-**1c** or QD-**1c**, the reaction at room temperature proceeded to completion in 15 minutes to afford chiral aldehyde **4Aa** in quantitative yield and 95% *ee* (entries 4–5, Table 1). Even with a catalyst loading of 0.1 mol%, highly enantiomerically enriched **4Aa** could still be produced in quantitative yield (entry 6, Table 1). The important role played by the 6′-OH group in the catalysis by cinchona alkaloid **1c** could be glimpsed from the dramatically lower enantioselectivity of the corresponding 6′-OMe cinchona alkaloid DHQD–PHN (entry 7 versus 3, Table 1).

Table 1: Asymmetric conjugate addition of **2A** to acrolein (**3a**) with cinchona-alkaloid catalysts.[a,b]



Entry	Catalyst	Loading [mol%]	*t*	Yield [%][c]	*ee* [%][d]
1	QD-**1a**	10.0	< 1 min	n.d.	39
2	QD-**1b**	10.0	< 1 min	n.d.	92
3	QD-**1c**	10.0	< 1 min	n.d.	95
4	QD-**1c**	1.0	15 min	100	95
5	Q-**1c**	1.0	15 min	100	95
6	Q-**1c**	0.1	7 h[e]	100	90
7	DHQD–PHN	10.0	< 5 min	n.d.	15

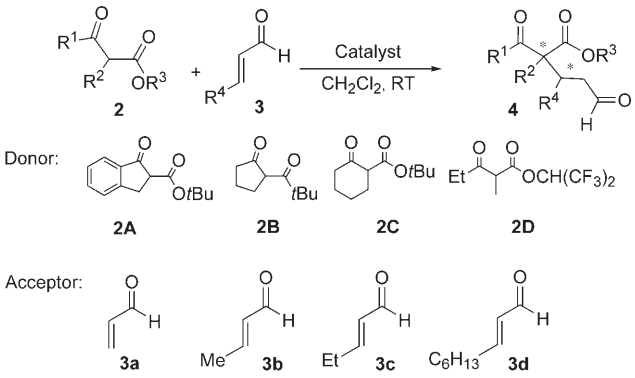
[a] Unless specified, the reaction was carried out with **2A** (0.5 M in CH_2Cl_2) and **3a** (2.5 equiv) in the presence of **1** at room temperature. [b] All the reactions went to completion in the indicated time. [c] Yield of the isolated product. [d] See the Supporting Information for the determination of the *ee* value. [e] Compound **2A** (0.2 mmol) was added to a solution of **1c** (0.5 mM) in CH_2Cl_2 (0.4 mL), and a solution of **3a** (0.26 mmol, 1.3 equiv) in CH_2Cl_2 (0.4 mL) was then added at a rate of 0.07 mL h^{-1}. n.d. = not determined.

Importantly, with Q-**1c** or QD-**1c**, conjugate additions of a wide range of cyclic and acyclic α-alkyl β-ketoesters (**2A–D**) to **3a** at room temperature generated the corresponding 1,4-adducts containing only an all-carbon quaternary stereocenter in 91–95% *ee* and virtually quantitative yield (entries 1–5, Table 2). Moreover, unprecedented highly diastereoselective and enantioselective conjugate additions to various β-substituted α,β-unsaturated aldehydes (**3b–d**) could be accomplished with 6′-OH cinchona alkaloid **1b** to afford the corresponding chiral aldehydes containing adjacent quaternary–tertiary stereocenters with 18–25:1 d.r. and 92–99% *ee* in nearly quantitative yield (entries 6–8, Table 2).

In light of the presence of all-carbon benzylic quaternary stereocenters in biologically interesting compounds,[12] we attempted the conjugate addition of α-phenyl α-cyanoacetate (**5A**) to **3a**. Unfortunately, all known 6′-OH cinchona alkaloids (**1a–e**),[11] including **1b** and **1c**, that demonstrated high enantioselectivity and considerable generality for the conjugate additions of α-alkyl β-ketoesters **2** with **3a** (see above) gave unsatisfactory enantioselectivities (entries 1–5, Table 3). Taking advantage of the readily tunable characteristics of 6′-OH cinchona alkaloids **1**, we explored the development of a new catalyst to attain an efficient enantioselective conjugate addition of **5A** to **3a**. Catalyst screening studies along this line of inquiry led to the discovery that catalyst **1f**, a structurally novel 6′-OH cinchona alkaloid,

 © 2006 Wiley-VCH Verlag GmbH & Co. KGaA, Weinheim

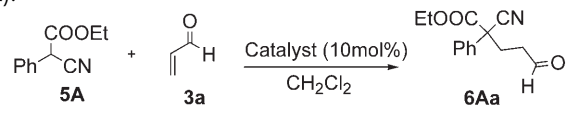
Table 2: Asymmetric conjugate addition of α-substituted-β-keto esters **2** to α,β-unsaturated aldehyde **3** with bifunctional cinchona-alkaloid catalysts **1b** and **1c**.[a]

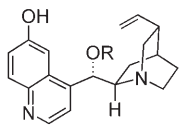


Entry	2	3	Catalyst	Loading [mol%]	*t*	Yield [%][b]	*ee* [%][c]	d.r.[d]
1[e]	**2A**	**3a**	QD-**1c** (Q-**1c**)	1.0	15 min	100 (100)	95 (95[f])	–
2[e]	**2A**	**3a**	Q-**1c**	0.1	7 h[g]	100	90[f]	–
3	**2B**	**3a**	QD-**1c** (Q-**1c**)	1.0	44 h	98 (99)	93[f] (90)	–
4	**2C**	**3a**	QD-**1c** (Q-**1c**)	10.0	30 h	98 (99)	98 (90)	–
5	**2D**	**3a**	QD-**1c** (Q-**1c**)	10.0	36 h[h]	100 (100)	91 (90)	–
6	**2A**	**3b**	QD-**1b**	10.0	8 h	100	99[i]	18:1
7	**2A**	**3c**	QD-**1b**	10.0	12 h	97	92[i]	20:1
8	**2A**	**3d**	QD-**1b**	10.0	24 h	98	98[i]	25:1

[a] Unless specified, the reaction was performed by treatment of **2** (0.3 mmol) with **3** (0.75 mmol, 2.5 equiv) and the catalyst in CH_2Cl_2 (0.6 mL) at 23 °C. The results in parentheses were obtained with Q-**1c**. [b] Yield of the isolated product. [c] See the Supporting Information for the determination of the *ee* value. [d] Determined by ^{1}H NMR spectroscopic analysis of the crude products. [e] The reaction was carried out with 1.3 equivalents of **3a**. [f] The absolute configuration was determined to be *R* (see the Supporting Information). [g] Compound **2A** (0.2 mmol) was added to a solution of **1c** (0.5 mM) in CH_2Cl_2 (0.4 mL), and a solution of **3a** (0.26 mmol, 1.3 equiv) in CH_2Cl_2 (0.4 mL) was then added at a rate of 0.07 mL h^{-1}. [h] A solution of **3a** (0.5 mmol, 2.5 equiv) in CH_2Cl_2(0.4 mL) was added to a solution of **2D** (0.2 mmol) and **1c** (0.02 mmol, 10.0 mol%) in CH_2Cl_2 (0.4 mL) at −36 °C and at a rate of 0.07 mL h^{-1}. [i] For the major diastereomer of **4**.

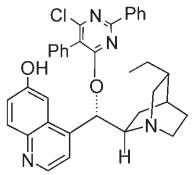
Table 3: Conjugate addition of α-phenyl α-cyanoacetate **5A** to acrolein (**3a**).[a,b]





QD-**1d** R=Benzoyl

QD-**1e** R=Acetyl



DHQD-**1f**

Entry	Catalyst	*T* [°C]	*t*	*ee* [%][c]
1	QD-**1a**	23	< 2 min	8
2	QD-**1b**	23	< 2 min	27
3	QD-**1c**	23	< 2 min	41
4	QD-**1d**	23	< 2 min	42
5	QD-**1e**	23	< 2 min	48
6	DHQD-**1f**	23	< 2 min	60
7	DHQD-**1f**	−50	< 20 min	85
8	DHQD-**1f**	−50	6 h[d]	91

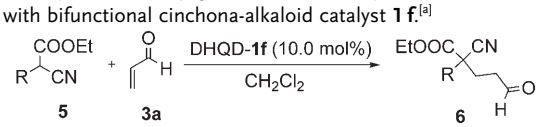
[a] Unless specified, the reaction was carried out with **5A** (0.5 M in CH_2Cl_2) and **3a** (1.3 equiv) in the presence of **1** (10 mol%) at the indicated temperature. [b] All the reactions went to completion in the indicated time. [c] See the Supporting Information for the determination of the *ee* value. [d] A solution of **3a** (0.26 mmol, 1.3 equiv) in CH_2Cl_2 (0.4 mL) was added to a solution of **5A** (0.2 mmol) and DHQD-**1f** (0.02 mmol, 10.0 mol%) in CH_2Cl_2 (0.4 mL) at a rate of 0.07 mL h^{-1}.

could afford significantly higher enantioselectivity than **1a–e** (entry 6 versus 1–5, Table 3). In particular, the conjugate addition of **5A** to **3a** with DHQD-**1f** at −50 °C afforded the corresponding 1,4-adduct **6A** in 85% *ee* (entry 7, Table 3). Upon a slow addition of **3a** to a solution of **5A** and DHQD-**1f** in dichloromethane, the enantioselectivity could be further improved to 91% *ee* (entry 8, Table 3). It should be noted that DHQD-**1f** was prepared on a multigram scale from dihydroquinidine by a four-step sequence[13] in 70% overall yield. Importantly, DHQD-**1f** afforded synthetically useful enantioselectivity and high yields for conjugate additions to **3a** with α-cyanoacetates (**5A–E**) bearing a range of α-aryl and -heteroaryl groups (entries 1–5, Table 4).

We applied this reaction to the development of a concise enantioselective total synthesis of (+)-tanikolide (**9**) to explore its synthetic utility.[14,15] Our approach features the conjugate addition of β-ketoester **2B** to **3a** catalyzed by QD-**1c** as the asymmetric induction step (see Scheme 3). We performed the conjugate addition at −25 °C with 10 mol% of QD-**1c** to achieve optimum enantioselectivity. The reaction occurred smoothly to provide the desired chiral aldehyde **4Ba** in quantitative yield with virtually perfect enantioselectivity (> 99% *ee*). The aliphatic side chain of **9** was then introduced by the olefination of aldehyde **4Ba** with 1,1-diiodooctane by following the procedure of Takai and co-workers with modifications.[16] Subsequent straightforward functional-group transformations converted keto ester **7** into keto alcohol **8** by a three-step sequence of in an overall yield of

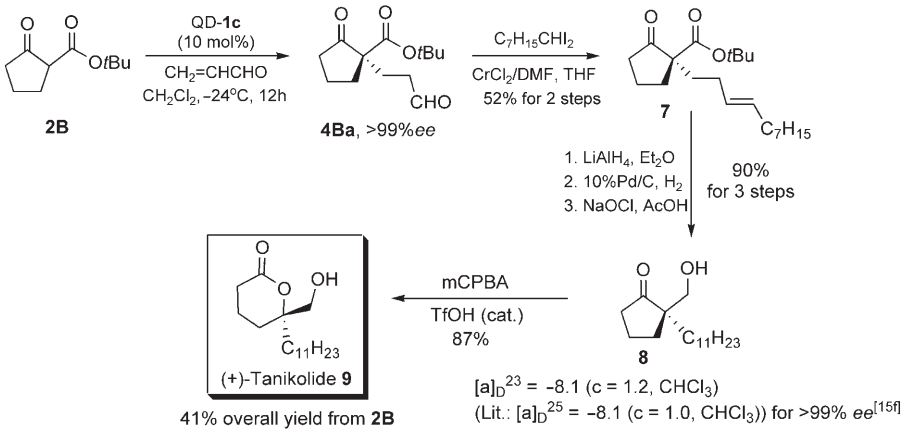
 © 2006 Wiley-VCH Verlag GmbH & Co. KGaA, Weinheim

Table 4: Asymmetric conjugate addition of α-cyano esters **5** to acrolein (**3a**) with bifunctional cinchona-alkaloid catalyst **1f**.[a]



Entry	5	R	*T* [°C]	*t* [h]	Yield [%][b]	*ee* [%][c]
1	**5A**	Ph	−50	6	100	91
2	**5B**	*p*-Cl-Ph	−50	6	98	88
3	**5C**	*m*-Cl-Ph	−50	8	100	80
4[d]	**5D**	*p*-MeO-Ph	−50	8	99	95
5	**5E**	2-thienyl	−78	8	90	87

[a] Unless specified, a solution of **3a** (0.26 mmol, 1.3 equiv) in CH_2Cl_2 (0.4 mL) was added to a solution of **5** (0.2 mmol) and DHQD-**1f** (0.02 mmol, 10.0 mol%) in CH_2Cl_2 (0.4 mL) at a rate of 0.07 mL h^{-1}. [b] Yield of the isolated product. [c] See the Supporting Information for the determination of the *ee* value. [d] A solution of **3a** (0.26 mmol, 1.3 equiv) in CH_2Cl_2 (0.4 mL) was added to a solution of **5D** (0.2 mmol) and DHQD-**1f** (0.02 mmol, 10.0 mol%) in CH_2Cl_2 (0.8 mL) at a rate of 0.07 mL h^{-1}.



Scheme 3. Catalytic enantioselective total synthesis of (+)-tanikolide. DMF = dimethylformamide, Tf = trifluoromethanesulfonyl.

90%. A Baeyer–Villiger oxidation of **8** with *m*-chloroperbenzoic acid (*m*CPBA) furnished **9** in 87% yield. In comparison to existing enantioselective syntheses of (+)-**9**,[15] our route is concise and affords tanikolide in virtually optically pure form and favorable overall yield. Moreover, this route should be useful for the asymmetric synthesis of analogues of tanikolide.

In summary, we have developed the first highly efficient and general asymmetric conjugate addition of carbonyl donors to α,β-unsaturated aldehydes. Critical to establishing a wide scope of carbonyl donors is the development of a new and readily accessible 6′-OH cinchona alkaloid catalyst **1f**, which is uniquely effective for conjugate additions to α,β-unsaturated aldehydes with α-aryl α-cyanoacetates as donors. With broad scope for both the α-substituted β-dicarbonyl donors and the α,β-unsaturated aldehydes and the use of readily available chiral organic catalysts that are easily recyclable[13] and compatible with air and moisture, the current reaction should open new opportunities for asymmetric synthesis that involve the construction of tetrasubstituted carbon stereocenters. This possibility is demonstrated in the development of a concise, high-yielding, and flexible enantioselective synthesis of the biologically interesting natural product tanikolide.

Received: March 6, 2006
Published online: May 31, 2006

Keywords: aldehydes · alkaloids · conjugate addition · natural products · organocatalysis

[1] For reviews of enamine catalysis, see: a) B. List, *Acc. Chem. Res.* **2004**, *37*, 548–557; b) W. Notz, F. Tanaka, C. F. Barbas III, *Acc. Chem. Res.* **2004**, *37*, 580–591.

[2] For the enantioselective α-oxidation of aldehydes, see: a) S. P. Brown, M. P. Brochu, C. J. Sinz, D. W. C. MacMillan, *J. Am. Chem. Soc.* **2003**, *125*, 10808–10809; for the enantioselective intramolecular α-alkylation of aldehydes, see: b) V. Vignola, B. List, *J. Am. Chem. Soc.* **2004**, *126*, 450–451; for the enantioselective α-chlorination and α-fluorination of aldehydes, see: c) M. P. Brochu, S. P. Brown, D. W. C. MacMillan, *J. Am. Chem. Soc.* **2004**, *126*, 4108–4109; d) T. D. Beeson, D. W. C. MacMillan, *J. Am. Chem. Soc.* **2005**, *127*, 8826–8828; e) M. Marigo, D. Fielenbach, A. Braunton, A. Kjærsgaard, K. A. Jørgensen, *Angew. Chem.* **2005**, *117*, 3769–3772; *Angew. Chem. Int. Ed.* **2005**, *44*, 3703–3706; for the asymmetric α-sulfenylation of aldehydes, see: f) M. Marigo, T. C. Wabnitz, D. Fielenbach, K. A. Jørgensen, *Angew. Chem.* **2005**, *117*, 804–807; *Angew. Chem. Int. Ed.* **2005**, *44*, 794–797; for cascade immonium–enamine organocatalysis, see: g) Y. Huang, A. M. Walji, C. H. Larsen, D. W. C. MacMillan, *J. Am. Chem. Soc.* **2005**, *127*, 15051–15053.

[3] For asymmetric Friedel–Crafts reactions with α,β-unsaturated aldehydes, see: a) J. F. Austin, S.-G. Kim, C. J. Sinz, W.-J. Xiao, D. W. C. MacMillan, *Proc. Natl. Acad. Sci. USA* **2004**, *101*, 5482–5487; b) N. A. Paras, D. W. C. MacMillan, *J. Am. Chem. Soc.* **2002**, *124*, 7894–7895; c) J. F. Austin, D. W. C. MacMillan, *J. Am. Chem. Soc.* **2002**, *124*, 1172–1173; for asymmetric cycloadditions with α,β-unsaturated aldehydes, see: d) K. A. Ahrendt, C. J. Borths, D. W. C. MacMillan, *J. Am. Chem. Soc.* **2000**, *122*, 4243–4244; e) A. B. Northrup, D. W. C. MacMillan, *J. Am. Chem. Soc.* **2002**, *124*, 2458–2459; f) W. S. Jen, J. J. M. Wiener, D. W. C. MacMillan, *J. Am. Chem. Soc.* **2000**, *127*, 11926–11927.

[4] J.-F. Paquin, C. Defieber, C. R. J. Stephenson, E. M. Carreira, *J. Am. Chem. Soc.* **2005**, *127*, 10850–10851.

[5] For the enantioselective conjugate addition of silyl nitronates to α,β-unsaturated aldehydes, see: a) T. Ooi, K. Doda, K. Maruoka, *J. Am. Chem. Soc.* **2003**, *125*, 9022–9023; b) T. Ooi, K. Morimoto, K. Doda, K. Maruoka, *Chem. Lett.* **2004**, *33*, 824–825.

[6] a) M. Sawamura, H. Hamashima, Y. Ito, *J. Am. Chem. Soc.* **1992**, *114*, 8295–8296; b) M. Sawamura, H. Hamashima, Y. Ito, *Tetrahedron* **1994**, *50*, 4439–4454.

[7] For rare examples of catalytic asymmetric C–C bond-forming Michael additions with α,β-unsaturated aldehydes, see: a) Y.

 © 2006 Wiley-VCH Verlag GmbH & Co. KGaA, Weinheim

Motoyama, Y. Koga, K. Kobayashi, K. Aoki, H. Nishiyama, *Chem. Eur. J.* **2002**, *8*, 2968 – 2975; b) G. Kumaraswamy, M. N. V. Sastry, N. Jena, *Tetrahedron Lett.* **2001**, *42*, 8515 – 8517; c) M. Yamaguchi, T. Shiraishi, M. Hirama, *J. Org. Chem.* **1996**, *61*, 3520 – 3530; d) M. Yamaguchi, T. Shiraishi, M. Hirama, *Angew. Chem.* **1993**, *105*, 1243 – 1244; *Angew. Chem. Int. Ed.* **1993**, *32*, 1176 – 1177.

[8] For an enantioselective conjugate addition of a cyclic α-substituted β-ketoester to acrolein catalyzed by a phase-transfer catalyst, see: T. Ooi, T. Miki, M. Taniguchi, M. Shiraishi, M. Takeuchi, K. Maruoka, *Angew. Chem.* **2003**, *115*, 3926 – 3928; *Angew. Chem. Int. Ed.* **2003**, *42*, 3796 – 3798.

[9] D. Basavaiah, A. J. Rao, T. Satyanarayana, *Chem. Rev.* **2003**, *103*, 811 – 891.

[10] J. Hang, S.-K. Tian, L. Tang, L. Deng, *J. Am. Chem. Soc.* **2001**, *123*, 12696 – 12697.

[11] a) H. Li, Y. Wang, L. Tang, L. Deng, *J. Am. Chem. Soc.* **2004**, *126*, 9906 – 9907; b) H. Li, Y. Wang, L. Tang, F. Wu, X. Liu, C. Guo, B. M. Foxman, L. Deng, *Angew. Chem.* **2005**, *117*, 107 – 110; *Angew. Chem. Int. Ed.* ***2005***, *44*, 105 – 108; c) H. Li, J. Song, X. Liu, L. Deng, *J. Am. Chem. Soc.* **2005**, *127*, 8948 – 8949; d) F. Wu, H. Li, R. Hong, L. Deng, *Angew. Chem.* **2006**, *118*, 961 – 964; *Angew. Chem. Int. Ed.* **2006**, *45*, 1947 – 1950; e) Y. Wang, X. Liu, L. Deng, *J. Am. Chem. Soc.* **2006**, *128*, 3928 – 3930.

[12] C. Cativiela, M. D. Díaz-de-Villegas, *Tetrahedron: Asymmetry* **1998**, *9*, 3517 – 3599.

[13] See the Supporting Information for details.

[14] I. P. Singh, K. E. Milligan, W. H. Gerwick, *J. Nat. Prod.* **1999**, *62*, 1333 – 1335.

[15] a) Y. Kita, S. Matsuda, E. Fujii, M. Horai, K. Hata, H. Fujioka, *Angew. Chem.* **2005**, *117*, 6007 – 6010; *Angew. Chem. Int. Ed.* **2005**, *44*, 5857 – 5860; b) T. Ohgiya, K. Nakamura, S. Nishiyama, *Bull. Chem. Soc. Jpn.* **2005**, *78*, 1549 – 1554; c) T. Ohgiya, S. Nishiyama, *Tetrahedron Lett.* **2004**, *45*, 8273 – 8275; d) J. M. Schomaker, B. Borhan, *Org. Biomol. Chem.* **2004**, *2*, 621 – 624; e) H. Mizutani, M. Watanabe, T. Honda, *Tetrahedron* **2002**, *58*, 8929 – 8936; f) H. Tanaka, Y. Kozuki, K. Ogasawara, *Tetrahedron Lett.* **2002**, *43*, 4175 – 4178; g) R. M. Kanada, T. Taniguchi, K. Ogasawara, *Synlett* **2000**, 1019 – 1021.

[16] T. Okazoe, K. Takai, K. Utimoto, *J. Am. Chem. Soc.* **1987**, *109*, 951 – 953.

 © 2006 Wiley-VCH Verlag GmbH & Co. KGaA, Weinheim

Organocatalysis

DOI: 10.1002/anie.200601025

Organocatalytic Conjugate Addition of Malonates to α,β-Unsaturated Aldehydes: Asymmetric Formal Synthesis of (−)-Paroxetine, Chiral Lactams, and Lactones**

*Sven Brandau, Aitor Landa, Johan Franzén, Mauro Marigo, and Karl Anker Jørgensen**

Chiral lactones and lactams are endowed with a large spectrum of biological properties[1] including very important pharmaceutical activities.[2] The chiral piperidines (−)-paroxetine hydrochloride **1**, marketed as paxil/seroxat, and (+)-femoxetine **2** are selective serotonin reuptake inhibitors and are used in the treatment of depression, obsessive-compulsive disorder, and panic (Figure 1).[3] The nonpeptide

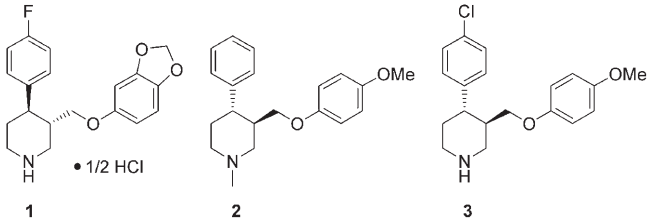


Figure 1. Antidepressants (−)-paroxetine **1**, (+)-femoxetine **2**, and peptidomimetic inhibitor Roche-1 **3**.

peptidomimetic type III inhibitor of renin, the piperidine Roche-1 **3**, was found to stabilize an enzyme conformation not previously observed for this enzyme.[4] All these compounds consist of a phenyl piperidine core structure with two *trans*-related substituents at C3 and C4. However, (−)-paroxetine **1** possesses the opposite enantiomeric configuration relative to (+)-femoxetine **2** and Roche-1 **3**.

The synthesis of the antidepressants (−)-paroxetine **1** and (+)-femoxetine **2** is focused on enzymatic asymmetric desymmetrization,[3a,5] chiral auxiliary-assisted,[6] or asymmetric

[*] Dr. S. Brandau, Dr. A. Landa, Dr. J. Franzén, Dr. M. Marigo, Prof. Dr. K. A. Jørgensen
The Danish National Research Foundation: Center for Catalysis
Department of Chemistry
Aarhus University
8000 Aarhus C (Denmark)
Fax: (+45) 8919-6199
E-mail: kaj@chem.au.dk

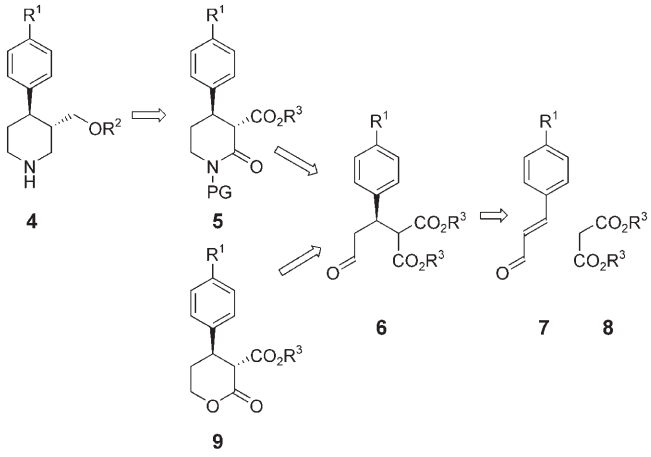
[**] This work was made possible by a grant from The Danish National Research Foundation. A.L. thanks *Eusko Jaurlaritza/Gobierno Vasco* for financial support (postdoctoral fellowship). J.F. thanks The Wenner–Gren Foundation for a grant. Thanks are expressed to Dr. Jacob Overgaard from the Department of Chemistry, Aarhus University for performing the X-ray crystal structure analysis.

Supporting information for this article is available on the WWW under http://www.angewandte.org or from the author.

 © 2006 Wiley-VCH Verlag GmbH & Co. KGaA, Weinheim

deprotonation[7] reactions. The total synthesis of these chiral compounds consists of approximately 12–14 steps. Herein we present a novel approach, based on organocatalysis employing chiral proline-derived catalysts, for a new, short, and simple methodology for the synthesis of chiral lactams and lactones of which the former can be converted to the phenyl piperidine serotonin reuptake inhibitors.

The retrosynthetic analysis of (−)-paroxetine **1** and (+)-femoxetine **2** leads to the phenyl piperidinone core structure **5**, which can be synthesized by a reductive amination sequence, starting from the optically active aldehyde **6** (Scheme 1). Moreover, compound **6** is also a precursor for



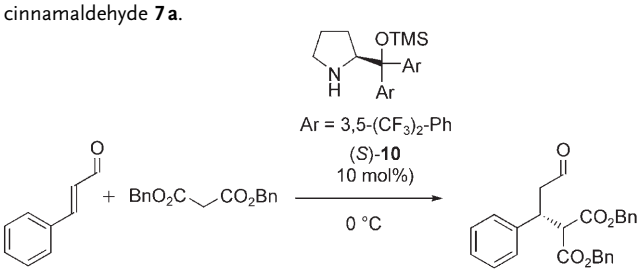
Scheme 1. Retrosynthetic analysis.

the formation of chiral lactones **9**, which are accessible through a reductive cyclization sequence. The formation of optically active **6** is derived from a conjugate addition reaction of malonates **8** to α,β-unsaturated aldehydes **7**. To date, no asymmetric organocatalytic reaction is reported for the conjugate addition of malonates to α,β-unsaturated aldehydes.[8,9]

The field of organocatalysis is a rapidly progressing area[10] and a large number of new asymmetric reactions have been developed. For the addition of nucleophiles to α,β-unsaturated compounds, a variety of different nucleophiles have been added to, for example, α,β-unsaturated aldehydes.[11] However, according to our knowledge, nucleophiles such as malonates that use iminium ion activation have only been added enantioselectively to α,β-unsaturated ketones.[12] Herein we will present the development of the first organocatalytic enantioselective addition of malonates to aromatic α,β-unsaturated aldehydes[13] with the purpose of creating a simple approach to optically active lactams and lactones, and also to show the potential of this new reaction for the formation of very important pharmaceutical compounds.

The organocatalytic enantioselective addition of malonates to aromatic α,β-unsaturated aldehydes was initially developed by reaction of cinnamaldehyde **7a** with dibenzyl malonate **8a** in different solvents at 0 °C by using the L-proline derivative (*S*)-2-[bis(3,5-bistrifluoromethylphenyl)trimethylsilanyloxymethyl]pyrrolidine (*S*)-**10**[11c,d,m,14] as the catalyst (Table 1).

Table 1: Solvent screening for the addition of dibenzyl malonate **8a** to cinnamaldehyde **7a**.



7a **8a** **6a**

Entry	Solvent	Conversion [%][b]	Yield [%][c]	*ee* [%][d]
1	CH_2Cl_2	0	–	-
2	Et_2O	0	–	-
3	CH_3CN	45	–	–
4	DMSO	46	28[e]	81
5	*n*-hexane	26	–	–
6	H_2O	12	–	–
7	$(CH_3)_2CO$	<5	–	–
8	MeOH	70	46[e]	92
9	EtOH	100	80	91
10	*n*PrOH	48	24[e]	86
11	*i*PrOH	<5	–	–

[a] All reactions were performed on a 0.25 mmol scale. [b] The conversion of **7a** into **6a** was estimated by ^{1}H NMR spectroscopy after 4 days at 0 °C. [c] Yield of the isolated product. [d] Determined by chiral HPLC after oxidation to the corresponding methyl ester. [e] Yield after oxidation.

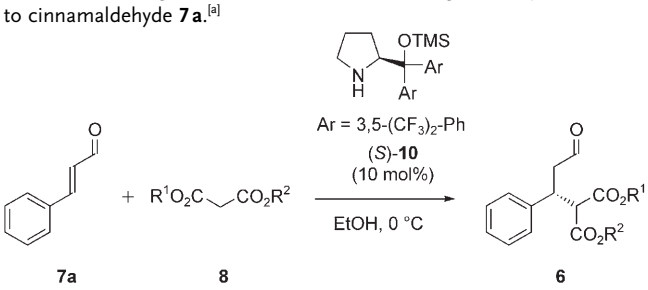
The screening of the reaction conditions in Table 1 shows that the reaction is very solvent dependent. Primary alcohols are the optimal solvent and the best results are obtained in MeOH and EtOH; in the latter solvent, full conversion is found after 4 days giving an 80 % yield of the addition product **6a** with an enantiomeric excess of 91 % *ee* (Table 1, entry 9). A slightly higher enantioselectivity (92 % *ee*) is obtained in MeOH (Table 1, entry 8); however, the conversion is much lower compared to EtOH. In *n*PrOH, a high enantioselectivity is also found (86 % *ee*) (Table 1, entry 10), but in this solvent a low conversion and yield have also been observed. It is notable that in all the other solvents, with the exception of dimethylsulfoxide (DMSO; Table 1, entry 4), no or low conversion is observed.

The reaction proceeds especially well for malonate derivatives with benzyl and methyl esters, **8a**,**b** (Table 2, entry 1, 2). For the ethyl ester **8c**, a lower yield is obtained (Table 2, entry 3), whereas no conversion is observed for the isopropyl ester **8d** (Table 2, entry 4). For the unsymmetrical malonate **8e** in Table 2, entry 5, a nondiastereoselective reaction takes place. The scope of the organocatalytic enantioselective addition of the dibenzyl **8a** and dimethyl malonates **8b** to a number of different aromatic α,β-unsaturated aldehydes **7a**–**k** catalyzed by (*S*)-**10** and (*R*)-**10** is presented in Table 3.

The results in Table 3 show the generality of this conjugate addition reaction with regard to aromatic α,β-unsaturated aldehydes. Very good to excellent enantioselectivities were obtained for all the addition products **6** ranging from 86–95 % *ee*. The addition of malonates to the aromatic α,β-unsaturated

 © 2006 Wiley-VCH Verlag GmbH & Co. KGaA, Weinheim

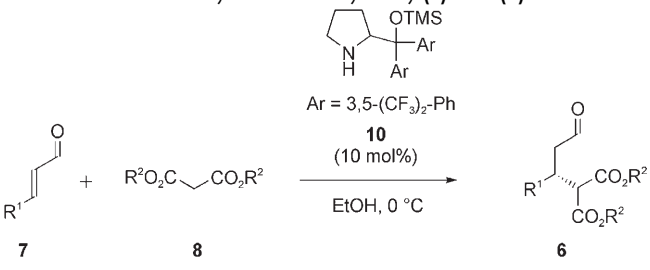
Table 2: Screening of various malonates for the organocatalytic addition to cinnamaldehyde **7a**.[a]



Entry	R^1	R^2	Yield [%][b]	d.r.[c]	*ee* [%][d]
1	Bn	Bn—**8a**	**6a**—80	–	91
2	Me	Me—**8b**	**6b**—85	–	94
3	Et	Et—**8c**	**6c**—42	–	89
4	*i*Pr	*i*Pr—**8d**	**6d**—0	–	–
5	Bn	Me—**8e**	**6e**—nd[e]	1:1	nd

[a] All reactions were performed on a 0.25 mmol scale. [b] Yield of the isolated product. [c] Estimated by ^{1}H NMR spectroscopy. [d] Determined by chiral HPLC after oxidation to the corresponding methyl ester. [e] No full conversion after 96 h.

Table 3: Reaction of dibenzyl **8a** and dimethyl malonates **8b** with different aromatic aldehydes **7a-k** catalyzed by ***(S)***- and ***(R)*-10**.[a]



Entry	R^1	R^2	Yield [%][b]	*ee* [%][c]
1	Ph—**7a**	Bn—**8a**	**6a**—80	91
2	Ph—**7a**	Bn—**8a**	**6a**—75	(−)90[d]
3	Ph—**7a**	Me—**8b**	**6b**—85	94
4	*p*-BrPh—**7b**	Bn—**8a**	**6f**—84	90
5	*p*-BrPh—**7b**	Me—**8b**	**6g**—31	95
6	*o*-BrPh—**7c**	Bn—**8a**	**6h**—34	88
7	*p*-MeOPh—**7d**	Bn—**8a**	**6i**—93	92
8	*p*-MeOPh—**7d**	Me—**8b**	**6j**—73	90
9	*p*-ClPh—**7e**	Bn—**8a**	**6k**—85	86
10	*p*-PhPh—**7f**	Bn—**8a**	**6l**—76	89
11	*p*-FPh—**7g**	Bn—**8a**	**6m**—72	86
12	*p*-CHOPh—**7h**	Bn—**8a**	**6n**—95	86
13	*p*-CH_3Ph—**7i**	Bn—**8a**	**6o**—95	88
14	2-Np—**7j**	Bn—**8a**	**6p**—69	88
15	2-Thiophene—**7k**	Bn—**8a**	**6q**—83	92

[a] All reactions were performed on a 0.25 mmol scale. [b] Yield of the isolated product. [c] Determined by chiral HPLC after oxidation to the corresponding methyl ester. [d] (*R*)-2-[bis(3,5-bistrifluoromethylphenyl)-trimethylsilanyloxymethyl]pyrrolidine (*R*)-**10** used as the catalyst.

aldehydes tolerates many functional groups in the *p*- or *o*-position of the aromatic ring, however, owing to steric interaction of the *o*-substituent (**7c**) to the malonate during the addition, a lower yield of **6h** is obtained (Table 3, entry 6). It is important to notice that aside from halogens, ethers, phenyl, and alkyl substituents, heteroaromatics and additional aldehydes are tolerated well in this reaction giving the addition products in high yields up to 95% and enantioselectivities up to 92% *ee* (Table 3, entry 12, 15). Use of the catalyst (*R*)-**10** for the addition of dibenzyl malonate **8a** to cinnamaldeyde **7a** afforded the enantiomeric (*S*)-configurated product **6a** in 75% yield and with an enantiomeric excess of 90% *ee* (Table 3).

The absolute configuration of the addition products **6** was confirmed by a single-crystal X-ray analysis of the methyl ester **11k** obtained by oxidation of **6k** (Figure 2).[15] The

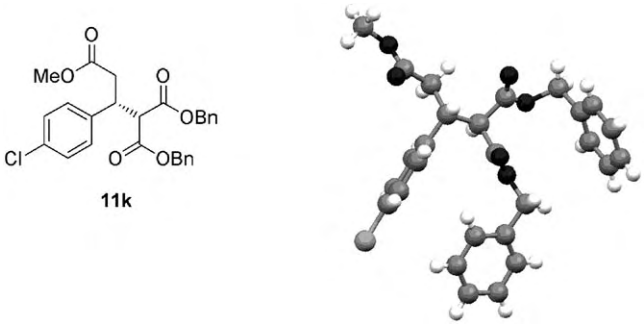
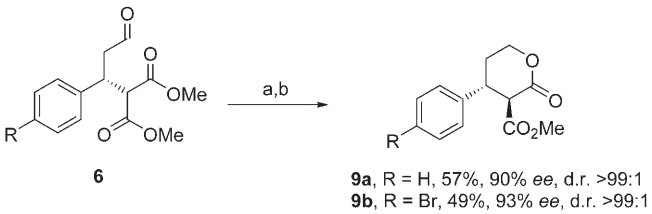


Figure 2. X-ray crystal structure of (*R*)-2-benzyloxycarbonyl-3-(4-chlorophenyl)petanedioic acid 5-benzyl ester 1-methyl ester, **11k**.

optically active compounds **6**, which are formed by the organocatalytic addition of dimethyl malonate **8b** to α,β-unsaturated aldehydes **7**, are valuable precursors for the formation of chiral lactones **9** (Scheme 1). In a reduction–cyclization procedure, the aldehyde function is reduced with $NaCNBH_3$ to the alcohol and then, in the presence of silica, a stereoselective cyclization reaction to the desired lactone takes place (Scheme 2).[16] We obtained the diastereomeri-

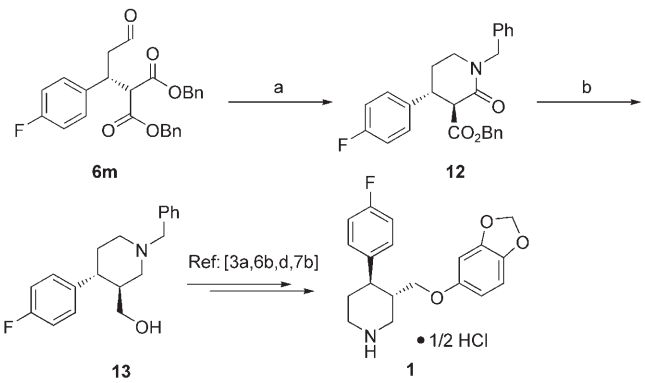


Scheme 2. Synthesis of chiral lactones **9**. Reagents: a) $NaCNBH_3$, AcOH, THF; b) SiO_2, CH_2Cl_2.

cally pure *trans*-lactones **9** in good yields and excellent enantioselectivities of up to 93% *ee*. However, we observed a minor loss of chirality of up to 2% *ee* during these reactions. The *trans* relationship of the substituents at C2 and C3 was confirmed by the ^3J coupling constants of the protons at C2 and C3 in the ^{1}H NMR spectra, showing a value of 10.5 Hz (**9a**) and 10.9 Hz (**9b**), respectively.

Compound **6** is also the building block for chiral lactam **12**, which can be easily synthesized by a reductive amination–cyclization sequence (Scheme 3).[17] We applied a tandem procedure of three reaction steps: imine formation, reduction, and lactamization, yielding the lactam **12** in 70% overall yield with an excellent diastereomeric ratio of 13:1 referring to the

 © 2006 Wiley-VCH Verlag GmbH & Co. KGaA, Weinheim



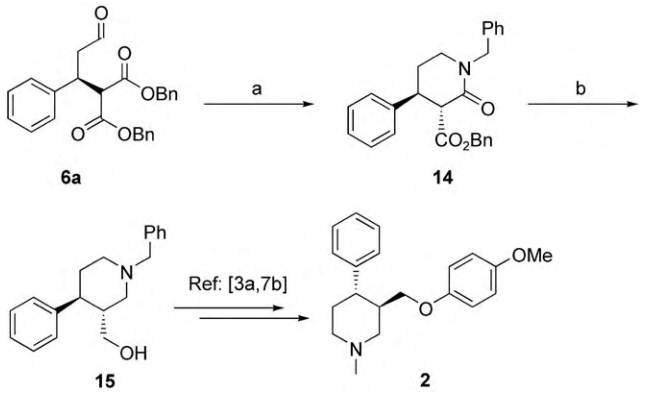
6m 12 13 1

Scheme 3. Synthesis of (−)-paroxetine **1**. Reagents: a) $PhCH_2NH_2$, $NaBH(OAc)_3$, dioxane, 70%; b) $LiAlH_4$, THF, Δ, 85%.

trans-lactam. The *trans* position of the substituents at C3 and C4 was confirmed by ^1H NMR spectroscopy. Lactam **12** has previously been transformed to (−)-paroxetine hydrochloride **1** in four steps (Scheme 3):[3a,6b,d,7b] Reduction of **12** with $LiAlH_4$ to give **13** in 85% yield as one diastereomer, etherification with sesamol, and hydrogenolysis of the benzyl group furnished (−)-paroxetine hydrochloride **1**. The 2-step asymmetric synthesis of **12** leads to (−)-paroxetine hydrochloride **1** in six steps overall.

Changing the catalyst for the malonate addition from (*S*)-2-[bis(3,5-bistrifluoromethylphenyl)trimethylsilanyloxymethyl]pyrrolidine, (*S*)-**10**, to (*R*)-2-[bis(3,5-bistrifluoromethylphenyl)trimethylsilanyloxymethyl]pyrrolidine, (*R*)-**10**, yields the Michael adduct **6a** and gives us the opportunity to synthesize the precursor for the chiral piperidine (+)-femoxetine **2** (Scheme 4) and (+)-paroxetine hydrochloride **1**. For the synthesis of (+)-femoxetine **2**, **6a** was transformed in a one-pot procedure to the *trans*-lactam **14** in 68% overall yield and with a diastereomeric ratio of 12:1. It has been reported that (+)-femoxetine **2** can be formed by subsequent reduction with $LiAlH_4$ in THF to give the piperidine **15** in 75% yield and as one diastereomers that can be converted to the desired product (+)-femoxetine **2**.[3a,7a]

In summary we reported the first organocatalytic enantioselective conjugate addition of malonates to aromatic α,β-unsaturated aldehydes resulting in the addition products in good yields and very good to excellent enantioselectivities. Furthermore, we developed new procedures for the formation of chiral lactones and lactams. These reactions proceed in a highly stereoselective manner leading to a simple synthesis of (−)-paroxetine in six steps overall and (+)-femoxetine in seven steps overall.



6a 14 15 2

Scheme 4. Synthesis of (+)-femoxetine **2**. Reagents: a) $PhCH_2NH_2$, $NaBH(OAc)_3$, dioxane, 68%; b) $LiAlH_4$, THF, Δ, 75%.

Experimental Section

General procedure for the organocatalytic addition of malonates to α,β-unsaturated aldehydes: **10** (15.0 mg, 0.025 mmol, 0.1 equiv) was added to a stirred ice-cooled (0 °C) solution of the α,β-unsaturated aldehyde **6** (0.50 mmol, 2.0 equiv) in solvent (1.0 mL) followed by the addition of malonate (0.25 mmol, 1.0 equiv). The reaction mixture was stirred for 96 h at 0 °C and then filtered through 1–2 cm bed of silica that was then washed through with Et_2O and CH_2Cl_2. The solvents were evaporated under vacuum. The crude product was subjected to flash chromatography on silica gel (Et_2O/*n*-pentane/CH_2Cl_2 1:10:0.1) to yield the desired addition product.

Received: March 15, 2006
Published online: April 28, 2006

Keywords: asymmetric synthesis · lactams · lactones · malonates · organocatalysis

[1] For an example, see: a) S. E. De Laszlo, B. L. Bush, J. J. Doyle, W. J. Greenlee, D. G. Hangauer, T. A. Halgren, R. J. Lynch, T. W. Schorn, P. K. S. Siegl, *J. Med. Chem.* **1992**, *35*, 833–846; b) H. Ebel, S. Knör, W. Steglich, *Tetrahedron* **2003**, *59*, 123–129; c) Z. H. Peng, K. A. Woerpel, *Org. Lett.* **2001**, *3*, 675–678; d) J. D. Connolly, R. A. Hill, *Dictionary of Terpenoids*, *Vol. 1*, Chapman and Hall, London, **1991**, pp. 476–541.

[2] For an example, see: a) P. Wei, G. W. Kaatz, R. J. Kerns, *Bioorg. Med. Chem. Lett.* **2004**, *14*, 3093–3097; b) P. E. Reed, J. A. Katzenellenbogen, *J. Med. Chem.* **1991**, *34*, 1162–1176; c) K. Bush, M. Macielag, M. Weidner-Wells, *Curr. Opin. Microbiol.* **2004**, *7*, 466–476; d) M. I. Konaklieva, B. J. Plotkin, *Med. Chem.* **2004**, *4*, 721–729; M. Kidwai, P. Sapra, K. R. Bhuskan, *Curr. Med. Chem.* **1999**, *6*, 195–215; e) D.-R. Hwang, Y.-S. Wu, C.-W. Chang, T.-W. Lien, W.-C. Chen, U.-K. Tan, J. T. A. Hsu, H.-P. Hsieh, *Bioorg. Med. Chem.* **2006**, *14*, 83–91.

[3] For an example, see: a) M. S. Yu, I. Lantos, Z.-Q. Peng, J. Yu, T. Cacchio, *Tetrahedron Lett.* **2000**, *41*, 5647–5651; b) G. M. Shutske, *Expert Opin. Ther. Pat.* **1994**, *4*, 335; c) J. A. Christensen, R. F. Squires, US Patent 3912743, **1975**; d) J. A. Christensen, R. F. Squires, US Patent 4007196, **1977**; e) E. A. Frank, R. T. Martin, US Patent 4902801, **1990**; f) I. Borza, L. Czibula, L. Dobay, K. Harsanyi, I. Hegedues, J. Kreidl, A. Nemes, E. Werkne Papp, I. Deutschne Juhasz, J. Nagyne Bagdy, WO Patent 98/01424, **1998**; g) C. M. Zepp, Y. Gao, D. L. Heefner, US Patent 5258517, **1993**; h) K. S. K. Murthy, A. W. Rey, US Patent 5962689, **1999**; i) B. M. Adger, M. E. Fox, G. A. Potter, US Patent 6066737, **2000**.

[4] For an example, see: M. G. Bursavich, D. H. Rich, *J. Med. Chem.* **2002**, *45*, 541–558.

[5] For an example, see: a) C. M. Zepp, Y. Gao, D. L. Heefner, *Chem. Abstr.* **1993**, *120*, 217289; b) G. de Gonzalo, R. Brieva, V. M. Sánchez, M. Bayod, V. Gotor, *J. Org. Chem.* **2001**, *66*, 8947–8953; c) J. M. Palomo, G. Fernández-Lorente, C. Mateo, R. Fernández-Lafuente, J. M. Guisan, *Tetrahedron: Asymmetry* **2002**, *13*, 2375–2381.

 © 2006 Wiley-VCH Verlag GmbH & Co. KGaA, Weinheim

[6] See *e.g.*: a) M. Amat, J. Hidalgo, J. Bosch, *Tetrahedron: Asymmetry* **1996**, *7*, 1591 – 1594; b) M. Amat, J. Hidalgo, J. Bosch, M. Cantó, M. Pérez, N. Llor, E. Molins, C. Miravitlles, M. Orozco, J. Luque, *J. Org. Chem.* **2000**, *65*, 3074 – 3084; c) J. Cossy, O. Mirguet, D. G. Pardo, J.-R. Desmurs, *Eur. J. Org. Chem.* **2002**, *42*, 3543 – 3551; d) L. Czibula, A. Nemes, F. Sebök, C. Szántay, Jr., M. Mák, *Eur. J. Org. Chem.* **2004**, *44*, 3336 – 3339.

[7] a) T. A. Johnson, D. O. Jang, B. W. Slafer, M. D. Curtius, P. Beak, *J. Am. Chem. Soc.* **2002**, *124*, 11689 – 11698; b) D. A. Greenhalgh, N. S. Simpkins, *Synlett* **2002**, *12*, 2074 – 2076; c) L. T. Liu, P.-C. Hong, H.-L. Huang, S.-F. Chen, C.-L. J. Wang, Y.-S. Wen, *Tetrahedron: Asymmetry* **2001**, *12*, 419 – 426; d) T. A. Johnson, M. D. Curtis, P. Beak, *J. Am. Chem. Soc.* **2001**, *123*, 1004 – 1005.

[8] For the addition of malonates to α,β-unsaturated aldehydes catalyzed by lewis acids, see, for example: a) S. Narasimhan, S. Velmathi, *Molecules* **2003**, *8*, 256 – 262; b) S. Velmathi, S. Swarnalakshmi, S. Narasimhan, *Tetrahedron: Asymmetry* **2003**, *14*, 113 – 117; c) K. A. Kochetkov, S. R. Harutyunyan, N. A. Kuz"mina, T. F. Savel"eva, V. I. Maleev, A. S. Peregudov, S. Vyskočil, A. S. Sagiyan, *Russ. Chem. Bull.* **2001**, *50*, 1620 – 1624.

[9] For a nonstereoselective organocatalytic addition of malonates to α,β-unsaturated aldehydes, see: M. Yamaguchi, N. Yokota, T. Minami, *J. Chem. Soc. Chem. Commun.* **1991**, 1088 – 1089.

[10] For reviews on organocatalysis, see, for example: a) P. I. Dalko, L. Moisan, *Angew. Chem.* **2004**, *116*, 5248 – 5286; *Angew. Chem. Int. Ed.* **2004**, *43*, 5138 – 5175; b) B. List, *Tetrahedron* **2002**, *58*, 5573 – 5590; c) A. Berkessel, H. Gröger, *Metal-Free Organic Catalysts in Asymmetric Synthesis*, Wiley-VCH, Weinheim, **2004**; d) A. Berkessel, H. Gröger, *Asymmetric Organocatalysis*, Wiley-VCH, Weinheim, **2005**; e) J. L. Methot, W. R. Roush, *Adv. Synth. Catal.* **2004**, *346*, 1035 – 1050; f) W. Notz, F. Tanaka, C. F. Barbas III, *Acc. Chem. Res.* **2004**, *37*, 580 – 591; g) J. Seayad, B. List, *Org. Biomol. Chem.* **2005**, *3*, 719 – 724; h) B. List, *Chem. Commun.* **2006**, 819 – 824.

[11] For recent examples of organocatalyzed additions to α,β-unsaturated aldehydes, see: a) R. K. Kunz, D. W. C. MacMillan, *J. Am. Chem. Soc.* **2005**, *127*, 3240 – 3241; b) H. Sunden, I. Ibrahem, A. Cordova, *Tetrahedron Lett.* **2005**, *47*, 99 – 103; c) M. Marigo, T. Schulte, J. Franzén, K. A. Jørgensen, *J. Am. Chem. Soc.* **2005**, *127*, 15710 – 15711; d) M. Marigo, J. Franzén, T. B. Poulsen, W. Zhuang, K. A. Jørgensen, *J. Am. Chem. Soc.* **2005**, *127*, 6964 – 6965; e) W. Wang, H. Li, J. Wang, *Org. Lett.* **2005**, *7*, 1637 – 1639; f) J. W. Yang, M. T. Hechavarria Fonseca, B. List, *Angew. Chem.* **2004**, *116*, 6829 – 6832; *Angew. Chem. Int. Ed.* **2004**, *43*, 6660 – 6662; g) S. G. Ouellet, J. B. Tuttle, D. W. MacMillan, *J. Am. Chem. Soc.* **2005**, *127*, 32 – 33; h) Y. Huang, A. M. Walji, C. H. Larsen, D. W. C. MacMillan, *J. Am. Chem. Soc.* **2005**, *127*, 15051 – 15053; i) J. W. Yang, M. T. Hechavarria Fonseca, B. List, *J. Am. Chem. Soc.* **2005**, *127*, 15036 – 15037; j) N. A. Paras, D. W. C. MacMillan, *J. Am. Chem. Soc.* **2002**, *124*, 7894 – 7895; k) J. F. Austin, S.-G. Kim, C. J. Sinz, W.-J. Xiao, D. W. C. MacMillan, *Proc. Natl. Acad. Sci. USA* **2004**, *101*, 5482 – 5487; l) S. P. Brown, N. C. Goodwin, D. W. C. MacMillan, *J. Am. Chem. Soc.* **2003**, *125*, 1192 – 1194; m) M. Marigo, S. Bertelsen, A. Landa, K. A. Jørgensen, *J. Am. Chem. Soc.* **2006**, *128*, published online. For the synthesis of the α,β-unsaturated aldehydes, see: G. Battistuzzi, S. Cacchi, G. Fabrizi, *Org. Lett.* **2003**, *5*, 777 – 780.

[12] a) N. Halland, P. S. Aburel, K. A. Jørgensen, *Angew. Chem.* **2003**, *42*, 685 – 689; *Angew. Chem. Int. Ed.* **2003**, *42*, 661 – 665; b) K. R. Knudsen, C. E. T. Mitchell, S. V. Ley, *Chem. Commun.* **2006**, 66 – 68; c) A. Kawara, T. Taguchi, *Tetrahedron Lett.* **1994**, *35*, 8805 – 8808; d) M. Yamaguchi, T. Shiraish, M. Hirama, *Angew. Chem.* **1993**, *105*, 1243 – 1245; *Angew. Chem. Int. Ed. Engl.* **1993**, *32*, 1176 – 1178; e) M. Yamaguchi, T. Shiraisi, M. Hirama, *J. Org. Chem.* **1996**, *61*, 3520 – 3530.

[13] Notably, aliphatic α,β-unsaturated aldehydes did not react with only malonates, but reacted with both the malonates and EtOH (solvent) under the present reaction conditions.

[14] For the use of this catalyst in organocatalysis, see, for example: a) J. Franzén, M. Marigo, D. Fielenbach, T. C. Wabnitz, A. Kjærsgaard, K. A. Jørgensen, *J. Am. Chem. Soc.* **2005**, *127*, 18296 – 18304; See also: b) Y. Hayashi, H. Gotoh, T. Hayashi, M. Shoji, *Angew. Chem.* **2005**, *117*, 4284 – 4287; *Angew. Chem. Int. Ed.* **2005**, *44*, 4212 – 4215.

[15] X-ray crystal structure analysis of **10h**: Formula $C_{27}H_{25}ClO_6$, weight 480.92 g mol^{-1}, colorless crystal. CCDC-601775 contains the supplementary crystallographic data for this paper. These data can be obtained free of charge from The Cambridge Crystallographic Data Centre via www.ccdc.cam.ac.uk/data_request/cif.

[16] E. Alvarez, T. Cuvigny, C. Harvé du Penhoat, *Tetrahedron* **1988**, *44*, 119 – 126.

[17] For the reductive amination see: A. F. Abdel-Magid, K. G. Carson, B. D. Harris, C. A. Marynoff, R. D. Shah, *J. Org. Chem.* **1996**, *61*, 3849 – 3862.

 © 2006 Wiley-VCH Verlag GmbH & Co. KGaA, Weinheim

Metallacarboranes

DOI: 10.1002/anie.200600890

Synthesis and Structure of 14- and 15-Vertex Ruthenacarboranes**

*Liang Deng, Jian Zhang, Hoi-Shan Chan, and Zuowei Xie**

Polyhedral expansion, a method developed by Hawthorne,[1] has proved to be very efficient for the synthesis of increasingly larger metallacarboranes.[2] This method has also been successfully applied to the synthesis of supercarboranes.[3] For example, by using carbon-atoms-adjacent (CAd) carborane anions as starting materials,[4] 13- and 14-vertex carboranes were prepared recently.[5,6] As theoretical calculations suggested that $[B_{14}H_{14}]^{2-}$ and $[B_{15}H_{15}]^{2-}$ have similar stability,[7] one may wonder whether such a cage-opening followed by boron or metal insertion would allow the preparation of 15-vertex clusters. This spurred us to prepare 15-vertex carboranes and metallacarboranes. Unfortunately, the reactions of Na_2-*nido*-$[(CH_2)_3C_2B_{12}H_{12}]$ with different borane reagents RBX_2 under various reaction conditions did not

[*] L. Deng, J. Zhang, H.-S. Chan, Prof. Dr. Z. Xie
Department of Chemistry and
Center of Novel Functional Molecules
The Chinese University of Hong Kong
Shatin, NT, Hong Kong (China)
Fax: (+852) 2603-5057
E-mail: zxie@cuhk.edu.hk

[**] This work was supported by a grant from the Research Grants Council of the Hong Kong Special Administration Region (Project No. 403805) and a Strategic Investments Scheme administrated by The Chinese University of Hong Kong.

© 2006 Wiley-VCH Verlag GmbH & Co. KGaA, Weinheim
InterScience

give any 15-vertex carborane, and rather afforded 14-vertex $(CH_2)_3C_2B_{12}H_{12}$ and a mixture of inseparable boron-containing species of high polarity. However, a metal fragment did insert into the 14-vertex *nido*-carborane cage to generate a 15-vertex metallacarborane. On the other hand, redox reactions were observed between *nido*-$[MR_2C_2B_{11}H_{11}]^{2-}$ and $R'BX_2$ or MX_2. These results are reported herein.

The starting material 2,3-$(CH_2)_3$-2,3-$C_2B_{12}H_{12}$ (**2**) was prepared from $[\{(CH_2)_3C_2B_{11}H_{11}\}\{Na_2(thf)_4\}]_n$ (**1**) by the method developed by us.[6] Single-crystal X-ray analysis[8] revealed that **2** is an isomer of 2,13-$(CH_2)_3$-2,13-$C_2B_{12}H_{12}$[6] (Figure 1). Treatment of **2** with an excess of finely cut sodium

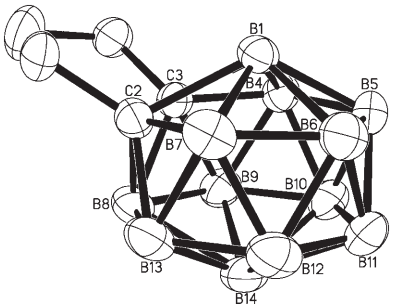
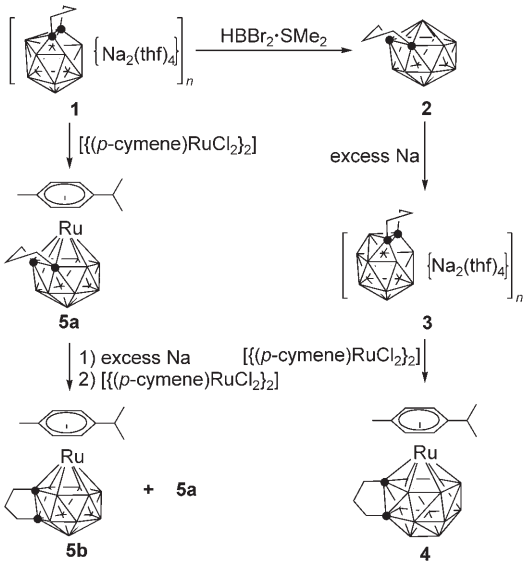


Figure 1. Molecular structure of **2**. Selected bond lengths [Å]: C2–C3 1.608(4), B1–C2 1.907(5), B1–C3 1.917(4), B1–B4 1.881(5), B1–B5 1.864(5), B1–B6 1.866(5), B1–B7 1.886(5).

metal in THF at room temperature gave, after recrystallization, 14-vertex *nido*-carborane salt $[\{(CH_2)_3C_2B_{12}H_{12}\}\{Na_2(thf)_4\}]_n$ (**3**) that was isolated in 80% yield (Scheme 1). Its ^{1}H NMR spectrum supported a molar ratio of four THF molecules per cage. The $^{11}B\{^1H\}$ NMR spectrum displayed a 1:2:2:3:2:1:1 pattern in the range 0.2 to −50.6 ppm, which was also observed in the reaction of **2** with an excess of lithium metal in THF. This result indicated that Group 1 metals can only reduce *closo*-$(CH_2)_3C_2B_{12}H_{12}$ to *nido*-$[(CH_2)_3C_2B_{12}H_{12}]^{2-}$, which suggests that *nido*-



Scheme 1. Synthetic routes to 14- and 15-vertex ruthenacarboranes.

$[(CH_2)_3C_2B_{12}H_{12}]^{2-}$ is a stronger reducing reagent than *nido*-$[(CH_2)_3C_2B_{10}H_{10}]^{2-}$, as the latter can be reduced to *arachno*-$[(CH_2)_3C_2B_{10}H_{10}]^{4-}$ by lithium metal.[4e] This high reducing power of **3** may prevent its capitation with $HBBr_2{\cdot}SMe_2$.

The molecular structure of **3** was confirmed by single-crystal X-ray diffraction (Figure 2).[8] It is a coordination polymer in which $[Na(thf)_2]^+$ ions connect *nido*-carborane

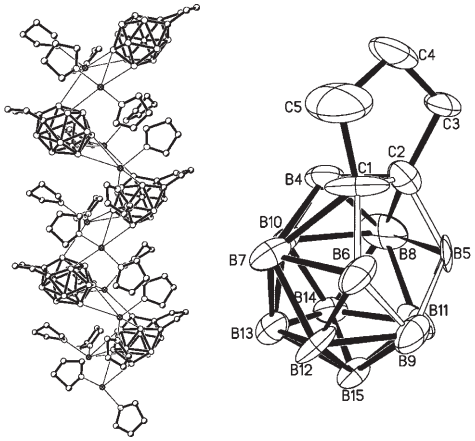


Figure 2. Left: a portion of the infinite polymeric chains in **3**. Right: structure of the anion in **3**. Selected bond lengths [Å]: C1–C2 1.404(3), C1–B6 1.696(2), C2–B5 1.605(3), B5–B9 1.684(3), B6–B9 1.840(3).

cages to form infinite one-dimensional zigzag chains. The 14-vertex *nido*-carborane dianion has an open bent pentagonal face with displacement of B9 by 0.55 Å out of the C1-C2-B5-B6 plane. This value is smaller than that of 0.68 Å in **1**.[4e] There are two seven-coordinate boron atoms (B7 and B8) in this cage. The average bond lengths between them and their neighboring vertices are 1.878(3) Å for B7 and 1.891(3) Å for B8, which are comparable to that of 1.902(3) Å in 2,13-$(CH_2)_3$-2,13-$C_2B_{12}H_{12}$.[6] Unlike 2,13-$(CH_2)_3$-2,13-$C_2B_{12}H_{12}$, the two hexagonal planes in **3** are not parallel; rather, they share the B4–B10 bond as common edge.[6]

Reaction of **3** with 0.5 equivalents of $[\{(p\text{-cymene})RuCl_2\}_2]$ in THF afforded 15-vertex ruthenacarborane 1,4-$(CH_2)_3$-7-(*p*-cymene)-7,1,4-$RuC_2B_{12}H_{12}$ (**4**) in 62% yield after column chromatographic separation (Scheme 1). To our knowledge compound **4** is one of the largest metallacarboranes known.[9,14] It is noteworthy that the reaction of **3** with $HBBr_2{\cdot}SMe_2$, $[NiCl_2(dppe)]$ (dppe = 1,2-bis(diphenylphosphanyl)ethane), or $[RuCl_2(PPh_3)_3]$ under various reaction conditions gave either the 14-vertex carborane 2,13-$(CH_2)_3$-2,13-$C_2B_{12}H_{12}$ or a mixture of inseparable products, and this indicates that the {(*p*-cymene)Ru} fragment is crucial for the formation of the 15-vertex species. Complex **4** is quite stable in air and soluble in polar organic solvents such as CH_2Cl_2, $CHCl_3$, and THF. It was fully characterized by ^{1}H, ^{13}C, and ^{11}B NMR spectroscopy, as well as high-resolution mass spectrometry. Its $^{11}B\{^1H\}$ NMR spectrum displayed a 1:2:1:2:1:1:1:1:1:1 pattern in the range 14.8 to −31.1 ppm, indicative of a species of low symmetry.

An X-ray analysis revealed that **4** adopts a *closo* structure with 26 triangular faces and has approximate D_{3h} symmetry with a C_3 axis passing through the centers of the C1-B2-B3

 © 2006 Wiley-VCH Verlag GmbH & Co. KGaA, Weinheim

and B13-B14-B15 planes if the tethering group is omitted and the differences among the Ru, B, and C atoms are ignored.[8] This geometry is very similar to that predicted for $[B_{15}H_{15}]^{2-}$ by theoretical calculations.[10] In this sandwich-type molecule (Figure 3), the arene ring is parallel to the hexagonal bonding face (C4-B2-B5-B10-B12-B15) of the carborane ligand with

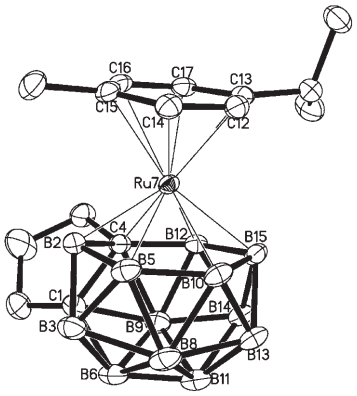


Figure 3. Molecular structure of **4**. Selected bond lengths [Å]: C1–C4 1.641(4), Ru7–C4 2.234(3), Ru7–B2 2.190(3), Ru7–B5 2.263(3), Ru7–B10 2.269(3), Ru7–B12 2.262(3), Ru7–B15 2.265(3).

an Ru–Ar(cent) distance of 1.78 Å and Ru–CB_5(cent) distance of 1.41 Å, which are comparable to the corresponding values of 1.73 and 1.46 Å in 14-vertex (*p*-cymene)$_2$Ru$_2$C$_2$B$_{10}$H$_{12}$.[9e] The average Ru–cage atom distance of 2.247(3) Å and average Ru–C(Ar) distance of 2.272(3) Å are very close to those of 2.249(3) and 2.225(3) Å in (*p*-cymene)$_2$Ru$_2$C$_2$B$_{10}$H$_{12}$.[9e] Examination of the structures of **3** and **4** shows that significant cage rearrangement occurred during the reaction. High-temperature ^{11}B NMR experiments suggested that **4** is a thermodynamically stable product.

After the successful preparation of **4**, we wondered if it could be synthesized by the capitation reaction of Na$_2$-*nido*-[(*p*-cymene)Ru{(CH$_2$)$_3$C$_2$B$_{12}$H$_{12}$}] with HBBr$_2$·SMe$_2$. The new 14-vertex metallacarborane 2,3-(CH$_2$)$_3$-1-(*p*-cymene)-1,2,3-RuC$_2$B$_{11}$H$_{11}$ (**5a**) was readily isolated in 72% yield from the reaction of 13-vertex *nido*-carborane salt [{(CH$_2$)$_3$C$_2$B$_{11}$H$_{11}$}-{Na$_2$(thf)$_4$}]$_n$ (**1**) with 0.5 equivalents of [{(*p*-cymene)RuCl$_2$}$_2$] in THF. Complex **5a** was treated with an excess of sodium metal in THF to produce a new species with an ^{11}B{^{1}H} NMR spectroscopic signature ($\delta = -11.50$ (1B), -14.88 (2B), and -32.81 ppm (8B)) distinct from those of **1** and **5a**, which was presumed to be Na$_2$-**5a**. This salt reacted with 2 equivalents of HBBr$_2$·SMe$_2$ in toluene to give **5a** and 2,13-(CH$_2$)$_3$-1-(*p*-cymene)-1,2,13-RuC$_2$B$_{11}$H$_{11}$ (**5b**) in 80 and 5% yield of isolated product, respectively, after column chromatographic separation (Scheme 1). This reaction was monitored by ^{11}B NMR spectroscopy, and no **4** was detected. In view of the successful preparation of 13- and 14-vertex bimetallic metallacarboranes (C$_5$H$_5$)$_2$Fe$_2$C$_3$B$_8$H$_{11}$,[11] (C$_5$H$_5$)$_2$Co$_2$C$_2$B$_{10}$H$_{12}$,[9d] and (*p*-cymene)$_2$Ru$_2$C$_2$B$_{10}$H$_{12}$,[9e] the reaction of Na$_2$-**5a** with 0.5 equivalents of [{(*p*-cymene)-RuCl$_2$}$_2$] in THF was then examined. Again, a redox reaction lead to **5a** and **5b** in a ratio similar to that mentioned above after column chromatographic separation. These results indicate that the reducing power of the 14-vertex *nido*-metallacarborane is much higher than those of 12- and 13-vertex *nido*-metallacarboranes.

Complexes **5a** and **5b** are air- and moisture-stable and soluble in polar organic solvents such as CH_2Cl_2, $CHCl_3$, and THF. They were fully characterized by various spectroscopic techniques. The ^{11}B{^{1}H} NMR spectrum of **5a** displayed a 3:3:3:2 pattern in the range $\delta = -3.8$ to -18.8 ppm, whereas that of **5b** showed a 1:1:2:1:1:1:1:2:1 pattern in the range 1.9 to -27.3 ppm, which indicates that **5a** has higher symmetry. The ^{1}H and ^{13}C NMR spectra also exhibited consistent symmetry patterns. Variable-temperature ^{11}B NMR experiments in *n*Bu$_2$O (20–140 °C) showed that both **5a** and **5b** are thermally stable and **5a** can not be transformed into **5b** under these conditions. Hence, **5b** must be formed in a redox reaction.

Single-crystal X-ray analyses revealed that **5a** and **5b** are isomers with a bicapped hexagonal antiprism geometry,[8] similar to that of 14-vertex carboranes.[6] The Ru atom occupies one of the apical vertices and the two cage carbon atoms are located in the 2,3- and 2,13-positions, respectively, as shown in Figures 4 and 5. The Ru–C$_2$B$_4$(cent) distance of 1.46 Å in **5a** and Ru–CB$_5$(cent) distance of 1.40 Å in **5b** are close to that of 1.41 Å in **4** and 1.46 Å in (*p*-cymene)$_2$Ru$_2$C$_2$B$_{10}$H$_{12}$.[9e] Examination of the structures of **1**[6] and

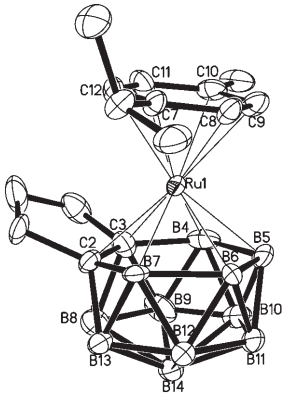


Figure 4. Molecular structure of **5a**. Selected bond lengths [Å]: C2–C3 1.644(12), Ru1–C2 2.268(8), Ru1–C3 2.251(9), Ru1–B4 2.258(11), Ru1–B5 2.288(10), Ru1–B6 2.280(9), Ru1–B7 2.252(8).

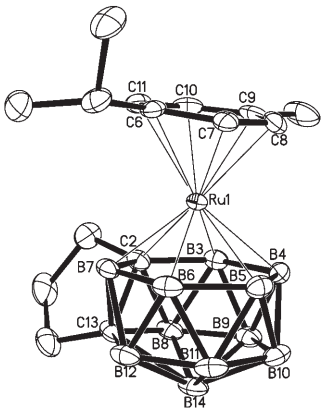


Figure 5. Molecular structure of **5b**. Selected bond lengths [Å]: C2–C13 1.631(5), Ru1–C2 2.192(3), Ru1–B3 2.231(4), Ru1–B4 2.275(4), Ru1–B5 2.290(4), Ru1–B6 2.276(4), Ru1–B7 2.199(4).

 © 2006 Wiley-VCH Verlag GmbH & Co. KGaA, Weinheim

5a,**b** indicates that significant cage rearrangement took place in the reaction of **1** with $[\{(p\text{-cymene})RuCl_2\}_2]$. A similar phenomenon was also observed in the formation of **4**.

In conclusion, we have prepared several new 14- and 15-vertex ruthenacarboranes. These supermetallacarboranes are air-, moisture-, and heat-stable. They are best described as $18e^-$ metal species in which the 13- and 14-vertex *nido*-carboranes act as $6e^-$ π ligands. This work clearly indicates that the reducing power of *nido*-carborane dianions increases with increasing cluster size and the *nido*-metallacarborane dianion is a very strong reductant, which limits success in the preparation of supercarboranes. Prevention of redox reactions is the key to obtaining successively larger clusters.[14]

Experimental Section

3: Finely cut sodium metal (100 mg, 4.35 mmol) was added to a solution of **2** (208 mg, 1.00 mmol) in THF (10 mL), and the mixture was stirred at room temperature for one week to give a clear yellow solution. After removal of excess sodium metal, the resulting yellow solution was concentrated to about 5 mL, and 4 mL of toluene was added. Complex **3** was obtained as colorless crystals after this solution was kept at room temperature for one week (434 mg, 80%). ^{1}H NMR (300 MHz, [D$_5$]pyridine): $\delta = 3.65$ (m, 16H), 1.60 (m, 16H; THF), 2.95 (m, 2H; $CH_2CH_2CH_2$), 2.55 ppm (m, 4H; $CH_2CH_2CH_2$); ^{13}C{^{1}H} NMR (100 MHz, [D$_5$]pyridine): $\delta = 67.84$, 25.47 (THF), 37.81 ($CH_2CH_2CH_2$), 31.70 ppm ($CH_2CH_2CH_2$), signals for the cage carbon atoms were not observed; ^{11}B{^{1}H} NMR (128 MHz, THF): $\delta = 0.21$ (1), −4.62 (2), −15.91 (2), −32.39 (3), −36.01 (2), −44.32 (1), −50.56 ppm (1); IR (KBr): $\tilde{\nu} = 2455\ cm^{-1}$ (vs; BH); C,H analysis (%) calcd for $C_{19}H_{46}B_{12}Na_2O_{3.5}$ (**3**−0.5 THF): C 45.08, H 9.16; found: C 44.74, H 9.02.

4: A solution of **3** (542 mg, 1.00 mmol) in THF (10 mL) was slowly added to a suspension of $[\{(p\text{-cymene})RuCl_2\}_2]$ (306 mg, 0.50 mmol) in THF (10 mL) at −78 °C, and the mixture was then stirred at room temperature for 12 h to give a deep brown solution. Removal of the precipitate and solvents gave a brown sticky solid. Chromatographic separation (SiO_2, 300–400 mesh, *n*-hexane/CH_2Cl_2 (1:4) as eluent) afforded **4** as a pale orange solid (275 mg, 62%). Single crystals suitable for X-ray analysis were grown from a THF solution. ^{1}H NMR (300 MHz, $CDCl_3$): $\delta = 5.89$ (d, $J = 6.6$ Hz, 1H), 5.81 (d, $J = 6.6$ Hz, 1H), 5.51 (d, $J = 6.3$ Hz, 1H), 5.35 (d, $J = 6.3$ Hz, 1H; $CH_3C_6H_4CH(CH_3)_2$), 3.27 (m, 1H; CH_2), 3.05 (m, 1H; CH), 2.72 (m, 1H; CH_2), 2.31 (s, 3H; $CH_3C_6H_4CH(CH_3)_2$), 2.09 (m, 4H; CH_2), 1.30 (d, $J = 6.6$ Hz, 3H), 1.26 ppm (d, $J = 6.6$ Hz, 3H; $CH_3C_6H_4CH(CH_3)_2$); ^{13}C{^{1}H} NMR (100 MHz, $CDCl_3$): $\delta = 122.9$, 112.9, 100.0, 97.13, 96.01, 92.79 ($CH_3C_6H_4CH(CH_3)_2$), 46.99, 36.53, 29.93, 28.14, 23.13, 22.13, 17.89 ppm, signals for the cage carbon atoms were not observed; ^{11}B{^{1}H} NMR (128 MHz, $CDCl_3$): $\delta = 14.83$ (1), 2.46 (2), −0.45 (1), −6.17 (2), −9.87 (1), −12.99 (1), −17.78 (1), −19.81 (1), −26.83 (1), −31.12 ppm (1); IR (KBr): $\tilde{\nu} = 2506$ (vs), 2450 cm^{-1} (s; BH); HRMS calcd for $[C_{15}H_{32}B_{12}Ru]^+$: *m*/*z* 444.2731; found: 444.2735.

5a: A solution of **1** (531 mg, 1.00 mmol) in THF (10 mL) was slowly added to a suspension of $[\{(p\text{-cymene})RuCl_2\}_2]$ (306 mg, 0.50 mmol) in THF (10 mL) at −78 °C, and the mixture was then stirred at room temperature for 12 h to give a deep brown solution. Removal of the precipitate and solvents gave a brown sticky solid. Chromatographic separation (SiO_2, 300–400 mesh, *n*-hexane/CH_2Cl_2 (1:4) as eluent) afforded **5a** as a yellow solid (310 mg, 72%). Single crystals of **5a**·THF suitable for X-ray analysis were grown from a THF solution. ^{1}H NMR (300 MHz, $CDCl_3$): $\delta = 5.51$ (d, $J = 6.6$ Hz, 2H), 5.41 (d, $J = 6.6$ Hz, 2H; $CH_3C_6H_4CH(CH_3)_2$), 3.76 (m, 4H), 1.85 (m, 4H; THF), 3.13 (m, 2H; CH_2), 2.95 (m, 1H; $CH_3C_6H_4CH(CH_3)_2$), 2.47 (m, 4H; CH_2), 2.29 (s, 3H; $CH_3C_6H_4CH(CH_3)_2$), 1.31 ppm (d, $J = 6.9$ Hz, 6H; $CH_3C_6H_4CH(CH_3)_2$); ^{13}C{^{1}H} NMR (100 MHz, $CDCl_3$): $\delta = 117.4$, 108.1, 94.87, 92.03 ($CH_3C_6H_4CH(CH_3)_2$), 67.96, 25.59 (THF), 42.38, 27.86 (CH_2), 30.20 (CH), 29.93, 22.43 ppm (CH_3), signals for the cage carbon atoms were not observed; ^{11}B{^{1}H} NMR (128 MHz, $CDCl_3$): $\delta = -3.84$ (3), −12.17 (3), −15.22 (3), −18.82 ppm (2); IR (KBr): $\tilde{\nu} = 2512\ cm^{-1}$ (vs; BH); HRMS calcd for $[C_{15}H_{31}B_{11}Ru]^+$: *m*/*z* 432.2560; found: 432.2550.

5b: Finely cut sodium metal (69 mg, 3.00 mmol) was added to a solution of **5a** (432 mg, 1.00 mmol) and naphthalene (13 mg, 0.10 mmol) in THF (10 mL), and the mixture was stirred at room temperature for two days to give a deep green solution. After removal of excess sodium metal, $[\{(p\text{-cymene})RuCl_2\}_2]$ (367 mg, 0.60 mmol) was added to the solution at −30 °C in one portion, and the mixture was stirred at room temperature for 6 h. Chromatographic separation (SiO_2, 300–400 mesh, *n*-hexane/CH_2Cl_2 (1:2) as eluent) afforded **5a** (346 mg, 80%) and **5b** (22 mg, 5%), both as yellow solids. Single crystals of **5b** suitable for X-ray analysis were grown from a THF solution. ^{1}H NMR (300 MHz, $CDCl_3$): $\delta = 5.51$ (m, 4H; $CH_3C_6H_4CH(CH_3)_2$), 2.69 (m, 6H; CH_2), 2.28 (m, 4H; $CH_3C_6H_4CH(CH_3)_2$), 1.11 ppm (s, 6H; $CH_3C_6H_4CH(CH_3)_2$); ^{13}C{^{1}H} NMR (100 MHz, $CDCl_3$): $\delta = 118.7$, 108.8, 95.16, 94.26, 91.88, 91.61 ($CH_3C_6H_4CH(CH_3)_2$), 42.82, 41.40, 30.24, 29.69, 22.99, 22.35, 18.37 ppm, signals for the cage carbon atoms were not observed; ^{11}B{^{1}H} NMR (128 MHz, $CDCl_3$): $\delta = 1.89$ (1), −1.67 (1), −6.62 (2), −9.23 (1), −11.01 (1), −20.39 (1), −23.62 (1), −24.81 (2), −27.28 ppm (1); IR (KBr): $\tilde{\nu} = 2517\ cm^{-1}$ (vs; BH); HRMS calcd for $[C_{15}H_{31}B_{11}Ru]^+$: *m*/*z* 432.2560; found: 432.2550.

Received: March 8, 2006
Published online: May 26, 2006

Keywords: boron · cage compounds · carboranes · cluster compounds · ruthenium

[1] M. F. Hawthorne, G. B. Dunks, *Science* **1972**, *178*, 462.
[2] a) A. K. Saxena, N. S. Hosmane, *Chem. Rev.* **1993**, *93*, 1081; b) R. N. Grimes in *Comprehensive Organometallic Chemistry II*, *Vol. 1* (Eds.: E. W. Abel, F. G. A. Stone, G. Wilkinson), Pergamon, Oxford, **1995**, pp. 371; c) R. N. Grimes, *Coord. Chem. Rev.* **2000**, *200*/202, 773; d) Z. Xie, *Coord. Chem. Rev.* **2002**, *231*, 23; e) Z. Xie, *Acc. Chem. Res.* **2003**, *36*, 1; f) N. S. Hosmane, J. A. Maguire, *Organometallics* **2005**, *24*, 1356.
[3] R. N. Grimes, *Angew. Chem.* **2003**, *115*, 1232; *Angew. Chem. Int. Ed.* **2003**, *42*, 1198.
[4] For CAd carborane anions, see: a) G. Zi, H.-W. Li, Z. Xie, *Organometallics* **2001**, *20*, 3836; b) G. Zi, H.-W. Li, Z. Xie, *Chem. Commun.* **2001**, 1110; c) G. Zi, H.-W. Li, Z. Xie, *Organometallics* **2002**, *21*, 5415; d) Z. Xie, *Pure Appl. Chem.* **2003**, *75*, 1335; e) L. Deng, M.-S. Cheung, H.-S. Chan, Z. Xie, *Organometallics* **2005**, *24*, 6244.
[5] A. Burke, D. Ellis, B. T. Giles, B. E. Hodson, S. A. MacGregor, G. M. Rosair, A. J. Welch, *Angew. Chem.* **2003**, *115*, 235; *Angew. Chem. Int. Ed.* **2003**, *42*, 225.
[6] L. Deng, H.-S. Chan, Z. Xie, *Angew. Chem.* **2005**, *117*, 2166; *Angew. Chem. Int. Ed.* **2005**, *44*, 2128.
[7] P. von R. Schleyer, K. Najafian, A. M. Mebel, *Inorg. Chem.* **1998**, *37*, 6765.
[8] Crystal data for **2**·$C_{10}H_8$: $C_{15}H_{26}B_{12}$, $M_r = 336.1$, monoclinic, space group $P2_1/c$, $a = 7.836(4)$, $b = 16.662(8)$, $c = 15.795(8)$ Å, $\beta = 100.69(1)°$, $V = 2027(2)$ Å^3, $T = 293$ K, $Z = 4$, $\rho_{calcd} = 1.102\ g\,cm^{-3}$, $2\theta_{max} = 50°$, $\mu(Mo_{K\alpha}) = 0.71073$ Å, absorption corrections applied by using SADABS,[12] relative transmission factors in the range 0.984–1.000. A total of 10927 reflections were collected and led to 3571 unique reflections, 3571 of which with $I > 2\sigma(I)$ were considered as observed, $R_1 = 0.0774$, wR_2-$(F^2) = 0.2060$. Crystal data for **3**: $C_{21}H_{50}B_{12}Na_2O_4$, $M_r = 542.3$,

 © 2006 Wiley-VCH Verlag GmbH & Co. KGaA, Weinheim

orthorhombic, space group $Pna2_1$, $a = 11.441(1)$, $b = 16.692(2)$, $c = 17.224(2)$ Å, $V = 3289(1)$ Å^3, $T = 293$ K, $Z = 4$, $\rho_{calcd} = 1.095$ g cm^{-3}, $2\theta_{max} = 50°$, $\mu(Mo_{K\alpha}) = 0.71073$ Å, absorption corrections applied by using SADABS,[12] relative transmission factors in the range 0.566–1.000. A total of 14726 reflections were collected and led to 4965 unique reflections, 4965 of which with $I > 2\sigma(I)$ were considered as observed, $R_1 = 0.0797$, $wR_2(F^2) = 0.1940$. Crystal data for **4**: $C_{15}H_{32}B_{12}Ru$, $M_r = 443.2$, monoclinic, space group $P2_1/c$, $a = 8.426(1)$, $b = 15.911(2)$, $c = 15.977(2)$ Å, $\beta = 101.63(1)°$, $V = 2098(1)$ Å^3, $T = 293$ K, $Z = 4$, $\rho_{calcd} = 1.403$ g cm^{-3}, $2\theta_{max} = 50°$, $\mu(Mo_{K\alpha}) = 0.71073$ Å, absorption corrections applied by using SADABS,[12] relative transmission factors in the range 0.794–1.000. A total of 11266 reflections were collected and led to 3695 unique reflections, 3695 of which with $I > 2\sigma(I)$ were considered as observed, $R_1 = 0.0266$, $wR_2(F^2) = 0.0646$. Crystal data for **5a**·THF: $C_{19}H_{39}B_{11}ORu$, $M_r = 503.5$, monoclinic, space group $P2_1/c$, $a = 15.893(5)$, $b = 10.347(3)$, $c = 16.159(5)$ Å, $\beta = 106.01(1)°$, $V = 2554(1)$ Å^3, $T = 293$ K, $Z = 4$, $\rho_{calcd} = 1.309$ g cm^{-3}, $2\theta_{max} = 50°$, $\mu(Mo_{K\alpha}) = 0.71073$ Å, absorption corrections applied by using SADABS,[12] relative transmission factors in the range 0.508–1.000. A total of 13305 reflections were collected and led to 4501 unique reflections, 4501 of which with $I > 2\sigma(I)$ were considered as observed, $R_1 = 0.0671$, $wR_2(F^2) = 0.1637$. Crystal data for **5b**: $C_{15}H_{31}B_{11}Ru$, $M_r = 431.4$, monoclinic, space group $P2_1/c$, $a = 14.427(2)$, $b = 8.281(1)$, $c = 17.514(3)$ Å, $\beta = 104.17(1)°$, $V = 2029(1)$ Å^3, $T = 293$ K, $Z = 4$, $\rho_{calcd} = 1.412$ g cm^{-3}, $2\theta_{max} = 50°$, $\mu(Mo_{K\alpha}) = 0.71073$ Å, absorption corrections applied by using SADABS,[12] relative transmission factors in the range 0.738–1.000. A total of 10671 reflections were collected and led to 3574 unique reflections, 3574 of which with $I > 2\sigma(I)$ were considered as observed, $R_1 = 0.0303$, $wR_2(F^2) = 0.0655$. These structures were solved by direct methods and refined by full-matrix least-squares techniques on F^2 by using the SHELXTL/PC package.[13] All non-hydrogen atoms were refined anisotropically and all hydrogen atoms were geometrically fixed by using the riding model. CCDC 600498–600502 (**2**·$C_{10}H_8$, **3**, **4**, **5a**·THF, **5b**) contain the supplementary crystallographic data for this paper. These data can be obtained free of charge from The Cambridge Crystallographic Data Centre via www.ccdc.cam.ac.uk/data_request/cif.

[9] Examples of 14-vertex metallacarboranes: $M_2C_4B_8$: a) W. M. Maxwell, R. F. Bryan, E. Sinn, R. N. Grimes, *J. Am. Chem. Soc.* **1977**, *99*, 4008; b) W. M. Maxwell, R. F. Bryan, E. Sinn, R. N. Grimes, *J. Am. Chem. Soc.* **1977**, *99*, 4016; c) J. R. Pipal, R. N. Grimes, *Inorg. Chem.* **1978**, *17*, 6. $M_2C_2B_{10}$: d) W. J. Evans, M. F. Hawthorne, *J. Chem. Soc. Chem. Commun.* **1974**, 38; e) D. Ellis, M. E. Lopez, R. McIntosh, G. M. Rosair, A. J. Welch, *Chem. Commun.* **2005**, 1917. MC_2B_{11}: f) L. Deng, H.-S. Chan, Z. Xie, *J. Am. Chem. Soc.* **2006**, *128*, 5219.

[10] J. Bicerano, D. S. Marynick, W. N. Lipscomb, *Inorg. Chem.* **1978**, *17*, 3443.

[11] B. Grüner, B. Štíbr, R. Kivekäs, R. Sillanpää, P. Stopka, F. Teixidor, C. Viñas, *Chem. Eur. J.* **2003**, *9*, 6115.

[12] G. M. Sheldrick, SADABS: Program for Empirical Absorption Correction of Area Detector Data, University of Göttingen, Germany, **1996**.

[13] G. M. Sheldrick, SHELXTL 5.10 for Windows NT: Structure Determination Software Programs, Bruker Analytical X-ray Systems, Inc., Madison, Wisconsin, USA, **1997**.

[14] Note added in proof: While this manuscript was in press we have learnt of the synthesis of another 15-vertex metallacarborane by a different group: R. D. McIntosh, D. Ellis, G. M. Rosair, A. J. Welch *Angew. Chem.* **2006**, *118*, 4419–4424; *Angew. Chem. Int. Ed.* **2006**, *45*, 4313–4316, next Communication in this issue.

 © 2006 Wiley-VCH Verlag GmbH & Co. KGaA, Weinheim

Metallacarboranes

DOI: 10.1002/anie.200601266

A 15-Vertex Heteroborane**

*Ruaraidh D. McIntosh, David Ellis, Georgina M. Rosair, and Alan J. Welch**

Following the synthesis[1] and characterization[1,2] of the first supraicosahedral heteroborane, 4-(η-C_5H_5)-4,1,6-*closo*-$CoC_2B_{10}H_{12}$, 35 years ago, experimental work in the area has advanced relatively slowly, with only sporadic reports of new species. Presently, the number of reported 13-vertex compounds, mainly MC_2B_{10}[3] (where M is a metal center) but occasionally $M_2C_2B_9$,[4] is only of the order of 150. Moreover, a mere handful of closed 14-vertex compounds have been reported, all except one being $M_2C_2B_{10}$,[5] and no examples of species with 15 or more vertices in the polyhedron.

The prevalence of metallacarboranes amongst the supraicosahedral heteroboranes reflects that such polyhedra generally contain an increasing number of degree-six vertices. Thus, for example, Brown and Lipscomb,[6] in considering hypothetical triangulated (deltahedral) structures for $[B_nH_n]^{2-}$ for $n = 13$–24, find that the number of degree-six vertices generally increases with increasing n, and the largest single-cage deltahedron currently known, Ge_{18}^{4-} (in $[Pd_2@Ge_{18}]^{4-}$), has recently been shown to contain six degree-six vertices.[7] Metal atoms or fragments, having relatively diffuse frontier orbital compared to {BH} fragments, are able to stabilize such structures, and thus in supraicosahedral metallacarboranes it is the metal atom(s) which tend to occupy the degree-six site(s).[3–5]

However, fuelled by the results of later theoretical calculations[8] suggesting that $[B_nH_n]^{2-}$ ions with $n \geq 16$ might adopt alternative structures which need not be fully triangulated and which are computed[9] to be progressively more favorable than the ubiquitous $[B_{12}H_{12}]^{2-}$ ion, we and others have renewed experimental efforts towards preparing progressively larger supraicosahedral heteroboranes with limited numbers of, or no, metal heteroatoms. As a result, the field of supraicosahedral heteroborane chemistry is currently undergoing an impressive renaissance. In 2003 we reported the first supraicosahedral carborane,[10] having 13 vertices and, interestingly in view of the predictions of

[*] R. D. McIntosh, Dr. D. Ellis, Dr. G. M. Rosair, Prof. A. J. Welch
School of Engineering & Physical Sciences
Heriot-Watt University
Edinburgh EH144AS (UK)
Fax: (+44) 131-451-3217
E-mail: a.j.welch@hw.ac.uk

[**] The chemistry described in this paper was part of presentation SP-B20 by R. D. McIntosh, K. J. Dalby, D. Ellis, M. E. Lopez, G. M. Rosair, A. J. Welch, and S. Zlatogorsky, at the 12th International Meeting on Boron Chemistry (IMEBORON-XII), Sendai, Japan, 15th September 2005. We thank the EPSRC and the Carnegie Trust for support, Dr. A. S. F. Boyd for NMR spectra, G. P. Smith for mass spectra, and C. Graham for microanalyses.

 © 2006 Wiley-VCH Verlag GmbH & Co. KGaA, Weinheim

Schleyer,[8] a non-triangulated (trapezoidal) face. This result was followed by the report by Xie and co-workers of a 14-vertex carborane.[11] In both these species the cage carbon atoms are joined by an exopolyhedral tether, to block the kinetic pathway to decomposition. We now report extensions to these studies—examples of 14-vertex MC_2B_{11} species, and a 15-vertex heteroborane.

The naphthalene-assisted sodium reduction of 1,2-μ-$(CH_2)_3$-1,2-*closo*-$C_2B_{11}H_{11}$[11] in THF and subsequent reaction with an equimolar (in Ru) amount of $[\{(p\text{-cymene})RuCl_2\}_2]$ yielded two bright yellow compounds, **1** and **2**, which were separated by thin layer chromatography. Mass spectrometric data on both were consistent with the anticipated molecular formula (*p*-cymene)$Ru(CH_2)_3C_2B_{11}H_{11}$ implying that **1** and **2** are isomers. The ^1H and ^{11}B NMR spectra of **1** suggest (time-averaged) C_s molecular symmetry, whereas **2** is clearly asymmetric with unique doublets for each of the four cymene aromatic H atoms, two doublets for the CH_3 protons of the cymene *i*Pr group, and eleven ^{11}B resonances of equal integral.

The structural identities of **1** and **2** were revealed by single-crystal X-ray diffraction.[12] Compound **1** (Figure 1) is a

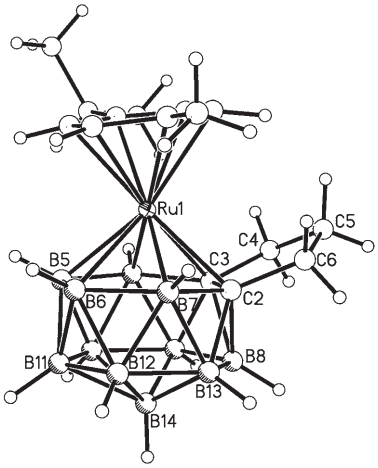


Figure 1. Perspective view of 1-(*p*-cymene)-2,3-μ-$(CH_2)_3$-1,2,3-*closo*-$RuC_2B_{11}H_{11}$ (**1**).

14-vertex ruthenacarborane with a bicapped hexagonal antiprismatic structure in which the metal atom occupies one degree-six vertex and B14 the other. Both cage carbon atoms are located in the upper hexagonal belt, adjacent to Ru1.

Although the crystallographic study of compound **2** is less precise owing to relatively poor crystal quality, it nevertheless unambiguously identifies **2** as also having a bicapped hexagonal antiprismatic cage (Figure 2). Again, the metal atom occupies one of the degree-six vertices, but this time only one cage carbon atom is adjacent to it; the other resides in the lower hexagonal belt.

Compounds **1** and **2** represent the first examples of 14-vertex MC_2B_{11} metallacarboranes. They are structural isomers, differing in the relative positions of one cage carbon atom, compound **1** having a 1,2,3-RuC_2B_{11} architecture whilst that of compound **2** is 1,2,8-RuC_2B_{11}. The isomeric relationship between **1** and **2** is similar to that between 3,1,2-MC_2B_9 and 4,1,2-MC_2B_9 icosahedral species, and we have recently been investigating the mechanism of the 3,1,2- to 4,1,2-MC_2B_9 isomerization (so-called "1,2→1,2" C atom isomerization) using vertex-substituted species.[13]

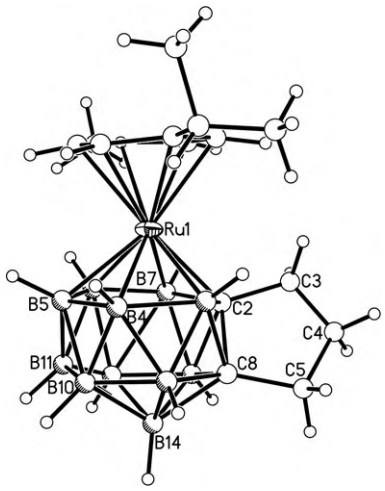


Figure 2. Perspective view of 1-(*p*-cymene)-2,8-μ-$(CH_2)_3$-1,2,8-*closo*-$RuC_2B_{11}H_{11}$ (**2**).

In an attempt to determine if there is any similar interconversion between **1** and **2**, toluene solutions of each were heated to reflux for 48 h. Compound **1** was recovered unchanged from this process, but compound **2** surprisingly gave way to a new species **3**, the mass spectrum of which suggested incorporation of an additional {BH} vertex. At room temperature, the ^1H NMR spectrum of **3** is consistent with a molecule with C_s symmetry whilst the ^{11}B-{^1H} NMR spectrum suggests near-coalescence, with broad, featureless, humps at $\delta \approx 20$, 15, 0, and -30 ppm superimposed upon which are sharper signals at $\delta \approx -11$ and -18 ppm. At 263 K, however, the ^{11}B-{^1H} spectrum consists of eight sharp integral-1 resonances and one (presumably co-incident) integral-4 resonance, consistent with a molecule lacking symmetry.

The molecular structure of **3** was revealed by crystallographic analysis[14] (Figure 3). It comprises a 15-vertex polyhedron with a degree-six Ru atom bound to an upper hexagonal B_6 belt (B2–B7), below which is an antiprismatic CB_5 belt (C8–B13). Below this, in turn, sits the C14B15 unit. Thus the gross polyhedral structure of **3** is related to the D_{3h}-symmetric hexacosahedron (26 faces) predicted[6,8] for the parent borane ion $[B_{15}H_{15}]^{2-}$. However, whilst the hexacosahedron, which contains three degree-six vertices, is fully triangulated (Figure 4), in **3** the B12–C14 connectivity, 2.383(5) Å, is formally missing, generating a quadrilateral B12-B13-C14-B15 face. Thus the polyhedron in **3** is formally a pentacosahedron (25 faces). The degree-six vertices are Ru1 and B9. If the B12–C14 connectivity were present then B12 would also be a degree-six vertex, and the cage would have effective mirror symmetry.

In compound **3**, the formal breaking of a connectivity between an otherwise degree-six boron atom and an otherwise degree-five carbon atom is highly reminiscent of the

 © 2006 Wiley-VCH Verlag GmbH & Co. KGaA, Weinheim

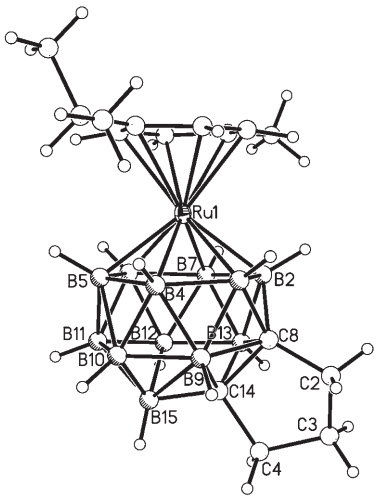


Figure 3. Perspective view of the 15-vertex ruthenacarborane 1-(*p*-cymene)-8,14-μ-$(CH_2)_3$-1,8,14-*closo*-$RuC_2B_{12}H_{12}$ (**3**).

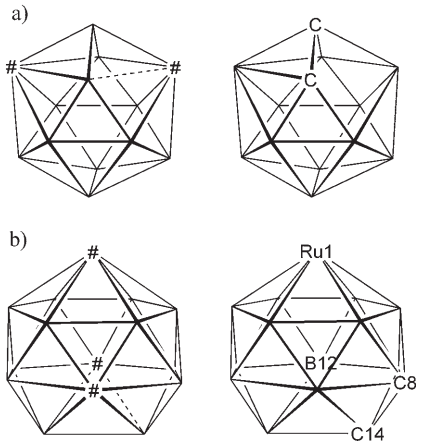


Figure 4. Topological relationships between; a) left: the docosahedron and right: the henicosahedron found in the 13-vertex carborane; b) left: the hexacosahedron and right: the pentacosahedron found in the 15-vertex ruthenacarborane. In each case the dashed bond in the left structure between a degree-six B atom and degree-five C atom (degree-six vertices shown as #) is formally absent in the right structure.

formal breaking of a similar B–C connectivity in the 13-vertex carborane,[10] transforming a docosahedron into a henicosahedron. Figure 4 shows the topological relationships between a) the docosahedron and henicosahedron, and b) the hexacosahedron and the pentacosahedron. As already noted, {BH} vertices are not particularly well-suited to degree-six vertices because their valence orbitals are not diffuse. A (relatively electronegative) cage C atom will cause further contraction of the valence orbitals of all adjacent B atoms, and this presumably results in the formal breaking of the former $B_{degree\text{-}six}$–C connectivity. In solution at elevated temperatures we assume a rapid (on the NMR timescale) fluctional process in which B12–C14 connection of **3** is made, and the B9–C14 connection broken, rendering the molecule C_s symmetric. This "square–diamond–square" rearrangement is exactly analogous to that which we have proposed to account for the final stereochemistry of B-substituted 13-vertex carborane,[10] and which we have subsequently shown is responsible for the fluctionality of unsubstituted 13-vertex carborane.[15]

The isolation of compound **3** from thermolysis of **2** was unexpected, and clearly involves adventitious capture of a {BH} fragment. To date we have not been able to prepare analogues of **3** by the more logical route of reduction of **2** followed by addition of BRX_2, but studies in this direction continue.

Compound **3** is to our knowledge the first 15-vertex heteroborane.[18] Its molecular structure, like that of the 13-vertex carborane, has responded to the presence of an unfavorable degree-six boron vertex by the formal breaking of a B–C connectivity. We are currently investigating ways of stabilizing degree-six boron vertices in supraicosahedral heteroboranes which may remove the need for such structural deformations. On the other hand, we are now only one vertex away from the size of polyhedron that Schleyer has suggested[8] (at least for $[B_nH_n]^{2-}$ ions) could form stable structures without degree-six vertices. We look forward to the next developments in this area with great anticipation.[18]

Experimental Section

1 and **2**: Reduction (Na/naphthalene) of 1,2-μ-$(CH_2)_3$-1,2-*closo*-$C_2B_{11}H_{11}$ (150 mg) in THF (20 mL), transfer to an equimolar THF suspension of $[\{(p\text{-cymene})RuCl_2\}_2]$ (234 mg) at −197 °C, warming to room temperature and overnight stirring afforded **1** and **2** in 22 % and 15 % yields (not optimized), respectively, subsequent work-up involving extraction into CH_2Cl_2, thin layer chromatography on SiO_2, and crystallization from CH_2Cl_2/petroleum ether.

1: IR (CH_2Cl_2): $\tilde{\nu}_{max}$ at 2584 cm^{-1} (BH); ^1H NMR (C_2D_6CO, 200 MHz, 298 K): $\delta = 5.78$ (d, $^3J \approx 8$ Hz, 2H, $CH_3C_6H_4CHMe_2$), 5.69 (d, $^3J \approx 8$ Hz, 2H, $CH_3C_6H_4CHMe_2$) 2.81–2.99 (m, 4H, CH_2 {3H} and $CH_3C_6H_4CHMe_2$ {1H}), 2.53 (m, 3H, CH_2), 2.19 (s, 3H, $CH_3C_6H_4CHMe_2$), 1.23 ppm (d, $^3J \approx 8$ Hz, 6H, $CH_3C_6H_4CHMe_2$); ^{11}B-{^1H} NMR (C_2D_6CO, 128 MHz, 298 K): $\delta = -5.86$ (3B), −13.58 (2B), −14.73 (1B), −17.39 (3B), −20.69 ppm (2B); MS (EI): *m*/*z* 430 [M^+]. Satisfactory microanalytical data were obtained.

2: IR (CH_2Cl_2): $\tilde{\nu}_{max}$ at 2591 cm^{-1} (B-H); ^1H NMR ($CDCl_3$, 200 MHz, 298 K): $\delta = 5.83$ (d, $^3J \approx 5$ Hz, 1H, $CH_3C_6H_4CHMe_2$), 5.77 (d, $^3J \approx 5$ Hz, 1H, $CH_3C_6H_4CHMe_2$), 5.45 (d, $^3J \approx 5$ Hz, 1H, $CH_3C_6H_4CHMe_2$), 5.39 (d, $^3J \approx 5$ Hz, 1H, $CH_3C_6H_4CHMe_2$), 3.22 (m, 1H, CH_2), 2.98 (m, 1H, $CH_3C_6H_4CHMe_2$), 2.56 (m, 1H, CH_2), 2.27 (s, 3H, $CH_3C_6H_4CHMe_2$), 2.24 (m, 2H, CH_2), 2.01 (m, 2H, CH_2), 1.27 (d, $^3J \approx 8$ Hz, 3H, $CH_3C_6H_4CHMe_2$), 1.21 ppm (d, $^3J \approx 8$ Hz, 3H, $CH_3C_6H_4CHMe_2$); ^{11}B-{^1H} NMR ($CDCl_3$, 128 MHz, 298 K): $\delta =$ 14.73 (1B), 3.38 (1B), 2.62 (1B), −0.70 (1B), −6.30 (1B), −10.11 (1B), −13.19 (1B), −18.03 (1B), −20.00 (1B), −27.03 (1B), −31.38 ppm (1B); MS (EI): *m*/*z* 430 [M^+]. Satisfactory microanalytical data were obtained.

3: Heating to reflux a toluene solution (20 mL) of **2** (35 mg) for 48 h afforded **3** in 67 % yield after work-up involving thin layer chromatography on SiO_2 (no other mobile bands were isolated) and crystallization from CH_2Cl_2/petroleum ether. IR (CH_2Cl_2): $\tilde{\nu}_{max}$ at 2529 cm^{-1} (B-H); ^1H NMR ($CDCl_3$, 200 MHz, 298 K): $\delta = 5.77$ (d, $^3J \approx 8$ Hz, 2H, $CH_3C_6H_4CHMe_2$), 5.66 (d, $^3J \approx 8$ Hz, 2H, $CH_3C_6H_4CHMe_2$), 2.64–2.90 (m, 3H, CH_2 {2H} and $CH_3C_6H_4CHMe_2$ {1H}), 2.39 (m, 2H, CH_2), 2.07 (s, 3H, $CH_3C_6H_4CHMe_2$), 1.92 (m, 2H, CH_2), 1.18 ppm (d, $^3J \approx 8$ Hz, 6H, $CH_3C_6H_4CHMe_2$); ^{11}B-{^1H} NMR (CD_2Cl_2, 128 MHz, 263 K): $\delta = 19.44$ (1B), 14.89 (1B), −0.98 (1B),

 © 2006 Wiley-VCH Verlag GmbH & Co. KGaA, Weinheim

−3.20 (1B), −11.92 (1B), −15.10 (1B), −18.49 (4B), −28.48 (1B), −31.34 ppm (1B); MS (EI): *m*/*z* 443 [M^+].

Received: March 31, 2006
Published online: May 26, 2006

Keywords: boron · cage compounds · carboranes · ruthenium · structure elucidation

[1] G. B. Dunks, M. M. McKown, M. F. Hawthorne, *J. Am. Chem. Soc.* **1971**, *93*, 2541.
[2] M. R. Churchill, B. G. DeBoer, *J. Chem. Soc. Chem. Commun.* **1972**, 1326.
[3] for example, a) D. F. Dustin, G. B. Dunks, M. F. Hawthorne, *J. Am. Chem. Soc.* **1973**, *95*, 1109; b) C. G. Salentine, M. F. Hawthorne, *J. Am. Chem. Soc.* **1975**, *97*, 426; c) C. G. Salentine, M. F. Hawthorne, *Inorg. Chem.* **1976**, *11*, 2872; d) J. D. Hewes, C. B. Knobler, M. F. Hawthorne, *J. Chem. Soc. Chem. Commun.* **1981**, 206; e) G. K. Barker, M. P. Garcia, M. Green, F. G. A. Stone, A. J. Welch, *J. Chem. Soc. Chem. Commun.* **1983**, 137; f) N. W. Alcock, J. G. Taylor, M. G. H. Wallbridge, *J. Chem. Soc. Dalton Trans.* **1987**, 1805; g) R. Khattar, C. B. Knobler, M. F. Hawthorne, *J. Am. Chem. Soc.* **1990**, *112*, 4962; h) R. Khattar, C. B. Knobler, M. F. Hawthorne, *Inorg. Chem.* **1990**, *29*, 2191; i) R. Khattar, C. B. Knobler, S. E. Johnson, M. F. Hawthorne, *Inorg. Chem.* **1991**, *30*, 1970; j) R. Khattar, M. J. Manning, C. B. Knobler, S. E. Johnson, M. F. Hawthorne, *Inorg. Chem.* **1992**, *31*, 268; k) S. Li, D. F. Mullica, E. L. Sappenfield, F. G. A. Stone, *J. Organomet. Chem.* **1994**, *467*, 95; l) K. Chui, H.-W. Li, Z. Xie, *Organometallics* **2000**, *19*, 5447; m) A. Burke, R. McIntosh, D. Ellis, G. M. Rosair, A. J. Welch, *Collect. Czech. Chem. Commun.* **2002**, *67*, 991; n) N. M. M. Wilson, D. Ellis, A. S. F. Boyd, B. T. Giles, S. A. Macgregor, G. M. Rosair, A. J. Welch, *Chem. Commun.* **2002**, 464; o) M. A. Laguna, D. Ellis, G. M. Rosair, A. J. Welch, *Inorg. Chim. Acta* **2003**, *347*, 161; p) D. Ellis, M. E. Lopez, R. McIntosh, G. M. Rosair, A. J. Welch, R. Quenardelle, *Chem. Commun.* **2005**, 1348; q) A. Burke, D. Ferrer, D. Ellis, D. L. Ormsby, G. M. Rosair, A. J. Welch, *Dalton Trans.* **2005**, 1716; r) R. McIntosh, D. Ellis, J. Gil-Lostes, K. J. Dalby, G. M. Rosair, A. J. Welch, *Dalton Trans.* **2005**, 1842.
[4] a) D. F. Dustin, W. J. Evans, M. F. Hawthorne, *J. Chem. Soc. Chem. Commun.* **1973**, 805; b) D. F. Dustin, M. F. Hawthorne, *J. Am. Chem. Soc.* **1974**, *96*, 3462; c) A. R. Kudinov, D. S. Perekalin, S. S. Rynin, K. A. Lyssenko, G. V. Grintselev-Knyazev, P. V. Petrovskii, *Angew. Chem.* **2002**, *114*, 4286; *Angew. Chem. Int. Ed.* **2002**, *41*, 4112.
[5] a) W. J. Evans, M. F. Hawthorne, *J. Chem. Soc. Chem. Commun.* **1974**, 38; b) W. M. Maxwell, R. F. Bryan, R. N. Grimes, *J. Am. Chem. Soc.* **1977**, *99*, 4016; c) W. M. Maxwell, R. F. Bryan, E. Sinn, R. N. Grimes, *J. Am. Chem. Soc.* **1977**, *99*, 4016; d) J. R. Pipal, R. N. Grimes, *Inorg. Chem.* **1978**, *17*, 6; e) D. Ellis, M. E. Lopez, R. McIntosh, G. M. Rosair, A. J. Welch, *Chem. Commun.* **2005**, 1917.
[6] L. D. Brown, W. N. Lipscomb, *Inorg. Chem.* **1977**, *16*, 2989.
[7] J. M. Goicoechea, S. C. Sevov, *J. Am. Chem. Soc.* **2005**, *127*, 7676.
[8] P. v. R. Schleyer, K. Najafian, A. M. Mebel, *Inorg. Chem.* **1998**, *37*, 6765.
[9] As defined by ΔH values computed for the reactions: $[B_{12}H_{12}]^{2-} + 4\,B_6H_{10} \rightarrow [B_{16}H_{16}]^{2-} + 4\,B_5H_9$ and $[B_{12}H_{12}]^{2-} + 5\,B_6H_{10} \rightarrow [B_{17}H_{17}]^{2-} + 5\,B_5H_9$. See equations (5) and (6) of ref. [8].
[10] A. Burke, D. Ellis, B. T. Giles, B. E. Hodson, S. A. Macgregor, G. M. Rosair, A. J. Welch, *Angew. Chem.* **2003**, *115*, 235; *Angew. Chem. Int. Ed.* **2003**, *42*, 225.
[11] L. Deng, H.-S. Chan, Z. Xie, *Angew. Chem.* **2005**, *117*, 2166; *Angew. Chem. Int. Ed.* **2005**, *44*, 2128.
[12] General crystallographic procedure: crystals were mounted in inert oil on a glass fiber and cooled to 100(2) K on a Bruker X8 APEX2 diffractometer equipped with $Mo_{K\alpha}$ X-ray radiation. Intensity data were corrected for absorption semi-empirically and structures solved by direct and difference-Fourier methods. Refinement[16] was by full-matrix least-squares analysis on F^2. Crystal data for **1**: $C_{15}H_{31}B_{11}Ru{\cdot}CH_2Cl_2$, $M_r = 516.3$, triclinic, $P\bar{1}$, $a = 8.5881(11)$, $b = 9.0273(13)$, $c = 16.032(2)$ Å, $\alpha = 86.703(7)$, $\beta = 79.245(7)$, $\gamma = 72.148(6)°$, $V = 1162.3(3)$ Å^3, $Z = 2$, $\rho = 1.475$ Mg m^{-3}, $\mu = 0.907$ mm^{-1}, $F(000) = 524$. 49377 data collected to θ_{max} 33.23°, 8880 independent reflections ($R_{int} = 0.0429$), $R_1 = 0.0293$, $wR_2 = 0.0705$ for data with $I > 2\sigma(I)$, $S = 1.019$, largest peak 1.05 and deepest hole −1.20 e Å^{-3}. Crystal data for **2**: $C_{15}H_{31}B_{11}Ru$, $M_r = 431.4$, monoclinic, $P2_1/c$, $a = 14.3739(19)$, $b = 8.4638(15)$, $c = 17.601(3)$ Å, $\beta = 104.756(6)°$, $V = 2070.7(6)$ Å^3, $Z = 4$, $\rho = 1.384$ Mg m^{-3}, $\mu = 0.754$ mm^{-1}, $F(000) = 880$. 80519 data collected to θ_{max} 25.38°, 3809 independent reflections ($R_{int} = 0.0728$), $R_1 = 0.0643$, $wR_2 = 0.1760$ for data with $I > 2\sigma(I)$, $S = 1.056$, largest peak 0.89 and deepest hole −1.05 e Å^{-3}. CCDC-603297 (**1**), CCDC-603298 (**2**), and CCDC-603299 (**3**) contains the supplementary crystallographic data for this paper. These data can be obtained free of charge from The Cambridge Crystallographic Data Centre via www.ccdc.cam.ac.uk/data_request/cif.
[13] a) R. M. Garrioch, P. Kuballa, K. S. Low, G. M. Rosair, A. J. Welch, *J. Organomet. Chem.* **1999**, *575*, 57; b) S. Robertson, D. Ellis, G. M. Rosair, A. J. Welch, *Appl. Organomet. Chem.* **2003**, *17*, 516; c) S. Robertson, R. M. Garrioch, D. Ellis, T. D. McGrath, B. E. Hodson, G. M. Rosair, A. J. Welch, *Inorg. Chim. Acta* **2005**, *358*, 1485.
[14] Crystal data for **3**: $C_{15}H_{32}B_{12}Ru$, $M_r = 443.2$, monoclinic, $P2_1/n$, $a = 11.2945(14)$, $b = 12.4801(12)$, $c = 15.5893(18)$ Å, $\beta = 109.112(5)°$, $V = 2076.3(4)$ Å^3, $Z = 4$, $\rho = 1.418$ Mg m^{-3}, $\mu = 0.754$ mm^{-1}, $F(000) = 904$. 36900 data collected to θ_{max} 33.20°, 7905 independent reflections ($R_{int} = 0.0252$), $R_1 = 0.0337$, $wR_2 = 0.0747$ for data with $I > 2\sigma(I)$, $S = 1.020$, largest peak 1.50 and deepest hole −1.43 e Å^{-3}.[17]
[15] M. Edie, S. A. Macgregor, A. J. Welch, unpublished computational results.
[16] G. M. Sheldrick, SHELXTL Version 5.1, Bruker AXS Inc., Madison, Wisconsin, **1999**.
[17] There is partial disorder in the crystallographic model, with atoms C3, C4, and B15 equally distributed over pairs of adjacent positions. We have associated C4 with B15 (as opposed to B15A) on the basis that C4 and C15 lie on opposite sides of the effective mirror plane through the cage.
[18] Note added in proof: While this manuscript was in press we have learnt of the synthesis of another 15-vertex metallacarborane by a different group: L. Deng, J. Zhang, H.-S. Chan, Z. Xie, *Angew. Chem.* **2006**, *118*, 4415–4419; *Angew. Chem. Int. Ed.* **2006**, *45*, 4309–4313, preceding Communication in this issue.

 © 2006 Wiley-VCH Verlag GmbH & Co. KGaA, Weinheim

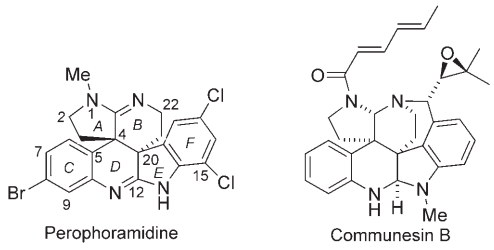
Natural Product Synthesis

DOI: 10.1002/anie.200601278

2-Thioindoles as Precursors to Spiro-Fused Indolines: Synthesis of (±)-Dehaloperophoramidine**

*Amir Sabahi, Alexei Novikov, and Jon D. Rainier**

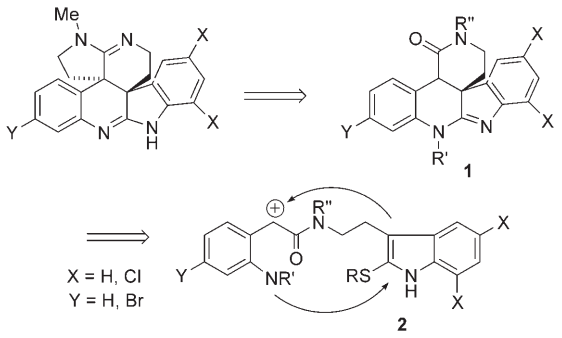
A large number of complex indole- and indoline-containing alkaloids have been isolated from the marine environment over the past decade.[1] Among these compounds is perophoramidine, which was isolated from the colonial ascidian *Perophora namei* by Ireland and co-workers.[2] The hexacyclic bisamidine skeleton of perophoramidine (see Scheme 1), which contains vicinal quaternary centers, was established with the help of extensive 2D NMR experiments and was later validated by the total synthesis developed by Fuchs and Funk.[3] Preliminary biological data indicated that perophoramidine is cytotoxic to HMT 116 colon carcinoma cells and is able to induce apoptosis by poly(adenosine-5′-diphosphate-ribose)polymerase (PARP) cleavage.[4]



Scheme 1. Structures of perophoramidine and communesin B.

Our interest in the synthetic chemistry of 2-thioindoles,[5–7] combined with the novel structural features of perophoramidine and its preliminary biological data, induced us to initiate a program to target its synthesis. Described herein are our preliminary results in this area and the synthesis of (±)-dehaloperophoramidine.

We considered several synthetic routes to the perophoramidine skeleton, but ultimately settled upon the approach illustrated in Scheme 2.[8] We envisioned that the intramolecular coupling between the 3-position of a 2-thioindole with a pendant electrophile would serve to generate one of the perophoramidine spiro-fused rings; the resulting thioimidate

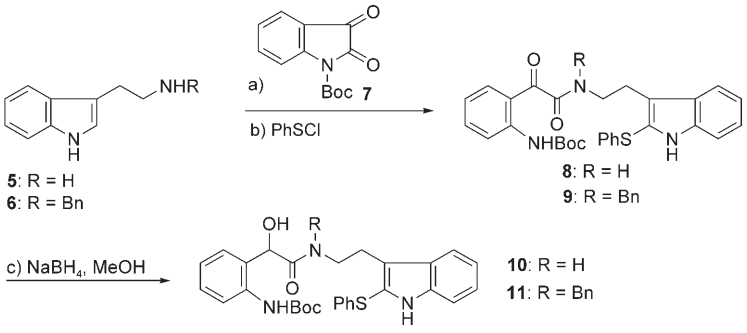


Scheme 2. Retrosynthetic analysis of perophoramidine.

would be nicely set up to undergo a subsequent cyclization with the pendant amine. The result of this cascade would be the generation of two rings, five of perophoramidine's six rings, and **1**. Incorporation of the remaining quaternary center and the A ring would provide perophoramidine. If successful, we were confident that the strategy outlined in Scheme 2 would not only enable us to efficiently synthesize perophoramidine but would also allow us to target other members of this family (namely, communesin B)[9] along with analogues for biological evaluation.

Clearly, the success of the strategy outlined in Scheme 2 depended upon the nucleophilicity of 2-thioindoles. As an indication of their reactivity, we had previously demonstrated that 2-thioindoles undergo "interrupted" Pictet–Spengler cyclizations to spiro-fused indolines (namely, **4**) when treated with the appropriate aldehyde in the presence of 4-Å molecular sieves (MS) at room temperature [Eq. (1)].[10] It is noteworthy that these conditions are milder than those used for related reactions of indoles that lack the thioether at the 2-position.[11]

With this in mind, we set out to investigate whether reactions related to that outlined in Equation (1) could be carried out to generate the dehaloperophoramidine skeleton. The synthesis of the requisite cyclization precursor is illustrated in Scheme 3. The coupling of tryptamine or benzyl-



Scheme 3. Synthesis of cyclization precursors **10** and **11**: a) *N*-Boc-isatin (**7**), THF, RT, 7 h (70%); b) PhSCl, CH_2Cl_2, 0°C→RT, 12 h (97%); c) $NaBH_4$, MeOH, 0°C, 0.5 h.

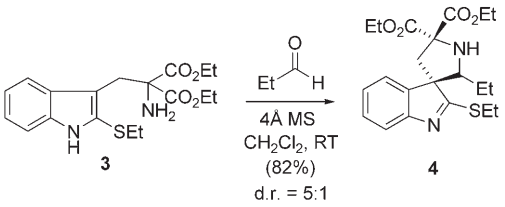
[*] A. Sabahi, Dr. A. Novikov, Prof. J. D. Rainier
Department of Chemistry
University of Utah
315 South, 1400 East, Salt Lake City, UT 84112 (USA)
Fax: (+1) 801-581-8433
E-mail: rainier@chem.utah.edu

[**] This research was supported by NIH General Medical Sciences (GM 61608) and the University of Utah. The authors thank Dr. Atta M. Arif, Dr. Charles L. Mayne, and Elliot M. Rachlin for help with the X-ray analysis, NMR spectroscopy, and mass spectrometry, respectively. Professor Chris M. Ireland is acknowledged for providing the spectral data of dehaloperophoramidine.

Supporting information for this article is available on the WWW under http://www.angewandte.org or from the author.

 © 2006 Wiley-VCH Verlag GmbH & Co. KGaA, Weinheim

protected tryptamine with *N*-*tert*-butyloxycarbonyl (*N*-Boc)-protected isatin followed by thioether incorporation and reduction with $NaBH_4$ provided cyclization precursors **10** and **11**, respectively.[12]

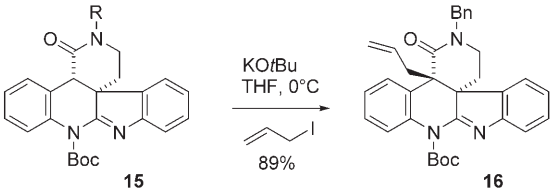


(1)

With a facile route to their synthesis in hand, we were prepared to examine the ability of **10** and **11** to undergo the key cyclization reaction. As a further indication of the nucleophilicity of 2-thioindoles, the desired cyclization occurred under the conditions used for the generation of the mesylate from **11** to give spirocycle **13** as a 1:1 mixture of C4 diastereomers. In contrast to the results with **11**, unprotected amide **10** did not undergo the desired cyclization but instead underwent competitive decomposition upon extended exposure to the reaction conditions. Presumably, this latter result is due to the inability of **10** to overcome the propensity of the amide to exist as its *s*-*trans* rotamer.[13]

The fact that **13** existed as a mixture of C4 diastereomers was inconsequential; treatment of the mixture with 1,8-diazabicyclo[5.4.0]undec-7-ene (DBU) led to equilibration at C4, and only one of the two diastereomers underwent a subsequent cyclization to give the C12 amidine **15** in 79% overall yield from **9**. Following optimization studies, we found it best to carry out both transformations in a single flask by concentrating the reaction mixture containing **13**, dissolving the resulting residue in CH_2Cl_2, and subjecting the resulting solution to DBU (Scheme 4).

With pentacycle **15** in hand, we examined the generation of the C4 quaternary center as a precursor to the A ring [Eq. (2)]. To achieve this goal, we ultimately settled upon an N,O-ketene acetal allylation reaction similar to that employed by Artman and Weinreb in their perophoramidine studies;[14] although they had used NaH, we found it best to employ KO*t*Bu as the base. Quenching the resulting ketene acetal with allyl iodide led to **16** as a single diastereomer in 89% yield.



(2)

Pentacycle **16** proved to be amenable to single-crystal X-ray analysis, thus firmly establishing that the reaction of **15** had resulted in the desired C4 and C20 diastereomer needed for the synthesis of perophoramidine (Figure 1).

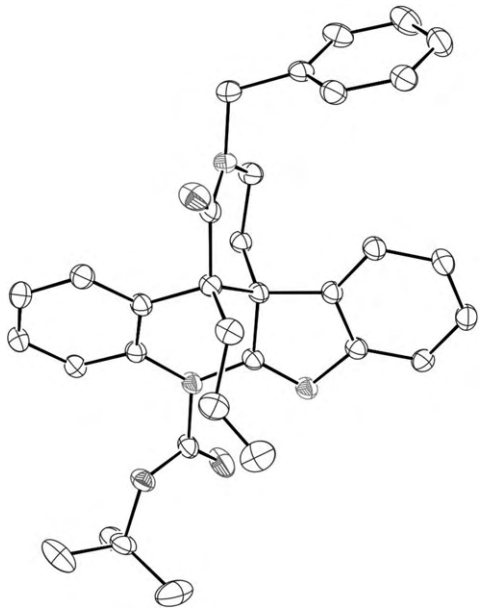
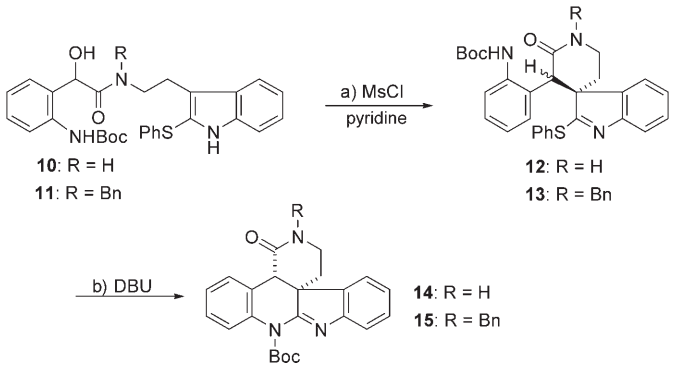


Figure 1. ORTEP drawing of **16** from X-ray crystallographic analysis.

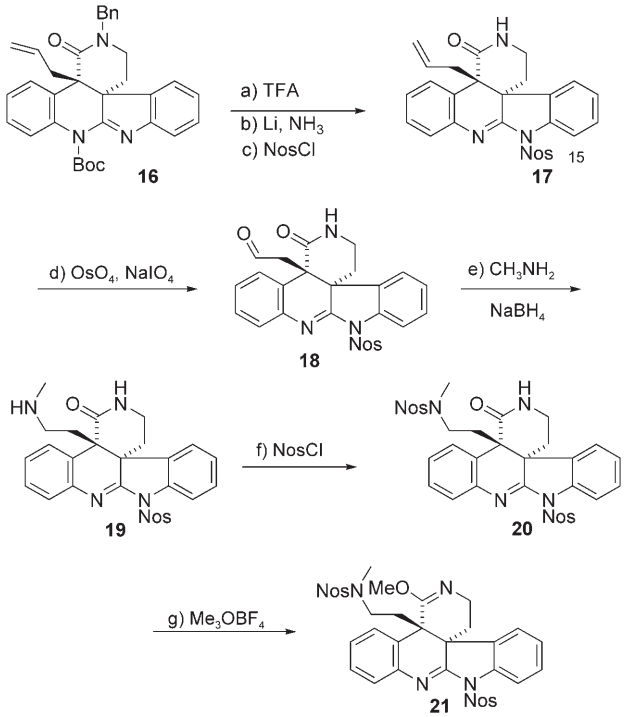
With ready access to **16**, all that remained to complete the synthesis of dehaloperophoramidine was the generation of the A ring (Scheme 1). We anticipated accomplishing this aim by converting the olefin in **16** into the corresponding amine, activating the lactam, and carrying out the requisite cyclization reaction to the C24 amidine. To accomplish these goals, we first needed to remove the benzyl group on the lactam. Although **16** decomposed when subjected to dissolving-metal conditions, we were able to affect the removal of the benzyl group when the N11 Boc group was absent. Thus, removal of the Boc group from **16** and subjecting the resulting compound to dissolving-metal conditions gave **17** after the selective formation of the *o*-nitrobenzensulfonyl (nosyl)-protected amidine. Interestingly, as evidenced by the downfield shift of the C15 proton in **17** relative to **16**, this latter reaction resulted in the selective formation of the N13 nosyl derivative. Oxidative cleavage of the alkene and reductive amination gave **19**. Conversion of the secondary amine into the



Scheme 4. Cyclization to the perophoramidine pentacycle: a) MsCl, pyridine, 0°C, 4 h; b) DBU, CH_2Cl_2, 0°C→RT (R = Bn: 79%, 3 steps; R = H: 0%). Ms = methanesulfonyl chloride.

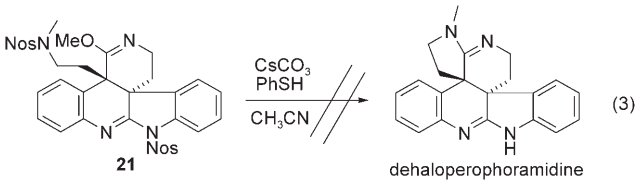
 © 2006 Wiley-VCH Verlag GmbH & Co. KGaA, Weinheim

corresponding nosyl derivative gave **21** after activation of the lactam through its conversion into the corresponding methyl imidate (Scheme 5).



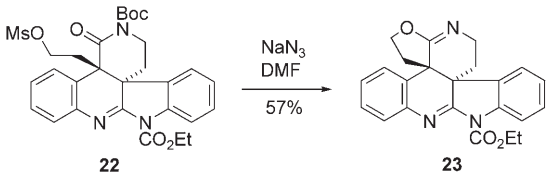
Scheme 5. Generation of the perophoramidine A-ring precursor: a) TFA, 0°C→RT, 12 h; b) Li, NH_3, THF, −78°C, 10 min; c) Boc_2O, NEt_3, THF, 0°C→RT, 8 h (69%, 3 steps); d) OsO_4, $NaIO_4$, NaOAc, THF, H_2O, 0°C, 3 h; e) CH_3NH_2·HCl, NaOAc, MeOH, RT, 7 h; $NaBH_4$, 0°C, 1 h; f) NosCl, NEt_3, THF, 0°C→RT, 12 h (42%, 3 steps); g) Me_3OBF_4, iPr_2NEt, CH_2Cl_2, 0°C, 1 h (44%). Nos = nosyl.

In the last critical transformation to dehaloperophoramidine, attempts to form the A ring under the conditions developed by Fuchs and Funk were completely unsuccessful in our hands.[15] As an indication of its lack of reactivity, we also were unable to convert the methyl imidate (or the corresponding imido triflate) in **21** into the corresponding amidine [Eq. (3)] through its intermolecular coupling with methyl amine or ammonia.



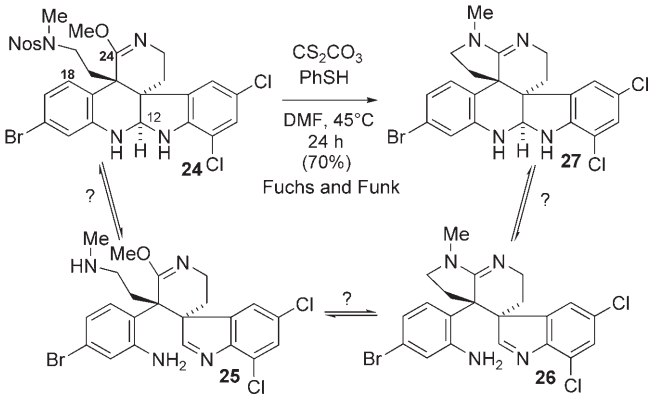
(3)

Interestingly, when we attempted to generate the azido substrate that corresponded to **22** as a precursor to a C24 amidine from an aza-Wittig reaction, we isolated *O*-alkylated adduct **23** [Eq. (4)]. Our attempts to use a similar reaction to form an acyclic amidine were unsuccessful as a result of our aforementioned inability to generate the requisite acyclic amidine precursor.



(4)

The significant difference between the successful substrate prepared by Fuchs and Funk (namely, **24**) and ours was the oxidation state of C12; they had employed a C12 aminal to our amidine. As we believe steric congestion at C24 to be the problem with imidate **21**, we suspected that the success of Fuchs and Funk with **24** might be related to its ability to undergo a reversible ring-opening reaction to temporarily relieve some of the congestion about C24 in the course of its conversion into **27** (Scheme 6).[16]

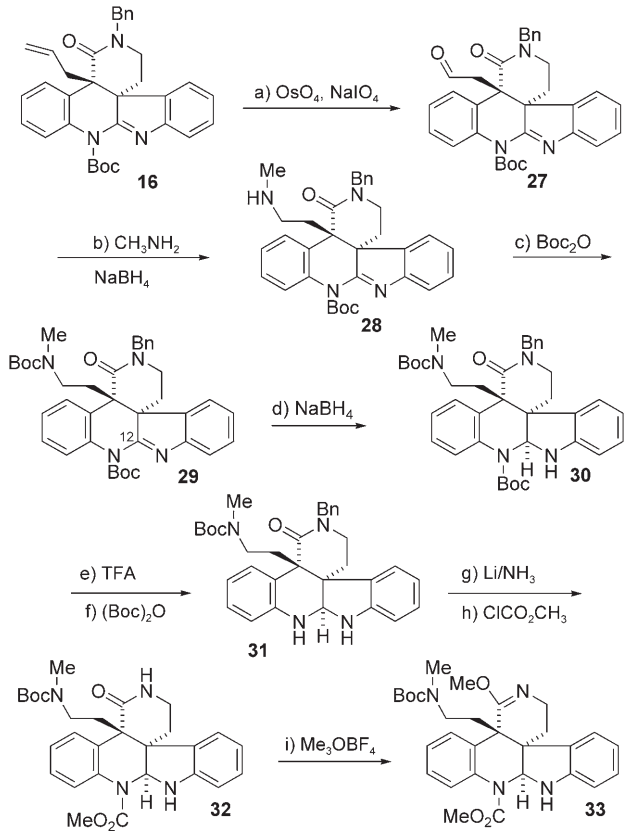


Scheme 6. Proposed mechanism for the cyclization to amidine **27** developed by Fuchs and Funk. DMF = dimethylformamide.

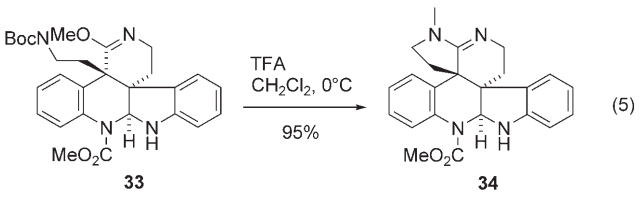
With this hypothesis driving our efforts, we synthesized the C12 aminal cyclization precursor from the allyl alkylation adduct **16** (Scheme 7). Oxidative cleavage and reductive amination gave **28**. Incorporation of the Boc group onto the secondary amine and reduction of the C12 amidine gave **30**. Note that reduction of the amidine did not occur during the reductive amination reaction. Aminal generation at C12 and global removal of the Boc groups gave **31** after reintroduction of the Boc moiety onto the secondary amine. Reductive removal of the benzyl group and selective incorporation of the methyl carbamate at N11 gave **32**.[17] Finally, conversion of the amide into the corresponding methyl imidate with trimethyloxonium tetrafluoroborate gave the targeted cyclization precursor **33**.

With **33** in hand, it remained to remove the Boc group and induce cyclization. We were pleased to find that exposure of **33** to trifluoroacetic acid (TFA) not only resulted in the removal of the Boc group but also led to the generation of the desired C24 amidine in 95% yield [Eq. (5)].

 © 2006 Wiley-VCH Verlag GmbH & Co. KGaA, Weinheim



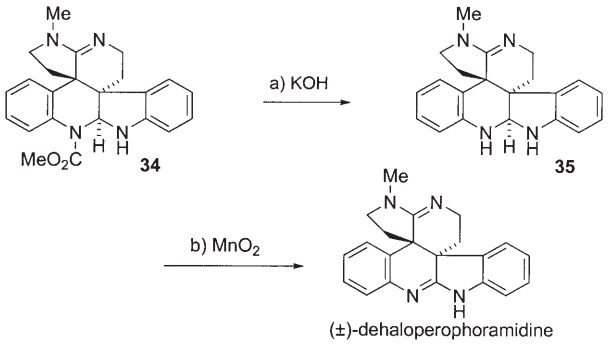
Scheme 7. Conversion of pentacycle **16** into imidate cyclization precursor **33**: a) OsO_4, $NaIO_4$, NaOAc, THF, H_2O, 0 °C, 3 h (72 %); b) CH_3NH_2·HCl, NaOAc, MeOH, RT, 7 h; $NaBH_4$, 0 °C, 1 h; c) Boc_2O, NEt_3, THF, 0 °C→RT, 12 h (82 %, 2 steps); d) $NaBH_4$, EtOH, 0 °C→RT, 18 h (89 %); e) TFA, CH_2Cl_2, 0 °C→RT, 8 h; f) Boc_2O, NEt_3, THF (97 %, 2 steps); g) Li, NH_3, THF, NH_4Cl, −78 °C; h) $ClCO_2CH_3$, pyridine, CH_2Cl_2, temp, time (88 %, 2 steps); i) Me_3OBF_4, $NaHCO_3$, CH_2Cl_2, 0 °C, 1 h (81 %).



(5)

To complete the synthesis of dehaloperophoramidine, it remained to remove the methyl carbamate and oxidize the aminal to the corresponding amidine. This occurred uneventfully; exposure of **34** to KOH and MeOH followed by oxidation with MnO_2 under the conditions developed by Fuchs and Funk gave (±)-dehaloperophoramidine, whose spectral data matched the data reported by Ireland and coworkers (Scheme 8).[2]

In conclusion, we have successfully generated (±)-dehaloperophoramidine from a highly efficient spirocyclization reaction of a readily available 2-thiotryptamine derivative. We are currently examining this reaction in the synthesis of other interesting alkaloids, including members of the communesin family. These efforts will be reported in due course.



Scheme 8. Completion of the preparation of (±)-dehaloperophoramidine: a) KOH, MeOH, H_2O, 100 °C, 6 h (71 %); MnO_2, CH_2Cl_2, RT, 0.5 h (64 %).

Received: April 1, 2006
Published online: May 30, 2006

Keywords: communesin · cyclization · natural products · perophoramidine · thioindoles

[1] For recent reviews, see: a) W. Gul, M. T. Hamann, *Life Sci.* **2005**, *78*, 442; b) J. W. Blunt, B. R. Copp, M. H. G. Munro, P. T. Northcote, M. R. Prinsep, *Nat. Prod. Rep.* **2006**, *23*, 26, and references therein.
[2] S. M. Verbitski, C. L. Mayne, R. A. Davis, G. P. Concepcion, C. M. Ireland, *J. Org. Chem.* **2002**, *67*, 7124.
[3] J. R. Fuchs, R. L. Funk, *J. Am. Chem. Soc.* **2004**, *126*, 5068.
[4] J.-B. Denault, G. S. Salvesen, *Chem. Rev.* **2002**, *102*, 4489.
[5] a) J. D. Rainier, A. R. Kennedy, *J. Org. Chem.* **2000**, *65*, 6213; b) J. D. Rainier, A. R. Kennedy, E. Chase, *Tetrahedron Lett.* **1999**, *40*, 6325.
[6] a) A. R. Kennedy, M. H. Taday, J. D. Rainier, *Org. Lett.* **2001**, *3*, 2407; b) A. N. Novikov, A. R. Kennedy, J. D. Rainier, *J. Org. Chem.* **2003**, *68*, 993; c) A. M. Nyong, J. D. Rainier, *J. Org. Chem.* **2005**, *70*, 746.
[7] For the use of 2-thioindoles to generate indolines with quaternary substitution at C3, see: K. S. Feldman, D. B. Vidulova, A. G. Karatjas, *J. Org. Chem.* **2005**, *70*, 6429.
[8] Our attempts to employ thionium ylide rearrangements to the perophoramidine skeleton were unsuccessful; for examples of this reaction, see reference [6].
[9] A. Numata, C. Takahashi, Y. Ito, T. Takada, K. Kawai, Y. Usami, E. Matsumura, M. Imachi, T. Ito, T. Hasegawa, *Tetrahedron Lett.* **1993**, *34*, 2355.
[10] A. R. Kennedy, PhD Dissertation, University of Arizona, **2001**.
[11] See R. B. Woodward, M. P. Cava, W. D. Ollis, A. Hunger, H. U. Daeniker, K. Schenker, *Tetrahedron* **1963**, *19*, 247.
[12] J. F. M. Da Silva, S. J. Garden, A. C. Pinto, *J. Braz. Chem. Soc.* **2001**, *12*, 273.
[13] W. E. Stewart, T. H. Siddall III, *Chem. Rev.* **1970**, *70*, 517.
[14] G. D. Artman III, S. M. Weinreb, *Org. Lett.* **2003**, *5*, 1523.
[15] We also explored a number of other basic and acidic conditions without success.
[16] An examination of molecular models of **21** and **24** indicates that approach of the amine onto the C24 imidate carbon is blocked by the C18 proton; the formation of **25** allows the aromatic ring to rotate, thus alleviating this problem.
[17] When the aminal was protected with a Boc group, reductive removal of the benzyl group resulted in the decomposition of the perophoramidine ring system.

 © 2006 Wiley-VCH Verlag GmbH & Co. KGaA, Weinheim

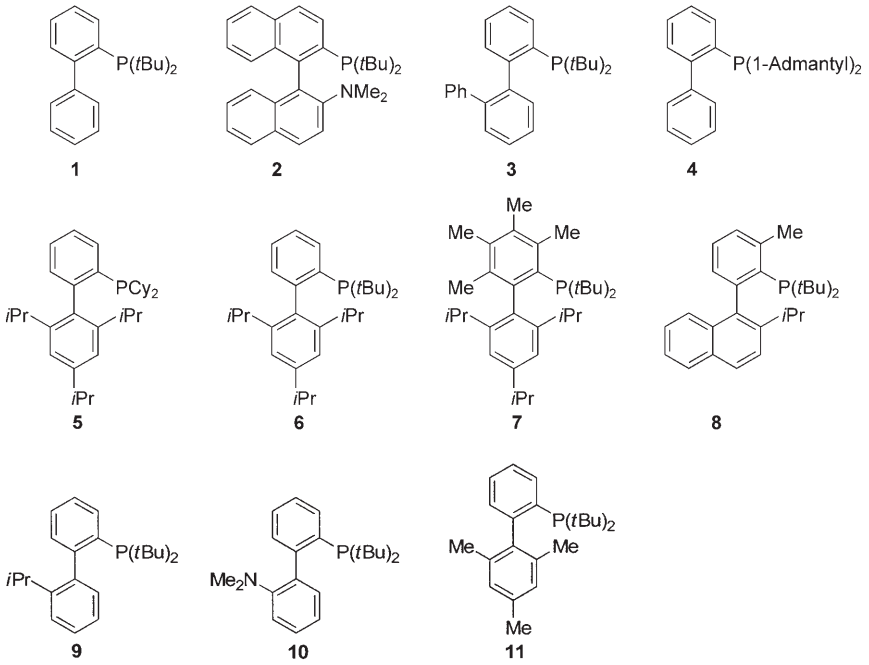
C–O Bond Formation

DOI: 10.1002/anie.200601253

Significantly Improved Method for the Pd-Catalyzed Coupling of Phenols with Aryl Halides: Understanding Ligand Effects**

*Carlos H. Burgos, Timothy E. Barder, Xiaohua Huang, and Stephen L. Buchwald**

The diaryl ether unit is a common structural feature in numerous natural products and biologically interesting compounds.[1,2] These ethers have traditionally been prepared by the reaction of aryl halides with sodium or potassium aryl oxides promoted by copper reagents (the classical Ullmann diaryl synthesis).[3] However, these classic conditions require elevated temperatures and stoichiometric amounts of copper and often result in yields that range from low to moderate. As such, this powerful transformation has limited utility, thus the development of new methods for the preparation of diaryl ethers under relatively mild reaction conditions has received much attention in recent years.[4–7] Even in view of recent improvements, reactions with certain substrate combinations remain difficult, hence the need for more general methods for the preparation of diaryl ethers. Our group, as well as those of Hartwig and Beller, has previously reported palladium-catalyzed procedures for diaryl ether formation.[7] Previously, we demonstrated that the cross-coupling of electron-deficient, electron-neutral, and electron-rich aryl halides and sulfonates with a variety of phenols could be conducted in high yield under relatively mild conditions.[7d] However, limitations still remain: little-to-no product was observed from the reactions of phenols with aryl halides that possess either strongly electron-withdrawing or electron-donating *ortho* substituents. Similarly, electron-deficient phenols were poor substrates. Additionally, the reaction of phenols that did not possess an *ortho* substituent at least as large as a methyl group were inefficient in most cases. The use, in many examples, of ligands that are neither commercially nor readily available further detracts from the utility of our previous method (compounds **2**–**4**, Scheme 1). These limitations provoked us to further investigate and develop catalyst systems that would allow for the efficient coupling of problematic substrate combinations. Herein, we report the expansion of this methodology by overcoming the above-mentioned difficulties as well as the coupling of heteroaryl halides with phenols through the use of two new ligands.



Scheme 1. Biaryl ligands for carbon–heteroatom bond-forming reactions.

The success of our previous methodology was based on the use of electron-rich, bulky biaryl dialkyl phosphines **1**–**4** as ligands (Scheme 1).[7d] Continuing studies in this area have led to the discovery of structural derivatives of these ligands that generate catalyst systems with both a greater degree of activity and stability. We previously reported that 2-dicyclohexylphosphino-2′,4′,6′-triisopropylbiphenyl (XPhos; **5**) is an excellent supporting ligand for Pd-catalyzed C–N and C–C bond-forming reactions.[8] During the course of these investigations, the use of 2-di-*tert*-butylphosphino-2′,4′,6′-triisopropylbiphenyl (di-*t*BuXPhos; **6**), the more hindered counterpart of **5**, was examined. Whereas the reactivity of catalysts based upon **6** in C–N and C–C bond-forming processes was less than those based on **5**, we hypothesized that the increased size of **6** would prove beneficial in C–O bond-forming reactions.[9] Subsequently, we prepared and tested the more hindered analogue **7** in coupling reactions of aryl halides and phenols. The one-pot preparation of **7** proceeded in 62% yield from 2,4,6-tri-isopropyl bromobenzene, 1,2-dibromo-3,4,5,6-tetramethylbenzene, and chloro(di-*tert*-butylphosphine) (Scheme 2).[10]

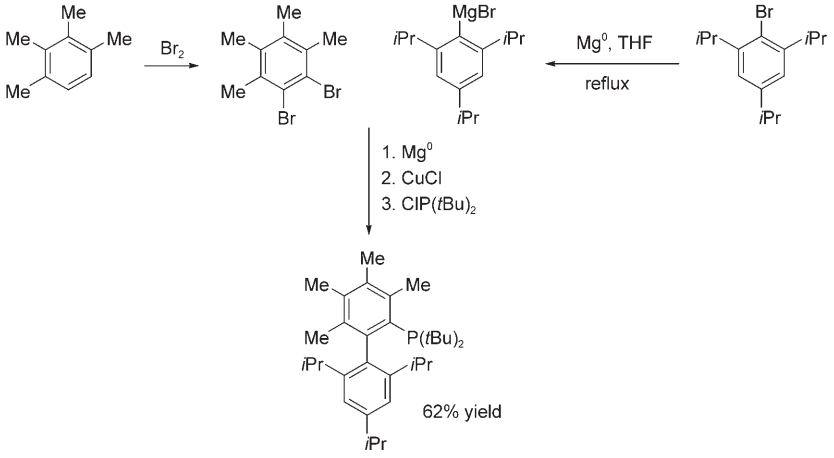
Initially, the reaction of a number of electron-deficient aryl halides with phenols with **6** as the supporting ligand was examined (Table 1). A variety of aryl bromides were coupled with a range of phenols in excellent yield. Common functional groups, including nitriles, aldehydes, ketones, esters, and trifluoromethyl groups, were tolerated under the reaction conditions employed. In contrast to previous results, good

[*] Dr. C. H. Burgos, T. E. Barder, Dr. X. Huang, Prof. Dr. S. L. Buchwald
Department of Chemistry
Room 18-490, Massachusetts Institute of Technology
Cambridge, MA 02139 (USA)
Fax: (+1) 617-253-3297
E-mail: sbuchwal@mit.edu

[**] We thank the National Institutes of Health (GM 58160) for funding and Merck, Amgen, and Boehringer-Ingelheim for additional unrestricted support.

Supporting information for this article is available on the WWW under http://www.angewandte.org or from the author.

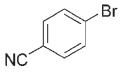
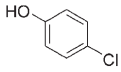
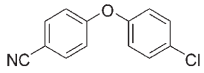
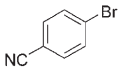
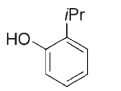
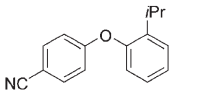
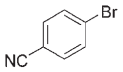
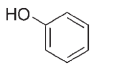
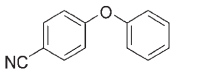
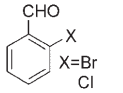
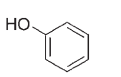
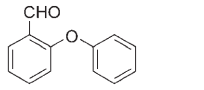
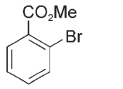
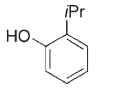
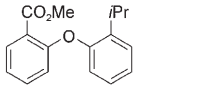
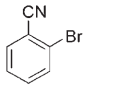
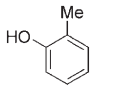
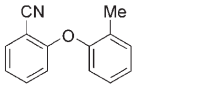
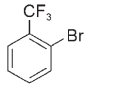
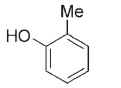
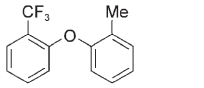
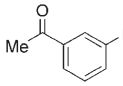
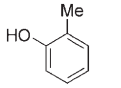
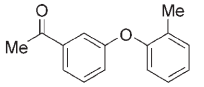
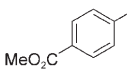
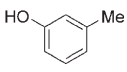
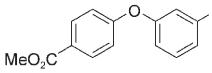
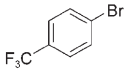
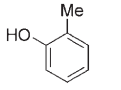
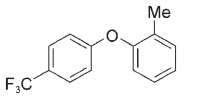
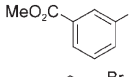
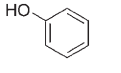
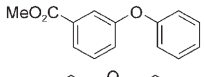
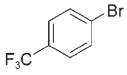
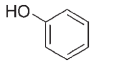
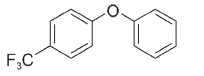
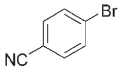
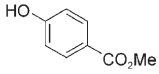
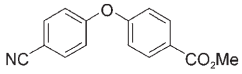
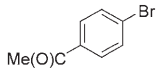
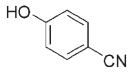
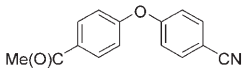
 © 2006 Wiley-VCH Verlag GmbH & Co. KGaA, Weinheim



Scheme 2. Synthesis of ligand **7**.

yields were observed with aryl halide substrates that possess electron-withdrawing groups in the *ortho* position (Table 1, entries 4–7). The exception to this outcome were reactions that involved 2-bromoacetophenone, which did not yield any product. Furthermore, whereas the coupling of electron-deficient phenols with aryl halides was problematic in previous reports (presumably because of the lower nucleophilicity of the corresponding phenolates), the use of a catalyst based upon **6** for these substrate combinations proved to be highly efficient. For example, we were able to couple methyl 4-hydroxybenzoate and 4-cyanophenol with 4-bromobenzonitrile and 4′-acetophenone, respectively, in high yield (Table 1, entries 1, 13, and 14).

Table 1: Pd-catalyzed C–O bond formation of electron-poor aryl halides with ligand **6**.[a]

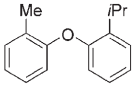
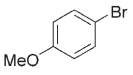
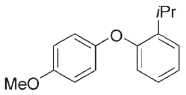
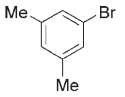
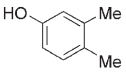
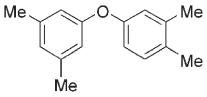
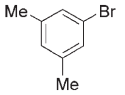
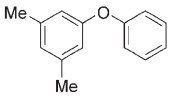
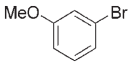
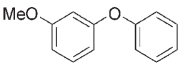
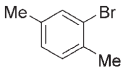
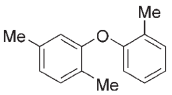
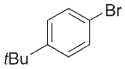
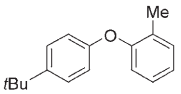
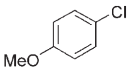
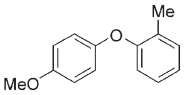
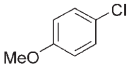
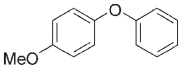
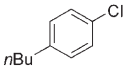
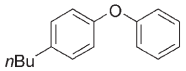
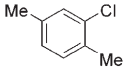
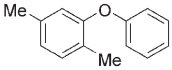
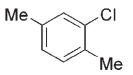
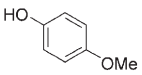
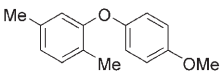
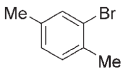
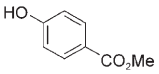
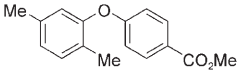
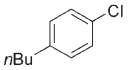
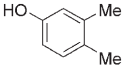
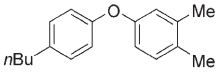
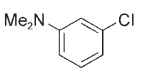
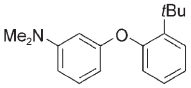
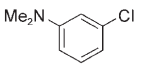
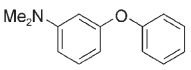
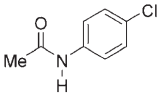
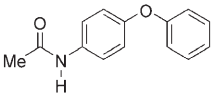
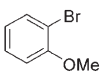
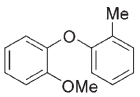
Entry	Halide	Phenol	Product	Pd [mol%]	Yield [%][b]
1				2	96
2				2	84
3				2	94
4				3	81[c] 85[c]
5				3	78[c]
6				2	91
7				3	85[c]
8				1	92
9				2	92
10				1	94
11				1	92
12				1	90
13				2	82
14				3	74[c]

[a] Reaction conditions: aryl halide (1 equiv), phenol (1.2 equiv), K_3PO_4 (2 equiv), **6** (3 mol%), toluene (0.3 M), 100 °C, 5–24 h; reaction times not optimized. [b] Yields based upon an average of two runs. [c] Reaction run with 5 mol% of **6** at 110 °C.

 © 2006 Wiley-VCH Verlag GmbH & Co. KGaA, Weinheim

Next, we investigated reactions of electron-neutral and electron-rich aryl halides with various phenols. Catalyst systems based upon **6** were efficient in many cases; however, certain combinations of substrates required the use of the more hindered ligand **7**. Table 2 illustrates that both electron-rich and electron-neutral aryl bromides and chlorides were

Table 2: Pd-catalyzed diaryl ether formation of electron-neutral and electron-rich aryl halides.[a]

Entry	Halide	Phenol	Product	Ligand	Pd [mol%]	Yield [%][b]
1				**6**	1	84
2				**6**	1	74
3				**6**	2	91
4				**6**	2	86
5				**7**	2	86
6				**6**	1	92
7				**6**	1	92
8				**6**	2	84
9				**7**	2	89
10				**7**	2	96
11				**7**	2	89
12				**7**	5	79
13				**6**	2	77[c]
14				**7**	2	94
15				**6**	2	88
16				**7**	2	84
17				**6**	2	95
18				**8**	2	84

[a] Reaction conditions: aryl halide (1.0 equiv), phenol (1.2 equiv), K_3PO_4 (2.0 equiv), ligand (3.0 mol%), toluene (0.3 M), 100°C, 5–24 h; reactions times were not optimized. [b] Yields based upon an average of two runs. [c] Reaction run with 7.0 mol% of ligand **8** at 115°C.

 © 2006 Wiley-VCH Verlag GmbH & Co. KGaA, Weinheim

excellent substrates with either **6** or **7**. For example, the reaction of an electron-rich aryl chloride, 4-chloroanisole, with phenolic derivatives afforded the corresponding diaryl ethers in > 80% yield (Table 2, entries 8 and 9). Of particular note, the reaction of *N*-(4-chlorophenyl)acetamide with phenol proceeded in 95% yield (Table 2, entry 17). To the best of our knowledge, there are no previous examples of the use of an aryl halide substrate bearing a secondary amide substituent in Pd-catalyzed diaryl ether synthesis. Additionally, we were able to couple an electron-deficient phenol, methyl 4-hydroxybenzoate, with an electron-neutral aryl bromide, 2-bromo-*p*-xylene, for the first time (Table 2, entry 13). However, more forcing conditions were required for this transformation: a reaction temperature of 115 °C and the use of 7 mol% of **6** and 5 mol% of $Pd(OAc)_2$. Disappointingly, 2-bromoanisole could not be coupled with phenols when employing ligands **6** and **7**, although this substrate could be coupled with *o*-cresol in 89% yield (Table 2, entry 18) with a naphthyl-substituted ligand **8** (Scheme 1). Although this ligand was effective, it was synthesized in low yield by using a modification of the standard benzyne-coupling protocol. Currently, we do not have a convenient high-yielding synthetic route for preparation of **8**.

The cross-coupling reactions of halopyridines and haloquinolines with phenols was also explored. Using the standard protocol with **6** and **7**, we were able to obtain heteroaryl ethers in good-to-excellent yield (Table 3). The majority of reactions required only 2 mol% of $Pd(OAc)_2$; however, two entries required higher catalyst loadings (Table 3, entries 2 and 3). Attempts to use 2- and 4-hydroxypyridine (that is, 2- and 4-pyridone) were entirely unsuccessful; neither C–O nor C–N bond formation was observed.

To identify structural features important for catalyst efficacy in Pd-catalyzed C–O bond-forming reactions, we undertook a structure–activity relationship study that employed various biaryl ligands (Figure 1). The four reactions shown in Scheme 3 [Eq. (1)–(4)] were conducted under identical conditions using seven different biaryl phosphine ligands (**1**, **5**–**7**, and **9**–**11**). These particular reactions were selected because of their relevance to the limitations of previous processes (see below) and to determine features that contribute to the success of particular ligands.

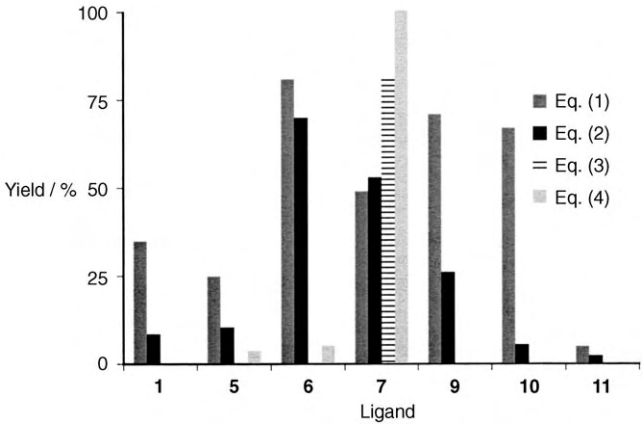
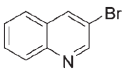
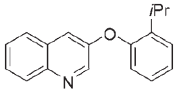
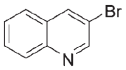
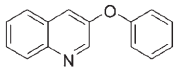
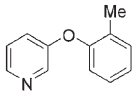
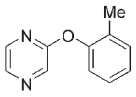
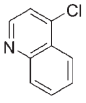
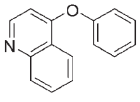
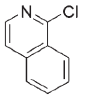
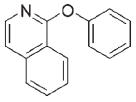
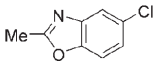
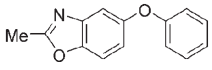


Figure 1. Illustration of the effects of various ligands on the four reactions in Scheme 3.

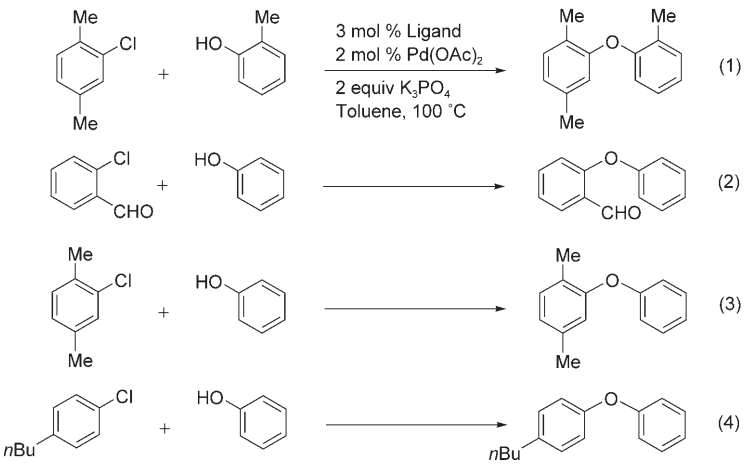
Arbitrarily, we set the level of acceptable yield at 50% for the reactions in Scheme 3. Consequently, ligands **1**, **5**, and **11**

Table 3: Pd-catalyzed heteroaryl ether formation.[a]

Entry	Halide	Phenol	Product	Ligand	Pd [mol%]	Yield [%][b]
1				**6**	2	90
2				**7**	4	75[c]
3				**6**	8	88[d]
4				**6**	2	87
5				**6**	2	86
6				**6**	2	90
7				**7**	2	91

[a] Reaction conditions: aryl halide (1.0 equiv), phenol (1.2 equiv), K_3PO_4 (2.0 equiv), ligand (3.0 mol%), toluene (0.3 M), 100 °C, 24 h; reactions times were not optimized. [b] Yields based upon an average of two runs. [c] Reaction run with 6.0 mol% of ligand **7** at 115 °C. [d] Reaction run with 10.0 mol% of ligand **10** at 115 °C.

 © 2006 Wiley-VCH Verlag GmbH & Co. KGaA, Weinheim

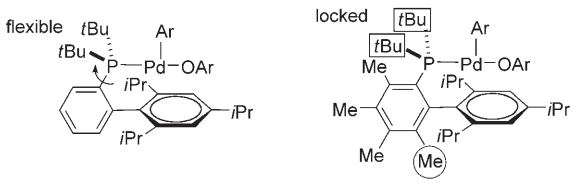


Scheme 3. Test reactions for comparison of ligands in Pd-catalyzed diaryl ether synthesis.

did not meet this requirement for any reaction in Scheme 3. For the coupling of chloro-*p*-xylene with *o*-cresol [Eq. (1)], four ligands (**6**, **7**, **9**, and **10**) were found to provide adequate results. This coupling is relatively easy and the data is consistent with previous reports with *ortho* alkyl-substituted phenols.[7d] However, the reaction of 2-chlorobenzaldehyde [Eq. (2)] with phenol was only found to be efficient with ligands **6** and **7**. Furthermore, the final two reactions in Scheme 3 [Eqs (3) and (4)] were catalyzed only with **7**, and a maximum of 10% yield was observed with ligands other than **7**. The coupling of 2-chloro-*p*-xylene with phenol [Eq. (3)] was effective with previous ligands; however, the reaction required sodium phenoxide in conjunction with **2** (79% yield). Pleasingly, the use of ligand **7** with a much weaker base, K_3PO_4, for this transformation affords an 88% yield of *p*-xylyl phenyl ether. The use of similarly harsh conditions were required for the coupling of 4-*n*-butylchlorobenzene with phenol [Eq. (4)]; for example, the use of sodium phenoxide with **2** at 115 °C. Again, the application of **7** in this reaction allows for the use of K_3PO_4 at 100 °C, with the product formed in a 96% yield. Based upon these results, it is clear that **7** possess(es) some structural feature(s) that generate a catalyst capable of promoting reactions of aryl halides with phenol that no other biaryl ligand has been able to achieve.

We believe the efficacy of reactions with these ligands depends on three steric factors: the substituents at the phosphorous center, the *ortho* substituents on the bottom ring, and the substituents on the top ring. For example, ligand **1** possesses two *tert*-butyl groups and a biphenyl unit at the phosphorous center. Under the conditions examined, this ligand is ineffective for all the reactions in Scheme 3. Ligand **5** is similarly ineffective as there are two cyclohexyl groups at the phosphorous center and three isopropyl groups at the 2′, 4′, and 6′ positions of the non-phosphine-containing ring of the ligand. It is believed this ligand is inefficient because the steric environment the cyclohexyl groups create directly around the phosphorous atom is relatively small. However, the combination of features in ligands **1** and **5** produce the much bulkier ligand **6**. Further increase in the size by addition of four methyl groups to the top ring of **6** yields **7**. Although **6** is less substituted than **7**, its use provides better results than **7** in Equations (1) and (2). Presuming that reductive elimination is the rate-limiting step in the reactions in Scheme 3, it is possible that in Equations (1) and (2) the added bulk of **7** is unnecessary to aid the reductive elimination from the [LPd(OAr)Ar] (L = ligand) intermediate. Furthermore, formation of the [LPd(OAr)Ar] intermediate with ligand **7** in Equation (1) may be slow because of the more difficult attack of the larger *o*-cresol versus phenoxide anion [for Eqs (3) and (4)] onto the [LPd(Ar)X] intermediate. However, once the [LPd(OAr)Ar] intermediate is formed, the inclusion of a greater degree of bulk (that is, the use of ligand **7**) can lead to a significantly enhanced rate of reductive elimination.

An addendum to this theory involves the requirement of permethylation of the top ring (the phosphine-containing ring) for certain reactions. It still remains difficult to understand the large influence of the methyl groups in the tetramethylated ring in **7**. It does not seem that the methyl groups increase the size of the ligand to such an extent that the reactivity is altered from minimal (for **6**) to excellent (for **7**) as it is in the last two reactions in Scheme 3. Therefore, it seems possible that the permethylated top ring may play another role in these reactions, namely, the methyl groups on **7** may "lock" the ligand into a certain conformation so that the methyl group *ortho* to the phosphorous center may act as a physical divide between the two *tert*-butyl groups (by locking them into a certain conformation). If this is the case, it is likely that the *tert*-butyl groups would be forced forward toward the Pd center, thereby ensuring that their influence is felt on the aryl and aryloxide units bound to the palladium center (Scheme 4). Additionally, the circled methyl group may instill



Scheme 4. Possible influences of methyl groups and lack thereof on **6** and **7**.

further conformational rigidity in the catalyst. We believe it is important for reductive elimination to occur rapidly, thereby minimizing the ability of the likely unstable [LPd(OAr)Ar] species to decompose or enter an alternate reaction manifold not leading toward the product. Further work is ongoing in our laboratories to determine the effects these various structural aspects of these bulky ligands on C–O bond-forming processes.

In summary, we have improved the scope and generality of Pd-catalyzed diaryl ether formation. This system allows the coupling of electron-deficient aryl halides almost without any restrictions. Additionally, we expanded this method to the cross-coupling reaction of halopyridines and quinolines. A

 © 2006 Wiley-VCH Verlag GmbH & Co. KGaA, Weinheim

structure–activity relationship study suggests the ligand bulk plays an important role in C–O bond-forming reactions possibly through instilling conformational rigidity in intermediates within the catalytic cycle.

Received: March 31, 2006
Published online: May 30, 2006

Keywords: biaryl phosphines · C–O bond formation · palladium · substituent effects · synthetic methods

[1] For reviews, see: a) J. Lindley, *Tetrahedron* **1984**, *40*, 1433 – 1456; b) J. S. Sawyer, *Tetrahedron* **2000**, *56*, 5045 – 5065.
[2] For examples of medicinally important diaryl ethers, see: a) S. Zenitani, S. Tashiro, K. Shindo, K. Nagai, K. Suzuki, M. Imoto, *J. Antibiot.* **2003**, *56*, 617 – 621; b) P. Cristau, J.-P. Vors, J. Zhu, *Tetrahedron* **2003**, *59*, 7859 – 7870; c) D. A. Evans, K. M. DeVries in *Glycopeptide Antibiotics, Drugs and the Pharmaceutical Sciences* (Ed.: R. Nagarajan), Marcel Decker, New York, **1994**, pp. 63 – 104; d) V. E. Deshpande, N. J. Gohkhale, *Tetrahedron Lett.* **1992**, *33*, 4213 – 4216; e) S. B. Singh, G. R. Pettit, *J. Org. Chem.* **1990**, *55*, 2797 – 2800; f) M. E. Jung, J. C. Rohloff, *J. Org. Chem.* **1985**, *50*, 4909 – 4913; for examples of agriculturally important diaryl ethers, see: g) R. A. Seldon, *Chirotechnology*, Marcel Dekker, New York, **1998**, pp. 62 – 65.
[3] a) F. Ullmann, *Ber. Dtsch. Chem. Ges.* **1904**, *37*, 853 – 854; for general reviews, see: Reference [1a].
[4] For recent examples of copper-catalyzed diaryl ether formation, see: a) Q. Cai, B. Zou, D. Ma, *Angew. Chem.* **2006**, *118*, 1298 – 1301; *Angew. Chem. Int. Ed.* **2006**, *45*, 1276 – 1279; b) D. Ma, Q. Cai, *Org. Lett.* **2003**, *5*, 3799 – 3802; c) E. Buck, Z. J. Song, D. Tschaen, P. G. Dormer, R. P. Volante, P. J. Reider, *Org. Lett.* **2002**, *4*, 1623 – 1626; d) R. K. Gujadhur, C. G. Bates, D. Venkataraman, *Org. Lett.* **2001**, *3*, 4315 – 4317; e) C. Palomo, M. Oiarbide, R. Lopez, E. Gomez-Bengoa, *Chem. Commun.* **1998**, 2091 – 2092; f) J.-F. Marcoux, S. Doye, S. L. Buchwald, *J. Am. Chem. Soc.* **1997**, *119*, 10539 – 10540.
[5] For recent examples of copper-catalyzed coupling reactions of aryl boronic acids or aryl boronates with phenols, see: a) D. M. T. Chan, K. L. Monaco, R. Li, D. Bonne, C. G. Clark, P. Y. S. Lam, *Tetrahedron Lett.* **2003**, *44*, 3863 – 3865; b) C. P. Decicco, S. Song, D. A. Evans, *Org. Lett.* **2001**, *3*, 1029 – 1032; c) P. Y. S. Lam, G. Vincent, C. Clark, S. Deudon, P. K. Jadhav, *Tetrahedron Lett.* **2001**, *42*, 3415 – 3418; d) M. E. Jung, T. I. Lazarova, *J. Org. Chem.* **1999**, *64*, 2976 – 2977; e) D. M. T. Chan, M. P. Winters, K. L. Monaco, R. Wang, *Tetrahedron Lett.* **1998**, *39*, 2933 – 2936; f) D. A. Evans, J. L. Katz, T. R. West, *Tetrahedron Lett.* **1998**, *39*, 2937 – 2940.
[6] For examples of microwave-irradiation-assisted aryl ether formation, see: a) H. He, Y.-J. Wu, *Tetrahedron Lett.* **2003**, *44*, 3445 – 3446; b) F. Li, Q. Wang, Z. Ding, F. Tao, *Org. Lett.* **2003**, *5*, 2169 – 2171; c) M. Chaouchi, A. Loupy, S. Marque, A. Petit, *Eur. J. Org. Chem.* **2002**, 1278; d) D. Bogdal, J. Pielichowski, A. Boron, *Synth. Commun.* **1998**, *28*, 3029.
[7] For examples of palladium-catalyzed diaryl ether formation, see: a) S. Harkal, K. Kumar, D. Michalik, A. Zapf, R. Jackstell, F. Rataboul, T. Riemeier, A. Monsees, M. Beller, *Tetrahedron Lett.* **2005**, *46*, 3237 – 3240; b) Q. Shelby, N. Kataoka, G. Mann, J. Hartwig, *J. Am. Chem. Soc.* **2000**, *122*, 10718; c) G. Mann, C. Incarvito, A. L. Rheigold, J. F. Hartwig, *J. Am. Chem. Soc.* **1999**, *121*, 3224; d) A. Aranyos, D. W. Old, A. Kiyomori, J. P. Wolfe, J. P. Sadighi, S. L. Buchwald, *J. Am. Chem. Soc.* **1999**, *121*, 4369 – 4378.
[8] a) X. Huang, K. W. Anderson, D. Zim, L. Jiang, A. Klapars, S. L. Buchwald, *J. Am. Chem. Soc.* **2003**, *125*, 6653 – 6655; b) H. N. Nguyen, X. Huang, S. L. Buchwald, *J. Am. Chem. Soc.* **2003**, *125*, 11818 – 11819.
[9] After this work was completed, the use of **6** for C–N bond-forming reactions with amide nucleophiles was reported: M. C. Willis, G. N. Brace, I. P. Holmes, *Synthesis* **2005**, 3229 – 3234.
[10] See the Supporting Information for details.

 © 2006 Wiley-VCH Verlag GmbH & Co. KGaA, Weinheim

Non-natural Base Pairs

DOI: 10.1002/anie.200601272

Efforts towards Expansion of the Genetic Alphabet: Pyridone and Methyl Pyridone Nucleobases**

*Aaron M. Leconte, Shigeo Matsuda, Gil Tae Hwang, and Floyd E. Romesberg**

A non-natural base pair, which is stable in duplex DNA and enzymatically synthesized with high efficiency and selectivity, would greatly expand the utility of nucleic acids, both in terms of their genetic-coding capacity and chemical functionality. Unlike the natural base pairs, a third base pair does not necessarily require H-bonding,[1] and we,[2] and others,[3] have demonstrated that hydrophobic and van der Waals forces can mediate the selective interbase interactions required for base-pair stability and synthesis.

Our early efforts focused on nucleotides bearing nucleobase analogues with large extended aromatic surfaces. A variety of self-pairs (formed between the same analogue) and heteropairs (formed between different analogues) were identified. These pairs were both stable in duplex DNA and efficiently synthesized by the exonuclease deficient Klenow fragment of DNA polymerase I (Kf).[2a,4] However, replication was consistently limited by poor extension (i.e. continued primer elongation after synthesis of the non-natural pair), which we reasoned could be the result of interbase intercalation of the large aromatic scaffolds that distort the newly formed primer terminus and prevent its efficient extension. Our second-generation non-natural base pairs were formed between nucleotides that bear small, aromatic nucleobase analogues that were designed to be too small to intercalate and therefore more likely to interact edge on. Although several base pairs have been found that are more efficiently extended by Kf, the rates remain insufficient.[2b,5] Further-

[*] A. M. Leconte, S. Matsuda, G. T. Hwang, Prof. Dr. F. E. Romesberg
Department of Chemistry
The Scripps Research Institute
La Jolla, CA 92037 (USA)
Fax: (+1) 858-784-7472
E-mail: floyd@scripps.edu

[**] Acknowledgement for financial support is given to the National Institutes of Health (GM60005 to F.E.R.).

Supporting information for this article is available on the WWW under http://www.angewandte.org or from the author.

WILEY InterScience DISCOVER SOMETHING GREAT
© 2006 Wiley-VCH Verlag GmbH & Co. KGaA, Weinheim

more, many of the smaller analogues bearing small hydrophobic nucleobases are also limited by facile and stable mispairing with dA.[2b,11] Thus, although small aromatic nucleobase analogues are promising, further optimization is required.

One factor that may contribute to the reduced Kf-mediated extension of the small aromatic pairs is their inability to engage the polymerase at a primer terminus. The natural base pairs have a similar geometric shape with a hydrogen bond acceptor located in an analogous position in the minor groove, N3 in purines or O2 in pyrimidines. When at the primer terminus, these H-bond acceptors have been shown to be important for polymerase-mediated extension.[6,7] Herein, we report the synthesis and characterization of nucleotides bearing pyridone-nucleobase analogues that are expected to position their carbonyl group into the minor groove (Figure 1a).

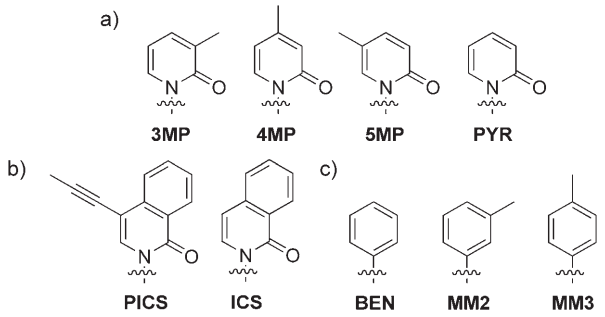


Figure 1. Non-natural nucleobases. a) Pyridone analogues, b) previously reported ICS analogues,[2a,4] and c) previously reported carbocyclic analogues.[9,11] 3MP = 3-methylpyridone, 4MP = 4-methylpyridone, 5MP = 5-methylpyridone, PYR = pyridone.

The β-nucleotides, triphosphates, and phosphoramidites of the pyridone analogues were synthesized by a modification of a literature procedure[8] as described in the Supporting Information. To evaluate the thermodynamic stability of the non-natural base pairs in duplex DNA, each non-natural nucleoside was incorporated into complementary oligonucleotides and the melting temperature (T_m) of the resulting duplexes was determined by thermal denaturation experiments (Table 1). The non-natural self-pairs are generally more stable than mispairs formed with natural nucleotides, with T_m values that range from 49.3 to 53.4 °C. With the exception of **3MP**, which is 3 °C more stable than the other self-pairs, the T_m values are only slightly dependent on methyl substitution. The relative stability of the **3MP** self-pair likely reflects optimized packing of the 3-position methyl groups in the interbase interface. Also, with the exception of **3MP**, these pyridone self-pairs are less stable than the self-pairs of the corresponding carbocyclic analogues (Figure 1c).[9] This relative destabilization may result from reduced hydrophobicity and/or from electrostatic repulsion between the carbonyl groups in the minor groove.

To examine the thermal orthogonality of the non-natural base pairs, we determined the duplex melting temperatures with the non-natural nucleotides paired opposite each natural nucleotide (Table 1). These mispairs are significantly less stable than even the least-stable self-pair, with the exception of the mispairs with dG. The relative stability of the mispairs with dG is likely due to the increased aromatic surface area of guanine, as well as its exocyclic minor-groove amine, which may H-bond with the pyridone-nucleobase analogues. In contrast, the fully carbocyclic analogues form their most stable mispairs with dA,[9] likely due to the increased hydrophobicity of adenine relative to the other natural nucleobases. Relative to substitution at the 4- or 5-position, substitution at the 3-position has a more variable effect on mispair stability: it has little effect on the mispair with dA, stabilizes the mispairs with dC and dT, and destabilizes the mispair with dG. The stability of the **3MP** self-pair and the destabilization of the **3MP**:dG mispair results in a self-pair thermal selectivity of 2–7 °C, which approaches that of a natural base pair.[10]

Table 1: T_m values of DNA duplexes.[a]

5′-dGCGTAC**X**CATGCG
3′-dCGCATG**Y**GTACGC

X	Y	T_m [°C]	X	Y	T_m [°C]
3MP	**3MP**	53.4	**5MP**	**5MP**	49.3
3MP	A	49.4	**5MP**	A	48.3
3MP	C	46.4	**5MP**	C	43.3
3MP	G	51.4	**5MP**	G	52.3
3MP	T	49.4	**5MP**	T	47.3
4MP	**4MP**	50.4	**PYR**	**PYR**	50.2
4MP	A	48.4	**PYR**	A	49.2
4MP	C	44.4	**4MP**	C	43.2
4MP	G	52.4	**PYR**	G	52.2
4MP	T	47.2	**PYR**	T	47.2
A	T	59.2[10]	A	G	55.4[10]

[a] For experimental details, see the Supporting Information.

The polymerase-mediated synthesis of these pyridone self-pairs was characterized by incorporating the analogues into template DNA and measuring the rate at which Kf incorporates the non-natural triphosphates (Table 2). Self-pair synthesis was inefficient, with second-order rate constants (k_{cat}/K_M) varying between $< 10^3$ and $4 \times 10^3\,M^{-1}\,min^{-1}$ (for comparison, a natural base pair is synthesized in a similar sequence context with a rate constant of $5 \times 10^7\,M^{-1}\,min^{-1}$ [4]). The **BEN** self-pair (Figure 1) was synthesized with a similar rate,[11] suggesting that the N-glycoside moiety does not facilitate non-natural base pair synthesis, at least not within the simple pyridone scaffold. The rates for pyridone self-pair synthesis are inefficient in contrast with self-pairs formed between other N-glycoside analogues bearing larger aromatic surface areas, such as **ICS** and **PICS** (Figure 1b), which are synthesized with second-order rate constants of approximately $10^5\,M^{-1}\,min^{-1}$.[2a,4] Perhaps the intercalation of the large

Table 2: Steady-state rate constants of Kf-mediated incorporation of dXTP with dX in the template.[a]

5′-dTAATACGACTCACTATAGGGAGA
3′-dATTATGCTGAGTGATATCCCTCT**X**GCTAGGTTACGGCAGGATCGC

X	k_{cat} [min^{-1}]	K_M [μM]	k_{cat}/K_M [$M^{-1}\,min^{-1}$]
3MP	0.15 ± 0.01	76 ± 23	2.0×10^3
4MP	1.1 ± 0.2	389 ± 96	2.8×10^3
5MP	0.53 ± 0.18	135 ± 65	3.9×10^3
PYR	n.d.[b]	n.d.[b]	$< 10^3$

[a] For experimental details, see the Supporting Information. [b] Rate too slow to determine k_{cat} and K_M independently.

 © 2006 Wiley-VCH Verlag GmbH & Co. KGaA, Weinheim

aromatic rings reorients the pyridone carboxy groups or provides sufficient stabilization in the transition state to overcome their forced desolvation.

To explore synthesis as a function of methyl group substitution, we examined the synthesis of the 12 possible heteropairs (see the Supporting Information). Although most heteropairs are synthesized only inefficiently (with k_{cat}/K_M between $< 10^3$ and $6 \times 10^3\,M^{-1}\,min^{-1}$), the triphosphate of **4MP** is inserted opposite **3MP** with an efficiency of $2 \times 10^4\,M^{-1}\,min^{-1}$, which is at least fivefold more efficient than either self-pair. The increased rate results largely from an increased k_{cat}, suggesting that the interbase interface is stabilized by packing interactions between the methyl groups in the developing transition state, and, importantly, that the pyridone scaffold may be optimized for synthesis.

To examine the kinetic orthogonality against pairing with the natural bases, we characterized the ability of the pyridone nucleobases to direct Kf to incorporate the natural deoxyribonucleotide triphosphates (dNTPs; see the Supporting Information). All of the mispairs are formed with a second-order rate constant of less than $5 \times 10^4\,M^{-1}\,min^{-1}$. The most efficiently synthesized mispairs resulted from insertion of deoxyguanosine triphosphate (GTP), which was inserted against the pyridone analogues significantly faster than against the corresponding carbocyclic analogues. For the carbocyclic analogues, each templates dGTP misincorporation at rates less than $2 \times 10^3\,M^{-1}\,min^{-1}$.[11] Methyl group substitution appears to have little effect on dGTP misincorporation, thus, it seems likely that the relatively efficient synthesis of the mispair is driven by a H-bond formed between the pyridone keto group and the dGTP amine.

After dGTP, the next most efficiently inserted natural triphosphate was generally deoxyadenosine triphosphate (dATP), which was inserted with a second-order rate constant ranging from 4×10^3–$2 \times 10^4\,M^{-1}\,min^{-1}$, with the exception of **3MP**, which did not template dATP insertion at a detectable rate ($k_{cat}/K_M < 10^3\,M^{-1}\,min^{-1}$). In contrast, the fidelity of the carbocyclic analogues is typically limited by facile insertion of dATP (often with rates in excess of $10^5\,M^{-1}\,min^{-1}$ [11]). This data further supports the previous suggestion that hydrophobic minor-groove functional groups increase the efficiency of dATP incorporation, possibly through a favorable packing interaction with the methyne group of dATP. Furthermore, the pyridones are more pyrimidine-like than their carbocyclic counterparts, and their mispairs with dA may be better recognized by the polymerase which evolved to discriminate against natural mispairs.[12]

The misincorporation of deoxythymidine triphosphate (dTTP) was inefficient ($k_{cat}/K_M < 5 \times 10^3\,M^{-1}\,min^{-1}$). Relative to the carbocyclic analogues,[11] inefficient incorporation of dTTP opposite the pyridone analogues generally appears to be due to weaker apparent binding of the natural triphosphate, again possibly reflecting forced desolvation of the minor-groove carbonyl groups in the transition state. dCTP was not incorporated opposite any pyridone analogue at a detectable rate ($k_{cat}/K_M < 10^3\,M^{-1}\,min^{-1}$).

As discussed above, the replication of predominantly hydrophobic non-natural base pairs is consistently limited by their extension.[5,11] Thus, understanding determinants of efficient extension is of great importance. To determine how the pyridone and methyl modifications impact this critical step, we examined the efficiencies with which Kf extended primers (by incorporation of the next correct triphosphate, deoxycytidine triphosphate; dCTP) that terminated with the self-pairs (Table 3). Both the **5MP** and **PYR** self-pairs were extended relatively efficiently at rates of 7×10^4 and $8 \times 10^4\,M^{-1}\,min^{-1}$, respectively, which is approximately 50-fold faster than the **BEN** self-pair.[11] The **4MP** and **3MP** self-pairs were extended less efficiently, at rates of 1×10^4 and $4 \times 10^3\,M^{-1}\,min^{-1}$. All of the pyridone self-pairs are extended significantly more efficiently than their carbocyclic analogues.[11] This is largely due to increased k_{cat} values. The large difference in k_{cat} between **PYR** and **BEN** self-pair extension suggests that the minor-groove H-bond is important for mediating interactions in the developing transition state. This agrees with previous studies that show that removing the minor groove H-bond acceptor from dG at a primer terminus results in a specific decrease in the extension k_{pol}.[13] As was suggested for the extension of a natural base pair,[6b] it seems likely that the pyridone minor groove H-bond acceptor stabilizes the rate-limiting transition state by engaging in a H-bonding network with Arg 668 of Kf and the ribosyl oxygen of the incoming dNTP.

Table 3: Selected rate constants for Kf-mediated extension of non-natural termini by incorporation of dCTP.[a]

5′-dTAATACGACTCACTATAGGGAGA**X**
3′-dATTATGCTGAGTGATATCCCTCT**Y**GCTAGGTTACGGCAGGATCGC

X	Y	k_{cat} [min^{-1}]	K_M [μM]	k_{cat}/K_M [$M^{-1}\,min^{-1}$]
3MP	**3MP**	1.1 ± 0.1	270 ± 107	3.9×10^3
4MP	**4MP**	2.9 ± 0.9	202 ± 56	1.5×10^4
5MP	**5MP**	7.3 ± 0.7	107 ± 12	6.8×10^4
PYR	**PYR**	9.6 ± 1.0	117 ± 32	8.2×10^4
5MP	**3MP**	13 ± 4	198 ± 21	6.4×10^4
5MP	**4MP**	16 ± 3	204 ± 56	7.8×10^4
PYR	**3MP**	14 ± 2	322 ± 76	4.3×10^4
PYR	**4MP**	16 ± 4	146 ± 56	1.1×10^5

[a] For experimental details and additional heteropair extension rate constants, see the Supporting Information.

To further explore extension as a function of methyl group substitution, we characterized the rates at which Kf extended a primer terminating at a heteropair (**X**:**Y**, in which **X** is the primer nucleobase and **Y** is the template nucleobase, Table 3 and the Supporting Information). Heteropairs formed between either **3MP** and **5MP** or **3MP** and **PYR** are extended at rates ranging from 4×10^4 to $9 \times 10^4\,M^{-1}\,min^{-1}$. These rates are 10- to 30-fold more efficient than those for the corresponding self-pairs and are similar to the extension of the **5MP** and **PYR** self-pairs. Likewise, heteropairs formed between **4MP** and either **5MP** or **PYR** were extended significantly faster than the **4MP** self-pair with rates ranging from 8×10^4 to $2 \times 10^5\,M^{-1}\,min^{-1}$. This suggests that steric interactions are responsible for the inefficient extension of the **3MP** and **4MP** self-pairs, and that shape complementarity is important for extension and possibly for the correct positioning of the minor groove H-bond acceptor to productively engage the polymerase. It is also interesting to note that the **4MP**:**5MP**, **PYR**:**4MP**, and **PYR**:**5MP** heteropairs are

 © 2006 Wiley-VCH Verlag GmbH & Co. KGaA, Weinheim

extended within twofold of the most efficiently extended non-natural base pairs reported to date.

The data have several important implications for future efforts to design non-natural base pairs. Generally, at least for the pyridone scaffold, shape complementarity is less important for mispair stability and synthesis than is H-bonding. However, shape complementarity between the nucleobase analogues does appear to be important for base pair synthesis and extension. It may contribute to efficient synthesis by forming a well-packed interbase interface that stabilizes the developing transition state. It may contribute to efficient extension by contributing to the formation of a primer terminus that properly orients the minor-groove H-bond acceptor for polymerase recognition. The effects of shape complementarity were generally less pronounced with pairs formed between larger nucleobase analogues, likely owing to their intercalative mode of interaction.[2a,4] The data also show that, compared to the fully carbocyclic analogues, the pyridone base pairs are generally extended with dramatically increased rates and are also more orthogonal to the natural nucleotides, especially dA.[11] In contrast with other classes of predominantly hydrophobic nucleobase analogues, non-natural base pairs formed between the pyridone analogues appear to be limited by their synthesis efficiencies. However, the relative efficiency with which the **4MP**:**3MP** pair is synthesized suggests that these rates might be increased by nucleobase optimization, as has been observed for other scaffolds.[2b,14] In addition, the synthesis might be optimized through the directed evolution of polymerases to more efficiently catalyze this step as it has for the **PICS** self-pair.[15] Thus, further exploring these non-natural base-pair scaffolds and evolving polymerases that more efficiently synthesize them represents a promising strategy for the expansion of the genetic alphabet.

Received: March 31, 2006
Published online: May 30, 2006

Keywords: DNA replication · genetic alphabet · hydrophobic effect · nucleobases · pyridones

[1] S. Moran, R. X.-F. Ren, S. Rumney, E. T. Kool, *J. Am. Chem. Soc.* **1997**, *119*, 2056 – 2057.
[2] a) D. L. McMinn, A. K. Ogawa, Y. Wu, J. Liu, P. G. Schultz, F. E. Romesberg, *J. Am. Chem. Soc.* **1999**, *121*, 11585 – 11586; b) A. A. Henry, A. G. Olsen, S. Matsuda, C. Yu, B. H. Geierstanger, F. E. Romesberg, *J. Am. Chem. Soc.* **2004**, *126*, 6923 – 6931.
[3] I. Hirao, Y. Harada, M. Kimoto, T. Mitsui, T. Fujiwara, S. Yokoyama, *J. Am. Chem. Soc.* **2004**, *126*, 13298 – 13305.
[4] A. K. Ogawa, Y. Wu, D. L. McMinn, J. Liu, P. G. Schultz, F. E. Romesberg, *J. Am. Chem. Soc.* **2000**, *122*, 3274 – 3287.
[5] G. T. Hwang, F. E. Romesberg, *Nucleic Acids Res.* **2006**, *34*, 2037 – 2045.
[6] a) J. C. Morales, E. T. Kool, *J. Am. Chem. Soc.* **1999**, *121*, 2323 – 2324; b) A. S. Meyer, M. Blandino, T. E. Spratt, *J. Biol. Chem.* **2004**, *279*, 33043 – 33046.
[7] a) Y. Li, G. Waksman, *Protein Sci.* **2001**, *10*, 1225 – 1233; b) S. J. Johnson, L. S. Beese, *Cell* **2004**, *116*, 803 – 816.
[8] F. E. Romesberg, C. Yu, S. Matsuda, A. A. Henry in *Current Protocols in Nucleic Acids Chemistry* (Eds.: S. L. Beaucage, D. E. Bergstrom, G. D. Glick, R. A. Jones), Wiley, New York, **2002**, pp. 1.5.1 – 1.5.36.
[9] S. Matsuda, F. E. Romesberg, *J. Am. Chem. Soc.* **2004**, *126*, 14419 – 14427.
[10] M. Berger, A. K. Ogawa, D. L. McMinn, Y. Wu, P. G. Schultz, F. E. Romesberg, *Angew. Chem.* **2000**, *112*, 3069 – 3071; *Angew. Chem. Int. Ed.* **2000**, *39*, 2940 – 2942.
[11] S. Matsuda, A. A. Henry, F. E. Romesberg, *J. Am. Chem. Soc.* **2006**, *128*, 6369 – 6375.
[12] K. Kincaid, J. Beckman, A. Zivkovic, R. L. Halcomb, J. W. Engels, R. D. Kuchta, *Nucleic Acids Res.* **2005**, *33*, 2620 – 2628.
[13] T. E. Spratt, *Biochemistry* **2001**, *40*, 2647 – 2652.
[14] a) A. K. Ogawa, Y. Wu, M. Berger, P. G. Schultz, F. E. Romesberg, *J. Am. Chem. Soc.* **2000**, *122*, 8803 – 8804; b) C. Yu, A. A. Henry, F. E. Romesberg, P. G. Schultz, *Angew. Chem.* **2002**, *114*, 3997 – 4000; *Angew. Chem. Int. Ed.* **2002**, *41*, 3841 – 3844.
[15] A. M. Leconte, L. Chen, F. E. Romesberg, *J. Am. Chem. Soc.* **2005**, *127*, 12470 – 12471.

 © 2006 Wiley-VCH Verlag GmbH & Co. KGaA, Weinheim

Chemical Genetics

DOI: 10.1002/anie.200600743

Mixed Isotope Photoaffinity Reagents for Identification of Small-Molecule Targets by Mass Spectrometry**

*Shane M. Lamos, Casey J. Krusemark, Christopher J. McGee, Mark Scalf, Lloyd M. Smith, and Peter J. Belshaw**

Identifying the protein targets of biologically active small molecules is often the rate-determining step in the process of elucidating protein function through chemical genetics.[1] A

[*] Prof. P. J. Belshaw
Departments of Chemistry and Biochemistry
University of Wisconsin, Madison
Madison, WI 53706 (USA)
Fax: (+1) 608-265-4534
E-mail: belshaw@chem.wisc.edu

S. M. Lamos,[+] Dr. M. Scalf, Prof. L. M. Smith
Department of Chemistry
University of Wisconsin, Madison
Madison, WI 53706 (USA)

C. J. Krusemark[+]
Department of Biochemistry
University of Wisconsin, Madison
Madison, WI 53706 (USA)

C. J. McGee
Department of Chemistry
University of California-Irvine
Irvine, CA 92697 (USA)

[+] S.M.L. and C.J.K. contributed equally to this work.

[**] We thank M. Shortreed for assistance with the MS studies, and also M. Cancilla and A. Hegeman for insightful discussions. C.J.K. was supported by a Biotechnology Training Grant fellowship. This work was supported by generous financial support from the NIH (GM065406) and NHLBI (N01-HV-28182).

Supporting information for this article is available on the WWW under http://www.angewandte.org or from the author.

© 2006 Wiley-VCH Verlag GmbH & Co. KGaA, Weinheim

classical approach for target identification is chromatography with immobilized ligands. Affinity chromatography approaches are often unsuccessful for identifying binding proteins with low affinity and low abundance because of contaminating nonspecifically purified proteins. These limitations have spurred the development of new methods for the discovery of target ligands.

Photoaffinity labeling (PAL) is an attractive alternative to affinity chromatography for the discovery of target ligands[2] since matrix and avidity effects of immobilized ligands are avoided. PAL methods using soluble probes are more amenable for the identification of low-affinity targets since the ligand concentration can be controlled. Photoaffinity probes also have the potential for use inside live cells, thus enabling affinity-based profiling of the entire proteome in its native state. However, biochemical purification and identification of labeled proteins, often facilitated by the addition of biotin or radioisotopes, remains a significant challenge in PAL. Here we describe the synthesis and application of target identification probe (TIP) reagents for addressing these issues. These reagents contain affinity, photoaffinity, and mixed isotope labels to facilitate the identification of binding proteins by mass spectrometry (MS).

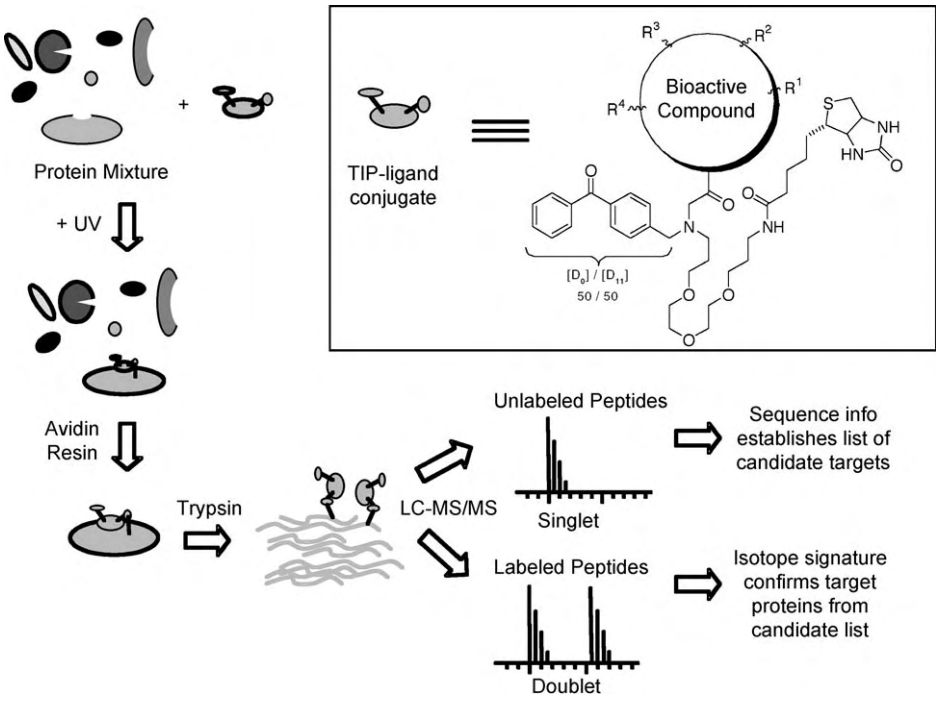


Figure 1. Strategy for determining the identity of small-molecule binding proteins.

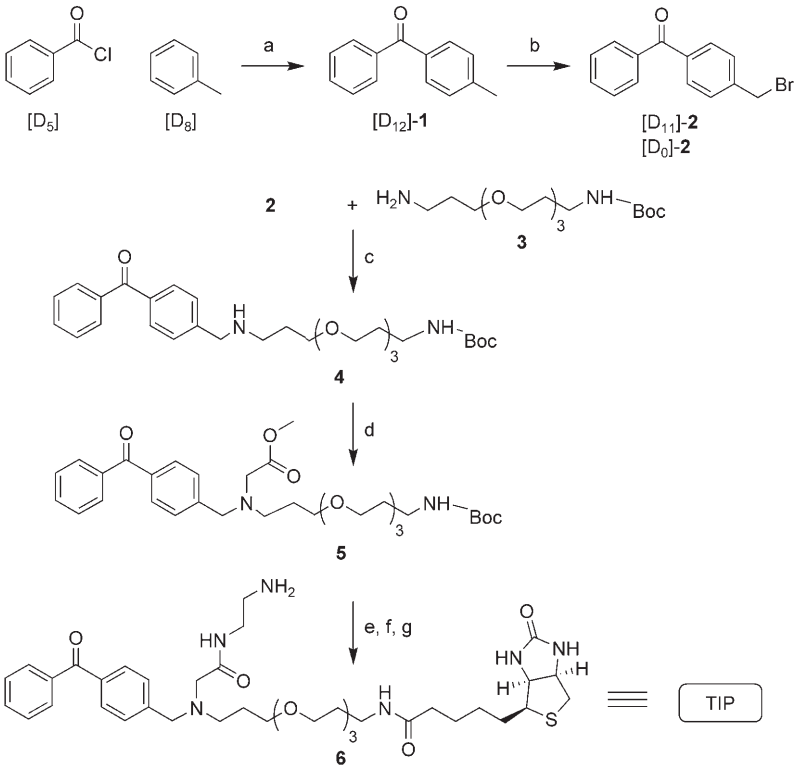
Stable mixed isotopes have been applied as selective identification tags in mass spectrometry. For example, drug metabolites can be easily identified, even in very complex mixtures, if isotopes are incorporated to give a unique isotopic pattern.[3] This approach has been used successfully in the identification of modification sites on proteins from covalently modifying inhibitors[4] and protein–protein cross-linking reagents.[5] The incorporation of mixed isotopes and photoaffinity labels into peptide ligands has been shown to aid the identification of receptor binding pockets[6] and has been suggested as an approach to aid the identification of small-molecule PAL targets.[7] To generalize this approach we employ mixed isotopes within a modular photoaffinity-labeling reagent to clearly identify labeled proteins in the presence of contaminants commonly observed in affinity purification and MS.

Our approach is outlined in Figure 1. After suitable attachment of the TIP to a bioactive small molecule, the conjugate is incubated in a protein mixture and covalently photoincorporated into target proteins. Avidin affinity chromatography is used to purify intact labeled proteins, which are proteolyzed and analyzed by mass spectrometry. Sequence information from MS/MS analysis of purified unlabeled peptides enables a list of candidate binding proteins to be established. Conclusive determination of labeled proteins is made possible by the presence of peptides bearing the unique isotopic signature (M, $M+11$) of the probe.

This strategy for characterizing the labeled and unlabeled peptides of chemically modified proteins is advantageous for identification. Relying on a probe-labeled peptide alone to identify a protein can be problematic,[8] particularly for photo-cross-linked peptides.[9] Photo-cross-linking reactions generally modify peptides with little site specificity, thereby producing isobaric peptides representing a number of chemical species.[10] Indeed, the MS fragmentation of the probe itself often results in MS/MS data that are difficult to interpret.[11] This current approach obviates the need to sequence labeled peptides, while providing high sequence coverage and confidence in identifying labeled proteins even in the presence of contaminants.

The synthesis of the probe began with the preparation of deuterated benzophenone $[D_{12}]$-**1** by a Friedel–Crafts acylation using commercially available $[D_8]$toluene and $[D_5]$benzoyl chloride (Scheme 1). In this way, a large isotopic mass difference ($[D_0]$ versus $[D_{11}]$) can be incorporated in a compact and economical manner. Radical bromination of $[D_{12}]$-**1** with NBS in the presence of a catalytic amount of AIBN yielded the benzophenone $[D_{11}]$-**2**. The commercially available benzophenone $[D_0]$-**2** was used to prepare the unlabeled series of compounds. Primary amine **3** was alkylated with $[D_{11}]$-**2** or $[D_0]$-**2** to produce secondary amines $[D_{11}]$-**4** and $[D_0]$-**4**, respectively. These were further alkylated with methyl bromoacetate to afford $[D_{11}]$-**5** and $[D_0]$-**5**. These compounds were converted into probes $[D_{11}]$-**6** and $[D_0]$-**6** by sequential cleavage of the Boc protecting groups, coupling to biotin (DIC/HOBt/DIPEA), and amidation with neat ethylene diamine. The resulting compounds $[D_{11}]$-**6** and $[D_0]$-**6**

 © 2006 Wiley-VCH Verlag GmbH & Co. KGaA, Weinheim



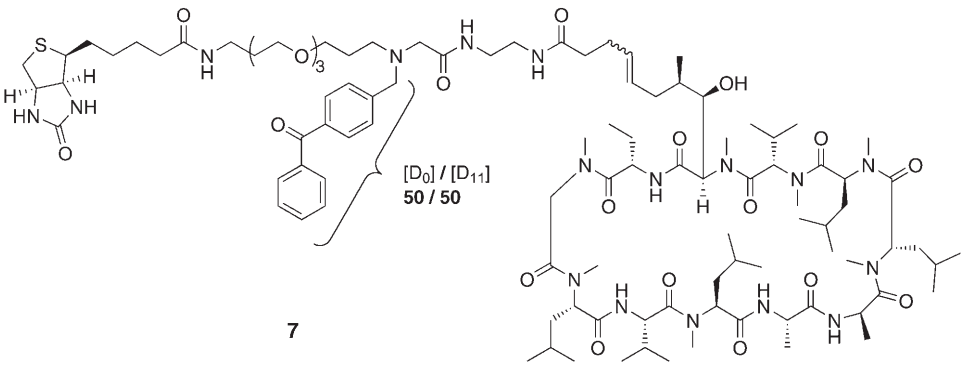
Scheme 1. a) [D_8]Toluene, [D_5]benzoyl chloride, $AlCl_3$; b) NBS, AIBN, CCl_4, reflux 3 h; c) **3**, K_2CO_3, CH_3CN/CH_2Cl_2 (5:2); d) methyl bromoacetate, DIPEA, CH_2Cl_2; e) 40% TFA in CH_2Cl_2; f) biotin, DIC, HOBt, DIPEA, DMF; g) neat ethylenediamine. Unlabeled compounds are derived from commercially available bromomethylbenzophenone ([D_0]-**2**). Boc = *tert*-butoxycarbonyl, NBS = *N*-bromosuccinimide, AIBN = azobisisobutyronitrile, DIPEA = *N*,*N*-diisopropylethylamine, DIC = diisopropylcarbodiimide, HOBt = 1-hydroxy-1*H*-benzotriazole, TFA = trifluoroacetic acid.

represent our modular multifunctional scaffold for preparing photoaffinity reagents.

For a proof of principle experiment, we chose the immunosuppressive drug CsA, whose biological activity is mediated through binding to cyclophilin A (CypA).[12] We derivatized CsA by olefin metathesis to its *N*-methyl-(4*R*)-4-[(*E*)-2-butenyl)-4-methyl]-L-threonine (MeBmt) residue, as previously described.[13] The modified CsA was appended onto [D_{11}]-**6** and [D_0]-**6** to give the heavy and light CsA–TIP conjugates [D_{11}]-**7** and [D_0]-**7**, respectively (Scheme 2). These were used as a 1:1 mixture for subsequent labeling experiments.

The photo-cross-linking specificity of the CsA conjugate was assessed within a protein mixture containing CypA. Upon UV irradiation, the reagent predominantly labeled CypA, as indicated by Western blot analysis (Figure 2b, lane 4). The addition of the photolabel produced an expected shift of the protein band to about 22 kDa. Photolabeling in the presence of excess CsA drastically reduced CypA labeling and slightly increased the labeling of bystander proteins (Figure 2b, lane 5). The results indicate that the photo-cross-linking is highly specific for CypA and is dependent on the ligand-binding interaction.

To demonstrate the applicability of the approach, labeled protein was purified from the protein mixture by using avidin resin (Figure 3, lane 2). Tryptic digests of eluted protein were analyzed directly by MS. A SEQUEST search of the database against the 4 protein sequences with MS/MS data identified 11 peptides from CypA corresponding to 59% sequence coverage. Single peptides from both FKBP and ovalbumin were also identified. A search of the full human database similarly identified CypA and a number of spurious proteins common to such searches, including ubiquitin and keratin. Only two peptides containing the unique isotopic signature were found in the mass spectra, and these were easily identified among many nonlabeled peptides (Figure 4). These corresponded in mass to labeled CypA peptides 92–118 and 56–82 (Figure 4c) and did not match with the theoretical labeled peptides from any of the other proteins identified. Both of the identified peptides are surface exposed and in proximity to the MeBmt side chain of the CypA–CsA complex.[14] Our results demonstrate that the presence of mixed-label peptides allows nonspecific proteins from both the affinity chromatography and MS analysis to be ignored, thereby allowing the target to be confidently determined. The incorporation of a large 11-Da mass difference permitted easy visual recognition of labeled peptides in the mass spectra. This mass difference enables the resolution of doublets for large peptides and even whole proteins (ca. 40 kDa), despite the presence of isotope manifolds (from natural abundance heavy isotopes) and thus could find utility in top-down proteomics applications. Further investigations with these reagents will include applications within live cells. In the event that the reagents are not



Scheme 2. Cyclosporin (CsA)/TIP conjugate.

 © 2006 Wiley-VCH Verlag GmbH & Co. KGaA, Weinheim

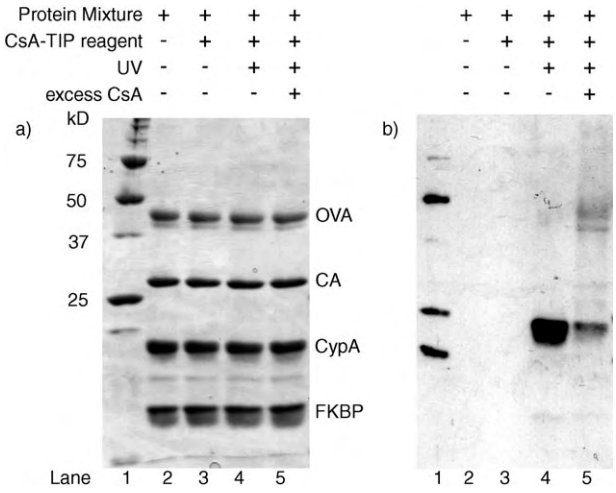


Figure 2. Detection of CsA binding proteins in a protein mixture. A protein mixture consisting of ovalbumin (OVA), carbonic anhydrase (CA), CypA, and FK binding protein (FKBP; 70 $\mu g\,mL^{-1}$ each) in phosphate-buffered saline (PBS) was incubated with CsA–TIP reagent (3.5 μM) and irradiated. Excess CsA (50 μM) was added where indicated. Portions of 15 μL were subjected to sodium dodecylsulfate/polyacrylamide gel electrophoresis (SDS-PAGE) analysis. a) Coomassie Blue stained gel. b) Duplicate Western blot visualized with streptavidin-alkaline phosphatase.

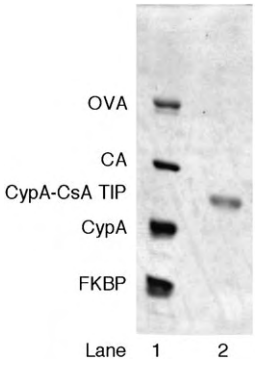


Figure 3. Purification of the CsA binding protein from the protein mixture. A protein mixture consisting of ovalbumin (OVA), carbonic anhydrase (CA), CypA, and FKBP (70 $\mu g\,mL^{-1}$ each) in PBS was incubated with CsA–TIP reagent (3.5 μM) and irradiated. Labeled species were purified with monomeric avidin resin (500 μL) and analyzed by SDS-PAGE. Lane 1: 15 μL of protein mixture, lane 2: elution from avidin stationary phase.

cell permeable, our modular design should readily enable modifications to increase cell permeability such as replacement of the purification tag and/or linkage to the bioactive molecule.

In summary, we have prepared a multifunctional reagent for the identification of small-molecule binding proteins through photoaffinity labeling and mass spectrometry. A facile and economic route for the incorporation of deuterated benzophenones (a widely used photoaffinity tag) into probes has been developed. Conjugates to the ligand CsA were prepared and used to identify a known target of CsA from a mixture of proteins. We have described a novel strategy for the high-confidence identification of photoaffinity-labeled

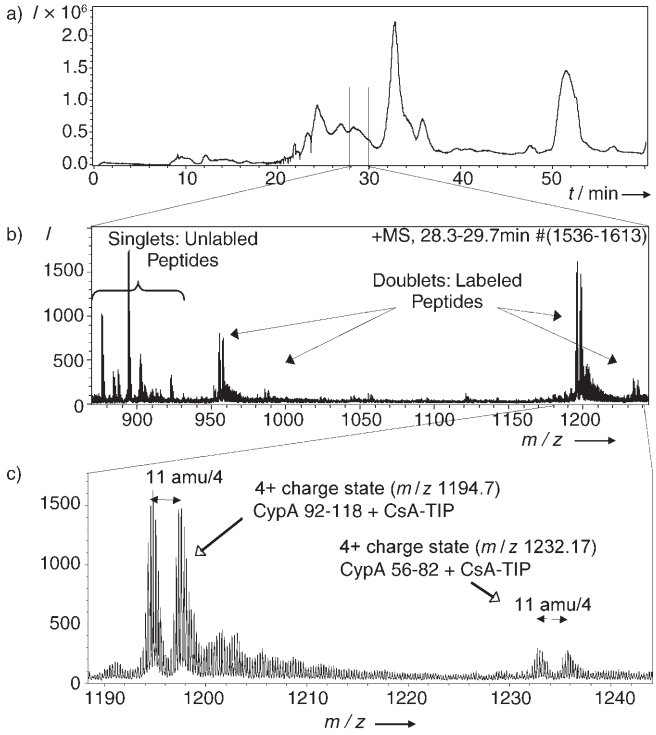


Figure 4. Identification of the two peptides containing the unique isotopic signature in the mass spectra. a) Chromatogram showing the total ion current; b,c) ms data.

proteins that combines unique isotope signatures with broad sequence coverage of purified, unlabeled peptide fragments. These approaches should be broadly applicable to MS analysis of chemically modified proteins.

Received: February 27, 2006
Published online: May 30, 2006

Keywords: chemical genetics · isotopic labeling · mass spectrometry · photoaffinity labeling · proteomics

[1] a) L. Burdine, T. Kodadek, *Chem. Biol.* **2004**, *11*, 593; b) G. Dorman, F. Darvas, *Chemical Genomics* (Eds.: F. Darvas, A. Guttman, G. Dorman), Marcel Dekker, New York, **2004**, p. 137.
[2] a) G. Dorman, *Bioorganic Chemistry of Biological Signal Transduction*, *Vol. 211* (Ed.: H. Waldman), Springer, Berlin, **2000**; b) G. Dorman, G. D. Prestwich, *Trends Biotechnol.* **2000**, *18*, 64; c) Y. Hatanaka, Y. Sadakane, *Curr. Top. Med. Chem.* **2002**, *2*, 271.
[3] T. A. Baillie, *Pharmacol. Rev.* **1981**, *33*, 81.
[4] N. L. Kelleher, R. B. Nicewonger, T. P. Begley, F. W. McLafferty, *J. Biol. Chem.* **1997**, *272*, 32215.
[5] a) D. R. Muller, P. Schindler, H. Towbi, U. Wirth, H. Voshol, S. Hoving, M. O. Steinmetz, *Anal. Chem.* **2001**, *73*, 1927; b) J. W. Back, V. Notenboom, L. J. de Koning, A. O. Muijsers, T. K. Sixma, C. G de Koster, L. de Jong, *Anal. Chem.* **2002**, *74*, 4417.
[6] E. Sachon, O. Tasseau, S. Lavielle, S. Sagan, G. Bolbach, *Anal. Chem.* **2003**, *75*, 6536.
[7] a) M. Daghish, L. Hennig, M. Findeisen, S. Giesa, F. Schumer, H. Hennig, A. G. Beck-Sickinger, P. Welzel, *Angew. Chem.* **2002**,

 © 2006 Wiley-VCH Verlag GmbH & Co. KGaA, Weinheim

114, 2404; *Angew. Chem. Int. Ed.* **2002**, *41*, 2293; b) M. Hashimoto, Y. Hatanaka, *Chem. Pharm. Bull.* **2004**, *52*, 1385.
[8] A. E. Speers, B. F. Cravatt, *J. Am. Chem. Soc.* **2005**, *127*, 10018.
[9] K. Fang, M. Hashimoto, S. Jockusch, N. J. Turro, K. Nakanishi, *J. Am. Chem. Soc.* **1998**, *120*, 8543.
[10] G. Dorman, G. D. Prestwich, *Biochemistry* **1994**, *33*, 5661.
[11] O. V. Borisov, M. B. Goshe, T. P. Conrads, V. S. Rakov, T. D. Veenstra, R. D. Smith, *Anal. Chem.* **2002**, *74*, 2284.
[12] R. E. Handschumacher, M. W. Harding, J. Rice, R. J. Drugge, D. W. Speicher, *Science* **1984**, *226*, 544.
[13] J. A. Smulik, S. T. Diver, F. Pan, J. O. Liu, *Org. Lett.* **2002**, *4*, 2051.
[14] C. Weber, G. Wider, B. Von Freyberg, R. Traber, W. Braun, H. Widmer, K. Wuthrich, *Biochemistry* **1991**, *30*, 6563.

 © 2006 Wiley-VCH Verlag GmbH & Co. KGaA, Weinheim

Cluster Compounds

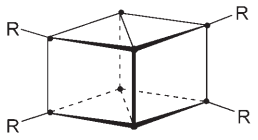
DOI: 10.1002/anie.200600292

Higher-Nuclearity Group 14 Metalloid Clusters: $[Sn_9\{Sn(NRR')\}_6]$**

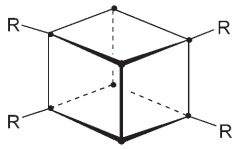
Marcin Brynda, Rolfe Herber, Peter B. Hitchcock, Michael F. Lappert,* Israel Nowik, Philip P. Power,* Andrey V. Protchenko, Aleš Růžička, and Jochen Steiner*

Dedicated to Professor Hansgeorg Schnöckel on the occasion of his 65th birthday

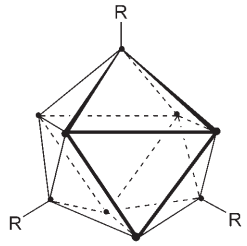
The term "metalloid cluster" was coined by Schnöckel and co-workers in the context of Al chemistry to designate those metal clusters in which "the number of metal–metal contacts exceeds the number of metal–ligand contacts and by the presence of metal atoms which participate exclusively in metal–metal interactions".[1] Reviews of such Al and Ga clusters have appeared[2] and were extended to those of the heavier Group 14 elements.[3] Previously reported tin clusters $[Sn_xR_y]$ $(x > y)$ include $[Sn_8R_4]$ (**I**),[4] $[Sn_8R_6]^{2-}$ (**II**),[5] $[Sn_9R_3]$ (**III**),[6] $[Sn_{10}R_3]^-$ (**IV**),[6] in each of which R represents an aryl or silyl ligand. In the spirit of Schnöckel's definition, we now present data on the highest-nuclearity Group 14 "metalloid" clusters to be reported thus far, the isoleptic compounds $[Sn_{15}Z_6]$ ($Z = N(2,6\text{-}iPr_2C_6H_3)(SiMe_2X)$; X = Me (**1**), Ph (**2**)). Compounds **1** and **2** are the first Group 14 metal clusters bearing amido ligands and are also unprecedented within this compound class for being body-centered and have as locus a tin atom with relatively close contacts (ca. 3.1 to 3.4 Å) to each of the remaining 14 tin atoms.



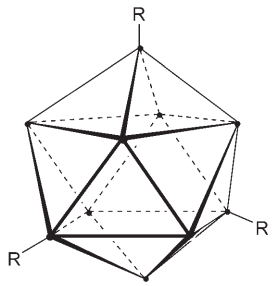
I R = $C_6H_3(C_6H_2Me_3\text{-}2,4,6)_2\text{-}2,6$



II R = $SitBu_3$



III R = $C_6H_3(C_6H_2iPr_3\text{-}2,4,6)_2\text{-}2,6$



IV R = $C_6H_3(C_6H_2Me_3\text{-}2,4,6)_2\text{-}2,6$

The best-known stable polyhedral clusters of the heavier Group 14 elements are the ligand-free Zintl anions, such as M_5^{2-} or M_9^{n-} (M = Ge, Sn, or Pb; $n = 2, 3, 4$).[7] An intriguing aspect of progressively higher-nuclearity metalloid clusters $[M_xR_y]$ (where x is large and $x \gg y$) is that their morphology should increasingly resemble sections of the bulk metal. Detailed structural data for such species may provide insight into changes that occur at or near the surface of the metal compared with those within its bulk. For main-group chemistry, relevant information was previously available only for Group 13 metalloid clusters, as in $[Al_{77}Z_{20}]^{2-}$ [8a] or $[Ga_{84}Z_{20}]^{3-}$ [8b] ($Z = N(SiMe_3)_2$). The characterization of $[Sn_{15}Z_6]$ (**1**, **2**) is now a step along the same path for clusters of Group 14 elements. A recent contribution in this area relates to the synthesis and X-ray structure of $[Si_8(SitBu_3)_6]$.[9]

The work herein was begun at the University of Sussex in 2003.[10] The crystalline compound **1** was isolated as small black crystals of space group *Pnnm* (**1**(*Pnnm*))by treatment of the colorless compound $[\{Sn[N(2,6\text{-}iPr_2C_6H_3)(SiMe_3)](\mu\text{-}Cl)\}_2]$ (**3**)[11] with KC_8 in Et_2O at about −30 °C and successive filtering, concentration of the filtrate, addition of PhMe, and prolonged storage at −27 °C. By this procedure compound

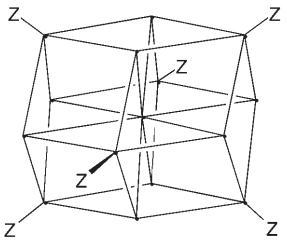
[*] Dr. P. B. Hitchcock, Prof. M. F. Lappert, Dr. A. V. Protchenko, Dr. A. Růžička
Department of Chemistry
University of Sussex
Brighton, BN1 9QJ (UK)
Fax: (+44) 1273-677-196
E-mail: m.f.lappert@sussex.ac.uk
Dr. M. Brynda, Prof. P. P. Power, Dr. J. Steiner
Department of Chemistry
University of California
One Shields Avenue, Davis, CA 95616 (USA)
Fax: (+1) 530-752-8995
E-mail: pppower@ucdavis.edu
Prof. R. Herber, Dr. I. Nowik
Racah Institute of Physics
The Hebrew University of Jerusalem
91904 Jerusalem (Israel)
Fax: (+972) 2-658-6347
E-mail: herber@vms.huji.ac.il

[**] We thank the EPSRC (A.V.P.) and the Royal Society (A.R.) for postdoctoral fellowships and the CRC Program of the U.S. National Science Foundation for financial support. R = 2,6-$iPr_2C_6H_3$; R′ = $SiMe_3$ or $SiMe_2Ph$.

Supporting information for this article is available on the WWW under http://www.angewandte.org or from the author.

 © 2006 Wiley-VCH Verlag GmbH & Co. KGaA, Weinheim

1 (*Pnnm*) was obtained in very low yield together with unreacted **3**.[10] A subsequent experiment, in which the crystallization was carried out at ambient temperature, furnished **1** ($R\bar{3}$) in very low yield as black (or dark red in thin layers) hexagonal prisms. The new crystalline amidotin(II) chloride **3**[11] was prepared in Et_2O from $SnCl_2$ and one equivalent of $Li[N(2,6\text{-}iPr_2C_6H_3)(SiMe_3)]$[12a] (76%) or $[Sn\{N(2,6\text{-}iPr_2C_6H_3)(SiMe_3)\}_2]$[12b] (93%). Attempted reduction of three other amidotin(II) compounds failed to yield isolable clusters. Reaction of $[Sn\{N(SiMe_3)_2\}_2]$ or $[\{Sn[N(SiMe_3)_2](\mu\text{-}Cl)\}_2]$ with KC_8 or $NaC_{10}H_8$ gave elemental tin, and reaction of $[\{Sn(tmp)(\mu\text{-}Cl)\}_2]$ (tmp = 2,2,6,6-tetramethylpiperidinato) with KC_8 yielded a tar of unidentified content.



1 Z = $N(C_6H_3iPr_2\text{-}2,6)(SiMe_3)$
2 Z = $N(C_6H_3iPr_2\text{-}2,6)(SiMe_2Ph)$

Complementary experiments were subsequently carried out at the University of California, Davis, where a new synthetic strategy was introduced, namely the use of a reductive elimination from a precursor metal chloride with $Li[BHsBu_3]$ (L-selectride). Thus, the cluster **1** (ca. 5%) was obtained by treatment of the in situ generated amidotin(II) chloride **3** with a less-than-stoichiometric amount of $Li[BHsBu_3]$ at −78 °C. Two forms of **1** were obtained by this route; crystallization from PhMe or hexane yielded X-ray-quality crystals **1** ($R\bar{3}c$) or **1** ($P2_1/n$), respectively. Compound **2** (7%) was obtained similarly from an analogue of **3** (prepared in situ from $[Sn\{N(2,6\text{-}iPr_2C_6H_3)(SiMe_2Ph)\}_2]$ and $SnCl_2$) and $Li[BHsBu_3]$. It is likely that a transient amidotin(II) hydride is an intermediate in these syntheses. In support of this postulate, we note that i) treatment of **3** with an equivalent of $[\{Cu(\mu\text{-}H)(PPh_3)\}_6]$ in C_6D_6 resulted in evolution of H_2 (NMR experiment) and ii) thermolysis of the sterically hindered Sn(II) hydride $[\{Sn[2,6\text{-}(2,4,6\text{-}iPr_3C_6H_2)_2C_6H_3](\mu\text{-}H)\}_2]$[13] in toluene afforded the $[Sn_9R_3]$ cluster **III**.[6]

Although single crystals of **1** were obtained in four different space groups (*Pnnm*, $R\bar{3}$, $R\bar{3}c$, $P2_1/n$),[14] the molecular structures that were deduced from each are essentially identical, and the various Sn–Sn distances are also closely similar to those of **2** (Table 1).[15] The structures of **1** and **2** are illustrated in Figure 1. The most striking feature of each structure is the body-centered arrangement of the 15 tin atoms, an architecture previously unknown for metalloid clusters of the Group 14 elements. The ligand-free tin atoms in **1** and **2** form a body-centered distorted cube, and each of the six faces is capped by an {Sn(NRR′)} moiety, as shown in Figure 2.

Table 1: Comparison of average bond lengths (Å) in clusters **1** and **2**.[a]

Compound	Sn1–Sn_A	Sn1–Sn_B	Sn_A–Sn_B	Sn_A–Sn_A
1 (*Pnnm*)	3.18 ± 0.03	3.36 ± 0.02	3.01 ± 0.03	3.67 ± 0.07
1 ($R\bar{3}$)	3.15 ± 0.03	3.40 ± 0.01	3.02 ± 0.02	3.64 ± 0.02
1 ($R\bar{3}c$)	3.16 ± 0.03	3.40 ± 0.01	3.02 ± 0.02	3.64 ± 0.03
1 ($P2_1/n$)	3.18 ± 0.02	3.33 ± 0.04	2.99 ± 0.02	3.67 ± 0.06
2 ($P2_1/n$)	3.15 ± 0.03	3.41 ± 0.02	3.02 ± 0.04	3.64 ± 0.04

[a] Sn1: central Sn atom; Sn_A: Sn atoms at cube apices; Sn_B: ligand-bound Sn atoms.

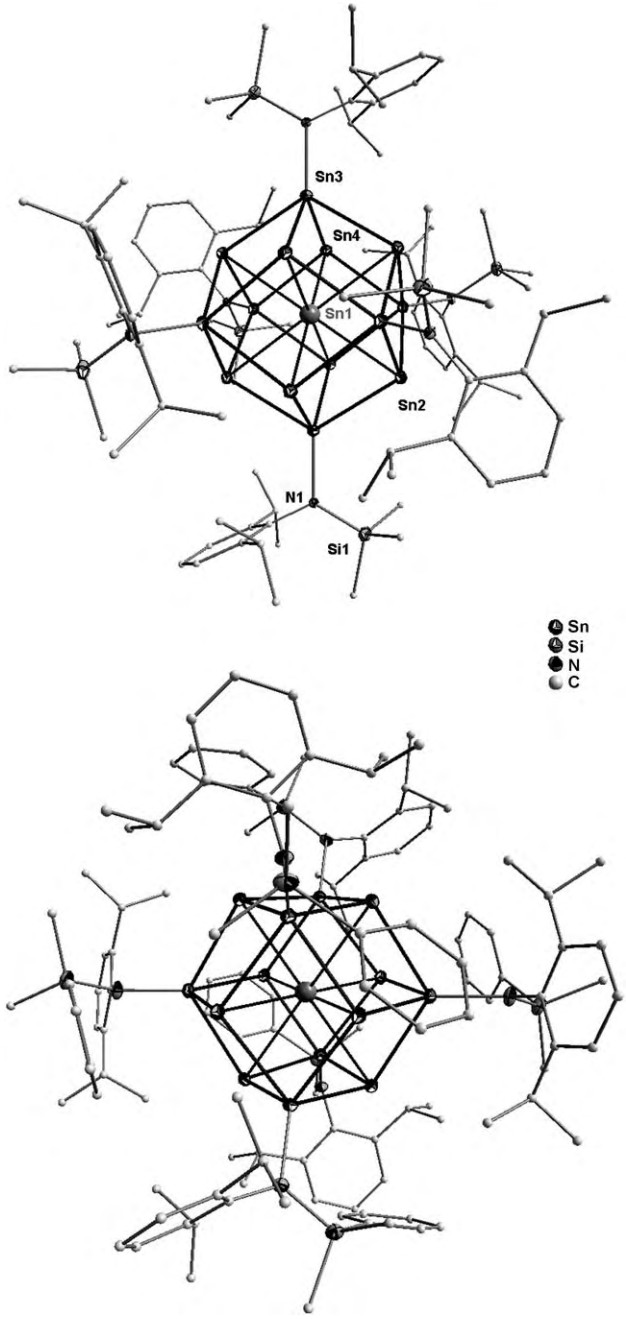


Figure 1. Thermal-ellipsoid plot (ellipsoids set at 50% probability) of **1** ($R\bar{3}c$) (upper) and **2** (lower) with isotropic representation of the C atoms and the central Sn atoms (H atoms are omitted for clarity).

 © 2006 Wiley-VCH Verlag GmbH & Co. KGaA, Weinheim

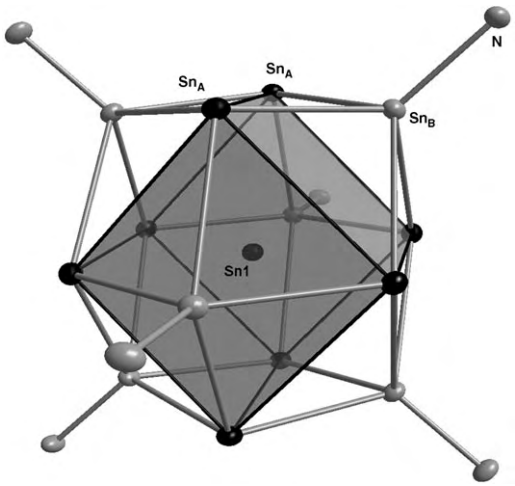


Figure 2. Polyhedral representation of the cluster core in **1** and **2** (unsubstituted Sn_A atoms black, N atoms and ligand-bound Sn_B atoms gray; only the N atoms of the amido ligands shown).

The metalloid character of **1** and **2** is revealed in the Sn–Sn interactions between the central tin atom (Sn1) and the eight tin atoms at the cube apices (Sn_A; Figure 2) of an Sn_8 cube. The Sn1–Sn_A distances have an average value close to 3.15 Å,[15] which is considerably longer than the average value of 2.81 Å in white tin (β-Sn), but closer to the average value of 3.10 Å in gray tin (α-Sn, diamond lattice). The Sn_A–Sn_B bonds between the amido-substituted tin atoms (Sn_B; Figure 2) and those at the apices of the cube (Sn_A) have an average length of 3.02 Å. The Sn_B–N bonds have an average length of 2.09 Å (for **1**) and 2.11 Å (for **2**), and are unexceptional (for comparison, Sn–N bond length in **3**: 2.068(2) Å).[11] The slightly larger average Sn_B–N bond length in **2** is probably a result of the greater steric demand of the silyl group of the ligand. The only main-group-metal cluster that possesses a structure similar to that of **1** and **2** is the neutral-atom cluster $[SiAl_8(AlCp^*)_6]$ ($Cp^* = \eta^5$-C_5Me_5), which has a bcc arrangement of Al atoms in which the central aluminum atom is replaced by a silicon atom and the faces are capped by {AlCp*} units.[16]

The structural motif of the Sn-centered core in **1** or **2** is similar to that of typical metallic structures. Thus, the bcc arrangement of the nine central tin atoms in **1** (black Sn atoms in Figure 2) corresponds to that in the α-iron structure, but not to those of white or gray tin. The bcc structure is observed for elemental tin only at high pressure, above 45 ± 5 GPa.[17] This relationship between the number of associated metal atoms in a molecular structure and high-pressure modifications of the corresponding bulk metal has also been observed in large clusters of Group 13 elements.[2]

Attempts to record solution ^{119}Sn NMR spectra of **1** and **2** failed possibly because of their very low solubility at ambient temperature as a result of their high symmetry and molecular weight. Heating the complex **1** (*Pnnm*) in [D_8]toluene led to precipitation of metallic tin. Moreover, the tin nuclei are in a rigid cage structure that forms part of a relatively large molecule, thus making NMR relaxation very slow, and the sample is thus quickly saturated.

Temperature-dependent ^{119}Sn Mössbauer spectroscopic experiments on a sample of **1** were carried out[18] to complement the above X-ray structural data. A representative spectrum is shown in Figure 3. Two distinct quadrupole-

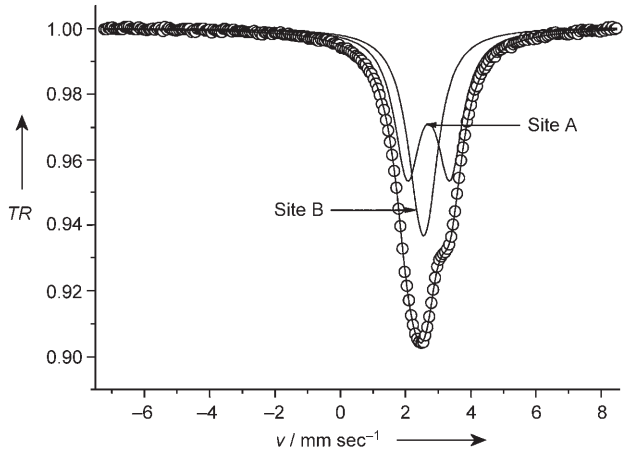


Figure 3. ^{119}Sn Mössbauer spectrum of **1** at 89 K (*TR* = relative transmission). The velocity scale is with respect to the centroid of a room-temperature $BaSnO_3$-absorber spectrum. The A site is ascribed to the core Sn_9 atoms, and the B site to the six ligand-bound Sn atoms.

splitting (QS) sites were revealed in a ratio of 1.5:1 at 90 K. These are assigned to the nine "naked" tin atoms Sn1 and Sn_A (site A) and the six ligand-bound atoms Sn_B (site B), respectively. Thus, the QS values of the A and B sites were determined to be 1.341 ± 0.012 (at 90 K) and 0.13 ± 0.01 mm s^{-1} (essentially temperature-independent), respectively.

The isomer shifts (IS) were found at 2.733 ± 0.011 and 2.63 ± 0.01 mm s^{-1} at 90 K for the A and B sites, respectively. These values are close to that of gray tin (α-Sn, 2.56 ± 0.02 mm s^{-1} at room temperature) or white tin (β-Sn, 2.68 mm s^{-1} [19]), and are within the range for bivalent tin compounds. For example, [{Sn[N(SiMe$_3$)$_2$](μ-Cl)}$_2$] has IS and QS values of 3.28 and 3.10 mm s^{-1}, respectively.[20] The IS values for quadrivalent organic tin compounds are substantially lower; for example, SnCl{CH(SiMe$_3$)$_2$}$_3$ has IS and QS values of 1.27 ± 0.03 and $2.18 \text{ mm} \pm 0.05$ mm s^{-1}, respectively.[21]

Detailed analysis of the temperature dependence of the Mössbauer spectra is provided in the Supporting Information, which shows that the ratio of the two tin sites B and A is 0.66 (ca. 6/9) in the temperature range 120–230 K. It has not been possible to analyze the Mössbauer data in terms of three distinct tin atom types, and the resonance associated with the larger quadrupole-splitting site includes that from the central tin atom, which is located in a distorted cubic environment.

The geometry optimization of the model tin cluster [Sn_9{Sn(NH$_2$)}$_6$] (**M1**) was performed in the gaseous phase by using DFT calculations. The geometry optimization was performed at the B3LYP/LanL2DZ level of theory by using the Gaussian 03 package.[22] The calculations reproduced the

 © 2006 Wiley-VCH Verlag GmbH & Co. KGaA, Weinheim

main features of the experimentally observed Sn_{15} cluster with the optimized bond lengths being about 3% larger than those observed in the crystal structures of complexes **1** and **2**. In the polyhedral representation of the cluster core, the symmetrically inequivalent tin atoms became fully symmetric after optimization. The calculated Sn_A–Sn_A distances are 3.78 Å, and the corresponding distances in the crystal structures of **1** and **2** vary over the range 3.60–3.74 Å (see Table 1). The Sn_B atoms are symmetrically distant from the central cube vertices by 3.15 Å (in contrast to the slightly asymmetric distribution of distances in the X-ray structures, 2.97 to 3.06 Å).

In conclusion, we report the crystalline metalloid clusters **1** and **2**, the first examples of a body-centered cluster of Group 14 elements.[23] Compounds **1** and **2** are also noteworthy for being i) the highest-nuclearity Group 14 clusters to be described, ii) unprecedented in this compound class for being body-centered, and iii) the first Group 14 metal clusters to have amido ligands. The inner cube of eight tin atoms (Sn_A) have the closer contacts to Sn1, and the distances between Sn1 and the remaining six tin atoms (Sn_B) are longer. The preferred method of synthesis of **1** and **2** involved a novel route, namely the reduction of the appropriate amidotin(II) chloride by the reducing agent Li[BH*s*Bu$_3$]. DFT calculations on the model cluster $[Sn_9\{Sn(NH_2)\}_6]$ reasonably reproduced the experimental Sn1–Sn_A, Sn1–Sn_B, Sn_A–Sn_B, and Sn_A–Sn_A distances. Mössbauer spectra of **1** are consistent with the X-ray structure in showing that there are two distinct quadrupole-splitting sites in the ratio 1.5:1, which correspond to the Sn_9 core and the six {Sn(NRR′)} moieties, but the Mössbauer data do not distinguish the Sn1 atom from the Sn_A atoms. The isomer shift of the atoms in the Sn_9 core is almost identical to that for β-tin.

Experimental Section

All manipulations were carried out under anaerobic and anhydrous conditions.

1(*Pnnm*, $R\bar{3}$): KC_8 (0.11 g, 0.81 mmol) was added with stirring to a solution of **3** (0.47 g, 0.55 mmol) in Et_2O (40 mL) at about −30 °C. The mixture was stirred for 5 h and filtered. The dark red-brown filtrate was concentrated to about 3 mL, toluene (10 mL) was added, and the mixture was stored at −27 °C for 3 months (initially, a black powder precipitated, which was filtered off and discarded) to yield several small black crystals of compound **1**(*Pnnm*) along with large pale crystals of unreacted **3**. In another experiment, when the crystals of unreacted **3** had precipitated, the remaining solution was decanted, concentrated again, and stored at room temperature to produce black (or dark red in thin layers) hexagonal prisms of compound **1**($R\bar{3}$).

1($R\bar{3}c$, $P2_1/n$): $[Sn\{N(2,6\text{-}iPr_2C_6H_3)(SiMe_3)\}_2]$ (1.23 g, 2 mmol) and $SnCl_2$ (0.38 g, 2 mmol) were mixed in freshly degassed THF (50 mL) at room temperature and stirred for 6 h. The reaction mixture was cooled to about −78 °C, and Li[BH*s*Bu$_3$] (L-selectride) (3.0 mL, 1.0 M solution in THF, 3.0 mmol) was added quickly. After slowly warming to room temperature, the solution was stirred for 48 h. The solvent was removed in vacuo, and the black residue was extracted into toluene (50 mL). The deep-black extract was filtered, and the filtrate was concentrated (ca. 30 mL). Storage of the solution at room temperature for 5 days afforded crystalline **1**($R\bar{3}c$) (0.045 g, 5%). The synthesis of **1**($P2_1/n$) was identical to that of **1**($R\bar{3}c$), except that the residue was extracted with hexane. Crystals of compound **1** were only sparingly soluble in hydrocarbons or ethers.

2: $[Sn\{N(2,6\text{-}iPr_2C_6H_3)(SiMe_2Ph)\}_2]$ (1.25 g, 1.75 mmol) and $SnCl_2$ (0.332 g, 1.75 mmol) were mixed in freshly degassed THF (40 mL) at room temperature and stirred for 6 h. The reaction mixture was cooled to about −78 °C, and Li[BH*s*Bu$_3$] (2.8 mL, 1.0 M solution in THF, 2.8 mmol) was added quickly. After slowly warming to room temperature, the solution was stirred for 24 h. The solvent was removed in vacuo, and the black residue was extracted into hexanes (30 mL). The deep-black extract was filtered, and the filtrate was concentrated (ca. 20 mL). Storage of the solution at room temperature for 2 days afforded crystalline **2** (0.057 g, 7%).

Received: January 23, 2006
Revised: April 25, 2006

Keywords: amide ligands · cluster compounds · Mössbauer spectroscopy · tin · X-ray diffraction

[1] A. Purath, R. Köppe, H. Schnöckel, *Angew. Chem.* **1999**, *111*, 3144; *Angew. Chem. Int. Ed.* **1999**, *38*, 2926.
[2] a) A. Schnepf, H. Schnöckel, *Angew. Chem.* **2002**, *114*, 3682; *Angew. Chem. Int. Ed.* **2002**, *41*, 3533; b) G. Linti, H. Schnöckel, W. Uhl, N. Wiberg, *Molecular Clusters of the Main Group Elements* (Eds.: M. Driess, H. Nöth), Wiley-VCH, Weinheim, **2004**, chap. 2.3, p. 126; c) H. Schnöckel, *Dalton Trans.* **2005**, 3131.
[3] a) N. Wiberg, P. P. Power, *Molecular Clusters of the Main Group Elements* (Eds.: M. Driess, H. Nöth), Wiley-VCH, Weinheim, **2004**, chap. 2.2, p. 188; b) A. Schnepf, *Angew. Chem.* **2004**, *116*, 680; *Angew. Chem. Int. Ed.* **2004**, *43*, 664.
[4] B. E. Eichler, P. P. Power, *Angew. Chem.* **2001**, *113*, 818; *Angew. Chem. Int. Ed.* **2001**, *40*, 796.
[5] N. Wiberg, H.-W. Lerner, S. Wagner, H. Nöth, T. Seifert, *Z. Naturforsch. B* **1999**, *54*, 877.
[6] A. F. Richards, B. E. Eichler, M. Brynda, M. M. Olmstead, P. P. Power, *Angew. Chem.* **2005**, *117*, 2602; *Angew. Chem. Int. Ed.* **2005**, *44*, 2546.
[7] J. D. Corbett, *Angew. Chem.* **2000**, *112*, 682; *Angew. Chem. Int. Ed.* **2000**, *39*, 670.
[8] a) A. Ecker, E. Weckert, H. Schnöckel, *Nature* **1997**, *387*, 379; b) A. Schnepf, H. Schnöckel, *Angew. Chem.* **2001**, *113*, 733; *Angew. Chem. Int. Ed.* **2001**, *40*, 712.
[9] G. Fischer, V. Huch, P. Mayer, S. K. Vasisht, M. Veith, N. Wiberg, *Angew. Chem.* **2005**, *117*, 8096; *Angew. Chem. Int. Ed.* **2005**, *44*, 7884.
[10] H. Cox, D. J. Doyle, P. B. Hitchcock, M. F. Lappert, L. J.-M. Pierssens, A. V. Protchenko, A. Růžička, J. R. Severn, XIth Int. Conf. on the Coordination and Organometallic Chemistry of Germanium, Tin, and Lead, Santa Fe, July **2004**, Abstracts Paper O-43.
[11] The synthesis and X-ray structure of **3** are described in the Supporting Information.
[12] a) B. Luo, V. G. Young, Jr., W. L. Gladfelter, *J. Organomet. Chem.* **2002**, *649*, 268; b) J. R. Babcock, L. Liable-Sands, A. L. Rheingold, L. R. Sita, *Organometallics* **1999**, *18*, 4437.
[13] B. E. Eichler, P. P. Power, *J. Am. Chem. Soc.* **2000**, *122*, 8785.
[14] Crystal data for **1**(*Pnnm*) with $Mo_{K\alpha}$ radiation ($\lambda = 0.7107$ Å) at 173(2) K: black block, orthorhombic, space group *Pnnm*, $a = 17.1182(2)$, $b = 17.1312(2)$, $c = 22.8882(2)$ Å, $V = 6712.09(13)$ Å^3, $Z = 2$, $R1$(obs. data) = 0.025, $wR2$(all data) = 0.092. Crystal data for **1**($R\bar{3}$) with $Mo_{K\alpha}$ radiation ($\lambda = 0.7107$ Å) at 173(2) K: black prism, trigonal, space group $R\bar{3}$, $a = 15.1565(2)$, $b = 15.1565(2)$, $c = 44.6776(10)$ Å, $\gamma = 120°$, $V = 8888.3(3)$ Å^3, $Z = 3$, $R1$(obs. data) = 0.036, $wR2$(all data) = 0.073. Crystal data for **1**($R\bar{3}c$)·PhMe with $Mo_{K\alpha}$ radiation ($\lambda = 0.7107$ Å) at 90(2) K: black block, hexagonal, space group $R\bar{3}c$, $a = 15.0335(2)$, $b = 15.0335(2)$, $c = 103.042(3)$ Å, $\beta = 120°$, $V = 20168.2(7)$ Å^3, $Z =$

 © 2006 Wiley-VCH Verlag GmbH & Co. KGaA, Weinheim

6, $R1$(obs. data) = 0.0262, $wR2$(all data) = 0.0560. Crystal data for **1** ($P2_1/n$) with $Mo_{K\alpha}$ radiation ($\lambda = 0.7107$ Å) at 90(2) K: black plate, monoclinic, space group $P2_1/n$, $a = 16.2048(6)$, $b = 24.0255(9)$, $c = 16.6026(6)$ Å, $\beta = 113.159(1)°$, $V = 5943.0(4)$ Å^3, $Z = 2$, $R1$(obs. data) = 0.0224, $wR2$(all data) = 0.0549. Crystal data for **2**·hexane with $Mo_{K\alpha}$ radiation ($\lambda = 0.7107$ Å) at 90(2) K: black block, monoclinic, space group $P2_1/n$, $a = 17.5916(6)$, $b = 18.8745(6)$, $c = 21.7499(7)$ Å, $\beta = 90.904(1)°$, $V = 7220.8(4)$ Å^3, $Z = 2$, $R1$(obs. data) = 0.0249, $wR2$(all data) = 0.0693. CCDC-295619–295624 contain the supplementary crystallographic data for this paper. These data can be obtained free of charge from The Cambridge Crystallographic Data Centre via www.ccdc.cam.ac.uk/data_request/cif.

[15] The Sn–Sn distances in each of **1** (*Pnnm*, $R\bar{3}$, $R\bar{3}c$, $P2_1/n$), **2**, and **III** are given in the Supporting Information.[6]

[16] A. Purath, C. Dohmeier, A. Ecker, R. Köppe, H. Krautscheid, H. Schnöckel, R. Ahlrichs, C. Stoermer, J. Friedrich, P. Jutzi, *J. Am. Chem. Soc.* **2000**, *122*, 6955.

[17] S. Desgreniers, Y. K. Vohra, A. L. Ruoff, *Phys. Rev. B* **1989**, *39*, 10360.

[18] Variable-temperature ^{119}Sn Mössbauer experiments were carried out by using a room-temperature $Ba^{119m}SnO_3$ source in transmission geometry as described previously.[19] Spectrometer calibration was effected by using an α-Fe absorber (10.52 mg Fe per cm^2). All isomer shifts are reported with respect to the centroid of a $BaSnO_3$ absorber spectrum at room temperature. Temperature control over the data acquisition periods (typically 8 to 24 h) was better than ± 0.2 K.

[19] R. H. Herber, G. I. Parisi, *Inorg. Chem.* **1966**, *5*, 769.

[20] H. Cox, P. B. Hitchcock, M. F. Lappert, L. J.-M. Pierssens, *Angew. Chem.* **2004**, *116*, 4600; *Angew. Chem. Int. Ed.* **2004**, *43*, 4500.

[21] J. D. Cotton, P. J. Davidson, M. F. Lappert, J. D. Donaldson, J. Silver, *J. Chem. Soc. Dalton Trans.* **1976**, 2286.

[22] Gaussian 98 (Revision A.7), M. J. Frisch, G. W. Trucks, H. B. Schlegel, G. E. Scuseria, M. A. Robb, J. R. Cheeseman, V. G. Zakrzewski, J. A. Montgomery, R. E. Stratmann, J. C. Burant, S. Dapprich, J. M. Millam, A. D. Daniels, K. N. Kudin, M. C. Strain, O. Farkas, J. Tomasi, V. Barone, M. Cossi, R. Cammi, B. Mennucci, C. Pomelli, C. Adamo, S. Clifford, J. Ochterski, G. A. Petersson, P. Y. Ayala, Q. Cui, K. Morokuma, D. K. Malick, A. D. Rabuck, K. Raghavachari, J. B. Foresman, J. Cioslowski, J. V. Ortiz, B. B. Stefanov, G. Liu, A. Liashenko, P. Piskorz, I. Komaromi, R. Gomperts, R. L. Martin, D. J. Fox, T. Keith, M. A. Al-Laham, C. Y. Peng, A. Nanayakkara, C. Gonzalez, M. Challacombe, P. M. W. Gill, B. G. Johnson, W. Chen, M. W. Wong, J. L. Andres, M. Head-Gordon, E. S. Replogle, J. A. Pople, Gaussian, Inc., Pittsburgh, PA, **1998**.

[23] Very recently a heterometallic Zintl compound containing a body-centered distorted cubic arrangement of nine Sn atoms was reported; see: E. N. Esenturk, J. C. Fettinger, B. W. Eichhorn, *J. Am. Chem. Soc.* **2006**, *128*, 12.

 © 2006 Wiley-VCH Verlag GmbH & Co. KGaA, Weinheim

Crystal Engineering

DOI: 10.1002/anie.200600376

Anisotropic Movements of Coordination Polymers upon Desolvation: Solid-State Transformation of a Linear 1D Coordination Polymer to a Ladderlike Structure**

*Mangayarkarasi Nagarathinam and Jagadese J. Vittal**

Despite the inherent strong barriers of simultaneous bond breaking and formation in more than one direction, many interesting transformations of one coordination polymer to another in the solid state have been studied widely in recent years.[1–4] A notable success has already been achieved in positioning the ligands with olefinic double bonds in a coordination polymer, and in the isolation of their photodimerized products through single-crystal-to-single-crystal (SCSC) transformation.[5] Generally, these photochemical [2+2] cycloadditions of the olefinic double bonds are expected to occur with the minimal atomic and molecular movements when they are aligned parallel and within the range of 3.0–4.1 Å.[5–8] There are also a few interesting reports on rare phenomena, such as the anisotropic long-range molecular-movement-induced/assisted [2+2] photodimerizations of organic molecules that have been visualized in single crystals only through grazing incidence diffraction, atomic force microscopy, and near-field optical microscopy.[9] Indeed, long-range molecular movements have been demonstrated in a few coordination complexes by SCSC transformation.[10] However, the studies have not been extended to crystals that have lost their crystallinity or undergone a mild change in the crystal structure as a result of the desolvation process. To the best of our knowledge, cooperative anisotropic molecular movements resulting from desolvation in a coordination polymer have not been observed to date.

While we were investigating the photochemical activity of coordination polymers, we found that the double bonds in the desolvated crystals of the single-stranded coordination polymers $[Ag(\mu_2\text{-bpe})]_n^{n+}$ (bpe = 4,4′-bipyridylethylene) undergo [2+2] cycloaddition under UV irradiation. This polymer has neither Ag···Ag interaction nor satisfies Schmidt's topochemical criteria in the solvated structure. Such a reaction can occur only when the bpe ligands are preorganized during desolvation.[5–9] The transformation from a single-stranded to

[*] Dr. M. Nagarathinam, Prof. J. J. Vittal
Department of Chemistry
National University of Singapore
3 Science Drive 3, Singapore 117543 (Singapore)
Fax: (+65) 6779-1691
E-mail: chmjjv@nus.edu.sg

[**] The National University of Singapore is thanked for its generous funding of this project. We thank Prof. L. L. Koh for his help with X-ray crystallography.

Supporting information for this article is available on the WWW under http://www.angewandte.org or from the author.

© 2006 Wiley-VCH Verlag GmbH & Co. KGaA, Weinheim

a ladder-type structure appears to be facilitated by Ag···Ag and π···π interactions accompanied by the anisotropic cooperative molecular movements of the adjacent linear chains upon desolvation. This notion has been further supported by X-ray powder diffraction experiments and IR spectroscopy. The details are presented herein.

Colorless thin crystals of $[Ag(\mu\text{-bpe})(H_2O)](CF_3CO_2)\cdot CH_3CN$ (**1**) were obtained by a layering method from equimolar solutions of bpe and $Ag(O_2CCF_3)\cdot H_2O$. The crystals became opaque immediately after removal from the mother liquor and disintegrated after some time. X-ray crystal structure determination at 223 K revealed the presence of linear 1D coordination polymers $[Ag(\mu\text{-bpe})]_n$ with the oxygen atom of a water molecule bonded to the Ag^I center (see Figure 1a). The nitrogen atom of the solvent CH_3CN is

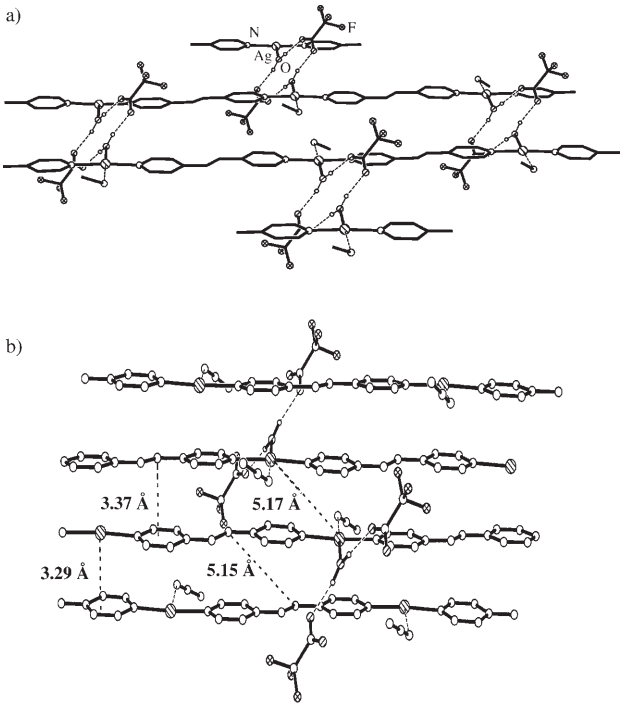


Figure 1. a) View of a portion of the hydrogen-bonded brick-wall-like structure in the crystal structure of **1**. b) View showing the non-alignment of double bonds and Ag atoms along the *b* axis in the packing. The disordered F atoms of the trifluoroacetate ions are not shown. The C–H hydrogen atoms have been omitted for clarity.

directed toward the Ag atom, and the Ag···N distance of 3.32 Å just exceeds the sum of the Van der Waals radii (3.27 Å). The hydrogen atoms of the coordinated water molecules from two neighboring polymeric strands bridge the oxygen atoms of two non-coordinated trifluoroacetate ions through hydrogen bonds (O–H···O, $d = 1.87$ Å, $D = 2.74$ Å, $\theta = 162°$) to form a 12-membered ring [notation $R_4^4(12)$],[11] similar to the analogous interactions reported in the literature.[12]

This connectivity leads to hydrogen-bonded, 2D brick-wall-like structures approximately in the *ac* plane, as a result of the *anti* dispositions of the Ag–O bonds in the polymer chains caused by crystallographic inversion at the double bonds. The closest Ag···Ag distances in this plane are 9.43 and 10.43 Å.

The adjacent polymeric strands are stacked along the *b* direction in such a way that the Ag^I atoms are close to a pyridyl ring (Ag···Py, 3.29 Å) and one carbon atom of the double bond is close to another pyridyl ring (C12···Py, 3.37 Å; see Figure 1b). The closest Ag···Ag and nonbonding interactions between the ethylenic carbon atoms of two consecutive layers are 5.17 and 5.15 Å, respectively. This finding clearly demonstrates that there is no Ag···Ag interaction, and that the silver atoms are not bridged by trifluoroacetate ligands and do not form the β-type motifs ((3.9 ± 0.2) Å), which can undergo photodimerizations with short-range molecular movements. Complex **1** satisfies the conditions for γ-type (> 5.1 Å) olefinic double bonds, which are clearly not expected to undergo photodimerizations in the solid state.[6,7]

As the crystal was desolvated and lost its crystallinity readily upon irradiation, the photoreactivity of the solvated crystal could not be studied. However, when a desolvated crystalline powder of **1** was irradiated by UV light for 8 h, complete conversion of the olefins to cyclobutane derivatives was observed. The ^1H NMR spectrum in $[D_6]$DMSO shows the complete disappearance of the olefinic proton signal at $\delta = 7.56$ ppm, a new signal attributable to cyclobutane protons at $\delta = 4.68$ ppm, and a shift in the bipyridyl proton signals from $\delta = 8.61$ and 7.65 ppm to $\delta = 8.35$ and 7.24 ppm, which confirms the formation of the expected photodimerized product (see Supporting Information).

Quantitative photodimerization on irradiation of desolvated **1** confirms that molecular movement occurs on removal of the solvents. The packing diagram of the crystal structure also shows clearly that there must be enough freedom for the reactive molecules to undergo the necessary lateral movements to reorganize once the solvents are removed.

The free movement of the coordination polymers, their reorganization from a linear 1D to a ladderlike structure, and the reorientation of the adjacent olefinic double bonds suitable for photodimerization in **1** on desolvation are evident from the isolation and characterization of colorless, platelike crystals of $[\{(\mu\text{-}O_2CCF_3)Ag\}_2(\mu\text{-bpe})_2]\cdot H_2O$ (**2**). Compound **2** was obtained on reaction of equimolar amounts of bpe and $Ag(O_2CCF_3)$ under different reaction conditions with the same solvents. The crystals obtained were of poor X-ray diffraction quality and readily lost lattice water to become opaque in air. Although the bpe ligands were severely disordered, which was further complicated by a crystallographic inversion center, the connectivity in the ladderlike 1D coordination polymeric structure has been proved beyond any doubt.

In **2** two linear polymers [(μ-bpe)Ag] are bridged by two trifluoroacetate ligands to form a double-stranded, molecular-ladder-like coordination polymer (Figure 2). The distances of Ag···Ag and two olefinic double bonds aligned in parallel are 3.15 and 3.62–4.06 Å, respectively. The π···π and Ag···Ag interactions provide thermodynamic stability to this ladder-type arrangement. The crystal structure of **2** signifies that we have successfully isolated a molecular-ladder-like coordina-

 © 2006 Wiley-VCH Verlag GmbH & Co. KGaA, Weinheim

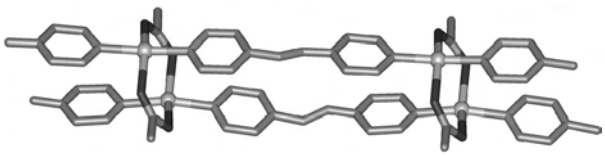


Figure 2. Perspective view of a portion of the 1D molecular ladder polymeric structure of **2**. Hydrogen atoms and disordered bpe ligands have been omitted for clarity.

tion polymer that satisfies the geometric criteria postulated by Schmidt for [2+2] photodimerizations.[6] Attempts to isolate crystals of **2** with better X-ray quality by changing the reaction conditions were in vain; they either resulted in crystals of poor X-ray quality, insoluble precipitate, or decomposition of the product to silver.

The desolvated crystalline powder of **2** was irradiated for 8 h and the ^{1}H NMR spectrum of the colorless product revealed that the product was completely photodimerized. This result supports the finding that the carboxylate-bridged silver dimer is a reliable supramolecular synthon for the alignment of bpe ligands as a silver coordination polymer. Furthermore, it confirms that the ladder structure is preserved in the desolvated **2**. But SCSC transformation was not observed because the single crystals disintegrated upon desolvation. The solvated **2** is not stable under UV irradiation similar to **1**.

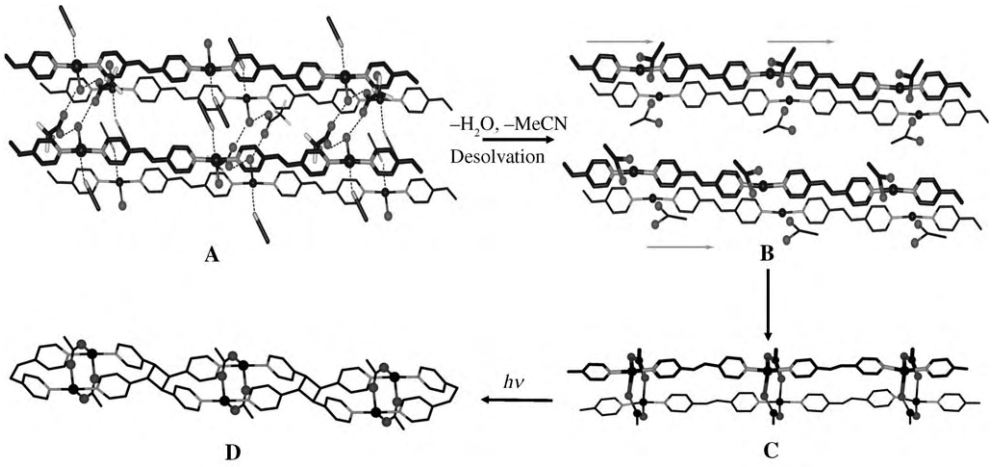
The X-ray powder diffraction pattern of desolvated **1** matched reasonably well with that of desolvated **2** (see Supporting Information), which implies that the crystal structure and the orientations of the coordination polymers in the desolvated lattice of **1** are similar to those present in desolvated **2**. This XRD result helps visualizing the anisotropic molecular movements in **1**.

The transformation of a linear 1D coordination polymer to a ladder-type polymeric structure is depicted in Scheme 1. Immediately after removal of the coordinated water molecule and the lattice CH_3CN, the crystal structure starts to collapse, which is transmitted throughout the stacked layers. To balance the stress, simultaneous cooperative lateral movements of the coordination polymers and $CF_3CO_2^-$ ions occur within the crystal (**B**). During this phase-rebuilding process, the thermodynamically favored Ag···Ag interaction becomes activated between the adjacent strands along the *b* axis, rather than with the parallel strands in the *ac* plane that are nearly 10 Å away. The average Ag···O distance between the silver atom and the oxygen atom of the $CF_3CO_2^-$ ions is about 4.45 Å in **A**.

It is proposed that the trifluoroacetate ions migrate to bridge the adjacent silver atoms in the *b* direction. Such movements of the carboxylate groups that form bonds to the metal are well documented.[3c,d,5a] For example, in the topochemical conversion of a hydrogen-bonded to a covalently bonded supramolecular network, a carboxylate oxygen atom of the reduced Schiff base ligand from the neighboring molecule forms a bond to Zn^{II} guided by N–H···O hydrogen bonds on thermal dehydration.[3c,d] In this transformation, the distance between Zn^{II} and the oxygen atoms of the carboxylate group changed from 3.736(2) to 2.010(2) Å. On the other hand, molecular rotation of the trifluoroacetate group competes for coordination and forms a bridge between two Ag atoms.[5a] Completion of phase transformation leads to the formation of a ladder structure (**C**), but the bond breaking and bond making probably create high strain and the crystal disintegrates. This reveals that the influence of strain generated by desolvation of the crystal and the Ag···Ag and π···π interactions in the resultant lattice leads to the transformation and hence the molecular reactions within the crystalline solid.

The proposed mechanism is further corroborated by the solid-state FTIR spectra of desolvated **1** and **2**, which are exactly the same, and the bridging of two carboxylate oxygen atoms of the trifluoroacetate ion that is seen from the $\Delta\tilde{\nu}$(COO) value of 200 cm^{-1}, that is, the difference between the ν_{as}(COO) at 1661 cm^{-1} and ν_s(COO) at 1461 cm^{-1}.[13] The relatively higher values of ν_{as}(COO) and the $\Delta\tilde{\nu}$(COO) are a result of the asymmetric O–Ag–O arrangement in **2** (Ag···O distances of 2.71 and 2.59 Å). In a mixture of solvents, $AgBF_4$ and bpe produced a 3D network structure of the photodimerized ligand over a long period of time.[14] Clearly, the metal and ligand have rearranged in solution to give this unexpected product.

A recent report by MacGillivray and co-workers on the desolvation-induced phase transition and partial loss of crystallinity of a compound that undergoes photodimerization describes that the alignment of bpe ligands through N–H···N interac-



Scheme 1. Transformation of linear 1D strands in the crystal structure of **1** to a ladderlike arrangement upon desolvation. **A**: A portion of the crystal structure, **B**: proposed intermediate stage after desolvation, **C**: formation of a ladderlike structure, and **D**: photodimerized product. For clarity only one strand is shown for **C** and **D**.

 © 2006 Wiley-VCH Verlag GmbH & Co. KGaA, Weinheim

tion was not disturbed on removal of the solvent.[8b] Although the influence of solvents on supramolecular transformation from linear 1D strands to a ladderlike coordination polymer on desolvation is not visualized through SCSC transformation, we have used Schmidt's criteria for the photodimerization[6] to investigate this phenomenon for the first time, along with X-ray powder diffraction, IR spectroscopy, and other analytical data. The detailed study of this type of cooperative, anisotropic, long-range molecular movement in a coordination polymer will not only give further insight into the solid-state reaction mechanism, but also direct inorganic coordination polymers toward materials science with great impact.

Experimental Section

1: A solution of bpe (0.018 g, 0.1 mmol) in CH_3OH (1 mL) was layered over an aqueous solution (1 mL) of $Ag(O_2CCF_3)\cdot 2H_2O$ (0.023 g, 0.1 mmol) with CH_3CN (3 mL) as a middle buffer layer. Colorless, dendrimer-shaped plates crystallized at the solvent junction. Yield: 0.07 g, 26%. IR (nujol mull): $\tilde{\nu}=1661$(m), 1604 (m), 1461(s), 1377(m), 1203(m), 1112(m), 1071(w), 829(m), 717 cm^{-1} (m). ^1H NMR (300 MHz, [D$_6$]DMSO, 298 K): $\delta=8.61$ (d, 4H; Py-H), 7.65 (d, 4H; Py-H), 7.56 ppm (s, 4H; CH=CH). C,H,N analysis (%) calcd for $C_{14}H_{10}F_3N_2OAg$ (desolvated **1**): C 41.71, H 2.50, N 6.95; found: C 41.67, H 2.36, N 6.78.

UV irradiation of **1**: Powdered **1** (15 mg) in between glass slides was irradiated with a Xe lamp (60 W) for approximately 8 h. IR (nujol mull): $\tilde{\nu}=1676$(m), 1604(m), 1462(s), 1377(m), 1200(m), 1112(m), 1067(w), 834 cm^{-1} (m). ^1H NMR (300 MHz, [D$_6$]DMSO, 298 K): $\delta=$ 8.35 (d, 4H; Py-H), 7.24 (d, 4H; Py-H), 4.68 ppm (s, 4H; CH-CH). C,H,N analysis (%) calcd for $C_{28}H_{20}F_6N_4O_4Ag_2$: C 41.71, H 2.50, N 6.95; found: C 41.67, H 2.36, N 6.92.

2: A solution of bpe (0.090 g, 0.5 mmol) in methanol (5 mL) was added to an aqueous solution (5 mL) of $Ag(O_2CCF_3)\cdot 2H_2O$ (0.115 g, 0.5 mmol), and the white precipitate formed was dissolved by further addition of CH_3CN (15 mL). The clear solution was filtered and the filtrate was slowly evaporated. Small, colorless, very thin, platelike crystals separated out after 3 days and were filtered and dried under vacuum. Yield: 0.08 g, 26%. IR (nujol mull): $\tilde{\nu}=1661$(m), 1602(m), 1461(s), 1377(m), 1203(m), 1112(m), 1071(w), 829(m), 717 cm^{-1} (m). ^1H NMR (300 MHz, [D$_6$]DMSO, 298 K): $\delta=8.61$ (s, 4H; Py-H), 7.65 (d, 4H; Py-H), 7.56 ppm (s, 4H; CH=CH). C,H,N analysis (%) calcd for $C_{14}H_{12}F_3N_2O_3Ag$: C 39.93, H 2.83, N 6.65; found: C 39.14, H 2.92, N 6.54; calcd for $C_{14}H_{10}F_3N_2O_2Ag$ (desolvated **2**): C 41.71, H 2.50, N, 6.95; found: C 41.67, H 2.47, N 6.78.

UV irradiation of **2**: Powdered **2** (15 mg) in between glass slides was irradiated with a Xe lamp (60 W) for approximately 8 h. IR (nujol mull): $\tilde{\nu}=1661$(m), 1602(m), 1461(s), 1377(m), 1203(m), 1112(m), 1071(w), 829(m), 717(m), 530 cm^{-1} (m). ^1H NMR (300 MHz, [D$_6$]DMSO, 298 K): $\delta=8.35$ (d, 4H; Py-H), 7.24 (d, 4H; Py-H), 4.68 ppm (s, 4H; CH–CH). C,H,N analysis (%) calcd for $C_{28}H_{20}F_6N_4O_4Ag_2$: C 41.71, H 2.50, N 6.95; found: C 41.67, H 2.36, N 6.92.

X-ray crystallography: Crystal data were collected on a Bruker APEX diffractometer with a CCD detector and graphite-monochromated $Mo_{K\alpha}$ radiation using a sealed tube (2.4 kW) at 223(2) K. Absorption corrections were made with the program SADABS[15] and the crystallographic package SHELXTL[16] was used for all calculations.

Crystal data for **1**: triclinic, space group $P\bar{1}$, $a=10.0330(8)$, $b=$ 10.2394(8), $c=10.9499(8)$ Å, $\alpha=104.260(2)$, $\beta=100.719(2)$, $\gamma=$ 118.696(1)°, $V=893.0(1)$ Å^3, $\rho_{calcd}=1.719$ g cm^{-1}, $Z=2$. In the final least-squares refinement cycles on $|F|^2$, the model converged at $R1=$ 0.0364, $wR2=0.0879$, GoF = 1.056 for 2896 ($I\geq 2\sigma(I)$) reflections.

Crystal data for **2**: monoclinic, space group $P2_1/m$, $a=7.349(2)$, $b=$ 17.781(5), $c=12.643(4)$ Å, $\beta=98.552(6)$°, $V=1633.6(8)$ Å^3, $Z=4$.

CCDC-295995 (**1**) contains the supplementary crystallographic data for this paper. These data can be obtained free of charge from The Cambridge Crystallographic Data Centre via www.ccdc.cam.ac.uk/data_request/cif.

Published online: May 31, 2006

Keywords: crystal engineering · ladder polymers · silver · solid-state reactions · stacking interactions

[1] For example, see: a) S. Rabe, U. Müller, *Z. Anorg. Allg. Chem.* **1999**, *625*, 1367–1370; b) U. Englert, B. Ganter, T. Wagner, W. Kläui, *Z. Anorg. Allg. Chem.* **1998**, *624*, 970–974; c) H. Li, M. Eddaoudi, M. O'Keefe, O. M. Yaghi, *Nature* **1999**, *402*, 276–279; d) C. J. Kepert, T. J. Prior, M. J. Rosseinsky, *J. Am. Chem. Soc.* **2000**, *122*, 5158–5168; e) E. Y. Lee, M. P. Suh, *Angew. Chem.* **2004**, *116*, 2858–2861; *Angew. Chem. Int. Ed.* **2004**, *43*, 2798–2801.

[2] a) L. Iordanidis, M. G. Kanatzidis, *Angew. Chem.* **2000**, *112*, 2004–2006; *Angew. Chem. Int. Ed.* **2000**, *39*, 1928–1930; b) L. Iordanidis, M. G. Kanatzidis, *J. Am. Chem. Soc.* **2000**, *122*, 8319–8320.

[3] a) B. Rather, M. J. Zaworotoko, *Chem. Commun.* **2003**, 830–831; b) K. Biradha, M. Fujita, *Angew. Chem.* **2002**, *114*, 3542–3545; *Angew. Chem. Int. Ed.* **2002**, *41*, 3392–3395; c) J. D. Ranford, J. J. Vittal, D. Wu, *Angew. Chem.* **1998**, *110*, 1159–1162; *Angew. Chem. Int. Ed.* **1998**, *37*, 1114–1116; d) J. D. Ranford, J. J. Vittal, D. Wu, X. Yang, *Angew. Chem.* **1999**, *111*, 3707–3710; *Angew. Chem. Int. Ed.* **1999**, *38*, 3498–3501.

[4] a) C.-L. Chen, A. M. Goforth, M. D. Smith, C.-Y. Su, H.-C. zur Loye, *Angew. Chem.* **2005**, *117*, 6831–6835; *Angew. Chem. Int. Ed.* **2005**, *44*, 6673–6677; b) D. Kumar, D. A. Jose, A. Das, P. Dastidar, *Inorg. Chem.* **2005**, *44*, 6933–6935; c) J. P. Ma, Y.-B. Dong, R. Q. Huang, D. M. Smith, C.-Y. Su, *Inorg. Chem.* **2005**, *44*, 6143–6145; d) J.-P. Chang, Y.-Y. Lin, W.-X. Zhang, X.-M. Chen, *J. Am. Chem. Soc.* **2005**, *127*, 14162–14163.

[5] a) Q. Chu, D. C. Swenson, L. R. MacGillivray, *Angew. Chem.* **2005**, *117*, 3635–3638; *Angew. Chem. Int. Ed.* **2005**, *44*, 3569–3572; b) G. S. Papaefstathiou, I. G. Georgia, T. Friščić, L. R. MacGillivray, *Chem. Commun.* **2005**, 3974–3976; c) N. L. Toh, M. Nagarathinam, J. J. Vittal, *Angew. Chem.* **2005**, *117*, 2277–2281; *Angew. Chem. Int. Ed.* **2005**, *44*, 2237–2240; d) G. S. Papaefsthathiou, Z. Zhong, L. Geng, L. R. MacGillivray, *J. Am. Chem. Soc.* **2004**, *126*, 9158–9159; e) C. R. Theocharis, A. M. Clark, S. E. Hopkin, P. Jones, *Mol. Cryst. Liq. Cryst.* **1988**, *156(Pt.A)*, 85–91.

[6] a) G. M. J. Schmidt, *J. Chem. Soc.* **1964**, 2014–2021; b) G. M. J. Schmidt, *Pure Appl. Chem.* **1971**, *27*, 647–678; c) G. Wegner, *Pure Appl. Chem.* **1977**, *49*, 443–454; d) *Photochemistry in Organized and Constrained Media* (Ed.: V. Ramamurthy), VCH, New York, **1991**; e) V. Ramamurthy, K. Venkatesan, *Chem. Rev.* **1987**, *87*, 433–481.

[7] a) P. Wagner, B.-S. Park in *Organic Photochemistry*, *Vol. 11* (Ed.: A. Padwa), Dekker, New York, **1991**, chap. 4; b) W. Jones, *Organic Molecular Solids: Properties and Applications*, CRC Press, Boca Raton, FL, **1997**; c) *Organic Solid State Reactions* (Ed.: F. Toda), *Top. Curr. Chem.*, *Vol. 254*, **2005**; d) A. E. Keating, M. A. Garcia-Garibay in *Organic and Inorganic Photochemistry* (Eds.: V. Ramamurthy, K. S. Schanze), Dekker, New York, **1998**, pp. 195–248; e) D. Braga, F. Grepioni, *Angew. Chem.* **2004**, *116*, 4092–4102; *Angew. Chem. Int. Ed.* **2004**, *43*, 4002–4011; f) A. Matsumoto, *Top. Curr. Chem.* **2005**, *254*, 263; g) W. L. Dilling, *Chem. Rev.* **1983**, *83*, 3–47; h) Y. Maekawa, S.

 © 2006 Wiley-VCH Verlag GmbH & Co. KGaA, Weinheim

Kato, K. Saigo, M. Hasegawa, *Macromolecules* **1991**, *24*, 2314 – 2322.
[8] a) L. R. MacGillivray, G. S. Papaefstathiou, T. Friščić, D. B. Varshney, T. D. Hamilton, *Top. Curr. Chem.* **2005**, *248*, 201 – 221; b) D. B. Varshney, X. Gao, T. Friščić, L. R. MacGillivray, *Angew. Chem.* **2006**, *118*, 662 – 666; *Angew. Chem. Int. Ed.* **2006**, *45*, 646 – 650.
[9] a) If the molecules are not interlocked but can migrate in the crystal lattice, the free molecular movement induces the photoreactive olefinic double bonds to reorganize and satisfy Schmidt's criteria for photochemical [2+2] cycloaddition; b) G. Kaupp, J. Naimi, M. Reza, *CrystEngComm* **2005**, *7*, 402 – 410; c) G. Kaupp, *Top. Curr. Chem.* **2005**, *254*, 95 – 183; d) G. Kaupp, J. Schmeyers, J. Boy, *Chemosphere* **2001**, *43*, 55 – 61; e) G. Kaupp in *Comprehensive Supramolecular Chemistry*, *Vol. 8* (Ed.: J. E. D. Davies), Elsevier, Oxford, **1996**, pp. 381 – 423.
[10] a) K. Hanson, N. Calin, D. Bugaris, M. Scancella, S. C. Sevov, *J. Am. Chem. Soc.* **2004**, *126*, 10502 – 10503; b) M. D. Hollingsworth, M. L. Peterson, K. L. Pate, B. D. Dinkelmeyer, M. E. Brown, *J. Am. Chem. Soc.* **2002**, *124*, 2094 – 2095.
[11] a) M. C. Etter, J. C. MacDonald, *Acta Crystallogr. B* **1990**, *46*, 256 – 258; b) J. Bernstein, R. E. Davis, L. Shimoni, N.-L. Chang, *Angew. Chem.* **1995**, *107*, 1689; *Angew. Chem. Int. Ed. Engl.* **1995**, *34*, 1555 – 1557.
[12] a) P. King, R. Clerac, C. E. Anson, A. K. Powell, *Dalton Trans.* **2004**, 852; b) M. Chatterjee, M. Maji, S. Ghosh, T. C. W. Mak, *J. Chem. Soc. Dalton Trans.* **1998**, 3641 – 3645.
[13] a) K. Nakamoto, *Infrared and Raman Spectra of Inorganic and Coordination Compounds*, 4th ed., Wiley, New York, **1986**, p. 191; b) G. B. Deacon, R. J. Philips, *Coord. Chem. Rev.* **1980**, 227 – 250.
[14] A. J. Blake, N. R. Champness, S. S. M. Chung, W. S. Li, M. Schröder, *Chem. Commun.* **1997**, 1675 – 1676.
[15] G. M. Sheldrick, SADABS, Software for Empirical Absorption Corrections, University of Göttingen (Germany), **2000**.
[16] SHELXTL Reference Manual, version 5.1, Bruker AXS, Analytical X-Ray Systems, Madison, WI, USA, **1997**.

 © 2006 Wiley-VCH Verlag GmbH & Co. KGaA, Weinheim

Phosphorus Heterocycles

DOI: 10.1002/anie.200600950

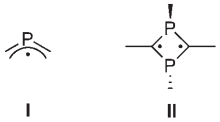
Preparation and Characterization of an Air-Tolerant 1,3-Diphosphacyclobuten-4-yl Radical**

Shigekazu Ito, Manabu Kikuchi, Masaaki Yoshifuji,* Anthony J. Arduengo, III, Tatyana A. Konovalova, and Lowell D. Kispert*

A radical is a species that contains an unpaired electron. These substances play an important role in organic, inorganic, physical, material, and biological chemistry from the point of view of reactivity, structure, and electronic properties. Radicals are generally highly reactive species with extremely short lifetimes; however, their stability can be improved thermodynamically by incorporation into a conjugated system. Kinetic enhancement of their stability can be accomplished through the use of steric encumbrance.[1,2]

The allyl radical is a fundamental organic radical and is an important research subject in both experimental and theoretical organic chemistry.[3] Streitwieser and co-workers reported the preparation and structure of stable pyridinium-substituted allyl radicals.[3c] Azuma et al. revealed the molecular and crystal structures of the 1,3-bis(diphenylene)-2-phenylallyl radical as complexes with benzene and acetone.[3d]

Parallels between the P=C and C=C double bonds have been formulated to develop phosphorus chemistry based on an organic chemistry model.[4] Allyl and 2-phosphaallyl radicals are examples of such "parallel" chemistry.[5] Schoeller et al. reported the generation of 2-phosphaallyl radical **I** by electrochemical reduction of 2-phosphaallyl cations and theoretical models of this radical provide insight into its structure.[6] We recently reported the synthesis



I II

[*] Dr. S. Ito, M. Kikuchi
Department of Chemistry
Graduate School of Science, Tohoku University
Aoba, Sendai 980-8578 (Japan)
Fax: (+81) 22-795-6562
E-mail: ito@synchem.chem.tohoku.ac.jp
Prof. M. Yoshifuji, Prof. A. J. Arduengo, III, Dr. T. A. Konovalova, Prof. L. D. Kispert
Department of Chemistry
University of Alabama
Tuscaloosa, AL 35487 (USA)
Fax: (+1) 205-348-4704
E-mail: myoshifuji@bama.ua.edu

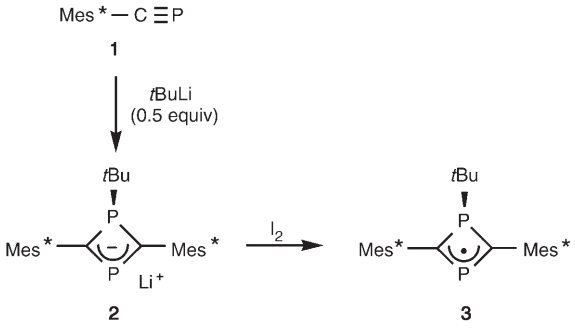
[**] This work was supported in part by Grants-in-Aid for Scientific Research (Nos 13304049 and 14044012) from the Ministry of Education, Culture, Sports, Science and Technology, Japan; the National Science Foundation (CHE-0413521, -0342921, and -0079498; USA); and the US Department of Energy (Grant DE-FG02-86ER13465). We thank Prof. Noboru Morita at Tohoku University for his helpful suggestions and comments.

Supporting information for this article is available on the WWW under http://www.angewandte.org or from the author.

© 2006 Wiley-VCH Verlag GmbH & Co. KGaA, Weinheim

of 1,3-diphosphacyclobutane-2,4-diyl biradicals of type **II** from a phosphaalkyne via a 1,3-diphosphacyclobutenyl anion.[7] Anions of **II** could also afford 1,3-diphosphacyclobuten-4-yl radicals (structure **I**) by an oxidative route. We now report the preparation and characterization of an air- and room-temperature-stable 1,3-diphosphayclobutenyl radical. A cyclobutenyl radical that is a C-congener of a 1,3-diphosphacyclobutenyl radical can be generated by H abstraction of cyclobutene or bicyclo[1.1.0]butane under cryogenic conditions,[8] thus suggesting that thermodynamic stabilization with phosphorus atoms and kinetic stabilization with the 2,4,6-tBu$_3$C$_6$H$_2$ (Mes*) groups are advantageous for producing stable organic radicals.

Phosphaalkyne **1** was treated with 0.5 equivalents of *tert*-butyllithium in THF to generate 1,3-diphosphaallyl anion **2** as a deep blue solution (Scheme 1).[7] When **2** was mixed with



Scheme 1. Preparation of **3**.

iodine, the solution turned deep red. After removal of the volatile materials, **3** was obtained and crystallized from dichloromethane. A single crystal was employed for X-ray crystallography structure analysis. Figure 1 displays the structure of **3** with a *Cs* symmetric form. The C_2P_2 four-membered ring is almost planar (Θ(P1-C1-P2-C2) = 7.7(3)°), whereas the two aromatic rings of the Mes* groups have torsional angles of 57.7(3) and 58.4(3)° with the C_2P_2 plane (thereby alleviating steric congestion). The sums of the bond angles at the C1

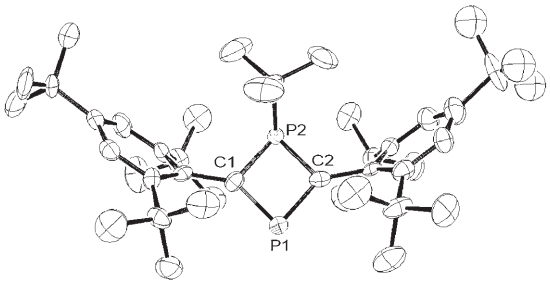
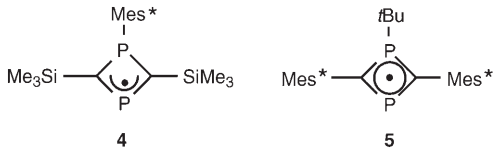


Figure 1. Molecular structure of **3** (ellipsoids set at 50% probability). Hydrogen atoms are omitted for clarity. The *p-tert*-butyl group in the Mes* group at C2 is disordered, and the atoms with the predominant occupancy factor (0.64) are displayed. Bond lengths [Å] and angles [°]: P1-C1 1.768(8), P1-C2 1.765(9), P2-C1 1.814(9), P2-C2 1.819(8), P2-C_{tBu} 1.881(8), C1-C_{Mes*} 1.48(1), C2-C_{Mes*} 1.49(1); C1-P1-C2 85.4(4), C1-P2-C2 82.5(4), P1-C1-P2 95.6(4), P1-C1-C_{Mes*} 142.3(7), P2-C1-C_{Mes*} 122.1(6), P1-C2-P2 95.5(4), P1-C2-C_{Mes*} 142.0(6), P2-C2-C_{Mes*} 122.3(6), C1-P2-C_{tBu} 109.8(4), C2-P2-C_{tBu} 110.2(3).

and C2 atoms are 360.0 and 359.8°, respectively, thus indicating sp^2 hybridizations. On the other hand, the P2 atom is strongly pyramidalized with a sum of the bond angles of 302.5°. Although the quality of structure refinement was not sufficient to allow discussion of the metric parameters in detail (because of the presence of disorder), the P2–C lengths in the four-membered ring indicate a P–C single bond, whereas the P1–C lengths are the same as the mean value between the P–C single- and the P=C double-bond lengths (ca. 1.85 Å[9] and 1.68 Å,[4] respectively). Compared with the 1,3-diphosphacyclobutane-2,4-diyls from our previous report,[7a,c] the transannular P1···P2 distance of 2.65 Å is longer than that for the biradical, whereas the C1···C2 distance of 2.40 Å is shorter. Accordingly, the bond angles of C1-P1-C2 and C1-P2-C2 are more acute than the corresponding data for the 1,3-diphosphacyclobutane-2,4-diyls.[7a,c] In spite of steric bulkiness, the Mes* groups tilt toward the *t*-butyl group, as was observed in the structure of a 1-*tert*-butyl-3-methyl-1,3-diphosphacyclobutane-2,4-diyl.[7a] Such structural properties might reflect a CH–π interaction[10] or the influence of crystal packing. The intermolecular P1···P1 distance (5.35 Å) indicates no substantial covalent bond and that the radical does not form dimers in the crystalline state.[11] Recently, Niecke and co-workers observed that the radical **4**, prepared through



cleavage of the P–C bond upon irradiation of a type **II** compound, undergoes a subsequent dimerization.[12a] This observation suggests that the radical moiety in **3** is successfully protected from dimerization as a result of the steric encumbrance.

In its crystalline state, radical **3** showed no apparent decomposition in air at room temperature for several months. The remarkable stability of **3** is likely derived from the electronic effect of the phosphorus atom in the allylic system and the adjacent phosphino moiety in addition to the steric encumbrance of the Mes* and the *tert*-butyl moieties. The UV/Vis spectrum of **3** in dichloromethane shows a relatively weak absorption at 759 nm and intense absorptions at 515 and 355 nm. Because of the broadening of the NMR spectrum of compound **3** as a result of the paramagnetic nature, no noticeable ^{31}P NMR signal was detected in the region between $\delta_P = 2000$ and -900 ppm ([D$_8$]toluene, 298 K).[13]

The electron paramagnetic resonance (EPR) spectrum of a solution of **3** in toluene ($T = 295$ K) exhibits a strong four-line signal with small outer peaks and the isotropic $g = 2.0025 \pm 0.0002$, which is characteristic of π–organic radicals[14] (see Figure 2a). The ^{31}P ($I = 1/2$) and ^{13}C ($I = 1/2$) isotropic hyperfine coupling (hfc) constants were determined by spectral simulation. The experimental spectrum was simulated by using the XSophe computer simulation software.[15] The best fit was obtained with the Lorentzian line width of 1.5 G, two different ^{31}P hfc constants $a_{P1} = 20.4$ G,

 © 2006 Wiley-VCH Verlag GmbH & Co. KGaA, Weinheim

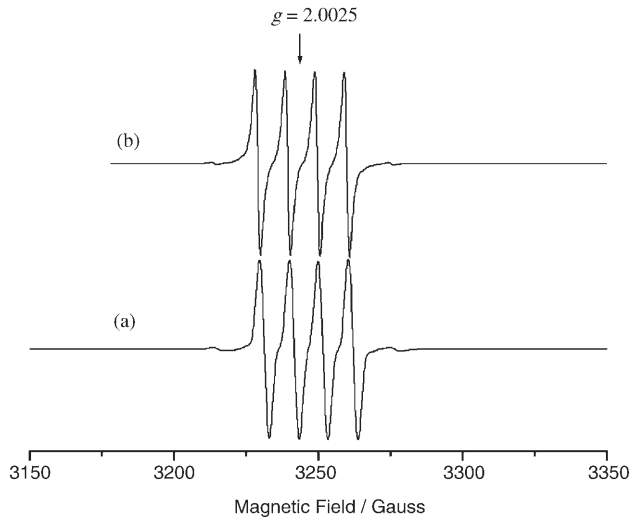
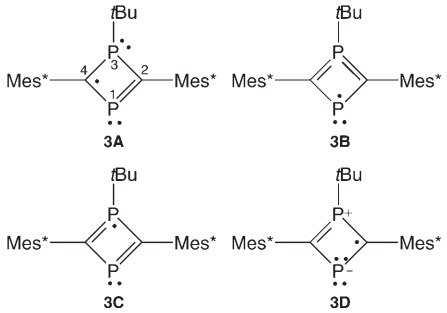


Figure 2. a) EPR spectrum of a solution of **3** in toluene at room temperature (experimental). EPR parameters: microwave frequency: 9.09823 GHz; modulation amplitude: 1 G; microwave power: 2 mW; gain 2×10^3. b) Simulated spectrum, see text.

$a_{P2} = 10.2$ G, and the ^{13}C isotropic hyperfine coupling of 30.2 G (Figure 2b). When hfc from naturally abundant ^{13}C was included in the simulation, small outer lines of the experimental spectrum were well reproduced. The large $^{31}P(a_{P1})$ hfc value corresponds to the phosphorus atom at P3 and the smaller $^{31}P(a_{P2})$ hfc value corresponds to that at P1 according to an ab initio calculation on $(P(CH)_2PCH_3)^{\bullet}$ as a model compound for **3**.[16] The Figure 3 shows that most of the electron spin density is concentrated on the C_2P_2 ring of the optimized structure, thus making the assignment of a_{P1} and a_{P2} possible. Contribution from the aromatic protons is probably negligible. The experimental spectrum was readily reproducible if the protons with a hfc value of < 1.0 G were used in the simulations. The ^{13}C hfc (30.2 G) determined from spectral simulations is consistent with the reported data for ^{13}C isotropic hfc.[17–20] This value is less than the ^{13}C isotropic coupling in the methyl radical $CH_3^{\bullet}$ (≈ 38 G)[17,18] and is more likely the observed ^{13}C isotropic coupling in the malonic radical $^{\bullet}CH(CO_2H)_2$ (≈ 33 G).[19,20] According to the EPR results and ab initio calculations, and based on the experimental ^{13}C couplings, 80–90% of the spin density in **3** will reside on the carbon atoms in the C_2P_2 ring and the remainder on the P atoms. This behavior explains small magnitudes of the ^{31}P hfc constants of **3**, which are considerably smaller than those of P-localized phosphinyl radicals $R_2P^{\bullet}$ (63–105 G)[1b,21] and diphosphanyl radicals $(R_2PPR)^{\bullet}$ (99–390 G).[1b,21c,22,23] On the other hand, the a_{P2} constant of **3** is similar to the ^{31}P hfc value of the 1,3-diphophaallyl radical $(R_2NP(CNR_2)PNR_2)^{\bullet}$ (R = *i*Pr, 9.4 G),[5a] thus featuring a spectroscopic property of organic radicals that contain conjugated P=C double bonds.

Both X-ray and EPR spectroscopic analysis support that the compound is well described as **3** (rather than fully delocalized **5**), as a resonance structure of **3A** and its symmetry equivalent, because the contribution of betaine structure **3D** (of **3A**) as well as **3B** and **3C** appears to be small based on the observed molecular geometry.



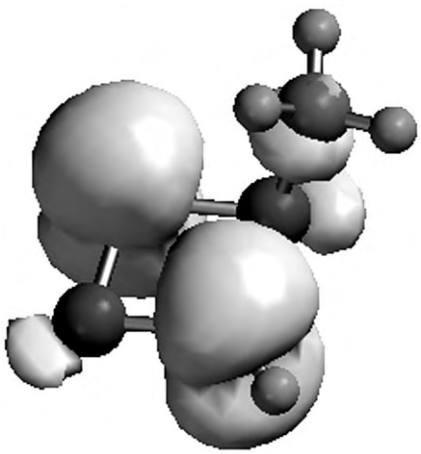


Figure 3. A visual map of electron spin density in the optimized structure of $[P(CH)_2PCH_3]^{\bullet}$ at the UHF/6-31G** level. Some important distances [Å] and angles [°] in the optimized structure: P-C(sp^2) 1.760, P(Me)-C(sp^2) 1.833, P-CH_3 1.856, C(sp^2)-P-C(sp^2) 83.31; P-C(sp^2)-P(Me) 98.33, 98.34, C(sp^2)-P(Me)-C(sp^2) 79.31, ΣP(Me) 287.59, ΣC-(sp^2) 359.70, P···P 2.721, C(sp^2)···C(sp^2) 2.340, Θ(P-C-P-C) 5.71. Total energy: −797.894357012 a.u.

A straightforward procedure for the preparation of the air-tolerant, thermally stable 1,3-diphosphacyclobutenyl radical **3** with a 2-phosphaallyl system has been developed. The radical structure was characterized by X-ray crystallographic and EPR spectroscopic analysis; furthermore, computational studies also support the proposed structure. Electronic perturbation of the phosphorus atoms and the spherical bulkiness of the Mes* groups provide the enormous stability of **3** in air by decreasing the reactivity of the radical. The unique properties of this class of compound will be further explored because stable radicals are expected to play an important role as starting compounds for intelligent materials, such as those employed in spintronics, molecular magnets, and spin-trapping.[24–26]

Experimental Section

Preparation of **3**: *tert*-Butyllithium (0.26 mmol, 1.4 M in hexanes) was added to a solution of **1** (150 mg, 0.52 mmol) in THF (3 mL) at −78 °C and stirred for 15 min. The reaction mixture was allowed to warm to room temperature, and subsequently mixed with iodine (0.26 mmol). The volatile materials were removed in vacuo, and the residue was extracted with hexane. The hexane extract was concentrated in vacuo,

 © 2006 Wiley-VCH Verlag GmbH & Co. KGaA, Weinheim

and practically pure **3** was obtained as a dark red solid (154 mg, 93%). Compound **3** was recrystallized as dark red needles from dichloromethane at 0°C. M.p. 130–132°C (decomp); UV/Vis (CH_2Cl_2): λ_{max} ($\varepsilon \times 10^{-3}$) 298 (12.3), 355 (16.1), 423 (3.6), 515 (11.7), 759 (1.3) nm; ESI-MS calcd for $C_{42}H_{67}P_2$: 633.4718; found: 633.4713; elemental analysis (%) calcd for $C_{42}H_{67}P_2$: C 79.57, H 10.65; found: C 79.05, H 10.66.

X-ray crystallography for **3**: $C_{42}H_{67}P_2$, $M_r = 633.94$, dark red needle (dichloromethane), $0.15 \times 0.15 \times 0.10\ mm^3$, triclinic, space group (no. 2), $a = 13.620(1)$, $b = 14.955(1)$, $c = 10.9292(7)$ Å, $\alpha = 98.130(7)$, $\beta = 98.918(8)$, $\gamma = 67.887(2)°$, $V = 2029.0(3)$ Å^3, $Z = 2$, $\rho_{calcd} = 1.038\ g\,cm^{-3}$, $F(000) = 698$, $\mu = 0.133\ mm^{-1}$, $T = 203$ K; a Rigaku RAXIS-IV imaging plate detector with graphite-monochromated $Mo_{K\alpha}$ radiation ($\lambda = 0.71070$ Å) was used; of 15420 reflections measured ($2\theta_{max} = 55.0°$), 8353 were observed ($R_{int} = 0.062$). The structure was solved by direct methods (SIR92),[27] expanded using Fourier techniques (DIRDIF94),[28] and then refined by full-matrix least squares on F^2 for 404 variable parameters. The non-hydrogen atoms without the disordered atoms in the *p-tert*-butyl group were refined anisotropically. Hydrogen atoms (calculated) were refined isotropically. $R1 = 0.116$ for $I > 2.0\sigma(I)$, and $R_w = 0.242$ for all data. Goodness of fit $S = 1.60$ for observed reflections. The maximum and minimum peaks on the final difference Fourier map corresponded to 0.60 and $-0.48\ e\,Å^{-3}$, respectively. The data were corrected for Lorentz polarization effect. Structure solution, refinement, and graphical representation were carried out using the teXsan package.[29] CCDC-295065 contains the supplementary crystallographic data for this paper. These data can be obtained free of charge from The Cambridge Crystallographic Data Centre via www.ccdc.cam.ac.uk/data_request/cif.

EPR measurement for **3**: EPR measurements at X-band (9.5 GHz) were carried out for **3** with a Varian E-12 EPR spectrometer, equipped with a rectangular cavity. The magnetic field was measured with a Bruker EPR 035M gaussmeter, and the microwave frequency was measured with a model HP 5245L frequency counter for *g* value determination.

Received: March 10, 2006
Published online: May 31, 2006

Keywords: EPR spectroscopy · phosphaalkynes · phosphorus heterocycles · radicals · steric hindrance

[1] a) M. Newcomb in *Reactive Intermediate Chemistry* (Eds.: R. A. Moss, M. Platz, M. Jones, Jr.), Wiley, Hoboken, NJ, **2004**, p. 121; b) P. P. Power, *Chem. Rev.* **2003**, *103*, 789.

[2] V. Lloveras, J. Vidal-Gancedo, D. Ruiz-Molina, T. M. Figueira-Duarte, J.-F. Nierengarten, J. Veciana, C. Rovira, *Faraday Discuss.* **2006**, *131*, 291.

[3] a) M. J. Plater, S. Kemp, E. Lattmann, *J. Chem. Soc. Perkin Trans. 1* **2000**, 971; b) B. Giese, W. Damm, R. Batra, *Chemtracts: Org. Chem.* **1994**, *7*, 355; c) S. G. DiMagno, K. C. Waterman, D. V. Speer, A. Streitwieser, *J. Am. Chem. Soc.* **1991**, *113*, 4679; d) N. Azuma, T. Ozawa, J. Yamauchi, *Bull. Chem. Soc. Jpn.* **1994**, *67*, 31.

[4] a) *Multiple Bonds and Low Coordination in Phosphorus Chemistry* (Eds.: M. Regitz, O. J. Scherer); Georg Thieme Verlag, Stuttgart, **1990**; b) K. B. Dillon, F. Mathey, J. F. Nixon, *Phosphorus: The Carbon Copy*, Wiley, Chichester, **1998**.

[5] a) Y. Canac, A. Baceiredo, W. W. Schoeller, D. Gigmes, G. Bertrand, *J. Am. Chem. Soc.* **1997**, *119*, 7579; b) M. Gouygou, C. Tachon, M. Koenig, A. Dubourg, J.-P. Declercq, J. Jaud, G. Etemad-Moghadam, *J. Org. Chem.* **1990**, *55*, 5750; c) M. Chentit, H. Sidorenkova, S. Choua, M. Geoffroy, Y. Ellinger, G. Bernardinelli, *J. Organomet. Chem.* **2001**, *634*, 136; d) D. Gigmes, Y. Berchadsky, J.-P. Finet, D. Siri, P. Tordo, *J. Phys. Chem. A* **2003**, *107*, 9652.

[6] W. W. Schoeller, W. Haug, J. Strutwolf, T. Busch, *J. Chem. Soc. Faraday Trans.* **1996**, *92*, 1751.

[7] a) H. Sugiyama, S. Ito, M. Yoshifuji, *Angew. Chem.* **2003**, *115*, 3932; *Angew. Chem. Int. Ed.* **2003**, *42*, 3802; b) H. Sugiyama, S. Ito, M. Yoshifuji, *Chem. Eur. J.* **2004**, *10*, 2700; c) M. Yoshifuji, H. Sugiyama, S. Ito, *J. Organomet. Chem.* **2005**, *690*, 2515.

[8] P. J. Krusic, J. P. Jesson, J. K. Kochi, *J. Am. Chem. Soc.* **1969**, *91*, 4566.

[9] F. H. Allen, O. Kennard, D. G. Watson, L. Brammer, A. G. Orpen, R. Taylor, *J. Chem. Soc. Perkin Trans. 2* **1987**, S1.

[10] S. Tsuzuki, K. Honda, T. Uchimaru, M. Mikami, K. Tanabe, *J. Am. Chem. Soc.* **2000**, *122*, 3746.

[11] Two additional phosphorus atoms (P3, P4) were observed with the small occupancy factor (0.06); the minor structure showed an intermolecular P···P distance of 4.24 Å.

[12] a) M. Sebastian, O. Schmidt, A. Fuchs, M. Nieger, D. Szieberth, L. Nyulászi, E. Niecke, *Phosphorus Sulfur Silicon Relat. Elem.* **2004**, *179*, 779; b) M. Sebastian, M. Nieger, D. Szieberth, L. Nyulászi, E. Niecke, *Angew. Chem.* **2004**, *116*, 647; *Angew. Chem. Int. Ed.* **2004**, *43*, 637.

[13] Compound **3** in [D_8]toluene showed small, broad, and complicated signals between $\delta_H = 2.0$ and 1.0 ppm in the ^{1}H NMR spectrum together with major residual signals of the solvent.

[14] L. D. S. Yadav, *Organic Spectroscopy*, Kluwer, Dordrecht, **2005**.

[15] XSophe Computer Simulation Software Suite, version 1.1.4, copyright **1993–2004**, developed in the Centre for Magnetic Resonance and Department of Mathematics, The University of Queensland (Brisbane, Queensland, Australia 4072) and Bruker Biospin GMBH (formerly Bruker Analytik; Rheinstetten, Germany).

[16] Ab initio calculations were performed at the UHF/6-31G** level using a SPARTAN'04 program package available from Wavefunction In. (Irvine, CA); the calculated optimized structure was very similar to the X-ray structure of **3** (see the Supporting Information for the computational results for coordinates and Mulliken net atomic charges).

[17] a) M. T. Rogers, L. D. Kispert, *J. Chem. Phys.* **1967**, *46*, 221; b) R. W. Fessenden, R. H. Schuler, *J. Chem. Phys.* **1965**, *43*, 2704.

[18] The methyl radical is known as a planar structure in which the unpaired spin density is localized on one $2p_\pi$ orbital and induces approximately 3% unpaired spin density in the carbon 2s orbital, thus resulting in the largest (≈ 38 G) isotropic ^{13}C coupling for one unpaired electron in a p orbital on a carbon atom; D. L. Beveridge, P. A. Dobosh, J. A. Pople, *J. Chem. Phys.* **1968**, *48*, 4802; K. Morokuma, L. Pedersen, M. Karplus, *J. Chem. Phys.* **1968**, *48*, 4801.

[19] a) T. Cole, C. Heller, *J. Chem. Phys.* **1961**, *34*, 1085; b) H. M. McConnell, R. W. Fessenden, *J. Chem. Phys.* **1959**, *31*, 1688.

[20] The ^{13}C isotropic hfc in the malonic radical is slightly less (≈ 33 G) than that in the methyl radical because not all of the unpaired spin density is localized on one carbon $2p_\pi$ orbital; some spin density is distributed on the rest of the radical orbitals.

[21] a) M. J. S. Gynane, A. Hudson, M. F. Lappert, P. P. Power, *J. Chem. Soc. Chem. Commun.* **1976**, 623; b) M. J. S. Gynane, A. Hudson, M. F. Lappert, P. P. Power, H. Goldwhite, *J. Chem. Soc. Dalton Trans.* **1980**, 2428; c) B. Cetinkaya, A. Hudson, M. F. Lappert, H. Goldwhite, *J. Chem. Soc. Chem. Commun.* **1982**, 609.

[22] M. Yoshifuji, K. Shibayama, N. Inamoto, T. Watanabe, *Chem. Lett.* **1983**, 585.

[23] S. Loss, M. Magistrato, L. Cataldo, S. Hoffmann, M. Geoffroy, U. Röthlisberger, H. Grützmacher, *Angew. Chem.* **2001**, *113*, 749; *Angew. Chem. Int. Ed.* **2001**, *40*, 725.

[24] D. A. Allwood, G. Xiong, C. C. Faulkner, D. Atkinson, D. Petit, R. P. Cowburn, *Science* **2005**, *309*, 1688.

 © 2006 Wiley-VCH Verlag GmbH & Co. KGaA, Weinheim

[25] E. Coronado, P. Day, *Chem. Rev.* **2004**, *104*, 5419.
[26] M. C. Krishna, S. English, K. Yamada, J. Yoo, R. Murugesan, N. Devasahayam, J. A. Cook, K. Golman, J. H. Ardenkjaer-Larsen, S. Subramanian, J. B. Mitchell, *Proc. Natl. Acad. Sci. USA* **2002**, *99*, 2216.
[27] A. Altomare, M. C. Burla, M. Camalli, M. Cascarano, C. Giacovazzo, A. Guagliardi, G. Polidori, *J. Appl. Crystallogr.* **1994**, *27*, 435.
[28] P. T. Beurskens, G. Admiraal, G. Beurskens, W. P. Bosman, R. de Gelder, R. Israel, J. M. M. Smits, The DIRDIF94 Program System, Technical Report of the Crystallography Laboratory, University of Nijmegen, The Netherlands, **1994**.
[29] Crystal Structure Analysis Package, Molecular Structure Corporation, The Woodlands, TX, **1985** and **1999**.

 © 2006 Wiley-VCH Verlag GmbH & Co. KGaA, Weinheim

Cascade Reactions

DOI: 10.1002/anie.200601208

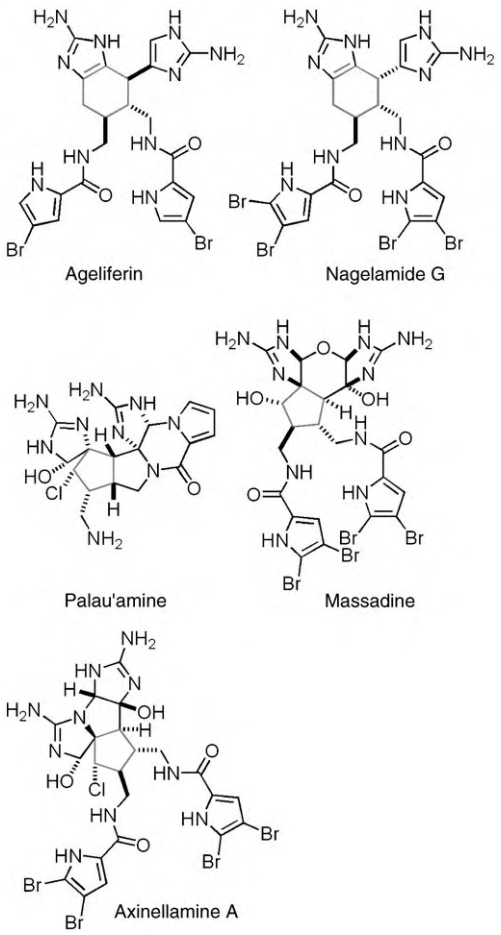
Regiocontrol in Mn^{III}-Mediated Oxidative Heterobicyclizations: Access to the Core Skeletons of Oroidin Dimers**

*Xianghui Tan and Chuo Chen**

Dedicated to Professor Tien-Yau Luh on the occasion of his 60th birthday

Pyrrole–imidazole alkaloids, also known as oroidin-family natural products, possess diverse molecular skeletons (Scheme 1) and many important biological properties, such as antibiotic, antiproliferative, and immunosuppressive activities.[1] The synthesis of polycyclic oroidin dimers remains a significant challenge.[1,2] To address this issue, we devised a radical cascade cyclization[3] strategy to construct the central cyclopentyl and cyclohexenyl core skeletons (**4** and **5**) of two classes of oroidin dimers, ageliferin/nagelamide and massadine/palau'amine/axinellamine. Herein, we describe two types of Mn^{III}-promoted cyclization cascades of allylic β-imidazolinonyl-β-ketoesters **1**, wherein two C–C bonds and three or four contiguous stereogenic centers are established in a single operation (Scheme 2).

Manganese(III) acetate is well known as an effective oxidant for enolizable carbonyl compounds.[4] Since the initial report of Corey and Kang on the intramolecular Mn^{III}-promoted oxidative cyclizations of β-dicarboxylates,[5] the reaction has grown in popularity and scope.[6,7] However, despite extensive investigations, applications of this method to unsaturated N-heterocyclic systems[8] and allylic β-ketoesters[9] are rare.



Scheme 1. Structures of oroidin dimers.

As outlined in Scheme 2, our strategy involves the oxidation of β-ketoester **1** with Mn^{III}, thus initiating a radical cascade cyclization reaction to give the ageliferin/nagelamide core skeleton **4** or the massadine/palau'amine/axinellamine core skeleton **5** after decarboxylation. With the controlling element X = H, the reaction proceeds through a 5-*exo*/6-*endo* cyclization pathway. On the other hand, the reaction can be directed to the 5-*exo*/5-*exo* cyclization pathway when X = Cl or CN. We have also developed an oxidative rearrangement reaction of **2** and **4** as an alternative approach to **3** and **5**.[10]

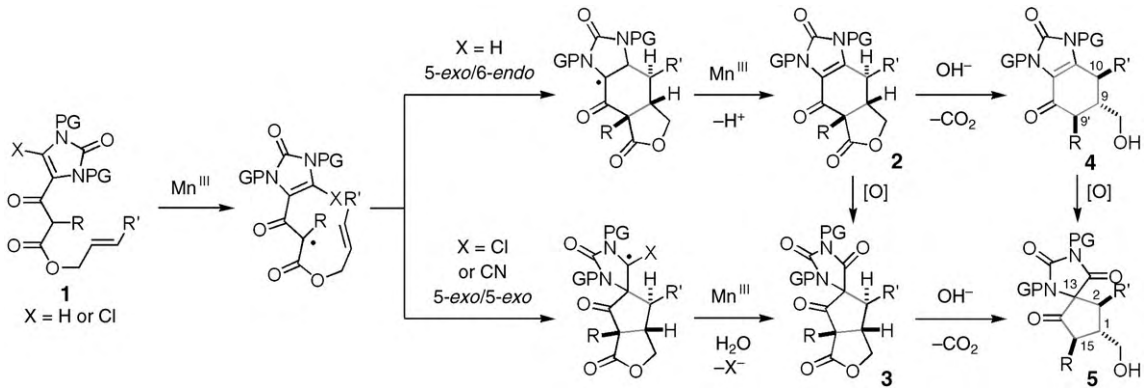
Our initial efforts focused on the 5-*exo*/6-*endo* cyclization of **1** (**1**→**2**). β-Ketoester **6**, which bears an α-methyl group, was oxidized cleanly by $[Mn(OAc)_3]$ in HOAc at 60 °C to give the ageliferin skeleton **7** in 63 % yield of the isolated product (Table 1, entry 1). No monocyclization products and other diastereomers were observed in the ^1H NMR spectra of the crude product.[11] We found that $[Mn(OAc)_3]$ was the best oxidant and HOAc the optimal solvent. Addition of Cu-

[*] Dr. X. Tan, Prof. Dr. C. Chen
Department of Biochemistry
University of Texas
Southwestern Medical Center at Dallas
5323 Harry Hines Boulevard, Dallas, TX 75390 (USA)
Fax: (+1) 214-648-0320
E-mail: Chuo.Chen@UTSouthwestern.edu

[**] We gratefully acknowledge the Southwestern Medical Foundation and the Welch Foundation for financial support. We also thank Dr. Radha Akella for the X-ray analyses.

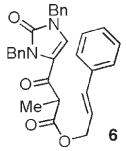
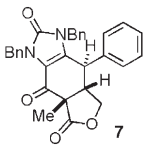
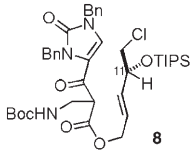
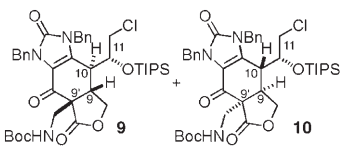
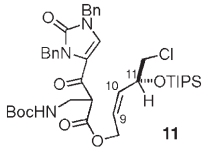
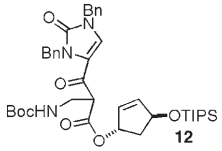
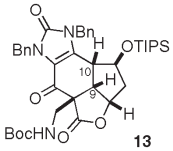
Supporting information for this article is available on the WWW under http://www.angewandte.org or from the author.

 © 2006 Wiley-VCH Verlag GmbH & Co. KGaA, Weinheim



Scheme 2. Synthetic approach to the oroidin dimers.

Table 1: Mn^{III}-promoted 5-*exo*/6-*endo* radical cyclization reactions.[a]

Entry	Substrate	Product(s)	Yield [%]
1	 **6**	 **7**	63
2	 **8**	 **9** + **10**	59 (2.1:1)
3	 **11**	**9** + **10**	50[b] (1:1.5)
4	 **12**	 **13**	60

[a] Reaction conditions: $[Mn(OAc)_3]$ (3.0 equiv), HOAc, 60 °C. [b] 80 °C.

$(OAc)_2$ or $[Yb(OTf)_3]$ (Tf = trifluoromethanesulfonyl) has no significant effects.

We next explored the scope of this radical cascade reaction. (*E*)-Allylic β-ketoester **8**, bearing all the necessary functional groups for the ageliferin synthesis, was oxidized cleanly to **9** and **10** in 59% yield (d.r. = 2.1:1; entry 2). Only two out of eight possible diastereomers were obtained. The C11 stereogenic center controlled the diastereoselectivity of this transformation through a moderate $A^{1,3}$ strain.[12] The α-radical of β-ketoester **8** added to the olefin preferentially from the less-hindered β face to give **9** as the major diastereomer. Lactones **9** and **10** contain the proper configurations at C9, C9′, and C10 for the ageliferin and *ent*-ageliferin synthesis. It is interesting to note that the oxidation of (*Z*)-**11** proceeded with "epimerization" at C10 and also afforded **9** and **10** (d.r. = 1:1.5; entry 3).[13,14] Constraining the (*Z*)-olefin in a cyclic system not only improved the diastereoselectivity but eliminated the issue of stereospecificity. Lactone **13** was obtained as the only product from the oxidation of **12** with $[Mn(OAc)_3]$ (entry 4).

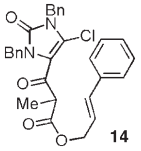
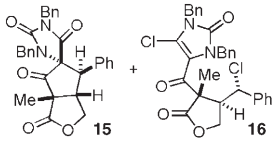
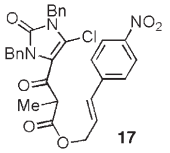
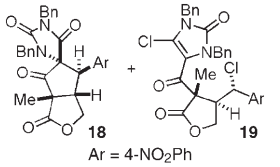
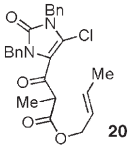
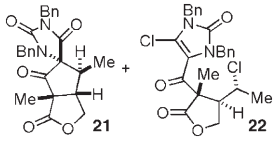
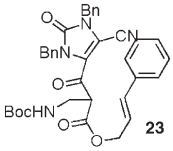
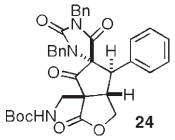
We then turned our attention to the synthesis of the massadine/palau'amine core skeleton and introduced a Cl atom as X to direct the second cyclization toward the 5-*exo* pathway (**1**→**3**). Oxidation of **14** proceeded through a 5-*exo*/5-*exo* cyclization to give **15**[15] along with the monocyclization products **16** in an approximate 1:1 ratio (Table 2, entry 1). No 6-*endo* products and other diastereomers were observed in the ^1H NMR spectra of the crude product. Introduction of an electron-withdrawing nitro group to the cinnamyl ester did not change the product ratio significantly (entry 2). Oxidation of the crotyl ester **20** also gave a mixture of **21** and **22** (entry 3). Remarkably, formation of the monocyclization product can be suppressed with X = CN. Hydantoin **24** was obtained as the only product from the oxidation of **23** in 60% yield (entry 4).

The temporary ester linkage used in the intramolecular reaction with $[Mn(OAc)_3]$ can be removed under decarboxylative conditions (Scheme 3). For example, briefly treating **9** with LiOH revealed the ageliferin core **25**. We also demonstrated that the ageliferin core skeleton **25** could be oxidatively rearranged to the massadine core **26** by mCPBA (namely, **4**→**5**) despite epimerization at C15. Notably, in contrast to the system developed by Dilley and Romo,[10a] ring contraction was achieved directly without competing migration of the olefin.

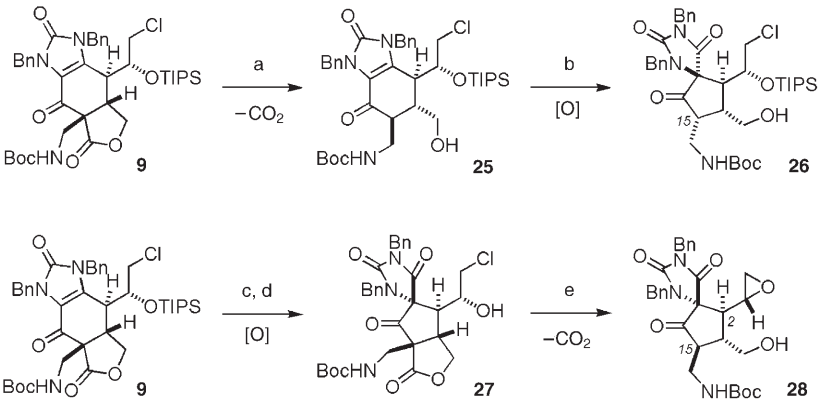
Lactone **9** can also be oxidized by mCPBA after deprotection of the triisopropylsilyl (TIPS) group (namely, **2**→**3**). In contrast to the oxidation of **9**, the reaction proceeded with opposite facial selectivity to afford hydantoin **27**, which bears the palau'amine spiro configuration. The ester linker of **27** can be removed with concomitant epoxide formation to provide **28**. The modifiable C2 and C15 stereogenic centers of **28** are opposite to those of palau'amine.

 © 2006 Wiley-VCH Verlag GmbH & Co. KGaA, Weinheim

Table 2: Mn^{III}-promoted 5-*exo*/5-*exo* radical cyclization reactions.[a]

Entry	Substrate	Product(s)	Yield [%]
1	 **14**	 **15** + **16**	87 (1:1.2)
2	 **17**	 **18** + **19** Ar = 4-NO_2Ph	69 (1:1)
3	 **20**	 **21** + **22**	61 (1:1.4)
4	 **23**	 **24**	60

[a] Reaction conditions: $[Mn(OAc)_3]$ (2.5 equiv), HOAc, 60 °C.



Scheme 3. Reaction conditions: a) LiOH, THF/H_2O, 50 °C, 15 min, 59% yield; b) mCPBA, $CHCl_3$, 23 °C, 16 h, 78% yield; c) NH_4F, HOAc, MeOH, 60 °C, 12 h, 83% yield; d) mCPBA, $CHCl_3$, 60 °C, 16 h, 78% yield; e) LiOH, THF/H_2O, 60 °C, 12 h, 72% yield. Boc = *tert*-butyloxycarbonyl, mCPBA = *m*eta-chloroperoxybenzoic acid.

In summary, we have devised a Mn^{III}-promoted radical cascade cyclization reaction to deliver the core skeletons of two types of oroidin dimers, ageliferin/nagelamide and massadine/palau'amine/axinellamine. Two C–C bonds and three or four contiguous stereogenic centers are established in one step. We have also demonstrated that the ageliferin cores thus obtained can be oxidatively rearranged to the massadine/palau'amine core skeletons with controlled installation of either spiro configurations. Efforts to synthesize selected oroidin dimers are currently in progress.

Received: March 27, 2006
Published online: May 31, 2006

Keywords: cascade reactions · natural products · radical reactions · rearrangement · synthetic methods

[1] For a review of the pyrrole–imidazole family of natural products, see: H. Hoffmann, T. Lindel, *Synthesis* **2003**, 1753–1783.

[2] For concise syntheses of sceptrin, see: a) P. S. Baran, A. L. Zografos, D. P. O'Malley, *J. Am. Chem. Soc.* **2004**, *126*, 3726–3727; b) V. B. Birman, X.-T. Jiang, *Org. Lett.* **2004**, *6*, 2369–2371; for an elegant synthesis of ageliferin, see: c) P. S. Baran, K. Li, D. P. O'Malley, C. Mitsos, *Angew. Chem.* **2006**, *118*, 255–258; *Angew. Chem. Int. Ed.* **2006**, *45*, 249–252; d) P. S. Baran, D. P. O'Malley, A. L. Zografos, *Angew. Chem.* **2004**, *116*, 2728–2731; *Angew. Chem. Int. Ed.* **2004**, *43*, 2674–2677; for synthetic approaches to palau'amine, see: e) H. Garrido-Hernandez, M. Nakadai, M. Vimolratana, Q. Li, T. Doundoulakis, P. G. Harran, *Angew. Chem.* **2005**, *117*, 775–779; *Angew. Chem. Int. Ed.* **2005**, *44*, 765–769, and references therein; for a synthetic approach to axinellamine, see: f) J. T. Starr, G. Koch, E. M. Carreira, *J. Am. Chem. Soc.* **2000**, *122*, 8793–8794.

[3] For a review of radical cascade cyclizations, see: a) A. J. McCarroll, J. C. Walton, *Angew. Chem.* **2001**, *113*, 2282–2307; *Angew. Chem. Int. Ed.* **2001**, *40*, 2224–2248; for reviews of cascade reactions, see: b) K. C. Nicolaou, T. Montagnon, S. A. Snyder, *Chem. Commun.* **2003**, 551–564; c) P. J. Parsons, C. S. Penkett, A. J. Shell, *Chem. Rev.* **1996**, *96*, 195–206.

[4] a) E. I. Heiba, R. M. Dessau, W. J. Koehl, Jr., *J. Am. Chem. Soc.* **1968**, *90*, 5905–5906; b) J. B. Bush, Jr., H. Finkbeiner, *J. Am. Chem. Soc.* **1968**, *90*, 5903–5905.

[5] E. J. Corey, M.-c. Kang, *J. Am. Chem. Soc.* **1984**, *106*, 5384–5385.

[6] For an example of an application of this reaction to complex natural-product synthesis, see: D. Yang, X.-Y. Ye, M. Xu, K.-W. Pang, K.-K. Cheung, *J. Am. Chem. Soc.* **2000**, *122*, 1658–1663.

[7] For reviews, see: a) G. G. Melikyan, *Org. React.* **1997**, *49*, 427–675; b) B. B. Snider, *Chem. Rev.* **1996**, *96*, 339–363.

[8] a) C.-P. Chuang, S.-F. Wang, *Tetrahedron Lett.* **1994**, *35*, 1283–1284; b) C.-P. Chuang, S.-F. Wang, *Synth. Commun.* **1994**, *24*, 1493–1505; c) A. Citterio, R. Sebastiano, M. C. Carvayal, *J. Org. Chem.* **1991**, *56*, 5335–5341.

[9] There is only one report of the oxidation of allylic β-ketoesters with Mn^{III}, wherein the thermodynamic *trans*-5-*exo* cyclization products were obtained: K. Sung, Y. Y. Wang, *J. Org. Chem.* **2003**, *68*, 2771–2778; the Mn^{III}-promoted cyclization of allylic β-dicarboxylate is more common, for example, Ref. [5].

 © 2006 Wiley-VCH Verlag GmbH & Co. KGaA, Weinheim

[10] For a two-step oxidation of imidazolinone with dimethyldioxirane (DMDO)/*N*-chlorosuccinimide (NCS) to construct the palau'amine core skeleton, see: a) A. S. Dilley, D. Romo, *Org. Lett.* **2001**, *3*, 1535–1538; for a similar DMDO-promoted oxidation of imidazole, see: b) C. J. Lovely, H. Du, Y. He, H. V. R. Dias, *Org. Lett.* **2004**, *6*, 735–738.

[11] The ^{1}H NMR spectra of the crude product indicated a clean transformation; however, the cyclization products were not stable to column chromatography on silica gel (among all the isolation conditions examined, Davisil 633 silica gel provided the best yields of the isolated products).

[12] For a review of $A^{1,3}$ strain, see: R. W. Hoffmann, *Chem. Rev.* **1989**, *89*, 1841–1860.

[13] For a similar stereospecificity issue, see: Ref. [6].

[14] A slightly higher temperature (80 °C) was required to suppress the formation of the monocyclization product; however, the diastereoselectivity was compromised.

[15] CCDC-290044 (**15**) contains the supplementary crystallographic data for this paper. These data can be obtained free of charge from The Cambridge Crystallographic Data Centre via www.ccdc.cam.ac.uk/data_request/cif.

 © 2006 Wiley-VCH Verlag GmbH & Co. KGaA, Weinheim

Main-Group-Element Compounds

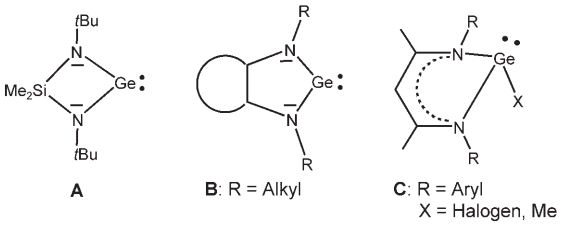
DOI: 10.1002/anie.200600237

A Heterofulvene-Like Germylene with a Betain Reactivity

Matthias Driess, Shenglai Yao, Markus Brym, and Christoph van Wüllen*

Dedicated to Professor Werner Kutzelnigg

Since the pioneering work on the synthesis of isolable germylenes (R_2Ge) reported by Lappert et al.,[1] remarkable progress has been made in tuning the reactivity of the low-coordinate Ge atom in germylenes through the presence of bulky and/or π-donor substituents R.[2] Sterically demanding amido or alkoxo substituents at the two-coordinate Ge atom lead to derivatives which can serve as ligands with different donor–acceptor abilities in coordination compounds.[3] Among the amido-substituted germylenes, the N-heterocyclic germylenes **A**,[4] **B**,[5] and **C**[6] deserve particular attention

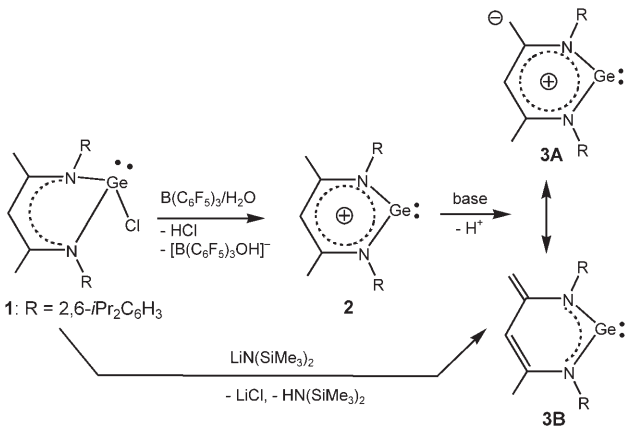


because they are versatile building blocks for the synthesis of germanium compounds with remarkable electronic features. Recent highlights include the synthesis of compounds with resonance-stabilized X–Ge=Y moieties (X = F, Cl, OH; Y = S,[7] Se,[8] NR[9]) and the formation of the N-heterocyclic germylenium cation **2**,[10] starting from the sterically encumbering β-diketiminato-substituted chlorogermylene **1** (Scheme 1).[6c]

The strikingly simple access to the planar GeN_2C_3 cation **2** from **1** and $B(C_6F_5)_3$ even in the presence of water suggests that π-electron resonance stabilization occurs.[10] The ready formation of the GeN_2C_3 cation **2** prompted us to investigate whether its π-resonance stabilization and planarity is retained even after monodeprotonation of a ring methyl group, and lead to the unprecedented cyclogermylene **3** which may exist as a dipolar resonance hybrid of **3A** and **3B** (Scheme 1).

[*] Prof. Dr. M. Driess, Dr. S. Yao, Dr. M. Brym, Prof. Dr. C. van Wüllen
Institute of Chemistry: Metalorganics and Inorganic Materials
Technische Universität Berlin
Strasse des 17. Juni 135, Sekr. C2, 10623 Berlin (Germany)
Fax: (+49) 30-314-22168
E-mail: matthias.driess@tu-berlin.de

Supporting information for this article is available on the WWW under http://www.angewandte.org or from the author.



Scheme 1. Synthesis of **2** and **3**, starting from the cyclic chlorogermylene **1**.

Herein, we report the synthesis of the new N-heterocyclic germylene **3** with an unexpected molecular structure and reactivity. Although, the desired germylene **3** is accessible by deprotonation of the germylene cation **2** by using strong bases (lithium diisopropylamide or $LiN(SiMe_3)_2$), it can only be isolated in low yield (< 10%). Fortunately, compound **3** is simply accessible in 79% yield from the direct reaction of chlorogermylene **1** with $LiN(SiMe_3)_2$ as a base in the molar ratio of 1:1.

The formation of **3** from **1** is mainly due to the steric congestion around the germanium atom which favors the base-assisted dehydrochlorination via monodeprotonation of a methyl group on the backbone of the β-diketiminato ligand instead of a nucleophilic $Cl/N(SiMe_3)_2$ substitution at germanium. Such a Cl substitution occurs when the analogous chlorogermylene with less-bulky phenyl substituents at the nitrogen atoms (R = Ph) is used, and leads solely to the corresponding $N(SiMe_3)_2$-substituted germylene.[6b] A similar deprotonation reaction at the backbone has been observed for the tautomerization of a iminogermane bearing the β-diketiminato ligand,[7b] for a cyclodiazaborane analogue[11] and for related calcium complexes.[12] The brown-red crystals of **3** have been fully characterized by EI-MS, combustion analysis, NMR spectroscopy (see Supporting Information), and X-ray diffraction analysis. The crystal structure revealed that the six-membered GeN_2C_3 ring is essentially planar (Figure 1).[13]

Interestingly, the Ge–N bond lengths in **3**, which are almost identical, are even slightly shorter (by 3 pm) than those in the germylene cation **2** whereas the endocyclic C–N bonds (N1–C2 and N2–C4) are significantly longer (by 5 pm). At the same time, the endocyclic C–C bond lengths of 140.2(3) (C2–C3) and 139.2(3) pm (C3–C4), and also the exocyclic C2–C1 double bond (141.3(3) pm) indicate conjugated double bonds. This situation suggests a larger contribution of the resonance form **3B** (Scheme 1) to the electronic ground state of **3**. Additionally, the X-ray structure of **3** shows that the terminal C4–C5 bond is unusual short (145.0(3) pm), this may result from disordering and/or packing effects which lead to shorter C4–C5 and longer C1–C2 bonds. The presence of alternating C–C bond lengths is supported by density

 © 2006 Wiley-VCH Verlag GmbH & Co. KGaA, Weinheim

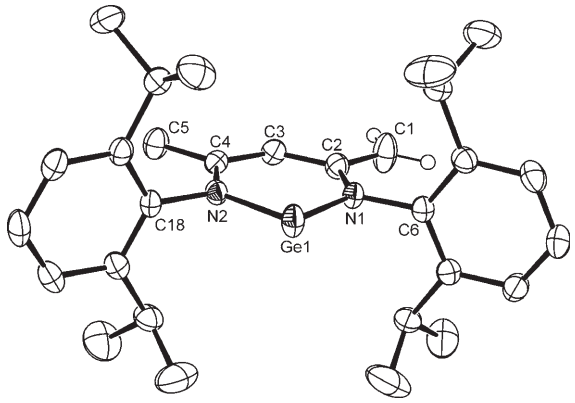
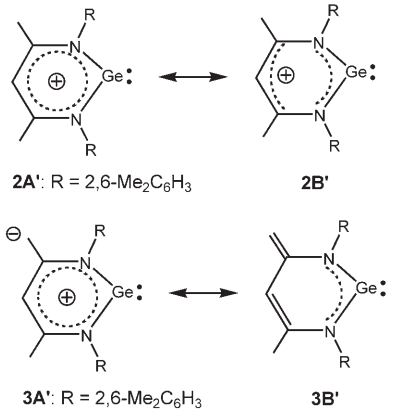


Figure 1. Molecular structure of **3**. The hydrogen atoms, except those at C1, have been omitted for clarity. Selected bond lengths [pm] and angles [°]: Ge1–N1 186.58(17), Ge1–N2 186.50(18), N1–C2 140.4(3), N1–C6 144.4(3), C1–C2 141.3(3), C2–C3 140.2(3), C3–C4 139.2(3), C4–C5 145.0(3), N2–C4 140.0(3), N2–C18 144.8(3); N1-Ge1-N2 95.84(8), Ge1-N1-C2 127.12(14), C2-C3-C4 129.9(2), N2-C4-C3 120.06(19), C1-C2-C3 120.2(2). Sum of bond angles at N1, N2, C2, and C4: 360°.

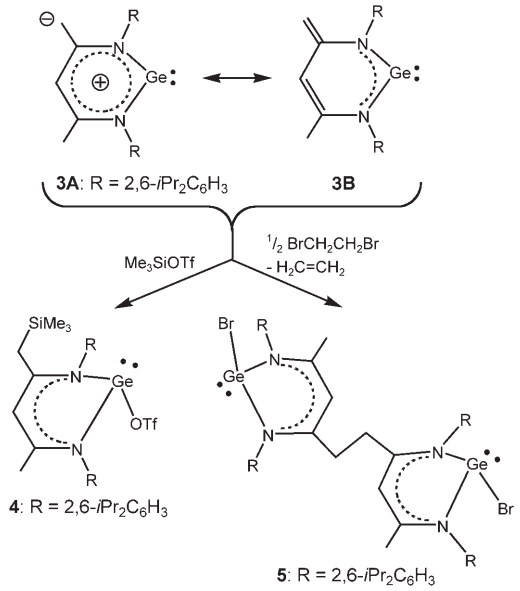
functional (DFT) calculations on the model compound **3′** in which the 2,6-diisopropylphenyl groups at nitrogen have been replaced by 2,6-dimethylphenyl substituents.[14] The calculations revealed alternating endo- and exocyclic C–C distances (C1–C2 135 pm, C2–C3 146 pm, C3–C4 135 pm, C4–C5 151 pm) as expected for substituted buta-1,3-diene derivatives. Remarkably, the calculations show also that the C–C bond-length equilibration is a shallow mode: only 10–15 kJ mol^{-1} are required to distort the minimum geometry of **3′** such that both endocyclic C–C bond lengths (C2–C3, C3–C4) and the exocyclic C1–C2 bond lengths amount to 140 pm. Additionally, the calculations indicate a preference for the mesomeric form **3B′** over **3A′** (Scheme 2). This situation is supported by quantum chemical calculations of the magnetic properties of **3′** (described by **3A′** and **3B′**) in comparison with those of the analogous model cation **2′** (described by the resonance forms **2A′** and **2B′**; Scheme 2). A cyclic delocalization of the 6 π electrons, as indicated by the resonance forms **3A′** and **2A′**, should lead to a ring current if the molecules are put into an external magnetic field perpendicular to the planes of the six-membered rings. This ring current affords a shielding of the ring center from the external magnetic field, and can be calculated by quantum chemical methods as the NICS (nucleus-independent chemical shift) value.[15a–d]

Cycles with negative NICS values are qualified by definition as aromatic. For the prototypical 6 π aromatic molecule, benzene, we calculate an isotropic NICS value of −10.0 ppm at the ring center (NICS(0)) which increases to −11.3 ppm 100 pm above this location (NICS(1)) in good agreement with results from calculations with smaller basis sets.[15] NICS values above the ring center offer a more robust criterion for aromaticity especially for inorganic ring systems since in these systems the σ-bond contributions are much smaller.[15b] The optimized geometries of **2′** and **3′** reveal different NICS(0) and NICS(1) values of −0.2 and −2.4 ppm, respectively, for **2′** and +3.0 and +1.3 ppm, respectively, for **3′**. This data supports the assumption that some aromatic character can be ascribed to **2′** but this is no longer the case for **3′**. Clearly, the cyclic delocalization of the π electrons in **3A′** is disfavored due to charge separation.

The electronic situation in **3** is reminiscent of that in fulvenes, especially heptafulvene. For heptafulvene, the calculated contribution of the zwitterionic aromatic resonance structure is rather small (from 5 %[16] to 8 %[17]), but this is enough to influence the properties of the molecule (see Supporting Information). In fact, **3** reacts like a betain, as shown by its gentle conversion with Me_3SiOTf (OTf = OSO_2CF_3) at −20 °C, leading to the *exo*-CH_2SiMe_3 substituted (trifluoromethylsulfonato)germylene **4** in 85 % yield (Scheme 3). The composition of **4** is consistent with the results by EI-MS, elemental analysis, and NMR spectroscopy, (see Supporting Information). An X-ray structure analysis of **4**[13] revealed a nonplanar GeN_2C_3 array (see Supporting Information) with bond lengths and angles similar to those observed for the analogous cyclic chlorogermylene **1**.[6c] The



Scheme 2. Resonance structures of **2′** and **3′**.



Scheme 3. Synthesis of **4** and **5**.

 © 2006 Wiley-VCH Verlag GmbH & Co. KGaA, Weinheim

unexpected bis(bromogermylene) **5** also results from the unusual betain-like reactivity of **3** which reacts with 1,2-dibromoethane in hexane at room temperature (Scheme 3). Compound **5** is the C–C homocoupling product of two germylene units under concomitant addition of bromine to each germanium atom. The yellow crystals of **5** can be isolated in 71% yield and consist of a mixture of diastereoisomers (racemic *RR*, *SS*, and *meso-RS*) as demonstrated by ^{1}H and ^{13}C NMR spectroscopy (see Supporting Information).

Apparently, in this reaction, 1,2-dibromoethane serves as a chemical equivalent of elemental bromine under release of ethene (^{1}H NMR spectroscopic monitoring). In line with this idea, compound **5** is also accessible by the reaction of **3** with Br_2 in the molar ratio of 1:1 but the yield is much lower (ca. 30%) and separation from side-products is difficult.

A X-ray diffraction analysis[13] shows that the crystals of **5** are the *meso* form (*RS*) with a center of symmetry and two nonplanar GeN_2C_3 rings coupled by a C–C bond (Figure 2). The bond lengths and angles of the GeN_2C_3 skeleton in **5** are similar to those of **1** and the C1–C1′ distance indicates the presence of an undisturbed C(sp^3)–C(sp^3) single bond.

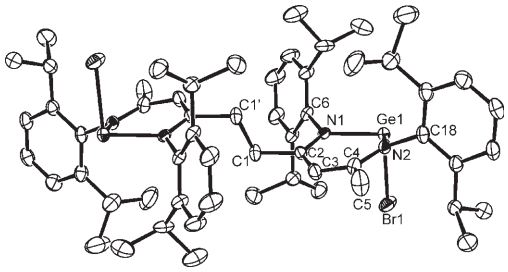


Figure 2. Molecular structure of **5**. H atoms have been omitted for clarity. Selected bond lengths [pm] and angles [°]: Ge1–Br1 247.16(5), Ge1–N1 200.1(2), Ge1–N2 198.1(3), N1–C2 132.8(4), N1–C6 145.9(4), C1–C2 152.4(4), C1–C1′ 152.5(6), C2–C3 138.2(5), C3–C4 141.0(4), C4–C5 149.9(5), N2–C4 132.8(4), N2–C18 145.6(4); N1-Ge1-Br1 93.68(7), N2-Ge1-Br1 95.35(7), N1-Ge-N2 91.17(10), C2-N1-Ge1 122.9(2), C3-C2-N1 124.1(3), C4-C3-C2 127.6(3), N2-C4-C3 121.7(3), N1-C2-C1 120.2(3), C1-C2-C3 115.4(3), C5-C4-C3 117.2(3), C5-C4-N2 121.0(3), C2-C1-C1′ 109.9(3). Sum of bond angles at Ge1: 280.3°.

In summary, we have shown that the N-heterocyclic germylene **3** is simply accessible from dehydrochlorination of **1** and has a planar GeN_2C_3 arrangement with a dipolar resonance structure analogous to the fulvenes. Although the less-polar resonance form **3B** is favored in the ground state, compound **3** shows a betain-like reactivity because of the contribution of dipolar resonance structure **3A**. Further investigations are currently underway to use **3** as a dipolar donor–acceptor ligand for the stabilization of σ,π-sandwich complexes of transition metals in unusual oxidation states.

Received: January 19, 2006
Published online: June 7, 2006

Keywords: betains · C–C coupling · fulvenes · germylenes · heteroarenes

[1] a) D. H. Harris, M. F. Lappert, J. B. Pedley, G. J. Sharp, *J. Chem. Soc. Dalton Trans.* **1976**, 945; P. J. Davidson, D. H. Harris, M. F. Lappert, *J. Chem. Soc. Dalton* **1976**, 2268.

[2] Reviews: a) J. Barrau, J. Escudié, J. Satgé, *Chem. Rev.* **1990**, *90*, 283; b) M. Weidenbruch, *Eur. J. Inorg. Chem.* **1999**, 373–381; c) "Recent Advances in structural chemistry of organic germanium, tin and lead compounds": K. W. Klinkhammer in *The Chemistry of Organic Germanium, Tin and Lead Compounds*, *Vol. 2* (Ed.: Z. Rappoport), Wiley, New York, **2002**, chap. 4, pp. 284–332; d) O. Kühl, Coord. *Chem. Rev.* **2004**, *248*, 411–427; e) P. Jutzi, S. Keitemeyer, B. Neumann, H.-G. Stammler, *Organometallics* **1999**, *18*, 4778–4784; f) M. Driess, N. Dona, K. Merz, *Dalton Trans.* **2004**, 3176.

[3] a) A. Castel, P. Riviere, J. Satge, M. Ahbala, *J. Organomet. Chem.* **1987**, *331*, 11–21; b) J. E. Bender IV, A. J. Shusterman, M. M. Banaszak Holl, J. W. Kampf, *Organometallics* **1999**, *18*, 1547–1552; c) J. Barrau, G. Rima, T. El Amraoui, *J. Organomet. Chem.* **1998**, *570*, 163–174; d) M. Knorr, E. Hallauer, V. Huch, M. Veith, P. Braunstein, *Organometallics* **1996**, *15*, 3868–3875; e) W. A. Herrmann, H. J. Kneuper, E. Herdtweck, *Chem. Ber.* **1989**, *122*, 433–436.

[4] a) M. Veith, M. Grosser, *Z. Naturforsch. B* **1982**, *37*, 1375; b) Review: M. Veith, *Angew. Chem.* **1987**, *99*, 1; *Angew. Chem. Int. Ed. Engl.* **1987**, *26*, 1.

[5] a) A. Meller, C.-P. Gräbe, *Chem. Ber.* **1985**, *118*, 2020; b) J. Pfeiffer, W. Maringgele, M. Noltemeyer, A. Meller, *Chem. Ber.* **1989**, *122*, 245; c) W. A. Herrmann, M. Denk, J. Behm, W. Scherer, F.-R. Klingan, H. Bock, B. Solouki, M. Wagner, *Angew. Chem.* **1992**, *104*, 1489; *Angew. Chem. Int. Ed. Engl.* **1992**, *31*, 1485; d) C. Heinemann, W. A. Herrmann, W. Thiel, *J. Organomet. Chem.* **1994**, *474*, 73; e) A. Schäfer, W. Saak, M. Weidenbruch, *Z. Anorg. Allg. Chem.* **1998**, *624*, 1405–1408, and references therein; see also reference [2c].

[6] a) A. E. Ayers, T. Klapötke, H. V. R. Dias, *Inorg. Chem.* **2001**, *40*, 1000; b) A. Akkari, J. J. Byrne, I. Saur, G. Rima, H. Gornitzka, J. Barreau, *J. Organomet. Chem.* **2001**, *622*, 190; c) Y. Ding, H. Hao, H. W. Roesky, M. Noltemeyer, H.-G. Schmidt, *Organometallics* **2001**, *20*, 4806.

[7] a) L. W. Pineda, V. Jancik, H. W. Roesky, R. Herbst-Irmer, *Angew. Chem.* **2004**, *116*, 5650–5652; *Angew. Chem. Int. Ed.* **2004**, *43*, 5534–5536; b) Y. Ding, Q. Ma, H. W. Roesky, R. Herbst-Irmer, I. Uson, M. Noltemeyer, H.-G. Schmidt, *Organometallics* **2002**, *21*, 5216–5220.

[8] a) Y. Ding, Q. Ma, H. W. Roesky, I. Uson, M. Noltemeyer, H.-G. Schmidt, *Dalton Trans.* **2003**, 1094–1098; b) I. Saur, G. Rima, H. Gornitzka, K. Miqueu, J. Barrau, *Organometallics* **2003**, *22*, 1106–1109.

[9] a) Y. Ding, Q. Ma, H. W. Roesky, R. Herbst-Irmer, I. Uson, M. Noltemeyer, H.-G. Schmidt, *Organometallics* **2002**, *21*, 5216–5220; b) Y. Ding, H. Hao, H. W. Roesky, M. Noltemeyer, H.-G. Schmidt, *Organometallics* **2001**, *20*, 4806–4811.

[10] M. Stender, A. D. Phillips, P. P. Power, *Inorg. Chem.* **2001**, *40*, 5314–5315.

[11] B. Qian, S. W. Baek, M. R. Smith III, *Polyhedron* **1999**, *18*, 2405.

[12] S. Harder, *Angew. Chem.* **2003**, *115*, 3553–3556; *Angew. Chem. Int. Ed.* **2003**, *42*, 3430–3434.

[13] **3**: monoclinic, space group $P2_1/n$, $a = 12.5801(3)$, $b = 16.2194(4)$, $c = 13.8696(4)$ Å, $\beta = 105.3620(10)°$, $V = 2728.86(12)$ Å^3, $Z = 4$, $\rho_{calcd} = 1.191$ Mg m^{-3}, $\mu(Mo_{K\alpha}) = 1.14$ mm^{-1}, 25012 collected reflections, 8320 crystallographically independent reflections ($R_{int} = 0.0523$), 5282 reflections with $I > 2\sigma(I)$, $\theta_{max} = 30.53°$, $R(F_o) = 0.0469$ ($I > 2\sigma(I)$), $wR(F_o^2) = 0.0901$ (all data), 298 refined parameters. **4**: monoclinic, space group $P2_1/n$, $a = 11.5855(4)$, $b = 23.3854(7)$, $c = 13.4704(4)$ Å, $\beta = 96.0450(10)°$, $V = 3629.3(2)$ Å^3, $Z = 4$, $\rho_{calcd} = 1.302$ Mg m^{-3}, $\mu(Mo_{K\alpha}) = 0.98$ mm^{-1}, 34090 collected reflections, 11087 crystallographi-

 © 2006 Wiley-VCH Verlag GmbH & Co. KGaA, Weinheim

cally independent reflections ($R_{int} = 0.0977$), 7812 reflections with $I > 2\sigma(I)$, $\theta_{max} = 30.56°$, $R(F_o) = 0.0473$ ($I > 2\sigma(I)$), $wR(F_o^2) = 0.0765$ (all data), 417 refined parameters. **5**: monoclinic, space group $P2_1/n$, $a = 9.6029(3)$, $b = 13.4481(5)$, $c = 22.5907(7)$ Å, $\beta = 99.7560(10)°$, $V = 2875.19(17)$ Å^3, $Z = 4$, $\rho_{calcd} = 1.315$ Mg m^{-3}, $\mu(Mo_{K\alpha}) = 2.47$ mm^{-1}, 26898 collected reflections, 8821 crystallographically independent reflections ($R_{int} = 0.1391$), 4961 reflections with $I > 2\sigma(I)$, $\theta_{max} = 30.60°$, $R(F_o) = 0.0549$ ($I > 2\sigma(I)$), $wR(F_o^2) = 0.1180$ (all data), 307 refined parameters. Crystals were each mounted on a glass capillary in perfluorinated oil and measured in a cold N_2 flow. The data of **3**, **4**, and **5** were collected on a Bruker-AXS SMART CCD diffractometer at 173(2) K using $Mo_{K\alpha}$ radiation ($\lambda = 0.71073$ Å). The structures were solved by direct methods and were refined on F^2 with the SHELX-97[23] software package. The positions of the H atoms were calculated and considered isotropically according to a riding model. Absorption corrections were done using the SADABS program.[24] CCDC-294818 (**3**), CCDC-294819 (**4**), and CCDC-294820 (**5**) contain the supplementary crystallographic data for this paper. These data can be obtained free of charge from The Cambridge Crystallographic Data Centre via www.ccdc.cam.ac.uk/data_request/cif.

[14] Geometry optimizations have been performed with the Gaussian03 program[18] at density functional level using the B3LYP[20] hybrid exchange-correlation functional and polarized valence triple zeta (TZVP)[19] basis sets. Nucleus-independent chemical shifts (NICS)[15] have been calculated by the (Hartree-Fock) IGLO[21] method with its integral-direct implementation.[22] NICS values have been obtained at the ring centers (NICS(0) value) as well as 100 pm above (NICS(1) value).

[15] a) P. von R. Schleyer, C. Maerker, A. Dransfeld, H. Jiao, N. J. R. van Eikema Hommes, *J. Am. Chem. Soc.* **1996**, *118*, 6317; b) P. von R. Schleyer, H. Jiao, N. J. R. van Eikema Hommes, V. G. Malkin, O. L. Malkina, *J. Am. Chem. Soc.* **1997**, *119*, 12669; c) Z. Chen, C. S. Wannere, C. Corminboeuf, R. Puchta, P. von R. Schleyer, *Chem. Rev.* **2005**, *105*, 3842; d) P. von R. Schleyer, *Chem. Rev.* **2005**, *105*, 3433.

[16] A. P. Scott, I. Agranat, P. U. Biedermann, N. V. Riggs, L. Radom, *J. Org. Chem.* **1997**, *62*, 2026.

[17] H. Möllerstedt, M. C. Piqueras, R. Crespo, H. Ottoson, *J. Am. Chem. Soc.* **2004**, *126*, 13938.

[18] Gaussian 03, Revision C.02, M. J. Frisch et al. See Supporting Information.

[19] A. Schäfer, C. Huber, R. Ahlrichs, *J. Chem. Phys.* **1994**, *100*, 5829.

[20] a) P. J. Stephens, F. J. Devlin, C. F. Chabalowski, M. J. Frisch, *J. Phys. Chem.* **1994**, *98*, 11623; b) A. D. Becke, *J. Chem. Phys.* **1993**, *98*, 5648; c) A. D. Becke, *Phys. Rev. A* **1988**, *38*, 3098; d) C. Lee, W. Yang, R. G. Parr, *Phys. Rev. B* **1988**, *37*, 785.

[21] W. Kutzelnigg, U. Fleischer, M. Schindler in *NMR Basic Principles and Progress*, *Vol. 213*, Springer, Berlin, **1991**, p. 165.

[22] U. Meier, C. van Wüllen, M. Schindler, *J. Comput. Chem.* **1992**, *13*, 551.

[23] G. M. Sheldrick, *SHELX-97, Program for Crystal Structure Determination*, University of Göttingen (Germany), **1997**.

[24] G. M. Sheldrick, *SADABS, Program for Empirical Absorption Correction of Area Detector Data*, University of Göttingen (Germany), **1996**.

 © 2006 Wiley-VCH Verlag GmbH & Co. KGaA, Weinheim

Borylene Complexes

DOI: 10.1002/anie.200601237

Molecular Structure and Cluster Formation of a *tert*-Butylborylene Complex**

Holger Braunschweig, Christian Burschka, Michael Burzler, Stephanie Metz, and Krzysztof Radacki*

In 1995 we reported on the first spectroscopically characterized borylene complexes $[\mu\text{-}BX\{(\eta^5\text{-}C_5H_4R)Mn(CO)_2\}_2]$ (**1**: X = NMe_2, R = H; **2**: X = *t*Bu, R = Me)[1] and the molecular structure of **1**. During the past decade, intense research efforts were focused on borylene complexes,[2] and many different coordination modes for ligands of the type B–R were described and include terminal,[3] hetero-dinuclear,[4] and semibridging[5] species, thus experimentally proving the predicted close relationship between borylene ligands and CO.[6,7] More recent studies focused on the reactivity of borylene complexes and revealed some interesting characteristics of these species, for example, i) the potential of terminal borylene ligands to be transferred to metallic[8] and non-metallic[9] substrates, ii) the strong tendency of some terminal borylene ligands to add metal bases of the type $[M(PR_3)_n]$ (M = Pd, Pt),[5,10] and iii) the exceptional stability of the central Mn_2B framework in **1**.[7] This stability allowed for elusive substitution reactions at the borylene center without cleavage of the metal–boron framework.[11] Given the pronounced thermodynamic stability of these compounds with respect to M–B dissociation,[6,7] the latter finding may appear surprising; DFT calculations revealed a build-up of positive charge at the boron center, and hence, the M–B bond is kinetically labile and susceptible to nucleophilic cleavage.[7]

Despite significant progress in this area, the choice of boron-bound substituents that sufficiently stabilize the metal-coordinated borylene ligand is very much restricted to mainly π-stabilizing heteroatoms such as N and O. Only very few substituents with little or no π stabilization were reported, such as sterically very demanding aryl[3b] or hypersilyl groups.[3c] The *tert*-butylborylene complex **2** is in a way a unique example, as it still represents the only alkylborylene complex and, accordingly, has attracted much interest.[12] Because of the highly unsaturated nature of the boron center in **2**, a reactivity pattern has to be expected that is

[*] Prof. Dr. H. Braunschweig, Dr. C. Burschka, M. Burzler, S. Metz, Dr. K. Radacki
Institut für Anorganische Chemie
Bayerische Julius-Maximilians-Universität Würzburg
Am Hubland, 97074 Würzburg (Germany)
Fax: (+49) 931-888-4623
E-mail: h.braunschweig@mail.uni-wuerzburg.de

[**] This work was supported by the Deutsche Forschungsgemeinschaft. We are grateful to BASF AG for a donation of chemicals. H.B. thanks Prof. T. P. Fehlner (Notre Dame) for very helpful discussions.

Supporting information for this article is available on the WWW under http://www.angewandte.org or from the author.

© 2006 Wiley-VCH Verlag GmbH & Co. KGaA, Weinheim

significantly different from that of its amino-stabilized counterpart **1**. Herein we report the synthesis and crystal structure of [μ-B*t*Bu{(η^5-C_5H_5)Mn(CO)$_2$}$_2$] (**3**), as well as the unprecedented reactivity of its methyl-substituted analogue [μ-B*t*Bu{(η^5-C_5H_4Me)Mn(CO)$_2$}$_2$] (**2**) towards [Pd(PCy$_3$)$_2$] (Cy = cyclohexyl) to yield a novel heterometallic boron cluster.

Since attempts to obtain suitable single crystals of **2** failed, its unsubstituted counterpart [μ-B*t*Bu{(η^5-C_5H_5)Mn(CO)$_2$}$_2$] (**3**) was prepared by an analogous procedure[13] from K[{(η^5-C_5H_5)Mn(CO)$_2$}H] and B$_2$*t*Bu$_2$Cl$_2$ and recrystallized from hexanes at −35 °C.

Compound **3** crystallizes in the space group $P2_1/n$ and displays the expected central three-membered Mn$_2$B ring with an exocyclic B1–C5 bond length of 1.610(2) Å,[14] which is in the normal range for *tert*-butylboranes (Figure 1).[15]

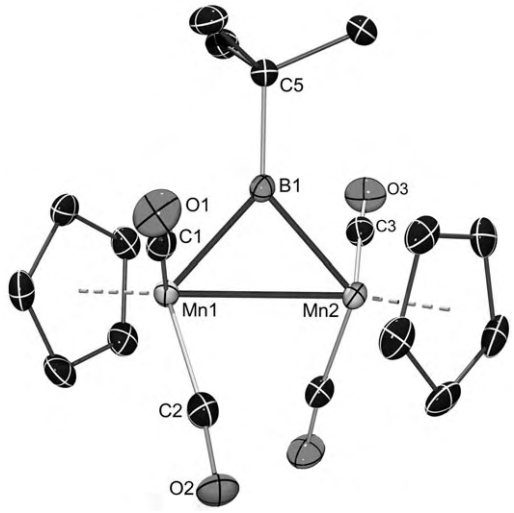
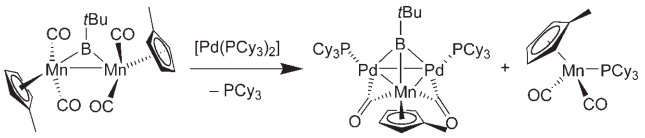


Figure 1. Molecular structure of **3** (thermal ellipsoids set at 50% probability). Bond lengths [Å] and angles [°]: B1–Mn1 2.0288(16), B1–Mn2 2.0309(16), Mn1–Mn2 2.7952(5), B1–C5 1.610(2); Mn1-B1-Mn2 87.03(7), B1-Mn2-Mn1 46.45(5).

Despite the absence of π stabilization from the boron-bound substituent, the geometry of the central Mn$_2$B moiety, with two nearly identical B–Mn bond lengths of 2.0288(16) Å (B1–Mn1) and 2.0309(16) Å (B1–Mn2) and a Mn–Mn bond length of 2.7952(5) Å, closely resembles that of the corresponding amino-[1] or chloroborylene[16] complexes.

In contrast to the similarities with respect to their molecular structures, **1** and **3** show markedly different reactivity, as already indicated by the extreme sensitivity of **3** in stark contrast to the stability of **1** even towards air and water. The aminoborylene species also proved unreactive towards [Pd(PCy$_3$)$_2$], whereas **2** underwent a clean, albeit slow, reaction with [Pd(PCy$_3$)$_2$] to form the unprecedented trimetallic species [(μ$_3$-B*t*Bu){[(η^5-C_5H_4Me)Mn(CO)$_2$][Pd(PCy$_3$)]$_2$}] (**4**).

A 1:2 mixture of **2** and [Pd(PCy$_3$)$_2$] in C_6D_6 was monitored by multinuclear NMR spectroscopy at ambient temperature. After a few hours, a slowly increasing new ^{11}B NMR spectroscopic resonance at $\delta = 150$ ppm was detected, which



2 **4** **5**

is 20 ppm highfield-shifted with respect to that of **3**, thus indicating the formation of **4**. The ^{31}P NMR spectrum revealed signals at $\delta = 10$ (PCy$_3$), 92 ([(η^5-C_5H_4Me)Mn(CO)$_2$PCy$_3$][17] (**5**)), and 27 ppm (**4**), as well as the signal from [Pd(PCy$_3$)$_2$] at $\delta = 39$ ppm. After three weeks the reaction was complete, and no additional signals indicative of further byproducts were detected. The new complex **4** was isolated as red crystals in 25% yield after repeated recrystallization from hexane. The formation of **4** requires the extrusion (and trapping by PCy$_3$) of one {(η^5-C_5H_4Me)Mn(CO)$_2$} fragment from **2**, thereby formally giving a terminal borylene complex "[(η^5-C_5H_4Me)(OC)$_2$Mn=B*t*Bu]",[18] which is subsequently stabilized by two {Pd(PCy$_3$)} moieties. Neither the controlled degradation of the thermodynamically very stable Mn$_2$B core under thermal conditions nor the multiple addition of metal bases to a boryl or borylene center has any precedence in metal–boron chemistry, and the occurrence of these transformations is here ascribed to the presence of the boron-bound alkyl substituent. Complex **4** crystallizes in the space group $P\bar{1}$ and consists of an MnPd$_2$ isosceles triangle (bond lengths: Mn1–Pd1 2.6426(10) Å, Mn1–Pd2 2.6458(10) Å, Pd1–Pd2 2.8423(7) Å) which is capped in a μ$_3$ fashion by the *tert*-butylborylene ligand (Figure 2).[14] The B1–Mn1 bond length of 1.987(7) Å is close to that of **1**, while the B–Pd bond lengths (B1–Pd1 2.144(7) Å, B1–Pd2 2.128(8) Å) are comparable to those of [(η^5-C_5Me_5)Fe(μ-CO)$_2$(μ-BCl$_2$)Pd(PCy$_3$)] (2.062(4) Å),[19] thus indicating M–B single bonds in **4**.

Compound **4** can be viewed as the first example of a *hetero*metallic μ$_3$-borylene complex. The class of μ$_3$-borylene

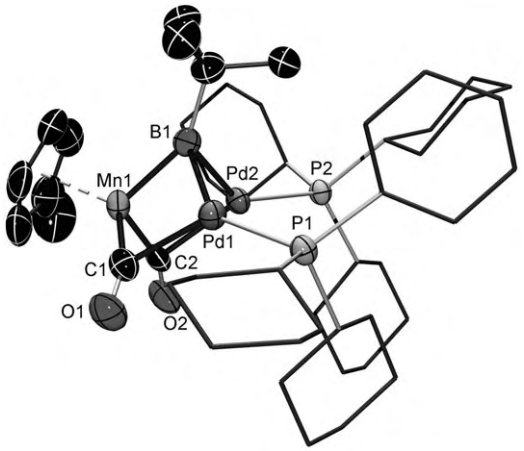


Figure 2. Molecular structure of **4** (thermal ellipsoids set at 50% probability). Bond lengths [Å] and angles [°]: Mn1–Pd1 2.6426(10), Mn1–Pd2 2.6458(10), Pd1–Pd2 2.8423(7), B1–Mn1 1.987(7), B1–Pd1 2.144(7), B1–Pd2 2.128(8); O1-C1-Mn1 158.9(5), O2-C2-Mn1 160.1(5).

 © 2006 Wiley-VCH Verlag GmbH & Co. KGaA, Weinheim

compounds is restricted to very few examples that exclusively consist of *homo*metallic frameworks of either Co[20] or, more commonly, Ru centers.[21] A formal electron count (each of the fragments {*t*BuB}, {Cy_3PPd},[22] and {(η^5-C_5H_4Me)$Mn(CO)_2$} contributes two electrons to the cluster framework) is in agreement with a metallaborane that is two electrons short of a *closo* species (that is, *hypercloso*). DFT studies, however, suggest a more localized bonding picture.[23] Natural bond orbital (NBO) calculations indicate a rather strong covalent Mn–B bond (Wiberg bond index, WBI = 0.8) and somewhat weaker Pd–B interactions (WBI = 0.42 and 0.48). The Pd–Pd interaction (WBI = 0.05), however, was calculated to be almost nonexistent. This description is reflected by electron localization function (ELF) computations (Figure 3), which revealed two fused basins between the

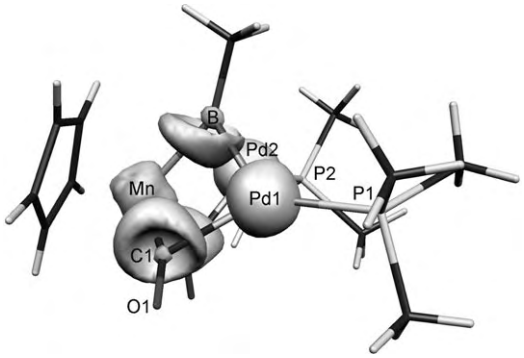


Figure 3. ELF = 0.6 plot for the model of complex **4**. The ELF contributions of ligand atoms are omitted for clarity.

boron and manganese atoms that also affect both palladium centers, thus representing two (3c, 2e) Mn-B-Pd bonds. Furthermore, no basins indicative of a typical metallaborane cluster were found over any triangular face of the {$BMnPd_2$} core.

This description is reminiscent of the bonding situation found in metal-base-stabilized amino-[5] and metallaborylene[10] complexes. In sharp contrast to these {$(Me_3Si)_2N$}- and {$Cp^*Fe(CO)_2$}-substituted borylenes, however, the presence of the non-π-stabilizing *tert*-butyl group in **4** allows for the unprecedented addition of two metal bases to the boron center.

Experimental Section

All manipulations were conducted in an atmosphere of dry argon by employing either standard Schlenk techniques or a glovebox.

4: [$Pd(PCy_3)_2$] (0.200 g, 0.300 mmol) was added to a solution of **2** (0.060 g, 0.134 mmol) in C_6D_6 (0.8 mL) at room temperature. The course of the reaction was monitored by multinuclear NMR spectroscopy. After three weeks the reaction was judged to be complete. The solvent was removed in vacuo, and hexane was added to the residue. Compound **4** was separated by fractional crystallization and recrystallization from hexanes at −35 °C as red crystals (0.035 g, 25 % yield). ^{1}H NMR (500 MHz, C_6D_6, 25 °C, TMS): δ = 4.59(m, 2H, $C_5H_4CH_3$), 4.54 (m, 2H, $C_5H_4CH_3$), 2.04 (s, 3H, $C_5H_4CH_3$), 1.65 (s, 9H, *t*Bu), 2.15–1.15 ppm (m, 66H, Cy); ^{13}C{^{1}H} NMR (126 MHz, C_6D_6, 25 °C): δ = 98.3 (*ipso*-C, $C_5H_4CH_3$), 83.4, 79.4 (C_5H_4Me), 35.2 (d, $^1J_{CP}$ = 10.5 Hz, Cy), 32.1, 31.8 (br s, Cy), 30.7 (s, *t*Bu), 28.6, 28.5, 27.3 (s, Cy), 12.7 ppm (s, $C_5H_4CH_3$), the signal for the semibridging CO ligand was not observed; ^{11}B{^{1}H} NMR (64 MHz, C_6D_6, 25 °C): 150 ppm (br s); ^{31}P{^{1}H} NMR (202 MHz, C_6D_6, 25 °C): 27.1 ppm; IR (benzene): $\tilde{\nu}$ = 1811, 1770 cm^{-1}

Received: March 29, 2006
Published online: June 1, 2006

Keywords: boron · borylene complexes · cluster compounds · manganese · palladium

[1] H. Braunschweig, T. Wagner, *Angew. Chem.* **1995**, *107*, 904 – 905; *Angew. Chem. Int. Ed. Engl.* **1995**, *34*, 825 – 826.
[2] a) H. Braunschweig, D. Rais, *Heteroat. Chem.* **2005**, *16*, 566 – 571; b) S. Aldridge, D. Coombs, *Coord. Chem. Rev.* **2004**, *248*, 535 – 559; c) H. Braunschweig, *Adv. Organomet. Chem.* **2004**, *51*, 163 – 192; d) H. Braunschweig, M. Colling, *Coord. Chem. Rev.* **2001**, *223*, 1 – 51; e) H. Braunschweig, *Angew. Chem.* **1998**, *110*, 1882 – 1898; *Angew. Chem. Int. Ed.* **1998**, *37*, 1786 – 1801; f) H. Braunschweig, M. Colling, *Eur. J. Inorg. Chem.* **2003**, 393 – 403; g) H. Braunschweig, M. Colling, *J. Organomet. Chem.* **2000**, *614*, 18 – 26.
[3] a) H. Braunschweig, K. Radacki, D. Scheschkewitz, G. R. Whittell, *Angew. Chem.* **2005**, *117*, 1685 – 1688; *Angew. Chem. Int. Ed.* **2005**, *44*, 1658 – 1661; b) D. L. Coombs, S. Aldridge, C. Jones, D. J. Willock, *J. Am. Chem. Soc.* **2003**, *125*, 6356 – 6357; c) H. Braunschweig, M. Colling, C. Kollann, K. Merz, K. Radacki, *Angew. Chem.* **2001**, *113*, 4327 – 4329; *Angew. Chem. Int. Ed.* **2001**, *40*, 4198 – 4200; d) H. Braunschweig, C. Kollann, U. Englert, *Angew. Chem.* **1998**, *110*, 3355 – 3357; *Angew. Chem. Int. Ed.* **1998**, *37*, 3179 – 3180.
[4] H. Braunschweig, K. Radacki, D. Rais, F. Seeler, K. Uttinger, *J. Am. Chem. Soc.* **2005**, *127*, 1386 – 1387.
[5] H. Braunschweig, D. Rais, K. Uttinger, *Angew. Chem.* **2005**, *117*, 3829 – 3832; *Angew. Chem. Int. Ed.* **2005**, *44*, 3763 – 3766.
[6] C. Boehme, J. Uddin, G. Frenking, *Coord. Chem. Rev.* **2000**, *197*, 249 – 276, and references therein.
[7] A. W. Ehlers, E. J. Baerends, F. M. Bickelhaupt, U. Radius, *Chem. Eur. J.* **1998**, *4*, 210 – 221.
[8] a) H. Braunschweig, M. Colling, C. Kollann, H.-G. Stammler, *Angew. Chem.* **2001**, *113*, 2359 – 2361; *Angew. Chem. Int. Ed.* **2001**, *40*, 2298 – 2300; b) H. Braunschweig, M. Colling, C. Hu, K. Radacki, *Angew. Chem.* **2003**, *115*, 215 – 218; *Angew. Chem. Int. Ed.* **2003**, *42*, 205 – 208.
[9] a) H. Braunschweig, T. Herbst, D. Rais, F. Seeler, *Angew. Chem.* **2005**, *117*, 7627 – 7629; *Angew. Chem. Int. Ed.* **2005**, *44*, 7461 – 7463; b) D. L. Kays, J. K. Day, L. Ooi, S. Aldridge, *Angew. Chem.* **2005**, *117*, 7623 – 7626; *Angew. Chem. Int. Ed.* **2005**, *44*, 7457 – 7460.
[10] H. Braunschweig, K. Radacki, D. Rais, F. Seeler, *Angew. Chem.* **2006**, *118*, 1087 – 1090; *Angew. Chem. Int. Ed.* **2006**, *45*, 1066 – 1069.
[11] H. Braunschweig, M. Müller, *Chem. Ber.* **1997**, *130*, 1295 – 1298.
[12] a) H. Braunschweig in *Inorganic Chemical Highlights* (Eds.: G. Meyer, D. Naumann, L. Wesemann), Wiley-VCH, Weinheim, **2001**, pp. 213 – 218; b) C. Elschenbroich, *Organometallchemie*, 4th ed., Teubner, Wiesbaden, **2002**.
[13] H. Braunschweig, B. Ganter, *J. Organomet. Chem.* **1997**, *545*, 163 – 167.
[14] The X-ray diffraction data for **3** and **4** were collected on a Stoe-IPDS diffractometer with an image plate by using graphite-monochromated $Mo_{K\alpha}$ radiation. The structures were solved by using direct methods, expanded by Fourier techniques, and refined with the SHELX software package (G. M. Sheldrick, SHELX-97 Universität Göttingen, **1997**) All non-hydrogen

 © 2006 Wiley-VCH Verlag GmbH & Co. KGaA, Weinheim

atoms were refined anisotropically. Hydrogen atoms were placed in idealized positions and included in the structure-factor calculations. CCDC-602961 (**3**) and CCDC-602990 (**4**) contain the supplementary crystallographic data for this paper. These data can be obtained free of charge from The Cambridge Crystallographic Data Centre via www.ccdc.cam.ac.uk/data_request/cif. Crystal data for **3**: $C_{18}H_{19}BMn_2O_4$, $M_r = 420.02$, dark red polyhedra, $0.5 \times 0.5 \times 0.4$ mm^3, monoclinic, space group $P2_1/n$, $a = 8.5604(9)$, $b = 13.3225(10)$, $c = 15.7316(17)$ Å, $\beta = 95.861(13)°$, $V = 1784.7(3)$ Å^3, $Z = 4$, $\rho_{calcd} = 1.563$ g cm^{-3}, $\mu = 1.433$ mm^{-1}, $F(000) = 856$, $T = 173(2)$ K, R(all data): $R_1 = 0.0267$, $wR_2 = 0.0641$, $2.60° < \theta < 28.01°$, 20339/4062 reflections collected/unique, $R_{int} = 0.0340$, 229 parameters. Crystal data for **4**: $C_{48}H_{82}BMnO_2P_2Pd_2$, $M_r = 1031.63$, red prisms, $0.2 \times 0.2 \times 0.1$ mm^3, triclinic, space group $P\bar{1}$, $a = 10.7449(9)$, $b = 21.7062(16)$, $c = 33.376(3)$ Å, $\alpha = 72.686(9)$, $\beta = 82.471(10)$, $\gamma = 77.668(9)°$, $V = 7241.2(10)$ Å^3, $Z = 6$, $\rho_{calcd} = 1.419$ g cm^{-3}, $\mu = 1.097$ mm^{-1}, $F(000) = 3228$, $T = 173(2)$ K, $R(I > 2\sigma(I))$: $R_1 = 0.0535$, $wR_2 = 0.1218$, $2.48° < \theta < 26.55°$, 58283/27614 reflections collected/unique, $R_{int} = 0.0741$, 1536 parameters. Three molecules were found in the independent part of the cell and differ essentially only by rotation of the PCy_3 groups; all bond lengths and angles given in the text are for the same molecule.

[15] R. Littger, H. Nöth, M. Suter, *Eur. J. Inorg. Chem.* **2000**, 1571 – 1579.

[16] H. Braunschweig, M. Colling, C. Hu, K. Radacki, *Angew. Chem.* **2002**, *114*, 1359 – 1361; *Angew. Chem. Int. Ed.* **2002**, *41*, 1415 – 1417.

[17] A. G. Ginzburg, L. A. Fedorov, P. V. Petrovskii, E. I. Fedin, V. N. Setkina, D. N. Kursanov, *J. Organomet. Chem.* **1974**, *73*, 77 – 84.

[18] The analogous chloroborylene complex $[(\eta^5\text{-}C_5H_4Me)(OC)_2Mn{=}BCl]$ is believed to be a key intermediate in the photochemically induced formation of the cluster $[B_2Cl_2\{(\eta^5\text{-}C_5H_4Me)Mn(CO)_2\}_2]$.[16]

[19] H. Braunschweig, K. Radacki, D. Rais, G. R. Whittell, *Angew. Chem.* **2005**, *117*, 1217 – 1219; *Angew. Chem. Int. Ed.* **2005**, *44*, 1192 – 1194.

[20] J. Feilong, T. P. Fehlner, A. L. Rheingold, *Angew. Chem.* **1988**, *100*, 400 – 402; *Angew. Chem. Int. Ed. Engl.* **1988**, *27*, 424 – 426.

[21] R. Okamura, K. Tada, K. Matsubara, M. Oshima, H. Suzuki, *Organometallics* **2001**, *20*, 4772 – 4774.

[22] Pd and Pt complexes are often stable with 16 electrons, and corresponding fragments can release two more electrons to bonding cluster MOs; see for example, C. E. Housecroft, *Boranes and Metallaboranes*, 2nd ed., Ellis Horwood, New York, **1994**, p. 120.

[23] Electronic-structure calculations were performed with Gaussian 03 Rev. B.04 (M. J. Frisch et al., Gaussian, Inc., Wallingford CT, **2004**). The electron localization function (ELF) was computed with the TopMoD program package (S. Noury, X. Krokidis, F. Fuster, B. Silvi, TopMoD, Université Pierre et Marie Curie, **1997**). The natural bond orbital (NBO) analysis was performed with the NBO 5.0G program (E. D. Glendening, J. K. Badenhoop, A. E. Reed, J. E. Carpenter, J. A. Bohmann, C. M. Morales, and F. Weinhold, Theoretical Institute, Univeristy of Wisconsin, Madison, **2001**). See the Supporting Information for details.

 © 2006 Wiley-VCH Verlag GmbH & Co. KGaA, Weinheim

Microcontact Printing

DOI: 10.1002/anie.200600310

Universal Ink for Microcontact Printing**

Dirk Burdinski, Milan Saalmink, Jeroen P. W. G. van den Berg, and Cees van der Marel*

Among the various soft lithographic patterning techniques, microcontact printing (μCP) has proven to be most versatile for surface modification needs in material as well as in life science applications.[1–3] Metal surfaces covering tens of square centimeters are now routinely structured by a combination of μCP and etching in numerous research laboratories typically with a surprisingly simple experimental setup. Current μCP research efforts, therefore, either attempt to push the routinely achievable resolution below the 100-nm limit,[4–6] or aim at further developing a μCP-based production technology with universal applicability for various patterning needs over large areas.[7–10] Herein we report a μCP method for the patterning of metal as well as metal oxide surfaces with a single ink composition. This marks an important step towards the development of μCP to become a really simple and universal patterning technique.

In μCP, a target substrate, which is typically comprised of a top metal layer, is modified with a patterned self-assembled monolayer (SAM) of organic molecules. The SAM is formed by printing with an elastomeric malleable stamp that bears the desired surface relief structure and is loaded with an appropriate ink solution. Only in the direct contact areas is a SAM deposited on the substrate. This can be employed as an etch-resistant mask to transcribe the pattern into the underlying metal layers by etching, as a template for further selective material deposition, or to achieve a surface functionalization for another purpose.

Among the materials that in experimental settings are now patterned routinely by μCP are the coinage metals Au, Ag, Cu, and Pd, as well as those exhibiting oxide surfaces,

[*] Dr. D. Burdinski, M. Saalmink
Department of Bio-Molecular Engineering
Philips Research
High Tech Campus Eindhoven
5656 AE Eindhoven (The Netherlands)
Fax: (+31) 40-27-43350
E-mail: dirk.burdinski@philips.com
J. P. W. G. van den Berg, Dr. C. van der Marel
Department of Materials Analysis
Philips Research
High Tech Campus Eindhoven
5656 AE Eindhoven (The Netherlands)

[**] We are grateful to our colleagues J. H. M. Snijders for performing XPS analyses, H. A. G. Nulens for AFM measurements, and G. L. T. van den Heuvel for analysis support. We thank M. Nollen (Philips IP&S) and M. M. J. Decré (Philips Research) for many stimulating discussions.

Supporting information for this article is available on the WWW under http://www.angewandte.org or from the author.

© 2006 Wiley-VCH Verlag GmbH & Co. KGaA, Weinheim

such as Si and Al. For each of these substrate types, a different class of ink molecules is usually required. SAMs on coinage metals are most readily formed from alkanethiol derivatives that strongly interact with the metal surface through the formation of metal–sulfide bonds.[11] Metal oxides, on the other hand, are patterned readily by using SAMs of acid-functionalized aliphatic ink molecules, such as carboxylic or phosphonic acids, or derivatives thereof including reactive halides.[12–17] This binding to the oxide surface occurs through simple condensation reactions.

The requirement for material-specific inks is a significant drawback of μCP compared with conventional patterning methods, in particular photolithography, in which a single etch-resistant material can be used universally for structuring a wide range of materials. The patterning of devices that exhibit multiple materials on a single surface can therefore not easily be achieved. Furthermore, reloading a once-inked stamp with a different ink is intrinsically difficult. This is a particular disadvantage as the production of the stamp is currently the most time-consuming and hence most-expensive step in the μCP process.

To solve these problems, we have investigated the use of ink compositions comprised of ink molecules that are suitable for SAM formation on chemically different materials as universally applicable inks for μCP. Considering their potentially wide applicability, this initial study focused on mixtures of octadecanethiol (ODT) and octadecylphosponic acid (ODPA) for μCP with poly(dimethylsiloxane) (PDMS) stamps. Taking into account their different surface binding mechanisms, a high selectivity of ink transfer and SAM formation during printing with such mixed ink solutions was expected.

Figure 1 shows optical micrographs of patterned gold and aluminum substrates after μCP with a mixed ODT-ODPA ink

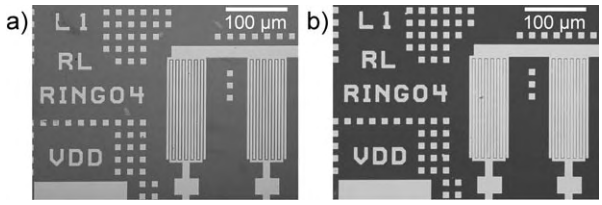


Figure 1. Optical micrographs of gold (a) and aluminum substrates (b) that were microcontact printed with a PDMS stamp after inking with a solution composed of ODT (2 mM) and ODPA (10 mM) in ethanol followed by wet chemical etching.

followed by chemical etching. For both substrates, clearly resolved patterns were obtained, which stimulated us to study this stamp–ink system in more detail. For gold patterning experiments, PDMS stamps are commonly inked with approximate 2 mM solutions of ODT in ethanol. Printing with ODPA on aluminum or silicon substrates was found earlier to require a higher ink concentration of about 10 mM in the respective inking solution to deposit sufficiently stable SAMs.[18] Importantly, the ink concentration in the bulk of the PDMS stamp (c_{stamp}), which serves as the ink reservoir during printing, can differ significantly from the concentration in the used inking solution (c_{soln}).[19] We therefore determined c_{stamp} of PDMS stamps that were immersed in ODT, ODPA, or mixed ODT-ODPA solutions of different concentrations for at least four hours by elemental analysis of the phosphate and sulfate products obtained after total combustion of the inked stamps (Figure 2).

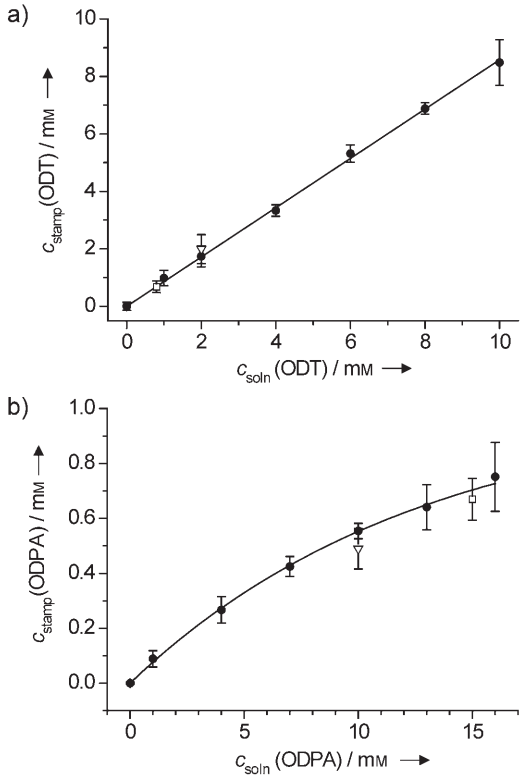


Figure 2. Concentrations of ODT (a) and ODPA (b) in PDMS stamps after inking as a function of their concentration in respective pure ink solutions in ethanol (●). Stamp concentrations were determined by ion chromatography (for sulfur analysis) and inductive coupled plasma atomic emission spectroscopy (ICP-AES; for phosphorus analysis) after the total combustion of stamp material (see the Supporting Information). The experimental data were fitted according to the following equations: a) $c_{stamp}(ODT) = 0.86\, c_{soln}(ODT)$, b) $c_{stamp}(ODPA) = 1.02\ mM\ (1-\exp(-c_{soln}(ODPA)/12.8\ mM))$. □ and ▽ represent results obtained from PDMS stamps inked with mixed ink solutions (▽: $c_{soln}(ODT) = 2.0$ mM and $c_{soln}(ODPA) = 10$ mM, □: $c_{soln}(ODT) = 0.8$ mM and $c_{soln}(ODPA) = 15$ mM). Error bars indicated three times the difference between experimental (c_{exp}) and average concentration values (c_{avg}) of two independent experiments ($\pm\sigma = 3\times|c_{exp}-c_{avg}|$).

For pure ODT solutions with a concentration of up to 10 mM, c_{stamp}(ODT) increased linearly with c_{soln}(ODT) (Figure 2a). No indication of stamp saturation was observed even close to the solubility limit of ODT in ethanol ($\approx$10 mM). The c_{stamp}/c_{soln} ratio of 0.86 for ODT in PDMS is higher than that reported earlier for the more hydrophilic mercaptohexadecanoic acid ink ($c_{stamp}/c_{soln} = 0.2$), which is apparently less compatible with the hydrophobic PDMS matrix.[19] In contrast, a substantially lower c_{stamp}/c_{soln} ratio of at most 0.1 was determined for the ODPA ink (Figure 2b). This ink furthermore exhibited a saturation behavior, from which a saturation concentration of ODPA in PDMS of 1.0 mM could be

 © 2006 Wiley-VCH Verlag GmbH & Co. KGaA, Weinheim

extrapolated. Inking of PDMS stamps with mixed ink solutions had no influence on the individual concentrations of both inks in the stamp when compared to single ink solutions (□ and ▽ in Figure 2). We confirmed experimentally that equal ODT and ODPA stamp concentrations of about 0.7 mM can be obtained by using solution concentrations of 0.8 mM and 15 mM, respectively (□).

To further correlate the composition of the deposited SAMs with that of the respective inking solutions, gold and aluminum substrates were analyzed with X-ray photoelectron spectroscopy (XPS) after printing with an unstructured ("flat") PDMS stamp. Typical contact times were used for these materials (Table 1). Curve fitting and quantification of the XPS spectra provided raw (apparent) surface concentrations for C, S, and P. These data were, based on a model calculation, converted to real atomic concentrations in the SAM-layer, layer thicknesses, and values of the surface coverage with sulfur and phosphorus.[20] A complete ODT monolayer on a Au[111] surface corresponds to a sulfur surface coverage of 4.67×10^{14} atoms cm^{-2}.[21] For ODT solution concentrations of 0.8 and 2 mM, gold surface coverages of about 70 and 80%, respectively, were found after printing. This shows that the surface coverage of ODT was not significantly influenced by the presence of ODPA in the inking solution. ODPA was nevertheless found as an impurity in, or on top of, the printed ODT SAMs in amounts that depended on its concentration in the inking solution and thus in the stamp. In the case of the same ODT and ODPA stamp concentrations, a preferred transfer of ODT over ODPA was observed. For aluminum substrates, on the other hand, ODPA was transferred with a very high selectivity over ODT. The ODPA surface coverage on aluminum substrates was found to be independent of the presence of ODT in the stamp. No ODT was detected in this case.

From an application point of view, the etch resistance of these printed SAMs is a valuable criterion. To test this property, aluminum patterns were developed with an alkaline hydrogen peroxide etching bath. The quality of the patterns obtained on substrates printed with pure ODPA or with mixed inks comprising ODPA concentrations of not less than 10 mM were virtually identical (Figure 3). Although for all aluminum substrates an expected ink spreading of about 0.4–0.6 μm was deduced from the increased size of the developed structures, the extent of spreading was found to be independent of the presence of ODT in the stamp (Table 1).

Printed gold samples were developed with an alkaline thiosulfate-based etching bath to yield a pattern quality that, similar to the aluminum case, was independent of the presence of the second ink (Figure 3). The spreading of ODT on gold was expectedly smaller than that of ODPA on aluminum (Table 1). Remarkably the simultaneous deposition of ODPA during the printing of ODT SAMs on gold did not detectibly compromise the provided etch resistance. This may be ascribed to a defect healing effect that was reported earlier for aliphatic alcohols and sulfonic acids in specially tailored etching solutions.[10,22]

We have thus shown that mixed solutions of aliphatic thiols and phosphonic acids constitute suitable ink compositions for μCP with PDMS stamps on coinage metal as well as on metal oxide surfaces. In preliminary experiments we have likewise successfully utilized mixtures of 2-alkyl-1,3-dithio-

Table 1: Results from XPS and tapping mode AFM experiments.[a]

				XPS		AFM	
Metal	c_{soln}(ODT) [mM]	c_{soln}(ODPA) [mM]	d [nm]	[S] $\times10^{-14}$ [at cm^{-2}]	[P] $\times10^{-14}$ [at cm^{-2}]	L_{line} [μm]	L_{square} [μm]
Au	0	10	1.5	–	2.5	×	×
Au	2	0	2.6	3.9	–	3.8	10.0
Au	2	10	2.8	3.6	0.8	3.9	10.2
Au	0	15	2.2	–	3.2	×	×
Au	0.8	0	2.5	3.4	–	3.8	9.9
Au	0.8	15	2.9	3.3	2.4	3.8	10.0
Al	0	10	2.0	–	4.8	4.4	10.5
Al	2	0	0.4	0.2	–	×	×
Al	2	10	2.0	–	4.6	4.4	10.4
Al	0	15	2.2	–	5.0	4.5	10.6
Al	0.8	0	0.5	–	–	×	×
Al	0.8	15	2.1	–	4.6	4.5	10.7

[a] The experiments were performed on gold (15 s contact time) and aluminum substrates (300 s contact time) onto which SAMs comprised of ODT and/or ODPA were deposited by μCP with unpatterned (for XPS) or patterend (for AFM) PDMS stamps. The stamps were loaded with solutions of ODT and/or ODPA in ethanol with the indicated concentrations. [S] and [P] denote the total surface coverage ($\pm0.2\times10^{14}$ atoms cm^{-2}) by sulfur and phosphorus, respectively, d denotes the average layer thickness as determined from the XPS results.[20] AFM samples were developed by wet chemical etching after printing. The analyzed lines and squares had a nominal width of $L_{line}=3.80$ μm and $L_{square}=10.00$ μm, respectively. Reported feature widths are average values with an error of ±0.1 μm. – = below detection limit of $0.2\cdot10^{14}$ at cm^{-2}. × = no pattern.

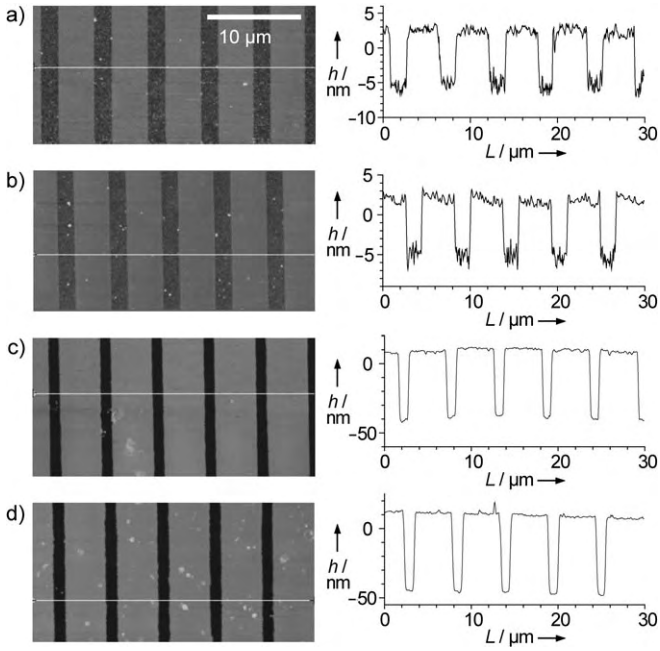


Figure 3. Tapping mode AFM micrographs and height profiles of gold (a and b, 10 nm Au) and aluminum substrates (c and d, 50 nm Al) patterned by μCP with ODT (a), ODPA (c), or mixed ODT/ODPA inks (b and d) and subsequent wet etching. Light areas correspond to elevated features. The elevated line features have a nominal width of 3.8 μm. The measured average (over at least two different substrate samples) widths are (3.8 ± 0.1) μm (a), (3.9 ± 0.1) μm (b), (4.4 ± 0.1) μm (c), and (4.4 ± 0.1) μm (d).

 © 2006 Wiley-VCH Verlag GmbH & Co. KGaA, Weinheim

lanes and alkylsilylchlorides for the patterning of gold, aluminum, and silicon oxide surfaces by μCP.[12,23] In general, we consider such universally applicable ink compositions to be useful for repeated printing with the same stamp on different materials or on surfaces that expose the same material in different modifications. Furthermore printing simultaneously on a single substrate that exposes different materials on its surface could be advantageous to increase the patterning reliability by extending SAMs to adjacent materials.

Utilizing mixed ink compositions even in spin coating and similar processes may prove valuable, for instance, in the packaging of electronic devices, to achieve good adhesion of an overmolded compound to all surface parts of the substrate, or in the fabrication of biosensors or other medical devices. Microfluidic systems comprised of walls made of different materials could likewise be modified easily to expose a homogeneous surface to the fluid. Clearly universal ink compositions have a wide range of potential applications, far beyond the limits of the μCP technique.

In conclusion, we have demonstrated the soft lithographic patterning of a metal (gold) as well as a metal oxide (aluminum) substrate by μCP with a single mixed ink composition and wet chemical etching. The process takes advantage of the intrinsic selectivity of the transfer of specific molecules from the mixed ink to different substrate materials. This method marks an important step in our continuing efforts to further develop μCP towards becoming a really simple and universal pattern technique.

Received: January 24, 2006
Published online: May 31, 2006

Keywords: microcontact printing · monolayers · phosphonic acids · self-assembly · thiols

[1] B. D. Gates, Q. Xu, J. C. Love, D. B. Wolfe, G. M. Whitesides, *Annu. Rev. Mater. Res.* **2004**, *34*, 339 – 372.
[2] A. P. Quist, E. Pavlovic, S. Oscarsson, *Anal. Bioanal. Chem.* **2005**, *381*, 591 – 600.
[3] R. K. Smith, P. A. Lewis, P. S. Weiss, *Prog. Surf. Sci.* **2004**, *75*, 1 – 68.
[4] K. M. Choi, J. A. Rogers, *J. Am. Chem. Soc.* **2003**, *125*, 4060 – 4061.
[5] H.-W. Li, B. V. O. Muir, G. Fichet, W. T. S. Huck, *Langmuir* **2003**, *19*, 1963 – 1965.
[6] M. Leufgen, A. Lebib, T. Muck, U. Bass, V. Wagner, T. Borzenko, G. Schmidt, J. Geurts, L. W. Molenkamp, *Appl. Phys. Lett.* **2004**, *84*, 1582 – 1584.
[7] J. A. Rogers, Z. Bao, K. Baldwin, A. Dodabalapur, B. Crone, V. R. Raju, V. Kuck, H. Katz, K. Amundson, J. Ewing, P. Drzaic, *Proc. Natl. Acad. Sci. USA* **2001**, *98*, 4835 – 4840.
[8] E. Delamarche, J. Vichiconti, S. A. Hall, M. Geissler, W. Graham, B. Michel, R. Nunes, *Langmuir* **2003**, *19*, 6567 – 6569.
[9] M. M. J. Decré, R. Schneider, D. Burdinski, J. Schellekens, M. Saalmink, R. Dona, *Mater. Res. Soc. Symp. Proc.* **2004**, *EXS-2*, 59 – 61.
[10] D. Burdinski, H. J. A. Brans, M. M. J. Decré, *J. Am. Chem. Soc.* **2005**, *127*, 10786 – 10787.
[11] J. C. Love, L. A. Estroff, J. K. Kriebel, R. G. Nuzzo, G. M. Whitesides, *Chem. Rev.* **2005**, *105*, 1103 – 1169.
[12] S. Onclin, B. J. Ravoo, D. N. Reinhoudt, *Angew. Chem.* **2005**, *117*, 6438 – 6462; *Angew. Chem. Int. Ed.* **2005**, *44*, 6282 – 6304.
[13] Y. Harada, G. S. Girolami, R. G. Nuzzo, *Langmuir* **2004**, *20*, 10878 – 10888.
[14] I. L. Liakos, R. C. Newman, E. McAlpine, M. R. Alexander, *Surf. Interface Anal.* **2004**, *36*, 347 – 354.
[15] L. B. Goetting, T. Deng, G. M. Whitesides, *Langmuir* **1999**, *15*, 1182 – 1191.
[16] N. L. Jeon, K. Finnie, K. Branshaw, R. G. Nuzzo, *Langmuir* **1997**, *13*, 3382 – 3391.
[17] T. L. Breen, P. M. Fryer, R. W. Nunes, M. E. Rothwell, *Langmuir* **2002**, *18*, 194 – 197.
[18] M. Geissler, H. Wolf, R. Stutz, E. Delamarche, U.-W. Grummt, B. Michel, A. Bietsch, *Langmuir* **2003**, *19*, 6301 – 6311.
[19] R. B. A. Sharpe, D. Burdinski, J. Huskens, H. J. W. Zandvliet, D. N. Reinhoudt, B. Poelsema, *Langmuir* **2004**, *20*, 8646 – 8651.
[20] C. van der Marel, M. Yildirim, H. R. Stapert, *J. Vac. Sci. Technol. A* **2005**, *23*, 1456 – 1470.
[21] XRD experiments indicate that the used gold surfaces exhibit a [111] orientation. A surface density of $[S]_{max} = 4.67 \times 10^{14}$ atoms cm^{-2} corresponds to an area coverage of 0.214 nm^2 per thiolate on an ideal smooth surface.
[22] M. Geissler, H. Schmid, A. Bietsch, B. Michel, E. Delamarche, *Langmuir* **2002**, *18*, 2374 – 2377.
[23] D. Burdinski (Philips Electronics N.V.), Patent Application, WO 049741, **2005**.

 © 2006 Wiley-VCH Verlag GmbH & Co. KGaA, Weinheim

Hydroalumination

DOI: 10.1002/anie.200504428

Facile Formation of a Persistent Butadien-2-yl Cation Stabilized by Hyperconjugation with an Al–C Bond**

Werner Uhl, Jörg Grunenberg, Alexander Hepp, Madhat Matar, and Andrej Vinogradov*

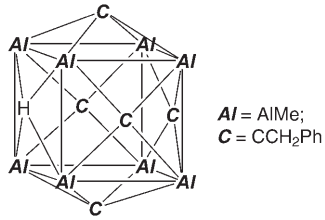
The addition of Al–H or Ga–H bonds to unsaturated organic compounds (hydroalumination, hydrogallation) has been reported in numerous publications and covered for many decades in standard textbooks.[1] However, we recently observed that the corresponding reactions with alkynes proceed through much more complicated pathways than

[*] Prof. Dr. W. Uhl, Dr. A. Hepp, Dr. M. Matar, A. Vinogradov
Institut für Anorganische und Analytische Chemie
Westfälische Wilhelms-Universität Münster
Corrensstrasse 30, 48149 Münster (Germany)
Fax: (+49) 251-833-6610
E-mail: uhlw@uni-muenster.de
Dr. J. Grunenberg
Institut für Organische Chemie
Universität Braunschweig
Hagenring 30, 38106 Braunschweig (Germany)

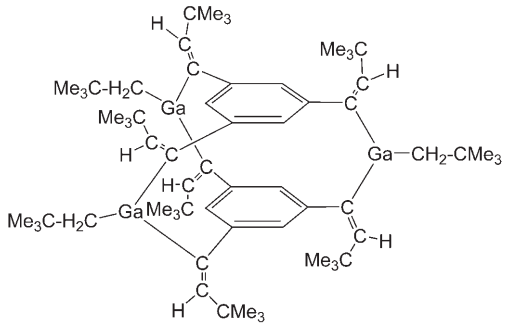
[**] This work was supported by the Deutsche Forschungsgemeinschaft and the Fonds der Chemischen Industrie. We are grateful to Prof. Dr. A. Berndt (Marburg) for valuable discussions.

WILEY InterScience DISCOVER SOMETHING GREAT
© 2006 Wiley-VCH Verlag GmbH & Co. KGaA, Weinheim

those suggested in the literature. The simple addition products which are usually expected were not obtained in many cases; instead, secondary reactions occurred with the release of trialkylaluminum or -gallium compounds. Novel products possessing unprecedented structures resulted, two of which are depicted in Scheme 1. Double hydroalumination



1

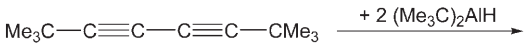


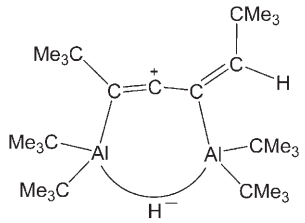
2

Scheme 1. Carbaalane **1** and [3,3,3]cyclophane derivative **2**.

and release of trimethylalane afforded the carbaalane **1** in high yield when dimethylaluminum hydride was treated with dimethylaluminum phenylethynide.[2] The similarly selective reaction of 1,3,5-tri(*tert*-butylethynyl)benzene with dineopentylgallium hydride gave the [3,3,3]cyclophane derivative **2** by hydrogallation and elimination of trineopentylgallane.[3] Generally, the regioselectivity of these addition reactions is determined by the substituents that are attached to the carbon atoms of the triple bonds, whereby dialkylelement (E = Al, Ga) or trimethylsilyl groups possess the strongest directing influence. Accordingly, the aluminum or gallium atoms of the hydrides attack preferentially those carbon atoms which already bear silicon or aluminum atoms. Hence, the reaction of 1,4-bis(trimethylsilyl)butadiyne with $(Me_3C)_2AlH$ yielded a product in high yield[4] in which both $Al(CMe_3)_2$ groups are attached to the terminal carbon atoms of the original butadiyne moiety. Under similar conditions, the reaction with 1,4-di(*tert*-butyl)butadiyne afforded an unexpected product, which is described herein.

The reaction of 1,4-di(*tert*-butyl)butadiyne with two equivalents of di(*tert*-butyl)aluminum hydride in *n*-pentane [Eq. (1)] yielded a yellow solution from which yellow crystals of the product **3** precipitated upon concentration and cooling of the solution to −45 °C. Crystal structure determination[5] of **3** (Figure 1) revealed that condensation with release of the corresponding trialkylalane, as analogous to the reactions of





3

(1)

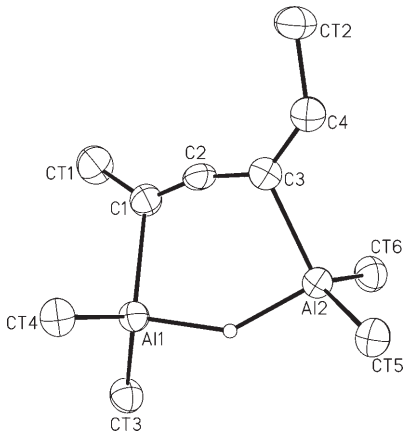


Figure 1. Molecular structure of **3** (thermal ellipsoids are set at 40% probability); methyl groups and the hydrogen atom attached to C4 are omitted. Selected bond lengths [pm] and angles [°]: C1-C2 125.6(3), C2-C3 136.7(3), C3-C4 133.9(3), Al1-C1 216.3(2), Al1-CT3 201.4(2), Al1-CT4 200.6(2), Al1-H1 172(2), Al2-C3 205.8(2), Al2-CT5 199.6(2), Al2-CT6 200.5(2), Al2-H1 172(2); CT1-C1-C2 135.0(2), Al1-C1-C2 99.9(2), C1-C2-C3 162.9(2), C2-C3-C4 135.3(2), C3-C4-CT2 129.5(2), C4-C3-Al2 117.7(2).

alkyl ethynes described before, did not occur. Instead, two intact di(*tert*-butyl)aluminum groups were found in the structure. The aluminum atom Al2 is bound to one of the inner carbon atoms of the original butadiyne moiety (C3) and thus does not have a close contact to the terminal *tert*-butyl group that is attached to C4. The associated triple bond in the original butadiyne (C3−C4) was hydroaluminated (bond length of C3=C4: 133.9(3) pm). In contrast, the second aluminum atom (Al1) is linked to a terminal carbon atom of the original butadiyne unit (C1) so that the vicinal arrangement of the dialkylaluminum groups does not occur, probably as a result of steric and electrostatic repulsion. The aluminum atoms are connected through a three-center, two-electron Al-H-Al bridge, and at first glance, the second triple bond of the butadiyne reactant remains unaffected and was not hydroaluminated. The C1−C2 bond length (125.6(3) pm) is between the standard bond lengths[6] of double (134 pm) and triple bonds (120 pm). Furthermore, the bond length between the inner carbon atoms C2−C3 (136.7(3) pm; expected value for $C(sp^2)$−C(sp): 143 pm) is relatively short. The dicoordinated carbon atom C2 does not possess a linear arrangement (∢(C1-C2-C3): 162.9(2)°). Standard Al−C bond

 © 2006 Wiley-VCH Verlag GmbH & Co. KGaA, Weinheim

lengths were detected only for the bonds involving the *tert*-butyl groups (average: 200.5 pm), and relatively long Al–C bond lengths resulted for the bonds involving the unsaturated carbon atoms of the π system (Al1–C1 216.3(2) pm; Al2–C3 205.8(2) pm). Thus, in accordance with quantum-chemical calculations, a relatively weak Al–C bond is observed in particular to Al1.

To understand the unusual structural parameters, quantum-chemical calculations[7] at the B3LYP/6-31G(d) level were carried out in which the entire molecule **3** was considered. According to the calculations, compound **3** should be described as bearing a butadien-2-yl cation. As based on an NBO (natural bond orbital) analysis, the positive charge is localized at the carbon atom C2, and the negative charge is essentially concentrated at the hydridic hydrogen atom (NBO charge: −0.55). The following charge distribution results for the inner C_4 portion of the molecule: C1 −0.41, C2 +0.15, C3 −0.53, C4 −0.14. Compound **3** may thus be described as a zwitterionic molecule which is soluble in nonpolar solvents. The occurrence of a butadien-2-yl cation is further supported by the calculated static bond strengths.

The DFT compliance constants[7] verify the alternating bond orders in this part of the molecule (C3=C4 0.12, C2–C3 0.23, C1=C2 0.12 Å mdyn^{-1}), which excellently agree with the bond lengths obtained by crystal structure determination. A higher value indicates weaker bonding since the compliance constants reflect the displacement of an internal coordinate by application of an external force. The butadienyl cation is stabilized by delocalization of the π electrons and particularly efficiently by a rarely observed hyperconjugation with an Al–C bond (Al1–C1).[8] The latter interaction results in a lengthening and weakening of the Al1–C1 bond (compliance constant: 1.56 Å mdyn^{-1}) compared with the Al2–C3 bond (compliance constant: 1.20 Å mdyn^{-1}). The stabilization of the cation by hyperconjugation is further supported by the fact that the C1–C2 bond length approaches that of a triple bond and by the unusually small Al1-C1-C2 angle (99.9°; for comparison, ∢(Al2-C3-C4) 117.7°), which favors the overlap of the Al–C σ orbital with the empty p orbital of the cationic carbon atom.

The calculated shift of the ^{13}C NMR spectroscopic resonance of the cationic carbon atom C2 ($\delta = 160$ ppm) is in excellent accordance with the experimentally obtained value ($\delta = 161.3$ ppm; remaining values for the butadiene skeleton: observed: $\delta = 116.7$ (C1), 129.9 (C3), 156.0 ppm (C4); calculated: $\delta = 108$ (C1), 120 (C3), 140 ppm (C4)). Interestingly, the four *tert*-butyl groups which are attached to the aluminum atoms exhibit only one proton resonance at room temperature. A splitting into two resonances, in accordance with the strongly differing chemical environments of these groups, was detected only upon cooling of a sample to −30 °C. We are not able to present a reasonable mechanism for this fast and unexpected exchange process. The spectroscopic resonances of the butadienyl part of the molecule with two chemically independent *tert*-butyl groups do not show any differences in dependency on the temperature. Thus, we believe that the exchange is restricted to the dialkylaluminum parts of the molecule and may proceed by a transition state which involves bridging *tert*-butyl groups.

To our knowledge, butadien-2-yl cations analogous to **3** have been detected previously only in superacidic media by NMR spectroscopy.[9] Quantum-chemical calculations on the simplest cation, $H_2C{=}C^+{-}CH{=}CH_2$, afforded structural parameters of the butadienyl skeleton[9] which are quite similar to those of compound **3**. According to the calculations, an effective hyperconjugation to both terminal C–H bonds of the $-C^+{=}CH_2$ moiety stabilizes the cationic center and results in a C=C bond length which approaches that of a C–C triple bond. In compound **3**, a similar interaction with an Al–C bond results in stabilization of the cation. Interestingly, the electrophilicity of the cationic carbon atom (C2) of **3** is not strong enough to remove the hydridic hydrogen atom from the Al-H-Al bridge. The coordinatively unsaturated aluminum atoms act as a very strong chelating Lewis acid and coordinate the hydride anion so effectively that rearrangement and bonding to the carbon atom C2 becomes unfavorable. Compounds related to **3** include the vinyl cations $R_2C{=}C^+R'$, one of which was characterized only recently by Müller et al. by a crystal structure determination.[10,11] Compound **3** has the advantages of easy accessibility by a facile route, its relatively high stability, and its solubility in nonpolar solvents. These properties will be useful for a thorough investigation of its chemical behavior and reactivity.

Experimental Section

3: *n*-Pentane was dried over $LiAlH_4$. 2,2,7,7-Tetramethyl-3,5-octadiyne (0.285 g, 1.76 mmol, Aldrich) was dissolved under argon in *n*-pentane (25 mL) and cooled to −20 °C. A solution of di(*tert*-butyl)aluminum hydride[12] (0.500 g, 3.52 mmol) in *n*-pentane (25 mL) was added dropwise. The color of the solution changed to yellow. The mixture was slowly warmed to room temperature and further stirred for 1 h. After concentration and cooling of the mixture to −45 °C, yellow crystals of **3** precipitated over several days (yield: 0.554 g, 71 %). M.p. (under argon, sealed capillary) 55 °C (decomp); ^{1}H NMR (400 MHz, [D$_8$]toluene, 275 K): $\delta = 6.00$ (s, 1H, C=CH), 2.73 (br s, 1H, Al-H), 1.28 (s, 36H, Al-CMe$_3$), 1.24 (s, 9H, C1-CMe$_3$), 0.99 ppm (s, 9H, C4-CMe$_3$); ^{1}H NMR (400 MHz, [D$_8$]toluene, 185 K): $\delta = 6.04$ (s, 1H, C=CH), 2.76 (br s, 1H, Al-H), 1.44 (s, 18H, Al2-CMe$_3$), 1.38 (s, 18H, Al1-CMe$_3$), 1.16 (s, 9H, C1-CMe$_3$), 0.94 ppm (s, 9H, C4-CMe$_3$); ^{13}C NMR (100 MHz, [D$_8$]toluene, 275 K): $\delta = 161.3$ ($^3J_{CH} = 17$ Hz, cationic C2), 156.0 ($^1J_{CH} = 156.0$ Hz, C4), 129.9 ($^2J_{CH} = 10$ Hz, C3), 116.7 (C1), 39.8 (C1-*C*Me$_3$), 37.6 (C4-*C*Me$_3$), 33.0 (C1-C*Me*$_3$), 31.5 (Al-C*Me*$_3$), 29.3 (C4-C*Me*$_3$), 19.4 ppm (Al-*C*Me$_3$); ^{13}C NMR (100 MHz, [D$_8$]toluene, 185 K): $\delta = 161.5$ (cationic C2), 156.9 (C4), 129.1 (C3), 115.2 (C1), 40.1 (C1-*C*Me$_3$), 37.8 (C4-*C*Me$_3$), 32.9 (C1-C*Me*$_3$), 31.82 (Al2-C*Me*$_3$), 31.75 (Al1-C*Me*$_3$), 29.3 (C4-C*Me*$_3$), 20.7 (Al1-*C*Me$_3$), 19.1 ppm (Al2-*C*Me$_3$); IR (nujol, CsBr): $\tilde{\nu} =$ 1851 br vs, 1681 br vs, 1594 vs ν(AlH), ν(C=C), 1464 vs, 1386 vs (nujol), 1362 vs, 1257 m δ(CH$_3$), 1218 vs, 1203 vs, 1176 vs, 1083 w, 1053 m, 1005 vs, 934 vs, 894 m, 855 w, 808 vs, 785 w, 762 w, 741 m ν(CC), ρ(CH$_3$), 661 vs, 631 vs, 604 w, 581 m, 539 s, 524 m, 508 m, 451 cm^{-1} s ν(AlC); UV/Vis (*n*-hexane): λ_{max} (log ε) = 321 (2.4), 400 nm (2.3); MS (20 eV): *m*/*z* (%): 446 (3.5) [*M*$^+$], 389 (100) [*M*$^+$−CMe$_3$], higher masses through decomposition.

Received: December 13, 2005
Revised: April 4, 2006
Published online: June 1, 2006

Keywords: aluminum · hydroalumination · hyperconjugation · structure elucidation · vinyl cation

 © 2006 Wiley-VCH Verlag GmbH & Co. KGaA, Weinheim

[1] C. Elschenbroich, *Organometallchemie*, 4th ed., Teubner, Stuttgart, **2003**; Hollemann-Wiberg, *Lehrbuch der Anorganischen Chemie*, deGruyter, Berlin, **1995**.

[2] W. Uhl, F. Breher, *Angew. Chem.* **1999**, *111*, 1578; *Angew. Chem. Int. Ed.* **1999**, *38*, 1477; W. Uhl, F. Breher, A. Lützen, W. Saak, *Angew. Chem.* **2000**, *112*, 414; *Angew. Chem. Int. Ed.* **2000**, *39*, 406; W. Uhl, *Inorganic Chemistry Highlights* (Eds.: G. Meyer, D. Naumann, L. Wesemann), Wiley-VCH, Weinheim, **2002**, p. 229.

[3] W. Uhl, F. Breher, S. Haddadpour, *Organometallics* **2005**, *24*, 2210; W. Uhl, S. Haddadpour, M. Matar, *Organometallics* **2006**, *25*, 159.

[4] W. Uhl, F. Breher, *J. Organomet. Chem.* **2000**, *608*, 54.

[5] Crystal structure of **3**: Single crystals from *n*-pentane at −45 °C, $C_{28}H_{56}Al_2$, monoclinic, space group $P2_1/c$; $a = 880.66(6)$, $b = 1871.8(1)$, $c = 1902.1(1)$ pm, $\beta = 94.638(5)°$, $V = 3125.2(3)$ Å^3, $Z = 4$, $\rho_{calcd} = 0.949$ g cm^{-3}, crystal dimensions $0.25 \times 0.21 \times 0.09$ mm^3, Stoe IPDS diffractometer, $Mo_{K\alpha}$ radiation, 193 K, measurement range $3.0 < 2\Theta < 52.4°$, 6252 independent reflections, 3961 reflections for $F > 4\sigma(F)$, $\mu = 0.104$ mm^{-1}, programs SHELXTL PLUS REL 4.1 and SHELXL-98 (G. M. Sheldrick, SHELXL-98, Program for the Refinement of Crystal Structures, Universität Göttingen, **1998**), 417 parameters, $R1 = 0.051$ and w$R2$(all data) = 0.129, max./min. residual electron density: $0.207/-0.268 \times 10^{30}$ e m^{-3}. The *tert*-butyl groups of CT1 and CT2 are rotationally disordered. The methyl groups were refined in three positions with occupancy factors of 0.3333 (each position at CT1) and 0.5000, 0.2500, and 0.2500 (CT2) with restrictions of bond lengths and angles. CCDC-292841 (**3**) contains the supplementary crystallographic data for this paper. These data can be obtained free of charge from The Cambridge Crystallographic Data Centre via www.ccdc.cam.ac.uk/data_request/cif.

[6] J. March, *Advanced Organic Chemistry*, 3rd ed., Wiley, New York, **1985**, p. 19.

[7] Geometry optimizations, calculation of frequencies, and NMR parameters (B3LYP 6-31G(d) GIAO) were conducted with the Gaussian program package: Gaussian 03, Revision C.02, M. J. Frisch, G. W. Trucks, H. B. Schlegel, G. E. Scuseria, M. A. Robb, J. R. Cheeseman, J. A. Montgomery, Jr., T. Vreven, K. N. Kudin, J. C. Burant, J. M. Millam, S. S. Iyengar, J. Tomasi, V. Barone, B. Mennucci, M. Cossi, G. Scalmani, N. Rega, G. A. Petersson, H. Nakatsuji, M. Hada, M. Ehara, K. Toyota, R. Fukuda, J. Hasegawa, M. Ishida, T. Nakajima, Y. Honda, O. Kitao, H. Nakai, M. Klene, X. Li, J. E. Knox, H. P. Hratchian, J. B. Cross, V. Bakken, C. Adamo, J. Jaramillo, R. Gomperts, R. E. Stratmann, O. Yazyev, A. J. Austin, R. Cammi, C. Pomelli, J. W. Ochterski, P. Y. Ayala, K. Morokuma, G. A. Voth, P. Salvador, J. J. Dannenberg, V. G. Zakrzewski, S. Dapprich, A. D. Daniels, M. C. Strain, O. Farkas, D. K. Malick, A. D. Rabuck, K. Raghavachari, J. B. Foresman, J. V. Ortiz, Q. Cui, A. G. Baboul, S. Clifford, J. Cioslowski, B. B. Stefanov, G. Liu, A. Liashenko, P. Piskorz, I. Komaromi, R. L. Martin, D. J. Fox, T. Keith, M. A. Al-Laham, C. Y. Peng, A. Nanayakkara, M. Challacombe, P. M. W. Gill, B. Johnson, W. Chen, M. W. Wong, C. Gonzalez, J. A. Pople, Gaussian, Inc., Wallingford CT, **2004**. The generalized compliance constants were calculated with the program *Compliance* (K. Brandhorst, J. Grunenberg, Braunschweig, **2005**) and are based on the B3LYP/6-13G(d) Cartesian force constants. For details of this method, see: G. v. Frantzius, R. Streubel, K. Brandhorst, J. Grunenberg, *Organometallics* **2006**, *25*, 118.

[8] W. Uhl, T. Spies, R. Koch, W. Saak, *Organometallics* **1999**, *18*, 4598.

[9] H.-U. Siehl, H. Mayr, *J. Am. Chem. Soc.* **1982**, *104*, 909; theory: H.-U. Siehl, S. Brixner, *J. Phys. Org. Chem.* **2004**, *17*, 1039; Y. Apeloig, A. Stanger, *J. Org. Chem.* **1982**, *47*, 1462; K. van Alem, G. Lodder, H. Zuilhof, *J. Phys. Chem. A* **2002**, *106*, 10681; K. van Alem, G. Lodder, H. Zuilhof, *J. Phys. Chem. A* **2000**, *104*, 2780; A. Cunje, C. F. Rodriquez, M. H. Lien, A. C. Hopkinson, *J. Org. Chem.* **1996**, *61*, 5212.

[10] T. Müller, M. Juhasz, C. A. Reed, *Angew. Chem.* **2004**, *116*, 1569; *Angew. Chem. Int. Ed.* **2004**, *43*, 1546; T. Müller, D. Margraf, Y. Syha, *J. Am. Chem. Soc.* **2005**, *127*, 10852; T. Müller, R. Meyer, D. Lennartz, H.-U. Siehl, *Angew. Chem.* **2000**, *112*, 3203; *Angew. Chem. Int. Ed.* **2000**, *39*, 3074, and references therein.

[11] L. I. Zakharkin, V. V. Kobak, *J. Organomet. Chem.* **1984**, *270*, 229.

[12] W. Uhl, L. Cuypers, R. Graupner, J. Molter, A. Vester, B. Neumüller, *Z. Anorg. Allg. Chem.* **2001**, *627*, 607.

 © 2006 Wiley-VCH Verlag GmbH & Co. KGaA, Weinheim

Hydrogels

DOI: 10.1002/anie.200504539

Switchable Hydrogels Obtained by Supramolecular Cross-Linking of Adamantyl-Containing LCST Copolymers with Cyclodextrin Dimers**

*Oliver Kretschmann, Soo Whan Choi, Masahiko Miyauchi, Itsuro Tomatsu, Akira Harada, and Helmut Ritter**

Intelligent hydrogels that are sensitive to external stimuli like temperature, light, pH, or salt effects are of increasing interest because of potential applications in materials science and medicine.[1] Not only covalently cross-linked gels but also associatively cross-linked gels are of interest. Various types of polymer inclusion complexes (PICs) formed by noncovalent host–guest interactions have been reported and investigated extensively for the construction of supramolecular systems.[2–4] Cyclodextrins (CDs) have been the most widely used host molecules because they are water-soluble and capable of selectively including a wide range of hydrophobic guest molecules.[5,6] Low-molecular-weight as well as polymeric molecules can interact with one or more CD molecules.[7] Since the first report in 1992, which described a "molecular necklace", CD-based PICs have been investigated extensively. They are important in fundamental research on, for example, noncovalent binding based on macromolecular

[*] O. Kretschmann, Dr. S. W. Choi, Prof. Dr. H. Ritter
Heinrich-Heine-Universität Düsseldorf
Institut für Organische Chemie und Makromolekulare Chemie
Universitätsstrasse 1, 40225 Düsseldorf (Germany)
Fax: (+49) 211-811-5840
E-mail: h.ritter@uni-duesseldorf.de
Dr. M. Miyauchi, I. Tomatsu, Prof. Dr. A. Harada
Department of Macromolecular Science
Graduate School of Science
Osaka University
Toyonaka, Osaka, 560-0043 (Japan)

[**] LCST = lower critical solution temperature.

© 2006 Wiley-VCH Verlag GmbH & Co. KGaA, Weinheim

recognition.[7–9] Tonelli et al. prepared various PICs and demonstrated several interesting applications.[8]

In 2003 we reported on the influence of polymer-bound adamantyl and cyclohexyl components in an *N*-isopropylacrylamide copolymer on the lower critical solution temperature (LCST),[9a] and more recently we described the synthesis of physical polymeric gels from CD-mediated *tert*-butyl methacrylate.[9b] We have introduced many PICs and pseudopolyrotaxanes by a series of combination of CDs, usually α-, β-, and γ-CD (six, seven, and eight glucose units, respectively), and the corresponding linear polymers.[10] We also reported on a thermosensitive PIC formed from a polymethacrylamide and randomly methylated β-CD which shows solubility behavior similar to that of established LCST polymers.[10f] In related work Huh et al. prepared a hydrogel with supramolecular structure, which shows a reversible phase transition, by inclusion complexation between poly(ethylene glycol)-grafted dextran and α-CD.[11] Li et al. introduced a PIC-based supramolecular hydrogel for an injectable delivery system.[12] Pluronics (commercial triblock copolymers of poly(ethylene oxide) and poly(propylene oxide)) were used for complexation with α-CD. Wenz et al. showed that the formation of a physical gel can be achieved by a specific host–guest interaction between CD polymers and suitable guest polymers.[13]

Recently we also studied the interaction between a polymer bearing β-CD moieties and a polymer bearing azobenzene moieties. We found that the β-CD polymer interacted with the polymer having *trans* azobenzene units to form a gel-like mixture. In contrast, the polymer with *cis* azobenzene units did not lead to formation of a gel under the same conditions.[14] More recently, we have successfully constructed aqueous systems that undergo gel-to-sol and sol-to-gel transitions and a photosensitive hydrogel system utilizing the formation of inclusion complexes of α-CD with dodecyl side chains in modified poly(acrylic acid).[15] We report here on a new type of supramolecular cross-linked hydrogel that shows LCST behavior and consists of polymers complexed to CD dimers.

Adamantyl groups are known to be included and held strongly in β-CD. To obtain noncovalent cross-linked gel structures, we used a CD dimer and adamantyl-containing polymers for our study. Guest copolymers **5**–**7** were prepared in DMF by free-radical copolymerization; the molar ratio of 1-adamantylacrylamide (**3**) or 6-acryloylaminohexanoic acid 1-adamantylamide (**4**) to *N*-isopropylacrylamide (NIPAAM, **1**) or *N*,*N*-dimethylacrylamide (DMAA, **2**) was 1:20. The polymers were characterized by ^{1}H and ^{13}C NMR spectroscopy, differential scanning calorimetry (DSC), and gel permeation chromatography (GPC). The molecular weights and compositions of the copolymers used in this study are listed in Table 1. The β-CD dimer **8** was prepared by condensation of terephthalic acid with 2 equiv of 6-amino-β-CD using *N*,*N*′-dicyclohexylcarbodiimide (DCC) and 1-hydroxy-1*H*-benzotriazole (HOBT) in DMF.[16]

The strong supramolecular cross-linking between the CD dimer **8** and copolymers **5**–**7** at 10 °C became evident by zero-shear viscosity measurements. Aqueous solutions of **5**–**7** were mixed with a defined amount of CD dimer **8**. To evaluate the viscosity data, pure copolymers **5**–**7** and mixtures of the copolymers and monofunctional β-CD were investigated and compared (Figure 1).

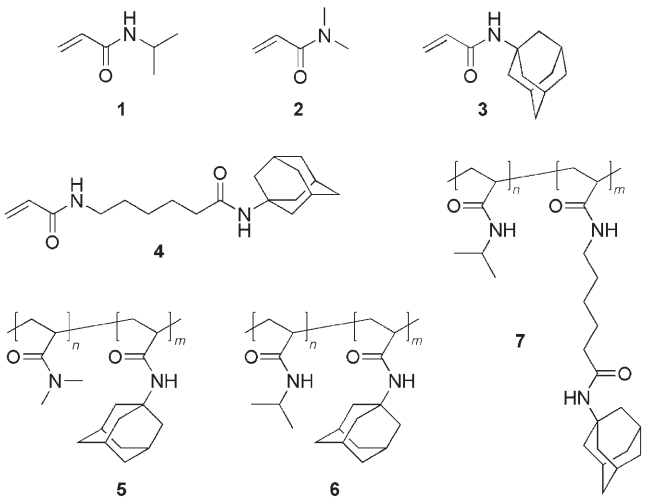
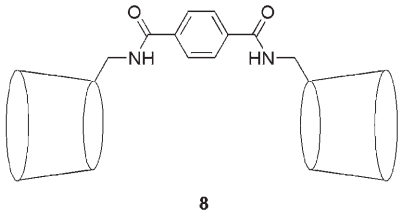


Table 1: Copolymerization of **1** and **2** and the adamantyl-containing monomers **3** and **4** with AIBN in DMF.

Copolymer	Monomers	*n*/*m*	M_n [g mol^{-1}][a]	PD[a]	T_g [°C][b]
5	**2**+**3**	20:1	50000	2.0	101
6	**1**+**3**	20:1	66000	3.1	139
7	**1**+**4**	20:1	76000	3.2	135

[a] M_n and PD were calculated by GPC. [b] The glass temperatures (T_g) were estimated by DSC.



As expected, the viscosity of the solutions of pure polymers increased with increasing molecular weight. However, the comparison can only be qualitative because of the different kinds of monomers used for copolymerization. Addition of native β-CD or methylated β-CD (me-β-CD) to these polymer solutions had no significant effect on the viscosity. The slight decrease of viscosity in the case of polymer **7** after addition of β-CD might result from the disruption of some intermolecular assemblies when the hydrophobic side chains are included into the β-CD cavity. In the case of polymers **5** and **6**, a decrease in viscosity after addition of β-CD could not be observed. These copolymers do not bear a flexible side group. Apparently no aggregates are formed that could be disrupted by complex formation.

Interestingly, when aqueous solutions of copolymers **5**–**7** were mixed with the CD dimer **8**, the viscosity of the solutions increased dramatically. Within seconds, stable gels formed. This demonstrates successful complex formation between the

 © 2006 Wiley-VCH Verlag GmbH & Co. KGaA, Weinheim

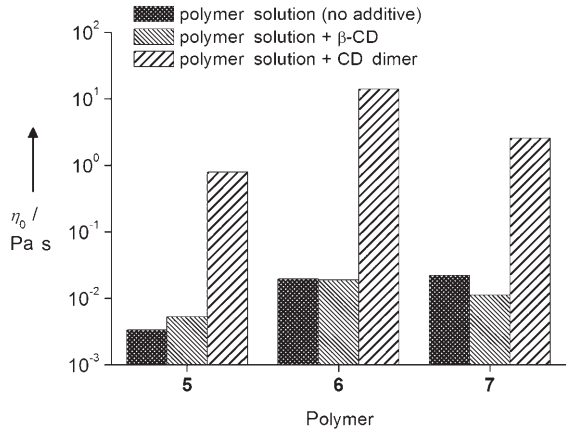


Figure 1. Comparison of zero-shear viscosities of polymer solutions without CDs, with β-CD, and with the CD dimer: $C_P = 50\ g\,L^{-1}$, $C_{CD} = 25\ g\,L^{-1}$, and $C_{CD\ dimer} = 25\ g\,L^{-1}$, 10 °C.

CD dimer **8** and the adamantyl units of the copolymers. As expected, the CD dimer acts as a noncovalent cross-linker between the adamantyl-containing copolymers, leading to hydrogels with supramolecular structure (Figure 2).

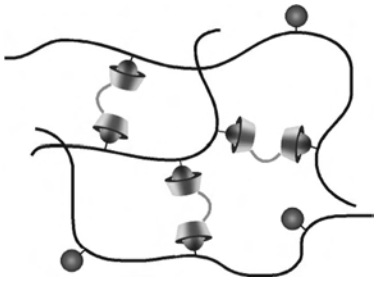


Figure 2. Estimated structure of the obtained hydrogels.

The thermosensitive properties of aqueous solutions of copolymers **5**–**7** and of their noncovalent cross-linked networks were investigated by monitoring the changes of turbidity as a function of temperature. As expected, the *N*,*N*-dimethylacrylamide-containing copolymer **5** shows no turbidity point at temperatures between 10 °C and 90 °C in water. For copolymer **6** we obtained the LCST transition at 23 °C (Figure 3a); for copolymer **7** we found a cloud point of 21 °C (Figure 3b). Both copolymers showed a sharp phase transition in response to a small temperature change. The fact that the turbidity points of copolymers **6** and **7** are significantly lower than that of poly(NIPAAM) itself (35 °C) is caused by the hydrophobic adamantyl units in the copolymers; copolymers **6** and **7** are less soluble in water than a homopolymer of NIPAAM is.

To investigate the effect of adding monomeric and dimeric CD on the change of phase transition temperature of the polymers **6** and **7**, we performed turbidity measurements at the same polymer concentration as above in the presence of a defined amount of me-β-CD and CD dimer, respectively. As reported previously, [9] we found that addition of me-β-CD led to cloud points of polymers **6** and **7** of 35 °C, which correlates

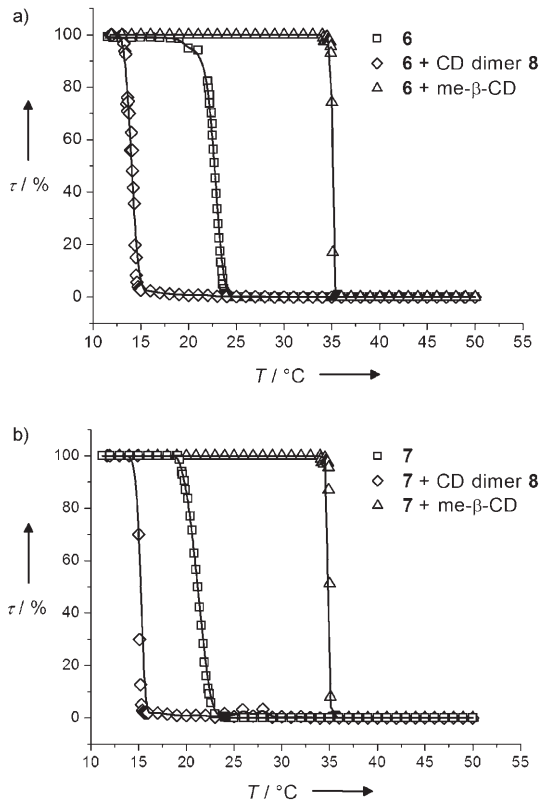


Figure 3. Turbidity measurements of aqueous solutions of the polymers a) **6** and b) **7** without addition of host molecules and measurements of the supramolecular complexes of the polymers with CD dimer **8** and me-β-CD respectively. $C_P = 10\ g\,L^{-1}$, $C_{me\text{-}\beta\text{-}CD} = 10\ g\,L^{-1}$, and $C_{CD\ dimer} = 5\ g\,L^{-1}$, 10 °C.

to the LCST of pure poly(NIPAAM). This increase of the cloud points relative to the cloud points of pure **6** and **7** results from the inclusion of the hydrophobic adamantyl units by me-β-CD.[9a]

When the CD dimer was added to the aqueous polymer solutions at half the molar ratio (relative to the amount of me-β-CD), the cloud points decreased significantly. This observed effect again can be explained by the cross-linkage of single polymer chains upon complexation of the CD dimer. The resulting supramolecular structures are restricted in their mobility and solubility, which is reflected in cloud points of 14.0 °C for polymer **6** and 15.7 °C for polymer **7**. As a result of the LCST behavior of the polymer/CD dimer mixtures the obtained hydrogels show different transparencies. The gel formed from copolymer **5** is transparent at room temperature, whereas those from polymers **6** and **7** are turbid at room temperature and transparent below their cloud points of 14.0 °C and 15.7 °C, respectively.

Supramolecular hydrogels were constructed by the formation of inclusion complexes between adamantyl-containing copolymers and CD dimers. Interactions between the copolymers and CD dimers have been studied below the LCST by viscometry. These inclusion complexes show different macroscopic behavior relative to complexes with β-CD. In addition, the LCSTs of the supramolecular networks consisting of NIPAAM copolymers and CD dimers are significantly lower

 © 2006 Wiley-VCH Verlag GmbH & Co. KGaA, Weinheim

than those of pure NIPAAM copolymers. The obtained hydrogels show a switchable transparency in a narrow temperature range and can be constructed easily by mixing two low-viscosity aqueous solutions. As a result of their hydrophilic and uncharged structure they are of potential interest for applications in biomedical science.

Experimental Section

Materials: β-CD was purchased from Tokyo Kasei Inc. and Wacker and used after recrystallization and drying at 80 °C under vacuum. Methylated β-CD (me-β-CD)(CAVASOL, W7M, technical grade) was purchased from Wacker. *para*-Toluenesulfonyl chloride, sodium hydroxide, sodium azide, 28% ammonium solution, triphenylphosphine, DCC, and HOBT were obtained from Nacalai Tesque Inc. Mono-6-*para*-toluenesulfonyl-β-CD[17–19] and mono-6-amino-β-CD[20] were prepared according to literature methods.

Measurements: GPC analyses were performed with a Viscotek GPCmax VE2001, using DMF as the eluent at 60 °C (flow rate: 1 mL min^{-1}). Samples of 100 μL were injected on the arrangement of columns consisting of one Viscotek TSK guard column H_{HR}-H 6.0 mm(ID) × 4 cm(L) and two Viscotek TSK GMH_{HR}-M 7.8 mm(ID) × 30 cm(L) columns. A Viscotek Viscometer model 250 and a Viscotek VE 3500 RI detector were used for detection. Evaluation was performed using OmniSEC 4.0 software. Polystyrene standards were used for universal calibration. MALDI-TOF-MS was performed on a Bruker Ultraflex TOF mass spectrometer using a 337-nm nitrogen laser. NMR spectra were recorded with a Bruker AC500 instrument at 20 °C. Chemical shifts were referenced to the solvent values ($\delta = 2.50$ ppm for [D$_6$]DMSO and $\delta = 4.70$ ppm for HOD). Cloud points were determined by transmission changes (at 500 nm) of the solutions heated at 0.1–0.2 K min^{-1} in a magnetically stirred cell; values of the cloud points were defined as the temperature at which the transmission decreases by 50%. DSC measurements were performed on a Mettler DSC-30 instrument in a temperature range of −40 to 150 °C at a heating rate of 10 K min^{-1}. For calibration, standard tin, indium, and zinc samples were used. The T_g values are reported as the average of three measurements using the midpoint method. Viscosity measurements were performed with a REOLOGICA DynAlyser 100 stress-controlled rheometer equipped with a cone and plate at 10 °C and using a circulating water bath. The radius of the cone was 25 mm, and the angle between the cone and plate was 4 °C. Zero-shear viscosities were estimated from the shear-rate dependence of the viscosities measured under applied stress of 0.1–2 Pa.

Synthesis of monomer **3**: A solution of 1-adamantylamine (7.56 g, 0.050 mol) and triethylamine (7.66 mL, 0.055 mol) in THF (200 mL) was cooled down to 0 °C. Subsequently a solution of acryloyl chloride (4.47 mL, 0.055 mol) in THF (50 mL) was added dropwise within 30 min. After complete addition the solution was stirred at room temperature for 2 h. The precipitate was filtered off, and the solvent was removed under reduced pressure. The obtained crude product was purified by column chromatography (hexane/ethyl acetate 3:1). Yield: 95%. ^{1}H NMR (500 MHz, $CDCl_3$): $\delta = 6.22$ (dd, $J = 1.6$ Hz, 1H), 6.02 (dd, $J = 10.3$ Hz, 1H), 5.56 (dd, $J = 1.4$ Hz, 1H), 5.24 (br s, 1H), 2.06 (m, 9H), 1.69 ppm (m, 6H); ^{13}C NMR (500 MHz, $CDCl_3$): $\delta = 164.51$, 132.18, 125.57, 52.10, 41.61, 36.36, 29.44 ppm; MS (70 eV, EI): m/z: 205 [M^+].

Synthesis of monomer **4**: 6-*N*-Acrylamidohexanoic acid was synthesized according to known procedures.[9a,21] A solution of 6-*N*-acrylamidohexanoic acid (1.85 g, 0.01 mol) and triethylamine (1.39 mL) in THF (50 mL) was cooled to 0 °C. Subsequently ethylchloroformiate (0.96 mL, 0.01 mol) was added. After 40 min, 1-adamantylamine (1.51 g, 0.01 mol) was added. The reaction mixture was stirred at 0 °C for 2 h. After further stirring for 16 h at room temperature, the mixture was filtrated. The filtrate was diluted with diethyl ether (100 mL) and allowed to crystallize in the refrigerator overnight. The precipitate was collected and purified by column chromatography (CH_2Cl_2/CH_3OH 19:1). Yield: 52%. ^{1}H NMR (500 MHz, $CDCl_3$): $\delta = 6.30$ (br s (overlapped), 1H), 6.26 (dd, 1H), 6.10 (dd, J = 9.8, 2.4 Hz, 1H), 5.56 (dd, $J = 17.0$ Hz, 1H), 5.25 (m, 1H), 3.30 (pseudo-q, 2H), 2.06 (t, $J = 7.3$ Hz, 2H), 2.04 (m, 3H), 1.98 (m, 6H), 1.64 (m, 6H), 1.16–1.60 ppm (br m, 2H); ^{13}C NMR (500 MHz, $CDCl_3$): $\delta = 172.23$, 165.70, 131.12, 126.09, 51.90, 41.68, 36.36, 37.25, 29.43, 28.85, 26.13, 24.50 ppm; MS (70 eV, EI): m/z: 316.2 [M^+]; elemental analysis calcd (%) for $C_{19}H_{26}N_2O_2$: C 72.12, H 8.92; found: C 71.96, H 9.12.

Representative synthesis of copolymers **5**–**7**: synthesis of copolymer **5**: *N*,*N*-dimethylacrylamide (4.16 mL, 4.00 g, 40 mmol) and 1-adamantylacrylamide (410.6 mg, 2 mmol) were dissolved in DMF (16 mL). The solution was flushed with argon for 30 min and AIBN (34.5 mg, 0.21 mmol) was added under argon atmosphere. The mixture was heated to 65 °C and stirred overnight. The solvent was removed under reduced pressure. The dry polymeric material was dissolved in water, dialyzed, and freeze-dried. Composition, glass temperatures, and GPC data of all synthesized copolymers are reported in Table 1.

Synthesis of the cyclodextrin dimer **8**: Terephthalic acid bridged β-CD-dimer was synthesized according to known procedures.[16] A solution of mono-6-amino-β-CD (2.96 g, 2.61 mmol) in DMF (50 mL) was treated with terephthalic acid (114 mg, 0.686 mmol). After the solution was cooled to 0 °C, 1-hydroxybenzotriazole (223 mg, 1.65 mmol) and *N*,*N*′-dicyclohexylcarbodiimide (367 mg, 1.78 mmol) were added. The resulting mixture was stirred at room temperature for seven days. After the insoluble materials were removed by filtration, the filtrate was poured into acetone (1.5 L). The precipitate was collected, washed with acetone, and dried under vacuum to give 3.36 g of the crude product. The crude product was purified by column chromatography on DIAION HP-20 (eluting with water/methanol 100:0 to 50:50). The 60:40 (water/methanol) fraction of the eluent was concentrated and the residue recrystallized from water/ethanol to give 1.08 g of the desired product. Yield: 65%. ^{1}H NMR (500 MHz, [D$_6$]DMSO): $\delta = 8.24$ (br s, 2H), 7.88 (s, 4H), 5.82–5.65 (m, 28H), 4.96–4.84 (m, 14H), 4.44–4.30 (m, 18H), 3.85–3.16 ppm (m, overlaps with HOD); ^{13}C NMR (500 MHz, [D$_6$]DMSO): $\delta = 165.90$, 136.40, 127.01, 101.87, 83.70, 81.50, 72.98, 72.37, 72.03, 59.93, 56.00 ppm; MALDI-TOF: m/z: 2419.3 [M^+−Na]; elemental analysis calcd (%) for $C_{92}H_{144}N_2O_{70}\cdot 9.4H_2O$: C 43.04, H 6.39, N 1.09; found: C 43.05, H 6.43, N 1.30.

Zero-shear viscosities were determined in water at 10 °C using following concentrations of polymers and cyclodextrins: $C_P = 50$ g L^{-1}, $C_{CD} = 25$ g L^{-1}, $C_{CD\ dimer} = 25$ g L^{-1}.

Turbidity measurements were performed in aqueous solutions at 10 °C using following concentrations of polymers and cyclodextrins: $C_P = 10$ g L^{-1}, $C_{me\text{-}\beta\text{-}CD} = 10$ g L^{-1}, $C_{CD\ dimer} = 5$ g L^{-1}.

Received: December 21, 2005
Revised: March 9, 2006
Published online: May 31, 2006

Keywords: cyclodextrins · host–guest systems · hydrogels · LCST · supramolecular chemistry

[1] a) M. Annaka, T. Tanaka, *Nature* **1992**, *355*, 430–432; b) Y. Osada, J. P. Gong, *Adv. Mater.* **1998**, *10*, 827–837; c) C. Alvarez-Lorenzo, O. Guney, T. Oya, Y. Sakai, M. Kobayashi, T. Enoki, Y. Takeoka, T. Ishibashi, K. Kuroda, K. Tanaka, G. Q. Wang, A. Y. Grosberg, S. Masamune, T. Tanaka, *Macromolecules* **2000**, *33*, 8693–8697; d) S. Varghese, A. K. Lele, D. Srinivas, M. Sastry, R. A. Mashelkar, *Adv. Mater.* **2001**, *13*, 1544–1548; e) A. P. Nowak, V. Breedveld, L. Pakstis, B. Ozbas, D. J. Pine, D. Pochan, T. J. Deming, *Nature* **2002**, *417*, 424–428; f) N. M. Sangeetha, U.

 © 2006 Wiley-VCH Verlag GmbH & Co. KGaA, Weinheim

Maitra, *Chem. Soc. Rev.* **2005**, *34*, 821 – 836; g) R. Yoshida, *Curr. Org. Chem.* **2005**, *9*, 1617 – 1641.
[2] A. Harada, *Coord. Chem. Rev.* **1996**, *148*, 115 – 133.
[3] M. Ceccato, P. L. Nostro, P. Baglioni, *Langmuir* **1997**, *13*, 2436 – 2439.
[4] W. Herrmann, B. Keller, G. Wenz, *Macromolecules* **1997**, *30*, 4966 – 4972.
[5] G. Wenz, *Angew. Chem.* **1994**, *33*, 851 – 870; *Angew. Chem. Int. Ed. Engl.* **1994**, *33*, 803 – 822.
[6] J. Szejtli, *Chem. Rev.* **1998**, *98*, 1743 – 1754.
[7] a) A. Harada, M. Kamachi, *Macromolecules* **1990**, *23*, 2821 – 2823; b) A. Harada, J. Li, M. Kamachi, *Nature* **1992**, *356*, 325 – 327; c) G. Wenz, B. Keller, *Angew. Chem. Int. Ed. Engl.* **1992**, *31*, 197 – 199; d) A. Harada, M. Okada, M. Kamachi, *Macromolecules* **1995**, *28*, 8406 – 8411; e) A. Harada, Y. Kawaguchi, T. Nishiyama, M. Kamachi, *Macromol. Rapid Commun.* **1997**, *18*, 535 – 539.
[8] a) L. Huang, E. Allen, A. E. Tonelli, *Polymer* **1999**, *40*, 3211 – 3221; b) C. Rusa, A. E. Tonelli, *Macromolecules* **2000**, *33*, 1813 – 1818; c) C. C. Rusa, C. Luca, A. E. Tonelli, *Macromolecules* **2001**, *34*, 1318 – 1322; d) J. Lu, P. A. Mirau, A. E. Tonelli, *Macromolecules* **2001**, *34*, 3276 – 3284.
[9] a) H. Ritter, O. Sadowski, E. Tepper, *Angew. Chem.* **2003**, *115*, 3279 – 3281; *Angew. Chem. Int. Ed.* **2003**, *42*, 3171 – 3173; Corrigendum: H. Ritter, O. Sadowski, E. Tepper, *Angew. Chem.* **2005**, *117*,6253; *Angew. Chem. Int. Ed.* **2005**, *44*, 6099; b) S. W. Choi, H. Ritter, *J. Macromol. Sci. Part A* **2004**, *42*, 321 – 325.
[10] a) A. Harada, J. Li, M. Kamachi, *Macromolecules* **1993**, *26*, 5698 – 5703; b) A. Harada, M. Okada, M.; Kamachi, *Macromolecules* **1995**, *28*, 8406 – 8409; c) A. Harada, J. Li, M. Kamachi, *Chem. Lett.* **1993**, 237 – 240; d) J. Li, A. Harada, M. Kamachi, *Bull. Chem. Soc. Jpn.* **1994**, *67*, 2808 – 2818; e) A. Harada, S. Suzuki, M. Okada, M. Kamachi, *Macromolecules* **1996**, *29*, 5611 – 5614; f) S. Schmitz, H. Ritter, *Angew. Chem.* **2005**, *117*, 5803 – 5806; *Angew. Chem. Int. Ed.* **2005**, *44*, 5658 – 5661.
[11] K. M. Huh, T. Ooya, W. K. Lee, S. Sasaki, I. C. Kwon, S. Y. Jeong, N. Yui, *Macromolecules* **2001**, *34*, 8657 – 8662.
[12] a) J. Li, X. Li, Z. Zhou, Z. Ni, K. W. Leong, *Macromolecules* **2001**, *34*, 7236 – 7237; b) J. Li, A. Harada, M. Kamachi, *Polym. J.* **1994**, *26*, 1019 – 1026.
[13] a) M. Weickenmeier, G. Wenz, J. Huff, *Macromol. Rapid Commun.* **1996**, *17*, 731 – 736; b) M. Weickenmeier, G. Wenz, J. Huff, *Macromol. Rapid Commun.* **1997**, *18*, 1117 – 1123; c) G. Wenz, M. Weickenmeier, J. Huff, in *Associative Polymers in Aqueous Solutions*, ACS Symposium Series *Vol. 765* (Ed.: E. Glass), Oxford Univ. Press, Oxford, **2000**, pp. 271 – 283.
[14] Y. Takashima, T. Nakayama, M. Miyauchi, Y. Kawaguchi, H. Yamaguchi, A. Harada, *Chem. Lett.* **2004**, *33*, 890 – 891.
[15] I. Tomatsu, A. Hashidzume, A. Harada, *Macromol. Rapid Commun.* **2005**, *26*, 825 – 829.
[16] K. Ohga, Y. Takashima, H. Takahashi, Y. Kawaguchi, H. Yamaguchi, A. Harada, *Macromolecules* **2005**, *38*, 5897 – 5904.
[17] K. Takahashi, K. Hattori, F. Toda, *Tetrahedron Lett.* **1984**, *25*, 3331 – 3334.
[18] R. C. Petter, J. S. Salek, C. T. Sikorski, G. Kumaravel, F.-T. Lin, *J. Am. Chem. Soc.* **1990**, *112*, 3860 – 3868.
[19] N. Zhong, H.-S. Byun, R. Bittman, *Tetrahedron Lett.* **1998**, *39*, 2919 – 2920.
[20] L. D. Melton, K. N. Slessor, *Carbohydr. Res.* **1971**, *18*, 29 – 37.
[21] H. Yamada, E. Fujita, S.-I. Nishmura, *Carbohydr. Res.* **1998**, *305*, 443 – 461.

 © 2006 Wiley-VCH Verlag GmbH & Co. KGaA, Weinheim

Solid-State Structures

DOI: 10.1002/anie.200600431

Mysterious Platinum Nitride**

*Jörg von Appen, Marck-Willem Lumey, and Richard Dronskowski**

In 2004, the spectacular high-pressure synthesis of platinum nitride was communicated;[1] PtN was prepared by compressing Pt metal and N_2 at pressures of 45–50 GPa and temperatures above 2000 K. According to X-ray diffraction, this phase possesses a face-centered cubic (fcc) unit cell with $a = 4.8041(2)$ Å. On the basis of Raman spectroscopy, an NaCl-type ([NaCl]; rock salt) structure was rejected, and the structure was assigned to the ZnS type ([ZnS]; zinc blende). Furthermore, an extraordinarily high bulk modulus of (372 ± 5) GPa was determined, and analytical profiles revealed a nearly daltonide composition of PtN_{1-x} ($x < 0.05$).

The first density functional theory (DFT) investigations of PtN confirmed all of the experimental results.[2] Other research groups also verified both the structure type and the lattice parameter by using various functionals.[3,4] Nonetheless, some oddities were encountered. For example, the experimentalists found[1] that the molar volume of PtN is larger than the volume of the starting materials ($Pt + {}^1/_2 N_2$) at pressures above 12 GPa. This situation is paradoxical, because the reaction mixture increases its volume upon pressurization, in contradiction to Le Chatelier's principle. In addition, all of the theoretical studies mentioned above concluded that the [NaCl] structure becomes more favorable than the [ZnS] structure above 4–17.5 GPa. Another theoretical study dealing with the calculation of single-crystal elastic constants questioned the stability of PtN,[5] and suggested the alternative composition PtN_2, first in a CaF_2-type ([CaF_2]; fluorite) structure and later in a FeS_2-type ([FeS_2]; pyrite) structure.[6] Indeed, the crystal structure of PtN seems to be a matter of debate.[7] Therefore, we decided to perform more comprehensive calculations and to consider other possible structure types. Moreover, we have calculated the total energies of the PtN polymorphs with respect to the energy of the elements. We also introduce the heat of formation ΔH_f as a new theoretical aspect.

The electronic structures of PtN in the [ZnS] and [NaCl] structures were first compared to the results of the previous studies. Our findings, based on either full-potential linearized

[*] J. von Appen, Dr. M.-W. Lumey, Prof. Dr. R. Dronskowski
Institut für Anorganische Chemie
Rheinisch-Westfälische Technische Hochschule (RWTH) Aachen
Landoltweg 1, 52056 Aachen (Germany)
Fax: (+49) 241-80-92642
E-mail: drons@HAL9000.ac.rwth-aachen.de

[**] We would like to thank the supercomputing centers of the RWTH Aachen and the Research Center Jülich for having provided us with their computer resources. Financial support from the Deutsche Forschungsgemeinschaft and the Fonds der Chemischen Industrie is also gratefully acknowledged.

 © 2006 Wiley-VCH Verlag GmbH & Co. KGaA, Weinheim

augmented plane wave (FLAPW) or pseudopotential calculations, in combination with local or gradient-corrected exchange-correlation functionals, are displayed in Table 1.

Table 1: Experimental data, and calculated relative energies ΔE, lattice parameters a, bulk moduli B_0, and transition pressures p_T for PtN in the [ZnS] and [NaCl] structures. The theoretical methods, as well as the exchange-correlation functionals are indicated.

	ΔE [eV]	a [Å]	B_0 [GPa]	p_T [GPa]
Experiment[1]		4.8041(2)	372 ± 5	
FLAPW		PBE-GGA		
[ZnS]	0	4.80	192	
[NaCl]	+0.48	4.45	232	16.5
Pseudopotentials	GGA/LDA	GGA/LDA	GGA/LDA	GGA/LDA
[ZnS]	0	4.80/4.70	190/232	
[NaCl]	+0.48/+0.36	4.50/4.41	230/288	17.6/13.3

At ambient pressure, [ZnS]-PtN is more stable than [NaCl]-PtN, and seems to be thermodynamically stable at first sight; this result corresponds with previous findings.[2,3] Also in agreement with previous investigations, our high-pressure calculations predict that [ZnS]-PtN will undergo a phase transition to [NaCl]-PtN at 17.6 GPa (GGA).[2,3] It therefore seems rather unlikely that [ZnS]-PtN would be produced at an experimental pressure of 45–50 GPa, unless the phase was formed upon depressurization. Another disagreement is that the experimentally reported and extraordinarily large bulk modulus of (372 ± 5) GPa cannot be reproduced by our calculations, which give values only half as large for [ZnS]-PtN. According to our experience, such discrepancies cannot be attributed to failures of theory alone. In a next step, the calculations were expanded by including PtS-type ([PtS]; cooperite), [CaF_2], and [FeS_2] structures.

In [PtS]-PtN, the N atoms are tetrahedrally coordinated by Pt (as Raman spectroscopy indicated for PtN[1]); the [PtS] structure is also adopted by PtO. While in [ZnS]-PtN all of the NPt_4 tetrahedra are corner-sharing, in [PtS]-PtN one-dimensional chains of edge-sharing tetrahedra are interconnected by corner-sharing between tetrahedra (Figure 1). As a consequence, the Pt atoms have square-planar coordination environments in [PtS]-PtN. In [CaF_2]-PtN_2, each NPt_4 tetrahedron shares all of its edges with neighboring tetrahedra, whereas [FeS_2]-PtN_2 (not shown) can be described as a [NaCl] structure, in which N_2 units occupy the Cl positions.

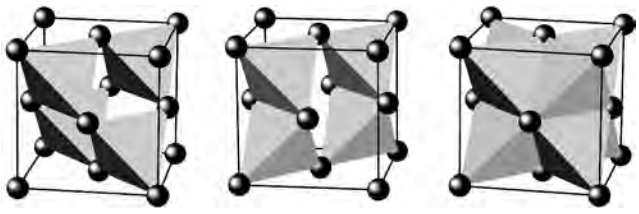


Figure 1. The [ZnS]-PtN (left), [PtS]-PtN (middle), and [CaF_2]-PtN_2 (right) structures differ in the connectivity of the incorporated NPt_4 tetrahedra. The spheres represent the fcc Pt lattices.

On the basis of the total energies of the elements as a function of their volumes, the heats of formation ΔH_f of the PtN and PtN_2 phases can be calculated, allowing theoretical access to thermodynamic stabilities and necessary synthesis pressures.[8] The results of these calculations are depicted in an energy–volume plot, as well as an enthalpy–pressure diagram derived from this plot (Figure 2).

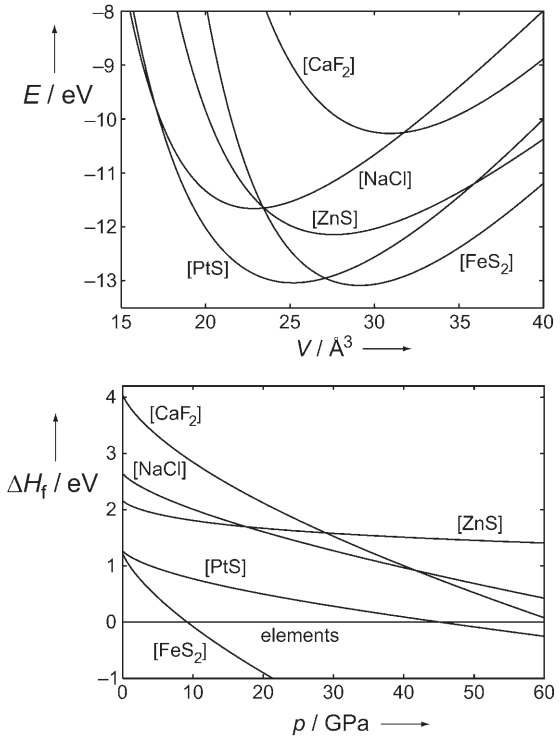


Figure 2. Plots of energy E as a function of volume V (per formula unit; top), and of enthalpy of formation ΔH_f as a function of pressure p (bottom), calculated (GGA) for PtN and PtN_2 in different structure types.

The results for the [ZnS] and [NaCl] structures have already been discussed above. The enthalpy–pressure diagram directly shows the transition pressure at which the [NaCl] structure becomes more favorable than the [ZnS] structure for PtN. At ambient pressure, [CaF_2]-PtN_2 is quite unstable, but it becomes more favorable than [ZnS]-PtN above approximately 30 GPa, and is more stable than the elements above approximately 60 GPa. The calculated lattice parameter of the [CaF_2] structure ($a_{GGA} = 4.98$ Å) is almost 4% larger than the experimentally reported one. The [FeS_2] structure is also thermodynamically unstable at ambient conditions, but is significantly more stable than the elements above approximately 10 GPa. The theoretical lattice parameter for [FeS_2]-PtN_2 ($a_{GGA} = 4.89$ Å) is in good accordance with that from another calculation.[6] For our further calculations, we will not consider the possibility of a [FeS_2] structure, because the experimentalists committed themselves to a 1:1 (and not 1:2) composition for platinum nitride.[1]

For the 1:1 daltonide PtN, Figure 2 reveals the puzzling finding that [ZnS]-PtN is an entirely unstable structure at any pressure. While chemists have, of course, succeeded in

 © 2006 Wiley-VCH Verlag GmbH & Co. KGaA, Weinheim

synthesizing thermodynamically unstable (but kinetically stable) materials, the synthesis of PtN in a structure type of lower density (relative to that of the starting materials) is impossible to realize using high pressure. Another interesting result is that [PtS]-PtN is 0.90 eV (GGA) more stable than [ZnS]-PtN at standard pressure. To exclude systematic errors, we tried to disprove our results using other methods, but always found similar energy lowerings (0.90–1.05 eV) for [PtS]-PtN relative to [ZnS]-PtN.

These relative stabilities are also obvious from the chemical bonding in both structures, which was analyzed by calculating crystal orbital Hamilton populations (COHPs; Figure 3, left and middle). For both structures, there are deep-lying Pt–N bonding regions arising from N 2p and Pt 5d orbitals. The instability of the two polymorphs results from the presence of antibonding Pt–N interactions (black) below the Fermi level, a scenario that nature usually tries to avoid. It is these repulsive interactions that must be counteracted by using pressure. As can easily be seen, more antibonding Pt–N levels are present near the Fermi level of [ZnS]-PtN, as expected. It must be remembered that the molar volume of [PtS]-PtN is smaller than that of [ZnS]-PtN; therefore, high pressure cannot stabilize [ZnS]-PtN. In contrast, increasing pressure stabilizes [PtS]-PtN, which is stable relative to the elements above 45 GPa, and is approximately 1.5 eV more stable than [ZnS]-PtN at this pressure. Nonetheless, the theoretical bulk modulus of 215 GPa (GGA; LDA: 240 GPa) is smaller than the experimental one. Also, the [PtS] structure is tetragonal ($a_{GGA} = 4.20$ Å, $c_{GGA} = 5.68$ Å) and, thus, inconsistent with the X-ray diffraction data.

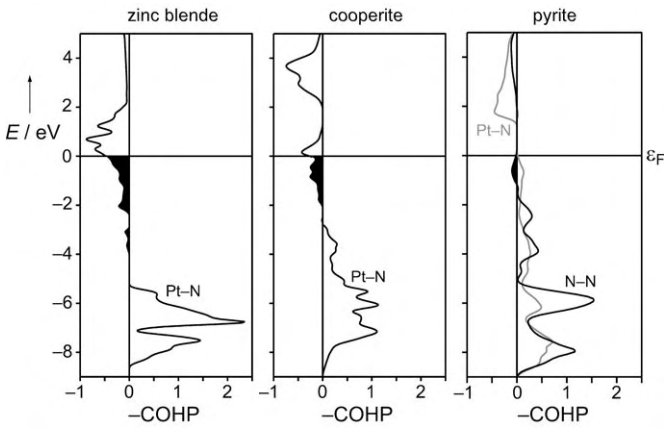


Figure 3. COHP analyses of the Pt–N interactions in [ZnS]-PtN (zinc blende; left) and [PtS]-PtN (cooperite; middle), and of the Pt–N and N–N interactions in [FeS_2]-PtN_2 (pyrite; right). Occupied antibonding states are emphasized in black.

Because of the problems encountered for the 1:1 phases, we searched for alternative structures with four-coordinate N atoms that, on one hand, are in harmony with the diffraction data, and on the other hand, contain the energetically advantageous structural motif of [PtS]-PtN, namely the edge-sharing NPt_4 tetrahedra. One possibility is a structure, which we label as [CaF], in which half of the tetrahedral holes in an fcc Pt lattice are statistically occupied by N atoms. In addition, the energy of the same model with a small excess or deficiency of N atoms (labeled [CaF_x]) was calculated to examine the effect on the lattice parameters.[9] For the N-deficient phases, a model containing a selective distribution of N atoms over the tetrahedral sites that are occupied in the [ZnS] structure (labeled [ZnS_x], $x \leq 1$) was also examined.

Plots of the volumes and energies of the PtN_x phases as a function of composition are displayed in Figure 4. As expected, the volumes generally increase with increasing N content (and vice versa) for both the [CaF_x] and [ZnS_x] structures. All volumes for the [ZnS_x] ($x \leq 1$) structure are much smaller than the published value for PtN. For the [CaF_x] structure, an N content of $x > 1.2$ is needed to reach the experimental volume of PtN. The phase with $x = 1$, [CaF]-PtN, exhibits a volume between those of the remarkably voluminous [ZnS]-PtN and the very dense [PtS]-PtN. The higher density of [PtS]-PtN is a reason for the increased stabilization of this polymorph relative to [ZnS]-PtN with increasing pressure (Figure 2, bottom).

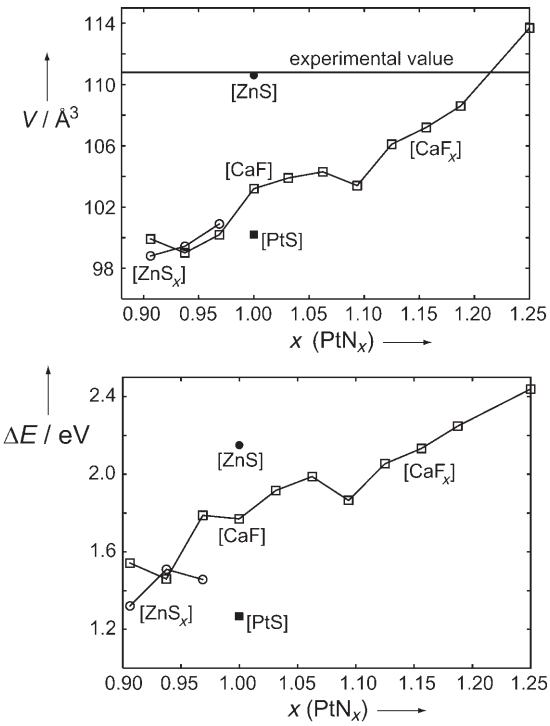


Figure 4. Plots of unit-cell volumes V (top) and relative energies ΔE (bottom) calculated (GGA) for PtN_x in different structure types (see text for details), as a function of the N content x.

As revealed by the plot of relative energy versus composition (Figure 4, bottom), all of the PtN_x phases become less stable with increasing N content. In the region of N-deficient PtN_x ($x < 1$) phases, the [ZnS_x] structure is generally more favorable than the [CaF_x] structure. The enormous energy stabilization and volume reduction of [ZnS_x]-PtN_x relative to stoichiometric [ZnS]-PtN are due to the large structural distortions around the N defects. For a precise 1:1 composition, the [CaF] structure, which contains a random N distribution, is less stable than the [PtS] structure,

 © 2006 Wiley-VCH Verlag GmbH & Co. KGaA, Weinheim

but more stable than the [ZnS] structure. Neither the relative energies nor the volumes of these phases match with the experimental results for PtN. In the region of N-rich PtN_x ($x>1$) phases, the volumes agree with experiment, but these phases are very unstable. The most stable phases, on the other hand, have volumes that are much smaller than that measured for PtN.

Another way to solve the problems with respect to the existence of platinum nitride is to simply ignore the experimental chemical analysis. In contrast to PtN, which is unstable over the entire pressure range in the [ZnS] structure and below 45 GPa in the [PtS] structure, the 1:2 phase [FeS_2]-PtN_2 is stable above 10 GPa (Figure 2, bottom) and has a molar volume that is smaller than that of the elements, thereby fulfilling Le Chatelier's principle. Indeed, a fascinating experimental report on the synthesis and characterization of [FeS_2]-PtN_2,[10] with a lattice constant of $a = 4.8$ Å, came to our attention during the revision of our manuscript (March 3, 2006). This result resolves all of the discrepancies between theory and experiment[1] mentioned above, by refuting the experiment. The stability of the [FeS_2] structure can, again, be explained through a COHP analysis of the Pt–N and N–N bonds (Figure 3, right). The Pt–N interactions, which were antibonding near the Fermi level in the PtN structures, are now bonding over the entire region below the Fermi level. Instead, antibonding N–N quasimolecular states are now located just below the Fermi level. Their occupation enlarges the N≡N triple bond of 1.10 Å to a double bond of 1.42 Å (experimental: 1.41 Å[10]). Thus, the very large bulk modulus of 265 GPa (GGA; LDA: 334 GPa) calculated for PtN_2 is immediately understandable, because of the high molecular stiffness of the negatively charged N_2 molecule whose antibonding π^* states have been partially filled. We note that similar diazenide (or pernitride) anions have been found experimentally in SrN_2[11] and BaN_2,[12] which were also synthesized under high pressure. Therefore, the reported "platinum nitride" PtN_2[10] would be better described as platinum diazenide (or pernitride).

In summary, there has been no convincing evidence for the synthesis of platinum nitride, PtN, to date. However, platinum diazenide, PtN_2, has been prepared recently, and its properties are in excellent agreement with theory. Nonetheless, PtN may be accessible by incorporating atomic N into an fcc Pt lattice at pressures above 45 GPa. We predict that the equilibrium phase of PtN will crystallize in the [PtS] structure, but that [PtS]-PtN will be thermodynamically unstable with respect to decomposition into PtN_2 and Pt. Thus, the synthesis would have to exploit the potential kinetic stability of PtN, which is a true challenge for experimentalists. Despite the low X-ray scattering contribution of the N atoms relative to the Pt atoms, the tetragonal [PtS]-PtN will be easy to detect, even using powder methods.

Theoretical Methodology

The first-principles electronic-structure calculations were performed using the Vienna ab initio simulation package,[13,14] with plane-wave basis sets and ultrasoft pseudopotentials. We also used the FLAPW method[15] and carried out tight-binding linear muffin-tin orbital atomic-sphere approximation (TB-LMTO-ASA) calculations.[16–20] Chemical bonds were analyzed using the COHP technique.[21] Electronic energies were calculated by DFT, using a cut-off energy of 500 eV. Exchange-correlation contributions were treated both in the local-density approximation (LDA),[22–24] as well as in the generalized-gradient approximation (GGA).[25]

Received: February 1, 2006
Revised: April 18, 2006
Published online: May 31, 2006

Keywords: density functional calculations · diazenides · high-pressure phases · nitrides · platinum nitride

[1] E. Gregoryanz, C. Sanloup, M. Somayazulu, J. Badro, G. Fiquet, H.-K. Mao, R. J. Hemley, *Nat. Mater.* **2004**, *3*, 294.
[2] B. R. Sahu, L. Kleinman, *Phys. Rev. B* **2005**, *71*, 041101. Note that these authors later revised their original bulk moduli: B. R. Sahu, L. Kleinman, *Phys. Rev. B* **2005**, *72*, 119901. In this paper, the first doubts about the 1:1 composition of PtN are expressed.
[3] J. Uddin, G. E. Scuseria, *Phys. Rev. B* **2005**, *72*, 035101.
[4] M. B. Kanoun, S. Goumri-Said, *Phys. Rev. B* **2005**, *72*, 113103.
[5] R. Yu, X. F. Zhang, *Appl. Phys. Lett.* **2005**, *86*, 121913.
[6] R. Yu, Q. Zhan, X. F. Zhang, *Appl. Phys. Lett.* **2006**, *88*, 051913.
[7] C.-Z. Fan, L.-L. Sun, Y.-X. Wang, Z.-J. Wei, R.-P. Liu, S.-Y. Zeng, W.-K. Wang, *Chin. Phys. Lett.* **2005**, *22*, 2637.
[8] R. Dronskowski, *Computational Chemistry of Solid State Materials*, Wiley-VCH, Weinheim, New York, **2005**. For the system under study, solid molecular N_2 in its α phase and fcc-Pt were used as the energy reference.
[9] For the calculations involving structures with random N distributions, various supercells consisting of eight conventional cells and containing 32 Pt atoms, and 32 N atoms distributed over 64 tetrahedral sites were set up.
[10] J. C. Crowhurst, A. F. Goncharov, B. Sadigh, C. L. Evans, P. G. Morrall, J. L. Ferreira, A. J. Nelson, *Science* **2006**, *311*, 1275.
[11] G. Auffermann, Y. Prots, R. Kniep, *Angew. Chem.* **2001**, *113*, 565; *Angew. Chem. Int. Ed.* **2001**, *40*, 547.
[12] G. V. Vajenine, G. Auffermann, Y. Prots, W. Schnelle, R. K. Kremer, A. Simon, R. Kniep, *Inorg. Chem.* **2001**, *40*, 4866.
[13] G. Kresse, J. Hafner, *Phys. Rev. B* **1993**, *47*, 558; G. Kresse, J. Hafner, *Phys. Rev. B* **1994**, *49*, 14251.
[14] G. Kresse, J. Furthmüller, *Comput. Mater. Sci.* **1996**, *6*, 15; G. Kresse, J. Furthmüller, *Phys. Rev. B* **1996**, *55*, 11169.
[15] P. Blaha, K. Schwarz, G. Madsen, D. Kvasnicka, J. Luitz, *WIEN2k*, Technische Universität Wien, **1999**.
[16] G. Krier, O. Jepsen, A. Burkhardt, O. K. Andersen, *The TB-LMTO-ASA program, version 4.7*, Max-Planck-Institut für Festkörperforschung, Stuttgart, Germany.
[17] O. K. Andersen, *Phys. Rev. B* **1975**, *12*, 3060.
[18] H. Skriver, *The LMTO Method*, Springer, Berlin, **1984**.
[19] O. K. Andersen in *The Electronic Structure of Complex Systems* (Eds.: P. Phariseau, W. M. Temmerman), Plenum, New York, **1984**.
[20] O. K. Andersen, O. Jepsen, *Phys. Rev. Lett.* **1984**, *53*, 2571.
[21] R. Dronskowski, P. E. Blöchl, *J. Phys. Chem.* **1993**, *97*, 8617.
[22] U. von Barth, L. Hedin, *J. Phys. C* **1972**, *5*, 1629.
[23] J. P. Perdew, A. Zunger, *Phys. Rev. B* **1981**, *23*, 5048.
[24] D. M. Ceperley, B. J. Alder, *Phys. Rev. Lett.* **1980**, *45*, 1814.
[25] J. P. Perdew in *Electronic Structure of Solids '91* (Eds.: P. Ziesche, H. Eschrig), Akademie Verlag, Berlin, **1991**.

 © 2006 Wiley-VCH Verlag GmbH & Co. KGaA, Weinheim

Hydrogen Bonds

DOI: 10.1002/anie.200601093

[Rb([18]crown-6)$(NH_3)_3$]Au·NH_3: Gold as Acceptor in N–H···Au^- Hydrogen Bonds**

*Hanne Nuss and Martin Jansen**

Dedicated to Professor Hansgeorg Schnöckel on the occasion of his 65th birthday

With increasing atomic number of the elements, the discrepancies between the results of nonrelativistic and relativistic electronic-structure calculations grow.[1] These differences are particularly striking in the case of gold. Relativistic treatment leads to a strong decrease in the energy of the 6s orbital, which is accompanied by a contraction of the corresponding orbital (direct relativistic effect) and an increase of the 5d levels (indirect relativistic effect). These characteristics are directly reflected in the ionization potentials and in a remarkably high first electron affinity. In recent experiments it has been possible to provide a number of examples that prove the influence of the relativistic effects on the chemistry of gold.[2] For instance, the stability of the Au^- ion in the solid state[3,4] and in solution[5] and its role as an integral part of transport processes are mentionable in this context.[6] Furthermore, the anionic character of gold is emphasized by its similarities to the heavier halides Br^- and I^-, and such similarities are apparent from crystal-chemical analogies[7] or from the disproportionation of elemental gold.[8] For example, [(NMe_4)Au], the first colorless auride compound,[9] crystallizes isotypically to (NMe_4)Br.[10]

Halides are characteristically good acceptors in hydrogen-bonded systems.[11,12] If the concept of similarity holds up as described above, it should be possible to synthesize compounds with hydrogen bonds that involve Au^- ions as acceptors. In [(NMe_4)Au][9] the hydrogen atoms of the methyl groups and the auride anion come as close as 292(10) pm (d_{min}(C···Au^-) = 366.3(1) pm) to each other. This separation is in the range of the sum of the van der Waals radii of hydrogen and Au^- (Σr_{vdW}(H···Au^-) = 290–310 pm;[13] Σr_{vdW}(C···Au^-) = 360 pm), which formerly were taken as criteria for the existence of hydrogen bonding.[14] Whether this contact is a true hydrogen bond or not has not yet been proven, as short N^+–C–H···X^- distances are often the result of attractive Coulomb interactions between N^+ and X^- centers, and the H···X^- contacts prevent a further approach of the anion for steric reasons.[12]

Herein we introduce a new compound in which hydrogen bonds between neutral ammonia molecules as donors and auride anions as acceptors have been found for the first time. Furthermore, the title compound is the first characterized representative of a class of aurides in which the alkali-metal cation of the reactant MAu (M = Rb, Cs) is complexed by crown ethers. Up to now, related compounds have been reported only with cryptands as ligands. Their crystal structures, however, have not yet been determined.[15,16] Complexation with these kinds of ligands leads to separated auride ions, and this separation manifests itself in the colorlessness of these compounds (for comparison: RbAu is metallic black, CsAu is yellow).

[Rb([18]crown-6)$(NH_3)_3$]Au·NH_3 was prepared by the reaction of RbAu with [18]crown-6 in liquid ammonia at 200 K. Evaporation of the solvent yielded colorless, extremely air- and temperature-sensitive crystals (storage within the reaction flask in ammonia atmosphere at 200 K is possible only for 7 days). Decomposition of the compound to elemental gold becomes clearly visible as the color of the compound changes to black.

According to the single-crystal X-ray structure determination,[17] [Rb([18]crown-6)$(NH_3)_3$]Au·NH_3 crystallizes in the monoclinic space group $P2_1/n$ (no. 14). The [6+3]-coordinated rubidium atom within the [Rb([18]crown-6)$(NH_3)_3$]$^+$ cation is shifted about 105 pm from the center of gravity of the crown ether (Figure 1). This "sunrise conformation"[18] is typically found in coordination compounds of [18]crown-6 and the heavier alkali metals rubidium and cesium, for which the ionic radii of 152 and 167 pm, respectively, are too large for this crown ether (of 260–320 pm diameter).[18]

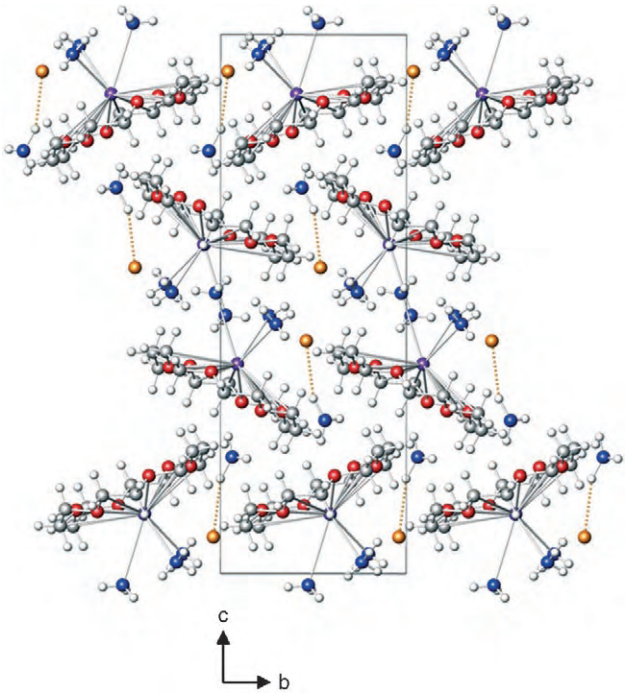


Figure 1. Structure of [Rb([18]crown-6)$(NH_3)_3$]Au·NH_3. C gray, H white, N blue, O red, Au orange, Rb violet. Orange dotted lines: N–H···Au^- hydrogen bonds with d(H···Au^-) = 258(1) pm.

[*] Dipl.-Chem. H. Nuss, Prof. Dr. Dr. h.c. M. Jansen
Max Planck Institute for Solid State Research
Heisebergstrasse 1, 70569 Stuttgart (Germany)
Fax: (+49) 711-689-1502
E-mail: m.jansen@fkf.mpg.de

[**] We wish to thank A. Müller for her preparative assistance, Dr. J. Nuss for the helpful discussion, and the Fonds der Chemischen Industrie for financial support.

© 2006 Wiley-VCH Verlag GmbH & Co. KGaA, Weinheim

Both the rubidium cations and the auride anions form 6^3 nets of *cis*-connected, six-membered rings with chair conformations. These nets are stacked parallel to the (101) plane in such a way that the rubidium and gold atoms together occupy the same positions as the phosphorus atoms in black phosphorus (Figure 2).

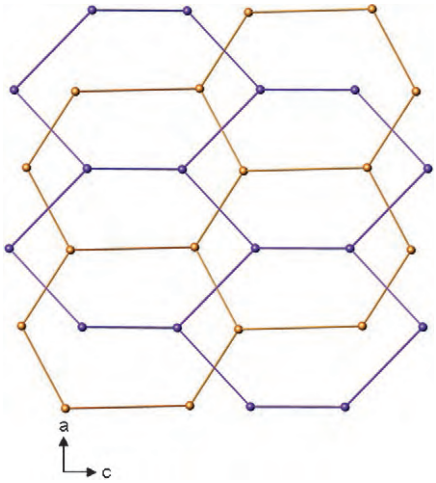


Figure 2. Crystal packing of cations (Rb^+ violet) and anions (Au^- orange) in $[Rb([18]crown\text{-}6)(NH_3)_3]Au{\cdot}NH_3$. Connecting lines highlight the 6^3 nets.

Figure 3 shows the area around of the auride anions and their coordination to hydrogen atoms. A distorted tetrahedral

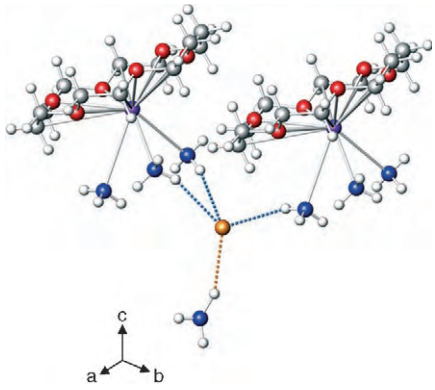


Figure 3. Environment of the auride anions in $[Rb([18]crown\text{-}6)(NH_3)_3]Au{\cdot}NH_3$. C gray, H white, N blue, O red, Au orange, Rb violet. Orange dotted line: N–H···Au^- hydrogen bond with $d(H{\cdots}Au^-) = 258(1)$ pm. Blue dotted lines: other N–H···Au^- hydrogen bonds.

geometry around the Au^- center is formed by four NH_3 molecules. Three of the NH_3 molecules are further coordinated to rubidium centers (average $d(N{\cdots}Au^-) = 373$ pm), and the forth one ($d(N{\cdots}Au^-) = 363$ pm) is uncoordinated. The hydrogen-atom sites were located by difference Fourier synthesis and their positional and displacement parameters were subsequently refined. As a result, an H···Au^- separation (258(1) pm) could be determined for the first time. The N-H-Au angle amounts to 158(1)°. These values lie exactly in the ranges commonly observed for N–H···Br^- and N–H···I^- hydrogen bonds (Table 1).

So-called nonconventional hydrogen bonds, that is, 3c-4e X–H···A bonds, in which the acceptor A is a transition metal

Table 1: Average distances [pm] in N–H···A^- hydrogen bonds with $\theta > 140°$.[a]

Donor	Br^-	I^-	Distance
$-NH_2$	252(2)	279(2)	d(H···A^-)
	346(1)	366(1)	d(N···A^-)
$-N^+H_3$	249(2)	272(2)	d(H···A^-)
	344(1)	368(2)	d(N···A^-)
R_3N^+H	229(1)	254(4)	d(H···A^-)
	324.7(7)	350(3)	d(N···A^-)

[a] Acceptor $A^- = Br^-$, I^-; all values are from reference [12].

without free pairs of electrons (in contrast to conventional acceptors such as F, N, O, Cl, Br), have been studied in depth since the 1990s. A number of examples are already known in which inter- and intramolecular hydrogen bonds exist in late-transition-metal complexes (for example, d^8 metal centers: Ni^{II}, Rh^{I}, Pd^{II}, Ir^{I}, Pt^{II}; d^{10} metal centers: Co^{-I}, Ni^{0}).[19] In a review article dealing with this topic,[20] Brammer et al. described some criteria for the characterization of such interactions. According to these criteria, the bridging hydrogen atom should be bonded to a rather electronegative element, and the acceptor metal atom should be electron-rich (late transition metals with filled d shells). Moreover, the arrangement of such (intermolecular) interactions should be approximately linear and typically be built by electronically saturated 18-valence-electron (18-VE) complexes.

$[Rb([18]crown\text{-}6)(NH_3)_3]Au{\cdot}NH_3$ fulfills these criteria well, even though the acceptor is not the center of a coordination compound, but rather, an unprecedented "naked" transition-metal anion. The Au^- ion is however a late transition metal with a filled d shell (VE configuration: $5d^{10}6s^2$), the proton-donor nitrogen atom is highly electronegative, and the N-H-Au angle (158(1)°) is in the range of typical values for X–H···M bonds.[21]

To our knowledge, only theoretical investigations on gold as an acceptor in hydrogen bonds exist up to now. Kryachko and Remacle have reported DFT studies on N–H···Au interactions between formamide or DNA bases as donors and gold atoms from small Au_n ($n = 3, 4$) clusters as acceptors.[22] The calculated distances d(N···Au(cluster)) range from 258.0 to 289.0 pm and the corresponding angles from 160.8 to 179.7°. Taking into account that in the case of the title compound the hydrogen bonds involve negatively charged auride ions instead of neutral gold atoms of a cluster, the experimental values, which are at the lower limit of the calculated ones, agree very well with the calculations. The N–H···Au^- interaction that is described here satisfies both models equally, Au^- as pseudohalide and Au^- as electron-rich transition-metal center.

$[Rb([18]crown\text{-}6)(NH_3)_3]Au{\cdot}NH_3$ is the first crystallographically characterized compound with N–H···Au^- hydro-

 © 2006 Wiley-VCH Verlag GmbH & Co. KGaA, Weinheim

gen bonds. This compound illustrates, as a further example, the outstanding diversity of the chemistry of gold.

Experimental Section

All experiments were carried out under argon (modified Schlenk technique or glovebox (M. Braun); H_2O, $O_2 < 0.1$ ppm). Ammonia (Westfalen AG, 3.8) was stored as a potassium–ammonia solution at 195 K until use. RbAu was synthesized according to the literature procedure for the preparation of CsAu[23] from the elements in liquid ammonia. [18]crown-6 (99%, Acros Organics) was carefully melted in vacuum prior to use to remove any traces of water.

An H-shaped reaction vessel with a glass frit (porosity 3) was charged with [18]crown-6 (100 mg, 0.38 mmol) and RbAu (106.9 mg, 0.38 mmol). The apparatus was cooled to about 200 K (ethanol/dry ice) and filled with NH_3 (ca. 10 mL) by condensation. The reaction mixture was brought to the boiling point several times to dissolve the largest possible amount of the reactants. After 5 h, the slightly yellow-colored solution was filtered and reduced to about half of its volume. After the solution was stored at 200 K for 1–2 days, it yielded colorless block-shaped crystals. Owing to the extreme sensitivity of this compound, crystals suitable for crystal-structure determination were selected directly from the mother liquor by using a nylon loop which was moistened with perfluorinated oil (galden). The selected crystal was transferred to the diffractometer under cooling with liquid N_2.[24]

Received: March 20, 2006
Published online: May 24, 2006

Keywords: auride · crown compounds · hydrogen bonds · X-ray diffraction

[1] a) I. P. Grant, *Adv. Phys.* **1970**, *19*, 747–811; b) J.-P. Desclaux, *At. Data Nucl. Data Tables* **1973**, *12*, 311–406; c) P. Pyykkö, *Angew. Chem.* **2004**, *116*, 4512–4557; *Angew. Chem. Int. Ed.* **2004**, *43*, 4412–4456.
[2] M. Jansen, *Solid State Sci.* **2005**, *7*, 1464–1474, and references therein.
[3] a) W. Biltz, F. Weibke, H. J. Ehrhorn, R. Wedemeyer, *Z. Anorg. Allg. Chem.* **1938**, *236*, 12–23; b) A. Sommer, *Nature* **1943**, *152*, 215–215.
[4] a) C. Feldmann, M. Jansen, *Angew. Chem.* **1993**, *105*, 1107–1108; *Angew. Chem. Int. Ed. Engl.* **1993**, *32*, 1049–1050; b) C. Feldmann, M. Jansen, *J. Chem. Soc. Chem. Commun.* **1994**, 1045–1046; c) "The Chemistry of Gold Oxides": M. Jansen, A.-V. Mudring in *Gold—Progress in Chemistry, Biochemistry and Technology* (Ed.: H. Schmidbaur), Wiley-VCH, Weinheim, **1999**, pp. 747–793.
[5] A.-V. Mudring, M. Jansen, J. Daniels, S. Krämer, M. Mehring, J. P. P. Ramalho, A. H. Romero, M. Parrinello, *Angew. Chem.* **2002**, *114*, 128–132; *Angew. Chem. Int. Ed.* **2002**, *41*, 120–124.
[6] C. Feldmann, M. Jansen, *Z. Anorg. Allg. Chem.* **1995**, *621*, 201–206.
[7] C. Feldmann, M. Jansen, *Z. Anorg. Allg. Chem.* **1995**, *621*, 1907–1912.
[8] a) A.-V. Mudring, M. Jansen, *Angew. Chem.* **2000**, *112*, 3194–3196; *Angew. Chem. Int. Ed.* **2000**, *39*, 3066–3067; b) A.-V. Mudring, J. Nuss, U. Wedig, M. Jansen, *J. Solid State Chem.* **2000**, *155*, 29–36.
[9] P. D. C. Dietzel, M. Jansen, *Chem. Commun.* **2001**, 2208–2209.
[10] K. M. Harmon, I. Gennick, S. L. Madeira, *J. Phys. Chem.* **1974**, *78*, 2585–2591.
[11] T. Steiner, *Angew. Chem.* **2002**, *114*, 50–80; *Angew. Chem. Int. Ed.* **2002**, *41*, 48–76.
[12] G. R. Desiraju, T. Steiner, *The Weak Hydrogen Bond in Structural Chemistry and Biology*, Oxford University Press, Oxford, **1999**, pp. 246–253.
[13] The value for the van der Waals radius of the hydrogen atom varies: 120 pm in: A. Bondi, *J. Phys. Chem.* **1964**, *68*, 441–451; 110 pm in the most chosen source for van der Waals radii: R. S. Rowland, T. Taylor, *J. Phys. Chem.* **1996**, *100*, 7384–7391.
[14] Lately, the "van der Waals criterion" has been regarded as too strict (see references [11] and [12]).
[15] R. J. Batchelor, T. Birchall, R. C. Burns, *Inorg. Chem.* **1986**, *25*, 2009–2015.
[16] R. C. Burns, J. D. Corbett, *J. Am. Chem. Soc.* **1981**, *103*, 2627–2632.
[17] Crystal data for $[Rb([18]crown\text{-}6)(NH_3)_3]Au{\cdot}NH_3$: monoclinic, space group $P2_1/n$ (no. 14), $a = 1108.6(4)$, $b = 820.2(3)$, $c = 2385.4(7)$ pm, $\beta = 91.80(1)°$, $V = 2168.0(2) \times 10^6$ pm^3, $\rho_{calcd} = 1.884$ g cm^{-3}, $Z = 4$, $\mu(Mo_{K\alpha}) = 9.05$ mm^{-1}, $F(000) = 1200$, $\lambda = 71.073$ pm, Bruker AXS Smart APEX diffractometer, graphite monochromator, $T = 100$ K, ω scan, 19427 measured reflections, 4484 symmetry independent reflections ($2\theta_{max} = 53.21°$), 223 refined parameters; semiempirical absorption correction (SADABS[25]); structure solution and refinement with SHELXTL:[26] $R_1 = 0.0517$, $wR_2 = 0.1169$ ($2014 F_0 > 4\sigma(F_0)$), $R_1 = 0.1119$, $wR_2 = 0.1608$ (all data); residual electron density $2.02/-1.14 \times 10^{-6}$ e pm^{-3}. CCDC-602496 contains the supplementary crystallographic data for this paper. These data can be obtained free of charge from The Cambridge Crystallographic Data Centre via www.ccdc.cam.ac.uk/data_request/cif.
[18] J. W. Steed, *Coord. Chem. Rev.* **2001**, *215*, 171–221.
[19] L. Brammer, J. M. Charnock, P. L. Goggin, R. J. Goodfellow, T. F. Koetzle, A. G. Orpen, *J. Chem. Soc. Dalton Trans.* **1991**, 1789–1798.
[20] L. Brammer, D. Zhao, F. T. Ladipo, J. Braddock-Wilking, *Acta Crystallogr. Sect. B* **1995**, *51*, 632–640.
[21] D. Braga, F. Grepioni, E. Tedesco, K. Biradha, G. R. Desiraju, *Organometallics* **1997**, *16*, 1846–1856.
[22] a) E. S. Kryachko, F. Remacle, *Chem. Phys. Lett.* **2005**, *404*, 142–149; b) E. S. Kryachko, F. Remacle, *Nano Lett.* **2005**, *5*, 735–739.
[23] W. J. Peer, J. J. Lagowski, *J. Am. Chem. Soc.* **1978**, *100*, 6260–6261.
[24] a) T. Kottke, D. Stalke, *J. Appl. Crystallogr.* **1993**, *26*, 615–619; b) D. Stalke, *Chem. Soc. Rev.* **1998**, *27*, 171–178.
[25] G. M. Sheldrick, SADABS Version 2.0, program for absorption correction, Bruker AXS, Madison, USA, **2001**.
[26] G. M. Sheldrick, SHELXTL Version 6.12, program suite for the solution and refinement of crystal structures, Bruker AXS, Madison, USA, **2000**.

 © 2006 Wiley-VCH Verlag GmbH & Co. KGaA, Weinheim

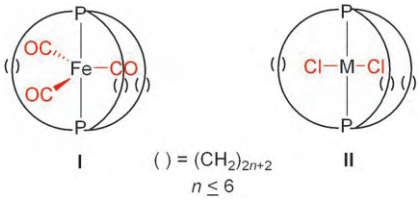
DOI: 10.1002/anie.200601191

"Giant" Gyroscope-Like Molecules Consisting of Dipolar Cl-Rh-CO Rotators Encased in Three-Spoke Stators That Define 25–27-Membered Macrocycles**

*Leyong Wang, Frank Hampel, and John A. Gladysz**

There is intense current interest in molecular rotors,[1] which are comprised of a "stator", a "rotator", and a connecting axis. One important objective is the synthesis of assemblies in which the rotators are partially "enclosed" or sterically shielded from their environments.[1–6] This approach follows by analogy to macroscopic machines in which rotating components are often for safety or mechanical reasons encased in protective housings. Two prominent classes of molecular rotors are compasses and gyroscopes.[3,4] When rotators feature dipole moments, they can be aligned in static electric fields, similar to compasses, or forced to turn unidirectionally in rotating electric fields,[1] similar to gyroscopes. In all cases, it is desirable that rotation be as "frictionless" as possible, without interference from nearby molecules or ions.

We have found that the trigonal-bipyramidal iron tricarbonyl complexes *trans*-$[Fe(CO)_3(P\{(CH_2)_nCH{=}CH_2\}_3)_2]$ (n = 4–6) and square-planar palladium and platinum dichloride complexes *trans*-$[MCl_2(P\{(CH_2)_nCH{=}CH_2\}_3)_2]$ ($n = 6$, M = Pd, Pt) undergo threefold intramolecular alkene metatheses that couple the *trans* phosphine ligands. Hydrogenations afford cage molecules of the types **I** and **II**, which bear a clear



resemblance to toy gyroscopes.[5,6] The three $(CH_2)_{2n+2}$ "spokes" or bridges provide a high degree of steric insulation. When these define seventeen-membered macrocycles ($n = 6$), rotation of the $\{ML_m\}$ moiety is rapid on the NMR time scale at room temperature. Although the iron complexes could be converted into cationic $[Fe(CO)_2(NO)]^+$ and $[HFe(CO)_3]^+$ analogues, which feature dipolar rotators, the accompanying anions are undesirable: they are capable of dipole–dipole interactions with the rotator, which can increase the rotational energy barriers.

Another challenge associated with such molecules is the construction of larger stators that would accommodate extended rotators. Thus, we sought in this study to 1) probe whether significantly longer bridges might be accessible by alkene metathesis, 2) introduce more rigid architectural units that would enforce a minimum dimensionality, 3) apply this chemistry to neutral complexes with dipolar rotors, and 4) map the effective size of the stator through ligand substitution and NMR spectroscopy experiments.

Pursuant the first two objectives, alkene-containing triarylphosphine ligands were sought. Accordingly, 4-bromophenol, the α,ω-bromoalkenes $Br(CH_2)_nCH{=}CH_2$ (**a** $n = 4$, **b** $n = 5$, **c** $n = 6$), and the base K_2CO_3 (1:1:1.5) were combined in DMF at 55 °C. Workup gave the corresponding ethers *p*-$BrC_6H_4O(CH_2)_nCH{=}CH_2$ (**1a–c**) in 92–95 % yields. As shown in Scheme 1, Grignard reagents were subsequently generated, and reactions with PCl_3 gave the phosphines $P\{p\text{-}C_6H_4O(CH_2)_nCH{=}CH_2\}_3$ (**2a–c**) in 84–92 % yields. The new compounds **1–2** and all the others below were characterized by microanalyses and the usual spectroscopic methods, as summarized in the Supporting Information.[7]

Square-planar complexes featuring two *trans*-disposed ligands **2** and two unlike ligands L′/L″ were sought. Using a standard procedure,[8] the rhodium chloride $[\{(cod)Rh(\mu\text{-}Cl)\}_2]$, **2a–c**, and CO were combined. As shown in Scheme 1, workup gave the bis(phosphine) carbonyl chloride complexes **3a–c** in 88–82 % yields. The NMR spectra showed the usual ^{103}Rh and virtual couplings associated with such compounds.[8] Next, **3b** (ca. 0.001 M in CH_2Cl_2) was treated with the Grubbs catalyst (15 mol %, or 5 %/new C=C linkage). Chromatography gave the intramolecular metathesis product **4b,** which features three 25-membered macrocycles, in 45 % yield. The ^{31}P NMR spectrum indicated a 60:30:10 mixture of C=C isomers. The sample was hydrogenated (4 atm H_2, 15 mol % PtO_2), giving the target molecule **5b** in 91 % yield.

A similar sequence with **3c** gave **4c** (49 %) and then **5c** (87 % with a purity of 90 % or 53 % with a purity of > 98 %). These complexes feature 27-membered macrocycles. However, **3a** did not afford detectable quantities of monorhodium products. The ^{13}C NMR spectra of **5b,c** exhibited a single set of signals for the CH_2 groups, indicating rapid rotation of the Cl-Rh-CO moieties about the P-Rh-P axes on the NMR time scale. No decoalescence was observed at −120 °C in $CDFCl_2$, although the peaks became severely broadened. Also, the PC_6H_4O moieties gave rise to only two CH ^{13}C and ^1H NMR signals (*o*, *m*), indicating rapid interconversion of the *meso* and *rac* PAr_3 propeller diastereomers.[9] Importantly, the ^{31}P signal and CO ^{13}C signal remained coupled to ^{103}Rh at room temperature, excluding dissociative mechanisms for rendering the above-mentioned groups equivalent.

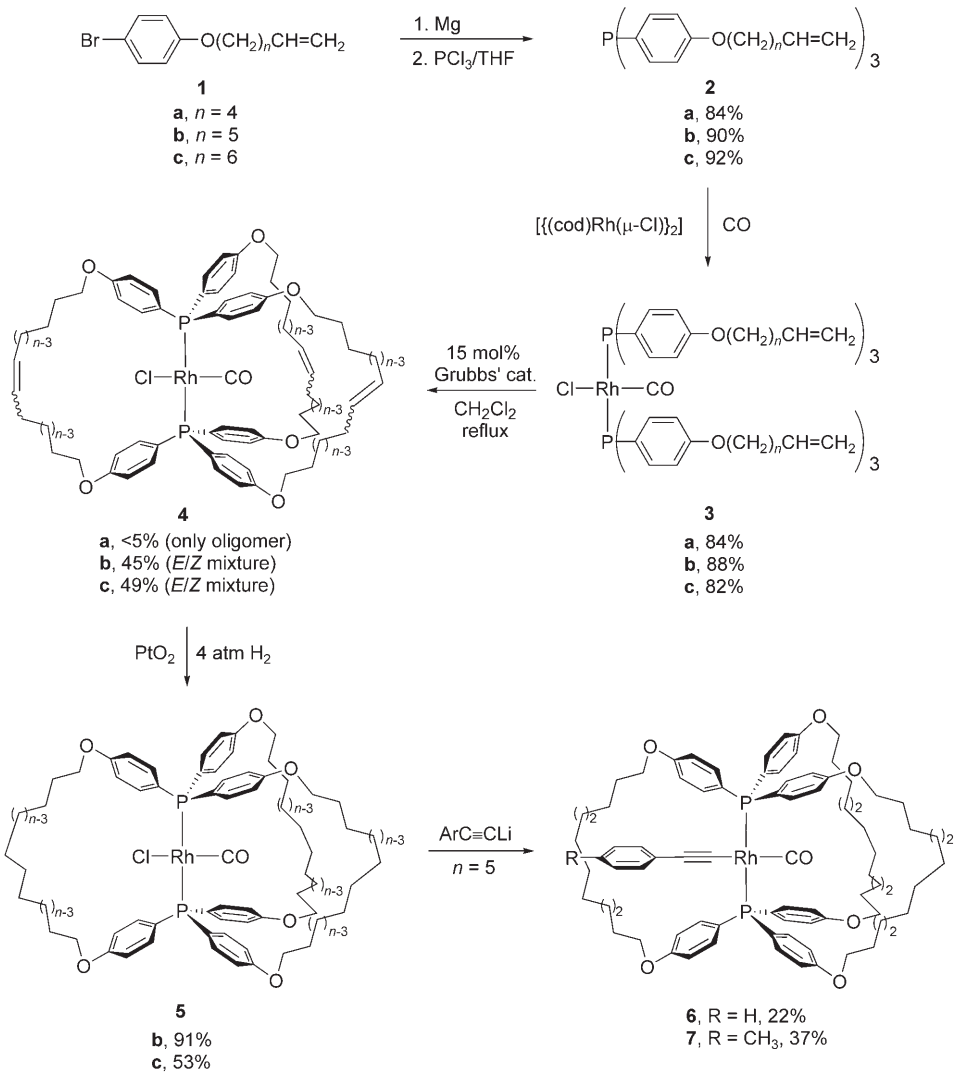
To help visualize the spatial relationships in these molecules, the crystal structures of the solvates **5b**·$(C_6H_6)_{1.5}$·

[*] Dr. L. Wang, Dr. F. Hampel, Prof. Dr. J. A. Gladysz
Institut für Organische Chemie
Friedrich-Alexander-Universität Erlangen-Nürnberg
Henkestrasse 42, 91054 Erlangen (Germany)
Fax: (+49) 9131-85-26865
E-mail: gladysz@organik.uni-erlangen.de

[**] We thank the Deutsche Forschungsgemeinschaft (DFG, GL 300/1-3), the Humboldt Foundation (Fellowship to L.W.), and Johnson Matthey PMC (rhodium loan) for support.

Supporting information for this article is available on the WWW under http://www.angewandte.org or from the author.

InterScience
© 2006 Wiley-VCH Verlag GmbH & Co. KGaA, Weinheim



Scheme 1. Synthesis and reactions of "giant" rhodium gyroscope-like molecules; cod = cycloocta-1,5-diene.

$(H_2O)_{0.5}$ and **5c**·$(C_6H_6)_{1.5}$·(CH_3OH) were determined (see Supporting Information). As shown in Figure 1 A and B, the molecular structures are similar, with P-Rh-P angles of 176–179° and nearly eclipsed C_{ipso}-P-P-C_{ipso} moieties (torsion angles 4.8–7.6°). In the horizontal dimension of Figure 1 A and B both molecules exhibit a large amount void space between the Cl-Rh-CO rotators and the diphosphine stators, enforced in part by the rigid arene spacers; in the vertical dimension, there are very slight van der Waals contacts (Figure 1 C). The Rh–Cl and *Rh–CO* distances (2.36 Å and 2.94 Å) can be compared with those from the rhodium to the distal carbon atoms of the bridges (10.24–10.72 Å for **5b**; 10.46–12.05 Å for **5c**). When the van der Waals radius of chlorine or oxygen[10] is added to the Rh–Cl and *Rh–CO* distances, and that of carbon is subtracted from the rhodium to the distal carbon distance, substantial clearance remains (4.11 Å and 4.46 Å versus 8.54–9.02 Å and 8.76–10.35 Å).

However, in contrast to the smaller iron-based systems **I**, the stators in **5b**,**c** are "porous", or capable of intercalation. For example, for **5b**·$(C_6H_6)_{1.5}$·$(H_2O)_{0.5}$, one benzene molecule occupies a cleft. The closest rhodium–carbon distance is 5.87 Å, or 4.17 Å after subtracting the van der Waals radius of carbon. Figure 1 D illustrates how a bridge of one molecule nestles quite close to the rotator of another in the crystal. The closest intermolecular rhodium–carbon distances are 4.84 Å (**5b**) and 4.80 Å (**5c**), or 3.14 Å and 3.10 Å after subtracting the van der Waals radius of carbon. This proximity should severely impede Cl-Rh-CO rotation in the crystalline state.

Given the rapid rotation of the Cl-Rh-CO moieties of **5b**,**c** in solution, we sought to replace the chloride by a bulkier ligand that would function as a "brake". Reactions of $[Rh(CO)(Cl)(L)_2]$ species and acetylide nucleophiles have been reported.[11] Thus, LiC≡CC_6H_5 and **5b** were combined in THF at −80 °C. ^{31}P NMR spectra indicated a nearly quantitative conversion. Workup gave the phenylacetylide complex **6** (Scheme 1), which was somewhat labile in all solvents investigated, in 22 % yield. The NMR spectroscopic properties of **6** were very similar to those of the triphenylphosphine analogue *trans*-$[Rh(CO)(C{\equiv}CC_6H_5)(PPh_3)_2]$.[12] In the crystal structure of the latter,[12] the distance from rhodium to the *p*-C_6H_5 hydrogen is 8.32 Å. When the van der Waals radius of hydrogen is added, the distance is similar to the horizontal clearance offered by the stator in **5b** (9.52 vs. 8.54–9.02 Å). However, NMR spectra of **6** in CD_2Cl_2 at −70 °C showed only one bridge (e.g., six signals for CH_2 groups in the ^{13}C NMR spectrum), indicating rapid rotation of the $C_6H_5C{\equiv}C$-Rh-CO moiety on the NMR time scale.

A similar reaction was conducted with a slightly "longer" acetylide, LiC≡CC_6H_4-*p*-CH_3. Workup gave the corresponding complex **7** (37 %, Scheme 1), for which a distance of 8.89 Å from rhodium to the *p*-methyl carbon atom can be estimated. When the van der Waals radius of carbon is added (10.59 Å), this becomes distinctly greater than the clearance offered by the stator. Accordingly, NMR spectra in CD_2Cl_2 at room temperature showed two types of bridges. As illustrated in Figure 2, twelve signals arising from CH_2 groups were detected in the ^{13}C NMR spectrum. These signals consist of two sets in an approximately 2:1 ratio. Two sets of PC_6H_4O ^{13}C

 © 2006 Wiley-VCH Verlag GmbH & Co. KGaA, Weinheim

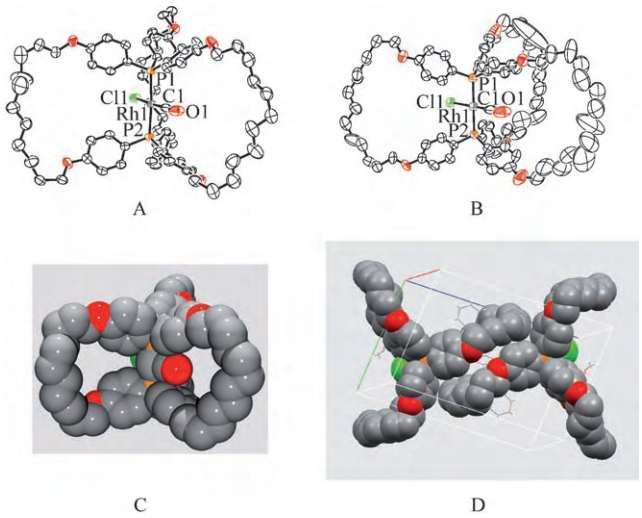


Figure 1. A,B) ORTEP (thermal ellipsoids set at 50% probability) and C,D) space-filling representations of the crystal structures of **5b**·$(C_6H_6)_{1.5}$·$(H_2O)_{0.5}$ and **5c**·$(C_6H_6)_{1.5}$·(CH_3OH): A) **5b** and B) **5c** with solvate molecules omitted; C) **5b** with solvate molecules omitted; D) packing view for **5c** showing intercalation of neighboring molecules. Selected bond lengths [Å] and angles [°], **5b**/**5c**: Rh1–C1 1.790(5)/1.791(8), Rh1–P1 2.3223(11)/2.3251(14), Rh1–Cl1 2.3646(10)/2.3651(15), C1–O1 1.153(5)/1.148(9); C1-Rh1-P1 91.00(15)/90.7(2), C1-Rh1-Cl1 174.73(17)/178.0(3), P1-Rh1-Cl1 88.18(4)/89.02(5), P1-Rh1-P2 175.87(4)/179.26(6), O1-C1-Rh1 176.4(5)/178.8(8).

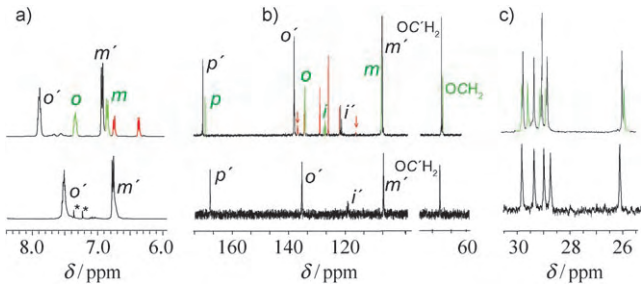
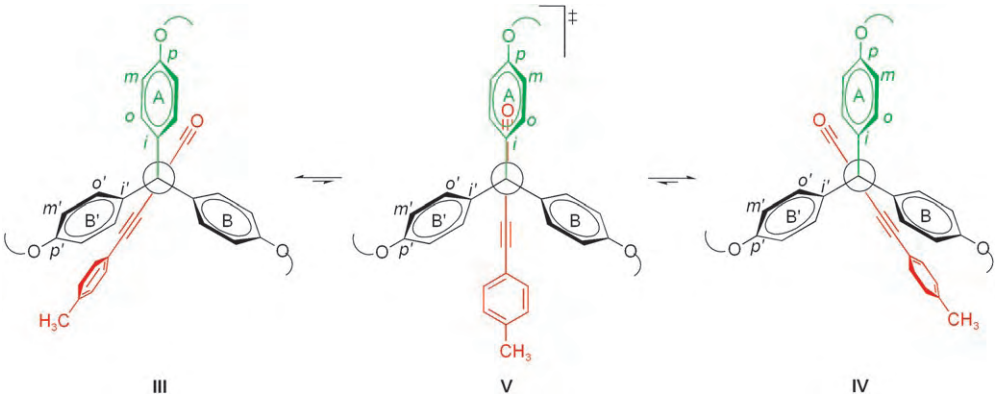


Figure 2. NMR spectra of **7** (top, CD_2Cl_2) and **5b** (bottom, $CDFCl_2$, −20 °C): a) ^{1}H NMR (400 MHz), aryl region; b) and c) ^{13}C NMR (100 MHz). Signals associated with the C≡C moiety and solvent are indicated by arrows and asterisks, respectively. The red signals originate from the acetylide ligand.

and ^{1}H signals (2:1) were also observed. These features persisted in spectra recorded in C_6D_5Cl at 120 °C, under which conditions **7** concurrently decomposed. These data are best modeled by a rapid equilibrium involving the quasi-enantiomeric structures **III** and **IV** and the transition state **V**.[13] This process entails passage of the shorter CO ligand of the rotator



between aryl ring A (in **III**–**V**) and the corresponding ring below, with the longer C≡CC_6H_4-*p*-CH_3 ligand remaining confined within a < 120° arc between rings B and B′ (in **III**–**V**). The PAr_3 propeller chirality must also rapidly invert. The time-averaged result is two types of bridges and aryl rings (B/B′:A, 2:1).

In summary, we have demonstrated that it is possible to synthesize "giant" gyroscope-like molecules that feature dipolar X-Rh-CO rotators and three-spoke stators that incorporate rigid *p*-disubstituted benzene rings. When X = Cl, the rotators rapidly rotate within the 25 to 27-membered macrocycles in solution. However, when the Rh–X length becomes greater than 10 Å, such as with *p*-$CH_3C_6H_4C{\equiv}C{-}Rh$, this motion is effectively "braked". These assemblies are structurally porous, such that solvent or neighboring molecules can intercalate between the spokes. This intercalation blocks rotation in the solid state. Future efforts will include restricting access to this space through the introduction of bulky groups and/or interbridge connections, and exploiting the dipole moments of the rotators to achieve directed rotary motion.

Received: March 25, 2006
Published online: May 26, 2006

Keywords: alkynyl ligands · hydrogenation · macrocycles · metathesis · rhodium

[1] G. S. Kottas, L. I. Clarke, D. Horinek, J. Michl, *Chem. Rev.* **2005**, *105*, 1281.
[2] a) T. C. Bedard, J. S. Moore, *J. Am. Chem. Soc.* **1995**, *117*, 10662; b) O. Hirata, M. Takeuchi, S. Shinkai, *Chem. Commun.* **2005**, 3805.
[3] M. A. Garcia-Garibay, *Proc. Natl. Acad. Sci. USA* **2005**, *102*, 10771, and references therein.
[4] a) Z. Dominguez, H. Dang, M. J. Strouse, M. A. Garcia-Garibay, *J. Am. Chem. Soc.* **2002**, *124*, 7719; b) Z. Dominguez, T.-A. Khuong, H. Dang, C. N. Sanrame, J. E. Nuñez, M. A. Garcia-Garibay, *J. Am. Chem. Soc.* **2003**, *125*, 8827; c) C. E. Godinez, G. Zepeda, C. J. Mortko, H. Dang, M. A. Garcia-Garibay, *J. Org. Chem.* **2004**, *69*, 1652; d) S. D. Karlen, R. Ortiz, O. L. Chapman, M. A. Garcia-Garibay, *J. Am. Chem. Soc.* **2005**, *127*, 6554.
[5] T. Shima, F. Hampel, J. A. Gladysz, *Angew. Chem.* **2004**, *116*, 5653; *Angew. Chem. Int. Ed.* **2004**, *43*, 5537.
[6] A. J. Nawara, T. Shima, F. Hampel, J. A. Gladysz, *J. Am. Chem. Soc.* **2006**, *128*, 4962.
[7] NMR and IR spectroscopic, mass spectral, and microanalytical data are summarized in the supporting information. CCDC-601307 and CCDC-601308 contain the supplementary crystallo-

 © 2006 Wiley-VCH Verlag GmbH & Co. KGaA, Weinheim

graphic data for this paper. These data can be obtained free of charge from The Cambridge Crystallographic Data Centre via www.ccdc.cam.ac.uk/data_request/cif.

[8] a) K. R. Dunbar, S. C. Haefner, *Inorg. Chem.* **1992**, *31*, 3676; b) J. Ruwwe, J. M. Martín-Alvarez, C. R. Horn, E. B. Bauer, S. Szafert, T. Lis, F. Hampel, P. C. Cagle, J. A. Gladysz, *Chem. Eur. J.* **2001**, *7*, 3931.

[9] Selected references: a) H. Brunner, R. Oeschey, B. Nuber, *Angew. Chem.* **1994**, *106*, 941; *Angew. Chem. Int. Ed. Engl.* **1994**, *33*, 866; b) S. G. Davies, A. E. Derome, J. P. McNally, *J. Am. Chem. Soc.* **1991**, *113*, 2854.

[10] A. Bondi, *J. Phys. Chem.* **1964**, *68*, 441.

[11] a) B. Cetinkaya, M. F. Lappert, J. McMeeking, D. E. Palmer, *J. Chem. Soc. Dalton Trans.* **1973**, 1202; b) W. Weng, T. Bartik, M. Brady, B. Bartik, J. A. Ramsden, A. M. Arif, J. A. Gladysz, *J. Am. Chem. Soc.* **1995**, *117*, 11922.

[12] J.-C. Choi, K. Osakada, T. Yamamoto, *Organometallics* **1998**, *17*, 3044.

[13] Interestingly, as can be inferred from Figure 1C, **5b** crystallizes in a conformation very similar to **V**, with OC-Rh-P-C_{ipso} torsion angles of $-3.4(2)°$ and $11.1(2)°$ (values for **5c**: $-7.0(4)°$ and $10.0(4)°$). Perhaps **V** can sometimes be a local minimum, closely straddled by two transition states leading to **III** and **IV**.

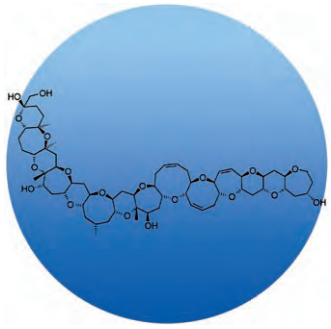
 © 2006 Wiley-VCH Verlag GmbH & Co. KGaA, Weinheim

Cover Picture

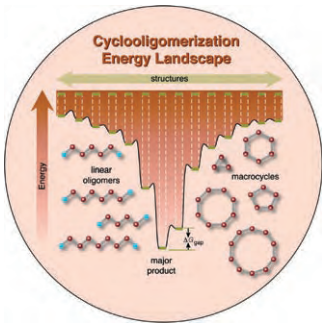


Tongxin Wang, An-Wu Xu,* and Helmut Cölfen*

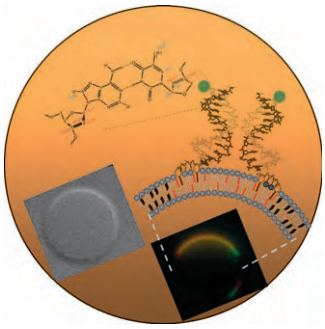
The Belousov–Zhabotinsky reaction with its typical concentric ring pattern is described for a precipitation for the first time by T. Wang, A.-W. Xu, and H. Cölfen in their Communication on page 4451 ff. The formation and self-organization of $BaCO_3$ nanoparticles can be directed with a new phosphonated block copolymer: short to ultralong nanofibers and, ultimately, ring patterns are obtained. This system could help to explain natural pattern formation. The cover picture shows observed and simulated Belousov–Zhabotinsky ring patterns, as well as the molecular structure of the block copolymer.



Biosynthesis
In their Essay on page 4406 ff., J. B. Spencer and A. R. Gallimore propose a simple model that can explain the biosynthesis of the ring structure of all the marine polyether ladders thus far characterized, including maitotoxin.



Shape-Persistent Macrocycles
The application of dynamic covalent chemistry for the preparation of shape-persistent macrocycles is described by J. S. Moore and W. Zhang in their Review on page 4416 ff. The advantages of thermodynamic over kinetic reaction pathways are highlighted.



Nanobiotechnology
J. Liebscher et al. report in their Communication on page 4440 ff. that oligonucleotides anchored to a lipid bilayer congregate in the liquid-disordered membrane domains of giant vesicles and can bind complementary oligonucleotide strands.

Contents

The following Communications have been judged by at least two referees to be "very important papers" and will be published online at www.angewandte.org soon:

*A. Abo-Riziq, B. Crews, M. Callahan, L. Grace, M. de Vries**
Spectroscopy of Isolated Gramicidin Peptides

C. Ye, Y. Bando, G. Shen, D. Golberg*
Formation of Single-Crystalline $SrAl_2O_4$ Nanotubes by a Roll-Up and Post-Annealing Approach

*A. Narayanaswamy, H. Xu, N. Pradhan, X. Peng**
Single-Crystal Nanoflowers with Different Chemical Compositions and Physical Properties Grown by Limited Ligand Protection

*A. Tao, P. Sinsermsuksakul, P. Yang**
Polyhedral Silver Nanocrystals with Distinct Scattering Signatures

J. van Bokhoven, C. Louis, J. Miller, M. Tromp, O. Safonova, P. Glatzel*
Activation of Oxygen on Gold-Alumina Catalysts: In Situ High-Energy Resolution Fluorescence and Time-Resolved X-ray Spectroscopy

M. Brynda, R. Herber, P. Hitchcock, M. Lappert,* I. Nowik, P. Power,* A. Protchenko, A. Ruzicka, J. Steiner*
Higher Nuclearity Group 14 Metalloid Clusters: $[Sn_9\{Sn(NRR')\}_6]$ ($R = 2,6\text{-}iPr_2C_6H_3$; $R' = SiMe_3$ or $SiMe_2Ph$)

Meeting Reviews

Functional Molecular Assemblies — *J. A. Thomas* — *4396*

Books

Nanoparticle Assemblies and Superstructures — Nicholas A. Kotov — *reviewed by M. Brust* — 4399

Biofunctionalization of Nanomaterials Nanotechnologies for the Life Sciences, Vol. 1 — Challa Kumar — *reviewed by G. Wittstock* — 4400

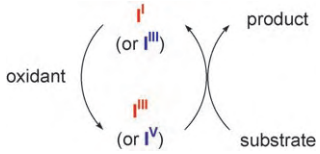
Highlights

Hypervalent Iodine Compounds

R. D. Richardson, T. Wirth* **4402 – 4404**

Hypervalent Iodine Goes Catalytic

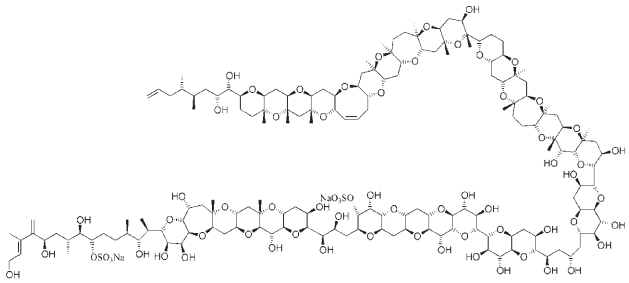
A dash of iodine: Different reactions relying on the power of hypervalent iodine reagents can now be performed with catalytic amounts of these compounds and a stoichiometric oxidant. Oxidations of alcohols, α-functionalizations of ketones, and spirocyclizations of phenol derivatives are possible.



InterScience

© 2006 Wiley-VCH Verlag GmbH & Co. KGaA, Weinheim

Essays



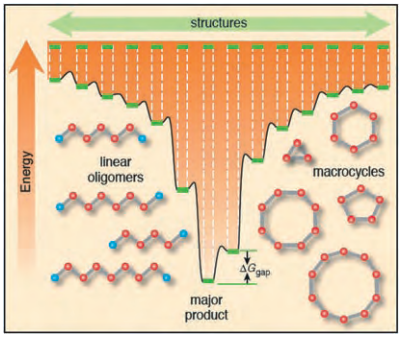
Odd one out: Marine polyether ladders are probably the most well-known of all marine natural products, not only for their fascinating structures, but also for their characteristic toxicity. A very straightforward model for the biosynthesis of all known polyether ladders, including maitotoxin (the largest and most toxic of this structural family; see formula) is described, but is the structure of this giant molecule really known?

Biosynthesis

A. R. Gallimore, J. B. Spencer* ——— **4406 – 4413**

Stereochemical Uniformity in Marine Polyether Ladders—Implications for the Biosynthesis and Structure of Maitotoxin

Reviews



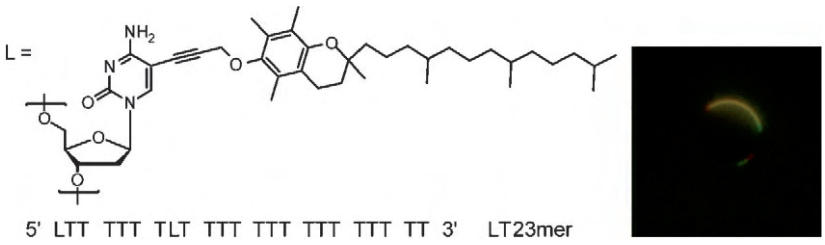
Balance control: Kinetically controlled cyclooligomerization is impeded by the formation of higher oligomers ("overshooting"). Under reversible conditions, the product distribution is determined by the thermodynamic stability, which is balanced by both entropic and enthalpic factors. Methods based on dynamic covalent chemistry and the use of the energy gap principle enable the formation of target macrocycles by cyclooligomerization to be controlled.

Macrocycle Synthesis

W. Zhang, J. S. Moore* ——— **4416 – 4439**

Shape-Persistent Macrocycles: Structures and Synthetic Approaches from Arylene and Ethynylene Building Blocks

Communications



Anchoring for DNA: A lipophilic oligonucleotide consisting of 21 thymidine units and two lipophilic nucleotides L was synthesized and bound to vesicular surfaces (see fluorescence image). The membrane-bound oligonucleotide binds complementary DNA strands by formation of Watson–Crick base pairs. The lipid-anchored oligonucleotide is preferentially enriched in liquid-disordered membrane domains.

Nanobiotechnology

A. Kurz, A. Bunge, A.-K. Windeck, M. Rost, W. Flasche, A. Arbuzova, D. Strohbach, S. Müller, J. Liebscher,* D. Huster,* A. Herrmann* ——— **4440 – 4444**

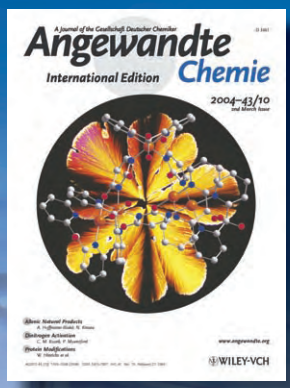
Lipid-Anchored Oligonucleotides for Stable Double-Helix Formation in Distinct Membrane Domains

For the USA and Canada:
ANGEWANDTE CHEMIE International Edition (ISSN 1433-7851) is published weekly by Wiley-VCH PO Box 191161, D 69451 Weinheim, Germany. Air freight and mailing in the USA by Publications Expediting Inc. 200 Meacham Ave., Elmont, NY 11003. Periodicals postage paid at Jamaica NY 11431. US POSTMASTER: send address changes to *Angewandte Chemie*, Wiley-VCH, 111 River Street, Hoboken, NJ 07030. Annual subscription price for institutions: US$ 5685/5168 (valid for print and electronic / print or electronic delivery); for individuals who are personal members of a national chemical society prices are available on request. Postage and handling charges included. All prices are subject to local VAT/sales tax.

© 2006 Wiley-VCH Verlag GmbH & Co. KGaA, Weinheim

The best in chemistry –

for more than a hundred years



A Journal of the Gesellschaft Deutscher Chemiker

Angewandte
International Edition **Chemie**

www.angewandte.org

1888: ***The beginning of a success story***

Constant Innovations

1962: *First issue of the International Edition*
1976: *Graphical abstracts*
1979: *Cover pictures*
1988: *Centenary of Angewandte*
1989: *Routine use of color*
1991: *New section: Highlights*
1992: *Computerized editorial tracking system*
1995: *Internet service for readers*
1998: *Regular press service; full-text online*
2000: *New section: Essays; EarlyView: Communications available online ahead of the printed version*
2001: *New section: Minireviews*
2002: *Online submission of manuscripts*
2003: *Weekly publication; new section: News; new layout*
2004: *Backfiles (1962-1997); ManuscriptXpress: Online system for authors and referees*



Angewandte's advisors...

Ulrich Stilz
Aventis, Frankfurt/Main

» With its interdisciplinary and international orientation ***Angewandte Chemie*** *has set the benchmark for publishing innovative results. The editorial team is acknowledged for the success of this renowned journal, that provides scientists with a unique forum, in which to discuss their discoveries. «*

Angewandte Chemie International Edition *is a journal of the German Chemical Society (GDCh)*

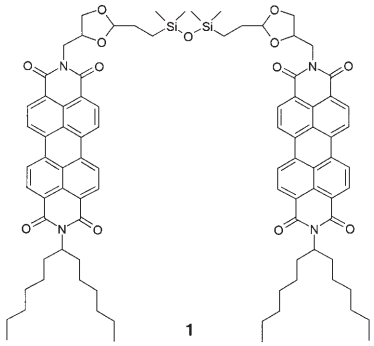
GDCh

WILEY InterScience® DISCOVER SOMETHING GREAT

WILEY-VCH

1198140_4_gu

Enantiomer or racemate? For compound **1** this question can be answered with one glance. Racemic starting material forms the *meso* form of **1** with the expected UV/Vis spectra of the chromophore, whereas the enantiomeric compounds display color shifts and large CD effects indicative of strong intramolecular exciton interactions.



1

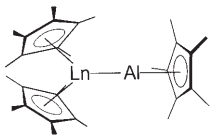
Exciton Interactions

H. Langhals,* O. Krotz ____ **4444 – 4447**

Chiral, Bichromophoric Silicones: Ordering Principles of Structural Units in Complex Molecules

---

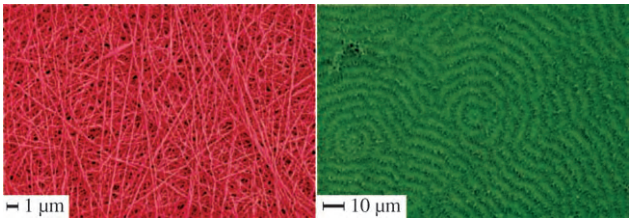
Opposites attract: The compounds $[(\eta^5\text{-}C_5Me_5)_2Ln{-}Al(\eta^5\text{-}C_5Me_5)]$ (Ln = Eu, Yb; see scheme) represent the first compounds with a bond between aluminum and a 4f metal. The bonds are predominantly electrostatic with insignificant charge-transfer and covalent contributions.



Metal–Metal Interactions

M. T. Gamer, P. W. Roesky,* S. N. Konchenko, P. Nava, R. Ahlrichs ____ **4447 – 4451**

Al–Eu and Al–Yb Donor–Acceptor Bonds



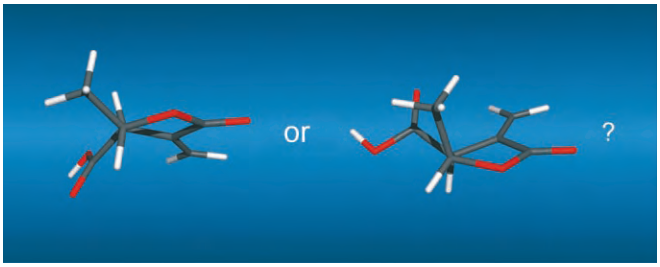
Intelligent design? Depending on the starting pH, ultralong nanofibers (see picture; left) or patterns of concentric circles (right) are produced in the polymer-controlled crystallization of $BaCO_3$. The ring patterns are the first examples of nanoparticle self-organization that can be described by a Belousov–Zhabotinsky formalism.

Pattern Formation in Crystals

T. X. Wang, A.-W. Xu,* H. Cölfen* ____ **4451 – 4455**

Formation of Self-Organized Dynamic Structure Patterns of Barium Carbonate Crystals in Polymer-Controlled Crystallization

---



***syn*- or *anti*-pathy?** Determination of the relative configuration of the α-methylene-γ-butyrolactone **1** failed by conventional NMR methods, because structures in the conformational space of both diastereoisomers exist that fulfill the restraints from NOE and ^3J coupling data equally well. Homo- and heteronuclear residual dipolar couplings were measured which indicate that **1** is *trans* configured.

NMR Methods

C. M. Thiele,* A. Marx, R. Berger, J. Fischer, M. Biel, A. Giannis ____ **4455 – 4460**

Determination of the Relative Configuration of a Five-Membered Lactone from Residual Dipolar Couplings

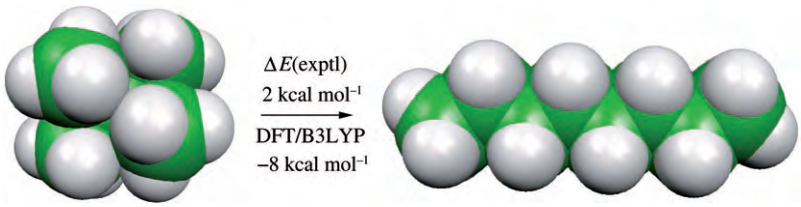
© 2006 Wiley-VCH Verlag GmbH & Co. KGaA, Weinheim

Contents

Theoretical Chemistry

S. Grimme* ——— **4460 – 4464**

Seemingly Simple Stereoelectronic Effects in Alkane Isomers and the Implications for Kohn–Sham Density Functional Theory

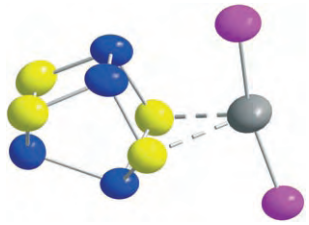


A theoretical disaster: In contrast to general opinion, modern density functional methods are not able to even qualitatively describe the overall energetics of simple alkylation reactions (see scheme). The main reason is that the currently used hybrid functionals almost completely neglect the generally relevant electron correlation effects for medium-range electron–electron distances.

Solid-State Structures

M. F. Bräu, A. Pfitzner* ——— **4464 – 4467**

$HgI_2 \cdot As_4S_4$: An Adduct from HgI_2 Molecules and Undistorted As_4S_4 Cages

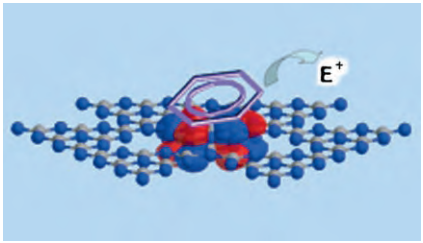


Unrattled cage: From the reaction of HgI_2, As, and S, an adduct of linear HgI_2 units and undistorted As_4S_4 cages is formed with only weak intermolecular interactions (see picture; Hg gray, I violet, S yellow, As blue). For the first time in this class of compounds, no polycationic network of Hg and S atoms is obtained. The optimization of the total energy prevents the formation of Hg–S bonds and the cleavage of the As_4S_4 cage.

Metal-Free Heterogeneous Catalysis

F. Goettmann, A. Fischer, M. Antonietti, A. Thomas* ——— **4467 – 4471**

Chemical Synthesis of Mesoporous Carbon Nitrides Using Hard Templates and Their Use as a Metal-Free Catalyst for Friedel–Crafts Reaction of Benzene

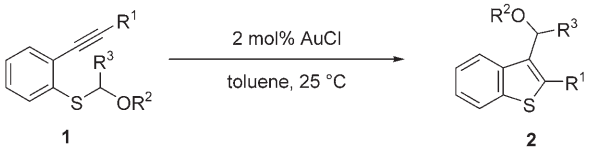


In the footsteps of Liebig and Berzelius: A material first synthesized in 1834, carbon nitride (C_3N_4), was synthesized in a graphitic mesoporous form by using silica nanoparticles as templates. The resulting electron-rich solid is an active catalyst for the Friedel–Crafts acylation of benzene with hexanoyl chloride. Presumably the catalysis arises from a shift of electron density from the MOs of the catalyst to the unoccupied orbitals of benzene (see picture).

Synthetic Methods

I. Nakamura,* T. Sato, Y. Yamamoto ——— **4473 – 4475**

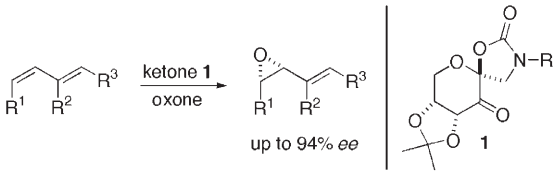
Gold-Catalyzed Intramolecular Carbothiolation of Alkynes: Synthesis of 2,3-Disubstituted Benzothiophenes from (α-Alkoxy Alkyl) (*ortho*-Alkynyl Phenyl) Sulfides



1 2

Gold forms rings: AuCl-catalyzed cyclization of (α-alkoxy alkyl) (*ortho*-alkynyl phenyl) sulfides **1** proceeds under mild conditions to give 3-(α-alkoxy alkyl) benzothiophenes **2** in high yields for a wide range of substrates (see scheme). The starting materials are readily available through acetalization of *ortho*-bromobenzenethiol and subsequent Sonogashira coupling. This methodology provides an atom-economic route to sulfur-containing heteroarenes.

© 2006 Wiley-VCH Verlag GmbH & Co. KGaA, Weinheim

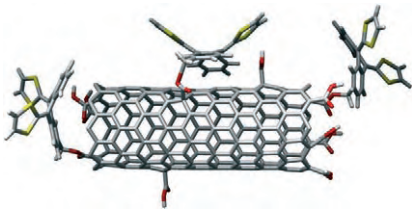


Putting the O into olefins: A highly regio- and enantioselective epoxidation of conjugated dienes was developed using glucose-derived ketone **1** as catalyst and oxone ($KHSO_5$) as oxidant to form vinyl *cis*-epoxides (see scheme).

Asymmetric Epoxidation

C. P. Burke, Y. Shi* ——— **4475 – 4478**

Regio- and Enantioselective Epoxidation of Dienes by a Chiral Dioxirane: Synthesis of Optically Active Vinyl *cis*-Epoxides

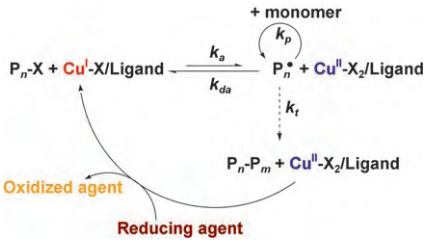


Spaced out: Single-walled carbon nanotubes (SWNTs) with covalently linked tetrathiafulvalene (TTF) derivatives have been synthetized and fully characterized as potential donor–acceptor nanoconjugates. Near-infrared flourescence and transient absorption measurements showed that the charge recombination dynamics is a function of the spacer linking the two moieties and the donor ability of the different TTF derivatives.

Donor–Acceptor Systems

M. Á. Herranz, N. Martín,* S. Campidelli, M. Prato,* G. Brehm, D. M. Guldi* ——— **4478 – 4482**

Control over Electron Transfer in Tetrathiafulvalene-Modified Single-Walled Carbon Nanotubes



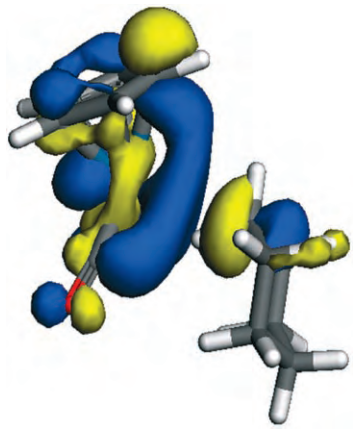
Staying active: The title method allows continuous and controlled polymerization with significantly less Cu catalyst than is required for conventional atom-transfer radical polymerization (as low as 10^{-3} mol% vs. monomer). The Cu^I activator is constantly regenerated by a reducing agent, which compensates for any loss of Cu^I as a result of radical termination reactions (see scheme).

Controlled Radical Polymerization

W. Jakubowski, K. Matyjaszewski* ——— **4482 – 4486**

Activators Regenerated by Electron Transfer for Atom-Transfer Radical Polymerization of (Meth)acrylates and Related Block Copolymers

Which bonds bind better? According to NMR experiments with the alkane complex [$CpRe(CO)_2$(cyclohexane)] at low temperatures, complexation with an axial proton is preferred over that through an equatorial one by about 1.5 kJ mol^{-1}. Calculations support this order of binding energies. The preference is proposed to be due to stronger electron donation through hyperconjugation from a C–H bond than from a C–C bond.



Alkane Ligands

D. J. Lawes, T. A. Darwish, T. Clark,* J. B. Harper,* G. E. Ball* ——— **4486 – 4490**

A Rhenium–Cyclohexane Complex with Preferential Binding of Axial C–H Bonds: A Probe into the Relative Ability of C–H, C–D, and C–C Bonds as Hyperconjugative Electron Donors?

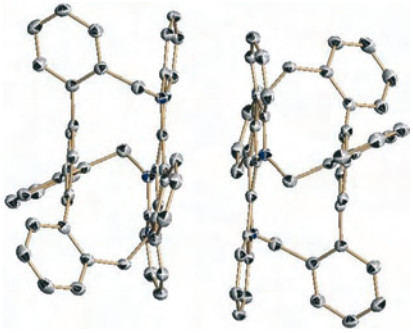
© 2006 Wiley-VCH Verlag GmbH & Co. KGaA, Weinheim

Contents

Cyclophane Structure and Behavior

B. Gómez-Lor,* G. Hennrich, B. Alonso, A. Monge, E. Gutierrez-Puebla, A. M. Echavarren* _____ **4491 – 4494**

A Redox-Active C_3-Symmetric Triindole-Based Triazacyclophane



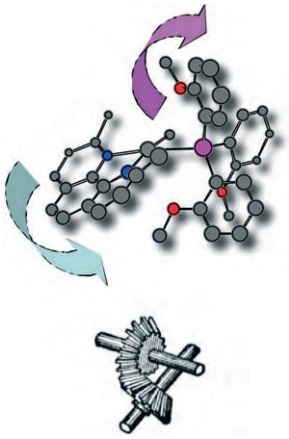
Spreading the charge: The highly stable dimeric radical cation of a C_3-symmetric triazacyclophane (see picture), with the positive charge delocalized over the two molecules, offers an excellent model for the study of intermolecular communication depending on hole hopping.

Synchronized Motion of Ligands

R. Romeo,* S. Carnabuci, L. Fenech, M. R. Plutino, A. Albinati ___ **4494 – 4498**

Overcrowded Organometallic Platinum(II) Complexes That Behave as Molecular Gears

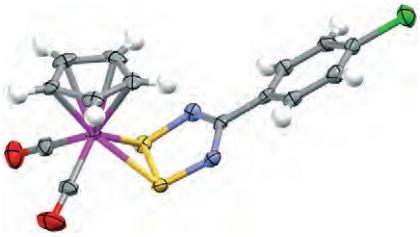
In gear: Dynamic ^{1}H NMR studies on some organometallic platinum(II) compounds reveal a synchronism between rotation around the Pt–P bond and the oscillation of a phenanthroline ligand between two nonequivalent exchanging sites. The system behaves as a molecular-sized analogue of a mechanical gear (see picture; C gray, N blue, O red, P purple) whose dynamic properties can be tuned through small structural changes.



Sulfur–Chromium Complex

H. F. Lau, V. W. L. Ng, L. L. Koh, G. K. Tan, L. Y. Goh,* T. L. Roemmele, S. D. Seagrave, R. T. Boeré* **4498 – 4501**

Cyclopentadienylchromium Complexes of 1,2,3,5-Dithiadiazolyls: η^2 π Complexes of Cyclic Sulfur–Nitrogen Compounds

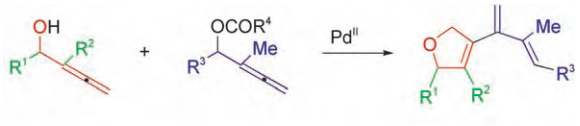


Diamagnetic π complexes are formed in the reaction between $[\{CpCr(CO)_3\}_2]$ and dithiadiazolyl dimers $[S_2N_2CR]_2$ (R = substituted phenyl rings) in which the heterocycles are η^2-coordinated to the metal in *endo* (depicted) or *exo* fashion. The isomers interconvert in solution at room temperature. These complexes are remarkable for retaining intact the S–S bonds of the dithiadiazolyl radicals (C gray, H white, O red, Cr purple, S yellow, N blue, Cl green).

Cross-Coupling Reactions

B. Alcaide,* P. Almendros,* T. Martínez del Campo ___ **4501 – 4504**

Reaction of Two Different α-Allenols in a Heterocyclization/Cross-Coupling Sequence: Convenient Access to Functionalized Buta-1,3-dienyl Dihydrofurans

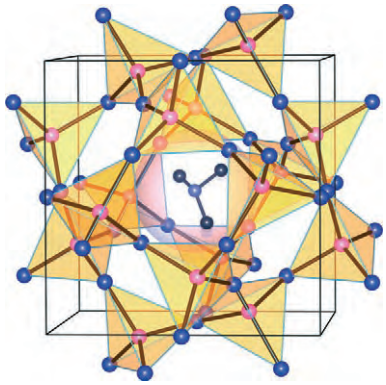


R^1, R^3 = alkyl, heteroalkyl, aryl, heteroaryl; R^2 = Me, Ph; R^4 = alkyl, aryl

In a single step a highly functionalized buta-1,3-dienyl-substituted 2,5-dihydrofuran unit can be formed from two different α-allenol derivatives through a novel heterocyclization/cross-coupling sequence (see scheme). The reactions are fast and totally chemo- and regioselective: No homocoupling products or heterocycles other than the five-membered oxacycle are formed.

© 2006 Wiley-VCH Verlag GmbH & Co. KGaA, Weinheim

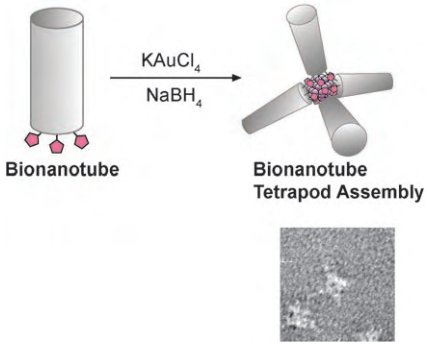
A new structure type, predicted as a possible candidate clathrasil structure, is exhibited by $P_4N_4(NH)_4(NH_3)$, which is the first microporous nitridic clathrate (see picture; blue N, pink P, dark gray H). $P_4N_4(NH)_4(NH_3)$ was synthesized at 11 GPa and 600 °C, and its crystal structure was determined by powder X-ray diffraction. The presence of intercalated ammonia was verified by mass chromatography and IR spectroscopy.



N,P Clathrates

F. Karau, W. Schnick* ____ **4505 – 4508**

A Nitridic Clathrate: $P_4N_4(NH)_4(NH_3)$

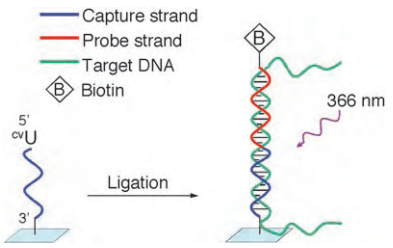


Tubular balls: Self-assembly of an Au nanocluster with bionanotubes of bacteriophage T4 gene product 5 (gp5) trimers has been demonstrated (see picture). The triad of His_6 fragments at the C terminus of $(gp5–His_6)_3$ contributed to the construction of an ordered tetrapod-like bionanotube assembly and the formation of Au nanoclusters with uniform size distribution.

Nanocluster Assembly

T. Ueno,* T. Koshiyama, T. Tsuruga, T. Goto, S. Kanamaru, F. Arisaka, Y. Watanabe* ____ **4508 – 4512**

Bionanotube Tetrapod Assembly by In Situ Synthesis of a Gold Nanocluster with $(Gp5–His_6)_3$ from Bacteriophage T4

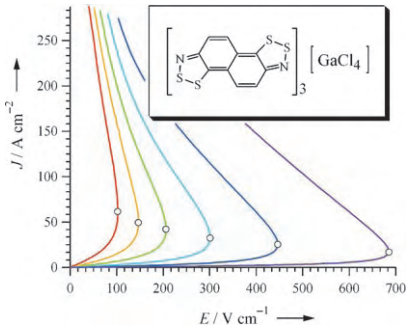


A chip for single mismatches: Results obtained with a photochemical-ligation-based DNA chip for enhanced discrimination of single-nucleotide polymorphisms (see scheme) show that the reaction takes place over a period of hours, with the 50% stage reached within 10 minutes. A single mismatch in the target sequence yielded extremely little ligated product (a rate 10^3-fold lower than for the complementary case).

DNA Recognition

S. Ogasawara, K. Fujimoto* **4512 – 4515**

SNP Genotyping by Using Photochemical Ligation



Resistance is useful: A thiazyl-radical salt, $[NT]_3[GaCl_4]$ (see structural diagram), exhibits negative resistance (see graph) in a charge-ordered state of the square columnar network of NT molecules. As the negative-resistance effect is observed at low electrical fields and high temperatures (290 K), it is potentially attractive for applications such as electrical devices.

Electron Transport

K. Okamoto, T. Tanaka, W. Fujita, K. Awaga,* T. Inabe ____ **4516 – 4518**

Low-Field Negative-Resistance Effect in a Charge-Ordered State of Thiazyl-Radical Crystals

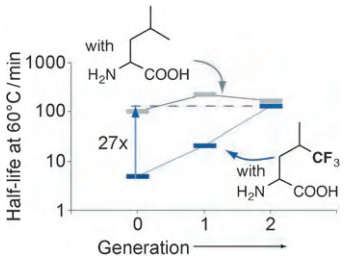
© 2006 Wiley-VCH Verlag GmbH & Co. KGaA, Weinheim

Contents

Directed Evolution

J. K. Montclare, D. A. Tirrell* **4518 – 4521**

Evolving Proteins of Novel Composition



Changing its nature: Global incorporation of noncanonical amino acids can alter the behavior of proteins in useful ways. In some cases, however, replacement of natural amino acids by noncanonical analogues (blue bars in picture) can cause loss of protein stability. After several generations, functional proteins of non-natural composition were prepared through residue-specific incorporation combined with directed evolution.

Sources

Product and Company Directory

You can start the entry for your company in "Sources" in any issue of *Angewandte Chemie*.

If you would like more information, please do not hesitate to contact us.

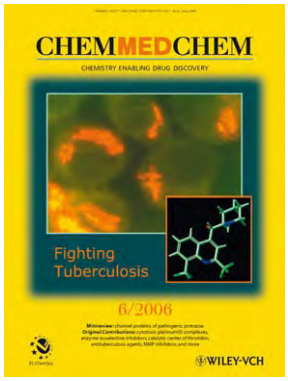
Wiley-VCH Verlag – Advertising Department
Tel.: 0 62 01 - 60 65 65
Fax: 0 62 01 - 60 65 50
E-Mail: MSchulz@wiley-vch.de

Service

Keywords — **4522**

Authors — **4523**

Preview — **4525**



For more information on ChemMedChem see www.chemmedchem.org

© 2006 Wiley-VCH Verlag GmbH & Co. KGaA, Weinheim



Functional Molecular Assemblies**

Jim A. Thomas

In the last decade, nanotechnology has moved from science-fiction novels into the research lab. As a result, "designer" molecular materials have become increasingly important. To construct and understand these systems requires an approach that often stretches over the whole of chemistry and into physics, biology, or materials science. However, judging from the excitement communicated by the participants of a recent meeting, it seems that although navigating this terra incognita is daunting, the intellectual rewards more than make up for it.

The organizing committee of the Royal Society of Chemistry Dalton Discussion 9 Meeting (DD9), held on April 19–21, 2006, interpreted its theme, Functional Molecular Assemblies, very widely. So, although this was an inorganic-chemistry meeting, participants from a wide range of molecular-based science attended.

The meeting was divided into four specific sub-themes, each introduced by a leading researcher. An unusual aspect was the time allocated to discussion—after several presentations, the floor was opened for contributions from the audience leading to exchanges that lasted for up to 45 minutes.

The opening session was on surface chemistry, and topics ranged from the use of rotaxane dyes as photographic inks to the synthesis of dendrimer-encapsulated quantum dots. Highlights included a fascinating talk by Bart Jan Ravoo from the Reinhoudt group (University of Twente) who explained a "molecular print-board" approach[1] for precisely positioning molecules in two dimensions. By using cyclodextrins immobilized on a surface as a substrate, the group "prints" molecules—through multivalent noncovalent interactions, stable positioning of guests such as ferrocene-terminated dendrimers is achieved. Ravoo explained how this method is being used to construct devices such as field-effect transistors.

One question that arose during the associated discussion was "when do noncovalent interactions between phases become more important than the interaction between molecules of a phase?" Another issue was the problem of reading and writing at the molecule scale. Since it was raised by Richard Feynman in his agenda-setting "Room at the Bottom" talk,[2] this problem has remained a great challenge to functional nanotechnology. A paper in this session outlined one approach to meeting this challenge. Mario Ruben of the Institute of Nanotechnology in Karlsruhe discussed the construction of coordination complex based nanoarchitectures and demonstrated that by employing current imaging tunneling spectroscopy (CITS), it is possible to image individual metal centers in 2×2 Co^{II}-based grids (Figure 1a). Later, during the second session on magnetic materials, Laurie Thompson (Memorial University, Newfoundland) showed images of a 3×3 Mn^{II}-based grid obtained by the same technique (Figure 1b). He also discussed bulk studies revealing that individual grid redox states are switchable, leading to changes in the magnetic properties of the grid. Furthermore, both researchers described successful strategies to produce extended structural arrangements. Given these observations it seems clear that high-density storage media based upon single molecules *are* possible.

Several presentations during the second session involved oligonuclear metal complexes and their possible use in molecular-based devices, for example, as candidates for quantum bits in quantum computational architectures. During his keynote lecture and the resulting discussion, Joel Miller of the University of Utah pointed out that although these latter systems are frequently called single molecular magnets they are often weakly coupled in the long range and hence are not true (bulk) magnets. In his talk, Miller elucidated how molecule-based bulk magnets can be designed and why such materials often have strikingly different properties from those of traditional atom-based systems. This point is illustrated by just one of the many systems described. Magnets based on second-row transition-metal complexes are comparatively rare; consequently Miller and colleagues have been investigating structures containing "paddle wheels" based on $[Ru_2(O_2CMe)_4]^+$ units. By

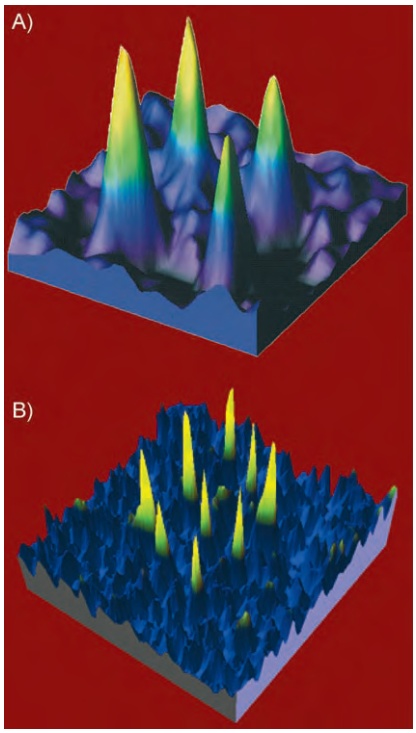


Figure 1. A) A 2×2 Co^{II} grid and B) a 3×3 Mn^{II} grid imaged with CITS. Adapted from references [3 and 4]; reproduced with permission of the Royal Society of Chemistry.

[*] Dr. J. A. Thomas
Department of Chemistry
University of Sheffield
Brook Hill, Sheffield S3 7HF (UK)
Fax: (+44) 114-273-8673
E-mail: james.thomas@sheffield.ac.uk

[**] Dalton Discussion 9: Functional Molecular Assemblies, April 19–21, 2006, Manchester (UK)

InterScience
© 2006 Wiley-VCH Verlag GmbH & Co. KGaA, Weinheim

using $[Cr(CN)6]^{3-}$ as a second charge-compensating unit, a 3D structure of interpenetrated cubic lattices was obtained. This system magnetically orders below 100 K and displays magnetic hysteresis. Interestingly, the hysteresis loop takes an unusual constricted form (Figure 2), and magnetic saturation occurs at magnetic-field strengths 30% higher than that of a related non-interpenetrated structure.

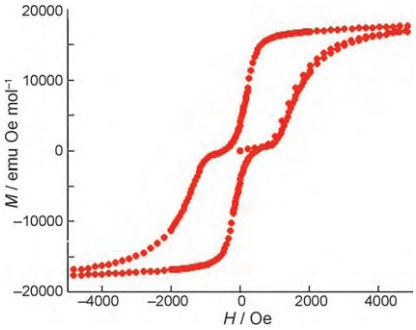


Figure 2. Constricted magnetic hysteresis for the interpenetrated cubic lattice structure of $[Ru_2(O_2CMe)_4]_3[Cr(CN)_6]$. Adapted from reference [5]; reproduced with permission of the Royal Society of Chemistry.

A third session, on self-assembly, began with Makoto Fujita of the University of Tokyo explaining how square-planar metal centers template the assembly of a wide range of discrete architectures with hydrophobic cavities; these cavities provide a nanospace for a number of unusual phenomena: For example, mixed-valence tetrathiafulvalene dimers can be generated and studied, common reactions such as Diels–Alder cyclization produce entirely new products, and previously short-lived intermediates in photochemical reactions of metal-carbonyl complexes can be structurally characterized.

After this, Markus Albrecht (RWTH-Aachen) described the self-assembly of large $[Ti_4L_4]^{8+}$ tetrahedral cages, and Rolf W. Saalfrank of the University of Erlangen–Nürnberg illustrated how the interactions of simple ligands with Fe^{III} that usually lead to metallacoronands assembly[6] can produce tetranuclear "stars". Two talks then illustrated how additional interactions can be used in assembly processes.

Lee Cronin (University of Glasgow) described triangular isopolyoxotungstate analogues of crown ethers, hypothesizing that the assembly of the structures is a result of symmetry transfer from the triethanolamine cations used in their preparation. Ed Constable of the University of Basel discussed the self-assembly of metal complexes driven by π stacking in the bulk phase and on surfaces. This latter study reinforced observations previously raised by Mario Ruben that self-assembly at surfaces lowers the symmetry and introduces new weak interactions, leading to new structures not found in crystals.

In this session, Sijbren Otto of the University of Cambridge introduced a thought-provoking concept—that secondary interactions *within* a receptor reinforce substrate binding. Suppose binding of a substrate by a protein is enthalpically favored but, owing to the loss of freedom in the final assembly, is entropically disfavored (Figure 3a); if binding to the substrate is accompanied by creation of intrareceptor interactions that only form on assembly of the host–guest complex (Figure 3b and c) then the entropic cost of creating two favorable interactions is only paid once. Otto then outlined how this effect could be used in synthetic receptors.

The subject of the last half day was photoactive materials. Papers by David Parker and Stephen Faulkner concerned the distinctive luminescent properties of lanthanide complexes. In his keynote lecture, Parker discussed his group's work at the University of Durham on complexes that sense specific ions and biomolecules. A point that clearly emerged from discussion was that the commonly made assumption that charged species are only appropriate for in vitro studies is incorrect. For example, Parker described how tricationic complexes that sense citrate or B-DNA in vitro are localized within nuclei in cellulo. More surprisingly, neutral and anionic analogues of one of these complexes show almost no cellular uptake. Faulkner then outlined how lanthanide centers can be photosensitized by coordination of suitable chromophores. He showed that phosphonate ligands yield complexes that are substitutionally robust, even in the presence of competing phosphate. Raymond Ziessel of ULP Strasbourg then showed that fluorescent boron dipyrromethane systems can be used for a variety of device applications including as hybrid materials such as luminescent zeolites.

Both the final two papers involved self-assembly *and* optical studies. In the first, Rainer Glaser of the University of Missouri-Columbia demonstrated how highly anisotropic materials with perfect polar order and layer stacking could be constructed from relatively simple aromatic azine building blocks. These materials have very high nonlinear optical responses with second-harmonic generation so efficient that it can be detected by the naked eye. In the last paper, Jim Thomas (University of Sheffield) discussed a general procedure for the assembly of kinetically robust mixed-valence molecular bowls constructed from ruthenium centers and hindered nucleobases.

In concluding remarks, Richard Winpenny applauded the speakers' readiness to present "work in progress" that was perhaps still not fully understood. As he and his fellow organizer Faulkner pointed out, this added fuel to the informal and stimulating conversations that took place within (and out-

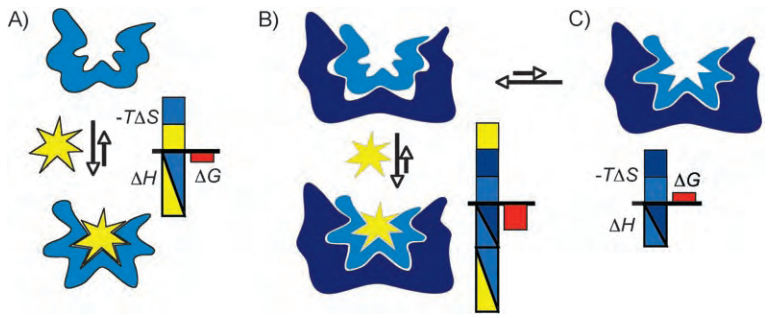


Figure 3. Thermodynamics of a protein binding to a ligand. A) Ligand binding with no intrareceptor interactions. B) Ligand binding with intrareceptor interactions. C) Intrareceptor interactions that cannot be formed without binding. Adapted from reference [7].

© 2006 Wiley-VCH Verlag GmbH & Co. KGaA, Weinheim

side) the lecture theater. A forthcoming special edition of *Dalton Transactions* will include all the DD9 presentations.

[1] T. Auletta, B. Dordi, A. Mulder, A. Santori, S. Onclin, C. M. Bruinink, M. Péter, C. A. Nijhuis, H. Beijleveld, H. Schönherr, G. J. Vancso, A. Casnati, R. Ungaro, B. J. Ravoo, J. Huskens, D. N. Reinhoudt, *Angew. Chem.* **2004**, *116*, 373; *Angew. Chem. Int. Ed.* **2004**, *43*, 369.

[2] "There's plenty of room at the bottom": R. P. Feynman in *Miniaturization* (Ed.: H. D. Hilbert), Reinhold, New York, **1961**, p. 282.

[3] N. Lin, S. Stepanow, F. Vidal, K. Kern, M. S. Alam, S. Strömsdörfer, V. Dremov, P. Müller, A. Landa, M. Ruben, *Dalton Trans.* **2006**, 2794.

[4] V. A. Milway, S. M. T. Abedin, V. Niel, T. L. Kelly, L. N. Dawe, S. K. Dey, D. W. Thompson, D. O. Miller, M. S. Alam, P. Müller, L. K. Thompson, *Dalton Trans.* **2006**, 2835.

[5] J. S. Miller, *Dalton Trans.* **2006**, 2742.

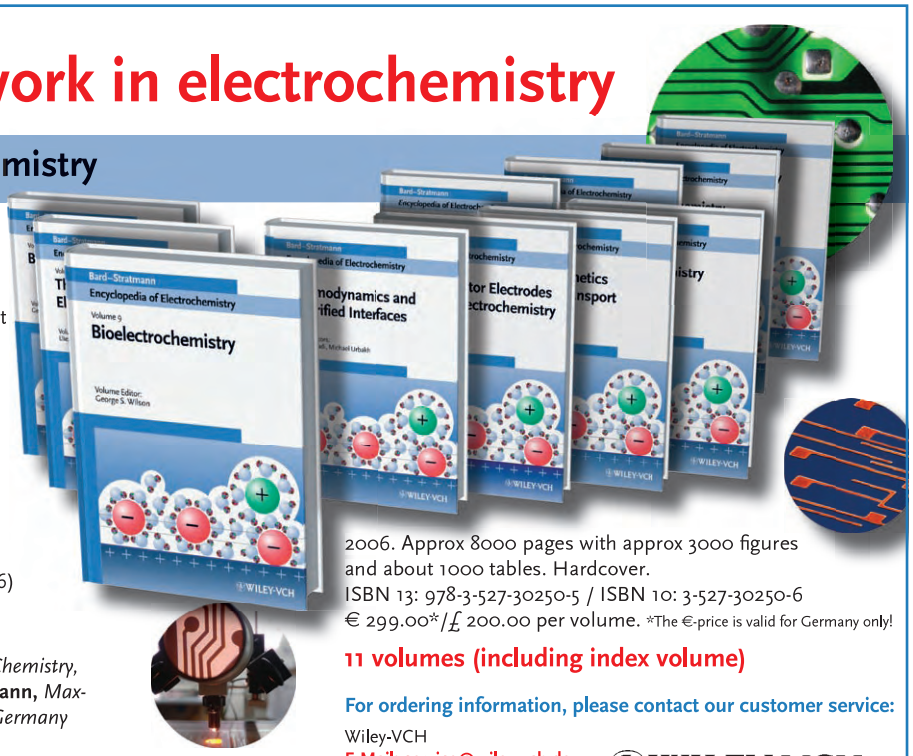
[6] See for example: R. W. Saalfrank, C. Deutcher, H. Maid, A. M. Ako, S. Dperner, T. Nakajima, W. Bauer, F. Hampel, B. A. Heß, N. J. R. van Eikema Hommes, R. Puchta, F. W. Heiemann, *Chem. Eur. J.* **2004**, *10*, 1899.

[7] S. Otto, *Dalton Trans.* **2006**, 2861.

DOI: 10.1002/anie.200602068

The definitive work in electrochemistry

Encyclopedia of Electrochemistry



Available Volumes:

1: Thermodynamics and Electrified Interfaces
2: Interfacial Kinetics and Mass Transport
3: Instrumentation and Electroanalytical Chemistry
4: Corrosion and Oxide Films
6: Semiconductor Electrodes and Photoelectrochemistry
7A+7B: Inorganic Electrochemistry
8: Organic Electrochemistry
9: Bioelectrochemistry

Forthcoming Volumes:

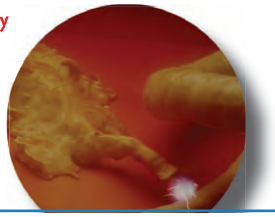
5: Electrochemical Engineering (Fall 2006)
10: Modified Electrodes (Fall 2006)
11: Index (Jan. 2007)

Editors-in-Chief: **Allen J. Bard,** *Department of Chemistry, University of Texas, Austin, USA/* **Martin Stratmann,** *Max-Planck-Institute for Iron Research, Duesseldorf, Germany*

Stay up-to-date in electrochemistry

- a total of 11 volumes makes this **the first and only** complete reference on electrochemistry
- covering **all aspects**, from fundamental research to applications in industry
- **easy access** to electrochemical topics

www.wiley-vch.de/bard/eoe



2006. Approx 8000 pages with approx 3000 figures and about 1000 tables. Hardcover.
ISBN 13: 978-3-527-30250-5 / ISBN 10: 3-527-30250-6
€ 299.00*/£ 200.00 per volume. *The €-price is valid for Germany only!

11 volumes (including index volume)

For ordering information, please contact our customer service:

Wiley-VCH
E-Mail: service@wiley-vch.de
www.wiley-vch.de

John Wiley & Sons, Inc.
E-Mail: custserv@wiley.com
www.wiley.com

John Wiley & Sons, Ltd.
E-Mail: cs-books@wiley.co.uk
www.wiley.com

WILEY-VCH
WILEY
WILEY InterScience® DISCOVER SOMETHING GREAT

26522604_gu

© 2006 Wiley-VCH Verlag GmbH & Co. KGaA, Weinheim

Hypervalent Iodine Compounds

DOI: 10.1002/anie.200601817

Hypervalent Iodine Goes Catalytic

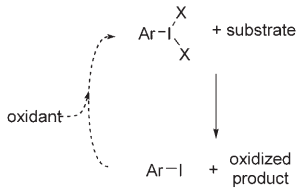
*Robert D. Richardson and Thomas Wirth**

Keywords:
catalysis · hypervalent compounds · iodine · oxidation · synthetic methods

The impressive development of hypervalent iodine chemistry in recent years is reflected by the growing number of publications and reviews[1] in this area. The synthesis of the first hypervalent iodine compound was accomplished more than one hundred years ago, but only recently have these compounds mutated from curiosities into useful reagents in organic synthesis.

Their main use is as very mild oxidants for the conversion of alcohols to carbonyl compounds, which tolerates various functionalities on highly complex molecules, but this is by no means the only area where these reagents can be employed. The use of hypervalent iodine compounds in the formation of carbon–carbon bonds in phenol coupling reactions or as precursors in the synthesis of benzyne can be very beneficial. In addition, a range of carbon–heteroatom bonds can be formed by using appropriate hypervalent iodine reagents. Activation of carbon–hydrogen bonds is also possible, and depending on the substrate, rearrangements or fragmentations can be induced by these reagents. With these nonmetallic oxidizing agents, issues of toxicity, which arise for many of the transition metals commonly involved in such processes, are avoided. Therefore, hypervalent iodine compounds offer high potential for the improvement of known reactions, not only from the environmental point of view; they are also potentially interesting reagents for the development of completely new synthetic transformations.

Until now, stoichiometric amounts and often even an excess of the hypervalent iodine reagents have been necessary to achieve the desired transformation. However, several recent publications have shown that it is indeed possible to use only a catalytic amount of an iodine-containing molecule together with a stoichiometric oxidant.[2] The oxidant generates the hypervalent iodine reagent in situ, and after the oxidative transformation, the reduced iodine-containing molecule is re-oxidized. This catalytic cycle is shown in Scheme 1 for a trivalent iodine compound.



Scheme 1. Catalytic cycle with hypervalent iodine compounds; Ar = aryl ligand; X = ligand (OH, OAc, OTs, $OCOCF_3$).

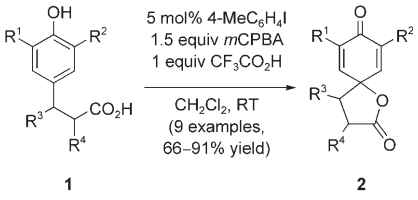
The basic requirement for a successful reaction generating and using hypervalent iodine compounds in only catalytic amounts is the ability of the stoichiometric oxidant to selectively generate the hypervalent iodine compound in the presence of the substrate. The oxidant must not react with the substrate, as the substrate should only be oxidized by the hypervalent iodine species. The stoichiometric oxidant has to be carefully selected to achieve the re-oxidation of the iodine compound under homogeneous reaction conditions.

A two-phase reaction using phase-transfer conditions should be particularly suitable to fulfill the requirements of a catalytic reaction, as the oxidant and the substrate could be separated in two different phases. This method would, however, require that the iodine-containing catalyst change its solubility properties with its oxidation state: the oxidized (hypervalent) form should be more soluble in the phase in which the substrate is soluble, and the reduced form more soluble in the other.

Known oxidants for the preparation of hypervalent iodine compounds from iodine-containing precursors include peracetic acid, sodium perborate, nitric acid, and hydrogen peroxide. Kita and co-workers recently introduced *meta*-chloroperbenzoic acid (*m*CPBA) as oxidant in the synthesis of novel and recyclable adamantane-based hypervalent iodine reagents.[3] This result paved the way for the development of catalytic reactions with hypervalent iodine compounds.

The same research group then reported the use of catalytic amounts of hypervalent iodine(III) reagents in the spirocyclization of phenol derivatives **1**, as shown in Scheme 2.[4] Only 5 mol% iodotoluene[5] is used together with 1.5 equiv *m*CPBA and 1 equiv trifluoroacetic acid to achieve the spirocyclization to lactones **2** in 66–91% yield.

Other stoichiometric oxidants are less successful; only *m*CPBA allows a



1 **2**

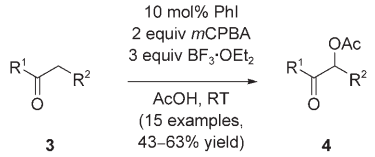
Scheme 2. Spirocyclization of phenol derivatives **1** with a catalytic amount of a hypervalent iodine reagent; R^1, R^2 = H, Me, Br; R^3, R^4 = H, Me.

[*] Dr. R. D. Richardson, Prof. Dr. T. Wirth
School of Chemistry
Cardiff University
Park Place, Cardiff CF10 3AT (UK)
Fax: (+44) 29-2087-6968
E-mail: wirth@cf.ac.uk

InterScience
© 2006 Wiley-VCH Verlag GmbH & Co. KGaA, Weinheim

catalytic reaction in high yield. Although the nature of the ligands X in the iodine(III) reagent (Scheme 1) is not defined, various acids, such as trifluoroacetic acid, enhance the yield of **2** in the catalytic reactions. The oxidant *m*CPBA does not react with substrate **1**, allowing a catalytic reaction.

The α-oxygenation of carbonyl compounds with hypervalent iodine reagents is a well established reaction. Ochiai and co-workers reported the combination of a catalytic amount of an iodoarene with *m*CPBA as oxidant for the α-acetoxylation of ketones **3** (Scheme 3).[6] The addition of 3 equiv



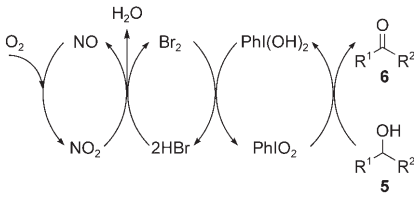
Scheme 3. α-Acetoxylation of ketones **3** with a catalytic amount of a hypervalent iodine reagent; R^1 = alkyl, allyl, aryl; R^2 = H, Me.

$BF_3{\cdot}OEt_2$ and 5 equiv water was essential. The reaction was performed in acetic acid (AcOH), and hence, α-acetoxylated ketones **4** were obtained in moderate to good yields (43–63%). Screening of different iodoarenes revealed that iodobenzene resulted in the highest yields; the introduction of either electron-withdrawing or electron-donating substituents decreased the catalytic efficiency of the iodoarene. The use of 10 mol% iodobenzene is necessary. When smaller amounts are used, the reaction slows, and Baeyer–Villiger oxidation products resulting from a direct reaction of *m*CPBA and the ketone are observed.

An extension of this reaction through the use of *para*-toluenesulfonic acid in acetonitrile, instead of acetic acid, was reported recently for the α-tosylation of ketones.[7] In this version, the boron trifluoride diethyl ether complex was not necessary, and the α-tosylated ketones were obtained in good yields (63–88%, 9 examples). Even a polystyrene-supported iodoarene could be employed successfully as a catalyst.

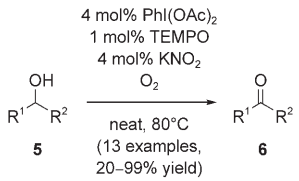
Some oxidations of alcohols to carbonyl compounds can also be effected with iodine(III) reagents in the presence of catalytic amounts of 2,2,6,6-tetramethyl-1-piperidinyl-oxyl (TEMPO)[8] or metal complexes,[9] but usually iodine(V) reagents are used for the oxidation of carbon–heteroatom bonds. Their generation from catalytic amounts of an iodine(III) or iodine(I) compound with an oxidant is the prerequisite for a successful catalytic oxidation protocol.

Examples of both strategies, oxidation with catalytic amounts of iodine(III) or iodine(V), have already been published. The use of oxygen as the stoichiometric oxidant is environmentally benign and has been coupled with an NO to NO_2 oxidation to catalytically generate elemental bromine, as shown in Scheme 4. The bromine then oxidizes iodine(III) to iodine(V).



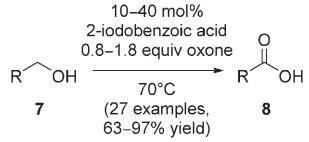
Scheme 4. Catalytic generation of hypervalent iodine compounds coupled with oxidation of alcohols **5** using air as stoichiometric oxidant; R^1 = alkyl, aryl; R^2 = H, alkyl.

The success of this approach is based on the catalytic cascade reaction observed by Liang, Hu, and co-workers in a TEMPO-mediated oxidation of alcohols.[10] Liu and co-workers replaced TEMPO with iodoxybenzene ($PhIO_2$) and developed conditions for oxidations of alcohols **5** to ketones **6** in water (Scheme 4).[11] Another oxygen-driven conversion of alcohols to carbonyl compounds, reported by Li and co-workers, uses catalytic amounts of iodine(III) reagents in a TEMPO-mediated reaction (Scheme 5).[12]



Scheme 5. Oxidation of alcohols **5** with a catalytic amount of a hypervalent iodine reagent using oxygen as stoichiometric oxidant; R^1 = alkyl, allyl, aryl; R^2 = H, Me..

The compound 1-hydroxy-1,2-benziodoxol-3(1*H*)-one-1-oxide (IBX)[13] is a well-established reagent for oxidation reactions and has also attracted theoretical interest.[14] The simple one-step oxidation of 2-iodobenzoic acid to IBX with oxone[15] has served as a basis for the development of catalytic reactions. Vinod and co-workers,[16] and Schulze and Giannis[17] have recently published such IBX oxidations with oxone as stoichiometric oxidant. Whereas Vinod and co-workers used an mixture of acetonitrile/water as solvent, the research group of Giannis applied a similarly efficient biphasic (ethyl acetate/water) solvent system with an additional phase-transfer catalyst (nBu_4NHSO_4). Aliphatic primary alcohols **7** are oxidized to the corresponding carboxylic acids **8** under these reaction conditions (Scheme 6). Only benzyl alcohol yielded the corresponding aldehyde and was not oxidized further.



Scheme 6. Oxidation of alcohols **7** with a catalytic amount of IBX using oxone as stoichiometric oxidant; R = alkyl.

The catalytic reactions presented herein will surely lead to the increased application of reactions mediated by hypervalent iodine reagents. It is no longer necessary to prepare the hypervalent iodine compounds, as the iodide precursors can be used. The transfer of established protocols using hypervalent iodine reagents to procedures using only catalytic amounts of iodide precursors and a stoichiometric oxidant should lead to improved synthetic strategies. If dealing with more sensitive substrates or other heteroatoms (sulfur, nitrogen), the development of catalytic transformations using a stoichiometric oxidant will be more difficult, and a fine-tuning of reaction rates and reactivities will be necessary.

[1] a) T. Wirth, *Angew. Chem.* **2005**, *117*, 3722–3731; *Angew. Chem. Int. Ed.* **2005**, *44*, 3656–3665; b) R. M. Moriarty, *J.*

 © 2006 Wiley-VCH Verlag GmbH & Co. KGaA, Weinheim

Org. Chem. **2005**, *70*, 2893 – 2903; c) Ed.: T. Wirth, *Top. Curr. Chem.* **2003**, *224*; d) V. V. Zhdankin, P. J. Stang, *Chem. Rev.* **2002**, *102*, 2523 – 2584.

[2] T. Dohi, Y. Kita, *Kagaku* **2006**, *61*, 68 – 69.

[3] a) H. Tohma, A. Maruyama, A. Maeda, T. Maegawa, T. Dohi, M. Shiro, T. Morita, Y. Kita, *Angew. Chem.* **2004**, *116*, 3679 – 3682; *Angew. Chem. Int. Ed.* **2004**, *43*, 3595 – 3598; b) T. Dohi, A. Maruyama, M. Yoshimura, K. Morimoto, H. Tohma, M. Shiro, Y. Kita, *Chem. Commun.* **2005**, 2205 – 2207.

[4] T. Dohi, A. Maruyama, M. Yoshimura, K. Morimoto, H. Tohma, Y. Kita, *Angew. Chem.* **2005**, *117*, 6349 – 6352; *Angew. Chem. Int. Ed.* **2005**, *44*, 6193 – 6196.

[5] Instead of the iodoarene, a catalytic amount of a hypervalent iodine reagent can be used as well.

[6] M. Ochiai, Y. Takeuchi, T. Katayama, T. Sueda, K. Miyamoto, *J. Am. Chem. Soc.* **2005**, *127*, 12244 – 12245.

[7] Y. Yamamoto, H. Togo, *Synlett* **2006**, 798 – 800.

[8] a) A. Dondoni, A. Massi, E. Minghini, S. Sabbatini, V. Bertolasi, *J. Org. Chem.* **2003**, *68*, 6172 – 6183; b) A. De Mico, R. Margarita, L. Parlanti, A. Vescovi, G. Piancatelli, *J. Org. Chem.* **1997**, *62*, 6974 – 6977.

[9] a) W. Sun, H. Wang, C. Xia, J. Li, P. Zhao, *Angew. Chem.* **2003**, *115*, 1072 – 1074; *Angew. Chem. Int. Ed.* **2003**, *42*, 1042 – 1044; b) R. S. Varma, R. Dahiya, R. K. Saini, *Tetrahedron Lett.* **1997**, *38*, 7029 – 7032.

[10] R. Liu, X. Liang, C. Dong, X. Hu, *J. Am. Chem. Soc.* **2004**, *126*, 4112 – 4113.

[11] R. Mu, Z. Liu, Z. Yang, Z. Liu, L. Wu, Z.-L. Liu, *Adv. Synth. Catal.* **2005**, *347*, 1333 – 1336.

[12] C. I. Herrerías, T. Y. Zhang, C.-J. Li, *Tetrahedron Lett.* **2006**, *47*, 13 – 17.

[13] a) T. Wirth in *Organic Synthesis Highlights V* (Eds.: H.-G. Schmalz, T. Wirth), Wiley-VCH, Weinheim, **2003**, pp. 144 – 150; b) T. Wirth, *Angew. Chem.* **2001**, *113*, 2893 – 2895; *Angew. Chem. Int. Ed.* **2001**, *40*, 2812 – 2814.

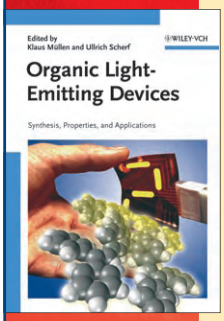
[14] a) M. J. Gallen, R. Goumont, T. Clark, F. Terrier, C. M. Williams, *Angew. Chem.* **2006**, *118*, 2995 – 3000; *Angew. Chem. Int. Ed.* **2006**, *45*, 2929 – 2934; b) J. T. Su, W. A. Goddard III, *J. Am. Chem. Soc.* **2005**, *127*, 14146 – 14147.

[15] M. Frigerio, M. Santagostino, S. Sputore, *J. Org. Chem.* **1999**, *64*, 4537 – 4538.

[16] A. P. Thottumkara, M. S. Bowsher, T. K. Vinod, *Org. Lett.* **2005**, *7*, 2933 – 2936.

[17] A. Schulze, A. Giannis, *Synthesis* **2006**, 257 – 260.

Wiley-VCH BOOK SHOP



K. Müllen / U. Scherf (eds.)

Organic Light Emitting Devices

Synthesis, Properties and Applications

Reflecting a decade of intense research, the contributions here from academic and industrial leaders combine the fundamentals and latest research results with application know-how and examples of functioning displays, covering all four important aspects.

ISBN 3-527-31218-8, 426 pp, cl, € 139.00



N. E. Schore

Arbeitsbuch Organische Chemie

Wer die didaktischen Qualitäten des „Vollhardt“ wirklich ausschöpfen und sich gründlich auf die Prüfung vorbereiten will, braucht zur Selbstkontrolle und zur Vertiefung dieses Ergänzungswerk. Das Lehrbuch und das Arbeitsbuch: Auch in der 4. Auflage ein bewährtes Gespann.

ISBN 3-527-31526-8, approx. 340 pp, pr, approx. € 34.90

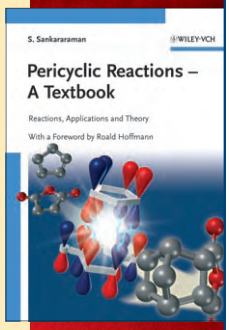
S. Sankararaman

Pericyclic Reactions – A Textbook

Reactions, Applications and Theory

This long awaited textbook presents Diels-Alder reactions, electrocyclic reactions, sigmatropic rearrangements plus many more topics in a highly didactic way, with both classical and new examples explained in detail. With a foreword by Nobel Laureate Roald Hoffmann.

ISBN 3-527-31439-3, 432 pp, pr, € 49.90



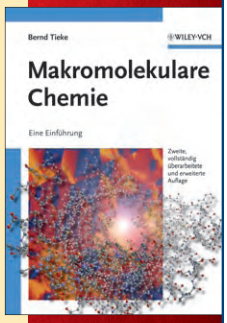
B. Tieke

Makromolekulare Chemie

Eine Einführung

Für Chemiker, Polymerchemiker und besonders für Chemiestudenten ist der „Tieke“ ein gelungenes und ausgewogenes Lehrbuch über das Basiswissen in der Makromolekularen Chemie. Mit bereits bewährter Didaktik wird der Stoff in verständlicher Form und klar gegliedert dargestellt.

ISBN 3-527-31379-6, 391 pp, pr, € 39.90



You can order online via **http://www.wiley-vch.de**
Wiley-VCH Verlag GmbH & Co. KGaA · POB 10 11 61 · D-69451 Weinheim, Germany
Phone: 49 (0) 6201/606-400 · **Fax:** 49 (0) 6201/606-184 · **E-Mail:** service@wiley-vch.de

WILEY-VCH

BS_0512_OC3_4c_1~2h_gu

 © 2006 Wiley-VCH Verlag GmbH & Co. KGaA, Weinheim

Biosynthesis

DOI: 10.1002/anie.200504284

Stereochemical Uniformity in Marine Polyether Ladders—Implications for the Biosynthesis and Structure of Maitotoxin**

*Andrew R. Gallimore and Jonathan B. Spencer**

Keywords:
antibiotic · biosynthesis · epoxidation · polyether ladders · polyketide synthase

The largest known, nonpolymeric natural product, maitotoxin, is a 3422 Da polyketide-derived polycyclic ether isolated from the marine dinoflagellate, *Gambierdiscus toxicus*.[1] The structure of maitotoxin consists of four extended fused-ring systems termed polyether ladders, A–D (Figure 1). The family of marine polyether ladders (Figure 1 and Figure 2) can be grouped into 14 backbone structures and has gained much notoriety in being responsible for countless cases of human food poisoning and massive fish kills.[2] Maitotoxin itself displays the highest toxicity of any nonproteinaceous natural product isolated thus far.[3]

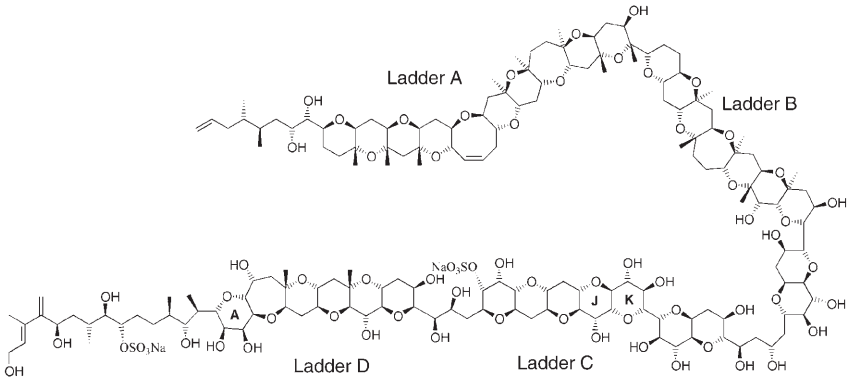


Figure 1. Maitotoxin.

The biogenesis of the polyether ladders, whilst attracting speculation, has advanced little further than the identification of their polyketide origin. Although labeling studies have shed some light on the construction of the obligatory polyketide chain precursor,[4] anything further than this remains speculative. However, the most closely analogous non-marine molecules, the polyether antibiotics, have been helpful in generating biosynthetic models for the more elaborate marine structures. In particular, monensin, a polyether ionophore antibiotic isolated from *Streptomyces cinnamonensis*,[5] has been studied fairly extensively.[6] A biosynthetic proposal was first put forward by Cane, Celmer, and Westley.[7] The Cane–Celmer–Westley model involves a polyketide-derived triene intermediate, "premonensin", which is subsequently epoxidized and cyclized in a cascade of S_N2 epoxide openings (Scheme 1). This hypothesis has remained foremost and has received widespread acceptance. $^{18}O_2$ labeling and sequencing of the gene cluster support this model.[8,9] Crucially, inactivation of the gene thought to be responsible for epoxidation of the double bonds recently led to the isolation of a triene shunt metabolite by our group.[10] Obviously, this strongly suggests that a triepoxide intermediate precedes monensin. The structures of the marine toxins also suggest that cyclization of a polyepoxide precursor may be a general biosynthetic strategy for the construction of polycyclic ethers. Indeed, both Shimizu and Nakanishi have independently proposed such a model for brevetoxin A—an octaepoxide precursor cyclizes in a cascade of S_N2 epoxide openings, mechanistically similar to that proposed for monensin (Scheme 2).[11] Indirect evidence for such a mechanism is provided by the $^{18}O_2$-labeling pattern of okadaic acid, a related marine polyether, suggesting an epoxide intermediate.[12] Also, the isolation of 27,28-epoxy-brevetoxin-B (the double bond in the 8-membered H ring is epoxidized) may suggest the extraneous over-epoxidation of a polyene precursor.[13]

Although a polyepoxide intermediate may be feasible en route to the brevetoxin skeleton, a straightforward extrapolation of the Cane–Celmer–Westley cyclization mechanism cannot be considered wholly satisfactory. The most notable concern is the manner in which the polyepoxide must cyclize to

[*] A. R. Gallimore, Dr. J. B. Spencer
University Chemical Laboratory
University of Cambridge
Cambridge CB21EW (UK)
Fax: (+44) 1223-336-362
E-mail: jbs20@cam.ac.uk

[**] We thank the EPSRC for a studentship to A.R.G.

Supporting information for this article is available on the WWW under http://www.angewandte.org or from the author.

WILEY InterScience DISCOVER SOMETHING GREAT
© 2006 Wiley-VCH Verlag GmbH & Co. KGaA, Weinheim

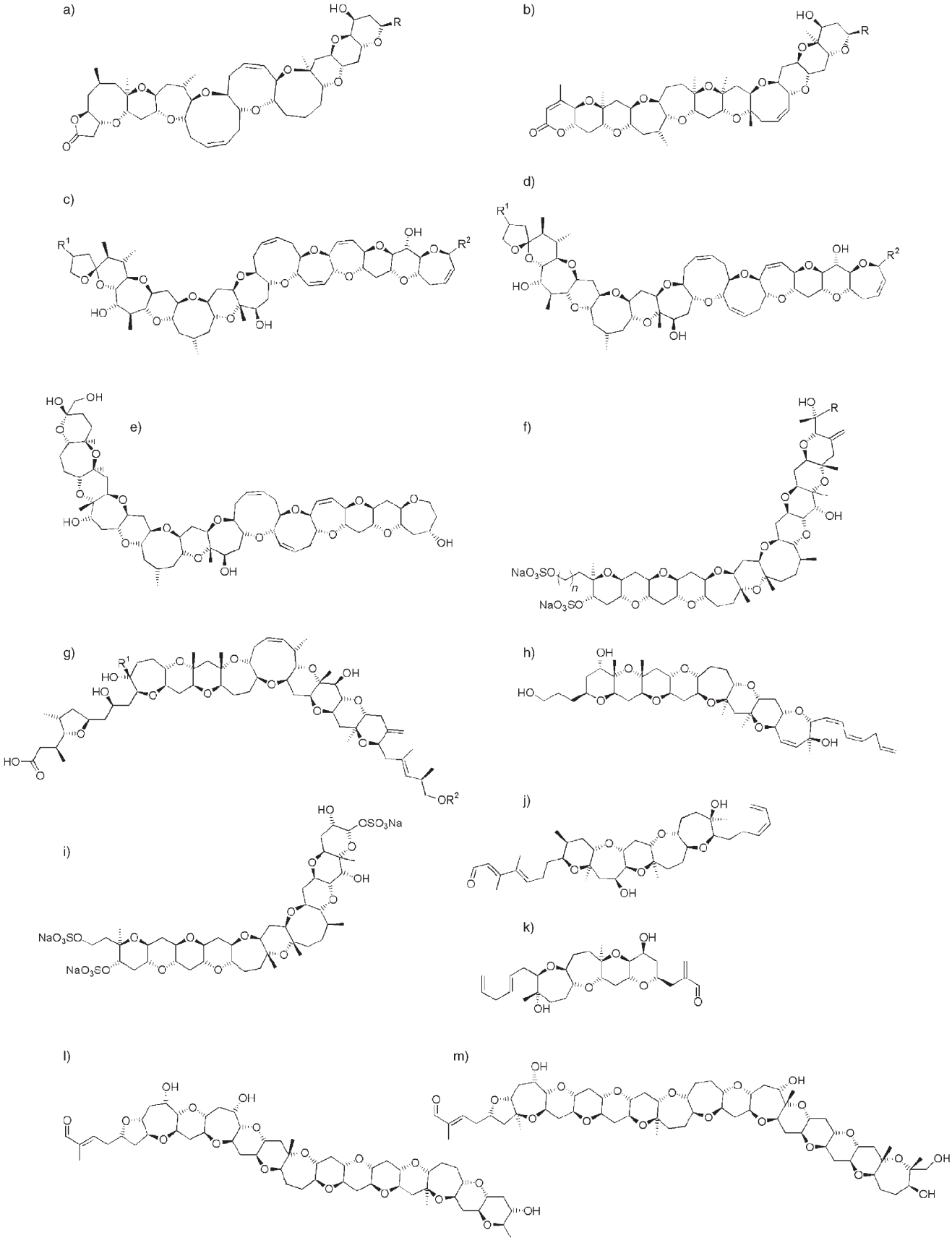
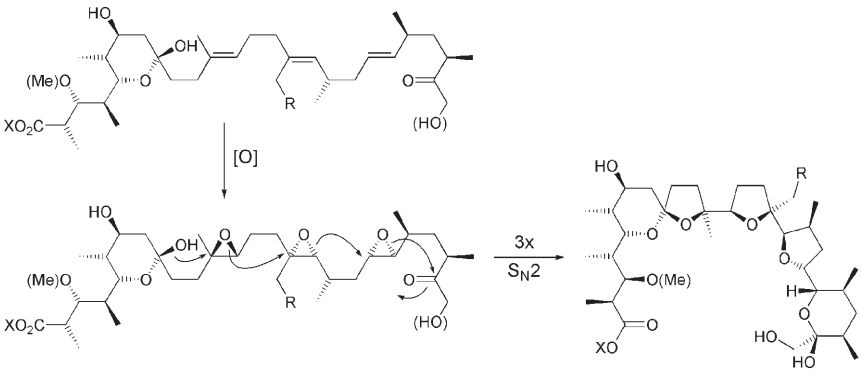
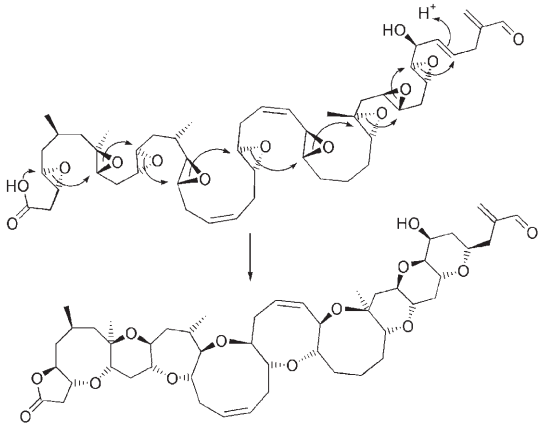


Figure 2. Marine polyether-ladder backbones. a) Brevetoxin type 1, b) Brevetoxin type 2, c) Ciguatoxin type 1, d) Ciguatoxin type 2, e) C-CTx-1, f) Yessotoxin, g) Gambieric Acid, h) Gambierol, i) Adriatoxin, j) Brevenal, k) Hemibrevetoxin B, l) Gymnocin A, m) Gymnocin B.

© 2006 Wiley-VCH Verlag GmbH & Co. KGaA, Weinheim



Scheme 1. Cane–Celmer–Westley model for monensin biosynthesis.



Scheme 2. Shimizu/Nakanishi cascade mechanism for brevetoxin A cyclization.

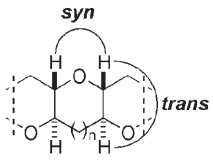
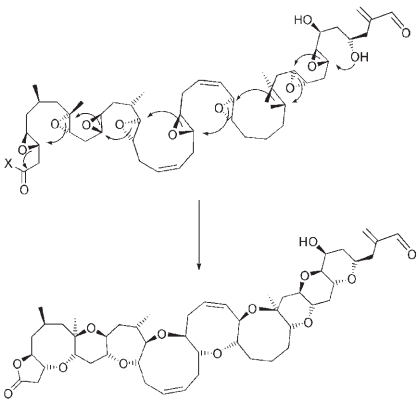


Figure 3. Common structural features of ladder ring junctions.

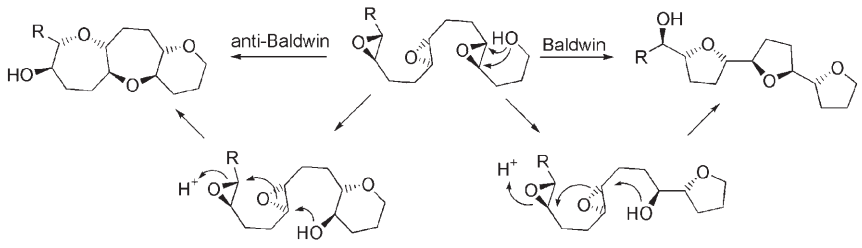
generate the contiguous fused ether rings characteristic of these toxins. Unlike the monensin triepoxide intermediate, which must cyclize in a series of favored *exo*-tet S_N2 closures, a pre-brevetoxin polyepoxide would entail nine disfavored *endo*-tet closures, each violating Baldwin's rules (Scheme 3)[14] As of yet, no satisfying and unifying hypothesis has been proposed for all the polyether ladders beyond the idea of a pre-brevetoxin polyepoxide intermediate.

A characteristic feature of these toxins is the *syn/trans* stereochemistry of the ring junctions (Figure 3). Examination of all known polyether ladders demonstrates that this feature is conserved across the family. This prompted us to carry out the retrobiosynthetic analyses to their hypothetical polyepoxide precursors. This has revealed, for the first time, that all of the contiguous rings, in any single polyether, can be derived from stereochemically identical, either all (*R*,*R*) or all (*S*,*S*), *trans* epoxides. As the mechanism of terminal ring formation is unclear in some cases, this rule can only be generally applied to ring junctions. However, when terminal ring closure does appear to involve a *trans* epoxide, then our rule is not deviated from. Further, the direction of cyclization is always, to some degree, ambiguous. To illustrate this, Shimizu and Nakanishi show the cyclization from a series of (*R*,*R*)-*trans* epoxides that terminates in the protonation of a double bond.[11] However, by simply invoking a series of (*S*,*S*)-*trans* epoxides, the cyclization may proceed from the opposite direction, terminating by closure of the lactone ring (probably more likely) and yielding the same structure (Scheme 4). What is important is the



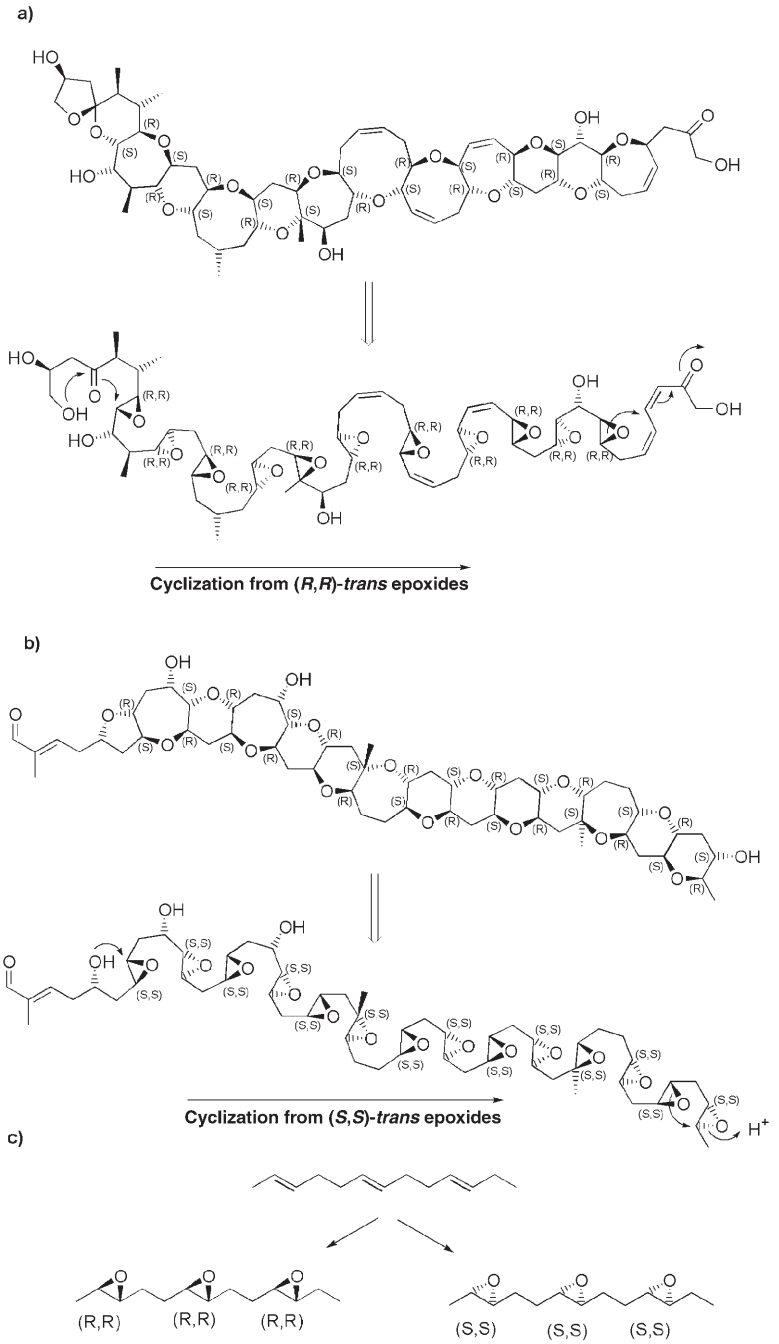
Scheme 4. An alternative to the Shimizu/Nakanishi brevetoxin cyclization mechanism from all (*S*,*S*)-*trans* epoxides (compare with Scheme 2).

relative stereochemistry of the epoxides and, thus, likewise of the final cyclized structure. This, of course, applies to any of the ladders (a–m) in Figure 2 in which the absolute stereochemistry has not yet been established. It follows that all of the *trans* double bonds in the polyene precursor are epoxidized from the same face and thus a single monooxygenase could be responsible for all of the *trans* epoxides (Scheme 5). The polyene intermediate may contain over twenty double bonds, as would be the case with maitotoxin. Differential epoxidation of these would, obviously, require them to be distinguished by their individual monooxygenase enzymes. Intuitively, this seems unlikely and examination of the ladder structures supports this view. A broadly specific monooxygenase could effect all of the asymmetric epoxidations from one face of the polyene without difficulty. This rule is shown to apply to all the polyether ladders thus far characterized—namely, the brevetoxins and hemibrevetoxin B[15], the yessotoxins (and the truncated adriatoxin),[16] the Pacific and Caribbean ciguatoxins,[17] the gambieric acids and gam-



Scheme 3. Epoxide opening showing a Baldwin versus anti-Baldwin pathway.

© 2006 Wiley-VCH Verlag GmbH & Co. KGaA, Weinheim



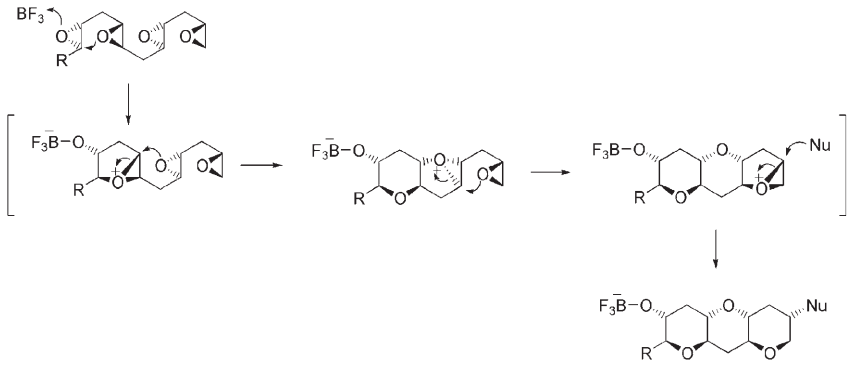
Scheme 5. Retrobiosynthetic analyses of a) Ciguatoxin (CTX); b) Gymnocin A; c) Epoxidation patterns. Arrows depicting the epoxide cyclization process have been omitted for clarity. However, see Scheme 2 for a general mechanism.

bierol,[18] the gymnocins[19] and brevenal[20] (see the Supporting Information). Interestingly, maitotoxin appears exceptional, but this will be returned to later.

Assuming a polyepoxide precursor to the polyether ladders, the mechanism of cyclization is of fundamental concern. The cyclization of polyepoxide precursors, in the construction of fused polycyclic ethers, has been explored as an approach to total synthesis, as well as facilitating mechanistic proposals for their biosynthesis. Although synthetic models have shown that formation of polycyclic ethers from polyepoxides is facile, Baldwin's rules are adhered to in simple, acid-catalyzed reactions.[21] However, there have been three distinct biomimetic approaches taken to effect apparent *endo*-selective epoxide opening in ring closure.[22] The first method uses successive ring closure of a hydroxy polyepoxide, which is analogous to the Cane–Celmer–Westley mechanism. However, the attack is guided electronically by substituents on the *endo* position of the epoxide. In the early work of Nicolaou, for example, an electron-rich double bond is placed adjacent to the *endo* position and stabilizes the *endo* transition state by electron donation from the π orbital. This has been effective in achieving both 6-*endo* over 5-*exo* selectivity, as well as 7-*endo* over 6-*exo* selectivity, in such epoxide openings.[23] The putative biosynthetic polyepoxides do not have such directing groups, however, so the selectivity could not occur in this manner. The second method that has been used to obtain *endo* selectivity is a successive ring expansion of a polyepoxide, in which the epoxide acts as a nucleophile (Scheme 6). This methodology typically employs a suitable Lewis acid to activate the terminal epoxide.[24] The first step in such a reaction is the intramolecular attack by an adjacent epoxide on the activated terminal epoxide to generate a bridged oxonium ion intermediate—the initiation step. The next step is the nucleophilic attack of the second epoxide, either *exo* or *endo*, to open the oxonium ion. Thus, the first ether ring is completed and a second oxonium ion is formed. This forms the electrophilic site for the next epoxide, and so on. The *endo* regioselectivity has been explained by minimization of ring strain in the formation of each oxonium ion. *Endo* attack, although disfavored in terms of Baldwin's rules, generates a less-strained oxonium ion, an effect that appears to dominate.[25] In theory, the Lewis acid mediated initiation step, or its enzymatic equivalent, could generate the complete polycyclic structure. This could be an elegant biosynthetic strategy and may be considered as a feasible alternative to the Cane–Celmer–Westley extrapolation. However, the synthetic methodology has serious limitations in terms of the number of rings that may be assembled as well as the substituents and ring sizes, perhaps making it less appealing as a general biosynthetic proposal for the polyether ladders.[26]

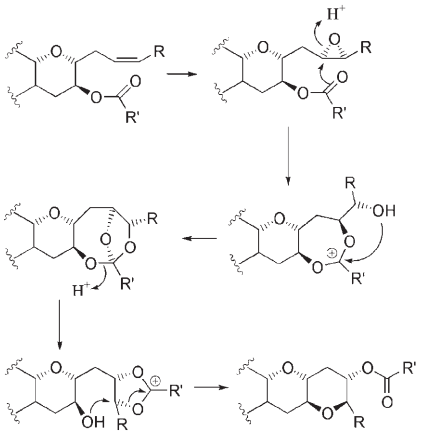
The third approach, developed by Giner, involves the rearrangement of an epoxy ester and is a very different mode of cyclization from the other two bio-

 © 2006 Wiley-VCH Verlag GmbH & Co. KGaA, Weinheim



Scheme 6. Lewis acid initiated ring-expansion approach to polyether synthesis.

mimetic models (Scheme 7).[27] Extrapolating this synthetic strategy to the biosynthesis of polyethers would require an all-*cis* polyene precursor, noted as



Scheme 7. Formation of a fused polycyclic ether through an epoxy ester rearrangement.

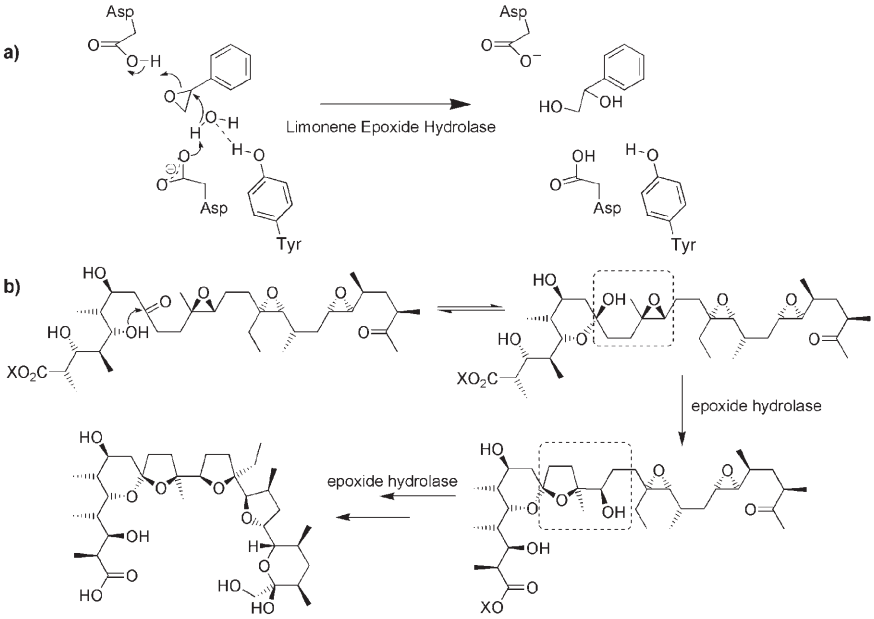
advantageous in explaining the *cis* bonds in the brevetoxins and ciguatoxins. Although an inventive synthetic approach to obtaining *endo* selectivity, it seems rather overcomplicated for an enzyme-catalyzed reaction.

Perhaps the most straightforward biosynthetic methodology would involve the stepwise closure of each ring by an epoxide hydrolase. The role of the enzyme would simply be to protonate the epoxide and direct the hydroxy nucleophile so as to close the ring in an *endo*-selective manner. Recently, we provided evidence for the involvement of epoxide hydrolases in the cyclization of monensin.[28] The enzymes have homology to limonene epoxide hydrolase, an enzyme that employs simple acid–base chemistry[29] and, unlike classical epoxide hydrolases, does not involve an enzyme-bound intermediate (Scheme 8).[30] Further to this, the uniform stereochemistry of the proposed marine polyepoxides suggests a single epoxide hydrolase could be responsible for all of the ring closures.

Although a stepwise cyclization accomplished by an epoxide hydrolase is a rational model, the inherent reactivity of the hypothetical polyepoxide intermediate may itself be a cause for concern. All of the double bonds of the prerequisite polyene must each be epoxidized and only when this is complete may the process of cyclization begin, so as to effect the smooth conversion of the polyepoxide to a polycyclic ether. An in trans epoxidation process, in which each double bond is epoxidized as it is formed on the polyketide synthase, would provide a more closely controlled sequential model. However, potentially there is also the problem of avoiding nonenzymatic side reactions during the construction of a series of somewhat reactive epoxides. So far, gymnocin B contains the largest number of contiguous rings (15) of any polyether ladder. However, there is no reason to suggest that gymnocin B represents the ceiling level in this respect. Any sequential biosynthetic model would, ideally, be applicable to any hypothetical polyether ladder of any length.

By coupling the epoxidation and cyclization steps more closely, this concern could be circumvented—the epoxidation of the first double bond creates the substrate for the epoxide hydrolase and the first ring is then closed. Epoxidation of the second double bond then presents the epoxide hydrolase with its next substrate. This iterative process continues until the final polycyclic structure is realized. The epoxidase and hydrolase enzymes would thus work in close cooperation, perhaps as a multienzyme complex. This bis-enzymatic model avoids constructing a polyepoxide prior to cyclization and may in fact be simplified further.

Janda et al. have utilized a "catalytic antibody" to direct the *endo* cyclization of hydroxy epoxides.[31] These antibodies are generated by means of a hapten that mimics the *endo* transition state. The suitably programmed antibody



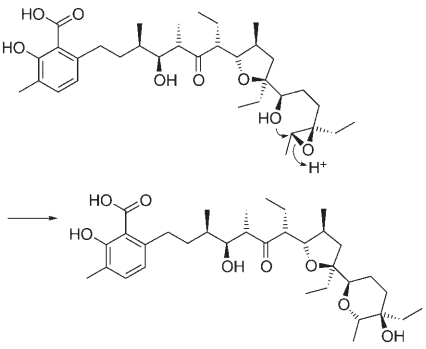
Scheme 8. a) Mechanism of styrene oxide hydrolysis by limonene epoxide hydrolase; b) Putative role of epoxide hydrolases in monensin cyclization.

 © 2006 Wiley-VCH Verlag GmbH & Co. KGaA, Weinheim

merely intercedes at, or near, the transition state to alter the energy balance in favor of the otherwise disfavored reaction pathway (Scheme 9). It is hypothesized that, through suitably placed charged residues, the antibody simply stabilizes the *endo* transition state relative to the *exo* as the tethered hydroxy group attacks. Applying this to polyether construction, it is feasible that, as the monooxygenase epoxidizes each double bond of the polyene, the bound enzyme acts in such a manner and facilitates *endo* attack of the hydroxy nucleophile. The size of the ring being closed would be largely irrelevant (the nine-membered ring of brevetoxin A may represent a realistic limit in this regard). The role of the enzyme at this stage would be no more than to bind and activate the newly formed epoxide, thus ensuring that the energy of the *endo* transition state is lowered relative to the *exo*. Once the ring is closed, the enzyme dissociates and moves on to the next double bond (Scheme 10). A distinct hydrolase enzyme that catalyzes ring closure may be superfluous. The oxidation–cyclization may be considered a single step and, overall, a single enzyme converts a simple polyene chain to a more sophisticated polyether ladder.

It is highly significant that neither of these models inherently place any limitation on the number of contiguous rings that may be constructed. Once the polyene precursor is assembled, conversion to the polycyclic structure is relatively straightforward. This could provide an explanation as to how polyether biosynthesis can be effected on such a grand scale, as exemplified by maitotoxin. Considering the remarkable biological activity of this structure, such scaling has clearly been a successful strategy.

Although the genes responsible for the formation of marine polyethers are difficult to obtain, it is noteworthy that the terminal ring of the ionophore, lasalocid A, produced by *Streptomyces lasaliensis,* also appears to be formed from a disfavored, *endo*-tet, epoxide opening (Scheme 11).[32] Interestingly, a very small quantity of the *exo*-tet product (<1%) has also been isolated,

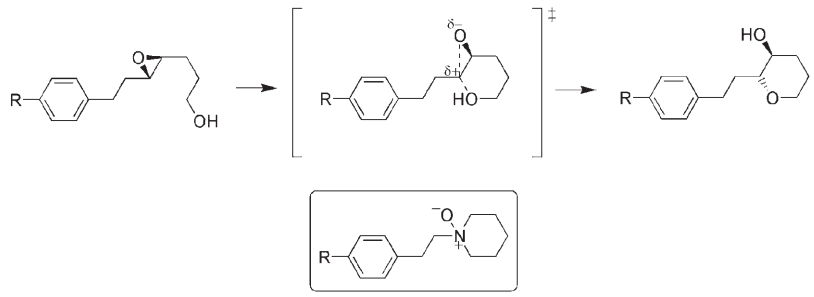


Scheme 11. Proposed formation of lasalocid through an *endo*-tet epoxide opening.

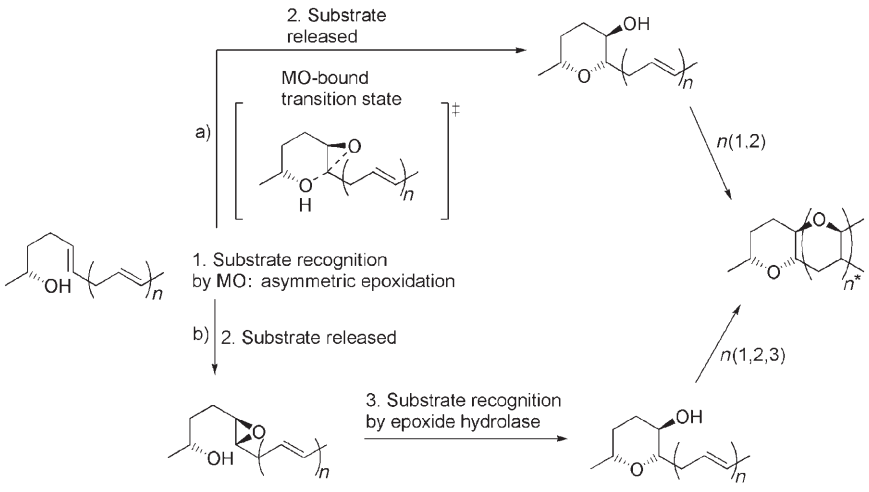
presumably resulting from the chemically favored, nonenzymatic cyclization. Alborixin, salinomycin, and narasin also have such terminal rings.[33] The gene clusters for lasalocid A and the other three polyethers should be obtainable as the organisms can be cultured, and this could confirm a role of *endo*-directing epoxide hydrolases in polyether biosynthesis.

As mentioned earlier, maitotoxin appears to be exceptional.[1] The main body of the molecule consists of four separate ladder sections (A–D), as well as a central "hinge" consisting of two identical bicyclic structures. This identicality suggests a common mechanism of construction distinct from the ladder sections. Although conforming to our stereochemical model in three of the ladder sections (see the Supporting Information), retrobiosynthetic analysis of ladder C reveals an epoxide with the opposite stereochemistry to the others (Scheme 12). This is striking as it leads to the only example of an exceptional ring junction (the "J–K ring junction") in any of the known polyether ladders.

From the 28 *trans* double bonds that must be epoxidized to construct the maitotoxin ladders, the selective discrimination of one double bond appears unrealistic. Without exception, none of the other polyether ladders that are derived from considerably fewer double bonds display any such stereochemical variation. As discussed, a single monooxygenase is likely to be responsible for epoxidation of all the *trans* double

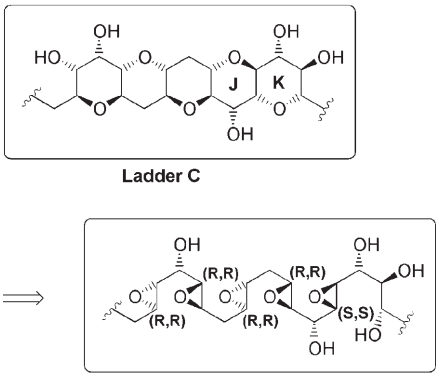


Scheme 9. Antibody-mediated *endo* cyclization. Antibody generated from hapten (boxed) that mimics the *endo* transition state.



Scheme 10. a) Mono-enzymatic route to a fused polyether; b) Bis-enzymatic route. MO = monooxygenase, * = alternating orientation of the oxane ring.

 © 2006 Wiley-VCH Verlag GmbH & Co. KGaA, Weinheim



Ladder C

Scheme 12. Retrobiosynthetic analysis of maitotoxin ladder C showing an exceptional (*S*,*S*)-*trans* epoxide.

bonds in any single polyether. To arrive at maitotoxin, this enzyme would be required to skip the double bond in question despite having broad enough specificity to recognize all of the others. Differential epoxidation of this double bond would certainly require a separate enzyme. Referring to the complete stereochemical assignment by Satake et al.,[34] it is striking that this region of the molecule is specifically noted as being highly challenging. In fact, the communication discusses this particular difficulty exclusively. Owing to overlap of signals in the ^{1}H NOESY NMR spectra, advanced 3D NMR experiments were required to assign the stereochemistry in this area of the molecule. In light of this and the results of our analyses, we propose that this assignment should be re-examined.

In conclusion, until now, mechanistic hypotheses for marine polyether ladder biosynthesis have not been considered in detail. Beyond the original Cane–Celmer–Westley extrapolation, as initially proposed by Shimizu and Nakanishi, only fragments of other models have been proposed or, often, only alluded to. These have been restricted to the brevetoxins. Herein we show that contiguous rings, in any single polyether, can be derived from stereochemically identical *trans* epoxides. This has allowed us to put forward a simple model that can explain the biosynthesis of the ring structure of all the marine polyether ladders thus far characterized. Finally, we propose that the established structure of the largest known non-polymeric natural product, maitotoxin, may justifiably be questioned.

Received: December 2, 2005
Published online: June 12, 2006

[1] a) M. Murata, T. Iwashita, A. Yokoyama, M. Sasaki, T. Yasumoto, *J. Am. Chem. Soc.* **1992**, *114*, 1975; b) M. Murata, H. Naoki, T. Iwashita, S. Matsunaga, M. Sasaki, A. Yokoyama, T. Yasumoto, *J. Am. Chem. Soc.* **1993**, *115*, 2060; c) M. Sasaki, N. Matsumori, T. Maruyama, M. Murata, K. Tachibana, T. Yasumoto, *Angew. Chem.* **1996**, *108*, 1782; *Angew. Chem. Int. Ed. Engl.* **1996**, *35*, 1672; d) T. Nonomura, M. Sasaki, N. Matsumori, M. Murata, K. Tachibana, T. Yasumoto, *Angew. Chem.* **1996**, *108*, 1786; *Angew. Chem. Int. Ed. Engl.* **1996**, *35*, 1675; e) W. Zheng, J. DeMattei, J.-P. Wu, J.-W. Duan, L. R. Cook, H. Oinuma, Y. Kishi, *J. Am. Chem. Soc.* **1996**, *118*, 7946.

[2] a) S. Khan, O. Arakawa, Y. Onoue, *Aquacult. Res.* **1997**, *28*, 9; b) S. Pratt, *Geotimes* **2005**, *50*, 8.

[3] M. Murata, H. Naoki, S. Matsunaga, M. Satake, T. Yasumoto, *J. Am. Chem. Soc.* **1994**, *116*, 7098.

[4] a) H.-N. Chou, Y. Shimizu, *J. Am. Chem. Soc.* **1987**, *109*, 2184; b) M. S. Lee, G.-w. Qin, K. Nakanishi, M. G. Zagorski, *J. Am. Chem. Soc.* **1989**, *111*, 6234.

[5] A. Agatarap, J. W. Chamberlin, M. Pinkerton, L. Steinrau, *J. Am. Chem. Soc.* **1967**, *89*, 5737.

[6] H. Patzelt, J. A. Robinson, *J. Chem. Soc. Chem. Commun.* **1993**, *16*, 1258.

[7] a) J. W. Westley, R. H. Evans, G. Harvey, R. G. Pitcher, D. L. Pruess, *J. Antibiot.* **1974**, *27*, 288; b) D. E. Cane, W. B. Celmer, J. W. Westley, *J. Am. Chem. Soc.* **1983**, *105*, 3594.

[8] a) A. A. Ajaz, J. A. Robinson, *Chem. Commun.* **1983**, *12*, 679; b) A. A. Ajaz, J. A. Robinson, D. L. Turner, *J. Chem. Soc. Perkin Trans. 1* **1987**, 27.

[9] P. F. Leadlay, J. Staunton, M. Oliynyk, C. Bisang, J. Cortes, E. Frost, Z. A. Hughes-Thomas, M. A. Jones, S. G. Kendrew, J. B. Lester, P. F. Long, H. A. I. McArthur, E. L. McCormick, Z. Oliynyk, C. B. W. Stark, C. J. Wilkinson, *J. Ind. Microbiol. Biotechnol.* **2001**, *27*, 360.

[10] A. Bhatt, C. B. W. Stark, B. M. Harvey, A. R. Gallimore, Y. A. Demydchuk, J. B. Spencer, J. Staunton, P. F. Leadlay, *Angew. Chem.* **2005**, *117*, 7237; *Angew. Chem. Int. Ed.* **2005**, *44*, 7075.

[11] a) Y. Shimizu, *Natural Toxins: Animal, Plant and Microbial* (Ed.: J. B. Harris), Clarendon, Oxford, **1986**, p. 123; b) K. Nakanishi, *Toxicon* **1985**, *23*, 473.

[12] a) M. Murata, M. Izumikawa, K. Tachibana, T. Fujita, H. Naoki, *J. Am. Chem. Soc.* **1998**, *120*, 147; b) M. Izumikawa, M. Murata, K. Tachibana, T. Fujita, H. Naoki, *Eur. J. Biochem.* **2000**, *267*, 5179.

[13] H.-N. Chou, Y. Shimizu, G. Van Duyne, J. Clardy, *Tetrahedorn Lett.* **1985**, *26*, 2865.

[14] *endo*-Tet is disfavoured as the oxygen nucleophile has more difficulty in achieving the geometry of attack for inversion at the epoxide carbon leading to the larger and, subsequently, fused rings. Attack at the alternative position (*exo*-tet) is favoured in this regard and leads to rings that are separated by a carbon–carbon bond. J. E. Baldwin, *J. Chem. Soc. Chem. Commun.* **1976**, 734.

[15] a) Y. Shimizu, H. N. Chou, H. Bando, G. Vanduyne, J. C. Clardy, *J. Am. Chem. Soc.* **1986**, *108*, 514; b) A. V. K. Prasad, Y. Shimizu, *J. Am. Chem. Soc.* **1989**, *111*, 6476.

[16] a) H. Takahashi, T. Kusumi, Y. Kan, M. Satake, T. Yasumoto, *Tetrahedron Lett.* **1996**, *37*, 7087; b) P. Ciminiello, E. Fattorusso, M. Forino, S. Magno, R. Viviani, *Tetrahedron Lett.* **1998**, *39*, 8897.

[17] a) M. Murata, A. M. Legrand, Y. Ishibashi, M. Fukui, T. Yasumoto, *J. Am. Chem. Soc.* **1990**, *112*, 4380; b) R. J. Lewis, J.-P. Vernoux, I. M. Brereton, *J. Am. Chem. Soc.* **1998**, *120*, 5914.

[18] a) H. Nagai, *J. Org. Chem.* **1992**, *57*, 5448; b) A. Morahashi, M. Satake, T. Yasumoto, *Tetrahedron Lett.* **1998**, *39*, 97.

[19] a) M. Satake, M. Shoji, Y. Oshima, H. Naoki, T. Fujita, T. Yasumoto, *Tetrahedron Lett.* **2002**, *43*, 5829; b) M. Satake, Y. Tanaka, Y. Ishikura, Y. Oshima, H. Naoki, T. Yasumoto, *Tetrahedron Lett.* **2005**, *46*, 3537.

[20] A. J. Bourdelais, H. M. Jacocks, J. L. C. Wright, P. M. Bigwarfe, D. G. Baden, *J. Nat. Prod.* **2005**, *68*, 2–6.

[21] a) I. Paterson, I. Boddy, I. Mason, *Tetrahedron Lett.* **1987**, *28*, 5205; b) U. Koert, *Synthesis* **1995**, 115.

[22] N. Hayashi, K. Fujiwara, A. Murai, *Tetrahedron* **1997**, *53*, 12425.

[23] a) K. C. Nicolaou, C. V. C. Prasad, P. K. Somers, C.-K. Hwang, *J. Am. Chem. Soc.* **1989**, *111*, 5330; b) K. C. Nicolaou, C. V. C. Prasad, P. K. Somers, C.-K. Hwang, *J. Am. Chem. Soc.* **1989**, *111*, 5335.

[24] K. Fujiwara, N. Hayashi, T. Tokiwano, A. Murai, *Heterocycles* **1999**, *50*, 561.

[25] J. C. Valentine, F. E. McDonald, W. A. Neiwert, K. I. Hardcastle, *J. Am. Chem. Soc.* **2005**, *127*, 4586.

[26] F. E. McDonald, F. Bravo, X. Wang, X. Wei, M. Toganoh, J. R. Rodriguez, B. Do, W. A. Neiwert, K. I. Hardcastle, *J. Org. Chem.* **2002**, *67*, 2515.

[27] J. Giner, *J. Org. Chem.* **2005**, *70*, 721.

[28] A. R. Gallimore, C. B. W. Stark, A. Bhatt, B. M. Harvey, Y. Demydchuk, V.

 © 2006 Wiley-VCH Verlag GmbH & Co. KGaA, Weinheim

Bolanos-Garcia, D. J. Fowler, J. Staunton, P. F. Leadlay, J. B. Spencer, *Chem. Biol.* **2006**, *13*, 453.
[29] M. Arand, B. M. Hallberg, J. Zou, T. Bergfors, F. Oesch, M. J. van der Werf, J. A. M. de Bont, T. A. Jones, S. L. Mowbray, *EMBO J.* **2003**, *22*, 2583.
[30] a) R. N. Armstrong, *CRC Crit. Rev. Biochem.* **1987**, *22*, 39; b) M. A. Argiriadi, C. Morisseau, B. D. Hammock, D. W. Christianson, *Proc. Natl. Acad. Sci. USA* **1999**, *96*, 10637.
[31] K. D. Janda, C. G. Shevlin, R. A. Lerner, *Science* **1993**, *259*, 490.
[32] J. W. Westley, J. F. Blount, R. H. Evans, A. Stemple, J. Berger, *J. Antibiot.* **1974**, *27*, 597.
[33] C. J. Dutton, B. J. Banks, C. B. Cooper, *Nat. Prod. Rep.* **1995**, *12*, 165.
[34] M. Satake, S. Ishida, T. Yasumoto, *J. Am. Chem. Soc.* **1995**, *117*, 7019.

Life's Simple Pleasures!



13286407_gu

No need to waste precious time looking for the right information – Register now for the free **Wiley-VCH Alerting Service.**

It's simple – and it's fast.

To receive regular news per e-mail tailored precisely to your needs and interests, just fill in the registration form at **www.wiley-vch.de/home/pas/**

WILEY-VCH

© 2006 Wiley-VCH Verlag GmbH & Co. KGaA, Weinheim

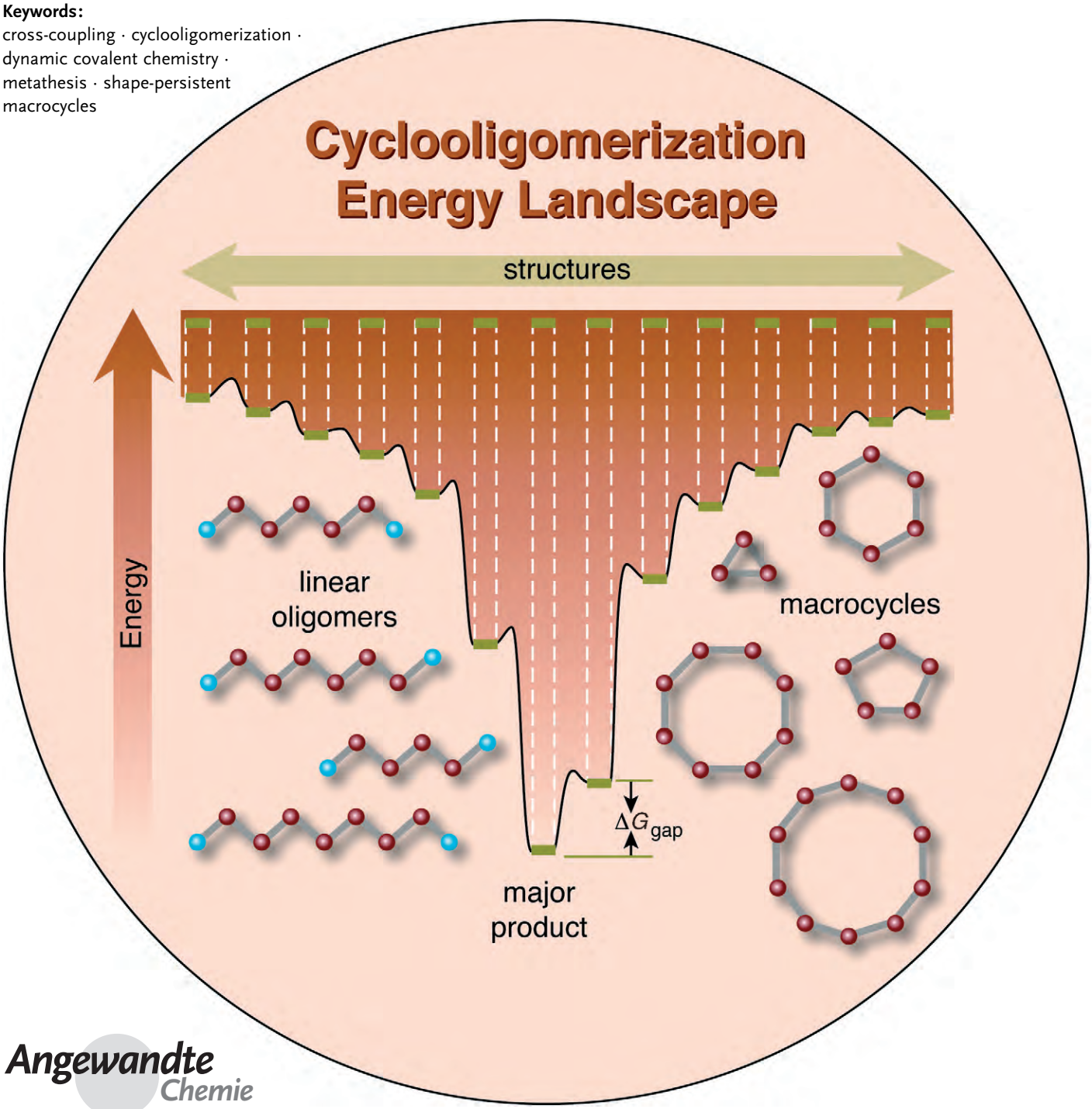
DOI: 10.1002/anie.200503988

Macrocycle Synthesis

Shape-Persistent Macrocycles: Structures and Synthetic Approaches from Arylene and Ethynylene Building Blocks

*Wei Zhang and Jeffrey S. Moore**

Keywords:
cross-coupling · cyclooligomerization · dynamic covalent chemistry · metathesis · shape-persistent macrocycles



© 2006 Wiley-VCH Verlag GmbH & Co. KGaA, Weinheim

Shape-persistent arylene ethynylene macrocycles have attracted much attention in supramolecular chemistry and materials science because of their unique structures and novel properties. In this Review we describe recent examples of macrocycle synthesis by cross-coupling (Sonogashira: aryl acetylene macrocycle or Glaser: aryl diacetylene macrocycle) and dynamic covalent chemistry. The primary disadvantage of the coupling methods is the kinetically determined product distribution, since a significant portion of oligomers grow beyond the length of the cyclic targets ("overshooting"). Better results have been obtained recently by a dynamic covalent approach involving reversible metathesis reactions that afford macrocycles in one step. Mechanistic studies demonstrate that macrocycle formation is thermodynamically controlled by this route. Remaining synthetic challenges include the efficient preparation of site-specifically functionalized structures and larger, more complex two- and three-dimensional molecules.

From the Contents

1. Introduction 4417
2. Kinetically Controlled Synthesis of Shape-Persistent Macrocycles 4419
3. Thermodynamically Controlled Synthesis of Arylene Ethynylene Macrocycles 4428
4. Conclusion and Outlook 4437

1. Introduction

In recent years there has been intense interest in shape-persistent arylene ethynylene macrocycles with respect to their roles as large, supramolecular building blocks that generate π-stacked structures in solution, noncollapsable nanoporous solids, and tubular ordered fluid phases.[1–11] In contrast to conformationally flexible cycles, shape-persistent macrocycles generally have a regular repeating unit with few degrees of conformational freedom. Their rigid backbones give rise to large molecular surfaces that organize into order structures. The ethynylene functional group is an attractive building block for these structures as a result of: 1) its potential for extended conjugation, 2) its simple linear geometry, 3) its pure carbon composition, which is especially attractive for the preparation of carbon-rich materials, Figure 1),[8,9] and 4) its wide accessibility through a wide-range of syntheses.[11,12] Shape-persistent macrocycles have an interior and an exterior at which site-specific substitution with functional groups can be accomplished. All these properties make shape-persistent macrocycles from arylene and ethynylene building blocks attractive structures for organic materials.[13]

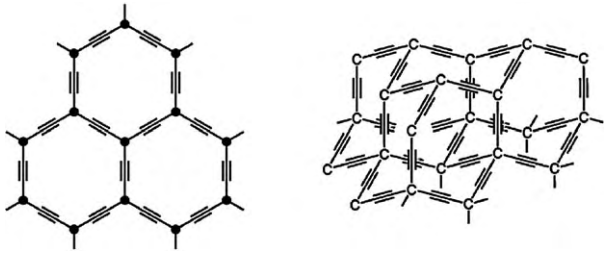


Figure 1. Two-dimensional and three-dimensional carbon network from tri- and tetra-substituted ethynylene-containing monomers. Each black dot represents a monomer unit.

Carbon–carbon coupling reactions play a critical role in the synthesis of arylene ethynylene macrocycles (Figure 2). Macrocycle preparation has benefited tremendously from the progress in the area of cross-coupling reactions between sp- or sp^2-hybridized carbon atoms.[12] This chemistry includes the palladium-catalyzed alkyne version of the Heck reaction,[14] which with copper salts is known as the Sonogashira cross-coupling,[15–19] the Negishi cross-coupling[20] between aryl halide and alkynylzinc halides, Glaser-type homocoupling[21–32] between terminal alkynes, as well as the Cu-promoted Castro–Stephens coupling.[33] These coupling reactions have high tolerance of functional groups, generally give high yields in individual steps, and the required precursors are readily available. Recently, with the rapid progress and growing interest in alkyne metathesis,[34] this type of carbon–carbon bond construction has also been applied to the synthesis of ethynylene-containing molecular structures.

Strategies that have been used in macrocycle syntheses can be classified into four major types (Figure 3): 1) cyclooligomerization;[35] 2) intramolecular ring closure of α,ω-difunctionalized oligomers; 3) intermolecular coupling between two or more oligomeric fragments followed by unimolecular cyclization; 4) templated cyclization of two or more fragments. When the cyclooligomerization approach (strategy 1) involves irreversible reactions (for example, cross-coupling), the problem of product "overshooting" significantly diminishes the theoretical yield. This problem will be discussed in detail in Section 2.1. Strategies 2 and 3 are the most commonly used in macrocycle synthesis by cross-coupling reactions, and they will be covered in Sections 2.2 and 2.3, respectively. Template-directed macrocycle syntheses (strategy 4) will be discussed in Section 2.4.

Dynamic covalent chemistry (DCC) concerns reversible reactions conducted under equilibrium conditions. Reversi-

[*] Dr. W. Zhang, Prof. J. S. Moore
Department of Chemistry and Materials Science & Engineering
University of Illinois at Urbana-Champaign
600 South Mathews Avenue, Urbana, IL 61801 (USA)
Fax: (+1) 217-244-8024
E-mail: jsmoore@uiuc.edu

© 2006 Wiley-VCH Verlag GmbH & Co. KGaA, Weinheim

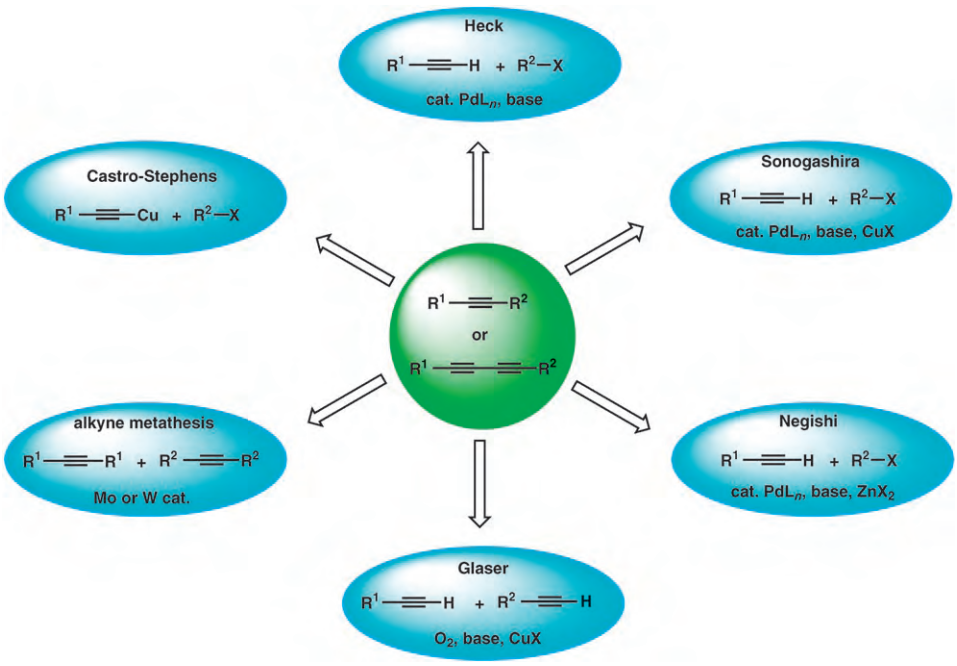


Figure 2. Carbon–carbon bond constructions involving the ethynylene functional group.

bility offers the potential to avoid the chemical "defects" that are introduced in kinetically controlled processes. Synthetic approaches based on DCC as well as theoretical calculations on the thermodynamic stabilities of generated macrocycles are covered in Section 3. Although there have been several previous reviews addressing related topics,[1,3–11] here we emphasize the most recently developed approaches for the synthesis of arylene ethynylene macrocycles.

Despite the availability of a variety of cross-coupling synthetic approaches, the efficient preparation of macrocycles is challenged by the disadvantage that these are kinetically controlled reactions; this is especially problematic for cyclooligomerization. Undesired bond formations (for example, higher oligomers overshooting the length of the target macrocycle) cannot be corrected because of the irreversible nature of the reaction. Therefore, intramolecular ring closure or intermolecular coupling of oligomers is employed to achieve a high yield of cyclic products. However, macrocycle preparations by these routes usually involve a large number of synthetic steps and the ring-closure step requires dilute conditions (< 1 mM). Overall yields by these routes are often still low.[5,7,36]

On the other hand, dynamic covalent chemistry[34,37–42] has been successfully applied to the preparation of macrocycles in high yield. A wide variety of molecular architectures such as macrocyclic compounds,[43] molecular capsules,[44] and interlocked structures[45] have been prepared by DCC. These successful cases illustrate favorable examples of the energy-gap principle discussed in Section 3.2.3.



Wei Zhang was born in China in 1977. After completing his BS in chemistry in 2000 at Peking University and one year graduate study in University of Utah, he transferred to the University of Illinois at Urbana-Champaign in 2001, where he completed his PhD in chemistry with Prof. Jeffrey Moore, working on the development of a molybdenum-based alkyne metathesis catalyst and its application in the synthesis of shape-persistent macrocycles and conjugated polymers (2005). In March 2006 he assumed a postdoctoral position at MIT with Prof. Timothy M. Swager.



Jeffrey Moore was born near Joliet, IL in 1962. He received his BS in chemistry (1984) from the University of Illinois, and his PhD in Materials Science and Engineering with Samuel Stupp (1989). After a NSF position at Caltech with Robert Grubbs and research at the University of Michigan in Ann Arbor, he returned in 1993 to the University of Illinois, where he is currently the William H. and Janet G. Lycan Professor of Chemistry and Materials Science and Engineering. His research focuses on molecular self-assembly, structure-controlled macromolecules and foldamers, stimuli-responsive materials, and self-healing polymers.

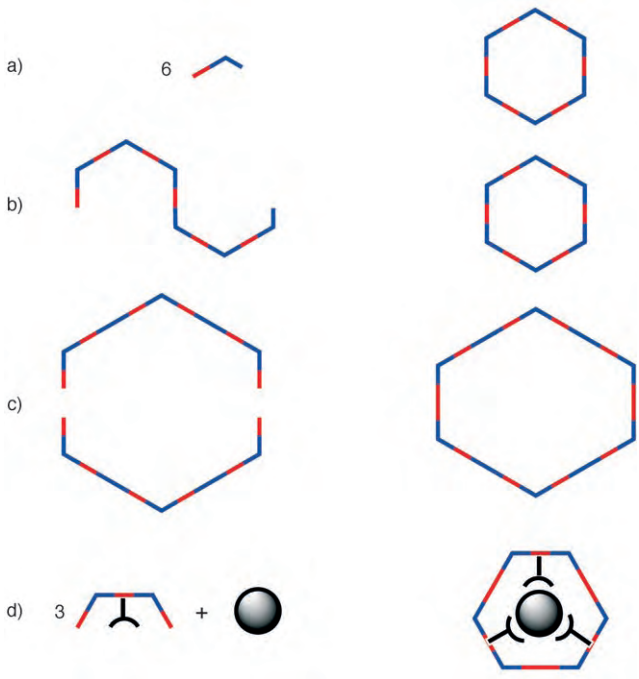


Figure 3. Schematic representation of cyclization strategies: a) cyclooligomerization; b) intramolecular cyclization; c) bimolecular coupling/unimolecular cyclization; d) templated cyclization.

© 2006 Wiley-VCH Verlag GmbH & Co. KGaA, Weinheim

For any thermodynamically controlled process, the successful generation of a unique species from a multitude of possible products depends on the relative free energies of all the species involved. The energies of these products define the so-called energy landscape, a term used widely in protein folding[46] but one that has broad applicability to other thermodynamically controlled processes involving a large ensemble of candidate structures. For cyclooligomerization, the number of possible products includes both cyclic and linear oligomers of various sizes. In cases where there is a large energy gap between the target macrocycle and other possible macrocyclic products, DCC is capable of generating the desired product in high yields, even when kinetic preferences initially give undesirable products (Figure 4). For systems constructed from conformationally flexible building blocks, entropy usually dominates and the smallest macrocycle (cyclic monomer or cyclic dimer) usually predominates. For shape-persistent macrocycles, small macrocycles such as cyclic monomers or cyclic dimers are often unfavorable because of high angle strain, which opens up the interesting possibility of generating large rings under thermodynamic control.

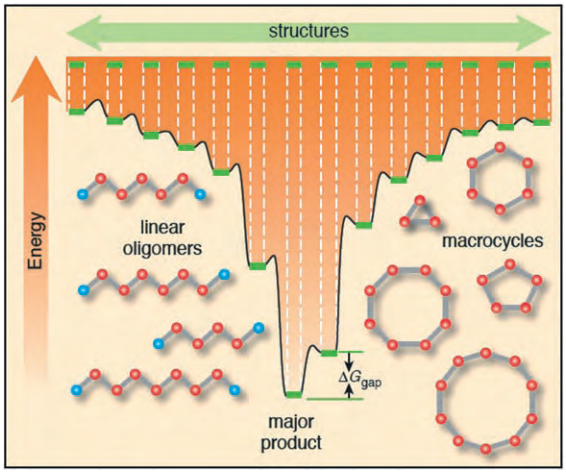


Figure 4. The cyclooligomerization energy landscape. As the degree of conversion increases, the end groups (blue spheres) are removed, which drives oligomers to grow in size and transform into cyclic products. Macrocyclic strain and entropy considerations determine the preferred ring size, with macrocycles having the smallest number of monomer units being entropically favored. The bond angles and conformational rigidity of the monomer determine if a particular macrocycle is strained or strain-free. The energy gap is the difference in energy between the most stable product and the second most stable product. The energy gap determines whether a unique product will be formed under reversible conditions.

2. Kinetically Controlled Synthesis of Shape-Persistent Macrocycles

2.1. Cyclooligomerization

2.1.1. Cyclization of AB- and AA-Type Monomers

Homocoupling (for example, the Glaser reaction) and cross-coupling reactions have been widely applied to the synthesis of arylene ethynylene macrocycle. The irreversible nature of these reactions means that undesired bond formation is incapable of being corrected and the product distribution is kinetically determined. One of the biggest drawbacks to kinetic cyclooligomerization is that oligomers grown by coupling difunctional monomers (for example, an alkynyl haloarene) may overshoot the length of the target macrocycles. Since these oligomers cannot be shortened, they cannot contribute to the yield of the desired product. The impact of "overshooting" in macrocycle synthesis can be analyzed by kinetic simulations of the cyclooligomerization process. Simulations of cyclotrimerization and cyclohexamerization are discussed below.[47]

Two types of monomers can be considered depending on whether homocoupling or cross-coupling reactions are used for cyclooligomerization. A difunctionalized monomer AB (which has two different functional groups A and B on the same molecule, and A can only react with B) is representative of cross-coupling cyclooligomerization, while a difunctionalized AA monomer (two identical functional groups A on the same molecule, and A can react with A) is representative of homocoupling cyclooligomerization. Figure 5 shows the reaction pathway for cyclotrimerization, and Table 1 shows the relevant oligomer M_i and cyclic C_3 products. In the simulation, monomers are allowed to grow in a stepwise fashion ($M_1 \rightarrow M_2$) until linear trimers (M_3) or higher oligomers are formed. The simulation assumes a best-case scenario in that all linear trimers instantly cyclize without further elongation, thus affording cyclic trimers (C_3). Any oligomers longer than trimers are treated as overshoot by-products (M_x). Based on these assumptions, only two species are present at the end of the reaction: target cyclic trimers (C_3) and overshoot oligomers (M_x, Table 1). The kinetic simulation gave a 50% yield of C_3 in this cyclooligomerization process (Figure 6).

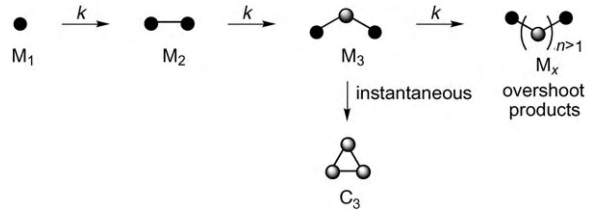


Figure 5. The reaction pathways involved in the cyclotrimerization of AB- or AA-type monomers.

Table 1: Possible bimolecular combinations used to model cyclotrimerization of AB- or AA-type monomers under irreversible conditions. Since M_3 is considered to instantaneously transform into C_3, there is no M_3 species in the table. M_x corresponds to any oligomer longer than a trimer.

Reactant	M_1	M_2	M_x
M_1	M_2	C_3	M_x
M_2	C_3	M_x	M_x
M_x	M_x	M_x	M_x

© 2006 Wiley-VCH Verlag GmbH & Co. KGaA, Weinheim

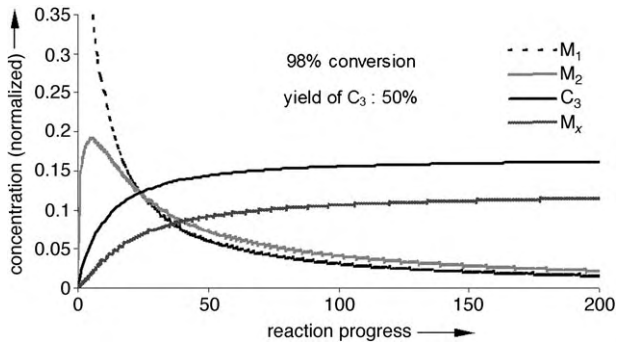


Figure 6. Simulation of oligomerization versus cyclotrimerization. The diagram shows how the concentration of each species changes in the cyclization/oligomerization process starting from AB- or AA-type monomers. The initial concentration of M_1 is normalized to 1.0. All rate constants (k) are normalized to 0.1.

Similarly, for simulations of the formation of a cyclic hexamer, oligomers grow in a stepwise fashion from M_1 to M_5 until linear hexamers M_6 are generated (Figure 7). In the best-

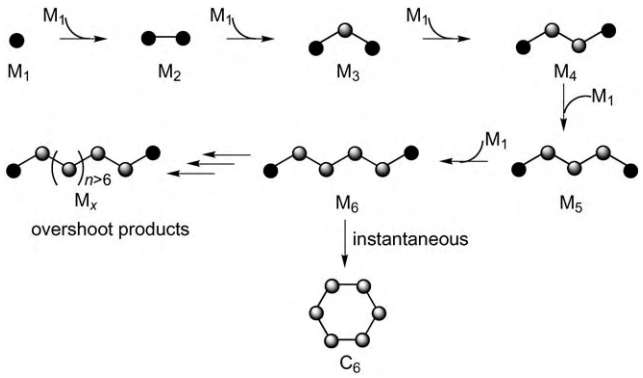


Figure 7. The reaction pathways involved in the cyclohexamerization of AB- or AA-type monomers.

case scenario all linear hexamers are assumed to instantly cyclize to afford hexacycle (C_6) with no other cyclic species generated. Oligomers longer than hexamers are treated as overshoot by-products (M_x). On the basis of these assumptions, only the target cyclic hexamers (C_6) and overshoot oligomers (M_x) are present at the end of the reaction (Table 2). The cyclohexamerization simulation predicts a 37% yield of C_6 (Figure 8). These best-case simulations show that the cyclooligomerization process is unlikely to be very efficient, and the efficiency decreases for larger rings.

Recently, Pan and co-workers have used AB-type monomers **1** to synthesize trimeric macrocycles **2** in the ionic liquid 1-butyl-3-methylimidazolium tetrafluoroborate (BMIM) through a Sonogashira coupling reaction [Eq. (1)].[48] The reaction is catalyzed by palladium(0) tetrakis(triphenylphosphine) at 80 °C and affords the trimeric macrocyclic products in one step directly from iodoarylacetylene monomers **1** in 11–37% yield. The distance from the center of the 12-membered dehydroannulene to the center of the carbon–carbon triple bonds in these conjugated cyclic trimers[49] is

Table 2: Possible bimolecular combinations used to model the cyclohexamerization of AB- or AA-type monomers under irreversible conditions. Since M_6 is considered to instantaneously transform into C_6, there is no M_6 species in the table. M_x corresponds to any oligomer longer than the hexamer.

Reactant	M_1	M_2	M_3	M_4	M_5	M_x
M_1	M_2	M_3	M_4	M_5	C_6	M_x
M_2	M_3	M_4	M_5	C_6	M_x	M_x
M_3	M_4	M_5	C_6	M_x	M_x	M_x
M_4	M_5	C_6	M_x	M_x	M_x	M_x
M_5	C_6	M_x	M_x	M_x	M_x	M_x
M_x	M_x	M_x	M_x	M_x	M_x	M_x

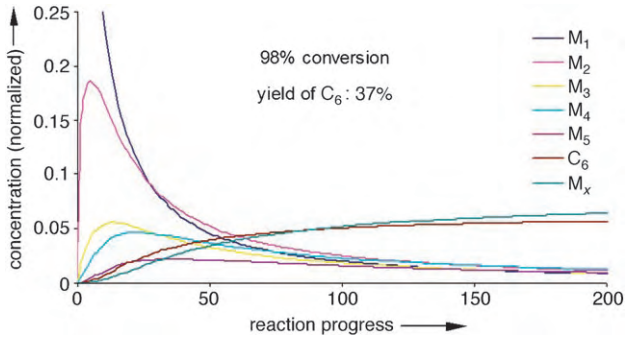
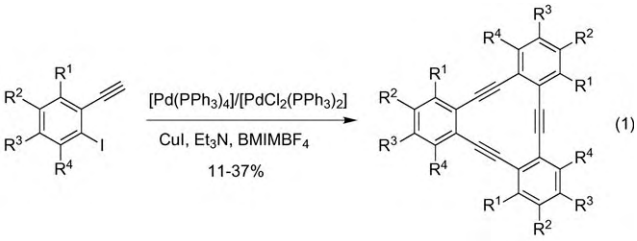


Figure 8. Simulation of oligomerization versus formation of the cyclohexamer. The diagram shows how the concentration of each species changes during the cyclization/oligomerization starting from AB- or AA-type monomers. The initial concentration of M_1 is normalized to 1.0. All rate constants (k) are normalized to 0.1.



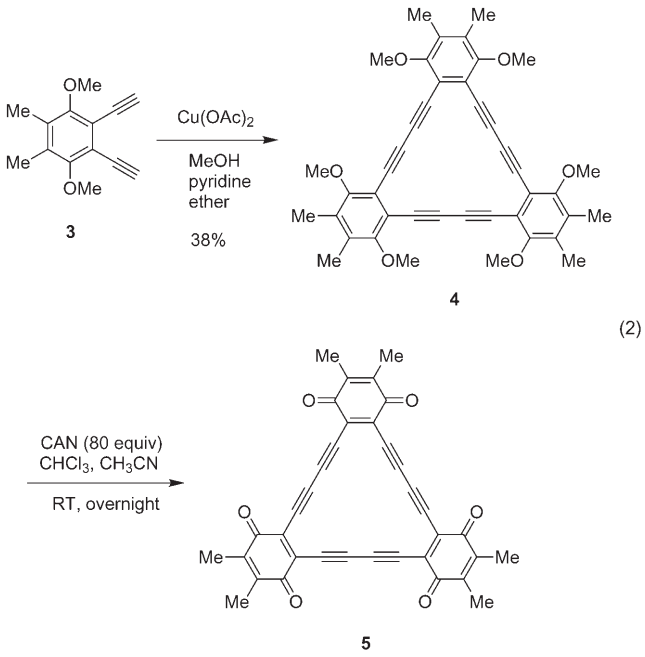
1a: $R^1=R^2=R^3=R^4=H$
1b: $R^1=R^2=H$, $R^3+R^4=PhH$
1c: $R^1=H$, $R^2=R^3=R^4=CH_3O$

2a: $R^1=R^2=R^3=R^4=H$
2b: $R^1=R^2=H$, $R^3+R^4=PhH$
2c: $R^1=H$, $R^2=R^3=R^4=CH_3O$

about 1.2 Å, which enables π-ethynylene/transition-metal bonding interactions to occur. The metal can be coordinated either in or out of the plane of the macrocycle. The interesting structural and conducting properties of the transition-metal complexes derived from those analogues have been explored.[50]

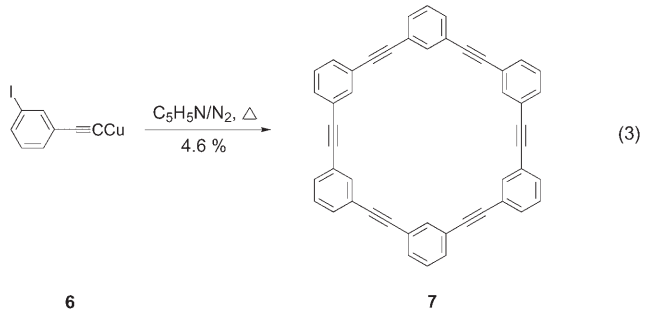
Komatsu and co-workers also used a one-step cyclooligomerization strategy to prepare another trimeric macrocycle, hexadehydro[18]annulene **4**, through copper-mediated oxidative coupling of the corresponding AA-type monomers 1,2-diethynylarene **3** [Eq. (2)].[51] Macrocycle **4** was obtained in 38% yield under Eglinton's conditions. Treatment of **4** with a large excess of ceric ammonium nitrate (CAN) provided the *p*-benzoquinone derivative **5**. Although **5** has both π-electron-

© 2006 Wiley-VCH Verlag GmbH & Co. KGaA, Weinheim



donating and -accepting groups, and can be regarded as a novel push-pull system,[52] the UV/Vis spectroscopic measurements and cyclic voltammetry (CV) revealed that the intramolecular charge transfer is small.

The first synthesis of hexameric arylene ethynylene macrocycles from AB-type monomers dates back 30 years, when Staab and Neunhoeffer prepared the hexameric phenyleneethynylene macrocycle **7** in 4.6% yield through sixfold Stephens–Castro coupling of the copper salt of *m*-iodophenylacetylene (**6**) [Eq. (3)].[53] This method represents an early



(3)

example of the application of the cyclooligomerization strategy to the preparation of shape-persistent macrocycles. The monomer grows into open-chain oligomers and the cyclization proceeds in competition with chain elongation. The low yield is probably due to the overshoot problem and possibly poor solubility of the growing oligomers.

These kinetic simulations and experimental results indicate that the yield of the macrocycle drops quickly as the ring size increases. For this reason, irreversible cyclooligomerization may not be suitable for synthesizing macrocycles containing a large number of monomeric units.

2.1.2. *Cyclooligomerization of A_2- and B_2-Type Monomers*

Reaction pathways for cyclohexamer formation by a process involving a pair of $A_2 + B_2$ monomers are shown in Figure 9. The assumptions used for kinetic simulations are the

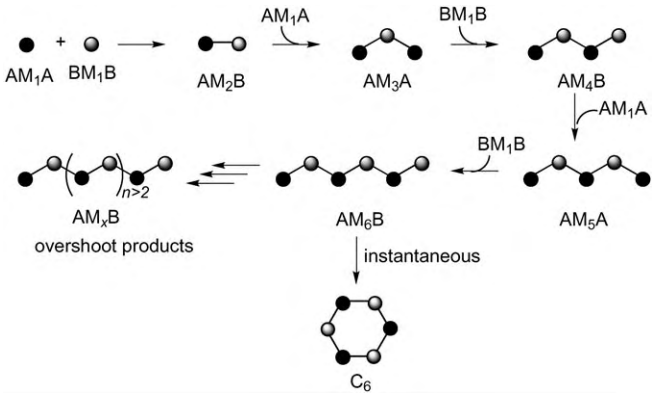


Figure 9. Reaction pathways for oligomerization and cyclohexamer formation from A_2- and B_2-type monomers.

same as for the AB best-case scenario; once the linear hexamer AM_6B is generated, it cyclizes to C_6 and no other cyclic species are formed. Any oligomers longer than hexamers are treated as overshoot by-products. At the end of the reaction two major species are present: target cyclic hexamers (C_6) and the ensemble of overshoot oligomers (Table 3, M_x includes AM_xB, AM_xA, and BM_xB). As

Table 3: Possible bimolecular combinations used to model cyclohexamerization of A_2- and B_2-type monomers under irreversible conditions. Since AM_6B is considered to instantaneously transform into C_6, there is no AM_6B species in the table. AMxB, AMxA, and BMxB correspond to oligomers longer than the hexamer.

Reactant	BM_1B	BM_2A	BM_3B	BM_4A	BM_5B	BM_xA/ BM_xB
AM_1A	AM_2B	AM_3A	AM_4B	AM_5A	C_6	AM_xB/ AM_xA
AM_2B	BM_3B	AM_4B	BM_5B	C_6	BM_xB	BM_xA/ BM_xB
AM_3A	AM_4B	AM_5A	C_6	AM_xA	AM_xB	AM_xB/ AM_xA
AM_4B	BM_5B	C_6	BM_xB	AM_xB	BM_xB	BM_xA/ BM_xB
AM_5A	C_6	AM_xA	AM_xB	AM_xA	AM_xB	AM_xB/ AM_xA
AM_xB/ AM_xA	BM_xA/ BM_xB	AM_xB/ AM_xA	BM_xA/ BM_xB	AM_xB/ AM_xA	BM_xA/ BM_xB	AM_xB/ AM_xA/ BM_xB

expected, the cyclooligomerization simulations gave similar results as for AB-type monomers. The simulation showed a 36% yield of C_6 (Figure 10). Therefore, product overshoot once again interferes with the efficient synthesis of the macrocycles.

Iyoda et al. have utilized palladium-catalyzed Sonogashira coupling to synthesize arylene ethynylene macrocycles

 © 2006 Wiley-VCH Verlag GmbH & Co. KGaA, Weinheim

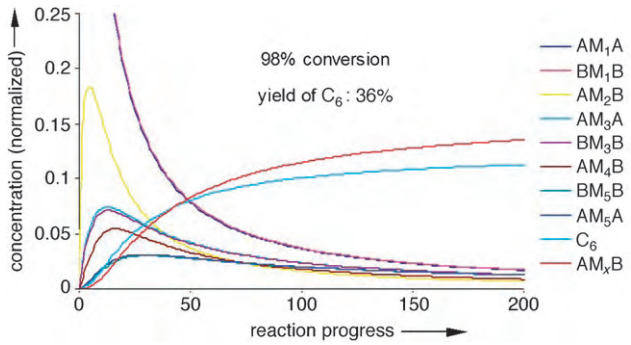
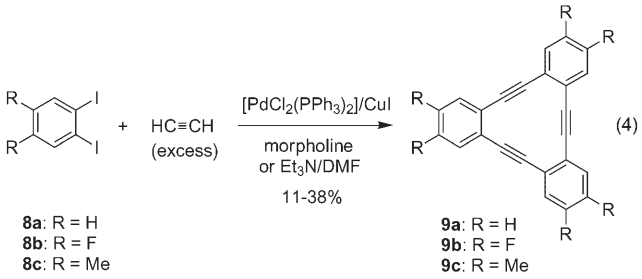


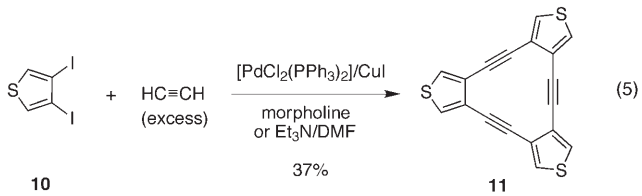
Figure 10. Simulation of oligomerization versus cyclohexamerization. The diagram shows how the concentration of each species changes in the cyclization/oliomerization process starting from A_2- and B_2-type monomers. The initial concentrations of AM_1A and BM_1B are normalized to 1.0. All rate constants (k) are normalized to 0.1.

containing three A_2 and three B_2 monomer units [Eq. (4)].[54] The direct reaction of *o*-diiodobenzene **8** (A_2-type monomer) with acetylene gas (B_2-type monomer) in the presence of



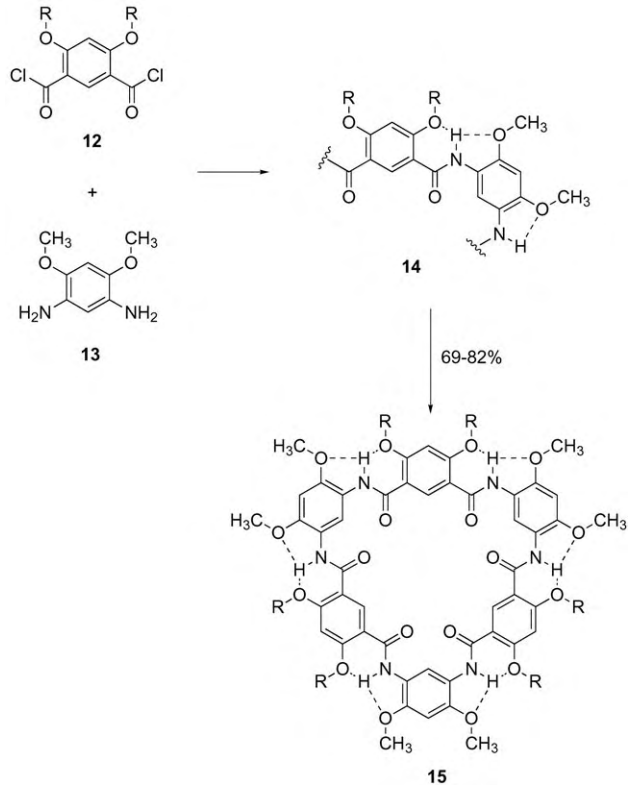
(4)

$[PdCl_2(PPh_3)_2]$ and CuI at 60 or 40 °C provided macrocycle **9** in 11–38 % yield. A similar reaction of the diiodide **10** with acetylene afforded the trithienocyclyne **11** in 37 % yield [Eq. (5)].



(5)

In an interesting recent example, Gong and co-workers reported their one-step synthesis of hexameric shape-persistent macrocycles through formation of an amide bond (Scheme 1).[55] Surprisingly, through this kinetically controlled approach, the reaction of diacid chloride **12** (A_2-type monomer) with 4,6-dimethoxy-1,3-phenylenediamine (**13**, B_2-type monomer), each at a concentration of 0.13 M, in the presence of triethylamine in CH_2Cl_2 provides high yields (69–82 %) of macrocycles **15**. Such high yields are inconsistent with the kinetic simulations. The folding and preorganization



Scheme 1. Macrocycle synthesis from A_2- and B_2-type monomers by amide formation. R = *n*-C_8H_{17} (69 %); $(CH_2)_3CO_2CH_2CH_3$ (82 %); $(CH_2CH_2O)_3CH_3$.[55]

of the uncyclized precursors **14** through hydrogen bonding are suggested to be responsible for the favored generation of cyclic oligoamides. It is still, however, difficult to understand how overshoot products are minimized. A detailed understanding of this successful $A_2 + B_2$ cyclization could lead to expedient synthesis of shape-persistent macrocycles in high yields.

The advantage of the cyclooligomerization procedure is that the target macrocycle is generated in a single step and the starting materials are readily accessible. However, as shown by most of the examples above, the yield of the target structure is inevitably low because of competition of the desired cyclic structure with the broad, statistical distribution of products, including a large collection of linear/cyclic oligomers and polymers of different chain lengths. Moreover, the separation and purification of the target macrocycle is difficult in the presence of large quantities of polydisperse by-products with similar structures. This crucial drawback makes the irreversible cyclooligomerization generally impractical for the large-scale synthesis of arylene ethynylene macrocycles. Alternative synthetic approaches, for example, the intramolecular ring-closure of difunctionalized oligomers, were developed to improve the low-yield synthesis, to simplify the purification process, and to produce site-specifically functionalized structures.

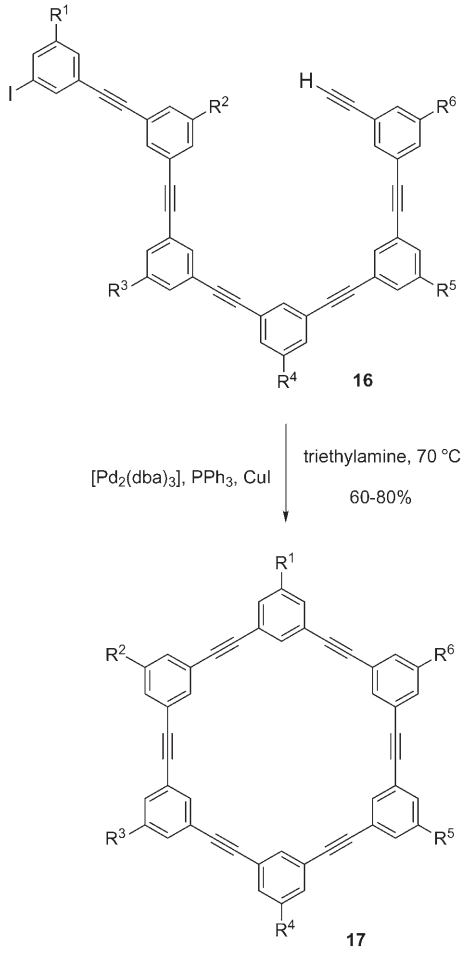
 © 2006 Wiley-VCH Verlag GmbH & Co. KGaA, Weinheim

2.2. Intramolecular Ring Closure of Difunctionalized Oligomers

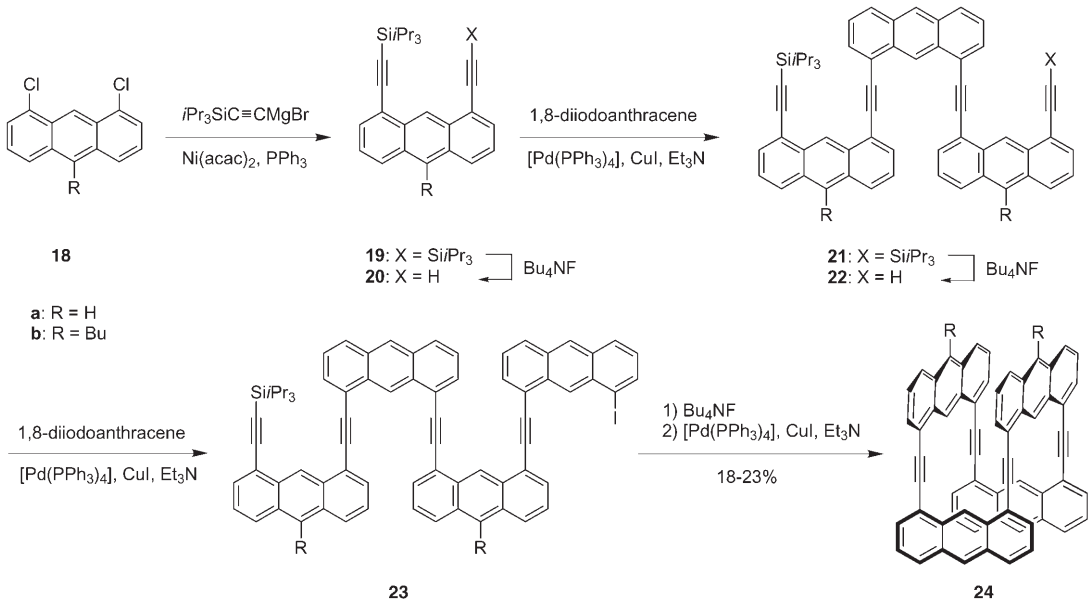
Motivated by precise structural control, we synthesized a series of macrocycles through intramolecular cyclization of difunctional oligomeric sequences (Scheme 2).[16] Instead of performing the oligomerization and cyclization in a one-pot procedure, a series of Sonogashira couplings between an aryl iodide and a terminal acetylene with orthogonal protecting groups on the chain ends were first used to prepare α-iodo-ω-ethynyl-functionalized *m*-phenyleneethynylene oligomers **16** with discrete lengths and specific homo- or heterosequences. Cyclization was then accomplished by using Sonogashira coupling under pseudo-high-dilution conditions (namely, slow addition of the oligomers to a catalyst solution) and the target macrocycles **17** were generated in moderately high yields (60–80% for the cyclization step).[17] The significantly improved yield of macrocycles was attributed to the preorganization of the cyclization precursor and the fact that unimolecular cyclization is kinetically more favorable than bimolecular coupling under pseudo-high-dilution conditions.

In addition to the improved yield, several other advantages of this intramolecular cyclization approach were realized. First, the stepwise synthesis allows for functional groups to be introduced at defined positions of the oligomeric sequence. Thus, the position of various side-chain functionalities can be precisely controlled according to the design requirements. Moreover, controlled incorporation of *ortho*-, *meta*-, and *para*-phenyleneethynylene fragments into the oligomer sequence could provide ready access to macrocycles with different geometrical shapes. Another advantage of this precursor approach is its adaptability to a wide variety of coupling reactions for synthesizing macrocycles with diverse backbone structures.[18,28–32]

Toyota et al. have synthesized the macrocyclic 1,8-anthryleneethynylene oligomers **24** by a sequential coupling/desilylation strategy (Scheme 3).[56] Monosilylated 1,8-diethynylan-



Scheme 2. Representative intramolecular cyclization using an α-iodo-ω-ethynyl-*m*-phenyleneethynylene oligomer precursor prepared through an iterative synthetic route.[16] dba = *trans*,*trans*-dibenzylideneacetone.



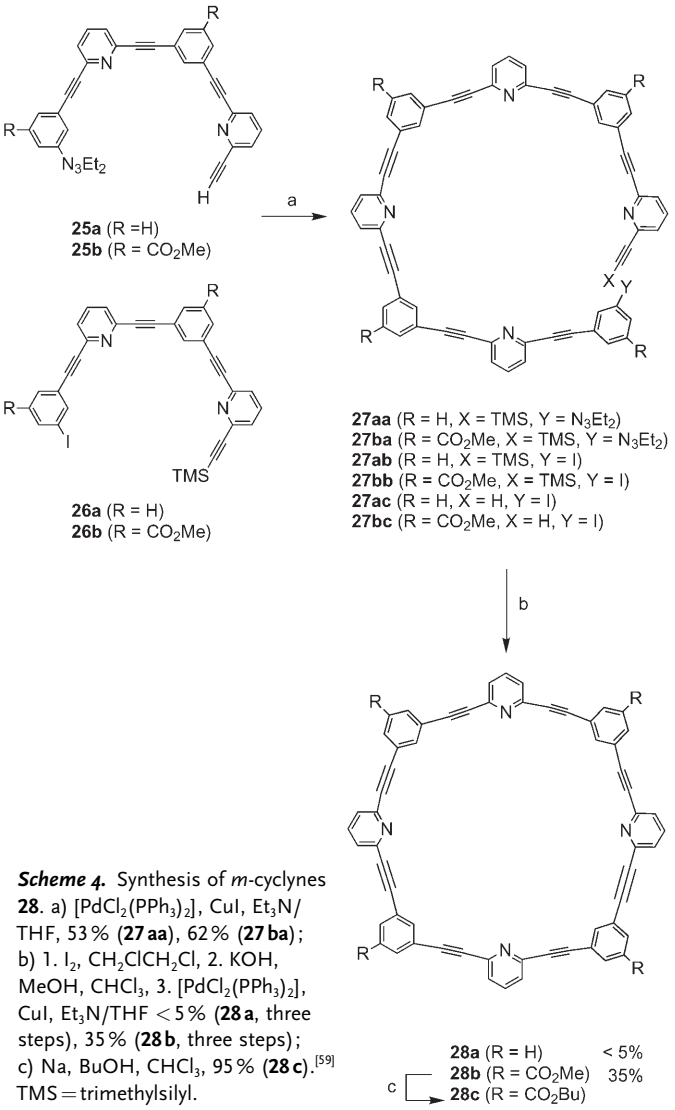
Scheme 3. Synthesis of cyclic oligomer **24**.[56]

 © 2006 Wiley-VCH Verlag GmbH & Co. KGaA, Weinheim

thracene (**20**) was prepared from **18** by a Ni-catalyzed coupling[57] followed by partial desilylation. Sonogashira coupling of **20** with 1,8-diiodoanthracene followed by similar desilylation provided compound **22**, which was coupled with an excess of 1,8-diiodoanthracene to afford acyclic tetramer **23**, the precursor of the target cyclic tetramer. The desilylation and coupling of **23** were conducted in a one-pot procedure in THF, and afforded cyclic compounds **24** in 23% (**24a**) and 18% (**24b**) yield. Although the positions of the absorption maxima of cyclic tetramer **24a** and acyclic **23a** were almost identical, the molar absorptivity of **24a** was less than **23a**.[58] Compound **24a** gave an intense and broad emission at $\lambda_{max} = 478$ nm, in contrast to the relatively sharp and structured bands of the acyclic oligomers. These characteristic electronic spectra are attributable to the π–π interactions between the anthracene chromophores. The synthesis of **24** could lead to a general approach for the preparation of aromatic compounds (the "panel/rod method") in which the degree of oligomerization and/or the type of building blocks could be varied.

Recently, Yoshida and co-workers have also utilized this intramolecular cyclization approach to prepare *m*-cyclynes **28** (Scheme 4).[59] Intermolecular coupling of terminal acetylene **25** with aryliodide **26** followed by replacement of the *N*,*N*-dialkyltriazene group with an iodo group by treatment with methyl iodide,[60] provided the desired linear precursor **27**. Open-chain compound **27** was then subjected to intramolecular coupling under high-dilution conditions to afford the target cyclyne **28**. These doughnut-shaped azamacrocycles with cavity dimensions of about 1 nm have strong light-emitting characteristics.[30,61] It is noteworthy that macrocycle **28b** can accommodate two molecules of $[Cu^{II}(hfac)_2]$ (hfac = 1,1,1,5,5,5-hexafluoro-2,4-pentanedione). The resulting pentacoordinate Cu^{II} complex emits remarkably strong fluorescence, contrary to conventional wisdom, and thus suggests that various transition-metal complexes of *m*-cyclynes **28** could find use as luminescent materials.

Haley and co-workers have utilized this precursor strategy to study the selectivity differences between Pd- and Cu-catalyzed cyclizations (Scheme 5).[62] Precursor polyyne **30** was constructed by a fourfold cross-coupling of diyne **29** to give 1,2,4,5-tetraiodobenzene. Glaser coupling catalyzed by $Cu(OAc)_2$ was tested to probe the possibility of the formation of either bis[15]annulene **31** (by cyclization across the *meta*-fused diyne unit) or bis[14]annulene **32** (by *ortho*-fused cyclization of the diyne unit), and annulenic **31** was isolated in 70% yield as the only significant cyclic product. In contrast, compound **32** was generated in 84% yield when Pd-mediated conditions were applied. The selectivity is rationalized by the different metal–acetylide intermediates in the Cu (**A**) and Pd-mediated (**B**) diacetylene-forming reactions (Scheme 6). The Cu-containing intermediate is proposed to arrange into a pseudo-*trans* configuration prior to reductive elimination,[63] which would require some systems to adopt a highly strained configuration for homocoupling to occur. However, in the case of the Pd catalyst, a variety of different ligands can be attached to the metal center which results in both *trans* and *cis* configurations being possible.

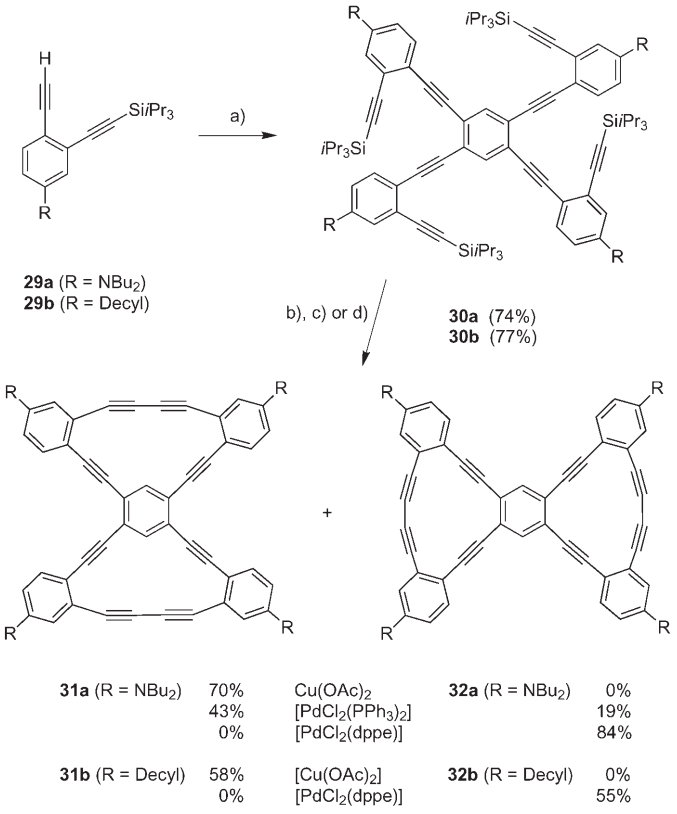


Scheme 4. Synthesis of *m*-cyclynes **28**. a) $[PdCl_2(PPh_3)_2]$, CuI, Et_3N/THF, 53% (**27aa**), 62% (**27ba**); b) 1. I_2, CH_2ClCH_2Cl, 2. KOH, MeOH, $CHCl_3$, 3. $[PdCl_2(PPh_3)_2]$, CuI, Et_3N/THF < 5% (**28a**, three steps), 35% (**28b**, three steps); c) Na, BuOH, $CHCl_3$, 95% (**28c**).[59] TMS = trimethylsilyl.

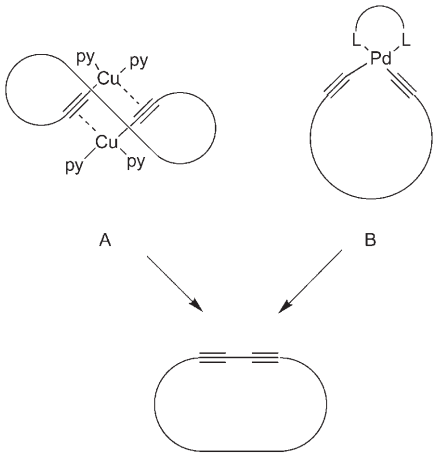
2.3. One-Pot Intermolecular Coupling Followed by Unimolecular Cyclization

Although the intramolecular ring-closure strategy provided the greatest versatility for structural control along with good cyclization yields, the labor-intensive and time-consuming synthesis and purification of the precursors impedes the efficient, large-scale preparation of macrocycles by these routes. An alternative strategy that capitalizes on the advantages while circumventing the shortcomings of the above two synthetic approaches was thus investigated by a number of research groups.[23,28,64–66] It was discovered that two oligomeric precursors with appropriate chain length and suitable terminal functionality can undergo an intermolecular coupling followed by an intramolecular cyclization in one pot, thereby affording target macrocycles in moderate yields. Although this combined step usually provides lower yields than the oligomer macrocyclization, the overall yield is often higher because fewer synthetic steps are used to synthesize

 © 2006 Wiley-VCH Verlag GmbH & Co. KGaA, Weinheim



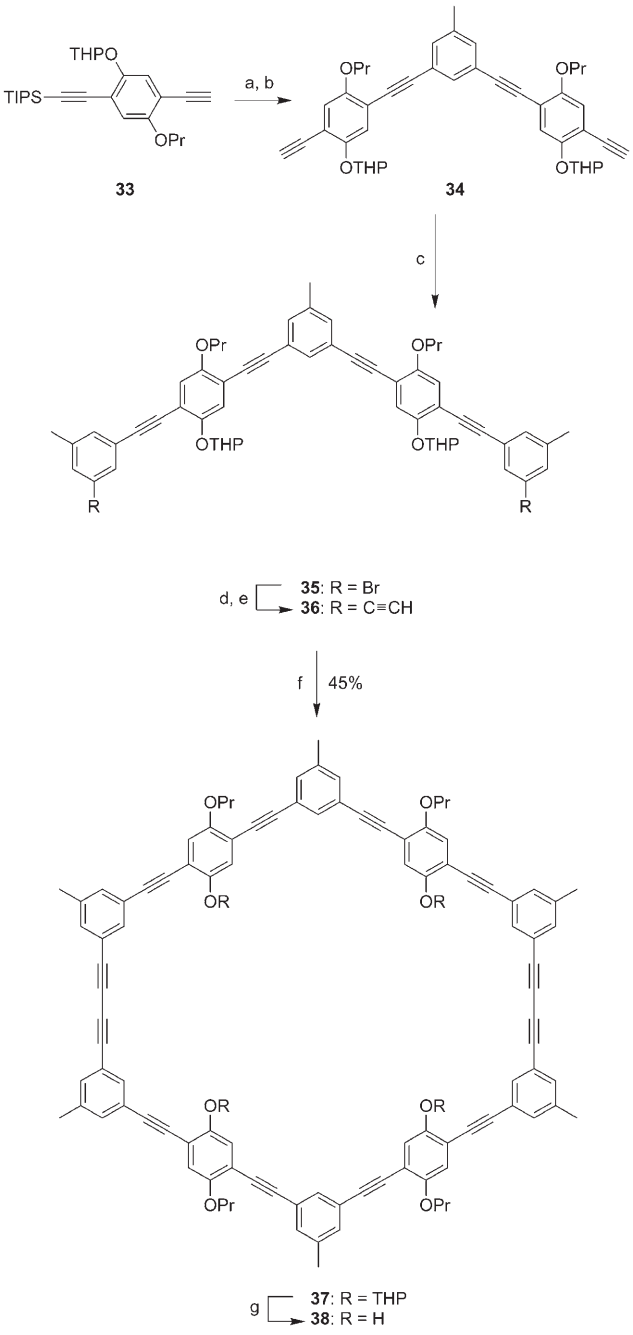
Scheme 5. a) 1,2,4,5-tetraiodobenzene, $[Pd(PPh_3)_4]$, CuI, iPr_2NH, THF, 40 °C; b) Bu_4NF, MeOH, THF; then $Cu(OAc)_2$, pyridine, 60 °C; c) Bu_4NF, MeOH, THF; then $[PdCl_2(PPh_3)_2]$, CuI, I_2, iPr_2NH, THF, 50 °C; d) Bu_4NF, MeOH, THF; then $[PdCl_2(dppe)]$, CuI, I_2, iPr_2NH, THF, 50 °C.[62] dppe = ethane-1,2-diylbis(diphenylphosphane).



Scheme 6. Proposed metalacetylide intermediates in Cu-mediated (**A**) and Pd-catalyzed (**B**) formation of diacetylene.[63] py = pyridyl.

the precursors, thus making this procedure more time-efficient.

Höger and Enkelmann applied this strategy to synthesize shape-persistent macrocyclic amphiphile **37** with a switchable arrangement of the polar (in their THP-protected form) and nonpolar functionalities (Scheme 7).[23] Palladium-catalyzed coupling of **33** with 3,5-diiodotoluene, followed by cleavage of the triisopropylsilylacetylene (TIPS) protecting group, provided tetrayne **34**, which was further coupled with 3-bromo-5-iodotoluene to give the dibromide **35**. Sonogashira coupling of **35** with trimethylsilylacetylene (TMSA), followed by removal of the TMS group, afforded the bisacetylene precursor **36**, which was subjected to an Eglington–Glaser coupling under high-dilution conditions to furnish the THP-protected macrocycle **37** in 45% yield. Acid-catalyzed

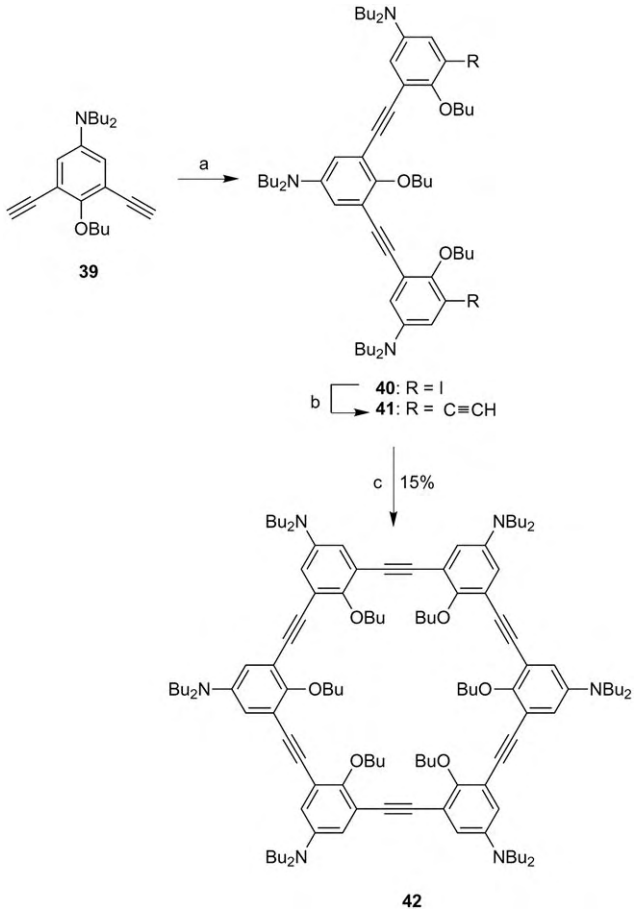


Scheme 7. a) 3,5-Diiodotoluene, $[PdCl_2(PPh_3)_2]$, CuI, piperidine, 55 °C, 14 h; b) Bu_4NF, THF, RT, 2 h (88%); c) 3-bromo-5-iodotoluene, $[PdCl_2(PPh_3)_2]$; CuI, piperidine, 55 °C, 14 h (84%); d) TMS-acetylene, $[PdCl_2(PPh_3)_2]$; CuI, piperidine, 55 °C, 4 d; e) NaOH, MeOH/THF, RT, 3 h (70%); f) $CuCl/CuCl_2$, pyridine, RT (45% yield); g) CH_2Cl_2/MeOH, H^+, 1 day (quantitative).[23] THP = tetrahydropyran.

 © 2006 Wiley-VCH Verlag GmbH & Co. KGaA, Weinheim

deprotection of **37** produced **38** in nearly quantitative yield. Macrocycle **38** represents the first example of an amphiphilic shape-persistent structure. A relatively free rotation about the diphenylacetylene units results in either a more hydrophilic or a more hydrophobic interior.

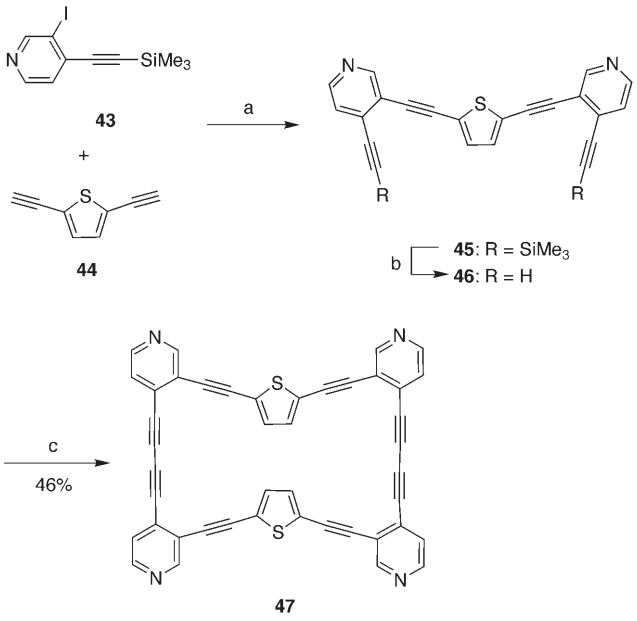
Cho and co-workers have also used a similar strategy to prepare a phenyleneethynylene macrocycle functionalized with dibutylamino and butyloxy groups (Scheme 8).[67,68] Diiodide **40** was obtained by the coupling of 1-butoxy-4-dibutylamino-2,6-diiodobenzene and **39** in a 2:1 ratio. Reaction of **40** with TMSA followed by deprotection of the TMS group under basic conditions provided terminal acetylene **41**. Subjecting a mixture of **41** and **40** to Sonogashira coupling conditions afforded the target macrocycle **42** in 15% yield.



Scheme 8. a) 1-Butoxy-4-dibutylamino-2,6-diiodobenzene (2 equiv), $[PdCl_2(PPh_3)_2]$, CuI, Et_3N/THF, RT, 18 h, 25%; b) 1. TMS-acetylene, $[PdCl_2(PPh_3)_2]$, CuI, Et_3N/THF, RT, 12 h, 80–95%, 2. KOH, MeOH/THF, RT, 1 h, 100%; c) **40**, $[PdCl_2(PPh_3)_2]$, CuI, Et_3N, RT, 48 h, 15%.[67]

An investigation of the photophysical properties of **42**[67] revealed it had a two-photon absorption behavior; the donor groups on the macrocycle increase the long-wavelength absorption maxima and the Stokes shift. The observed larger Stokes shift in a more polar solvent also indicates a significant degree of charge transfer in the excited state of macrocycle **42**.

Recently, Baxter prepared a new dehydroannulene-type macrocycle **47** comprised of a conjugated helical framework of thiophene (electron-donor) and pyridine (electron-acceptor) heterocyclic units (Scheme 9).[69] A Sonogashira

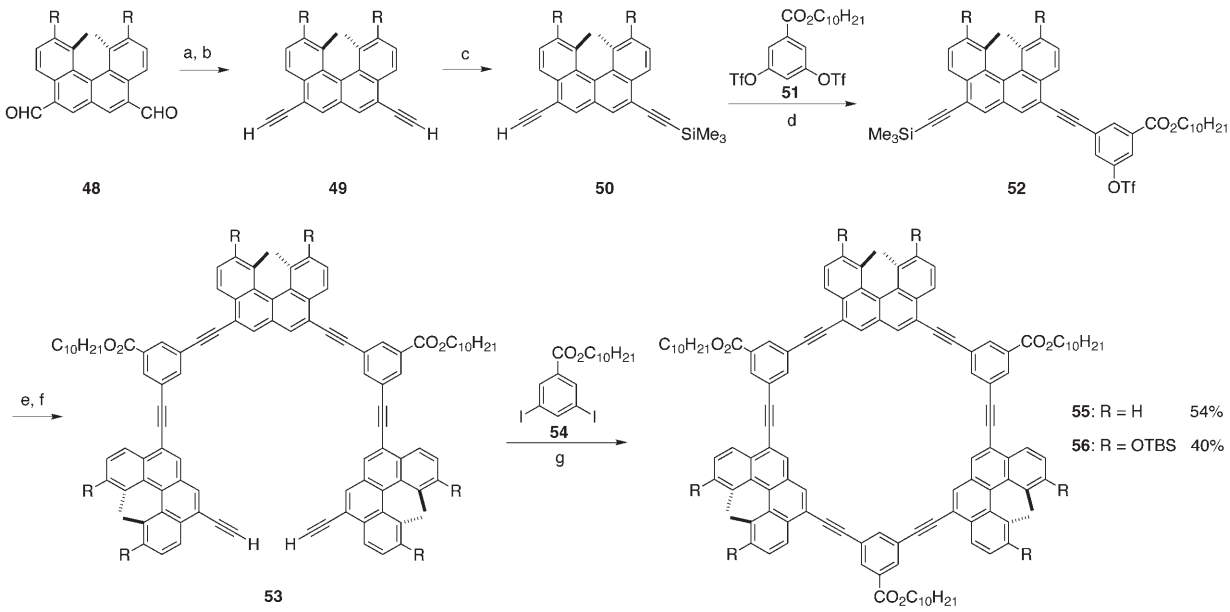


Scheme 9. a) $[PdCl_2(PPh_3)_2]$, CuI, toluene, Et_3N, 20°C, 5 days (54%); b) Bu_4NF, THF, H_2O, 20°C, 20 h (88%); c) $Cu_2(OAc)_4 \cdot 2H_2O$, pyridine, 20°C, 7 days (46%).[69]

reaction between **44** and two equivalents of **43** followed by desilylation provided dialkyne **46** in 88% yield. This oligomer was cyclized by using the Eglinton–Galbraith ethyne-coupling approach under moderate dilution conditions with an excess of $Cu_2(OAc)_4$ to afford macrocycle **47** in 46% yield. It was found that macrocycle **47** can function as a selective precipitation and fluorescence sensor[70–72] for specific metal ions such as Ag^I and it also exhibits reversible proton-triggered fluorescence quenching behavior. The unique donor–acceptor architecture and interesting spectroscopic properties of **47** indicate that such compounds may provide a platform for novel sensory functions.

Yamaguchi and co-workers prepared optically active helicene derivatives, such as chiral [3+3] cycloalkyne (*M*,*M*,*M*)-**55**, which is an arylene ethynylene macrocycle consisting of three (*M*)-helicenes and three *m*-phenylene units (Scheme 10).[73–75] Dialdehyde (*M*)-**48** was converted into the bis(dibromoolefin), then treated with excess *n*-butyllithium to give the diacetylene (*M*)-**49** in 99% yield. Monoprotected acetylene (*M*)-**50** was obtained in 62% yield from (*M*)-**49** by treatment with 1.1 equivalents of *n*-butyllithium. The Sonogashira coupling of (*M*)-**50** and 5 equivalents of ditriflate **51** gave (*M*)-**52**, which was coupled with (*M*)-**49**. Desilylation of the product afforded the trimeric precursor (*M*,*M*,*M*)-**53**. Cyclization of **53** with diiodobenzene **54** under highly dilute conditions furnished the [3+3] cycloalkynes (*M*,*M*,*M*)-**55** and (*M*,*M*,*M*)-**56** in yields of 54 and 40%, respectively. Macrocycle **55** (R = H) was found to form

 © 2006 Wiley-VCH Verlag GmbH & Co. KGaA, Weinheim



Scheme 10. a) PPh_3, CBr_4, CH_2Cl_2; b) *n*BuLi, THF; c) *n*BuLi, Me_3SiCl, THF; d) **51**, $[Pd_2(dba)_3]$, CuI, Mes_3P, PPh_3, Bu_4NI, NEt_3, DMF; e) **49**, $[Pd_2(dba)_3]$, CuI, Mes_3P, PPh_3, Bu_4NI, NEt_3, DMF; f) Bu_4NF, THF; g) **54**, $[Pd_2(dba)_3]$, CuI, Mes_3P, Bu_4NI, NEt_3, DMF, toluene (40–54%).[73,75] TBS = *tert*-butyldimethylsilyl, Tf = trifluoromethanesulfonyl.

a strong and selective bimolecular aggregate in $CHCl_3$ and benzene.[75] Its aggregation was ascribed to the π–π interactions between the nonplanar π-electron system of a helicene. Studies of derivatives of (*M*,*M*,*M*)-**55** revealed that the species with flexible linkers form intramolecular aggregates, while those with rigid and linear linkers form dimolecular aggregates.[74] Other [3+3] cycloalkyne derivatives (R = OTf, ONf, OAc, OH) were also prepared from (*M*,*M*,*M*)-**56**. It was found that the aggregation of the functionalized [3+3] cycloalkynes is stronger for the compounds with electron-withdrawing substituents than for those with electron-donating substituents.[73]

2.4. Templated Cyclization

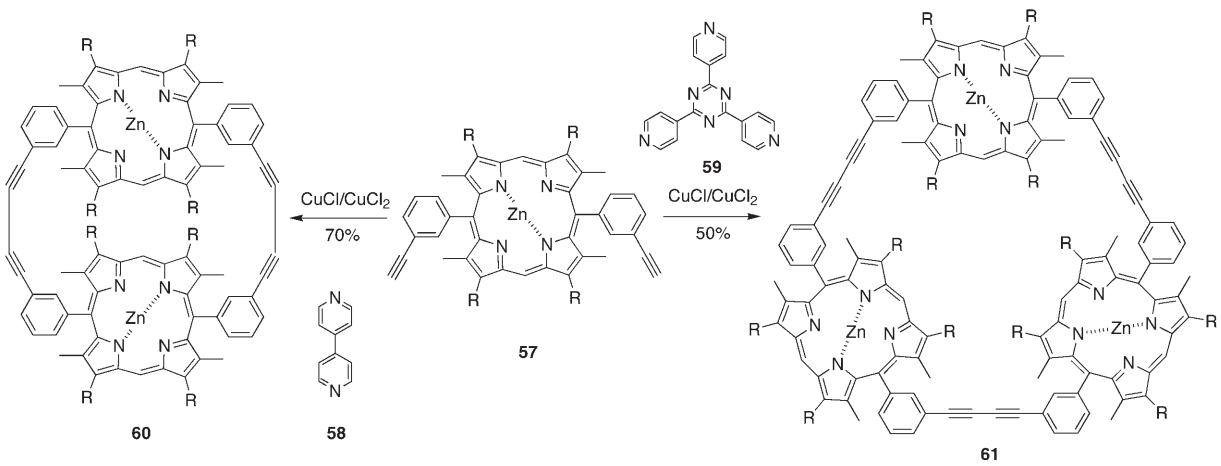
Although the macrocycle yield is greatly improved by preformation of oligomers, as shown in the previous section, the efficiency of the cyclization was still only modest in some cases. Further breaking down the cyclization precursors into three or more pieces led to lower cyclization yields.[24] Moreover, conducting the reaction under high-dilution conditions can only partially prevent oligomerization and it requires large amounts of solvent. A templated cyclization strategy was thus explored to more effectively promote the intramolecular coupling, and thus increase the ratio of cyclic to linear products.

Anderson and Sanders were the first to use the template methodology to synthesize shape-persistent macrocycles (Scheme 11).[76,77] Initially, the relatively small bisacetylene **57** was cyclized under oxidative conditions and a mixture of macrocycles of different size was obtained, as expected. However, when the cyclization was performed in the presence of an appropriate template, such as 4,4′-bipyridyl (**58**) or terpyridyl **59**, the cyclic dimer **60** or the cyclic trimer **61** was obtained in 70% and 50% yields, respectively. An arrangement of the precursors around the pyridyl derivative, which functions as a template, is suggested to be the reason for the kinetic selectivity in these reactions.

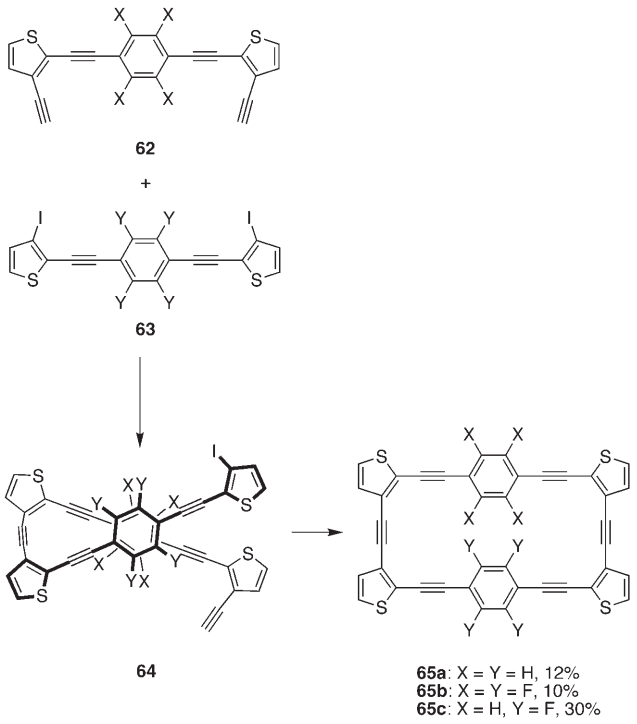
Marsella et al. synthesized the thiophene-containing arylene ethynylene macrocycles **65a–c** by Sonogashira coupling of dialkyne **62** with diiodide **63** (Scheme 12).[78] The electronic interactions between Ar_H and Ar_F units[79] were used to template the macrocycle synthesis in solution. The macrocyclization involved linear intermediate **64**, which is suggested to play a decisive role in the formation of the macrocycle by acting as both a substrate and template. As expected, macrocycle **65c** (X = H, Y = F), the structure in which π–π stacking is strongest, is obtained in the highest yield (30% for **65c** versus 12% and 10% for **65a** and **65b**, respectively). This represents the first example in which electrostatic interactions between perfluorophenyl and phenyl moieties were used as a noncovalent templating force in shape-persistent macrocycle synthesis.

Höger et al. utilized an ester linkage instead of noncovalent metal coordination or electrostatic interactions in their templated synthesis of phenyleneethynylene macrocycles (Scheme 13).[7,24,26] Initially, the polar alcohol functionality in diyne **66** was protected as a benzoate group to give **67**. When **67** was subjected to intermolecular cyclization under dilution conditions, the crude product contained mostly polymeric products along with cyclic trimer in only 20–25% yield. This cyclization roughly follows the expected statistics (see previous section). In contrast, cyclization of template-bound hexaacetylene **68**, also prepared from **66**, afforded a crude product that contained more than 95% of the template-

 © 2006 Wiley-VCH Verlag GmbH & Co. KGaA, Weinheim



Scheme 11. Synthesis of porphyrin oligomers **60** and **61** using noncovalent templates.[76,77]



Scheme 12. Synthesis of thiophene-containing macrocycles **65**. Reaction conditions: $[PdCl_2(PPh_3)_2]$, CuI, iPr_2NH, THF, 80 °C.[78]

bound cyclic trimer **69**. Base-catalyzed cleavage of the ester bonds generated the desired macrocycle **70** in nearly quantitative yield.

The basic concept behind templated cyclization involves an overall low concentration of reactive compounds in the reaction mixture (as a result of high-dilution conditions) together with a high local concentration of terminal acetylenes (as a consequence of the preorganization of the reaction precursors), thus greatly facilitating the cyclization process. In these templated reactions, the size of the macrocycle can be controlled by template design.[76,77] Covalently linked templates usually require the introduction of specific functional groups into the substrate and extra synthetic steps for attachment and cleavage. From the standpoint of synthetic effort, noncovalent templates may be superior to covalent ones given their reversible formation and the ease of template removal.

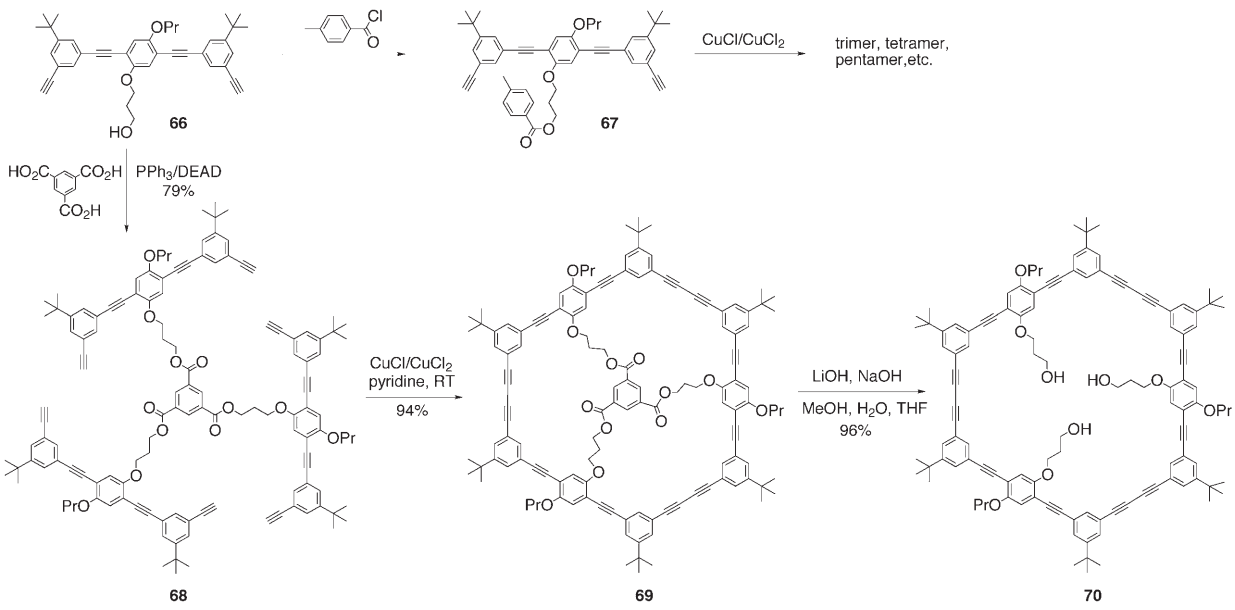
3. Thermodynamically Controlled Synthesis of Arylene Ethynylene Macrocycles

The primary disadvantage of coupling-based approaches is that the product distribution is kinetically determined and it is not possible to correct undesired bond formation. The formation of higher oligomers (overshooting) is an additional problem that lowers the yield of the desired product. Therefore, considerable effort must generally be put into developing synthetic strategies that avoid the formation of undesired oligomers.

The past decade has witnessed the use of thermodynamically controlled, noncovalent metal coordination interactions to prepare shape-persistent metal-linked macrocycles in high yield.[80] More recently, promising approaches based on dynamic covalent chemistry (DCC)[37,38] (imine metathesis[39] and alkyne metathesis[34,40–42]) have been successfully utilized, for example, to provide shape-persistent arylene ethynylene macrocycles in high yield. The reversible nature of dynamic covalent chemistry overcomes the formation of kinetically introduced, undesired bonds. The distribution of products depends on the relative stabilities of all possible structures. Provided there is a large enough energy gap between the desired macrocycle and other possible oligomeric and macrocyclic products, the target structure will be generated as the major product at equilibrium (see Figure 4).

A prerequisite for the selective generation of thermodynamically stable products in high yield is an appropriate chemical reaction.[37] As a reversible approach to joining difunctionalized monomer units, metathesis reactions ensure nearly equivalent bond energies on both sides of the equilibrium equation. Since the changes in bond energies do not significantly bias the reaction equilibrium, the product distribution is mainly determined by the thermodynamic stability of each species.

 © 2006 Wiley-VCH Verlag GmbH & Co. KGaA, Weinheim

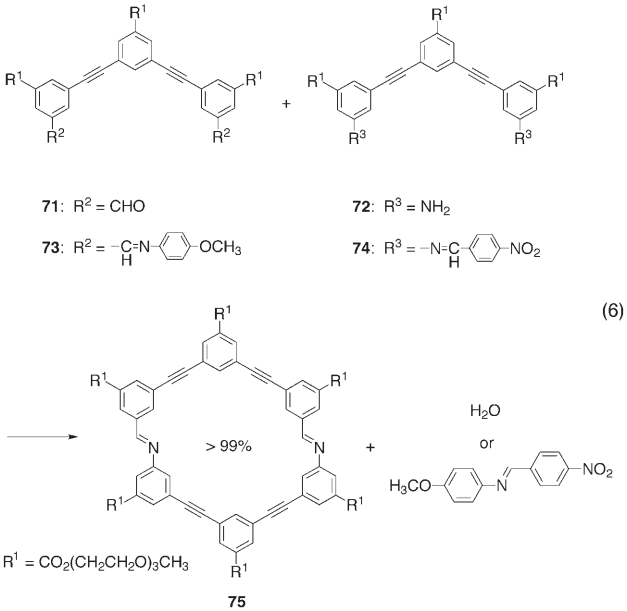


Scheme 13. Synthesis of macrocycle **70** using a covalently bound template.[7] DEAD = diethylazodicarboxylate.

3.1. Imine Metathesis

Our research group reported the synthesis of an imine-containing phenyleneethynylene macrocycles through a reversible imine metathesis [Eq. (6)].[81]

Reaction of dialdehyde **71** and diamine **72** at relatively high concentration in methanol at reflux provided a nearly quantitative conversion into macrocycle **75**. Surprisingly, even without any effort made to remove the condensation by-product (water) from the system, the reversible imine condensation proceeded to almost completion and afforded the macrocycle exclusively. Further studies showed that the imine metathesis between oligomer **73** and **74** through imine metathesis is dependent on the solvent: although the conversion into macrocycle **75** was nearly quantitative in acetonitrile, the yield was significantly lower in chloroform. These results can be rationalized by considering the aggregation behavior of the macrocycle. The generated macrocycle was found to be stabilized by intermolecular aromatic stacking interactions, which resulted in macrocycle aggregation in polar solvents such as acetonitrile and methanol.[81,82] The self-association behavior of **75** exhibited in both solution and the solid state suggests that the "geometry" of the imine bond is compatible with the *m*-phenyleneethynylene system and does not significantly interfere with π–π stacking interactions. Hence, the imine functionality can serve as a suitable reversible linking group, thus enabling exchange or metathesis reactions among *m*-phenyleneethynylene oligomers of various lengths and backbone structures.[39]

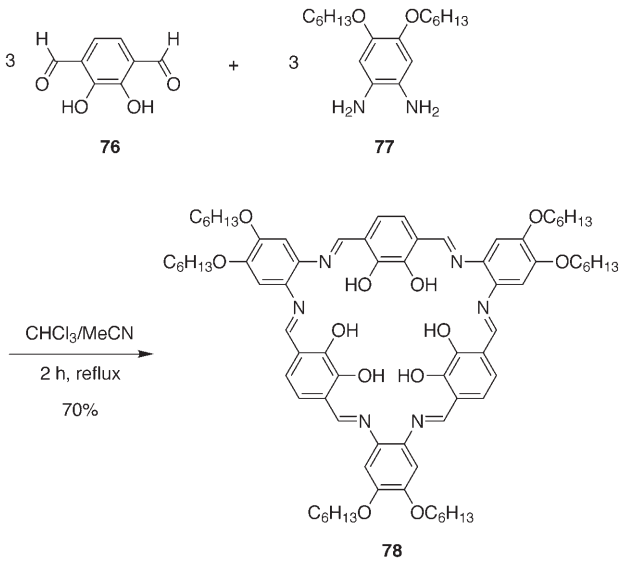


(6)

MacLachlan and co-workers have also used this Schiff base condensation approach to prepare shape-persistent conjugated macrocycles (Scheme 14).[83–85] Macrocycle **78** was prepared in 70% yield by cyclooligomerization of 3,6-diformylcatechol (**76**) and phenylenediamine **77**. The selective generation of macrocycle **78** was suggested to result from the reversibility of the imine condensation, which allows the reaction to reach the thermodynamically favored [3+3] macrocyclic condensation product. This reaction is an example of a cyclooligomerization of A_2- with B_2-type monomers under reversible conditions.

To illustrate that the energy gap principle accounts for the high yield of the [3+3] product, we performed simple calculations on the thermodynamic stability of the three possible macrocyclic products **78**, **79**, and **80** (Figure 11) generated by imine metathesis. We consider the distribution of products from [2+2] tetracycle **79** (2 equiv of **76** reacting with 2 equiv of **77**) to [4+4] octacycle **80** (4 equiv of **76** reacting with 4 equiv of **77**) by comparing their individual

 © 2006 Wiley-VCH Verlag GmbH & Co. KGaA, Weinheim



Scheme 14. Synthesis of conjugated Schiff base macrocycle **78**.[85]

stabilities relative to [3+3] hexacycle **78**. Entropy can play a decisive role in cyclooligomerization and tends to favor macrocycles having the fewest numbers of monomer units. The relative entropy change between the various macrocycles

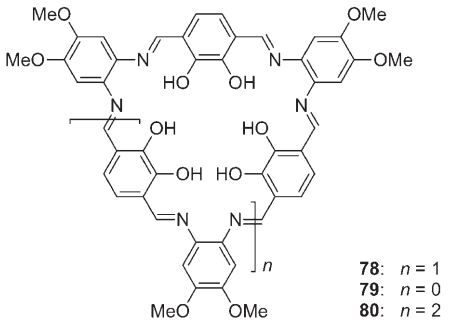


Figure 11. Macrocyclic products generated by imine metathesis.

can be estimated from a semiquantitative model,[86] and the relative enthalpy change can be estimated by using molecular mechanics models (Table 4).[87] With the entropy and

Table 4: Change in the Gibbs free energy (ΔG) in Reactions (7) and (8).

Equation	ΔH [kcal mol^{-1}]	ΔS [kcal mol^{-1} K]	ΔG [kcal mol^{-1}] (363 K)
7	16.8	0.029	6.2
8	0.39	−0.015	6.0

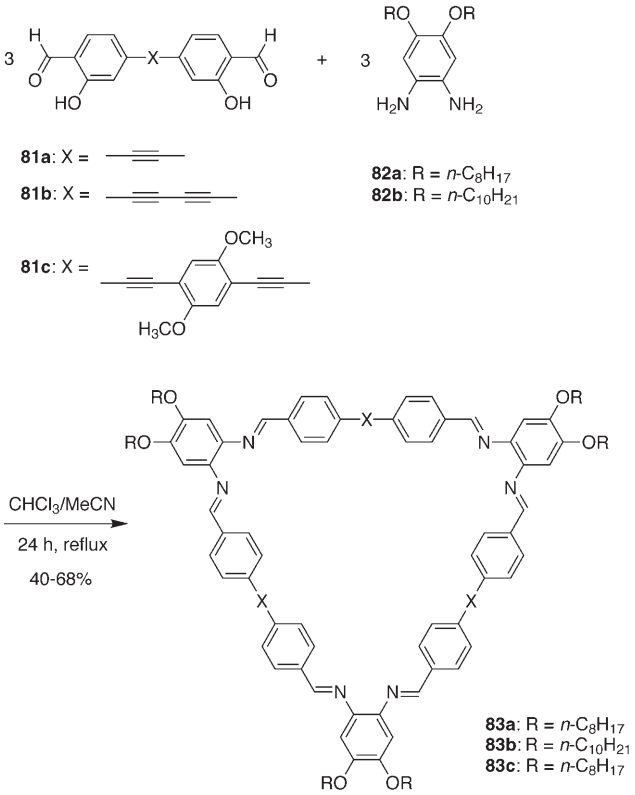
enthalpy values of these macrocycles in hand, the Gibbs free energy of each macrocycle ($n = 0$, 1, 2) relative to hexacycle **78** [Eqs. (7) and (8)] can be estimated. These

2 cyclic trimer $\rightleftharpoons$ 3 cyclic dimer (7)

4 cyclic trimer $\rightleftharpoons$ 3 cyclic tetramer (8)

calculations show that the [3+3] hexacycle **78** is more stable than the smaller tetacycle **79** because it is enthalpically favored as a result of less angle strain, while hexacycle **78** is entropically favored over the larger octacycle **80**. Therefore, **78** is the most favored among all the macrocycles generated during the imine metathesis. Calculations of this sort may find practical utility as a predictive tool for reversible cyclo-oligomerizations.

Gallant and MacLachlan have demonstrated that macrocycle **78** exhibits crown ether like behavior, in which the internal phenolic oxygen atoms coordinate to small cations seated at the center of the macrocycle.[85] However, **78** has a very small interior diameter and it adopts a nonplanar conformation even when coordinated to transition metals. Macrocycles with metals spaced farther apart are required for the construction of large, flat macrocycles that can assemble into nanotubes. MacLachlan and co-workers synthesized compound **81a–c** by either Pd-catalyzed Sonogashira coupling or Cu-catalyzed oxidative coupling, and subjected them to imine-condensation conditions with diamine **82**, thus affording target macrocycles **83a–c** in 40–68% yield (Scheme 15).[83] The incorporation of phenyleneethynylene spacers into the backbone of the macrocycles enables the facile preparation of large, planar macrocycles with tunable diameters. These macrocycles can bind multiple metals, thus forming soluble, luminescent complexes which offer potential opportunities for developing supramolecular materials and sensors triggered by metal–ligand coordination.



Scheme 15. Synthesis of conjugated Schiff base macrocycles **83**.[83]

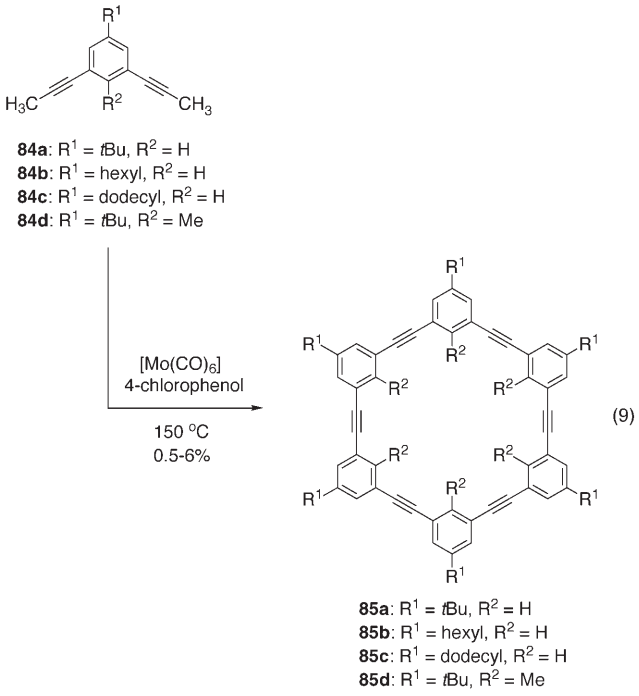
 © 2006 Wiley-VCH Verlag GmbH & Co. KGaA, Weinheim

3.2. Alkyne Metathesis

3.2.1. Conventional Vacuum-Driven Alkyne Metathesis

Analogous to alkene[88] and imine metathesis,[39] alkyne metathesis is a fast, reversible process. In the past few years, alkyne metathesis with either defined carbyne complexes[89,90] or catalysts generated in situ[91,92] has been used to synthesize saturated and unsaturated ring systems. The reversibility of the alkyne metathesis reaction[34,40–42] has attracted growing attention as a potentially powerful method for preparing arylene ethynylene macrocycles.

Bunz and co-workers were the first to use alkyne metathesis to prepare hexakis(phenyleneethynylene) macrocycles [Eq. (9)].[92] Monomers **84** were obtained from the corresponding diiodides by Pd-catalyzed propynylations. Reaction of **84**, with a metathesis catalyst generated in situ from $[Mo(CO)_6]$ and 4-chlorophenol (or 4-trifluoromethylphenol) in 1,2-dichlorobenzene at 150 °C under nitrogen provided macrocycles **85** in 0.5–6% yield. The high temperature required by the "instant" catalyst and the difficulty in product purification may mean that the isolated yield does not truly reflect the thermodynamically controlled product distribution. An X-ray crystal structure of **85a** revealed a porous solid with infinite elliptical channels. This structure demonstrates that shape-persistent hydrocarbon **85a** does not require hydrogen bonding or long alkyl chains to arrange into tubular structures with intrastack channels; van der Waals interactions alone are sufficient to line up these rings into tubular forms.



84a: R^1 = *t*Bu, R^2 = H
84b: R^1 = hexyl, R^2 = H
84c: R^1 = dodecyl, R^2 = H
84d: R^1 = *t*Bu, R^2 = Me

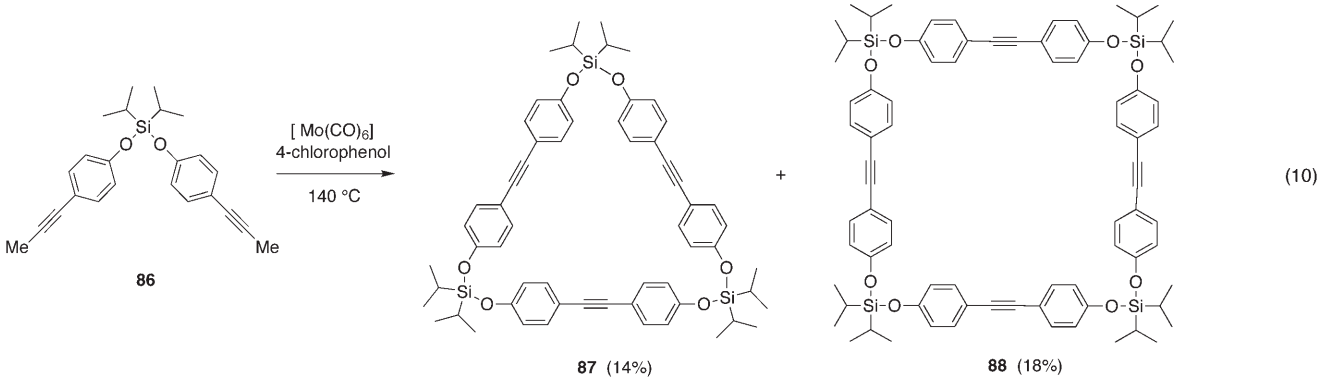
(9)

85a: R^1 = *t*Bu, R^2 = H
85b: R^1 = hexyl, R^2 = H
85c: R^1 = dodecyl, R^2 = H
85d: R^1 = *t*Bu, R^2 = Me

Similarly, alkyne metathesis of dialkyne **86** in the presence of $[Mo(CO)_6]$ and 4-chlorophenol at 140 °C in 1,2-dichlorobenzene afforded the silicon-containing phenyleneethynylene cyclic trimer **87** and tetramer **88** in yields of 14% and 18%, respectively [Eq. (10)].[91,93,94] Crystalline **88** exhibits a rhomboidal structure that contains a large interior cavity occupied by two molecules of hexane from the solvent from which it was crystallized. This feature indicates the potential application of these box-shaped molecules in host–guest chemistry.

Vollhardt and co-workers have utilized Schrock's catalyst to synthesize the trimeric *ortho*-dehydrobenzannulenes through alkyne metathesis [Eq. (11)].[95] Reactions of dialkyne monomer **89a–d** at 80 °C in toluene with 20 mol% catalyst loading provided the target cyclic trimers **90a–d** in yields of 12–54%.[96] However, the doubly *ortho*-substituted precursors **89e,f** did not undergo cyclization, presumably because the substituents cause steric hindrance at the alkyne groups which impedes the metathesis reactions.

Although carbyne complexes[95] and catalysts generated in situ[92,94] have led to clear advances in the synthesis of phenyleneethynylene macrocycles by alkyne metathesis, the required high reaction temperature and/or low yield greatly impede the exploration of broader substrate scope and makes large-scale preparation of the macrocycles impractical. For the purposes of low-temperature dynamic covalent approaches, it was necessary to utilize more active alkyne metathesis catalysts. The ideal catalyst should be convenient to synthesize, possess broad substrate compatibility, and exhibit catalytic activity at low temperature. Other possibilities for improving metathesis-based cyclooligomerizations would include adopting alternative driving forces that could efficiently remove the by-product and so favorably shift the monomer–oligomer equilibrium.



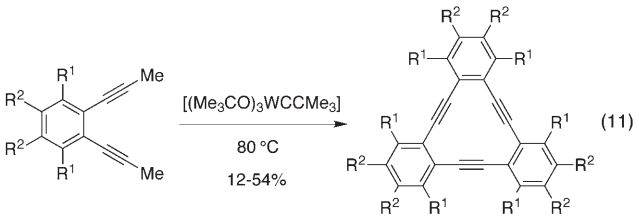
86

87 (14%)

88 (18%)

(10)

© 2006 Wiley-VCH Verlag GmbH & Co. KGaA, Weinheim

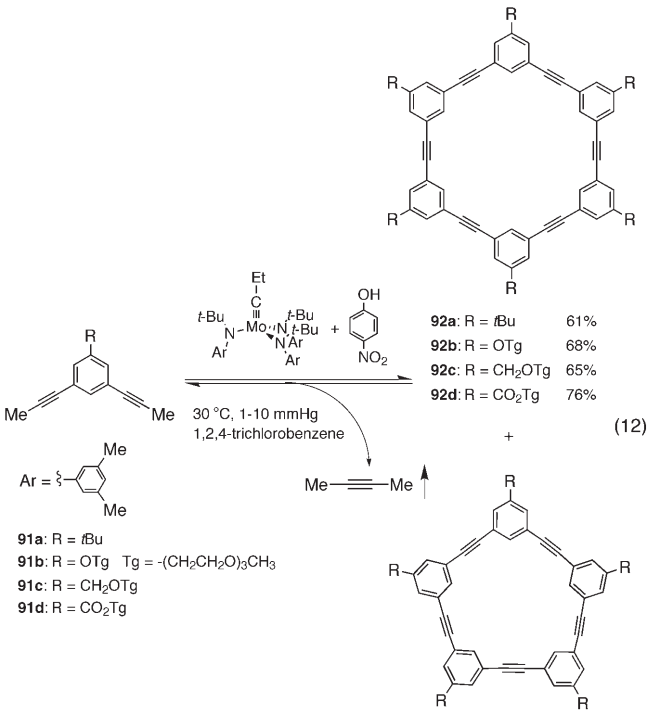


89a: $R^1 = R^2 = H$
89b: $R^1 = H$, $R^2 = Me$
89c: $R^1 = H$, $R^2 = OMe$
89d: $R^1 = H$, $R^2 = Br$
89e: $R^1 = R^2 = Me$
89f: $R^1 = Br$, $R^2 = H$

90a: $R^1 = R^2 = H$ (54%)
90b: $R^1 = H$, $R^2 = Me$ (27%)
90c: $R^1 = H$, $R^2 = OMe$ (28%)
90d: $R^1 = H$, $R^2 = Br$ (12%)
90e: $R^1 = R^2 = Me$ (0%)
90f: $R^1 = Br$, $R^2 = H$ (0%)

Molybdenum or tungsten complexes have been most widely used as alkyne metathesis catalysts in organic synthesis and polymer chemistry.[34,40,89–92] We developed a reductive recycle strategy[41] for conveniently preparing molybdenum(VI)–alkylidyne catalyst precursors, which are converted into a room-temperature-active catalyst compatible with a variety of functional groups and solvents simply by the addition of phenols.[42] The highly active catalysts in general allow arylene ethynylene macrocycles to be prepared in one synthetic step in high yield at room temperature.[97,98]

In the initial attempts, alkyne metatheses were conducted in a high-boiling solvent under conventional vacuum-driven conditions[89,97,99] to facilitate removal of by-products. The phenyleneethynylene macrocycles **92a–d** were obtained in good yields on a small scale (15–33 mg, 61–76% yield) from dialkyne monomers **91a–d** in the presence of alkylidynetris-amidomolybdenum(VI) complexes (10 mol%) and three equivalents of *p*-nitrophenol [Eq. (12)].[100] Although the substrates functionalized with electron-rich groups (for example, alkoxy groups) react much faster than those substituted with electron-poor groups (for example, ester groups),[42,101] the electronic effect of the substituents on the monomers does not affect the yield of the target macrocycles. In other words, the one-step alkyne metathesis is a general approach. Importantly, these reactions did not require high-dilution conditions to achieve good yields of the macrocyclic products.



91a: R = *t*Bu
91b: R = OTg Tg = -$(CH_2CH_2O)_3CH_3$
91c: R = CH_2OTg
91d: R = CO_2Tg

92a: R = *t*Bu 61%
92b: R = OTg 68%
92c: R = CH_2OTg 65%
92d: R = CO_2Tg 76%

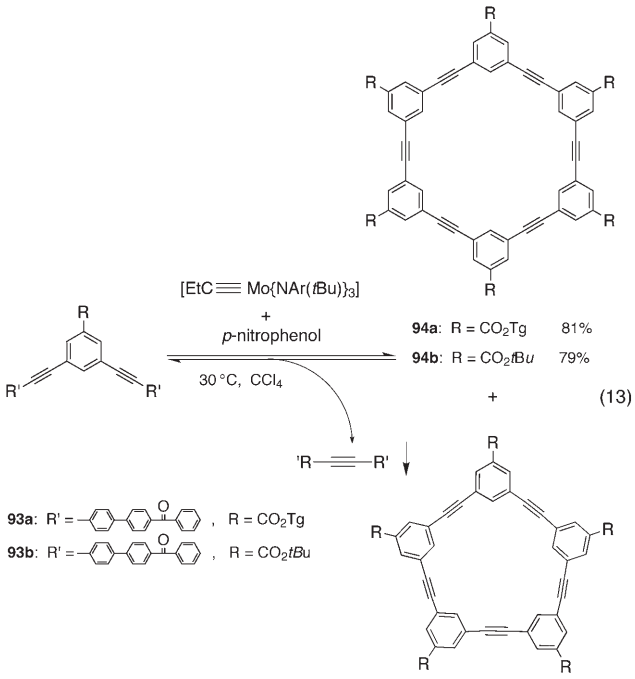
However, several attempts to increase the scale of the vacuum-driven strategy resulted in poor yields of the macrocycle, low conversions, and considerable amounts of oligomeric products. Failure to scale the reaction was thought to be due to the "pseudopoisoning" effect of the by-product on the metathesis catalyst.[102] Alkyl-substituted alkynes are more reactive than aryl alkynes in alkyne metathesis reactions and electron-deficient aryl alkynes react slower than electron-rich aryl alkynes.[42,101,103] Hence, the reaction of the Mo^{VI} catalyst with butyne is presumably favored over its reaction with oligomers. For the gram-scale preparation of macrocycle **92d**, the by-product 2-butyne (or 3-hexyne) was more difficult to remove efficiently than in small-scale syntheses. The catalyst thus performs unproductive butyne metathesis rather than the desired elongation and cyclization; the nonproductive route dominates the catalytic activity. Moreover, the catalyst is eventually deactivated by polymerization of the butyne by-product if its concentration becomes too high.[42] These results indicate that dialkyl-substituted alkyne by-products should be avoided (or efficiently removed) if the metathesis of electron-deficient aryl substrates is to proceed with high conversion.

3.2.2. Precipitation-Driven Alkyne Metathesis

To overcome the "pseudopoisoning" effect and improve the efficiency of alkyne metathesis for macrocycle preparation, we envisioned that a poorly soluble, less-reactive diarylacetylene by-product would enable the efficient removal of the by-product from the reaction mixture and thus allow the desired metathesis reaction to be performed in a closed system. Precipitation rather than evaporation thus serves as the driving force to shift the metathesis equilibrium. It was discovered that the metathesis of the benzoylbiphenyl-substituted monomers **93a–b** in the presence of a molybdenum(VI)–propylidyne catalyst at 30 °C provided macrocycles **94a,b** in high yields along with a small amount of pentacycles [Eq. (13)].[97] The diarylacetylene by-product is extremely insoluble in a variety of solvents: its solubility is only 1.09×10^{-6} mol L^{-1} in CCl_4 at 25 °C. Thus, removal of the by-product by precipitation is highly efficient. Multigram synthesis of **94a** was accomplished in one step by using the precipitation-driven approach under optimized conditions (5.68 g, 77%), and represents the first successful large-scale preparation of hexakisphenyleneethynylene macrocycles.

These results highlight the significant advantages of precipitation-driven alkyne metathesis over the traditional vacuum-driven approach. In particular, no extra effort is necessary to ensure efficient removal of the by-product, because once it is generated, it precipitates and does not interfere with the activity of the catalyst. Therefore, in addition to serving as the driving force for the metathesis

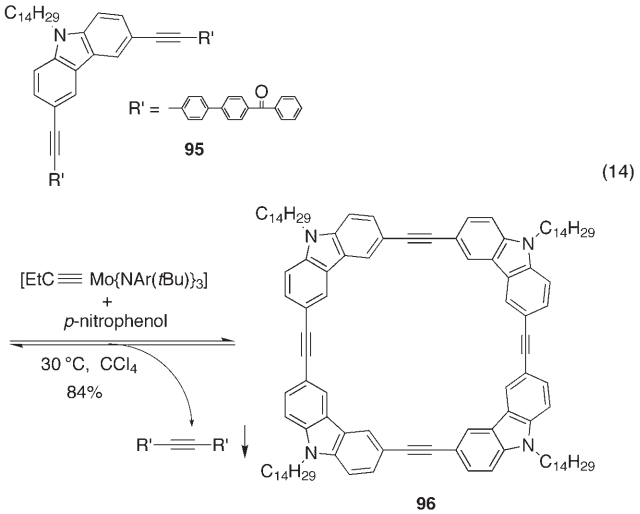
 © 2006 Wiley-VCH Verlag GmbH & Co. KGaA, Weinheim



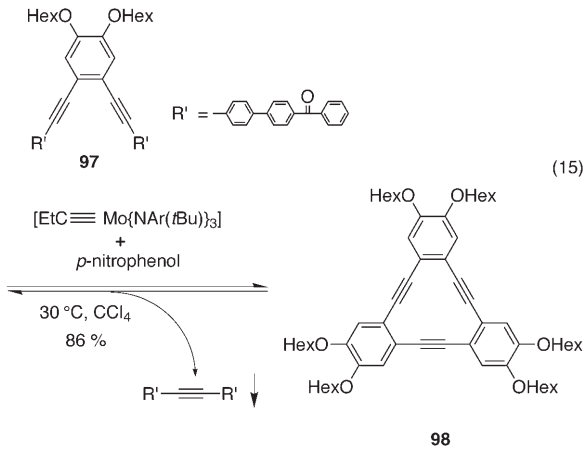
(13)

reaction, the precipitation of the by-product also prevents catalyst "pseudopoisoning". Moreover, the product is isolated simply by filtration followed by concentration of the solution.

The generality of this precipitation-driven strategy was further demonstrated by the successful syntheses of square-shaped macrocycle **96**[104] from dialkyne **95** [Eq. (14)].[97,105] The only product observed was tetracycle **96**, which was isolated in 84% yield. As a further illustration, triangle-shaped macrocycle **98** was successfully prepared in one step from monomer **97** in 86% yield [Eq. (15)],[106] which is significantly higher than the yields derived from cross-coupling reactions [**2** in Eq. (1), **9** in Eq. (4)]. All the reactions were performed in CCl_4 at 30 °C in closed reaction vessels. It is envisioned that the precipitation-driven, reversible alkyne metathesis may open the way to other two-dimensional or three-dimensional arylene ethynylene structures as well as alkyne-bridged oligomers and polymers.



(14)

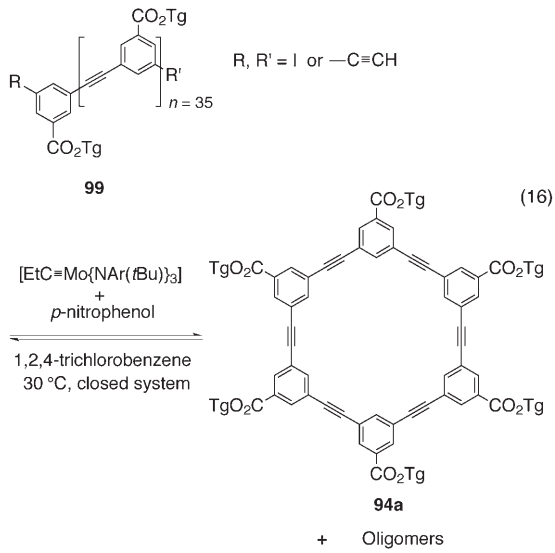


(15)

3.2.3. *Thermodynamic Stabilities of Arylene Ethynylene Macrocycles (Energy Gap Principle) and the Cyclooligomer Distribution*

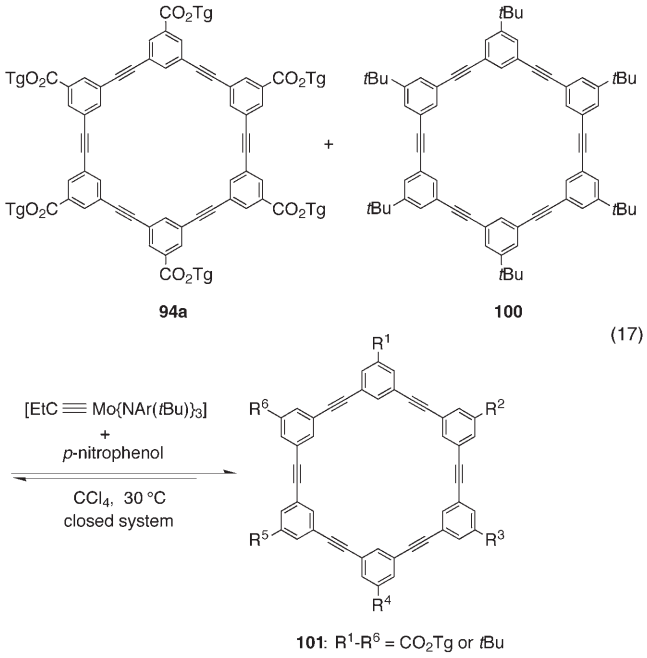
A series of experiments were conducted to reveal the underlying principles for the selective generation of certain arylene ethynylene macrocycles by alkyne metathesis and to demonstrate that the reaction is truly thermodynamically controlled.[102] One piece of evidence supporting the reversibility of all the steps in the formation of the macrocycle was obtained by subjecting a presynthesized phenyleneethynylene polymer to alkyne metathesis conditions [Eq. (16)]. Analysis of the reaction mixture by gel permeation chromatography (GPC) showed the transformation of polymer into shorter oligomers, with hexacycle **94a** as the major product.

Additional evidence was gained through a scrambling experiment, in which a 1:1 mixture of two different phenylene ethynylene macrocycles (**94a** and **100**) was subjected to metathesis [Eq. (17)]. A series of scrambled macrocyclic products having different combinations of Tg- and *t*Bu-substituted side chains were observed in the MALDI mass



(16)

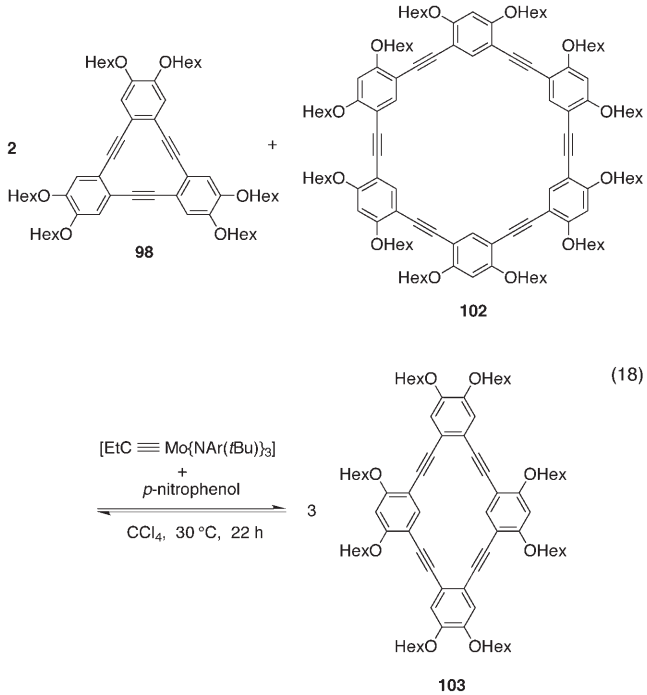
 © 2006 Wiley-VCH Verlag GmbH & Co. KGaA, Weinheim



(17)

spectrum, further demonstrating the reversibility of macrocycle formation.

A more interesting scrambling experiment was also performed in which a 2:1 mixture of macrocycles **98** and **102** was subjected to metathesis [Eq. (18)] followed by FD-MS analysis.[106] A tetrameric macrocycle, presumably structure **103** (*m*/*z* 1200) having two *ortho*-disubstituted units from **98** (*m*/*z* 900) and two *meta*-disubstituted units from **102** (*m*/*z* 1800), was observed. All the evidence indicates that the formation of phenyleneethynylene hexacycles under these conditions is thermodynamically controlled.



(18)

Theoretical calculations on the thermodynamic stabilities of shape-persistent macrocyclic compounds added further evidence in surpport of the observed product distribution as the equlibrium distribution. The distribution of products from tetracycle to octacycle [Eq. (13)] was calculated relative to the hexacycle,[86,87] with the Gibbs free energy of each macrocycle ($n = 4, 5, 7, 8$) estimated from the entropy and enthalpy values of these macrocycles (see Table 5 and Figure 12 as well as Equations (19)–(22)). These calculations show that the hexacycle is more stable than smaller macrocycles ($n = 4$, 5) at 30 °C because it is enthalpically favored as a result of less angle strain. In contrast, the conversion of hexacycle into large-sized macrocycles ($n = 7$, 8) is largely disfavored entropically. Therefore, the cyclic hexamer is the most favored product among all the macrocycles generated during metathesis. Under the reversible conditions used in the dynamic covalent approach, large macrocyclic compounds observed by MALDI-MS at an early stage in the cyclooligomerization process transform into the cyclic hexamer and a smaller amount of the cyclic pentamer, which is consistent with the expected thermodynamic equilibrium.

4 cyclic hexamer ⇌ 6 cyclic tetramer (19)

5 cyclic hexamer ⇌ 6 cyclic pentamer (20)

7 cyclic hexamer ⇌ 6 cyclic heptamer (21)

8 cyclic hexamer ⇌ 6 cyclic octamer (22)

Table 5: Change in the Gibbs free energy (ΔG) in Reactions (19)–(22).

Equation	ΔH [kcal mol^{-1}]	ΔS [kcal mol^{-1} K]	ΔG [kcal mol^{-1}] (303 K)
19	24.4	0.030	15.6
20	4.1	0.012	0.54
21	0.9	−0.009	3.53
22	1.2	−0.015	5.81

The calculations also rationalize the experimentally observed temperature dependence of the hexacycle to pentacycle ratio [see Eq. 13].[102] It was found that the ratio of cyclic hexamer to pentamer decreased from 6.5:1.0 at 30 °C to 2.9:1.0 at 95 °C. When pure cyclic hexamer **93a** was subjected to alkyne metathesis at 95 °C, a mixture of hexacycle and pentacycle in a 2.9:1.0 ratio was obtained. This ratio is similar to that obtained directly from monomers at this temperature. Moreover, when the purified macrocycle mixture from the metathesis reaction at 75 °C (3.3:1.0 hexacycle/pentacycle) was resubjected to alkyne metathesis at 30 °C, the ratio of cyclic hexamer to cyclic pentamer increased to 6:1 after 22 h. The decrease in the ratio of cyclic hexamer to cyclic pentamer at elevated temperatures reflects the entropically favored formation of smaller macrocycles. These results illustrate the importance of conducting the metathesis reaction at low temperatures to favor the formation of larger cyclic hexamers. In this case, the energy gap (Figure 4) is not sufficiently great to yield an exclusive product, although the gap begins to widen at lower temperatures.

The calculated thermodynamic stabilities of carbazole-based macrocyclic compounds **96**, **104**, and **105** (Figure 13)

 © 2006 Wiley-VCH Verlag GmbH & Co. KGaA, Weinheim

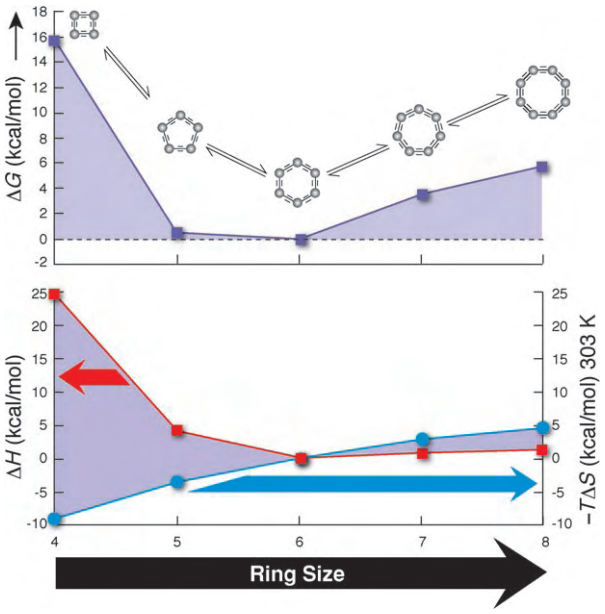


Figure 12. Approximate change in the Gibbs free energy of cyclic oligomers (tetracycle to octacycle) relative to the hexacycle. The plot of ΔH (red line) and $-T\Delta S$ (blue line) versus ring size shows that at 30 °C the hexacycle is more stable than smaller macrocycles (tetracycle and pentacycle) because it is enthalpically favored as a result of less angle strain. In contrast, the conversion of hexacycle into large-sized macrocycles (heptacycle and octacycle) is largely disfavored entropically.

are consistent with the observation of a single product (Table 6). As can be seen from Equations (23) and (24) as

3 cyclic teramer ⇌ 4 cyclic trimer (23)

5 cyclic teramer ⇌ 4 cyclic pentamer (24)

well as Table 6, tetrameric macrocycle **96** is thermodynamically more stable than its trimeric and pentameric species **104** and **105**, respectively. This result is consistent with our observation of the unique formation of tetracycle **96**.

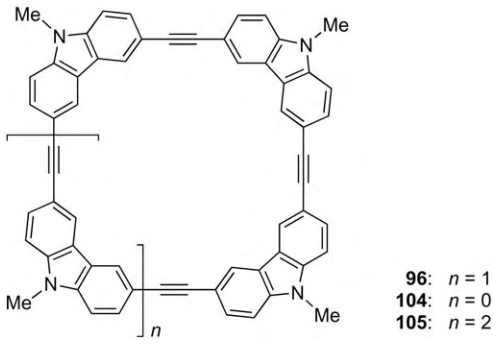


Figure 13. Carbazole-based macrocycles.

Similarly, the thermodynamic stabilities of catechol-based macrocyclic compounds were also calculated (Figure 14, Equations (25) and (26), Table 7). On the basis of the

Table 6: Change in the Gibbs free energy (ΔG) in Reactions (23) and (24).

Equation	ΔH [kcal mol^{-1}]	ΔS [kcal mol^{-1} K]	ΔG [kcal mol^{-1}] (303 K)
23	13.9	0.019	8.1
24	1.6	−0.012	5.2

2 cyclic trimer ⇌ 3 cyclic dimer (25)

4 cyclic trimer ⇌ 3 cyclic tetramer (26)

calculations it seems that trimeric macrocycle **98** is also thermodynamically more stable than the dimer **106** and tetramer **107**. This result is again consistent with our previously observed exclusive formation of cyclic trimer **98** and further demonstrates the importance of the energy gap principle to the favored formation of a unique macrocyclic product.

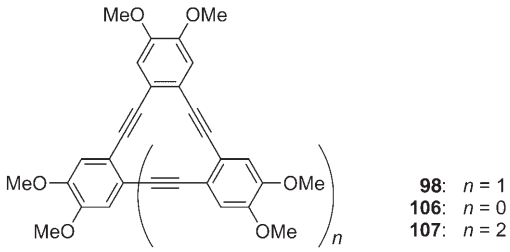


Figure 14. Catechol-based macrocycles.

Table 7: Change in the Gibbs free energy (ΔG) in Reactions (25) and (26).

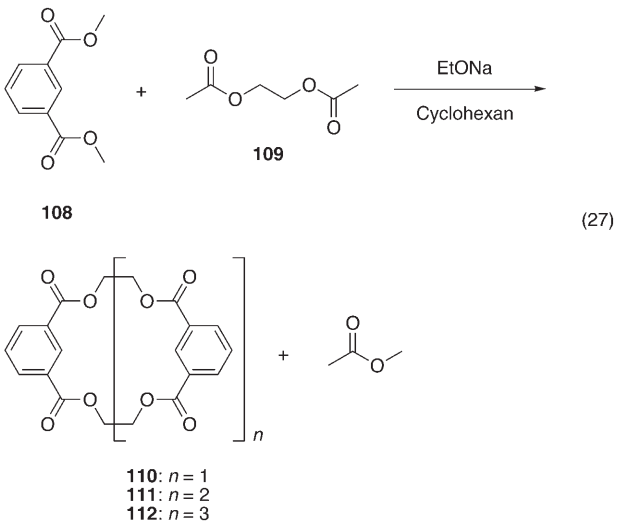
Equation	ΔH [kcal mol^{-1}]	ΔS [kcal mol^{-1} K]	ΔG [kcal mol^{-1}] (303 K)
25	57.2	0.026	49.2
26	0.42	−0.014	4.6

3.2.4. Considerations between Shape-Persistent and Non-Shape-Persistent Macrocycle Synthesis by DCC

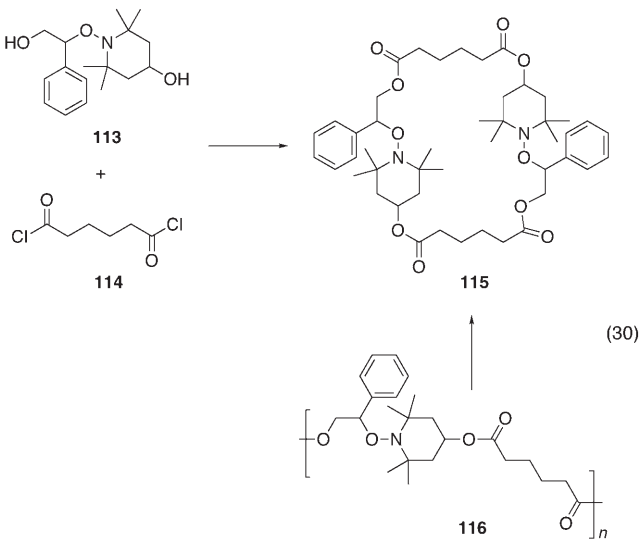
Macrocycles with flexible linkages in their backbones have similar angle strains irrespective of their size; their flexibility makes the enthalpic contribution less important to the thermodynamic stability. Therefore, in the case of flexible macrocycles, product formation is mainly entropically driven, and generally leads to the accumulation of macrocycles with the minimum number of monomer units under optimized conditions. This accounts for the broad applicability of ring-closing metathesis reactions which tend to yield monomeric cyclic products.[107]

This situation is illustrated by the successful selective and quantitative synthesis of macrocyclic ethylene isophthalate dimer **110**, which was reported by Nagahata and co-workers [Eq. (27)].[108] They found that isophthalic acid dimethyl ester (**108**) undergoes transesterification with one equivalent of ethylene glycol diacetate (EGA, **109**) in the presence of sodium ethoxide at 65 °C to provide cyclic dimer product **110** (considered as a dimer of two AB-type monomer units) in

 © 2006 Wiley-VCH Verlag GmbH & Co. KGaA, Weinheim



(27)



(30)

almost quantitive yield (97.6%). The thermodynamic stabilities of the ethylene isophthalate macrocycles calculated by the same approach mentioned before are presented in Table 8 [Eqs. (28) and (29)]. On the basis of the calculations, the

3 cyclic dimer ⇌ 2 cyclic trimer (28)

4 cyclic dimer ⇌ 2 cyclic tetramer (29)

dimeric macrocycle **110** is indeed predicted to be thermodynamically more stable than the trimer **111** and tetramer **112** mainly because of entropic considerations.

Table 8: Change in the Gibbs free energy (ΔG) in Reactions (28) and (29).

Equation	ΔH [kcal mol^{-1}]	ΔS [kcal mol^{-1} K]	ΔG [kcal mol^{-1}] (303 K)
28	−0.53	−0.018	5.6
29	0.10	−0.014	9.5

Similarly, alkoxyamine-based dimeric macrocycle **115** (considered as a dimer of two AB-type monomer units) with flexible linkages was prepared directly from alkoxyamine **113** and adipoyl chloride (**114**) under highly dilute conditions [Eq. (30)].[109] Cyclo-depolymerization[110] of poly(alkoxyamine) **116** at 125 °C provided cyclic dimer **115** as the major component, thus indicating the thermodynamic stability of the dimeric product over other macrocycles under such reaction conditions. Presumably, the favored formation of **115** is also entropically driven.[111]

Based on these examples and calculations, it seems that dimeric or monomeric (if the linkages are sufficiently long) macrocycles with flexible linkages are likely to be obtained in high yields under optimized conditions. Unlike shape-persistent macrocycles, which have encoded an enthalpic parameter into each monomer, the thermodynamic stabilities of non-shape-persistent macrocycles depend much less on enthalpy. Thus, attaining large macrocycles is not expected for non-shape-persistent structures prepared by a reversible process.

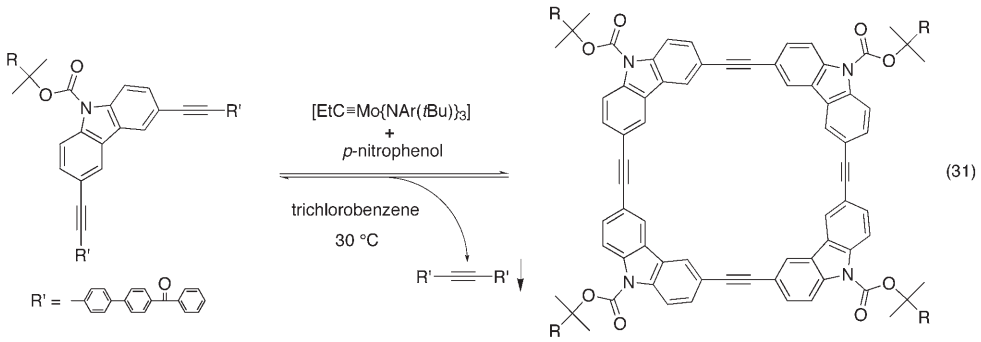
3.2.5. Limitations of Thermodynamically Controlled Cyclooligomerization Methods

Clearly, there are limitations with the thermodynamically controlled cyclooligomerization methods. First, this approach is generally not applicable to synthesizing strained molecular structures, which are enthalpically strongly disfavored. Second, the growing oligomers must remain soluble to approach equilibrium. To illustrate this concept, the precipitation-driven alkyne metathesis to prepare other carbazole-based tetrameric macrocycles functionalized with tertiary alkyl carboxylate groups on the nitrogen atoms was attempted.[105] Three dialkyne monomers **117a–c** functionalized with *tert*-butylcarboxylate, 1,1-dimethyloctylcarboxylate, and 1,1-dimethyltridecylcarboxylate, respectively, were subjected to standard metathesis conditions [Eq. (31)]. Nearly quantitative conversion of the starting monomers into insoluble materials was observed in the case of **117a** and **117b**. The insoluble material was believed to be intermediate oligomers and the diarylacetylene by-products. In contrast, metathesis of monomer **117c** proceeded well in 1,2,4-trichlorobenzene at 30 °C, and tetrameric macrocycle **118c** was obtained in high yield.

This example demonstrates the solubility requirement of longer arylene ethynylene oligomers, especially those that overshoot the target macrocycle length. All the intermediate compounds should remain soluble along the reaction pathway, which would allow the thermodynamically stable products to prevail through reversible alkyne metathesis. As the example in Equation (31) illustrates, it is not clear which materials are likely to remain soluble and which are likely to precipitate. This problem represents a synthetic challenge for the preparation of larger, more complex two-dimensional and three-dimensional molecular structures.

Another limitation of the cyclooligomerization approach is site-specific functionalization. The energy gap between macrocycles containing identical monomer units with those containing co-monomers is not likely to be large enough to favor the formation of a specific structure. In addition to variable composition, the preparation of macrocycles site-

 © 2006 Wiley-VCH Verlag GmbH & Co. KGaA, Weinheim



(31)

117a: R = Methyl
117b: R = Heptyl
117c: R = dodecyl

118a: R = Methyl < 5%
118b: R = Heptyl < 5%
118c: R = dodecyl 81%

specifically functionalized with a particular unit is also problematic under reversible conditions. New strategies and alternative driving forces will need to be developed to overcome these limitations.

4. Conclusion and Outlook

Within the past two decades there has been considerable progress in the synthesis and supramolecular chemistry of shape-persistent arylene ethynylene macrocycles. The development of versatile and efficient synthetic methodologies enables simplified access to the macrocycles, thus allowing a systematic investigation of their properties. The yields of the macrocycles obtained by irreversible cyclooligomerization reactions are usually limited by the formation of higher oligomers (overshooting). Repetitive (convergent/divergent) coupling reactions allow for absolute control over the size of the target macrocycles and placement of functional groups. Template-directed synthetic approaches involving preorganized precursors usually require fewer steps in the syntheses and high overall yield obtained, thus greatly facilitating the preparation of functionalized macrocycles under kinetically controlled conditions.

Metathesis reactions under thermodynamically controlled conditions have shown advantages in both easy accessibility of the starting materials and high product yields. The concept of the energy gap principle illustrated here for macrocyclization applies broadly to other dynamic covalent methods. The highly efficient one-step preparation of macrocycles using precipitation-driven alkyne metathesis may open the way to other two-dimensional or three-dimensional arylene ethynylene structures as well as alkyne-bridged oligomers and polymers. The convenient synthesis and the self-assembling capabilities of arylene ethynylene macrocycles make them promising modular building blocks for a variety of supramolecular structures, such as extended tubular channels, discotic liquid crystals, molecular electronics or optical devices, and microscopic reactors.

Work in our laboratory at the Frederick Seitz Materials Research Laboratory at the University of Illinois at Urbana-Champaign was supported by the National Science Foundation and the US Department of Energy, Division of Material Science.

Received: November 9, 2005
Published online: June 13, 2006

[1] S. Höger, *Angew. Chem.* **2005**, *117*, 3872; *Angew. Chem. Int. Ed.* **2005**, *44*, 3806.
[2] S. Höger, *Chem. Eur. J.* **2004**, *10*, 1320.
[3] D. Zhao, J. S. Moore, *Chem. Commun.* **2003**, 807.
[4] Y. Yamaguchi, Z. Yoshida, *Chem. Eur. J.* **2003**, *9*, 5430.
[5] C, Grave, A. D. Schlüter, *Eur. J. Org. Chem.* **2002**, 3075.
[6] F. Diederich, *Chem. Commun.* **2001**, 219.
[7] S. Höger, *J. Polym. Sci. Part A* **1999**, *37*, 2685.
[8] U. H. F. Bunz, Y. Rubin, Y. Tobe, *Chem. Soc. Rev.* **1999**, *28*, 107.
[9] M. M. Haley, J. J. Pak, S. C. Brand, *Top. Curr. Chem.* **1999**, *201*, 81.
[10] J. S. Moore, *Acc. Chem. Res.* **1997**, *30*, 402.
[11] J. K. Young, J. S. Moore in *Modern Acetylene Chemistry* (Eds.: P. J. Stang, F. Diederich), VCH, Weinheim, **1995**, chap. 12.
[12] K. Sonogashira, *Comprehensive Organic Synthesis*, *Vol. 3* (Eds.: B. M. Trost, I. Fleming), Pergamon, Oxford, **1991**, p. 521.
[13] Recently Yaghi and co-workers reported their synthesis of covalent organic frameworks (COFs) by condensation reactions of phenyldiboronic acid and hexahydroxytriphenylene. The highly crystalline products apparently formed expanded porous graphitic layers that are either staggered or eclipsed, as determined by powder x-ray diffraction studies (A. P. Côté, A. I. Benin, N. W. Ockwig, M. O'Keeffe, A. J. Matzger, O. M. Yaghi, *Science* **2005**, *310*, 1166).
[14] H. A. Dieck, F. R. Heck, *J. Organomet. Chem.* **1975**, *93*, 259.
[15] a) K. Sonogashira, Y. Tohda, N. Hagihara, *Tetrahedron Lett.* **1975**, *16*, 4467; b) L. Cassar, *J. Organomet. Chem.* **1975**, *93*, 253.
[16] J. S. Moore, J. Zhang, *Angew. Chem.* **1992**, *104*, 873; *Angew. Chem. Int. Ed. Engl.* **1992**, *31*, 922.
[17] J. Zhang, D. J. Pesak, J. L. Ludwick, J. S. Moore, *J. Am. Chem. Soc.* **1994**, *116*, 4227.
[18] S. Lahiri, J. L. Thompson, J. S. Moore, *J. Am. Chem. Soc.* **2000**, *122*, 11315.
[19] U. H. F. Bunz, *Chem. Rev.* **2000**, *100*, 1605.
[20] a) A. O. King, N. Okukado, E. Negishi, *J. Chem. Soc. Chem. Commun.* **1977**, 683; b) A. O. King, E. Negishi, F. J. Villani, Jr., A. Silveira, Jr., *J. Org. Chem.* **1978**, *43*, 358; c) E. Negishi, *Acc. Chem. Res.* **1982**, *15*, 340.
[21] a) G. Eglinton, A. R. Galbraith, *J. Chem. Soc.* **1959**, 889; b) O. M. Behr, G. Eglinton, A. R. Galbraith, R. A. Raphael, *J. Chem. Soc.* **1960**, 3614; c) D. O'Krongly, S. R. Denmeade, M. Y. Chiang, R. Breslow, *J. Am. Chem. Soc.*, **1985**, *107*, 5544.
[22] For a review on acetylene coupling, see P. Siemsen, R. C. Livingston, F. Diederich, *Angew. Chem.* **2000**, *112*, 2740; *Angew. Chem. Int. Ed.* **2000**, *39*, 2632.
[23] S. Höger, V. Enkelmann, *Angew. Chem.* **1995**, *107*, 2917; *Angew. Chem. Int. Ed. Engl.* **1995**, *34*, 2713.
[24] S. Höger, A. D. Meckenstock, H. Pellen, *J. Org. Chem.* **1997**, *62*, 4556.
[25] S. Höger, A. D. Meckenstock, S. Müller, *Chem. Eur. J.* **1998**, *4*, 2423.
[26] S. Höger, A. D. Meckenstock, *Chem. Eur. J.* **1999**, *5*, 1686.
[27] S. Höger, K. Bonrad, A. Mourran, U. Beginn, M. Möller, *J. Am. Chem. Soc.* **2001**, *123*, 5651.

 © 2006 Wiley-VCH Verlag GmbH & Co. KGaA, Weinheim

[28] Y. Tobe, N. Utsumi, K. Kawabata, K. Naemura, *Tetrahedron Lett.* **1996**, *37*, 9325.
[29] Y. Tobe, N. Utsumi, A. Nagano, K. Naemura, *Angew. Chem.* **1998**, *110*, 1347; *Angew. Chem. Int. Ed.* **1998**, *37*, 1285.
[30] Y. Tobe, A. Nagano, K. Kawabata, M. Sonoda, K. Naemura, *Org. Lett.* **2000**, *2*, 3265.
[31] A. Nomoto, M. Sonoda, Y. Yamaguchi, T. Ichikawa, K. Hirose, Y. Tobe, *J. Org. Chem.* **2006**, *71*, 401.
[32] Y. Tobe, N. Utsumi, K. Kawabata, A. Nagano, K. Adachi, S. Araki, M. Sonoda, K. Hirose, K. Naemura, *J. Am. Chem. Soc.* **2002**, *124*, 5350.
[33] C. E. Castro, R. D. Stephens, *J. Org. Chem.* **1963**, *28*, 2163.
[34] For reviews, see a) A. Fürstner, P. W. Davies, *Chem. Commun.* **2005**, 2307; b) R. R. Schrock, A. H. Hoveyda, *Angew. Chem.* **2003**, *115*, 4740; *Angew. Chem. Int. Ed.* **2003**, *42*, 4592; c) R. R. Schrock, *Chem. Rev.* **2002**, *102*, 145; d) A. Fürstner in *Handbook of Metathesis*, *Vol. 2* (Ed.: R. H. Grubbs), Wiley-VCH, Weinheim, **2003**, chap. 2.12; e) U. H. F. Bunz, *Acc. Chem. Res.* **2001**, *34*, 998.
[35] The formation of porphyrins and calixarenes by pyrrole- or phenol-aldehyde condensations, repectively, are cyclooligomerization examples, see a) A. Ghosh, *Angew. Chem.* **2004**, *116*, 1952; *Angew. Chem. Int. Ed.* **2004**, *43*, 1918; b) C. D. Gutsche, D. E. Johnston, Jr., D. R. Stewart, *J. Org. Chem.* **1999**, *64*, 3747; c) B. Dhawan, S.-I. Chen, C. D. Gutsche, *Makromol. Chem.* **1987**, *188*, 921; d) A. D. Adler, F. R. Longo, W. Shergalis, *J. Am. Chem. Soc.* **1964**, *86*, 3145.
[36] V. Prautzsch, S. Ibach, F. J. Vögtle, *J. Inclusion Phenom. Macrocyclic Chem.* **1999**, *33*, 427.
[37] S. J. Rowan, S. J. Cantrill, G. R. L. Cousins, J. K. M. Sanders, J. F. Stoddart, *Angew. Chem.* **2002**, *114*, 938; *Angew. Chem. Int. Ed.* **2002**, *41*, 898.
[38] J.-M. Lehn, *Chem. Eur. J.* **1999**, *5*, 2455.
[39] a) B. M. Trost, *Science* **1991**, *254*, 1471; b) K. Oh, K.-S. Jeong, J. S. Moore, *Nature* **2001**, *414*, 889; c) K. Oh, K.-S. Jeong, J. S. Moore, *J. Org. Chem.* **2003**, *68*, 8397; d) T. Nishinaga, A. Tanatani, K. Oh, J. S. Moore, *J. Am. Chem. Soc.* **2002**, *124*, 5934; e) D. Zhao, J. S. Moore, *Macromolecules* **2003**, *36*, 2712.
[40] a) R. R. Schrock, D. N. Clark, J. Sancho, J. H. Wengrovius, S. M. Rocklage, S. F. Pedersen, *Organometallics* **1982**, *1*, 1645; b) L. G. McCullough, R. R. Schrock, *J. Am. Chem. Soc.* **1984**, *106*, 4067; c) L. G. McCullough, R. R. Schrock, J. C. Dewan, J. C. Murdzek, *J. Am. Chem. Soc.* **1985**, *107*, 5987; d) J. M. Blackwell, J. S. Figueroa, F. H. Stephens, C. C. Cummins, *Organometallics* **2003**, *22*, 3351; e) Y.-C. Tsai, P. L. Diaconescu, C. C. Cummins, *Organometallics* **2000**, *19*, 5260; f) C. E. Laplaza, A. L. Odom, W. M. Davis, C. C. Cummins, J. D. Protasiewics, *J. Am. Chem. Soc.* **1995**, *117*, 4999; g) A. Mortreux, M. Blanchard, *J. Chem. Soc. Chem. Commun.* **1974**, 786; h) N. G. Pschirer, U. H. F. Bunz, *Tetrahedron Lett.* **1999**, *40*, 2481.
[41] W. Zhang, S. Kraft, J. S. Moore, *Chem. Commun.* **2003**, 832.
[42] W. Zhang, S. Kraft, J. S. Moore, *J. Am. Chem. Soc.* **2004**, *126*, 329.
[43] a) D. J. Brunelle, E. P. Boden, T. G. Shannon, *J. Am. Chem. Soc.* **1990**, *112*, 2399; b) S. J. Rowan, P. A. Brady, J. K. M. Sanders, *Angew. Chem.* **1996**, *108*, 2283; *Angew. Chem. Int. Ed. Engl.* **1996**, *35*, 2143; c) S. J. Rowan, J. K. M. Sanders, *J. Org. Chem.* **1998**, *63*, 1536; d) S. J. Rowan, D. G. Hamilton, P. A. Brady, J. K. M. Sanders, *J. Am. Chem. Soc.* **1997**, *119*, 2578.
[44] a) S.-W. Tam-Chang, J. S. Stehouwer, J. Hao, *J. Org. Chem.* **1999**, *64*, 334; b) S. Ro, S. J. Rowan, A. R. Pease, D. J. Cram, J. F. Stoddart, *Org. Lett.* **2000**, *2*, 2411.
[45] a) D. G. Hamilton, N. Feeder, S. J. Teat, J. K. M. Sanders, *New J. Chem.* **1998**, *22*, 1019; b) D. G. Hamilton, J. E. Davies, L. Prodi, J. K. M. Sanders, *Chem. Eur. J.* **1998**, *4*, 608; c) D. G. Hamilton, M. Montalti, L. Prodi, M. Fontani, P. Zanello, J. K. M. Sanders, *Chem. Eur. J.* **2000**, *6*, 608.
[46] a) J. N. Onuchic, H. Nymeyer, A. E. Garcia, J. Chahine, N. D. Socci, *Adv. Protein Chem.* **2000**, *53*, 87; b) D. J. Brockwell, D. A. Smith, S. E. Radford, *Curr. Opin. Struct. Biol.* **2000**, *10*, 16.
[47] All the simple kinetic simulations were performed by using a mechanism-based kinetics simulator located at http://www.stolaf.edu/depts/chemistry/courses/toolkits/126/js/kinetics/index.htm.
[48] Y. Li, J. Zhang, W. Wang, Q. Miao, X. She, X. Pan, *J. Org. Chem.* **2005**, *70*, 3285.
[49] C. Eickmeier, H. Junga, A. J. Matzger, F. Scherhag, M. Shim, K. P. C. Vollhardt, *Angew. Chem.* **1997**, *109*, 2194; *Angew. Chem. Int. Ed. Engl.* **1997**, *36*, 2103.
[50] a) J. D. Ferrara, C. Tessier-Youngs, W. J. Youngs, *J. Am. Chem. Soc.* **1985**, *107*, 6719; b) W. J. Youngs, J. D. Kinder, J. D. Bradshaw, C. A. Tessier, *Organometallics* **1993**, *12*, 2406; c) J. D. Ferrara, A. Djebli, C. Tessier-Youngs, W. J. Youngs, *J. Am. Chem. Soc.* **1988**, *110*, 647.
[51] T. Nishinaga, Y. Miyata, N. Nodera, K. Komatsu, *Tetrahedron* **2004**, *60*, 3375.
[52] P. N. Prasad, D. J. Williamsm, *Introduction to nonlinear optical effects in molecules and polymers*, Wiley, New York, **1991**, chap. 7, p. 132.
[53] H. A. Staab, K. Neunhoeffer, *Synthesis* **1974**, 424.
[54] M. Iyoda, A. Vorasingha, Y. Kuwatani, M. Yoshida, *Tetrahedron Lett.* **1998**, *39*, 4701.
[55] a) L. Yuan, W. Feng, K. Yamato, A. R. Sanford, D. Xu, H, Guo, B. Gong, *J. Am. Chem. Soc.* **2004**, *126*, 11120; the same research group reported similar syntheses of tetrameric aromatic sulfonamide macrocycles with alkoxy side chains in yields of 38–51%, see b) L. He, Y. An, L. Yuan, K. Yamato, W. Feng, O. Gerlitz, C. Zheng, B. Gong, *Chem. Commun.* **2005**, 3788–3790.
[56] S. Toyota, M. Goichi, M. Kotani, *Angew. Chem.* **2004**, *116*, 2298; *Angew. Chem. Int. Ed.* **2004**, *43*, 2248.
[57] H. E. Katz, *J. Org. Chem.* **1989**, *54*, 2179.
[58] For examples of hypsochromic effects observed in aromatic macrocycles and polymers with π–π interactions, see a) F. Vögtle, *Cyclophane Chemistry*, Wiley, Chichester, **1993**, p. 77; b) S. Dumitrescu, M. Grigoras, C. I. Simionescu, *Eur. Polym. J.* **1983**, *19*, 1137.
[59] Y. Yamaguchi, S. Kobayashi, S. Miyamura, Y. Okamoto, T. Wakamiya, Y. Matsubara, Z. Yoshida, *Angew. Chem.* **2004**, *116*, 370; *Angew. Chem. Int. Ed.* **2004**, *43*, 366.
[60] J. S. Moore, E. J. Weinstein, Z. Y. Wu, *Tetrahedron Lett.* **1991**, *32*, 2465.
[61] a) O. Henz, D. Lentz, A. D. Schlüter, *Chem. Eur. J.* **2000**, *6*, 2362; b) O. Henz, D. Lentz, A. Schater, P. Franke, A. D. Schlüter, *Chem. Eur. J.* **2002**, *8*, 357; c) S. Kobayashi, Y. Yamaguchi, T. Wakamiya, Y. Matsubara, K. Sugimoto, Z. Yoshida, *Tetrahedron Lett.* **2003**, *44*, 1469.
[62] J. A. Marsden, J. J. Miller, M. M. Haley, *Angew. Chem.* **2004**, *116*, 1726; *Angew. Chem. Int. Ed.* **2004**, *43*, 1694.
[63] F. Bohlmann, H. Schönowsky, E. Inhoffen, G. Grau, *Chem. Ber.* **1963**, *96*, 794.
[64] Z. Y. Wu, J. S. Moore, *Angew. Chem.* **1996**, *108*, 320; *Angew. Chem. Int. Ed. Engl.* **1996**, *35*, 297.
[65] Z. Y. Wu, S. Lee, J. S. Moore, *J. Am. Chem. Soc.* **1992**, *114*, 8730.
[66] V. Hensel, K. Lützow, J. Jacob, K. Gessler, W. Saenger, A. D. Schlüter, *Angew. Chem.* **1997**, *109*, 2768; *Angew. Chem. Int. Ed. Engl.* **1997**, *36*, 2654.
[67] O. S. Pyun, W. Yang, M.-Y. Jeong, S. H. Lee, K. M. Kang, S.-J. Jeon, B. R. Cho, *Tetrahedron Lett.* **2003**, *44*, 5179.
[68] Recently, a donor–acceptor-substituted phenyleneethynylene macrocycle was prepared through a similar approach: B. Traber, T. Oeser, R. Gleiter, *Eur. J. Org. Chem.* **2005**, 1283.
[69] P. N. W. Baxter, *J. Org. Chem.* **2004**, *69*, 1813.
[70] P. N. W. Baxter, *Chem. Eur. J.* **2003**, *9*, 2531.

 © 2006 Wiley-VCH Verlag GmbH & Co. KGaA, Weinheim

[71] P. N. W. Baxter, *Chem. Eur. J.* **2002**, *8*, 5250.
[72] P. N. W. Baxter, *J. Org. Chem.* **2001**, *66*, 4170.
[73] H. Sugiura, Y. Takahira, M. Yamaguchi, *J. Org. Chem.* **2005**, *70*, 5698.
[74] Y. Saiki, K. Nakamura, Y. Nigorikawa, M. Yamaguchi, *Angew. Chem.* **2003**, *115*, 5348; *Angew. Chem. Int. Ed.* **2003**, *42*, 5190.
[75] K. Nakamura, H. Okubo, M. Yamaguchi, *Org. Lett.* **2001**, *3*, 1097.
[76] H. L. Anderson, J. K. M. Sanders, *Angew. Chem.* **1990**, *102*, 1478; *Angew. Chem. Int. Ed. Engl.* **1990**, *29*, 1400.
[77] D. W. J. McCallien, J. K. M. Sanders, *J. Am. Chem. Soc.* **1995**, *117*, 6611.
[78] M. J. Marsella, Z.-Q. Wang, R. J. Reid, K. Yoon, *Org. Lett.* **2001**, *3*, 885.
[79] For discussion on the aryl–perfluoroaryl (Ar_H–Ar_F) interaction as a reliable way to generate supramolecular synthons in crystal engineering, see a) G. W. Coates, A. R. Dunn, L. M. Henling, J. W. Ziller, E. B. Lobkovsky, R. H. Grubbs, *J. Am. Chem. Soc.* **1998**, *120*, 3641; b) G. W. Coates, A. R. Dunn, L. M. Henling, D. A. Dougherty, R. H. Grubbs, *Angew. Chem.* **1997**, *109*, 290; *Angew. Chem. Int. Ed. Engl.* **1997**, *36*, 248.
[80] For reviews on metal-linked shape-persistent macrocycles, see a) M. Fujita, M. Tominaga, A. Hori, B. Therrien, *Acc. Chem. Res.* **2005**, *38*, 369; b) S. R. Seidel, P. J. Stang, *Acc. Chem. Res.* **2002**, *35*, 972; c) S. Leininger, B. Olenyuk, P. J. Stang, *Chem. Rev.* **2000**, *100*, 853.
[81] D. Zhao, J. S. Moore, *J. Org. Chem.* **2002**, *67*, 3548.
[82] D. J. Hill, J. S. Moore, *Proc. Natl. Acad. Sci. USA* **2002**, *99*, 5053.
[83] a) A. J. Gallant, J. K.-H. Hui, F. E. Zahariev, Y. A. Wang, M. J. MacLachlan, *J. Org. Chem.* **2005**, *70*, 7936; b) C. Ma, A. Lo, A. Abdolmaleki, M. J. MacLachlan, *Org. Lett.* **2004**, *6*, 3841.
[84] A. J. Gallant, B. O. Patrick, M. J. MacLachlan, *J. Org. Chem.* **2004**, *69*, 8739.
[85] A. J. Gallant, M. J. MacLachlan, *Angew. Chem.* **2003**, *115*, 5465; *Angew. Chem. Int. Ed.* **2003**, *42*, 5307.
[86] M. Mammen, E. I. Shakhnovich, J. M. Deutch, G. M. Whitesides, *J. Org. Chem.* **1998**, *63*, 3821; the entropy values of methoxy-substituted macrocycles are estimated.
[87] Spartan software (version 4.0; Wavefunction, Inc.; Irvine, California) at the AM1 level was used to estimate the heats of formation for the methoxy-substituted macrocycles.
[88] For reviews, see a) R. H. Grubbs, *Tetrahedron* **2004**, *60*, 7117; b) T. M. Trnka, R. H. Grubbs, *Acc. Chem. Res.* **2001**, *34*, 18; c) S. J. Connon, S. Blechert, *Angew. Chem.* **2003**, *115*, 1944; *Angew. Chem. Int. Ed.* **2003**, *42*, 4592; d) S. T. Diver, A. J. Giessert, *Chem. Rev.* **2004**, *104*, 1317; e) A. Fürstner, *Angew. Chem.* **2000**, *112*, 3140; *Angew. Chem. Int. Ed.* **2000**, *39*, 3012, and Ref. [34b].
[89] K. Weiss, A. Michel, E. M. Auth, U. H. F. Bunz, T. Mangel, K. Müllen, *Angew. Chem.* **1997**, *109*, 522; *Angew. Chem. Int. Ed. Engl.* **1997**, *36*, 506.
[90] a) A. Fürstner, O. Guth, A. Rumbo, G. Seidel, *J. Am. Chem. Soc.* **1999**, *121*, 11108; b) A. Fürstner, C. Mathes, C. W. Lehmann, *J. Am. Chem. Soc.* **1999**, *121*, 9453.
[91] a) L. Kloppenburg, D. Jones, U. H. F. Bunz, *Macromolecules* **1999**, *32*, 4194; b) N. G. Pschirer, W. Fu, R. D. Adams, U. H. F. Bunz, *Chem. Commun.* **2000**, 87.
[92] P.-H. Ge, W. Fu, W. A. Herrmann, E. Herdtweck, C. Campana, R. D. Adams, U. H. F. Bunz, *Angew. Chem.* **2000**, *112*, 3753; *Angew. Chem. Int. Ed.* **2000**, *39*, 3607.
[93] Analogous to the synthesis of macrocycle **85**, the yields reported herein are unlikely to truly reflect the distribution of the thermodynamically controlled products.
[94] For similar silicon-containing macrocycles, see a) F. Q. Liu, G. Harder, T. D. Tilley, *J. Am. Chem. Soc.* **1998**, *120*, 3271; b) S. S. H. Mao, F. Q. Liu, T. D. Tilley, *J. Am. Chem. Soc.* **1998**, *120*, 1193.
[95] O. Š. Miljanić, K. P. C. Vollhardt, G. D. Whitener, *Synlett* **2003**, 29.
[96] The reported yields may not truly reflect the thermodynamically controlled product distribution.
[97] W. Zhang, J. S. Moore, *J. Am. Chem. Soc.* **2004**, *126*, 12796.
[98] The same approach was also successfully applied to the synthesis of conjugated arylene ethynylene polymers with high molecular weight at room temperature, see W. Zhang, J. S. Moore, *Macromolecules* **2004**, *37*, 3973.
[99] a) A. Fürstner, G. Seidel, *Angew. Chem.* **1998**, *110*, 1758; *Angew. Chem. Int. Ed.* **1998**, *37*, 1734.
[100] A small amount of pentameric macrocycles are obtained as the major side product in these cases.
[101] J. H. Greudenberger, R. R. Schrock, M. R. Churchill, A. L. Rheingold, J. W. Ziller, *Organometallics* **1984**, *3*, 1563.
[102] W. Zhang, J. S. Moore, *J. Am. Chem. Soc.* **2005**, *127*, 11863.
[103] a) R. R. Schrock, *Acc. Chem. Res.* **1986**, *19*, 342; b) J. H. Wengrovius, J. Sancho, R. R. Schrock, *J. Am. Chem. Soc.* **1981**, *103*, 3932.
[104] The tetrameric carbazole macrocycle **96** was first synthesized in 14.3% yield by a cross-coupling approach: S. Maruyama, H. Hokari, T. Wada, H. Sasabe, *Synthesis* **2001**, 1794.
[105] Recently, another 1,1-dimethyltridecylcarboxylate-functionalized carbazole-based macrocycle has also been prepared through the precipitation-driven alkyne metathesis, W. Zhang, H. M. Cho, J. S. Moore, *Org. Synth.*, submitted.
[106] W. Zhang, S. M. Brombosz, J. L. Mendoza, J. S. Moore, *J. Org. Chem.* **2005**, *70*, 10198.
[107] a) A. Deiters, S. F. Martins, *Chem. Rev.* **2004**, *104*, 2199; b) A. Fürstner, *Angew. Chem.* **2003**, *115*, 3706; *Angew. Chem. Int. Ed.* **2003**, *42*, 3582.
[108] R. Nagahata, J. Sugiyama, Y. Nakao, M. Asai, K. Takeuchi, *Macromolecules* **2003**, *36*, 2582.
[109] G. Yamaguchi, Y. Higaki, H. Otsuka, A. Takahara, *Macromolecules* **2005**, *38*, 6316.
[110] For entropically driven cyclo-depolymerizations, see a) A. Ben-Haida, I, Baxter, H. M. Colquhoun, P. Hodge, F. H. Kohnke, D. J. Williams, *Chem. Commun.* **1997**, 1533; b) I. Baxter, A. Ben-Haida, H. M. Colquhoun, P. Hodge, F. H. Kohnke, D. J. Williams, *Chem. Commun.* **1998**, 2213; c) B.-H. Lim, S.-H. Kwon, E.-C. Kang, H. Park, H.-W Lee, W.-G. Kim, *J. Polym. Sci. Part A* **2003**, *41*, 881; d) P. Hodge, *React. Funct. Polym.* **2001**, *48*, 15; e) P. Hodge, Z. Yang, A. Ben-Haida, C. S. McGrail, *J. Mater. Chem.* **2000**, *10*, 1533; f) A. J. Hall, P. Hodge, C. S. McGrail, J. Rickerby, *Polymer* **2000**, *41*, 1239.
[111] Favored formation of cyclic dimers with flexible linkages by alkene metathesis was also reported: A. B. Smith III, S. A. Kozmin, C. M. Adams, D. V. Paone, *J. Am. Chem. Soc.* **2000**, *122*, 4984.

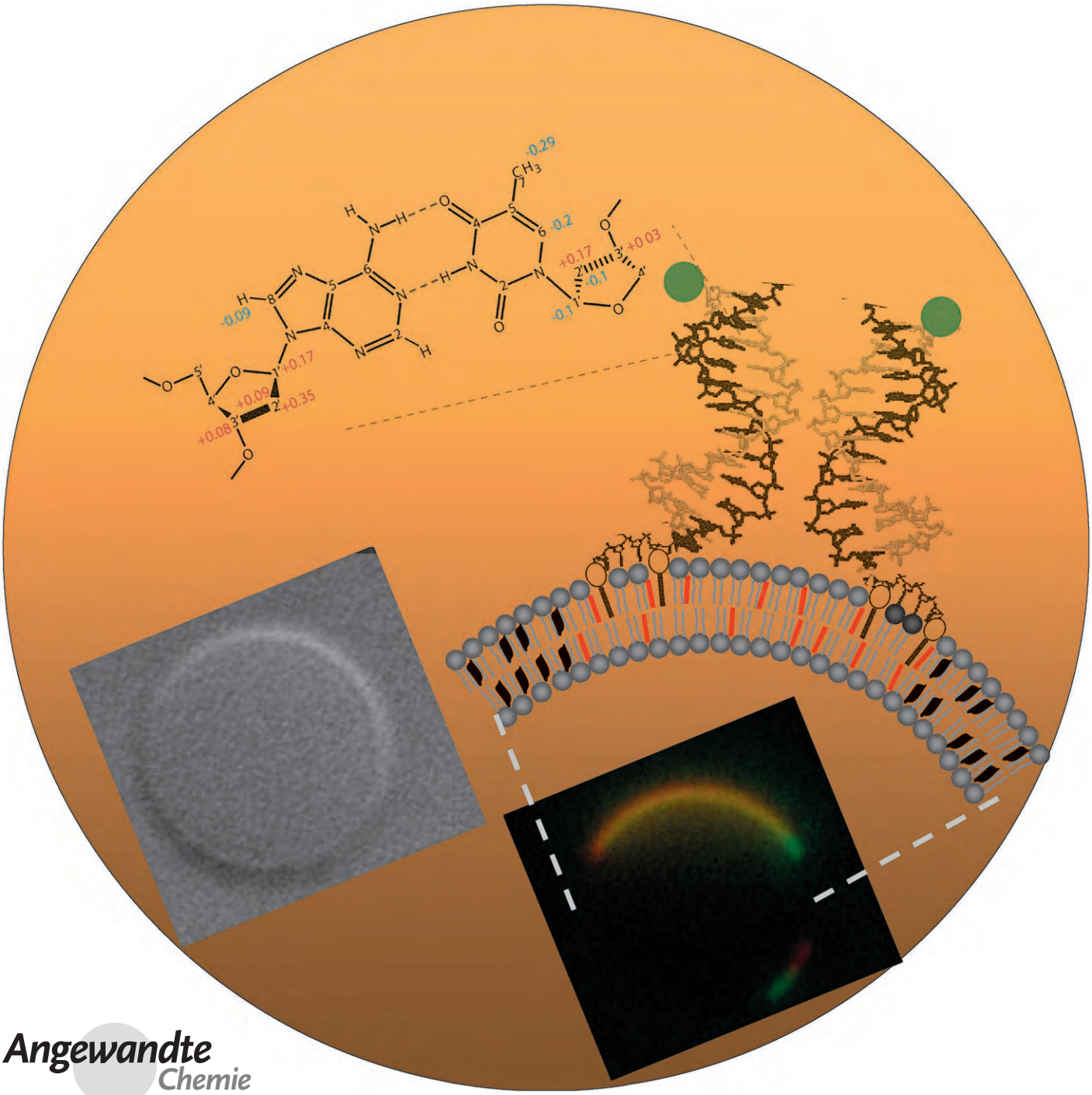
© 2006 Wiley-VCH Verlag GmbH & Co. KGaA, Weinheim

Nanobiotechnology

DOI: 10.1002/anie.200600822

Lipid-Anchored Oligonucleotides for Stable Double-Helix Formation in Distinct Membrane Domains**

Anke Kurz, Andreas Bunge, Anne-Katrin Windeck, Maximilian Rost, Wolfgang Flasche, Anna Arbuzova, Denise Strohbach, Sabine Müller, Jürgen Liebscher, Daniel Huster,* and Andreas Herrmann**

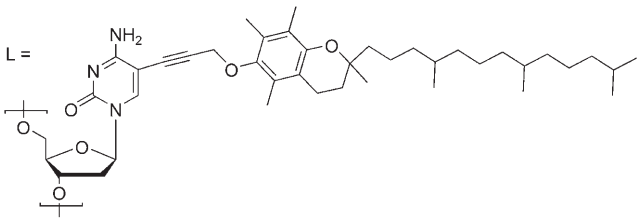


WILEY InterScience DISCOVER SOMETHING GREAT

© 2006 Wiley-VCH Verlag GmbH & Co. KGaA, Weinheim

Lipid-anchored RNA and DNA oligonucleotides have emerged as attractive chimeric molecules for various applications in nanobiotechnology, in cell biology, and for the development of therapeutic strategies in medicine.[1,2] For example, lipophilic oligonucleotides have been synthesized to improve cellular uptake of antisense single-stranded DNA (ssDNA) and interference RNA.[1,3] Recently, efficient silencing of an endogenous apolipoprotein B in mice has been reported upon injection of short interfering RNA molecules (siRNA) coupled to a cholesterol anchor.[4] Depending on the application, lipid-anchored oligonucleotides should meet various requirements, such as easy and flexible synthesis, efficient and stable membrane incorporation, and selective binding of complementary DNA strands. For various purposes a distinct lateral organization of oligonucleotides in membranes is desirable. By selecting appropriate lipid anchors, the enrichment of lipophilic oligonucleotides in specific lipid domains can be achieved[5] which allows distinct functional compartments to be created on a membrane surface. Herein we describe the synthesis and application of a lipidated ssDNA molecule that stably inserts into lipid membranes, displays the oligonucleotide on the vesicular surface, binds complementary DNA strands by formation of Watson–Crick base pairs, and preferentially sequesters into liquid-disordered membrane domains.

The oligonucleotide LT23mer is a 23mer consisting of 21 thymidine units and two lipophilic nucleotides L in positions 1 and 8 with α-tocopherol units as lipophilic anchors (Scheme 1). LT23mer was synthesized on a DNA synthesizer applying phosphoramidite methodology (Supporting Information). The lipophilic tocopherylpropinylcytidine L was obtained by Sonogashira coupling of 5-iodocytidine with racemic *O*-propargyltocopherol using a recently published procedure[6] and transformed into the 5′-DMTr-protected 3′-diisopropylaminocyanethylphosphor amidite by conventional methods. This method provides a high flexibility because lipophilic nucleotides can be introduced in any position of an oligonucleotide.



5′ LTT TTT TLT TTT TTT TTT TTT TT 3′ LT23mer

Scheme 1. Structure of the lipophilic nucleoside L building block used as a monomer in the synthesis of lipid modified oligonucleotides. The sequence of the LT23mer is given below

Fluorescence microscopy was used to visualize the membrane affinity of LT23mer and the ability to bind a complementary A20mer DNA strand. Giant unilamellar vesicles (GUVs) were prepared containing 1 mol% LT23mer and the fluorescent phospholipid analogue *N*-NBD-PE (0.5 mol%; see Experimental Section). To demonstrate binding of the complementary DNA strand, an adenosine 20mer tagged either on its 3′ (3′Rh-A20mer) or on its 5′ terminus (5′Rh-A20mer) with the fluorophore rhodamine (Rh) was added. The binding of these complementary strands to the LT23mer of the GUV membranes could be identified by the Rh fluorescence (Figure 1, only shown for 5′Rh-A20mer). Fluorescence was homogeneous over the whole membrane indicating that LT23mer is homogeneously distributed within the membrane. The GUVs could not be labeled by Rh-tagged T20mer. In the absence of LT23mer no labeling of GUVs with fluorescent A20mers was observed (not shown).

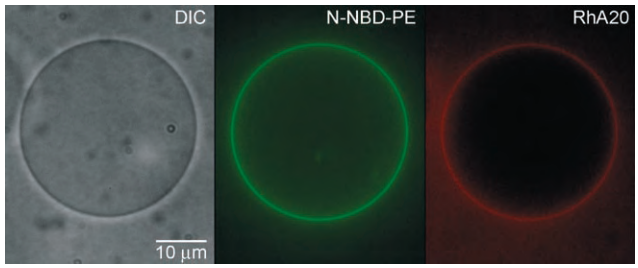


Figure 1. Binding of a Rh-A20mer to *N*-NBD-PE-labeled (0.5 mol%) POPC–GUVs containing LT23mer (about 1 mol%) at room temperature. Left: differential interference contrast (DIC) image. Middle: Fluorescence of *N*-NBD-PE and right: fluorescence of 5′Rh-A20mer.

To examine further binding of complementary adenine oligonucleotides to membrane-bound LT23mer we employed a fluorescence resonance energy transfer (FRET) assay.

[*] Dr. A. Kurz,[+] Dr. A.-K. Windeck, M. Rost, Dr. A. Arbuzova, Prof. Dr. A. Herrmann
Institute of Biology/Biophysics
Humboldt University of Berlin
Invalidenstrasse 42, 10115 Berlin (Germany)
Fax: (+49) 30-2093-8585
E-mail: andreas.herrmann@rz.hu-berlin.de
Dipl.-Phys. A. Bunge,[+] Priv.-Doz. Dr. D. Huster
Junior Research Group "Structural Biology of Membrane Proteins"
Institute of Biotechnology
Martin-Luther University Halle-Wittenberg
Kurt-Mothes-Strasse 3, 06120 Halle (Germany)
Fax: (+49) 345-55-27013
E-mail: daniel.huster@biochemtech.uni-halle.de
Dr. W. Flasche, Prof. Dr. J. Liebscher
Institute of Chemistry
Humboldt University Berlin
Brook-Taylor-Strasse 2, 12489 Berlin (Germany)
Fax: (+49) 30-2093-7552
E-mail: liebscher@chemie.hu-berlin.de
Dipl.-Chem. D. Strohbach, Prof. Dr. S. Müller
Institute of Biochemistry
Ernst-Moritz-Arndt University Greifswald
Soldmannstrasse 16, 17487 Greifswald (Germany)
[+] These authors contributed equally.
[**] This study was supported by the BMBF grant No. 0312018. We thank Mrs Charlott Peters for preparative support.
Supporting information for this article is available on the WWW under http://www.angewandte.org or from the author.

 © 2006 Wiley-VCH Verlag GmbH & Co. KGaA, Weinheim

Large unilamellar vesicles (LUVs) containing either POPC and LT23 mer or only POPC (control) were prepared in the presence of *N*-NBD-PE (0.5 mol %). The fluorescent NBD moiety, which serves as a donor for FRET, is covalently attached to the lipid head group. LUVs were incubated with the 3′Rh-A20 mer with Rh being the fluorescence acceptor. We measured a strong FRET when LUVs containing LT23 mer were incubated with 3′Rh-A20 mer (Figure 2a). FRET was not observed for control LUVs (Figure 2b).

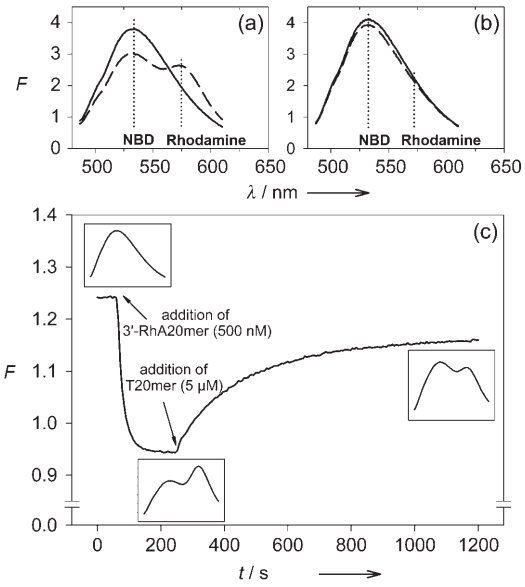


Figure 2. Fluorescence of *N*-NBD-PE-labeled POPC–LUVs a) with or b) without LT23 mer, were incubated in the absence (——) or presence (-----) of 3′Rh-A20 mer at room temperature. A strong FRET was observed when 3′Rh-A20 mers were added to LT23 mer containing LUVs (LT23 mer:3′Rh-A20 mer = 1:1). Vertical dotted lines are fluorescence maxima of NBD and rhodamine, respectively. c) Kinetics of 3′-RhA20 mer (500 nM) binding to LT23 mer-containing LUVs measured by the decrease of NBD fluorescence owing to FRET (excitation 460 nm; emission 532 nm). At $t = 280$ s an unlabelled T20 mer (5 μM) was added. For three selected time points fluorescence spectra are shown indicating the absence, increase, and decrease of FRET, respectively.

Binding of 3′Rh-A20 mer to membrane-bound LT23 mer was rapid, with a half time of about 20 s (Figure 2c), and reversible. When (unlabelled) T20 mers were added in 10-fold excess with respect to LT23 mer, a decrease of FRET was observed owing to the competition of the T20 mer for 3′Rh-A20 mer (Figure 2c).

The structure of the membrane-associated complex of LT23 mer and A20 mer was investigated by NMR spectroscopy. As a control, solution NMR studies of stoichiometric mixtures of A20 mer and T20 mer were carried out. Base-pair formation and stacking leads to characteristic changes of the chemical shifts.[7] Slices of the ^{1}H NOESY spectra are shown (Figure 3). In the presence of LUVs, 1D spectra also contained intense signals arising from lipids. In contrast, the NOESY slices only showed the signals of the base and the sugar moieties. Figure 3a depicts the ^{1}H NMR spectrum of

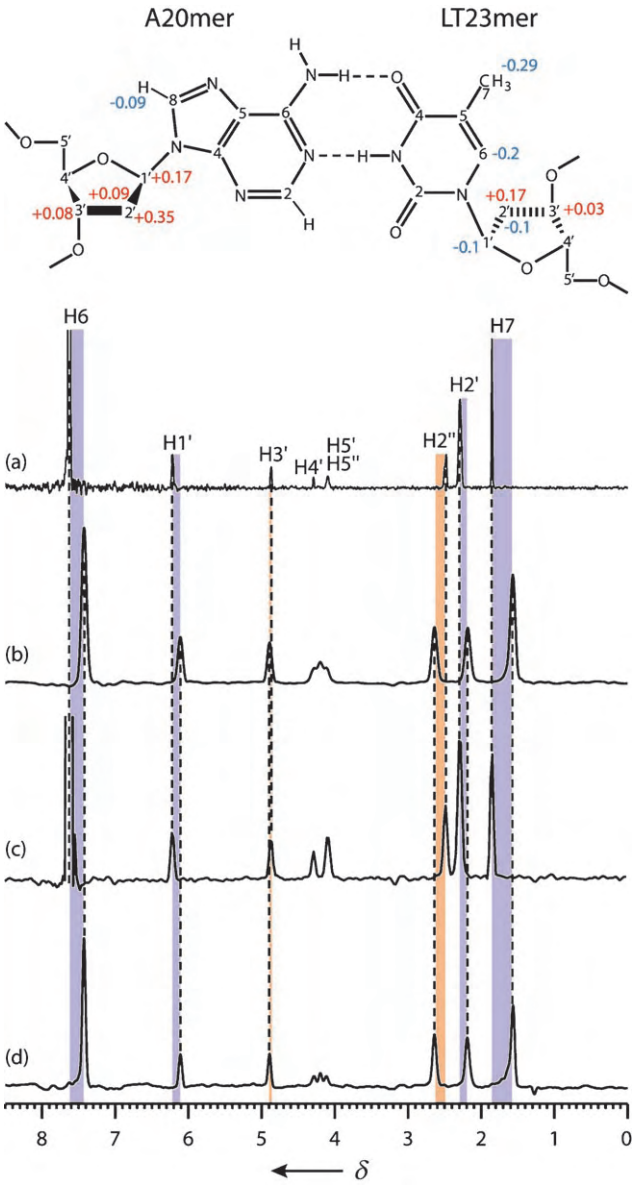


Figure 3. Slices of ^{1}H NOESY NMR spectra of free and membrane bound oligonucleotides in the absence and presence of a complementary strand. a) T20 mer in buffer, b) A20 mer and T20 mer (1:1) in buffer; c) LT23 mer associated with POPC membranes; d) LT23 mer associated with POPC membranes in the presence of A20 mers. Lines are drawn to guide the eye. Purple bars denote upfield and yellow bars denote downfield shifts. A summary of the chemical shift changes (in ppm) for the A and T moieties is given in the structural formula above. Slight chemical shift changes of the H5′/H5″ signals may indicate a conformational change in the furanose upon double-strand formation.

the T20 mer. In the presence of the complementary A20 mer strands, all the resonance signals were shifted in a specific manner (Figure 3b). The LT23 mer bound to POPC LUVs (Figure 3c) showed exactly identical ^{1}H NMR chemical shifts as isolated T20 mer (cf. Figure 3a). After addition of the complementary A20 mer, identical relative shifts compared to the A20 mer–T20 mer double helix were observed (Figure 3d). The chemical shift changes of A20 mer after binding

 © 2006 Wiley-VCH Verlag GmbH & Co. KGaA, Weinheim

to either T20 mer or LT23 mer were also identical (not shown). This result strongly suggests that very similar structures are formed and neither the lipid-anchor nor the membrane proximity interfere with the formation of the DNA double helix through Watson–Crick base pairing.

It has been shown that GUVs prepared from a lipid mixture of POPC, cholesterol, and sphingomyeline (1:1:1) form liquid-disordered and liquid-ordered domains.[8] Domains can be visualized through fluorescence microscopy by employing fluorescent lipid analogues, which preferentially enrich in one of the two domains. The lipophilic fluorophore Merocyanine 540 accumulates in the liquid-disordered domain[9] as verified by *N*-NBD-PE which is another domain marker for liquid-disordered domains (data not shown).[8b] GUVs of the above mentioned a lipid mixture (1:1:1 (molar ratio)) were used with LT23 mer (about 1 mol%) and Merocyanine 540. Subsequently, complementary oligonucleotides (5′FITC-A20 mer) were added. In contrast to the homogeneous distribution found in pure POPC–GUVs, the LT23 mer with the complementary strand 5′FITC-A20 mer was recruited into the liquid-disordered domain as identified by Merocyanine 540 staining (Figure 4). Such a preferential recruitment can be explained by the bulky α-tocopherol anchor which could pack more easily into a liquid-disordered phase. Preferential partitioning of isoprenylated proteins into liquid-disordered domains has also been observed.[10]

In summary, we have described a simple strategy to synthesize lipophilic nucleosides that can be used to produce large quantities of lipid-anchored oligonucleotides with variable length and primary structure. These molecules insert into lipid membranes and expose the ssDNA to the aqueous phase. Complementary strands are recognized and self-assemble into double stranded DNA with Watson–Crick base pairing. Thus, molecules, vesicles, drugs, or biologically active RNA can be associated with membrane or cellular surfaces at will. An important observation is the recruitment of lipid-anchored oligonucleotides to specific lipid domains. This property could be used to tether double-stranded DNA to specific domains of membrane surfaces and thus to functionalize these domains. Given that lipid domains play an important role in endocytosis,[11] enrichment of lipophilic oligonucleotides to those domains could be explored to enhance cellular uptake. Thus, nanostructures may be built and various cell biological or medical applications can be foreseen.

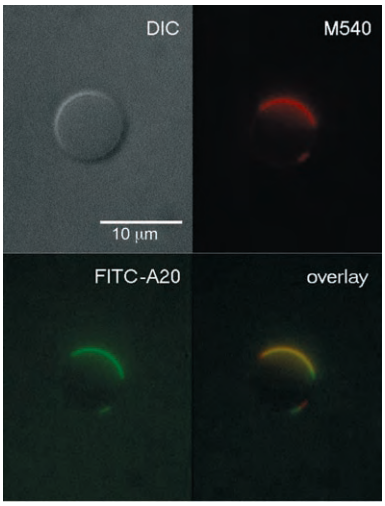


Figure 4. DIC and fluorescence images indicating that LT23 mer binds preferentially to liquid-disordered membrane domains. GUVs were prepared from a mixture of POPC/sphingomyeline/cholesterol (1:1:1 molar ratio) containing about 1 mol% LT23 mer and incubated with 5′FITC-A20 mer in KCl buffer (50 mM), pH 8.0, at room temperature. LT23 mer–5′FITC-A20 mer complexes are recruited to the liquid-disordered domain which was detected by Merocyanine 540 (M540). This dye is known to enrich in liquid-disordered domains.

Experimental Section

1-Palmitoyl-2-oleoyl-*sn*-glycerophosphocholine (POPC), sphingomyeline (SM), and the fluorescent lipid *N*-(7-nitro-2,1,3-benzoxadiazol-4-yl)-1,2-dipalmitoyl-*sn*-glycero-3-phosphatidyl-ethanolamine (*N*-NBD-PE) were obtained from Avanti Polar Lipids (Birmingham, USA). Cholesterol and Merocyanine 540 were from Sigma (Deisenhof, Germany). DNA-oligonucleotides with or without a covalently attached fluorophores (rhodamine (Rh) or fluorescein (fluorescein-isothiocyanate (FITC))) were synthesized by BioTez (Berlin-Buch, Germany). All solutions used were buffered with 10 mM HEPES, pH 8. The preparation of unilamellar vesicles was performed in sucrose solution (80 to 250 mM). For washing and dilution of the vesicles and preparation of multilamellar vesicles buffered KCl, KCl/glucose, or glucose solutions of equal osmolarity were used (see below).

For preparation of LUVs, the lipid mixture dissolved in chloroform was evaporated in a round-bottomed flask by a rotary evaporator forming a thin lipid layer on the flask wall. The lipid film was resuspended by manual swirling of the glass flask. Subsequently, LUVs were formed by subjecting this suspension to five freeze–thaw cycles and extrusion through a polycarbonate filter (Nucleopore GmbH, Tübingen, Germany) of 100 nm diameter using an extruder (Lipex Biomembranes, Vancouver).[12] For membrane incorporation, LT23 mer was added to an aliquot of the LUVs and the suspension was again subjected to five freeze–thaw cycles. Finally, LUVs were ultracentrifuged (120000 × g) and unbound LT23 mer and any micelles remaining were removed (supernatant).

GUVs were generated at room temperature by the electroformation technique in a chamber made of indium tin oxide (ITO) coated glass slides.[13] Lipids were dissolved in chloroform (0.25 mg lipid mL^{-1}) and 70 μL of solved lipids were deposited in small droplets on each slide. The solvent was evaporated in a desiccator (10 mbar) at room temperature for 60 min. Subsequently, the chamber was closed by sealed with silicon paste. The sucrose solution (250 mM sucrose, 10 mM HEPES, 0.02% NaN_3) was injected with a syringe through a micropore filter immediately before connecting the completely sealed chamber to the generator. LT23 mer was added to the sucrose solution to allow its incorporation during GUV preparation. The voltage of the applied AC-field was increased in steps every 6 min from 20 mV up to 1.1 V while continuously increasing the frequency from 4 Hz to 10 Hz within the first minute. The AC-field was applied for 3–12 h. To complete the procedure, voltage was raised to 1.3 V and the frequency lowered to 4 Hz. The chamber was then stored in a refrigerator at 4 °C.

Fluorescence spectra and kinetics were recorded using an Aminco Bowman spectrometer series 2 (SLM-Aminco, Rochester, NY). *N*-NBD-PE was excited at 460 nm (slit width 4 nm) and fluorescence spectra were recorded between 470 and 610 nm with a scan rate of 1 nm s^{-1} whereas for kinetic measurements the emission wavelength was set to 532 nm (slit width 4 nm). GUVs were examined

 © 2006 Wiley-VCH Verlag GmbH & Co. KGaA, Weinheim

with an Olympus IX-81 inverted fluorescence microscope (Olympus, Hamburg, Germany) equipped with a cooled CCD camera (SPOT slider, Visitron Systems, Puchheim, Germany). Images were acquired using 100× Plan-APO oil immersion objective with the appropriate differential interference contrast (DIC) optics and fluorescence filter sets: BP 470-490, FT 505, and BP 510-550 (NBD, FITC); BP 530–550, FT 580, and LP 590 (rhodamine, Merocyanine 540).

For NMR spectroscopy experiments, aliquots of LT23 mer were added to extruded 100 nm POPC vesicle suspensions (20 mM in D_2O buffer (10 mM HEPES, 100 mM NaCl, pD 7.0)) at a LT23 mer to POPC molar ratio of 1:100. NMR experiments were carried out on a Bruker DRX600 or Avance 700 NMR spectrometer at a resonance frequency of 600.13 MHz or 700.13 MHz, respectively, at 30 °C. Spectra were acquired at a spectral width of 7 kHz with a 90° pulse length of 10.3 μs. For phase sensitive NOESY experiments (mixing time 300 ms) 480 complex data points were collected in the t_1 dimensions with 32 or 64 scans per increment at a 4 s relaxation delay. Subsequently, aliquots of A20 mer was added at a 1:1 molar ratio with respect to LT23 mer and NMR spectra were collected again.

Received: March 2, 2006

Keywords: FRET (fluorescence energy resonance transfer) · molecular recognition · nanostructures · NMR spectroscopy · nucleic acids

[1] a) A. S. Boutorin, L. V. Gus'kova, E. M. Ivanova, N. D. Kobetz, V. F. Zarytova, A. S. Ryte, L. V. Yurchenko, V. V. Vlassov, *FEBS Lett.* **1989**, *254*, 129 – 132; b) R. G. Shea, J. C. Marsters, N. Bischofberger, *Nucleic Acids Res.* **1990**, *18*, 3777 – 3783.

[2] a) C. MacKellar, D. Graham, D. W. Will, S. Burgess, T. Brown, *Nucleic Acids Res.* **1992**, *20*, 3411 – 3417; b) J. M. Tomkins, K. J. Barnes, A. J. Blaker, W. J. Watkins, C. Abell, *Tetrahedron Lett.* **1997**, *38*, 691 – 694; c) S. Bonaccio, P. Walde, P. L. Luisi, *J. Phys. Chem.* **1994**, *98*, 6661 – 6663.

[3] a) A. M. Krieg, J. Tonkinson, S. Matson, Q. Zhao, M. Saxon, L. M. Zhang, U. Bhanja, L. Yakubov, C. A. Stein, *Proc. Natl. Acad. Sci. USA* **1993**, *90*, 1048 – 1052; b) C. Lorenz, P. Hadwiger, M. John, H. P. Vornlocher, C. Unverzagt, *Bioorg. Med. Chem. Lett.* **2004**, *14*, 4975 – 4977.

[4] J. Soutschek, A. Akinc, B. Bramlage, K. Charisse, R. Constien, M. Donoghue, S. Elbashir, A. Geick, P. Hadwiger, J. Harborth, M. John, V. Kesavan, G. Lavine, R. K. Pandey, T. Racie, K. G. Rajeev, I. Rohl, I. Toudjarska, G. Wang, S. Wuschko, D. Bumcrot, V. Koteliansky, S. Limmer, M. Manoharan, H. P. Vornlocher, *Nature* **2004**, *432*, 173 – 178.

[5] a) P. F. F. Almeida, A. Pokorny, A. Hinderliter, *Biochim. Biophys. Acta* **2005**, *1720*, 1 – 13; b) M. Edidin, *Annu. Rev. Biophys. Biomol. Struct.* **2003**, *32*, 257 – 283; c) R. G. Anderson, K. Jacobson, *Science* **2002**, *296*, 1821 – 1825.

[6] W. Flasche, C. Cismas, A. Herrmann, J. Liebscher, *Synthesis* **2004**, 2335 – 2341.

[7] a) S. R. LaPlante, E. A. Boudreau, N. Zanatta, G. C. Levy, P. N. Borer, J. Ashcroft, D. Cowburn, *Biochemistry* **1988**, *27*, 7902 – 7909; b) R. F. Epand, B. G. Sayer, R. M. Epand, *FEBS J.* **2005**, *272*, 1792 – 1803.

[8] a) J. Korlach, P. Schwille, W. W. Webb, G. W. Feigenson, *Proc. Natl. Acad. Sci. USA* **1999**, *96*, 8461 – 8466; b) C. Dietrich, L. A. Bagatolli, Z. N. Volovyk, N. L. Thompson, M. Levi, K. Jacobson, E. Gratton, *Biophys. J.* **2001**, *80*, 1417 – 1428; c) K. Bacia, P. Schwille, T. Kurzchalia, *Proc. Natl. Acad. Sci. USA* **2005**, *102*, 3272 – 3277; d) T. Baumgart, S. T. Weiss, W. W. Webb, *Nature* **2003**, *425*, 821 – 824; e) Z. Orynbayeva, S. Kolusheva, E. Livneh, A. Lichtenshtein, I. Nathan, R. Jelinek, *Angew. Chem.* **2005**, *44*, 1092 – 1096; *Angew. Chem. Int. Ed.* **2005**, *44*, 1092 – 1096; f) I. O. Benítez, D. R. Talham, *J. Am. Chem. Soc.* **2005**, *127*, 2814 – 2815.

[9] P. Williamson, K. Mattocks, R. A. Schlegel, *Biochim. Biophys. Acta* **1983**, *732*, 387 – 393.

[10] C. Nicolini, J. Baranski, S. Schlummer, J. Palomo, M. Lumbierres-Burgues, M. Kahms, J. Kuhlmann, S. Sanchez, E. Gratton, H. Waldmann, R. Winter, *J. Am. Chem. Soc.* **2006**, *128*, 192 – 201.

[11] R. G. Parton, A. A. Richards, *Traffic* **2003**, *4*, 724 – 738.

[12] M. J. Hope, M. B. Bally, G. Webb, P. R. Cullis, *Biochim. Biophys. Acta* **1985**, *812*, 55 – 65.

[13] a) M. Angelova, S. Soleau, P. Meleard, J. F. Faucon, P. Bothorel, *Prog. Lipid Res.* **1992**, *89*, 127 – 131; b) L. Mathivet, S. Cribier, P. F. Devaux, *Biophys. J.* **1996**, *70*, 1112 – 1121.

 © 2006 Wiley-VCH Verlag GmbH & Co. KGaA, Weinheim

Exciton Interactions

DOI: 10.1002/anie.200504477

Chiral, Bichromophoric Silicones: Ordering Principles of Structural Units in Complex Molecules**

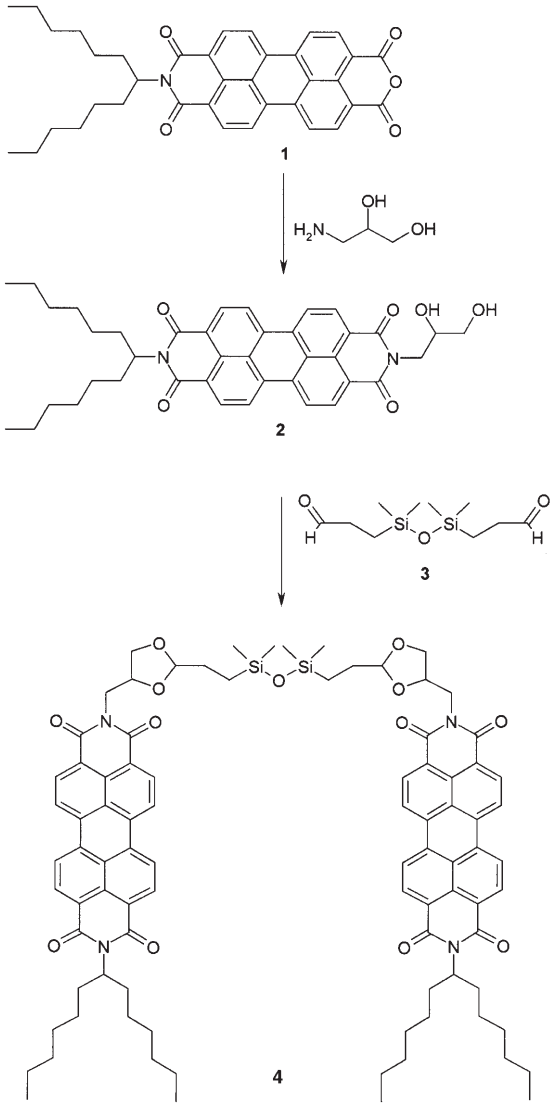
Heinz Langhals and Oswald Krotz*

Chromophores[1] are ideal sensors for intramolecular interactions. However, they have not been employed in investigations of the ordering principles in complex chiral molecules such as structures of fundamental importance for processes in life. In our research we have used a short, flexible chain of silicone as the basic structure and linked its termini to the strongly fluorescent perylene bisimides[2,3] by a chiral spacer (for the oscillator strengths and transition moment see reference [2]). To this end, the perylene dye **1**,[4] bearing long-chain *sec*-alkyl groups for increased solubility,[2,5] was condensed with 3-aminopropane-1,2-diol to form **2** (Scheme 1).[6,7] The bichromoporic dye **4** was formed by further condensation with the silicone dialdehyde **3**[8,9] with acid catalysis. When racemic **2** was allowed to react with **3** to form **4a**, an intensely yellow fluorescent material with the UV/Vis spectra characteristic of perylene bisimides[2] was obtained. Apparently the two chromophores in **4a** interact only neglibly (Figure 1, bottom). Remarkably, **4a** forms exclusively the *meso* form as could be shown by NMR spectroscopy; the amount of the racemic form is less than

[*] Prof. Dr. H. Langhals, Dipl.-Chem. O. Krotz
Department of Chemistry
LMU University of Munich
Butenandtstrasse 13, 81377 Munich (Germany)
Fax: (+49) 89-2180-77640
E-mail: Langhals@lrz.uni-muenchen.de

[**] This work was supported by the Deutsche Forschungsgemeinschaft and the Fonds der Chemischen Industrie. We thank Dr. D. Stephenson for the NOE measurements.

WILEY InterScience DISCOVER SOMETHING GREAT
© 2006 Wiley-VCH Verlag GmbH & Co. KGaA, Weinheim



Scheme 1. Synthesis of the dyes **4**.

0.4% (NMR spectrum at 20°C). This corresponds to a remarkable difference in free enthalpy of more than 13 kJ mol^{-1}.

A completely different situation was found when enantiopure **2** was allowed to react with **3**: The *R* enantiomer **2b** led to **4b** and the *S* enantiomer **2c** to **4c**. NOE measurements indicate that the newly formed stereogenic center in position 2 of the dioxolane rings of **4b** occurs as two-thirds *S* enantiomer and one-third *R* enantiomer, and vice versa for **4c**. One obtained red fluorescent materials in both cases; the fluorescence is bathochromically shifted and intensified at long wavelengths by exciton interactions.[10–13] Thus, it is easy to visually discriminate between racemic and enantiomeric **2**.

The exciton effects are based on intramolecular interactions in the bichromophoric dyes because when an artificial racemate was formed from the antipodes **4b** and **4c,** the spectra did not change with respect to the pure antipodes (Figure 1). Catalysis by acid (toluene sulfonic acid) transformed this artificial racemate composed of **4b** and **4c** into **4a**, and caused a change in the color of fluorescence from red

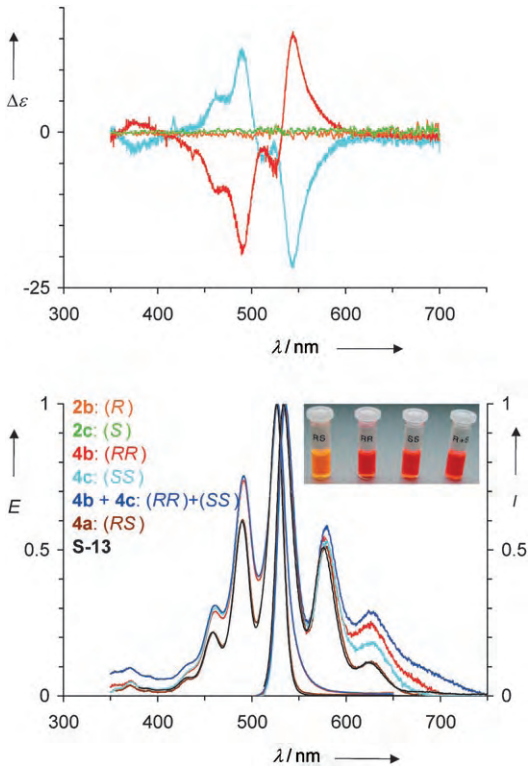


Figure 1. Top: CD spectra of **4b** (red) and **4c** (turquoise) in chloroform and neglible CD effect of the enantiomers **2b** (orange) and **2c** (green). Bottom: UV/Vis absorption (left) and fluorescence spectra (right) in chloroform. Blue: 1:1 Mixture of **4b** and **4c**, red: **4b**, turquoise: **4c**, brown: **4a**, black: reference of standard perylene dyes (S-13, 2,9-bis(1-hexylheptyl)anthra[2,1,9-*def*;6,5,10-*d′e′f′*]diisoquinoline-1,3,8,10-tetraone). **2a**, **4a**: racemate; **2b**, **4b**: (4*R*,4′*R*); **2c**, **4c**: (4*S*,4′*S*).

to yellow. This transformation proceeded precisely with pseudo-first-order kinetics (see the isosbestic point and the linear relation in Figure 2). The rate constant was determined by UV/Vis spectroscopy to be 2.0×10^{-5} s^{-1} at a concentration of acid of 7 mmol L^{-1} (in chloroform). Thus, the rate constant for the transformation is calculated to be 2.9 L mol^{-1} s^{-1}. In **4**

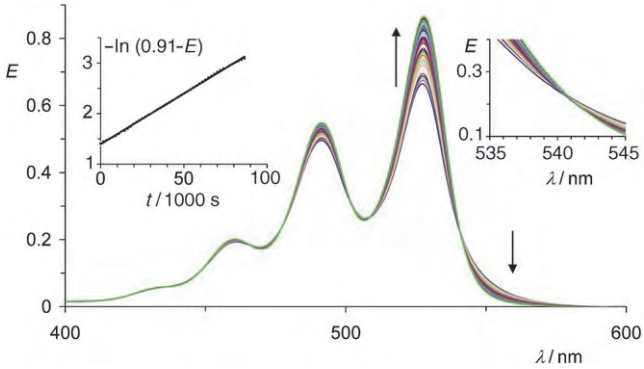


Figure 2. Change of the UV/Vis spectra caused by the acid-catalyzed transformation of a 1:1 mixture of **4b** and **4c** into **4a**. Right inset: amplification of the region of the isosbestic point at 541 nm. Left inset: kinetic analysis of the transformation according to pseudo first order at 527.2 nm: $k_1 = 2.0\times10^{-5}$ s^{-1} at $c_{H^+} = 7$ mmol L^{-1} (20°C in chloroform, $r = 0.9998$, $n = 46$).

© 2006 Wiley-VCH Verlag GmbH & Co. KGaA, Weinheim

the geometry suitable for the exciton interactions of the chromophores is apparently avoided. The driving force responsible arises from the interaction of the chromophores (cf. also Ref. [14]) because the terminal groups are so distant from each other that steric interactions cannot be important. The intensity of the interaction is remarkable.

The orientation[15,16] of the chromophores in **4b** and **4c** in solution can be determined by the CD effects of the dyes[17] (Figure 1, top). These are dominated[18] by exciton interactions[19] because very small CD effects are found for perylene dyes with chiral aliphatic N substituents; (Figure 1, top; cf. also Ref. [20]). On the other hand, a pronounced exciton effect with $\Delta\varepsilon = +16$ is found for **4b** and $\Delta\varepsilon = -21$ for **4c**. The transition moment for the electronic excitation of the perylene dye is parallel to the line connecting the two N atoms.[21] As a consequence, *P* chirality (right-handed screw sense) is given for the arrangement of chromophores in space for **4b** and *M* chirality (left-handed screw sense) for **4c**.

The transformation shown in Figure 2 is of interest because it offers insights not only into ordering processes of larger molecular structures but also for applications such as security marking and the detection of acids.

Experimental Section

2a: A solution of **1** (400 mg, 697 μmol), racemic 3-amino-1,2-propanediol (241 mg, 2.65 mmol), and imidazole (40 g) was heated with the exclusion of air and moisture (Ar atmosphere) for 4 h at 105 °C, quenched by the addition of a 1:1 mixture of 2 M HCl and acetic acid (100 mL), and stirred for 30 min. The precipitate was collected by vacuum filtration, dried in air (110 °C) for 16 h, and purified by column chromatography (silica gel, chloroform/ethanol 10:1). Yield 344 mg (76 %) dark red solid; R_f (silica gel, $CHCl_3$/EtOH 10:1) = 0.23; ^{1}H NMR (600 MHz, $CDCl_3$, 25 °C): $\delta = 0.83$ (t, $^3J_{H,H} =$ 6,9 Hz, 6H, CH_3), 1.23–1.37 (m, 16H, CH_2), 1.86–1.90 (m, 2H, CH_2), 2.22–2.27 (m, 2H, CH_2), 3.66–3.73 (m, 2H, CH_2-OH), 4.14–4.18 (m, 1H, *CH*-OH), 4.40–4.52 (m, 2H, CH_2-CHOH), 5.15–5.20 (m, 1H, α-CH), 8.55–8.67 ppm (m, 8H, arom. CH); ^{13}C NMR (151 MHz, $CDCl_3$, 25 °C): $\delta = 14.0$, 22.6, 27.0, 29.2, 31.8, 32.4, 42.9, 54.9, 63.8, 70.7, 122.4, 122.9, 123.4, 126.2, 126.4, 129.4, 131.9, 134.0, 135.3, 164.6 ppm; MS (DEI$^+$/70 eV): *m*/*z* (%): 646 (19) [M^+], 629 (8), 615 (11) [M^+-CH_3O], 614 (10), 586 (6), 572 (11) [$M^+-C_3H_6O_2$], 465 (18) [$M^+-C_{13}H_{25}$], 446 (15), 433 (43) [$M^+-C_{13}H_{26}-CH_3O$], 415 (12), 404 (100), 390 (68) [$M^+-C_{13}H_{26}-C_3H_6O_2$], 373 (21), 345 (14), 207 (16), 55 (17), 44 (22); IR (KBr): $\tilde{\nu} =$ 3436 (m), 2925 (m), 2855 (m), 1697 (m), 1656 (s), 1594 (s), 1578 (m), 1507 (w), 1438 (m), 1404 (m), 1343 (s), 1251 (m), 1171 (w), 1127 (w), 1106 (w), 1035 (w), 854 (w), 810 (m), 747 (m), 432 cm^{-1} (w); UV/Vis ($CHCl_3$): λ_{max} (ε) = 460 (16800), 491 (44700), 528 nm (73700 L mol^{-1} cm^{-1}); fluorescence ($CHCl_3$): $\lambda_{max} = 536$, 579 nm; fluorescence quantum yield ($CHCl_3$, $\lambda_{ex} = 489$ nm, $c = 6.9$ μmol L^{-1}, reference S-13 with $\Phi = 1.00$): 1.00; $C_{40}H_{42}N_2O_6$ (646.8): calcd: C 74.28, H 6.55, N 4.33; found: C 73.96, H 6.51, N 4.29.

2b: The reaction of (*R*)-3-amino-1,2-propanediol (241 mg, 2.65 mmol) was analogous to that of **2a**, and the product was purified analogously. Yield 187 mg (41 %) dark red solid; R_f (silica gel, $CHCl_3$/EtOH 10:1) = 0.23; ^{1}H NMR (600 MHz, $CDCl_3$, 25 °C): $\delta = 0.84$ (m, 6H, CH_3), 1.25–1.34 (m, 16H, CH_2), 1.87–1.90 (m, 2H, CH_2), 2.23–2.27 (m, 2H, CH_2), 3.71–3.78 (m, 2H, CH_2-OH), 4.16–4.19 (m, 1H, *CH*-OH), 4.37–4.51 (m, 2H, CH_2-CHOH), 5.15–5.18 (m, 1H, α-CH), 8.40–8.66 ppm (m, 8H, arom. CH); ^{13}C NMR (151 MHz, $CDCl_3$, 25 °C): $\delta = 14.1$, 22.6, 27.0, 29.2, 31.8, 32.4, 42.9, 54.9, 63.9, 70.6, 122.4, 122.8, 123.3, 126.1, 126.2, 129.3, 131.8, 133.8, 135.1, 164.4 ppm; MS (DEI$^+$/70 eV): *m*/*z* (%): 646 (76) [M^+], 629 (24), 612 (51), 573 (19), 465 (83), 446 (66), 430 (100), 415 (81), 404 (99), 391 (96), 373 (40), 345 (34); IR (KBr): $\tilde{\nu} =$ 3436.2 (m), 2955.0 (m), 2926.4 (m), 2856.3 (m), 1696.6 (s), 1655.8 (s), 1595.0 (s), 1578.2 (m), 1507.4 (w), 1438.4 (w), 1404.5 (m), 1344.0 (s), 1251.7 (m), 1172.0 (w), 1126.7 (w), 1107.6 (w), 1036.1 (w), 963.6 (w), 853.1 (w), 810.4 (m), 747.7 (m), 724.0 (w), 592.2 cm^{-1} (w); UV/Vis ($CHCl_3$): λ_{max} (ε) = 461 (17600), 492 (47700), 529 nm (78200 L mol^{-1} cm^{-1}); fluorescence ($CHCl_3$): $\lambda_{max} = 536$, 577 nm; fluorescence quantum yield ($CHCl_3$, $\lambda_{ex} = 490$ nm, $E_{490nm} =$ 0.226 cm^{-1}, reference S-13 with $\Phi = 1.00$): 1.00; HRMS ($C_{40}H_{42}N_2O_6$): calcd *m*/*z*: 646.3043, found *m*/*z*: 646.3018.

2c: The reaction of (*S*)-3-amino-1,2-propanediol (241 mg, 2.65 mmol) was analogous to that of **2a**, and the product was purified analogously. Yield 192 mg (43 %) dark red solid; R_f (silica gel, $CHCl_3$/EtOH 10:1): 0.23; ^{1}H NMR (600 MHz, $CDCl_3$, 25 °C): $\delta = 0.83$ (t, $^3J_{H,H} = 6.9$ Hz, 6H, CH_3), 1.23–1.34 (m, 16H, CH_2), 1.86–1.90 (m, 2H, CH_2), 2.22–2.28 (m, 2H, CH_2), 2.75–2.76 (m, 1H, OH), 3.08–3.09 (m, 1H, OH), 3.66–3.72 (m, 2H, CH_2-OH), 4.14–4.16 (m, 1H, *CH*-OH), 4.41–4.52 (m, 2H, CH_2-CHOH), 5.15–5.21 (m, 1H, α-CH), 8.61–8.70 ppm (m, 8H, arom. CH); ^{13}C NMR (151 MHz, $CDCl_3$, 25 °C): $\delta = 14.0$, 22.6, 26.9, 29.2, 31.8, 32.4, 42.9, 54.9, 63.8, 70.7, 122.5, 123.0, 123.5, 126.3, 126.5, 129.5, 131.1, 131.8, 132.0, 134.0, 135.4, 164.7 ppm; MS (DEI$^+$/70 eV): *m*/*z* (%): 646 (19) [M^+], 573 (18), 465 (24),446 (19), 433 (20), 430 (14), 404 (38), 391 (100), 373 (11), 347 (12); IR (KBr): $\tilde{\nu} =$ 3490.1 (m, br), 2921.8 (m), 2855.3 (m), 1688.8 (m), 1643.3 (s), 1593.1 (m), 1575.1 (w), 1438.6 (w), 1403.5 (w), 1342.0 (m), 1248.6 (w), 1170.8 (w), 1036.5 (w), 809.3 (m), 746.2 cm^{-1} (m); UV/Vis ($CHCl_3$): λ_{max} (ε) = 461 (16000), 492 (43300), 528 nm (70300 L mol^{-1} cm^{-1}); fluorescence ($CHCl_3$): $\lambda_{max} = 536$, 579 nm; fluorescence quantum yield ($CHCl_3$, $\lambda_{ex} = 491$ nm, $E_{491nm} = 0.319$ cm^{-1}, reference S-13 with $\Phi = 1.00$): 1.00; HRMS ($C_{40}H_{42}N_2O_6$): calcd *m*/*z*: 646.3043, found *m*/*z*: 646.3048.

4a: A mixture of **3** (62 mg, 17 μmol), **2a** (30 mg, 46 μmol), *p*-toluenesulfonic acid monohydrate (spatula tip), and anhydrous magnesium sulfate (spatula tip) in chloroform (5 mL) was stirred for 24 h. The magnesium sulfate was removed by filtration and the filtrate concentrated to dryness. The residue was purified by column chromatography (alumina, chloroform/ethanol 20:1). Yield 14 mg (56 %) dark red solid; R_f (silica gel, $CHCl_3$/EtOH 10:1) = 0.30; ^{1}H NMR (600 MHz, $CDCl_3$, 25 °C): $\delta = 0.07$–0.24 (m, 12H, Si-CH_3), 0.75–0.79 (m, 4H, Si-CH_2), 0.82–0.84 (m, 12H, CH_3), 1.23–1.37 (m, 32H, CH_2), 1.69–1.71 (m, 2H, Si-CH_2-CH_2), 1.77–1.81 (m, 2H, Si-CH_2-CH_2), 1.84–1.89 (m, 4H, CH_2), 2.22–2.28 (m, 4H, CH_2), 3.82–3.84 (m, 1H), 3.99–4.00 (m, 2H), 4.09–4.11 (m, 1H), 4.15–4.20 (m, 1H), 4.24–4.29 (m, 1H), 4.55–4.60 (m, 2H), 4.64–4.71 (m, 2H), 4.88–4.93 (m, 1H), 5.16–5.22 (m, 3H), 8.61–8.69 ppm (m, 16H, arom. CH); ^{13}C NMR (151 MHz, $CDCl_3$, 25 °C): $\delta = 14.0$, 22.6, 26.9, 29.2, 31.8, 32.4, 41.8, 42.9, 54.8, 68.4, 68.6, 73.7, 104.9, 106.2, 123.0, 123.2, 126.4, 126.6, 129.6, 131.1, 131.5, 131.7, 131.9, 134.3, 135.0, 163.5 ppm; MS (FAB$^-$/NBA, Xe 8 kV): *m*/z (%): 1503 (2) [M+H]$^+$, 913 (3), 836 (3), 774 (10), 762 (100), 612 (18), 585 (10), 579 (11), 571 (25), 388 (11), 360 (12), 153 (16); IR (KBr): $\tilde{\nu} =$ 2924.3 (m), 2855.8 (m), 1695.4 (s), 1651.7 (s), 1593.3 (s), 1577.1 (m), 1506.3 (w), 1436.0 (w), 1403.9 (m), 1338.6 (s), 1249.6 (m), 1173.0 (w), 1126.3 (w), 1037.8 (w), 840.6 (w), 808.1 (m), 744.9 cm^{-1} (m); UV/Vis ($CHCl_3$): λ_{max} (ε) = 461 (31800), 491 (80000), 527 nm (108300 L mol^{-1} cm^{-1}); fluorescence ($CHCl_3$): $\lambda_{max} =$ 535, 578 nm; fluorescence quantum yield ($CHCl_3$, $\lambda_{ex} = 490$ nm, $E_{490nm} = 0.245$ cm^{-1}, reference S-13 with $\Phi = 1.00$): 1.00; HRMS ($C_{90}H_{102}N_4O_{13}Si_2$): calcd *m*/*z*: 1502.6976, found *m*/*z*: 1502.6957.

4b: The reaction of **3** (217 mg, 59.5 μmol) and **2b** (100 mg, 155 μmol) in chloroform (15 mL) was analogous to the reaction of **2a**, and the product was purified in analogy to **4a**. Yield 31 mg (35 %) dark red solid; R_f (silica gel, $CHCl_3$/EtOH 10:1) = 0.30; ^{1}H NMR (600 MHz, $CDCl_3$, 25 °C): $\delta = -0.01$–0.16 (m, 12H, Si-CH_3), 0.57–0.75 (m, 4H, Si-CH_2), 0.83–0.84 (m, 12H, CH_3), 1.23–1.36 (m, 32H, CH_2), 1.51–1.73 (m, 4H, Si-CH_2-CH_2), 1.86–1.92 (m, 4H, CH_2), 2.24–2.27 (m, 4H, CH_2), 3.68–5.29 (div. m, 14H, N-CH/N-CH_2/acetal. CH/acetal. CH_2), 8.10–8.67 ppm (m, 16H, arom. CH); ^{13}C NMR (151 MHz, $CDCl_3$, 25 °C): $\delta = 0.2$, 14.0, 22.6, 26.9, 27.0, 29.2, 31.8,

 © 2006 Wiley-VCH Verlag GmbH & Co. KGaA, Weinheim

32.4, 37.8, 41.8, 42.9, 54.8, 54.9, 63.8, 68.3, 68.5, 68.6, 73.4, 73.6, 105.6, 105.8, 107.0, 107.3, 122.5, 122.8, 123.0, 123.2, 123.4, 125.9, 126.5, 129.2, 129.5, 131.1, 131.6, 131.9, 132.0, 133.8, 134.1, 134.3, 134.9, 135.3, 163.2, 163.5, 163.7, 164.6 ppm; MS (DEI$^+$/70 eV): m/z (%): 1502 (0.7) [M^+], 817 (32), 657 (100), 629 (30), 475 (13), 429 (16), 391 (26), 189 (15); IR (KBr): $\tilde{\nu}$ = 2924.4 (s), 2856.2 (m), 1695.5 (s), 1651.9 (s), 1593.7 (s), 1578.5 (w), 1435.5 (w), 1404.0 (w), 1339.6 (m), 1173.1 (w), 1126.7 (w), 1046.0 (w), 844.0 (w), 809.2 (w), 745.6 cm^{-1} (w); UV/Vis ($CHCl_3$): λ_{max} (ε) = 461 (30800), 492 (76800), 527 nm (101400 L mol^{-1} cm^{-1}); fluorescence ($CHCl_3$): λ_{max} = 534, 577 nm; fluorescence quantum yield ($CHCl_3$, λ_{ex} = 491 nm, $E_{491\ nm}$ = 0.224 cm^{-1}, reference S-13 with Φ = 1.00): 1.00; HRMS ($C_{90}H_{102}N_4O_{13}Si_2$): calcd m/z: 1502.6976, found m/z: 1502.6931; $C_{90}H_{102}N_4O_{13}Si_2$ (1504.0): calcd: C 71.87, H 6.84, N 3.73; found: C 71.07, H 6.93, N 3.58.

4c: The reaction of **3** (62 mg, 17 μmol) and **2c** (30 mg, 46 μmol) in chloroform (5 mL) was analogous to the reaction of **2a**, and the product was purified in analogy to **4a**. Yield 6 mg (24%); R_f (silica gel, $CHCl_3$/EtOH 10:1) = 0.30; ^{1}H NMR (600 MHz, $CDCl_3$, 25 °C): δ = −0.01–0.16 (m, 12H, Si-CH_3), 0.54–0.78 (m, 4H, Si-CH_2), 0.83–0.84 (m, 12H, CH_3), 1.24–1.37 (m, 32H, CH_2), 1.57–179 (m, 4H, Si-CH_2-CH_2), 1.83–1.93 (m, 4H, CH_2), 2.24–2.27 (m, 4H, CH_2), 3.66–5.28 (div. m, 14H, N-CH/N-CH_2/acetal. CH/acetal. CH_2), 8.06–8.67 ppm (m, 16H, arom. CH); ^{13}C NMR (151 MHz, $CDCl_3$, 25 °C): δ = 0.2, 11.7, 11.8, 14.1, 22.6, 27.0, 27.7, 27.9, 29.3, 31.8, 32.4, 37.8, 41.8, 42.0, 42.9, 43.3, 54.9, 63.9, 68.3, 68.4, 68.5, 68.6, 70.6, 73.6, 105.5, 105.8, 107.0, 107.2, 122.4, 122.5, 122.7, 123.1, 123.3, 124.0, 125.8, 126.3, 129.0, 129.2, 129.3, 129.4, 129.5, 130.7, 130.8, 131.0, 131.5, 131.6, 131.7, 131.8, 133.7, 134.0, 134.2, 134.8, 135.1, 163.0, 163.1, 163.3, 163.4, 164.3, 164.5 ppm; MS (DEI$^+$/70 eV): m/z (%): 1502 (0.4) [M^+], 817 (31), 657 (100), 629 (28), 475 (16), 429 (22), 391 (25), 189 (31), 99 (16), 55 (16); MS (TA/MALDI): m/z (%): 1526 [M+Na]$^+$, 629, 531, 515, 471, 437, 431, 402, 358; IR (KBr): $\tilde{\nu}$ = 2922.9 (m), 2855.1 (m), 1695.8 (s), 1655.9 (s), 1593.4 (s), 1578.1 (m), 1504.4 (w), 1434.1 (m), 1403.5 (m), 1339.9 (s), 1249.3 (m), 1173.7 (w), 1126.3 (w), 1103.9 (w), 1038.8 (m), 982.5 (w), 836.9 (w), 808.1 (m), 745.0 cm^{-1} (m); UV/Vis ($CHCl_3$): λ_{max} (ε) = 461 (32400), 491 (81300), 527 nm (107100 L mol^{-1} cm^{-1}); fluorescence ($CHCl_3$): λ_{max} = 534, 578 nm; fluorescence quantum yield ($CHCl_3$, λ_{ex} = 490 nm, $E_{490\ nm}$ = 0.236 cm^{-1}, reference S-13 with Φ = 1.00): 1.00; HRMS ($C_{90}H_{102}N_4O_{13}Si_2$): calcd m/z: 1502.6976, found m/z: 1502.6939.

Received: December 16, 2005
Published online: June 13, 2006

Keywords: dyes/pigments · exciton interactions · fluorescence spectroscopy · perylenes

[1] H. Zollinger, *Color Chemistry, Synthesis, Properties, and Applications of Organic Dyes and Pigments*, 3rd ed., Wiley-VCH, Zürich, **2003**, ISBN 3-906390-23-3.
[2] H. Langhals, *Helv. Chim. Acta* **2005**, *88*, 1309 – 1343.
[3] H. Langhals, *Heterocycles* **1995**, *40*, 477 – 500.
[4] H. Kaiser, J. Lindner, H. Langhals, *Chem. Ber.* **1991**, *124*, 529 – 535.
[5] H. Langhals, S. Demmig, T. Potrawa, *J. Prakt. Chem.* **1991**, *333*, 733 – 748.
[6] H. Langhals, K. Fuchs, *Collect. Czech. Chem. Commun.* **2006**, *1*, 625 – 634 .
[7] H. Langhals, K. Fuchs, Ger. Offen. DE 102004020542.6, 27. April, **2004**.
[8] E. Fritz-Langhals, *Org. Process Res. Dev.* **2005**, *9*, 577 – 582; *Chem. Abstr.* **2005**, *143*, 349015.
[9] W. E. Dennis, J. W. Ryan, *J. Org. Chem.* **1970**, *35*, 4180 – 4183.
[10] A. S. Davydov, *Zh. Eksp. Teor. Fiz.* **1948**, *18*, 210 – 218; *Chem. Abstr.* **1949**, *43*, 4575f.
[11] A. S. Davydov, *Theory of Molecular Excitations* (Eds.: H. Kasha, M. Oppenheimer, Jr.), McGraw-Hill, New York, **1962**.
[12] W. Kuhn, *Trans. Faraday Soc.* **1930**, *26*, 293 – 308.
[13] M. Kasha, H. R. Rawls, M. A. El-Bayoumi, *Pure Appl. Chem.* **1965**, *11*, 371 – 392.
[14] Y. Luo, J. Lin, H. Duan, J. Zhang, C. Lin, *Chem. Mater.* **2005**, *17*, 2234 – 2236.
[15] V. Prelog, G. Helmchen, *Angew. Chem.* **1982**, *94*, 614 – 631; *Angew. Chem. Int. Ed. Engl.* **1982**, *21*, 567 – 583.
[16] R. S. Cahn, C. Ingold, V. Prelog, *Angew. Chem.* **1966**, *78*, 413 – 447; *Angew. Chem. Int. Ed. Engl.* **1966**, *5*, 385 – 415.
[17] K. Nakanishi, N. Berova, *The Excitation Chirality Method* (Eds.: K. Nakanishi, N. Berova, R. W. Woody), VCH, Weinheim, **1994**, pp. 361 – 398.
[18] A. I. Kiprianov, *Russ. Chem. Rev.* **1971**, *40*, 594 – 607.
[19] H. Langhals, J. Gold, *Liebigs Ann.* **1997**, 1151 – 1153.
[20] J. Karolin, L. B.-Å. Johansson, U. Ring, H. Langhals, *Spectrochim. Acta Part A* **1996**, *52*, 747 – 753.
[21] L. B.-Å. Johansson, H. Langhals, *Spectrochim. Acta Part A* **1991**, *47*, 857 – 861.

 © 2006 Wiley-VCH Verlag GmbH & Co. KGaA, Weinheim

Metal–Metal Interactions

DOI: 10.1002/anie.200600423

Al–Eu and Al–Yb Donor–Acceptor Bonds**

Michael T. Gamer, Peter W. Roesky, Sergey N. Konchenko, Paola Nava, and Reinhart Ahlrichs*

Metal–metal bonds are of fundamental interest in many areas in natural science.[1] In the coordination chemistry of transition metals, single and multiple metal–metal bonds have

[*] Dr. M. T. Gamer, Prof. Dr. P. W. Roesky
Freie Universität Berlin
Institut für Chemie und Biochemie
Fabeckstrasse 34–36, 14195 Berlin (Germany)
Fax: (+49) 308-385-2440
E-mail: roesky@chemie.fu-berlin.de

Dr. S. N. Konchenko
Institute of Inorganic Chemistry
Siberian Division of RAS
Acad. Lavrentyev str. 3, Novosibirsk 630090 (Russia)
Fax: (+7) 3833-309-489
E-mail: konch@che.nsk.su

Dr. P. Nava, Prof. Dr. R. Ahlrichs
Institut für Physikalische Chemie
Lehrstuhl für Theoretische Chemie
Universität Karlsruhe (TH)
Kaiserstrasse 12, 76128 Karlsruhe (Germany)
Fax: (+49) 721-608-7225
E-mail: reinhart.ahlrichs@chemie.uni-karlsruhe.de

[**] We thank Arnim Hellweg and Florian Weigend for providing the auxiliary basis sets for Yb and Eu. This work was supported by the Deutsche Forschungsgemeinschaft (Center for Functional Nanostructures).

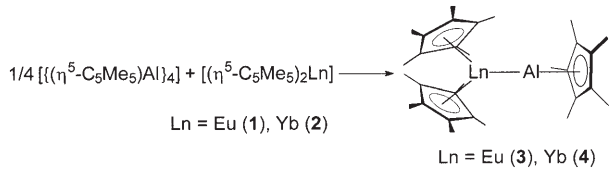
Supporting information for this article is available on the WWW under http://www.angewandte.org or from the author.

© 2006 Wiley-VCH Verlag GmbH & Co. KGaA, Weinheim

been well-established[2] since the mid-60s.[3] In contrast to the rapid development in main-group and transition-metal chemistry, metal–metal bonds in rare-earth complexes are virtually unknown because the 4f valence shell is embedded in the interior of the ion and shielded by the $5s^2$ and $5p^6$ orbitals.[4] To the best of our knowledge, only one example of a nonbridged metal–metal bond exists for a 4f metal, in $[(thf)(\eta^5\text{-}C_5H_5)_2Lu{-}Ru(CO)_2(\eta^5\text{-}C_5H_5)]$.[5] Herein we present the coordination of $[(\eta^5\text{-}C_5Me_5)Al]$ onto divalent lanthanide compounds.

For several years, the low-valent Al^I compound $[\{(\eta^5\text{-}C_5Me_5)Al\}_4]$ has been known.[6,7] The tetramer decays in solution and in the gas phase into the monomer unit $[(\eta^5\text{-}C_5Me_5)Al]$.[8,9] In late-transition-metal chemistry, a number of compounds[10–12] that contain aluminum, such as $[Fe(CO)_4\text{-}\{(\eta^5\text{-}C_5Me_5)Al\}]$, were reported.[13] In this context, the $\{(\eta^5\text{-}C_5Me_5)Al\}$ fragment is considered to be isolobal with CO and PR_3.[14] Theoretical studies have shown that the HOMO of $\{(\eta^5\text{-}C_5Me_5)Al\}$ distinctly exhibits the character of a lone pair, such that the alanediyl unit $\{(\eta^5\text{-}C_5Me_5)Al\}$ can act as a Lewis base.[15] The first example in main-group chemistry that featured the $\{(\eta^5\text{-}C_5Me_5)Al\}$ fragment as a pure donor ligand with no backbonding was the aluminum–boron donor–acceptor adduct $[(\eta^5\text{-}C_5Me_5)Al{-}B(C_6F_5)_3]$.[16] On the basis of these considerations we anticipated that the coordination of the $\{(\eta^5\text{-}C_5Me_5)Al\}$ fragment to a Lewis acidic lanthanide complex would result in an aluminum–lanthanide donor–acceptor bond.

Heating a 1:4 mixture of $[\{(\eta^5\text{-}C_5Me_5)Al\}_4]$ and solvent-free $[(\eta^5\text{-}C_5Me_5)_2Ln]$ (Ln = Eu (**1**), Yb (**2**))[17] in an evacuated ampoule at 120 °C for several days resulted in red (Ln = Eu) and green (Ln = Yb) crystals, respectively, of composition $[(\eta^5\text{-}C_5Me_5)_2Ln{-}Al(\eta^5\text{-}C_5Me_5)]$ (Ln = Eu (**3**), Yb (**4**)) in moderate yields (Scheme 1). Both compounds are very air-



Scheme 1.

sensitive and decompose quickly in aromatic solvents. The starting materials can be partly recovered from the reaction mixtures. The solid-state structures of both complexes were determined by single-crystal X-ray crystallography (Figure 1).[18] The structures consist of individual Lewis acid–base adducts with no unusually short intermolecular contacts. All three C_5Me_5 groups in each molecule are η^5-bound. The angle between the C_5Me_5 ring centroid (Cg), Al atom, and Ln atom is slightly bent in each case (161.82(1)° (**3**), 171.79(1)° (**4**)). These values are in agreement with those in $[(C_6F_5)_3B{-}Al(\eta^5\text{-}C_5Me_5)]$, which has a Cg-Al-B angle of 172.9(1)°. The average Al–C bond lengths of 2.251(2) Å (**3**) and 2.257(3) Å (**4**) are in the range of those in $[(C_6F_5)_3B{-}Al(\eta^5\text{-}C_5Me_5)]$ (2.171(3) Å), but are significantly shorter than those in the starting material $[\{(\eta^5\text{-}C_5Me_5)Al\}_4]$ (2.388(7) Å).

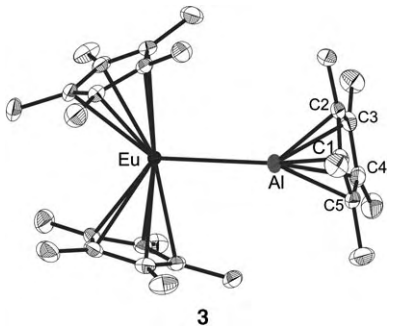


Figure 1. Perspective ORTEP view of the molecular structure of **3**. Thermal ellipsoids are set at the 50% probability level. Hydrogen atoms are omitted for clarity. Selected distances [Å] and angles [°]: Al–Eu 3.3652(10), Al–C1 2.249(2), Al–C2 2.257(2), Al–C3 2.257(2), Al–C4 2.248(2), Al–C5 2.247(2), Cg_{Al}–Al 1.8987(10), Cg_1–Eu 2.524(8), Cg_2–Eu 2.528(2); Cg_{Al}-Al-Eu 161.82(1), Cg_1-Eu-Cg_2 140.14(1), Cg_1-Eu-Al 107.75(1), Cg_2-Eu-Al 106.09(1). Selected distances [Å] and angles [°] for the isostructural compound **4** (not shown): Al–Yb 3.1981(11), Al–C1 2.258(3), Al–C2 2.265(3), Al–C3 2.259(3), Al–C4 2.248(3), Al–C5 2.254(3), Cg_{Al}–Al 1.9047(5), Cg_1–Yb 2.3941(3), Cg_2–Yb 2.3892(1); Cg_{Al}-Al-Yb 171.79(1), Cg_1-Yb-Cg_2 143.80(1), Cg_1-Yb-Al 107.44(1), Cg_2-Yb-Al 108.04(1). Cg = C_5Me_5 centroid.

The Cg–Ln distances (Cg_1–Eu 2.524(8), Cg_2–Eu 2.528(2), Cg_1–Yb 2.3941(3), Cg_2–Yb 2.3892(1) Å) are comparable to those in the starting materials $[(\eta^5\text{-}C_5Me_5)_2Ln]$, thus clearly indicating that the lanthanide element is still in the +2 oxidation state.[17] The Al–Ln bond lengths of 3.3652(10) Å (**3**) and 3.1981(11) Å (**4**) cannot be compared with other data since we present the first metal–metal bond between aluminum and a 4f metal.

The oxidation states of the metal centers in **3** and **4** correlate with those in the corresponding starting materials. Nevertheless, it is experimentally very difficult to disprove the presence of a bridging hydrido ligand by standard X-ray diffraction analysis. We were especially scrutinous because the $\{(\eta^5\text{-}C_5Me_5)Al\}$ fragment tends to insert into C–H bonds.[19] The EI mass spectrum of compound **3** shows decomposition into $[(\eta^5\text{-}C_5Me_5)Al]^+$, $[(\eta^5\text{-}C_5Me_5)_2Eu]^+$, and other ion fragments. The following experiments were made to disprove the presence of a hydrido species:

1) The ^1H NMR spectrum shows that compound **4** decomposes rapidly in solution; thus, a clear assignment of the spectroscopic signals was not possible. Nevertheless, the ^1H NMR spectrum shows that a diamagnetic product is obtained, which indicates that no oxidized $[(\eta^5\text{-}C_5Me_5)_2Yb{-}H]$ is present. Moreover, no Al–H signals were observed in the negative region of the ppm scale.[3]
2) The standard X-ray diffraction analyses were of high quality, and the hydrogen atoms could be freely refined. However, no bridging hydrido atoms were detected.
3) In the IR spectrum of $[(\eta^5\text{-}C_5Me_5)AlH_2]$, the ν(Al–H) stretching mode was determined as strong signals at 1795 and 1770 cm^{-1}.[20] The IR spectra of the hydrido-bridged complexes $[(\eta^5\text{-}C_5Me_5)_2YbAlH_3{\cdot}L]$ (L = NEt_3, thf, Et_2O) revealed signals between 1800 and 1660 cm^{-1}.[21] In contrast, neither the IR nor the Raman spectra of compounds **3** and **4** show any signal in the region between and 2720 and 1420 cm^{-1}.

 © 2006 Wiley-VCH Verlag GmbH & Co. KGaA, Weinheim

Further support for the absence of a bridging hydrido ligand is provided by the following theoretical studies. Calculations of the molecular electronic structure were carried out to provide a more complete characterization of **3** and **4**.[22,23] Here, only the DFT-BP86[24] results are discussed, as they are very similar to those from DFT-TPSS,[25] whereas Hartree-Fock, MP2, and hybrid functionals show serious deficiencies.[26] In Table 1 are shown the most important calculated structural parameters of **3** and **4**, as well as those of their constituents **1**, **2**, and [(η^5-C_5Me_5)Al] (**5**), together with experimental data.[6,8,17,27]

Table 1: Computed (BP86) and experimental (XRD, ED) structural parameters of compounds **1**–**5**.[a]

		BP86	XRD	ED
5	Cg_{Al}-Al	2.003	2.015[6]	2.063[8]
1	Cg-Eu	2.478	2.53[17c]	–
	Cg_1-Eu-Cg_2	151.3	140	–
2	Cg-Yb	2.338	2.38[17a]	2.326[17b]
	Cg_1-Yb-Cg_2	157.1	146	158
3	Al-Eu	3.384	3.365[b]	–
	Cg_{Al}-Al	1.947	1.899	–
	Cg_1-Eu	2.513	2.524	–
	Cg_1-Eu-Cg_2	142.7	140.1	–
4	Al-Yb	3.226	3.198[b]	–
	Cg_{Al}-Al	1.953	1.905	–
	Cg_1-Yb	2.385	2.394	–
	Cg_1-Yb-Cg_2	144.7	143.8	–

[a] XRD = data from single-crystal X-ray diffraction experiments, ED = data from electron-diffraction experiments in the gas phase. Experimental distances for **1**, **2**, and **5** are average values. Cg = C_5Me_5 centroid; distances given in Å, angles given in °. [b] This work.

The BP86 calculations show gratifying accuracy for **1** and **2**. The Cg–Yb distances and Cg-Yb-Cg angles agree with the gas-phase data to within 0.01 Å and 1°, respectively.[28] The calculations for **5** are slightly less accurate. The BP86 method yields a Cg–Al distance that is 0.06 Å smaller than the ED result, which, however, may itself be an overestimate of this value.[8] The situation is similar for the computed structure constants of **3** and **4** in comparison with the corresponding X-ray diffraction data. The Cg–Ln distances and the Cg-Ln-Cg angles, as well as the Cg–Al distances, show virtually identical deviations as for **1**, **2**, and **5**. The computed and measured Al–Ln bond lengths also agree to within 0.03 Å.[29] Since structural constants are very sensitive, for example with respect to addition of one or more hydrogen atoms, the BP86 computations confirm the chemical compositions of **3** and **4**.

The dissociation energy of **3**/**4** with respect to **1**/**2** and **5** is perhaps the most interesting quantity not yet available by experiment. From the BP86 calculations, we obtained the values shown for Eqs. (1) and (2) (TPSS values: 37 kJ mol^{-1} for Yb, 35 kJ mol^{-1} for Eu). The relatively small binding energy ΔE is consistent with the fact that **3** and **4** are not stable in solution (see above).

$$\mathbf{3} \rightarrow \mathbf{1} + \mathbf{5} \quad \Delta E = 29.7\ \text{kJ mol}^{-1} \tag{1}$$

$$\mathbf{4} \rightarrow \mathbf{2} + \mathbf{5} \quad \Delta E = 30.0\ \text{kJ mol}^{-1} \tag{2}$$

The main features of the molecular electronic structures of **3** and **4** show close similarities (Figure 2). In each case, the

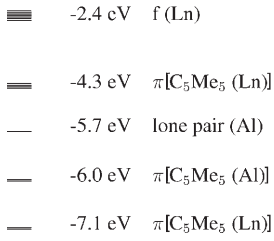


Figure 2. Molecular-orbital diagram of the highest occupied orbitals of **3** and **4**. The given energies refer to **4**.

HOMO is the 4f orbital of the Ln atom and is distributed over a range of only 0.2 eV (BP86).[30] The occupations $4f^{14}$ for Yb and $4f^7$ (all spins parallel) for Eu clearly prove the oxidation state of +2 for the Ln center and consequently +1 for the Al atom. The f electrons are followed on the molecular-orbital diagram by the π HOMO of the C_5Me_5 ligand on the Ln center. The π HOMO of the C_5Me_5 ligand on the Al center is about 1.7 eV lower in energy, thus indicating a much stronger C_5Me_5–Al than C_5Me_5–Ln interaction. The lone pair of electrons of the {C_5Me_5Al} fragment (Figure 3) is located

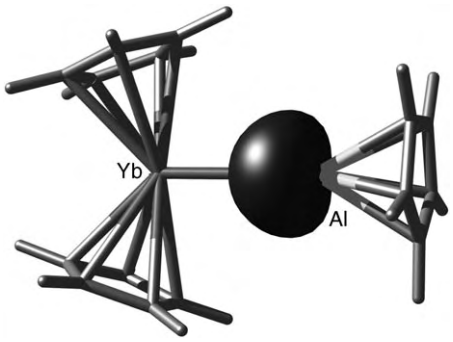


Figure 3. Orbital of the lone pair of electrons on the Al atom for the C_5H_5 analogue of **4**; the surface given corresponds to 0.075 atomic units (of the molecular orbital).

between the π MOs on the molecular-orbital diagram, and is relatively well separated from the higher- and lower-lying orbitals. As can be seen in Figure 3, there are only very small contributions from the Ln orbitals to this MO.[31] The interaction of **1** or **2** with **5** is predominantly electrostatic (computed BP86 dipole moments: 1.5 D for **2**, orientation $Yb^{\delta+}$; 1.7 D for **5**, orientation $Al^{\delta-}$) with insignificant charge-transfer and covalent contributions.

In summary, we have prepared the first complexes with bonds between aluminum and 4f metals. These largely electrostatic bonds possess insignificant charge-transfer and covalent contributions. The complexes are weekly bound

 © 2006 Wiley-VCH Verlag GmbH & Co. KGaA, Weinheim

(bond energies ca. 30 kJmol^{-1}), and only minor geometry distortions of constituent moieties are observed.

Experimental Section

All manipulations were carried out under anaerobic and anhydrous conditions. A solid mixture of solvent-free $[(\eta^5\text{-}C_5Me_5)_2Ln]$ (0.4 mmol) and yellow $[\{(\eta^5\text{-}C_5Me_5)Al\}_4]$ (65 mg, 0.1 mmol) was placed at the bottom of an ampoule (ca. 10 × 100 mm). The tube was evacuated (10^{-2} mbar) and flame sealed. Observable amounts of crystals appeared after two days of heating at 120 °C. After two weeks of heating, the ampoule was opened, and the crystals were collected. **3**: Yield: 20 mg (36 %), red crystals; M.p. 200 °C (decomp); IR (KBr): $\tilde{\nu}$ = 460 (s), 593 (s), 1030 (w), 1178 (m), 1198 (w), 1385 (s), 1417 (s), 2722 (w), 2901 cm^{-1} (m). **4**: 34 mg (56 %), green crystals; M.p. 145 °C (decomp); IR (KBr): $\tilde{\nu}$ = 460 (s), 668 (m), 1030 (w), 1178 (m), 1379 (s), 1440 (s), 2720 (w), 2852 (s), 2905 cm^{-1} (s).

Received: February 1, 2006
Published online: June 7, 2006

Keywords: aluminum · cluster compounds · lanthanides · metal–metal interactions · rare earths

[1] "Physics and Chemistry of Metal Cluster Compounds": *Physics and Chemistry of Materials with Low-Dimensional Structures, Vol. 18* (Eds.: F. Lévy, E. Mooser, L. J. de Jongh), Springer, Heidelberg, **1994**.
[2] *The Chemistry of Metal Cluster Complexes* (Eds.: D. F. Shriver, H. D. Kaesz, R. D. Adams), Wiley, New York, **1990**.
[3] F. A. Cotton, N. F. Curtis, C. B. Harris, B. F. G. Johnson, S. J. Lippard, J. T. Mague, W. R. Robinson, J. S. Wood, *Science* **1964**, *145*, 1305.
[4] A. J. Freeman, R. E. Watson, *Phys. Rev.* **1962**, *127*, 2058 – 2075.
[5] I. P. Beletskaya, A. Z. Voskoboynikov, E. B. Chuklanova, N. I. Kirillova, A. K. Shestakova, I. P. Parshina, A. I. Gusev, G. K.-I. Magomedov, *J. Am. Chem. Soc.* **1993**, *115*, 3156 – 3166.
[6] C. Dohmeier, C. Robl, M. Tacke, H. Schnöckel, *Angew. Chem.* **1991**, *103*, 594 – 595; *Angew. Chem. Int. Ed. Engl.* **1991**, *30*, 564 – 565.
[7] S. Schulz, H. W. Roesky, H. J. Koch, G. M. Sheldrick, D. Stalke, A. Kuhn, *Angew. Chem.* **1993**, *105*, 1828 – 1830; *Angew. Chem. Int. Ed. Engl.* **1993**, *32*, 1729 – 1731.
[8] A. Haaland, K.-G. Martinsen, S. A. Shlykov, H. V. Volden, C. Dohmeier, H. Schnöckel, *Organometallics* **1995**, *14*, 3116 – 3119. The measurements were carried out at 139 °C, which led to an Al–C vibrational amplitude of 0.12 Å.
[9] J. Gauss, U. Schneider, R. Ahlrichs, C. Dohmeier, H. Schnöckel, *J. Am. Chem. Soc.* **1993**, *115*, 2402 – 2408.
[10] C. Gemel, T. Steinke, M. Cokoja, A. Kempter, R. A. Fischer, *Eur. J. Inorg. Chem.* **2004**, 4161 – 4176.
[11] T. Steinke, C. Gemel, M. Winter, R. A. Fischer, *Chem. Eur. J.* **2005**, *11*, 1636 – 1646.
[12] T. Steinke, C. Gemel, M. Cokoja, M. Winter, R. A. Fischer, *Angew. Chem.* **2004**, *116*, 2349 – 2352; *Angew. Chem. Int. Ed.* **2004**, *43*, 2299 – 2302.
[13] J. Weiss, D. Stetzkamp, B. Nuber, R. A. Fischer, C. Boehme, G. Frenking, *Angew. Chem.* **1997**, *109*, 95 – 97; *Angew. Chem. Int. Ed. Engl.* **1997**, *36*, 70 – 72.
[14] J. Uddin, C. Boehme, G. Frenking, *Organometallics* **2000**, *19*, 571 – 582.
[15] A. H. Cowley, *Chem. Commun.* **2004**, 2369 – 2375.
[16] J. D. Gordon, A. Voigt, C. L. B. Macdonald, J. S. Silverman, A. H. Cowley, *J. Am. Chem. Soc.* **2000**, *122*, 950 – 951.
[17] a) M. Schultz, C. J. Burns, D. J. Schwarz, R. A. Andersen, *Organometallics* **2000**, *19*, 781 – 789; b) R. A. Andersen, R. Blom, J. M. Boncella, C. J. Burns, H. V. Volden, *Acta Chem. Scand. Ser. A* **1987**, *41*, 24 – 35; c) W. J. Evans, L. A. Hughes, T. P. Hanusa, *Organometallics* **1986**, *5*, 1285 – 1291.
[18] Single-crystal X-ray diffraction data for **3** were obtained with a Bruker SMART 1000 diffractometer with $Mo_{K\alpha}$ radiation (λ = 0.71073 Å); space group $P\bar{1}$ (No. 2), a = 9.899(2), b = 10.934(2), c = 14.878(2) Å, α = 75.228(11), β = 71.74(2), γ = 69.631(12)°, 133 K, Z = 2, V = 1414.3(4) Å^3, ρ = 1.373 g cm^{-3}, $2\theta_{max}$ = 61°, 17545 reflections collected, 8433 independent reflections (R_{int} = 0.0206). The structure was solved by Patterson methods and refined by full-matrix least-square techniques by using 7551 reflections with $I > 2\sigma(I)$ to R_1 = 0.0237 and wR_2 = 0.0659. Single-crystal X-ray diffraction data for **4** were obtained with a Bruker SMART 1000 diffractometer with $Mo_{K\alpha}$ radiation (λ = 0.71073 Å); space group $P\bar{1}$ (No. 2), a = 9.904(2), b = 10.682(2), c = 14.915(3) Å, α = 76.583(5), β = 74.427(5), γ = 70.670(4)°, 133 K, Z = 2, V = 1416.4(6) Å^3, ρ = 1.420 g cm^{-3}, $2\theta_{max}$ = 61°, 17380 reflections collected, 8375 independent reflections (R_{int} = 0.0249). The structure was solved by Patterson methods and refined by full-matrix least-square techniques by using 7394 reflections with $I > 2\sigma(I)$ to R_1 = 0.0331 and wR_2 = 0.0763. CCDC-296933 and CCDC-296934 contain the supplementary crystallographic data for this paper. These data can be obtained free of charge from The Cambridge Crystallographic Data Centre via www.ccdc.cam.ac.uk/data_request/cif.
[19] T. Steinke, M. Cokoja, C. Gemel, A. Kempter, A. Krapp, G. Frenking, U. Zenneck, R. A. Fischer, *Angew. Chem.* **2005**, *117*, 3003 – 3007; *Angew. Chem. Int. Ed.* **2005**, *44*, 2943 – 2946.
[20] H.-J. Himmel, J. Vollet, *Organometallics* **2002**, *21*, 5972 – 5977.
[21] S. Y. Kjazhanski, E. S. Kalyuzhnaya, L. E. E. Herrera, B. M. Bulychev, A. V. Khvostov, A. I. Sizov, *J. Organomet. Chem.* **1997**, *531*, 19 – 25.
[22] All calculations were performed with the program package TURBOMOLE; a) R. Ahlrichs, M. Bär, M. Häser, H. Horn, C. Kölmel, *Chem. Phys. Lett.* **1989**, *162*, 165 – 169; b) O. Treutler, R. Ahlrichs, *J. Chem. Phys.* **1995**, *102*, 346 – 354.
[23] We employed the newly developed def2-TZVP basis sets (triple zeta valence augmented by polarization functions, for example 2d1f for Al and C); a) F. Weigend, R. Ahlrichs, *Phys. Chem. Chem. Phys.* **2005**, *7*, 3297 – 3305. For Yb and Eu we used ECPs and segmented basis sets from M. Dolg, which are available from the EMSL http://www.emsl.pnl.gov/forms/basisform.html, with one set of g functions (exponent 0.306). Auxiliary basis sets were provided by F. Weigend for DFT and A. Hellweg for MP2; b) F. Weigend, *Phys. Chem. Chem. Phys.* **2006**, *8*, 1057 – 1065.
[24] a) A. D. Becke, *Phys. Rev. A* **1988**, *38*, 3098 – 3100; b) S. H. Vosko, L. Wilk, M. Nusair, *Can. J. Phys.* **1980**, *58*, 1200 – 1211; c) J. P. Perdew, *Phys. Rev. B* **1986**, *33*, 8822 – 8824; erratum: J. P. Perdew, *Phys. Rev. B* **1986**, *34*, 7406.
[25] J. Tao, J. P. Perdew, V. N. Staroverov, G. E. Scuseria, *Phys. Rev. Lett.* **2003**, *91*, 146401.
[26] Details are presented in the Supplementary Information.
[27] The computed structure constants are given for the most stable conformer. Structure optimizations were carried out by using analytical gradients together with a geometry relaxation procedure. a) M. von Arnim, R. Ahlrichs, *J. Chem. Phys.* **1999**, *111*, 9183 – 9190. We investigated possible rotations of methyl groups as well as staggered (lower in energy) and eclipsed conformations of $\{(\eta^5\text{-}C_5Me_5)_2Ln\}$ moieties. Final computations were done in C_s symmetry for **1**–**4**, and in C_{5v} symmetry for **5**.
[28] X-ray diffraction data for the solid phase are not directly comparable; these data indicate interactions of monomeric units[17] between a methyl group of one unit and the lanthanide atom of another unit (a weak "dative bond"). This interaction

 © 2006 Wiley-VCH Verlag GmbH & Co. KGaA, Weinheim

decreases the Cg-Ln-Cg angle and increases (slightly) the Cg–Ln distance.
[29] The only noticeable deviation between theory and experiment concerns the Ln-Al-Cg angle, which is almost linear (179°) according to the calculations. This deviation may be a result of effects of crystal packing in combination with the softness of the corresponding vibrational mode.
[30] The smallest computed vertical ionization potentials (energy difference between molecule and cation) are 5.3 eV for **3** and **4**.
[31] Mulliken analyses and natural-population analyses indicate a transfer of less than 0.2 electrons from $\{(C_5Me_5)Al\}$ to $\{(C_5Me_5)_2Ln\}$.

 © 2006 Wiley-VCH Verlag GmbH & Co. KGaA, Weinheim

Pattern Formation in Crystals

DOI: 10.1002/anie.200601038

Formation of Self-Organized Dynamic Structure Patterns of Barium Carbonate Crystals in Polymer-Controlled Crystallization**

Tongxin Wang, An-Wu Xu, and Helmut Cölfen**

The self-assembly of structural motifs and the self-organization of dynamic motifs into highly ordered one-, two-, or three-dimensional patterns with controlled structures have received much attention in recent years, because of their importance in basic research and their potential applications.[1] Recently, methods such as lithography, microstamping, or template-assisted synthesis have been employed to fabricate patterns with controlled structures.[2] Of the many challenges facing materials science, the development of bottom-up crystallization strategies enabling the direct growth of nanocrystal assemblies with patterns remains an attractive, but elusive goal.

[*] Dr. T. X. Wang,[+] Dr. A.-W. Xu, Dr. H. Cölfen
Max Planck Institute of Colloids and Interfaces
Department of Colloid Chemistry
Research Campus Golm, 14424 Potsdam (Germany)
Fax: (+49) 331-567-9502
E-mail: an-wu.xu@mpikg.mpg.de
coelfen@mpikg.mpg.de

[+] Current address:
Department of Materials Science and Engineering
University of Pennsylvania
3231 Walnut Street, Philadelphia, PA 19104 (USA)

[**] We thank the Max Planck Society for financial support and for a fellowship for T.X.W., and the Alexander von Humboldt Foundation for a research fellowship for A.-W.X. Prof. Markus Antonietti is thanked for the useful discussions. We also thank Antje Völkel for the ultracentrifugation, Ivoclar Vivadent AG (Liechtenstein) for the gift of the acrylate ethyl ester monomer, and Jan Krieger for providing his Brüsselator simulation program free of charge.

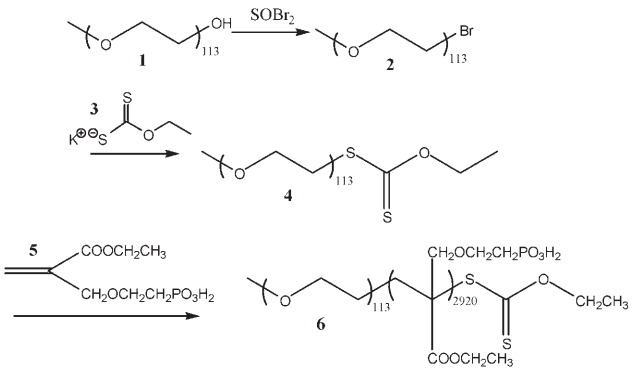
Supporting information for this article is available on the WWW under http://www.angewandte.org or from the author.

Living organisms accurately and routinely create complex, spatially well-defined functional mesoscopic superstructures, which can now be partly mimicked.[3] Specific additives, such as polymers, can exert a strong influence on crystal nucleation, growth, and self-organization into hierarchical architectures. A number of studies have already attempted to mimic biomineralization by using synthetic polymers as crystal-growth modifiers and superstructure-directing agents.[4] Recently, self-organized $CaCO_3$ crystals with submicrometer-scale periodicity were grown on a thin matrix of a hydrophobically modified polysaccharide in solution, in the presence of poly(acrylic acid) (PAA).[5] Micropatterning of a surface with single crystals of $CaCO_3$ was achieved by using a template-assisted method.[6] Synthetic approaches to the morphological control of inorganic minerals through polymer-controlled crystallization can produce a variety of inorganic superstructures, such as helical fibers, mesocrystals, complex spherical structures, hollow spheres, spongelike structures, and self-similar structures.[7]

Double hydrophilic block copolymers (DHBCs)[4a] consisting of a hydrophilic block that strongly interacts with inorganic minerals and a non-interacting hydrophilic block have recently been employed for the control of mineral crystallization and have proven to be highly effective, improved variants of the polyelectrolytes or amphiphiles used previously.[8] We reported the preparation of helical fibers of $BaCO_3$ using a racemic phosphonated block copolymer as additive.[9] This study demonstrated that the phosphonated group has a strong influence on the crystallization of $BaCO_3$.

In the present paper, we extend these observations through a systematic variation of pH and polymer concentration. We find experimental evidence that self-organization by reaction–diffusion processes, which govern pattern evolution and selection in many chemical and biological systems,[10] can also be realized in biomimetic mineralization. To our knowledge, this case is the first in which self-assembly and self-organization of the primary nanocrystalline building blocks occur in the same chemical system.

The phosphonated block copolymer **6** was synthesized through radical polymerization initiated by the new macroinitiator **4** (Scheme 1; see Supporting Information). Owing to the high steric demand of its functional side groups, the polymer is expected to be stiff, as suggested by computer modeling.[9] The polymer exhibits a high molar mass of



Scheme 1. Synthesis of the phosphonated DHBC **6**.

© 2006 Wiley-VCH Verlag GmbH & Co. KGaA, Weinheim

greater than 700 000 g mol^{-1} and a pH-independent polydispersity in the pH range 1.8–6.5 (see Supporting Information).

Crystallization of $BaCO_3$ through a gas-diffusion procedure (see Supporting Information) in $BaCl_2$ solution (20 mM) with polymer **6** (0.5 g L^{-1}) as additive at a starting pH of 3.5 led to ultralong $BaCO_3$ nanofibers, as shown in Figure 1. After 1 day of growth, the resulting $BaCO_3$ crystals consist

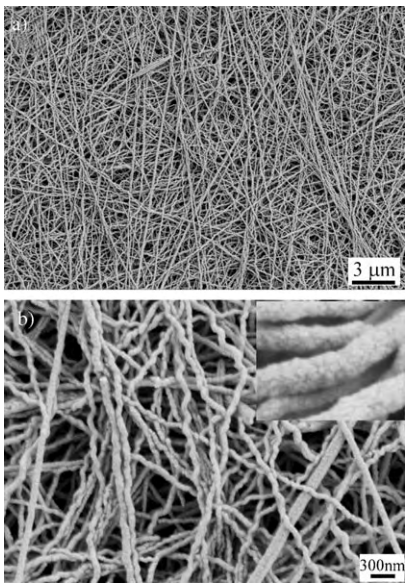


Figure 1. SEM images at different resolutions of ultralong nanofibers of $BaCO_3$ after 1 day of growth ([polymer] = 0.5 g L^{-1}, [Ba^{2+}] = 20 mM, starting pH 3.5); inset in (b) is an enlargement.

almost entirely of ultralong nanofibers with diameters of 40–140 nm and lengths of up to several millimeters. Moreover, some nanofibers display a helixlike structure, as observed in our previous study.[9] High-resolution scanning electron microscopy (SEM) images show that each nanofiber is composed of spherical nanoparticles with diameters of approximately 20 nm (Figure 1b, inset). The spherical nanoparticles self-assemble into the final helical objects. These nanofibers are clearly different from our previous helical fibers, which were assembled from nanorod building blocks.[9] The tectonic assembly of the nanoparticles into a helixlike structure is driven by the selective adsorption of the polymer on a specific crystal face.[9] An X-ray diffraction (XRD) pattern confirms the presence of pure witherite ($BaCO_3$; orthorhombic, space group *Pmcn*, $a = 5.316$, $b = 8.892$, $c = 6.428$ Å (JCPDS 71-2394); see Supporting Information). The primary particle size of 20 nm estimated by SEM agrees well with the XRD data, as evidenced by the reasonable coincidence between the experimental and simulated diffractograms for 20-nm particles of $BaCO_3$. A control experiment in the absence of polymer additive under otherwise similar conditions produced dendritic witherite crystals (see Supporting Information).

To investigate their effect on the final product, the polymer (0.5–2 g L^{-1}) and Ba^{2+} (2.5–20 mM) concentrations were varied. These experiments indicate that the concentration of polymer, the concentration of Ba^{2+}, and hence, the molar ratio of polymer to Ba^{2+} have a distinct influence on the morphology of the $BaCO_3$ crystals (see Supporting Information). At a fixed Ba^{2+} concentration, a lower polymer concentration favors long nanofibers of $BaCO_3$, implying that the phosphonated block copolymer exerts a strong control on the $BaCO_3$ crystallization. On the other hand, at a fixed polymer concentration, a higher Ba^{2+} concentration favors long nanofibers. At low Ba^{2+} concentrations, short fibers and irregular particles are formed. Our experiments show that a low polymer to Ba^{2+} ratio favors the formation of longer $BaCO_3$ nanofibers. This result might be caused by the strong crystallization-inhibition effect of phosphonated polymers, as shown for $BaSO_4$.[11a] The inhibition is dependent on the polymer concentration, such that the largest number of primary nanoparticles is expected for the lowest polymer and highest Ba^{2+} concentrations. Thus, more and smaller crystallization nuclei are present when CO_2 and NH_3 diffused into the solution.[11b]

In a second set of experiments, the influence of the pH on the morphology of the final products was examined. The solubility of $BaCO_3$ (as well as those of all other carbonates) depends on pH. A lower starting pH means that a larger amount of CO_2 must be added before the precipitation can begin, and therefore, that a higher reactant concentration is present at the point of nucleation. The pH upon dissolution of the polymer in a $BaCl_2$ solution is approximately 3.5. When the starting pH of the solution is 3.5 or 1.8 (adjusted by HCl) and all other conditions are constant, long $BaCO_3$ nanofibers are observed (Figure 2a,b). Thus, a lower starting pH favors long $BaCO_3$ nanofibers. On the other hand, when the starting pH of the solution is increased to 5.5, rather ill-defined short nanofibers and nanoparticles are observed (Figure 2c). The higher pH results in earlier nucleation at a lower concentration of reactants, which apparently disturbs the self-assembly into helical fibers. At an even higher pH of 6.5, nucleation leads to spherical $BaCO_3$ aggregates, which coexist with a small number of helical nanofibers (Figure 2d).

Analytical ultracentrifugation of reaction solutions at different starting pH values confirms that the Ba^{2+} ions form clusters upon hydrolysis at higher pH values, as evidenced by an increase in the sedimentation coefficient (see Supporting

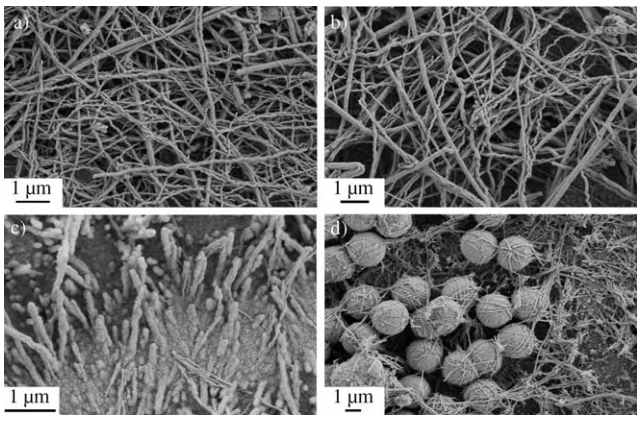


Figure 2. SEM images of $BaCO_3$ crystals after 1 day of growth at starting pH values of a) 1.8, b) 3.5, c) 5.5, and d) 6.5 ([polymer] = 1 g L^{-1}, [Ba^{2+}] = 10 mM).

 © 2006 Wiley-VCH Verlag GmbH & Co. KGaA, Weinheim

Information). Furthermore, the polymer–Ba^{2+} interaction is pH dependent, and the aggregate size and/or density increases with pH, whereas the polymer itself does not aggregate in the pH range investigated. The polymer–Ba^{2+} aggregation becomes very pronounced at a pH of 6.5, and macroscopic aggregates are formed.

At the critical point between the assembly of $BaCO_3$ into fibers or spheres, the short nanofibers obtained from polymer–Ba^{2+} aggregates at a starting pH of 5.5 self-organize into striking larger-scale structures. Typical SEM images of the quasiperiodic reaction–diffusion patterns observed after 1 day are shown in Figure 3. Light microscopy measurements

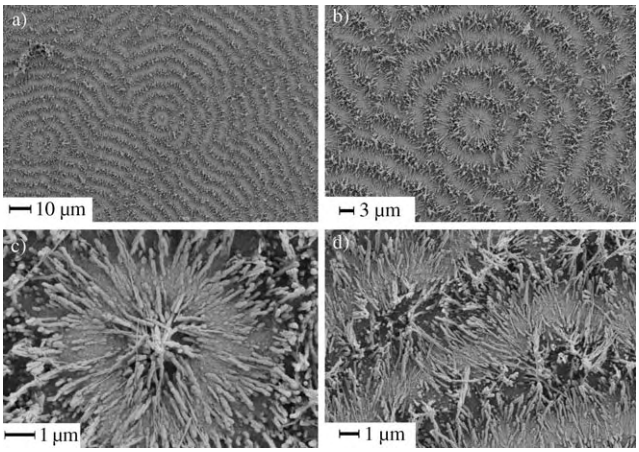


Figure 3. SEM images at different resolutions of the concentric ring patterns of $BaCO_3$ crystals after 1 day of growth ([polymer] = 1 g L^{-1}, [Ba^{2+}] = 10 mM, starting pH 5.5).

reveal that these patterns are formed in solution and are not induced by the drying process (see Supporting Information). The periodic wave pattern has multiple centers, from which concentric rings radiate outwards at even spacings (Figure 3a), and is reminiscent of Liesegang ring patterns[12] or the concentric wave patterns observed in the spatially extended Belousov–Zhabotinsky reaction.[13] On the substrate, many groups of concentric rings grow at the same time and stop before they merge into one another. The distance between adjacent rings is nearly constant at approximately 5 μm (Figure 3), excluding the possibility that these structures are formed by a Liesegang phenomenon. In Liesegang ring patterns, the distance between adjacent rings increases according to $X_n = Q(1+p)^n$, where X_n is the position of the nth band, p is the space coefficient (often in the range 0.05–0.4), and Q is a constant. In addition, Liesegang rings are usually formed by imposed concentration gradients in gels, but our ring patterns are formed in dilute solution.

The enlarged SEM images show that each ring (band) is composed of short nanorods (Figure 3c,d). These short nanorods stand, rather than lie, on the substrate and tend to form bundles that are organized in a circular pattern. Note that the experimental window for the formation of this ring pattern is narrow ([polymer] = 0.8–1.3 g L^{-1}, [Ba^{2+}] = 8–12 mM, starting pH 5.1–5.7).

We assume that the periodic pattern formation in the present study belongs to a self-organization process that results from an autocatalytic reaction in counterplay with a diffusion process.[14,15] Such phenomena are usually observed in gel media.[15] To understand the underlying mechanism of the formation of the dynamic ring patterns, we have to formulate the different processes that are equivalent to the elementary steps in a Belousov–Zhabotinsky reaction (see Supporting Information). The Belousov–Zhabotinsky reaction is a self-sustaining reaction–diffusion system;[13] in thin films, straight, spiral, or target oscillating waves of activity propagate as a result. Coupled chemical reactions cause changes in the concentrations of the reagents, which in turn, cause local changes in the oxidation potential of the solution. These potentials can be visualized with a redox indicator.

In our case, the formation of the polymer–Ba^{2+} complex is essential for the oscillating reaction. During complex formation, which is a key step in the autocatalytic cycle, Ba^{2+} ions bind to polymeric polyanions.[16] The formation of the polymer–Ba^{2+} complex can be demonstrated experimentally by titrating a polymer solution with Ba^{2+} and detecting the conductivity (data not shown). Dynamic light scattering measurements indicate that the average size of the polymer–Ba^{2+} complex formed when **6** is added to an aqueous Ba^{2+} solution is approximately 386 nm (data not shown), further confirming the formation of the complex.

Upon subsequent addition of CO_2, $BaCO_3$ is formed primarily in the vicinity of the polymers, which act as localized Ba^{2+} depots. Because of crystallization inhibition at the high local polymer concentration, amorphous nanoparticles of $BaCO_3$ are generated. SEM images of reaction products formed at different growth stages are presented in Figure 4. After 4 h of growth, the product consists of a film composed of particles of approximately 20–30 nm in size (Figure 4a). The corresponding electron diffraction (ED) pattern confirms that these nanoparticles are amorphous (Figure 4a, inset).

The amorphous $BaCO_3$ nanoparticles can aggregate. Although the crystallization of an amorphous particle is thermodynamically favored, kinetically inhibition makes it a rare event. If, however, a nanocrystal is formed, the majority of the polymer–Ba^{2+} complex is set free, because at its high local concentration the complex is not included in the crystal lattice, and it is only partially adsorbed onto the nanoparticle surface. The release of the polymer–Ba^{2+} complex upon crystallization is the important autocatalytic step in the observed oscillating reaction. The formation of a nanocrystal, not only results in the crystallization of other amorphous particles in the surrounding aggregate, but also in the attraction of additional amorphous nanoparticles. Similar behavior was also found for crystalline vaterite-type $CaCO_3$ particles formed by the oriented attachment of amorphous precursor particles.[17]

Therefore, the crystalline structure grows quickly and consumes all of the material in its direct surroundings. Consequently, diffusion processes come into play and begin to form the oscillating ring pattern (Figure 4b). The crystalline nanoparticles aggregate into short fibers, which have a tendency to stand on the substrate (Figure 4b, inset; similar to ZnO nanorods, which grow vertically on a substrate in solution[18]). The overall precipitation reaction in the presence of the phosphonated polymer **6** can be formulated as

 © 2006 Wiley-VCH Verlag GmbH & Co. KGaA, Weinheim

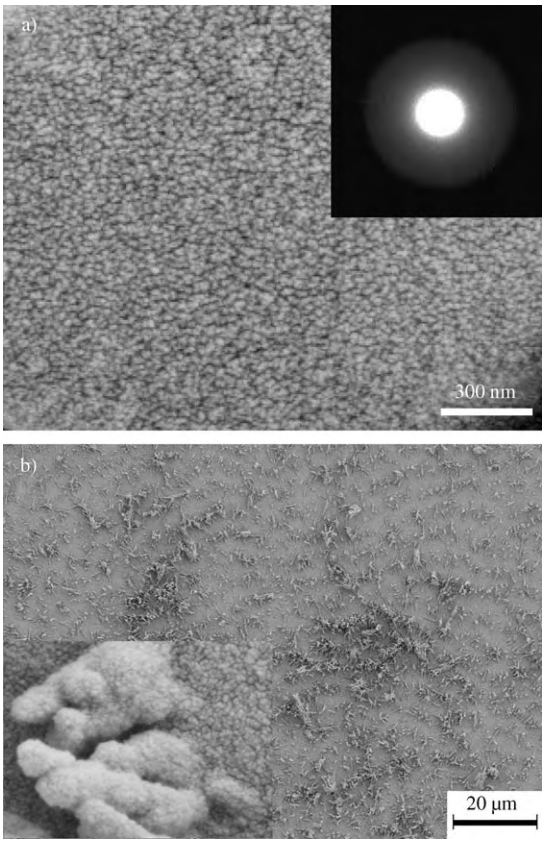


Figure 4. SEM images of the $BaCO_3$ particles after a) 4 h and b) 18 h of growth ([polymer] = 1 g L^{-1}, [Ba^{2+}] = 10 mM, starting pH 5.5); inset in (a) is the corresponding ED pattern; inset in (b) is an enlargement.

Equation (1) (see Supporting Information for partial reactions).

$$m\,Ba^{2+} + (m-x)\,H_2O_3P\text{-polymer-}PO_3H_2 + x\,CO_2 + x\,H_2O \rightarrow [BaCO_{3\,cryst}]_x \downarrow + (m-x)\,[\text{polymer-}(PO_3H)_2Ba] + 2m\,H^+ \quad (1)$$

This autocatalytic precipitation reaction coupled with diffusion of the nanoparticles establishes a reaction–diffusion system that leads to a concentric ring pattern. With time, a series of rings propagate out from a common center. To further substantiate that the observed oscillating precipitation reaction is of the Belousov–Zhabotinsky type, we carried out numerical simulations of the reaction–diffusion system using a Brusselator model (see Supporting Information).[19] The simulated pattern evolution in time and space qualitatively agrees with the experimental observations, supporting the oscillating character of our precipitation reaction. Note that similar patterns, although not derived from a Belousov–Zhabotinsky reaction, are also found in biominerals. For example, spiral patterns have been observed on the growing inner surface of nacre (aragonite-type $CaCO_3$); the exact origin of the patterns has not been fully explained.[20]

Many physical, chemical, and biological systems self-organize into periodic patterns characteristic of reaction–diffusion processes.[12–15,21] Examples include periodic precipitation fronts, Liesegang rings, Belousov–Zhabotinsky reactions, chemical turbulence, cardiac waves, and bacterial colonies.

Nature often uses oscillating reactions and similar patterns as a means of producing structures and materials with unique properties that are expressed on scales ranging from macroscopic (for example, stripes in seashells, and annual rings in trees, agates, and rocks) to microscopic (for example, cellular growth, chemotaxis, and biological waves).[21,22] This study adds a new example of spontaneous, self-organized pattern formation in solution by biomimetic mineralization. The resulting patterns are similar to those in a variety of physical, chemical, and natural systems, but are formed by a mesoscale transformation process.

In summary, we report the first Belousov–Zhabotinsky reaction for a self-organized system consisting of nanoparticles. In this system, the coupled reaction partners are not in the same aggregate state (in solution). The relationship between time and space in the observed ring patterns can be elucidated on the basis of the formalism for Belousov–Zhabotinsky oscillating reactions combined with nanoparticle assembly. The formulation of the underlying coupled reactions shows that the autocatalytic step is the formation of a polymer–Ba^{2+} complex. The reaction–diffusion system results in the spontaneous (that is, without external manipulation of concentration, temperature, or any other parameter) formation of micrometer-sized periodic rings of nanocrystalline $BaCO_3$. This ring pattern is grown on a substrate in an aqueous solution containing a new synthetic DHBC. Such a spontaneous generation of a pattern with remarkable regularity on the submicrometer scale is unexpected and indicates that the Belousov–Zhabotinsky reaction may be generalized to systems in different aggregation states (for example, liquid and solid).

The phosphonated block copolymers applied herein interact strongly with inorganic minerals and effectively control the crystallization of $BaCO_3$. A single DHBC can control both crystallization and self-organization by multiple reaction pathways determined by subtle changes in the experimental parameters.

Received: March 15, 2006

Keywords: barium carbonate · Belousov–Zhabotinsky reaction · block copolymers · reaction–diffusion system · self-organization

[1] a) A. H. Heuer, D. J. Fink, V. J. Laraia, J. L. Arias, P. D. Calvert, K. Kendall, G. L. Messing, J. Blackwell, P. C. Rieke, D. H. Thompson, A. P. Wheeler, A. Veis, A. I. Caplan, *Science* **1992**, *255*, 1098; b) C. B. Murray, C. R. Kagan, M. G. Bawendi, *Science* **1995**, *270*, 1335; c) G. M. Whitesides, B. Grzybowski, *Science* **2002**, *295*, 2418; d) M. Antonietti, *Nat. Mater.* **2003**, *2*, 9; e) H. Cölfen, S. Mann, *Angew. Chem.* **2003**, *115*, 2452; *Angew. Chem. Int. Ed.* **2003**, *42*, 2350.

[2] a) *Handbook of Microlithography, Micromachining, and Microfabrication* (Ed.: P. R. Choudhury), SPIE, Bellingham, **1997**; b) B. D. Gates, Q. B. Xu, M. Stewart, D. Ryan, C. G. Willson, G. M. Whitesides, *Chem. Rev.* **2005**, *105*, 1171.

[3] a) H. A. Lowenstam, S. Weiner, *On Biomineralization*, Oxford University Press, New York, **1989**; b) S. Mann, *Biomineralization. Principles and Concepts in Bioinorganic Materials Chemis-*

 © 2006 Wiley-VCH Verlag GmbH & Co. KGaA, Weinheim

try, Oxford University Press, Oxford, **2001**; c) E. Bäuerlein, *Biomineralization*, Wiley-VCH, Weinheim, **2000**.
[4] a) H. Cölfen, *Macromol. Rapid Commun.* **2001**, *22*, 219; b) F. C. Meldrum, *Int. Mater. Rev.* **2003**, *48*, 187; c) S. H. Yu, H. Cölfen, *J. Mater. Chem.* **2004**, *14*, 2124.
[5] A. Sugawara, T. Ishii, T. Kato, *Angew. Chem.* **2003**, *115*, 5457; *Angew. Chem. Int. Ed.* **2003**, *42*, 5299.
[6] J. Aizenberg, D. A. Muller, J. L. Grazul, D. R. Hamann, *Science* **2003**, *299*, 1205.
[7] a) L. A. Gower, D. A. Tirrell, *J. Cryst. Growth* **1998**, *191*, 153; b) T. Sugawara, Y. Suwa, K. Ohkawa, H. Yamamoto, *Macromol. Rapid Commun.* **2003**, *24*, 847; c) H. Cölfen, M. Antonietti, *Angew. Chem.* **2005**, *117*, 5714; *Angew. Chem. Int. Ed.* **2005**, *44*, 5576; d) S. H. Yu, H. Cölfen, A. W. Xu, W. F. Dong, *Cryst. Growth Des.* **2004**, *4*, 33; e) A. Bigi, E. Boanini, D. Walsh, S. Mann, *Angew. Chem.* **2002**, *114*, 2267; *Angew. Chem. Int. Ed.* **2002**, *41*, 2163; f) L. M. Qi, H. Cölfen, M. Antonietti, M. Li, J. D. Hopwood, A. J. Ashley, S. Mann, *Chem. Eur. J.* **2001**, *7*, 3526.
[8] a) J. M. Marentette, J. Norwig, E. Stockelmann, W. H. Meyer, G. Wegner, *Adv. Mater.* **1997**, *9*, 647; b) M. Antonietti, M. Breulmann, C. G. Göltner, H. Cölfen, K. K. W. Wong, D. Walsh, S. Mann *Chem. Eur. J.* **1998**, *4*, 2493; c) K. L. Robinson, J. V. M. Weaver, S. P. Armes, E. D. Marti, F. C. Meldrum, *J. Mater. Chem.* **2002**, *12*, 890; d) S. H. Yu, H. Cölfen, M. Antonietti, *Chem. Eur. J.* **2002**, *8*, 2937; e) F. Bouyer, C. Gerardin, F. Fajula, J. L. Putaux, T. Chopin, *Colloids Surf. A* **2003**, *217*, 179; f) A. Taubert, D. Palms, O. Weiss, M. T. Piccini, D. N. Batchelder, *Chem. Mater.* **2002**, *14*, 2594.
[9] S. H. Yu, H. Cölfen, K. Tauer, M. Antonietti, *Nat. Mater.* **2005**, *4*, 51.
[10] J. D. Murray, *Mathematical Biology*, Springer, Berlin, **1989**.
[11] a) M. Li, H. Cölfen, S. Mann, *J. Mater. Chem.* **2004**, *14*, 2269; b) T. X. Wang, H. Cölfen, M. Antonietti, *J. Am. Chem. Soc.* **2005**, *127*, 3246.
[12] R. E. Liesegang, *Naturwiss. Wochenschr.* **1896**, *11*, 53.
[13] a) A. N. Zaikin, A. M. Zhabotinsky, *Nature* **1970**, *225*, 535; b) I. R. Epstein, K. Showalter, *J. Phys. Chem.* **1996**, *100*, 13132; c) "Eine periodische Reaktion und ihr Mechanismus": B. P. Belousov in *Selbstorganisation chemischer Strukturen* (Eds.: L. Kuhnert, U. Niedersen), Harry Klein, Frankfurt/Main, **1981**, p. 71.
[14] a) H. K. Henisch, *Periodic Precipitation*, Pergamon, Oxford, **1991**; b) B. Hess, A. Mikhailov, *Science* **1994**, *264*, 223; c) K. Iwamoto, S. Mitomo, M. Seno, *J. Colloid Interface Sci.* **1984**, *102*, 477; d) M. Tsapatsis, D. G. Vlachos, S. Kim, H. Ramanan, G. R. Gavalas, *J. Am. Chem. Soc.* **2000**, *122*, 12864.
[15] a) A. Turing, *Philos. Trans. R. Soc. London Ser. B* **1952**, *237*, 37; b) H.-J. Krug, H. Brandtstädter, *J. Phys. Chem. A* **1999**, *103*, 7811; c) S. C. Müller, J. Ross, *J. Phys. Chem. A* **2003**, *107*, 7997; d) R. Klajn, M. Fialkowski, I. T. Bensemann, A. Bitner, C. J. Campbell, K. Bishop, S. Smoukov, B. A. Grzybowski, *Nat. Mater.* **2004**, *3*, 729.
[16] C. G. Sinn, R. Dimova, M. Antonietti, *Macromolecules* **2004**, *37*, 3444.
[17] N. Gehrke, H. Cölfen, N. Pinna, M. Antonietti, N. Nassif, *Cryst. Growth Des.* **2005**, *5*, 1317.
[18] K. Govender, D. S. Boyle, P. B. Kenway, P. O'Brien, *J. Mater. Chem.* **2004**, *14*, 2575.
[19] a) W. Jahnke, A. T. Winfree, *Int. J. Bifurcation Chaos Appl. Sci. Eng.* **1991**, *1*, 445; b) T. Turányi, L. Györgyi, R. J. Field, *J. Phys. Chem.* **1993**, *97*, 1931; c) I. Prigogine, R. Lefever, *J. Chem. Phys.* **1968**, *4*, 1695; d) We used the Brusselator simulation program written by Jan Krieger for his "Facharbeit Chemie, Bundeswettbewerb Jugend forscht 2001". This program is based on: J. R. Weimar, *Simulation with Cellular Automata*, Logos, Berlin, **1997**.
[20] K. Wada, *Nature* **1966**, *211*, 1427.
[21] a) M. Tsapatsis, D. G. Vlachos, S. Kim, H. Ramanan, G. R. Gavalas, *J. Am. Chem. Soc.* **2000**, *122*, 12864; b) P. Ortoleva, *Geochemical Self-Organization*, Oxford University Press, Oxford, New York **1994**; c) L. Kuhnert, U. Niedersen, *Selbstorganisation chemischer Strukturen. Ostwalds Klassiker der exakten Wissenschaften*, *Vol. 272*, Geest & Portig, Leipzig, **1987**.
[22] a) P. Ball, *The Self-Made Tapestry: Pattern Formation in Nature*, Oxford University Press, Oxford, **1999**; b) D. Thompson, *On Growth and Form*, Cambridge University Press, Cambridge, **1992**; c) H. Meinhardt, *Models of Biological Pattern Formation*, Academic Press, London, **1982**.

 © 2006 Wiley-VCH Verlag GmbH & Co. KGaA, Weinheim

NMR Methods

DOI: 10.1002/anie.200503247

Determination of the Relative Configuration of a Five-Membered Lactone from Residual Dipolar Couplings **

Christina M. Thiele, Andreas Marx, Robert Berger, Jana Fischer, Markus Biel, and Athanassios Giannis*

The determination of the relative configuration of stereogenic centers in organic molecules by NMR spectroscopy is in general an interlinked problem of simultaneous determination of conformation and configuration. This is usually accomplished using distance restraints from NOE data[1]

[*] Dr. C. M. Thiele,[+] Dipl.-Chem. A. Marx
Institut für Analytische Chemie
Universität Leipzig (Germany)
E-mail: cmt@punk.oc.chemie.tu-darmstadt.de

Dr. R. Berger
Frankfurt Institute for Advanced Studies
Johann Wolfgang Goethe Universität
Max-von-Laue-Strasse 1, 60438 Frankfurt am Main (Germany)

Dipl.-Chem. J. Fischer, Dipl.-Chem. M. Biel, Prof. Dr. A. Giannis
Institut für Organische Chemie
Universität Leipzig
Johannisallee 29, 04103 Leipzig (Germany)

[+] Present address:
Clemens-Schöpf-Institut für Organische Chemie und Biochemie
Technische Universität Darmstadt
Petersenstrasse 22, 64287 Darmstadt (Germany)
Fax: (+49) 6151-16-5531

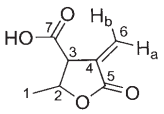
[**] C.M.T. thanks Prof. Dr. M. Reggelin for his support, Dr. L. Hennig for helpful discussions, Dr. B. Luy and Prof. Dr. H. Kessler for a gift of PS sticks, and Dr. F. Delaglio for providing the program NMRPIPE and for helping us use it. C.M.T. acknowledges the Fonds der Chemischen Industrie and the Deutsche Forschungsgemeinschaft (TH1115/1-1) for grants. R.B. acknowledges financial support by the Volkswagen Foundation as well as computer time provided by the Norddeutscher Verbund für Hoch- und Höchstleistungsrechnen (HLRN) and the Center for Scientific Computing (CSC).

Supporting information for this article is available on the WWW under http://www.angewandte.org or from the author.

© 2006 Wiley-VCH Verlag GmbH & Co. KGaA, Weinheim
InterScience

and/or angular restraints from ^3J coupling constants.[2–4] Information concerning interatomic angles can also be extracted on basis of the recently introduced projection angle restraints from cross-correlated relaxation.[5–7]

Reasons why these conventional approaches may fail are manifold. The stereogenic centers that are to be related can be highly substituted or remote; conformational equilibria can lead to averaging of the observed parameters. If only one diastereoisomer is available, structures in the conformational space of the configurational isomers can exist that possess very similar distances or angles encoding the same coupling constant. This latter aspect, which occurs for the five-membered lactone **1** (Scheme 1), is the one that will be resolved in the present communication using residual dipolar couplings (RDCs).



Scheme 1. α-Methylene-γ-butyrolactone (**1**) and numbering of its atoms.

RDCs have proven to provide valuable additional geometrical restraints in the structure determination of biomacromolecules[8] and were recently reintroduced for the structure determination of small organic molecules.[9–20] Distance and angle information can be obtained that is complementary to that extracted from NOE and ^3J coupling data. As an added benefit parametrization is not needed. The measurement of RDCs relies on the weak alignment of a solute with respect to an external magnetic field. There is a wide variety of alignment media to induce a convenient degree of anisotropy for water-soluble compounds.[21,22] For organic molecules partial orientation is typically achieved either by liquid crystals[23–25] or by strain-induced alignment in a gel.[19,26–28] Most applications to organic molecules so far have dealt with rigid molecules. In the determination of the relative configuration of the nonrigid lactone **1**, however, different conformations must be taken into account.

We are interested in these compounds because of their biological activity. Knowledge of the relative configuration of the two stereogenic centers is therefore essential. From synthesis[29] the *trans* configuration may be expected in **1**, and the strong NOE contact between the methyl group (on C2) and proton H3 as well as the weak contact between the protons H2 and H3 also seem to indicate a *trans* configuration of the two stereogenic centers. A closer look at the intensities of the NOE crosspeaks, the $^3J_{H2\text{-}H3}$ coupling constants, the long-range coupling constants $^3J_{H3\text{-}C1}$ and $^3J_{H2\text{-}C7}$, and the possible conformations of the two configurational isomers, however, reveals ambiguities: A $^3J_{H2\text{-}H3}$ coupling constant of 6.2 Hz encodes for dihedral angles of 20–30° or 130–140° (depending on parametrization[2–4,30] and ignoring possible conformational averaging). The long-range coupling constants $^3J_{H3\text{-}C1} = 5.1$ Hz and $^3J_{H2\text{-}C7} = 5.3$ Hz are both in the region of dihedral angles of 40° or 130° based on a parametrization for aliphatic hydrocarbons.[31] Note that very few parametrizations for $^3J_{C\text{-}H}$ are available for non-biomolecules,[30] which leads to a high uncertainty in the obtained dihedral angle. We therefore consider $^3J_{C\text{-}H}$ to be less restrictive restraints than $^3J_{H\text{-}H}$ or the NOE. The NOE between Me (on C2) and H3 can be converted into a distance of 3.1 to 3.5 Å (±0.2 Å) after multiplicity and pseudoatom correction (0.4 Å),[32] when the NOE data are extracted from the spectrum at 400-ms mixing time (initial-rate approximation valid) and calibrated with the fixed distance of the two protons of the exocyclic double bond (1.85 Å). The distance H2–H3 cannot be determined owing to very weak peak intensity (low signal-to-noise ratio, therefore large error).

For insight into the different conformers for the two diastereoisomers, we computed equilibrium structures on the density functional theory (DFT) level using the hybrid functional B3LYP[33] as implemented in the program Gaussian 03[34] and employing a basis set of triple-zeta quality[35] augmented by diffuse functions[36] (aug-cc-pVTZ) (Table 1).

Table 1: Distances *r* (in Å) and dihedral angles ∢ (in °) about the C2–C3 bond in the conformers of the two diastereoisomers of **1**.[a]

	cis					*trans*	
Conformer	1a	1b	2a	2b	2c	1a	1b
r(H3,Me)	3.93	3.93	3.60	3.62	3.62	3.00	2.99
∢(H2,H3)	−24.7	−22.1	29.0	27.6	27.0	148.6	150.2
∢(H3,C1)	−151.3	−148.2	−95.0	−96.3	−97.4	23.8	24.9
∢(H2,C7)	92.6	92.7	147.5	150.7	147.6	28.1	29.6

[a] Obtained from DFT calculations using the B3LYP hybrid functional and the aug-cc-pVTZ basis set.

For the *cis* configuration five energetically low-lying conformers were obtained, for the *trans* configuration only two. Some of the structures differ mainly in the conformation about the C3–C7 single bond (orientation of the carboxylic acid group), which is of only minor importance for the present study. The conformers obtained are therefore grouped according to the ring conformations, giving two ring conformers (*cis*-1 with Me pseudo-axial and COOH pseudo-equatorial as well as *cis*-2 with Me pseudo-equatorial and COOH pseudo-axial) for the *cis* configuration and one (*trans*-1 with Me and COOH pseudo-equatorial) for the *trans* configuration. Their geometries were used later on as input structures for the calculations within PALES.[37] Other conformers that are expected to have much higher energy (e.g. structures with *trans* conformation within the carboxylic group) have not been studied further.

The examination of the various conformers reveals that structures in the conformational space of both diastereoisomers exist that are compatible with the experimental data ($^3J_{H2\text{-}H3}$ and NOE) to quite a similar degree (conformers *cis*-2 and *trans*-1). The long-range coupling constants do not fit in any case, which could be indicative of conformational averaging. Therefore it seems not to be possible to assign the relative configuration based on these data alone.

It is known that compounds of this type can be oriented in chiral (enantiomerically pure) polyglutamates[38] in order to obtain RDCs, but this was not considered to be useful in this case as **1** is obtained as a racemic mixture.[29] Therefore achiral alignment media, namely polystyrene (PS) sticks[26] and lamellar phases[39,40] were tested for this molecule, which is soluble both in water and organic solvents. Owing to the limited stability of **1** in DMSO,[41] pentaethylene glycol monododecyl ether ($C_{12}E_5$)/*n*-hexanol/D_2O was chosen as alignment medium, which was prepared as described[39] to

 © 2006 Wiley-VCH Verlag GmbH & Co. KGaA, Weinheim

give a quadrupolar splitting $\Delta_\nu Q(D_2O)$ of 11.6 Hz at the chosen temperature of 293 K.

All NMR measurements were performed using a Bruker Avance NMR spectrometer operating at a proton frequency of 700 MHz and equipped with a cryo-TXI probe. The $^1J_{C\text{-}H}$ and $^1D_{C\text{-}H}$ were measured using heteronuclear single quantum coherences (HSQCs) without decoupling during aquisition as described previously.[12,42] The RDC of the methyl group was converted into a $^1D_{C\text{-}C}$ using the formula given in reference [13] (see also the Supporting Information). These five RDCs are not sufficient to obtain structural information, so homo- and heteronuclear RDCs ($^nD_{H\text{-}H}$ and $^nD_{C\text{-}H}$ $(n>1)$) were measured, with special emphasis placed on the determination of their sign. For $^1D_{C\text{-}H}$ the sign determination is straightforward if the degree of alignment is small enough, as is the case here ($^1J_{C\text{-}H}$ is known to be positive). For $^nD_{C\text{-}H,H\text{-}H}$ signs are more difficult to extract, because the scalar couplings are much smaller. The relative signs of coupling constants are usually obtained from spectra using the E.COSY principle.[43,44] We found HETLOC[45,46] (for $^nJ_{C\text{-}H}/^nD_{C\text{-}H}$) and XLOC[47] (for $^nJ_{H\text{-}H}/^nD_{H\text{-}H}$) most useful, as the displacement vector is spanned by $^1J_{C\text{-}H}/^1D_{C\text{-}H}$, the sign of which is known unequivocally, and the coupling in question ($^nJ_{C\text{-}H}/^nD_{C\text{-}H}$ and $^nJ_{H\text{-}H}/^nD_{H\text{-}H}$, respectively). So even the absolute sign of the coupling can be determined (see Figure 1).

The $^nD_{C\text{-}H,H\text{-}H}$ values for the protons of the methyl group cannot be included owing to averaging of distances and angles by fast rotation. The 14 remaining RDCs with known sign (four $^1D_{C\text{-}H}$, one $^1D_{C\text{-}C}$, two $^3D_{H\text{-}H}$, and seven $^nD_{C\text{-}H}$, $(n>1)$; see the Supporting Information) are used in the program PALES (bestFit module)[37] to determine by means of singular value decomposition[48] those alignment tensors of the various computed structures that give the best agreement between measured and calculated RDCs. Smaller root mean square deviations (RMSD) between experimental and calculated RDCs indicate better agreement between computed and experimentally observed structure. The RMSD values are herein considered to be a measure for the correctness of the input structure and its conformation and configuration. We assume the fit to be good only if the RMSD is below or on the same order of magnitude as the error in the coupling measurement (up to 0.5 Hz in this case). No threshold value of RMSD for a good fit can be given, as this also depends on the number of couplings used, etc. Therefore also the Q values are given in the Supporting Information.

The smallest RMSDs are obtained for the *trans*-configured conformers. The RMSDs for all conformers having *cis* configuration are considerably larger (see Table 2), which suggests that lactone **1** has *trans* configuration. The fit of calculated vs. observed couplings is satisfactory for *trans*-1a and *trans*-1b and remains reasonable when further nine long-range RDCs, the signs of which are not known (RDCs to quarternary carbons, determined using CT-J-HMBC,[49,50] see the Supporting Information), are introduced. (Note that only RMSDs of calculations with the same set of RDCs can be compared.)

Although the fitting procedure gave satisfactory results for the two *trans*-configured conformers, we were led by the scalar long-range C-H couplings ($^3J_{C\text{-}H}$), which indicate conformational averaging (as they do not fit to any of the obtained conformers, see above), to explore if further low-energy ring conformers of **1** exist. Therefore, we computed energetically low-lying conformers of **1** on the level of second-order Møller–Plesset perturbation theory (MP2) with a basis set of double-zeta quality[35] augmented by diffuse functions[36]

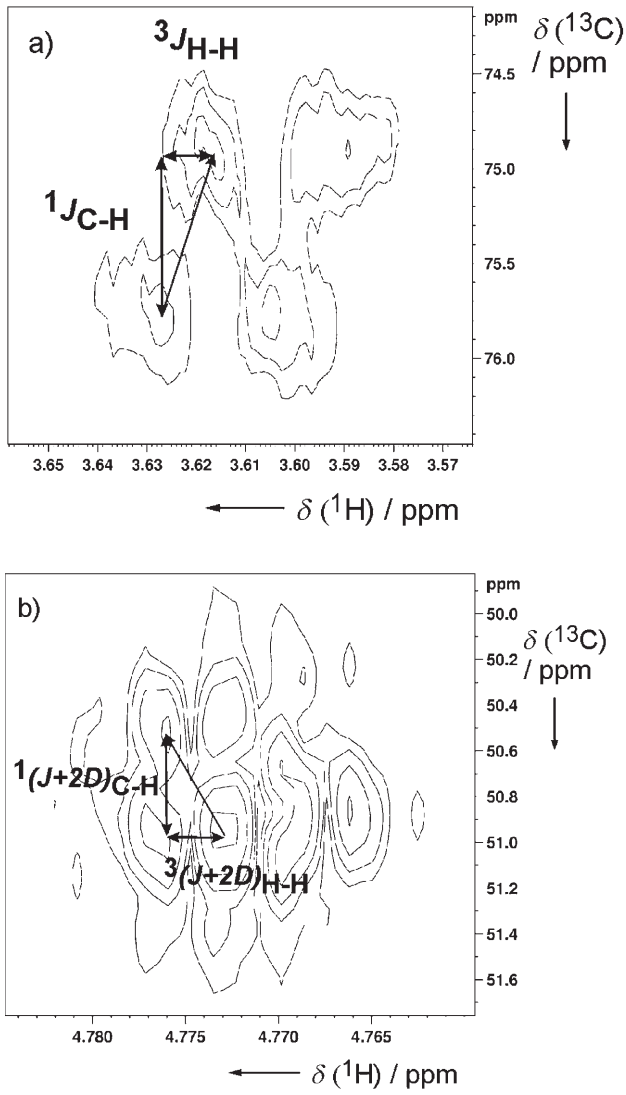


Figure 1. Determination of the sign and size of $^3D_{H2\text{-}H3}$ from XLOC a) crosspeak C2–H3 in isotropic solution $^3J_{H2\text{-}H3}=6.4$ Hz; b) crosspeak C3–H2 in anisotropic solution $^3(J+2D)_{H2\text{-}H3}=-2.7$ Hz (^{1}H NMR frequency: 700 MHz)

Table 2: RMSDs (in Hz) between measured and calculated RDCs for the various conformers of the two diastereoisomers of **1**.[a]

	cis					*trans*	
	1a	1b	2a	2b	2c	1a	1b
$n=14$	1.65	1.59	4.61	4.54	4.41	0.53	0.57
$n=23$	2.08	2.05	3.62	3.57	3.48	0.65	0.70

[a] Obtained on the DFT level with the B3LYP hybrid functional and the aug-cc-pVTZ basis set (n = number of RDCs used).

 © 2006 Wiley-VCH Verlag GmbH & Co. KGaA, Weinheim

(aug-cc-pVDZ). With this method, a second ring conformer for the *trans*-configured lactone (*trans*-2 with Me and COOH pseudo-axial) was obtained with *trans*-2a being less than 2 kJ mol^{-1} higher in energy than *trans*-1a. The corresponding structure on the DFT level is also only slightly higher in energy than the *trans*-1a conformer, but the potential energy hypersurface on the B3LYP hybrid density functional level is extremely shallow so that no equilibrium structure could be localized.

When, however, solvent effects were included within the framework of the polarizable continuum model (PCM) and water was assumed as a solvent, an equilibrium structure corresponding to the *trans*-configured ring conformer 2 was also obtained on the DFT level. Otherwise, no significant conformational changes of the lactone ring are observed upon the transition from gas phase to aqueous solution on the present DFT level.

A conventional analysis with the structures in Table 3 reveals that no conformer satisfies simultaneously all the experimental restraints (NOE and $^3J_{\text{H-H,C-H}}$). The *cis* conformers 2 (a and c) comply with $^3J_{\text{H-H}}$ and NOE, but are at odds with one of the two $^3J_{\text{C-H}}$ values; the *trans* conformers 1 (a and b) fulfill both $^3J_{\text{C-H}}$ and the NOE, but violate the restraints from $^3J_{\text{H-H}}$. For the structures calculated on the MP2 level (see Table 4) the situation is similar.

Table 3: Distances *r* (in Å) and dihedral angles ∢ (in °) in the conformers of the two diastereoisomers of **1**.[a]

Conformer	*r*(H3,Me)	∢(H2,H3)	∢(H3,C1)	∢(H2,C7)	RMSD *n* = 14	RMSD *n* = 23
cis-1a	4.00	−24.3	152.9	92.7	1.83	2.29
cis-1b	3.99	−23.6	151.7	91.6	1.80	2.31
cis-2a	3.63	31.3	94.6	150.4	5.00	3.93
cis-2c	3.63	32.3	93.9	153.6	5.06	3.99
trans-1a	3.06	154.1	27.2	34.5	0.77	0.96
trans-1b	3.07	157.8	30.5	36.4	0.94	1.10
trans-2a	3.00	111.0	16.1	10.4	0.53	0.73
trans-2b	3.00	109.3	17.5	11.0	0.61	0.80

[a] Obtained from DFT calculations using the B3LYP hybrid functional, the 6–31++G(d,p) basis set,[51] and the PCM for inclusion of solvent effects. RMSD (in Hz) from calculations of D_{calc} vs. D_{obs} within PALES.

Using the experimentally measured RDCs, we calculated the alignment tensors for the two sets of additional structures as described above. Again the RMSD is used as a measure for the quality of the fit and the structure (see Table 3 and Table 4). The RMSDs values from Table 3 and Table 4 clearly indicate that **1** is *trans* configured, as the corresponding conformers computed on the B3LYP/6-31++G(d,p) PCM and on the MP2/aug-cc-pVDZ level exhibit the smallest RMSDs, the latter structures being rather similar to the former.

As the next step we also calculated the transition structures for the interconversion of 1a to 2a for each diastereoisomer on the MP2 level (Table 4, *cis*-ts and *trans*-ts, respectively). The barriers computed for the interconversion process are very small for the *trans* diastereoisomer (below 3 kJ mol^{-1}) with the two equilibrium structures having nearly the same energy (to within 1.5 kJ mol^{-1}). To a first approximation, the transition structures should resemble an averaged structure of the two conformers and might therefore be expected to give the smallest RMSD. This is indeed observed if one employs the transition structure *trans*-ts, which provides evidence for averaging resulting from the existence of two almost equally populated minima separated by a small barrier.

Table 4: Distances *r* (in Å) and dihedral angles ∢ (in °) in the conformers of the two diastereoisomers of **1**.[a]

Conformer	*r*(H3,Me)	∢(H2,H3)	∢(H3,C1)	∢(H2,C7)	RMSD *n* = 14	RMSD *n* = 23
cis-1a	3.95	−29.4	156.9	89.6	1.76	2.17
cis-1b	3.95	−29.0	156.1	86.9	1.74	2.24
cis-2a	3.56	34.5	90.4	153.6	4.96	3.92
cis-2c	3.57	34.2	91.0	156.0	4.91	3.88
cis-ts	3.79	5.40	120.1	125.0	2.27	2.06
trans-1a	3.02	155.8	30.5	34.0	0.75	0.82
trans-1b	3.02	157.6	31.4	35.2	0.84	0.91
trans-2a	2.96	105.2	21.5	18.2	0.64	0.86
trans-2b	2.96	103.0	23.2	19.2	0.82	1.00
trans-ts	2.93	125.6	0.1	3.3	0.51	0.48

[a] Calculated on the MP2 level using the aug-cc-pVDZ basis set. RMSD (in Hz) from calculations of D_{calc} vs. D_{obs} within PALES.

We note in passing that a more rigorous numerical treatment would require the solution of the one- or multi-dimensional Schrödinger equation for the tunneling dynamics and the determination of the motional-state-dependent average dipolar couplings between the nuclei followed by thermal averaging of the various levels.

Another way of accounting for an ensemble of conformers is to fit the RDC data to an ensemble of structures for each of which proper averaging would be required (see for instance reference [52] for a discussion of numerical approaches). The more approximate averaging of the contributions of equilibrium structures employed herein (assuming equal population) was performed using the tcl script dcEnsemble.tcl available in NMRPIPE.[53] This leads to an RMSD of 0.47, which is almost equal to that obtained using the transition structure *trans*-ts only. This value is, however, of little significance as data from only one alignment medium were used. Fitting of RDC data to two conformers reduces the degrees of freedom (for SVD) by a factor of two, hampering therefore a direct comparison. Further research towards the determination of the conformation of **1** using different alignment media is under way.

An analogous analysis based on $^3J_{\text{H-H,C-H}}$ and NOE data alone, in contrast, is not conclusive: for both diastereomers $^3J_{\text{C-H,H-H}}$ and NOE for an ensemble of structures (equally weighted or weighted according to their energy differences, see Table 5) are in line with the experimental data. The values of $^3J_{\text{C-H}}$ given in Table 5 are, however, coarse estimates because of the lack of a suitable parametrization.

The importance of measuring more than six RDCs and the determination of the sign for $^3D_{\text{H2-H3}}$ becomes evident from Table 6. When using only the five $^1D_{\text{C-H}}$ and $^3D_{\text{H2-H3}}$ values, the size of which can be easily determined by 1D ^{1}H NMR spectroscopy, without knowing its sign, it is not possible to assign the configuration. One would possibly even be led to a

 © 2006 Wiley-VCH Verlag GmbH & Co. KGaA, Weinheim

Table 5: Calculated coupling constants (from Karplus-type relationships[30,31]) for the conformers 1a and 2a and ensembles of conformers.[a]

Conformer	∢(H2,H3)	∢(H3,C1)	∢(H2,C7)	$^3J_{H2\text{-}H3,\,pred}$ [Hz][30]	$^3J_{C1\text{-}H3,pred}$ [Hz][31]	$^3J_{C7\text{-}H2,pred}$ [Hz][31]
cis-1a	−29.4	156.9	89.6	7.24	8	0–1
cis-2a	34.5	90.4	153.6	5.66	0–1	8
cis-ts	5.40	120.1	125.0	7.97	3	3
ensemble(1:1)				6.45	4–5	4–5
ensemble(4:3)				6.56	5	5
trans-1a	155.8	30.5	34.0	9.67	6	6
trans-2a	105.2	21.5	18.2	2.08	7	7
trans-ts	125.6	0.1	3.3	3.88	8	8
ensemble(1:1)				5.87	6–7	6–7
ensemble(5:3)				6.82	5	5

[a] Ensembles of conformers (1a and 1b, equally weighted or weighted according to their energy difference) for the both diastereoisomers of **1** (MP2 structures used).

Table 6: RMSDs (in Hz) between measured and calculated RDCs for the various conformers of the two diastereoisomers of **1** for six RDCs with correct or wrong sign for $D_{H2\text{-}H3}$.[a]

	cis					*trans*				
	1a	1b	2a	2c	ts	1a	1b	2a	2b	ts
correct	0.22	0.25	3.14	3.10	0.41	0.13	0.19	0.31	0.37	0.17
wrong	0.54	0.51	1.56	1.51	0.01	1.36	1.36	1.30	1.34	1.01

[a] Obtained on the MP2 level using the aug-cc-pVDZ basis set.

wrong conclusion. $^3D_{H2\text{-}H3}$ is one of the crucial distance and angular restraints for the determination of the relative configuration in **1**. A wrong sign for this coupling leads to a significantly smaller RMSD for *cis*-ts than the RMSD obtained for the *trans* conformer *trans*-1a and *trans*-ts using the correct sign (0.01 for *cis*-ts with the wrong sign vs. 0.13 for *trans*-1a with the correct sign; see Table 6). It is therefore of particular importance to choose a method that yields not only the size but also the sign of the coupling constant.

We have demonstrated that RDCs carry important information complementary to NOE data and *J* coupling constants. For molecules like the five-membered lactone **1**, in which the conformational flexibility impedes conventional structure determination, it is possible to assign the relative configuration of the stereogenic centers (in the present case to be *trans*) with the help of RDCs. An extension of this methodology to more flexible molecules will be one of the further topics of our research.

Received: September 13, 2005
Revised: March 28, 2006
Published online: June 8, 2006

Keywords: alignment media · configuration determination · lactones · NMR spectroscopy · residual dipolar couplings

[1] D. Neuhaus, M. P. Williamson, *The Nuclear Overhauser Effect in Structural and Conformational Anaylsis*, 2nd ed., Wiley-VCH, New York, **2000**.
[2] M. Karplus, *J. Chem. Phys.* **1959**, *30*, 11–15.
[3] E. Díez, J. San-Fabián, J. Guilleme, C. Altona, L. A. Donders, *Mol. Phys.* **1989**, *68*, 49–63.
[4] C. A. G. Haasnoot, F. A. A. M. De Leeuw, C. Altona, *Tetrahedron* **1980**, *36*, 2783–2792.
[5] B. Reif, M. Hennig, C. Griesinger, *Science* **1997**, *276*, 1230–1233.
[6] S. Ravindranathan, X. Feng, T. Karlsson, G. Widmalm, M. H. Levitt, *J. Am. Chem. Soc.* **2000**, *122*, 1102–1115.
[7] B. Reif, H. Steinhagen, B. Junker, M. Reggelin, C. Griesinger, *Angew. Chem.* **1998**, *110*, 2006–2007; *Angew. Chem. Int. Ed.* **1998**, *37*, 1903–1906.
[8] J. H. Prestegard, C. M. Bougault, A. I. Kishore, *Chem. Rev.* **2004**, *104*, 3519–3540, and references therein.
[9] A. Saupe, *Angew. Chem.* **1968**, *80*, 99–115; *Angew. Chem. Int. Ed. Engl.* **1968**, *7*, 97–112.
[10] J. W. Emsley, J. C. Lindon, *NMR Spectroscopy Using Liquid Crystal Solvents*, Pergamon, Oxford, **1975**.
[11] A. Mangoni, V. Esposito, A. Randazzo, *Chem. Commun.* **2003**, 154–155.
[12] C. M. Thiele, S. Berger, *Org. Lett.* **2003**, *5*, 705–708.
[13] L. Verdier, P. Sakhaii, M. Zweckstetter, C. Griesinger, *J. Magn. Reson.* **2003**, *163*, 353–359.
[14] C. Aroulanda, V. Boucard, F. Guibé, J. Courtieu, D. Merlet, *Chem. Eur. J.* **2003**, *9*, 4536–4539.
[15] J. Yan, A. D. Kline, H. Mo, M. J. Shapiro, E. R. Zartler, *J. Org. Chem.* **2003**, *68*, 1786–1795.
[16] C. M. Thiele, *J. Org. Chem.* **2004**, *69*, 7403–7413.
[17] J. Yan, F. Delaglio, A. Kaerner, A. D. Kline, H. Mo, M. J. Shapiro, T. A. Smitka, G. A. Stephenson, E. R. Zartler, *J. Am. Chem. Soc.* **2004**, *126*, 5008–5017.
[18] T. N. Pham, S. L. Hinchley, D. W. H. Rankin, T. Liptaj, D. Uhrín, *J. Am. Chem. Soc.* **2004**, *126*, 13100–13110.
[19] J. C. Freudenberger, P. Spiteller, R. Bauer, H. Kessler, B. Luy, *J. Am. Chem. Soc.* **2004**, *126*, 14690–14691.
[20] R. M. Gschwind, *Angew. Chem.* **2005**, *117*, 4744–4746; *Angew. Chem. Int. Ed.* **2005**, *44*, 4666–4668.
[21] J. H. Prestegard, A. I. Kishore, *Curr. Opin. Chem. Biol.* **2001**, *5*, 584–590, and references therein.
[22] K. Kobzar, H. Kessler, B. Luy, *Angew. Chem.* **2005**, *117*, 3205–3207; *Angew. Chem. Int. Ed.* **2005**, *44*, 3145–3147.
[23] M. Sarfati, P. Lesot, D. Merlet, J. Courtieu, *Chem. Commun.* **2000**, 2069–2081, and references therein.
[24] C. Aroulanda, M. Sarfati, J. Courtieu, P. Lesot, *Enantiomer* **2001**, *6*, 281–287.
[25] B. Bendiak, *J. Am. Chem. Soc.* **2002**, *124*, 14862–14863.
[26] B. Luy, K. Kobzar, H. Kessler, *Angew. Chem.* **2004**, *116*, 1112–1116; *Angew. Chem. Int. Ed.* **2004**, *43*, 1092–1094.
[27] P. Haberz, J. Farjon, C. Griesinger, *Angew. Chem.* **2005**, *117*, 431–433; *Angew. Chem. Int. Ed.* **2005**, *44*, 427–429.
[28] J. C. Freudenberger, S. Knörr, K. Kobzar, D. Heckmann, T. Paululat, H. Kessler, B. Luy, *Angew. Chem.* **2005**, *117*, 427–430; *Angew. Chem. Int. Ed.* **2005**, *44*, 423–426.
[29] M. Biel, A. Kretsovali, E. Karatzali, J. Papamatheakis, A. Giannis, *Angew. Chem.* **2004**, *116*, 4065–4067; *Angew. Chem. Int. Ed.* **2004**, *43*, 3974–3976, zit. Lit.
[30] C. Altona in *Encyclopedia of NMR* (Eds.: D. M. Grant, R. Morris), Wiley, New York, **1996**, pp. 4909–4923.
[31] R. Aydin, H. Günther, *Magn. Reson. Chem.* **1990**, *28*, 448–457.

 © 2006 Wiley-VCH Verlag GmbH & Co. KGaA, Weinheim

[32] C. M. Fletcher, D. N. M. Jones, R. Diamond, D. Neuhaus, *J. Biomol. NMR* **1996**, *8*, 292 – 310.
[33] P. J. Stephens, F. J. Devlin, M. J. Frisch, C. F. Chabalowski, *J. Phys. Chem.* **1994**, *98*, 11 623 – 11 627.
[34] Gaussian 03, Revision C.02, M. J. Frisch et al., see the Supporting Information.
[35] R. A. Kendall, T. H. Dunning, R. J. Harrison, *J. Chem. Phys.* **1992**, *96*, 6796 – 6806.
[36] T. H. Dunning, *J. Chem. Phys.* **1989**, *90*, 1007 – 1023.
[37] M. Zweckstetter, A. Bax, *J. Am. Chem. Soc.* **2000**, *122*, 3791 – 3792.
[38] P. Lesot, Y. Gounelle, D. Merlet, A. Loewenstein, J. Courtieu, *J. Chem. Phys.* **1995**, *99*, 14 871 – 14 875.
[39] M. Rückert, G. Otting, *J. Am. Chem. Soc.* **2000**, *122*, 7793 – 7797.
[40] V. V. Klochkov, A. V. Klochkov, C. M. Thiele, S. Berger, *J. Magn. Reson.* **2006**, *179*, 58 – 63.
[41] J. Fischer, M. Biel, C. M. Thiele, A. Giannis, unpublished results.
[42] C. M. Thiele, *Angew. Chem.* **2005**, *117*, 2847 – 2850; *Angew. Chem. Int. Ed.* **2005**, *44*, 2787 – 2790.
[43] C. Griesinger, O. W. Sørensen, R. R. Ernst, *J. Magn. Reson.* **1987**, *75*, 474 – 492, and references therein.
[44] H. Neubauer, J. Meiler, W. Peti, C. Griesinger, *Helv. Chim. Acta* **2001**, *84*, 243 – 258.
[45] M. Kurz, P. Schmieder, H. Kessler, *Angew. Chem.* **1991**, *103*, 1341 – 1342; *Angew. Chem. Int. Ed. Engl.* **1991**, *30*, 1329 – 1331.
[46] D. Uhrin, G. Batta, V. J. Hubry, P. N. Barlow, K. E. Köver, *J. Magn. Reson.* **1998**, *130*, 155 – 161.
[47] A. Meissner, O. W. Sørensen, *Magn. Reson. Chem.* **2001**, *39*, 49 – 51.
[48] J. A. Losonczi, M. Andrec, M. W. F. Fischer, J. H. Prestegard, *J. Magn. Reson.* **1999**, *138*, 334 – 342.
[49] K. Furihata, H. Seto, *Tetrahedron Lett.* **1999**, *40*, 6271 – 6275.
[50] Sign determination: J. Yan, A. D. Kline, H. Mo, M. J. Shapiro, E. R. Zartler, *Magn. Reson. Chem.* **2004**, *42*, 962 – 967.
[51] W. J. Hehre, R. Ditchfield, J. A. Pople, *J. Chem. Phys.* **1972**, *56*, 2257 – 2261; T. Clark, J. Chandrasekhar, G. W. Spitznagel, P. von R. Schleyer, *J. Comput. Chem.* **1983**, *4*, 294 – 301; P. C. Hariharan, J. A. Pople, *Theor. Chim. Acta* **1973**, *28*, 213 – 222.
[52] E. E. Burnell, C. A. de Lange, *NMR of Ordered Liquids*, Kluwer, Dordrecht, **2003**.
[53] F. Delaglio, S. Grzesiek, G. Vuister, G. Zhu, J. Pfeifer, A. Bax, *J. Biomol. NMR* **1995**, *6*, 277 – 293.

 © 2006 Wiley-VCH Verlag GmbH & Co. KGaA, Weinheim

Theoretical Chemistry

DOI: 10.1002/anie.200600448

Seemingly Simple Stereoelectronic Effects in Alkane Isomers and the Implications for Kohn–Sham Density Functional Theory**

*Stefan Grimme**

The concept of stereoelectronic (SE) effects is widely applied especially in organic chemistry.[1] Substituents are typically described as electron-density-donating or -withdrawing or responsible for sterically interacting with, for example, reagents. The rational application of SE design rules is of utmost importance in synthetic chemistry where target structures are often kinetically or thermodynamically favored. Important SE effects can be introduced by alkylation (methylation in the following discussion for simplicity) of strategic positions in a molecule. The resulting energetic changes can be qualitatively separated into so-called electronic (bonding) and nonbonding (through-space, i.e., attractive van der Waals (vdW) and electrostatic, and repulsive Pauli) interactions. While a meaningful definition and separation of these individual terms is quite difficult at a rigorous quantum mechanical level, it is generally believed that modern quantum chemical methods are at least able to describe the overall energetic effects quantitatively. It is shown in this Communication that this does not hold for the widely used Kohn–Sham density functional theory (DFT)[2] with all state-of-the-art density functionals; this approach does not provide even a qualitatively correct picture for an important class of chemical problems.

The problem has become evident in recent years since larger molecular systems have been studied more routinely. In general it appears when a first-row atom or group X (X = B, C, N) is successively alkylated. Gilbert[3] found increasing errors of the B3LYP functional (up to 20 kcal mol^{-1}) for the dissociation reaction (1) when R = H is replaced by CH_3.

$$R_3N{-}BR_3 \rightarrow NR_3 + BR_3 \qquad (1)$$

Similar results were reported later[4,5] for the C–C bond dissociation reaction (2) and [2+2] cycloadditions and CH_2-

$$R_3C{-}CR_3 \rightarrow R_3C^{\bullet} + {}^{\bullet}CR_3 \qquad (2)$$

[*] Prof. Dr. S. Grimme
Theoretische Organische Chemie
Organisch-Chemisches Institut der Universität Münster
Corrensstrasse 40, 48149 Münster (Germany)
Fax: (+49) 251-833-6515
E-mail: grimmes@uni-muenster.de

[**] This work was supported by the Deutsche Forschungsgemeinschaft in the framework of the SFB 424 ("Molekulare Orientierung als Funktionskriterium in chemischen Systemen"). The author thanks C. Mück-Lichtenfeld for technical assistance and helpful discussions.

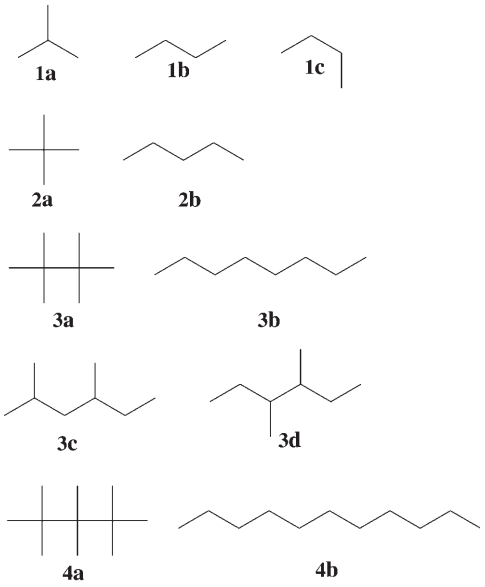
 WILEY InterScience DISCOVER SOMETHING GREAT © 2006 Wiley-VCH Verlag GmbH & Co. KGaA, Weinheim

alkene insertions with substrates of various sizes[5] and for radical stabilization energies.[6] Related to the problem are several observations[7–9] of increasing errors for DFT/B3LYP-derived enthalpies of formation with increasing size of the molecules (hydrocarbons in particular, for example, 0.7 kcal mol^{-1} per CH_2 group[8,9] in *n*-alkanes and 25 kcal mol^{-1} for adamantane[7]).

The origin of these very unusual errors has been subject to speculations or special ad hoc explanations that range from "self-interaction error" (for Eq. (2)) to "problems with dative C–C bonds in general,"[3,5] to the failure of most density functionals (DFs) to describe the attractive long-range vdW interaction (cf. Ref. [10] and references therein). This latter consideration is quite obvious as increasing alkylation decreases the average nonbonding distances, which, along with with a too repulsive vdW potential, would systematically destabilize the more substituted species (i.e., the left sides in Equations (1) and (2)). This was also our first working hypotheses because these intramolecular vdW effects can be quite large even in medium-sized molecules.[11] However, as will be shown here, the failure of common DFs to account for vdW interactions plays only a secondary role; rather, the fact that all semi-local(hybrid) DFs neglect medium-range electron correlation (EC) effects is of general relevance. It seems important to stress at this point that we do not question the usefulness of current DFT in general. However, we think that especially because DFT (and B3LYP in particular) is being used more and more as a computational tool by nonexperts, it is necessary to reveal the strengths and weaknesses of the theoretical method. We furthermore offer a possible solution to the problem within the framework of DFT that incorporates parts of conventional wave function methods (B2PLYP functional[12]).

The examples we use in our analysis are not dissociation reactions (which have their own special problems) but seemingly simple isomerizations of branched to linear alkanes. In all these reactions, the number of C–H and C–C bonds as well as the formal hybridization states remain the same. The typical errors for the calculated isomerization energy branched→linear (ΔE) are already apparent for butane and increase with the size of the system. We consider in detail two isomers (the most branched isomer is labeled **a** and the linear **b**) of butane (**1**), pentane (**2**), octane (**3**), and undecane (**4**) (Scheme 1). To separate the SE effect into electronic and steric parts, the transition state for the *gauche–gauche* rotation of *n*-butane (**1c**) (in which the steric $CH_3\cdots CH_3$ interaction is similar to that in isomers **3a** and **4a**) and of two different hexanes (isomers of octane, **3c** and **3d**) were investigated.

In order to demonstrate that we are not discussing tiny and probably unimportant effects but a problem of general importance, the calculated and experimental isomerization energies for octane are shown in Table 1. Beside traditional wave function methods that are based on second-order Møller–Plesset perturbation theory (MP2 or its improved version SCS-MP2[13]) all types of modern DFs (pure GGA: BLYP[14] and PBE;[15] hybrid GGA: B3LYP[16] and BHLYP;[17] meta-hybrid: TPSSh;[18] GGA with empirical vdW corrections: D-BLYP[10]) were employed.[19]



Scheme 1.

Table 1: Isomerization energies for octane.[a]

Method	ΔE(**3b**–**3a**) [kcal mol^{-1}]
MP2	4.6 (2.7)
exptl	**1.9** ± **0.5**
SCS-MP2	1.4 (0.5)
B2PLYP	−3.5 (−5.4)
PBE	−5.5 (−7.4)
D-BLYP	−5.5 (−7.4)
TPSSh	−6.3 (−8.2)
BHLYP	−7.2 (−9.1)
B3LYP	−8.4 (−10.3)
BLYP	−9.9 (−11.8)
HF	−11.5 (−13.4)

[a] Errors with respect to experimental results in parentheses. For reference to the experimental value see the Method Section; the theoretical data refer to the cQZV3P//MP2/TZV(d,p) level.

A brief inspection of these data reveals a disastrous situation for DFT: none of the functionals can describe even the correct energetic order of the isomers (branched lower in energy than linear). The errors are surprisingly large, ranging from −7.4 (PBE) to −11.8 kcal mol^{-1} (BLYP). Errors of this magnitude are unacceptable and disqualify DFT application in polymer science or in investigations of, for example, alkane combustion, where branching is an important aspect. From the theoretical point of view it is further intriguing that the DFT results are only slightly better than calculations at the uncorrelated Hartree–Fock (HF) level (error of −13.4 kcal mol^{-1}). This means that the main SE effect (which results completely from EC) is not described correctly by any of the DFs, although it is generally believed that at least the main EC effects are incorporated in current DFs. The finding that EC is the decisive factor for the relative stability of alkane isomers is also not well-known in the literature; quite recently a (wrong) explanation of the effect on the basis of orbital considerations was published[20] (for a good review on the

 © 2006 Wiley-VCH Verlag GmbH & Co. KGaA, Weinheim

topic including many older works and a quite new concept see Ref. [21]). It seems also noteworthy that the usual explanation of these SE effects as resulting from hyperconjugation can be ruled out because this is mostly included already at the HF level (by superposition of $A^{\cdot\cdot}B$, A^+B^-, A^-B^+ valence bond structures for a covalent AB bond).

The correlated wave function methods have only minor problems with this system (MP2 "overshoots" as usual), and SCS-MP2 in particular yields here (and for other alkanes as well) results accurate to within experimental error. Also surprising is the finding that the portion of "exact" exchange in a hybrid functional (e.g. 20 and 50% in B3LYP and BHLYP, respectively), which usually influences the results considerably, has almost no effect on ΔE. So-called meta functionals involving derivatives of the occupied orbitals (kinetic energy density) also fail completely; in other words, TPSSh is not better than its predecessor PBE.

Table 2 shows results for the other systems investigated; we have included only PBE, B3LYP, and B2PLYP and note in passing that other DFs yield similar results. In contrast to **1**–**3**, the linear isomer of undecane is the most stable as a result of many very unfavorable short contacts between methyl groups. In general the methods behave similarly, as in the case of octane. The errors increase with the size of the system, for example, 1.0, 1.5, 10.3, and about 17 kcal mol^{-1} for B3LYP in the series **1** to **4**. Thus, the error seems to accumulate; this was also found in the studies of dissociation reactions.[3,5] In the calculations of octane, the HF errors are larger than with B3LYP and the PBE errors are smaller.

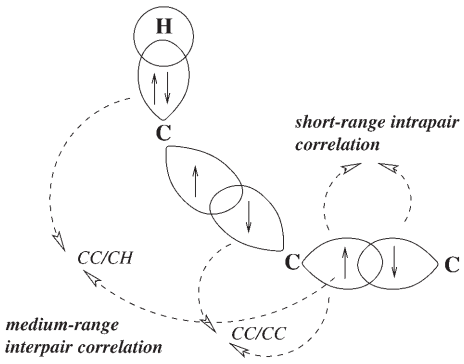
Table 2: Calculated relative energies ΔE of alkane isomers.[a]

Isomer	ΔE [kcal mol^{-1}]						
	exptl	SCS-MP2	MP2	HF	B3LYP	PBE	B2PLYP
			butane				
1b	1.5	1.5	1.8	0.3	0.5	0.8	1.0
1c[b]	5.5	5.7	5.7	6.4	5.7	5.5	5.7
			pentane				
2b	2.8	3.0	3.6	0.1	1.3	1.6	2.1
			octane				
3b	1.9	1.4	4.6	−11.5	−8.4	−5.5	−3.5
3c	1.0	0.7	1.6	−3.0	−2.4	−1.7	−0.9
3d	2.0	2.1	3.8	−4.8	−3.5	−2.1	−0.8
			undecane				
4b	–	−9.4	−3.4	−34.4	−26.8	−21.0	−17.9

[a] With respect to the branched isomer **a**; cQZV3P//MP2/TZVP level. [b] Transition state for C2–C3 rotation (*gauche–gauche*) with respect to *n*-butane. For the reference value see Ref. [22].

For a further analysis of the problem it is important to answer the question how large the "steric" contributions to ΔE are. It is not rigorously possible to separate these effects (from a formal point of view the "steric" part is also of electronic origin), but there is strong evidence that the vdW aspect (and the usual DFT problems for that) is not a major factor: 1) The effect on ΔE when diffuse basis functions are added (they are usually necessary to accurately describe vdW interactions) is small at the SCS-MP2 level (0.5 kcal mol^{-1} difference for ΔE when the aug-cc-pVTZ is used instead of the cc-pVTZ AO basis); 2) The empirical vdW correction[13] works in the right direction (stabilizing **a** with respect to **b**), but the BLYP error is reduced by less than 40% for **3** (see Table 1); 3) The *gauche–gauche* transition state for the rotation around C2–C3 in *n*-butane that is sterically very similar to the situation in, for example, **3a** (shortest nonbonding C–C distances of about 3.2 Å compared to 2.9 Å in **1c**) is described reasonably well by all DFs; 4) For the energy difference between **3c** and **3d**, which have the same type of branching but branching points at different positions, the DFT errors are opposite to what would be expected when the vdW interaction is dominant (i.e., **3d** is incorrectly lower in energy than **3c**).

Clearly the reason for the failure to describe the SE alkylation effect lies primarily in the electronic (through-bond) part. As already emphasized, it is entirely due to electron correlation (EC) and our analysis is thus based on a rigorous partitioning of the EC energy. Owing to the localized electronic structure of alkanes this is possible by considering the $N_o(N_o+1)/2$ pair correlation energies $[\varepsilon]_{ij}$ (N_o is the number of occupied orbitals) that sum up to the total correlation energy. When localized molecular orbitals (LMO) are used as the basis in the MP2 or SCS-MP2 treatment, the correlation energies $[\varepsilon]_{ij}$ can be assigned to different regions in space (electron pairs) and correlation types (inter- or intrapair correlations, see Scheme 2, where the dashed arrows indicate "electron collisions and correlations"). Note that the LMO treatment does not change the total correlation energy.



Scheme 2.

The partitioned pair correlation energies and contributions to the isomerization energy of pentane and octane are listed in Table 3. In Figure 1 contributions to ΔE are partitioned according to the estimated distance between the correlating electrons.

In perusing Table 3, one finds that the intrapair correlation (last column) contributes almost nothing to ΔE. These tiny differences between the quite large correlation energy values (< 0.1%) strongly support the common picture of the simple electronic structure (transferrable, localized σ bonds) of alkanes. According to further analysis, the EC effect on the ΔE values results entirely from interpair correlations between orbitals of the same type (CC/CC and CH/CH), which favor the branched form, compared to CC/CH correlations, which lower the energy of the linear isomer. This can be simply

 © 2006 Wiley-VCH Verlag GmbH & Co. KGaA, Weinheim

Table 3: Pair correlation energies (in $-m\,E_h$) at the SCS-MP2/TZV(d,p) level using localized CC and CH orbitals.[a]

Isomer	Sum of pair correlation energy				
	CC/CC	CH/CH	CH/CC	Total	CC + CH (intrapair)
2a	128	460	183	771	449.3
2b	153 (15.7)	482 (13.8)	142 (−25.7)	777 (3.8)	448.8
3a	232	679	308	1219	699.6
3b	289 (35.8)	728 (30.7)	224 (−52.7)	1241 (13.8)	699.7

[a] Values in parentheses are the correlation energy contributions to ΔE (in kcal mol^{-1}). The ΔE values at the HF/TZV(d,p) level are 0.5 and −10.6 kcal mol^{-1} for pentane and octane, respectively, which yields together with the values in the fifth column total SCS-MP2 ΔE values of 4.3 and 3.2 kcal mol^{-1}, respectively.

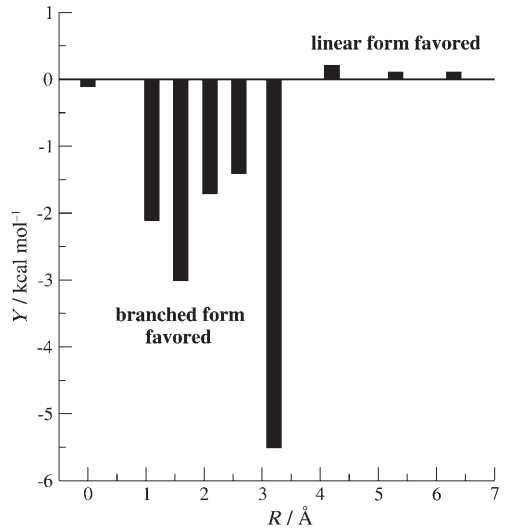


Figure 1. Contribution of the pair correlation energy to the isomerization energy of octane as a function of the distance R between the center-of-charge of the respective pair of LMOs.

rationalized by the sheer number of (atomic) 1,3-interactions in the two isomers (CC: 6 (**2a**) vs. 3 (**2b**), HH: 12 (**2a**) vs. 9 (**2b**), CH: 12 (**2a**) vs. 18 (**2b**)). Figure 1 shows that the correlations that determine ΔE occur on a medium-range length scale (1.5–3.5 Å), and one may indeed classify these as correlating 1,3-interactions. This important result can be considered as the quantum mechanical basis for the recently proposed 1,3-interaction model for alkane stabilities.[21] Since we have already pointed out the minor importance of vdW effects, it comes as no surprise that the long-range correlations actually favor the linear form (see Figure 1).

These findings also very clearly lead to an explanation for the failure of current DF: the exchange functionals introduce a localized exchange-hole around each electron that mimics effects of static EC (the intrapair terms), but this contributes nothing to ΔE. Because the correlation functionals are also too local, the 1,3-correlations and thus the entire SE effect is more or less absent. The hybrid functionals also do not work because the exchange hole is not delocalized in saturated systems. Significantly better (but still qualitatively wrong) results for all alkanes are obtained from the new B2PLYP functional,[12] which includes (beside standard exchange and correlation components) perturbative (orbital-dependent) terms similar to MP2 or SCS-MP2.

In summary, it has been shown that the seemingly simple stereoelectronic alkylation effect (and this also holds for substitutions at other main-group elements) is entirely due to electron correlation and that vdW-type interactions (the "stereo" part) are only moderately (less than 30 % for about ten close-lying carbon atoms) responsible. However, the intramolecular vdW interaction should not be ignored as it is an essential part of the internal energy and its inclusion is absolutely necessary to obtain reasonable agreement with experiment.[11] For the explanation of the serious failure of all common semilocal density functionals, however, the vdW problem is only of secondary importance. Rather, medium-range but nonlocal electron correlations originating from different (perfectly) localized σ orbitals contribute almost exclusively to the energy difference between linear and branched forms. The different correlation energies are mainly determined by the spatial distribution of the different bond types in the isomers. This explains the success of simple additivity schemes (group, bond, or 1,3-interaction increments) and furthermore holds for most of the DFT problems mentioned in the introduction.[23]

This, however, is bad news for standard Kohn–Sham DFT as it seems difficult to obtain the necessary information about electron pairs and their interactions from simple considerations of the electron density alone. Of course we are not questioning the exactness and usefulness of the Hohenberg–Kohn theorems or the Kohn–Sham approach in general, but just the human ability to find accurate density functionals in practice. The better results with the new virtual orbital-dependent B2PLYP functional that includes in part the necessary terms shows, however, the way to go in the future. In this sense the reaction **3a**→**3b**, for which no current DF provides even the right sign for ΔE,[24] is suggested as a mandatory benchmark for new density functionals.

Methods

The (SCS-)MP2 and DFT calculations were performed with slightly modified versions of the Turbomole suite of programs.[25]. As the AO basis, the split-valence (SV), triple-zeta (TZV), or quadruple-zeta (QZV) sets of Ahlrichs et al. [26] or the correlation-consistent sets of Dunning[27] (cc-pVXZ, X = D, T, Q) were employed. In the (SCS-)MP2 and B2PLYP treatments the RI approximation for the two-electron integrals was used,[28] and all electrons were correlated. The geometries were optimized at the MP2/TZV(d,p) level, and single-point calculations on these structures were performed with a cQZV3P AO basis set which includes (3d2f/2pd) polarization functions, (2pd) core-polarization/correlation functions, and an additional single diffuse s function ($\alpha = 0.05$) on carbon. This basis set provides results to within ±0.1 kcal mol^{-1} of the basis set limit for ΔE (as estimated from aug-cc-pVXZ (X = T, Q) treatments for **3**) and furthermore yields quite small intramolecular basis set superposition errors. The effect of choosing geometries optimized at a different level than MP2 in the single-point calculations (e.g. DFT) was estimated to be on the order of ±0.2 kcal mol^{-1} for ΔE in the case of octane. The experimental ΔE values were derived from experimental standard enthalpies of formation[29] by correcting for vibrational zero-point energies, internal $H(0)-H(298)$ contributions, and corrections due to

 © 2006 Wiley-VCH Verlag GmbH & Co. KGaA, Weinheim

thermal population of higher-lying conformers. The harmonic vibrational frequency calculations were performed at the (unscaled) DFT-PBE/SV(d,p) level; the MM3(1996)[30] force field was used for the conformational searches. Since for undecane no experimental data are available, the accurate SCS-MP2 values were used as reference. The experimental enthalpies have quoted error bars of $\pm(0.2–0.4)$ kcal mol^{-1}, which yields an estimate for the uncertainty of the ΔE(exptl) values used of about ± 0.5 kcal mol^{-1}.

Received: February 2, 2006
Revised: March 21, 2006
Published online: May 31, 2006

Keywords: ab initio calculations · alkanes · density functional calculations · isomerization · stereoelectronic effects

[1] "Stereoelectronic Effects in Organic Chemistry": P. Delongchamps in *Organic Chemistry Series*, *Vol. 1* (Ed.: J. E. Baldwin), Pergamon, Oxford, **1983**, pp. 5–20; A. J. Kirby, *The Anomeric Effect and Related Stereoelectronic Effects at Oxygen*, Springer, New York, **1983**; *Interactions in Molecules: Electronic and Steric Effects* (Ed.: S. D. Peyerimhoff), Wiley-VCH/DFG, Weinheim, **2003**.
[2] R. G. Parr, W. Yang, *Density-Functional Theory of Atoms and Molecules*, Oxford University Press, Oxford, **1989**; W. Koch, M. C. Holthausen, *A Chemist's Guide to Density Functional Theory*, Wiley-VCH, New York, **2001**.
[3] T. M. Gilbert, *J. Phys. Chem. A* **2004**, *108*, 2550–2554.
[4] X.-Q. Yao, X.-J. Hou, H. Jiao, H.-W. Xiang, Y.-W. Li, *J. Phys. Chem. A* **2003**, *107*, 9991–9996.
[5] C. E. Check, T. M. Gilbert, *J. Org. Chem.* **2005**, *70*, 9828–9834.
[6] E. I. Izgorodina, M. L. Coote, L. Radom, *J. Phys. Chem. A* **2005**, *109*, 7558–7566.
[7] S. Grimme, *J. Phys. Chem. A* **2005**, *109*, 3067–3077.
[8] P. C. Redfern, P. Zapol, L. A. Curtiss, K. Raghavachari, *J. Phys. Chem. A* **2000**, *104*, 5850–5854.
[9] L. A. Curtiss, K. Raghavachari, P. C. Redfern, J. A. Pople, *J. Chem. Phys.* **2000**, *112*, 7374–7383.
[10] S. Grimme, *J. Comput. Chem.* **2004**, *25*, 1463–1476.
[11] S. Grimme, C. Diedrich, M. Korth, *Angew. Chem.* **2006**, *118*, 641–645; *Angew. Chem. Int. Ed.* **2006**, *45*, 625–629.
[12] S. Grimme, *J. Chem. Phys.* **2006**, *124*, 034108–034116.
[13] S. Grimme, *J. Chem. Phys.* **2003**, *118*, 9095–9102.
[14] A. D. Becke, *Phys. Rev. A* **1988**, *38*, 3098–3100; C. Lee, W. Yang, R. G. Parr, *Phys. Rev. B* **1988**, *37*, 785.
[15] J. P. Perdew, K. Burke, M. Ernzerhof, *Phys. Rev. Lett.* **1996**, *77*, 3865–3868.
[16] A. D. Becke, *J. Chem. Phys.* **1993**, *98*, 5648–5652; P. J. Stephens, F. J. Devlin, C. F. Chablowski, M. J. Frisch, *J. Phys. Chem.* **1994**, *98*, 11623–11627.
[17] A. D. Becke, *J. Chem. Phys.* **1993**, *98*, 1372.
[18] V. N. Staroverov, G. E. Scuseria, J. Tao, J. P. Perdew, *J. Chem. Phys.* **2003**, *119*, 12129.
[19] Only nonempirical or semiempirical density functionals containing a few parameters were tested. Very empirical forms including many (>10) parameters are not expected to give good accuracy for a broad range of different molecules.
[20] J. Ma, S. Ingaki, *J. Am. Chem. Soc.* **2001**, *123*, 1193–1198.
[21] S. Gronert, *J. Org. Chem.* **2006**, *71*, 1209–1219.
[22] N. L. Allinger, J. T. Fermann, W. D. Allen, H. F. Schaefer III, *J. Chem. Phys.* **1997**, *106*, 5143–5150.
[23] Our explanation is also in agreement with the findings of Curtiss et al.[9] that "… *the B3LYP errors are not systematic and can not be removed by a simple molecule-independent correction.*"
[24] There are mixtures of different GGA components with the LDA exchange term possible (e.g. 50% LDA + 50% B88 + LYP) that yield the right ΔE value (due to the strong overbinding tendency of LDA), but such functionals provide very inaccurate results for most other chemically relevant problems and are thus not considered further.
[25] R. Ahlrichs, M. Bär, M. Häser, H. Horn, C. Kölmel, *Chem. Phys. Lett.* **1989**, *162*, 165–169. Turbomole (Version 5.6): R. Ahlrichs et al., Universität Karlsruhe, **2003**. See also: http://www.turbomole.com.
[26] A. Schäfer, H. Horn, R. Ahlrichs, *J. Chem. Phys.* **1992**, *97*, 2571–2577; A. Schäfer, C. Huber, R. Ahlrichs, *J. Chem. Phys.* **1994**, *100*, 5829–5835; F. Weigend, F. Furche, R. Ahlrichs, *J. Chem. Phys.* **2003**, *119*, 12753–12762. The basis sets are available from the Turbomole homepage via the FTP server button (in the subdirectories basen, jbasen, and cbasen). See http://www.turbomole.com.
[27] T. H. Dunning, *J. Chem. Phys.* **1989**, *90*, 1007–1023.
[28] F. Weigend, M. Häser, *Theor. Chem. Acc.* **1997**, *97*, 331–340; F. Weigend, A. Köhn, C. Hättig, *J. Chem. Phys.* **2002**, *116*, 3175–3183.
[29] NIST Standard Reference Database. See http://webbook.nist.gov/chemistry/.
[30] N. L. Allinger, Y. H. Yuh, J.-H. Lii, *J. Am. Chem. Soc.* **1989**, *111*, 8551–8566.

 © 2006 Wiley-VCH Verlag GmbH & Co. KGaA, Weinheim

Solid-State Structures

DOI: 10.1002/anie.200600690

$HgI_2 \cdot As_4S_4$: An Adduct from HgI_2 Molecules and Undistorted As_4S_4 Cages**

*Michael F. Bräu and Arno Pfitzner**

Dedicated to Professor Herbert Jacobs on the occasion of his 70th birthday

Copper(I) halides have been successfully established as a preparative tool for the synthesis of neutral and low-charge molecules of the fifth and sixth main-group elements. Inspired by publications of Rabenau et al.[1–3] as well as Möller and Jeitschko,[4] a whole series of phosphorus,[5] phosphorus chalcogenide,[6] and heteroatomic chalcogen molecules[7] were obtained in a copper halide matrix. Mixed phosphorus–arsenic polymers can also be obtained in this way.[8] The catalytic influence of Cu^+ ions and the structural flexibility of the copper halide are the major reasons for the success of this approach. A possible stabilizing influence of the matrix on the embedded molecules must also be taken into account. Thus,

[*] M. F. Bräu, Prof. Dr. A. Pfitzner
Universität Regensburg
Institut für Anorganische Chemie
Universitätsstrasse 31, 93040 Regensburg (Germany)
Fax: (+49) 941-943-4983
E-mail: arno.pfitzner@chemie.uni-regensburg.de

[**] We thank Prof. Dr. H. Haeuseler and Regina Stötzel, Universität Siegen, for recording the Raman spectra.

WILEY InterScience DISCOVER SOMETHING GREAT
© 2006 Wiley-VCH Verlag GmbH & Co. KGaA, Weinheim

the heteroatomic chains $^1_\infty$[SeTe] and $^1_\infty$[STe] decompose and release elemental tellurium upon separation from the copper halide. In contrast, the phosphorus polymers $^1_\infty$[P8]P4(4)[and $^1_\infty$[P10]P2[can be obtained from their adducts $(CuI)_8P_{12}$ and $(CuI)_3P_{12}$, respectively, by separation of the copper halide matrix.[9] The isostructural arsenic-bearing polymers can be obtained in the same way.[8]

After the successful synthesis of a number of otherwise unknown or inaccessible phosphorus chalcogenides in a matrix of copper halides,[6] the next challenging task was the synthesis of binary cages As_4Q_4 (Q = S, Se) that are coordinated as neutral ligands to a transition metal. To date, these molecules, which are also known as minerals, could not be built into complex structures without fragmentation.[10] Reaction of the cage molecules with transition-metal compounds typically leads to cleavage of the As–As bond or further fragmentation. For this kind of reaction, d^{10} ions should be preferable according to the present state of knowledge. A larger number of such adducts are known, especially with Cu^+ ions. However, a few phosphorus chalcogenide adducts are also known with d^0 ions.[11] In order to suppress the formation of pnicogen–halogen bonds, the metals should be used in the form of metal iodides. Herein, we present our first results for the HgI_2/As_4S_4 system.

Mercury forms halides of the composition Hg_2X_2 and HgX_2, which exist in molecular form as the linear molecules X–Hg–Hg–X and X–Hg–X, respectively. At room temperature, these molecules are stable in the solid state only for X = Cl and Br. In contrast, HgI_2 exists in a yellow high-temperature form that is composed of such molecules as well as in two futher modifications that consist of layers of corner-sharing HgI_4 tetrahedra.[12] The red modification is stable at room temperature. With increasing temperature, it is transformed into an orange modification, and ultimately into the yellow form at even higher temperature. In the ternary mercury/arsenic/halogen system, the family of mercury pnicogen halides is known and forms compounds of different compositions and structures.[13] The ternary compounds $Hg_3Q_2X_2$ (Q = S, Se, Te; X = F, Cl, Br, I) are built of Hg_3Q pyramids, sharing common corners to result in one-, two-, or three-dimensional networks.[14] The vacancies in these cationic networks are occupied by the halide counterions. The quaternary compounds Hg_3AsQ_4X (Q = S, Se; X = Cl, Br, I) are built of Hg_3Q pyramids and AsQ_3 units that are connected to cationic layers, between which the halide counterions are embedded.[15] In each of these compounds, covalent bonds are observed exclusively between the mercury and chalcogen atoms, but no contacts between the mercury and halide atoms are formed. Adducts of mercury halides and molecular arsenic chalcogenides have not yet been reported.

The crystal structure of $HgI_2{\cdot}As_4S_4$ was determined from single-crystal X-ray diffraction data. In the crystal, nearly linear HgI_2 molecules and As_4S_4 cages are observed. The coordination sphere of mercury consists of two iodide ions, as well as two sulfur atoms of an As_4S_4 cage with Hg–S distances of 2.984 and 3.236 Å. These adducts form centrosymmetric dimers, in which the mercury atoms coordinate to one sulfur atom of a second cage with a Hg–S distance of 3.596 Å (Figure 1). Because of this irregular environment of mercury,

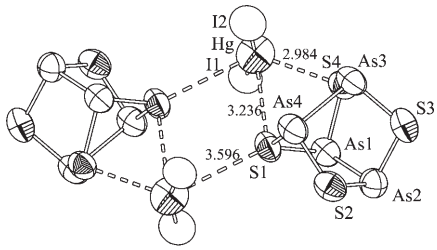


Figure 1. Coordination of mercury atoms by I and As_4S_4 cages in $HgI_2{\cdot}As_4S_4$. Two linear molecules of HgI_2 and the two coordinating As_4S_4 cage molecules are shown. Broken lines show d(Hg–S) in Å. Ellipsoids are set at 80% probability.

the HgI_2 molecules are more significantly bent (I-Hg-I 165.92°) than in yellow mercury iodide (178.3°). Figure 2 shows the three-dimensional arrangement of the dimeric units in the crystal structure. The centers of the dimers form the motif of a distorted cubic close packing. The shortest distances between the dimers are observed between the sulfur atoms and are greater than 3.7 Å.

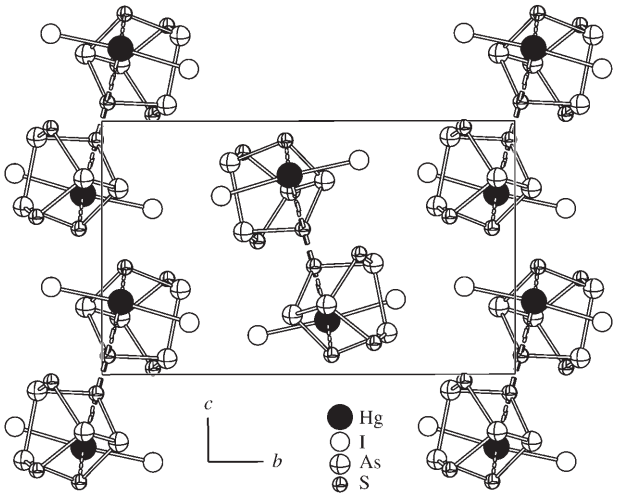


Figure 2. Excerpt of the crystal structure of $HgI_2{\cdot}As_4S_4$. The centers of the dimers shown in Figure 1 form the motif of a distorted cubic close packing.

A question arises about the bonds between the HgI_2 molecules and the As_4S_4 cages, and initial insights can be derived from the crystal structure. In this solid state, all atoms occupy the general position 4*e* in the space group $P2_1/c$. Hence, the ideal symmetry of the As_4S_4 cage is not determined by the space-group symmetry. The point group D_{4d} of the free molecule is nearly preserved in the adduct $HgI_2{\cdot}As_4S_4$. The intramolecular distances show only minor influences from the coordination of the sulfur atoms to the mercury centers. Thus, the bond lengths d(S–As) for the sulfur atoms S1 and S4 are elongated only by 0.02 Å as compared to those of the noncoordinating atoms S2 and S3. The elongation of the bond lengths for S4 is slightly more pronounced than for S1, which might be a result of the shorter Hg–S4 distance (2.984 Å) as compared to Hg–S1 (3.236 Å). If

 © 2006 Wiley-VCH Verlag GmbH & Co. KGaA, Weinheim

the decuple of the standard deviation is used as a criterion for significance, the distances d(S–As) are not significantly different. The same observation holds true for the distances d(As–As), for which the differences are also minimal. The Hg–I bond lengths (ca. 2.60 Å) are not significantly different from those in yellow HgI_2 when the higher temperature for the crystal structure determination of yellow HgI_2 is taken into account. As mentioned above, the I-Hg-I angle (165.92°) is, however, distinctly smaller.

As interatomic distance is no real criterion for the strength of a bond, further insight into the influence of the coordination of the As_4S_4 cage to mercury can be obtained by Raman spectroscopy. Earlier investigations showed that vibrational frequencies of such embedded molecular units are quite sensitive to bonding interactions with the environment.[16] The Raman spectrum of $HgI_2{\cdot}As_4S_4$ is shown in Figure 3, and Table 1 gives the assignment of the observed

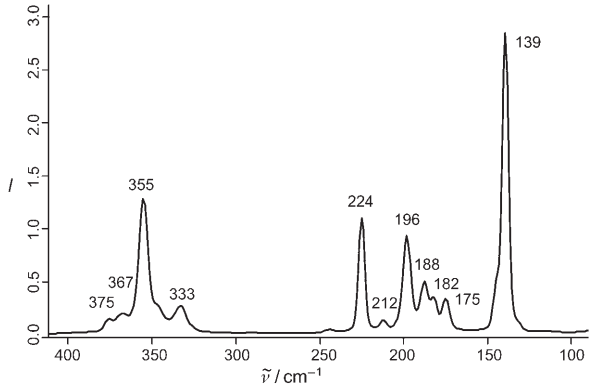


Figure 3. Raman spectrum of $HgI_2{\cdot}As_4S_4$, resolution = 2 cm^{-1}, T = 25 °C. The peaks correspond to As_4S_4 and yellow HgI_2.

Table 1: Comparison of the Raman frequencies for $HgI_2{\cdot}As_4S_4$ and realgar (all frequencies in cm^{-1}).

Assignment	Intensity	$HgI_2As_4S_4$	Realgar[17]
ν(As-S)	very weak	375	376
ν(As-S)	very weak	367	370
ν(As-S)	strong	355	355
ν(As-S)	weak	333	330
ω(As-S)	strong	225	222
δ(As-S)	very weak	212	212
δ(As-S-As)	strong	196	196
ν(As-As)	weak	188	184
–	very weak	182	–
ν(As-As)	weak	175	173
ν(HgI_2)	very strong	139	–

peaks. The linear stretching vibration of the HgI_2 unit (139 cm^{-1}) differs only slightly from the one observed in yellow HgI_2 (133 cm^{-1}), and the different temperatures of the measurements have to be taken into account. The vibrational frequencies of the As_4S_4 cage in $HgI_2{\cdot}As_4S_4$ and the free As_4S_4 cage agree within the experimental errors.[18] Thus, the Raman spectrum of the adduct compound can be interpreted as a combination of the spectra of yellow HgI_2 and realgar (arsenic sulfide). Vibrational spectroscopy demonstrates that the molecular units in this compound show only very weak interactions, in agreement with the structural data.

Finally the question remains as to why no cationic network of mercury and sulfur atoms is formed in $HgI_2{\cdot}As_4S_4$ and why molecular units are favored in contrast to all known compounds in this system. As based on available data for compounds in the ternary and quaternary systems $Hg_3Q_2X_2$ and Hg_3AsQ_4X, one might expect preferential formation of Hg–S bonds and of a polycationic network that incorporates arsenic. Obviously the total energy of the system, which is supposed to be the crucial factor for thermodynamically controlled reactions, is optimum when linear HgI_2 molecules, which are usually unstable at room temperature, are weakly coordinated by As_4S_4 cages. Structural and spectroscopic investigations show that the interactions between the molecular units are very weak. Thus, it is possible to preserve the As_4S_4 cage for the first time in an undistorted manner.

Experimental Section

$HgI_2{\cdot}As_4S_4$ was obtained by heating HgI_2 (Merck, 99.9%), gray arsenic (Merck, 99.999%), and sulfur (Merck, 99.9995%) in the molar ratio 1:4:4 in evacuated quartz ampoules. The reactants were molten at 400 °C and then annealed at 200 °C for two weeks. $HgI_2{\cdot}As_4S_4$ was obtained in good yield as orange crystals along with red HgI_2 and As_4S_4. $HgI_2{\cdot}As_4S_4$ decomposes peritectically at 212 °C and cannot be obtained directly from the melt.

X-ray structure analysis and crystallographic data: $HgI_2As_4S_4$, M_r = 882.31 g mol^{-1}, monoclinic, space group $P2_1/c$, a = 9.433(3), b = 14.986(9), c = 11.624(5) Å, β = 127.72(2)°, V = 1299(1) Å^3 (lattice constants from powder data, transmission geometry, STOE STADI P), Z = 4, ρ_{calcd} = 4.509 g cm^{-3}, $F(000)$ = 1528, T = 293 K, $\lambda(Mo_{K\alpha})$ = 0.71073 Å. Single-crystal diffraction data were collected on a STOE IPDS I: 16111 measured reflections, 2244 independent reflections (R_{int} = 0.0616). Absorption correction with X-Red[19] after optimizing the shape of the crystal with X-Shape,[20] structure solution with SIR92,[21] refinement with SHELX-97,[22] 100 parameters, $R1(I \geq 2\sigma(I))$ = 0.0380, $wR2(I \geq 2\sigma(I))$ = 0.0861, $R1$(all) = 0.0479, $wR2$(all) = 0.0899, GooF = 1.073, residual electron density = 1.675/–1.051 Å^{-1}. Further details on the crystal structure investigations may be obtained from the Fachinformationszentrum Karlsruhe, 76344 Eggenstein-Leopoldshafen, Germany (fax: (+49) 7247-808-666; E-mail: crysdata@fiz-karlsruhe.de), on quoting the depository number CSD-416258.

Raman spectra were recoded on a Bruker RFS100/S FT spectrometer equipped with a Nd:YAG laser (λ = 1064 nm) and a Ge detector cooled with liquid nitrogen.

Thermal analyses were performed on a Setaram TG-DTA in evacuated quartz ampoules with a heating rate of 2 °C min^{-1}.

Received: February 21, 2006
Revised: March 30, 2006
Published online: June 7, 2006

Keywords: arsenic · cage compounds · cocrystallization · mercury · structure elucidation

[1] W. Milius, *Z. Anorg. Allg. Chem.* **1990**, *586*, 175.
[2] J. Fenner, *Acta Crystallogr. Sect. B* **1976**, *32*, 3084.
[3] W. Milius, A. Rabenau, *Mater. Res. Bull.* **1987**, *22*, 1493.
[4] M. H. Möller, W. J. Jeitschko, *J. Solid State Chem.* **1986**, *65*, 178.

 © 2006 Wiley-VCH Verlag GmbH & Co. KGaA, Weinheim

[5] A. Pfitzner, E. Freudenthaler, *Z. Kristallogr.* **1995**, *210*, 59; A. Pfitzner, E. Freudenthaler, *Angew. Chem.* **1995**, *107*, 1784; *Angew. Chem. Int. Ed. Engl.* **1995**, *34*, 1647; E. Freudenthaler, A. Pfitzner, *Z. Kristallogr.* **1997**, *212*, 103; A. Pfitzner, E. Freudenthaler, *Z. Naturforsch. B* **1997**, *52*, 199; E. Freudenthaler, A. Pfitzner, *Solid State Ionics* **1997**, *101–103*, 1053.
[6] A. Pfitzner, S. Reiser, *Inorg. Chem.* **1999**, *38*, 2451; A. Pfitzner, S. Reiser, H.-J. Deiseroth, *Z. Anorg. Allg. Chem.* **1999**, *625*, 2196; A. Pfitzner, S. Reiser, T. Nilges, *Angew. Chem.* **2000**, *112*, 4328; *Angew. Chem. Int. Ed.* **2000**, *39*, 4160; S. Reiser, G. Brunklaus, J. H. Hong, J. C. C. Chan, H. Eckert, A. Pfitzner, *Chem. Eur. J.* **2002**, *8*, 4228; T. Nilges, S. Reiser, A. Pfitzner, *Z. Anorg. Allg. Chem.* **2003**, *629*, 563; G. Brunklaus, J. C. C. Chan, H. Eckert, S. Reiser, T. Nilges, A. Pfitzner, *Phys. Chem. Chem. Phys.* **2003**, *5*, 3768; S. Nilges, T. Nilges, H. Haeuseler, A. Pfitzner, *J. Mol. Struct.* **2004**, *706*, 89.
[7] A. Pfitzner, S. Zimmerer, *Z. Anorg. Allg. Chem.* **1995**, *621*, 969; A. Pfitzner, S. Zimmerer, *Z. Anorg. Allg. Chem.* **1996**, *622*, 853; A. Pfitzner, S. Zimmerer, *Z. Kristallogr.* **1997**, *212*, 203; A. Pfitzner, S. Zimmerer, *Angew. Chem.* **1997**, *109*, 1031; A. Pfitzner, S. Zimmerer, *Angew. Chem. Int. Ed. Engl.* **1997**, *36*, 982; A. Pfitzner, F. Baumann, W. Kaim, *Angew. Chem.* **1998**, *110*, 2057; *Angew. Chem. Int. Ed.* **1998**, *37*, 1955; J. Stanek, P. Fornal, S. S. Hafner, A. Pfitzner, *Acta Phys. Pol. A* **2001**, *100*(5), 807; T. Nilges, S. Zimmerer, D. Kurowski, A. Pfitzner, *Z. Anorg. Allg. Chem.* **2002**, *628*, 2809.
[8] B. Jayasekera, K. Somaskandan, S. L. Brock, *Inorg. Chem.* **2004**, *43*, 6902; B. Jayasekera, S. L. Brock, A. Y. H. Lo, R. W. Schurko, G. Nazri, *Chem. Eur. J.* **2005**, *11*, 3762.
[9] A. Pfitzner, M. F. Bräu, J. Zweck, G. Brunklaus, H. Eckert, *Angew. Chem.* **2004**, *116*, 4324; *Angew. Chem. Int. Ed.* **2004**, *43*, 4228.
[10] J. Wachter, *Angew. Chem.* **1998**, *110*, 782; *Angew. Chem. Int. Ed.* **1998**, *37*, 750.
[11] H. Nowottnick, K. Stumpf, R. Blachnik, H. Reuter, *Z. Anorg. Allg. Chem.* **1999**, *625*, 693; A. Pfitzner, D. Hoppe, *Z. Anorg. Allg. Chem.*, in press.
[12] M. Hostettler1, H. Birkedal, D. Schwarzenbach, *Helv. Chim. Acta* **2003**, *86*, 1410.
[13] A. Shevel'kov, E. Dikarev, B. Popovkin, *J. Solid State Chem.* **1996**, *126*, 324.
[14] Yu. Minets, Yu. Voroshilov, V. Panko, *J. Alloys Compd.* **2004** *367*, 109.
[15] J. Beck, S. Hedderich, K. Köllisch, *Inorg. Chem.* **2000**, *39*, 5847.
[16] A. Pfitzner, *Chem. Eur. J.* **1997**, *3*, 2032.
[17] M. Muniz-Miranda, G. Sbrana, P. Bonazzi, S. Menchetti, G. Pratesi, *Spectrochim. Acta Part A* **1996**, *52*, 1391.
[18] A. Banerjee, J. O. Jensen, J. L. Jensen, *J. Mol. Struct.* **2003**, *662*, 63.
[19] X-RED, STOE, Darmstadt, **1999**.
[20] X-SHAPE, Crystal Optimization for Numerical Absorption Correction, STOE, Darmstadt, **1999**.
[21] A. Altomare, G. Cascarano, C. Giacovazzo, A. Gualardi, *J. Appl. Crystallogr.* **1993**, *26*, 343.
[22] G. M. Sheldrick, SHELX-97, Program for the solution and refinement of crystal structures, University of Göttingen, Germany, **1997**.

 © 2006 Wiley-VCH Verlag GmbH & Co. KGaA, Weinheim

Metal-Free Heterogeneous Catalysis

DOI: 10.1002/anie.200600412

Chemical Synthesis of Mesoporous Carbon Nitrides Using Hard Templates and Their Use as a Metal-Free Catalyst for Friedel–Crafts Reaction of Benzene**

*Frederic Goettmann, Anna Fischer, Markus Antonietti, and Arne Thomas**

Carbon nitride is presumably the most promising (and the most sought after) candidate to complement carbon in materials applications. Diamond-like β-C_3N_4 is predicted to be of similar hardness as diamond but less compressible.[1,2] However, it is assumed that like carbon, at ambient conditions a graphitic-C_3N_4 allotrope (g-C_3N_4) is the most stable form. Accordingly, the attempted bulk synthesis of this material is the subject of an even larger number of reports in the literature.[3] Historically, the synthesis of g-C_3N_4 derivatives started with the observations of Berzelius described by Liebig[4] in 1834. They reported the first synthesis of a less defined, hydrogen-containing, polymeric precursor ("melon"), which however already had the correct connectivity patterns and an approximately correct C/N ratio. g-C_3N_4 is a potentially useful substitute for amorphous and graphitic carbon in a variety of applications, for example, as a catalytic support and for gas storage.[5] Therefore, novel procedures yielding more defined carbon nitrides, in particular mesoporous forms with large accessible areas, are eagerly awaited. Vinu et al. recently reported the synthesis of mesoporous carbon nitride by nanocasting techniques.[6] Their material featured a large surface area; however, the C/N molar ratio (≈ 5) indicated the loss of the vast majority of nitrogen, while X-ray diffraction measurements showed low crystallinity of the pore walls.

In this paper we employ a recently developed[7] synthetic scheme based on the self-condensation of cyanamide, dicyandiamide, or melamine accompanied by elimination of ammonia to generate mesoporous g-C_3N_4 materials with high local order. As C_3N_4 synthesis is a high-temperature procedure, appropriate templates that withstand 600 °C for at least 12 h are needed for the scaffolding of the mesoporous system. Recently, porous silicas were used successfully as templates for the generation of g-C_3N_4 nanoparticles.[8] Herein, a

[*] Dr. F. Goettmann, A. Fischer, Prof. Dr. M. Antonietti, Dr. A. Thomas
Max-Planck-Institute of Colloids and Interfaces
Department of Colloid Chemistry
Research Campus Golm, 14424 Potsdam (Germany)
Fax: (+49) 331-567-9502
E-mail: arne.thomas@mpikg.mpg.de

[**] We thank Rona Pitschke for technical help throughout electron microscopy. The Max Planck Society is acknowledged for support within the framework of the project house "ENERCHEM".

Supporting information for this article is available on the WWW under http://www.angewandte.org or from the author.

© 2006 Wiley-VCH Verlag GmbH & Co. KGaA, Weinheim

similar, but inverted, template approach is applied to the carbon nitride system, using so-called hard templates, that is, inorganic nanoparticles, which can be removed after condensation. Silica nanoparticles, which have already been used successfully for the generation of mesoporous carbon,[9] are found to act as suitable templates.

Ideally, these silica nanoparticles could be dispersed homogeneously in the starting monomers, that is, in cyanamide. In our case, such a dispersion is favored by appropriate surface interactions between the silica surface and the amine and, later, aromatic nitrogen groups. Condensation of the monomers at elevated temperatures (two condensation procedures were applied; see the Experimental Section) resulted in carbon nitride/silica hybrids, in which the silica nanoparticles remain well-dispersed in a solid C_3N_4 matrix. The silica template was dissolved with ammonium hydrogen fluoride solution and removed to yield various mesoporous materials of the type mpg-$C_3N_{4/r}$. (In the following the "g" is omitted when the first heat treatment was used, in other words, when the material is not sufficiently graphitic; *r* refers to the initial silica/cyanamide mass ratio (0.5, 1, 1.6).) These materials were fully characterized by using transmission electron microscopy (TEM), nitrogen adsorption, wide- and small-angle X-ray scattering, elemental analysis, and FTIR spectroscopy.

Figure 1 shows TEM pictures of a sample with an initial cyanamide/silica mass ratio of 1:1 that was condensed for 4 h at 550 °C and freed of the template. The TEM pictures indicate that the pore size and connectivity of those powders

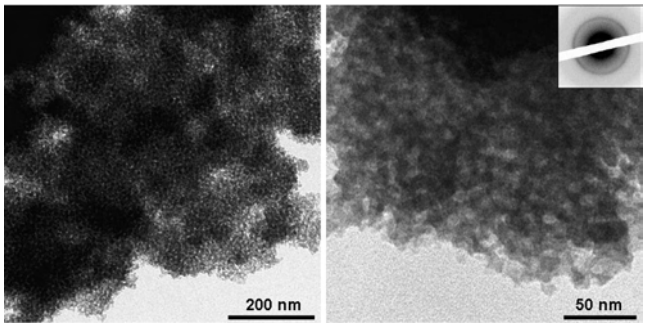


Figure 1. TEM images and an electron diffraction pattern of mp-$C_3N_{4/1}$ after removal of the silica nanoparticles.

exactly reflect the geometric properties of the original template. The disordered pore system of spherical pores with a mean diameter of 12 nm can be regarded as a direct image, or more appropriately, a negative image of the structure of the silica sol. In addition, electron diffraction of a selected area proves the high partial crystallinity of the pore walls, which is revealed by one intense diffraction ring corresponding to the stacking distance of g-C_3N_4 ($d =$ 0.33 nm).

Figure 2 shows nitrogen adsorption/desorption isotherms of three mp-C_3N_4 samples prepared with different silica/cyanamide ratios. The curves show a small hysteresis typical for the existence of randomly connected spherical pores, only

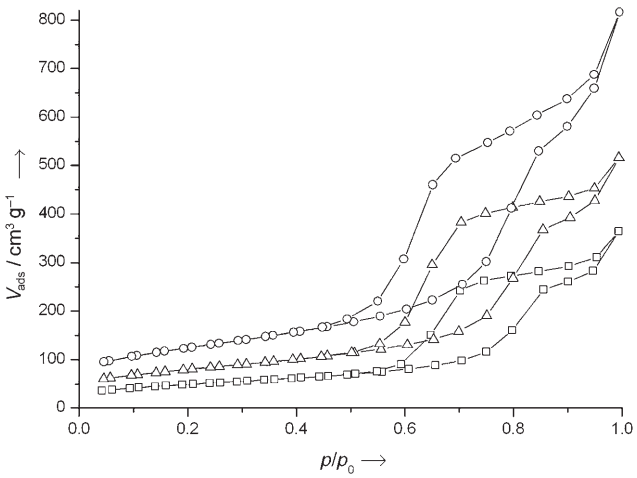


Figure 2. Nitrogen gas adsorption isotherms for different mp-C_3N_4 samples reflecting different template concentrations. □ mp-$C_3N_{4/0.5}$, △ mp-$C_3N_{4/1}$, ○ mp-$C_3N_{4/1.6}$.

weak microporosity, and surface areas between 86 and 439 $m^2 g^{-1}$, depending on the template content.

To evaluate the degree of condensation and the structure of the pore walls, we performed wide-angle X-ray scattering (WAXS) measurements and elemental analysis. The data along with those of an appropriately condensed bulk g-C_3N_4 are shown in Figure 3. The X-ray diffraction patterns reveal

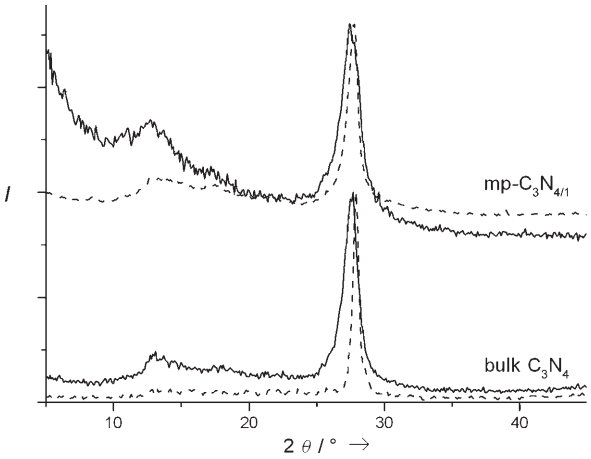


Figure 3. Comparison of the WAXS diagram of mp-$C_3N_{4/1}$ with that of the corresponding nonporous material after two different heat treatments: 550 °C for 4 h in closed but unsealed quartz tubes (——); additional heating at 600 °C for 10 h in sealed quartz ampules (-----).

the graphite-like stacking of C_3N_4 layers in both the bulk and the mesoporous material. The (002) peaks correspond to interlayer distances of $d = 0.326$ nm (material prepared at 550 °C) and $d = 0.319$ nm (material prepared at 600 °C). The X-ray patterns recorded for the mesoporous materials do not differ significantly from those of the nonporous materials, except for a slight broadening of the (002) peak and a decrease in the overall intensity. This can be attributed to a reduced correlation length introduced by the spherical

 © 2006 Wiley-VCH Verlag GmbH & Co. KGaA, Weinheim

porogens. The ordering in the pore walls is significantly increased by the second tempering step (600 °C/10 h) prior to the removal of the silica template. For the bulk and the mesoporous materials, a pronounced additional peak is found at $2\theta = 13.1°$, corresponding to a distance $d = 0.675$ nm, which can be attributed to an in-plane structural packing motif, for example, the hole-to-hole distance of the nitride pores (Figure 4). For the mesoporous materials this peak is broadened, again reflecting the effect of the geometric confinement in the nanosized pore walls.

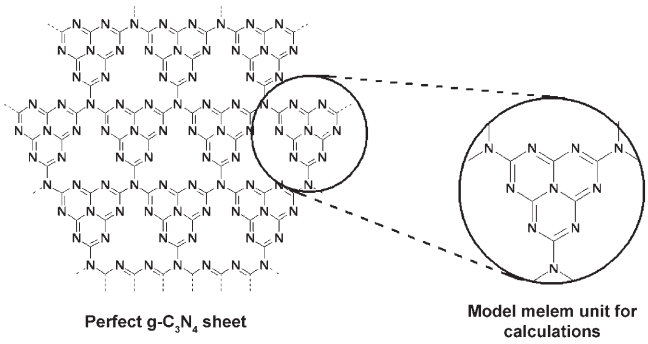


Figure 4. Representation of a perfect graphitic C_3N_4 and of the melem unit used for modeling purposes.

Elemental analyses were performed several times on different batches of the prepared material. An average value of 0.71 was determined for the C/N ratio (theoretical value of C_3N_4: 0.75). We attribute the additional small amounts of hydrogen (1.5%) to (minor) structural defects, surface termination effects by uncondensed amino functions (which is supported by the fact that the H content increases with surface area), and adsorbed water (as evidenced by FTIR spectroscopy). Although this material does not exhibit perfect crystallinity, its X-ray diffraction pattern indicates an organization level that differs strongly from Liebig's "melon".

For a long time the field of mesoporous materials was restricted to inorganic solids[10] and resulted in their numerous applications especially as catalysts and catalytic supports.[11] Based on its unique electronic properties and large surface area, mpg-C_3N_4 should be an alternative catalyst complementary to the high-surface-area metal oxides usually used. According to Kroke et al.[12] the basic motifs of a g-C_3N_4 sheet are melem rings linked by nitrogen bridges. We performed DFT calculations using the Gaussian O3 package with the B3LYP functional on a model melem unit to gain insight into the local electronic structure of g-C_3N_4. The optimized geometry is shown in Figure 5. It is worth noticing that even in the uncondensed form the amino groups are planar, indicating sp^2 hybridization. In this case the lone pairs of these atoms interact with the π system of the arene. The three highest occupied molecular orbitals feature π symmetry, whereas HOMO-3 is an antibonding combination of the atomic orbitals describing the lone pairs of the "aromatic" nitrogen atoms. These results are in good qualitative agreement with results reported by Le Breton et al. in 1984;[13] the HOMO consists exclusively of the p_z orbitals of the heterocyclic nitrogens, which is exactly the symmetry of the highest unoccupied π-type orbital in the Hückel model of benzene. It should thus be possible for the melem units to transfer electron density to arenes through overlapping of those orbitals, resulting in a very unusual arene activation.

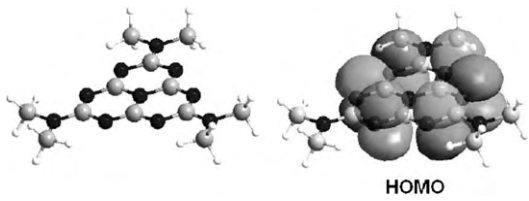


Figure 5. Optimized geometry (DFT) of the model melem ring (left) and the a representation of the HOMO (right).

A perfect infinite g-C_3N_4 sheet, however, is likely to feature an electronic band structure (theoretical investigations are currently underway that support this idea) and thus no electron localization in the π states. The above-mentioned activation might therefore only be possible on defects, which promote electron relocalization. In the case of graphite it is well known that defects such as edges,[14] curvature,[15] and doping atoms[16] can induce electron relocalization. In addition, such defects have recently been demonstrated to be catalytically active sites in the oxidative dehydrogenation of ethylbenzene.[17,18] mpg-C_3N_4 features almost all of these structures in combination with a high surface area, which implies that this material should contain a large number of potentially catalytic active sites. For this reason we investigated the activity of mpg-C_3N_4 as a catalyst for the activation of aromatic compounds.

A typical process for the C–H activation of aromatic molecules is the Friedel–Crafts acylation. Usually the electrophile is activated, although activation of the nucleophile should, in principle, yield the same results. In fact, graphite particles have already been used to promote Friedel–Crafts reactions. However, because of the large excess of graphite required, it is not clear whether this is catalytic activation.[19,20]

For our purpose, we analyzed six samples of mesoporous C_3N_4 with varying surface area (amount of template) and degree of organization (heat treatment; Table 1). We first investigated the effect of various solvents (benzene, heptane, anisole) on the acylation of benzene with hexanoyl chloride using mp-$C_3N_{4/1}$ as the catalyst. The corresponding conversion rates are listed in Table 2. In all cases, medium to high conversion was found; that is, mp-C_3N_4 indeed acts as an activation catalyst. The observed difference between reactions conducted in benzene and heptane is likely to result from passivation of the surface of mp-C_3N_4 by a large excess of benzene. We are currently examining this assumption by

Table 1: Specific surface areas (in m^2g^{-1}) of the different mesoporous nitrides synthesized for catalytic applications.

	$C_3N_{4/0.5}$	$C_3N_{4/1}$	$C_3N_{4/1.6}$
mp-	136	190	440
mpg-	86	141	327

 © 2006 Wiley-VCH Verlag GmbH & Co. KGaA, Weinheim

Table 2: Catalytic activity of mp-$C_3N_{4/1}$ in the Friedel–Crafts acylation of benzene with hexanoyl chloride in different solvents.

	Benzene	Heptane	Anisole
T [°C]	80	90	150
Conversion [%]	16	80	60

spectroscopy. The choice of anisole as a solvent might be surprising as it is well known to be much more reactive than benzene as a Friedel–Crafts substrate. Indeed, in mixtures of benzene and anisole the only product formed is *n*-hexanophenone. This finding indicates that anisole does not react as long as benzene is present. As the catalysis is supposed to originate from electron donation from melem units to the aromatic substrate, substrates having lower-lying molecular orbitals should interact more strongly with the C_3N_4 surface. On the other hand, substitutions on the aromatic ring alter the symmetry of the molecular orbitals, resulting in an inferior overlap with the HOMO of localized melem units. These two considerations together with steric effects make it difficult to predict the reactivity of individual arenes.

Since heptane was found to be a suitable solvent for the Friedel–Crafts acylation (Table 2), it was used in subsequent experiments. We set out to analyze the effect of the surface and crystallinity of the catalysts. The acylations were performed with hexanoyl chloride (50 mg) and benzene (150 mg) in heptane (5 g) for 20 h at 90 °C using 25 mg of the corresponding carbon nitride as the catalyst. The products of the reactions were analyzed by GC with an internal standard for quantification. Some results are summarized in Table 3. Most of the mesoporous carbon nitrides used are indeed active catalysts for the Friedel–Crafts acylation, whereas the bulk carbon nitride was inactive. As a reference, graphite particles (1 μm in diameter) were used under the same conditions and were found to be far less active.

Table 3: Catalytic activity of mpg-C_3N_4 in the Friedel–Crafts acylation of benzene.[a]

Catalyst	Conversion [%]	TOF × 100 [h^{-1}][b]
mp-$C_3N_{4/0.5}$	52	3.6
mp-$C_3N_{4/1}$	80	5.5
mp-$C_3N_{4/1.6}$	52	3.6
mpg-$C_3N_{4/0.5}$	90	6.2
bulk g-C_3N_4	0	–
graphite	1	–

[a] Reaction conditions: A mixture of benzene (150 mg), hexanoyl chloride (50 mg), and (C_3N_4) in heptane (5 g) was stirred at 90 °C for 20 h. The products were analyzed by gas chromatography. [b] Turnover frequency: *n*(hexanoyl chloride) per *n*(melem units) per hour.

No clear correlation can be found between the specific surface area and the catalytic activity of samples that were submitted to the same heat treatment, as the activity appears to go through a maximum. This can also indicate that only the pore walls of a certain minimal thickness have a suitable electronic structure. The second heat treatment at 600 °C and the resulting increase in organization and condensation seem to improve the catalytic activity, and the best results were obtained for mpg-$C_3N_{4/0.5}$ (90 % conversion).

To conclude, we have synthesized a mesoporous, high-surface-area graphitic carbon nitride by using colloidal silica nanoparticles as a template, and its catalytic properties were tested in Friedel–Crafts reactions. Remarkable activity enhancement was found for reactions with benzene as the coupling partner. We are currently trying to prove experimentally that this catalysis arises from back-donation of electron density from molecular orbitals of the catalyst to unoccupied orbitals of the arene. As defects in the graphitic layers appear to be responsible for the catalytic activity, in future work we will focus on determining the structure of the catalyst more precisely to gain better insight into the underlying activation mechanism.

Most of the solids used in heterogeneous catalysis are Lewis acids.[21] We hope that mpg-C_3N_4 described here will pave the way for metal-free heterogenous catalysts with Lewis-base character. This would be an important step towards metal-free coordination chemistry and catalysis. Moreover, this system is likely to be active for other C–C coupling and C–H activation reactions. It is remarkable that this was achieved with a material first described by Berzelius and Liebig, one of the first organic solid-state materials made.

Experimental Section

TEM images were recorded on a Zeiss EM91 microscope. WAXS spectra were recorded on a Bruker D8 Advance diffractometer and the SAXS spectra on a Enraf Nonius FR590. FTIR spectra were recorded on a BioRad FTS 6000 spectrometer.

Synthesis of g-C_3N_4: Molten cyanamide (1 g, 24 mmol; Aldrich) was heated and stirred at 70 °C, and different amounts of a 40 % dispersion of 12-nm SiO_2 particles (Ludox HS40, Aldrich) in water were added dropwise (1.25, 2.0, 4.0 g Ludox for the $r = 0.5, 1, 1.6$). The resulting transparent mixtures were then heated at a rate of 4.5 K min^{-1} over 2 h to reach a temperature of 550 °C and then tempered at this temperature for another 4 h. To prepare mp-C_3N_4, the resulting brown–yellow powder was treated with a 4 M NH_4HF_2 for two days to remove the silica template. The powders were then centrifuged and washed three times with distilled water and twice with ethanol. Finally the powders were dried at 70 °C under vacuum for several hours. To prepare mpg-C_3N_4, samples resulting from the first heat treatment (without silica extraction) were heated to 600 °C for 10 h under static vacuum in a sealed quartz ampule. To remove the silica templates, the obtained light-brown powders were treated with NH_4HF_2 as described above.

All computations were performed using the Gaussian 03 suite of programs[22] and gradient-corrected density functional theory by using the B3LYP functional.[23] Optimizations were carried out using the 6-21G basis set.

Catalysis experiments: A sample of mesoporous C_3N_4 (25 mg, 0.5 mmol melem units) was suspended in a solution of benzene (2 mmol) and hexanoyl chloride (50 mg, 0.75 mmol) in the respective solvent (5 g). The mixture was heated to reflux. After 20 h reaction time, an aliquot of the mixture was poured into ethanol and analyzed by GC. The structure of the product was confirmed by ^{1}H NMR spectroscopy.

Received: January 31, 2006
Published online: June 13, 2006

 © 2006 Wiley-VCH Verlag GmbH & Co. KGaA, Weinheim

Keywords: carbon nitrides · Friedel–Crafts acylation · mesoporous materials · metal-free catalysis

[1] A. Y. Liu, M. L. Cohen, *Science* **1989**, *245*, 841.
[2] M. L. Cohen, *Phys. Rev. B* **1985**, *32*, 7988.
[3] E. Kroke, M. Schwarz, *Coord. Chem. Rev.* **2004**, *248*, 493.
[4] J. Liebig, *Ann. Pharm.* **1834**, *10*, 10.
[5] X. D. Bai, D. Y. Zhong, G. Y. Zhang, X. C. Ma, S. Liu, E. G. Wang, Y. Chen, D. T. Shaw, *Appl. Phys. Lett.* **2001**, *79*, 1552.
[6] A. Vinu, K. Ariga, T. Mori, T. Nakanishi, S. Hishita, D. Golberg, Y. Bando, *Adv. Mater.* **2005**, *17*, 1648.
[7] B. Jürgens, E. Irran, J. Senker, P. Kroll, H. Müller, W. Schnick, *J. Am. Chem. Soc.* **2003**, *125*, 10288.
[8] M. Groenewolt, M. Antonietti, *Adv. Mater.* **2005**, *17*, 1789.
[9] S. J. Han, K. Sohn, T. Hyeon, *Chem. Mater.* **2000**, *12*, 3337.
[10] G. J. D. Soler-Illia, C. Sanchez, B. Lebeau, J. Patarin, *Chem. Rev.* **2002**, *102*, 4093.
[11] A. Taguchi, F. Schüth, *Microporous Mesoporous Mater.* **2005**, *77*, 1.
[12] E. Kroke, M. Schwarz, E. Horath-Bordon, P. Kroll, B. Noll, A. D. Norman, *New J. Chem.* **2002**, *26*, 508.
[13] M. Shahbaz, S. Urano, P. R. Lebreton, M. A. Rossman, R. S. Hosmane, N. J. Leonard, *J. Am. Chem. Soc.* **1984**, *106*, 2805.
[14] T. Enoki, Y. Kobayashi, *J. Mater. Chem.* **2005**, *15*, 3999.
[15] S. Tomita, T. Sakurai, H. Ohta, M. Fujii, S. Hayashi, *J. Chem. Phys.* **2001**, *114*, 7477.
[16] M. Endo, T. Hayashi, S. H. Hong, T. Enoki, M. S. Dresselhaus, *J. Appl. Phys.* **2001**, *90*, 5670.
[17] D. S. Su, N. Maksimova, J. J. Delgado, N. Keller, G. Mestl, M. J. Ledoux, R. Schlögl, *Catal. Today* **2005**, *102*, 110.
[18] J. A. Macia-Agullo, D. Cazorla-Amoros, A. Linares-Solano, U. Wild, D. S. Su, R. Schlögl, *Catal. Today* **2005**, *102*, 248.
[19] C. Laporte, P. Baules, A. Laporterie, J. R. Desmurs, J. Dubac, *C. R. Acad. Sci. Ser. IIc* **1998**, *1*, 141.
[20] M. Kodomari, Y. Suzuki, K. Yoshida, *Chem. Commun.* **1997**, 1567.
[21] A. Corma, H. Garcia, *Chem. Rev.* **2003**, *103*, 4307.
[22] Gaussian 98 (Revision A.7), M. J. Frisch et al., Gaussian, Inc., Pittsburgh, PA, **1998**.
[23] A. D. Becke, *J. Chem. Phys.* **1993**, *98*, 5648.

 © 2006 Wiley-VCH Verlag GmbH & Co. KGaA, Weinheim

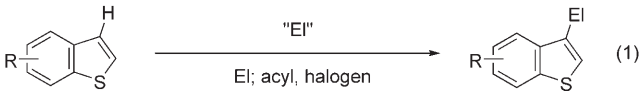
Synthetic Methods

DOI: 10.1002/anie.200601178

Gold-Catalyzed Intramolecular Carbothiolation of Alkynes: Synthesis of 2,3-Disubstituted Benzothiophenes from (α-Alkoxy Alkyl) (*ortho*-Alkynyl Phenyl) Sulfides

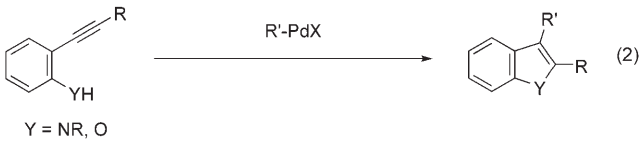
Itaru Nakamura, Takuma Sato, and Yoshinori Yamamoto*

Facile synthesis of benzothiophenes bearing a substituent at the C3 position is of great interest as this structural framework is often seen in biologically active compounds such as raloxifene and sertaconazole.[1,2] In general, functionalization of the C3 position is carried out by electrophilic substitution reactions such as Friedel–Crafts acylation and halogenation [Eq. (1)].[3] However, it is difficult to attach an alkyl group



(1)

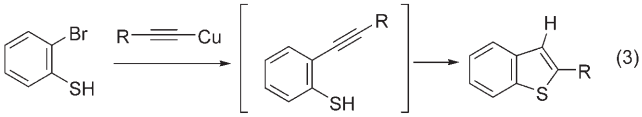
such as (α-alkoxy alkyl), benzyl, or allyl group because the corresponding alkyl halides are less reactive than acyl halides; in those cases, lithiation at the C3 position by using *sec*-BuLi is required prior to alkylation.[4] Cyclization of *ortho*-alkynyl anilines and *ortho*-alkynyl phenols with organopalladium species is one of the common methods for the direct synthesis of 2,3-disubstituted indoles and benzofurans [Eq. (2)].[5] This



Y = NR, O

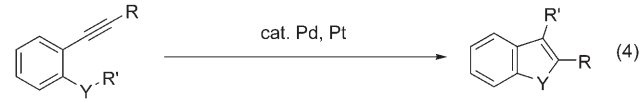
(2)

methodology is, however, inapplicable to the direct synthesis of 2,3-disubstituted benzothiophenes as the substrates, *ortho*-alkynyl benzenethiols, are not accessible by Sonogashira coupling of *ortho*-halo benzenethiols; the palladium-catalyzed reaction does not proceed due to catalyst poisoning by the mercapto group. The substrates can be synthesized through a stoichiometric reaction by using copper acetylides, but they are immediately cyclized under the reaction conditions to give 2-monosubstituted benzothiophenes [Eq. (3)].[6] Accordingly, the direct synthesis of 2,3-disubstituted benzothiophenes is not possible, which is in contrast to the syntheses of 2,3-disubstituted indoles and benzofurans.



(3)

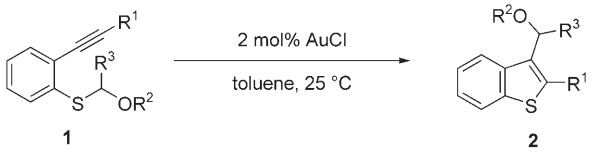
Recently, several groups, including ourselves, developed the transition metal-catalyzed cyclization of *ortho*-alkynyl anilines and (*ortho*-alkynyl phenyl) ethers, which have a migration group (R′), such as an allyl,[7] propargyl,[8] acyl,[9] (α-alkoxy alkyl),[10] or (*para*-methoxyphenyl)methyl group,[10b] at the Y position. The migration of R^1 from Y to the C3 position takes place readily to produce the corresponding 2,3-disubstituted indoles and benzofurans in excellent yields [Eq. (4)].



(4)

Y = NR, O
R' = allyl, propargyl, acyl,
(α-alkoxy alkyl),
(*p*-methoxyphenyl)methyl

It occurred to us that a similar migration may take place in (*ortho*-alkynyl phenyl) sulfides by judicious choice of catalyst. Herein, we report the gold-catalyzed cyclization of (α-alkoxy alkyl) (*ortho*-alkynyl phenyl) sulfides, **1**, under mild conditions to give 2,3-disubstituted benzothiophenes, **2**, in excellent yields (Scheme 1).[11] The starting materials, **1**, are available through acetalization of *ortho*-bromobenzenethiol followed by Sonogashira coupling.



1 2

Scheme 1. Gold-catalyzed cyclization of (α-alkoxy alkyl) (*ortho*-alkynyl phenyl) sulfides, **1**.

The results are summarized in Table 1. The reaction of methoxymethyl-*ortho*-(1-pentynyl)phenyl sulfide (**1a**) in the presence of 2 mol% of AuCl in toluene at 25 °C gave 2-methoxymethyl-3-propylbenzothiophene (**2a**) in 93% yield (Table 1, entry 1). The reaction of **1a** in the presence of $AuCl_3$ or $PtCl_2$ instead of AuCl gave **2a** in a similar yield, whereas $AuBr_3$, $PtCl_4$, AgOTf, or $InCl_3$ did not induce the reaction. Other catalysts, such as $PdCl_2$, PdI_2, $CuCl_2$, and $Yb(OTf)_3$, also did not promote any reaction. The reaction in hexane as solvent, instead of toluene, proceeded slowly over 24 h and gave **2a** in 95% yield, whereas the reaction in CH_2Cl_2 gave **2a**

[*] Dr. I. Nakamura, T. Sato, Prof. Dr. Y. Yamamoto
Department of Chemistry
Graduate School of Science
Tohoku University
Sendai 980-8578 (Japan)
Fax: (+81) 22-795-6784
E-mail: itaru-n@mail.tains.tohoku.ac.jp

Supporting information for this article is available on the WWW under http://www.angewandte.org or from the author.

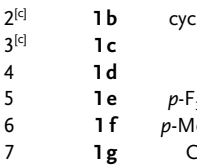
© 2006 Wiley-VCH Verlag GmbH & Co. KGaA, Weinheim

Table 1: Gold(I)-catalyzed cyclization of (α-alkoxy alkyl) (*ortho*-alkynyl phenyl) sulfides **1**.[a]

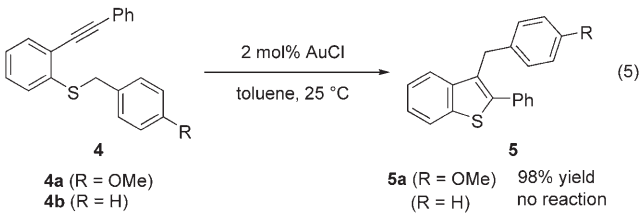
Entry	1	R^1	R^2	R^3	2	Yield [%][b]
1	**1a**	*n*Pr	Me	H	**2a**	93
2[c]	**1b**	cyclohexyl	Me	H	**2b**	92
3[c]	**1c**	*t*Bu	Me	H	**2c**	96
4	**1d**	Ph	Me	H	**2d**	99
5	**1e**	*p*-$F_3CC_6H_4$	Me	H	**2e**	quant.
6	**1f**	*p*-$MeOC_6H_4$	Me	H	**2f**	96
7	**1g**	CO_2Et	Me	H	**2g**	85
8	**1h**	Ph	TBS[d]	H	**2h**	99
9	**1i**	Ph	MPM[e]	H	**2i**	95
10	**1j**	Ph	TMSE[f]	H	**2j**	92
11	**1k**	*n*Pr	Et	Me	**2k**	92
12	**1l**	Ph	Et	Me	**2l**	98
13	**1m**	*n*Pr	$-(CH_2)_4-$		**2m**	98
14	**1n**	Ph	$-(CH_2)_4-$		**2n**	93

[a] The reaction of **1** (0.25 mmol) was carried out in the presence of AuCl (2 mol%) in toluene (1.25 mL) at 25 °C for 2 h. [b] Yield of isolated product. [c] 10 mol% of AuCl was used. [d] TBS = *tert*-butyldimethylsilyl. [e] MPM = (*p*-methoxyphenyl)methyl. [f] TMSE = 2-(trimethylsilyl)ethyl.

in 73% yield along with a small amount (16%) of bis(benzothienyl) methane **3** as a by-product. The use of CH_3CN, THF, or MeOH did not give any reaction. Substrates **1b** and **1c**, which have bulkier substituents at the R^1 position, afforded the desired products, **2b** and **2c**, respectively, in excellent yields with 10 mol% AuCl (Table 1, entries 2 and 3). The reactions of **1d**, **1e**, and **1f**, which bear an aryl group on the alkynyl moiety, gave the corresponding 2-aryl benzothiophenes **2d**, **2e**, and **2f**, respectively, in excellent yields (Table 1, entries 4–6). Ynoate **1g** was converted into the corresponding 2-benzothiophene carboxylate, **2g**, in 85% yield (Table 1, entry 7).[12] Substrates **1h**, **1i**, and **1j**, which had protective groups at the R^3 position, gave the corresponding protected 3-benzothienyl methanols **2h**, **2i**, and **2j** in 99, 95, and 92% yields, respectively (Table 1, entries 8–10). The reactions of 1-ethoxyethyl sulfides, **1k** and **1l**, and tetrahydropyranyl sulfides, **1m** and **1n**, proceeded smoothly (Table 1, entries 11–14). The (*p*-methoxyphenyl)methyl sulfide, **4a**, was converted into the corresponding benzothiophene, **5a**, in 98% yield in the presence of 2 mol% of AuCl, whereas benzyl sulfide **4b** did not react at all [Eq. (5)]. The reaction of



3



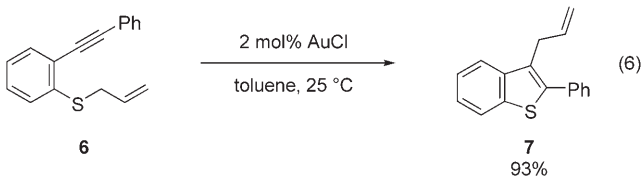
4 **5**

4a (R = OMe)
4b (R = H)

5a (R = OMe) 98% yield
(R = H) no reaction

(5)

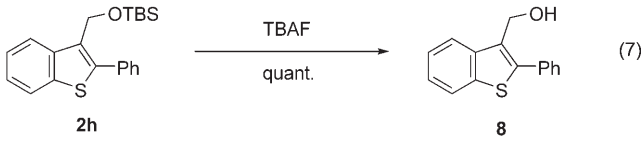
the allyl sulfide **6** proceeded smoothly to give the 3-allylbenzothiophene **7** in 93% yield [Eq. (6)]. (2-Phenylbenzothien-3-yl)methanol (**8**) was obtained quantitatively



6 **7**
93%

(6)

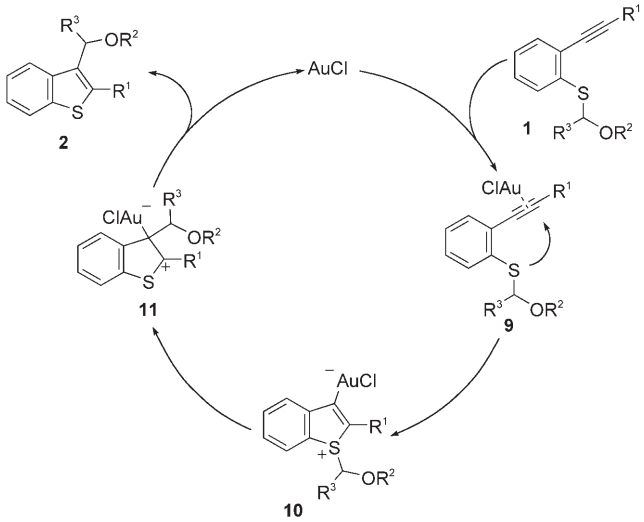
from **2h** by treatment with tetra-*n*-butylammonium fluoride [TBAF, Eq. (7)].



2h **8**

(7)

A plausible mechanism for the gold-catalyzed reaction of **1** is illustrated in Scheme 2. Gold(I) chloride is coordinated by



Scheme 2. Plausible mechanism for the catalytic formation of **2** from **1**.

the triple bond of substrate. Nucleophilic attack of the sulfur atom of **9** at the alkynyl moiety gives the cyclized intermediate **10**. Migration of the (α-alkoxy alkyl) group of **10** to the carbon atom bonded to the gold atom produces the intermediate **11**. Elimination of gold chloride from **11** gives the product **2**; the nature of this migration is not yet known.

In conclusion, we are now in a position to synthesize 2,3-disubstituted benzothiophenes in an efficient manner. As the present reaction proceeds through carbon–sulfur bond addition, so-called carbothiolation,[13] this methodology provides an atom-economic way of synthesizing sulfur-containing heteroarenes. Although multisubstituted benzothiophenes are often seen in biologically active compounds and organic materials, the catalytic construction of benzothiophene skeletons has been rarely investigated.[14] We expect this methodology to be useful in synthesizing biologically active or molecular-materials-oriented benzothiophene derivatives.[15]

 © 2006 Wiley-VCH Verlag GmbH & Co. KGaA, Weinheim

Experimental Section

Substrate **1** (0.25 mmol) in toluene (0.5 mL) was added to AuCl (1.16 mg, 0.005 mmol) in toluene (0.75 mL) in a pressure vial under an argon atmosphere. After the reaction mixture had been stirred at 25 °C for 2 h, it was filtered through a short column of silica gel by using ethyl acetate as eluent. The crude product was purified by silica-gel column chromatography with hexane/ethyl acetate as eluent to give **2**.

2a: IR (neat): $\tilde{\nu}$ = 3060, 2959, 2929, 2871, 2817, 1573, 1460, 1436, 1093, 760, 732 cm^{-1}; ^1H NMR (600 MHz, $CDCl_3$): δ = 1.01 (t, J = 7.2 Hz, 3H), 1.75 (m, 2H), 2.93 (t, J = 7.8 Hz, 2H), 3.38 (s, 3H), 4.46 (s, 2H), 7.27 (ddd, J = 8.4, 7.2, 1.2 Hz, 1H), 7.35 (ddd, J = 8.4, 7.2, 1.2 Hz, 1H), 7.76 ppm (m, 1H), 7.79 (m, 1H); ^{13}C NMR (150 MHz, $CDCl_3$): δ = 13.82, 24.99, 30.47, 57.76, 65.62, 121.75, 121.99, 123.71, 124.07, 127.60, 138.18, 140.10, 145.28 ppm; HRMS (ESI): m/z calcd for $C_{13}H_{16}OS$: 243.0814 $[M+Na]^+$; found: 243.0815.

Received: March 24, 2006
Published online: June 12, 2006

Keywords: cyclization · gold · homogeneous catalysis · sulfur heterocycles · synthetic methods

[1] C. D. Jones, M. G. Jevnikar, A. J. Pike, M. K. Peters, L. J. Black, A. R. Thompson, J. F. Falcone, J. A. Clemens, *J. Med. Chem.* **1984**, *27*, 1057 – 1066.
[2] M. Raga, C. Palacin, J. M. Castello, J. A. Ortiz, M. R. Cuberes, M. Moreno-Manas, *Eur. J. Med. Chem.* **1986**, *21*, 329 – 332.
[3] Acylation: a) C. Hansch, H. G. Lindwall, *J. Org. Chem.* **1945**, *10*, 381 – 385; b) K. C. Lee, B. S. Moon, J. H. Lee, K.-H. Chung, J. A. Katzenellenbogen, D. Y. Chi, *Bioorg. Med. Chem.* **2003**, *11*, 3649 – 3658. Halogenation: c) J. Szmuszkovicz, E. J. Modest, *J. Am. Chem. Soc.* **1950**, *72*, 571 – 577.
[4] a) A. R. Katritzky, S. N. Denisenko, D. C. Oniciu, I. Ghiviriga, *J. Org. Chem.* **1998**, *63*, 3450 – 3453; b) S. Kamila, C. Mukherjee, S. S. Mondal, A. De, *Tetrahedron* **2003**, *59*, 1339 – 1348; c) T. K. Pradhan, S. C. Ghosh, A. De, *ARKIVOC* **2003**, *9*, 158 – 173.
[5] For reviews, see: a) G. Battistuzzi, S. Cacchi, G. Fabrizi, *Eur. J. Org. Chem.* **2002**, 2671 – 2681; b) S. Cacchi, G. Fabrizi, A. Goggiomani, *Heterocycles* **2002**, *56*, 613 – 632; c) G. Balme, D. Bouyssi, T. Lomberget, N. Monteiro, *Synthesis* **2003**, *14*, 2115 – 2134; d) I. Nakamura, Y. Yamamoto, *Chem. Rev.* **2004**, *104*, 2127 – 2198; e) G. Zeni, R. C. Larock, *Chem. Rev.* **2004**, *104*, 2285 – 2309. For a recent report, see f) A. S. K. Hashmi, T. M. Frost, J. W. Bats, *Org. Lett.* **2001**, *3*, 3769 – 3771.
[6] A. M. Malte, C. E. Castro, *J. Am. Chem. Soc.* **1967**, *89*, 6770.
[7] For examples of palladium(0)-catalyzed *endo* cyclization, see: a) S. Cacchi, G. Fabrizi, L. Moro, *Synlett* **1998**, 741 – 745; b) N. Monterio, G. Balme, *Synlett* **1998**, 746 – 747; c) S. Cacchi, G. Fabrizi, P. Pace, *J. Org. Chem.* **1998**, *63*, 1001 – 1011; d) A. Arcadi, S. Cacchi, M. Del Rosario, G. Fabrizi, F. Marinelli, *J. Org. Chem.* **1996**, *61*, 9280 – 9288. For $PtCl_2$-catalyzed cyclizations, see: e) A. Fürstner, H. Szillat, F. Stelzer, *J. Am. Chem. Soc.* **2000**, *122*, 6785 – 6786; f) A. Fürstner, F. Stelzer, H. Szillat, *J. Am. Chem. Soc.* **2001**, *123*, 11863 – 11869.
[8] S. Cacchi, G. Fabrizi, L. Moro, *Tetrahedron Lett.* **1998**, *39*, 5101 – 5104.
[9] T. Shimada, I. Nakamura, Y. Yamamoto, *J. Am. Chem. Soc.* **2004**, *126*, 10546 – 10547.
[10] a) I. Nakamura, Y. Mizushima, Y. Yamamoto, *J. Am. Chem. Soc.* **2005**, *127*, 15022 – 15023; b) A. Fürstner, P. W. Davies, *J. Am. Chem. Soc.* **2005**, *127*, 15024 – 15025.
[11] For reviews on gold-catalyzed reaction, see: a) A. S. K. Hashmi, *Angew. Chem.* **2005**, *117*, 7150 – 7154; *Angew. Chem. Int. Ed.* **2005**, *44*, 6990 – 6993; b) S. Ma, S. Yu, Z. Gu, *Angew. Chem.* **2006**, *118*, 206 – 209; *Angew. Chem. Int. Ed.* **2006**, *45*, 200 – 203.
[12] $PtCl_2$ showed similar catalytic activity to that of AuCl towards the reaction. However, the reaction of **1g** in the presence of $PtCl_2$, instead of AuCl, did not proceed at all.
[13] a) K. Sugoh, H. Kuniyasu, T. Sugae, A. Ohtaka, Y. Takai, A. Tanaka, C. Machino, N. Kambe, H. Kurosawa, *J. Am. Chem. Soc.* **2001**, *123*, 5108 – 5109; b) M. Toyofuku, S.-I. Fujiwara, T. Shinike, H. Kuniyasu, N. Kambe, *J. Am. Chem. Soc.* **2005**, *127*, 9706 – 9707.
[14] M. C. Willis, D. Taylor, A. T. Gillmore, *Org. Lett.* **2004**, *6*, 4755 – 4757.
[15] For a review, see: a) C. M. Rayner, M. A. Graham, *Sci. Synth.* **2001**, *10*, 155 – 184; b) T. Y. Zhang, J. O'Toole, C. S. Proctor, *Sulfur Rep.* **1999**, *22*, 1 – 47; c) E. T. Pelkey, *Prog. Heterocycl. Chem.* **1999**, *11*, 102 – 123; d) C. Bianchini, A. Meli, *Synlett* **1997**, 643 – 649.

 © 2006 Wiley-VCH Verlag GmbH & Co. KGaA, Weinheim

Asymmetric Epoxidation

DOI: 10.1002/anie.200600840

Regio- and Enantioselective Epoxidation of Dienes by a Chiral Dioxirane: Synthesis of Optically Active Vinyl *cis*-Epoxides**

*Christopher P. Burke and Yian Shi**

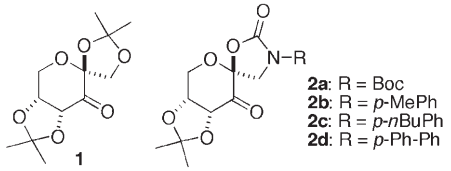
Optically active vinyl epoxides are very useful synthetic intermediates,[1] and enantioselective monoepoxidation of conjugated dienes presents an efficient approach to these compounds.[2,3] Enantioselective epoxidation of conjugated dienes using chiral (salen)Mn catalysts has been shown to proceed predominantly at the *cis*-olefin with high regioselectivity and high enantioselectivity.[3] In the case of acyclic dienes, the epoxidation gave optically active vinyl *trans*-epoxides as major products.[3a,b,d] Earlier, we reported that fructose-derived ketone **1** (Scheme 1) is effective for the regioselective epoxidation of conjugated dienes to provide vinyl *trans*- and trisubstituted epoxides with high *ee* values [Eq. (1)].[4,5] Nevertheless, an efficient synthesis of chiral vinyl *cis*-epoxides is still highly desirable.

[*] C. P. Burke, Prof. Dr. Y. Shi
Department of Chemistry
Colorado State University
Fort Collins, CO 80523 (USA)
Fax: (+1) 970-491-1801
E-mail: yian@lamar.colostate.edu

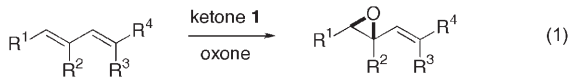
[**] We are grateful to the generous financial support from the General Medical Sciences of the National Institutes of Health (GM59705-07).

Supporting information for this article, including the characterization of epoxides and the data for the determination of the enantiomeric excesses of the epoxides, is available on the WWW under http://www.angewandte.org or from the author.

© 2006 Wiley-VCH Verlag GmbH & Co. KGaA, Weinheim

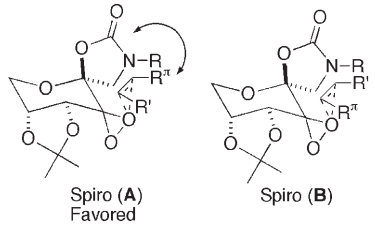


Scheme 1. Boc = *tert*-butyloxycarbonyl.



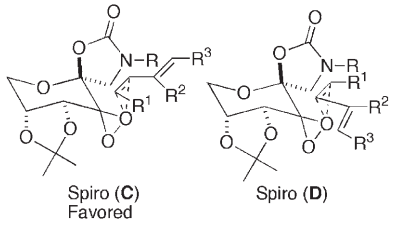
(1)

Recently, we found that oxazolidinone-containing ketone **2** provides high enantiomeric excesses for certain *cis*-olefins and styrenes.[6,7] Earlier studies suggest that spiro transition state **A** is favored over competing spiro **B** owing to an attraction between the R^{π} group of the olefin and the oxazolidinone moiety of the ketone catalyst (Scheme 2).[6,7]



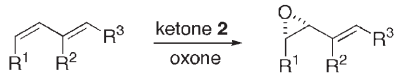
Scheme 2.

Up to this point, the R^{π} group has been primarily limited to aromatic groups. As part of our continuing efforts to further understand the interaction and expand the scope of this epoxidation, we examined the asymmetric epoxidation of conjugated dienes with ketone **2**. This study allows us to investigate whether alkenes can be effective directing groups to favor spiro transition state **C** (Scheme 3) and lead to the



Scheme 3.

synthesis of optically active vinyl *cis*-epoxides [Eq. (2)]. Herein, we report our preliminary efforts on this subject.



(2)

The epoxidation of conjugated dienes was carried out with ketone **2** as catalyst and oxone as oxidant. A variety of dienes are shown to be effective substrates, giving vinyl *cis*-epoxides with high *ee* values (Table 1).[8] The reactions were generally clean as judged by the ^{1}H NMR spectra of the crude reaction mixtures. The reactions were also stereospecific in that *cis*-olefins yielded only *cis*-epoxides, with no isomerization observed. The low isolated yields compared with the conversions in some cases were a result of the high sensitivity of vinyl epoxides towards flash column chromatography using silica gel.

Some of the reaction trends are highlighted as follows. Regioselectivity for the epoxidation is dependent on the type of diene. For *cis*/*trans*-dienes, it was found that the *cis*-olefins were epoxidized preferentially with high regioselectivity.[9] The epoxide derived from the *trans*-olefin was only detected in one case (Table 1, entry 7). A conjugated triene (Table 1, entry 9) also proved to be an effective substrate. As expected, *cis*/trisubstituted dienes showed competition for epoxidation between the two olefins. The degree of trisubstituted olefin epoxidation varied depending on the steric and electronic properties of the diene. If the trisubstituted olefin was deactivated electronically and/or sterically, *cis*-olefin epoxidation was favored (Table 1, entries 10 and 11).

In most cases, no further epoxidation of vinyl *cis*-epoxides was found, presumably due to the deactivation of the olefin by the epoxide. For entry 8 in Table 1, bis(epoxide) was detected. In this case, the *ee* value of the mono(epoxide) did not change at different conversions, thus indicating that no significant kinetic resolution occurred during the reaction. However, for entry 10 in Table 1, it was found that the *ee* value of the vinyl epoxide increased with the conversion, which suggests that kinetic resolution may be occurring.

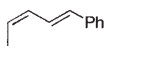
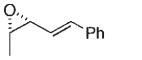
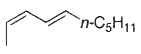
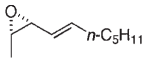
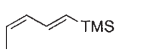
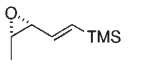
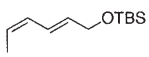
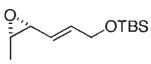
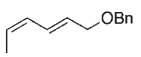
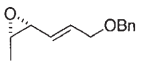
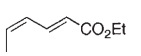
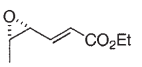
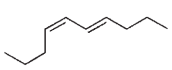
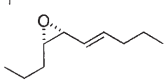
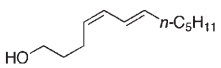
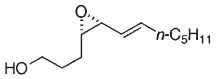
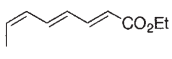
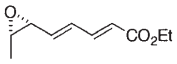
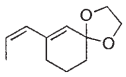
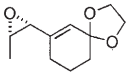
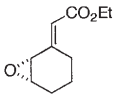
Changing the group on the 4-position of the aromatic ring of the catalyst had an effect on the enantioselectivity, likely due to additional interactions (possibly hydrophobic in nature) between this group and the substrate. The hydrophobic and hydrophilic nature of the R^1 and R^3 groups of the diene (Scheme 3) also have significant effects on the enantioselectivity of the epoxidation. Lower *ee* values were observed when the R^1 group was hydrophobic (Table 1, entry 7), presumably due to the increased hydrophobic interactions between the R^1 group and the N substituent of the catalyst in the competing spiro transition state **D** (Scheme 3). Conversely, higher *ee* values could be expected with more hydrophilic R^1 and/or more hydrophobic R^3 groups, thus further favoring spiro transition state **C** over **D** (for example, see Table 1, entry 8).

The stereochemistry of the epoxides shown in Table 1 is assigned on the basis of transition state spiro **C**. To further validate this model and the assigned stereochemistry, the absolute configurations of two representative examples (Table 1, entries 1 and 11) were determined [Eq. (3) and (4)] by converting the epoxide into a compound with known configuration.[10,11] The results in both cases support the initial assignment based on transition state spiro **C**.

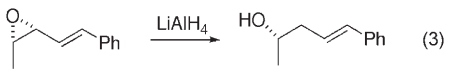
In summary, we report that a conjugating olefin is an effective group for the attraction between the oxazolidinone of the catalyst and the substrate. A variety of conjugated

 © 2006 Wiley-VCH Verlag GmbH & Co. KGaA, Weinheim

Table 1: Asymmetric epoxidation of dienes by ketone **2**.[a]

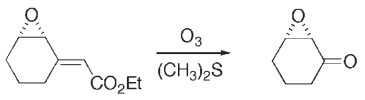
Entry	Diene	Epoxide	Ketone	Yield (Conv.) [%][b]	*ee* [%]
1			**2b**	66 (>95)[c,d]	85[e]
2			**2c**	47 (89)[f–h]	89[e]
3			**2d**	58 (100)[f,i]	92[j]
4			**2d**	64 (85)[f,g,k]	90[l]
5			**2d**	62 (98)[i]	90[l]
6			**2b**	64 (99)[i]	94[l]
7			**2d**	66 (88)[g,i,m,n]	76[l]
8			**2c**	80 (100)[c,f,i,o,p]	89[e]
9			**2b**	74 (99)[i]	94[l]
10			**2a**	61 (100)[f,i,q]	93[l]
11			**2b**	67 (>95)[c,i,r] [3b]	91[s]

[a] All reactions were carried out at −10°C with diene (1 equiv), ketone (0.1–0.3 equiv), oxone (1.6 equiv), and K_2CO_3 (6.7 equiv) in DME/DMM (3:1, v/v) and buffer (0.1 M K_2CO_3/AcOH in 1×10^{-4} M aq. EDTA, pH 9.3) for 4 h, unless otherwise stated. TMS = trimethylsilyl; TBS = *tert*-butyldimethylsilyl; Bn = benzyl; DME = 1,2-dimethoxyethane; DMM = dimethoxymethane; EDTA = ethylenediaminetetraacetic acid. [b] The conversion was determined by GC analysis of the crude reaction mixture. [c] The conversion was determined by ^{1}H NMR spectroscopy of the crude reaction mixture. [d] 0.10 equiv catalyst used. [e] Enantioselectivity was determined by chiral HPLC (Chiralcel OJ column). [f] Oxone and K_2CO_3 were added over 8 h. [g] 2.4 equiv oxone and 10.1 equiv K_2CO_3 were used. [h] 0.20 equiv catalyst used. [i] 0.25 equiv catalyst used. [j] Enantioselectivity was determined by chiral shift ^{1}H NMR spectroscopy with Eu(hfc)$_3$ (hfc = 3-(heptafluoropropylhydroxymethylene)-D-camphorate). [k] 0.30 equiv catalyst used. [l] Enantioselectivity was determined by Chiral GC (Chiraldex B-DM column). [m] Oxone and K_2CO_3 were added over 10 h. [n] 12:1 ratio of *cis*/*trans*-epoxides (regioselectivity) observed; the yield and *ee* for the *cis*-epoxide is given. [o] 0.96 equiv oxone and 4.0 equiv K_2CO_3 were used. [p] 10:1 ratio of mono/bis(epoxide)s observed; the yield and *ee* for the mono(epoxide) is given. [q] 1.8 equiv oxone and 4.0 equiv K_2CO_3 were used. [r] The isolated product is a mixture of *cis*-/trisubstituted epoxides (3.3:1); the *ee* value is given for the *cis*-epoxide. [s] Enantioselectivity was determined by chiral HPLC (Chiralcel OD column).



(3)

Configuration known



(4)

Configuration known

dienes can be epoxidized with high enantioselectivity using glucose-derived catalysts **2a–d** and oxone as oxidant. The epoxidations are stereospecific and no isomerization is observed to give *cis*-epoxides exclusively from *cis*-olefins. The regio- and enantioselectivity of the reaction are dependent on the substitution pattern of the diene system. With this methodology, a variety of enantioenriched vinyl *cis*-epoxides are now readily available.

Experimental Section

Representative procedure for asymmetric epoxidation (Table 1, entry 6). Buffer (0.1 M K_2CO_3/AcOH in 4×10^{-4} M aqueous EDTA, pH 9.3; 5 mL) and Bu_4NHSO_4 (0.0075 g, 0.02 mmol) were added with stirring to a solution of the diene (0.070 g, 0.50 mmol) and ketone **2b** (0.042 g, 0.125 mmol) in DME/DMM (3:1, v/v; 7.5 mL). The mixture was cooled to about −10°C (NaCl–ice bath temperature), and then a solution of oxone (0.20 M; 0.49 g, 0.80 mmol) in aqueous EDTA (4×10^{-4} M, 4.0 mL) and a solution of K_2CO_3 (0.84 M, 0.46 g, 3.36 mmol) in aqueous EDTA (4×10^{-4} M, 4.0 mL) were added dropwise simultaneously over a period of 4 h through a syringe pump. The reaction was then quenched with the addition of petroleum ether and extracted with a mixture (1:1, v/v) of petroleum ether/diethyl ether. The combined organic layers were washed with water and brine, dried (Na_2SO_4), filtered and concentrated, and the residue was purified by flash chromatography (the silica gel was buffered with 1% Et_3N in petroleum ether; petroleum ether/diethyl ether (1:0 to 19:1, v/v) was used as eluent) to give the *cis*-epoxide as a colorless oil (0.050 g, 64% yield, 94% *ee*).

Received: March 4, 2006
Published online: June 9, 2006

Keywords: asymmetric synthesis · dienes · epoxidation · synthetic methods

[1] For leading references on synthetic applications of vinyl epoxides, see: a) B. M. Trost, *Angew. Chem.* **1989**, *101*, 1199; *Angew. Chem. Int. Ed. Engl.* **1989**, *28*, 1173; b) J. A. Marshall, *Chem. Rev.* **1989**, *89*, 1503; c) H. C. Kolb, M. S. VanNieuwenhze, K. B. Sharpless, *Chem. Rev.* **1994**, *94*, 2483.

[2] For leading references on enantioselective monoepoxidations of conjugated dienes directed by hydroxy groups, see: a) R. A. Johnson, K. B. Sharpless in *Catalytic Asymmetric Synthesis* (Ed.: I. Ojima), VCH, New York, **1993**, Chap. 4.1; b) T. Katsuki, V. S. Martin, *Org. React.* **1996**, *48*, 1.

[3] For leading references on enantioselective epoxidation of *cis*-olefins of conjugated dienes using chiral (salen)Mn catalysts,

 © 2006 Wiley-VCH Verlag GmbH & Co. KGaA, Weinheim

see: a) N. H. Lee, E. N. Jacobsen, *Tetrahedron Lett.* **1991**, *32*, 6533; b) S. Chang, N. H. Lee, E. N. Jacobsen, *J. Org. Chem.* **1993**, *58*, 6939; c) S. Chang, R. M. Heid, E. N. Jacobsen, *Tetrahedron Lett.* **1994**, *35*, 669; d) W. Zhang, N. H. Lee, E. N. Jacobsen, *J. Am. Chem. Soc.* **1994**, *116*, 425; e) T. Hamada, R. Irie, T. Katsuki, *Synlett* **1994**, 479; f) D. Mikame, T. Hamada, R. Irie, T. Katsuki, *Synlett* **1995**, 827–828; g) M. F. Hentemann, P. L. Fuchs, *Tetrahedron Lett.* **1997**, *38*, 5615.

[4] M. Frohn, M. Dalkiewicz, Y. Tu, Z.-X. Wang, Y. Shi, *J. Org. Chem.* **1998**, *63*, 2948.

[5] For leading reviews on chiral ketone catalyzed asymmetric epoxidations, see: a) S. E. Denmark, Z. Wu, *Synlett* **1999**, 847; b) M. Frohn, Y. Shi, *Synthesis* **2000**, 1979; c) Y. Shi, *Acc. Chem. Res.* **2004**, *37*, 488; d) D. Yang, *Acc. Chem. Res.* **2004**, *37*, 497.

[6] a) H. Tian, X. She, L. Shu, H. Yu, Y. Shi, *J. Am. Chem. Soc.* **2000**, *122*, 11551; b) H. Tian, X. She, H. Yu, L. Shu, Y. Shi, *J. Org. Chem.* **2002**, *67*, 2435; c) L. Shu, P. Wang, Y. Gan, Y. Shi, *Org. Lett.* **2003**, *5*, 293; d) L. Shu, Y. Shi, *Tetrahedron Lett.* **2004**, *45*, 8115.

[7] a) H. Tian, X. She, J. Xu, Y. Shi, *Org. Lett.* **2001**, *3*, 1929; b) M. Hickey, D. Goeddel, Z. Crane, Y. Shi, *Proc. Natl. Acad. Sci. USA* **2004**, *101*, 5794; c) D. Goeddel, L. Shu, Y. Yuan, O. A. Wong, B. Wang, Y. Shi, *J. Org. Chem.* **2006**, *71*, 7115.

[8] For some examples of racemic epoxidations of conjugated dienes and polyenes with dimethyldioxirane, see: a) R. Curci, M. Fiorentino, L. Troisi, J. O. Edwards, R. H. Pater, *J. Org. Chem.* **1980**, *45*, 4758; b) W. Ebenezer, G. Pattenden, *Tetrahedron Lett.* **1992**, *33*, 4053; c) R. Curci, A. Detomaso, T. Prencipe, G. B. Carpenter, *J. Am. Chem. Soc.* **1994**, *116*, 8112; d) R. Curci, A. Detomaso, M. E. Lattanzio, G. B. Carpenter, *J. Am. Chem. Soc.* **1996**, *118*, 11089; e) R. W. Murray, M. Singh, N. Rath, *Tetrahedron Lett.* **1996**, *37*, 8671; f) R. W. Murray, M. Singh, N. Rath, *J. Org. Chem.* **1997**, *62*, 8794; g) D. Yang, M.-K. Wong, K.-K. Cheung, E. W. C. Chan, Y. Xie, *Tetrahedron Lett.* **1997**, *38*, 6865.

[9] It was observed that *cis*-olefins were epoxidized faster than *trans*-olefins with dimethyldioxirane, see: A. L. Baumstark, C. J. McCloskey, *Tetrahedron Lett.* **1987**, *28*, 3311.

[10] T. Hayashi, M. Konishi, M. Kumada, *J. Org. Chem.* **1983**, *48*, 281.

[11] M. Aoki, D. Seebach, *Helv. Chim. Acta* **2001**, *84*, 187.

 © 2006 Wiley-VCH Verlag GmbH & Co. KGaA, Weinheim

Donor–Acceptor Systems

DOI: 10.1002/anie.200504354

Control over Electron Transfer in Tetrathiafulvalene-Modified Single-Walled Carbon Nanotubes**

M. Ángeles Herranz, Nazario Martín, Stéphane Campidelli, Maurizio Prato,* Georg Brehm, and Dirk M. Guldi**

Fullerenes and, more recently, carbon nanotubes (CNTs) have emerged as an innovative and new class of nanoscale carbon-based materials that are currently under intensive investigation.[1] The excitement in this area is, by large, a consequence of their promising functions in molecular-scale electronic applications. In stark contrast to the wealth of [60]fullerene-based donor–acceptor dyads studied so far,[2] the incorporation of single-walled carbon nanotubes (SWNTs) into donor–acceptor ensembles has been scarcely explored, and only a few examples involving the covalent linkage of electroactive species are known.[3] For example, some of us reported the functionalization of SWNTs with electron-donating ferrocene and confirmed that in this particular case electron transfer occurred from the ferrocene to the photoexcited SWNT. This initial work stimulated the use of SWNT nanoconjugates in solar energy conversion applications.[4] However, control over the electron transfer in SWNTs remains a central but unsolved topic.

[*] Dr. M. Á. Herranz, Prof. Dr. N. Martín
Departamento de Química Orgánica
Facultad de Química
Universidad Complutense
28040 Madrid (Spain)
Fax: (+34) 91-394-4103
E-mail: nazmar@quim.ucm.es

Dr. S. Campidelli, Prof. Dr. M. Prato
Dipartimento di Scienze Farmaceutiche
Università di Trieste
Piazzale Europa, 1, 34127 Trieste (Italy)
Fax: (+39) 040-52-572
E-mail: prato@unis.it

Dr. G. Brehm, Prof. Dr. D. M. Guldi
Friedrich-Alexander-Universität Erlangen-Nürnberg
Institute for Physical Chemistry
Egerlandstrasse 3, 91058 Erlangen (Germany)
Fax: (+49) 9131-852-8307
E-mail: dirk.guldi@chemie.uni-erlangen.de

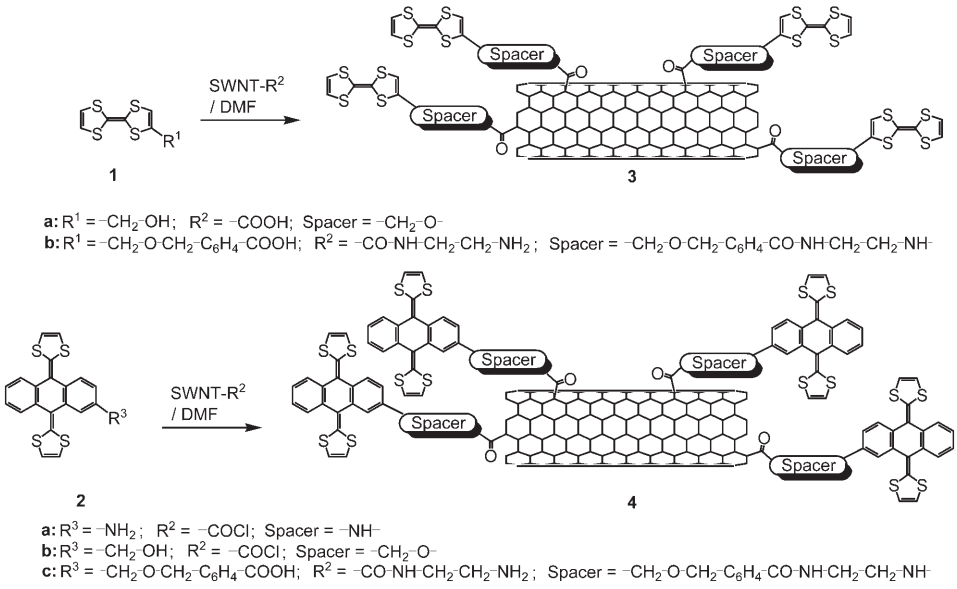
[**] This work was supported by the MEC of Spain (project CTQ2005-02609/BQU), the CAM (project P-PPQ-000225-0505), the UCM (project PR1/05), the European Union (TRN network WONDERFULL), the MIUR (PRIN 2004, no. 2004035502), the Deutsche Forschungs-gemeinschaft (SFB 583), FCI, and the Office of Basic Energy Sciences of the US Department of Energy (NDRL no. 4661). We thank Christian Ehli and G. M. Aminur Rahman for their useful discussions. M.A.H. would like to acknowledge the CICYT for a "Ramón y Cajal" contract.

Supporting information for this article is available on the WWW under http://www.angewandte.org or from the author.

WILEY InterScience DISCOVER SOMETHING GREAT
© 2006 Wiley-VCH Verlag GmbH & Co. KGaA, Weinheim

Herein, we focus on the first series of structurally well-defined and electronically fine-tuned donor–acceptor SWNT nanoconjugates, in which tetrathiafulvalene (TTF) and/or π-extended tetrathiafulvalene (exTTF) are integrated as electron donors. Previous studies have illustrated the remarkable and numerous benefits of utilizing TTF or exTTF in electron-transfer events.[5] Here we provide, for the first time, a complete spectroscopic characterization of charge-separation products in photoexcited TTF–SWNT and exTTF–SWNT conjugates, that is, the generation of reduced and oxidized components, and a kinetic analysis that documents the successful control over the charge recombination processes by structural variation.

In our strategy, the as-prepared HIPco SWNTs were purified, shortened, and modified with carboxylic groups by treatment with HNO_3 and H_2SO_4/H_2O_2 (Scheme 1).[6] Compound **3a** was obtained by an esterification reaction between



Scheme 1. Synthesis of TTF- and exTTF-functionalized SWNTs.

the short SWNT containing carboxylic acid groups and hydroxymethyl-substituted TTF (**1a**)[7] in the presence of 3-(3-dimethylaminopropyl)-1-ethylcarbodiimide (EDC) and 1-hydroxy-1*H*-benzotriazole (HOBt). For the synthesis of compounds **4a**,**b**, suitably functionalized short SWNTs (SWNT-COOH) were first treated with thionyl chloride to generate the respective acyl chloride functionalities and then treated with amine **2a**[8] or alcohol **2b**.[8] The TTF–SWNT and exTTF–SWNT nanoconjugates **3b** and **4c**, respectively, were obtained upon esterification of the corresponding carboxylic acids (**1b** and **2c**)[9] with short SWNTs, previously treated with ethylenediamine, in the presence of EDC and HOBt (see the Supporting Information for experimental details).

Compounds **3a**,**b** and **4a–c** were fully characterized by standard analytical and spectroscopic techniques such as FTIR, Raman, UV/Vis, thermogravimetric analysis (TGA), transmission electron microscopy (TEM), and atomic force microscopy (AFM). Importantly, the recorded FTIR spectra reveal the characteristic fingerprints of the amide and/or ester functionalities in the SWNT nanoconjugates (**3a**,**b** and **4a–c**). Although some of the characteristic van Hove singularities of the SWNTs are observed in the near-infrared region of the absorption spectra (see the Supporting Information), the TTF and exTTF features—predominantly in the visible range—are nearly entirely masked. The Raman spectra, on the other hand, of all the SWNT samples (SWNT-COOH, SWNT–TTF **3a**,**b**, SWNT–exTTF **4a–c**) reveal intense disorder bands (D band) prior to and after the condensation reaction. However, a decrease in the relative intensities, using the G band as internal reference, of these bands was observed upon condensation (see the Supporting Information). This behavior has previously been observed in some related systems.[10] In addition, the G band is noticeably downfield shifted in the spectra of the donor–acceptor nanoconjugates (**3a**,**b** and **4a–c**) relative to that seen in the reference SWNT. This observation is consistent with studies of charge-transfer reactions of SWNTs doped with either donor or acceptor groups.[11]

The functionalization of the nanotubes has also been investigated by TGA under nitrogen. Both SWNT-COOH and SWNT-$CONHCH_2CH_2NH_2$ present a weight loss of about 23% between 200 and 600 °C which corresponds to the destruction of the organic groups present on the surface of the nanotubes. The functionalized nanotubes **3a**,**b** and **4a–c** exhibit a weight loss of about 27–34% in the same temperature range (see the Supporting Information). Thus the TGA results indicate that the SWNT–TTF and SWNT–exTTF nanoconjugates all show a similar behavior upon heating. As expected, the increased weight loss compared to their respective precursors stems from the covalent linkage of the TTF/exTTF moieties to the sidewalls of the nanotubes.

The presence of SWNTs in all the studied samples was corroborated by means of TEM and AFM (a representative TEM picture is shown in the Supporting Information). SWNTs are present as aggregates of several micrometers length and also as small bundles with diameters of 20 to 50 nm, in which very thin bundles or individual tubes can be seen at the edges. These characteristics are fundamentally different from those of the starting HIPco SWNTs (www.cnanotech.com), which exhibit thick and long bundles exclusively. Complementary AFM investigations (Figure 1) permitted a more detailed insight into the SWNT–TTF and SWNT–exTTF nanoconjugates. The samples were prepared by spin coating solutions of SWNT–TTF and SWNT–exTTF in DMF on to silicon wafers. This technique allowed us to visualize very thin bundles (several hundreds of nanometers long and 3 to 10 nm in diameter) as well as individual tubes (100–500 nm long and 1.2–1.7 nm in diameter).

 © 2006 Wiley-VCH Verlag GmbH & Co. KGaA, Weinheim

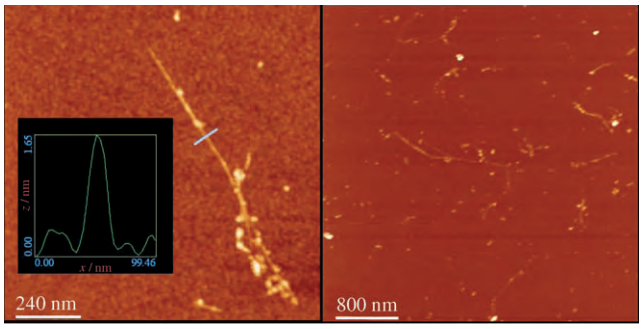


Figure 1. AFM images of SWNT–exTTF nanoconjugate **4a** on a silicon wafer. Right: a general view of the sample, left: a small aggregate of nanotubes.

The electrochemical properties of **3a**,**b** and **4a–c** were investigated in saturated solutions of DMF and THF containing 0.1 M nBu$_4$NClO$_4$ in an argon atmosphere. The voltammograms display a continuum of diffusion-controlled cathodic current, with an onset at around −0.4 V, which is attributed (in accordance with previous studies[12]) to the reductive charging of the SWNTs. Single two-electron and chemically reversible oxidation processes are clearly discernible for derivatives **4a–c**. We assign them to exTTF-centered processes, even though they are positively shifted by approximately 100 mV relative to the reference systems **2a–c** (Figure 2). These shifts are likely a result of weak intramolecular electronic interactions between the electroactive units in the nanoconjugates. In sharp contrast, the characteristic two one-electron and chemically reversible oxidation steps of TTF in **3a**,**b** were observed as a broad peak, most probably involving both oxidation processes (see the Supporting Information). Based on the electrochemical data, the lowest energy levels of the (SWNT)$^{\bullet-}$–(TTF)$^{\bullet+}$ or (SWNT)$^{\bullet-}$–(exTTF)$^{\bullet+}$ conjugates are estimated to lie between 0.65 and 0.80 eV.

Notably, our approach towards dispersable donor–acceptor nanoconjugates preserves, although not entirely but at least in part, the electronic structure of the SWNTs.[13] The presence of the van Hove singularities in the near-infrared region further supports this assumption. Consequently, near-infrared fluorescence spectroscopy emerges as a viable method to probe excited state interactions (that is, photoinduced charge separation) between photoexcited SWNTs (that is, with radiative lifetimes and nonradiative lifetimes as long as 3 μs and 500 ps, respectively[14]) and the covalently linked donor moieties. An illustration is given in Figure 3, from which two important observations were deduced. Firstly, sets of fluorescence features are seen mirror imaged to the absorptive transitions. A likely rationale implies fluorescence from the semiconducting SWNTs. Secondly, a systematic quenching trend is discernable when comparing the fluorescence of the SWNTs with that of the SWNT–TTF or SWNT–exTTF conjugates. The quenching is significantly enhanced when shorter linkers are used to connect the TTF or exTTF units to the SWNTs.

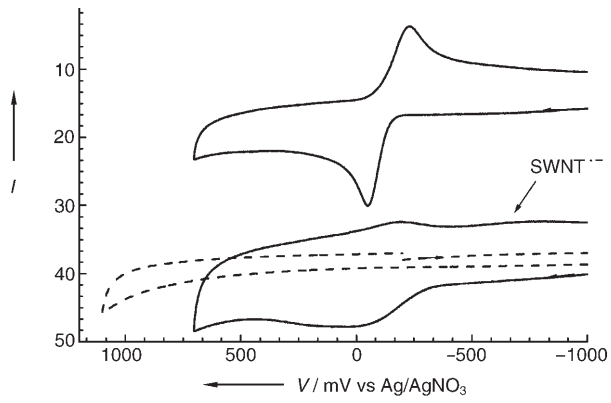


Figure 2. Cyclic voltammograms obtained for **2b** (0.5 mM; top) and **4b** (saturated solution, bottom) in a 0.1 M nBu$_4$NClO$_4$/DMF solution. Sweep rate = 500 mV s^{-1}, T = 25 °C, working electrode: glassy carbon, reference electrode: Ag/AgNO$_3$, and counter electrode: Pt wire. The dashed line corresponds to the background signal.

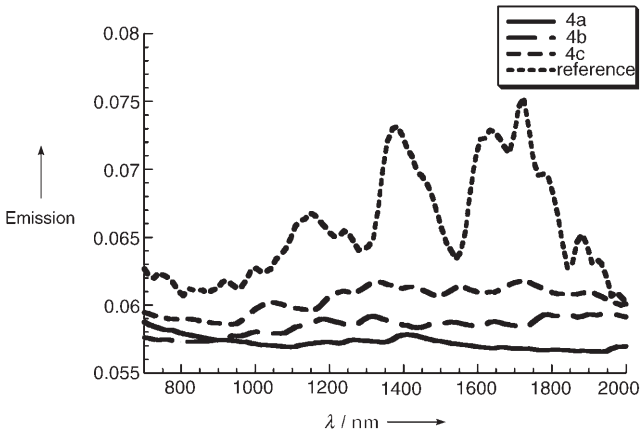


Figure 3. Near-infrared fluorescence of SWNT-COOH and SWNT–exTTF nanoconjugates **4a–c** with matching absorption at 600 nm.

Spectroscopic confirmation for the assumed charge separation came from transient absorption measurements performed with SWNT-COOH as well as the SWNT–TTF and SWNT–exTTF ensembles. Under the chosen conditions, laser excitation at 308, 337, or 355 nm, respectively, the reference conjugate SWNT-COOH in THF shows a fairly broad and long-lived transient species (see the Supporting Information). In stark contrast, nanosecond excitation of fine dispersions of SWNT–TTF and SWNT–exTTF in THF gave rise in the visible range (Figure 4) to the well-known signatures, namely, transitions at 440 nm and 660 nm, respectively, of the TTF and exTTF radical cations.[15] To gather evidence for the reduction of the SWNTs we examined the near-infrared region of the spectrum. In this region, the radical cation absorptions of the donor fragments are negligible and the van Hove singularities of the SWNTs constitute the major absorbing species. In fact, pulse radiolytic reduction experiments with aqueous suspensions of SWNTs, either in the form of a covalent nanoconjugate (SWNT–PSS) or noncovalent nanohybrid (SWNT/pyrene$^+$), led to characteristic spectra.[16] The fact that we found such features in the present cases (Figure 4) lead us to postulate that the SWNTs are indeed reduced. In conclusion, the spectra recorded after nanosecond photolysis appear as

 © 2006 Wiley-VCH Verlag GmbH & Co. KGaA, Weinheim

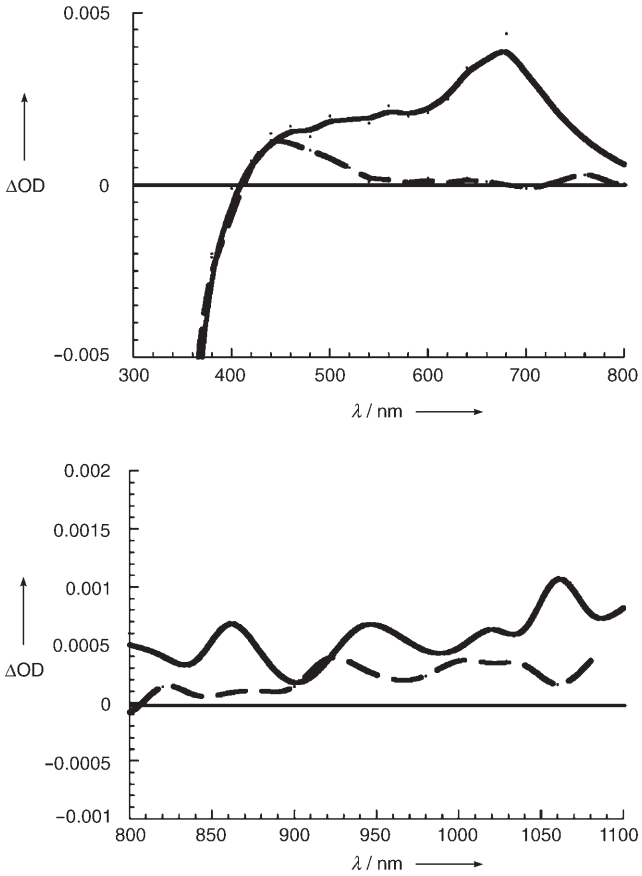


Figure 4. Differential absorption spectra (Vis: top and NIR: bottom) obtained upon nanosecond flash photolysis (532 nm) of **3b** (dashed line) and **4c** (solid line) in nitrogen-saturated THF solutions with a time delay of 150 ns.

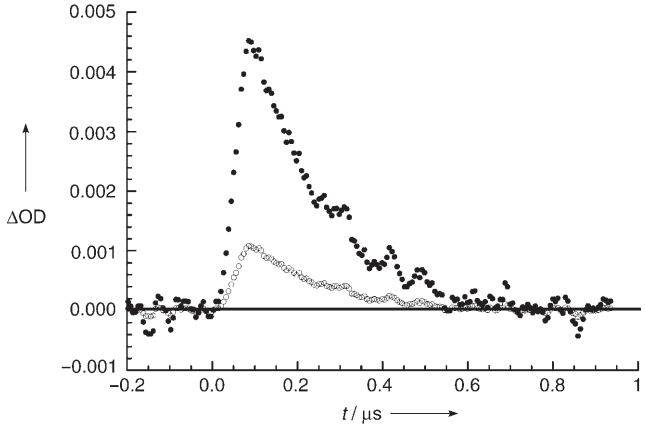


Figure 5. Time absorption profiles of the decay of the radical ion pairs of **4c** at 660 nm (filled circles: oxidized exTTF) and 1060 nm (open circles: reduced SWNT).

composite spectra showing the attributes of the oxidized donor and the reduced acceptor components within the photoexcited SWNT–TTF or SWNT–exTTF nanoconjugates.[17]

Kinetic analysis of the different SWNT–TTF and SWNT–exTTF nanoconjugates allowed evaluation of the fate of the charge-separated state, that is, evaluation of the charge-recombination dynamics as a function of the donor–acceptor separation. An example of the decay profiles is given in Figure 5. Interestingly, extending the linkage length leads to a stabilization of the charge-separated states, despite some structural flexibility. The lifetimes, on the other hand, in the exTTF-containing nanoconjugates (**4a**: 160 ns; **4b**: 275 ns; **4c**: 335 ns) are appreciably extended relative to the analogous TTF nanoconjugates (**3a**: 190 ns; **3b**: 230 ns).

Two energy levels are important when considering the absorption of photons in SWNTs: the one that relates to free carrier thresholds, that is, free electron/hole pair continuum, and the one that relates to exciton thresholds, that is, strongly correlated electron-hole pairs (see the Supporting Information).[14] When photons that are equal to or greater in energy than the band gap are absorbed the elementary excitation is strongly excitonic in nature, based on the fairly high exciton binding energies (Coulomb interactions). It is implicit that the spatial separation is tunable by many means. Secondary processes can, however, still afford the free electron/hole pair continuum. Alternatively, nonradiative processes from the lower lying exciton threshold are likely to populate longer-lived trap states. However, the important question about the nature of the precursor of the radical ion pair state still remains to be properly assessed.

In conclusion, time-resolved spectroscopy has helped to identify reduced SWNT and oxidized TTF and/or exTTF as metastable states in a series of donor–acceptor nanoconjugates. Overall, remarkable lifetimes in the range of hundreds of nanoseconds have been noted. Most importantly, we have succeeded for the first time in controling the rate of electron transfer, namely, charge separation and charge recombination, by either systematically altering the relative donor–acceptor separations (**4a** versus **4b** versus **4c**) or by integrating different electron donors (**3** versus **4**).

Received: December 7, 2005
Revised: March 29, 2006
Published online: June 12, 2006

Keywords: charge separation · donor–acceptor systems · electron transfer · nanotubes · tetrathiafulvalenes

[1] a) *Carbon Nanotubes: Synthesis, Structure, Properties and Applications* (Eds.: M. S. Dresselhaus, G. Dresselhaus, P. Avouris), Springer, Berlin, **2001**; b) S. Reich, C. Thomsen, J. Maultzsch, *Carbon Nanotubes: Basic Concepts and Physical Properties*, Wiley-VCH, Weinheim, **2004**.

[2] For recent reviews, see: a) H. Imahori, *J. Phys. Chem. B* **2004**, *108*, 6130–6143; b) L. Sánchez, N. Martín, D. M. Guldi, *Angew. Chem.* **2005**, *117*, 5508–5516; *Angew. Chem. Int. Ed.* **2005**, *44*, 5374–5382; c) J. L. Segura, N. Martín, D. M. Guldi, *Chem. Soc. Rev.* **2005**, *34*, 31–47; d) L. Sánchez, M. A. Herranz, N. Martín, *J. Mater. Chem.* **2005**, *15*, 1409–1421.

[3] For representative examples, see: a) L. W. Qu, R. B. Martin, W. J. Huang, K. F. Fu, D. Zweifel, Y. Lin, Y.-P. Sun, C. E. Bunker, B. A. Harruff, J. R. Gord, L. F. Allard, *J. Chem. Phys.* **2002**, *117*, 8089–8094; b) N. Nakashima, Y. Tomonari, H. Murakami, *Chem. Lett.* **2002**, 638–639; c) M. Alvaro, P. Atienzar, P. de la Cruz, J. L. Delgado, H. García, F. Langa, *J. Phys. Chem.*

 © 2006 Wiley-VCH Verlag GmbH & Co. KGaA, Weinheim

B **2004**, *108*, 12691 – 12697; d) H. Li, R. B. Martin, B. A. Harruff, R. A. Carino, L. F. Allard, Y.-P. Sun, *Adv. Mater.* **2004**, *16*, 896 – 900; e) D. Baskaran, J. W. Mays, X. P. Zhang, M. S. Bratcher, *J. Am. Chem. Soc.* **2005**, *127*, 6916 – 6917.

[4] D. M. Guldi, M. Marcaccio, D. Paolucci, F. Paolucci, N. Tagmatarchis, D. Tasis, E. Vázquez, M. Prato, *Angew. Chem.* **2003**, *115*, 4338 – 4341; *Angew. Chem. Int. Ed.* **2003**, *42*, 4206 – 4209.

[5] See our studies on fullerene-based systems: a) N. Martín, L. Sánchez, D. M. Guldi, *Chem. Commun.* **2000**, 113 – 114; b) M. A. Herranz, N. Martín, J. Ramey, D. M. Guldi, *Chem. Commun.* **2002**, 2968 – 2969; c) L. Sánchez, I. Pérez, N. Martín, D. M. Guldi, *Chem. Eur. J.* **2003**, *9*, 2457 – 2468; d) M. Segura, L. Sánchez, J. de Mendoza, N. Martín, D. M. Guldi, *J. Am. Chem. Soc.* **2003**, *125*, 15093 – 15100; e) F. Giacalone, J. L. Segura, N. Martín, D. M. Guldi, *J. Am. Chem. Soc.* **2004**, *126*, 5340 – 5341; f) F. Giacalone, N. Martín, J. Ramey, D. M. Guldi, *Chem. Eur. J.* **2005**, *11*, 4819 – 4834, and references therein.

[6] a) J. Liu, A. G. Rinzler, H. Dai, J. H. Hafner, R. K. Bradley, P. J. Boul, A. Lu, T. Iverson, K. Shelimov, C. B. Huffman, F. Rodriguez-Marcias, Y.-S. Shon, T. R. Lee, D. T. Colbert, R. E. Smalley, *Science*, **1998**, *280*, 1253 – 1256; b) K. J. Ziegler, Z. Gu, H. Peng, E. L. Flor, R. H. Hauge, R. E. Smalley, *J. Am. Chem. Soc.* **2005**, *127*, 1541 – 1547.

[7] J. Garín, J. Orduna, S. Uriel, A. J. Moore, M. R. Bryce, S. Wegener, D. S. Yufit, A. K. J. Howard, *Synthesis* **1994**, 489 – 493.

[8] a) See the Supporting Information for the synthesis and full characterization of compound **2a**; b) for the preparation of **2b** see: S. González, N. Martín, D. M. Guldi, *J. Org. Chem.* **2003**, *68*, 779 – 791.

[9] a) Compound **1b** was prepared following a modified procedure by: A. Kanibolotsky, S. Roquet, M. Cariou, P. Leriche, C.-O. Turrin, R. de Bettignies, A.-M. Caminade, J.-P. Majoral, V. Khodorkovsky, A. Gorgues, *Org. Lett.* **2004**, *6*, 2109 – 2112; b) see the Supporting Information for the synthesis and full characterization of **2c**.

[10] M. Prato, M. Meneghetti, unpublished data.

[11] U. J. Kim, C. A. Furtado, X. Liu, G. Chen, P. C. Eklund, *J. Am. Chem. Soc.* **2005**, *127*, 15437 – 15445.

[12] M. Melle-Franco, M. Marcaccio, D. Paolucci, F. Paolucci, V. Georgakilas, D. M. Guldi, M. Prato, F. Zerbetto, *J. Am. Chem. Soc.* **2003**, *125*, 1646 – 1647.

[13] For donor–acceptor SWNT ensembles preserving the electronic structure of SWNT, see for example: a) D. M. Guldi, G. M. A. Rahman, N. Jux, N. Tagmatarchis, M. Prato, *Angew. Chem.* **2004**, *116*, 5642 – 5646; *Angew. Chem. Int. Ed.* **2004**, *43*, 5526 – 5530; b) D. M. Guldi, G. M. A. Rahman, M. Prato, N. Jux, Sh. Qin, W. Ford, *Angew. Chem.* **2005**, *117*, 2051 – 2054; *Angew. Chem. Int. Ed.* **2005**, *44*, 2015 – 2018; c) D. M. Guldi, H. Taieb, G. M. A. Rahman, N. Tagmatarchis, M. Prato, *Adv. Mater.* **2005**, *17*, 871 – 875; d) D. M. Guldi, G. M. A. Rahman, N. Jux, D. Balbinot, U. Hartnagel, N. Tagmatarchis, M. Prato, J. *Am. Chem. Soc.* **2005**, *127*, 9830 – 9838.

[14] a) C. S. Sheng, Z. V. Vardeny, A. B. Dalton, R. H. Baughman, *Synth. Met.* **2005**, *155*, 254 – 257; b) A. Hagen, M. Steiner, M. R. Raschke, C. Lienau, T. Hertel, H. Qian, A. J. Meixner, A. Hartschuh, *Phys. Rev. Lett.* **2005**, *95*, 197401; c) F. Wang, G. Dukovic, L. E. Brus, T. F. Heinz, *Science* **2005**, *308*, 838 – 841; d) Y. Z. Ma, L. Valkunas, S. M. Bachilo, G. R. Fleming, *J. Phys. Chem. B* **2005**, *109*, 15671 – 15674; e) F. Wang, G. Dukovic, L. E. Brus, T. F. Heinz, *Phys. Rev. Lett.* **2004**, *92*, 177401.

[15] D. M. Guldi, L. Sanchez, N. Martín, *J. Phys. Chem. B* **2001**, *105*, 7139 – 7144.

[16] D. M. Guldi, G. M. A. Rahman, V. Sgobba, N. A. Kotov, D. Bonifazi, M. Prato, *J. Am. Chem. Soc.* **2006**, *128*, 2315 – 2323.

[17] The fact that the transient features on the nanosecond time scale are instantaneous rules out any intermolecular processes.

 © 2006 Wiley-VCH Verlag GmbH & Co. KGaA, Weinheim

Controlled Radical Polymerization

DOI: 10.1002/anie.200600272

Activators Regenerated by Electron Transfer for Atom-Transfer Radical Polymerization of (Meth)acrylates and Related Block Copolymers**

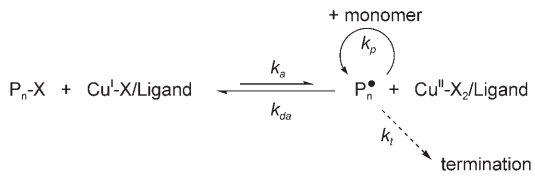
*Wojciech Jakubowski and Krzysztof Matyjaszewski**

Atom-transfer radical polymerization (ATRP) is a controlled or living radical polymerization (CRP) technique[1,2] that enables the preparation of new nanostructured materials that are not accessible by conventional free-radical polymerization (FRP). Reported herein is the ATRP of polar monomers such as (meth)acrylates and related block copolymers by means of a new initiating/catalytic method based on activators regenerated by electron transfer (ARGET) with ppm (10^{-4} mol% vs. monomer) amounts of Cu catalyst.[3]

ATRP[4–7] provides a simple route to many well-defined (co)polymers with precisely controlled functionalities, topologies, and compositions.[8–10] It has been very successfully applied to the preparation of many nanocomposites, hybrids, and bioconjugates.[11–23] The advantages of ATRP, in comparison with other CRP processes, include the large range of available monomers and (macro)initiators, the simplicity of reaction setup, and the ability to conduct the process over a large range of temperatures, solvents, and dispersed media.[6,7,24]

ATRP (Scheme 1) is a repetitive atom-transfer process between a macromolecular alkyl halide P_n–X and a redox-active transition-metal complex Cu^I–X/ligand in which $P_n^\bullet$ radicals propagate (rate constant of propagation k_p) and are reversibly formed (rate constants k_a and k_{da}). The growing radicals also terminate by coupling or disproportionation (rate constant k_t).

An inherent feature, but also a limitation of ATRP, is the presence of a catalyst (a transition-metal complex with



Scheme 1. Mechanism for ATRP.

[*] W. Jakubowski, Prof. K. Matyjaszewski
Center for Macromolecular Engineering
Department of Chemistry
Carnegie Mellon University
4400 Fifth Avenue, Pittsburgh, Pennsylvania 15213 (USA)
Fax: (+1) 412-268-6897
E-mail: km3b@andrew.cmu.edu

[**] The authors thank the National Science Foundation (DMR-05-49353 and CHE-04-05627) and the members of the CRP Consortium at Carnegie Mellon University for financial support, and Ke Min for the synthesis of P*n*BA using glucose as reducing agent in ARGET ATRP.

InterScience
© 2006 Wiley-VCH Verlag GmbH & Co. KGaA, Weinheim

various ligands). The catalyst is not bound to the end of the chain, as it is in coordination polymerization, and can therefore be used in a controlled or living process with substoichiometric amounts with respect to the initiator. Nevertheless, it is typically used at concentrations ranging from 0.1 to 1 mol% with respect to the monomer and therefore needs to be removed from the final polymer. There have been several attempts to remove and recycle the catalyst efficiently by extraction, precipitation, immobilization, or by using biphasic systems.[24–30] However, there is always some loss of polymerization control in biphasic systems or added cost associated with catalyst preparation.

Thus, another approach to reduce the amount of ATRP catalyst, while preserving a similar reaction rate, is to enhance the rate of activation significantly (augmenting the equilibrium constant by increasing the k_a/k_{da} ratio; Scheme 1). Indeed, CuBr complexed by tetradentate ligands such as tris[2-(dimethylamino)ethyl]amine (Me_6TREN) and tris(2-pyridylmethyl)amine (TPMA) is 10^3–10^5 times more active than the originally used CuBr/bipyridine complexes.[31–35] However, the catalyst concentration can not simply be reduced by 10^3 (from a concentration equimolar with the initiator (i.e., 1 mol% vs. monomer) to 10 ppm vs. monomer) owing to the radical termination and concurrent irreversible oxidation of the catalyst (Cu^I to Cu^{II}). All Cu^I species would be converted to Cu^{II} when less than 1% of the growing chains terminate. Furthermore, some impurities, such as oxygen or various radical inhibitors, deactivate these minute amounts of very active catalyst, and thus stringent purification methods and procedures similar to those used in ionic polymerizations are required.

These limitations can be overcome by the addition of an appropriate reducing agent, such as tin(II) 2-ethylhexanoate ($Sn(EH)_2$), which has been approved by the Food and Drug Administration (FDA), or sugars such as glucose. The $Sn(EH)_2$ reductant can reduce the Cu^{II} species that accumulate when radicals irreversibly terminate to restore the original Cu^I state needed for activation (Scheme 2). In this process, the activators are continuously regenerated by electron transfer (ARGET).

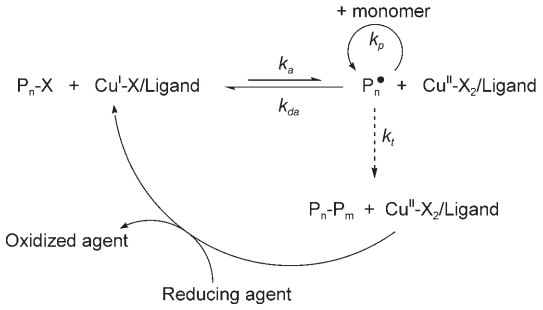
Furthermore, the process can be started with the oxidatively stable Cu^{II} species, which can be reduced in situ to the Cu^I state as in a previously reported AGET process (activators generated by electron transfer).[36,37] However, in AGET ATRP, the oxidatively stable Cu^{II} catalyst, present at a considerably higher concentration (>0.1 mol% vs. monomer), was reduced with nearly stoichiometric amounts of ascorbic acid or $Sn(EH)_2$. Other reducing agents were previously used to accelerate ATRP, but the concentration of copper catalyst was always very high, essentially equal to that of the initiator.[38–41]

In the ARGET system, a tiny amount of Cu catalyst is used together with a sufficiently large excess of reducing agent, which not only reduces Cu^{II} to Cu^I but is also responsible for scavenging oxygen and radical inhibitors. The concentration of the reducing agent and related rate of reduction can greatly influence the ARGET ATRP. Herein, we report the optimized conditions for the studied system; investigations of different reducing agents and rates of reduction will be presented elsewhere. ARGET provides a real breakthrough in ATRP since the repetitive reduction cycle enables the amount of catalyst to be decreased significantly (down to single digit ppm vs. monomer). For some applications, ARGET could even allow the residual copper to be left in the final, colorless products.

We have recently reported that ARGET ATRP of styrene with 10 ppm $CuCl_2/Me_6$TREN catalyst in the presence of an excess of $Sn(EH)_2$ was well controlled and gave polymers with low polydispersities ($M_w/M_n < 1.2$) and molecular weights that agreed excellently with theoretical values.[3] Control of the molecular weight was also good even with 1 ppm Cu, but the polydispersities were higher ($M_w/M_n \approx 1.6$), which indicated that there was not enough Cu to assure fast exchange between active and dormant species.

Herein, we present results of ARGET ATRP of *n*-butyl acrylate (*n*BA) and methyl methacrylate (MMA). These systems are more challenging, since the more polar acrylates coordinate more strongly to Cu[42,43] than does styrene, which could potentially affect the catalyst performance.

Table 1 presents the experimental conditions and properties of poly(*n*-butyl acrylate) (P*n*BA) prepared by ARGET ATRP. The polymerization of *n*BA was initiated by ethyl 2-bromoisobutyrate (EtBrIB), and a final molecular weight $M_n = 20000\ g\,mol^{-1}$ was targeted. A constant amount (10 mol% vs. initiator; 0.07 mol% vs. monomer) of $Sn(EH)_2$



Scheme 2. Mechanism for ARGET ATRP: The Cu^I activator is constantly regenerated by environmentally acceptable reducing agents (e.g. FDA-approved compounds, sugars etc.), which compensate for any loss of Cu^I as a result of radical termination.

Table 1: Experimental conditions and properties of P*n*BA prepared by ARGET ATRP.

Entry[a]	Cu[c] [ppm]	*t* [min]	Conv. [%]	$M_{n,theo}$[d] [g mol^{-1}]	$M_{n,GPC}$ [g mol^{-1}]	M_w/M_n
1	500	1210	97	19400	19600	1.18
2	50	370	91	18100	19400	1.26
3	10	360	90	17900	19100	1.40
4	2	1150	97	19500	24400	2.48
5[b]	50	1320	71	14300	15100	1.16
6[b]	10	1320	84	16800	19300	1.33
7[b]	2	1260	88	17600	23500	1.56

[a] Ratio of reactants: $[nBA]_0/[EtBrIB]_0/[Me_6TREN]_0/[Sn(EH)_2]_0 = 160/1/0.1/0.1$; $[nBA]_0 = 5.88$ M; $T = 60$ °C, in anisole (20% v/v vs. monomer); [b] TPMA (0.03 equiv) was used as a ligand instead of Me_6TREN; [c] molar ratio vs. monomer; [d] $M_{n,theo} = ([nBA]_0/[EtBrIB]_0) \times \text{conversion} \times M_{monomer}$.

 © 2006 Wiley-VCH Verlag GmbH & Co. KGaA, Weinheim

and variable concentrations of the Cu-based catalyst with Me_6TREN and TPMA as ligands were employed. The amount of copper was varied from 500 down to 2 ppm vs. monomer (Table 1).

Figure 1 presents the evolution of the molecular weights and polydispersities with conversion for polymerization of *n*BA with 50 ppm $CuCl_2$/Me_6TREN catalyst. Control of the molecular weight was excellent according to theoretical values based on quantitative initiation. However, with 2 ppm Cu catalyst, the molecular weights and polydispersities were higher (Table 1, entry 4), which indicates that there was not enough Cu to assure fast exchange between active and dormant species.

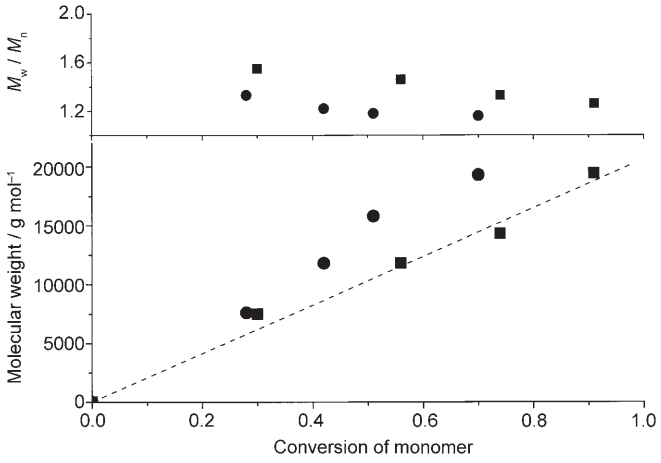


Figure 1. Molecular weights and polydispersities of poly(*n*-butyl acrylate) and poly(methyl methacrylate) as a function of degree of conversion of (■) *n*BA and (●) MMA. Experimental conditions for *n*BA are given in Table 1, entry 2 and for MMA in Table 2, entry 1.

Better results were obtained with the TPMA ligand, which binds more strongly to Cu than does Me_6TREN[44,45] (Table 1, entries 5–7). Although TPMA forms slightly less active complexes than Me_6TREN,[32,34,46] better control over polymerization was observed. This observation can be ascribed to a higher real concentration of Cu species in the system, since TPMA binds more strongly to Cu.

ARGET ATRP of *n*BA was also carried out in the presence of glucose (an organic reducing agent). Under conditions similar to those presented in Table 1, entry 5 (*n*BA/EtBrIB/$CuCl_2$/TPMA/glucose = 160/1/0.0078/0.03/0.1; 50 ppm Cu vs. monomer; $t = 2640$ min; $T = 80\,^{\circ}C$, in 20% v/v anisole), P*n*BA was formed in 48% yield with $M_n = 10\,500\ g\,mol^{-1}$ and $M_w/M_n = 1.47$ ($M_{n,theo} = 9600\ g\,mol^{-1}$).

Table 2 presents the experimental conditions and properties of poly(methyl methacrylate) (PMMA) prepared by ARGET ATRP. Ethyl α-bromophenylacetate (EtBPA) was used as initiator and TPMA as a ligand. As in the case of *n*BA, MMA was polymerized by ARGET ATRP with varied amounts of Cu catalyst. The molecular weight and polydispersity of the polymer with 50 ppm Cu catalyst as a function of degree of conversion are shown in Figure 1. Figure 2 shows a kinetic plot and the evolution of the molecular-weight distribution with polymerization (2 ppm Cu catalyst). The molecular weight was well controlled; a gradual increase in the molecular-weight distribution was observed, and the final polydispersity was relatively low ($M_w/M_n = 1.36$).

Table 2: Experimental conditions and properties of PMMA prepared by ARGET ATRP.

Entry[a]	Cu[b] [ppm]	t [min]	Conv. [%]	$M_{n,theo}$[c] [g mol^{-1}]	$M_{n,GPC}$ [g mol^{-1}]	M_w/M_n
1	50	360	70	14 000	19 300	1.16
2	10	370	61	12 200	15 900	1.34
3	2	335	66	13 300	15 300	1.36

[a] Ratio of reactants: $[MMA]_0/[EtBPA]_0/[TPMA]_0/[Sn(EH)_2]_0 = 200/1/0.03/0.1$; $[MMA]_0 = 6.23$ M; $T = 90\,^{\circ}C$, in anisole (50% v/v vs. monomer); [b] molar ratio vs. monomer; [c] $M_{n,theo} = ([MMA]_0/[EtBPA]_0) \times \text{conversion} \times M_{monomer}$.

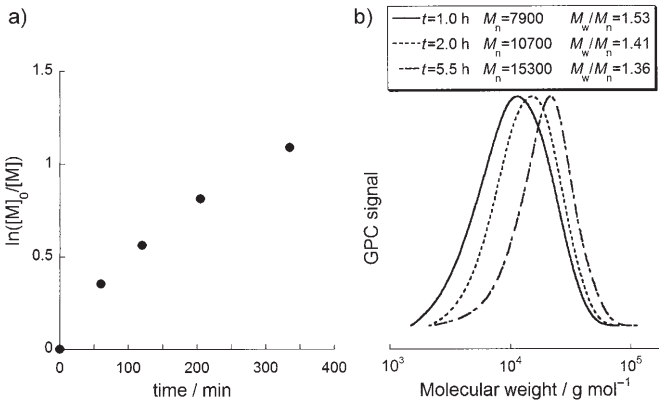


Figure 2. a) Kinetic plot and b) evolution of GPC traces during ARGET ATRP of MMA. Experimental conditions are given in Table 2, entry 3.

The new system was also successfully applied to the synthesis of block copolymers P*n*BA-*b*-PS and PS-*b*-P*n*BA (PS = polystyrene). Initially a P*n*BA block was prepared by using ARGET ATRP of *n*BA with 50 ppm Cu complex ($M_{n,GPC} = 19\,400\ g\,mol^{-1}$, $M_{n,theo} = 18\,100\ g\,mol^{-1}$, $M_w/M_n = 1.26$), and then it was used as a macroinitiator. Chain extension of the P*n*BA macroinitiator with styrene by ARGET ATRP with 15 ppm Cu catalyst was very efficient ($M_{n,GPC} = 34\,900\ g\,mol^{-1}$, $M_{n,theo} = 37\,000\ g\,mol^{-1}$, $M_w/M_n = 1.18$).

Figure 3 presents the size-exclusion chromatography (SEC) traces recorded after each step. The reactions were well controlled, as evidenced by the monomodal gel-permeation chromatography (GPC) traces. PS macroinitiator, also prepared by ARGET ATRP with 15 ppm Cu catalyst ($M_{n,GPC} = 17\,100\ g\,mol^{-1}$, $M_{n,theo} = 15\,300\ g\,mol^{-1}$, $M_w/M_n = 1.18$) was chain extended with *n*BA (50 ppm Cu catalyst) to provide a block copolymer with $M_{n,GPC} = 26\,300\ g\,mol^{-1}$ ($M_{n,theo} = 28\,900\ g\,mol^{-1}$) and $M_w/M_n = 1.33$.

In summary, we report the successful polymerization of the polar monomers *n*-butyl acrylate and methyl methacrylate by ARGET ATRP with ppm quantities of Cu catalyst. Better control was obtained with TPMA as a ligand which binds to copper more strongly than does Me_6TREN. The new ARGET system was also successfully applied to the efficient synthesis of styrene and *n*-butyl acrylate block copolymers. It is

 © 2006 Wiley-VCH Verlag GmbH & Co. KGaA, Weinheim

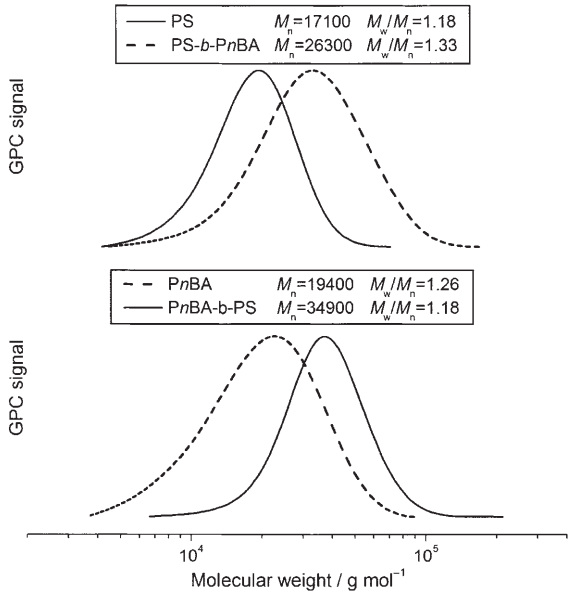


Figure 3. GPC traces after each step of the synthesis of block copolymers PS-*b*-P*n*BA (top) and P*n*BA-*b*-PS (bottom). Experimental conditions for the polymerization of *n*BA: *n*BA/EtBrIB/Cu^{II}/Me_6TREN/$Sn(EH)_2$ = 160/1/0.0078/0.1/0.1; $[nBA]_0$ = 5.88 M, Cu catalyst: 50 ppm vs. monomer, T = 60 °C, in anisole (20% v/v vs. monomer). Experimental conditions for polymerization of styrene: styrene/P*n*BA/$CuCl_2$/Me_6TREN/$Sn(EH)_2$ = 200/1/0.003/0.1/0.1; $[styrene]_0$ = 5.82 M, Cu catalyst: 15 ppm vs. monomer, T = 110 °C, in anisole (50% v/v vs. monomer).

anticipated that ARGET ATRP will facilitate the commercial application of ATRP and simplify the preparation of many new materials, including molecular hybrids, bioconjugates, and nanocomposites.

Experimental Section

Styrene (Aldrich, 99%), *n*-butyl acrylate (*n*BA) (Acros, 99 + %), and methyl methacrylate (MMA) (Acros, 99%) were passed through a column filled with neutral alumina, dried over calcium hydride, and distilled under reduced pressure. Tris[2-(dimethylamino)ethyl]amine (Me_6TREN),[31] tris(2-pyridylmethyl)amine (TPMA)[47] were synthesized following previously reported procedures. Ethyl 2-bromoisobutyrate (EtBrIB) (Acros, 98%), ethyl α-bromophenylacetate (EtBrPA) (Aldrich, 97%), copper(II) chloride (Acros, 99%), tin(II) 2-ethylhexanoate ($Sn(EH)_2$) (Aldrich), and anisole (Aldrich, 99%) were used as received.

General procedure for ARGET ATRP of *n*BA, (targeted number-average degree of polymerization (DP_n) = 160; 50 ppm Cu catalyst): Degassed *n*BA (5.0 mL, 35 mmol) and anisole (0.5 mL) were transferred via degassed syringes to a dry, nitrogen-purged Schlenk flask, and the Cu complex ($CuCl_2$ 0.24 mg, 0.18×10^{-2} mmol; Me_6TREN 0.51 μL, 0.18×10^{-2} mmol) in degassed anisole (0.5 mL) was added. The resulting mixture was stirred for 10 minutes, and then a purged solution of $Sn(EH)_2$ (7.29 μL, 2.2×10^{-2} mmol) and Me_6TREN (5.8 μL, 2.2×10^{-2} mmol) in anisole (0.5 mL) was added. EtBrIB (32.4 μL, 22.1×10^{-2} mmol) was added to initiate the polymerization. An initial sample was taken, and the sealed flask was placed in an oil bath at 60 °C. Samples were taken at timed intervals and analyzed by gas chromatography (GC) and gel-permeation chromatography (GPC) to follow the progress of the reaction. The polymerization was stopped after 6.2 h ($M_{n,GPC}$ = 19400, M_w/M_n = 1.26, conversion = 91%) by opening the flask and exposing the catalyst to air.

Synthesis of diblock copolymer P*n*BA-*b*-PS by ARGET ATRP: A P*n*BA macroinitiator (M_w = 19400, M_w/M_n = 1.26, 2.35 g, 0.12 mmol) was dissolved in styrene monomer (2.75 mL, 24.0 mmol) in a 25-mL Schlenk flask and bubbled with nitrogen for 15 minutes. Next, a solution of Cu complex ($CuCl_2$ 4.84×10^{-2} mg, 0.36×10^{-3} mmol; Me_6TREN 0.10 μL, 0.36×10^{-3} mmol) in degassed anisole (0.7 mL) was added. The resulting mixture was stirred for 10 minutes, and then a purged solution of $Sn(EH)_2$ (3.9 μL, 1.2×10^{-2} mmol) and Me_6TREN (3.2 μL, 1.2×10^{-2} mmol) in anisole (0.7 mL) was added. An initial sample was taken and the sealed flask was placed in an oil bath at 110 °C. Samples were taken at timed intervals and analyzed by GC and GPC. The polymerization was stopped after 30.8 h ($M_{n,GPC}$ = 34900, M_w/M_n = 1.18, conversion = 88%) by opening the flask and exposing the catalyst to air.

Analysis: Molecular weight and polydispersity were determined by GPC (Waters 515 pump and Waters 2414 differential refractometer, PSS columns (Styrogel 10^5, 10^3, 10^2 Å), THF eluent, T = 35 °C, flow rate = 1 mL min^{-1}). Linear polystyrene and poly(methyl methacrylate) standards were used for calibration. The conversion of the monomers was determined by using a Shimadzu GC 14-A gas chromatograph (FID detector, J&W Scientific 30 m DB WAX Megabore column, anisole internal standard). The injector and detector temperatures were kept constant at 250 °C. The analysis was carried out isothermally at 60 °C for 2 min, and then the temperature was increased to 140 °C at a rate of 40 °C min^{-1} and held at 140 °C for 2 min. The degree of conversion was calculated by measuring the decrease of the peak area of the monomer relative to the peak areas of the standards.

Received: January 21, 2006
Published online: June 13, 2006

Keywords: atom-transfer radical polymerization · block copolymers · polymerization · redox chemistry

[1] K. Matyjaszewski, T. P. Davis, *Handbook of Radical Polymerization*, Wiley-Interscience, New York, **2002**.
[2] A. Goto, T. Fukuda, *Prog. Polym. Sci.* **2004**, *29*, 329.
[3] W. Jakubowski, K. Min, K. Matyjaszewski, *Macromolecules* **2006**, *39*, 39.
[4] T. E. Patten, J. Xia, T. Abernathy, K. Matyjaszewski, *Science* **1996**, *272*, 866.
[5] J.-S. Wang, K. Matyjaszewski, *J. Am. Chem. Soc.* **1995**, *117*, 5614.
[6] K. Matyjaszewski, J. Xia, *Chem. Rev.* **2001**, *101*, 2921.
[7] M. Kamigaito, T. Ando, M. Sawamoto, *Chem. Rev.* **2001**, *101*, 3689.
[8] T. E. Patten, K. Matyjaszewski, *Adv. Mater.* **1998**, *10*, 901.
[9] V. Coessens, T. Pintauer, K. Matyjaszewski, *Prog. Polym. Sci.* **2001**, *26*, 337.
[10] K. A. Davis, K. Matyjaszewski, *Adv. Polym. Sci.* **2002**, *159*, 2.
[11] D. Bontempo, H. D. Maynard, *J. Am. Chem. Soc.* **2005**, *127*, 6508.
[12] H.-A. Klok, *J. Polym. Sci. Part A* **2005**, *43*, 1.
[13] K. Matyjaszewski, *Prog. Polym. Sci.* **2005**, *30*, 858.
[14] T. Sun, H. Liu, W. Song, X. Want, L. Jiang, L. Li, D. Zhu, *Angew. Chem.* **2004**, *116*, 4763; *Angew. Chem. Int. Ed.* **2004**, *43*, 4663.
[15] C. Tang, K. Qi, K. L. Wooley, K. Matyjaszewski, T. Kowalewski, *Angew. Chem.* **2004**, *116*, 2843; *Angew. Chem. Int. Ed.* **2004**, *43*, 2783.
[16] M. L. Becker, J. Liu, K. L. Wooley, *Chem. Commun.* **2003**, 180.
[17] J. Pyun, S. Jia, T. Kowalewski, G. D. Patterson, K. Matyjaszewski, *Macromolecules* **2003**, *36*, 5094.
[18] K. Koh, K. Ohno, Y. Tsujii, T. Fukuda, *Angew. Chem.* **2003**, *115*, 4326; *Angew. Chem. Int. Ed.* **2003**, *42*, 4194.

 © 2006 Wiley-VCH Verlag GmbH & Co. KGaA, Weinheim

[19] K. Kamata, Y. Lu, Y. Xia, *J. Am. Chem. Soc.* **2003**, *125*, 2384.
[20] S. Liu, S. P. Armes, *Angew. Chem.* **2002**, *114*, 1471; *Angew. Chem. Int. Ed.* **2002**, *41*, 1413.
[21] S. Nuss, H. Bottcher, H. Wurm, M. L. Hallensleben, *Angew. Chem.* **2001**, *113*, 4137; *Angew. Chem. Int. Ed.* **2001**, *40*, 4016.
[22] T. von Werne, T. E. Patten, *J. Am. Chem. Soc.* **2001**, *123*, 7497.
[23] J. Pyun, T. Kowalewski, K. Matyjaszewski, *Macromol. Rapid Commun.* **2003**, *24*, 1043.
[24] J. Qiu, B. Charleux, K. Matyjaszewski, *Prog. Polym. Sci.* **2001**, *26*, 2083.
[25] D. M. Haddleton, D. Kukulj, A. P. Radigue, *Chem. Commun.* **1999**, 99.
[26] P. Kubisa, *Prog. Polym. Sci.* **2004**, *29*, 3.
[27] S. C. Hong, K. Matyjaszewski, *Macromolecules* **2002**, *35*, 7592.
[28] G. Barre, D. Taton, D. Lastecoueres, J.-M. Vincent, *J. Am. Chem. Soc.* **2004**, *126*, 7764.
[29] J. Pyun, K. Matyjaszewski, T. Kowalewski, D. Savin, G. Patterson, G. Kickelbick, N. Huesing, *J. Am. Chem. Soc.* **2001**, *123*, 9445.
[30] Y. Shen, H. Tang, S. Ding, *Prog. Polym. Sci.* **2004**, *29*, 1053.
[31] J. Xia, S. G. Gaynor, K. Matyjaszewski, *Macromolecules* **1998**, *31*, 5958.
[32] J. Qiu, K. Matyjaszewski, L. Thouin, C. Amatore, *Macromol. Chem. Phys.* **2000**, *201*, 1625.
[33] J. Queffelec, S. G. Gaynor, K. Matyjaszewski, *Macromolecules* **2000**, *33*, 8629.
[34] J. Xia, K. Matyjaszewski, *Macromolecules* **1999**, *32*, 2434.
[35] K. Matyjaszewski, T. E. Patten, J. Xia, *J. Am. Chem. Soc.* **1997**, *119*, 674.
[36] W. Jakubowski, K. Matyjaszewski, *Macromolecules* **2005**, *38*, 4139.
[37] K. Min, H. Gao, K. Matyjaszewski, *J. Am. Chem. Soc.* **2005**, *127*, 3825.
[38] K. Matyjaszewski, S. Coca, S. G. Gaynor, M. Wei, B. E. Woodworth, *Macromolecules* **1997**, *30*, 7348.
[39] A. de Vries, B. Klumperman, D. de Wet-Roos, R. D. Sanderson, *Macromol. Chem. Phys.* **2001**, *202*, 1645.
[40] Y. Gnanou, G. Hizal, *J. Polym. Sci. Part A* **2004**, *42*, 351.
[41] G. Hizal, U. Tunca, S. Aras, H. Mert, *J. Polym. Sci. Part A* **2005**, *44*, 77.
[42] W. A. Braunecker, N. V. Tsarevsky, T. Pintauer, R. R. Gil, K. Matyjaszewski, *Macromolecules* **2005**, *38*, 4081.
[43] W. A. Braunecker, T. Pintauer, N. V. Tsarevsky, G. Kickelbick, K. Matyjaszewski, *J. Organomet. Chem.* **2005**, *690*, 916.
[44] G. Golub, A. Lashaz, H. Cohen, P. Paoletti, A. Bencini, B. Valtancoli, D. Meyerstein, *Inorg. Chim. Acta* **1997**, *255*, 111.
[45] E. A. Ambundo, M.-V. Deydier, A. J. Grall, N. Aguera-Vega, L. T. Dressel, T. H. Cooper, M. J. Heeg, L. A. Ochrymowycz, D. B. Rorabacher, *Inorg. Chem.* **1999**, *38*, 4233.
[46] T. Pintauer, K. Matyjaszewski, *Coord. Chem. Rev.* **2005**, *249*, 1155.
[47] Z. Tyeklar, R. R. Jacobson, N. Wei, N. N. Murthy, J. Zubieta, K. D. Karlin, *J. Am. Chem. Soc.* **1993**, *115*, 2677.

 © 2006 Wiley-VCH Verlag GmbH & Co. KGaA, Weinheim

Alkane Ligands

DOI: 10.1002/anie.200600313

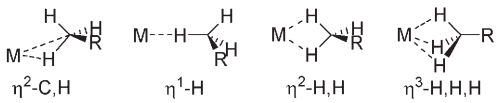
A Rhenium–Cyclohexane Complex with Preferential Binding of Axial C–H Bonds: A Probe into the Relative Ability of C–H, C–D, and C–C Bonds as Hyperconjugative Electron Donors?**

Douglas J. Lawes, Tamim A. Darwish, Timothy Clark, Jason B. Harper,* and Graham E. Ball**

Dedicated to Professor Gernot Frenking on the occasion of his 60th birthday

Formation of alkane σ complexes with agostic-like interactions is widely accepted as being a prerequisite for C–H activation by transition-metal centers and has therefore received considerable attention by experimental and theoretical chemists.[1–3] One important aspect of σ-complex or agostic interactions is their specificity. Do, for instance, such interactions prefer η^2-C,H, η^1-H, η^2-H,H, or η^3-H,H,H binding (Scheme 1)[1b] and can this preference be influenced by electronic differences between the hydrogen atoms?

We now describe experimental (NMR) and theoretical investigations of an alkane complex, $[CpRe(CO)_2$-(cyclohexane)] (**1**), in which competition exists between axial and equatorial C–H bonds for binding to the metal



Scheme 1. Possible binding modes for σ-complex or agostic interactions.

[*] Prof. Dr. T. Clark
Computer-Chemie-Centrum
Friedrich-Alexander-Universität Erlangen-Nürnberg
Nägelsbachstrasse 25, 91052 Erlangen (Germany)
Fax: (+49) 9131-8526565
E-mail: Tim.Clark@chemie.uni-erlangen.de
D. J. Lawes, T. A. Darwish, Dr. J. B. Harper, Dr. G. E. Ball
School of Chemistry
University of New South Wales
Sydney NSW 2052 (Australia)
Fax: (+61) 2-9385-6141
E-mail: j.harper@unsw.edu.au
g.ball@unsw.edu.au

[**] We acknowledge Prof. W. Adcock (Flinders University) and Prof. M. Paddon-Row (UNSW) for early communication of results and helpful discussions, and the Australian Research Council for funding and an Australian Postgraduate Award to D.J.L. The work at Erlangen was supported by the Deutsche Forschungsgemeinschaft as part of SFB583 "Redox-active metal complexes: Control of reactivity via molecular architecture".

Supporting information for this article is available on the WWW under http://www.angewandte.org or from the author.

WILEY InterScience DISCOVER SOMETHING GREAT
© 2006 Wiley-VCH Verlag GmbH & Co. KGaA, Weinheim

center. Given the role of alkane complexes as intermediates in the C–H activation reaction, knowledge of the selectivity of alkane coordination sites may prove relevant to directing the site selectivity of C–H activation products. Complex **1** allows the order of relative hyperconjugative donor strengths of bonds, C–H > C–D > C–C, to be probed experimentally. Our experiments and calculations suggest that the interaction of the alkane with the metal is primarily with one hydrogen atom of the methylene unit and that the axially complexed isomer is preferred.

Some of us have previously reported the direct NMR observation of an alkane complex in solution, [CpRe(CO)$_2$-(cyclopentane)].[3a,b] This complex was generated through exposure of a photolabile rhenium precursor, [CpRe(CO)$_3$], dissolved in cyclopentane to UV/visible light at 180 K [Eq. (1)]. A resonance is observed at $\delta = -2.32$ ppm and

$$[\mathrm{CpRe(CO)_3}] \xrightarrow[\text{cyclopentane, } -\mathrm{CO}]{h\nu,\ 180\ \mathrm{K}} [\mathrm{CpRe(CO)_2(cyclopentane)}] \quad (1)$$

assigned to the protons of the bound methylene unit. The fact that a single resonance is observed, coupled with a highly shielded ^{13}C resonance and a large equilibrium isotope shift accompanying deuterium incorporation,[3c] suggests a fast exchange between two equivalent complexes in which one of the C–H bonds in this methylene unit is complexed with the metal center. A rapid, mutual exchange between two alternative η^2-C,H structures renders the two protons equivalent, and the net result is that each proton is directly complexed with the metal center half of the time.

More recently, we have demonstrated that three isomeric pentane complexes, [CpRe(CO)$_2$(pentane-η^2-C^x,H^x)], ($x = 1$–3) are observable in which the pentane ligand may bind using either of the methylene or the methyl moieties.[3c] Using partially deuterated, bound methyl groups in [CpRe-(CO)$_2$(pentane-η^2-C^1,H^1)], it was demonstrated that: 1) one hydrogen (deuterium) atom is directly complexed with the metal center at any given instant and there is a rapid exchange of which hydrogen (deuterium) atom is engaged in this direct interaction; 2) binding of hydrogen is preferred over that of deuterium ($K_{H/D} = 2.02$); 3) the observed shielding in the ^{1}H NMR spectrum is directly related to the fraction of time a hydrogen atom spends directly complexed with the metal center. Similarly, the ^1J(C,H) value decreases as the fraction of time that a hydrogen atom spends directly complexed with the metal center increases.

We have now extended our studies to the binding of cyclohexane, since, at the temperatures used, it exists in a chair form and the exchange between the chair forms is slow.[4] Hence, axial and equatorial protons with discrete NMR shifts are present and it is possible to observe an alkane complex that exhibits preferential complexation of one hydrogen atom within a CH_2 unit. The discrete shifts for axial and equatorial hydrogen atoms will be retained in a complex-bound cyclohexane even if, as expected, there is rapid exchange between the two isomeric structures.

When photolysis experiments similar to those described previously[2,3] [see Eq. (1)] are carried out at 173 K in the presence of cyclohexane, two new signals of similar intensity are observed in the ^{1}H NMR spectrum at $\delta = -6.17$ and 0.49 ppm (Figure 1a). These resonances are due to the formation of [CpRe(CO)$_2$(cyclohexane)] (**1**). The experiment was performed using either 60:40 [D_{12}]pentane/cyclohexane or 8:82:10 [D_{12}]pentane/isobutene/cyclohexane to allow very

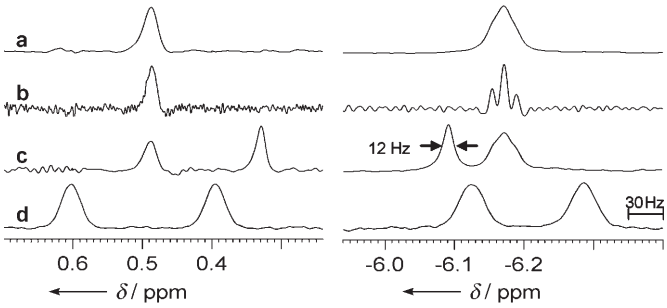


Figure 1. Signals due to the protons of a bound methylene unit in a, b) [CpRe(CO)$_2$(cyclohexane)] (**1**), c) a mixture of **1** and [CpRe(CO)$_2$([2,2,3,3,5,5,6,6-D_8]cyclohexane-η^2-C^1,H^1)] ([D_8]-**1**), and d) [CpRe(CO)$_2$([$^{13}C_6$]cyclohexane)] ([$^{13}C_6$]-**1**) in their ^{1}H NMR spectra at 173 K.[5] The spectra in (a), (c), and (d) have line broadening of 5 Hz and the spectrum in (b) is resolution-enhanced with Gaussian multiplication. All spectra shown were obtained for 8:82:10 [D_{12}]pentane/isobutene/cyclohexane solvent mixtures.

low temperatures to be used with the otherwise high-melting cyclohexane. Any bound [D_{12}]pentane (formation of [CpRe(CO)$_2$([D_{12}]pentane)]) is not observed in the ^{1}H NMR spectra as it is fully deuterated. When isobutane is also present as solvent, a resonance due to formation of the isobutane complex [CpRe(CO)$_2$(isobutane-η^2-C^1,H^1)] ($\delta = -2.13$ ppm (d, ^3J(H,H) = 6 Hz)) is also seen.

Repeating the experiment using uniformly ^{13}C-labeled cyclohexane (Figure 1d) confirms this molecule to be an alkane complex, with large ^1J(C,H) coupling constants of (96.5 ± 0.5) and (125.0 ± 0.5) Hz for the resonances at $\delta = -6.17$ and 0.49 ppm, respectively. The latter is close to the ^1J(C,H) coupling constants found in free cyclohexane at this temperature (≈128 Hz). A ^{1}H-^{13}C HSQC experiment confirms that both protons are attached to the same carbon atom with a shielded shift ($\delta = -22.4$ ppm) characteristic of a bound alkane. We attribute the two ^{1}H NMR resonances to the axial and equatorial protons, respectively, of a bound methylene unit. The axial hydrogen atom would be anticipated to show a large coupling ($J > 8$ Hz) to three other hydrogen nuclei (geminal, 2 × *trans*), whereas the equatorial hydrogen atom is expected to have only one large coupling (geminal). After resolution enhancement (Figure 1b), a triplet structure is evident for the signal at $\delta = -6.17$ ppm, indicating *two* large coupling constants of (9.8 ± 0.5) Hz. No large coupling constants were resolved for the signal at $\delta = 0.49$ ppm. This suggests that the geminal ^2J(H,H) splitting is unexpectedly small.

In order to confirm assignment of these resonances, [1,1,2,2,4,4,5,5-D_8]cyclohexane was prepared.[6] When this [D_8]cyclohexane was used as alkane ligand under the same conditions, signals were observed at $\delta = -6.09$ and 0.33 ppm, the former having a line width of about 7 Hz (Figure 1c) due to [CpRe(CO)$_2$([2,2,3,3,5,5,6,6-D_8]cyclohexane-η^2-C^1,H^1)]

 © 2006 Wiley-VCH Verlag GmbH & Co. KGaA, Weinheim

([D_8]-**1**). As all vicinal H,H couplings have been removed through deuteration, this confirms that the geminal H,H coupling constant is small (< 6 Hz) and that the signal at $\delta = -6.09$ ppm corresponds to a bound axial hydrogen atom. This geminal coupling is weak, possibly because this formally two-bond (H–C–H) coupling now contains a three-bond component (H···Re···C–H) of opposite sign to the two-bond component, and our calculations indicate an increase of the H-C-H angle to 118.5° (MP2, most stable conformation), both of which would reduce the coupling strength.[7] The calculated value for this geminal ^2J(H,H) coupling in the most stable conformation is < 5 Hz (Table 1), and the value for the *trans* diaxial ^3J(H,H) coupling between the bound axial proton and vicinal axial protons is calculated to be in the range 7.9–10.6 Hz, consistent with our experimental observation.[8]

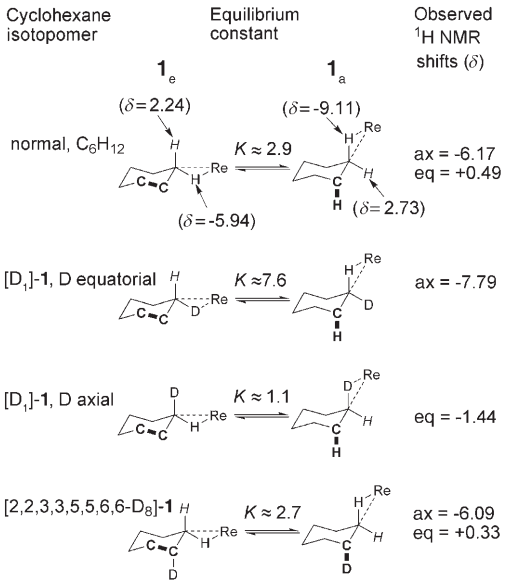
Table 1: NMR parameters of **1** obtained from calculations[a] and from experiments.

Isomer	$\delta(H_a)$ [ppm]/ ^1J(C,H) [Hz]	$\delta(H_e)$ [ppm]/ ^1J(C,H) [Hz]	^2J(H,H) [Hz]	$K_{\mathbf{1}_a/\mathbf{1}_e}$[b]
$\mathbf{1}_a$	−9.74/101.3	+2.33/156.4	−4.73	2.4
$\mathbf{1}_e$	+2.38/156.6	−9.78/103.4	−4.65	5.6
experimental values	−6.17/96.5	+0.49/125	< 6	2.4–3.4

[a] In each case, the values shown are calculated using the lowest-energy conformation as predicted by the MP2 calculations. Calculations were performed using B3LYP-GIAO on the HCTH-optimized geometries and the default SCRF-PCM treatment in cyclohexane solvent.[8] [b] The equilibrium constant calculated is the value required to give the observed δ at 173 K assuming that the calculated δ values are correct.

The observed chemical shift of both the axial and equatorial protons is the result of an equilibrium between two isomeric complexes, $\mathbf{1}_a$ and $\mathbf{1}_e$ which have the axial and the equatorial hydrogen atom, respectively, directly complexed with the metal center (Scheme 2). Interconversion of $\mathbf{1}_a$ and $\mathbf{1}_e$ is fast on the NMR timescale at the temperatures employed. This is confirmed by variable-temperature NMR experiments on **1**. Decreasing the temperature results in a significant increase in the separation of the axial and equatorial shifts, indicative of an increasing equilibrium constant at lower temperatures. The separation of the two shifts increases from 6.65 ppm at 173 K to 6.91 ppm at 145 K. The amount of shielding can be used to estimate the proportion of time that each type of C–H bond is complexed with the rhenium center. Likewise, the reduction of the C–H coupling gives an independent measure of the same parameters. Given that the axial proton is highly shielded, by about 7.4 ppm compared to free cyclohexane, and ^1J(C,H) is greatly reduced (96.5 Hz compared to 128 Hz in free cyclohexane), while the shielding (by ≈1.2 ppm) and reduction in coupling (^1J(C,H) = 125 Hz) is much smaller for the equatorial proton, it is clear that binding of the axial proton is significantly preferred in this system.

It is not possible to extract a precise equilibrium constant, $K_{\mathbf{1}_a/\mathbf{1}_e}$, for this case of axially vs. equatorially complexed as only the weighted-averaged chemical shifts and ^1J(C,H) values are observed and the values of these parameters for the axial and



Scheme 2. Equilibria between axially and equatorially complexed species for various isotopomers with midrange-fitted empirical equilibrium constants. All equilibria are in fast exchange on the NMR timescale at the temperatures employed resulting in only weighted-averaged shifts being observed. In each case one of the two (equivalent) bonds antiperiplanar to the complexed bond is shown in bold. Chemical shifts in brackets are estimated values based on empirical data for each proton that would be observed if no exchange were occurring.

equatorial protons in the two isomers are not known. However, further measurements such as equilibrium isotope effect (isotopic perturbation of resonance) experiments on [$CpRe(CO)_2$([1-D_1]cyclohexane-η^2-C^1,H^1)] ([D_1]-**1**) aid the prediction of the chemical shifts and coupling constants of both the complexed and uncomplexed hydrogen atoms in the two isomers of the complex. Combined with knowledge of the pentane system, sensible estimates for the equilibrium constants and NMR parameters can be extracted. In the case of the bound methyl group of [$CpRe(CO)_2$(pentane-η^2-C^1,H^1)], an analytical solution was possible: the directly complexed hydrogen atom has a shielded shift of $\delta = -8.22$ ppm and the uncomplexed hydrogen atoms within the same methyl group a shift of $\delta = 1.12$ ppm, slightly deshielded (by ≈0.20 ppm) compared to a free methyl group. By making assumptions about the chemical-shift change upon binding of the more remote proton in a bound methylene group (i.e., the hydrogen atoms shown in italics in Scheme 2) it is possible to extract values for the equilibrium constants $K_{\mathbf{1}_a/\mathbf{1}_e}$ and $K_{H/D}$.

We have chosen to make assumptions about the chemical shift of this type of proton as it is likely to be less affected by different binding situations than the strongly complexed proton. Using a range of values for the change in chemical shift for this uncomplexed proton that vary from 0 to +2.5 ppm, a range that brackets the observed value for pentane (deshielded by 0.20 ppm) and the larger deshielding predicted by calculations (up to 1.24 ppm), a range of values for $K_{\mathbf{1}_a/\mathbf{1}_e} = 3.4$–2.4 and $K_{H/D} = 4.7$–1.9, respectively, is obtained.[9] Using a value for this deshielding of 1 ppm relative to free cyclohexane leads to the midrange values shown in Scheme 2, $K_{\mathbf{1}_a/\mathbf{1}_e} = 2.9$ and $K_{H/D} = 2.6$. Note that in

 © 2006 Wiley-VCH Verlag GmbH & Co. KGaA, Weinheim

general, there is no reason to assume that the $K_{H/D}$ value will be the same for cyclohexane as for pentane, or indeed that the same value applies to axial and equatorial sites.

Ab initio and DFT calculations[8] on **1** give structures in which the alkane is complexed through one hydrogen atom at any time. The PW91 and HCTH DFT calculations prefer the more stable axially complexed isomer $\mathbf{1}_a$ by 1.3 and 0.4 kJ mol^{-1}, respectively, and ab initio MP2 calculations prefer it by 4.2 kJ mol^{-1} relative to the equatorially complexed isomer $\mathbf{1}_e$; in comparison a value of 1.5 kJ mol^{-1} is estimated from the empirical data. In contrast, the B3LYP hybrid density functional prefers $\mathbf{1}_e$ by 1.2 kJ mol^{-1}. As seen in calculated structures of smaller alkanes,[10] the Re-H-C angle for the complexed C–H moiety is large: the lowest-energy conformations of $\mathbf{1}_a$ and $\mathbf{1}_e$ have values of 114.4° and 112.6°, respectively (MP2), although these values can be as large as 128° in the other conformations.

The barrier to exchange between the two isomers is calculated to be 10.0 and 14.6 kJ mol^{-1} at the HCTH and MP2 levels, respectively. This energy barrier is sufficiently low for the two isomers to remain in fast exchange on the NMR timescale even at the lowest temperatures employed in this study, consistent with our observations. The calculated barriers for 1,2-(axial-equatorial) and 1,3-(axial-axial) hydrogen shifts are 21 and 29 kJ mol^{-1}, respectively, at HCTH and 52 and 13 kJ mol^{-1}, respectively, at MP2. Experimental data indicate that these 1,2 and 1,3 shifts are not occurring rapidly on the NMR timescale and that these barriers are underestimated. The calculated binding energies at the different levels vary widely but in the expected fashion. PW91 and MP2 apparently overestimate the binding, whereas B3LYP and HCTH agree moderately well. Given the disagreement between B3LYP and the other methods as to the relative stabilities of the isomers, the HCTH binding energies are probably most reliable.

In agreement with experiment, calculations predict very different NMR parameters (δ and J) for the complexed and uncomplexed hydrogen atoms within the bound methylene group (Table 1).

Our empirical data suggest that the calculated shifts of the complexed hydrogen atoms are slightly more extreme than the experimental ones, but the basic principle is well demonstrated. The ^1J(C,H) values are clearly overestimated as they cannot give a weighted average of 96.5 Hz as was observed in the case of the axial C–H coupling. However, they do predict the reduction of ^1J(C,H) upon complexation and an increase of it for the uncomplexed hydrogen atom compared to the free alkane. This behavior was observed empirically in the case of [CpRe(CO)$_2$(pentane-η^2-C^1,H^1)] (^1J(C,H) of the complexed H: 85 Hz; of the uncomplexed: 132 Hz).

The expected mode of complexation of cyclohexane to the rhenium center, confirmed by our calculations, is shown in Scheme 2, with the metal center positioned between the axial and equatorial C–H bonds.[1] Steric interactions with the cyclohexane ligand would be expected to disfavor any other options. From this, it is not apparent that a steric argument could account for the selective formation of the complex of an axial C–H bond of cyclohexane. At best, complexation of the axial and equatorial C–H bonds would be the same, although long-range steric interactions with the ring would favor the equatorially complexed isomer. This is supported by the crystal structure of a complex of uranium with a very bulky hexadentate ligand with the equatorial C–H bond of methylcyclohexane being complexed,[11] though it is noted that this is in the solid state rather than in solution as observed here and stabilizing interactions between the cyclohexane ring and the co-ligand may be significant. Below, we propose an electronic argument to explain the observed preference for binding.

In 1981, Cieplak proposed a radical argument to account for the selectivity observed in nucleophilic additions to cyclohexanones.[12a] The Cieplak model relies on the assumption that a C–H bond is a better electron donor than a C–C bond when both are available for hyperconjugation, for example, when they have an antiperiplanar relationship to an electron-depleted bond. This assumption sparked some controversy and has stimulated many groups to examine its validity.[12–17] The earliest experimental evidence supporting Cieplak's hypothesis used the ^{19}F NMR chemical shifts of bicycloalkyl fluorides as probes to the extent of delocalization of electrons from C–X bonds into the σ* orbital of the C–F bond.[13a,b] This indicated that alkyl groups are electron-withdrawing when compared to hydrogen. Subsequent experimental studies, including those examining the hydrochlorination and fluorination of 5-substituted adamant-2-ols,[13e] the reduction of 5-substituted adamantan-2-ones,[14a,b] and the conformations of α,β-unsaturated esters and aldehydes,[15a] further support this model.

While these experimental results indicate that C–H bonds are better hyperconjugative donors than C–C bonds, the magnitude of this difference has not been derived experimentally. Computational studies of 2-substituted 1-fluoroethanes[18a] and 2,5-dimethyl-2-adamantyl cations[18b] report the difference as about 4 and 1.6 kJ mol^{-1}, respectively.

The preference for axial coordination in **1** is an electronic, not a vibrational effect. The slightly weaker axial C–H bonds are better donors than their equatorial counterparts. There is a stereoelectronic preference for conformations in which the best donor lone pair or bond is antiperiplanar to the best acceptor bond.[19] A C–H bond complexed with a rhenium center is more electron-deficient than a regular C–H bond (as there is insignificant electron back donation from the metal center[20]) and thus is a better electron acceptor. Since axial C–H bonds in chair conformations of cyclohexanes are antiperiplanar to some of the other C–H bonds, while the equatorial C–H bonds are antiperiplanar to certain C–C bonds (Scheme 2), the selectivity described in this paper suggests that a C–H bond is a better hyperconjugative donor than a C–C bond. Taking into account that two such effects are operating in each case, this corresponds to an energy difference of about 0.75 kJ mol^{-1}, which is in reasonable agreement with the computed differences, given the small magnitude of the effect.[8]

It is worth noting that preferential reaction of equatorial C–H bonds has been found in the monooxygenation of methylene C–H bonds in substituted cyclohexanes.[21] This was explained qualitatively using long-range hyperconjuga-

 © 2006 Wiley-VCH Verlag GmbH & Co. KGaA, Weinheim

tive stabilization, though this difference could not be quantified.

The equilibrium constant $K_{\mathbf{1}_a/\mathbf{1}_e}$ is reduced somewhat by the introduction of deuterium into vicinal sites (using [D_8]cyclohexane). Assuming that the "normal" deuterium isotope shifts are similar for axial and equatorial protons, which is the case in free cyclohexane, it is apparent (Figure 1c) that the shifts of the two protons are closer together in this isotopomer and that the equilibrium constant is therefore reduced (from $\approx$2.9 to $\approx$2.7). Ascribing this effect entirely to the replacement of two *trans*-diaxial C–H bonds by two C–D bonds leads to a reduction in energy of about 46 J mol^{-1} per bond. This is consistent with the fact that the stronger C–D bond is less likely to donate its electrons. This observation adds further weight to the hypothesis that the observed phenomenon is indeed caused by an electronic effect since the steric effect of replacing hydrogen with deuterium in vicinal sites is expected to be negligible.

Qualitative MO arguments also suggest that the axial hydrogen atoms are better electron donors than the equatorial ones. The degenerate HOMOs of cyclohexane are delocalized over the C–C and equatorial C–H bonds. However, the contribution on each equatorial hydrogen atom is only 5.6% (sum of the squared coefficients of the two H basis functions in the Eigenvector). Three occupied combinations of essentially pure axial σ_{C-H} orbitals are only roughly 0.5 eV lower in energy than the HOMO and provide more effective electron donation than the HOMOs.[22] These orbitals reflect exactly the hyperconjugation arguments given above.

In conclusion, we have identified an alkane complex, [$CpRe(CO)_2$(cyclohexane)], in which binding occurs preferentially through the axial C–H bond of a methylene group. The ratio of the complexation of each type of C–H bond in cyclohexane ($K_{\mathbf{1}_a/\mathbf{1}_e} \approx 2.9$) suggests the difference in the electron-donating abilities of C–H, C–C, and even C–D bonds may be determined, assuming that there is no steric preference for either mode of complexation.

Received: January 24, 2006
Published online: June 13, 2006

Keywords: ab initio calculations · alkane ligands · C–H activation · hyperconjugation · NMR spectroscopy

[1] a) S. Zarić, M. B. Hall, *J. Phys. Chem. A* **1997**, *101*, 4646, and references therein; b) C. Hall, R. N. Perutz, *Chem. Rev.* **1996**, *96*, 3125.

[2] Reviews: a) J. A. Labinger, J. E. Bercaw, *Nature* **2002**, *417*, 507; b) R. H. Crabtree, *J. Chem. Soc. Dalton Trans.* **2001**, *17*, 2437; c) W. D. Jones, *Acc. Chem. Res.* **2003**, *36*, 140; d) M. Lersch, M. Tilset, *Chem. Rev.* **2005**, *105*, 2471; e) S. R. Klei, J. T. Golden, P. Burger, R. G. Bergman, *J. Mol. Catal. A* **2002**, *189*, 79.

[3] a) S. Geftakis, G. E. Ball, *J. Am. Chem. Soc.* **1998**, *120*, 9953; b) S. Geftakis, G. E. Ball, *J. Am. Chem. Soc.* **1999**, *121*, 6336; c) D. J. Lawes, S. Geftakis, G. E. Ball, *J. Am. Chem. Soc.* **2005**, *127*, 4134.

[4] The barrier to ring inversion of cyclohexane is 43 kJ mol^{-1} (F. R. Jensen, D. S. Noyce, C. H. Sederholm, A. J. Berlin, *J. Am. Chem. Soc.* **1960**, *82*, 1256); so the rate of interconversion of the chair forms of cyclohexane is ca. 1 s^{-1} at 180 K.

[5] See the Supporting Information for details of experimental NMR procedures.

[6] See the Supporting Information for the preparation of labeled alkanes.

[7] J. Geertsen, J. Oddershede, W. T. Raynes, *Magn. Reson. Chem.* **1993**, *31*, 722.

[8] See the Supporting Information for details of the quantum mechanical calculations.

[9] Details of the derivation of these values are given in the Supporting Information.

[10] For calculated structures of [$CpRe(CO)_2$(ethane)] and [$CpRe(CO)_2$(methane)], respectively, see: a) H. Yang, M. C. Asplund, K. T. Kotz, M. J. Wilkens, H. Frei, C. B. Harris, *J. Am. Chem. Soc.* **1998**, *120*, 10154; b) R. G. Bergman, T. R. Cundari, A. M. Gillespie, T. B. Gunnoe, W. D. Harman, T. R. Klinckman, M. D. Temple, D. P. White, *Organometallics* **2003**, *22*, 2331.

[11] I. Castro-Rodriguez, H. Nakai, P. Gantzel, L. N. Zakharov, A. L. Rheingold, K. Meyer, *J. Am. Chem. Soc.* **2003**, *125*, 15734.

[12] a) A. S. Cieplak, *J. Am. Chem. Soc.* **1981**, *103*, 4540; b) C. T. Johnson, B. D. Tait, A. S. Cieplak, *J. Am. Chem. Soc.* **1987**, *109*, 5875; c) A. S. Cieplak, *J. Org. Chem.* **1998**, *63*, 521; d) A. S. Cieplak, *Chem. Rev.* **1999**, *99*, 1265.

[13] a) W. Adcock, A. N. Abeyrickrema, *J. Org. Chem.* **1982**, *47*, 2957; b) W. Adcock, A. N. Abeyrickrema, G. B. Kok, *J. Org. Chem.* **1984**, *49*, 1387; c) W. Adcock, V. S. Iyer, *J. Org. Chem.* **1988**, *53*, 5259; d) W. Adcock, N. A. Trout, *J. Org. Chem.* **1991**, *56*, 3229; e) W. Adcock, J. Cotton, N. A. Trout, *J. Org. Chem.* **1994**, *59*, 1867; f) W. Adcock, N. J. Head, N. R. Lokan, N. A. Trout, *J. Org. Chem.* **1997**, *62*, 6177; g) W. Adcock, N. A. Trout, *Magn. Reson. Chem.* **1998**, *36*, 181; h) W. Adcock, N. A. Trout, *Chem. Rev.* **1999**, *99*, 1415.

[14] a) C. K. Cheung, L. T. Tseng, M. H. Lin, S. Srivastava, W. J. le Noble, *J. Am. Chem. Soc.* **1986**, *108*, 1598; b) M. Xie, W. J. le Noble, *J. Org. Chem.* **1989**, *54*, 3836; c) V. R. Bodepudi, W. J. le Noble, *J. Org. Chem.* **1991**, *56*, 2001; d) W.-S. Chung, N. J. Turro, S. Srivastava, W. J. le Noble, *J. Org. Chem.* **1991**, *56*, 5020; e) H. Li, J. E. Silver, W. H. Watson, R. P. Kashyap, W. J. le Noble, *J. Org. Chem.* **1991**, *56*, 5932; f) H. Li, W. J. le Noble, *Recl. Trav. Chim. Pays-Bas* **1992**, *111*, 199; g) V. R. Bodepudi, W. J. le Noble, *J. Org. Chem.* **1994**, *59*, 3265; h) M. Kaselj, W.-S. Chung, W. J. le Noble, *Chem. Rev.* **1999**, *99*, 1287.

[15] a) B. W. Gung, M. M. Yanik, *J. Org. Chem.* **1996**, *61*, 947; b) B. W. Gung, *Tetrahedron* **1996**, *52*, 5263; c) B. W. Gung, *Chem. Rev.* **1999**, *99*, 1377.

[16] a) M. D. Rozeboom, K. N. Houk, *J. Am. Chem. Soc.* **1982**, *104*, 1189; b) Y.-D. Wu, K. N. Houk, *J. Am. Chem. Soc.* **1987**, *109*, 908; c) Y.-D. Wu, J. A. Tucker, K. N. Houk, *J. Am. Chem. Soc.* **1991**, *113*, 5018.

[17] a) T. Laube, H. U. Stilz, *J. Am. Chem. Soc.* **1987**, *109*, 5876; b) T. Laube, T.-K. Ha, *J. Am. Chem. Soc.* **1988**, *110*, 5511; c) T. Laube, S. Hollenstein, *J. Am. Chem. Soc.* **1992**, *114*, 8812.

[18] a) P. R. Rablen, R. W. Hoffmann, D. A. Hrovat, W. T. Boron, *J. Chem. Soc. Perkin Trans. 2* **1999**, 1719; b) A. Filippi, N. A. Trout, P. Brunelle, W. Adcock, T. Sorenson, M. Speranza, *J. Org. Chem.* **2004**, *69*, 5537.

[19] P. Deslongchamps, *Stereoelectronic Effects in Organic Chemistry*, Pergamon, Oxford, **1983**.

[20] G. J. Kubas, *J. Organomet. Chem.* **2001**, *635*, 37.

[21] M. E. González-Núñez, G. Castellano, C. Andrew, J. Royo, M. Báguena, R. Mello, G. Asensio, *J. Am. Chem. Soc.* **2001**, *123*, 7487.

[22] See: R. Koch, T. Clark, *The Chemist's Electronic Book of Orbitals*, Springer, Berlin, **1999**.

 © 2006 Wiley-VCH Verlag GmbH & Co. KGaA, Weinheim

Cyclophane Structure and Behavior

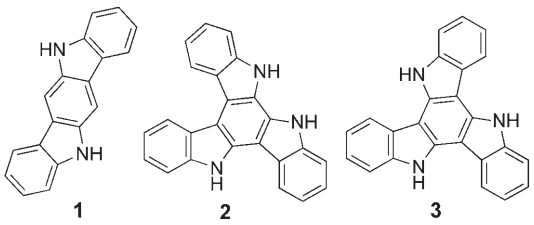
DOI: 10.1002/anie.200600526

A Redox-Active C_3-Symmetric Triindole-Based Triazacyclophane**

Berta Gómez-Lor, Gunther Hennrich, Beatriz Alonso, Angeles Monge, Enrique Gutierrez-Puebla, and Antonio M. Echavarren**

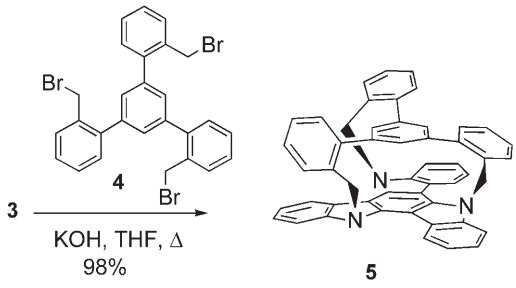
Interest in carbazole-based compounds has grown over the last few years due to their photoconductive properties and ability to transport positive charges (holes). Many carbazole-containing polymers and oligomers have been synthesized for electronic applications.[1] In fields like nonlinear optics, xerography, photorefractives, and organic light-emitting diodes, the photoconductivity or hole-transport properties of the carbazolyl groups are being extensively utilized.[2] In addition, new carbazole-related molecules such as indolo[3,2-*b*]carbazole (**1**)[3] and 6,11-dihydro-5*H*-diindolo[2,3-*a*;2′,3′-*c*]carbazole (**2**)[4] have been prepared which show extended π systems in which two or three carbazole units, respectively, share an aromatic ring (Scheme 1). These structures are being widely investigated in the field of organic electronics.

In contrast to compound **2**, which is easily obtained by oxidative trimerization of indole, the symmetrical analogue 10,15-dihydro-5*H*-5,10,15-triazadiindeno[1,2-*a*;1′,2′-*c*]fluorene (**3**) has been very rarely studied, probably due to difficulties in its synthesis.[5] Owing to its extended π system and its planar, disk-like structure, this C_3-symmetric molecule offers great potential as a central core for the construction of columnar liquid crystals for one-dimensional conduction.[6] We have recently reported the convenient synthesis of **3**[7] from a known symmetrical hexabromotriindole[8] by palladium-catalyzed reductive debromination with triethylammonium formate. The ready availability of **3** on the multigram scale prompted us to investigate the electron-donating nature of this platform.



Scheme 1. Carbazole-based molecules with extended π systems.

Herein we report on the high-yielding synthesis of a new triazacyclophane based on this triindole platform, its crystal structure and redox behavior, and the characterization by X-ray diffraction of the corresponding radical cation. Triindole platform **3** is *N*-alkylated in order to avoid N–N coupling, which is one of the undesired chemical side reactions that can cause irreversible cyclic voltammetry behavior of carbazole derivatives upon oxidation. The alkylation of **3** with tris(benzylbromide)benzene **4** was performed with the aim to get a cyclophane as their unique geometry forces the aromatic rings into a cofacial arrangement that makes them perfect models for charge-transport processes.[9] Triazacyclophane **5** was obtained as a white powder in almost quantitative yield (Scheme 2).[10]



Scheme 2. Synthesis of cyclophane **5**.

Recrystallization of **5** from $CHCl_3$ furnishes colorless crystals suitable for X-ray diffraction. The X-ray crystal structure determination indicates that the central rings of the triindole and the triphenylbenzene are practically parallel (0.7(4)°) and are held at a distance of 3.223(4) Å, with the central benzene units being slightly rotated (≈9°) with respect to each other (Figure 1). The molecules of **5** pack in the crystal in pairs of enantiomers, isolated by solvent molecules, with a staggered face-to-face arrangement of the triphenylbenzene moiety (distance between the centroids of the central ring: 5.787(4) Å). Crystallographic packing (Figure 2) shows no evidence for a triindole/triindole interaction.

Cyclophane **5** shows NMR data consistent with C_3 symmetry (Figure 3a). As a result of the rigid structure, the methylene hydrogen atoms appear as AX systems with a coupling constant of $J = 14.7$ Hz. Unequivocal ^{1}H NMR signal assignments were made on the basis of COSY and HMQC experiments. Addition of trifuoroacetic acid (TFA) to the $CDCl_3$ solution yielded a dark-blue solution, for which all the NMR signals except H6–H9 are broadened or have even

[*] Dr. B. Gómez-Lor, Prof. Dr. A. Monge, Prof. Dr. E. Gutierrez-Puebla
Instituto de Ciencia de Materiales de Madrid
Cantoblanco, 20849 Madrid (Spain)
Fax: (+34) 91-372-0623
E-mail: bgl@icmm.csic.es
Prof. Dr. A. M. Echavarren
Institut Català d'Investigació Química (ICIQ)
43007 Tarragona (Spain)
Fax: (+34) 97-792-0218
E-mail: aechavarren@iciq.es
Dr. G. Hennrich, Dr. B. Alonso
Departamento de Química Orgánica
Departamento de Química Inorgánica
Universidad Autónoma de Madrid
Cantoblanco, 20849 Madrid (Spain)

[**] We are grateful to the Ministerio de Educación y Ciencia (MEC; grant nos. CTQ2004-02865/BQU to B.G.-L. and CTQ2004-02869 to A.M.E. and Ramón y Cajal contract to G.H.), the Comunidad Autónoma de Madrid (project no. 200580M133), and the ICIQ Foundation for financial support. We also thank Prof. J. Elguero for helpful comments.

 © 2006 Wiley-VCH Verlag GmbH & Co. KGaA, Weinheim

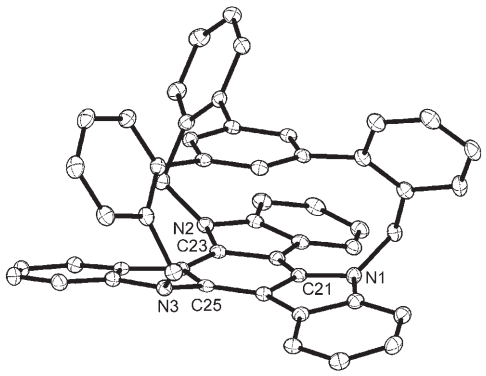


Figure 1. ORTEP plot of **5**.

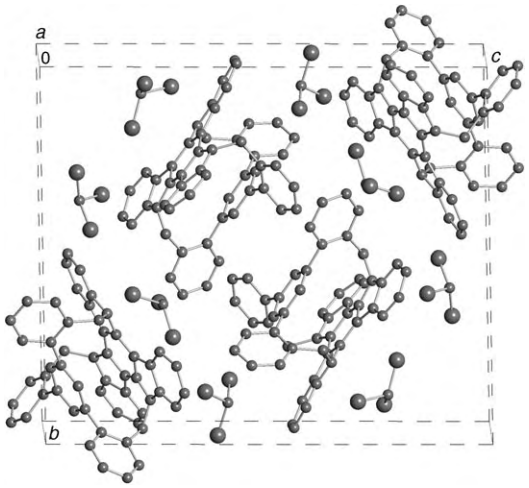


Figure 2. Unit cell of **5**–$(CHCl_3)_2$.

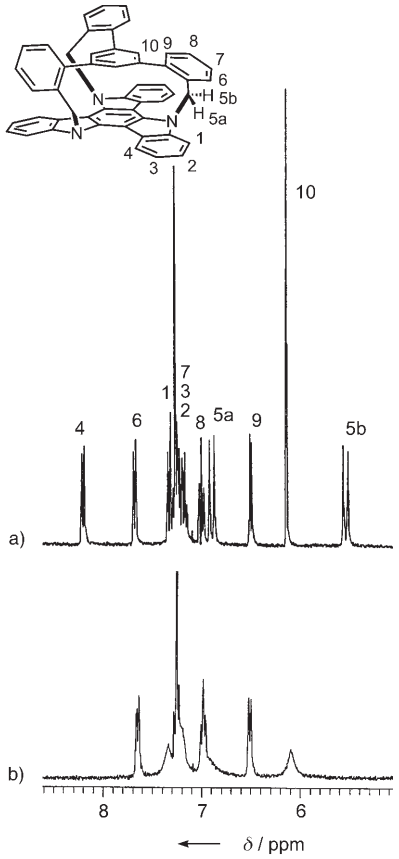


Figure 3. NMR signals for cyclophane **5** a) before and b) after addition of TFA.

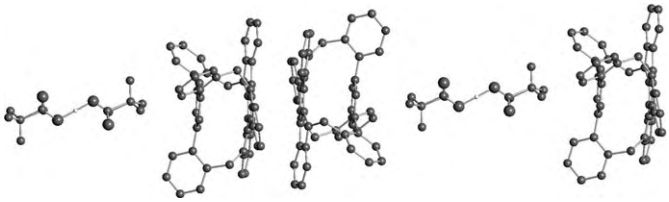


Figure 4. Alternation of the dimeric stacks of $(\mathbf{5})_2^{\bullet+}$ and the anions ($CF_3COO^-\cdot CF_3COOH$) along the direction (111).

vanished (Figure 3b).[11] TFA has been used as a one-electron oxidant to generate radical cations,[12] even though there is controversy about how the oxidation actually occurs.[13] The broadening of the proton signals is presumably due to fast electron exchange between the radical cation and the neutral parent molecule, and it reveals the electron spin density on the different sites of the radical cation. Broadening of the H10 NMR signal therefore suggests a spin delocalization through space.

From oxidized solutions of **5**, black crystals suitable for X-ray crystallography were obtained; these crystals are surprisingly stable at room temperature for several weeks. X-ray analysis indicates the structure to be the dimeric radical cation $(\mathbf{5})_2^{\bullet+}$, with the positive charge delocalized over the two molecules within the dimeric structure[14,15] and with two disordered hydrogen-bonded trifluoroacetate molecules acting as counterions for each dimer.[16] Related trifluoroacetate dimers have been previously reported as counterions.[17] The crystal packing shows infinite stacks in which two cyclophane enantiomers are in a staggered face-to-face arrangement of the triindole moieties, with a separation of 3.270(4) Å (centroid–centroid distance of the central rings), isolated by the anions (Figure 4). The close distance, shorter than the sum of normal van der Waals separation, is also indicative of the formation of discrete radical cation dimers. These dimers are considered to be the smallest supramolecular unit that can carry a delocalized positive charge.[14b,18]

Structure comparison of the neutral and the radical-cation dimers shows some differences, in spite of the molecular strain of cyclophane **5**. The most notable difference is a shortening in the distance between the central rings of the triindole and the triphenylbenzene (3.169(4) Å in the radical cation), thereby suggesting a through-space interaction. Another difference is the contraction of the bonds connecting each nitrogen atom with the central benzene ring in the radical cation (N1–C21 1.377(4), N2–C23 1.394(4), N3–C25 1.376(4) Å) relative to those in the neutral donor (N1–C21 1.397(3), N2–C23 1.407(3), N3–C25 1.392(3) Å). This reflects delocalization of the charge over the triindole platform. No other remarkable geometrical changes were observed.

The chemical oxidation of **5** was monitored by UV/Vis spectroscopy. Upon addition of phenyliodine(III) bis(trifluor-

 © 2006 Wiley-VCH Verlag GmbH & Co. KGaA, Weinheim

oacetate) (PIFA) to a solution of **5** in CH_2Cl_2, dramatic changes occur in three spectral regions (Figure 5). Diminution of the major triindole absorption (306 nm) is accompanied by an increase of two bands in the visible region (412 (minor) and 682 nm (major)) and the appearance of a broad, weak band in the near infrared (900–1030 nm). The spectral changes are time-dependent and are completed after 15 min under the chosen experimental conditions.

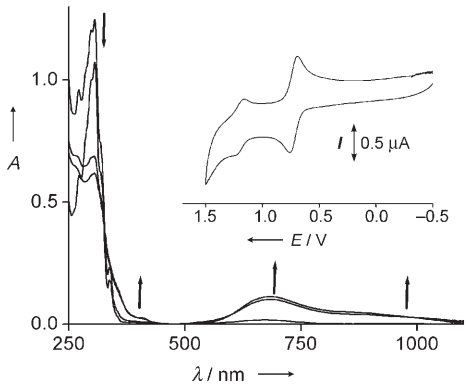


Figure 5. Change in the UV/Vis absorption of **5** in CH_2Cl_2 ($c = 10^{-5}$ mol L^{-1}) upon addition of PIFA (10 equiv), after 0.5, 10, and 15 min. Inset: Cyclic voltammogram of **5** ($c = 10^{-5}$ mol L^{-1}) recorded in CH_2Cl_2/0.1 M tetra-*n*-butylammonium hydroxide (TBAH) with a Pt working electrode. Scan rate: 0.1 V s^{-1}.

We attribute these changes to the formation of a radical cation species with characteristic absorption in the visible region.[19] The radical species would immediately form a dimeric charge-resonance (CR) complex between the initially formed radical cation and its neutral counterpart, thereby yielding a distinctive CR band in the near infrared.[20] The coexistence of all three species (the neutral, monomeric radical cation, and CR complex species) gives rise to a complex absorption spectrum with broad, overlapping bands. The time dependence of the formation of the new species is influenced by the oxidation agent used, as demonstrated for comparable systems.[21] However, the spectra observed after 15 min remain practically unchanged for hours, a result that indicates the stability of the generated radical and complex species.

Cyclic voltammograms of **5** show two well-defined reversible redox processes at 0.8 and 1.2 V (Figure 5, inset). Interestingly, the anodic peak current of the second wave is lower than the i_p value of the first oxidation step and is concentration-dependent, decreasing as the effective concentration of **5** lowers, most likely due to the formation of dimeric assemblies, as shown previously.

In conclusion, a novel triazacyclophane, **5**, based on the C_3-symmetric indole trimer **3**, that forms unusually stable radical cation–neutral molecule dimers upon oxidation has been synthesized. X-ray evaluation of the differences in the structure of the neutral and oxidized species has been achieved; this is usually a difficult task due to the characteristic instability of radical species. This crystallographic study revealed a dimeric association of $(\mathbf{5})_2^{\bullet+}$ through the triindole platform. In solution, the presence of the radical species, forming dimeric resonance-transfer complexes, is confirmed by employing UV/Vis spectroscopy. The intriguing structural and electronic properties of the novel cyclophane reported herein hold great promise for potential applications of trindole-based materials in the field of molecular electronics. Research in this direction is ongoing.

Experimental Section

X-ray structure determinations: Colorless crystals of **5** and dark-blue crystals of $\mathbf{5}^{\bullet+}$ showing well-defined faces were mounted on a Bruker-Siemens Smart CCD diffractometer equipped with a low-temperature device, a normal focus, and a 2.4-kW sealed-tube X-ray source ($Mo_{K\alpha}$ radiation, $\lambda = 0.71067$ Å) operating at 50 kV and 20 mA. Low-temperature data (173 K) were collected over a hemisphere of the reciprocal space by a combination of three exposure sets. Each exposure of 10 s covered 0.3° in ω over the ranges $2° < \theta < 29°$ (for **5**) and $2° < \theta < 27°$ (for $\mathbf{5}^{\bullet+}$).The first 100 frames were recollected at the end of the data collection to monitor crystal decay. The intensities were corrected for Lorentz and polarization effects. The structures were solved by the Multan and Fourier methods. Crystal data for **5**–$(CHCl_3)_2$: crystal dimensions: $0.20 \times 0.20 \times 0.16$ mm^3; unit cell dimensions: $a = 10.710(1)$, $b = 18.399(2)$, $c = 21.948(3)$ Å; monoclinic, space group $P2(1)/c$, $\beta = 99.948(2)°$, $V = 4259.9(8)$ $Å^3$, $Z = 4$, $\rho_{calcd} = 1.445$ mg m^{-3}. **5**–$(CHCl_3)_2$ was refined anisotropically: $R1(F) = 0.1021$ for all data; $R1(F) = 0.0771$ for observed data with $I > 2\sigma(I)$; GOF(F2) = 1.10. Crystal data for $(\mathbf{5})_2^{\bullet+}$–$(CF_3COO^-\cdot CF_3COOH)$: crystal dimensions: $0.20 \times 0.20 \times 0.20$ mm^3; unit cell dimensions: $a = 12.1969(6)$, $b = 12.4372(6)$, $c = 13.0011(6)$ Å; triclinic, centrosymmetric space group $P\bar{1}$, $\alpha = 80.570(1)$, $\beta = 81.874(1)$, $\gamma = 83.194(1)°$, $V = 1916.8(2)$ $Å^3$, $Z = 1$, $\rho_{calcd} = 1.388$ mg m^{-3}. $(\mathbf{5})_2^{\bullet+}$–$(CF_3COO^-\cdot CF_3COOH)$ was refined anisotropically: $R1(F) = 0.1060$ for all data; $R1(F) = 0.0851$ for observed data with $I > 2\sigma(I)$; GOF(F2) = 1.06. The trifuoracetate groups are disordered and a model of disorder of the α carbon atoms was employed. The typical CF_3 disorder is also present but attempts to model it did not improve the refinement process. Most of the calculations were carried out with SMART[22] software for data collection and reduction and the SHELXTL[23] software for structure solution and refinements. CCDC 297289 and CCDC 297290 contain the supplementary crystallographic data for this paper. These data can be obtained free of charge from The Cambridge Crystallographic Data Centre via www.ccdc.cam.ac.uk/data_request/cif.

Cyclophane **5**: A mixture of **3** (102 mg, 0.3 mmol) and KOH (168 mg, 3 mmol) in THF (40 mL) was heated under reflux for 15 min. Tribromide **4** (176 mg, 0.3 mmol) was then added and the mixture was heated for 16 h. The mixture was diluted with EtOAc, washed with 10% aqueous HCl and saturated aqueous NaCl solution, dried (Na_2SO_4), and evaporated. The residue was purified by chromatography with CH_2Cl_2/hexanes (1:1) to give **5** as a white solid (200 mg, 98%): m.p. = 154–156 °C; ^{1}H NMR (300 MHz, $CDCl_3$): $\delta = 8.18$ (d, $J = 7.6$ Hz, 3H), 7.66 (d, $J = 7.0$ Hz, 3H), 7.32–7.13 (m, 4H), 7.01 (t, $J = 7.4$ Hz, 3H), 6.89 (d, $J = 14.7$ Hz, 3H), 6.49 (d, $J = 6.5$ Hz, 3H), 6.12 (s, 6H), 5.53 ppm (d, $J = 14.7$ Hz, 3H); ^{13}C NMR ($CDCl_3$, 75 MHz): $\delta = 142.51$, 142.21, 141.40, 141.01, 136.04, 132.64, 132.05, 127.37, 126.62, 125.14, 122.68, 121.68, 129.12, 114.45, 104.55, 52.07 ppm; FAB MS: m/z (%): 687 [M^+] (29), 307 (31), 154 (100); HR-MS (FAB): calcd for $C_{51}H_{34}N_3$: 688.2752; found: 688.2724.

Received: February 8, 2006
Published online: June 13, 2006

Keywords: charge transfer · cyclophanes · heterocycles · oxidation · radical ions

 © 2006 Wiley-VCH Verlag GmbH & Co. KGaA, Weinheim

[1] a) F. Dierschkle, A. C. Grimsdale, K. Müllen, *Macromol. Chem. Phys.* **2004**, *205*, 1147 – 1154; b) Y. Takihana, M. Shiotsuki, F. Sanda, T. Masuda, *Macromolecules* **2004**, *37*, 7578 – 7583; c) K. Brunner, A. van Dijken, H. Börner, J. J. A. M. Bastiaansen, N. M. M. Kliggen, B. M. W. Langeveld, *J. Am. Chem. Soc.* **2004**, *126*, 6035 – 6042; d) H. Li, Y. Zhang, Y. Hu, L. Ma, X. Jing, F. Wang, *Macromol. Chem. Phys.* **2004**, *205*, 247 – 255; e) N. Drolet, J.-F. Morin, N. Leclerc, S. Wakin, Y. Tao, M. Leclerc, *Adv. Funct. Mater.* **2005**, *15*, 1671 – 1682.

[2] For a recent review, see: J. V. Grazulevivius, P. Strohriegl, J. Pielichowski, K. Pielichowski, *Prog. Polym. Sci.* **2003**, *28*, 1297 – 1353.

[3] a) N.-X. Hu, X. Shuang, Z. Popovic, B. Ong, A.-M. Hoor, *J. Am. Chem. Soc.* **1999**, *121*, 5097 – 5098; b) S. Wakim, J. Bouchard, M. Simard, N. Drolet, Y. Tao, M. Leclerc, *Chem. Mater.* **2004**, *16*, 4386 – 4388; c) Y. Wu, Y. Li, S. Gadner, B. S. Ong, *J. Am. Chem. Soc.* **2005**, *127*, 614 – 618; d) Y. Wu, Y. Li, S. Gadner, B. S. Ong, *Adv. Mater.* **2005**, *7*, 849 – 853.

[4] a) A. R. Mount, M. T. Robertson, *Phys. Chem. Chem. Phys.* **1999**, *1*, 5169 – 5177; b) P. Jennings, A. C. Jones, A. R. Mount, *Phys. Chem. Chem. Phys.* **2000**, *2*, 1241 – 1248; c) L. Greci, G. Tommasi, R. Petrucci, G. Marrosu, A. Trazza, P. Sgarabotto, L. Righi, A. Alberti, *J. Chem. Soc. Perkin Trans. 2* **2000**, 2337 – 2342.

[5] Compound **3** has been prepared by the acid-catalyzed reaction between indole and 3-bromoindole, which furnishes a complex mixture of indole dimers and trimers from which **3** can be obtained only in low yield: V. Bocchi, G. Palla, *Tetrahedron* **1986**, *42*, 5019 – 5024.

[6] J. M. Warman, P. M. de Haas, G. Dicker, F. C. Grozema, J. Piris, M. G. Debije, *Chem. Mater.* **2004**, *16*, 4600 – 4609.

[7] B. Gómez-Lor, A. M. Echavarren, *Org. Lett.* **2004**, *6*, 2993 – 2996.

[8] N. Robertson, S. Parsons, E. J. MacLean, R. A. Coxall, R. A. Mount, *J. Mater. Chem.* **2000**, *10*, 2043 – 2047.

[9] a) B. Speisser in *Modern Cyclophane Chemistry* (Eds: R. Gleiter, H. Hopf), Wiley-VCH, Weinheim, **2004**; b) G. B. Bartholemew, G. C. Bazan, *Acc. Chem. Res.* **2001**, *34*, 30 – 39.

[10] We have previously reported the synthesis of the all-carbon analogue: a) Ó. de Frutos, B. Gómez-Lor, T. Granier, M. A. Monge, E. Gutiérrez-Puebla, A. M. Echavarren, *Angew. Chem.* **1999**, *111*, 1552 – 1555; *Angew. Chem. Int. Ed.* **1999**, *38*, 205 – 207; b) Ó. de Frutos, B. Gómez-Lor, T. Granier, M. A. Monge, E. Gutiérrez-Puebla, A. M. Echavarren, *Chem. Eur. J.* **2002**, *8*, 2879 – 2890.

[11] a) V. M. Domingo, X. Burelons, E. Brillas, J. Carrilla, J. Rius, X. Torrelles, L. Juliá, *J. Org. Chem.* **2000**, *65*, 6847 – 6855; b) L. R. Milgrom, W. D. Flitter, *Tetrahedron* **1993**, *49*, 507 – 514; c) L. Eberson, F. Radner, *J. Chem. Soc. Chem. Commun.* **1991**, 1233 – 1234.

[12] A. Alberti, B. Ballarin, M. Guerra, D. Macciantelli, A. Mucci, F. Parenti, L. Schenetti, R. Seeber, C. Zanardi, *ChemPhysChem* **2003**, *4*, 1216 – 1225.

[13] a) R. Rathore, C. Zu, S. V. Lindeman, J. K. Kochi, *J. Chem. Soc. Perkin Trans. 2* **2000**, 1837 – 1840; b) L. Eberson, F. Radner, *Acta Chem. Scand.* **1998**, *52*, 114 – 130.

[14] Aromatic donor molecules tend to self-associate with their corresponding radical cations, thereby yielding dimeric electronically delocalized structures: a) J. K. Kochi, R. Rathore, P. Le Maguerés, *J. Org. Chem.* **2000**, *65*, 6826 – 6836, and references therein; b) D.-L. Sun, S. V. Rosokha, S. V. Lindeman, J. K. Kochi, *J. Am. Chem. Soc.* **2003**, *125*, 15950 – 15963; c) M. Yoshizawa, K. Kumazawa, M. Fujita, *J. Am. Chem. Soc.* **2005**, *127*, 13456 – 13457.

[15] The compound crystallizes in the triclinic system. Given that, in this system, the space group is not unequivocally determined through the systematic extinctions, the structure was solved in both the $P1$ and $P\bar{1}$ space groups. After careful analysis of the results in the acentric group, no significant geometrical differences were observed either in the independent cyclophane molecules or in the dimeric anion. Consequently, the structure presented here corresponds to that solved in the $P\bar{1}$ group: A. L. Spek, PLATON, A Multipurpose Crystallographic Tool, Utrecht University, Utrecht, The Netherlands, **2005**.

[16] The shared hydrogen atom in the trifluoroacetate dimer has been observed in a Δ Fourier map in both the P1 and $P\bar{1}$ space groups.

[17] a) A. Kunze, R. Gleiter, F. Rominger, *Chem. Commun.* **1999**, 171 – 172; b) J. Pawlas, M. Kawatsura, J. F. Hartwig, *J. Am. Chem. Soc.* **2002**, *124*, 3669 – 3679.

[18] P. Le Maguerés, S. V. Lindeman, J. K. Kochi, *Org. Lett.* **2000**, *2*, 3567 – 3570.

[19] S. I. Hauck, K. V. Lakshimi, J. F. Hartwig, *Org. Lett.* **1999**, *1*, 2057 – 2060.

[20] a) See reference [14a]; b) P. Le Maguerés, S. V. Lindeman, J. K. Kochi, *J. Chem. Soc. Perkin Trans. 2* **2001**, 1180 – 1185; c) D. Sun, S. V. Rosokha, J. K. Kochi, *J. Am. Chem. Soc.* **2004**, *126*, 1388 – 1401.

[21] A. Ito, K. Tanaka, K. Kanemoto, T. Kato, *J. Org. Chem.* **2002**, *67*, 491 – 498. The same trends were observed for trifluoroacetic acid (slow) and $SbCl_5$ (fast). We refrained from using $SbCl_5$ due to the strong spectral overlap in the UV and Vis region.

[22] Software for the SMART system, V.5.04, Bruker-Siemens Analytical X-ray Instruments, Inc., Madison, WI, USA, **1998**.

[23] G. M. Sheldrick, SHELXL97, Program for Crystal Structure Refinement, University of Göttingen, Germany, **1997**.

 © 2006 Wiley-VCH Verlag GmbH & Co. KGaA, Weinheim

Synchronized Motion of Ligands

DOI: 10.1002/anie.200600827

Overcrowded Organometallic Platinum(II) Complexes That Behave as Molecular Gears**

Raffaello Romeo, Salvatore Carnabuci, Lucia Fenech, Maria Rosaria Plutino, and Alberto Albinati*

The bottom-up approach to functional materials and the development of molecular-sized analogues of mechanical devices, such as shuttles,[1] rotors,[2] brakes,[3] ratchets,[4]

[*] Prof. R. Romeo, Dr. S. Carnabuci, Dr. L. Fenech
Dipartimento di Chimica Inorganica, Chimica Analitica
e Chimica Fisica
Università di Messina
Salita Sperone 31, 98166 Vill. S. Agata, Messina (Italy)
Fax: (+39) 090-393-756
E-mail: rromeo@unime.it

Dr. M. R. Plutino
ISMN-CNR, Unità di Messina (Italy)

Prof. A. Albinati
Dipartimento di Chimica Strutturale e Stereochimica Inorganica
e Facoltà di Farmacia, Università di Milano
20133, Milano (Italy)

[**] We are grateful to the Ministero dell'Università e della Ricerca Scientifica e Tecnologica (MIUR), PRIN 2004, and to the University of Messina (PRA 2003) for funding this work, and to Prof. Brian Mann and Prof. Pablo Espinet for helpful discussions.

WILEY InterScience DISCOVER SOMETHING GREAT
© 2006 Wiley-VCH Verlag GmbH & Co. KGaA, Weinheim

gears,[5] and even molecular elevators,[6] constitute a challenge for chemists. All these nanosystems act on external chemical stimuli, such as pH changes, photoactivation, or charge injection.

We have recently reported on the fluxional motion of the 2,9-dimethyl-1,10-phenanthroline (dmphen) ligand between nonequivalent exchanging sites in cationic complex ions of the type $[Pt(Me)(dmphen)(L)]^+$, where L is a neutral S- or P-donor ligand.[7–9] The mechanism is switchable between associative and dissociative pathways. A fine-tuning of the rate and mechanism of the dynamic exchange of the coordinated dmphen ligand can be achieved by varying the solvent, the counterion, the nature and concentration of added nucleophiles, and the electronic and steric characteristics of the ligand L. The driving force for the fluxional motion is the steric distortion of the dmphen ligand, as measured by the dihedral angle between the dmphen plane and the coordination plane, the steric congestion at the metal, and a marked lengthening of the platinum–nitrogen bonds. A free-energy surface constructed for the reacting system by use of the quantitative analysis of ligand effects (QALE)[10] predicts a very fast flipping of dmphen when using phosphanes with a high cone angle. No restricted rotation was observed for any phosphane around the Pt–P or P–C_{ipso} bonds.

When we turned our interest to the dynamic behavior of $[Pt(Me)(dmphen)(PR_3)]^+$ complexes bearing bulky *o*-methoxyphenyl groups on the phosphorus donor atom we observed a very interesting phenomenon: contrary to our expectations, the fluxional motion of dmphen decreases with increasing steric congestion at PR_3, and for tris(2-methoxyphenyl)phosphane and bis(2-methoxyphenyl)phenylphosphane the rate of flipping of dmphen appears to be identical to that of phosphane rotation.

The rate of flipping of dmphen in **1** (see Figure 1 for structure) was monitored using the broadening of the signals of the substituent methyl groups in the 2- and 9-positions of the dmphen ligand (Me_a and Me_b, respectively, in Figure 2) as a probe. The rate of phosphane rotation was followed by monitoring the changes of the signals of the methyl groups of the *ortho*-methoxy groups (Me_x, Me_y, and Me_z in Figure 2). The rate constants of both the dynamic processes were determined separately or by a full line-shape analysis of the spectra (Figure 2) using the computer program gNMR 4.0,[11] and were found to be practically identical ($\Delta G^{\neq} = (55.4 \pm 0.3)\ kJ\,mol^{-1}$).

Compound **2** (Figure 1) has a static structure in solution as far as the planar 1,10-phenanthroline ligand is concerned, although its rate of phosphane rotation is essentially identical to that of compound **1** ($\Delta G^{\neq} = (55.6 \pm 0.2)\ kJ\,mol^{-1}$), the difference between the free-energies of activation being in the range of the statistical error at 340 K (see data in Table 1). The ^1H NMR resonance for Pt–Me of both **1** and **2** is practically unaffected by an increase of temperature, apart from a small shift to higher frequency and a sharpening of the ^{195}Pt satellites.[12]

The steric congestion in the coordination plane of the substrate is responsible for the two dynamic motions in compound **1** and for the restricted rotation around the Pt–P bond in **2**. As shown in the ORTEP view of compound **1** (Figure 1), two methoxy groups of the phenyl rings of the phosphane lie above and below the coordination plane in such a way that it resembles a "pseudo-octahedral" complex.[13] The steric clash between the bulky *ortho*-methoxy substituents and the adjacent methyl group of the phenanthroline ligand determines a tetrahedral distortion of the square-planar coordination geometry, a loss of planarity of the dmphen ligand, and, most remarkably, a rotation of the dmphen moiety around the N1–N2 vector to form a dihedral angle of 35.7(2)° with the mean-square coordination plane. A comparison with compound **2**, in which the unsubstituted phenanthroline moiety is coplanar with the coordination plane, shows that methyl substitution on dmphen is crucial in dictating its geometry and dynamic motion but hardly affects the rate of phosphane rotation. In other words, the two phosphane-containing moieties of **1** and **2** are identical from a structural and dynamic viewpoint, but the remaining two are totally different. The Pt–N1 and Pt–N2 bonds are somewhat longer in **1** than in **2** (2.156(4) and 2.134(4) vs. 2.139(5) and 2.105(5) Å, respectively).

When addressing the question of how the connection between the two dynamic motions in compound **1** is

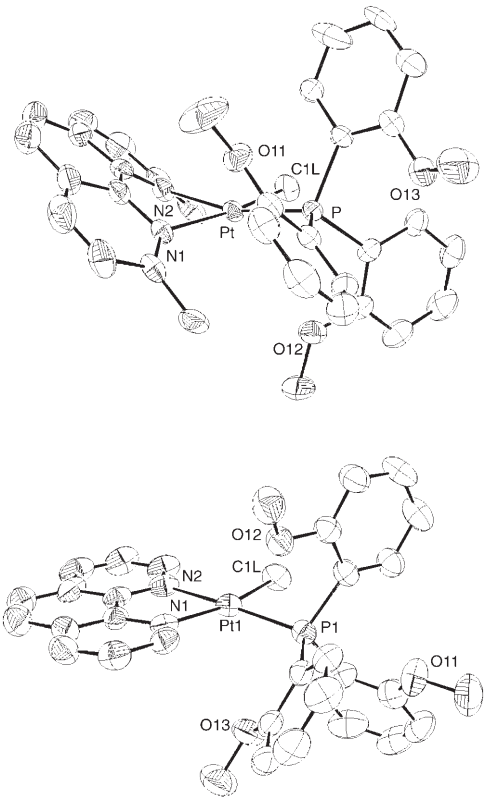


Figure 1. ORTEP drawings of the cationic complexes [Pt(Me)(dmphen){P(2-$MeOC_6H_4)_3$}] (**1**; top) and [Pt(Me)(phen){P(2-$MeOC_6H_4)_3$}] (**2**; bottom); thermal ellipsoids are at 50% probability. Selected bond lengths [Å] and bond and torsion angles [°] for compounds **1** and **2**, respectively: Pt1–C1L 2.057(5), 2.065(5); Pt1–P1 2.227(1), 2.242(2); Pt1–N1 2.156(4), 2.139(5); Pt1–N2 2.134(4), 2.105(5); N1-Pt1-N2 77.0(2), 78.1(2); P1-Pt1-C1L 83.3(2), 86.0(2); C1L-Pt1-N2 93.8(2), 91.5(2); P1-Pt1-N1 105.3(1), 104.7(1); Pt1-N1-N2-C10 36.8(5), 5.0(5).

 © 2006 Wiley-VCH Verlag GmbH & Co. KGaA, Weinheim

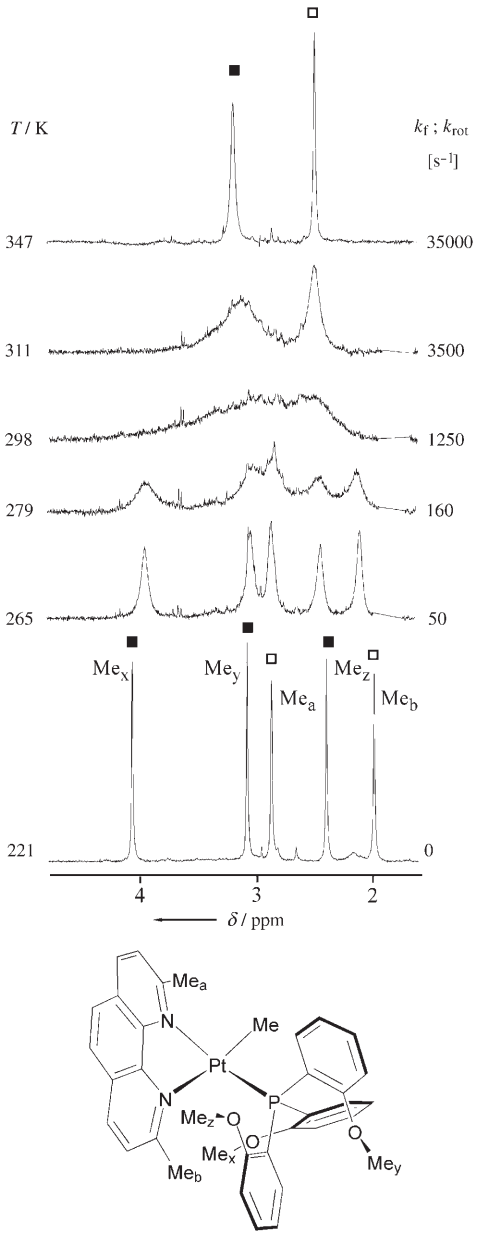


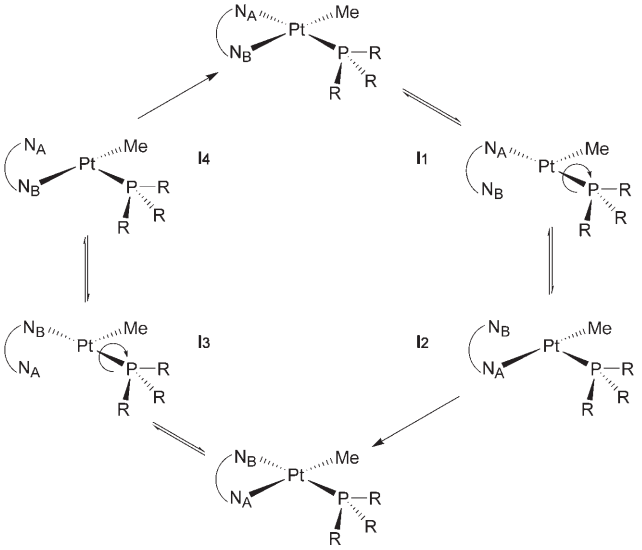
Figure 2. ^{1}H DNMR spectrum of **1** (300 MHz, $CDCl_3$, TMS) showing the phenanthroline methyl protons (open squares) and the methyl groups of the phosphane ligand (filled squares).

Table 1: Kinetic features for dynamic processes in the cationic $[Pt(Me)(N\text{-}N)(PR_3)]^+$ complexes in $CDCl_3$.

	N-N	PR_3	k_f[a] [10^3 s^{-1}]	k_{rot}[b] [10^3 s^{-1}]	$\Delta G^{\neq}$[c] [kJ mol^{-1}]
1	dmphen	P(2-MeOC$_6$H$_4$)$_3$	21.8 ± 0.2	21.8 ± 0.2	55.4 ± 0.3
2	phen	P(2-MeOC$_6$H$_4$)$_3$		19.0 ± 0.1	55.6 ± 0.2
3	dmphen	P(2-MeOC$_6$H$_4$)$_2$Ph	195 ± 1	195 ± 1	48.7 ± 0.1
4	dmphen	P(2-MeOC$_6$H$_4$)Ph$_2$	579 ± 2		46.2 ± 0.1

[a] Rate of N-N flipping at 340 K. [b] Rate of phosphane rotation at 340 K. [c] At 340 K.

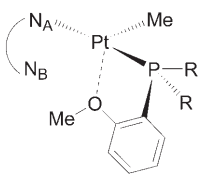
generated, we must take into account two main observations: 1) the rate of phosphane rotation is not greatly influenced by the coordination environment or whether the phenanthroline is flat or distorted; rather, the contrary seems to be true, namely the fluxional motion of dmphen in **1** is controlled by the rotation rate of the crowded phosphane; 2) the fluxional motion of dmphen in compound **1** is not affected by the nature of the counterion, the solvent (including CD_3OD), or by deliberate addition of weak nucleophiles (sulfoxides or sulfides) to the solution;[8] no traces of free PR_3 were observed by $^{31}P\{^1H\}$ NMR spectroscopy. These observations are perfectly in keeping with the dissociative mechanism established for these compounds.[7–9] Scheme 1 shows the suggested steps



Scheme 1. A dissociative mechanism involving three-coordinate, T-shaped intermediates (**I1**–**I4**) for the coupled rotation/flipping motion.

for the coupled process: 1) platinum–nitrogen bond breaking and the formation of two T-shaped, three-coordinate intermediates **I1** and **I3** containing η^1-coordinated dmphen, 2) their isomerization into the corresponding intermediates **I2** and **I4**, and 3) final ring closure. During the oscillation of dmphen between the two nonequivalent exchanging sites, the phosphane ligand rotates by 120° around the platinum–phosphorus bond. Restricted rotation about a platinum–phosphorus bond is a well-known phenomenon which often depends on the bulk of the ligand, although other causes have been found to participate in this dynamic process.[14]

A reasonable hypothesis is that one step of the dissociative mechanism, presumably ring closing of the monodentate three-coordinate intermediate complex $[Pt(Me)(\eta^1\text{-dmphen})\{P(2\text{-MeO-}C_6H_4)_3\}]^+$ (**I1** and **I3**), can be slowed down by the presence of methoxy groups on the phenyl rings of the phosphane projecting towards the metal center. The coordinative and electronic unsaturation of the 14-electron species[15] is somewhat compensated by a temporary electronic assistance from one oxygen of a methoxy group (Scheme 2) and, as a consequence, isomerization of the intermediate and the ring closing must await the



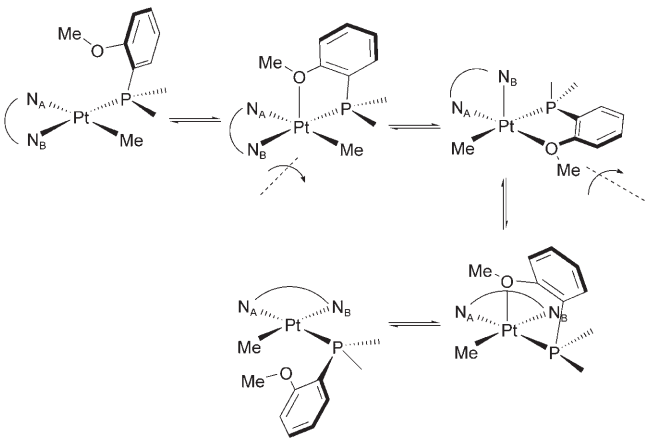
Scheme 2. Postulated interactions in the intermediates **I1** and **I3**.

 © 2006 Wiley-VCH Verlag GmbH & Co. KGaA, Weinheim

liberation of the coordination site from this oxygen atom before taking place.

This idea is supported by the steady increase in the coupled motion upon removal of one or two methoxy groups from the phosphane ligand. Table 1 shows that, on passing from P(2-$MeOC_6H_4)_3$ (in **1**) to P(2-$MeOC_6H_4)_2Ph$ (in **3**) a tenfold increase in the value of the two rates can be measured. On going from P(2-$MeOC_6H_4)_2Ph$ (in **3**) to P(2-$MeOC_6H_4)Ph_2$ (in **4**), we can no longer measure the rate of phosphane rotation. However, based on the free-energy surface that represents the way in which any single P-donor ligand can affect the energy of the transition state in the absence of any additional effect,[9] the value of $\Delta G^{\neq}$, (46.2 ± 0.1) kJ mol^{-1}, for the flipping of dmphen appears to be in the range expected from the value of the cone angle of P(2-$MeOC_6H_4)Ph_2$. Thus, we are inclined to conclude that the connection between the two motions in compound **4** is lost or becomes very weak.

A reasonable mechanistic alternative to dissociation could be a direct intramolecular attack at the metal center by the oxygen atom of the methoxy group. A variety of associative mechanisms could then be envisaged that involve 1) a sequence of nucleophilic substitution reactions that take place with retention of configuration, or 2) an intramolecular rearrangement from a five-coordinate intermediate, such as a Berry pseudorotation or a "turnstile" mechanism, as shown in Scheme 3.



Scheme 3. Turnstile mechanism involving simultaneous rotation of ligands on the triangular faces of a square-pyramidal adduct.

No distinction can be made among the possible reaction pathways on the basis of the kinetic data alone. However, we observe that 1) the flipping motion of dmphen in these complexes features an uncatalyzed intramolecular geometrical isomerization that, in platinum(II) complexes, is known to proceed with a dissociative mechanism very similar to that described in Scheme 1,[16] 2) if the addition of a fifth ligand is a prerequisite for the occurrence of the process we would have expected activation of fluxional motion of phen in **2** and an acceleration and a catalytic effect in **1**, **3**, and **4** by the addition of external nucleophiles that are much stronger than the oxygen of the methoxy group,[8] and 3) an associative attack should be facilitated by the number of oxygen atoms on the phosphane ligand, while the rates increase sharply along the series of complexes in the order **1** < **3** < **4**. Therefore, we conclude that release of steric congestion in these compounds confers a further impetus to ring opening, as expected from the results of previous studies, but ring closing is impeded by the contemporary slow rotation about the Pt–P bond.

The fascinating synchronism between the two motions—the fluxionality of dmphen and the rotation of the phosphane ligand—in complexes **1** and **3**, together with the possibility of being able to fine-tune the rates and the activation pathways, opens the way to the design of molecular gears whose dynamics can be controlled by intrinsic stereoelectronic properties (dissociative mechanism) or by external chemical stimuli (associative mechanism).

Received: March 2, 2006
Revised: April 12, 2006
Published online: June 13, 2006

Keywords: fluxionality · molecular devices · N ligands · NMR spectroscopy · platinum

[1] a) P. L. Anelli, N. Spencer, J. F. Stoddart, *J. Am. Chem. Soc.* **1991**, *113*, 5131–5133; b) P. R. Ashton, R. Ballardini, V. Balzani, I. Baxter, A. Credi, M. C. T. Fyfe, M. T. Gandolfi, M. Gomez-Lopez, M. V. Martinez-Diaz, A. Piersanti, N. Spencer, J. F. Stoddart, M. Venturi, A. J. P. White, D. J. Williams, *J. Am. Chem. Soc.* **1998**, *120*, 11932–11942; c) A. M. Brouwer, C. Frochot, F. G. Gatti, D. A. Leigh, L. Mottier, F. Paolucci, S. Roffia, G. W. H. Wurpel, *Science* **2001**, *291*, 2124–2128; d) J. P. Collin, C. Dietrich-Buchecker, P. Gavina, M. C. Jimenez-Molero, J. P. Sauvage, *Acc. Chem. Res.* **2001**, *34*, 477–487.

[2] a) M. F. Hawthorne, J. I. Zink, J. M. Skelton, M. J. Bayer, C. Liu, E. Livshits, R. Baer, D. Neuhauser, *Science* **2004**, *303*, 1849–1851; b) N. Koumura, R. W. J. Zijlstra, R. A. van Delden, N. Harada, B. L. Feringa, *Nature* **1999**, *401*, 152–155; c) T. R. Kelly, *Acc. Chem. Res.* **2001**, *34*, 514–522.

[3] T. R. Kelly, M. C. Bowyer, K. V. Bhaskar, D. Bebbington, A. Garcia, F. R. Lang, M. H. Kim, M. P. Jette, *J. Am. Chem. Soc.* **1994**, *116*, 3657–3658.

[4] T. R. Kelly, I. Tellitu, J. P. Sestelo, *Angew. Chem.* **1997**, *109*, 1969–1972; *Angew. Chem. Int. Ed. Engl.* **1997**, *36*, 1866–1868.

[5] a) G. S. Kottas, L. I. Clarke, D. Horinek, J. Michl, *Chem. Rev.* **2005**, *105*, 1281–1376; b) J. Clayden, J. H. Pink, *Angew. Chem.* **1998**, *110*, 2040–2043; *Angew. Chem. Int. Ed.* **1998**, *37*, 1937–1939.

[6] a) J. D. Badjic, V. Balzani, A. Credi, S. Silvi, J. F. Stoddart, *Science* **2004**, *303*, 1845–1849; b) V. Balzani, A. Credi, M. Venturi in *Molecular Devices and Machines—A Journey Into the Nano World*, Wiley-VCH, Weinheim, **2003**, pp. 269–277.

[7] R. Romeo, L. Fenech, L. M. Scolaro, A. Albinati, A. Macchioni, C. Zuccaccia, *Inorg. Chem.* **2001**, *40*, 3293–3302.

[8] R. Romeo, L. Fenech, S. Carnabuci, M. R. Plutino, A. Romeo, *Inorg. Chem.* **2002**, *41*, 2839–2847.

[9] R. Romeo, S. Carnabuci, M. R. Plutino, A. Romeo, S. Rizzato, A. Albinati, *Inorg. Chem.* **2005**, *44*, 1248–1262.

[10] http://www.bu.edu/qale. This Web site collects sets of data, protocols for the analysis, program packages, parameters of ligands, leading references, etc.

[11] *gNMR*, version 4.0, Cherwell Science, Oxford, **1997**.

[12] P. Pregosin in *Platinum NMR Spectroscopy*, *Vol. 17*, Academic Press, London, **1986**, pp. 285–349.

 © 2006 Wiley-VCH Verlag GmbH & Co. KGaA, Weinheim

[13] Crystal data for **1**(SbF_6)·H_2O: $C_{36}H_{38}F_6N_2O_4PPtSb$, M_r = 1024.48, triclinic, space group $P\bar{1}$, a = 10.3925(7), b = 11.9207(8), c = 16.264(1) Å, α = 73.956(2), β = 76.621(2), γ = 84.545(2)°, V = 1882.8(2) Å^3, Z = 2, ρ_{calcd} = 1.804 g cm^{-3}, μ($Mo_{K\alpha}$) = 45.41 cm^{-1}. 22382 Reflections were collected at room temperature with a Bruker SMART CCD diffractometer, of which 8975 were unique (R_{int} = 0.0394). An empirical absorption correction was applied using the program SADABS (transmission factors in the range 1.000–0.606). Structure solution was by Patterson and Fourier methods and refinement by full-matrix least-squares on F^2 (programs WinGx ver. 1.70 and SHELX-PC), using anisotropic displacement parameters for all atoms except the hydrogens (in calculated positions), which were treated as riding atoms. Final agreement factors were R_1 = 0.0406, wR_2 = 0.0967 for 6916 observed reflections ($I \geq 2\sigma(I)$) and 459 refined parameters; GOF = 1.052. Crystal data for **2**(PF_6): $C_{34}H_{32}F_6N_2O_3P_2Pt$, M_r = 887.65, triclinic, space group $P\bar{1}$, a = 8.717(3), b = 12.286(3), c = 15.654(4) Å, α = 91.40(3)°, β = 96.65(4)°, γ = 96.52(3)°, V = 1653.2(8) Å^3, Z = 2, ρ_{calcd} = 1.783 g cm^{-3}, μ($Mo_{K\alpha}$) = 45.13 cm^{-1}. 5766 Independent reflections were collected at room temperature with a NONIUS CAD4 diffractometer. An empirical absorption correction was applied using the azimuthal (Ψ) scans of three reflections (transmission factors in the range 1.000–0.676). The structure solution was by Patterson and Fourier methods and refined as described above. Final agreement factors were R_1 = 0.0310, wR_2 = 0.0726 for 4463 observed reflections [$I \geq 2\sigma(I)$] and 433 refined parameters; GOF = 1.008. CCDC-299811 and -299812 contain the supplementary crystallographic data for this paper. These data can be obtained free of charge from The Cambridge Crystallographic Data Centre via www.ccdc.cam.ac.uk/data_request/cif.

[14] An exhaustive series of references can be found in P. Mastrorilli, C. F. Nobile, M. Latronico, V. Gallo, U. Englert, F. P. Fanizzi, O. Sciacovelli, *Inorg. Chem.* **2005**, *44*, 9097 – 9104.

[15] for an extensive discussion on 14-electron, three-coordinate platinum(II) species, see: M. R. Plutino, L. M. Scolaro, A. Albinati, R. Romeo, *J. Am. Chem. Soc.* **2004**, *126*, 6470 – 6484.

[16] R. Romeo, G. Alibrandi, *Inorg. Chem.* **1997**, *36*, 4822 – 4830 and references cited therein.

 © 2006 Wiley-VCH Verlag GmbH & Co. KGaA, Weinheim

Sulfur–Chromium Complex

DOI: 10.1002/anie.200600724

Cyclopentadienylchromium Complexes of 1,2,3,5-Dithiadiazolyls: η^2 π Complexes of Cyclic Sulfur–Nitrogen Compounds**

Hiu Fung Lau, Victor Wee Lin Ng, Lip Lin Koh, Geok Kheng Tan, Lai Yoong Goh, Tracey L. Roemmele, Sonja D. Seagrave, and René T. Boeré**

The analogy of the Hückel $4n+2$-electron rule has proven to be a useful guide to the diverse chemistry of unsaturated sulfur–nitrogen compounds since it was first suggested in 1972.[1] While these electron-rich unsaturated compounds provide numerous examples of "forbidden" $4n$-electron species,[2] the most-stable and dominant ring compounds obey the rule.[3] At the same time there has been an intensive, and thus far unsuccessful, search for organometallic derivatives that show polyene-like π bonding to low-valent metal fragments. An early suggestion that cyclo-S_2N_2 might form η^4 complexes for example, with a {CpMn} fragment ($Cp = \eta^5$-C_5H_5)[4] may be contrasted with the fact that known metal complexes of binary S–N compounds are either σ bonded through an N lone pair (rare) or ring-opened by oxidative addition to the metal center (common).[5]

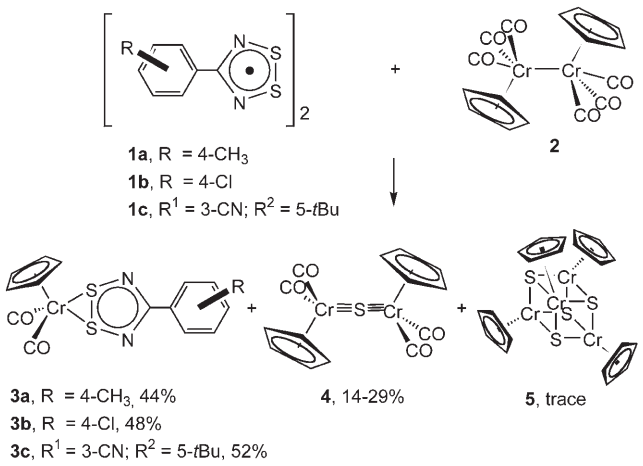
Many examples of the cyclo-1,2,3,5-dithiadiazolyl, XCN_2S_2 (X is a halogen or H atom, or an organic group),[6] which are thermally much more robust than S_2N_2, have been isolated as the 6π-electron cation or as the 7π-electron radical, which forms weak dimers, **1**, in the solid state (Scheme 1).[7] Reactions of these heterocycles with low-valent transition metals also lead exclusively to ring-opened adducts in which the S–S bond ($d_{S\text{-}S} \approx 2.1$ Å) is oxidatively added to iron ($d_{S\text{-}S} = 2.929$),[8,9] nickel ($d_{S\text{-}S} = 2.905$),[10] palladium ($d_{S\text{-}S} = 3.035$),[11] and platinum ($d_{S\text{-}S} = 3.066$ Å) atoms.[12] Recently, paramagnetic complexes of intact dithiadiazolyls, which coordinate to metal centers through nitrogen atoms

[*] H. F. Lau, V. W. L. Ng, L. L. Koh, G. K. Tan, Dr. L. Y. Goh
Department of Chemistry
National University of Singapore
Kent Ridge 119260 (Singapore)
Fax: (+65) 6779-1691
E-mail: chmgohly@nus.edu.sg
T. L. Roemmele, S. D. Seagrave, Prof. R. T. Boeré
Department of Chemistry and Biochemistry
University of Lethbridge
Lethbridge, AB, T1K3M4 (Canada)
Fax: (+1) 403-329-2057
E-mail: boere@uleth.ca

[**] The authors gratefully acknowledge financial support from the Natural Sciences and Engineering Research Council (Canada), and the National University of Singapore for Academic Research Grant no. R143-000-209-112

Supporting information for this article is available on the WWW under http://www.angewandte.org or from the author.

© 2006 Wiley-VCH Verlag GmbH & Co. KGaA, Weinheim



Scheme 1. Reaction of aryl-substituted dithiadiazolyl dimers **1a–c** with **2**.

with the assistance of 2-pyridyl groups, have been reported.[13] Such complexes are being exploited as potential molecular magnets from the interaction of the ligand and unpaired electrons of the metal atom.

To date, reactions with organometallic radicals have not been reported. Our studies on the reactivity of $[\{CpCr(CO)_3\}_2]$ (**2**) towards P–P- and S–S-bonded substrates—for example, polyatomic main-group elements,[14] or various classes of organic substrates—[15] have shown that the reactions are initiated by the 17-electron radical $[CpCr(CO)_3]^\bullet$ (**2A**), into which **2** readily dissociates in solution.[16] Thus, the resulting primary products from diphenyl dichalcogenide Ph_2E_2 (E = S, Se, Te),[17] $[Ph_2P(S)S]_2$,[18] the analogous $[(i\mathrm{PrO})_2P(S)S]_2$,[19] tetraalkyldiphosphine disulfide,[20] $[R_2NC(S)S]_2$,[21] $[(C_6H_4)NSCS]_2$,[22] $(C_5H_4NS)_2$,[23] and $(C_6H_5N_4CS)_2$[24] are inevitably generated in the coupling of **2A** with organic sulfur- or phosphorus-centered radicals. We therefore reasoned that **2A** represents a very mild reagent for radical-coupling reactions with **1**, although S–S bond-cleavage reactions are still expected to dominate.

Three aryl-substituted dithiadiazolyl dimers, **1a–c**, have been investigated in reactions with **2** (Scheme 1). In each case, exhaustive chromatography on silica gel led to isolation of intense red crystals of new adducts **3a–c** in yields of about 50% together with previously observed compounds **4**[25] and **5**[26] as well as green residues that could not be eluted or extracted from the support.[27] Structures of the adducts **3a–c** obtained from single-crystal X-ray diffraction are depicted in Figure 1.[28] Noteworthy, and unprecedented among metal complexes of **1**, is the virtually unchanged value of the S–S separation in the metal complexes ($d_{S\text{-}S} = 2.114(1)$ in **3a**, 2.132(2) in **3b**, 2.146(3) Å in **3c**) compared to that found in the dithiadiazolyl dimers[29] ($d_{S\text{-}S} = 2.096(7)$ in **1b**,[30] 2.101(2) Å in **1c**, unknown in **1a**). Hence ring-opening from oxidative addition has not occurred, and the S–S bond is retained in the metal complexes.

In the crystal structures, **3a** is found as the *exo* isomer, while **3b** and **3c** exist as the *endo* isomers (Scheme 2). It has been previously demonstrated that the influence of the R groups on RCN_2S_2 reactivity is minimal as a consequence of the nodal properties of the frontier orbitals of the rings, which

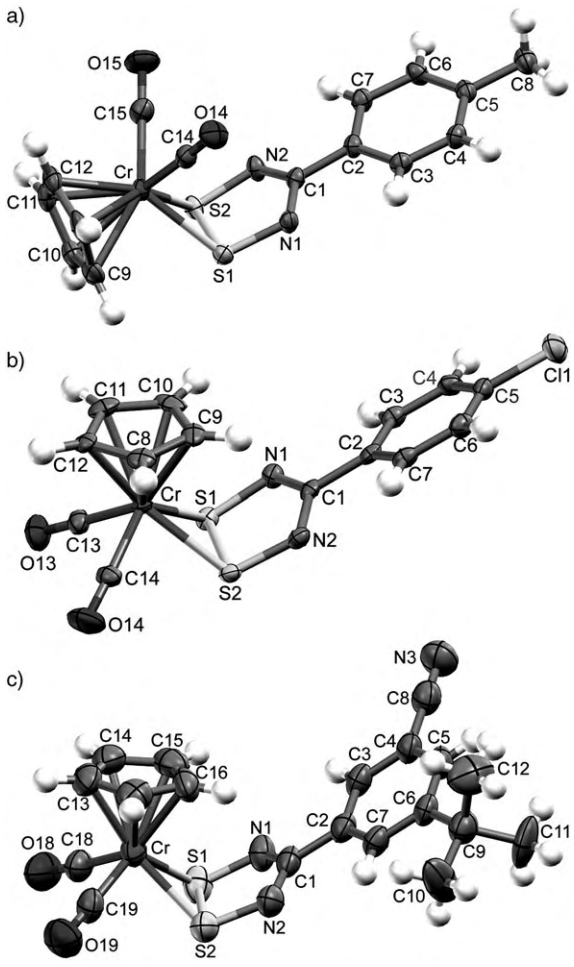
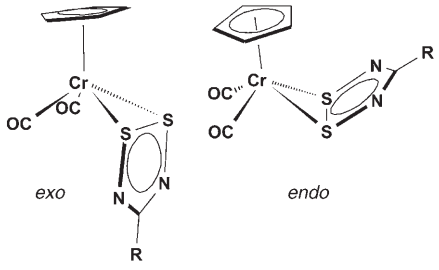


Figure 1. Thermal ellipsoid plots of the molecular structures in crystals of: a) **3a**, selected bond lengths [Å] and bond angles [°]: Cr–S1 2.3463(9), Cr–S2 2.3454(9), S1–N1 1.640(3), S2–N2 1.644(2), S1–S2 2.114(1); S1-Cr-S2 53.57(3), N1-S1-S2 94.77(9), N1-S1-Cr 114.76(10), S2-S1-Cr 63.19(3), N2-S2-S1 93.62(9), N2-S2-Cr 113.17(9), S1-S2-Cr 63.24(3); b) **3b**: Cr–S1 2.3602(13), Cr–S2 2.3537(12), S1–N1 1.642(4), S2–N2 1.635(4), S1–S2 2.1315(15); S1-Cr-S2 53.77(4), N1-S1-S2 93.79(13), N1-S1-Cr 112.62(14), S2-S1-Cr 62.96(4), N2-S2-S1 93.79(14), N2-S2-Cr 114.00(14), S1-S2-Cr 63.27(4); c) **3c**: Cr–S1 2.3540(19), Cr–S2 2.361(2), S1–N1 1.636(5), S2–N2 1.632(5), S1–S2 2.146(3); S1-Cr-S2 54.14(7), N1-S1-S2 93.3(2), N1-S1-Cr 110.99(19), S2-S1-Cr 63.10(7), N2-S2-S1 93.5(2), N2-S2-Cr 112.6(2), S1-S2-Cr 62.76(7).



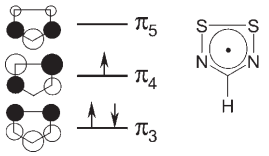
Scheme 2. Bonding modes for the dithiadiazolyl ligand of **3**.

suggests that the R groups are not responsible electronically for the observed isomerism.[7] To probe the energetic preference for the two isomers, we have performed hybrid DFT calculations on the model system $[CpCrS_2N_2CH]$.

 © 2006 Wiley-VCH Verlag GmbH & Co. KGaA, Weinheim

Geometry-optimized models within C_s symmetry at the B3PW91/6-311 + G(2d,2p)//B3PW91/6-31G + (d) level of theory[31] have metric parameters in close agreement with the values determined from the crystal structures and indicate that the *endo* form is more stable than the *exo* by only 2.5 kJ mol^{-1}, a difference that is not significant at this level of theory. In solution at room temperature, ^{1}H NMR spectra of **3a** and **3b** in C_6D_6 display a single, sharp Cp resonance signal, and the expected AB doublets for the *ortho*- (lower frequency) and *meta*-aryl H atoms (higher frequency). In all three complexes, the *ortho* resonances are substantially line-broadened (see the Supporting Information), which is suggestive of dynamic effects in solution. Indeed, when $C_6D_5CD_3$ solutions of the metal complexes are cooled below −20 °C, the AB doublets split into two sets and the Cp resonances also separate. The resulting signals sharpen upon further cooling and the low-temperature spectra integrate to approximately equal intensities, which is consistent with the predictions from the calculations that the two isomers are quite similar in energy. We therefore attribute the low-temperature spectra to the presence of *exo* and *endo* isomers in approximately equal proportions, and the distribution of isomers in the obtained crystal structures to either crystal packing effects or fortuitous crystal selection.

The calculations also provide insight into the bonding in both isomers.[31] The three highest occupied molecular orbitals (HOMOs) of the complexes correspond approximately to the well-known Cr d-centered "t_{2g}-like" orbitals, and the HOMO itself consists of the interaction of the π_4 singly occupied molecular orbital (SOMO) of the 7π-electron dithiadiazolyl ring with one of these metal orbitals (Scheme 3). A second molecular orbital with considerable



Scheme 3. Frontier orbitals of dithiadiazolyl radicals.

overlap between the metal and ring fragments lies seventh in sequence of filled orbitals and results from the interaction of the doubly occupied π_3 orbital of the ring with metal orbitals. This interpretation is consistent with the notion that the S_2N_2CR moiety acts as a three-electron π donor towards the 15-electron $[CpCr(CO)_2]$ moiety, which results in 18-electron compounds that bear a formal resemblance to the very recently reported $[CpCr(CO)_2\{R_2CC(R)CR_2\}]$ π-allyl complexes.[32] The lower π orbitals of the heterocycle are of no consequence in metal binding owing to the high effective electronegativity of both the nitrogen and sulfur atoms.[2] It is therefore not surprising, in retrospect, that the stable products from the interaction of $[CpCr(CO)_x]$ ($x = 0$–3) with S_2N_2CR are the observed $[(\eta^5\text{-Cp})Cr(CO)_2(\eta^2\text{-}S_2N_2CR)]$ structures in which the heterocycle acts as a three-electron donor, rather than the hypothetical $[(\eta^5\text{-Cp})Cr(\eta^5\text{-}S_2N_2CR)]$ in which the heterocycle would need to supply seven π electrons. It is likely that one of the hindrances to the preparation of π complexes from unsaturated sulfur–nitrogen and C,N,S-ring compounds has been a too-strict adherence to the metallocene paradigm.

Further investigations into the electronic,[33] structural, and dynamic behavior of these unprecedented metal complexes are in progress in our laboratories. In conclusion, we have prepared three RCN_2S_2 dithiadiazolyl complexes with $[CpCr(CO)_2]$ in which the rings are coordinated as three-electron π donors with approximately equal-energy *exo* and *endo* isomers in dynamic exchange. These examples are the first π complexes of unsaturated C,N,S rings.

Received: February 24, 2006
Revised: April 17, 2006
Published online: June 8, 2006

Keywords: chromium · cyclopentadienyl ligands · pi interactions · radicals · S ligands

[1] A. J. Banister, *Nature Phys. Sci.* **1972**, *237*, 92; A. J. Banister, *Nature Phys. Sci.* **1972**, *239*, 69.
[2] R. T. Oakley, *Prog. Inorg. Chem.* **1988**, *36*, 299.
[3] T. Chivers, *A Guide to Chalcogen-Nitrogen Chemistry*, World Scientific, Singapore, **2005**.
[4] M. Bénard, *Nouv. J. Chim.* **1986**, *10*, 529.
[5] a) T. Chivers, F. Edelmann, *Polyhedron* **1986**, *5*, 1661; b) C. A. Ghilardi, S. Midollini, S. Moneti, A. Orlandini, *J. Organomet. Chem.* **1986**, *312*, 383; c) R. Jones, C. P. Warrens, D. J. Williams, J. D. Woollins, *J. Chem. Soc. Dalton Trans.* **1987**, 907; d) R. Jones, P. F. Kelly, D. J. Williams, J. D. Woollins, *J. Chem. Soc. Dalton Trans.* **1988**, 803; e) R. Jones, P. F. Kelly, D. J. Williams, J. D. Woollins, *J. Chem. Soc. Dalton Trans.* **1988**, 1569; f) P. S. Belton, I. P. Parkin, D. J. Williams, J. D. Woollins, *J. Chem. Soc. Chem. Commun.* **1988**, 1479; g) C. A. O'Mahoney, I. P. Parkin, D. J. Williams, J. D. Woollins, *J. Chem. Soc. Dalton Trans.* **1989**, 1179; h) T. Chivers, J. Fait, K. J. Schmidt, *Inorg. Chem.* **1989**, *28*, 3018; i) M. B. Hursthouse, M. Motevalli, P. F. Kelly, J. D. Woollins, *Polyhedron* **1989**, *8*, 997; j) V. C. Ginn, P. F. Kelly, A. M. Z. Slawin, D. J. Williams, J. D. Woollins, *J. Chem. Soc. Dalton Trans.* **1992**, 963; k) D. Hanssgen, M. Jansen, W. Assenmacher, H. Salz, *J. Organomet. Chem.* **1993**, *445*, 61; l) R. T. Boeré, B. Klassen, K. H. Moock, *J. Organomet. Chem.* **1994**, *467*, 127; m) F. Kunkel, K. Harms, H.-C. Kang, W. Massa, K. Dehnicke, *Z. Naturforsch. B* **1997**, *52*, 193; n) S. M. Aucott, P. Bhattacharyya, H. L. Milton, A. M. Z. Slawin, J. D. Woollins, *New J. Chem.* **2003**, *27*, 1466; o) S. M. Aucott, A. M. Z. Slawin, J. D. Woollins, *Can. J. Chem.* **2002**, *80*, 1481; p) J. Van Droogenbroeck, C. Van Alsenoy, S. M. Aucott, J. D. Woollins, A. D. Hunter, F. Blockhuys, *Organometallics* **2005**, *24*, 1004; q) W.-K. Wong, C. Sun, W.-Y. Wong, D. W. J. Kwong, W.-T. Wong, *Eur. J. Inorg. Chem.* **2000**, 1045.
[6] For reviews, see: a) A. W. Cordes, R. C. Haddon, R. T. Oakley, *Stud. Inorg. Chem.* **1992**, *14*, 295; b) J. M. Rawson, A. J. Banister, I. Lavender, *Adv. Heterocycl. Chem.* **1995**, *62*, 137; c) T. Torroba, *J. Prakt. Chem./Chem.-Ztg.* **1999**, *341*, 99.
[7] The existence of the 8π anion has only been demonstrated electrochemically on the time scale of cyclic voltammetry. R. T. Boeré, T. L. Roemmele, *Coord. Chem. Rev.* **2000**, *210*, 369.
[8] A. J. Banister, I. May, J. M. Rawson, *J. Organomet. Chem.* **1998**, *550*, 241.
[9] a) A. J. Banister, I. B. Gorrell, W. Clegg, K. A. Jørgensen, *J. Chem. Soc. Dalton Trans.* **1989**, 2229; b) R. T. Boeré, K. H. Moock, V. Klassen, J. Weaver, D. Lentz, H. Michael-Schulz, *Can. J. Chem.* **1995**, *73*, 1444.
[10] A. J. Banister, I. B. Gorrell, W. Clegg, K. A. Jørgensen, *J. Chem. Soc. Dalton Trans.* **1991**, 1105.

 © 2006 Wiley-VCH Verlag GmbH & Co. KGaA, Weinheim

[11] a) A. J. Banister, J. A. K. Howard, I. May, J. M. Rawson, *Chem. Commun.* **1997**, 1763; b) A. J. Banister, I. B. Gorrell, J. A. K. Howard, S. E. Lawrence, C. W. Lehman, I. May, J. M. Rawson, B. K. Tanner, C. I. Gregory, A. J. Blake, S. P. Fricker, *J. Chem. Soc. Dalton Trans.* **1997**, 377; c) J. E. Davies, R. J. Less, I. May, J. M. Rawson, *New J. Chem.* **1998**, *22*, 763.

[12] a) A. J. Banister, I. B. Gorrell, S. E. Lawrence, C. W. Lehmann, I. May, G. Tate, A. J. Blake, J. M. Rawson, *J. Chem. Soc. Chem. Commun.* **1994**, 1779; b) N. Feeder, R. J. Less, J. M. Rawson, J. N. B. Smith, *J. Chem. Soc. Dalton Trans.* **1998**, 4091.

[13] a) M. Jennings, K. E. Preuss, J. Wu, *Chem. Commun.* **2006**, 341; b) N. R. G. Hearns, K. E. Preuss, J. F. Richardson, S. Bin-Salamon, *J. Am. Chem. Soc.* **2004**, *126*, 9942.

[14] a) L. Y. Goh, *Coord. Chem. Rev.* **1999**, *185–186*, 257, and references therein; b) L. Y. Goh, W. Chen, R. C. S. Wong, *Chem. Commun.* **1999**, 1481; c) L. Y. Goh, W. Chen, R. C. S. Wong, *Organometallics* **1999**, *18*, 306.

[15] Z. Weng, L. Y. Goh, *Acc. Chem. Res.* **2004**, *37*, 187, and references therein.

[16] a) R. D. Adams, D. E. Collins, F. A. Cotton, *J. Am. Chem. Soc.* **1974**, *96*, 749; b) T. Madach, H. Vahrenkamp, *Z. Naturforsch. B* **1978**, *33*, 1301; c) L. Y. Goh, M. J. D'Aniello, Jr., S. Slater, E. L. Muetterties, I. Tavanaiepour, M. I. Chang, M. F. Fredrich, V. W. Daz, *Inorg. Chem.* **1979**, *18*, 192; d) S. J. McLain, *J. Am. Chem. Soc.* **1988**, *110*, 643; e) M. C. Baird, *Chem. Rev.* **1988**, *88*, 1217; f) L. Y. Goh, Y. Y. Lim, *J. Organomet. Chem.* **1991**, *402*, 209; g) D. C. Woska, Y. Ni, B. B. Wayland, *Inorg. Chem.* **1999**, *38*, 4135.

[17] a) L. Y. Goh, M. S. Tay, T. C. W. Mak, R.-J. Wang, *Organometallics* **1992**, *11*, 1711; b) L. Y. Goh, M. S. Tay, Y. Y. Lim, T. C. W. Mak, Z.-Y. Zhou, *J. Chem. Soc. Dalton Trans.* **1992**, 1239; c) L. Y. Goh, M. S. Tay, W. Chen, *Organometallics* **1994**, *13*, 1813.

[18] L. Y. Goh, W. K. Leong, P.-H. Leung, Z. Weng, I. Haiduc, *J. Organomet. Chem.* **2000**, *607*, 64.

[19] L. Y. Goh, Z. Weng, W. K. Leong, I. Haiduc, K. M. Lo, R. C. S. Wong, *J. Organomet. Chem.* **2001**, *631*, 67.

[20] L. Y. Goh, Z. Weng, W. K. Leong, J. J. Vittal, I. Haiduc, *Organometallics* **2002**, *21*, 5287.

[21] a) L. Y. Goh, Z. Weng, W. K. Leong, P. H. Leung, *Angew. Chem.* **2001**, *113*, 3336; *Angew. Chem. Int. Ed.* **2001**, *40*, 3236; b) L. Y. Goh, Z. Weng, W. K. Leong, P. H. Leung, *Organometallics* **2002**, *21*, 4398; c) L. Y. Goh, Z. Weng, T. S. Andy Hor, W. K. Leong, *Organometallics* **2002**, *21*, 4408.

[22] L. Y. Goh, Z. Weng, W. K. Leong, J. J. Vittal, *J. Am. Chem. Soc.* **2002**, *124*, 8804.

[23] V. W. L. Ng, W. K. Leong, L. L. Koh, G. K. Tan, L. Y. Goh, *J. Organomet. Chem.* **2004**, *689*, 3210.

[24] V. W. L. Ng, Z. Weng, J. J. Vittal, L. L. Koh, G. K. Tan, L. Y. Goh, *J. Organomet. Chem.* **2005**, *690*, 1157.

[25] a) T. J. Greenhough, B. W. S. Kolthammer, P. Legzdins, J. Trotter, *Inorg. Chem.* **1979**, *18*, 3543; b) L. Y. Goh, T. W. Hambley, G. B. Robertson, *J. Chem. Soc. Chem. Commun.* **1983**, 1458; c) L. Y. Goh, T. W. Hambley, G. B. Robertson, *Organometallics* **1987**, *6*, 1051.

[26] W. Chen, L. Y. Goh, T. C. W. Mak, *Organometallics* **1986**, *5*, 1997.

[27] The complexes **3a–c** were found to be air-stable as solids for up to two weeks, as monitored by the carbonyl stretches in the IR spectra. ^{1}H NMR spectra of solutions of the complexes indicated significant decomposition to $[Cp_4Cr_4S_4]$ (**5**; identified by its spectral characteristics: ^{1}H NMR: $\delta(Cp) = 4.90$ ppm in $[D_6]$benzene)[26] after two days at ambient temperature. Full details of the synthesis and characterization of the new complexes are provided in the Supporting Information.

[28] Crystal data: **3a** and **3c** crystallize in $P\bar{1}$ with $Z = 2$ while **3b** and **1c** are found in *Pbca* with $Z = 8$. CCDC-297903, 297904, 297905, and 299596 contain the supplementary crystallographic data for this paper. These data can be obtained free of charge from the Cambridge Crystallographic Data Centre via www.ccdc.cam.ac.uk/data_request/cif.

[29] The value of $d_{S\text{-}S}$ in monomeric dithiadiazolyl radicals and in the diamagnetic dimers is expected to be different, but quantum calculations show the difference to be small.[30] In a cobalt bis(hexafluoroacetonato) complex of a monomeric dithiadiazolyl with only σ coordination through a nitrogen atom and a substituent group, leaving the sulfur atoms uncoordinated, $d_{S\text{-}S} = 2.091$ Å.[13b]

[30] R. T. Boeré, K. H. Moock, M. Parvez, *Z. Anorg. Allg. Chem.* **1994**, *620*, 1589.

[31] C. N. Carlson, J. D. Smith, T. P. Hanusa, W. W. Brennessel, V. G. Young, Jr., *J. Organomet. Chem.* **2003**, *683*, 191. Details of the calculations are presented in the Supporting Information, including the calculated geometry, comparison to π allyl bonding, and an orbital-interaction diagram.

[32] D. W. Norman, M. J. Ferguson, J. M. Stryker, *Organometallics* **2004**, *23*, 2015.

[33] Preliminary voltammetric results for **3a** are provided in the Supporting Information.

 © 2006 Wiley-VCH Verlag GmbH & Co. KGaA, Weinheim

Cross-Coupling Reactions

DOI: 10.1002/anie.200601055

Reaction of Two Different α-Allenols in a Heterocyclization/Cross-Coupling Sequence: Convenient Access to Functionalized Buta-1,3-dienyl Dihydrofurans**

Benito Alcaide, Pedro Almendros,* and Teresa Martínez del Campo*

In memory of Marcial Moreno-Mañas

Dihydrofurans are an important class of oxygenated heterocycles that have attracted much interest because of the biological activity of naturally occurring representatives. They

[*] Prof. Dr. B. Alcaide, Dipl.-Chem. T. Martínez del Campo
Departamento de Química Orgánica I
Universidad Complutense de Madrid
Facultad de Química, 28040-Madrid (Spain)
Fax: (+34) 91-394-4103
E-mail: alcaideb@quim.ucm.es

Dr. P. Almendros
Instituto de Química Orgánica General
Consejo Superior de Investigaciones Científicas
Juan de la Cierva 3, 28006 Madrid (Spain)
Fax: (+34) 91-564-4853
E-mail: iqoa392@iqog.csic.es

[**] Support for this work by the DGI-MCYT (Project BQU2003-07793-C02-01) is gratefully acknowledged. T.M.C. thanks the MEC for a predoctoral grant. We thank Rocio Carrascosa for her help in the preparation of some materials.

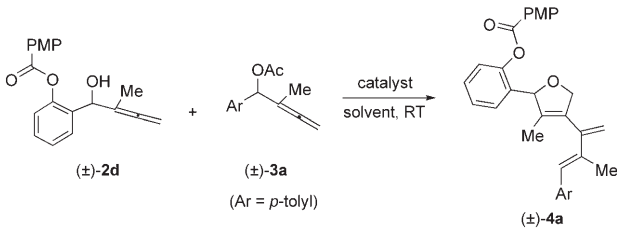
Supporting information for this article is available on the WWW under http://www.angewandte.org or from the author.

© 2006 Wiley-VCH Verlag GmbH & Co. KGaA, Weinheim
InterScience

are also useful building blocks in organic synthesis.[1] Allenes, once a rarity, have become established as an extremely useful functional group in modern synthetic organic chemistry.[2] In particular, the transition-metal-catalyzed cyclization of functionalized allenes that contain a nucleophilic center has attracted much attention.[3] However, the cross-coupling of two different allenes has scarcely been mentioned; only Ma and co-workers have described reactions of this type in recent reports on the coupling of 2,3-allenoic acids with 2,3-allenols or 1,2-allenyl ketones.[4] In continuation of our research in heterocyclic and allene chemistry,[5] we report herein an efficient cross-coupling reaction between two different α-allenol derivatives to give functionalized dihydrofurans in a single step.

The precursors for dihydrofuran formation, α-allenols **2a–j**, were readily prepared in good overall yield from the appropriate carbaldehyde **1a–i** (Table 1) through a regioselective indium-mediated Barbier-type carbonyl-allenylation reaction in an aqueous medium.[6] When the indium-mediated allenylation of enantiomerically pure aldehydes **1** did not take place with complete diastereoselectivity, the diastereomeric α-allenols **2** and *anti*-**2** could be separated readily by gravity flow chromatography.[7,8]

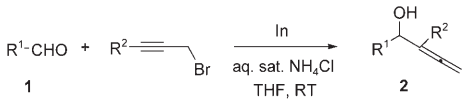
Some α-allenols **2** were protected as the corresponding acetates or *p*-nitrobenzoate **3a–c** by using standard procedures. Initial studies evaluated the effectiveness of different α-allenol derivatives and catalysts. Aromatic α-allenols were selected as initial test substrates. Our early efforts focused on the reaction between α-allenol **2d** and α-allenol **2b** protected as its acetate **3a** (Ar = *p*-MeC_6H_4). The use of $AuCl_3$ resulted in a complex mixture of unidentified products. Fortunately, palladium catalysts such as $Pd(OAc)_2$ and $PdCl_2$ in the absence of an oxidant effectively promoted this new heterocyclization/cross-coupling sequence in solvents such as MeCN and DMF at ambient temperature (Scheme 1, Table 2). It was

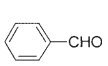
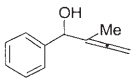
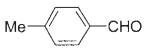
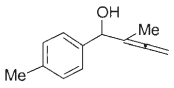
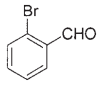
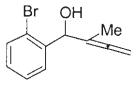
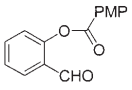
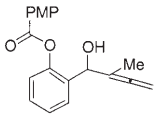
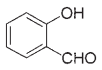
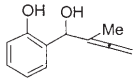
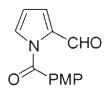
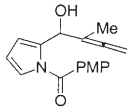
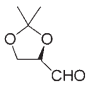
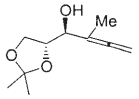
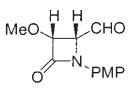
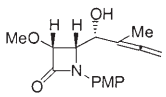
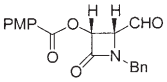
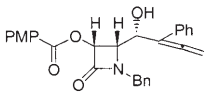
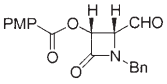
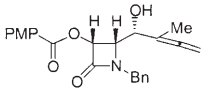


Scheme 1. Synthesis of the 2,3,4-trisubstituted 2,5-dihydrofuran **4a** through palladium(II)-catalyzed heterocyclization/cross-coupling of α-allenol derivatives **2d** and **3a**. PMP = 4-$MeOC_6H_4$.

discovered that the treatment of α-allenol **2d** with $PdCl_2$ (5 mol%) in DMF (0.2 M) led to the desired cyclization adduct **4a** in an impressive 90% yield when the protected α-allenol **3a** was used as the coupling partner (Table 2, entry 4). No homodimerization products were detected. Furthermore, the domino cyclization reaction is totally regioselective, with exclusive formation of the five-membered oxacycle. The free α-allenol component undergoes heterocyclization to give a 2,5-dihydrofuran, and the protected α-allenol cross-coupling partner becomes attached to the C4 carbon atom of the oxacycle as a substituted buta-1,3-diene functionality.

Table 1: Indium-mediated Barbier-type carbonyl allenylation of aldehydes **1**.



Entry	R^1CHO	R^2	Product	Yield [%][a]
1	 **1a**	Me	 (±)-**2a**	99
2	 **1b**	Me	 (±)-**2b**	66
3	 **1c**	Me	 (±)-**2c**	97
4	 **1d**	Me	 (±)-**2d**	77
5	 **1e**	Me	 (±)-**2e**	96
6	 **1f**	Me	 (±)-**2f**	58
7	 (−)-**1g**	Me	 (−)-**2g**	67
8	 (+)-**1h**	Me	 (+)-**2h**	70
9	 (−)-**1i**	Ph	 (+)-**2i**	74
10	 (−)-**1i**	Me	 (+)-**2j**	68

[a] Yield of the pure, isolated product with correct analytical and spectral data. Bn = benzyl, PMP = 4-$MeOC_6H_4$.

 © 2006 Wiley-VCH Verlag GmbH & Co. KGaA, Weinheim

Table 2: Reaction of α-allenol derivatives **2d** and **3a** under different conditions: palladium(II)-catalyzed heterocyclization/cross-coupling.[a]

Entry	Catalyst[a]	Solvent	*t* [h]	Yield [%][b]
1	$AuCl_3$	CH_2Cl_2	24	[c]
2	$Pd(OAc)_2$	DMF	24	10
3	$Pd(OAc)_2$	MeCN	48	[c]
4	$PdCl_2$	DMF	4	90
5	$PdCl_2$	MeCN	9	55

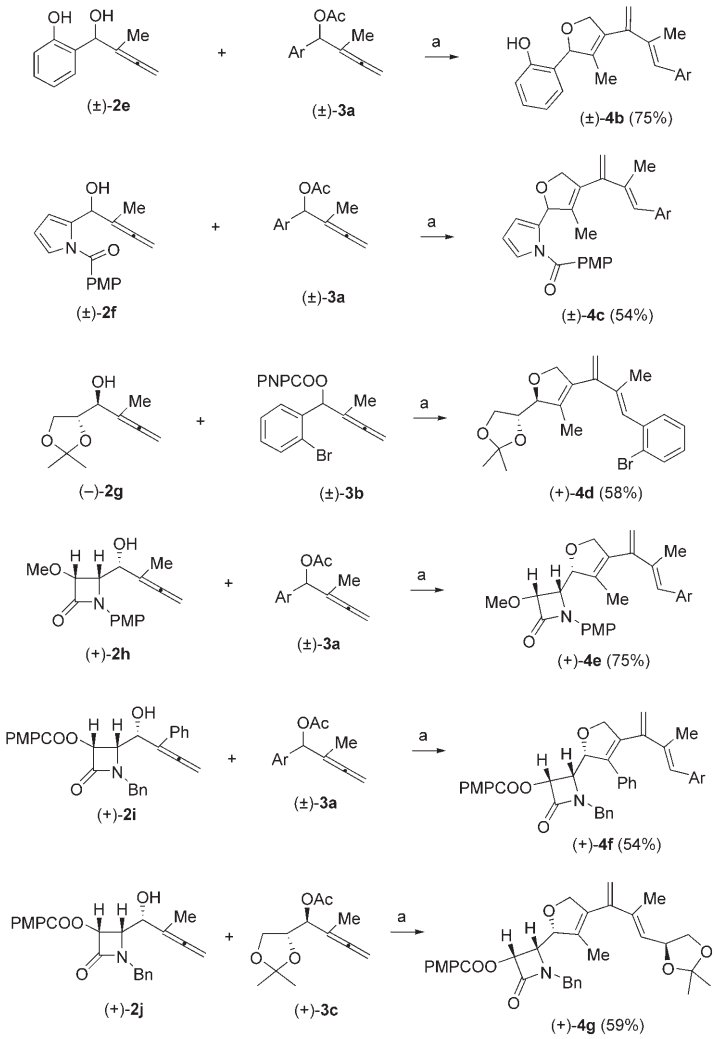
[a] All reactions were conducted with 5 mol% of the catalyst. [b] Yield of the pure, isolated product with correct analytical and spectral data. The disappearance of the starting material **2d** was observed in all cases. [c] A complex mixture of unidentified products was obtained. DMF = *N*,*N*-dimethylformamide.

To further probe the scope of this transformation, we tested the tolerance of the Pd^{II}-catalyzed heterocyclization/cross-coupling to structural alterations to both the α-allenol and protected α-allenol moieties. As expected, γ-allenols were found to be completely unreactive under these conditions. It was possible to couple chemoselectively the protected α-allenol **3a** with compound **2e**, which contains both α- and γ-allenol functionalities. None of the coupled γ-allenol was obtained, but instead the product **4b** was formed exclusively by selective coupling to the α-allenol moiety (Scheme 2). Next, we decided to use heteroaromatic α-allenol derivatives as the reactants (Scheme 2). Buta-1,3-dienyl dihydrofuran **4c** was obtained in a reasonable yield from **2f** and **3a**.

Satisfied with the above results, we set out to evaluate the cross-coupling process for substrates that contain stereocenters. Thus, a series of aliphatic enantiomerically pure α-allenol derivatives were tested (Scheme 2). The α-allenols **2g–j** were converted smoothly into the desired functionalized optically active dihydrofuran derivatives **4d–g**. These results indicate that stereochemical integrity is conserved at the carbinol carbon atom of the allenol as well as at the distal stereocenters in the course of the allene–allene cross-coupling process. The sterically more encumbered phenyl-substituted allenol derivative **2i** readily underwent the cyclization/coupling sequence under identical conditions. Remarkably, the heterocyclization/cross-coupling reaction between the 2-azetidinone-tethered allenol **2j** and the 1,3-dioxolane-tethered protected allenol **3c** gave the β-lactam–dihydrofuran hybrid **4g** in 59% yield. Thus, it was shown that the heterocyclization/cross-coupling of two different α-allenol derivatives can be considered in the planning of a complex synthetic route.

In this study, the assignment of the configuration of the newly formed 1,3-diene moiety of dihydrofurans **4** was a crucial problem, which we thought we might solve conveniently by means of X-ray crystallography. However, the reluctance of most of these compounds to form suitable crystals for X-ray analysis prompted us to consider an alternative method. We focused our attention on NMR spectroscopic methods for the determination of the geometry of substituted alkenes. Indeed, qualitative homonuclear NOE difference spectra allowed us to assign the *E* configuration as depicted in Schemes 1 and 2.

The formation of buta-1,3-dienyl dihydrofurans **4** can be rationalized through a novel heterocyclization/cross-coupling

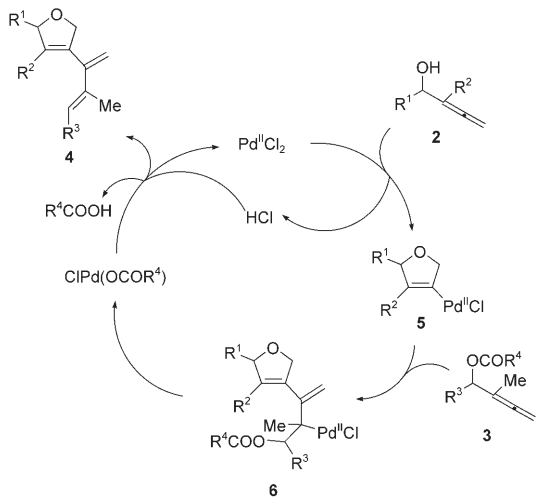


Scheme 2. Synthesis of 2,3,4-trisubstituted 2,5-dihydrofurans **4b–g** through palladium(II)-catalyzed heterocyclization/cross-coupling of α-allenol derivatives **2** and **3**. Reagents and conditions: a) $PdCl_2$ (5 mol%), DMF, RT; **4b**: 6 h (at 0°C); **4c**: 2.5 h; **4d**: 4 h; **4e**: 4 h; **4f**: 4 h (at 0°C); **4g**: 5 h. Ar = *p*-tolyl, PMP = 4-$MeOC_6H_4$, PNP = 4-$NO_2C_6H_4$.

reaction between α-allenols and protected allenols. A possible catalytic cycle is shown in Scheme 3. Regioselective palladium(II)-mediated intramolecular oxypalladation of the free allenol component **2** generates a palladadihydrofuran intermediate **5**, which then undergoes a cross-coupling reaction with the protected allenol partner **3**. The coupling of vinyl palladium(II) intermediates **5** with protected allenols **3** to give species **6** takes place regioselectively at the central allene carbon atom of **3**. Finally, *trans*-β-deacyloxypalladation generates a buta-1,3-dienyl dihydrofuran **4** in a highly stereoselective manner with exclusive formation of the *E* isomer and concomitant regeneration of the palladium(II) species.

In conclusion, we have developed a mild, palladium(II)-catalyzed heterocyclization/cross-coupling reaction to form 2,3,4-trifunctionalized 2,5-dihydrofurans from two different α-allenols that is applicable to compounds with a wide range of substitution patterns. As our studies indicate high levels of regioselectivity as well as the possibility of using optically

 © 2006 Wiley-VCH Verlag GmbH & Co. KGaA, Weinheim



Scheme 3. Mechanistic explanation for the Pd^{II}-catalyzed heterocyclization/cross-coupling of α-allenols and protected α-allenols.

active substrates, this is a potentially attractive method for organic synthesis. Current work is aimed at exploring the scope of the reaction with respect to both α-allenols and protected α-allenols, and identifying applications in complex-molecule synthesis.

Experimental Section

General procedure: $PdCl_2$ (0.005 mmol) was added to a stirred solution of an α-allenol **2** (0.10 mmol) and the appropriate protected α-allenol **3** (0.30 mmol) in *N*,*N*-dimethylformamide (1.0 mL). The reaction mixture was stirred under an argon atmosphere until the starting material had disappeared (monitored by TLC). Water (0.5 mL) was then added, and the reaction mixture was extracted with ethyl acetate (3 × 4 mL). The organic phase was washed with water (2 × 2 mL), dried ($MgSO_4$), and concentrated under reduced pressure. Chromatography of the residue with mixtures of hexanes and ethyl acetate as the eluent gave analytically pure 2,3,4-trisubstituted 2,5-dihydrofurans **4**. (+)-**4e**: Prepared from (+)-**2h** (55 mg, 0.19 mmol); chromatographic purification of the crude product (hexanes/ethyl acetate 20:1) gave (+)-**4e** (64 mg, 75%) as a colorless oil; $[\alpha]_D = +45.5$ ($c = 2.1$, $CHCl_3$); ^{1}H NMR (300 MHz, $CDCl_3$, 25 °C): $\delta = 7.48$ (d, $J = 9.0$ Hz, 2H), 7.11 (d, $J = 8.0$ Hz, 2H), 6.97 (d, $J = 8.0$ Hz, 2H), 6.79 (d, $J = 9.0$ Hz, 2H), 6.17 (br s, 1H), 5.28–5.30 (m, 1H), 5.21 (d, $J = 1.2$ Hz, 1H), 4.72 (d, $J = 5.6$ Hz, 1H), 4.67–4.69 (m, 2H), 4.58 (d, $J = 1.2$ Hz, 1H), 4.55–4.57 (m, 1H), 3.67 (s, 3H), 3.65 (s, 3H), 2.33 (d, $J = 0.7$ Hz, 3H), 1.84 (d, $J = 1.2$ Hz, 3H), 1.66–1.68 ppm (m, 3H); ^{13}C NMR (75 MHz, $CDCl_3$, 25 °C): $\delta = 164.9$, 156.3, 144.2, 136.2, 135.9, 134.9, 134.5, 133.5, 130.4, 129.3, 129.1, 128.6, 118.9, 114.2, 114.1, 86.9, 82.7, 77.6, 61.7, 59.4, 55.3, 21.1, 15.1, 12.0 ppm; IR ($CHCl_3$): $\tilde{\nu} = 1742$ cm^{-1}; MS (ESI): *m*/*z* (%): 446 (100) $[M+H]^+$, 445 (11) $[M]^+$; elemental analysis calcd (%) for $C_{28}H_{31}NO_4$ (445.5): C 75.48, H 7.01, N 3.14; found: C 75.72, H 7.06, N 3.10.

Received: March 16, 2006
Published online: June 7, 2006

[1] For selected reviews, see: a) T. G. Kilroy, T. P. O'Sullivan, P. J. Guiry, *Eur. J. Org. Chem.* **2005**, 4929; b) X.-L. Hou, Z. Yang, K.-S. Yeung, H. N. C. Wong in *Progress in Heterocyclic Chemistry*, *Vol. 17* (Eds.: G. W. Gribble, J. A. Joule), Elsevier, Oxford, **2005**, pp. 142–171; c) X.-L. Hou, Z. Yang, K.-S. Yeung, H. N. C. Wong in *Progress in Heterocyclic Chemistry*, *Vol. 16* (Eds.: G. W. Gribble, J. A. Joule), Elsevier, Oxford, **2004**, pp. 156–197; d) *The Chemistry of Heterocycles: Structure, Reactions, Syntheses, and Applications* (Eds.: T. Eicher, J. S. Hauptmann), Wiley-VCH, Weinheim, **2003**; e) B. M. Fraga, *Nat. Prod. Rep.* **1992**, *9*, 217; f) A. T. Merrit, S. V. Ley, *Nat. Prod. Rep.* **1992**, *9*, 243; g) K. Nakanishi, *Natural Products Chemistry*, Kodansha Academic, New York, **1974**; h) A. I. Meyers, *Heterocycles in Organic Synthesis*, Wiley, New York, **1974**; i) F. M. Dean in *Advances in Heterocyclic Chemistry*, *Vol. 30* (Ed.: A. R. Katritzky), Academic, New York, **1982**, pp. 167–238; j) H. Heaney, J. S. Ahn in *Comprehensive Heterocyclic Chemistry II*, *Vol. 2* (Ed.: C. W. Bird), Elsevier, **1995**, chap. 2.06, pp. 297–350.

[2] For general and comprehensive reviews, see: a) S. Ma, *Chem. Rev.* **2005**, *105*, 2829; b) *Modern Allene Chemistry* (Eds.: N. Krause, A. S. K. Hashmi), Wiley-VCH, Weinheim, **2004**; c) R. Zimmer, C. U. Dinesh, E. Nandanan, F. A. Khan, *Chem. Rev.* **2000**, *100*, 3067.

[3] For selected reviews, see: a) A. Hoffmann-Röder, N. Krause, *Org. Biomol. Chem.* **2005**, *3*, 387; b) S. Ma, *Acc. Chem. Res.* **2003**, *36*, 701; c) R. W. Bates, V. Satcharoen, *Chem. Soc. Rev.* **2002**, *31*, 12; d) A. S. K. Hashmi, *Angew. Chem.* **2000**, *112*, 3737; *Angew. Chem. Int. Ed.* **2000**, *39*, 3590.

[4] a) S. Ma, Z. Gu, *J. Am. Chem. Soc.* **2005**, *127*, 6182; b) S. Ma, Z. Gu, Z. Yu, *J. Org. Chem.* **2005**, *70*, 6291; c) S. Ma, Z. Yu, *Chem. Eur. J.* **2004**, *10*, 2078; d) S. Ma, Z. Yu, *Angew. Chem.* **2002**, *114*, 1853; *Angew. Chem. Int. Ed.* **2002**, *41*, 1775.

[5] a) B. Alcaide, P. Almendros, C. Aragoncillo, M. C. Redondo, M. R. Torres, *Chem. Eur. J.* **2006**, *12*, 1539; b) B. Alcaide, P. Almendros, J. M. Alonso, *Chem. Eur. J.* **2006**, *12*, 2874; c) B. Alcaide, P. Almendros, R. Rodríguez-Acebes, *J. Org. Chem.* **2006**, *71*, 2346–2351; d) B. Alcaide, P. Almendros, R. Rodríguez-Acebes, *Chem. Eur. J.* **2005**, *11*, 5708; e) B. Alcaide, P. Almendros, G. Cabrero, M. P. Ruiz, *Org. Lett.* **2005**, *7*, 3981; f) B. Alcaide, P. Almendros, R. Rodríguez-Acebes, *J. Org. Chem.* **2005**, *70*, 2713.

[6] a) B. Alcaide, P. Almendros, C. Aragoncillo, M. C. Redondo, *Eur. J. Org. Chem.* **2005**, 98; b) B. Alcaide, P. Almendros, C. Aragoncillo, *Chem. Eur. J.* **2002**, *8*, 1719; c) M. B. Isaac, T.-H. Chan, *J. Chem. Soc. Chem. Commun.* **1995**, 1003; the α-allenol (−)-**2g** had been prepared previously as a mixture of regio- and diastereoisomers by stannane chemistry: d) A. McCluskey, I. W. Muderawan, Muntari, D. J. Young, *J. Org. Chem.* **2001**, *66*, 7811.

[7] Complete diastereoselectivity was observed in all cases except for the reaction of the aldehyde (+)-**1h**.

[8] The configuration at the carbinol stereogenic center of the enantiomerically pure α-allenols **2g–j** was established by comparison of the ^{1}H NMR chemical shifts of the corresponding acetylmandelates according to the method developed by Trost and co-workers: a) B. M. Trost, J. L. Belletire, S. Godleski, P. G. McDougal, J. M. Balkovec, J. J. Baldwin, M. E. Christy, G. S. Ponticello, S. L. Varga, J. P. Springer, *J. Org. Chem.* **1986**, *51*, 2370; b) K. M. Sureshan, T. Miyasou, S. Miyamori, Y. Watanabe, *Tetrahedron: Asymmetry* **2004**, *15*, 3357; for a review, see: c) J. M. Seco, E. Quiñoá, R. Riguera, *Chem. Rev.* **2004**, *104*, 17.

Keywords: allenes · cross-coupling · domino reactions · heterocycles · palladium

 © 2006 Wiley-VCH Verlag GmbH & Co. KGaA, Weinheim

N,P Clathrates

DOI: 10.1002/anie.200600551

A Nitridic Clathrate: $P_4N_4(NH)_4(NH_3)$**

*Friedrich Karau and Wolfgang Schnick**

In molecular and solid-state chemistry, some phosphorus- and nitrogen-containing compounds exhibit specific similarities and analogies to silicon–oxygen compounds. This resemblance is explained by the isolobal relation between P–N and Si–O bonds.[1,2] Simple examples are phosphorus nitride imide, PN(NH),[3,4] and phosphorus oxide nitride, PON,[5] which are both isoelectronic with silica, SiO_2. Accordingly, both compounds crystallize in β-cristobalite-analogous network structures and are made up of corner-sharing PX_4 tetrahedra (X = O, N). The ternary nitridophosphates $NaPN_2$ and $LiPN_2$[6–9] have filled isoelectronic $[PN_2]^-$ network structures and are structurally related to PON and PN(NH), as they adopt the chalcopyrite structure type. More complex silica analogues are represented by the class of nitridosodalites[10–13] and related oxonitridosodalites.[14] Recently, we synthesized and identified the first oxonitridic zeolite,[15] namely, $Li_xH_{12-x-y+z}[P_{12}O_yN_{24-y}]X_z$ with X = Cl, Br.[16] The $[P_{12}O_yN_{24-y}]$ framework of this new framework type (NPO[17]) contains large 12-ring channels and is solely made up of 3-rings (i.e., rings composed of 12 or 3 corner-sharing tetrahedra, respectively) as fundamental building units (FBUs).[16] The specific topology of the framework type NPO has been identified previously as a possible candidate structure for microporous SiO_2,[18] but this prediction has not been proven by experiment so far.

Besides the diverse and manifold substance class of zeolites[19] and zeosils,[20] another group of microporous solids is formed by clathrasils and clathralites[20,21] (generic term: clathrate). Usually these compounds contain uncharged SiO_2 framework structures of corner-sharing SiO_4 tetrahedra with neutral molecules (or nothing) in their cagelike pores. Herein we report on the first nitridic clathrate $[P_4N_4(NH)_4](NH_3)$ (**1**), which is based on a novel PN(NH) framework structure.

$[P_4N_4(NH)_4](NH_3)$ (**1**) was obtained by a high-pressure high-temperature reaction[22–25] at 600 °C and 11 GPa in a Walker-type multianvil assembly starting from a mixture of ammonium azide NH_4N_3[26] and P_3N_5[27] [Eq. (1)]. In the past,

$$21\,NH_4N_3 + 16\,P_3N_5 \rightleftharpoons 12\,P_4N_4(NH)_4(NH_3) + 28\,N_2 \quad (1)$$

we have employed the multianvil technique for the synthesis and investigation of the high-pressure behavior of silica-analogous phosphorus nitrides[9,22,25] and recently we synthesized the high-pressure polymorph γ-P_3N_5.[28] We have frequently used high N_2 partial pressures, generated in situ by thermolysis of azides, in our synthetic approaches to metal-containing nitridophosphates starting from the respective metal azide and P_3N_5. Thereby, phosphorus nitride P_3N_5 (thermal decomposition > 850 °C at normal pressure[22]) is prevented from dissociation into the elements [Eq. (2)] at the

$$P_3N_5 \rightarrow 3\,PN + N_2 \rightarrow {}^3/_4\,P_4 + {}^5/_2\,N_2 \quad (2)$$

high reaction temperatures[22] above 1000 °C that are usually necessary for the crystallization of the desired metal nitridophosphates.

In the current work we utilized the thermolysis of ammonium azide NH_4N_3 under high pressure and high temperature to provide the high partial pressures of both N_2 and NH_3 which are concurrently necessary for an ammonolysis reaction and thermal stabilization of P_3N_5 [cf. Eq. (1)]. Under normal pressure NH_4N_3 decomposes into NH_3 and HN_3 at 133 °C.[26] Above approximately 300 °C highly exothermic explosive decomposition occurs frequently and nitrogen is formed as well [Eq. (3)]. At moderate pressures (ca. 2–

$$3\,NH_4N_3 \rightarrow 4\,NH_3 + 4\,N_2 \quad (3)$$

3 MPa) and temperatures around 580 °C ammonolysis of P_3N_5 [Eq. (4)] made available crystalline phosphorus nitride imide PN(NH) (**2a**).[3]

$$P_3N_5 + NH_3 \rightleftharpoons 3\,PN(NH) \quad (4)$$

Under the extreme synthesis conditions of $P_4N_4(NH)_4(NH_3)$ (**1**), NH_3 apparently is incorporated into the growing PN(NH) framework structure and therefore acts as a template molecule. Thus, in contrast to nonintercalated **2a**, a topologically different host lattice of PN(NH) and formation of the clathrate $P_4N_4(NH)_4(NH_3)$ (**1**) with NH_3-filled cages is observed. In addition, we found that pure PN(NH) (**2a**) forms a high-pressure (hp) polymorph hp-PN(NH) (**2b**) that is still structurally related to the β-cristobalite-type normal-pressure phase **2a**. This displacive phase transition occurs between 7 and 11.5 GPa.[29]

The crystal structure of $P_4N_4(NH)_4(NH_3)$ (**1**) was determined on the basis of powder X-ray diffraction analysis (Figure 1) by direct methods and refined by the Rietveld method.[30] The reflections of the powder pattern of **1** were indexed in the tetragonal crystal system[31] and space group $P\bar{4}n2$ was derived unambiguously.

Nitridic clathrate **1** has an unprecedented PN(NH) framework structure of corner-sharing PN_4 tetrahedra that form 4-rings and 8-rings as FBUs (Figures 2 and 3). According to the literature[32] the formula of **1** can be written as $|(NH_3)_2|$

[*] Dipl.-Chem. F. Karau, Prof. Dr. W. Schnick
Department Chemie und Biochemie
Lehrstuhl für Anorganische Festkörperchemie
Ludwig-Maximilians-Universität
Butenandtstrasse 5–13(D), 81377 München (Germany)
Fax: (+49) 89-2180-77440
E-mail: wolfgang.schnick@uni-muenchen.de

[**] The authors thank Dr. Robert G. Bell, University College London, for helpful advice and Dr. Gerd Fischer, Ludwig-Maximilians-Universität München, for collecting the mass chromatograms and mass spectra. Generous financial support by the Fonds der Chemischen Industrie and the Deutsche Forschungsgemeinschaft, project SCHN 377/11-1, is gratefully acknowledged.

 © 2006 Wiley-VCH Verlag GmbH & Co. KGaA, Weinheim

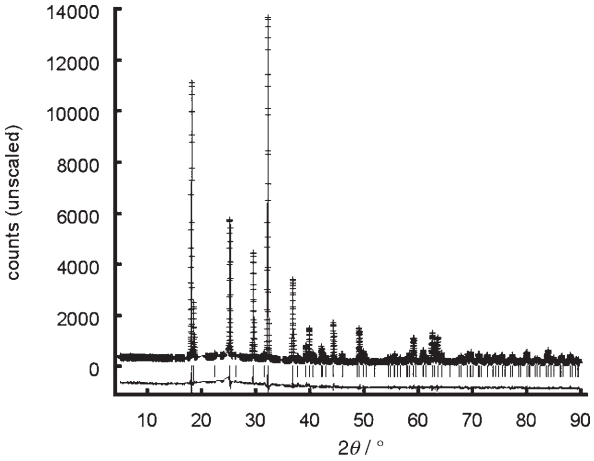


Figure 1. Observed (crosses) and calculated (line) X-ray powder diffraction pattern as well as the difference profile of the Rietveld refinement of **1**. Allowed peak positions are marked by vertical lines.

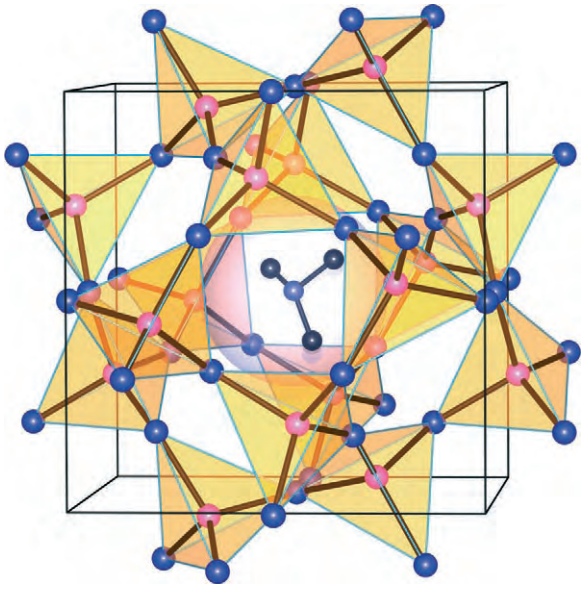


Figure 2. Crystal structure of **1**, viewed approximately along [001]; blue N, pink P, dark gray H. The enclosed and rotationally disordered NH_3 molecule with its center of gravity on the site [000] is surrounded by a sphere representing the van der Waals radius of NH_3 (3.1 Å). The cavity is built up from one 8-ring (in the image plane) and two 4-rings (above and below the image plane).

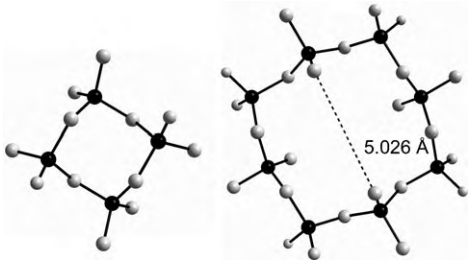


Figure 3. Ball-and-stick model of the 4-ring and the 8-ring, viewed along [001]. The diameter of the 8-ring (between two opposite N atoms) is indicated by a dotted line.

$[P_8^{+V[8]}N_8^{-III[2]}(N_8^{-III[2]}H_8)]_h\{3[4^28^4]\}_p\{0[4^28^4](P\bar{4}n2)\}$ to emphasize the topology of the pores and the host network. The cycle class sequence of this framework (i.e., the relative frequency of occurrence of $[P_nN_n]$ ring sizes in the network of **1** for $n = 1$, 2, 3 …) was calculated with the program TOPOLAN[33] and amounts to {–, 0, 0, 4, 0, 0, 0, 36, 0, 168, …}. The characteristic cages of this novel clathrate structure are formed by bent 8-rings which adopt the boat form and are capped by two 4-rings situated above and below the ring plane of the 8-rings. Each 8-ring is connected to two neighboring 4-rings through two tetrahedral corners (Figure 4). The thus-formed cages each

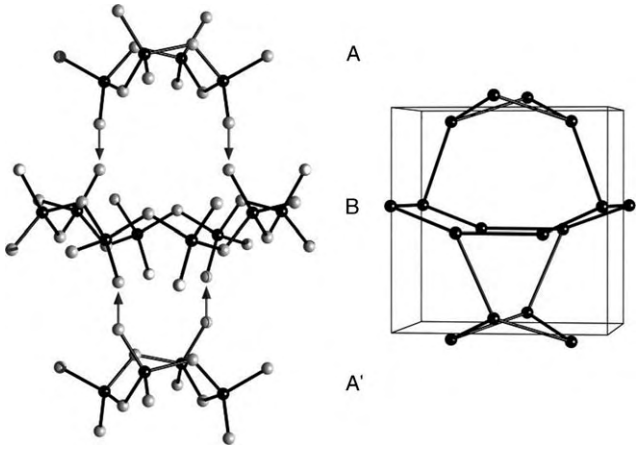


Figure 4. Exploded view of the framework structure in **1**, viewed approximately along [010]. The upper and lower 4-rings (A and A′) are both connected through two P-N-P bridges to the middle 8-ring. On the right, the resulting framework topology in the unit cell of **1** is illustrated by simply connecting the tetrahedral centers (P) in **1**. For clarity, the intercalated NH_3 molecule is omitted in both drawings. The pore symbol[40] for **1** is $[4^28^4]$.

contain one NH_3 molecule, which is presumably rotationally disordered. The inclusion of ammonia in **1** was proved both by temperature-programmed mass spectrometry and FTIR spectroscopy (see Experimental Section). The diameter of the cavities is about 5 Å considering the centers of the atoms, and about 3.5 Å with respect to their van der Waals radii. According to its mean van der Waals radius of 3.1 Å[34] the NH_3 molecule fits quite well into the cavities (see Figure 2). The topology of porous structures can be illustrated clearly by simply connecting the tetrahedral centers of the framework (here the P atoms), and such a representation for **1** is displayed in Figure 5.

The $P_4N_4(NH)_4$ framework of **1** has not been observed in any porous structure or clathrate so far. However, its topology was already predicted theoretically by Bell et al.[35] and Treacy et al.,[36] who adopted the tiling theorem in a systematic search for structure candidates of hitherto unknown zeolites and clathrasils. However, during those investigations the specific framework structure realized in **1** was assumed to be unstable in the case of a silica (SiO_2) framework, while nitridic frameworks were not taken into account at that time. Presumably, the bond angles T-X-T (T = Si, P; X = O, N) in this framework type are unfavorably small[37] in the case of the hypothetical SiO_2 polymorph (theoretically refined values: Si-

 © 2006 Wiley-VCH Verlag GmbH & Co. KGaA, Weinheim

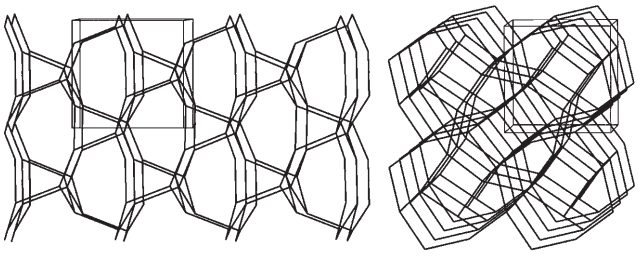


Figure 5. Framework topology of **1**. For clarity, the N, NH groups, and NH_3 molecules are omitted and the tetrahedral centers (P) are directly connected.

O1-Si 125°, Si-O2-Si 134°, and Si-O3-Si 134°),[35,36] while the experimentally observed angles in **1** (P-N1-P 121.4(3)°, P-N2-P 123.4(2)°, P-N3-P 153.8(3)°) fit well into the usual range observable in phosphorus nitrides and imides.[3,7,9,22,25] The same holds for the P–N bond lengths in **1** (1.59(2)–1.67(2) Å).[3,7,9,22,25]

Nitridic clathrate **1** exhibits remarkable thermal stability with respect to evolution of ammonia. According to temperature-programmed mass spectrometry (see Experimental Section) the intercalated NH_3 in **1** is not expelled below 550 °C. At such temperatures **1** transforms presumably into a crystalline phase of normal-pressure PN(NH) [Eq. (5)].

$$P_4N_4(NH)_4(NH_3) \rightarrow 4\,PN(NH) + NH_3 \quad (5)$$

Above 810 °C condensation of the thus-formed PN(NH) framework with further evolution of NH_3 is observed in mass chromatograms, which essentially represents the reverse of the ammonolysis reaction of P_3N_5 [Eq. (4)]. This finding compares well with the condensation (with evolution of NH_3) of crystalline PN(NH) (**2a**) that we observed in mass chromatograms at 860 °C. Amorphous and relatively undefined PN(NH) (**2c**) is much more sensitive towards condensation to P_3N_5, which already starts at temperatures as low as 100 °C (see Experimental Section). In accordance with our previous results[22] we finally observed thermolysis of the thus-formed amorphous P_3N_5 into the constituting elements [cf. Eq. (2)] above 890 °C.

At first glance, the high-pressure approach seems to be quite unusual for the synthesis of porous compounds, as these conditions are expected to destabilize less dense framework structures, which usually have lower density than related phases of higher thermodynamic stability. The success of this approach for the synthesis of **1** may be rationalized by assuming that the increase in density (**1** vs. **2b** + NH_3) is the driving force of the high-pressure reaction in a closed system. The density of **1** (2.642 g cm^{-3}) is comparable to that of 2.67 g cm^{-3} for hp-PN(NH) (**2b**),[29] but for a quantitative estimation of the driving force for pressure-driven formation of **1** (as compared with the possibly competing formation of hp-PN(NH) + NH_3), the respective temperature- and pressure-dependent values for **1** and **2b**, as well as the contribution of NH_3, must be considered; however, these are not available as yet. Further experimental and theoretical investigations are planned to shed light on this issue and to further broaden this novel high-pressure approach to hitherto unknown porous structures.

Experimental Section

$P_4N_4(NH)_4(NH_3)$ (**1**) was synthesized from the starting materials NH_4N_3[26] and P_3N_5[27] by high-pressure high-temperature synthesis in a similar way as outlined in the literature[22] in a Walker-type multianvil[24,38] module. Octahedra with an edge length of 14 mm (Ceramic Substrates, Isle of Wight) were used, and the sample was placed into a capsule made of hexagonal boron nitride (Henze, Kempten). The mixture was heated over 10 min to 600 °C at 11 GPa, the temperature was maintained for 15 min, and the reaction was finally quenched by cooling to room temperature. About 0.5 mm^3 of **1** were obtained per batch as a colorless and crystalline powder.

The thermal behavior of **1** was investigated by temperature-dependent mass spectroscopy on a JEOL M-station J-MS 700 mass spectrometer. The sample was heated by an electric furnace to 900 °C in an evacuated silica glass tube connected to the gas inlet of the mass spectrometer (heating rate 10 °C min^{-1}). The mass chromatograms exhibit two discrete peaks which are indicative of formation of NH_3 (m/z 17): The first peak, at 565 °C, represents evolution of intercalated NH_3 [Eq. (5)]. The second peak, at 810 °C, represents evolution of NH_3 from condensation of the PN(NH) framework to yield phosphorus(V) nitride P_3N_5 [Eq. (4)]. The last peak, observed at 890 °C for m/z 28 (N_2), comes from the thermolysis of P_3N_5 [Eq. (2)]. The setup of our apparatus did not allow for the detection of low-volatility phosphorus(III) nitride PN as an intermediate. However, small amounts of P_4 (m/z 124) were identified in the mass spectrum at 900 °C [Eq. (2)].

The experiment was repeated with crystalline PN(NH) (**2a**) as reference.[3,4] Condensation of **2a** has been observed at 860 °C, whereas the condensation of amorphous PN(NH) (**2c**) already starts at approximately 80 °C.

The FTIR spectrum[39] of **1** exhibits a significant band at 1091 cm^{-1} for the δ_s(H-N-H) deformation mode and at 1635 cm^{-1} for the δ_{as}(H-N-H) mode originating from the intercalated NH_3 molecule. The PN(NH) framework only shows N–H valence modes because of the absence of NH_2 groups. The observed N–H valence modes result from both imide groups of the framework and N–H vibrational modes of the ammonia molecules and they resemble those of crystalline PN(NH).[3,29]

Received: February 10, 2006
Published online: May 31, 2006

Keywords: high-pressure chemistry · high-temperature chemistry · microporous materials · nitrides · phosphorus

[1] W. Schnick, *Angew. Chem.* **1993**, *105*, 846; *Angew. Chem. Int. Ed. Engl.* **1993**, *32*, 806.
[2] U. Wannagat, D. Burgdorf, H. Buerger, G. Pawelke, *Z. Naturforsch. B* **1991**, *46*, 1039.
[3] W. Schnick, J. Lücke, *Z. Anorg. Allg. Chem.* **1992**, *610*, 121.
[4] N. Jacobs, R. Nymwegen, S. Doyle, T. Wroblewski, W. Kockelmann, *Z. Anorg. Allg. Chem.* **1997**, *623*, 1467.
[5] L. Boukbir, R. Marchand, Y. Laurent, P. Bacher, G. Roult, *Ann. Chim.* **1989**, *14*, 475.
[6] P. Eckerlin, C. Langereis, I. Maak, A. Rabenau, *Angew. Chem.* **1960**, *72*, 268; P. Eckerlin, C. Langereis, I. Maak, A. Rabenau in *Special Ceramics*, *Vol. 3* (Ed.: P. Popper) Academic Press, London, **1965**, pp. 79.
[7] W. Schnick, J. Lücke, *Z. Anorg. Allg. Chem.* **1990**, *588*, 19.
[8] A. Vitola, J. Ronis, T. Millers, *Latv. PSR Zinat. Akad. Vestis Kim. Ser.* **1990**, 35.

 © 2006 Wiley-VCH Verlag GmbH & Co. KGaA, Weinheim

[9] K. Landskron, S. Schmid, W. Schnick, *Z. Anorg. Allg. Chem.* **2001**, *627*, 2469.
[10] W. Schnick, J. Lücke, *Angew. Chem.* **1992**, *104*, 208; *Angew. Chem. Int. Ed. Engl.* **1992**, *31*, 213.
[11] W. Schnick, J. Lücke, *Z. Anorg. Allg. Chem.* **1994**, *620*, 2014.
[12] W. Schnick, N. Stock, J. Lücke, M. Volkmann, M. Jansen, *Z. Anorg. Allg. Chem.* **1995**, *621*, 987.
[13] F. Wester, W. Schnick, *Z. Anorg. Allg. Chem.* **1996**, *622*, 1281.
[14] N. Stock, E. Irran, W. Schnick, *Chem. Eur. J.* **1998**, *4*, 1822.
[15] Because $Li_xH_{12-x-y+z}[P_{12}O_yN_{24-y}]X_z$ (X = Cl, Br) is made up of a network strukture of $(P/O,N)_4$ tetrahedra, it should be named a "nitridic zeotype" according to F. Liebau, *Microporous Mesoporous Mater.* **2003**, *58*, 15.
[16] S. Correll, O. Oeckler, N. Stock, W. Schnick, *Angew. Chem.* **2003**, *115*, 3674; *Angew. Chem. Int. Ed.* **2003**, *42*, 3549.
[17] International Zeolite Association, *Atlas of Zeolite Framework Types*, http://topaz.ethz.ch/IZA-SC/StdAtlas.htm.
[18] M. O'Keeffe, *Acta Crystallogr. Sect. A* **1992**, *48*, 670.
[19] A. K. Cheetham, G. Fèrey, T. Loiseau, *Angew. Chem.* **1999**, *111*, 3466; *Angew. Chem. Int. Ed.* **1999**, *38*, 3268.
[20] F. Schüth, W. Schmidt, *Adv. Mater.* **2002**, *14*, 629.
[21] L. McCusker, *J. Appl. Crystallogr.* **1988**, *21*, 305.
[22] F. Karau, W. Schnick, *J. Solid State Chem.* **2005**, *178*, 135.
[23] H. Huppertz, *Z. Kristallogr.* **2004**, *219*, 330.
[24] D. Walker, M. A. Carpenter, C. M. Hitch, *Am. Mineral.* **1990**, *75*, 1020.
[25] F. Karau, W. Schnick, *Z. Anorg. Allg. Chem.* **2006**, *632*, 231.
[26] W. J. Frierson, *Inorg. Synth.* **1946**, *8*, 136.
[27] V. Schultz-Coulon, W. Schnick, *Z. Anorg. Allg. Chem.* **1997**, *623*, 69.
[28] K. Landskron, H. Huppertz, J. Senker, W. Schnick, *Angew. Chem.* **2001**, *113*, 2713; *Angew. Chem. Int. Ed.* **2001**, *40*, 2643; K. Landskron, H. Huppertz, J. Senker, W. Schnick, *Z. Anorg. Allg. Chem.* **2002**, *628*, 1465.
[29] F. Karau, W. Schnick, unpublished results.
[30] Crystal data for $[P_4N_4(NH)_4](NH_3)$: Stoe StadiP diffractometer; $Cu_{K\alpha1}$ ($\lambda = 1.5415$ Å); $2\Theta = 5$–$90°$, internal step width of $2\Theta = 0.01°$, detector (linear PSD, $\Delta 2\Theta = 5°$) step width of $2\Theta = 0.25°$, 7810 data points, $N_{obsd} = 86$, 32 variables, number of thermal displacement parameters refined: 5, background function: cosine Fourier series with 12 coefficients; tetragonal, space group $P\bar{4}n2$ (no. 118), $a = 6.73436(5)$, $c = 7.03995(8)$ Å, $V = 319.273(6)$ Å^3, $Z = 2$, $\rho_{calcd} = 2.642\ g\,cm^{-3}$, framework density 25.06 T/1000 Å^3; max. atom shift 0, $R(F^2) = 0.0620$, $wR_p = 0.0773$, $R_p = 0.0580$; structure solution by direct methods: EXPO (A. Altomare, M. C. Burla, B. Carrozzini, G. Cascarano, C. Giacovazzo, A. Guagliardi, A. G. G. Moliterni, G. Polidori, R. Rizzi, *J. Appl. Crystallogr.* **1999**, *32*, 339), Rietveld refinement: GSAS (A. C. Larson, R. B. v. Dreele, *Los Alamos Natl. Lab.* **2000**, *86*, 768). Further details on the crystal structure investigations may be obtained from the Fachinformationszentrum Karlsruhe, 76344 Eggenstein-Leopoldshafen, Germany (fax: (+49) 7247-808-666; e-mail: crysdata@fiz-karlsruhe.de), on quoting the depository number CSD-416155.
[31] P.-E. Werner, *Z. Kristallogr.* **1964**, *120*, 375.
[32] L. B. McCusker, F. Liebau, G. Engelhardt, *Pure Appl. Chem.* **2001**, *73*, 381.
[33] G. Thimm, S. Schumacher, W. Uhr, W. E. Klee, TOPOLAN, Topological analysis of crystal structures, Institut für Kristallographie der Universität Karlsruhe, Germany, **2001**.
[34] G. M. Barrow, *Physikalische Chemie*, 6th ed., Friedrich Vieweg, Braunschweig, **1984**.
[35] M. D. Foster, O. D. Friedrichs, R. G. Bell, F. A. A. Paz, J. Klinowski, *J. Am. Chem. Soc.* **2004**, *126*, 9769.
[36] M. M. J. Treacy, K. H. Randall, S. Raho, J. A. Perry, D. J. Z. Chadi, *Z. Kristallogr.* **1997**, *212*, 768.
[37] F. Liebau, *Structural Chemistry of Silicates*, Springer, Berlin, Heidelberg, New York, Tokyo, **1985**.
[38] D. Walker, *Am. Mineral.* **1991**, *76*, 1092.
[39] IR data of $[P_4N_4(NH)_4](NH_3)$: 1091: δ_s(H-N-H); 1366, 1409: ν(P–N); 1635: δ_{as}(H-N-H); 3130 ν_s(N–H); 3427 cm^{-1} ν_{as}(N–H).
[40] F. Liebau, *Microporous Mesoporous Mater.* **2003**, *58*, 15.

 © 2006 Wiley-VCH Verlag GmbH & Co. KGaA, Weinheim

Nanocluster Assembly

DOI: 10.1002/anie.200504588

Bionanotube Tetrapod Assembly by In Situ Synthesis of a Gold Nanocluster with $(Gp5–His_6)_3$ from Bacteriophage T4**

Takafumi Ueno, Tomomi Koshiyama, Toshimitsu Tsuruga, Toshiaki Goto, Shuji Kanamaru, Fumio Arisaka, and Yoshihito Watanabe**

Utilization of biomolecules for the synthesis of novel materials is a very important strategy for the fabrication of new nanomaterials.[1–3] A number of proteins with a diverse range of structures (tube, ball, and cage) have been employed as frameworks for the construction of multidimensional

[*] Dr. T. Ueno
Research Center for Materials Science
Nagoya University
Nagoya 464-8602 (Japan)
Fax: (+81) 52-789-2953
E-mail: taka@mbox.chem.nagoya-u.ac.jp

T. Koshiyama, T. Tsuruga, Prof. Dr. Y. Watanabe
Department of Chemistry, Graduate School of Science
Nagoya University
Nagoya 464-8602 (Japan)
Fax: (+81) 52-789-2953
E-mail: yoshi@nucc.cc.nagoya-u.ac.jp

T. Goto
Department of Physics, Graduate School of Science
Nagoya University
Nagoya 464-8602 (Japan)

Dr. S. Kanamaru, Prof. Dr. F. Arisaka
Department of Biomolecular Engineering
Graduate School of Bioscience and Biotechnology
Tokyo Institute of Technology
B-39 4259 Nagatsuta-cho, Midori-ku, Yokohama 226-8501 (Japan)

[**] We thank Prof. S. Aono and S. Inagaki (Okazaki Institute for Integrative Bioscience, National Institutes of Natural Sciences, Japan) for suggestions. This work was supported by the Advanced Technology Institute, Grants-in-Aid for Scientific Research (grants no. 18685019 to T.U. and no. 16074208 on Priority Area "Chemistry of Coordination Space" to Y.W.) from the Ministry of Education, Science, Sports and Culture, Japan, and a grant from the 21st Century COE program "Establishment of COE on Materials Science: Elucidation and Creation of Molecular Functions" of Nagoya University for T.K. Gp5 = gene product 5.

Supporting information for this article is available on the WWW under http://www.angewandte.org or from the author.

 WILEY InterScience DISCOVER SOMETHING GREAT

© 2006 Wiley-VCH Verlag GmbH & Co. KGaA, Weinheim

devices,[4–16] since proteins are useful materials for the deposition of metal composites and the mineralization of metal ions. Metal composites with important electronic, magnetic, and optical properties can be introduced either on the surface of or inside proteins by attaching peptide fragments to the proteins.[11–17] For example, native and synthetic histidine-rich peptide fragments exhibit a high affinity for metal cations and nanoclusters,[11,15,18–20] and have been used for this purpose: 1) synthetic His_6 fragments introduced into viruses and chaperonin have been applied for metal-cluster patterning[11,15] and 2) native histidine-rich fragments have been demonstrated to control the size distribution in nanocluster syntheses for various metals.[18,19]

However, it is still difficult to assemble proteins on metal composites and regulate their structures.[14,16] If we could control multidimensional protein assembly on metal composites, it would be a significant advance in the field of bionanodevice self-assembly. We have chosen gene product 5 (gp5) of bacteriophage T4 as an attractive model for work in this direction. Rossmann and co-workers, including two of the present authors, have reported the crystal structure of $(gp5)_3$ complexed with $(gp27)_3$ (Figure 1a).[21] Gp5 has three domains, namely the N-terminal domain (gp5N), which possesses an oligonucleotide/oligosaccharide (OB) fold, the lysozyme domain, and the C-terminal domain (gp5C), which forms a three-stranded β helix as $(gp5C)_3$ that may be called a bionanotube (Figure 1b and c). Gp5C functions as a needle to penetrate the outer membrane of *Escherichia coli*. Gp5 is one of the essential tail proteins in the assembly of bacteriophage T4. The complexes of $(gp27–gp5)_3$, $(gp5)_3$, and $(gp5C)_3$ were overexpressed and purified with the aid of a His_6 fragment introduced onto the C terminus of gp5 as described in previous reports.[21,22] We then studied the self-assembly of trimeric gp5 coupled with the in situ synthesis of Au nanoclusters (NCs). The three histidine-rich regions form a triad at the C termini of $(gp5–His_6)_3$ (Figure 1a). The triad of His_6 fragments is expected to assist in the synthesis of an Au NC at the C termini of the β-helical nanotube, $(gp5C–His_6)_3$. In this paper, we report the in situ preparation of Au NCs bearing a tetrapod assembly of the bionanotubes (Figure 2).

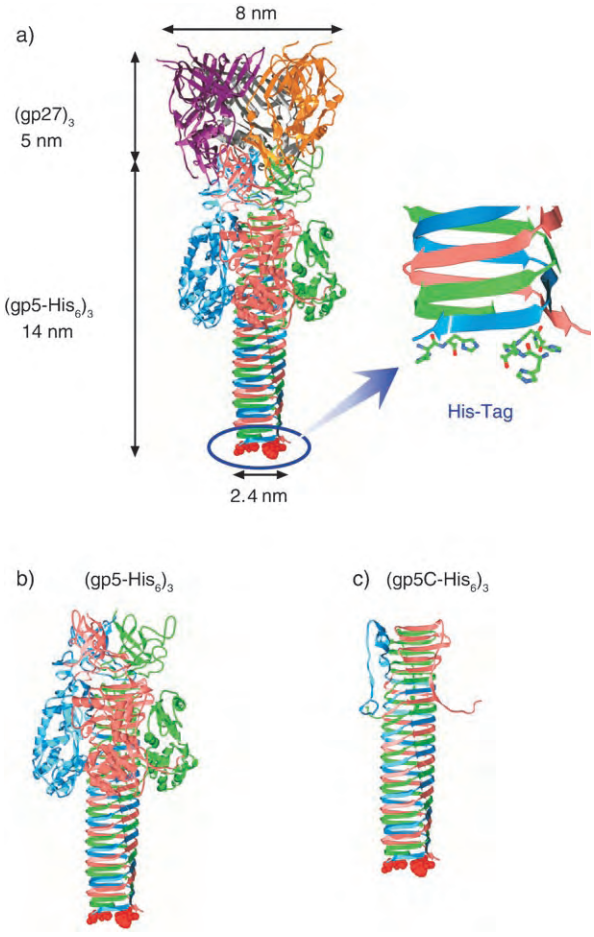


Figure 1. Structures of a) the membrane-puncturing bionanotube complexes of $(gp27–gp5–His_6)_3$ from bacteriophage T4 with a close-up view of the His_6 fragment region showing the histidine residues, b) $(gp5–His_6)_3$, and c) $(gp5C–His_6)_3$ (Protein DataBank file code: 1K28). The His_6 triad is displayed as a space-filling model in red.

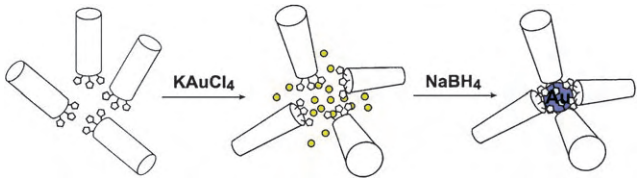


Figure 2. Self-assembly of $(gp5–His_6)_3$ through an Au nanocluster.

The $gp5–His_6$ trimer was treated with 300 equivalents of $KAuCl_4$ to obtain a homogeneous pale-yellow solution at pH 9.0 (20 mM tris(hydroxymethyl)aminomethane (Tris)/HCl and 0.2 M NaCl) and 4 °C. The Au^{III} ions were reduced with 2.5 equivalents of $NaBH_4$ to yield the Au NCs. Upon the reduction, the spectrum of the solution was changed significantly; there was the expected plasmon resonance absorption maximum for an Au NC at 530 nm (Figure 3a).[23] Under the same conditions, dark-purple precipitates were observed in a protein-free control experiment, while the solution containing only $(gp5–His_6)_3$ remained a clear purple color. These results suggest that $(gp5–His_6)_3$ can make Au NCs soluble in aqueous solution by covering the NCs, as previously reported for Au-NC-binding peptides.[24] Finally, the $Au/\{(gp5–His_6)_3\}_4$ composite was purified with size-exclusion chromatography (Sephacryl S300, fractionation range 1×10^4–1.5×10^6 Da) by monitoring the absorption both at 280 nm (protein) and at 530 nm (Au NC). The coelution of the protein and metal components through the column is a clear indication of the composite nature of the material (Figure 3b). The N- and C-terminal domains indicated in Figure 3c arise from processing, where $gp5–His_6$ is cleaved on the C-terminus side of Ser351, which is in a loop between the lysozyme and C-terminal domains. The two resultant fragments remain associated after the reaction with Au.[25]

We examined the structure of the $Au/(gp5–His_6)_3$ composites by transmission electron microscopy to understand the role of the His_6 fragments upon formation of the Au NCs. The TEM image of Au NCs with $(gp5–His_6)_3$ shows monodisperse NCs with a diameter of 2.7 nm (Figure 4a and the Au NCs histogram). The surface area of the Au NCs is 22.9 nm^2 on the

 © 2006 Wiley-VCH Verlag GmbH & Co. KGaA, Weinheim

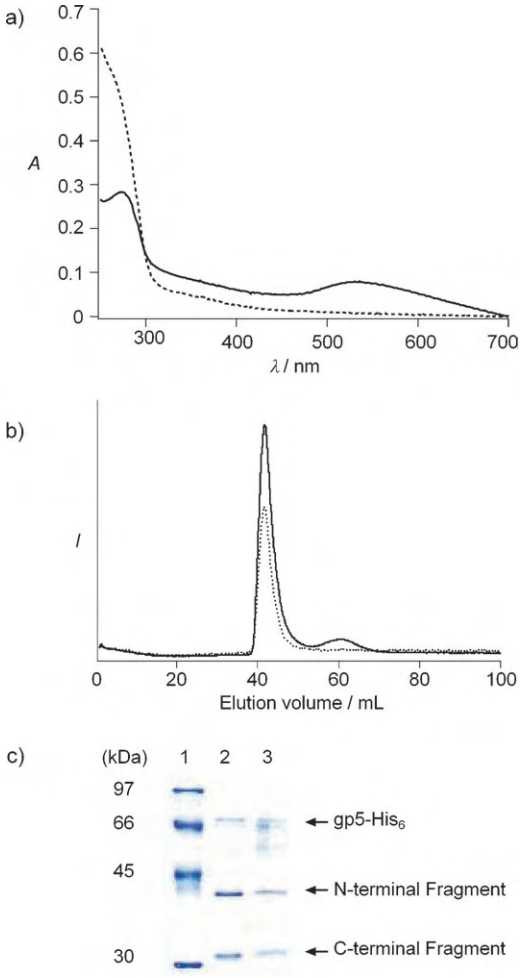


Figure 3. a) UV/Vis spectra of $KAuCl_4$/$(gp5–His_6)_3$ solution before (broken line) and after (solid line) reduction, b) size-exclusion-chromatography elution profile of Au/$\{(gp5–His_6)_3\}_4$ monitored at 280 nm (solid line) and 530 nm (broken line), and c) sodium dodecylsulfate (SDS) PAGE of a molecular-weight marker (lane 1), $(gp5–His_6)_3$ (lane 2), and Au/$\{(gp5–His_6)_3\}_4$ (lane 3). The gel (12.5%) was stained with Coomassie brilliant blue.

basis of the TEM results. The crystal structure of $(gp5–His_6)_3$ shows that the base area of the C-terminal region is 6.1 nm^2 when the $(gp5–His_6)_3$ tube is assumed to be a cylinder (Figure 1a). Thus, four $(gp5–His_6)_3$ units are expected to bind on the surface of each Au NC. In fact, close-up views of the composites indicate that an Au NC is covered with four proteins which are approximately 14 nm in length (Figure 4b). The protein size, which is identical to that of $(gp5–His_6)_3$ (Figure 1b), is in agreement with our proposed structure for composites consisting of four $(gp5–His_6)_3$ units and the Au NC in a tetrapod arrangement, as shown in Figure 4c.

The tetrapod assemblies were formed in a yield of 60% at pH 9.0, although only nonuniform aggregations of Au/protein composites occurred at pH 8.0 and 10.[26] The yield was decreased with addition of excess $KAuCl_4$ (500 equiv) because the Au NCs were formed with nonuniform size and shape.[26] In order to confirm that $(His_6)_3$ directs the composite formation and the Au NC size, $KAuCl_4$ was mixed with $(gp5)_3$ that had no His_6 fragments attached and then the mixture was reduced with $NaBH_4$ at pH 9.0. The prepared Au NCs were larger (diameter 3.3 nm) with polydispersion, and the proteins assembled more randomly around the Au NCs than in those composites prepared in the presence of $(gp5–His_6)_3$ (Figure 4d). Furthermore, $(gp27–gp5–His_6)_3$ and $(gp5C–His_6)_3$ also gave polydisperse and larger Au NCs under the same conditions (Figure 4e and f). In addition, these composites with Au NCs were also not shaped into uniform structures at pH 8.0 and 10.[26] These results clearly indicate that the specific Au/protein tetrapod composite was constructed by the reaction of $(gp5–His_6)_3$ with 300 equivalents of Au at pH 9.0 (Figure 4a).

The crystal structure of $(gp27–gp5–His_6)_3$ shows that the His_6 fragments located at the C-terminus of gp5 are 2.4 nm apart from each other in the trimer structure (Figure 1a). It has been previously reported that such periodical location of histidine-rich fragments results in the formation of size-regulated metal particles on an artificial peptide nanotube.[19] $(Gp5)_3$ with no His_6 fragments gave the polydisperse and larger Au NCs in the composites, with random binding of the proteins to the Au NCs (Figure 4d). Thus, the formation of the monodisperse Au NCs in Au/$\{(gp5–His_6)_3\}_4$ (2.7 nm) is expected to be restricted by the specific location of the His_6 fragments on the gp5 trimer.

The pH value of the reaction is also an important factor in generating the tetrapod assembly on an Au NC. Conformation change of histidine-rich peptides is induced in the presence of metal ions between pH 8.0 and 10.[27] The reduction of Au ions with $(gp5–His_6)_3$ at pH 8.0 gives random Au/$(gp5–His_6)_3$ assemblies with polydisperse Au-NC size. This is because the conformations of the His_6 fragments and the other surface residues are inappropriate for the formation of tetrapod assemblies at pH 8.0. At pH 10, few Au NCs were formed, due to low reactivity of $NaBH_4$ at high pH values.[26,28] It is expected that the structure of the His_6 fragment in $gp5–His_6$ at pH 9.0 is more suitable for binding Au atoms than that at other pH values.

Furthermore, the assembly of proteins on an Au NC is influenced by the electrostatic potential of the tube proteins. Au NCs are stabilized in solution when they are covered with negatively charged molecules, such as citrate anions.[29] The electrostatic potential map of $(gp5–His_6)_3$ (calculated with the Grasp software) clearly shows a negatively charged region located at the C termini of the $gp5–His_6$ units (Figure 5b). On the other hand, $(gp5C–His_6)_3$ has negative patches at the N and the C termini and the negative charge at the N terminus prevents the specific binding of the C terminus with an Au NC (Figure 5c). In the case of $(gp27–gp5–His_6)_3$, the negatively charged regions are located only at the C terminus (Figure 5a); however, the gp27 fragment has many exposed methionine and cysteine residues with high affinity for Au^{III} cations and Au NCs.[29] Thus, Au NCs nonspecifically bind on the $(gp27–gp5–His_6)_3$ surface (Figure 4d). Furthermore, the isoelectric point of $(gp5–His_6)_3$ is estimated to be 6.0 (calculated with the Protein Calculator v3.2 software).[30] These considerations suggest that the tetrapod structure, Au/$\{(gp5–His_6)_3\}_4$, is held through the cooperative effects of

 © 2006 Wiley-VCH Verlag GmbH & Co. KGaA, Weinheim

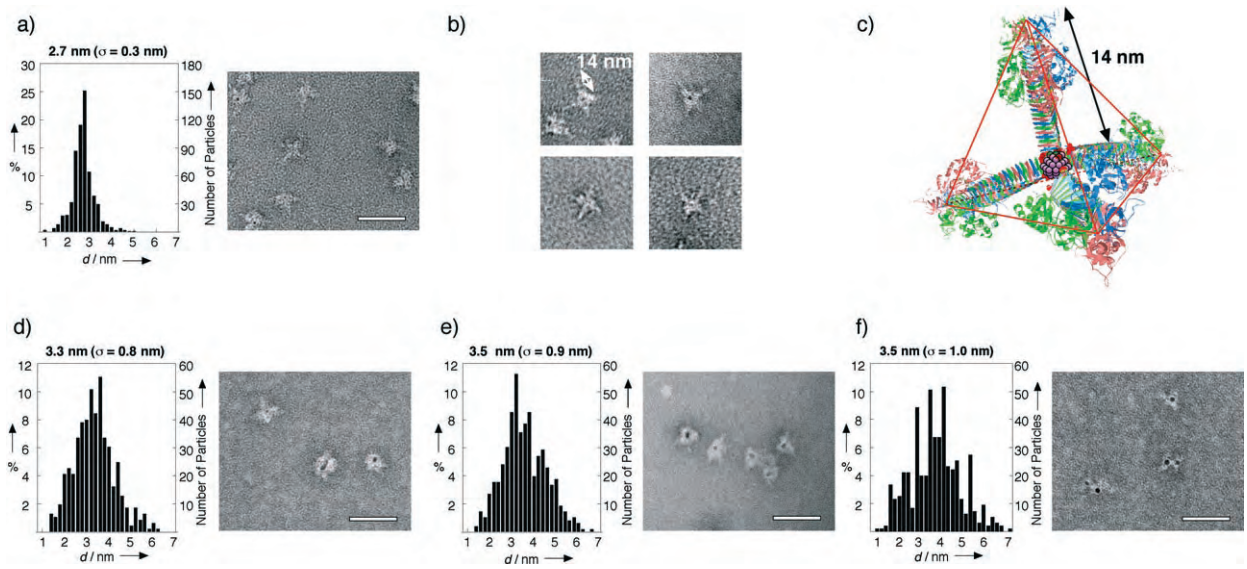


Figure 4. Au nanocluster size distribution and TEM images for a) Au/{(gp5–His_6)$_3$}$_4$, d) Au/(gp5)$_3$, e) Au/(gp27–gp5–His_6)$_3$, and f) Au/(gp5C–His_6)$_3$. b) Close-up TEM image of single Au/{(gp5–His_6)$_3$}$_4$ composites. Scale bar: 50 nm. All reactions were carried out at pH 9.0. TEM grids were stained with 2% uranyl acetate. c) The proposed structure of the composite.

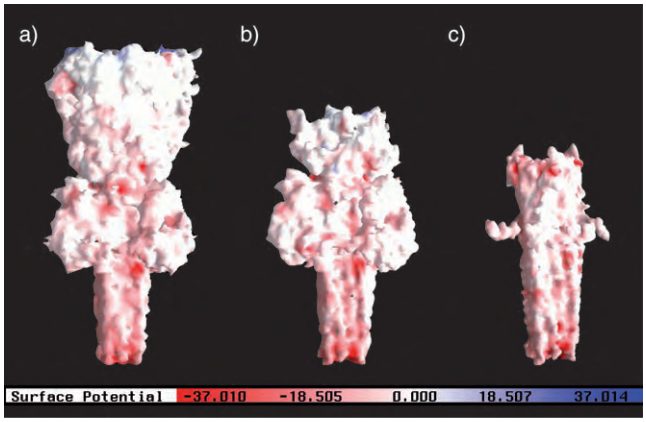


Figure 5. Electrostatic potential maps for a) (gp27–gp5–His_6)$_3$, b) (gp5–His_6)$_3$, and c) (gp5C–His_6)$_3$. The surface is colored according to its potential (blue positive, red negative). The maps were generated by calculations with the Grasp software.[31]

the His_6 triad, the negative charge of the C termini, and the electrostatic repulsion between each (gp5–His_6)$_3$ on an Au NC at pH 9.0 (Figure 4a).

In summary, we have prepared a tetrapod assembly of bionanotubes by in situ synthesis of Au NCs with (gp5–His_6)$_3$ from bacteriophage T4 (Figure 2). The three-dimensional structure is regulated cooperatively by the location of His_6 fragments and the surface electrostatic potential on the (gp5–His_6)$_3$ nanotube. The results indicate that if His_6 fragments are introduced at desired positions in proteins, it could be possible to design various architectures of protein assembly on metals by using in situ metal nanocluster formation. Modification of the surface charge may further facilitate the specific assembly of the tetrapod. This presents a novel strategy for the fabrication of nanoscale metal composites.

Experimental Section

Reagents were purchased from Nacalai Tesque and Sigma–Aldrich, and used without further purification. The expression and purification of proteins containing His_6 fragments were performed as reported previously.[21,22] The proteins were checked by SDS PAGE and MALDI-TOF MS (Voyager instrument, PE Biosystems). All reactions were carried out at 4 °C.

Preparation of gp5 without a His_6 fragment: Gp5 without a His_6 fragment was isolated by the glutathione *S*-transferase (GST) fusion method. Cell pellets that expressed the GST–gp5 fusion proteins were resuspended in buffer solution (10 mM Na_2HPO_4, 1.8 mM KH_2PO_4, 140 mM NaCl, 2.7 mM KCl, pH 7.3) and lyzed by sonication. The mixture was centrifuged at 17500 rpm for 20 min. The supernatant was loaded onto a GSTrap FF column (Amersham Biosciences). GST–gp5 was eluted from the column with 50 mM Tris/HCl and 10 mM glutathione buffer at pH 8.0. The eluted solution was dialyzed against 10 mM Na_2HPO_4, 1.8 mM KH_2PO_4, 140 mM NaCl, and 2.7 mM KCl at pH 7.3. The GSTs of the GST–gp5 proteins were digested with thrombin protease for 6 h. The free GSTs were then trapped with the GSTrap FF column. Finally, the gp5 proteins were purified with a Superdex G200 column on an ÄKTA explorer 100 FPLC system (Amersham Biosciences).

Preparation of Au/{(gp5–His_6)$_3$}$_4$: A $KAuCl_4$ solution (1 mM, 480 μL in 20 mM Tris/HCl and 0.2 M NaCl buffer, pH 9.0) was added to a solution of (gp5–His_6)$_3$ (0.4 μM, 4 mL in 20 mM Tris/HCl and 0.2 M NaCl buffer, pH 9.0). The mixture was stirred for 30 min, and then a solution of $NaBH_4$ (2.5 mM, 480 μL in 20 mM Tris/HCl and 0.2 M NaCl buffer, pH 9.0) was added. After stirring for 30 min, the mixture was centrifuged at 15000 rpm for 10 min to remove precipitate. The resulting solution was purified on a size-exclusion column (Sephacryl S300) equilibrated with 20 mM Tris/HCl and 0.2 M NaCl buffer (pH 9.0).

Transmission electron microscopy: A solution of Au/{(gp5–His_6)$_3$}$_4$ (3 μL) was applied to a copper grid covered with a thin amorphous carbon film for 1 min, and then excess solution was removed with a filter paper. The grid was washed with water (3 μL) for 1 min and then stained with 2% uranyl acetate (3 μL) for 1 min. The images of the negatively stained samples were recorded on a

 © 2006 Wiley-VCH Verlag GmbH & Co. KGaA, Weinheim

JEM-4010N microscope (300 kV). Other samples were prepared and observed with the same procedure.

Received: December 26, 2005
Revised: March 31, 2006
Published online: June 13, 2006

Keywords: bacteriophages · biomineralization · gold · nanotubes · self-assembly

[1] C. M. Niemeyer, *Angew. Chem.* **2001**, *113*, 4254 – 4287; *Angew. Chem. Int. Ed.* **2001**, *40*, 4128 – 4158.
[2] N. L. Rosi, C. A. Mirkin, *Chem. Rev.* **2005**, *105*, 1547 – 1562.
[3] D. M. Vriezema, M. C. Aragones, J. A. A. W. Elemans, J. J. L. M. Cornelissen, A. E. Rowan, R. J. M. Nolte, *Chem. Rev.* **2005**, *105*, 1445 – 1490.
[4] T. Douglas, M. Young, *Nature* **1998**, *393*, 152 – 155.
[5] J. C. Falkner, M. E. Turner, J. K. Bosworth, T. J. Trentler, J. E. Johnson, T. Lin, V. L. Colvin, *J. Am. Chem. Soc.* **2005**, *127*, 5274 – 5275.
[6] R. A. McMillan, C. D. Paavola, J. Howard, S. L. Chan, N. J. Zaluzec, J. D. Trent, *Nat. Mater.* **2002**, *1*, 247 – 252.
[7] W. Shenton, D. Pum, U. B. Sleytr, S. Mann, *Nature* **1997**, *389*, 585 – 587.
[8] W. Shenton, T. Douglas, M. Young, G. Stubbs, S. Mann, *Adv. Mater.* **1999**, *11*, 253 – 256.
[9] T. Ueno, M. Suzuki, T. Goto, T. Matsumoto, K. Nagayama, Y. Watanabe, *Angew. Chem.* **2004**, *116*, 2581 – 2584; *Angew. Chem. Int. Ed.* **2004**, *43*, 2527 – 2530.
[10] Q. Wang, T. Lin, L. Tang, J. E. Johnson, M. G. Finn, *Angew. Chem.* **2002**, *114*, 477 – 480; *Angew. Chem. Int. Ed.* **2002**, *41*, 459 – 462.
[11] A. Chatterji, W. F. Ochoa, T. Ueno, T. Lin, J. E. Johnson, *Nano Lett.* **2005**, *5*, 597 – 602.
[12] T. Douglas, E. Strable, D. Willits, A. Aitouchen, M. Libera, M. Young, *Adv. Mater.* **2002**, *14*, 415 – 418.
[13] R. M. Kramer, C. Li, D. C. Carter, M. O. Stone, R. R. Naik, *J. Am. Chem. Soc.* **2004**, *126*, 13282 – 13286.
[14] S.-W. Lee, C. Mao, C. E. Flynn, A. M. Belcher, *Science* **2002**, *296*, 892 – 895.
[15] R. A. McMillan, J. Howard, N. J. Zaluzec, H. K. Kagawa, R. Mogul, Y.-F. Li, C. D. Paavola, J. D. Trent, *J. Am. Chem. Soc.* **2005**, *127*, 2800 – 2801.
[16] S. R. Whaley, D. S. English, E. L. Hu, P. F. Barbara, A. M. Belcher, *Nature* **2000**, *405*, 665 – 668.
[17] M. Sarikaya, C. Tamerler, A. K.-Y. Jen, K. Schulten, F. Beneyx, *Nat. Mater.* **2003**, *2*, 577 – 585.
[18] I. A. Banerjee, L. Yu, H. Matsui, *Proc. Natl. Acad. Sci. USA* **2003**, *100*, 14678 – 14682.
[19] R. Djalali, Y.-F. Chen, H. Matsui, *J. Am. Chem. Soc.* **2003**, *125*, 5873 – 5879.
[20] J. M. Slocik, J. T. Moore, D. W. Wright, *Nano Lett.* **2002**, *2*, 169 – 173.
[21] S. Kanamaru, P. G. Leiman, V. A. Kostyuchenko, P. R. Chipman, V. V. Mesyanzhinov, F. Arisaka, M. G. Rossmann, *Nature* **2002**, *415*, 553 – 557.
[22] S. Kanamaru, N. C. Gassner, N. Ye, S. Takeda, F. Arisaka, *J. Bacteriol.* **1999**, *181*, 2739 – 2744.
[23] J. P. Wilcoxon, J. E. Martin, P. Provencio, *J. Chem. Phys.* **2001**, *115*, 998 – 1008.
[24] J. M. Slocik, D. W. Wright, *Biomacromolecules* **2003**, *4*, 1135 – 1141.
[25] S. Kanamaru, Y. Ishiwata, T. Suzuki, M. G. Rossmann, F. Arisaka, *J. Mol. Biol.* **2005**, *346*, 1013 – 1020.
[26] See the Supporting Information.
[27] G. Pappalardo, G. Impellizzeri, R. P. Bonomo, T. Campagna, G. Grasso, M. G. Saita, *New J. Chem.* **2002**, *26*, 593 – 600.
[28] S. Liu, J. V. M. Weaver, M. Save, S. P. Armes, *Langmuir* **2002**, *18*, 8350 – 8357.
[29] C. J. Sandroff, D. R. Herschbach, *Langmuir* **1985**, *1*, 131 – 135.
[30] The website of this software is http://www.scripps.edu/~cdputnam/protcalc.html.
[31] A. Nicholls, K. A. Sharp, B. Honig, *Proteins Struct. Funct. Genet.* **1991**, *11*, 281 – 296.

 © 2006 Wiley-VCH Verlag GmbH & Co. KGaA, Weinheim

DNA Recognition

DOI: 10.1002/anie.200600790

SNP Genotyping by Using Photochemical Ligation**

*Shinzi Ogasawara and Kenzo Fujimoto**

A DNA chip for analysis of biomedical features, such as single-nucleotide polymorphisms (SNPs), is a most powerful and useful tool, which allows the simultaneous detection of many different target molecules present in a sample.[1] However, the technology is not yet widely used in routine clinical settings, because it requires improvement in terms of fidelity, reproducibility, and expedition, all of which are essential for standardization and human-gene diagnosis. Whether electrochemical detection[2] or fluorescence detection,[3] the reaction principle that underlies the DNA-chip assays is hybridization with allele-specific oligonucleotide (ASO) probes. In allele-specific hybridization, the difference in thermal stability between perfectly matched and mismatched ASO probes with the DNA target is used to distinguish between SNP alleles. This difference can be very small and can vary based on sequence context. Therefore, although ASO probes can distinguish single-nucleotide differences based on small changes in hybridization efficiency, the

[*] S. Ogasawara, Prof. Dr. K. Fujimoto
School of Materials Science
Japan Advanced Institute of Science and Technology
Asahidai, Nomi, Ishikawa 923-1292 (Japan)
Fax: (+81) 761-51-1671
E-mail: kenzo@jaist.ac.jp
Prof. Dr. K. Fujimoto
PRESTO
Japan Science and Technology Agency (JST)
Kawaguchi 332-0012 (Japan)

[**] This work was supported by Precursory Research for Embryonic Science and Technology (PRESTO), Japan Science and Technology Agency (JST), Japan. Partial support by a Grant-in-Aid for Scientific Research from the Ministry of Education, Culture, Sports, Science, and Technology, Japan, is also acknowledged. SNP = single-nucleotide polymorphism.

Supporting information for this article is available on the WWW under http://www.angewandte.org or from the author.

WILEY InterScience DISCOVER SOMETHING GREAT
© 2006 Wiley-VCH Verlag GmbH & Co. KGaA, Weinheim

selectivity and sensitivity seen for ASO probes of 15 oligodeoxynucleotides or longer is relatively small.

As a result of this problem, there has been considerable recent work to find molecular strategies for increasing selectivity toward such small genetic differences. One of the most common strategies currently used to engender high specificity in sequence detection is the use of DNA-ligation enzymes.[4] Ligases, such as the T4 and Tth enzyme, are quite sensitive to base mismatches at the ligation junction, and selectivity against single mismatches is high, in the order of 10- to 10^2-fold. Although they are quite useful, enzymatic ligation methods for sequence detection also face some limitations. For example, the ligation efficiency on the solid phase is relatively lower than in a solution.[5] In addition, there are the limits in the most suitable conditions, including temperature, pH value, and salt concentration, caused by the use of an enzyme. Indeed, the available range of salt (Mg^{2+}) concentrations for the use of T4 ligase was 10–100 mM, as shown in a separate experiment (see the Supporting Information). DNA ligases also show low activity with RNAs.[6] Finally, ligase-mediated approaches are unlikely to be useful with modified probes that contain non-natural DNA backbones, such as peptide nucleic acids, phosphoramidate DNA, or 2′-*O*-methyl RNA. Even relatively simple modifications, such as conjugation with biotin or fluorescent labels, may be expected to cause difficulties near the ligation junction.

Therefore, as a more useful strategy, the consideration of alternatives to ligase enzymes in the joining of DNA strands seems justified for some applications. A number of nonenzymatic methods that involve the addition of ligating reagents to the DNA have been described.[7] However, even with an autoligation approach, which is considered to be the most useful method for single-mismatch discrimination, the ligation efficiency reached only 80% after 7 hours.[7c] Additional efforts are thus needed to create more broadly applicable methods that would allow accurate, rapid, and selective identification of SNPs. Herein, we describe a novel SNP-typing method which is based on template-directed[8] photochemical ligation of DNA, by using 5-carboxyvinyldeoxyuridine (^{cv}U) as previously reported.[9] The photochemical-ligation approach offers the potential advantages of rapid analysis, sequence selectivity, less-restricted reaction conditions, and high efficiency on RNA targets, thereby rivaling the use of ligase enzymes.[9d] In our method, an unusual salt-concentration-dependent hybridization behavior associated with the probe strand was exploited to achieve selectivity without an annoying requirement for thermal stringency during the photochemical-ligation reaction.

Figure 1A shows a schematic representation of the strategies employed. We chose a strand design that involved the ligation of a 9-mer strand (capture) containing ^{cv}U at the 5′-end and a biotin-tagged 21-mer strand (probe), which can afford very high sequence specificity because of the high mismatch selectivity of the shorter capture strand. The capture and probe strands were complementary to a sequence encompassing amino acid residue 248, called a hot spot, on exon 7 of the human oncogene p53,[10] which has been found to be mutated in more than 50% of known human cancers.

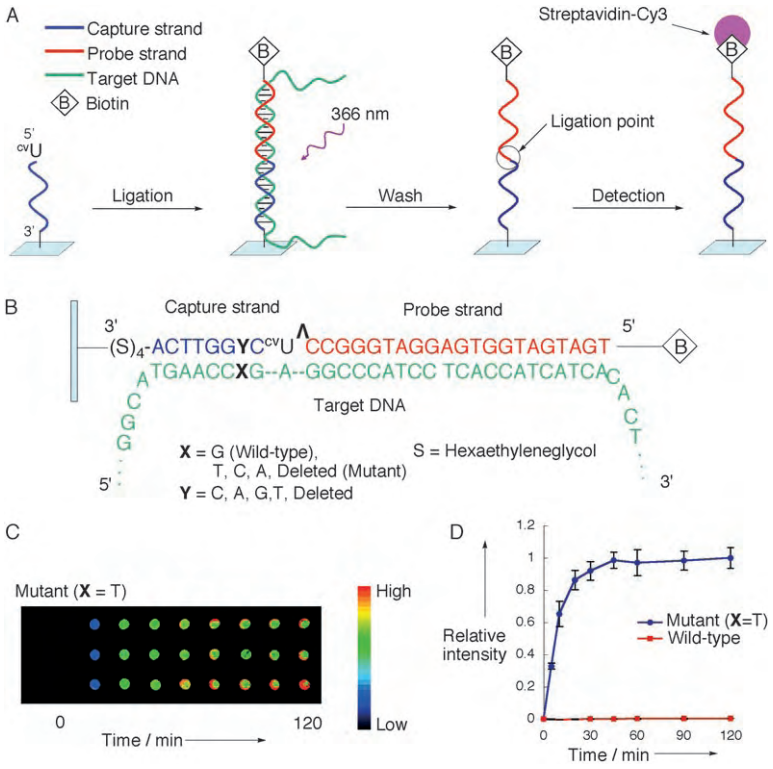


Figure 1. Scheme, sequence, and progress of the photochemical ligation. A) Conceptual scheme showing how the target is detected by photochemical-ligation and hybridization specificity. B) Capture, probe, and target sequences used in this study. C) Fluorescence image for a time course of mutant detection. The capture strands (**Y** = A) were attached to all 27 spots, and three longitudinal spots were irradiated at 366 nm during the same period. D) Differing rates of photochemical ligation of matched and singly mismatched target DNA strands with the mutant-detection capture strand (**Y** = A).

To investigate the difference in the ligation rate between the matched and mismatched sequences on the DNA chip, we prepared two capture strands (mutation and wild type) and target strands with the p53 mutant sequence (Figure 1B). Capture strands were immobilized onto the activated glass surface by spotting with solutions of the appropriate 3′-amino-modified capture strands in sodium cacodylate buffer (see the Experimental Section and Supporting Information). Ligations were carried out on the DNA chip by 366-nm irradiation at room temperature with the 5′-biotin-tagged probe and the target, in a tris(hydroxymethyl)aminomethane–HCl (Tris-HCl) buffer containing Mg^{2+} ions. After the chip was washed twice with phosphate-buffered-saline (PBS) solution and once with ultrapure water at 98 °C for 10 minutes, streptavidin-Cy3 conjugate was added. Surface fluorescence measurements were performed on a CRBIO IIe microscanner array (Hitachi Software Engineering Co.) after washing twice with a PBS solution at room temperature. The results show that the reaction takes place on the target over a period of hours and reaches the 50% stage within 10 minutes (Figure 1C,D). Significantly, a single mismatch in the target sequence yielded very little ligated product, with a measured rate that was 10^3-fold lower than that of the complementary case.

© 2006 Wiley-VCH Verlag GmbH & Co. KGaA, Weinheim

In such a ligation reaction, there are two possible sources of specificity: the ligation reaction itself and the hybridization selectivity between the target and capture strands. We also carried out mutation detection in the conventional way for the same target to verify the potential selectivity of our photochemical ligation for SNP detection. A conventional way of increasing target selectivity is to wash the DNA chip with a buffer solution at an adequate temperature, which results in the dehybridization of DNA duplexes formed from noncomplementary strands. In the mutation detection by the traditional method, which shows only hybridization specificity, the observed selectivity for the matched (mutant) sequence was about 8, even after washing with a stringent solution at the appropriate temperature (Figure 2A). One possible reason for the decrease in selectivity is the loss of DNA duplexes of matched sequences, particularly during the washing step employed to remove noncomplementary strands from the DNA chip. A second possible source of low selectivity is incomplete washing of the mismatched sequences (wild type). By contrast, the fluorescence image after use of the photochemical-ligation method showed no loss of the biotin-tagged probe strand, due to covalent bonding between the capture and probe strands (Figure 2B). Moreover, mismatched duplexes and other components with the potential to harm the fluorescence imaging were eliminated completely by high temperatures (Figure 2C,D). The influence of the washing conditions is summarized in Figure 2E.

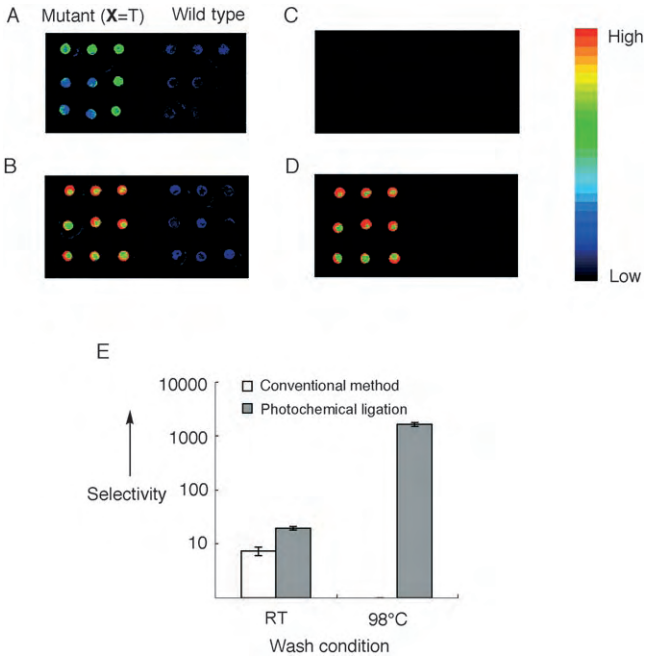


Figure 2. Influence of washing and photochemical ligation on specificity. In all four fluorescence images, the capture strands (**Y** = A) were attached to the surface, and the targets (left: **X** = T, 3×3 spots; right: **X** = G, 3×3 spots) were applied. A) Use of only hybridization specificity and washing with buffer under stringent conditions (room temperature). B) Use of both hybridization specificity and photochemical-ligation specificity and washing with buffer under stringent conditions. C) Use of only hybridization specificity and washing with ultrapure water at 98 °C for 10 min. No signal was observed. D) Use of both hybridization specificity and photochemical-ligation specificity and washing with ultrapure water at 98 °C for 10 min. E) Selectivity for different washing conditions.

Finally, to demonstrate the generality of sequence discrimination, we constructed a set of five closely related targets (all in the p53 context) with a single variable base (A, G, C, T, or deleted (D)), along with 9-mer immobilized capture strands with the same five bases. We then carried out kinetic measurements for all 25 possible combinations of capture and target strands (Table 1). The ligation of each of the 20 possible mismatched sequences is presented as a ratio between the ligation efficiency of each mismatched reaction and that of the corresponding matched one. Most mismatches are discriminated by a factor greater than 10^3-fold, as compared to the corresponding matched sequence (G–A, G–D, G–G, C–T, C–D, C–C, A–C, A–G, A–D, A–A, T–C, D–T, D–C), and almost all of the remaining sequences are discriminated by greater than 10^2-fold (Figure 3).

Table 1: Survey of photochemical-ligation rates for all base-pairing combinations in the context of the p53 system.

Base pair (**X**–**Y**)[a]	Relative intensity[b]	Base pair (**X**–**Y**)[a]	Relative intensity[b]
G–C	1.0 ± 0.18	T–D	0.0029 ± 0.0039
G–T	0.013 ± 0.008	T–T	0.016 ± 0.001
G–A	0[c]	A–T	1.0 ± 0.15
G–D	0[c]	A–C	0[c]
G–G	0[c]	A–G	0[c]
C–G	1.0 ± 0.18	A–D	0[c]
C–T	0[c]	A–A	0[c]
C–A	0.012 ± 0.008	D–D	1.0 ± 0.13
C–D	0.0009 ± 0.0021	D–T	0[c]
C–C	0[c]	D–C	0.0010 ± 0.0089
T–A	1.0 ± 0.16	D–A	0.0031 ± 0.0022
T–C	0.0005 ± 0.0013	D–G	0.0021 ± 0.0051
T–G	0.018 ± 0.014		

[a] D stands for nucleic base **X** or **Y** deleted. [b] Intensity of the mismatched-ligation signal divided by that of the corresponding correctly matched-ligation signal; three data points were used in each case. [c] The average intensity as measured is approximately equal to zero.

In summary, we have developed a new SNP-typing method with high selectivity and sensitivity by introducing a form of photochemical-ligation technology into an existing allele-specific hybridization. Washing of a DNA chip after photoirradiation without thermal stringency and combination of photochemical-ligation specificity with hybridization specificity between the target and capture strands is shown to produce discrimination of point mutations up to 10^3-fold and more. In principle, one might use other types of photosensitive molecules, such as *p*-carbamoylvinyl phenol nucleosides,[11] to catch target molecules directly without the extra probe strand. This new protocol should facilitate the expeditious, reliable, and parallel screening of important SNPs and could be readily scaled up for a high-throughput automated operation.

 © 2006 Wiley-VCH Verlag GmbH & Co. KGaA, Weinheim

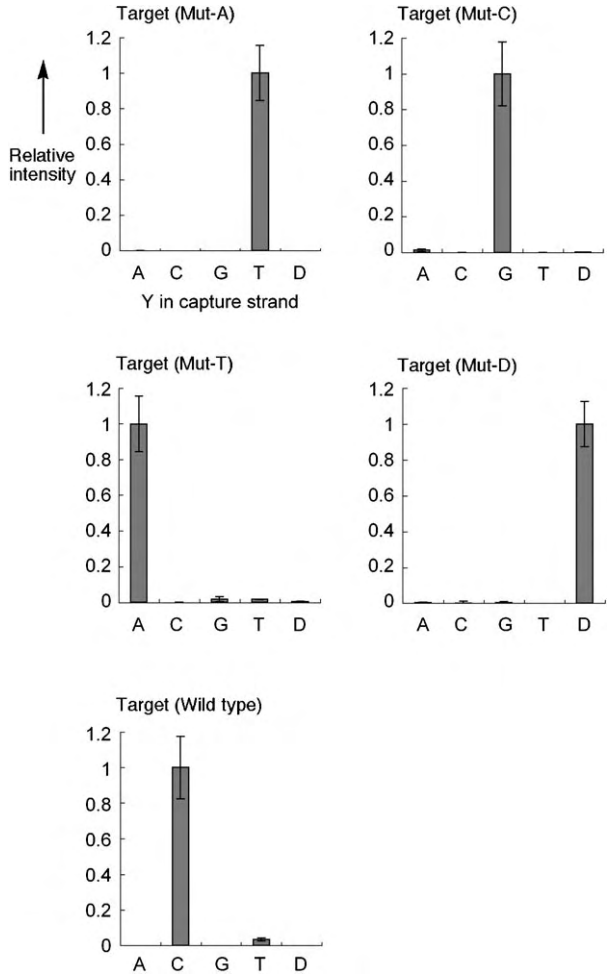


Figure 3. Relative intensity for all 25 possible combinations of capture and target strands. Each experiment was repeated at least three times.

Experimental Section

^{cv}U was synthesized from 5-iodo-2′-deoxyuridine; the method was reported previously.[8] ^{cv}U-containing capture strands were prepared by the β-cyanoethylphosphoramidite method on a 3′-amino-modified C7 CPG 500 resin (purchased from Glen Research) by using an Applied Biosystems 3400 DNA synthesizer and the standard method. After automated synthesis, the oligomers were cleaved and deprotected with concentrated aqueous ammonia at 55 °C for 17 h, and purified by HPLC. The capture strands were characterized by MALDI-TOF MS.

The amino-modified capture strands were diluted to a concentration of 30 μM in 100 mM sodium cacodylate buffer (pH 7.4) and 100 mM NaCl. DNA solution (1 μL) was dispensed onto the aldehyde glass slide (purchased from Nalge Nunc International Co.) and incubated for 12 h in a desiccator. After incubation, the glass slides were washed twice with 0.15% sodium dodecylsulfate (SDS) and twice with ultrapure water and were then incubated for 5 min with blocking solution (10 mg $NaBH_4$ dissolved in PBS (4 mL) and 100% ethanol (1 mL)). After the blocking, the slide was dipped 20 times into ultrapure water and then dried.

The photochemical-ligation reaction was performed by exposure of the surface to 1 nM target (5 attomoles), 1 μM 5′-biotin-labeled probe strand in Tris-HCl buffer (pH 7.6), and 250 mM $MgCl_2$. A 5-μL drop of this solution was placed onto the DNA chip and then spread over the entire surface by placing a clean quartz cover glass on top of the sample, after which the DNA chip was photoirradiated at 366 nm with transilluminator. The photochemical-ligation reaction was allowed to proceed for 60 min at room temperature, after which the surface was rinsed twice with 0.15% SDS and twice with ultrapure water at 98 °C for 10 min.

Received: March 1, 2006
Published online: May 31, 2006

Keywords: biosensors · DNA recognition · ligation reactions · medicinal chemistry · photochemistry

[1] a) A. Marshall, J. Hodgson, *Nat. Biotechnol.* **1998**, *16*, 27–31; b) G. Ramsay, *Nat. Biotechnol.* **1998**, *16*, 40–44.
[2] a) G. C. King, D. A. Giusto, W. A. Wlassoff, S. Giesebrecht, E. Flening, G. D. Tyrelle, *Hum. Mutat.* **2004**, *23*, 420–425; b) J. Wang, G. O. Liu, A. Merkoci, *J. Am. Chem. Soc.* **2003**, *125*, 3214–3215; c) F. Patolsky, E. Katz, I. Willner, *Angew. Chem.* **2002**, *114*, 3548–3552; *Angew. Chem. Int. Ed.* **2002**, *41*, 3398–3402; d) J. Park, T. A. Taton, C. A. Mirkin, *Science* **2002**, *295*, 1503–1505; e) E. M. Boon, D. M. Ceres, T. G. Drummond, M. G. Hill, J. K. Barton, *Nat. Biotechnol.* **2000**, *18*, 1096–1100.
[3] a) H. Matsuzaki, S. Dong, H. Loi, X. Di, G. Liu, E. Hubbell, J. Law, T. Berntsen, M. Chadha, H. Hui, G. Yang, G. Kennedy, T. A. Webster, S. Cawley, P. S. Walsh, K. W. Jones, S. P. A. Fodor, R. Mei, *Nat. Methods* **2004**, *1*, 109–111; b) D. A. Hinds, L. L. Sture, G. B. Nilson, E. Halperin, E. Eskin, D. G. Ballinger, K. A. Frazer, D. R. Cox, *Science* **2005**, *307*, 1072–1079; c) C. Y. Zhang, H. C. Yen, M. T. Kuroki, T. H. Wang, *Nat. Mater.* **2005**, *4*, 826–831.
[4] a) H. Baron, S. Fung, A. Aydin, S. Bahring, F. C. Luft, H. Schuster, *Nat. Biotechnol.* **1996**, *14*, 1279–1282; b) N. P. Gerry, N. E. Witowski, J. P. Day, R. P. Hammer, G. Barany, F. Barany, *J. Mol. Biol.* **1999**, *292*, 251–262; c) R. Favis, J. P. Day, N. P. Gerry, C. Phelan, S. Narod, F. Barany, *Nat. Biotechnol.* **2000**, *18*, 561–564.
[5] A. G. Frutos, L. M. Smith, R. M. Corn, *J. Am. Chem. Soc.* **1998**, *120*, 10277–10282.
[6] M. Nilson, G. Barbany, D. Antson, K. Gerton, U. Landegren, *Nat. Biotechnol.* **2000**, *18*, 791–793.
[7] a) Z. Y. Zhan, D. G. Lynn, *J. Am. Chem. Soc.* **1997**, *119*, 12420–12421; b) P. Lou, J. C. Leitzel, Z. Y. Zhan, D. G. Lynn, *J. Am. Chem. Soc.* **1998**, *120*, 3019–3031; c) S. Sando, E. T. Kool, *J. Am. Chem. Soc.* **2002**, *124*, 2096–2097.
[8] a) M. M. Rozeman, D. R. Liu, *ChemBioChem* **2006**, *7*, 253–256; b) X. Li, D. R. Liu, *Angew. Chem.* **2004**, *116*, 4956–4979; *Angew. Chem. Int. Ed.* **2004**, *43*, 4848–4870.
[9] a) K. Fujimoto, S. Matsuda, N. Takahashi, I. Saito, *J. Am. Chem. Soc.* **2000**, *122*, 5646–5647; b) S. Ogasawara, K. Fujimoto, *ChemBioChem* **2005**, *6*, 1756–1760; c) M. Ogino, Y. Yoshimura, A. Nakazawa, I. Saito, K. Fujimoto, *Org. Lett.* **2005**, *7*, 2853–2856; d) Y. Yoshimura, Y. Noguchi, H. Sato, K. Fujimoto, *Nucleic Acid Symp. Ser.* **2005**, *49*, 143–144.
[10] P. Hainaut, T. Hernandez, A. Robinson, P. Rodriguez-Tome, T. Flores, M. Hollstein, C. C. Harris, R. Montesano, *Nucleic Acids Res.* **1998**, *26*, 205–213.
[11] Y. Yoshimura, Y. Ito, K. Fujimoto, *Bioorg. Med. Chem. Lett.* **2005**, *15*, 1295–1298.

 © 2006 Wiley-VCH Verlag GmbH & Co. KGaA, Weinheim

Electron Transport

DOI: 10.1002/anie.200600596

Low-Field Negative-Resistance Effect in a Charge-Ordered State of Thiazyl-Radical Crystals**

Kentaro Okamoto, Toshiyuki Tanaka, Wataru Fujita, Kunio Awaga, and Tamotsu Inabe*

Nonlinear electrical transport in inorganic semiconductors has been utilized in various electric devices such as sensors, switches, diodes, and thyristors.[1] Recent developments in organic electric devices strongly indicate the importance of materials research for non-ohmic electrical behavior in organic compounds.[2] In fact, current–voltage characteristics of organic materials have been studied extensively, and nonlinear electrical transport phenomena, such as a switching effect with a so-called negative-(differential)-resistance effect, have been already discovered as a characteristic feature of organic semiconductors.[3–7] However, these effects were found to occur at low temperature in a high electric field, in an insulating state caused by charge ordering, neutral–ionic transition, and on-site Coulomb repulsion (Mott–Hubbard insulator). Thus, it is very important to develop organic materials that exhibit this nonlinear behavior under mild conditions.

Heterocyclic thiazyl radicals have unique chemical and physical properties.[8–15] Their molecular skeletons exhibit large electronic polarization, which leaves a positive charge on the sulfur atom and a negative charge on the nitrogen atom. Thiazyl-radical solids always involve a multidimensional network consisting of face-to-face π–π overlaps and side-by-side S···N contacts. Herein, we describe the crystal structure and the nonlinear electrical transport of the 3:1 salt of a thiazyl radical, naphtho[2,1-*d*:6,5-*d*′]bis([1,2,3]dithiazole), abbreviated as NT (Figure 1 a).

Single crystals of $[NT]_3[GaCl_4]$ were obtained by an electrochemical method. X-ray crystal analysis was carried out at 173 K.[16] The crystal structure includes two crystallographically independent 2D layers of NT molecules, layers **A** and **B** (Figure 1 b), though their structures are nearly the same. Each layer consists of a 2D square network of NT molecules with short intermolecular S···N contacts, in which the molecular planes of the NT molecules are parallel to the layer. The short S···N contacts reflect a large electric polarization of the NT molecular skeleton. Layer **A** includes the NT molecules **1** and **2**, and layer **B** includes the molecules **3** and **4**. Figure 1 c depicts a side view of the layered structure and shows the **BABBAB** stacking with large π–π overlaps. Four NT molecules of slightly different structure are included in the 3D network. The $GaCl_4^-$ counterion (not shown in Figure 1 b) is located in a cavity surrounded by four stacking columns of NT molecules.

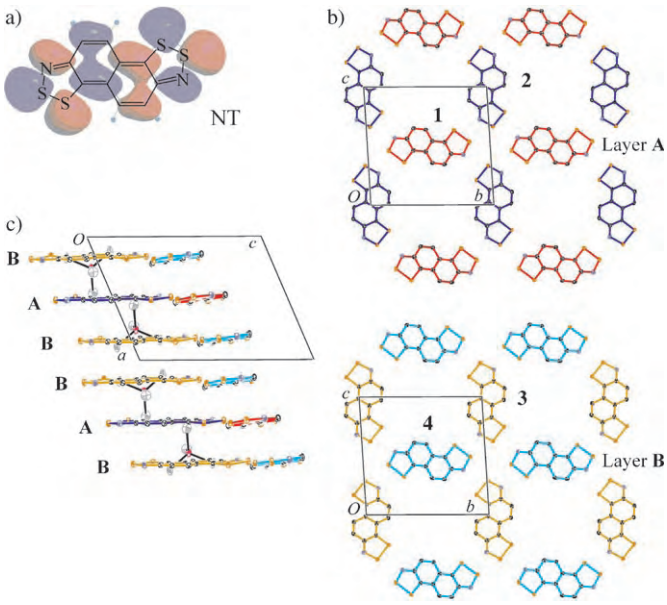


Figure 1. a) The HOMO of NT. b) Layers **A** and **B**, which consist of 2D square networks of NT molecules **1**–**4**, in the crystal structure of $[NT]_3[GaCl_4]$. c) Side view of the layered structure, showing the location of the $GaCl_4^-$ counterions. The colors of the NT molecules express their charges (see Figure 2 for color key).

It is well known that the S–N bond length is a good indicator of the charge on the thiazyl and thiazole compounds; removal of an electron from the highest occupied molecular orbital (HOMO) results in a shortening of the bond length, because the HOMO has antibonding character of the S–N bond (Figure 1 a). Figure 2 depicts the relation between the average S–N bond length l_{SN} and the charge ρ on NT for the neutral NT molecule,[17] the NT^+ cation in [NT]Cl,[18] and the cation in [NT][TCNQ], which is in a mixed valence state (TCNQ is 7,7,8,8-tetracyanoquinodimethane).[18] For [NT][TCNQ], l_{SN} is 1.626 Å and ρ can be estimated to be 0.60 from the C–N stretching frequency (2199 cm^{-1}).[19] Figure 2 indicates an empirical linear relation between l_{SN} and ρ (gray line) that is similar to that of the thiazyl compound, 1,3,2-benzodithiazolyl (BDTA).[20] In the crystal structure of $[NT]_3[GaCl_4]$, the average S–N bond lengths of the NT molecules are as follows: **1** 1.617, **2** 1.645, **3** 1.626, **4** 1.643 Å. The standard deviations for these lengths are all less than 0.004 Å. By fitting the empirical relation to these interatomic distances, the values of ρ were roughly estimated to be: **1** 0.8, **2** 0, **3** 0.5, **4** 0.1. The colors of the NT molecules in Figure 1 were taken from the color bar in Figure 2.

[*] K. Okamoto, T. Tanaka, Dr. W. Fujita, Prof. K. Awaga
Research Center for Materials Science & Department of Chemistry
Nagoya University
Furo-cho, Chikusa-ku, Nagoya 464-8602 (Japan)
Fax: (+81) 52-789-2484
E-mail: awaga@mbox.chem.nagoya-u.ac.jp
Prof. T. Inabe
Division of Chemistry
Faculty of Science
Hokkaido University
Kita-ku, Sapporo 060-0810 (Japan)

[**] This work was supported by a Grant-in-Aid for Scientific Research from the Ministry of Education, Culture, Sports, Science and Technology (MEXT).

InterScience
© 2006 Wiley-VCH Verlag GmbH & Co. KGaA, Weinheim

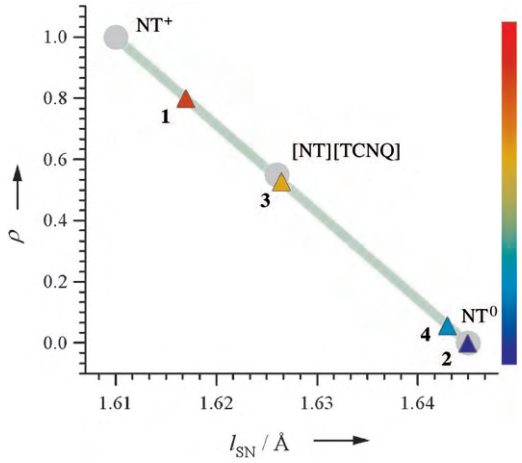


Figure 2. Correlation between the charge ρ and the S–N bond length l_{SN} in NT compounds; the gray line expresses the empirical linear relation between them; l_{SN} = 1.645 Å for NT^0 [17] and 1.610 Å for NT^+.[18] The right side bar is a color key for the charge on NT.

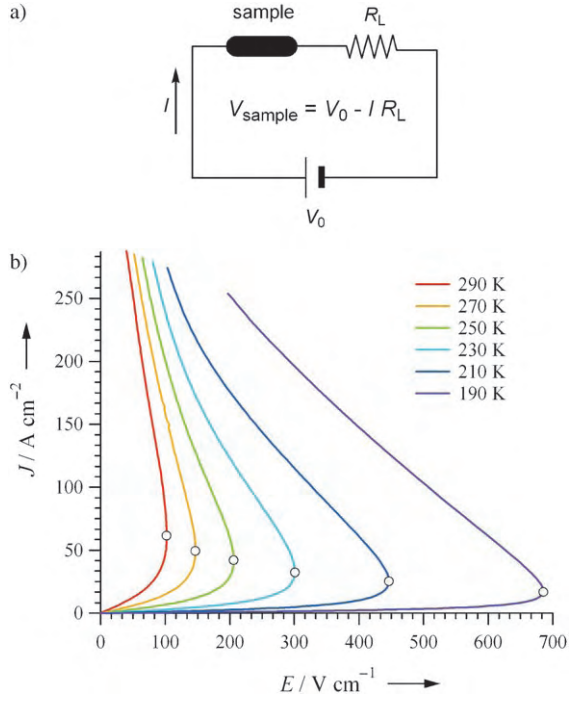


Figure 3. a) Electric circuit used to measure the current–voltage characteristics of samples. b) Plot of J versus E for a crystal of $[NT]_3[GaCl_4]$ at various temperatures, measured with a pulse field (25-ms width and 300-ms interval). The open circles show the turning points for the negative-resistance effect.

Since the unit cell includes one each of NT molecules **1** and **2**, and two each of **3** and **4**, the average charge on NT is calculated as: $[0.8+0+(2\times0.5)+(2\times0.1)]/6=0.33$. This value, which is estimated from the molecular structures, is in good agreement with the chemical formula $[NT]_3[GaCl_4]$ with $\rho=0.33$ and thus justifies the analysis presented in Figure 2. From this analysis, we conclude that the present crystal includes a significant charge disproportionation; molecules **1** and **3** are charge-rich (R), while **2** and **4** are charge-poor (P). Figure 1 depicts the alternation of charges in the 3D crystal structure; the charge-rich and charge-poor molecules alternate according to the pattern RRPRRP or PPRPPR along the a axis (π-stacking direction) and occupy the warp and weft positions in the 2D square network parallel to the bc plane such that the combination of P–P or R–R is ruled out. This 3D charge alternation is gaining much attention as a characteristic insulating state induced by intermolecular Coulomb repulsions in strongly correlated systems.[21,22]

Electrical transport measurements were carried out by using a conventional two-terminal method on samples with typical dimensions of length $l=1$ mm (along the a axis) and area $S=0.1\,mm^2$ in cross section. Variable-temperature conductivity measurements revealed semiconductivity with a room-temperature conductivity of $\sigma_{RT}=0.5\,S\,cm^{-1}$ and a band gap of $\Delta E=0.18$ eV, despite the material being in a mixed-valence state and having a 3D network structure. This result could be ascribed to the charge ordering shown in Figure 1.

The current–voltage (I–V_0) characteristics were measured along the a axis by using an electric circuit in series with a load resistor R_L of 20 ko (Figure 3a), which was connected in series to the sample to prevent a sudden burst of current. Since sample heating is generally a problem for these I–V_0 measurements, we used a pulse current/voltage source with a pulse width of 25 ms and a pulse interval of 300 ms. We confirmed that the data are independent of R_L, the pulse width, and the pulse interval. Figure 3b depicts the current density J in the crystal as related to the applied electric field E, which were obtained from the equations $J=I/S$ and $E=(V_0-IR_L)/l$. At room temperature (290 K), the J–E curve exhibits a steep nonlinear rise and clearly indicates a negative-differential-resistance effect after passing through the turning point indicated by an open circle (Figure 3). This nonlinearity is caused by a partial melting of the charge ordering because, if there is no charge ordering, the material should have a five-sixths-filled band that brings about metallic conduction. The threshold values for the electric field E_T and the current density J_T are $100\,V\,cm^{-1}$ and $60\,A\,cm^{-2}$, respectively. It is very rare that this type of negative-resistance effect is observed at room temperature in organic materials. In addition, the E_T value obtained for $[NT]_3[GaCl_4]$ is much lower than those of the other organic materials that show nonlinear conductivity.[3–7] Lowering the temperature from 290 K, the values of E_T and J_T exhibit a significant increase and decrease, respectively, making the negative-resistance effect more drastic.

We have revealed a negative-resistance effect in $[NT]_3[GaCl_4]$, which includes the charge ordering on the 3D network of the NT molecules. Surprisingly, this effect occurs under a very low electric field at room temperature. In a recent report, this type of nonlinear transport in a charge-ordered state had thyristor properties (conversion from direct current to alternating current), though this behavior was found only at liquid-helium temperatures.[23] Our results may be applicable to organic electric devices such as switching units, information storage media, and thyristors, in which room-temperature, low-field performance is extremely advantageous.

 © 2006 Wiley-VCH Verlag GmbH & Co. KGaA, Weinheim

Experimental Section

The parent compound NT was prepared according to a previously reported method.[17] Single crystals of $[NT]_3[GaCl_4]$ were obtained by electrochemical oxidation of NT (20 mg), with the electrolyte $[(n\text{-}C_4H_9)_4N][GaCl_4]$ (50 mg) in a 1:1 mixture of 1,2-dichloroethane and CS_2 at a constant current of 1 μA. Green needles were grown on the anodic electrode within 3–5 days.

Received: February 15, 2006
Revised: March 30, 2006
Published online: June 7, 2006

Keywords: electron transport · negative resistance · radicals · semiconductors

[1] S. M. Sze, *Semiconductor Devices: Physics and Technology*, Wiley, New York, **2002**.
[2] T. W. Kelley, P. F. Baude, C. Gerlach, D. E. Ender, D. Muyres, M. A. Haase, D. E. Vogel, S. D. Theiss, *Chem. Mater.* **2004**, *16*, 4413, and references therein.
[3] a) P. S. Potember, T. O. Poehler, D. O. Cowan, *Appl. Phys. Lett.* **1979**, *34*, 405; b) P. S. Potember, T. O. Poehler, R. C. Benson, *Appl. Phys. Lett.* **1982**, *41*, 548.
[4] Y. Tokura, H. Okamoto, T. Koda, T. Mitani, G. Saito, *Phys. Rev. B* **1988**, *38*, 2215.
[5] a) Y. Iwasa, T. Koda, Y. Tokura, S. Koshihara, N. Iwasawa, G. Saito, *Appl. Phys. Lett.* **1989**, *55*, 2111; b) Y. Iwasa, T. Koda, Y. Tokura, S. Koshihara, N. Iwasawa, G. Saito, *Phys. Rev. B* **1989**, *39*, 10441.
[6] R. Kumai, Y. Y. Okimoto, Y. Tokura, *Science* **1999**, *284*, 1645.
[7] M. M. Matsushita, T. Sugawara, *J. Am. Chem. Soc.* **2005**, *127*, 12450.
[8] R. T. Oakley, *Prog. Inorg. Chem.* **1988**, *36*, 299.
[9] a) J. M. Rawson, A. J. Banister, I. Lavender, *Adv. Heterocycl. Chem.* **1995**, *62*, 137; b) J. M. Rawson, G. D. McManus, *Coord. Chem. Rev.* **1999**, *189*, 135; c) J. M. Rawson, F. Palacio, *Struct. Bonding (Berlin)* **2001**, *100*, 94.
[10] K. Awaga, T. Tanaka, T. Shirai, M. Fujimori, Y. Suzuki, H. Yoshikawa, W. Fujita, *Bull. Chem. Soc. Jpn.* **2006**, *79*, 25.
[11] C. D. Bryan, A. W. Cordes, R. M. Fleming, N. A. George, S. H. Glarum, R. C. Haddon, R. T. Oakley, T. T. M. Palstra, A. S. Perel, L. F. Schneemeyer, J. V. Waszczak, *Nature* **1993**, *365*, 821.
[12] F. Palacio, G. Antorrena, M. Castro, R. Burriel, J. Rawson, J. N. B. Smith, N. Bricklebank, J. Novoa, C. Ritter, *Phys. Rev. Lett.* **1997**, *79*, 2336.
[13] a) W. Fujita, K. Awaga, *Science* **1999**, *286*, 261; b) W. Fujita, K. Awaga, H. Matsuzaki, H. Okamoto, *Phys. Rev. B* **2002**, *65*, 064434.
[14] J. L. Brusso, O. P. Clements, R. C. Haddon, M. E. Itkis, A. A. Leitch, R. T. Oakley, R. W. Reed, J. F. Richardson, *J. Am. Chem. Soc.* **2004**, *126*, 8256; J. L. Brusso, O. P. Clements, R. C. Haddon, M. E. Itkis, A. A. Leitch, R. T. Oakley, R. W. Reed, J. F. Richardson, *J. Am. Chem. Soc.* **2004**, *126*, 14692.
[15] S. S. Staniland, W. Fujita, Y. Umezono, K. Awaga, S. J. Clark, H. B. Cui, H. Kobayashi, N. Robertson, *Chem. Commun.* **2005**, 3204.
[16] X-ray diffraction data were collected with graphite-monochromated $Mo_{K\alpha}$ radiation ($\lambda = 0.71073$ Å) on a Rigaku Mercury CCD diffractometer. The absorption correction was applied by integration based on the crystal shape. The structures were solved by direct methods (SHELXS-97). A full-matrix least-squares method on F^2 with anisotropic thermal parameters was employed for the structural refinements (SHELXL-97). Hydrogen atoms were found by difference Fourier syntheses and were refined. Crystal data for $[NT]_3[GaCl_4]$: $C_{30}H_{12}Cl_4GaN_6S_{12}$ ($M_r = 1052.70$), green needle, $1.0 \times 0.3 \times 0.3$ mm^3, *triclinic*, $P\bar{1}$, $a = 10.870(3)$, $b = 13.591(4)$, $c = 13.823(4)$ Å, $\alpha = 88.382(13)$, $\beta = 67.244(7)$, $\gamma = 78.073(12)°$, $V = 1839.5(9)$ Å^3, $Z = 2$, $\rho_{calcd} = 1.901$ g cm^{-1}, $T = 173$ K, $2\theta_{max} = 54.92°$, $F(000) = 1050$, reflections collected/unique 14980/8057 ($R_{int} = 0.0518$), parameters 478, final $R1 = 0.0551$ ($I > 2\sigma(I)$), $wR2 = 0.1311$ (all data), $S = 1.038$ (all data). CCDC-297988 contains the supplementary crystallographic data for this paper. These data can be obtained free of charge from The Cambridge Crystallographic Data Centre via www.ccdc.cam.ac.uk/data_request/cif.
[17] T. M. Barclay, I. J. Burgess, A. W. Cordes, R. T. Oakley, R. W. Reed, *Chem. Commun.* **1998**, 1939.
[18] K. Okamoto, T. Takana, W. Fujita, K. Awaga, unpublished work. CCDC-297989 ([NT]Cl) and CCDC-297990 ([NT][TCNQ]) contain the supplementary crystallographic data for this paper.
[19] J. S. Chappel, A. N. Bloch, W. A. Bryden, M. Maxfield, T. O. Poehler, D. O. Cowan, *J. Am. Chem. Soc.* **1981**, *103*, 2442.
[20] Y. Umezono, W. Fujita, K. Awaga, *J. Am. Chem. Soc.* **2006**, *128*, 1084.
[21] H. Seo, *J. Phys. Soc. Jpn.* **2000**, *69*, 805.
[22] H. Seo, C. Hotta, H. Fukuyama, *Chem. Rev.* **2004**, *104*, 5005.
[23] F. Sawano, I. Terasaki, H. Mori, T. Mori, M. Watanabe, N. Ikeda, Y. Nogami, Y. Noda, *Nature* **2005**, *437*, 522.

 © 2006 Wiley-VCH Verlag GmbH & Co. KGaA, Weinheim

Directed Evolution

DOI: 10.1002/anie.200600088

Evolving Proteins of Novel Composition**

*Jin Kim Montclare and David A. Tirrell**

The behavior of proteins can be altered significantly by the incorporation of noncanonical amino acids.[1–3] Changes in spectroscopic properties,[4] thermal stability,[5,6] and molecular recognition behavior[7,8] have been reported. In many cases,

[*] Prof. D. A. Tirrell
Division of Chemistry and Chemical Engineering
California Institute of Technology
1200 E. California Blvd.
Pasadena, CA 91125 (USA)
Fax: (+1) 626-793-8472
E-mail: tirrell@caltech.edu
J. K. Montclare
Department of Chemical and Biological Sciences
Polytechnic University
6 Metrotech Center
Brooklyn, NY 11201
and
Department of Biochemistry
SUNY Downstate Medical Center
450 Clarkson Street
Brooklyn, NY 11203 (USA)

[**] We thank Frances Arnold for use of several instruments. This work was supported by NIH GM 62523 and 5F32 GM67375-2 (D.A.T. and J.K.M.) and by the Beckman Institute of the California Institute of Technology (D.A.T.).

Supporting information for this article is available on the WWW under http://www.angewandte.org or from the author.

InterScience
© 2006 Wiley-VCH Verlag GmbH & Co. KGaA, Weinheim

however, introduction of novel amino acids causes loss of protein function.[9,10] Herein we describe a new approach to protein engineering in which amino acid replacement is combined with directed evolution to create functional proteins of novel composition. Global replacement of the leucine residues of chloramphenicol acetyltransferase (CAT) by 5′,5′,5′-trifluoroleucine (TFL) results in a 20-fold reduction in the half-life ($t_{1/2}$) of thermal inactivation of the enzyme at 60 °C. Two rounds of random mutagenesis and screening yielded a variant of CAT containing three amino acid substitutions, which in fluorinated form demonstrates a 27-fold improvement in $t_{1/2}$, recovering the loss in thermostability caused by fluorination.

CAT confers chloramphenicol resistance in bacteria by catalyzing acetyl-group transfer from acetyl coenzyme A to the hydroxy groups of the antibiotic. Because CAT is expressed readily in bacterial cells and can be assayed easily for activity and thermostability,[11,12] it provides a convenient test system for evaluation of the capacity of directed evolution to restore the loss of function that can accompany global amino acid replacement in recombinant proteins. The enzyme functions as a homotrimer in which each polypeptide chain consists of 219 amino acids, including 13 leucine residues.[11] We have shown previously that TFL serves as an effective leucine surrogate with respect to bacterial protein synthesis.[6,13] In the experiments described herein, CAT is expressed in media depleted of leucine and supplemented with 500 μM TFL. The extent of leucine replacement is 76 ± 4 %, as shown by amino acid analysis and MALDI-TOF MS.

Two parameters are used commonly to describe the thermostability of an enzyme: the half-life ($t_{1/2}$), which shows loss of activity at elevated temperature (in these experiments, 60 °C), and the temperature (T_{50}) at which half of the initial activity is lost after 30 min.[14,15] Global replacement of leucine by TFL yields a fluorinated CAT (CAT T) for which $t_{1/2} = 5$ min and $T_{50} = 57$ °C (Figures 1 a and 2 and Table 1). The corresponding values for wild-type CAT (CAT L) are 101 min and 66 °C.

A library of CAT variants was created through error-prone PCR under conditions that yielded an average of 1–2 amino acid substitutions per gene, and transformed into the leucine auxotrophic LAM 1000 strain of *E. coli*. In the first round, lysates from 1848 colonies were screened for retention of activity after incubation at 60 °C for 1 h. Rescreening the 25 most active clones led to the identification of one variant, L1-C10 T, that exhibited a fourfold increase in $t_{1/2}$ and a value of T_{50} that was 3 °C higher than that of CAT T (Figures 1 a and 2 and Table 1). This variant was used as the parent for a second round of random mutagenesis and screening. For this round, lysates from 1760 colonies were screened for retention of activity after heating to 60 °C for 1 h. The 12 best clones were rescreened and yielded one variant, L2-A1 T, which was characterized by values of $t_{1/2}$ and T_{50} equal or superior to those of wild-type CAT L (Figures 1 a and 2, Table 1, and the Supporting Information). Two rounds of mutagenesis and screening thus yielded a

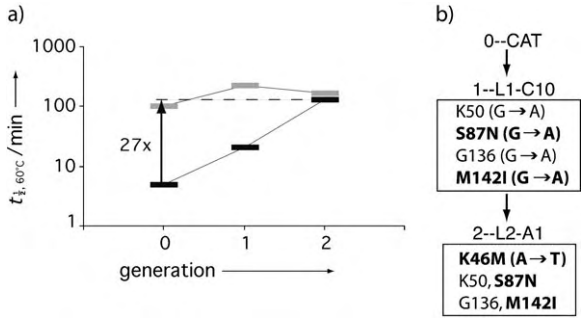


Figure 1. Thermostability landscape and identity of CAT and CAT variants. a) Evolutionary progression of thermostability of CAT and CAT variants expressed in media supplemented either with leucine (gray) or with TFL (black). Plot of the half-life for inactivation at 60 °C versus generation. The enzyme expressed in TFL-supplemented medium was screened for thermostability. b) Lineage and mutations in evolved CAT variants. Nucleotide mutations are shown in parentheses. Mutations that result in changes in protein sequence are shown in bold type. $t_{1/2,60°C}$ = half-life at 60 °C

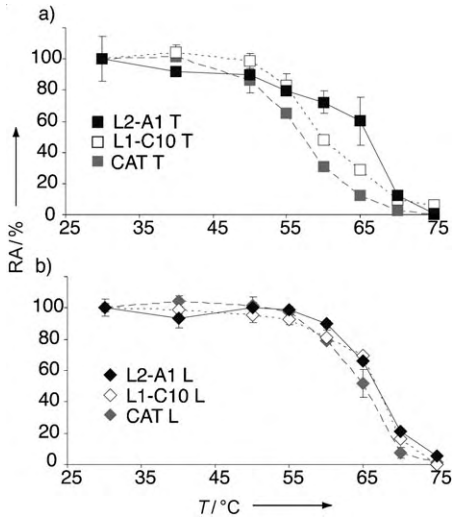


Figure 2. Residual activity versus temperature profiles. a) Residual activity versus temperature profiles of CAT T, L1-C10 T, and L2-A1 T. b) Residual activity versus temperature profiles of wild-type CAT L, L1-C10 L and L2-A1 L. All data represent an average of three trials in which error bars represent the standard deviation. Residual activity corresponds to the ratio of the activity after incubation for 30 min at the designated temperature divided by the initial activity at 30 °C. RA = residual activity.

Table 1: Kinetic parameters and thermostability of CAT variants.

Proteins	K_m [μM]		k_{cat}/K_m [10^4 μM^{-1} min^{-1}]		T_{50} [°C]		$t_{1/2}$ [min]			
	L	T	L	T	L	T	L[a]	T[a]	L[b]	T[b]
CAT	16.6 ± 3.0	19.9 ± 1.5	14.4 ± 2.7	8.4 ± 1.3	65.8	57	101	5	3	–
L1-C10	15.7 ± 2.4	11.3 ± 2.4	13.4 ± 2.2	7.7 ± 1.5	67	60	229	21	–	–
L2-A1	17.1 ± 2.4	10.0 ± 2.0	12.4 ± 1.9	12.0 ± 2.5	67	66.1	171	133	–	4

Kinetic parameters are the averages obtained in three experiments (± standard deviation). Values of $t_{1/2}$ and T_{50} are also averages from three experiments (standard deviation < 5 %). L represents enzyme expressed in leucine; T represents enzyme expressed in 5′,5′,5′-trifluoroleucine. [a] Half-life at 60 °C. [b] Half-life at 70 °C.

© 2006 Wiley-VCH Verlag GmbH & Co. KGaA, Weinheim

27-fold increase in $t_{1/2}$ and an increase of 9 °C in T_{50}. In contrast, little change in thermal stability was observed for CAT variants expressed in media supplemented with leucine.

The increase in thermostability observed in these experiments is accompanied by a modest increase in the specific activity of the fluorinated enzyme (Table 1). The first-generation variant, L1-C10 T, displayed no significant change in activity relative to CAT T; however, the specific activity of L2-A1 T was twice that of the fluorinated parent. For the enzymes expressed in leucine-supplemented media, the specific activity remained essentially unchanged (Table 1). This result was to be expected given that screening was conducted only on the fluorinated variants. The evolved variant L2-A1 T and wild-type CAT L were equally active under ambient conditions.

Mutations that improved the thermostability of CAT T were identified by DNA sequencing (Figure 1b). Among six nucleotide changes, three nonsynonymous mutations resulted in the amino acid substitutions K46M, S87N, and M142I (see the Supporting Information), and a non-sense mutation truncated the evolved polypeptide chain by one residue. None of the mutations were located in conserved positions of the enzyme as determined from sequence alignment. Of the three amino acid substitutions, only one (M142I) was reported in a homologous CAT protein (see the Supporting Information). Neither of the other two amino acid substitutions were identified in known CAT sequences, but both are considered conservative mutations.[16] Most significant, perhaps, was the fact that no leucine residues were eliminated from the protein.

A structural model of *E. coli* CAT I complexed with chloramphenicol revealed the sites of the mutations identified by directed evolution (Figure 3 and the Supporting Information).[17] Each of the mutations is located more than 15 Å from the chloramphenicol binding site, and none make direct contact with any of the TFL/leucine residues of the enzyme.

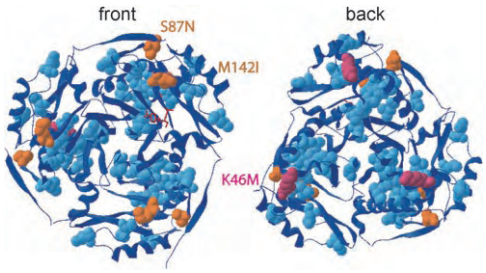


Figure 3. Structural model of the CAT trimer showing the three stabilizing mutations in L2-A1. Two of the mutations (S87N and M142I) from generation one are depicted in orange; the third mutation (K46M) from generation two is represented in pink. Residues highlighted in blue are the leucine/TFL residues of CAT; the chloramphenicol substrate is highlighted in red.

The work reported herein shows conclusively that it is possible to evolve functional proteins of novel composition. Although it is likely that incorporation of multiple copies of noncanonical amino acids into recombinant proteins will compromise function in many cases, directed evolution provides an effective means for adapting protein sequences to the inclusion of novel side chains and novel intramolecular interactions. We are exploring the limits of this approach to the engineering of proteins of novel composition, structure, and function. These results may also advance the more ambitious goal of evolving organisms with novel genetic codes.[18–20]

Experimental Section

Random mutagenesis: CAT libraries were created through error-prone PCR by using the GeneMorph Kit (Stratagene, La Jolla, CA) according to the manufacturer's protocols. The first-generation library was prepared by using template plasmid pCCCAT ($\approx$ 40 μg) and primers H1 (*Hind*III site in bold): 5′-cgt tct acc **aag ctt** cgc ccc gcc ctg cca ctc atc-3' and B1 (*Bam*HI site in bold): 5′-cgt tct acg c**gg atc c**at gga gaa aaa aat cac tgg ata tac cac c-3′. For the second-generation library, template plasmid (800 μg), and primers H2 (*Hind*III site in bold): 5′-gga gtc caa gct cag ctc tta **aag ctt** c-3′ and B2 (*Bam*HI site in bold): 5′-gca tca cca tca cca tca c**gg atc** cat g-3′ were employed. The library inserts and pCC vector (see the Supporting Information) were sequentially digested with *Hind*III and *Bam*HI, and ligated by using a insert/vector (3:1) ligation mixture for maximal ligation efficiency. The library was transformed into XL1 blue cells and grown in of 2XYT (100 mL) containing ampicillin (200 μg mL^{-1}). The amplified DNA was purified and transformed into leucine auxotrophic *E. coli* strain LAM1000 bearing the pREP4 plasmid, which carries the *lacI*^{q} gene for *lac* repressor.

Preparation of cell lysates for screening: Colonies of LAM1000/pCCCAT or pCCCAT mutants/pREP4 were transferred to a 96-deep-well plate containing M9 medium (200 μL) supplemented with glucose (0.2 %), thiamine (3.5 μg mL^{-1}), $MgSO_4$ (1 mM), $CaCl_2$ (0.1 mM), 20 amino acids (40 μg mL^{-1} of each amino acid), and antibiotics (ampicillin (200 μg mL^{-1}), kanamycin (35 μg mL^{-1})), and grown for 12 h at 30 °C at 80 % humidity at 250 rpm. The resulting starter culture plate was then used to inoculate a new 96-deep-well plate containing minimal M9 medium (400 μL, supplemented as above) and cells were grown for 12 h at 30 °C. The cells were washed twice with NaCl (0.9 %) solution prior to induction and resuspended in M9 medium supplemented with glucose (0.2 %), thiamine (3.5 μg mL^{-1}), $MgSO_4$ (1 mM), $CaCl_2$ (0.1 mM), 19 amino acids (40 μg mL^{-1} of each amino acid) plus TFL (500 μM), antibiotics (ampicillin (200 μg mL^{-1}), kanamycin (35 μg mL^{-1})), and isopropyl-β-D-galatopyranoside (IPTG; 1.0 mM), and induced for 6 h at 30 °C. Cells were harvested by centrifugation, stored at −80 °C, thawed at 37 °C in tris(hydroxymethyl)aminomethane (Tris)-Cl buffer solution (50 mM; pH 7.8) containing lysozyme (1.0 mg mL^{-1}; Sigma) and lysed by resuspension. The lysed cells were harvested by centrifugation and aliquots of the supernatant were used for analysis.

Thermostability screening: Lysed cells in 96-deep-well plates were heated in a water-bath set at 60 °C for 1 h for uniform heating. The lysates were clarified by centrifugation and aliquots (100 μL) were used for analysis. The activity of the lysates after heating was measured at room temperature as described in the Supporting Information.

Enzyme characterization: CAT and CAT variants grown in 20 amino acids and 19 amino acids plus TFL were expressed and characterized as described in the Supporting Information. The cell pellets were resuspended in Tris-Cl buffer solution (50 mM; pH 7.8) and lysozyme (0.5 mg mL^{-1}) on ice and lysed by sonication. Whole-cell lysates were clarified and subjected to purification by immobilized-metal affinity chromatography on Ni–nitrilotriacetic acid (NTA) columns according to the manufacturer's protocol (Qiagen). After loading, the column was washed with wash buffer 1A (Tris-Cl (50 mM; pH 7.8), imidazole (15 mM), glycerol (20 %), ethanol (5 %)), wash buffer 1B (Tris-Cl (50 mM; pH 7.8), imidazole (30 mM), glycerol

 © 2006 Wiley-VCH Verlag GmbH & Co. KGaA, Weinheim

(20%), ethanol (5%)), and wash buffer 2 (Tris-Cl (50 mM; pH 7.8), imidazole (35 mM), glycerol (20%)). Purified protein was eluted with elution buffer 1 (Tris-Cl (50 mM; pH 7.8), imidazole (125 mM)) and elution buffer 2 (Tris-Cl (50 mM; pH 7.8), imidazole (250 mM)). The purity of each protein sample was monitored by PAGE analysis and verified by MALDI-TOF MS and amino acid analysis.

Determination of $t_{1/2}$ and T_{50}: Residual activity (RA) at various temperatures was calculated as the ratio of activity after heating divided by the initial activity measured at 30°C. Plots of RA versus temperature were used to calculate the temperature at which 50% of the enzyme activity was lost during an incubation period of 30 min (T_{50}).[14] The half lives of thermal inactivation were obtained by incubating purified proteins at specific temperatures. Aliquots were taken at various time intervals and activities were monitored. The data were fit to a first-order exponential-decay equation $V = V_o e^{-kt}$, where V_o represents the initial enzyme activity, k represents the inactivation rate constant, and t is the time in minutes.

Received: January 9, 2006
Published online: June 8, 2006

Keywords: amino acids · directed evolution · enzymes · protein engineering · thermostability

[1] A. J. Link, M. L. Mock, D. A. Tirrell, *Curr. Opin. Biotechnol.* **2003**, *14*, 603.
[2] N. Budisa, *Angew. Chem.* **2004**, *116*, 6586; *Angew. Chem. Int. Ed.* **2004**, *43*, 6426.
[3] L. Wang, P. G. Schultz, *Angew. Chem.* **2005**, *117*, 34; *Angew. Chem. Int. Ed.* **2005**, *44*, 34.
[4] J. H. Bae, et al., *J. Mol. Biol.* **2003**, *328*, 1071 (see the Supporting Information).
[5] Y. Tang, D. A. Tirrell, *J. Am. Chem. Soc.* **2001**, *123*, 11089.
[6] Y. Tang, G. Ghirlanda, W. A. Petka, T. Nakajima, W. F. DeGrado, D. A. Tirrell, *Angew. Chem.* **2001**, *113*, 1542; *Angew. Chem. Int. Ed.* **2001**, *40*, 1494.
[7] B. Bilgicer, X. Xing, K. Kumar, *J. Am. Chem. Soc.* **2001**, *123*, 11815.
[8] B. Bilgicer, K. Kumar, *Proc. Natl. Acad. Sci. USA* **2004**, *101*, 15324.
[9] N. Budisa, R. Huber, R. Golbik, C. Minks, E. Weyher, L. Moroder, *Eur. J. Biochem.* **1998**, *253*, 1.
[10] L. Wang, J. M. Xie, A. A. Deniz, P. G. Schultz, *J. Org. Chem.* **2003**, *68*, 174.
[11] W. V. Shaw, *Meth. Enzymol.* **1975**, *43*, 737.
[12] S. L. Turner, G. C. Ford, A. Mountain, A. Moir, *Protein Eng.* **1992**, *5*, 535.
[13] T. Panchenko, W. W. Zhu, J. K. Montclare, *Biotechnol. Bioeng.* **2006**, in press.
[14] H. M. Zhao, F. H. Arnold, *Protein Eng.* **1999**, *12*, 47.
[15] V. G. H. Eijsink, G. Vriend, B. Vandervinne, B. Hazes, B. Vandenburg, G. Venema, *Proteins Struct. Funct. Genet.* **1992**, *14*, 224.
[16] M. O. Dayhoff, R. M. Schwartz, B. C. Orcutt in *Atlas of protein sequence and structure*, *Vol. 5* (ed.: M. O. Dayhoff), National Biomedical Research Foundation, Washington, **1978**, p. 345.
[17] A. G. W. Leslie, J. M. Liddell, W. V. Shaw, *J. Mol. Biol.* **1986**, *188*, 283.
[18] J. M. Bacher, R. A. Hughes, J. T. F. Wong, A. D. Ellington, *Trends Ecol. Evol.* **2004**, *19*, 69.
[19] J. M. Bacher, J. J. Bull, A. D. Ellington, *BMC Evol. Biol.* **2003**, *3*, 24.
[20] R. A. Hughes, A. D. Ellington, *Proc. Natl. Acad. Sci. USA* **2005**, *102*, 1273.

 © 2006 Wiley-VCH Verlag GmbH & Co. KGaA, Weinheim